

Springer Series in
OPTICAL SCIENCES

1

founded by H.K.V. Lotsch

Editor-in-Chief: W. T. Rhodes, Atlanta

Editorial Board: A. Adibi, Atlanta
T. Asakura, Sapporo
T. W. Hänsch, Garching
T. Kamiya, Tokyo
F. Krausz, Garching
B. Monemar, Linköping
H. Venghaus, Berlin
H. Weber, Berlin
H. Weinfurter, München

Springer Series in OPTICAL SCIENCES

The Springer Series in Optical Sciences, under the leadership of Editor-in-Chief *William T. Rhodes*, Georgia Institute of Technology, USA, provides an expanding selection of research monographs in all major areas of optics: lasers and quantum optics, ultrafast phenomena, optical spectroscopy techniques, optoelectronics, quantum information, information optics, applied laser technology, industrial applications, and other topics of contemporary interest.

With this broad coverage of topics, the series is of use to all research scientists and engineers who need up-to-date reference books.

The editors encourage prospective authors to correspond with them in advance of submitting a manuscript. Submission of manuscripts should be made to the Editor-in-Chief or one of the Editors. See also www.springer.com/series/624

Editor-in-Chief

William T. Rhodes

Georgia Institute of Technology

School of Electrical and Computer Engineering

Atlanta, GA 30332-0250, USA

E-mail:bill.rhodes@ece.gatech.edu

Editorial Board

Ali Adibi

School of Electrical and Computer Engineering

Van Leer Electrical Engineering Building

Georgia Institute of Technology

777 Atlantic Drive NW

Atlanta, GA 30332-0250

Email:adibi@ece.gatech.edu

Toshimitsu Asakura

Hokkai-Gakuen University

Faculty of Engineering

1-1, Minami-26, Nishi 11, Chuo-ku

Sapporo, Hokkaido 064-0926, Japan

E-mail:asakura@eli.hokkai-s-u.ac.jp

Theodor W. Hänsch

Max-Planck-Institut für Quantenoptik

Hans-Kopfermann-Strasse 1

85748 Garching, Germany

E-mail:t.w.haensch@physik.uni-muenchen.de

Takeshi Kamiya

Ministry of Education, Culture, Sports

Science and Technology

National Institution for Academic Degrees

3-29-1 Otsuka, Bunkyo-ku

Tokyo 112-0012, Japan

E-mail:kamiyat@niad.ac.jp

Ferenc Krausz

Ludwig-Maximilians-Universität München

Lehrstuhl für Experimentelle Physik

Am Coulombwall 1

85748 Garching, Germany

and

Max-Planck-Institut für Quantenoptik

Hans-Kopfermann-Straße I

85748 Garching, Germany

E-mail:ferenc.krausz@mpq.mpg.de

Bo Monemar

Department of Physics

and Measurement Technology

Materials Science Division

Linköping University

58183 Linköping, Sweden

E-mail:bom@ifm.liu.se

Herbert Venghaus

Heinrich-Hertz-Institut

für Nachrichtentechnik Berlin GmbH

Einsteinufer 37

10587 Berlin, Germany

E-mail:venghaus@hhi.de

Horst Weber

Technische Universität Berlin

Optisches Institut

Straße des 17. Juni 135

10623 Berlin, Germany

E-mail:weber@physik.tu-berlin.de

Harald Weinfurter

Ludwig-Maximilians-Universität München

Sektion Physik

Schellingstraße 4/III

80799 München, Germany

E-mail:harald.weinfurter@physik.uni-muenchen.de

Walter Koechner

Solid-State Laser Engineering

Sixth Revised and Updated Edition

With 447 Illustrations and 45 Tables



Dr. Walter Koechner
18496 Yellow Schoolhouse Rd.
Round Hill, VA 20141
U.S.A.

Library of Congress Control Number: 2005932556

ISBN-10: 0-387-29094-X e-ISBN: 0-387-29338-8
ISBN-13: 978-0387-29094-2

Printed on acid-free paper.

© 2006 Springer Science+Business Media, Inc.

All rights reserved. This work may not be translated or copied in whole or in part without the written permission of the publisher (Springer Science+Business Media, Inc., 233 Spring Street, New York, NY 10013, USA), except for brief excerpts in connection with reviews or scholarly analysis. Use in connection with any form of information storage and retrieval, electronic adaptation, computer software, or by similar or dissimilar methodology now known or hereafter developed is forbidden.

The use in this publication of trade names, trademarks, service marks, and similar terms, even if they are not identified as such, is not to be taken as an expression of opinion as to whether or not they are subject to proprietary rights.

Printed in the United States of America. (TB/MVY)

9 8 7 6 5 4 3 2 1

springer.com

To my wife Renate

Preface to the Sixth Edition

This book, written from an industrial vantage point, describes the characteristics, design, and operation of solid-state lasers. As the title implies, the emphasis is placed on the technical aspects of these systems rather than on theoretical concepts. Lengthy mathematical derivations have been avoided because the theory is not treated as an end in itself, but rather serves to explain the experimental results observed in the laboratory. However, there is sufficient theoretical background provided in each chapter to make the book self-contained.

Solid-State Laser Engineering is mainly intended for the practicing scientist or engineer who is interested in the design or use of solid-state lasers. The response from readers has shown that the comprehensive treatment of the subject makes the work useful also to students of laser physics who want to supplement their theoretical knowledge with the engineering aspects of lasers. Although not written in the form of a college text, the book might be used in an advanced college course on laser technology.

After a historical overview, the book starts with a review of the basic concepts of laser physics (Chap. 1). Analytical expressions of the threshold condition, gain, and output of laser oscillators are derived in Chap. 3. An oscillator followed by one or more amplifiers is a common architecture in pulsed solid-state laser systems to boost output energy. Energy storage and gain of amplifiers is discussed in Chap. 4.

Four chapters deal with the basic subsystems of solid-state lasers. These are the active medium, the optical resonator, the pumping system, and the thermal management. Properties of solid-state laser hosts and active ions are reviewed in Chap. 2. Beam divergence and line width of an oscillator are strongly dependent on the spatial and longitudinal mode structure of the resonator. Resonator configurations and characteristics are presented in Chap. 5. Different pump sources and configurations for transferring pump radiation to the active material are discussed in Chap. 6. Thermal gradients set up as a result of heat removal from the active medium have a profound impact on beam quality and output power limitations. Thermal effects and cooling techniques are treated in Chap. 7.

Three chapters are devoted to techniques and devices that can alter the temporal or spectral output of a laser, i.e., Q-switching, mode-locking, and nonlinear devices. Electro-optical, acousto-optical, and passive Q-switches are employed for the generation of laser pulses with a pulselwidth on the order of nanoseconds (Chap. 8). Ultrashort pulses with pulselwidths in the picosecond or femtosecond regime are obtained from solid-state lasers by passive or active mode-locking (Chap. 9). Nonlinear optical devices, such as harmonic generators, parametric oscillators, and Raman oscillators, provide a means of extending the frequency range of available laser sources, and

Brillouin scattering offers the possibility of minimizing distortions in laser amplifiers (Chap. 10). The last chapter discusses the fundamental limit of the output energy or power of a laser system, which is determined by optical damage occurring at the surface or within the bulk of optical components (Chap. 11).

Following the demonstration of the first laser over 45 years ago, an extraordinary number of different types of lasers have been invented using a wide variety of active media and pump techniques to create an inversion. Laser research and engineering has developed into many specialized disciplines depending on the laser medium (solid state, optical fiber, semiconductor, neutral or ionized gas, liquid) and excitation mechanism (optical pumping, electric current, gas discharge, chemical reaction, electron beam).

For historical reasons, solid-state lasers describe a class of lasers in which active ions in crystal or glass host materials are optically pumped to create a population inversion. Other types of lasers that employ solid-state gain media are semiconductor lasers and optical fiber lasers and amplifiers. However, since these lasers employ very specialized technologies and design principles, they are usually treated separately from conventional bulk solid-state lasers.

The design and performance characteristics of laser diode arrays are discussed in this book because these devices are employed as pump sources for solid-state lasers. Fiber lasers, although similar to conventional solid-state lasers as far as the active material and the pump source is concerned, are radically different with respect to beam confinement, mode structure, coupling of pump and laser beams, and the design of optical components.

Gratified by the wide acceptance of *Solid-State Laser Engineering*, I have updated and completely revised the material for this sixth edition. Obsolete material has been deleted, the presentation and organization of the material has been streamlined in some places, and new information has been added to account for recent developments in the areas of diode laser pumping, laser materials, and nonlinear crystals. The sections dealing with the theory of mode-locking, femtosecond lasers, high-efficiency harmonic generation, passive and acousto-optic Q-switching, semiconductor saturable absorber mirrors (SESAM), and periodically poled nonlinear crystals have been greatly expanded. In particular

- the theory of second and third harmonic conversion has been expanded to describe high-efficiency conversion by taking into account pump depletion as well as phase mismatch.
- concave–convex resonators in the presence of strong thermal focusing have been analyzed in more detail compared to previous editions.
- the important technique of mode-locking via a semiconductor saturable absorber mirror (SESAM) is described in some detail.
- a description of the Pound–Drever–Hall (PDH) servo system employed to achieve absolute frequency stability from a laser oscillator has been added.
- the high gain that can be achieved in diode pumped cw Nd:YAG laser amplifiers required a section on cw amplifiers.

- the edge-pumped, conductively cooled slab laser concept is introduced in the section on thermal effects.
- a separate section dealing with multipass amplifiers in rod, slab, and thin disk geometries has been added.
- the threshold condition and slope efficiency of quasi three-level lasers, such as Yb:YAG, has been included in the oscillator performance model.
- an analysis has been added to the phenomenological description of pulse formation in mode-locked lasers.
- the section on Bragg reflection that is fundamental to the operation of an acousto-optic-switch has been enlarged.

Solid-state lasers are a fascinating field to spend an entire scientific or engineering career, because working with these systems involves many scientific and technical disciplines, from solid-state physics and spectroscopy to laser physics, and to the engineering disciplines of optical and mechanical design and digital and analog electronic design.

The development of modern laser system represents a multidisciplinary effort. Based on the performance goals, the design of a new laser system typically starts with a laser physicist defining the system configuration and architecture. This conceptual effort is followed by a detailed optical and mechanical design of the laser components in parallel with the design of the analog and digital subsystems. In addition, manufacturing engineering and quality control play important roles in assuring producibility, reliability, and maintainability of the final product. These combined efforts result in highly reliable, computer-controlled turn-key laser systems employed in research, commercial, industrial, medical, and military applications. Solid-state lasers and systems represent a one-billion dollar industry, and they are the dominant class of lasers for the applications mentioned above.

The material presented in this book reflects the author's experience gained in directing solid-state laser R&D over a 35-year period. This book would not have been possible without the many contributions to the field of laser engineering that have appeared in the open literature and which have been used here as the basic source material. I apologize to any of my colleagues whose work has not been acknowledged or adequately represented in this book.

It is impossible to describe all the new materials, laser configurations, and pumping schemes which have been developed over the last several years. In doing so, the book would merely become a literature survey with commentaries. Readers interested in specific devices are referred to the original literature. Very good sources of information are the *IEEE Journal of Quantum Electronics*, *Optics Letters*, and the conference proceedings of the CLEO and solid-state laser conferences.

My wife Renate not only typed most of the new material for this edition, but without her patience and understanding this book could not have been written.

Contents

Preface.....	vii
Introduction.....	1
1. Energy Transfer Between Radiation and Atomic Transitions	11
1.1 Optical Amplification	11
1.2 Interaction of Radiation with Matter	12
1.2.1 Blackbody Radiation.....	12
1.2.2 Boltzmann's Statistics	13
1.2.3 Einstein's Coefficients.....	14
1.2.4 Phase Coherence of Stimulated Emission.....	17
1.3 Absorption and Optical Gain	18
1.3.1 Atomic Lineshapes.....	18
1.3.2 Absorption by Stimulated Transitions.....	22
1.3.3 Population Inversion	25
1.4 Creation of a Population Inversion	27
1.4.1 The Three-Level System.....	27
1.4.2 The Four-Level System.....	29
1.4.3 The Metastable Level	30
1.5 Laser Rate Equations.....	32
1.5.1 The Three-Level System	33
1.5.2 The Four-Level System.....	35
1.5.3 Comparison of Three- and Four-Level Lasers.....	36
2. Properties of Solid-State Laser Materials.....	38
2.1 Overview	40
2.1.1 Host Materials.....	40
2.1.2 Active Ions.....	45
2.2 Ruby.....	51
2.3 Nd:Lasers.....	54
2.3.1 Nd:YAG	54
2.3.2 Nd:Glass	61
2.3.3 Nd:Cr:GSGG.....	64
2.3.4 Nd:YLF.....	66
2.3.5 Nd:YVO ₄	69

2.4	Er:Lasers.....	73
2.4.1	Er:YAG.....	73
2.4.2	Er:Glass.....	75
2.5	Tunable Lasers	79
2.5.1	Alexandrite Laser.....	84
2.5.2	Ti:Sapphire	88
2.5.3	Cr:LiSAF.....	91
2.5.4	Tm:YAG.....	94
2.6	Yb:YAG.....	97
3.	Laser Oscillator	102
3.1	Operation at Threshold.....	103
3.2	Gain Saturation.....	108
3.3	Circulating Power.....	109
3.4	Oscillator Performance Model	111
3.4.1	Conversion of Input to Output Energy.....	112
3.4.2	Laser Output.....	118
3.5	Relaxation Oscillations	128
3.5.1	Theory.....	128
3.5.2	Spike Suppression.....	132
3.5.3	Gain Switching.....	133
3.6	Examples of Laser Oscillators.....	134
3.6.1	Lamp-Pumped cw Nd:YAG Laser.....	134
3.6.2	Diode Side-Pumped Nd:YAG Laser	139
3.6.3	End-Pumped Systems.....	148
3.7	Ring Laser.....	152
4.	Laser Amplifier	156
4.1	Single- and Multiple-Pass Pulse Amplifiers	157
4.1.1	Pulse Amplification.....	158
4.1.2	Nd:YAG Amplifiers	163
4.1.3	Nd:Glass Amplifiers	171
4.1.4	Multipass Amplifier Configurations.....	177
4.2	Regenerative Amplifiers	180
4.3	cw Amplifiers.....	188
4.4	Signal Distortions.....	190
4.4.1	Spatial Distortions.....	190
4.4.2	Temporal Distortions.....	193
4.5	Depopulation Losses	194
4.5.1	Amplified Spontaneous Emission	195
4.5.2	Prelasing and Parasitic Modes	198
4.5.3	Reduction of Depopulation Losses.....	199
4.6	Self-Focusing.....	200
4.6.1	Whole-Beam Self-Focusing	201

4.6.2	Examples of Self-focusing in Nd:YAG Lasers.....	203
4.6.3	Small-Scale Self-Focusing.....	206
4.6.4	Suppression of Self-Focusing.....	207
5.	Optical Resonator	210
5.1	Transverse Modes.....	210
5.1.1	Intensity Distribution.....	211
5.1.2	Characteristics of a Gaussian Beam	215
5.1.3	Resonator Configurations.....	217
5.1.4	Stability of Laser Resonators	221
5.1.5	Diffractiion Losses	223
5.1.6	Higher-Order Modes	224
5.1.7	Mode Selection.....	227
5.1.8	Active Resonator.....	231
5.1.9	Examples of Resonator Designs.....	238
5.1.10	Resonator Modeling and Software Packages	254
5.2	Longitudinal Modes	255
5.2.1	The Fabry-Perot Interferometer	255
5.2.2	Laser Resonator with Gain Medium.....	259
5.2.3	Longitudinal Mode Control	263
5.2.4	Injection Seeding.....	268
5.3	Intensity and Frequency Control.....	271
5.3.1	Amplitude Fluctuations	271
5.3.2	Frequency Tuning.....	274
5.3.3	Frequency Locking	276
5.4	Hardware Design.....	278
5.5	Unstable Resonators	282
5.5.1	Confocal Positive-Branch Unstable Resonator.....	284
5.5.2	Negative-Branch Unstable Resonator	287
5.5.3	Variable Reflectivity Output Couplers	289
5.5.4	Gain, Mode Size, and Alignment Sensitivity	295
5.6	Wavelength Selection	297
6.	Optical Pump Systems	300
6.1	Pump Sources.....	300
6.1.1	Flashlamps	303
6.1.2	Continuous Arc Lamps	334
6.1.3	Laser Diodes	340
6.2	Pump Radiation Transfer Methods	366
6.2.1	Side-Pumping with Lamps	368
6.2.2	Side-Pumping with Diodes.....	393
6.2.3	End-Pumped Lasers	407
6.2.4	Face-Pumped Disks.....	418

7. Thermo-Optic Effects	423
7.1 Cylindrical Geometry	426
7.1.1 Temperature Distribution.....	426
7.1.2 Thermal Stresses.....	437
7.1.3 Photoelastic Effects.....	440
7.1.4 Thermal Lensing.....	442
7.1.5 Stress Birefringence	445
7.1.6 Compensation of Optical Distortions	449
7.2 Slab and Disk Geometries.....	457
7.2.1 Rectangular-Slab Laser.....	458
7.2.2 Slab Laser with Zigzag Optical Path	461
7.2.3 Disk Amplifiers and Lasers.....	469
7.3 End-Pumped Configurations	473
7.3.1 Thermal Gradients and Stress.....	473
7.3.2 Thermal Lensing.....	477
7.3.3 Thermal Fracture Limit.....	479
7.4 Thermal Management.....	481
7.4.1 Liquid Cooling	481
7.4.2 Conduction Cooling	485
7.4.3 Air/Gas Cooling.....	486
8. Q-Switching	488
8.1 Q-Switch Theory.....	488
8.1.1 Fast Q-Switch.....	490
8.1.2 Slow Q-Switching	493
8.1.3 Continuously Pumped, Repetitively Q-Switched Systems	494
8.2 Mechanical Q-Switches.....	498
8.3 Electro-Optical Q-Switches	499
8.3.1 KDP and KD*P Pockels Cells	502
8.3.2 LiNbO ₃ Pockels Cells	506
8.3.3 Prelasing and Postlasing	508
8.3.4 Depolarization Losses.....	511
8.3.5 Drivers for Electro-Optic Q-Switches	514
8.4 Acousto-Optic Q-Switches	514
8.4.1 Bragg Reflection	516
8.4.2 Device Characteristics	519
8.5 Passive Q-Switches	522
8.6 Cavity Dumping.....	529
9. Mode Locking	534
9.1 Pulse Formation.....	535
9.2 Passive Mode Locking	542
9.2.1 Liquid Dye Saturable Absorber	543

9.2.2	Coupled-Cavity Mode Locking	546
9.2.3	Kerr Lens Mode Locking.....	548
9.2.4	Semiconductor Saturable Absorber Mirror (SESAM)	556
9.3	Active Mode Locking	560
9.3.1	cw Mode Locking.....	561
9.3.2	Transient Active Mode Locking.....	564
9.4	Picosecond Lasers.....	568
9.4.1	AM Mode Locking.....	569
9.4.2	FM Mode Locking	572
9.5	Femtosecond Lasers	575
9.5.1	Laser Materials	575
9.5.2	Dispersion Compensation	576
9.5.3	Examples of Kerr Lens or SESAM Mode-Locked Femtosecond Lasers	579
9.5.4	Chirped Pulse Amplifiers	584
10.	Nonlinear Devices.....	587
10.1	Nonlinear Optical Effects.....	587
10.1.1	Second-Order Nonlinearities.....	589
10.1.2	Third-Order Nonlinearities	590
10.2	Harmonic Generation.....	592
10.2.1	Basic Theory of Second Harmonic Generation.....	594
10.2.2	Phase Matching.....	602
10.2.3	Properties of Nonlinear Crystals.....	611
10.2.4	Intracavity Frequency Doubling.....	618
10.2.5	Third Harmonic Generation	625
10.2.6	Examples of Harmonic Generation	629
10.3	Optical Parametric Oscillators	634
10.3.1	Performance Modeling	637
10.3.2	Crystals.....	649
10.3.3	Quasi Phase Matching	652
10.3.4	Design and Performance	655
10.4	Raman Laser	662
10.4.1	Theory	663
10.4.2	Device Implementation.....	666
10.5	Optical Phase Conjugation	669
10.5.1	Basic Considerations	669
10.5.2	Material Properties	671
10.5.3	Focusing Geometry	673
10.5.4	Pump-Beam Properties	673
10.5.5	System Design	676
11.	Damage of Optical Elements.....	680
11.1	Surface Damage	681

11.2	Inclusion Damage	684
11.3	Damage Threshold of Optical Materials	684
11.3.1	Scaling Laws.....	685
11.3.2	Laser Host Materials.....	688
11.3.3	Optical Glass.....	689
11.3.4	Nonlinear Crystals	690
11.3.5	Dielectric Thin Films	694
11.4	System Design Considerations	698
11.4.1	Choice of Materials.....	698
11.4.2	Design of System.....	699
11.4.3	System Operation	700
Appendix A	Laser Safety	702
Appendix B	Conversion Factors and Constants	708
Appendix C	Definition of Symbols	711
References	716
Subject Index	742

Introduction

In this Introduction we will provide a short overview of the important milestones in the development of solid-state lasers, discuss the range of performance parameters possible with these lasers, and mention major applications. Besides the compactness and benign operating features, it was the enormous flexibility in design and output characteristics that led to the success of solid-state lasers over the last 40 years.

Major Milestones in the Development of Solid-State Lasers

Historically, the search for lasers began as an extension of stimulated amplification techniques employed in the microwave region. Masers, coined from microwave amplification by stimulated emission of radiation, served as sensitive preamplifiers in microwave receivers. In 1954 the first maser was built by C. Townes, who utilized the inversion population between two molecular levels of ammonia to amplify radiation at a wavelength of around 1.25 cm.

In 1955 an optical excitation scheme for masers was simultaneously proposed by N. Bloembergen, A.M. Prokhorov, and N.G. Basov. A few years later, masers were mostly built using optically pumped ruby crystals. In 1958, A. Schawlow and C. Townes proposed extending the maser principle to optical frequencies and the use of a Fabry–Perot resonator for feedback. However, they did not find a suitable material or the means of exciting it to the required degree of population inversion.

This was accomplished by T. Maiman who built the first laser in 1960. It was a pink ruby crystal (sapphire with trivalent chromium impurities), optically pumped by a helical flashlamp that surrounded the cylindrical laser crystal. The parallel ends of the ruby crystal were silvered, with a small hole at one end for observing the radiation. The reflective surfaces comprised the optical resonator. The output wavelength was 694 nm. It was T. Maiman who coined the name “laser,” in analogy to maser, as an abbreviation of light amplification by stimulated emission of radiation.

In early ruby laser systems the output consisted of a series of irregular spikes, stretching over the duration of the pump pulse. A key discovery made by R.W. Hellwarth in 1961 was a method called Q-switching for concentrating the output from the ruby laser into a single pulse. The Q-switch is an optical shutter which prevents laser action during the flashlamp pulse, and therefore the population inversion can reach large values. If the shutter is suddenly opened, stored energy will be released

in a time characterized by a few round trips between the resonator mirrors. Hellwarth initially proposed a Kerr cell, a device which rotates the plane of polarization when voltage is applied. This Q-switch, which consisted of a cell filled with nitrobenzene, required very high voltages for Q-switching; it was soon replaced by spinning one of the resonator mirrors. A further refinement was the insertion of a spinning prism between the fixed mirrors of the resonator.

The earliest application of the laser was in active range-finding by measuring the time of flight of a laser pulse reflected from a target. Investigation in this direction started immediately after the discovery of the ruby laser. Four years later, fully militarized rangefinders containing a flashlamp-pulsed ruby laser with a spinning prism Q-switch went into production. For about 10 years ruby-based rangefinders were manufactured; afterward the ruby laser was replaced by the more efficient neodymium doped yttrium aluminum garnet (Nd:YAG) laser.

Beside the use in rangefinders, the ruby laser was basically a research tool and, for the next 15 years, ruby lasers became the standard high-power radiation source in the visible region for research at university, government, and industrial laboratories. Applications in an industrial environment were rare, in large part due to the low-pulse repetition rate of the ruby laser (a pulse every few seconds), high cost of the equipment, and the unfamiliarity of the industry with this new radiation source. Some of the specialized applications included drilling holes in diamonds that are used as dies for drawing wires or spot welding in vacuum through the glass envelope of vacuum tubes. Another application was stress analysis by means of double pulse holography, in which surface deformation due to stress or temperature is measured interferometrically between two pulses.

The discovery of the ruby laser triggered an intensive search for other material, and in rapid succession laser action in other solids, gases, semiconductors, and liquids was demonstrated. Following the discovery of the ruby laser, the next solid-state material was uranium-doped calcium fluoride, which was lased in late 1960. The first solid-state neodymium laser was calcium tungstate doped with neodymium ions. This laser, discovered in 1961, was used in research facilities for a number of years until yttrium aluminate garnet, as a host material for neodymium, was discovered.

In 1961, E. Snitzer demonstrated the first neodymium glass laser. Since Nd:glass could be made in much larger dimensions and with better quality than ruby, it promised to deliver much higher energies. It was quickly realized that high energy, short pulses produced from large Nd:glass lasers possessed the potential to heat matter to thermonuclear temperatures, thus generating energy in small controlled explosions. Large budgets have been devoted to the development and installation of huge Nd:glass laser systems which became the worldwide systems of choice for laser fusion research and weapons simulation. The most powerful of these systems, the NOVA laser, completed in 1985, produced 100 kJ of energy in a 2.5-ns pulse. The NIF laser scheduled to be completed in 2005 is designed to generate 1.8 MJ.

Using a ruby laser, P.A. Franken demonstrated second harmonic generation in crystal quartz in 1961. Generation of harmonics is caused by the nonlinear behavior of the refractive index in the presence of a very high electric field strength. The conversion of the fundamental wavelength to the second harmonics was extremely

small because the interaction length of the beams was only a few wavelengths and the nonlinearity of quartz is very low.

Soon after these first nonlinear optics experiments were conducted it was realized that efficient nonlinear interactions require a means of achieving phase-velocity matching of the interacting waves over a distance of many wavelengths. Within a year, two basic approaches to achieve efficient harmonic generation were published in the literature. One approach, namely the use of birefringence to offset dispersion, is still the preferred method for most nonlinear processes in use today. Efficient harmonic generation was soon achieved in birefringence compensated potassium dihydrogen phosphate (KDP) crystals, a crystal which is still employed today for the generation of the third harmonic of large Nd:glass lasers. The other method, namely the use of a periodic modulation of the sign of the nonlinear coefficient to restore the optical phase, could only be realized 30 years later. In the early 1990s, lithographic processing techniques enabled the fabrication of quasi-phase-matched small crystals, using electric field poling of lithium niobate.

In 1962 the idea of parametric amplification and generation of tunable light was conceived, and a few years later the first experiment demonstrating parametric gain was achieved. Commercial parametric oscillators based on lithium niobate were introduced in 1971. Damage of the nonlinear material and the appearance of tunable dye lasers led to a decline in interest in optical parametric oscillators (OPOs) for almost 20 years. The discovery of damage-resistant nonlinear crystals with large nonlinear coefficients in the early 1990s revived interest in OPOs, and today tunable solid-state lasers covering the wavelength range from the visible to the near-infrared have found widespread application in spectroscopy, remote sensing, and wherever a tunable radiation source is required.

The possibility of laser action in a semiconductor was explored rather early. Initially, intrinsic semiconductors pumped by an electron beam or by optical radiation were considered. However, at the end of 1962, several groups succeeded in producing pulsed output from gallium–arsenide pn junctions cooled to cryogenic temperatures. About 10 years later, continuous operation at room temperature was achieved.

The first optical fiber amplifier was demonstrated in 1963 using a 1-m long neodymium-doped glass fiber wrapped around a flashlamp. However, the concept received little attention until the 1980s when low-loss optical fibers became available and the fiber-optic communications industry explored these devices for amplification of signals.

In 1964 the best choice of a host for neodymium ions, namely yttrium aluminum garnet (YAG), was discovered by J. Geusic. Since that time, Nd:YAG remains the most versatile and widely used active material for solid-state lasers. Nd:YAG has a low threshold which permits continuous operation, and the host crystal has good thermal, mechanical, and optical properties and can be grown with relative ease.

An immediate application was the replacement of ruby with Nd:YAG in military rangefinders. Since the system efficiency was about a factor of 10 higher with Nd:YAG as compared to ruby, the weight of storage-capacitors and batteries was drastically reduced. This allowed the transition from a tripod-mounted unit, the size of a briefcase, to a hand-held device only slightly larger than a binocular.

Continuously pumped, repetitively Q-Switched Nd:YAG lasers were the first solid-state lasers which found applications in a production environment, mainly in the semiconductor industry for resistor trimming, silicon scribing, and marking. The early systems were pumped with tungsten filament lamps and Q-switched with a rotating polygon prism. Reliability was a big issue because lamp-life was short—on the order of 40 hs—and the bearings of the high-speed motors employed in the rotating Q-switches did wear out frequently. The mechanical Q-switches were eventually replaced by acousto-optic Q-switches, and krypton arc lamps replaced tungsten filament lamps.

Up to this point, solid-state lasers were capable of generating very impressive peak powers, but average power was still limited to a few watts or at most a few tens of watts. However, at the end of the 1960s, continuously pumped Nd:YAG lasers with multihundred watts output power became commercially available.

During the first years of laser research, a particular effort was directed toward generation of short pulses from Nd:glass and ruby lasers. With Q-switching, several round trips are required for radiation to build up. Given the length of the resonator and available gain of these early systems, the pulses were on the order of 10 to 20 ns. The next step toward shorter pulses was a technique called cavity dumping, whereby the radiation in the resonator, as it reached its peak, was quickly dumped by a fast Q-switch. Pulses with a duration on the order of one round trip (a few nanoseconds) in the resonator could be generated with this method. In 1965, a technique termed “mode-locking” was invented. Mode-locking is a technique whereby passive loss modulation, with a fast response saturable absorber, or by active loss or frequency modulation, a fixed relationship among the phases of the longitudinal modes is enforced. With either passive or active mode-locking, pulses much shorter than a resonator round trip time can be generated; typically, pulses are on the order of 20–100 ps.

By the end of the 1960s, most of the important inventions with regard to solid-state laser technology had been made. Nd:YAG and Nd:glass proved clearly superior over many other solid-state laser materials; short-pulse generation by means of Q-switching and mode-locking, as well as frequency conversion with harmonic generators and parametric oscillators, was well understood. Xenon-filled flashlamps and krypton arc lamps had been developed as pump sources and laser diodes were recognized as an ideal pump source, but due to a lack of suitable devices the technology could not be implemented.

To gain wider acceptance in manufacturing processes, the reliability of the laser systems needed improvement and the operation of the lasers had to be simplified. During the 1970s, efforts concentrated on engineering improvement, such as an increase in component and system lifetime and reliability. The early lasers often worked poorly and had severe reliability problems. At the component level, damage resistant optical coatings and high-quality laser crystals had to be developed; and the lifetime of flash lamps and arc lamps had to be drastically improved. On the system side, the problems requiring solutions were associated with water leaks, corrosion of metal parts by the cooling fluid, deterioration of seals and other parts in the pump cavity due to the ultraviolet radiation of the flashlamp, arcing within the high-voltage section of the laser, and contamination of optical surfaces caused by the environment.

The application of solid-state lasers for military tactical systems proceeded along a clear path since there is no alternative for rangefinders, target illuminators, and designators. At the same time construction of large Nd:glass lasers began at many research facilities. Also solid-state lasers were readily accepted as versatile research tools in many laboratories.

Much more difficult and rather disappointing at first was the acceptance of the solid-state lasers for industrial and medical applications. Despite improvement in systems reliability and performance, it took more than two decades of development and engineering improvements before solid-state lasers moved in any numbers out of the laboratory and onto the production floor or into instruments used in medical procedures. Often applications that showed technical feasibility in the laboratory were not suitable for production because of economic reasons, such as high operating costs or limited processing speeds. Also, other laser systems provided strong competition for a relatively small market. The CO₂ laser proved to be a simpler and more robust system for many industrial and medical applications. Also, the argon ion laser was readily accepted and preferred over solid-state lasers for retinal photocoagulation. The dye laser was the system of choice for tunable laser sources. The entry of solid-state lasers into manufacturing processes started with very specialized applications, either for working with difficult materials, such as titanium, or for difficult machining operations, such as drilling holes in slanted surfaces; for example, in jet fuel nozzles or for precision material removal required in the semiconductor and electronics industry.

In the latter part of the 1970s, and into the 1980s, a number of tunable lasers were discovered, such as alexandrite, titanium-doped sapphire, and chromium-doped fluoride crystals. The most important tunable laser, Ti:sapphire, discovered in the mid-1980s, is tunable between 660 and 980 nm. This laser must be pumped with another laser in the blue-green wavelength region. Alexandrite, first operated in 1979, has a smaller tunable output but can be flashlamp-pumped. Chromium-doped fluoride crystals, such as lithium strontium aluminum fluoride and lithium calcium aluminum fluoride, are of interest because they can be pumped with laser diodes.

In the late 1980s, the combination of broadband tunable lasers in combination with ultrafast modulation techniques, such as Kerr lens mode-locking, led to the development of mode-locked lasers with pulse widths on the order of femtoseconds. The pulse width limit of a mode-locked laser is inversely proportional to the bandwidth of the laser material. For neodymium-based lasers, the lower limit for the pulse width is a few picoseconds. Laser media with a much larger gain bandwidth, such as Ti:sapphire, can produce much shorter pulses compared to neodymium lasers.

Over the years, the performance of diode lasers has been constantly improved as new laser structures and new material growth and processing techniques were developed. This led to devices with longer lifetimes, lower threshold currents, and higher output powers. In the 1970s, diode lasers capable of continuous operation at room temperature were developed. In the mid-1980s, with the introduction of epitaxial processes and a greatly increased sophistication in the junction structure of GaAs devices, laser diodes became commercially available with output powers of several watts. These devices had sufficient power to render them useful for the pumping of Nd:YAG lasers. The spectral match of the diode laser output with the

absorption of neodymium lasers results in a dramatic increase in system efficiency, and a reduction of the thermal load of the solid-state laser material. Military applications and the associated research and development funding provided the basis for exploring this new technology. Since the early laser diodes were very expensive, their use as pump sources could only be justified where diode pumping provided an enabling technology. Therefore the first applications for diode-pumped Nd:YAG lasers were for space and airborne platforms, where compactness and power consumption is of particular importance.

As diode lasers became less expensive, these pump sources were incorporated into smaller commercial solid-state lasers. At this point, laser diode-pumped solid-state lasers began their rapid evolution that continues, today. Diode pumping offers significant improvements in overall systems efficiency, reliability, and compactness. In addition, diode pumping has added considerable variety to the design possibilities of solid-state lasers. In many cases laser diode arrays were not just a replacement for flashlamps or arc lamps, but provided a means for designing completely new laser configurations. They also led to the exploration of several new laser materials. Radiation from laser diodes can be collimated; this provides great flexibility of designing solid-state lasers with regard to the shape of the laser medium and orientation of the pump beam. In end-pumped lasers, the pump beam and resonator axis are collinear which led to highly efficient lasers with excellent beam quality. In monolithic lasers, the active crystal also provides the resonator structure leading to lasers with high output stability and excellent spatial and temporal beam quality. New laser materials, such as Yb:YAG and Nd:YVO₄ which could not be pumped efficiently with flashlamps, are very much suited to laser diode pumping.

In this historical perspective we could sketch only briefly those developments that had a profound impact on the technology of solid-state lasers. Laser emission has been obtained from hundreds of solid-state crystals and glasses. However, most of these lasers are of purely academic interest. There is a big difference between laser research and the commercial laser industry, and there are many reasons why certain lasers did not find their way into the market or disappeared quickly after their introduction. Most of the lasers that did not leave the laboratory were inefficient, low in power, difficult to operate or, simply, less practical to use than other already established systems. Likewise, many pump schemes, laser configurations, and resonator designs did not come into use because of their complexity and commensurate high manufacturing and assembly costs or their difficulty in maintaining performance.

Typical Performance Parameters and Applications

Solid-state lasers provide the most versatile radiation source in terms of output characteristics when compared to other laser systems. A large range of output parameters, such as average and peak power, pulse width, pulse repetition rate, and wavelength, can be obtained with these systems.

Today we find solid-state lasers in industry as tools in many manufacturing processes, in hospitals and in doctors' offices as radiation sources for therapeutic, cosmetic, and surgical procedures, in research facilities as part of the diagnostic

instrumentation, and in military systems as rangefinders, target designators, and infrared countermeasure systems. The flexibility of solid-state lasers stems from the fact that:

- the size and shape of the active material can be chosen to achieve a particular performance.
- different active materials can be selected with different gain, energy storage, and wavelength properties.
- the output energy can be increased by adding amplifiers.
- a large number of passive and active components are available to shape the spectral, temporal, and spatial profile of the output beam.

In this section we will illustrate the flexibility of these systems and indicate the major applications that are based on particular performance characteristics.

Average Output Power. The majority of solid-state lasers available commercially have output powers below 20 W. The systems are continuously pumped, typically equipped with a Q-switch, and often combined with a wavelength converter. Continuously pumped, repetitively Q-switched lasers generate a continuous stream of short pulses at repetition rates between 5 and 100 kHz depending on the material. Since the peak power of each pulse is at least three orders of magnitude above the average power, breakdown of reflective surfaces and subsequent material removal by melting and vaporization is facilitated.

The electronics and electrical industry represents the largest market for application such as soldering, wire bonding and stripping, scribing of wafers, memory repair, resistor and integrated circuit trimming. In addition, industrywide, these lasers found uses for marking of parts, precision spot and seam welding, and for general micro-machining tasks. In the medical fields solid-state lasers have found applications in ophthalmology for vision correction and photocoagulation, skin resurfacing, and as replacements for scalpels in certain surgical procedures. In basic research, solid-state lasers are used in scientific and biomedical instrumentation, Raman and laser-induced breakdown spectroscopy. Application for these lasers are far too broad and diverse to provide a comprehensive listing here.

Higher power solid-state lasers with output powers up to 5 kW are mainly employed in metals working, such as seam and spot welding, cutting, drilling, and surface treatment. In particular, systems with output powers of a few hundred watts have found widespread applications in the manufacturing process. The higher power levels allow for faster processing speed and working with thicker materials.

At the low end of the power scale are very small lasers with output powers typically less than 1 W. These lasers are pumped by diode lasers and have in most cases the resonator mirrors directly coated onto the crystal surfaces. The neodymium-doped crystals are typically only a few millimeters in size. These lasers have an extremely stable, single frequency output and are employed in interferometric instruments, spectroscopic systems, and instruments used in analytical chemistry. They also serve as seed lasers for larger laser systems.

The majority of solid-state lasers with outputs up to 20 W are pumped with diode arrays, whereas systems at the multihundred watt level are for the most part pumped

by arc lamps because of the high cost of laser diode arrays, although diode-pumped systems with up to 5 kW of output power are on the market.

Peak Power. Pulsed systems with pulsedwidths on the order of 100 μ s and energies of several joules are employed in manufacturing processes for hole drilling. The peak power of these systems is on the order of several tens of kilowatts. Substantially higher peak powers are obtained with solid-state lasers that are pulse-pumped and Q-switched. For example, military systems such as rangefinders and target designators have output energies of 10–200 mJ and pulsedwidths of 10–20 ns. Peak power for these systems is on the order of several megawatts. Laser generated plasmas investigated in research facilities require peak powers in the gigawatt regime. Typically, lasers for this work have output energies of several joules and pulsedwidths of a few nanoseconds. The highest peak powers from solid-state lasers are generated in huge Nd:glass lasers employed for inertial confinement fusion experiments. The largest of these systems had an energy output of 600 J and pulsedwidth of 0.5 ps which resulted in a peak power of 1.25 petawatt.

Pulse Width. Solid-state lasers can span the range from continuous operation to pulses as short as one cycle of the laser frequency which is on the order of 1 fs. Long pulses in the milli- and microsecond regime are generated by adjusting the length of the pump pulse. Hole drilling and surface hardening of metals is typically performed with pulses around 100 μ s in duration. Continuously pumped Q-switched Nd:YAG lasers generate pulses with pulsedwidths on the order of hundreds of nanoseconds.

A reduction in pulsedwidth is achieved in lasers that are pulse-pumped and Q-switched. These lasers have pulsedwidths from a few nanoseconds to about 20 ns. All military rangefinders and target designators fall into this category. The pulsedwidth of pulse-pumped Q-switched lasers is shorter than their continuously pumped counterparts because a higher gain is achieved in pulse-pumped systems. The technique of mode-locking the longitudinal modes provides a means of generating pulses in the picosecond regime with neodymium lasers. Since pulsedwidth and gain-bandwidth are inversely related, even shorter pulses are obtained with tunable lasers due to their broad spectrum. For example, with Ti:sapphire lasers, pulses in the femtosecond regime are generated. These short pulses enable researchers, for example, to study dynamic processes that occur during chemical reactions.

Pulse Repetition Rate. At the low end are lasers employed in inertial fusion experiments. In these systems laser pulses are single events with a few experiments conducted each day because the heat generated during each pulse has to be dissipated between shots. Also, some hand-held rangefinders for surveillance purposes are single-shot devices. Most military rangefinders and target designators operate at 20 pulses per second. Welders and drillers, if they are pulse-pumped, generate pulses at a repetition rate of few hundred pulses per second. Continuously pumped and Q-switched lasers provide a continuous train of pulses between 5 and 100 kHz. A large number of materials-processing applications fall into this mode of operation. Mode-locking generates pulses with repetition rates of several hundred megahertz. These systems are mainly used in photochemistry or in specialized materials processing applications. In the latter applications, material is removed by ablation that prevents heat from penetrating the surrounding area.

Linewidth. The linewidth of a laser is the result of the gain-bandwidth of the laser material and the number of longitudinal modes oscillating within the resonator. The output of typical laser is comprised of many randomly fluctuating longitudinal modes, each mode representing a spectral line within the bandwidth of the output beam. The typical linewidth of an Nd:YAG laser is on the order of 10 GHz or 40 pm. Compared to the wavelength, lasers are very narrow-bandwidth radiation sources and therefore for most applications the linewidth of the laser is not important. Exceptions are applications of the laser in coherent radar systems or in interferometric devices. Also, in lasers that operate at peak powers close to the damage threshold of optical components, it is beneficial to restrict operation to a single longitudinal mode to avoid power spikes as a result of the random superposition of the output from several modes.

Single mode operation of solid-state lasers is most readily achieved with small monolithic devices, having resonators which are so short as to allow only one longitudinal mode to oscillate. Only a few lasers, such as used in interferometers designed for gravitational wave detection, require close to quantum noise-limited performance. Careful temperature and vibration control combined with feedback systems have reduced the bandwidth of these lasers to a few kilohertz.

Spectral Range. A direct approach to tunable output is the use of tunable laser, such as Ti:sapphire or the alexandrite laser. However, these sources are limited to the spectral region between 600 and 900 nm. The most well-developed and efficient lasers, such as the neodymium-based systems, are essentially fixed wavelength radiation sources with output around 1 μm . Nonlinear crystals employed in harmonic generators will produce second, third, and fourth harmonics, thus providing output in the visible and ultraviolet spectrum. Tunable spectral coverage can be obtained from optical parametric oscillators that convert a portion of the output beam into two beams at longer wavelength. Depending on the region over which tunable output is desired, the optical parametric oscillator can be pumped directly with the fundamental beam of the laser or with one of its harmonics.

The limits of spectral range for solid-state lasers in the ultraviolet region is reached by quadrupled neodymium lasers at around 266 nm. The longest wavelength at useful power levels is produced around 4 μm by neodymium or erbium lasers operating at 1 or 2 μm , which are shifted to the longer wavelength with optical parametric oscillators. The limits at the short and long wavelengths are determined mainly by a lack of nonlinear crystals with a sufficiently high-damage threshold or nonlinear coefficient.

Many industrial, medical, and military applications require a different wavelength than the fundamental output available from standard lasers. For example, most materials have higher absorptions at shorter wavelengths, therefore frequency-doubled neodymium lasers are often preferred over fundamental wavelength operation. Also, the smallest spot size diameter that can be achieved from a laser is proportional to the wavelength. The fine structures of integrated circuits and semiconductor devices require operation of the laser at the shortest wavelength possible. Also, by matching the wavelength of a laser to the peak absorption of a specific material, the top layer of a multilayer structure can be removed selectively without damage to the layers underneath.

All Nd:glass lasers employed in inertial confinement fusion experiments are operated at the third harmonic, i.e., 352 nm, because the shorter wavelength is more optimum for pellet compression compared to the fundamental output. Medical applications require solid-state lasers operating in a specific spectral range for control of the absorption depth of the radiation in the skin, tissue, or blood vessels. Frequency agility is required from lasers employed in instruments used for absorption measurements, spectroscopy, sensing devices, analytical chemistry, etc. A fixed or tunable laser in conjunction with harmonic generators and/or an optical parametric oscillator is usually employed to meet these requirements.

Military rangefinders need to operate in a region that does not cause eye damage because most of the time these systems are employed in training exercises. A wavelength of 1.5 μm poses the least eye hazard. This wavelength is obtained from Q-switched erbium lasers or from neodymium lasers that are wavelength-shifted with an optical parametric oscillator or Raman cell. Lasers designed to defeat missile threats, so-called infrared countermeasure lasers, have to operate in the 2–4 μm region. Output in this spectral range can be obtained from neodymium or erbium lasers, wavelength-shifted with one or two optical parametric amplifiers.

Spatial Beam Characteristics. Virtually all laser applications benefit from a diffraction-limited beam. Such a beam has the lowest beam divergence and produces the smallest spot if focused by a lens. However, there is a trade-off between output power and beam quality. Lasers in the multihundred or kilowatt output range employed for metal cutting or welding applications have beams that are many times diffraction-limited. On the other hand, lasers that are employed for micromachining applications and semiconductor processing, where a minimum spot size and kerf-width is essential, are mostly operated very close to the diffraction limit.

Future Trends. The replacements of flashlamps and arc lamps with laser diode arrays will continue even for large solid-state lasers because the increase in systems efficiency, beam quality and reliability, is compelling. Even for advanced inertial confinement fusion lasers, diode pumped crystals are considered as replacement for flashlamp pumped Nd:Glass. Also, the push for solid-state lasers, with ever higher average output powers will continue. Concepts for lasers at 100 kW average power are already being developed. Most smaller lasers have output beams that are close to the diffraction limit. A particular challenge is to improve the beam quality of solid-state lasers with output powers in the multihundred or kilowatt regime.

The trend for smaller lasers, certainly for military lasers, is toward systems which do not require liquid cooling. Also, the search continues for new nonlinear crystals with high-damage thresholds and large nonlinear coefficients, particularly for the infrared and ultraviolet regions. Even with diode pumping, solid-state lasers are not particularly efficient radiation sources, converting at best about 10% of electric input into useful output. Further improvements in the efficiency of diode pump sources as a result of refinements in diode structure and processing techniques, coupled with a further optimization of laser materials and designs, could increase the efficiency of solid-state lasers to about 20 or 30%.

1. Energy Transfer Between Radiation and Atomic Transitions

In this introductory chapter we shall outline the basic ideas underlying the operation of solid-state lasers. In-depth treatments of laser physics can be found in a number of excellent textbooks [1.1, 2].

1.1 Optical Amplification

To understand the operation of a laser we have to know some of the principles governing the interaction of radiation with matter.

Atomic systems such as atoms, ions, and molecules can exist only in discrete energy states. A change from one energy state to another, called a transition, is associated with either the emission or the absorption of a photon. The wavelength of the absorbed or emitted radiation is given by Bohr's frequency relation

$$E_2 - E_1 = h\nu_{21}, \quad (1.1)$$

where E_2 and E_1 are two discrete energy levels, ν_{21} is the frequency, and h is the Planck's constant. An electromagnetic wave whose frequency ν_{21} corresponds to an energy gap of such an atomic system can interact with it. To the approximation required in this context, a solid-state material can be considered an ensemble of very many identical atomic systems. At thermal equilibrium, the lower energy states in the material are more heavily populated than the higher energy states. A wave interacting with the substance will raise the atoms or molecules from lower to higher energy levels and thereby experience absorption.

The operation of a laser requires that the energy equilibrium of a laser material be changed such that energy is stored in the atoms, ions, or molecules of this material. This is achieved by an external pump source which transfers electrons from a lower energy level to a higher one. The pump radiation thereby causes a "population inversion." An electromagnetic wave of appropriate frequency, incident on the "inverted" laser material, will be amplified because the incident photons cause the atoms in the higher level to drop to a lower level and thereby emit additional photons. As a result, energy is extracted from the atomic system and supplied to the radiation field. The release of the stored energy by interaction with an electromagnetic wave is based on stimulated or induced emission.

Stated very briefly, when a material is excited in such a way as to provide more atoms (or molecules) in a higher energy level than in some lower level, the material will be capable of amplifying radiation at the frequency corresponding to the energy

level difference. The acronym “laser” derives its name from this process: “Light Amplification by Stimulated Emission of Radiation.”

A quantum mechanical treatment of the interaction between radiation and matter demonstrates that the stimulated emission is, in fact, completely indistinguishable from the stimulating radiation field. This means that the stimulated radiation has the same directional properties, same polarization, same phase, and same spectral characteristics as the stimulating emission. These facts are responsible for the extremely high degree of coherence, which characterizes the emission from lasers. The fundamental nature of the induced or stimulated emission process has already been described by A. Einstein and M. Planck.

In solid-state lasers, the energy levels and the associated transition frequencies result from the different quantum energy levels or allowed quantum states of the electrons orbiting about the nuclei of atoms. In addition to the electronic transitions, multiatom molecules in gases exhibit energy levels that arise from the vibrational and rotational motions of the molecule as a whole.

1.2 Interaction of Radiation with Matter

Many of the properties of a laser may be readily discussed in terms of the absorption and emission processes which take place when an atomic system interacts with a radiation field. In the first decade of this century Planck described the spectral distribution of thermal radiation, and in the second decade Einstein, by combining Planck’s law and Boltzmann statistics, formulated the concept of stimulated emission. Einstein’s discovery of stimulated emission provided essentially all of the theory necessary to describe the physical principle of the laser.

1.2.1 Blackbody Radiation

When the electromagnetic radiation in an isothermal enclosure, or cavity, is in thermal equilibrium at temperature T , the distribution of radiation density $\varrho(v) dv$, contained in a bandwidth dv , is given by Planck’s law

$$\varrho(v) dv = \frac{8\pi v^2}{c^3} \frac{hv}{e^{hv/kT} - 1}, \quad (1.2)$$

where $\varrho(v)$ is the radiation energy density per unit frequency ($(J s)/cm^3$), k is Boltzmann’s constant, and c is the velocity of light. The spectral distribution of thermal radiation energy vanishes at $v = 0$ and $v \rightarrow \infty$, and has a peak, which depends on the temperature.

The factor

$$\frac{8\pi v^2}{c^3} = p_n \quad (1.3)$$

in (1.2) gives the density of radiation modes per unit volume and unit frequency interval. The factor p_n can also be interpreted as the number of degrees of freedom associated with a radiation field, per unit volume, per unit frequency interval. The expression for the mode density p_n ((modes s)/cm³) plays an important role in connecting the spontaneous and the induced transition probabilities.

For a uniform, isotropic radiation field, the following relationship is valid:

$$W = \frac{\varrho(\nu)c}{4}, \quad (1.4)$$

where W is the blackbody radiation (W/cm²), which will be emitted from an opening in the cavity of the blackbody. Many solids radiate like a blackbody. Therefore, the radiation emitted from the surface of a solid can be calculated from (1.4).

According to the Stefan–Boltzmann equation, the total black body radiation is

$$W = \sigma T^4, \quad (1.5)$$

where $\sigma = 5.68 \times 10^{-12}$ W/(cm² K⁴). The emitted radiation W has a maximum which is obtained from Wien's displacement law

$$\frac{\lambda_{\max}}{\mu\text{m}} = \frac{2893}{T/\text{K}}. \quad (1.6)$$

For example, a blackbody at a temperature of 5200 K has its radiation peak at 5564 Å, which is about the center of the visible spectrum.

A good introduction to the fundamentals of radiation and its interaction with matter can be found in [1.2].

1.2.2 Boltzmann's Statistics

According to a basic principle of statistical mechanics, when a large collection of similar atoms is in thermal equilibrium at temperature T , the relative populations of any two energy levels E_1 and E_2 , such as the ones shown in Fig. 1.1, must be related by the Boltzmann ratio

$$\frac{N_2}{N_1} = \exp\left(\frac{-(E_2 - E_1)}{kT}\right), \quad (1.7)$$

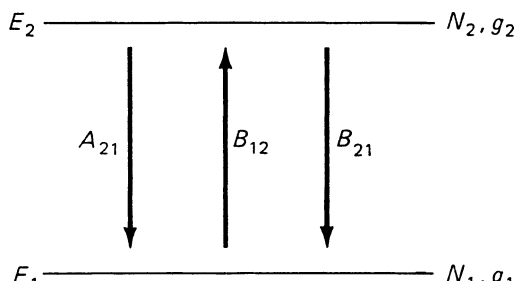


Fig. 1.1. Two energy levels with populations N_1 , N_2 and degeneracies g_1 , g_2 , respectively

where N_1 and N_2 are the number of atoms in the energy levels E_1 and E_2 , respectively. For energy gaps large enough that $E_2 - E_1 = h\nu_{21} \gg kT$, the ratio is close to zero, and there will be very few atoms in the upper energy level at thermal equilibrium. The thermal energy kT at room temperature ($T \approx 300$ K) corresponds to an energy gap $\hbar\nu$ with $\nu \approx 6 \times 10^{12}$ Hz, which is equivalent in wavelength to $\lambda \approx 50$ μm. Therefore, for any energy gap whose transition frequency ν_{21} lies in the near-infrared or visible regions, the Boltzmann exponent will be very small at normal temperatures. The number of atoms in any upper level will then be very small compared to the lower levels. For example, in ruby the ground level E_1 and the upper laser level E_2 are separated by an energy gap corresponding to a wavelength of $\lambda \approx 0.69$ μm. Since $h = 6.6 \times 10^{-34}$ W s², then $E_2 - E_1 = hc/\lambda = 2.86 \times 10^{-19}$ W s. With $k = 1.38 \times 10^{-23}$ (W s)/K and $T = 300$ K, it follows that $N_2/N_1 \approx \exp(-69)$. Therefore at thermal equilibrium virtually all the atoms will be in the ground level.

Equation (1.7) is valid for atomic systems having only nondegenerate levels. If there are g_i different states of the atom corresponding to the energy E_i , then g_i is defined as the degeneracy of the i th energy level.

We recall that atomic systems, such as atoms, ions, molecules, can exist only in certain stationary states, each of which corresponds to a definite value of energy and thus specifies an energy level. When two or more states have the same energy, the respective level is called degenerate, and the number of states with the same energy is the multiplicity of the level. All states of the same energy level will be equally populated therefore the number of atoms in levels 1 and 2 is $N_1 = g_1 N'_1$ and $N_2 = g_2 N'_2$, where N'_1 and N'_2 refer to the population of any of the states in levels 1 and 2, respectively. It follows then from (1.7) that the populations of the energy levels 1 and 2 are related by the formula

$$\frac{N_2}{N_1} = \frac{g_2}{g_1} \frac{N'_2}{N'_1} = \frac{g_2}{g_1} \exp\left(\frac{-(E_2 - E_1)}{kT}\right). \quad (1.8)$$

At absolute zero temperature, Boltzmann's statistics predicts that all atoms will be in the ground state. Thermal equilibrium at any temperature requires that a state with a lower energy be more densely populated than a state with a higher energy. Therefore, N_2/N_1 is always less than unity for $E_2 > E_1$ and $T > 0$. This means that optical amplification is not possible in thermal equilibrium.

1.2.3 Einstein's Coefficients

We can most conveniently introduce the concept of Einstein's A and B coefficients by loosely following Einstein's original derivation. To simplify the discussion, let us consider an idealized material with just two nondegenerate energy levels 1 and 2 having populations of N_1 and N_2 , respectively. The total number of atoms in these two levels is assumed to be constant

$$N_1 + N_2 = N_{\text{tot}}. \quad (1.9)$$

Radiative transfer between the two energy levels which differ by $E_2 - E_1 = h\nu_{21}$ is allowed. The atom can transfer from state E_2 to the ground state E_1 by emitting energy; conversely, transition from state E_1 to E_2 is possible by absorbing energy. The energy removed or added to the atom appears as quanta of $h\nu_{21}$. We can identify three types of interaction between electromagnetic radiation and a simple two-level atomic system: absorption, spontaneous emission, and stimulated emission.

Absorption. If a quasimonochromatic electromagnetic wave of frequency ν_{21} passes through an atomic system with energy gap $h\nu_{21}$, then the population of the lower level will be depleted at a rate proportional to both the radiation energy density $\varrho(\nu)$ and the population N_1 of that level

$$\frac{\partial N_1}{\partial t} = -B_{12}\varrho(\nu)N_1, \quad (1.10)$$

where B_{12} is a constant of proportionality with dimensions $\text{cm}^3/(\text{s}^2 \text{ J})$.

The product $B_{12}\varrho(\nu)$ can be interpreted as the probability per unit frequency for which transitions are induced by the effect of the field.

Spontaneous Emission. After an atom has been raised to the upper level by absorption, the population of the upper level decays spontaneously to the lower level at a rate proportional to the upper level population.

$$\frac{\partial N_2}{\partial t} = -A_{21}N_2, \quad (1.11)$$

where A_{21} is a constant of proportionality with dimensions s^{-1} . The quantity A_{21} , being a characteristic of the pair of energy levels in question, is called the spontaneous transition probability because this coefficient gives the probability that an atom in level 2 will spontaneously change to a lower level 1 within a unit of time.

Spontaneous emission is a statistical function of space and time. With a large number of spontaneously emitting atoms there is no phase relationship between the individual emission processes; the quanta emitted are incoherent. Spontaneous emission is characterized by the lifetime of the electron in the excited state, after which it will spontaneously return to the lower state and radiate away the energy. This can occur without the presence of an electromagnetic field.

Equation (1.11) has a solution

$$N_2(t) = N_2(0) \exp\left(\frac{-t}{\tau_{21}}\right), \quad (1.12)$$

where τ_{21} is the lifetime for spontaneous radiation of level 2. This radiation lifetime is equal to the reciprocal of the Einstein's coefficient,

$$\tau_{21} = A_{21}^{-1}. \quad (1.13)$$

In general, the reciprocal of the transition probability of a process is called its lifetime.

Stimulated Emission. Emission takes place not only spontaneously but also under stimulation by electromagnetic radiation of appropriate frequency. In this case, the atom gives up a quantum to the radiation field by “induced emission” according to

$$\frac{\partial N_2}{\partial t} = -B_{21}\varrho(\nu_{21})N_2, \quad (1.14)$$

where B_{21} again is a constant of proportionality.

Radiation emitted from an atomic system in the presence of external radiation consists of two parts. The part whose intensity is proportional to A_{21} is the spontaneous radiation; its phase is independent of that of the external radiation. The part whose intensity is proportional to $\varrho(\nu)B_{21}$ is the stimulated radiation; its phase is the same as that of the stimulating external radiation.

The probability of induced transition is proportional to the energy density of external radiation in contrast to spontaneous emission. In the case of induced transition there is a firm phase relationship between the stimulating field and the atom. The quantum which is emitted to the field by the induced emission is coherent with it.

But we shall see later that the useful parameter for laser action is the B_{21} coefficient; the A_{21} coefficient represents a loss term and introduces into the system photons that are not phase-related to the incident photon flux of electric field. Thus the spontaneous process represents a noise source in a laser.

If we combine absorption, spontaneous, and stimulated emission, as expressed by (1.10, 11, and 14), we can write for the change of the upper and lower level populations in our two-level model

$$\frac{\partial N_1}{\partial t} = -\frac{\partial N_2}{\partial t} = B_{21}\varrho(\nu)N_2 - B_{12}\varrho(\nu)N_1 + A_{21}N_2. \quad (1.15)$$

The relation

$$\frac{\partial N_1}{\partial t} = -\frac{\partial N_2}{\partial t} \quad (1.16)$$

follows from (1.9).

In thermal equilibrium, the number of transitions per unit time from E_1 to E_2 must be equal to the number of transitions from E_2 to E_1 . Certainly, in thermal equilibrium

$$\frac{\partial N_1}{\partial t} = \frac{\partial N_2}{\partial t} = 0. \quad (1.17)$$

Therefore we can write

$$\begin{array}{lll} N_2 A_{21} & + & N_2 \varrho(\nu) B_{21} \\ \text{Spontaneous} & \text{Stimulated} & = N_1 \varrho(\nu) B_{12} \\ \text{emission} & \text{emission} & \text{Absorption.} \end{array} \quad (1.18)$$

Using the Boltzmann equation (1.8) for the ratio N_2/N_1 , we then write the above expression as

$$\varrho(\nu_{21}) = \frac{(A_{21}/B_{21})}{(g_1/g_2)(B_{12}/B_{21}) \exp(h\nu_{21}/kT) - 1}. \quad (1.19)$$

Comparing this expression with the blackbody radiation law (1.2), we see that

$$\frac{A_{21}}{B_{21}} = \frac{8\pi\nu^2h\nu}{c^3} \quad \text{and} \quad B_{21} = \frac{g_1 B_{12}}{g_2}. \quad (1.20)$$

The relations between the A 's and B 's are known as Einstein's relations. The factor $8\pi\nu^2/c^3$ in (1.20) is the mode density p_n given by (1.3).

In solids the speed of light is $c = c_0/n$, where n is the index of refraction and c_0 is the speed of light in vacuum.

For a simple system with no degeneracy, that is, one in which $g_1 = g_2$, we see that $B_{21} = B_{12}$. Thus, the Einstein coefficients for stimulated emission and absorption are equal. If the two levels have unequal degeneracy, the probability for stimulated absorption is no longer the same as that for stimulated emission.

1.2.4 Phase Coherence of Stimulated Emission

The stimulated emission provides a phase-coherent amplification mechanism for an applied signal. The signal extracts from the atoms a response that is directly proportional to, and phase-coherent with, the electric field of the stimulating signal. Thus the amplification process is phase-preserving. The stimulated emission is, in fact, completely indistinguishable from the stimulating radiation field. This means that the stimulated emission has the same directional properties, same polarization, same phase, and same spectral characteristics as the stimulating emission. These facts are responsible for the extremely high degree of coherence, which characterizes the emission from lasers. The proof of this fact is beyond the scope of this elementary introduction, and requires a quantum mechanical treatment of the interaction between radiation and matter. However, the concept of induced transition, or the interaction between a signal and an atomic system, can be demonstrated, qualitatively, with the aid of the classical electron-oscillator model.

Electromagnetic radiation interacts with matter through the electric charges in the substance. Consider an electron which is elastically bound to a nucleus. One can think of electrons and ions held together by spring-type bonds which are capable of vibrating around equilibrium positions. An applied electric field will cause a relative displacement between electron and nucleus from their equilibrium position. They will execute an oscillatory motion about their equilibrium position. Therefore, the model exhibits an oscillatory or resonant behavior and a response to an applied field. Since the nucleus is so much heavier than the electron, we assume that only the electron moves. The most important model for understanding the interaction of light and matter is that of the harmonic oscillator. We take as our model a single electron, assumed to be bound to its equilibrium position by a linear restoring force. We may visualize the electron as a point of mass suspended by springs. Classical electromagnetic theory asserts that any oscillating electric charge will act as a miniature antenna or dipole and will continuously radiate away electromagnetic energy to its surroundings.

A detailed description of the electric dipole transition and the classical electron-oscillator model can be found in [1.3].

1.3 Absorption and Optical Gain

In this section we will develop the quantitative relations that govern absorption and amplification processes in substances. This requires that we increase the realism of our mathematical model by introducing the concept of atomic lineshapes. Therefore, the important features and the physical processes which lead to different atomic lineshapes will be considered first.

1.3.1 Atomic Lineshapes

In deriving Einstein's coefficients we have assumed a monochromatic wave with frequency ν_{21} acting on a two-level system with an infinitely sharp energy gap $h\nu_{21}$. We will now consider the interaction between an atomic system having a finite transition linewidth $\Delta\nu$ and a signal with a bandwidth $d\nu$.

Before we can obtain an expression for the transition rate for this case, it is necessary to introduce the concept of the atomic lineshape function $g(\nu, \nu_0)$. The distribution $g(\nu, \nu_0)$, centered at ν_0 , is the equilibrium shape of the linewidth-broadened transitions. Suppose that N_2 is the total number of ions in the upper energy level considered previously. The spectral distribution of ions per unit frequency is then

$$N(\nu) = g(\nu, \nu_0)N_2. \quad (1.21)$$

If we integrate both sides over all frequencies we have to obtain N_2 as a result:

$$\int_0^\infty N(\nu) d\nu = N_2 \int_0^\infty g(\nu, \nu_0) d\nu = N_2. \quad (1.22)$$

Therefore the lineshape function must be normalized to unity:

$$\int_0^\infty g(\nu, \nu_0) d\nu = 1. \quad (1.23)$$

If we know the function $g(\nu, \nu_0)$, we can calculate the number of atoms $N(\nu) d\nu$ in level 1 which are capable of absorbing in the frequency range ν to $\nu + d\nu$, or the number of atoms in level 2 which are capable of emitting in the same range. From (1.21) we have

$$N(\nu) d\nu = g(\nu, \nu_0) d\nu N_2. \quad (1.24)$$

From the foregoing it follows that $g(\nu, \nu_0)$ can be defined as the probability of emission or absorption per unit frequency. Therefore $g(\nu) d\nu$ is the probability that a given transition will result in an emission (or absorption) of a photon with energy between $h\nu$ and $h(\nu + d\nu)$. The probability that a transition will occur between $\nu = 0$ and $\nu = \infty$ has to be 1.

It is clear from the definition of $g(\nu, \nu_0)$ that we can, for example, rewrite (1.11) in the form

$$-\frac{\partial N_2}{\partial t} = A_{21}N_2g(\nu, \nu_0) d\nu, \quad (1.25)$$

where N_2 is the total number of atoms in level 2 and $\partial N_2/\partial t$ is the number of photons spontaneously emitted per second between ν and $\nu + d\nu$.

The linewidth and lineshape of an atomic transition depends on the cause of line broadening. Optical frequency transitions in gases can be broadened by lifetime, collision, or Doppler broadening, whereas transitions in solids can be broadened by lifetime, dipolar or thermal broadening, or by random inhomogeneities. All these linewidth-broadening mechanisms lead to two distinctly different atomic lineshapes, the homogeneously and the inhomogeneously broadened line [1.4].

The Homogeneously Broadened Line

The essential feature of a homogeneously broadened atomic transition is that every atom has the same atomic lineshape and frequency response, so that a signal applied to the transition has exactly the same effect on all atoms in the collection. This means that within the linewidth of the energy level each atom has the same probability function for a transition.

Differences between homogeneously and inhomogeneously broadened transitions show up in the saturation behavior of these transitions. This has a major effect on the laser operation. The important point about a homogeneous lineshape is that the transition will saturate uniformly under the influence of a sufficiently strong signal applied anywhere within the atomic linewidth.

Mechanisms which result in a homogeneously broadened line are lifetime broadening, collision broadening, dipolar broadening, and thermal broadening.

Lifetime Broadening. This type of broadening is caused by the decay mechanisms of the atomic system. Spontaneous emission or fluorescence has a radiative lifetime. Broadening of the atomic transition due to this process is related to the fluorescence lifetime τ by $\Delta\omega_a\tau = 1$, where $\Delta\omega_a$ is the bandwidth.

Actually, physical situations in which the lineshape and linewidth are determined by the spontaneous emission process itself are vanishingly rare. Since the natural or intrinsic linewidth of an atomic line is extremely small, it is the linewidth that would be observed from atoms at rest without interaction with one another.

Collision Broadening. Collision of radiating particles (atoms or molecules) with one another and the consequent interruption of the radiative process in a random manner leads to broadening. As an atomic collision interrupts either the emission or the absorption of radiation, the long wave train which otherwise would be present becomes truncated. The atom restarts its motion after the collision with a completely random initial phase. After the collision the process is restarted without memory of the phase of the radiation prior to the collision. The result of frequent collisions is the presence of many truncated radiative or absorptive processes.

Since the spectrum of a wave train is inversely proportional to the length of the train, the linewidth of the radiation in the presence of collision is greater than that of an individual uninterrupted process.

Collision broadening is observed in gas lasers operated at higher pressures, hence the name pressure broadening. At higher pressures collisions between gas atoms limit their radiative lifetime. Collision broadening, therefore, is quite similar to lifetime broadening, in that the collisions interrupt the initial state of the atoms.

Dipolar Broadening. Dipolar broadening arises from interactions between the magnetic or electric dipolar fields of neighboring atoms. This interaction leads to results very similar to collision broadening, including a linewidth that increases with increasing density of atoms. Since dipolar broadening represents a kind of coupling between atoms, so that excitation applied to one atom is distributed or shared with other atoms, dipolar broadening is a homogeneous broadening mechanism.

Thermal Broadening. Thermal broadening is brought about by the effect of the thermal lattice vibrations on the atomic transition. The thermal vibrations of the lattice surrounding the active ions modulate the resonance frequency of each atom at a very high frequency. This frequency modulation represents a coupling mechanism between the atoms, and therefore a homogeneous linewidth is obtained. Thermal broadening is the mechanism responsible for the linewidth of the ruby laser and Nd:YAG laser.

The lineshape of homogeneous broadening mechanisms lead to a Lorentzian lineshape for atomic response. For the normalized Lorentz distribution, the equation

$$g(\nu) = \left(\frac{\Delta\nu}{2\pi} \right) \left[(\nu - \nu_0)^2 + \left(\frac{\Delta\nu}{2} \right)^2 \right]^{-1} \quad (1.26)$$

is valid. Here, ν_0 is the center frequency and $\Delta\nu$ is the width between the half-power points of the curve. The factor $\Delta\nu/2\pi$ assures normalization of the area under the curve according to (1.23). The peak value for the Lorentz curve is

$$g(\nu_0) = \frac{2}{\pi \Delta\nu}. \quad (1.27)$$

The Inhomogeneously Broadened Line

Mechanisms which cause inhomogeneous broadening tend to displace the center frequencies of individual atoms, thereby broadening the overall response of a collection without broadening the response of individual atoms. Different atoms have slightly different resonance frequencies on the same transition, for example, owing to Doppler shifts. As a result, the overall response of the collection is broadened. An applied signal at a given frequency within the overall linewidth interacts strongly only with those atoms whose shifted resonance frequencies lie close to the signal frequency. The applied signal does not have the same effect on all the atoms in an inhomogeneously broadened collection.

Since in an inhomogeneously broadened line interaction occurs only with those atoms whose resonance frequencies lie close to the applied signal frequency, a strong

signal will eventually deplete the upper laser level in a very narrow frequency interval. The signal will eventually “burn a hole” in the atomic absorption curve. Examples of inhomogeneous frequency-shifting mechanisms include Doppler broadening and broadening due to crystal inhomogeneities.

Doppler Broadening. The apparent resonance frequencies of atoms undergoing random motions in a gas are shifted randomly so that the overall frequency response of the collection of atoms is broadened. A particular atom moving with a velocity component v relative to an observer in the z direction will radiate at a frequency measured by the observer as $\nu_0(1 + v/c)$. When these velocities are averaged, the resulting lineshape is Gaussian. Doppler broadening is one form of inhomogeneous broadening, since each atom emits a different frequency rather than one atom having a probability distribution for emitting any frequency within the linewidth. In the actual physical situation, the Doppler line is best visualized as a packet of homogeneous lines of width $\Delta\nu_n$, which superimpose to give the observed Doppler shape. The He-Ne laser has a Doppler-broadened linewidth. Most visible and near-infrared gas laser transitions are inhomogeneously broadened by Doppler effects.

Line Broadening Due to Crystal Inhomogeneities. Solid-state lasers may be inhomogeneously broadened by crystalline defects. This happens only at low temperatures where the lattice vibrations are small. Random variations of dislocations, lattice strains, etc., may cause small shifts in the exact energy level spacings and transition frequencies from ion to ion. Like Doppler broadening, these variations do not broaden the response on an individual atom, but they do cause the exact resonance frequencies of different atoms to be slightly different. Thus random crystal imperfection can be a source of inhomogeneous broadening in a solid-state laser crystal.

A good example of an inhomogeneously broadened line occurs in the fluorescence of neodymium-doped glass. As a result of the so-called glassy state, there are variations, from rare earth site to rare earth site, in the relative atomic positions occupied by the surrounding lattice ions. This gives rise to a random distribution of static crystalline fields acting on the rare earth ions. Since the line shifts corresponding to such crystal-field variations are larger, generally speaking, than the width contributed by other factors associated with the transition, an inhomogeneous line results.

The inhomogeneous-broadened linewidth can be represented by a Gaussian frequency distribution. For the normalized distribution, the equation

$$g(\nu) = \frac{2}{\Delta\nu} \left(\frac{\ln 2}{\pi} \right)^{1/2} \exp \left[- \left(\frac{\nu - \nu_0}{\Delta\nu/2} \right)^2 \ln 2 \right] \quad (1.28)$$

is valid, where ν_0 is the frequency at the center of the line and $\Delta\nu$ is the linewidth at which the amplitude falls to one-half. The peak value of the normalized Gaussian curve is

$$g(\nu_0) = \frac{2}{\Delta\nu} \left(\frac{\ln 2}{\pi} \right)^{1/2}. \quad (1.29)$$

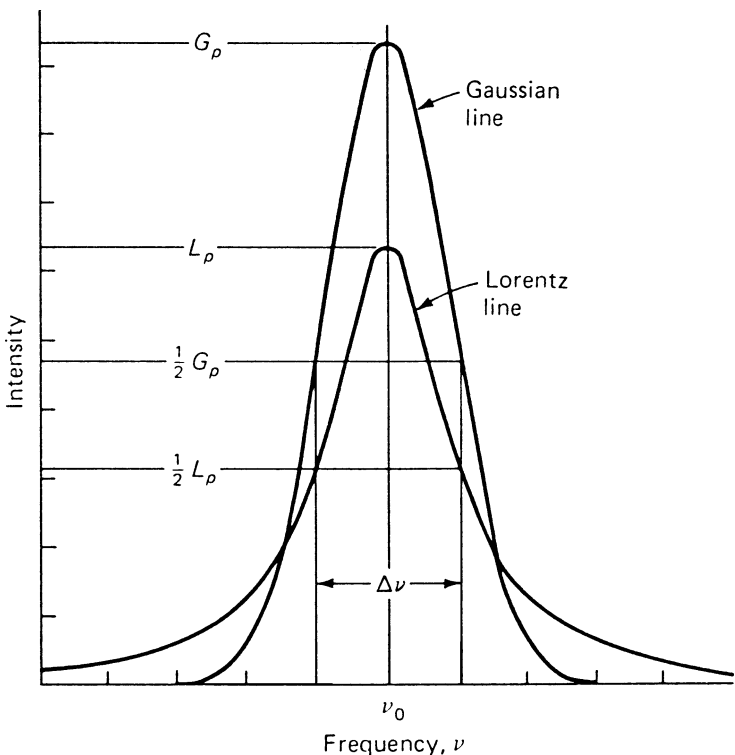


Fig. 1.2. Gaussian and Lorentz lines of common linewidth (G_p and L_p are the peak intensities)

In Fig. 1.2 the normalized Gaussian and Lorentz lines are plotted for a common linewidth.

1.3.2 Absorption by Stimulated Transitions

We assume a quasicollimated beam of energy density per frequency $\varrho(\nu)$ incident on a thin absorbing sample of thickness dx ; as before, we consider the case of an optical system that operates only between two energy levels as illustrated schematically in Fig. 1.1. The populations of the two levels are N_1 and N_2 , respectively. Level 1 is the ground level and level 2 is the excited level. We consider absorption of radiation in the material and emission from the stimulated processes but neglect the spontaneous emission. From (1.15 and 1.20) we obtain

$$-\frac{\partial N_1}{\partial t} = \varrho(\nu)B_{21} \left(\frac{g_2}{g_1}N_1 - N_2 \right). \quad (1.30)$$

As we recall, this relation was obtained by considering infinitely sharp energy levels separated by $h\nu_{21}$ and a monochromatic wave of frequency ν_{21} .

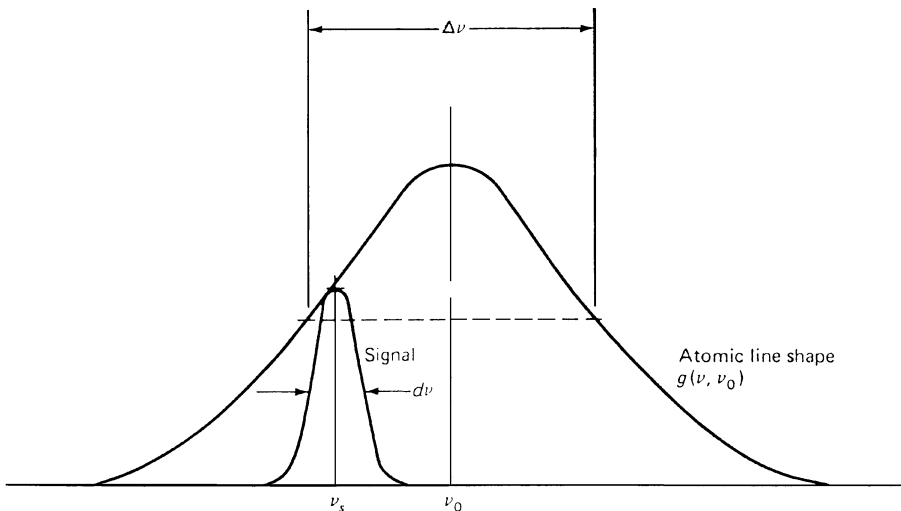


Fig. 1.3. Linewidth-broadened atomic transition line centered at ν_0 and narrow band signal centered at ν_s

We will now consider the interaction between two linewidth-broadened energy levels with an energy separation centered at ν_0 , and a half-width of $\Delta\nu$ characterized by $g(\nu, \nu_0)$ and a signal with center frequency ν_s and bandwidth $d\nu$. The situation is shown schematically in Fig. 1.3. The spectral width of the signal is narrow, as compared to the linewidth-broadened transition. If N_1 and N_2 are the total number of atoms in level 1 and level 2, then the number of atoms capable of interacting with a radiation of frequency ν_s and bandwidth $d\nu$ are

$$\left(\frac{g_2}{g_1} N_1 - N_2 \right) g(\nu_s, \nu_0) d\nu. \quad (1.31)$$

The net change of atoms in energy level 1 can be expressed in terms of energy density $\varrho(\nu) d\nu$ by multiplying both sides of (1.30) with photon energy $h\nu$ and dividing by the volume V . We will further express the populations N_1 and N_2 as population densities n_1 and n_2 .

Equation (1.30) now becomes

$$-\frac{\partial}{\partial t} [\varrho(\nu_s) d\nu] = \varrho(\nu_s) d\nu B_{21} h \nu g(\nu_s, \nu_0) \left(\frac{g_2}{g_1} n_1 - n_2 \right). \quad (1.32)$$

This equation gives the net rate of absorbed energy in the frequency interval $d\nu$ centered around ν_s . In an actual laser system the wavelength of the emitted radiation, corresponding to the signal bandwidth $d\nu$ in our model, is very narrow as compared to the natural linewidth of the material. Ruby, for example, has a fluorescent linewidth of 5 Å, whereas the linewidth of the laser output is typically 0.1–0.01 Å. The operation of a laser, therefore, can be fairly accurately characterized as the interaction of linewidth-broadened energy levels with a monochromatic wave. The photon

density of a monochromatic radiation of frequency ν_0 can then be represented by a delta function $\delta(\nu - \nu_0)$. After integrating (1.32) in the interval $d\nu$, we obtain, for a monochromatic signal of frequency ν_s and a linewidth-broadened transition,

$$-\frac{\partial \varrho(\nu_s)}{\partial t} = \varrho(\nu_s) B_{21} h \nu_s g(\nu_s, \nu_0) \left(\frac{g_2}{g_1} n_1 - n_2 \right). \quad (1.33)$$

The signal will travel through the material of thickness dx in the time $dt = dx/c = (n/c_0)dx$. Then, as the wave advances from x to $x + dx$, the decrease of energy in the beam is

$$-\frac{\partial \varrho(\nu_s)}{\partial x} = h \nu_s \varrho(\nu_s) g(\nu_s, \nu_0) B_{21} \left(\frac{g_2}{g_1} n_1 - n_2 \right) \frac{1}{c}. \quad (1.34)$$

Integration of (1.34) gives

$$\frac{\varrho(\nu_s)}{\varrho_0(\nu_s)} = \exp \left[-h \nu_s g(\nu_s, \nu_0) B_{21} \left(\frac{g_2}{g_1} n_1 - n_2 \right) \frac{x}{c} \right]. \quad (1.35)$$

If we introduce an absorption coefficient $\alpha(\nu_s)$,

$$\alpha(\nu_s) = \left(\frac{g_2}{g_1} n_1 - n_2 \right) \sigma_{21}(\nu_s), \quad (1.36)$$

where

$$\sigma_{21}(\nu_s) = \frac{h \nu_s g(\nu_s, \nu_0) B_{21}}{c}. \quad (1.37)$$

Then we can write (1.35) as

$$\varrho(\nu_s) = \varrho_0(\nu_s) \exp[-\alpha(\nu_s)x]. \quad (1.38)$$

Equation (1.38) is the well-known exponential absorption equation for thermal equilibrium condition $n_1 g_2 / g_1 > n_2$. The energy of the radiation decreases exponentially with the depth of penetration into the substance. The maximum possible absorption occurs when all atoms exist in the ground state n_1 . For equal population of the energy states $n_1 = (g_1/g_2)n_2$, the absorption is eliminated and the material is transparent. The parameter σ_{21} is the cross section for the radiative transition $2 \rightarrow 1$. The cross section for stimulated emission σ_{21} is related to the absorption cross section σ_{12} by the ratio of the level degeneracies:

$$\frac{\sigma_{21}}{\sigma_{12}} = \frac{g_1}{g_2}. \quad (1.39)$$

The cross section is a very useful parameter to which we will refer in the following chapters. If we replace B_{21} by the Einstein relation (1.20), we obtain σ_{21} in a form which we will find most useful:

$$\sigma_{21}(\nu_s) = \frac{A_{21} \lambda_0^2}{8\pi n^2} g(\nu_s, \nu_0). \quad (1.40)$$

As we will see later, the gain for the radiation building up in a laser resonator will be highest at the center of the atomic transitions. Therefore, in lasers we are mostly dealing with stimulated transitions which occur at the center of the linewidth.

If we assume $\nu \approx \nu_s \approx \nu_0$, we obtain for the spectral stimulated emission cross section at the center of the atomic transition for a Lorentzian lineshape

$$\sigma_{21} = \frac{A_{21}\lambda_0^2}{4\pi^2 n^2 \Delta\nu}, \quad (1.41)$$

and for a Gaussian lineshape

$$\sigma_{21} = \frac{A_{21}\lambda_0^2}{4\pi n^2 \Delta\nu} \left(\frac{\ln 2}{\pi} \right)^{1/2}. \quad (1.42)$$

Here we have introduced into (1.40) the peak values of the lineshape function, as given in (1.27 and 1.29) for the Lorentzian and Gaussian curves, respectively. For example, in the case of the R_1 line of ruby, where $\lambda_0 = 6.94 \times 10^{-5}$ cm, $n = 1.76$, $\tau_{21} = (1/A_{21}) = 3$ ms, and $\Delta\nu = 330$ GHz one finds, according to (1.41), $\sigma_{21} = 4.0 \times 10^{-20}$ cm². In comparing this value with the data provided in Table 2.2, we have to distinguish between the spectroscopic cross section and the effective stimulated emission cross section. (This will be discussed in Sect. 2.3.1 for the case of Nd:YAG). The effective stimulated emission cross section is the spectroscopic cross section times the occupancy of the upper laser level relative to the entire manifold population. In ruby, the upper laser level is split into two sublevels and therefore the effective stimulated emission cross section is about half of the value calculated from (1.41).

1.3.3 Population Inversion

According to the Boltzmann distribution (1.7), in a collection of atoms at thermal equilibrium there are always fewer atoms in a higher-lying level E_2 than in a lower level E_1 . Therefore the population difference $N_1 - N_2$ is always positive, which means that the absorption coefficient $\alpha(\nu_s)$ in (1.36) is positive and the incident radiation is absorbed (Fig. 1.4).

Suppose that it were possible to achieve a temporary situation such that there are more atoms in an upper energy level than in a lower energy level. The normally positive population difference on that transition then becomes negative, and the normal stimulated absorption is correspondingly changed to stimulated emission or amplification of the applied signal. That is, the applied signal gains energy as it interacts with the atoms and hence is amplified. The energy for this signal amplification is supplied by the atoms involved in the interaction process. This situation is characterized by a negative absorption coefficient $\alpha(\nu_s)$ according to (1.36). From (1.34) it follows that $\partial Q(\nu)/\partial x > 0$.

The essential condition for amplification is that there are more atoms in an upper energy level than in a lower energy level, i.e., for amplification,

$$N_2 > N_1 \quad \text{if} \quad E_2 > E_1, \quad (1.43)$$

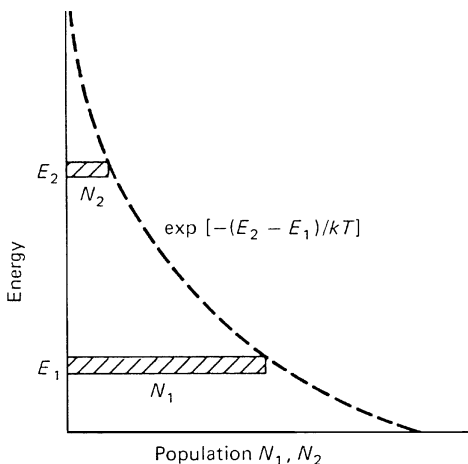


Fig. 1.4. Relative populations in two energy levels as given by the Boltzmann relation for thermal equilibrium

as illustrated in Fig. 1.5. The resulting negative sign of the population difference ($N_2 - g_2 N_1 / g_1$) on that transition is called a population inversion. Population inversion is clearly an abnormal situation; it is never observed at thermal equilibrium. The point at which the population of both states is equal is called the “inversion threshold.”

Stimulated absorption and emission processes always occur side by side independent of the population distribution among the levels. So long as the population of the higher energy level is smaller than that of the lower energy level, the number of absorption transitions is larger than that of the emission transitions, so that there is an overall attenuation of the radiation. When the numbers of atoms in both states are equal, the number of emissions becomes equal to the number of absorptions; the material is then transparent to the incident radiation. As soon as the population of the higher level becomes larger than that of the lower level, emission processes predominate and the radiation is enhanced collectively during passage through the

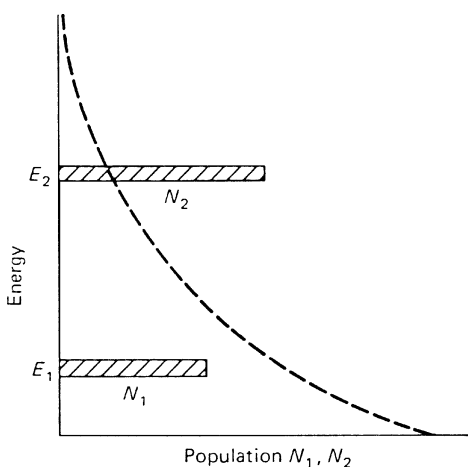


Fig. 1.5. Inverted population difference required for optical amplification

material. To produce an inversion requires a source of energy to populate a specified energy level; we call this energy the pump energy.

In Sect. 1.4 we will discuss the type of energy level structure an atomic system must possess in order to make it possible to generate an inversion. Techniques by which the atoms of a solid-state laser can be raised or pumped into upper energy levels are discussed in Sect. 6.1. Depending on the atomic system involved, an inverted population condition may be obtainable only on a transient basis, yielding pulsed laser action; or it may be possible to maintain the population inversion on a steady-state basis, yielding continuous-wave (cw) laser action.

The total amount of energy which is supplied by the atoms to the light wave is

$$E = \Delta N h\nu, \quad (1.44)$$

where ΔN is the total number of atoms which are caused to drop from the upper to the lower energy level during the time the signal is applied. If laser action is to be maintained, the pumping process must continually replenish the supply of upper-state atoms. The size of the inverted population difference is reduced not only by the amplification process but also by spontaneous emission, which always tends to return the energy level populations to their thermal equilibrium values.

1.4 Creation of a Population Inversion

In this section we discuss how the necessary population inversion for laser action is obtained in solid-state lasers. We can gain considerable understanding on how laser devices are pumped and how their population densities are inverted by studying some simplified but fairly realistic models.

The discussion up to this point has been based on a hypothetical $2 \leftrightarrow 1$ transition and has not been concerned with how the levels 2 and 1 fit into the energy level scheme of the atom. This detached point of view must be abandoned when one tries to understand how laser action takes place in a solid-state medium. As already noted, the operation of the laser depends on a material with narrow energy levels between which electrons can make transitions. Usually these levels are due to impurity ions in a host crystal. The pumping and laser processes in real laser systems typically involve a very large number of energy levels, with complex excitation processes and cascaded relaxation processes among all these levels. Operation of an actual laser material is properly described only by a many-level energy diagram. The main features can be understood, however, through the familiar three-level or four-level idealizations of Figs. 1.6 and 1.7. More detailed energy level diagrams of some of the most important solid-state laser materials are presented in Chap. 2.

1.4.1 The Three-Level System

Figure 1.6 shows a diagram which can be used to explain the operation of an optically pumped three-level laser, such as ruby. Initially, all ions of the laser material are

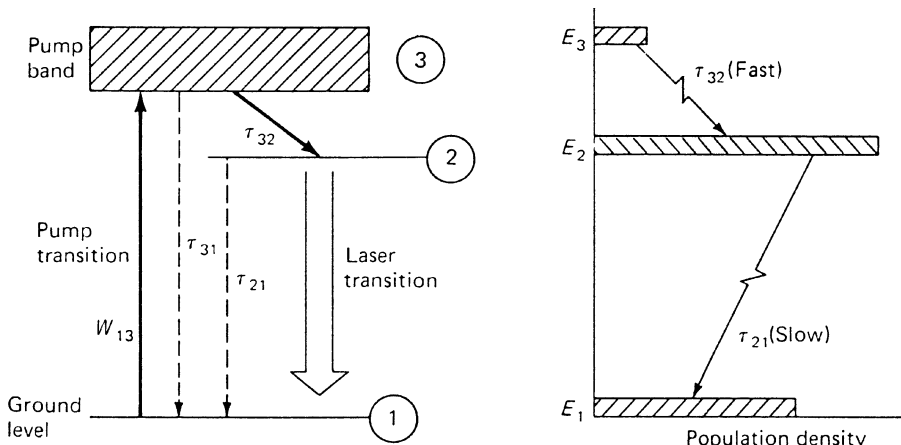


Fig. 1.6. Simplified energy level diagram of a three-level laser

in the lowest level 1. Excitation is supplied to the solid by radiation of frequencies which produce absorption into the broadband 3. Thus, the pump light raises ions from the ground state to the pump band, level 3. In general, the “pumping” band, level 3, is actually made up of a number of bands, so that the optical pumping can be accomplished over a broad spectral range. Most of the excited ions are transferred by fast radiationless transitions into the intermediate sharp level 2. In this process the energy lost by an electron is transferred to the lattice. Finally, the electron returns to the ground level by the emission of a photon. It is this last transition that is responsible for the laser action. If pumping intensity is below laser threshold, ions in level 2 predominantly return to the ground state by spontaneous emission. Ordinary fluorescence acts as a drain on the population of level 2. After the pump radiation is extinguished, level 2 is emptied by fluorescence at a rate that varies from material to material. In ruby, at room temperature, the lifetime of level 2 is 3 ms. When the pump intensity is above laser threshold, the decay from the fluorescent level consists of stimulated as well as spontaneous radiation; the stimulated radiation produces the laser output beam. Since the terminal level of the laser transition is the highly populated ground state, a very high population must be reached in the E_2 level before the $2 \rightarrow 1$ transition is inverted.

It is necessary, in general, that the rate of radiationless transfer from the uppermost level to the level at which the laser action begins be fast compared with the other spontaneous transition rates in a three-level laser. Therefore, the lifetime of the E_2 state should be large in comparison with the relaxation time of the $3 \rightarrow 2$ transition, i.e.,

$$\tau_{21} \gg \tau_{32}. \quad (1.45)$$

The number of ions N_3 in level E_3 is then negligible compared with the number of ions in the other two states, i.e., $N_3 \ll N_1, N_2$. Therefore,

$$N_1 + N_2 \approx N_{\text{tot}}. \quad (1.46)$$

A vital aspect of the three-level system is that the ions are in effect pumped directly from level 1 into the metastable level 2 with only a momentary pause as they pass through level 3. With these conditions, we can calculate as if only two levels were present. In order that an equal population is achieved between the E_2 and E_1 levels, one-half of all atoms must be excited to the E_2 level:

$$N_2 = N_1 = \frac{N_{\text{tot}}}{2} \quad (1.47)$$

In order to maintain a specified amplification, the population of the second level must be larger than that of the first level. In most cases which are of practical importance, however, the necessary inversion ($N_2 - N_1$) is small compared with the total number of all ions. The pump power necessary for maintaining this inversion is also small compared with the power necessary for achieving equal population of the levels.

The disadvantage of a three-level system is that more than half of the ions in the ground state must be raised to the metastable level E_2 . There are thus many ions present to contribute to the spontaneous emission. Moreover, each of the ions which participate in the pump cycle transfer energy into the lattice from the $E_3 \rightarrow E_2$ transition. This transition is normally radiationless, the energy being carried into the lattice by phonons.

1.4.2 The Four-Level System

The four-level laser system, which is characteristic of the rare earth ions in glass or crystalline host materials, is illustrated in Fig. 1.7. Note that a characteristic of the three-level laser material is that the laser transition takes place between the excited laser level 2 and the final ground state 1, the lowest energy level of the system. This leads to low efficiency. The four-level system avoids this disadvantage. The pump

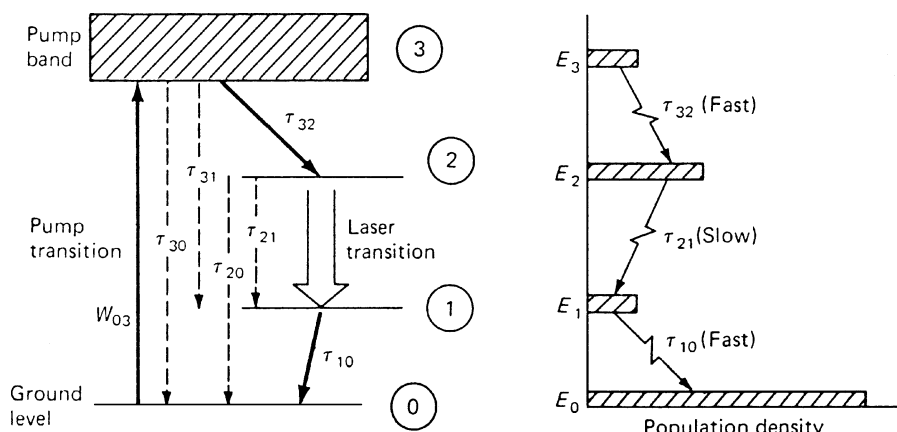


Fig. 1.7. Simplified energy level diagram of a four-level laser

transition extends again from the ground state (now level E_0) to a wide absorption band E_3 . As in the case of the three-level system, the ions so excited will proceed rapidly to the sharply defined level E_2 . The laser transition, however, proceeds now to a fourth, terminal level E_1 , which is situated above the ground state E_0 . From here the ion undergoes a rapid nonradiative transition to the ground level. In a true four-level system, the terminal laser level E_1 will be empty. To qualify as a four-level system a material must possess a relaxation time between the terminal laser level and the ground level, which is fast compared to the fluorescent lifetime, i.e., $\tau_{10} \ll \tau_{21}$. In addition the terminal laser level must be far above the ground state so that its thermal population is small. The equilibrium population of the terminal laser level 1 is determined by the relation

$$\frac{N_1}{N_0} = \exp\left(\frac{-\Delta E}{kT}\right), \quad (1.48)$$

where ΔE is the energy separation between level 1 and the ground state, and T is the operating temperature of the laser material. If $\Delta E \gg kT$, then $N_1/N_0 \ll 1$, and the intermediate level will always be relatively empty. In some laser materials the energy gap between the lower laser level and the ground state is relatively small and therefore they must be cooled to function as four-level lasers. In a four-level system an inversion of the $2 \rightarrow 1$ transition can occur even with vanishingly small pump power, and the high pump rate, necessary to maintain equilibrium population in the aforementioned three-level system, is no longer needed. In the most favorable case, the relaxation times of the $3 \rightarrow 2$ and $1 \rightarrow 0$ transitions in the four-level system are short compared with the spontaneous emission lifetime of the laser transition τ_{21} . Hence we can also carry out the calculations as if only the E_1 and E_2 states were populated.

1.4.3 The Metastable Level

After this brief introduction to the energy level structure of solid-state lasers we can ask the question, “what energy level scheme must a solid possess to make it a useful laser?” As we have seen in the previous discussion, the existence of a metastable level is of paramount importance for laser action to occur. The relatively long lifetime of the metastable level provides a mechanism by which inverted population can be achieved. Most transitions of ions show rapid nonradiative decay because the coupling of the internal atomic oscillations to the surrounding lattice is strong. Radiative decay processes can occur readily, but most have short lifetimes and broad linewidths. Only a few transitions of selected ions in solids turn out to be decoupled from the lattice vibrations. These transitions have a radiative decay, which leads to relatively long lifetimes.

In typical laser systems with energy levels, such as illustrated by Figs. 1.6 and 7, the $3 \rightarrow 2$ transition frequencies as well as the $1 \rightarrow 0$ transition frequencies all fall within the frequency range of the vibration spectrum of the host crystal lattice. Therefore, all these transitions can relax extremely rapidly by direct nonradiative decay, i.e., by emitting a phonon to the lattice vibrations, with $\tau_{32}, \tau_{10} \approx 10^{-8}-10^{-11}$ s.

However, the larger $3 \rightarrow 0$, $3 \rightarrow 1$, $2 \rightarrow 0$, and $2 \rightarrow 1$ energy gaps in these atoms often correspond to transition frequencies that are higher than the highest possible vibration frequency of the crystal lattice. Such transitions cannot relax via simple single-phonon spontaneous emission, since the lattice simply cannot accept phonons at those high frequencies. These transitions must then relax either by radiative (photon) emission or by multiple-phonon processes. Since both these processes are relatively weak compared to direct single-phonon relaxation, the high-frequency transitions will have much slower relaxation rates ($\tau_{21} \approx 10^{-5}\text{--}10^{-3}$ s in many cases). Therefore, the various levels lumped into level 3 will all relax mostly into level 2 while level 2 itself is metastable and long-lived because there are no other levels located close below it into which it can decay directly.

The existence of metastable levels follows from quantum mechanical considerations that will not be discussed here. However, for completeness we will explain the term “forbidden transition.” As we have seen in Sect. 1.2.4, the mechanism by which energy exchange takes place between an atom and the electromagnetic fields is the dipole radiation. As a consequence of quantum mechanical considerations and the ensuing selection rules, transfer between certain states cannot occur due to forbidden transitions. The term “forbidden” means that a transition among the states concerned does not take place as a result of the interaction of the electric dipole moment of the ion with the radiation field. As a result of the selection rules, an ion may get into an excited state from which it will have difficulty returning to the ground state. A state from which all dipole transitions to lower energy states are forbidden is metastable; an ion entering such a state will generally remain in that state much longer than it would in an ordinary excited state from which escape is comparatively easy.

In the absence of a metastable level, the ions which become excited by pump radiation and are transferred to a higher energy level will return either directly to the ground state by spontaneous radiation or by cascading down on intermediate levels, or they may release energy by phonon interaction with the lattice. In order for the population to increase at the metastable laser level, several other conditions have to be met. Let us consider the more general case of a four-level system illustrated in Fig. 1.7. (Note that a three-level system can be thought of as a special case of a four-level scheme where level 1 and level 0 coincide.) Pumping takes place between two levels and laser action takes place between two other levels. Energy from the pump band is transferred to the upper laser level by fast radiationless transitions. Energy is removed from the lower laser level again by fast radiationless transitions.

For electrons in the pump band at level 3 to transfer to level 2 rather than return directly to the ground state, it is required that $\tau_{30} \gg \tau_{32}$. For population to build up, relaxation out of the lower level 1 has to be fast, $\tau_{21} \gg \tau_{10}$. Thus, as a first conclusion, we may say that if the right relaxation time ratio exists between any two levels (such as 3 and 2) in an energy level system, a population inversion should be possible. If so, then obtaining a large enough inversion for successful laser operation becomes primarily a matter of the right pumping method. The optical pumping method is generally feasible only in laser materials which combine a narrow laser emission line with a broad absorption transition, so that a broadband intense light source can be used as the pump source. An exception is a solid-state laser which is pumped by

another laser, such as a diode laser. In this case the requirement for a broad absorption range for the pump band can be relaxed.

Having achieved population inversion in a material by correct combination of relaxation times and the existence of broad pump bands, the linewidth of the laser transition becomes very important. In the following chapter we will see that the optical gain for a given population inversion is inversely proportional to linewidth. Therefore, the metastable level should have a sufficiently narrow linewidth.

1.5 Laser Rate Equations

The dynamic behavior of a laser can be described with reasonable precision by a set of coupled rate equations [1.5]. In their simplest forms, a pair of simultaneous differential equations describe the population inversion and the radiation density within a spatially uniform laser medium. We will describe the system in terms of the energy-level diagrams shown in Figs. 1.6 and 1.7. As we have seen in the preceding discussions, two energy levels are of prime importance in laser action: the excited upper laser level E_2 and the lower laser level E_1 . Thus for many analyses of laser action an approximation of the three- and four-level systems by a two-level representation is very useful.

The rate-equation approach used in this section involves a number of simplifying assumptions; in using a single set of rate equations we are ignoring longitudinal and radial variations of the radiation within the laser medium. In spite of these limitations, the simple rate-equation approach remains a useful tool and, if properly used, provides a great deal of insight into the behavior of real solid-state laser devices. We will derive from the rate equations the threshold condition for laser actions, and obtain a first-order approximation of the relaxation oscillations in a solid-state laser. Furthermore, in Chap. 4 we will use the rate equations to calculate the gain in a laser amplifier.

In general, the rate equations are useful in predicting the gross features of the laser output, such as average and peak power, Q-switched pulse-envelope shape, threshold condition, etc. On the other hand, many details of the nature of the laser emission are inaccessible from the point of view of a simple rate equation. These include detailed descriptions of the spectral, temporal, and spatial distributions of the laser emission. Fortunately, these details can often be accounted for independently.

In applying the rate equations to the various aspects of laser operation, we will find it more convenient to express the probability for stimulated emission $\varrho(v)B_{21}$ by the photon density ϕ and the stimulated emission cross section σ .

With (1.37) we can express the Einstein coefficient for stimulated emission B_{21} in terms of the stimulated emission cross section $\sigma_{21}(v)$,

$$B_{21} = \frac{c}{hvg(v)}\sigma_{21}(v), \quad (1.49)$$

where $c = c_0/n$ is the speed of light in the medium. The energy density per unit frequency $\varrho(v)$ is expressed in terms of the lineshape factor $g(v)$, the energy $h\nu$, and

the photon density ϕ (photons/cm³) by

$$\varrho(v) = h\nu g(v)\phi. \quad (1.50)$$

From (1.49 and 50) we obtain

$$B_{21}\varrho(v) = c\sigma_{21}(v)\phi. \quad (1.51)$$

1.5.1 The Three-Level System

In order to approximate the three-level system with a two-level scheme, we assume that the transition from the pump band to the upper laser level is so fast that $N_3 \approx 0$. Therefore pumping does not affect the other processes at all except to allow a mechanism of populating the upper level and thereby obtaining population inversion ($N_2 > N_1$).

Looking at Fig. 1.6, this assumption requires that the relaxation time ratio τ_{32}/τ_{21} be very small. In solid-state lasers $\tau_{32}/\tau_{21} \approx 0$ is a good approximation. Spontaneous losses from the pump band to the ground state can be expressed by the quantum efficiency η_Q . This parameter, defined as

$$\eta_Q = \left(1 + \frac{\tau_{32}}{\tau_{31}}\right)^{-1} \leq 1, \quad (1.52)$$

specifies what fraction of the total ions excited to level 3 drop from there to level 2, thus becoming potentially useful for laser action. A small η_Q obviously requires a correspondingly larger pump power.

The changes in the electron population densities in a three-level system, based on the assumption that essentially all of the laser ions are in either level 1 or level 2, are

$$\frac{\partial n_1}{\partial t} = \left(n_2 - \frac{g_2}{g_1}n_1\right)c\phi\sigma + \frac{n_2}{\tau_{21}} - W_p n_1 \quad (1.53)$$

and

$$\frac{\partial n_2}{\partial t} = -\frac{\partial n_1}{\partial t}, \quad (1.54)$$

since

$$n_{\text{tot}} = n_1 + n_2, \quad (1.55)$$

where W_p is the pumping rate (s⁻¹).

The terms on the right-hand side of (1.53) express the net stimulated emission, the spontaneous emission, and the optical pumping.

The time variation of the population in both levels due to absorption, spontaneous, and stimulated emission is obtained from (1.15). Note that the populations N_1 and N_2 are now expressed in terms of population densities n_1 and n_2 . To take into account the effect of pumping, we have added the term $W_p n_1$, which can be thought of as the rate of supply of atoms to the metastable level 2. More precisely, $W_p n_1$ is the number

of ions transferred from the ground level to the upper laser level per unit time per unit volume. The pump rate W_p is related to the pump parameter W_{13} in Fig. 1.6 by

$$W_p = \eta_Q W_{13}. \quad (1.56)$$

The negative sign in front of $W_p n_1$ in (1.53) indicates that the pump mechanism removes atoms from the ground level 1 and increases the population of level 2.

If we now define the inversion population density by

$$n = n_2 - \frac{g_2 n_1}{g_1} \quad (1.57)$$

we can combine (1.53, 54, and 57) to obtain

$$\frac{\partial n}{\partial t} = -\gamma n \phi \sigma c - \frac{n + n_{\text{tot}}(\gamma - 1)}{\tau_f} + W_p(n_{\text{tot}} - n), \quad (1.58)$$

where

$$\gamma = 1 + \frac{g_2}{g_1} \quad \text{and} \quad \tau_f = \tau_{21}. \quad (1.59)$$

In obtaining (1.58) we have used the relations

$$n_1 = \frac{n_{\text{tot}} - n}{1 + g_2/g_1} \quad \text{and} \quad n_2 = \frac{n + (g_2/g_1)n_{\text{tot}}}{1 + g_2/g_1}. \quad (1.60)$$

Another equation, usually regarded together with (1.58), describes the rate of change of the photon density within the laser resonator,

$$\frac{\partial \phi}{\partial t} = c \phi \sigma n - \frac{\phi}{\tau_c} + S, \quad (1.61)$$

where τ_c is the decay time for photons in the optical resonator and S is the rate at which spontaneous emission is added to the laser emission.

If we consider for the moment only the first term on the right, which is the increase of the photon density by stimulated emission, then (1.61) is identical to (1.33). However, for the time variation of the photon density in the laser resonator we must also take into account the decrease of radiation due to losses in the system and the increase of radiation due to a small amount of spontaneous emission which is added to the laser emission. Although very small, this term must be included because it provides the source of radiation which initiates laser emission.

An important consideration for initiation of laser oscillation is the total number p of resonant modes possible in the laser resonator volume V_R , since in general only a few of these modes are initiated into oscillations. This number is given by the familiar expression (1.3),

$$p = 8\pi v^2 \frac{\Delta\nu V_R}{c^3}, \quad (1.62)$$

where v is the laser optical frequency and $\Delta\nu$ is the bandwidth of spontaneous emission. Let p_L be the number of modes of the laser output. Then S can be expressed as the rate at which spontaneous emission contributes to stimulated emission,

namely,

$$S = \frac{p_L n_2}{p \tau_{21}}. \quad (1.63)$$

Refer to Chap. 3 for a more detailed description of the factor τ_c which appears in (1.61). For now we only need to know that τ_c represents all the losses in an optical resonator of a laser oscillator. Since τ_c has the dimension of time, the losses are expressed in terms of a relaxation time. The decay of the photon population in the cavity results from transmission and absorption at the end mirrors, “spillover” diffraction loss due to the finite apertures of the mirrors, scattering and absorptive losses in the laser material itself, etc. In the absence of the amplifying mechanism, (1.61) becomes

$$\frac{\partial \phi}{\partial t} = -\frac{\phi}{\tau_c}, \quad (1.64)$$

the solution of which is $\phi(\tau) = \phi_0 \exp(-t/\tau_c)$.

The importance of (1.61) should be emphasized by noting that the right-hand side of this equation describes the net gain per transit of an electromagnetic wave passing through a laser material.

1.5.2 The Four-Level System

We will assume again that the transition from the pump band into the upper laser level occurs very rapidly. Therefore, the population of the pump band is negligible, i.e., $n_3 \approx 0$. With this assumption the rate of change of the two laser levels in a four-level system is

$$\frac{dn_2}{dt} = W_p n_0 - \left(n_2 - \frac{g_2}{g_1} n_1 \right) \sigma \phi c - \left(\frac{n_2}{\tau_{21}} + \frac{n_2}{\tau_{20}} \right), \quad (1.65)$$

$$\frac{dn_1}{dt} = \left(n_2 - \frac{g_2}{g_1} n_1 \right) \sigma \phi c + \frac{n_2}{\tau_{21}} - \frac{n_1}{\tau_{10}}, \quad (1.66)$$

$$n_{\text{tot}} = n_0 + n_1 + n_2. \quad (1.67)$$

From (1.65) it follows that the upper laser level population in a four-level system increases due to pumping and decreases due to stimulated emission and spontaneous emissions into level 1 and level 0. The lower level population increases due to stimulated and spontaneous emission and decreases by a radiationless relaxation process into the ground level. This process is characterized by the time constant τ_{10} . In an ideal four-level system the terminal level empties infinitely fast to the ground level. If we let $\tau_{10} \approx 0$, then it follows from (1.66) that $n_1 = 0$. In this case the entire population is divided between the ground level 0 and the upper level of the laser transition. The system appears to be pumping from a large source that is independent of the lower laser level. With $\tau_{10} = 0$ and $n_1 = 0$, we obtain the following rate equation for the ideal four-level system:

$$n = n_2 \quad (1.68)$$

and

$$n_{\text{tot}} = n_0 + n_2 \approx n_0 \quad \text{since} \quad n_2 \ll n_0. \quad (1.69)$$

Therefore, instead of (1.58), we have

$$\frac{\partial n_2}{\partial t} = -n_2\sigma\phi c - \frac{n_2}{\tau_f} + W_p n_0. \quad (1.70)$$

The fluorescence decay time τ_f of the upper laser level is given by

$$\frac{1}{\tau_f} = \frac{1}{\tau_{21}} + \frac{1}{\tau_{20}}, \quad (1.71)$$

where $\tau_{21} = A_{21}^{-1}$ is the effective radiative lifetime associated with the laser line. In the equation for the rate of change of the upper laser level we have again taken into account the fact that not all ions pumped to level 3 will end up at the upper laser level. It is

$$W_p = \eta_Q W_{03}, \quad (1.72)$$

where the quantum efficiency η_Q depends on the branching ratios, which are the relative relaxation rates for the ions along the various possible downward paths,

$$\eta_Q = \left(1 + \frac{\tau_{32}}{\tau_{31}} + \frac{\tau_{32}}{\tau_{30}} \right)^{-1} \leq 1. \quad (1.73)$$

As already indicated in the case of a three-level system the quantum efficiency is the probability of an absorbed pump photon producing an active atom in the upper laser level. Some of the absorbed pump photons will not produce an active ion in the upper laser level. Some, for example, may decay to manifolds other than the manifold containing the upper laser level while others may decay to the ground level by radiationless transitions. The equation which describes the rate of change of the photon density within the laser resonator is the same as in the case of the three-level system.

1.5.3 Comparison of Three- and Four-Level Lasers

The rate equation applicable to three- and four-level systems can be expressed by a single pair of equations, namely, (1.58 and 61), where $\gamma = 1 + g_2/g_1$ for a three-level system and $\gamma = 1$ for a four-level system. The factor γ can be thought of as an “inversion reduction factor” since it corresponds to the net reduction in the population inversion after the emission of a single photon. In a four-level system, see (1.70), we have $\gamma = 1$ since the population inversion density is reduced only by one for each photon emitted. For a three-level system, see (1.58), we have $\gamma = 2$ if we assume no degeneracy, i.e., $g_2/g_1 = 1$. This reflects the fact that in this case the population inversion is reduced by two for each stimulated emission of a photon because the

emitting photon is not only lost to the upper laser level, but also increases the lower laser level by one. The parameters τ_f and W_p are defined by (1.56, 59, 71, and 72) for the three- and four-level systems. The factor S in (1.61), which represents the initial noise level of ϕ due to spontaneous emission at the laser frequency, is small and needs to be considered only for initial starting of the laser action. It will be dropped from this point on.

A more detailed analysis of the laser rate equations can be found in [1.1, 3].

2. Properties of Solid-State Laser Materials

Materials for laser operation must possess sharp fluorescent lines, strong absorption bands, and a reasonably high quantum efficiency for the fluorescent transition of interest. These characteristics are generally shown by solids (crystals or glass) that incorporate in small amounts elements in which optical transitions can occur between states of inner, incomplete electron shells. Thus the transition metals, the rare earth (lanthanide) series, and the actinide series are of interest in this regard. The sharp fluorescence lines in the spectra of crystals doped with these elements result from the fact that the electrons involved in transitions in the optical regime are shielded by the outer shells from the surrounding crystal lattice. The corresponding transitions are similar to those of the free ions.

Most solid-state lasers emit radiation in the spectral region ranging from 400 nm to 3 μm that is based on 4f–4f transitions of rare earth and 3d–3d transitions of transition-metal-doped crystals. The spectroscopic properties of the laser transition determine the way the laser system may be designed and operated. The laser transition is characterized by its upper level lifetime τ_f , emission cross section σ , and gain bandwidth $\Delta\nu$.

For the continuous wave (cw) operation, the threshold for laser action is inversely proportional to the product $(\sigma \tau_f)$. Therefore, the value of $\sigma \tau_f$ is an important criterion whether a laser can be operated in the cw mode. For pulsed operation, the threshold becomes independent of the lifetime when the pump pulse duration is much shorter than τ_f . In Q-switching, energy storage time prior to Q-switching is limited by the upper level lifetime, while the emission cross section determines the magnitude of the gain. A long upper state lifetime permits the use of a long pump pulse, thereby increasing energy storage. This is particularly important for diode-pumped lasers where the pump source is power-limited, rather than energy-limited.

The gain bandwidth $\Delta\nu$ limits the tuning range of the laser system and determines the minimum pulselwidth that can be achieved in a mode-locked laser. Transition-metal ions mostly exhibit broadband emission, which offers broad tunability and generation of extremely short pulses.

In addition to a favorable combination of parameters describing the laser transition, a viable laser material must also possess pump bands that are within the emission spectrum of readily available pump sources, such as arc lamps and diode laser arrays. A broad absorption band is required of efficient arc lamp pumping, whereas a relatively narrow spectral pump band is acceptable for diode pumping.

The location of the lower laser level within the energy level diagram also has a profound impact on the pump source requirement. As explained in the previous

chapter, we have to distinguish between three- and four-level laser systems. In a four-level system, the lower laser level is above the ground state by an energy gap $\Delta E \gg kT$. Under these conditions the lower laser level is not thermally populated and it requires less energy to generate population inversion compared to a three-level laser where laser action terminates at the ground level and ground-state absorption overlaps laser emission.

In between the three- and four-level systems are the so-called quasi-three-level or quasi-four-level lasers. In these lasers the laser transition terminates at a level close to the ground level and is, therefore, thermally populated. The disadvantage of three-level and quasi-three-level lasers of requiring high pump intensities to reach threshold can be overcome to some extent if the laser material has other favorable characteristics which will be discussed later in this chapter.

The three principal elements leading to gain in a solid-state laser are as follows:

- *The host material* with its macroscopic mechanical, thermal, and optical properties, and its unique microscopic lattice properties.
- *The activator/sensitizer ions* with their distinctive charge states and free-ion electronic configurations.
- *The optical pump source* with its particular geometry, spectral irradiance, and temporal characteristic.

These elements are interactive and must be selected self-consistently to achieve a given system performance.

In this chapter we consider the properties of various host materials and activator/sensitizer combinations and we will describe some of the features of the most prominent laser materials.

The ruby laser, still in use today, provides a good illustration of a three-level system.

Nd:YAG, because of its high gain and good thermal and mechanical properties, is by far the most important solid-state laser for scientific, medical, industrial, and military applications. Nd:glass is important for laser fusion drivers because it can be produced in large sizes. Nd:YLF is a good material for a number of applications; the crystal exhibits lower thermal birefringence and has a higher energy storage capability (due to its lower gain coefficient) compared to Nd:YAG. The crystal Nd:YVO₄ has become a very attractive material for small diode-pumped lasers because of its large emission cross section and strong absorption at 809 nm.

The Nd:Cr:GSGG laser is an example of the application of a codoped laser material where the Cr³⁺ ions provide broad absorption bands for efficient flashlamp pumping and the energy absorbed by Cr³⁺ is transferred to the upper laser level of the Nd³⁺ ions.

Highly doped Er:YAG emits at a wavelength around 3 μm. This is an attractive wavelength for certain medical applications. Er:glass is of special importance because the laser output at 1.55 μm is in the eye-safe region of the spectrum.

The group of tunable lasers includes alexandrite, Ti:sapphire, and Cr:LiSAF. Laser emission is achieved by the 3d-electron of Cr³⁺ or Ti³⁺. In these “vibronic” lasers the emission of photons is closely coupled to the emissions of phonons in the

crystal lattice (vibrational quanta). Broad wavelength tunability is achieved because the energy of the laser transition can be partitioned between photons and phonons in a continuous fashion. In the Tm:YAG laser the considerable phonon broadening and high multiplicity of the Stark level of the 4f-electron provides tunability around $2\text{ }\mu\text{m}$.

The Yb:YAG laser is an example of a quasi-three-level laser. This diode-pumped laser has become a very important system for high power applications in the kilowatt range.

Overviews of laser host materials and active ions, as well as compilations of useful laser and materials parameters, can be found in a number of handbooks and summary articles [2.1–7].

2.1 Overview

The conditions for laser action at optical frequencies were first described by Schawlow and Townes [2.8] in 1958. The first demonstration of laser action by Maiman [2.9] was achieved in 1960 using ruby ($\text{Cr}^{3+}:\text{Al}_2\text{O}_3$), a crystalline solid system. The next step in the development of solid-state lasers was the operation of trivalent uranium in CaF_2 and divalent samarium in CaF_2 .

Laser action in neodymium-doped glass and the first continuously operating crystal laser using $\text{Nd}^{3+}:\text{CaWO}_4$ were reported in 1961. Since then laser action has been achieved from trivalent rare earths ($\text{Nd}^{3+}, \text{Er}^{3+}, \text{Ho}^{3+}, \text{Ce}^{3+}, \text{Tm}^{3+}, \text{Pr}^{3+}, \text{Gd}^{3+}, \text{Eu}^{3+}, \text{Yb}^{3+}$), divalent rare earths ($\text{Sm}^{2+}, \text{Dy}^{2+}, \text{Tm}^{2+}$), transition metals ($\text{Cr}^{3+}, \text{Ni}^{2+}, \text{Co}^{2+}, \text{Ti}^{3+}, \text{V}^{2+}$), and the actinide ion U^{3+} embedded in various host materials. Optically pumped laser action has been demonstrated in hundreds of ion-host crystal combinations covering a spectral range from the visible to the mid-infrared.

The exceptionally favorable characteristics of the trivalent neodymium ion for laser action were recognized at a relatively early stage in the search for solid-state laser materials. Thus, Nd^{3+} was known to exhibit a satisfactorily long fluorescence lifetime and narrow fluorescence linewidths in crystals with ordered structures, and to possess a terminal state for the laser transition sufficiently high above the ground state so that cw operation at room temperature was readily feasible. Therefore, this ion was incorporated as a dopant in a variety of host materials, that is, glass, CaWO_4 , CaMoO_4 , CaF_2 , LaF_3 , and so forth, in an effort to make use of its great potential. However, most of these early hosts displayed undesirable shortcomings, either from the standpoint of their intrinsic physical properties or because of the way in which they interacted with the Nd^{3+} ions. Finally, yttrium aluminum garnet (YAG) was explored by Geusic et al. [2.10] as a host for Nd^{3+} , and its superiority to other host materials was quickly demonstrated.

2.1.1 Host Materials

Solid-state host materials may be broadly grouped into crystalline solids and glasses. The host must have good optical, mechanical, and thermal properties to withstand the

severe operating conditions of practical lasers. Desirable properties include hardness, chemical inertness, absence of internal strain and refractive index variations, resistance to radiation-induced color centers, and ease of fabrication.

Several interactions between the host crystal and the additive ion restrict the number of useful material combinations. These include size disparity, valence, and spectroscopic properties. Ideally, the size and valence of the additive ion should match that of the host ion it replaces.

In selecting a crystal suitable for a laser ion host one must consider the following key criteria:

- (a) The crystal must possess favorable optical properties. Variations in the index of refraction lead to inhomogeneous propagation of light through the crystal, which results in poor beam quality.
- (b) The crystal must possess mechanical and thermal properties that will permit high-average-power operation. The most important parameters are thermal conductivity, hardness, and fracture strength.
- (c) The crystal must have lattice sites that can accept the dopant ions and that have local crystal fields of symmetry and strength needed to induce the desired spectroscopic properties. In general, ions placed in a crystal host should have long radiative lifetimes with emission cross sections near 10^{-20} cm^2 .
- (d) It must be possible to scale the growth of the impurity-doped crystal, while maintaining high optical quality and high yield.

Glasses

Glasses form an important class of host materials for some of the rare earths, particularly Nd^{3+} . The outstanding practical advantage compared to crystalline materials is the tremendous size capability for high-energy applications. Rods up to 1 m in length and over 10 cm in diameter and disks up to 90 cm in diameter and several centimeters thick have been produced. The optical quality is excellent, and glass, of course, is easily fabricated and takes a good optical finish. Laser ions placed in glass generally show a larger fluorescent linewidth than in crystals as a result of the lack of a unique and well-defined crystalline field surrounding the individual active atoms. Therefore, the laser thresholds for glass lasers have been found to run higher than their crystalline counterparts. Also, glass has a much lower thermal conductivity than most crystalline hosts. The latter factor leads to a large thermally induced birefringence and optical distortion in glass laser rods when they are operated at high average powers.

For bulk solid-state lasers, glass doped with Nd^{3+} or Er^{3+} is important and will be discussed in Sects. 2.3.2 and 2.4.2. In fiber oscillators and amplifiers, Er^{3+} -doped and Yb^{3+} -doped glass provides the active medium.

Oxides

A large number of crystalline host materials have been investigated since the discovery of the ruby laser. Crystalline laser hosts generally offer as advantages over glasses their

higher thermal conductivity, narrower fluorescence linewidths, and, in most cases, greater hardness. However, the optical quality and doping homogeneity of crystalline hosts are often poorer, and the absorption lines are generally narrower.

Sapphire. The first laser material to be discovered (ruby laser) employed sapphire as a host. The Al_2O_3 (sapphire) host is hard, with high thermal conductivity, and transition metals can readily be incorporated substitutionally for the Al. The Al site is too small for rare earths, and it is not possible to incorporate appreciable concentrations of these impurities into sapphire. Besides ruby, which is still used today, Ti-doped sapphire has gained significance as a tunable laser material. The properties of ruby and Ti-sapphire will be discussed in Sects. 2.2 and 2.5.2.

Garnets. Some of the most useful laser hosts are the synthetic garnets: yttrium aluminum garnet, $\text{Y}_3\text{Al}_5\text{O}_{12}$ (YAG); gadolinium gallium garnet, $\text{Gd}_3\text{Ga}_5\text{O}_{12}$ (GGG); and gadolinium scandium aluminum garnet, $\text{Gd}_3\text{Sc}_2\text{Al}_3\text{O}_{12}$ (GSGG). These garnets have many properties that are desirable in a laser host material. They are stable, hard, optically isotropic, and have good thermal conductivities, which permits laser operation at high average power levels.

In particular, yttrium aluminum garnet doped with neodymium (Nd:YAG) has achieved a position of dominance among solid-state laser materials. YAG is a very hard, isotropic crystal, which can be grown and fabricated in a manner that yields rods of high optical quality. At the present time, it is the best commercially available crystalline laser host for Nd^{3+} , offering low threshold and high gain. The properties of Nd:YAG are discussed in more detail in Sect. 2.3.1.

Besides Nd^{3+} , the host crystal YAG has been doped with Tm^{3+} , Er^{3+} , Ho^{3+} , and Yb^{3+} . Important members of this group of lasers include Yb:YAG, Er:YAG, Tm:YAG, and Nd:Cr:GSGG, which will be discussed in Sects. 2.6, 2.4.1, 2.5.4, and 2.3.3, respectively.

Aluminate. In 1969 a crystal host derived from the same $\text{Y}_2\text{O}_3\text{--}\text{Al}_2\text{O}_3$ system as YAG was discovered [2.11]. The crystal yttrium ortho aluminate (YAlO_3), termed YALO or YAP is the 1:1 compound or perovskite phase (YAG is the 3:5 compound or garnet phase). Many physical properties of YAP such as hardness and thermal conductivity are similar to those of YAG. In contrast to YAG, which is cubic and isotropic, YAP is orthorhombic and anisotropic. The anisotropy of the spectral properties of YAlO_3 enables one to select crystallographic orientations of the laser rod which optimize particular performance characteristics. Thus rod orientations can be chosen for high gain and low thresholds or, alternatively, for low gain and high energy storage required for Q-switching operation.

The fluorescence in Nd:YAlO₃ occurs predominantly in three strong lines at 1.0645, 1.0725, and 1.0795 μm . For light propagating along the *b* axis of the crystal, the gain is maximum at 1.0795 μm and is comparable to that of the 1.064- μm line in Nd:YAG. For a beam propagating along the *c* axis of Nd:YAlO₃, the gain is maximum at 1.064 μm , but it is only about one-half of that in Nd:YAG. Laser action in YAP has been achieved with ions including Nd^{3+} , Er^{3+} , Ho^{3+} , and Tm^{3+} .

Despite several major potential advantages of YAP over YAG, such as a polarized output, the capability of accepting a higher concentration of Nd, the possibility of varying gain by changing the rod axis, and lower costs because of faster crystal growth, the material disappeared from the market only 2 years after its introduction. YAP's disadvantages were lower efficiency than expected and erratic performance. It was found, for example, that during the growth process Fe^{3+} impurities enter the single crystal, which increase the absorption loss at $1.06\ \mu\text{m}$ and cause fluorescence quenching. However, over the years it has been possible to improve the optical quality of the YAP crystals and the material is commercially available again. For example, a diode-pumped Nd:YALO laser with 100 W output was reported in [2.12].

Oxysulfide. The application of rare earth oxysulfides as laser host materials has also been explored. The entire oxysulfide series, from lanthanum oxysulfide through lutetium oxysulfide and yttrium oxysulfide, possess the same (uniaxial) crystal structure. Thus, solid solutions of any concentration of rare earth activator in any other rare earth oxysulfide host are possible. Host materials which are transparent from 0.35 to $7\ \mu\text{m}$ include lanthanum, gadolinium, yttrium, and lutetium oxysulfide. Laser action was observed at $1.075\ \mu\text{m}$ for Nd and $\text{La}_2\text{O}_2\text{S}$. The lasing transition cross section of Nd:LOS was measured to be about one-third of that of Nd:YAG [2.13]. The optical quality of LOS crystals is far below the quality of YAG crystals.

Phosphates and Silicates

Laser oscillations have been produced in crystals of Nd^{3+} -doped calcium fluorophosphate or $\text{Ca}_5(\text{PO}_4)_3\text{F}$. The host crystal has the mineral name fluorapatite, from which the name FAP was coined [2.14]. This material is unique in that the Nd^{3+} fluorescence spectrum is predominantly concentrated in a single narrow and intense line, whereas the absorption spectrum is relatively broad and intense. Fluorapatites have low oscillation thresholds and high slope efficiencies, but they are soft, are susceptible to the formation of color centers, and their low thermal conductivity leads to strong thermal distortions. Because of these latter properties, FAP did not become a popular laser material. In 1972 another apatite became available: silicate oxyapatite or CaLaSOAP. In contrast to FAP, CaLaSOAP is considerably harder; however, its thermal conductivity is nearly equal to that of FAP and is only one-ninth the thermal conductivity of YAG.

The energy storage in Nd:SOAP is about five times that of YAG. In addition to SOAP's high energy storage, the material has the potential that large crystals can be grown inexpensively. Crystals 15 cm long with diameters as large as 1.2 cm have been grown at growth rates of 2–3 mm/h. It was reported that the optical quality of SOAP rods 7.5 by 0.6 cm was comparable to the quality of YAG rods with undetectable scattering and less than 0.5 fringe. The main disadvantages of SOAP are low laser damage threshold and low thermal conductivity. Physical, spectroscopic, and laser characteristics of neodymium-doped silicate oxyapatite are reported in [2.15].

Laser action has been achieved in the neodymium pentaphosphates $\text{YNdP}_5\text{O}_{14}$, $\text{LaNdP}_5\text{O}_{14}$, and $\text{ScNdP}_5\text{O}_{14}$ [2.16–19]. An outstanding property of these materials is

the high gain which can be achieved as a result of the favorable position of the $^4I_{15/2}$ manifold relative to the upper laser states. As a result of the high gain, cw oscillation at room temperature has been obtained in $\text{ScNdP}_5\text{O}_{14}$ with a pump power of only 4 mW, using an argon laser as a pump source [2.19].

Tungstates, Molybdates, Vanadates, and Beryllates

CaWO_4 was the most popular material for Nd before YAG became commercially available. The rare earth substitutes for Ca, but only in the trivalent oxidation state, and hence charge compensation is needed. The material is very prone to fracture, even when well annealed, and thus considerable care is required when the boules are being fabricated into laser rods. The thermal conductivity is three to four times greater than that of the glasses.

Sodium rare earth molybdates and tungstates have served as host materials for active ions. In these materials, which are similar to CaWO_4 and CaMoO_4 , one-half of the calcium atoms are randomly replaced with sodium and the other half with rare earth. Laser action has been observed from Nd^{3+} in $\text{NaLa}(\text{MoO}_4)_2$ and $\text{NaGd}(\text{WO}_4)_2$ and from $\text{NaNd}(\text{WO}_4)_2$. Interest in $\text{Nd:NaLa}(\text{MoO}_4)_2$ stems from the fact that this material has a low gain, intermediate to Nd:glass and Nd:YAG, and thus is capable of higher efficiencies than the former material and greater energy storage than the latter material. The thermal conductivity of $\text{Nd:NaLa}(\text{MoO}_4)$ is three times that of the Nd:glass. However, the lower thermal conductivity and the higher thermal expansion coefficient of $\text{Nd:NaLa}(\text{MoO}_4)_2$ as compared to Nd:YAG result in a Nd:NaLa(MoO_4)₂ laser rod having much greater thermal stress than a Nd:YAG rod when both are subjected to the same average input power during lasing action.

Nd^{3+} -doped yttrium orthovanadate (YVO_4) was known for a long time as a material having a low threshold [2.21]. However, early studies of this crystal were hampered by severe crystal growth problems, and as a result YVO_4 was discarded as a host. With the emergence of diode pumping, Nd:YVO₄ has become an important solid-state laser material because it has very attractive features, such as a large stimulated emission cross section and a high absorption of the pump wavelength. Also the growth problem has been overcome for the small crystals required with diode pump sources. Details of this laser crystal will be discussed in Sect. 2.3.5.

Gadolinium vanadate (Nd:GdVO₄) is an interesting laser crystal because it has a thermal conductivity similar to that of Nd:YAG and an absorption and emission cross section similar to that of Nd:YVO₄. Recently high quality Nd:GdVO₄ crystals have been grown with a floating zone method [2.20].

A candidate of the beryllates is Nd^{3+} -doped lanthanum beryllate (Nd:La₂Be₂O₅) [2.22]. Since La³⁺ is the largest of the rare earth ions, La₂Be₂O₅ (BEL) has large distribution coefficients for other trivalent rare earth ions. For this reason boules of BEL with high concentrations of rare earth ions are much more readily grown than are YAG and other hosts based on the yttrium ion. Since the thermal conductivity and the cross section are considerably lower than those of YAG the material has not found applications.

Fluorides

The divalent fluorides are relatively soft, isotropic crystals. Rare earth-doped CaF₂ crystals have been studied extensively [2.23, 24], since this material was the host of many early solid-state lasers.

Doping of fluorides with trivalent rare earth ions requires charge compensation which complicates the crystal growth process. The important representative of this crystal family is yttrium lithium fluoride (YLiF₄), a uniaxial crystal. YLiF₄ is transparent to 150 nm. Therefore, high-current-density xenon flashlamps which emit strongly in the blue and near-ultraviolet can be used as pump sources without damage to the material. The most common dopant of YLF is Nd³⁺. Nd:YLF offers a reduction in thermal lensing and birefringence combined with improved energy storage relative to Nd:YAG. The thermomechanical properties of Nd:YLF, however, are not as good as those of Nd:YAG. Details of Nd:YLF are discussed in Sect. 2.3.4.

Ceramics

In recent years, polycrystalline Nd:YAG ceramics have been produced with good optical quality. Lasers that have incorporated a Nd:YAG ceramic as active element have achieved power outputs and efficiencies comparable to single crystal Nd:YAG lasers [2.25–27]. Previously, transparent Nd:doped ceramics were plagued with high-scattering losses. Improved fabrication methods in the ceramic formation and sintering process have led to polycrystalline materials with very narrow grain boundaries and a very low porosity. These new highly transparent Nd:YAG ceramics are characterized by a very low-scattering loss.

Compared to Nd:YAG single crystals, Nd:YAG ceramics can be produced with higher Nd concentration and larger size. Nd:YAG ceramics are promising candidates for microchip lasers because they combine the advantage of Nd:YAG and Nd:YVO₄, which are the two leading materials for these applications. Ceramics can be highly doped for efficient pump absorption similar to Nd:YVO₄, and the material has the conductivity of Nd:YAG, which is twice as high as that of Nd:YVO₄.

2.1.2 Active Ions

Before proceeding to a discussion of the active laser ions, we will review briefly the nomenclature of atomic energy levels.

Different energy states of electrons are expressed by different quantum numbers. The electrons in an atom are characterized by a principal quantum number n , an orbital angular momentum l , the orientation of the angular momentum vector m , and a spin quantum number s . A tradition from the early days of line series allocation has established the following method of designating individual electronic orbits: a number followed by a letter symbolizes the principal quantum number n and the angular momentum number l , respectively. The letters s, p, d, f stand for $l = 0, 1, 2, 3$, respectively. For example, a 3d electron is in an orbit with $n = 3$ and $l = 2$.

To designate an atomic energy term one uses by convention capital letters with a system of subscripts and superscripts. The symbol characterizing the term is of the form $^{2S+1}L_J$, where the orbital quantum numbers $L = 0, 1, 2, 3, 4, 5$, are expressed by the capital letters S, P, D, F, G, H, I. A superscript to the left of the letter indicates the value $(2S + 1)$, that is, the multiplicity of the term due to possible orientation of the resultant spin S . Thus a one-electron system ($S = 1/2$) has a multiplicity 2. L and S can combine to a total angular momentum J , indicated by a subscript to the right of the letter. Thus the symbol $^2P_{3/2}$ shows an energy level with an orbital quantum number $L = 1$, a spin of $S = 1/2$, and a total angular momentum of $J = 3/2$. The complete term description must include the configuration of the excited electron, which precedes the letter symbol. Thus the ground state of lithium has the symbol $2s\ ^2S_{1/2}$.

When an atom contains many electrons, the electrons that form a closed shell may be disregarded and the energy differences associated with transitions in the atom may be calculated by considering only the electrons outside the closed shell.

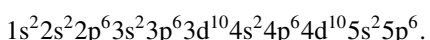
In describing the state of a multielectron atom, the orbital angular momenta and the spin angular momenta are added separately. The sum of the orbital angular momenta are designated by the letter L , and the total spin is characterized by S . The total angular momentum J of the atom may then be obtained by vector addition of L and S . The collection of energy states with common values of J , L , and S is called a term.

In the following section, a qualitative description is given of some of the prominent features of the most important rare earth, actinide, and transition metal ions.

Rare Earth Ions

The rare earth ions are natural candidates to serve as active ions in solid-state laser materials because they exhibit a wealth of sharp fluorescent transitions representing almost every region of the visible and near-infrared portions of the electromagnetic spectrum. It is a characteristic of these lines that they are very sharp, even in the presence of the strong local fields of crystals, as a result of the shielding effect of the outer electrons.

The ground-state electronic configuration of the rare earth atom consists of a core which is identical to xenon, plus additional electrons in higher orbits. In xenon, the shells with quantum numbers $n = 1, 2, 3$ are completely filled. The shell $n = 4$ has its s, p, and d subshells filled, whereas the 4f subshell capable of accommodating 14 electrons is completely empty. However, the $n = 5$ shell has acquired its first 8 electrons which fill the 5s and 5p orbits. The electronic configuration for xenon is

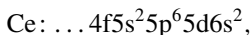


Elements beyond xenon, which has the atomic number 54, have this electronic structure and, in addition, have electrons in the 4f, 5d, 6s, etc., orbits. Cesium, barium, and lanthanum are the elements between xenon and the rare earths. Cs has one, Ba has two 6s electrons, and La has in addition one electron in the 5d orbit. Rare earth

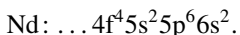
Table 2.1. Electronic configuration of trivalent rare earths

Element number	Trivalent rare earth	Number of 4f electrons	Ground state
58	Cerium, Ce ³⁺	1	² F _{5/2}
59	Praseodymium, Pr ³⁺	2	³ H ₄
60	Neodymium, Nd ³⁺	3	⁴ I _{9/2}
61	Promethium, Pm ³⁺	4	⁵ I ₄
62	Samarium, Sm ³⁺	5	⁶ H _{5/2}
63	Europium, Eu ³⁺	6	⁷ F ₀
64	Gadolinium, Gd ³⁺	7	⁸ S _{7/2}
65	Terbium, Tb ³⁺	8	⁷ F ₆
66	Dysprosium, Dy ³⁺	9	⁶ H _{15/2}
67	Holmium, Ho ³⁺	10	⁵ I ₈
68	Erbium, Er ³⁺	11	⁴ I _{15/2}
69	Thulium, Tm ³⁺	12	³ H ₆
70	Ytterbium, Yb ³⁺	13	² F _{7/2}
71	Lutetium, Lu ³⁺	14	¹ S ₀

elements begin with the filling of the inner vacant 4f orbitals. For example, the first rare earth element cerium has only one electron in the f orbit:



and the important rare earth neodymium has four electrons in the f orbit

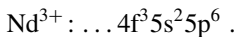


Since the first nine shells and subshells up to 4d¹⁰ are completely filled, only the outer electron configuration is indicated.

In crystals, rare earth ions are normally trivalent, but under appropriate conditions the valence state can also be divalent. When a trivalent ion is formed the atom gives up its outermost 6s electrons; the atom loses also its 5d electron if it has one, otherwise one of the 4f electrons is lost. For example, trivalent Ce has the electronic configuration



and trivalent Nd has the configuration



As one can see, the trivalent ions of rare earths have a simpler configuration than the corresponding atoms. Ions from the rare earths differ in electronic structure only by the number of electrons in the 4f shell as illustrated in Table 2.1. When a divalent rare earth ion is formed, the atom gives up its outermost 6s electrons.

The fluorescence spectra of rare earth ions arise from electronic transitions between levels of the partially filled 4f shell. Electrons present in the 4f shell can be raised by light absorption into unoccupied 4f levels. The 4f states are well shielded by the filled 5s and 5p outer shells. As a result, emission lines are relatively narrow and the energy level structure varies only slightly from one host to another. The

effect of the crystal field is normally treated as a perturbation on the free-ion levels. The perturbation is small compared to spinorbit and electrostatic interactions among the 4f electrons. The primary change in the energy levels is a splitting of each of the free-ion levels in many closely spaced levels as a result of the Stark effect of the crystal field. In crystals the free-ion levels are then referred to as manifolds. Figure 2.2 provides a nice illustration of the splitting of the Nd³⁺ manifolds into sublevels as a result of the YAG crystal field.

Neodymium. Nd³⁺ was the first of the trivalent rare earth ions to be used in a laser, and it remains by far the most important element in this group. Stimulated emission has been obtained with this ion incorporated in at least 100 different host materials, and a higher power level has been obtained from Nd lasers than from any other four-level material. The principal host materials are YAG and glass. In these hosts, stimulated emission is obtained at a number of frequencies within three different groups of transitions centered at 0.9, 1.06, and 1.35 μm. Radiation at these wavelengths results from $^4F_{3/2} \rightarrow ^4I_{9/2}$, $^4I_{11/2}$, $^4I_{13/2}$ transitions, respectively.

The nomenclature of the energy levels may be illustrated by a discussion of the Nd³⁺ ion. This ion has three electrons in the 4f subshell. In the ground state their orbits are so aligned that the orbital angular momentum adds up to $3 + 2 + 1 = 6$ atomic units. The total angular momentum $L = 6$ is expressed by the letter I. The spins of the three electrons are aligned parallel to each other, providing an additional $3/2$ units of angular momentum, which, when added antiparallel to the orbital angular momentum, gives a total angular momentum of $6 - 3/2 = 9/2$ units. According to the quantum rules for the addition of angular momenta, the vector sum of an orbital angular momentum of 6 and a spin angular momentum of $3/2$ may result in the following four values of the total angular momentum: $9/2$, $11/2$, $13/2$, and $15/2$. The levels corresponding to these values are $^4I_{9/2}$, $^4I_{11/2}$, $^4I_{13/2}$, and $^4I_{15/2}$. The first of these, which has the lowest energy, is the ground state; the others are among the first few excited levels of Nd³⁺. These levels are distinguished by the orientation of the spins with respect to the resultant orbital angular momentum. Other excited levels are obtained when another combination of the orbital angular momenta is chosen.

The most important Nd laser materials are described in Sect. 2.3.

Erbium. Laser action in erbium has been demonstrated in a variety of garnets, fluorides, and glasses. Erbium laser performance is not very impressive in terms of efficiency or energy output. However, erbium has attracted attention because of two particular wavelengths of interest. A crystal such as YAG highly doped with erbium produces an output around 2.9 μm, and erbium-doped phosphate glass generates an output at 1.54 μm (see Sect. 2.4). Both of these wavelengths are absorbed by water, which leads to interesting medical applications in the case of the 2.9 μm lasers and to eye safe military rangefinders in the case of the shorter wavelength.

The wavelength at 1.54 μm arises from a transition between the $^4I_{13/2}$ state and the $^4I_{15/2}$ ground state of Er³⁺. At room temperature all levels of the terminal $^4I_{15/2}$ manifold are populated to some degree; thus, this transition forms a three-level laser scheme with a correspondingly high threshold.

The wavelength at 2.9 μm stems from a laser transition from the $^4\text{I}_{11/2}$ to the $^4\text{I}_{13/2}$ state. The lower laser level of this transition is considerably above the ground state, similar to the 1.06 μm transition in Nd^{3+} . Therefore this transition is four level in nature. However, complicated energy transfer mechanisms between the levels and a lower laser level which has a longer lifetime compared to the upper laser level has prevented cw operation at this transition.

Holmium. Laser action in Ho^{3+} has been reported in many different host materials [2.28]. Because the terminal level is only about 250 cm^{-1} above ground level, the lower laser level has a relatively high thermal population at room temperature. While Ho:YAG and Ho:YLF have proven to be efficient lasers, operation has been limited in most cases to cryogenic temperatures, which will depopulate the lower laser level. Previous efforts in flashlamp pumped 2 μm lasers have concentrated on Er:Tm:Ho doped YAG and YLF.

It was discovered that Cr-sensitized Tm:Ho:YAG offers several advantages over the Er-sensitized materials. In a Cr:Tm:Ho:YAG laser, a very efficient energy transfer process between the co-dopants takes place. Cr^{3+} acts to efficiently absorb flashlamp energy, which is then transferred to Tm with a transfer quantum efficiency approaching 2 (two photons in the IR for each pump photon). From Tm the energy is efficiently transferred to Ho . Lasing occurs at the $^5\text{I}_7 - ^5\text{I}_8$ Ho transition at a wavelength of 2080 nm [2.29]. Laser diode pumping of a Tm:Ho:YAG laser via an absorption line in Tm^{3+} at 780 nm is also possible [2.30]. Chromium doping is not necessary in this case (see also Sect. 2.5.4).

Thulium. Efficient flashlamp and laser diode-pumped laser operation has been achieved in $\text{Tm}^{3+}:\text{YAG}$ and $\text{Tm}^{3+}:\text{YLF}$ codoped either with Cr^{3+} or Ho^{3+} . The output wavelength for the $^3\text{F}_4 - ^3\text{H}_6$ transition is 2.01 μm . The thulium ion has an absorption at 785 nm, which is useful for diode pumping. With diode pumping Tm:YAG lasers have been designed with output powers in excess of 100 W. Cr doping provides for efficient absorption of the flashlamp radiation. Flashlamp-pumped Cr:Tm:YAG can achieve tunable output between 1.945 and 1.965 μm .

Thulium- and thulium-sensitized holmium lasers have outputs in the 2 μm region, a wavelength of interest for coherent radar systems, remote sensing, and medical applications. The possibility of pumping thulium-doped crystals, with readily available powerful GaAlAs laser diodes at 785 nm, has stimulated interest in these materials. Energy transfer and other relevant spectroscopic data of the Tm:YAG laser are covered in Sect. 2.5.4.

Praseodymium, Gadolinium, Europium, Ytterbium, Cerium. Laser action in all these triply ionized rare earths has been reported; however, only marginal performance was obtained in hosts containing these ions with the exception of ytterbium. Diode-pumped Yb:YAG has become an important laser and is described in Sect. 2.6.

Recently another Yb-doped crystal, namely Yb:KGW which is yttrium tungstate, $\text{KGd}(\text{WO}_4)_2$ has found applications in mode locked lasers. This crystal has a high

emission cross section, broad emission spectrum from 1020 to 1060 nm, and can be pumped with diode lasers at 940 or 980 nm. Diode-pumped Yb:KGW lasers have been developed for the generation of femto second pulses at an output wavelength of 1048 nm.

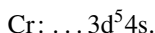
Samarium, Dysprosium, Thulium. The divalent rare earths Sm^{2+} , Dy^{2+} , and Tm^{2+} have an additional electron in the 4f shell, which lowers the energy of the 5d configuration. Consequently, the allowed 4f–5d absorption bands fall in the visible region of the spectrum. These bands are particularly suitable for pumping the laser systems. Tm^{2+} , Dy^{2+} , and Sm^{2+} have been operated as lasers, all in a CaF_2 host. For laser operation, these crystals must be refrigerated to at least 77 K.

Actinide Ions

The actinides are similar to the rare earths in having the 5f electrons partially shielded by 6s and 6p electrons. Most of the actinide elements are radioactive, and only uranium in CaF_2 has been successfully used in a laser [2.24]. The host was doped with 0.05% uranium. Laser action occurred at $2.6\ \mu\text{m}$ between a metastable level and a terminal level some $515\ \text{cm}^{-1}$ above the ground state.

Transition Metals

Important members of the transition-metal group include chromium and titanium. The chromium atom has 18 electrons in orbitals which make up the filled core. The outer configuration includes six electron in the d and s orbitals:

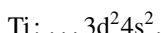


The trivalent chromium ion has given up three electrons from these outer two sets of orbitals

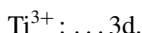


leaving three electrons in the 3d orbitals. These electrons determine the optical properties of the ion. Since they are unshielded by outer shells of electrons, in contrast to rare earth ions, the optical properties of transition-metal ions are strongly influenced by the host crystal field.

The titanium atom has the same electronic configuration as chromium, but only four electrons in the d and s orbitals:



The trivalent titanium has only a single electron in the d orbital:



Transition metal/host crystal combinations that have resulted in important lasers include ruby ($\text{Cr}^{3+}:\text{Al}_2\text{O}_3$), alexandrite ($\text{Cr}^{3+}:\text{BeAl}_2\text{O}_4$), $\text{Cr}^{3+}:\text{LiSAF}$

(Cr³⁺:LiSrAlF₆), and Ti-sapphire (Ti³⁺:Al₂O₃) lasers, which are discussed in separate sections.

In addition, Cr:forsterite (Cr⁴⁺:Mg₂SiO₄) need to be mentioned because this laser is employed in the generation of femtosecond pulses. Both pulsed and cw laser operation has been achieved in Cr⁴⁺:Mg₂SiO₄ with Nd:YAG lasers at 1.06 μm and 532 nm as pump sources. The tuning range covers the spectral region from 1167 to 1345 nm. A distinguishing feature of laser actions in Cr⁺:Mg₂SiO₄ is that the lasing ion is not trivalent chromium (Cr³⁺) as in the case with other chromium-based lasers, but the active ion in this crystal is tetravalent chromium (Cr⁴⁺) which substitutes for silicon (Si⁴⁺) in a tetrahedral site.

Several other transition-metal-based lasers that have been offered commercially at one time or another include Cr:GSGG, Cr:KZnF₃, and Co:MgF₂. We will briefly come back to these lasers in Sect. 2.5.

2.2 Ruby

The ruby laser, Cr³⁺:Al₂O₃, is a three-level system, which makes it necessary to pump the crystal at high intensity to achieve at least inversion. Consequently, the overall system efficiency is very low, which is the main reason for its limited use today. Ruby chemically consists of sapphire (Al₂O₃) in which a small percentage of the Al³⁺ has been replaced by Cr³⁺. This is done by adding small amounts of Cr₂O₃ to the melt of highly purified Al₂O₃. Sapphire has the best thermomechanical properties of all solid-state laser materials. The crystal is very hard, has high thermal conductivity, and can be grown to very high quality by the Czochralski method. The Cr³⁺ ion has three d electrons in its unfilled shell; the ground state of the free ion is described by the spectroscopic symbol ⁴A. The amount of doping is nominally 0.05 wt.% Cr₂O₃.

A simplified energy level diagram of ruby is shown in Fig. 2.1. In ruby lasers, population inversion with respect to the ²E level is obtained by optically pumping Cr³⁺ ions from the ⁴A₂ ground state to the broad pump bands ⁴T₂ and ⁴T₁. The lifetime at the pump bands, which are each about 1000-nm wide, located in the green (18,000 cm⁻¹) and in the violet (25,000 cm⁻¹), is extremely short, with the ions returning to a metastable state ²E that has a fluorescent life-time of 3 ms. This metastable level is split into two sublevels with a separation of $\Delta E = 29 \text{ cm}^{-1}$. The upper sublevel is the $2\bar{\text{A}}$ and the lower one the $\bar{\text{E}}$ sublevel. The two transitions ($\bar{\text{E}} \rightarrow {}^4\bar{\text{A}}_2$ and $2\bar{\text{A}} \rightarrow {}^4\text{A}_2$) are referred to as the R_1 and R_2 lines, which are located at the end of the visible region at 594.3 and 692.9 nm, respectively. The width of these fluorescent lines is $\Delta\nu = 330 \text{ GHz}$ at room temperature and they are homogeneously broadened because of the interaction of the Cr³⁺ ions with lattice vibrations. The two R lines are connected to each other by a very fast nonradiative decay; thermalization of the population occurs, and this results in the lower-lying $\bar{\text{E}}$ level being the more heavily populated.

At thermal equilibrium the difference in population between the $\bar{\text{E}}$ and $2\bar{\text{A}}$ level is determined by the Boltzmann factor $\kappa = \exp(\Delta E/kT)$. At room temperature the Boltzmann factor is $\kappa = 0.87$. The R_1 line attains laser threshold before the R_2 line

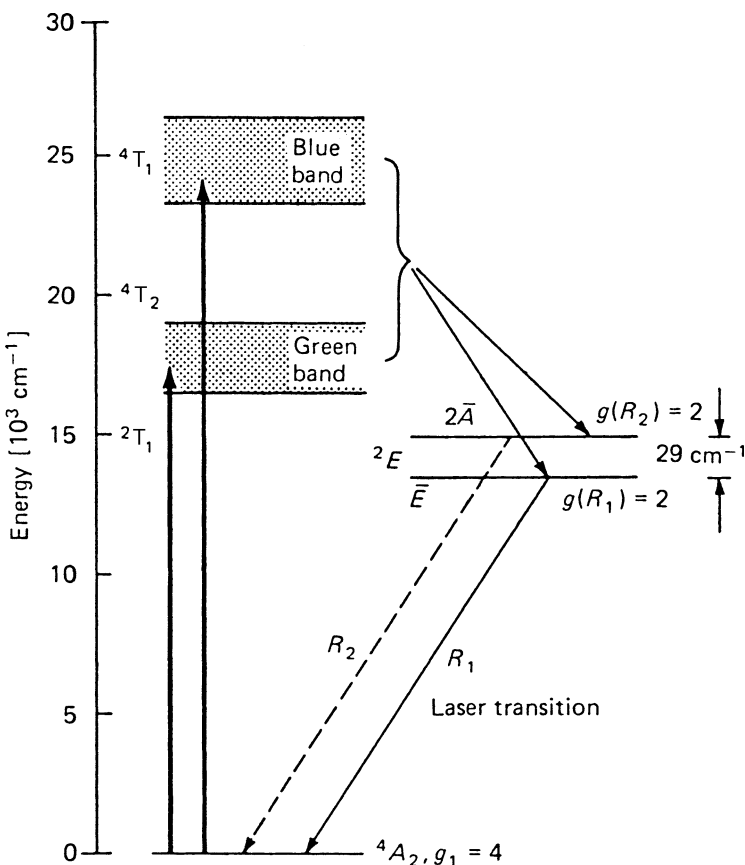


Fig. 2.1. Important energy levels of Cr^{3+} in ruby (separation of $2E$ levels not to scale)

because of the higher inversion. Once laser action commences in the R_1 line, the \bar{E} level becomes depleted and population transfer from the nearby $2\bar{A}$ level proceeds at such a fast rate that the threshold level is never reached for the R_2 line. Therefore, the entire initial population of the two states decays through R_1 emission. If we compare the energy-level diagram of ruby with our simplified scheme of a three-level system in Fig. 1.6, the levels 4T_1 and 4T_2 jointly constitute level 3, whereas 2E and $^2\bar{A}_2$ states represent levels 2 and 1, respectively. We can write

$$n_2 = n_2(R_1) + n_2(R_2) \quad (2.1)$$

for the metastable level and n_1 for the ground level. Threshold and gain in ruby depends only on the population of level $n_2(R_1)$. However, in relating gain and threshold to the population of the ground level n_1 or to the total number of Cr^{3+} ions n_{tot} , one has to take the population of $n_2(R_2)$ into account. In ruby all levels are degenerate, that is,

$$g(n_1) = 4, \quad g(R_1) = g(R_2) = 2. \quad (2.2)$$

Because of the higher degeneracy of the ground state, amplification occurs when the R_1 level is at least one-half as densely populated as the ground state. Since

$$n_2(R_1) + n_2(R_2) + n_1 = n_{\text{tot}}, \quad (2.3)$$

we have the following population at threshold (300 K)

$$\begin{aligned} n_2(R_1) &= \frac{n_{\text{tot}}}{3 + \kappa} = 0.26n_{\text{tot}}, \\ n_2(R_2) &= \frac{\kappa n_{\text{tot}}}{3 + \kappa} = 0.22n_{\text{tot}}, \\ n_1 &= \frac{2n_{\text{tot}}}{3 + \kappa} = 0.52n_{\text{tot}}. \end{aligned} \quad (2.4)$$

Thus we must have just under one-half of the atoms in the two upper levels in order to reach threshold. With a Cr³⁺ concentration of $n_{\text{tot}} = 1.58 \times 10^{19} \text{ cm}^{-3}$ and a photon energy of $h\nu = 2.86 \times 10^{-19} \text{ W s}$, we obtain for the energy density at the metastable level required to achieve transparency in ruby according to (2.4),

$$J_{\text{th}} = \left(\frac{\kappa + 1}{\kappa + 3} \right) n_{\text{tot}} h\nu = 2.18 \text{ J/cm}^3. \quad (2.5)$$

The small-signal gain coefficient in ruby is

$$g_0 = \sigma \left[n_2(R_1) - \frac{g(R_1)n_1}{g(n_1)} \right], \quad (2.6)$$

where σ is the stimulated emission cross section of the R_1 line and $n_2(R_1)$ is the population density of the E level.

Since $\sigma = \sigma_{12}g(n_1)/g(R_1)$, the gain coefficient can be expressed as (assuming $\kappa = 1$)

$$g_0 = \alpha_0 \left(\frac{2n_2}{n_{\text{tot}}} - 1 \right), \quad (2.7)$$

where $\alpha_0 = \sigma_{12}n_{\text{tot}}$ is the absorption coefficient of ruby. Ruby has an absorption cross section of $\sigma_{12} = 1.22 \times 10^{-10} \text{ cm}^2$ and an absorption coefficient of $\alpha_0 = 0.2 \text{ cm}^{-1}$. With all the chromium ions in the ground state ($n_2 = 0$), the gain of the unpumped ruby crystal is $g_0 = -\alpha_0$. With all the ions in the upper levels ($n_2 = n_{\text{tot}}$), the maximum gain coefficient is $g_0 = \alpha_0$. (with the approximation $\kappa = 1$)

The example of ruby illustrates very clearly the drawbacks of a three-level system.

- (a) Compared to a four-level laser, three-level lasers such as ruby and Er:glass, and quasi-three-level lasers such as Yb:YAG require high-pump intensities because a certain amount of pump power is required just to achieve transparency in the material.
- (b) Since three-level and quasi-three-level lasers absorb at the laser wavelength unless pumped to inversion, any portion of the laser crystal which is shielded from the pump light, for example, by the rod holder, will present a high absorption loss.

Despite these obvious drawbacks, three-level lasers have other redeeming features, such as desirable wavelength or a particular efficient pump method, which makes these lasers attractive. For example, the ruby laser emits in the visible region, has broad absorption bands at a wavelength region particularly well-suited for flashlamp pumping, and has a long fluorescent lifetime and a reasonably large stimulated emission cross section.

2.3 Nd:Lasers

From the large number of Nd:doped materials, the lasers discussed in more detail in this chapter have gained prominence. Nd:YAG, because of its high gain and good thermal and mechanical properties, is by far the most important solid-state laser for scientific, medical, industrial, and military applications. Nd:glass is important for laser fusion drivers because it can be produced in large sizes. Nd:Cr:GSGG has received attention because of the good spectral match between the flashlamp emission and the absorption of the Cr ions. An efficient energy transfer between the Cr and Nd ions results in a highly efficient Nd:laser. Nd:YLF is a good material for a number of applications, because the output is polarized, and the crystal exhibits low thermal birefringence. It has a higher energy storage capability (due to its low gain coefficient) compared to Nd:YAG and its output wavelength matches that of phosphate Nd:glass, therefore modelocked and Q-switched Nd:YLF lasers have become the standard oscillators for large glass lasers employed in fusion research. Nd:YVO₄ has become a very attractive material for small diode-pumped lasers because of its large emission cross section and strong absorption at 809 nm.

2.3.1 Nd:YAG

The Nd:YAG laser is by far the most commonly used solid-state laser. Neodymium-doped yttrium aluminum garnet (Nd:YAG) possesses a combination of properties uniquely favorable for laser operation. The YAG host is hard, of good optical quality, and has a high thermal conductivity. Furthermore, the cubic structure of YAG favors a narrow fluorescent linewidth, which results in high gain and low threshold for laser operation. In Nd:YAG, trivalent neodymium substitutes for trivalent yttrium, so charge compensation is not required.

Physical Properties

In addition to the very favorable spectral and lasing characteristics displayed by Nd:YAG, the host lattice is noteworthy for its unusually attractive blend of physical, chemical, and mechanical properties. The YAG structure is stable from the lowest temperatures up to the melting point, and no transformations have been reported in the solid phase. The strength and hardness of YAG are lower than ruby but still high enough so that normal fabrication procedures do not produce any serious breakage problems.

Table 2.2. Physical and optical properties of Nd:YAG

Chemical formula	Nd:Y ₃ Al ₅ O ₁₂
Weight % Nd	0.725
Atomic % Nd	1.0
Nd atoms/cm ³	1.38×10^{20}
Melting point	1970°C
Knoop hardness (kg/mm ²)	1320
Density	4.56 g/cm ³
Tensile strength	200 MPa
Modulus of elasticity	310 Gpa
Poisson ratio	0.30
Thermal expansion coefficient	
[100] orientation	$8.2 \times 10^{-6}/^\circ\text{C}$,
[110] orientation	$7.7 \times 10^{-6}/^\circ\text{C}$,
[111] orientation	$7.8 \times 10^{-6}/^\circ\text{C}$,
Linewidth	120 GHz
Stimulated emission cross section	
$R_2 - Y_3$	$\sigma = 6.5 \times 10^{-19} \text{ cm}^2$
${}^4\text{F}_{3/2} - {}^4\text{I}_{11/2}$	$\sigma = 2.8 \times 10^{-19} \text{ cm}^2$
Fluorescence lifetime	230 μs
Photon energy at 1.06 μm	$h\nu = 1.86 \times 10^{-19} \text{ J}$
Index of refraction	1.82 (at 1.0 μm)

Pure Y₃Al₅O₁₂ is a colorless, optically isotropic crystal which possesses a cubic structure characteristic of garnets. In Nd:YAG about 1% of Y³⁺ is substituted by Nd³⁺. The radii of the two rare earth ions differ by about 3%. Therefore, with the addition of large amounts of neodymium, strained crystals are obtained, indicating that either the solubility limit of neodymium is exceeded or that the lattice of YAG is seriously distorted by the inclusion of neodymium. Some of the important physical properties of YAG are listed in Table 2.2 together with optical and laser parameters [2.31–38]. Thermal properties of Nd:YAG are summarized in Table 2.3.

When operating a laser cw, or at a pulse repetition frequency higher than the inverse of the fluorescence lifetime, maintaining good extraction efficiency depends on having a beam intensity significantly larger than the saturation intensity $I_s = h\nu/\sigma \tau_f$, where $h\nu$ is the photon energy, σ is the emission cross section, and τ_f is the fluorescence lifetime. In low repetition rate pulsed systems the fluence in the resonator must be

Table 2.3. Thermal properties of Nd:YAG

Property	Units	300 K	200 K	100 K
Thermal conductivity	W cm ⁻¹ K ⁻¹	0.14	0.21	0.58
Specific heat	W s g ⁻¹ K ⁻¹	0.59	0.43	0.13
Thermal diffusivity	cm ² s ⁻¹	0.046	0.10	0.92
Thermal expansion	K ⁻¹ × 10 ⁻⁶	7.5	5.8	4.25
$\partial n/\partial T$	K ⁻¹	7.3×10^{-6}	—	—

higher than the saturation fluence $J_s = h\nu/\sigma$. From the parameters listed in Table 2.2 it follows that for Nd:YAG a saturation intensity $I_s = 2.9 \text{ kW/cm}^2$ and a saturation fluence $J_s = 0.67 \text{ J/cm}^2$.

Laser Properties

Figure 2.2 depicts the energy level diagram of Nd:YAG. Stark splitting of the manifolds are shown on the right-hand side. Each of the $^{2S+1}L_J$ manifolds is split by the crystal field into $J + 1/2$ sublevels. The actual laser transitions occur between these individual Stark levels. The heavy line in Fig. 2.2 indicates the main laser transition in Nd:YAG having a wavelength of 1064 nm. The dashed lines represent transitions leading to 1.3 μm and 946 nm radiation.

The laser transition at 1064 nm occurs between the upper Stark level of the $^4F_{3/2}$ manifold (R_2 sublevel) and a Stark level within the $^4I_{11/2}$ manifold (Y_3 sublevel). At room temperature only 40% of the $^4F_{3/2}$ population is at level R_2 ; the remaining 60%

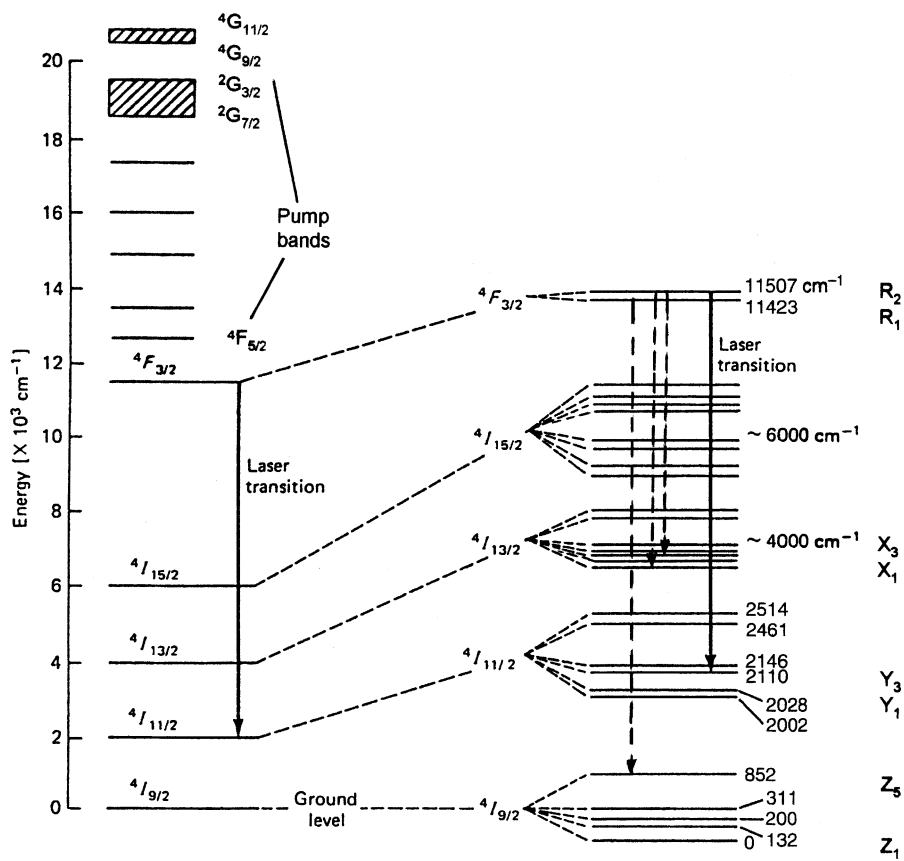


Fig. 2.2. Energy level diagram of Nd:YAG. The solid line represents the major transition at 1064 nm, and the dashed lines are the transitions at 1319, 1338, and 946 nm.

are at the lower sublevel R_1 according to Boltzmann's law. Lasing takes place only by R_2 ions whereby the R_2 level population is replenished from R_1 by thermal transitions. The ground level of Nd:YAG is the $^4I_{9/2}$ level. The terminal laser level is 2110 cm^{-1} above the ground state, and thus the population is a factor of $\exp(\Delta E/kT) \approx \exp(-10)$ of the ground-state density. Since the terminal level is not populated thermally, Nd:YAG is a four-level laser and the threshold condition is easy to obtain.

The fluorescence lifetime of the $^4F_{3/2}$ manifold is about $230\text{ }\mu\text{s}$ for Nd doping concentrations around 1% [2.38].

The branching ratios for room temperature fluorescence from the upper laser level to the various manifolds are as follows [2.5]: $^4F_{3/2} \rightarrow ^4I_{9/2} = 0.30$, $^4F_{3/2} \rightarrow ^4I_{11/2} = 0.56$, $^4F_{3/2} \rightarrow ^4I_{13/2} = 0.14$, and $^4F_{3/2} \rightarrow ^4I_{15/2} < 0.01$. The strongest fluorescence output is from the upper manifold to the lower manifold containing the laser transition at 1064 nm.

Above the upper laser level are located the pump bands starting with the manifold $^4F_{5/2}$, which is responsible for absorption around 808 nm. The highest laying manifold in Fig. 2.2 causes absorption in the visible region. Ions excited into these various pump bands relax efficiently to the upper laser level.

At room temperature the main $1.06\text{ }\mu\text{m}$ line in Nd:YAG is homogeneously broadened by thermally activated lattice vibrations. The spectroscopic cross section for the individual transition between Stark sublevels has been measured [2.33] to be $\sigma(R_2 - Y_3) = 6.5 \times 10^{-19}\text{ cm}^2$. At a temperature of 295 K, the Maxwell-Boltzmann fraction in the upper Stark sublevel is 0.427, implying an effective cross section for Nd:YAG of $\sigma(^4F_{3/2} - ^4I_{11/2}) = 2.8 \times 10^{-19}\text{ cm}^2$. The effective stimulated-emission cross section is the spectroscopic cross section times the occupancy of the upper laser level relative to the entire $^4F_{3/2}$ manifold population.

Figure 2.3 shows the fluorescence spectrum of Nd^{3+} in YAG near the region of the laser output with the corresponding energy levels for the various transitions. The

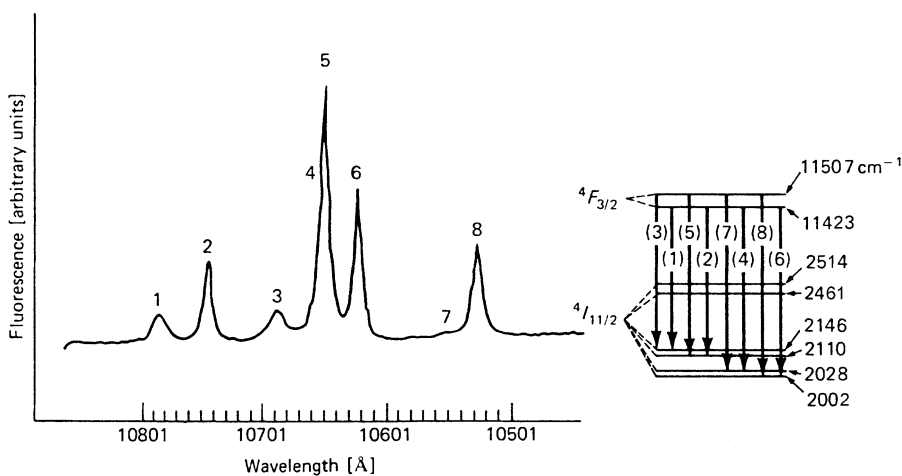


Fig. 2.3. Fluorescence spectrum of Nd^{3+} in YAG at 300 K in the region of $1.06\text{ }\mu\text{m}$ [2.10, 38].

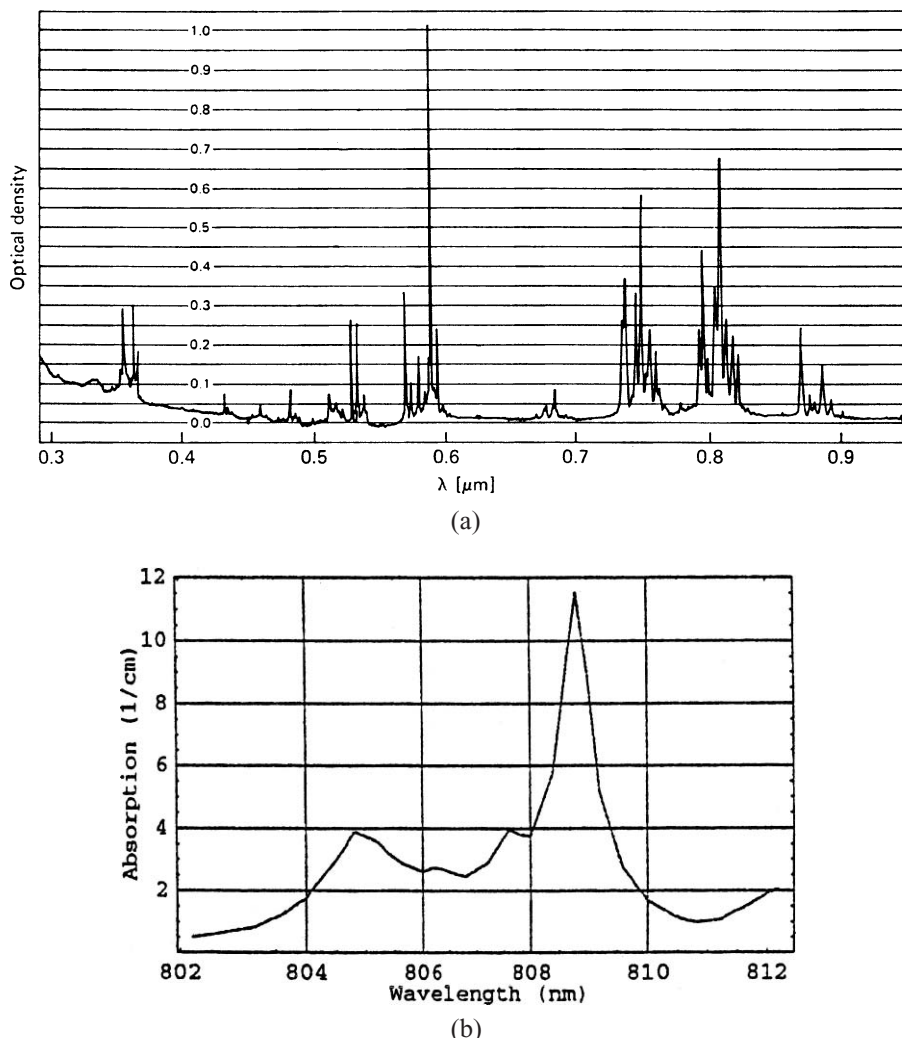


Fig. 2.4. (a) Absorption spectrum of Nd:YAG from 0.3 to 0.9 μm and (b) expanded scale around 808 nm.

absorption of Nd:YAG in the range of 0.3–0.9 μm is shown in Fig. 2.4a. In Fig. 2.4b the absorption spectrum is expanded around the wavelength of 808 nm, which is important for laser diode pumping.

We can relate the absorption spectrum Fig. 2.4a to the energy level diagram in Fig. 2.2. The absorption peaks shown around 870 nm are caused by a transition from the ground level directly to the manifold containing the upper laser level $^4\text{I}_{9/2} \rightarrow ^4\text{F}_{3/2}$. The absorption around 808 nm is the result of the $^4\text{I}_{9/2} \rightarrow ^4\text{F}_{5/2}$ transition. The manifold $^4\text{F}_{5/2}$, comprising three Stark sublevels and located at about $12,776\text{ cm}^{-1}$, is the lowest pump band on the energy scale shown in Fig. 2.2. This is the main absorption

pump band for laser diode pumping at 808 nm. The absorption around 750 nm is the result of the manifold immediately above $^4F_{5/2}$. Both absorption regions around 810 and 750 nm are important for pumping Nd:YAG with cw arc lamps. The absorption peaks around 540 and 590 nm relate to the upper energy levels around 19,000 and 20,500 cm⁻¹ shown in Fig. 2.2. The pump bands are important for flashlamp-pumped Nd:YAG lasers because flashlamps produce a large amount of radiation in the visible region.

Nd:YAG Laser Crystals

Commercially available laser crystals are grown exclusively by the Czochralski method. Growth rates, dopants, annealing procedures, and final size generally determine the manufacturing rate of each crystal. The boule axis or growth direction is customarily in the [111] direction. The high manufacturing costs of Nd:YAG are mainly due to the very slow growth rate of Nd:YAG, which is of the order of 0.5 mm/h. Typical boules of 10–15 cm in length require a growth run of several weeks.

Boules grown from Nd:YAG typically contain very few optically observable scattering centers and show negligible absorption at the lasing wavelength. However, all Nd:YAG crystals grown by Czochralski techniques show a bright core running along the length of the crystal when positioned between crossed polarizers. Strain flares are also visible, radiating from the core toward the surfaces of the crystal. Electron microprobe studies have revealed that in the core region the Nd concentration can run as much as twice as high as in the surrounding areas. The cores originate from the presence of facets on the growth interface which have a different distribution coefficient for neodymium than the surrounding growth surface. These compositional differences cause corresponding differences in thermal expansion coefficients which, in turn, give rise to the observed stress patterns during the cool down of the crystals from the growth temperature. Annealing does not seem to eliminate the cores and, thus far, no way has been found of avoiding the formation of facets on the growth interface. However, by choosing the growth direction carefully and by maintaining as steep an interface angle as is practical, the stresses can be confined to a very localized region and high-optical quality rods can be fabricated from the surrounding material. This means, of course, that in order to provide rods of a given diameter, the crystal must be grown with a diameter that is somewhat more than twice as large. The boules are processed by quartering into sections. Rods can be fabricated with maximum diameters of about 15 mm and lengths of up to 150 mm. The optical quality of such rods is normally quite good and comparable to the best quality of Czochralski ruby or optical glass. For example, 6 mm by 100 mm rods cut from the outer sections of 20 mm by 150 mm boules typically may show only 1–2 fringes in a Twyman–Green interferometer.

Neodymium concentration by atom percent in YAG has been limited to 1.0–1.5%. Higher doping levels tend to shorten the fluorescent lifetime, broaden the linewidth, and cause strain in the crystal, resulting in poor optical quality. The Nd doping level in YAG is sometimes expressed in different concentration units: A concentration

of 1.0% Nd atoms in the lattice is equivalent to 0.727% Nd or 0.848% Nd_2O_3 by weight, respectively. The concentration of Nd^{3+} sites in these cases is $1.386 \times 10^{20} \text{ cm}^{-3}$.

In specifying Nd:YAG rods, the emphasis is on size, dimensional tolerance, doping level, and passive optical tests of rod quality. Cylindrical rods with flat ends are typically finished to the following specifications: end flat to $\lambda/10$, ends parallel to ± 4 arc seconds, perpendicularity to rod axis to ± 5 min, and rod axis parallel to within $\pm 5^\circ$ to [111] direction. Dimensional tolerances typically are ± 0.5 mm on length and ± 0.025 mm on diameter. Most suppliers furnish the laser crystals with a photograph showing the fringe pattern of the crystal as examined by a Twyman-Green interferometer. A double-pass Twyman-Green interferometer quickly reveals strained areas, small defects, or processing errors.

In a particular application the performance of a Nd:YAG laser can be somewhat improved by the choice of the optimum Nd concentration. As a general guideline, it can be said that a high-doping concentration (approximately 1.2%) is desirable for Q-switch operation because this will lead to high energy storage. For cw operation, a low-doping concentration (0.6–0.8%) is usually chosen to obtain good beam quality.

It is worth noting that in contrast to a liquid or a glass, a crystal host is not amenable to uniform dopant concentration. This problem arises as a result of the crystal-growth mechanism. In the substitution of the larger Nd^{3+} for a Y^{3+} in $\text{Y}_3\text{Al}_5\text{O}_{12}$, the neodymium is preferentially retained in the melt. The increase in the concentration of Nd from the seed to the terminus of a 20-cm long boule is about 20–25%. For a laser rod 3–8 cm long, this end-to-end variation may be 0.05–0.10% of Nd_2O_3 by weight.

Different Laser Transitions in Nd:YAG

Nd:YAG can produce other useful wavelength besides the familiar 1064 nm. From Fig. 2.2 it follows that there are 14, 12, and 10 transitions possible from the manifold $^4\text{F}_{3/2}$ to the $^4\text{I}_{13/2}$, $^4\text{I}_{11/2}$, $^4\text{I}_{9/2}$ manifolds respectively. The peak cross section and fluorescence branching ratios for fluorescence of these transitions are listed in [2.5]. Laser action has been achieved in many of these transitions [2.39–44].

In Nd:YAG the 1064 nm and 1061 nm transitions $^4\text{F}_{3/2} \rightarrow ^4\text{I}_{11/2}$ have the highest emission cross sections. At room temperature the 1064 nm line $R_2 \rightarrow Y_3$ is dominant, while at low temperatures the 1061 line $R_1 \rightarrow Y_1$ has the lower threshold [2.45].

Several low-gain transitions, one at 946 nm and two at 1.3 μm , are of particular interest in Nd:YAG because frequency doubling of these wavelengths is attractive for producing powerful beams in the blue and red region of the spectrum. The transitions at 946 nm and at 1.3 μm are indicated by dashed lines in Fig. 2.2. Effective cross sections are listed in Table 2.4. To obtain output at these wavelengths, parasitic oscillations at the higher gain transitions are typically suppressed by dichroic mirrors and intra-cavity dispersive prisms.

There are two strong transitions in the 1.3 μm region from the $^4\text{F}_{3/2}$ to the $^4\text{I}_{13/2}$ manifold which have almost the same cross section and the laser output typically

Table 2.4. Important transitions in Nd:YAG [2.5, 7, 43]

Wavelength (nm)	Transition	Cross section (10^{-19} cm^2)
1064.1	${}^4\text{F}_{3/2} \rightarrow {}^4\text{I}_{11/2}, (R_2 \rightarrow Y_3)$	2.8
1338.1	${}^4\text{F}_{3/2} \rightarrow {}^4\text{I}_{13/2}, (R_2 \rightarrow X_3)$	1.0
1318.7	${}^4\text{F}_{3/2} \rightarrow {}^4\text{I}_{13/2}, (R_2 \rightarrow X_1)$	0.95
946	${}^4\text{F}_{3/2} \rightarrow {}^4\text{I}_{9/2}, (R_1 \rightarrow Z_5)$	0.5

contains both wavelength. One is the $R_2 \rightarrow X_1$ transition at 1319 nm and the other is the $R_2 \rightarrow X_3$ line at 1338 nm. Nd:YAG lasers that have been operated in this wavelength region are reported in [2.43, 46–49].

A flashlamp-pumped pulsed system achieved up to 165 W average power at 1.3 μm [2.46]. Intracavity doubling of a diode-pumped Nd:YAG laser operating at 1319 nm generated 6.1 W of cw red radiation at 659.5 nm. Efficiency and stability was improved by suppressing the 1338-nm line by inserting a thin etalon into the resonator [2.47]. With laser diode side pumping cw powers in excess of 100 W at 1319 nm have been reported [2.48].

The 946-nm emission originates from the R_1 Stark level of the ${}^4\text{F}_{3/2}$ manifold and terminates at the highest Stark level Z_5 of the ground manifold ${}^4\text{I}_{9/2}$. Because the lower laser level is only 852 cm^{-1} above the ground state, there is a thermal population of about 0.7% at room temperature. This residual population induces a partial reabsorption of the laser radiation which increases the threshold. Therefore, the laser operating at 946 nm emission is a quasi-three-level laser.

There is great interest in these transitions since frequency doubling of the 946 nm leads to the blue spectral region. An all solid-state blue laser could become an alternative to the argon-ion laser. Laser operating at 946 nm are reported in [2.44, 50–52]. Intracavity frequency doubling of a diode pumped system generated 4.6 W of output at 946 nm, which produced 2.8 W at the blue wavelength of 473 nm [2.52].

2.3.2 Nd:Glass

There are a number of characteristics that distinguish glass from other solid-state laser host materials. Its properties are isotropic. It can be doped at very high concentrations with excellent uniformity, and it can be made in large pieces of diffraction-limited optical quality. In addition, glass lasers have been made, in a variety of shapes and sizes, from fibers a few micrometers in diameter to rods 2 m long and 7.5 cm in diameter and disks up to 90 cm in diameter and 5 cm thick.

The most common commercial optical glasses are oxide glasses, principally silicates and phosphates, that is, SiO_2 and P_2O_5 based. Table 2.5 summarizes some important physical and optical properties of commercially available silicate and phosphate glasses.

Phosphate glasses have a larger emission cross section and a smaller nonlinear coefficient as compared to silicate glasses. These two attributes make Nd-doped

Table 2.5. Physical and optical properties of Nd-doped glasses

Spectroscopic properties	Glass type					
	Q-246 Silicate (Kigre)	Q-88 Phosphate (Kigre)	LHG-5 Phosphate (Hoya)	LHG-8 Phosphate (Hoya)	LG-670 Silicate (Schott)	LG-760 Phosphate (Schott)
Peak wavelength (nm)	1062	1054	1054	1054	1061	1054
Cross section ($\times 10^{-20}$ cm 2)	2.9	4.0	4.1	4.2	2.7	4.3
Fluorescence lifetime (μ s)	340	330	290	315	330	330
Linewidth FWHM (nm)	27.7	21.9	18.6	20.1	27.8	19.5
Density (gm/cm 3)	2.55	2.71	2.68	2.83	2.54	2.60
Index of refraction (Nd)	1.568	1.545	1.539	1.528	1.561	1.503
Nonlinear coefficient (10^{-16} cm 2 /W)	3.74	2.98	3.48	3.10	3.78	2.90
$dn/dt(20 - 40^\circ\text{C})$ ($10^{-6}/^\circ\text{C}$)	2.9	-0.5	8.6	-5.3	2.9	-6.8
Thermal coefficient of optical path (20 – 40°C)($10^{-6}/^\circ\text{C}$)	+8.0	+2.7	+4.6	+0.6	8.0	—
Transformation point (°C)	518	367	455	485	468	—
Thermal expansion coefficient (20 – 40°C)($10^{-7}/^\circ\text{C}$)	90	104	86	127	92.6	138
Thermal conductivity (W/m °C)	1.30	0.84	1.19	—	1.35	0.67
Specific heat (J/g °C)	0.93	0.81	0.71	0.75	0.92	0.57
Knoop hardness	600	418	497	321	497	—
Young's modulus (kg/mm 2)	8570	7123	6910	5109	6249	—
Poisson's ratio	0.24	0.24	0.237	0.258	0.24	0.27

phosphate glasses the material of choice for large laser systems employed in fusion research [2.53–57].

There are two important differences between glass and crystal lasers. First, the thermal conductivity of glass is considerably lower than that of most crystal hosts. Second, the emission lines of ions in glasses are inherently broader than in crystals. A wider line increases the laser threshold. Nevertheless, this broadening has an advantage. A broader line offers the possibility of obtaining and amplifying shorter light pulses and, in addition, it permits the storage of larger amounts of energy in the amplifying medium for the same linear amplification coefficient. Thus, glass and crystalline lasers complement each other. For continuous or very high repetition-rate operation, crystalline materials provide higher gain and greater thermal conductivity. Glasses are more suitable for high-energy pulsed operation because of their large size, flexibility in their physical and optical parameters, and the broad fluorescent line width.

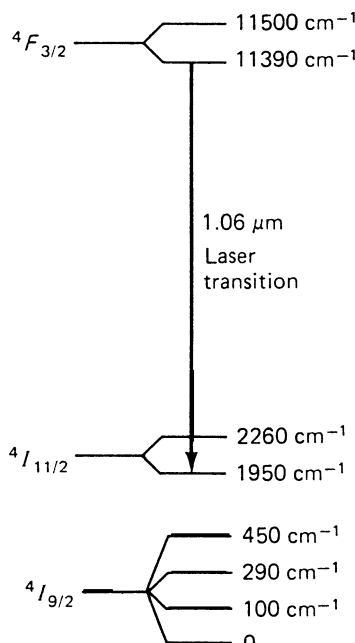


Fig. 2.5. Partial energy level diagram of Nd^{3+} in glass

Unlike many crystals, the concentration of the active ions can be very high in glass. The practical limit is determined by the fact that the fluorescence lifetime and, therefore the efficiency of stimulated emission, decreases with higher concentrations. In silicate glass, this decrease becomes noticeable at a concentration of 5% Nd_2O_3 .

Figure 2.5 shows a simplified energy level diagram of Nd:glass. The Nd^{3+} ion in glass represents a four-level system. The upper laser level indicated in Fig. 2.5 is the lower-lying component of the $^4F_{3/2}$ pair with a several hundred microsecond spontaneous emission lifetime. The terminal laser level is the lower-lying level of the pair in the $^4I_{11/2}$ multiplet. The $^4I_{11/2}$ group empties spontaneously by a radiationless phonon transition to the $^4I_{9/2}$ ground state about 1950 cm^{-1} below.

Because of the large separation of the terminal laser level from the ground state even at elevated temperatures there is no significant terminal-state population and, therefore, no degradation of laser performance. In addition, the fluorescent linewidth of the neodymium ion in glass is quite insensitive to temperature variation; only a 10% reduction is observed in going from room temperature to liquid nitrogen temperature. As a result of these two characteristics, it is possible to operate a neodymium-doped glass laser with little change in performance over a temperature range of -100 to $+100^\circ\text{C}$.

Figure 2.6 shows the pump bands of Nd:glass. In comparing Fig. 2.6 with Fig. 2.4, one notes that the locations of the absorption peaks in Nd:YAG and Nd:glass are about the same; however, in Nd:glass the peaks are much wider and have less fine a structure compared to Nd:YAG.

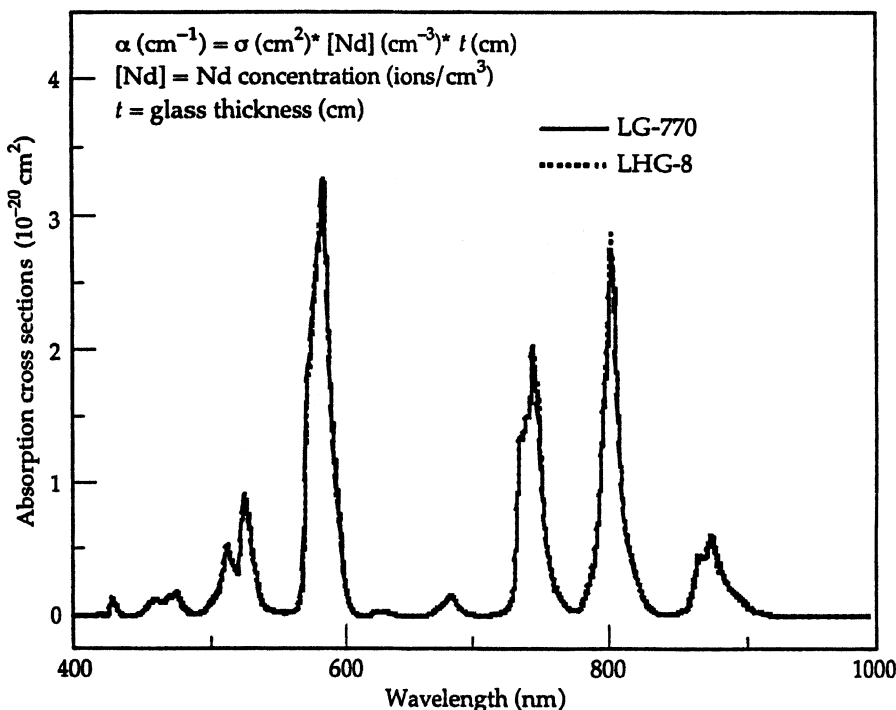


Fig. 2.6. Absorption spectra for two phosphate glasses [2.58]

Data Sources on Laser Glasses. Useful reviews on glass lasers can be found in [2.1, 2, 59, 60]. Pertinent materials parameters are listed in the data sheets of the major Nd:glass manufacturers.

2.3.3 Nd:Cr:GSGG

Soon after the invention of the Nd:YAG laser attempts were made to increase the absorption of pump radiation from flashlamps by incorporating a second dopant called a sensitizer into the laser crystal. A particularly attractive sensitizer is Cr³⁺ because the broad absorption bands of chromium can efficiently absorb light throughout the whole visible region of the spectrum. The concept of improving efficiency by codoping a Nd laser crystal with Cr³⁺ ions is based on absorption of pump radiation by the broad absorption bands of Cr and nonradiative energy transfer to the Nd ions. No improvement was achieved with the host crystal YAG because of an inefficient transfer process. However, it was discovered [2.61,62] that a nearly 100% transfer efficiency could be achieved in the codoped garnet crystal GSGG. In Nd:Cr:YAG the Cr³⁺ → Nd³⁺ transfer time of 6.2 ms prevents the Cr³⁺ from being an effective sensitizer, because the transfer time has to be shorter than the 230 μs fluorescence decay time of Nd³⁺. In Nd:Cr:GSGG the Cr³⁺ → Nd³⁺ transfer time has been measured to be

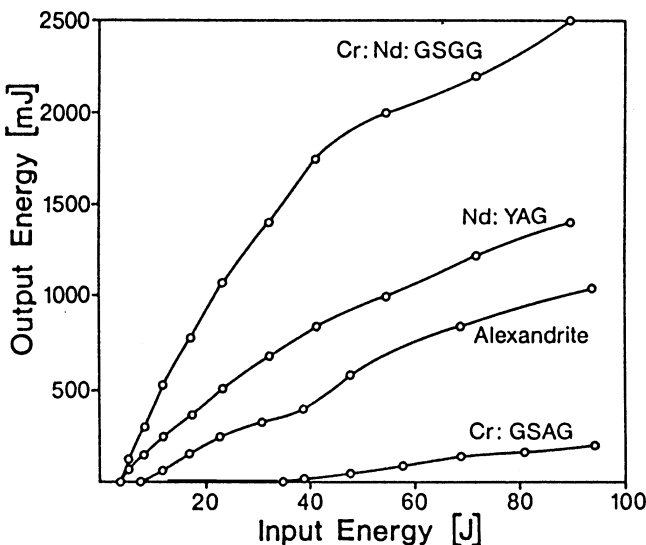


Fig. 2.7. Output energy versus input energy for Cr:Nd:GSGG, Nd:YAG, alexandrite, and Cr:GSAG [2.64]

17 μ s [2.62]. This is due to a favorable red shift of the 4T_1 energy band of Cr^{3+} . It was found that the pumping efficiency improvement is not a strong function of the Cr concentration for the range of $1\text{--}2 \times 10^{20}/\text{cm}^3$ [2.63].

Figure 2.7 illustrates the high efficiency which can be achieved with this material by comparing it to Nd:YAG and to tunable lasers such as alexandrite and Cr:GSAG [2.64]. The experiments were carried out in a silver-plated single-ellipse pump cavity using a $5 \times 75 \text{ mm}^2$ flashlamp. The laser rods were $6 \times 75 \text{ mm}^2$ in an identical laser-resonator configuration but with output coupling optimized for the particular laser. The flashlamp pump efficiency of Nd:Cr:GSGG is about twice that of Nd:YAG.

The explanation for the high efficiency of codoped GSGG follows from Fig. 2.8, which shows the absorption spectrum of this material. Two high-intensity Cr^{3+} absorption bands having maxima at 450 and 640 nm covering an appreciable part of the visible region and narrow Nd lines can be observed.

The higher pump efficiency of Nd:Cr:GSGG does not automatically translate into better system performance because Nd:Cr:GSGG does exhibit much stronger thermal focusing and stress birefringence, as compared to Nd:YAG.

The crystal Nd:Cr:GSGG has a thermal conductivity that is about 2.5 times lower compared to Nd:YAG. Furthermore, the blue and red Cr absorption bands produce substantial quantum defect heating because of the large energy difference between pump and laser photons. As a consequence, thermal lensing is six to nine times more severe compared to Nd:YAG along with a three times greater thermally induced birefringence [2.66–68].

Therefore, if beam brightness is the criteria rather than output energy, the enhanced flashlamp pump efficiency advantage of Nd:GSGG compared to Nd:YAG

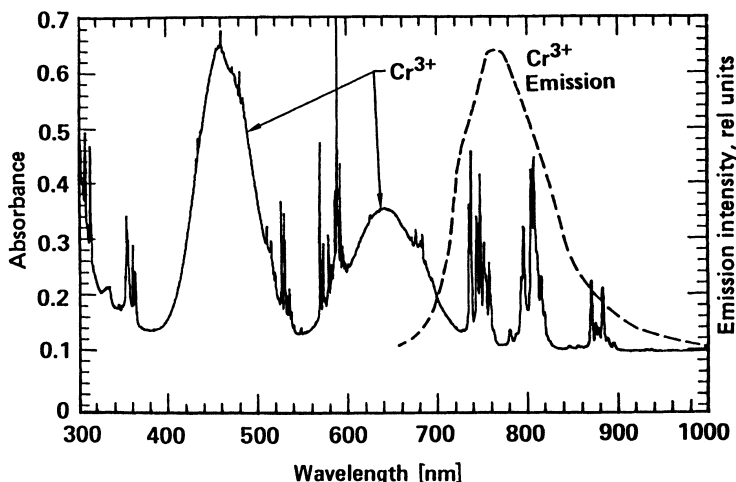


Fig. 2.8. Absorption spectra of Cr:Nd:GSGG [2.65]

is diminished because of larger thermally induced beam distortions. Measurements at the author's laboratory have shown that under single-shot and low-repetition-rate operation, beam brightness in a GSGG system is about twice as high as compared to YAG. However, as the repetition rate is increased, this difference became smaller and beam brightness for a given input was about equal in both systems at 25 Hz for a Q-switched system at 100 mJ output.

By incorporating advanced thermal lensing and birefringence compensation techniques, good beam quality and stable performance over a broad operating range was achieved from a Nd:Cr:GSGG laser [2.68]. The laser produced 150 mJ pulses at repetition rates of up to 20 Hz. Thermal lensing and astigmatism were corrected with a cylindrical telescope and an adjustable negative lens-rear mirror combination. Birefringence was partially compensated by adding a third resonator mirror and a Faraday rotator. This so-called reentrant resonator as well as the thermal lensing compensation technique are applicable to any solid-state laser and will be discussed further in Chap. 7.

2.3.4 Nd:YLF

The crystal $\text{Nd}^{3+}:\text{LiYF}_4$ has a number of attributes that offer an advantage over Nd:YAG in certain applications. The natural birefringence of this uniaxial crystal dominates thermally induced birefringence and the polarized output eliminates the thermal depolarization losses of optically isotropic hosts like YAG.

The transition of Nd:YLF at 1053 nm matches the peak gain of Nd-doped phosphate and fluorophosphate glasses. Since Nd:YLF can be cw pumped and mode-locked, a Nd:YLF oscillator provides a stable output for the selection of an individual short

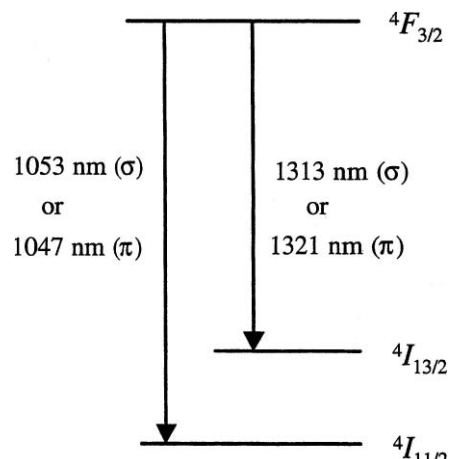


Fig. 2.9. Simplified energy level diagram of Nd:YLF

pulse. For this reason Nd:YLF is used in the master oscillators of Nd:glass amplifier chains.

The material also has advantages for diode pumping since the fluorescence lifetime in Nd:YLF is twice as long as in Nd:YAG. Laser diodes are power limited and, therefore a larger pump time afforded by the longer fluorescence time provides for twice the energy storage from the same number of diodes.

For laser diode pumping, Nd:YLF exhibits three absorption maxima, namely, at 792, 797, and 806 nm [2.69]. The largest absorption occurs at 792 nm, but the more powerful cw laser diodes are available at 806 nm. In some Nd:YLF lasers the pump wavelength of 797 nm is chosen as a compromise [2.70].

Fig. 2.9 shows a simplified energy level diagram of Nd:YLF. All lines originate on the same Stark split $^4F_{3/2}$ upper level. Depending on the polarization, two lines are obtained around 1.05 and 1.3 μm . The birefringence of Nd:YLF makes the gain of these lines a function of the laser polarization. For example, with an intracavity polarizer one can select either the 1047 nm (extraordinary beam) or the 1053 nm (ordinary beam) transition. The same can be done for the two 1.3 μm transition; however, in addition lasing at the 1.05 μm lines has to be suppressed. The main reason for lasing Nd:YLF at one of the 1.3 μm transitions is for the production of red light [2.71, 72].

Material properties of Nd:YLF are listed in Table 2.6. Nd:YLF is a mechanically weaker and softer crystal compared to Nd:YAG with a lower thermal conductivity and emission cross section. Since the thermomechanical properties of Nd:YAG are far superior to those of Nd:YLF, the latter crystal is employed only in low- to medium-power systems.

For lasers requiring moderate Q-switch energies, the lower gain of Nd:YLF actually offers some advantages in system architecture over the high gain material Nd:YAG. The energy storage in Q-switched operation of Nd oscillators and amplifiers

Table 2.6. Properties of Nd-doped lithium yttrium fluoride (YLF)

Lasing wavelength (nm)	1053 (σ)
	1047 (π)
Index of refraction, $\lambda = 1.06\mu\text{m}$	$n_0 = 1.4481$
	$n_e = 1.4704$
Fluorescent lifetime	480 μs
Stimulated emission	$1.8 \times 10^{-19}(\pi)$
Cross section (cm^2)	$1.2 \times 10^{-19}(\sigma)$
Density (g/cm^3)	3.99 (undoped)
Hardness (Mohs)	4–5
Elastic modulus (N/m^2)	7.5×10^{10}
Strength (N/m^2)	3.3×10^7
Poisson's ratio	0.33
Thermal conductivity ($\text{W}/(\text{cm K})$)	0.06
Thermal expansion coefficient ($^\circ\text{C}^{-1}$)	a axis: 13×10^{-6} c axis: 8×10^{-6}
Melting point ($^\circ\text{C}$)	825

is constrained by the onset of parasitic oscillations. To first order, the energy storage limit of two materials is inversely proportional to the ratio of the stimulated emission cross sections. Therefore, higher storage densities are obtained in the lower cross section material Nd:YLF as compared to Nd:YAG.

Figure 2.10 shows the performance of a Q-switched YLF oscillator, producing an output of 400 mJ [2.73]. This output level would require the addition of an amplifier in the case of a Nd:YAG laser. Single oscillators with up to 0.5 J Q-switched output and oscillator-amplifier configurations with several Joules output usually result in less complicated structures if designed with Nd:YLF rods as compared to Nd:YAG [2.74, 75]. The weaker thermal lensing in Nd:YLF coupled with its natural

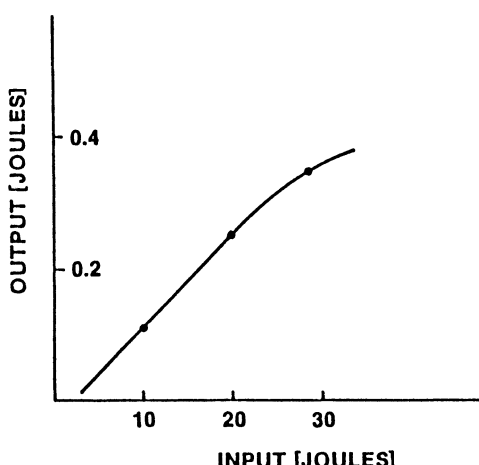


Fig. 2.10. Performance of a Q-switched YLF oscillator (laser rod: 0.25×2.5 inch 2 ; output coupler: 30% reflectivity; wavelength: $1.053\mu\text{m}$) [2.73]

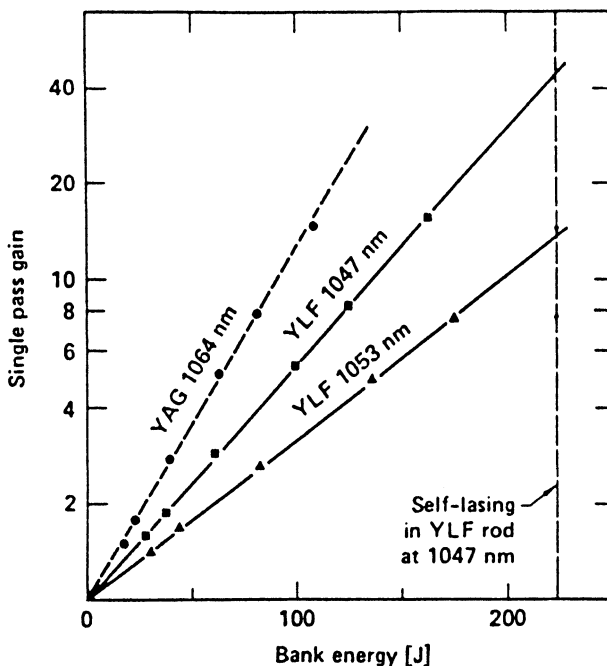


Fig. 2.11. Single-pass gain versus pump energy for YLF and YAG [2.74]

birefringence provide additional advantages in certain applications compared to Nd:YAG.

Figure 2.11 shows measured single-pass gain versus pump energy for the two transitions [2.74]. The measurements of the Nd:YLF amplifier were performed on a 10 mm diameter \times 76 mm YLF rod with 1% Nd doping. The crystal was pumped in a silver-coated double elliptical pumping head. The YAG data were obtained by replacing the Nd:YLF with a 10 mm diameter Nd:YAG rod in the same amplifier head.

2.3.5 Nd:YVO₄

Neodymium-doped yttrium vanadate has several spectroscopic properties that are particularly relevant to laser diode pumping. The two outstanding features are a large stimulated emission cross section which is five times higher than Nd:YAG, and a strong broadband absorption at 809 nm.

The potential of Nd:YVO₄ as an important laser material has been recognized in 1966 [2.21]. However, crystals could not be grown free of scattering centers and absorbing color center defects. The unavailability of high-quality crystals of the size required for flashlamp pumping proved to be the major obstacle to further development. The high gain achievable in Nd:YVO₄ and the strong absorption of diode pump radiation require crystals only a few millimeters in length. With the constraint of large

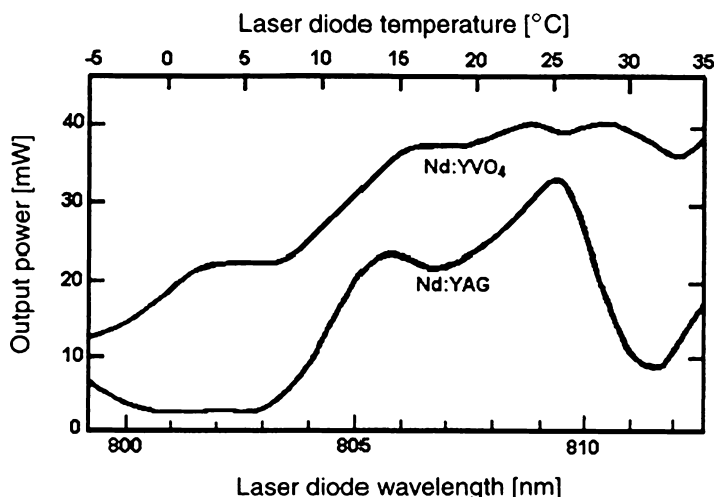


Fig. 2.12. Output from a Nd:YVO₄ and Nd:YAG laser as a function of diode pump temperature and wavelength [2.77]

crystal size removed, and with further improvements in the crystal growth process, material of high-optical quality became available.

The vanadate crystal is naturally birefringent and laser output is linearly polarized along the extraordinary π direction. The polarized output has the advantage that it avoids undesirable thermally induced birefringence.

Pump absorption in this uniaxial crystal is also polarization dependent. The strongest absorption occurs for pump light polarized in the same direction as the laser radiation. The absorption coefficient is about seven times higher compared to Nd:YAG in the π direction. The sublevels at the $^4F_{5/2}$ pump band are more resolved in Nd:YAG, whereas in Nd:YVO₄ Stark splitting is smaller and the multiple transitions are more compacted. The result is a broader and less spiky absorption profile of Nd:YVO₄ compared to Nd:YAG around the pump wavelength of 809 nm. Figure 2.12 gives an indication of the broader and smoother absorption profile of this material as compared to Nd:YAG. From this data follows also that Nd:YVO₄ laser performance is more tolerant to diode temperature variations because of the large pump bandwidth. If one defines this bandwidth as the wavelength range where at least 75% of the pump radiation is absorbed in a 5 mm thick crystal, then one obtains for Nd:YVO₄ a value of 15.7 nm and a value of 2.5 nm for Nd:YAG [2.78].

Table 2.7 summarizes important material parameters for Nd:YVO₄. The two outstanding features of this crystal, as already mentioned, are the high emission cross section and the large absorption coefficient for pump radiation at 809 nm. Major short comings of Nd:YVO₄ are a relatively low thermal conductivity and a short fluorescence lifetime.

The low thermal conductivity (about one-third that of Nd:YAG) prevents good heat dissipation, and the thermally induced fracture of the crystal raises a severe obstacle to scaling up to the operation to high power. This limitation can

Table 2.7. Material parameters for Nd:YVO₄ [2.78–80]

Laser cross section	$15.6 \times 10^{-19} \text{ cm}^2$
Laser wavelength	1064.3 nm
Linewidth	0.8 nm
Fluorescence lifetime	100 μs
Peak pump wavelength	808.5 nm
Peak absorption coefficient at 808 nm (cm^{-1})	34 (π polarization) 10 (σ polarization)
Nd doping	1% (atomic Nd)
Modulus of elasticity	133 Gpa
Tensile strength	53 MPa
Thermal conductivity	0.05 W/cm K
Poisson ratio	0.33
Knoop hardness	480 kg/mm ²

be, to some extent, circumvented by using low-doped crystals as discussed further below.

As expressed in (3.65), the pump input power to reach threshold for cw operation is inversely proportional to the product of emission cross section σ and effective lifetime τ_f . The large cross section in Nd:YVO₄ is partially offset by its shorter lifetime. However, the product ($\sigma \tau_f$) is still larger than in Nd:YAG, determining a low cw threshold.

Nd³⁺ ions in YVO₄ have a large absorption cross section at a wavelength around 809 nm, with a peak value of about $2.7 \times 10^{-19} \text{ cm}^2$ [2.80]. Thus, with a doping level of 1% at. Nd or $1.26 \times 10^{20} \text{ Nd ions/cm}^3$ the absorption coefficient is 34 cm^{-1} . The peak absorption cross section of Nd:YVO₄ for the π direction is about seven times larger than that of Nd:YAG at 808 nm ($4.1 \times 10^{-20} \text{ cm}^2$).

The intense pump absorption of 809 nm laser diode radiation allows the use of short crystals that absorb most of the incident light. Since the divergence of the pump beam is typically much larger than that of the resonator mode, a crystal capable of absorbing pump radiation in a short length can best match the spot size of the resonator mode. In particular, fiber-coupled diode sources, because of their relatively poor beam quality, have a short Rayleigh range when focused to a small spot size.

Although a high absorption and short active region is desirable from a mode matching point of view, it is in contrast to the requirement of adequate heat dissipation required for high-power operation. A small pump volume increases the thermal gradients and the mechanical stress. It has been shown that the pump power fracture limit of Nd:YVO₄ is inversely proportional to the doping concentration [2.81]. For this reason it was found that for higher power operation with pump sources on the order of 30 W the optimum concentration for a Nd:YVO₄ crystal is in the range of 0.25–0.4% Nd [2.82].

Figure 2.13 depicts the $E||c$ polarized spectra of a 10 mm long crystal with a 0.27% doping [2.83]. Peak absorption is centered at 808.7 nm with a line width at room temperature of 2.5 nm FWHM. The broader pedestal absorption arises from other weak Nd lines.

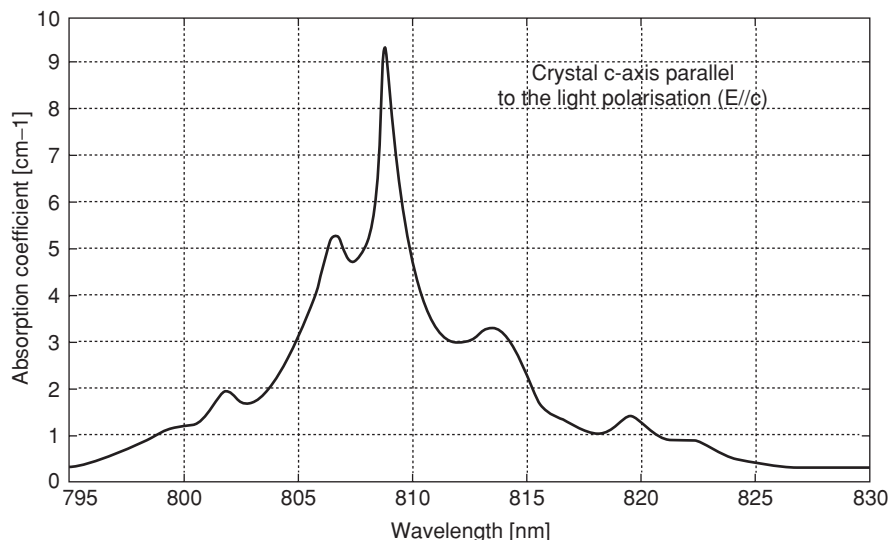


Fig. 2.13. Absorption spectrum of a 0.27% doped Nd:YVO₄ crystal in the region of the 808 nm pump band (after [2.83].)

In an attempt to reduce thermal heating in Nd:YVO₄ a number of systems [2.84, 85] have been pumped at 880 nm directly into the upper laser level as illustrated in Fig. 2.14. The laser emission in Nd:YVO₄ at 1064 nm is the transition $^4F_{3/2}(R_1) \rightarrow ^4I_{11/2}(Y_1)$. The Nd:YVO₄ crystals are traditionally pumped into the strongly absorbing

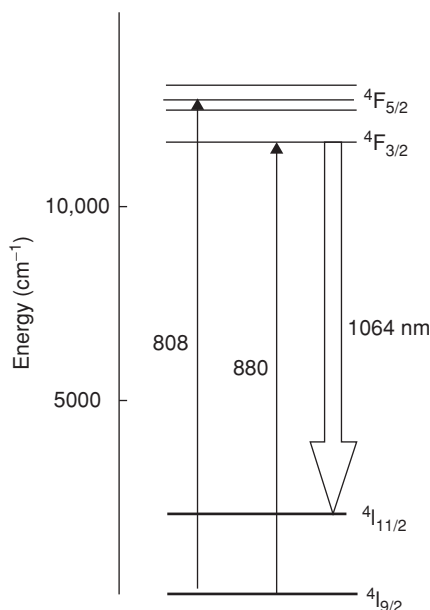


Fig. 2.14. Pumping of Nd:YVO₄ at 808 or 879 nm.

$^4F_{5/2}$ level at 809 nm. An alternative pump transition for Nd:YVO₄ is $^4I_{9/2}(Z_1) \rightarrow ^4F_{3/2}(R_1)$ at 880 nm. Pumping directly into the upper laser level leads to a reduction of quantum defect heating on account of the smaller difference of the wavelength of the pump and laser radiation. Pumping at the longer wavelength increases the quantum defect efficiency (Stokes factor η_s) from 0.76 to 0.83. An optical-to-optical slope efficiency of 75% with diode laser pumping at 880 nm was reported for a 1 mm thick Nd:YVO₄ crystal doped at 1% [2.84].

The properties of Nd:YVO₄ can best be exploited in an end-pumped configuration and a number of commercial lasser systems are based on fiber-coupled diode arrays pumping a small vanadate crystal. Actually, Nd:YVO₄ is the material of choice for cw endpumped lasers with output power up to about 30 W[2.86–90]. These systems are often also internally frequency doubled to provide output at 532 nm. In endpumped systems the pump beam is usually highly focused and it is difficult to maintain a small beam waist over a distance of more than a few millimeters. In this case a material such as Nd:YVO₄, which has a high absorption coefficient combined with high gain, is very advantageous.

Impressive overall efficiencies have been achieved in Nd:YVO₄ as illustrated in the examples presented in Sects. 3.6.3 and 6.2.3. For cw-pumped, repetitively Q-switched operation, the relatively short upper-state lifetime of Nd:YVO₄ requires high pulse rates of 50–100 kHz in order to achieve average power close to cw performance. The high gain in combination with a short fluorescence lifetime produces relatively short Q-switch pulses compared to Nd:YAG and Nd:YLF. Pulsewidth in repetitively Q-switched systems is typically around 10 ns.

Like most other Nd-doped crystals, Nd:YVO₄ can also be used to generate 1.34 μm radiation. At this wavelength, the slope efficiency is reduced compared to 1.06 μm operation and thermal loading is higher due to the larger quantum defect. An end-pumped Nd:YVO₄ laser with a slope efficiency of 40% and producing 7.3 W of output power in a twice diffraction-limited beam has been reported in [2.83].

2.4 Er:Lasers

Erbium–laser performance is not very impressive in terms of efficiency or energy output. However, erbium has attracted attention because of two particular wavelengths of interest. A crystal, such as YAG, highly doped with erbium produces an output around 2.9 μm , and Er-doped phosphate glass generates an output at 1.54 μm . Both of these wavelenghts are absorbed by water, which leads to interesting medical applications in the case of the 2.9 μm lasers, and to eye safe military rangefinders in the case of the shorter wavelength.

2.4.1 Er:YAG

In 1975 Soviet researchers [2.91] discovered laser operation at room temperature in highly doped Er:YAG, i.e., erbium concentrations at around 50%. Laser emission

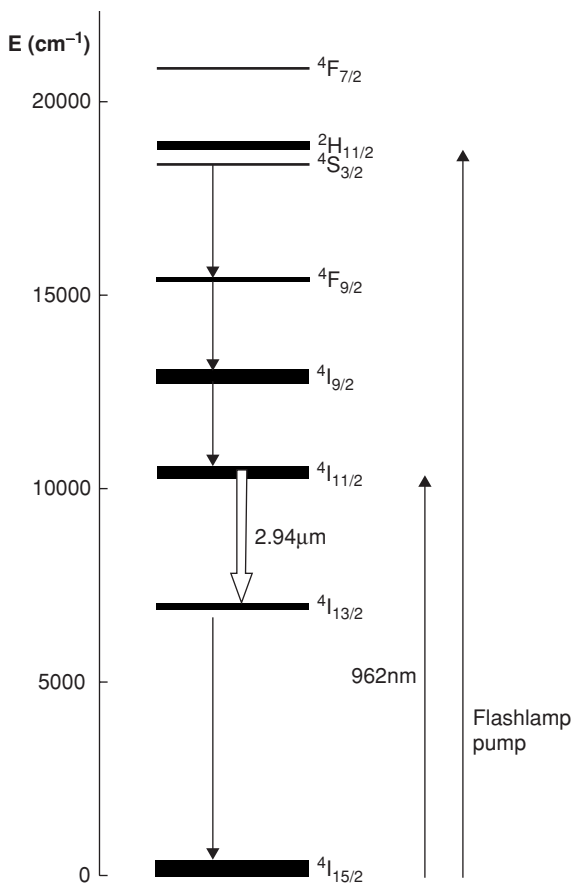


Fig. 2.15. Energy level diagram of Er:YAG for laser action at 2940 nm

occurs at 2940 nm. The laser is of particular interest because its wavelength coincides with a water absorption line. Optical absorption by the water in tissue is extremely large ($>3000\text{ cm}^{-1}$), making potential medical applications such as plastic surgery very attractive.

Figure 2.15 depicts a simplified energy level diagram of Er:YAG. The 2940 nm lasing transition is between the $^4I_{11/2}$ and $^4I_{13/2}$ states of the Er^{3+} ion. The system is a four-level laser because the lower laser level is separated from the ground state $^4I_{15/2}$ by almost 7000 cm^{-1} . The stimulated emission cross section for this laser transition is $\sigma = 3 \times 10^{-20}\text{ cm}^2$. Despite a much shorter lifetime of the emitting level ($^4I_{11/2}$) as compared to the terminal level ($^4I_{13/2}$), efficient 2.9 μm room temperature laser emission between these two levels is possible because of very complex energy transfer processes. As a result of up-conversion, and cross relaxation between neighboring Er^{3+} ions in the $^4I_{13/2}$ level, much of the lower laser level population is recycled into the upper laser level, thus overcoming the unfavorable lifetime of the two levels [2.92, 93]. Relatively long pump pulses are required because the up-conversion process in

Er:YAG takes about 100 μs for pumping at 962 nm to bring the system to the cw regime. For this reason there is a minimum pump duration below which the system efficiency decreases.

The most efficient pump process is direct excitation of the upper laser level $^4\text{I}_{11/2}$ by laser diodes emitting at a wavelength of 962 nm. Measured absorption coefficient of Er:YAG for the diode emission at this wavelength is 14 cm^{-1} . Excitation with flashlamp pumping is mainly at shorter wavelengths into the $^4\text{F}_{7/2}$, $^2\text{H}_{11/2}$, and $^4\text{S}_{3/2}$ levels as shown in Fig. 2.15. Major absorption occurs for these levels between 480 to 530 nm. The excitation from these higher energy levels of Er^{3+} cascades downward to the upper laser level.

Flashlamp-pumped Er:YAG lasers have a very low system efficiency. A contributing factor is the large quantum defect since the upper laser level of the 2940 nm transition is pumped mainly by light at a wavelength less than 600 nm. A typical example is a 75 mm long by 6.25 mm diameter 50% doped Er:YAG rod pumped by two flashlamps of 7 mm bore diameter in a double elliptical, silver-coated pump cavity [2.94]. At a pulse duration of 170 μs , the laser produced an output of 600 mJ at an input energy of 360 J per pulse. The repetition rate was 1 Hz. At higher repetition rates thermal lensing caused a reduction in efficiency and distorted the beam shape.

The system efficiency increases from a fraction of 1% to about 4–5% for laser diode pumped Er:YAG lasers. As an example, Fig. 2.16 depicts the output versus input characteristics of a 1.5-mm-thick Er:YAG hexagonal disk side-pumped with three laser diode bars [2.95]. This particular geometry provides for multiple internal reflection regions of the laser beam. The three quasi cw stacked-array diode lasers emitted at 962 nm with a spectral width of 5 nm (FWHM). The diodes were pulsed at 400 μs at a repetition rate of 100 Hz. The maximum output of 32 mJ of energy was achieved at 230 mJ of pump energy delivered to the crystal. This corresponds to an optical-to-optical efficiency of 14%.

The most efficient Er:YAG lasers are end-pumped monolithic designs. Power outputs around 1 W cw have been achieved [2.96]. Short pulses can be generated by Q-switching Er:YAG lasers with devices such as piezoelectrically controlled frustrated total internal reflection prisms[2.97] or passive devices using bleachable absorption[2.98].

Besides Er:YAG, the crystal Er:YLF is frequently employed for the generation of 2810 nm radiation. A 15% doped Er:YLF crystal, side-pumped by two 40 W diode bars emitting at 980 nm, generated up to 4 W cw output[2.99]. Using an intra-cavity quartz birefringent plate for wavelength selection, tunable output between 2700 and 2800 nm was obtained at specific lines corresponding to particular transitions between $^4\text{I}_{11/2}$ and $^4\text{I}_{13/2}$ manifolds.

2.4.2 Er:Glass

Erbium has been made to lase at 1.54 μm in both silicate and phosphate glasses. Because of the three-level behavior of erbium and the weak absorption of pump radiation codoping with other rare earth ions is necessary to obtain satisfactory system efficiency. In fact, erbium must be sensitized with ytterbium if the material is to lase

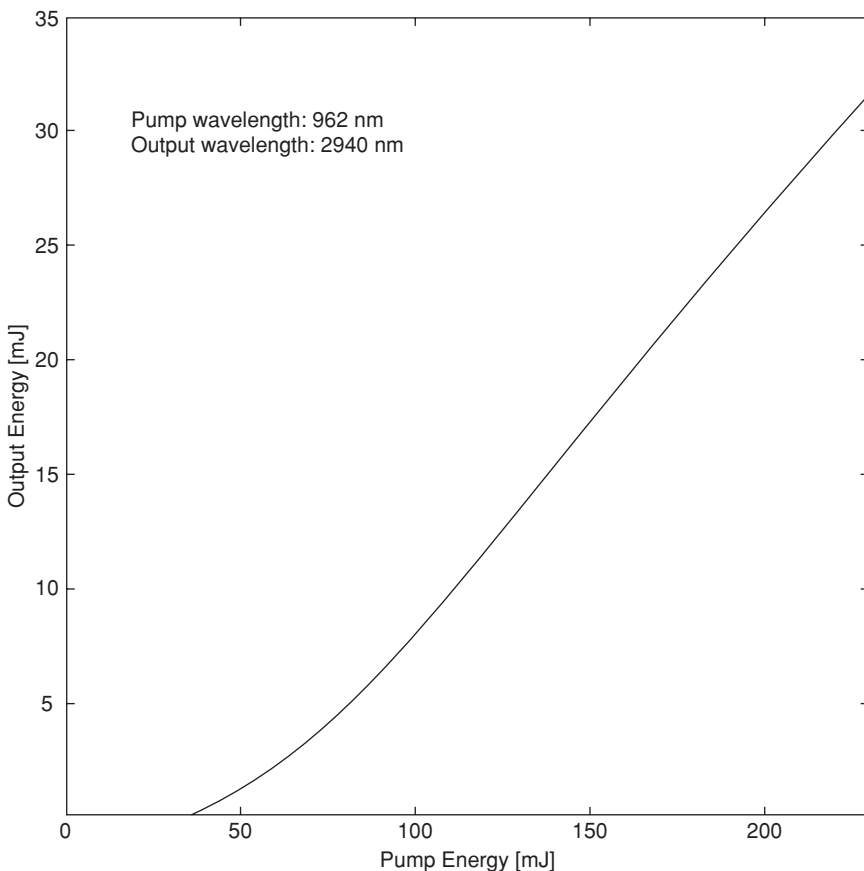


Fig. 2.16. Output vs. input curve for a diode pumped Er:YAG laser at 100 pps (after Ref.2.95)

at all at room temperature. Pump radiation is absorbed by ytterbium, which has an absorption band between 0.9 and 1 μm , and transferred to the erbium ions. The transfer is illustrated in Fig. 2.17. In the codoped Er:Yb:glass, radiation from a flashlamp or laser diode pumps the strong $^2\text{F}_{7/2} \rightarrow ^2\text{F}_{5/2}$ transition in Yb^{3+} . Because of the good overlap between the upper states of Yb^{3+} and Er^{3+} , the excited Yb^{3+} ions transfer energy to the $^4\text{I}_{11/2}$ level of Er^{3+} . The erbium ions then relax to the upper laser level $^4\text{I}_{13/2}$ and lasing occurs down to the $^4\text{I}_{15/2}$ manifold.

Laser action terminates at a Stark level within the ground manifold. At room temperature all levels of the terminal $^4\text{I}_{15/2}$ manifold are populated to some degree, thus this transition forms a three-level laser scheme with a correspondingly high threshold.

For flashlamp pumping, the efficiency of Er:glass can be further improved by adding Cr^{3+} in addition to Yb^{3+} . The Cr^{3+} ions absorb flashlamp radiation in two broadbands centered at 450 and 640 nm, and emit radiation in a broadband centered

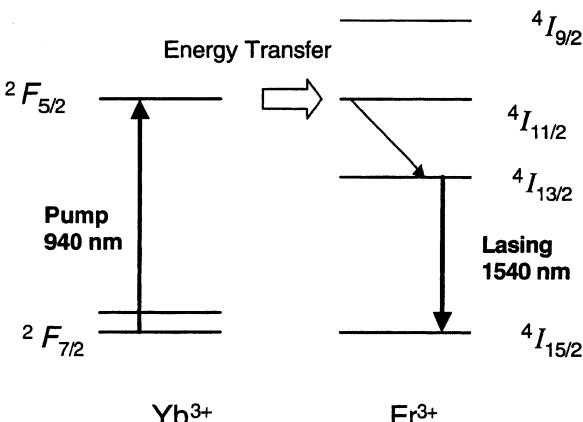


Fig. 2.17. Energy level diagram in codoped Er, Yb:glass

at 760 nm. This allows energy to be transferred from Cr^{3+} to the $^4\text{I}_{9/2}$ and $^4\text{I}_{11/2}$ states of Er^{3+} and the $^2\text{F}_{5/2}$ state of Yb^{3+} .

With the development of strained layer InGaAs laser diodes, which have emission between 0.9 and 1 μm , it is now possible to pump the strong Yb^{3+} transition $^2\text{F}_{7/2} - ^2\text{F}_{5/2}$. Diode pumping at 940 nm has dramatically improved the efficiency and average power achievable from Er:glass lasers.

The absorption of pump radiation by Yb^{3+} and efficient transfer to Er^{3+} is possible because the transfer rate from Yb to the Er transition is 10 times greater than the $^2\text{F}_{5/2}$ relaxation rate of Yb^{3+} . In particular the $^4\text{I}_{11/2}$ relaxation rate of Er is less than 10 μs , which allows rapid population of the Er^{3+} lasing state, while minimizing energy back transfer to Yb^{3+} .

The time required for transfer of energy from Yb^{3+} to Er^{3+} , and then for the $\text{Er}^{3+}\text{-}^4\text{I}_{11/2}$ manifold to relax to the $^4\text{I}_{13/2}$ state causes a time delay between the pump pulse and output laser pulse that is typical of Er:Yb:glass and depends on the pump level.

Because of the inhomogeneous broadening of the transition in glass, the absorption spectrum of Er:Yb:phosphate glass is smooth and continuous, allowing pumping at virtually any wavelength from 920 to 1000 nm as illustrated in Fig. 2.18. Material properties of Er:Yb:glass are listed in Table 2.8. The long fluorescence lifetime of Er^{3+} and the broad spectral absorption of Yb^{3+} are fortuitous for laser diode pumping.

The laser diode pumps of Er:glass lasers designed for military applications are typically operated at around 940 nm, rather than at the peak absorption wavelength shown in Fig. 2.18. At this wavelength, there is a broad absorption band where the absorption coefficient is between 4 and 6 cm^{-1} . Pumping in this spectral region allows operation of the pump laser diodes over a large temperature range without active temperature control. When compared with flashlamp pumping, the diode pump is over an order of magnitude more efficient and produces less heat.

Figure 2.19 illustrates the performance of a diode pumped Er:Yb: phosphate glass laser [2.100]. The 2 mm diameter and 10 mm long laser rod was side-pumped by two

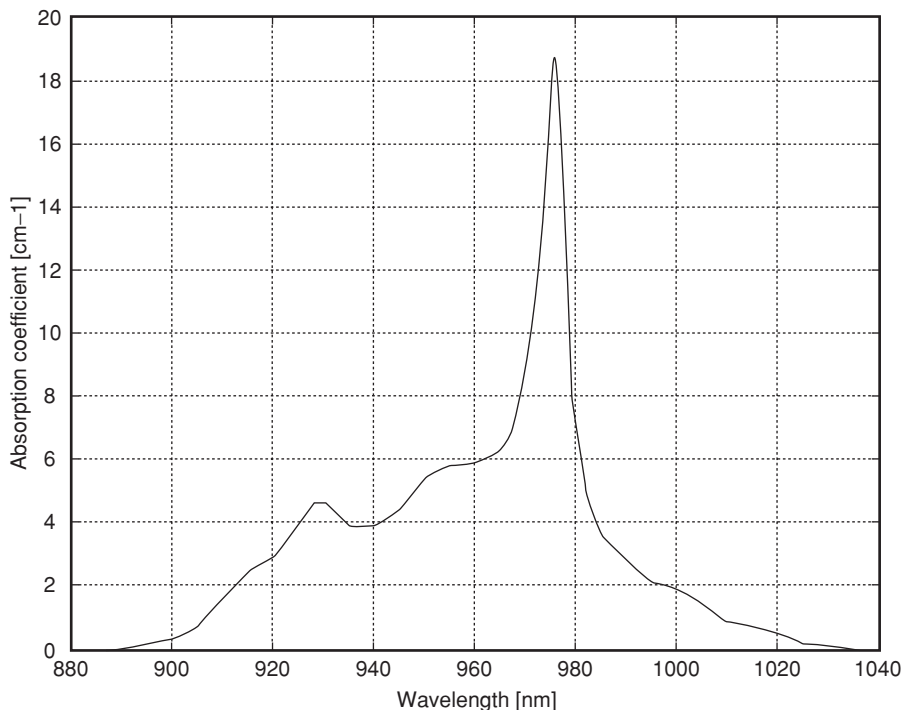


Fig. 2.18. Absorption spectrum of Er:Yb:phosphate glass [2.100]

diode arrays. Each array consisted of a stack of three 1-cm bars which had a 7-mm FWHM bandwidth peaked at 973 nm. The pulse width was limited by the power supply to 1 ms. At the maximum output of 20.5 mJ, the optical-to-optical efficiency was 8.6% and the system achieved a wall plug efficiency of 2.7%.

Small hand-held rangefinders are the major application of Er:glass lasers. For these applications the lasers have to be Q-switched. This is accomplished typically with spinning prisms, frustrated total internal reflection (FRIR) devices or intra-cavity bleachable absorbers.

A Q-switched Er:glass laser operating up to 50 Hz and producing 14 mJ Q-switched pulses at 25 Hz has been reported in [2.101]. The pump pulse width was

Table 2.8. Material properties of an erbium doped phosphate glass

Emission wavelength	1.54 μm
Fluorescent lifetime	8 ms
Index of refraction at 1.54 μm	1.531
$d\eta/dT$	$63 \times 10^{-7}/^\circ\text{C}$
Thermal expansion (α)	$124 \times 10^{-7}/^\circ\text{C}$
Thermo-optic coefficient (W)	$-3 \times 10^{-7}/^\circ\text{C}$

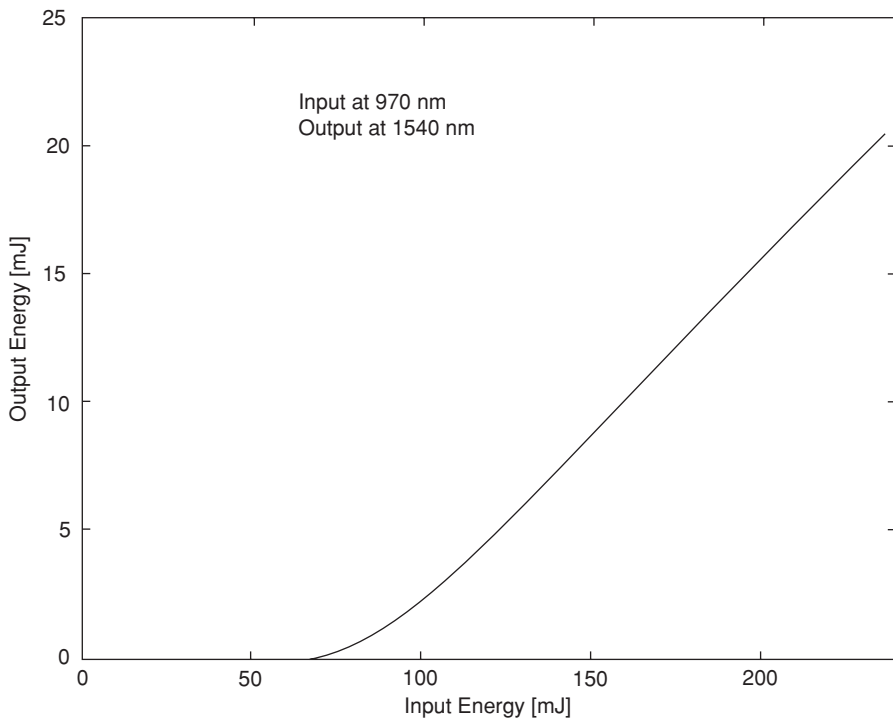


Fig. 2.19. Output vs. input of a diode pumped Er:Yb:phosphate glass laser [2.100]

5 ms with the diode arrays centered at 940 nm. The 2.5 mm diameter and 33 mm long Er:Yb:glass rod was side-pumped by 18 one centimeter bars. Total pump energy was 1.3 J. The Q-switch was a FTIR device. Since FTIR Q-switches are not polarization sensitive, thermal distortions that could lead to large depopulation losses in electro-optical Q-switches are not a problem.

A passively Q-switched microlaser producing 50 kw of peak power at 20 Hz has been described in [2.102]. The $\text{Co}^{2+}:\text{MgAl}_2\text{O}_4$ (Co:Spinel) saturable absorber Q-switch produced 2 ns pulses. In this design a single-stripe laser diode with 4 W output end-pumped a $2 \times 2 \times 3$ mm Er:doped phosphate glass “mini brick.” The complete laser can be packaged on a TO-3 header and the pulse energy of 100 μJ is sufficient for range applications up to 2 km.

2.5 Tunable Lasers

In a typical laser, such as Nd:YAG, the laser transition occurs between discrete energy states which produces a narrow line width output beam. Tunability of the emission in solid-state lasers is achieved when the stimulated emission of photons is intimately coupled to the emission of vibrational quanta (phonons) in a crystal lattice.

This electron–phonon coupling creates vibrational sublevels that spread the energy levels into bands, in this way laser transition can take place over a range of energies. In these “vibronic” lasers, the total energy of the lasing transition is fixed, but can be partitioned between photons and phonons in a continuous fashion. When a laser transition occurs between these coupled vibrational and electronic states, vibrational energy, i.e. a phonon, is either emitted or absorbed with each electronic transition.

Vibronic lasers have gain over a broad range of wavelengths which means they can produce either tunable output or ultra-short pulses (see Chap. 9). The large gain bandwidth of tunable lasers leads to some trade-off with other important material parameters. From (1.41) it follows that the excited state lifetime $\tau_f = 1/A_{21}$ and the cross section σ for stimulated emission is proportional to the inverse of the gain bandwidth $\Delta\nu$. By virtue of having a large bandwidth, tunable laser crystals have either a small stimulated emission cross section or a short fluorescence lifetime. Both parameters determine the operating characteristics of these lasers.

A small product $(\sigma\tau_f)$ leads to a high threshold for cw operation (see Chap. 3), a short fluorescence time τ_f makes pumping with flashlamps or laser diodes problematic or impossible, and a small σ requires a very intense pump source to reach threshold.

Typically, vibronic lasers are four-level systems and the laser transition occurs from the upper level to a vibrationally excited sublevel of the ground state. The ions in the lower laser level drop back to the ground level by releasing vibrational energy. The actual gain curve depends on temperature because the vibrational sublevels of the ground manifold—the lower laser level—are thermally populated. Higher temperatures populate higher vibrational levels, preventing the laser from oscillating at the shorter wavelength.

The history of tunable solid-state lasers can be traced back to work performed over 40 years ago at Bell Laboratories. In 1963, Bell-Labs researchers reported the first vibronic laser, a nickel-doped magnesium fluoride (Ni:MgF_2) device [2.103]. The same group later built a series of vibronic lasers using nickel, cobalt, or vanadium as the dopant and MnF_2 , MgO , MgF_2 , ZnF_2 , or KMgF_3 as the host crystal [2.104]. Tunable in the 1.12–2.17 μm range, these flashlamp-pumped lasers had a serious drawback: they operated only when cooled to cryogenic temperatures. Despite these early results, this field lay dormant for more than a decade, probably because of the need for cryogenic cooling of the laser material, the emergence of Nd:YAG, and the concentration on dye lasers and color-center lasers. The first room-temperature vibronic laser, reported by Bell Labs in 1974, was a flashlamp-pumped $\text{Ho:BaY}_2\text{F}_8$ device emitting at 2.17 μm [2.105].

In 1977, the crystal alexandrite (chromium-doped BeAl_2O_4) was made to lase on a vibronic transition [2.106, 107]. The crystal field strength at the chromium site in alexandrite is sufficiently low to permit thermal activation of broad ${}^4\text{T}_2$ fluorescence. The result is a low-gain, four-level laser tunable in the range of 0.7–0.8 μm .

During the mid-1970s, research started on a variety of divalent transition-metal doped crystals such as Ni^{2+} , V^{2+} , and Co^{2+} at MIT Lincoln Laboratory [2.108]. Most of the materials investigated, such as V:MgF_2 , suffered from excited state absorption, which reduces the net gain to an unacceptably low level. A notable exception is $\text{Co}^{2+}:\text{MgF}_2$, which turned out to be a useful laser.

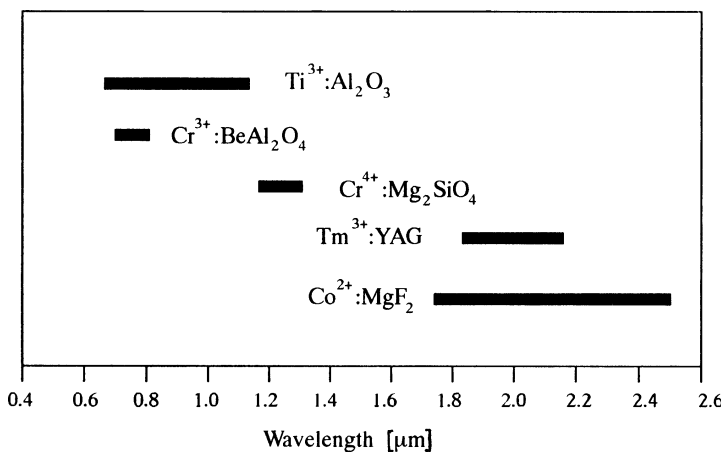


Fig. 2.20. Spectral range of several tunable lasers

If pumped by a $1.3 \mu\text{m}$ Nd laser, the cobalt laser is tunable from 1750 to 2500 nm. This earlier work resulted also in the discovery of the Ti:sapphire laser by Moulton in 1982 [2.109]. In the sapphire host, Ti^{2+} exhibits no appreciable excited-state absorption and therefore has a tuning range that spans virtually its entire fluorescence emission wavelength range.

The spectral ranges of typical tunable lasers are shown in Fig. 2.20.

Chromium Lasers

Chromium has enjoyed considerable success as a tunable-laser ion due to the special nature of its trivalent d^3 electronic configuration. Particular attributes of Cr over other transition metals are its chemical stability, broad pump bands, large energy-level splitting, and reduced excited state absorption (ESA). These advantages have led to at least a dozen crystals being demonstrated as good laser hosts for Cr. Chromium has a laser tuning range of about 100 nm, with the center wavelength shifted by the particular crystal host.

Alexandrite. Cr in chrysoberyl (BeAl_2O_4) lasers in the 700–800 nm range and was the first tunable ion solid-state laser considered for practical use. Details of this commercially available laser material are given in Sect. 2.5.1.

Cr:GdScGa-Garnet. Cr^{3+} -doped Ga garnets present a class of transition-metal ion lasers which can operate pulsed as well as cw at room temperature [2.110–113]. Because of a low-crystal field at the Cr site, the ${}^4\text{A}_2 - {}^4\text{T}_2$ splitting is nearly equal to the ${}^4\text{A}_2 - {}^4\text{T}_1$ separation. Thus, in contrast to ruby or alexandrite, the fluorescence is totally dominated by the broadband four-level ${}^4\text{T}_2 \rightarrow {}^4\text{A}_2$ transition.

Garnet crystals are described by the formula $\text{C}_3\text{A}_2\text{D}_3\text{O}_{12}$, where one chooses large ions $\text{A} = \text{Ga, Sc, Lu}$ for the octahedral site, $\text{D} = \text{Ga}$ for the tetrahedral site, and $\text{C} = \text{Y}$,

Gd, La, Lu for the dodecahedral site. Broadband four-level fluorescence has been obtained in the 700–950 nm spectral range from Cr-doped YGG, YScGG (YSGG), GGG, GdScGG(GSGG), and LaLuGG(LLGG) with lifetimes ranging from 240 to 70 μ s, respectively. The crystals are grown by the standard Czochralski technique at $\approx 1750^\circ\text{C}$.

One compound, Cr^{3+} -doped GdScGa-garnet, has received particular attention. In Cr^{3+} -doped GdScGa-garnet, the R-line fluorescence is totally absent and because of a large 2400 cm^{-1} Stokes shift of the ${}^4\text{T}_2$ Level, the whole fluorescence is channelled into the broadband (four level) ${}^4\text{T}_2 \rightarrow {}^4\text{A}_2$ transition. Pulsed and cw laser action has been obtained from Cr:GSGG over a tuning range from approximately 700 to 900 nm. The development of the alexandrite and Ti:sapphire lasers, which overlap the tuning range of Cr:GSGG have overshadowed this material, since the former can be flashlamp pumped and the latter has a wider tuning range.

Cr:KZnF₃. This fluorine perovskite was the second tunable solid-state laser material (after alexandrite) to be offered commercially [2.114]. Cr:KZnF₃ operates from 785 to 865 nm, with good slope efficiency when laser pumped between 650 and 700 nm. Like Cr:GSGG, this material has been displaced by the more versatile Ti:sapphire laser.

Cr:Forsterite. Both pulsed and cw laser operation has been achieved in Cr⁴⁺:Mg₂SiO₄ with Nd:YAG lasers at 1.06 μm or 532 nm as pump sources [2.115–117]. This laser is of interest because the tuning range covers the spectral region from 1167 to 1345 nm, which is not accessible with other lasers. A distinguishing feature of laser actions in Cr:Mg₂SiO₄ is that the lasing ion is not trivalent chromium (Cr^{3+}) as is the case with other chromium-based lasers but the active ion in this crystal is tetravalent chromium (Cr^{4+}) which substitutes for silicon (Si^{4+}) in a tetrahedral site. Single crystals of Cr-doped forsterite are grown by the Czochralski method. Forsterite has a fluorescence lifetime of 25 μs and therefore has to be pumped by another laser. Stimulated emission cross section is $1.44 \times 10^{-19} \text{ cm}^2$, about one-fourth of Nd:YAG.

One of the pump bands of forsterite spans the region ranging 850–1200 nm. Therefore, pulsed or cw Nd:YAG lasers are employed to pump forsterite lasers. Generation for short mode-locked pulses is the main attraction of this material (see Chap. 9).

Cr:LiSAF. Cr³⁺-doped LiSrAlF₆ has a tuning range from 780 to 920 nm and can be flashlamp and diode pumped. Very large crystals of high optical quality can be grown from this material. Cr:LiSAF lasers are particularly important for femtosecond pulse generation and will be discussed in Sect. 2.5.3 and Chap. 9.

Co:MgF₂

Interest in mid-IR lasers is stimulated by remote sensing and medical applications. Room temperature operation of Co-, Tm-, Ho-, and Er-doped materials has made this spectral region accessible to practical applications.

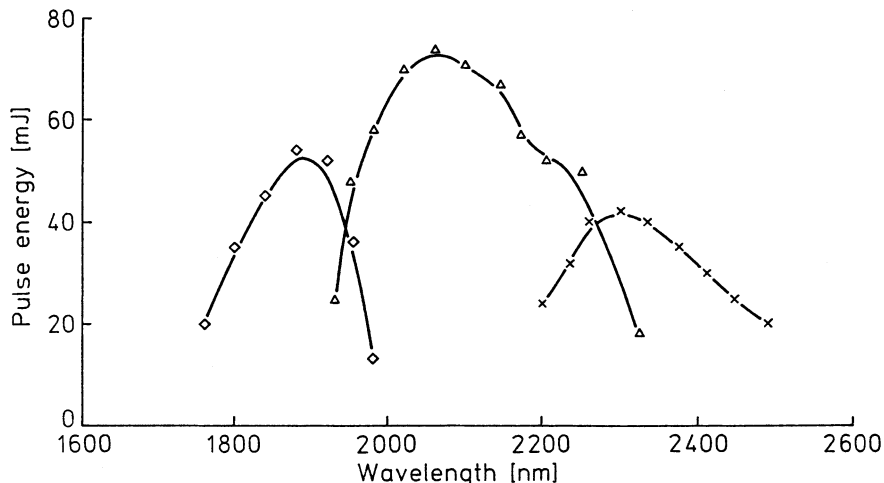


Fig. 2.21. Tuning range of the Co:MgF₂ laser [2.118]

Cobalt-doped magnesium fluoride (Co²⁺:MgF₂) has a particularly wide tuning range that extends from 1750 to 2500 nm. With flashlamp pumping, the laser requires cryogenic cooling. For this reason not much attention was given to this material. After it was discovered that room temperature operation is possible if the Co:MgF₂ crystal is pumped by a 1.32 μm Nd:YAG or Nd:YLF laser, commercial versions became available. Figure 2.21 shows the tuning range of the Co:MgF₂ laser, which requires different sets of optics to span the whole range.

Pulsed room temperature versions emit average powers on the order of a fraction of 1W. Powerful Co:MgF₂ lasers have achieved outputs up to 980 mJ at 10 Hz repetition rate [2.118]. Laser action is between the ⁴T₂ and ⁴T₁ state of Co²⁺. The role of the Co:MgF₂ as a tunable source for IR wavelengths has been diminished lately because Nd:YAG lasers, wavelength shifted with an OPO, can cover the same spectral region.

Titanium Laser

The Ti:sapphire laser has an exceptionally wide tuning range and a large gain cross section. Also, large, high-quality crystals are commercially available. These attributes have led to the use of this material for many laser applications. Further details will be discussed in Sect. 2.5.2.

Rare-Earth Tunable Lasers

Tm- and Ho-doped YAG, YLF, and YAP lasers are primarily employed as laser sources in the 2 μm region, a wavelength of interest for certain medical applications and coherent radar systems. However, limited tunability can also be achieved with these lasers. In the previous examples, tunability was afforded by the 3d electron of the transition-metal ions Cr³⁺ and Ti³⁺. In Tm³⁺:YAG, for example, the considerable

phonon broadening and high multiplicity of the Stark levels of the 4f electron provides tunability from 1.87 to 2.16 μm (Sect. 2.5.4). Similarly, holmium lasers have some tunability around 2.067 μm . For example, a diode-pumped Ho:Tm:YLF laser was tuned with an etalon between 2.06 and 2.07 μm [2.119]. Holmium lasers are usually codoped with Tm to provide increased absorption for the pump source. Although not particularly considered a tunable laser, Yb:YAG has tunability from 1.018 to 1.053 μm [2.120]. This laser is mainly of interest for high-power generation.

Tm, Ho, and Yb lasers have been known for years, but flashlamp pumping is not particularly efficient in these three-level lasers. The fact that these crystals can be pumped with laser diodes has generated renewed interest in these lasers materials. Tm:YAG is discussed in Sect. 2.5.4 and Yb:YAG in Sect. 2.6.

2.5.1 Alexandrite Laser

Alexandrite ($\text{BeAl}_2\text{O}_4:\text{Cr}^{3+}$) developed by Walling et al. [2.121] is the common name for chromium-doped chrysoberyl—one of the olivine family of crystals—with four units of BeAl_2O_4 forming an orthorhombic structure. The crystal is grown in large boules by the Czochralski method much like ruby and YAG. Laser rods up to 1 cm in diameter and 10 cm long with a nominal 2-fringe total optical distortion are commercially available. The chromium concentration of alexandrite is expressed in terms of the percentage of aluminum ions in the crystal which have been replaced by chromium ions. The Cr^{3+} dopant concentration, occupying the Al^{3+} sites, can be as high as 0.4 at.% and still yield crystals of good optical quality. A concentration of 0.1 at.% represents 3.51×10^{19} chromium ions per cubic centimeter.

Alexandrite is optically and mechanically similar to ruby, and possesses many of the physical and chemical properties of a good laser host. Hardness, strength, chemical stability, and high thermal conductivity (two-thirds that of ruby and twice that of YAG) enables alexandrite rods to be pumped at high average powers without thermal fracture. Alexandrite has a thermal fracture limit which is 60% that of ruby and five times higher than YAG. Table 2.9 lists the chrysoberyl material properties [2.122].

Table 2.9. Material parameters of alexandrite

Laser wavelength (nm)	700–818
Stimulated emission cross section (cm^2)	1.0×10^{-20}
Spontaneous lifetime (μs)	260 ($T = 298 \text{ K}$)
Doping density (at.%)	0.05–0.3
Fluorescent linewidth (nm)	100
Gain coefficient for 1 J/cm^3 stored energy (cm^{-1})	0.038–0.19
Index of refraction (750 nm)	$E b$ 1.7421
Thermal expansion	$ b 6.1 \times 10^{-6} / \text{K}$
Thermal conductivity (W/cm K):	0.23
Melting point ($^\circ\text{C}$)	1870
Hardness (kg/mm^2)	2000

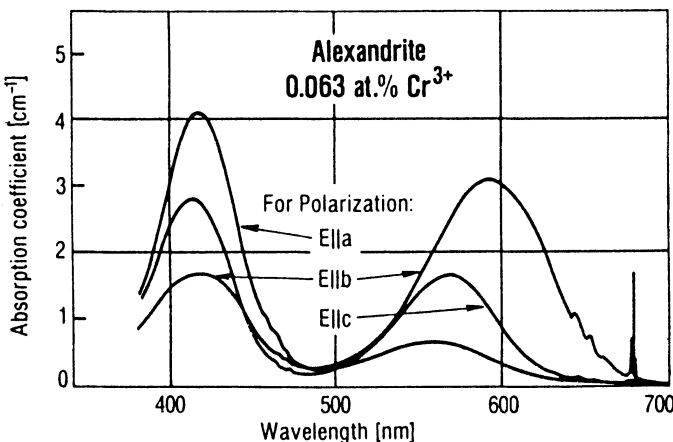


Fig. 2.22. Absorption spectrum of alexandrite [Allied Corps. Data Sheet]

Because of its orthorhombic structure, alexandrite is biaxial with the principal axes of the index ellipsoid along the crystallographic axes. Light emitted from the laser is polarized with the E vector parallel to the b axis. The gain in the $E \parallel b$ polarization is 10 times that in the alternate polarizations. Alexandrite lasers at room temperature with flashlamp pumping throughout the range 701–818 nm. The alexandrite absorption bands are very similar to those of ruby, and span the region from about 380 to 630 nm, with peaks occurring at 410 and 590 nm.

The absorption spectrum of alexandrite shown in Fig. 2.22 is compatible with pumping by flashlamps. Alexandrite lasers can also operate cw when pumped by arc lamps. But most commercial alexandrite lasers are pumped by flashlamps. The absorption peak near 680 nm shown in Fig. 2.22 has been exploited to pump alexandrite with diode lasers [2.123].

The laser gain cross section increases from $7 \times 10^{-21} \text{ cm}^2$ at 300 K to $2 \times 10^{-20} \text{ cm}^2$ at 475 K, which results in improved laser performance at elevated temperature. The 260 μs , room-temperature fluorescence lifetime permits effective energy storage and Q-switched operation.

Alexandrite can operate both as a four-level vibronic laser and as a three-level system analogous to ruby. As a three-level laser, it has a high threshold, fixed output wavelength (680.4 nm at room temperature), and relatively low efficiency. Obviously, the primary interest of alexandrite lies in its vibronic nature.

The basic physics of the four-level alexandrite laser can be discussed with reference to the energy level diagram (Fig. 2.23). The 4A_2 level is the ground state, and 4T_2 is the absorption state continuum. Vibronic lasing is due to emission from the 4T_2 state to excited vibronic states within 4A_2 . Subsequent phonon emission returns the system to equilibrium. Since alexandrite is an intermediate crystal field material ($E \approx 800 \text{ cm}^{-1}$) there is coupling between the 2E state and the 4T_2 . The lifetimes of each of these states is 1.5 ms and 6.6 μs , respectively. The two R lines emitted from 2E occur in the vicinity of 680 nm, as for ruby. The terminal laser level is a

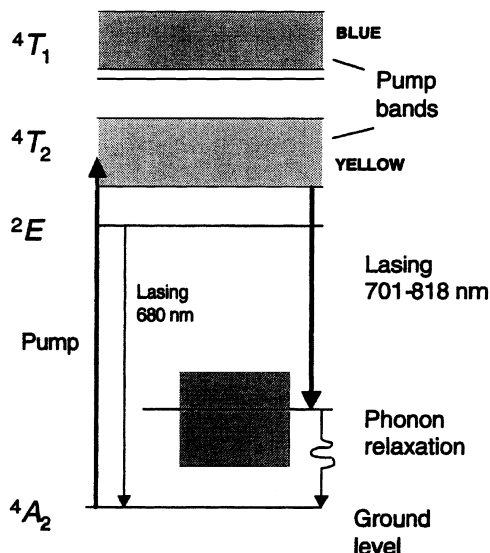


Fig. 2.23. Simplified energy level diagram for chromium ions in alexandrite

set of vibrational states well above the ground state. The initial laser level is a level 800 cm^{-1} above a long-lived storage level and in thermal equilibrium with it.

Because of the vibronic nature of the alexandrite laser, the emission of a photon is accompanied by the emission of phonons. These phonons contribute to thermalization of the ground-state vibrational levels. The laser wavelength depends on which vibrationally excited terminal level acts as the transition terminus; any energy not released by the laser photon will then be carried off by a vibrational phonon, leaving the chromium ion at its ground state.

As the temperature increases, the gain of alexandrite increases, the gain peak shifts to a longer wavelength, and the fluorescence lifetime decreases. The four-level model can be used to predict the temperature dependence of the laser performance. The 2E state acts as a storage level for 4T_2 . Thus, as the temperature of alexandrite increases, the vibronic continua in 4T_2 are successively populated from 2E in accordance with the Boltzmann distribution and the stimulated emission cross-section increases.

However, raising the temperature also tends to populate the terminal levels, especially those which lie closest to the ground level and which therefore correspond to the highest-energy (shortest-wavelength) photons. Since laser performance is highest with a maximally populated initial level and a minimally populated terminal level, it can be seen that increasing the temperature has two conflicting effects. The result is that performance is positively affected by temperature increases only for wavelengths above 730 nm.

Guch [2.124] evaluated the performance of a flashlamp-pumped alexandrite laser at temperatures from ambient to 310°C . As illustrated in Fig. 2.24a, the variation in laser output over the $34^\circ\text{--}310^\circ\text{C}$ range is dramatic. The threshold performance indicates that laser gain rises significantly, as temperature increases. Figure 2.24b illustrates laser output energy as a function of temperature for a fixed input to the

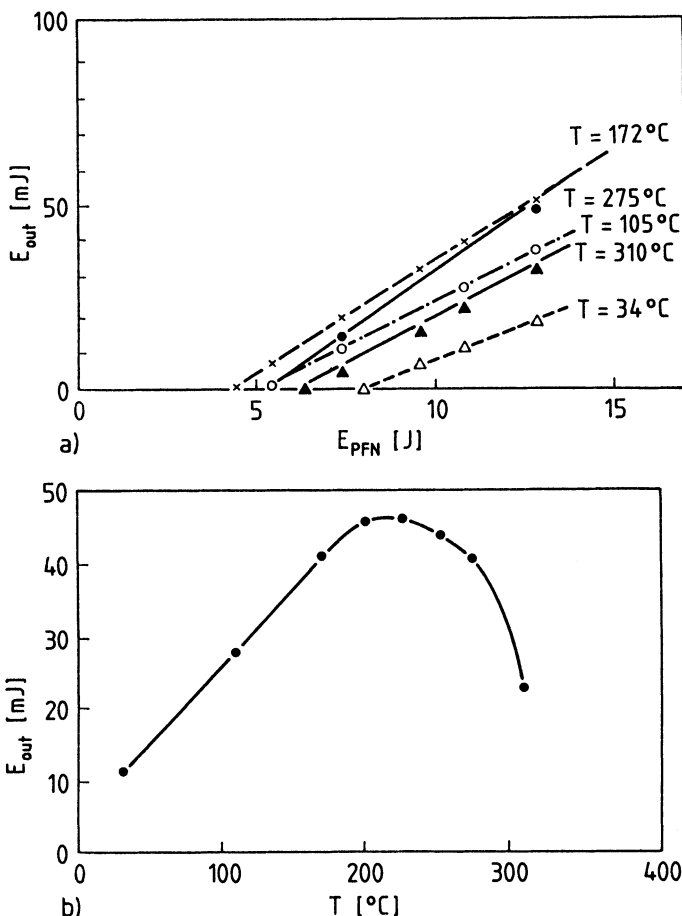


Fig. 2.24. Temperature dependence of alexandrite (a) Alexandrite laser energy as a function of pump energy at temperatures from 34 to 310°C . (b) Alexandrite laser output energy as a function of temperature for fixed 10.8-J flashlamp output [2.124]

flashlamp. The ability of alexandrite lasers to sustain high gain and efficiency at temperatures above those normally encountered in solid-state lasers is particularly striking.

For a fixed lamp pulse there is an optimum temperature at which the output peaks because the gain increases with temperature, but the fluorescent lifetime decreases. At higher temperatures the fluorescence lifetime becomes shorter than the flashlamp pulse duration and stored energy is lost as fluorescence.

The development of the alexandrite laser has reached maturity after over 20 years of efforts. Its high average-power performance is about 100 W if operated at 250 Hz [2.125]. Overall efficiency is close to 0.5%. Tunability over the range of approximately 700–818 nm has been demonstrated with tuning accomplished in a manner similar to dye lasers: a combination of etalons and birefringent filters. With these standard

spectral control devices 0.5 cm^{-1} linewidths and tunability over 150 nm has been achieved. Alexandrite has been lased in pulsed and cw modes; it has been Q-switched and mode locked.

A rod 10 cm long and 0.63 cm in diameter, when lased in a stable resonator, yields over 5 J long-pulsed and as much as 2 J with pulse duration less than 30 ns when Q-switched [2.122]. The reason for such high output energies is the fact that alexandrite is a low-gain medium.

2.5.2 Ti:Sapphire

Since laser action was first reported [2.109], the Ti:Al₂O₃ laser has been the subject of extensive investigations and today it is the most widely used tunable solid-state laser. The great interest in this material arises from the broad vibronic fluorescence band which allows tunable laser output between 670 and 1070 nm. Besides the broad tuning range of about 400 nm, Ti:sapphire possesses a large gain cross section that is comparable to Nd:YAG.

In this material, a Ti³⁺ ion is substituted for an Al³⁺ ion in Al₂O₃. Laser crystals, grown by the Czochralski method, consist of sapphire doped with 0.1% Ti³⁺ by weight. The absorption and fluorescence spectra for Ti:Al₂O₃ are shown in Fig. 2.25.

Crystals of Ti:Al₂O₃ exhibit a broad absorption band, located in the blue-green region of the visible spectrum with a peak around 500 nm. This is a wavelength region readily accessible with argon-ion and frequency-doubled Nd:YAG lasers. Both of these lasers are the most frequently employed pump sources for Ti:sapphire.

A relatively weak absorption band is observed in the IR region, which has been shown to be due Ti³⁺-Ti⁴⁺ pairs. The presence of Ti⁴⁺ ions causes detrimental absorption that interferes with efficient laser operation. Optimized crystal growth techniques and additional annealing processes have drastically reduced this absorption band compared to earlier crystals.

The fluorescence peaks at 780 nm, with a 180 nm bandwidth (FWHM). Therefore, the tunable output from commercial Ti:sapphire lasers is highest between about 700 and 900 nm.

A schematic energy level diagram of Ti:sapphire is shown in Fig. 2.26. The laser transition is between the ²E excited state and the ²T₂ ground state. Optical pumping excites Ti³⁺ to the upper laser level, which then relaxes to the bottom of the vibronic band before making the laser transition. Vibrational relaxation then drops ions to the bottom of the ground-level vibronic band. A strong interaction between the Ti atoms and host crystal, combined with a large difference in electron distribution between the two energy levels, makes the transition linewidth broad.

The energy level structure of the Ti³⁺ ion is unique among transition-metal laser ions in that there are no d-state energy levels above the upper laser level. The simple energy-level structure (3d¹ configuration) eliminates the possibility of excited-state absorption of the laser radiation, an effect which has limited the tuning range and reduced the efficiency of other transition-metal-doped lasers.

The laser parameters of Ti:Al₂O₃ are listed in Table 2.10. The outstanding features of Ti:sapphire are the broad fluorescence linewidth and the high stimulated emission cross-section. A drawback is the short fluorescence lifetime.

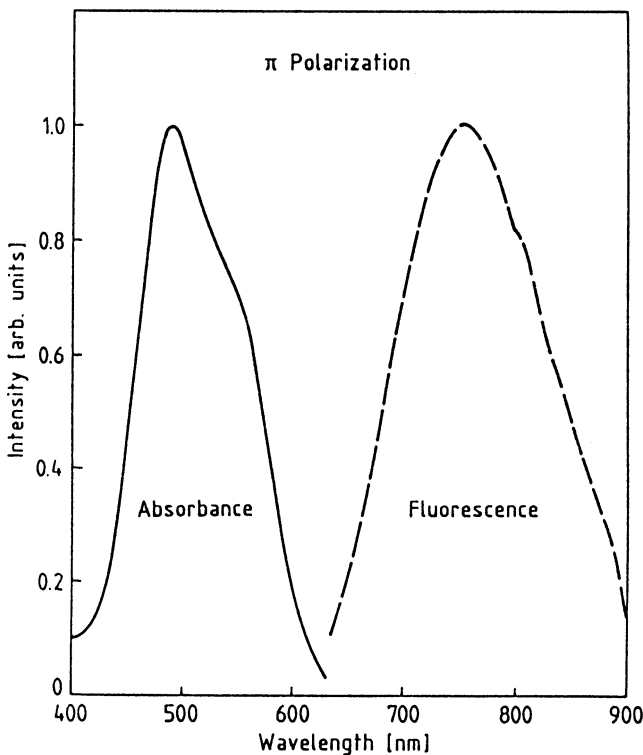


Fig. 2.25. Absorption and fluorescence spectra of the Ti^{3+} ion in Al_2O_3 (sapphire) [2.126]

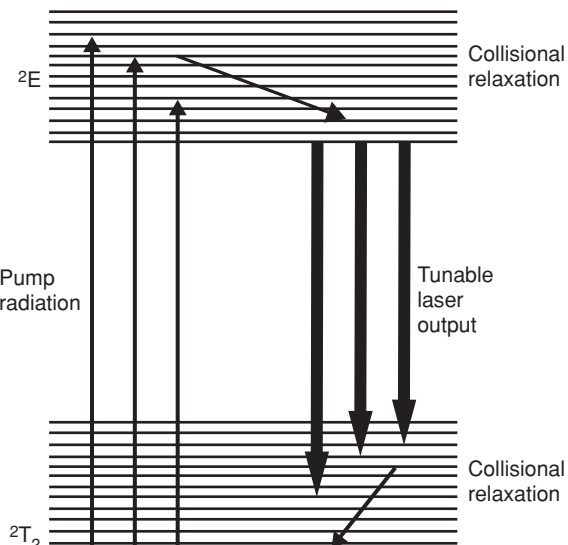


Fig. 2.26. Schematic energy level diagram of Ti:sapphire

Table 2.10. Laser parameters of Ti:Al₂O₃

Index of refraction	1.76
Fluorescent lifetime	3.2 μ s
Fluorescent linewidth (FWHM)	230 nm
Peak emission wavelength	780 nm
Peak stimulated emission cross section	
parallel to <i>c</i> -axis	$\sigma_{ } \sim 4.1 \times 10^{-19}$ cm ²
perpendicular to <i>c</i> -axis	$\sigma_{\perp} \sim 2.0 \times 10^{-19}$ cm ²
Stimulated emission cross section	
at 0.795 μ m	$\sigma_{ } = 2.8 \times 10^{-19}$ cm ²
Quantum efficiency of	
converting a 0.53 μ m photon	$n_Q \approx 1$
into an inverted site	
Saturation fluence at 0.795 μ m	$E_s = 0.9$ J/cm ²

Besides having favorable spectroscopic and lasing properties, one other advantage of Ti:Al₂O₃ are the material properties of the sapphire host itself, namely very high thermal conductivity, exceptional chemical inertness, and mechanical rigidity. Titanium sapphire is available from commercial vendors in sizes of 3.5 cm diameter by 15 cm long and, as a result of the well-developed growth technology for sapphire, of good optical quality.

Ti:sapphire lasers have been pumped with a number of sources such as argon and copper vapor lasers, frequency doubled Nd:YAG and Nd:YLF lasers, as well as flashlamps.

Flashlamp pumping is very difficult to achieve in Ti:sapphire because a very high pump flux is required. The reason is the short fluorescence lifetime of 3.2 μ s which results in a small product of stimulated emission cross-section times fluorescence lifetime ($\sigma \tau_f$). The population inversion in a laser required to achieve threshold is inversely proportional to $\sigma \tau_f$ as will be shown in Sect. 3.1. However, improvements in crystal quality, which lead to the removal of residual absorption bands, in combination with special flashlamps have resulted in output energies of 3 J per pulse at 2% efficiency. The flashlamps designed for high wall loadings were spectrally enhanced by using a dye surrounding the laser rod to convert near-UV light from the flashlamp into blue-green fluorescence which is within the absorption band of Ti:sapphire [2.127]. With design improvements in the lamp-discharge circuit and the pump cavity, an average power of 220 W at an efficiency of 2.2% has been achieved [2.128].

Commercial Ti:sapphire lasers are pumped by argon lasers to obtain cw output, and by frequency-doubled Nd:YAG or Nd:YLF lasers for pulsed operation. In the cw mode, typical performance is close to 1 W output with a 5 W argon pump.

Figure 2.27 depicts typical output characteristics of argon-ion pumped Ti:sapphire lasers. Without wavelength selection, the spectral output is near the peak of the gain curve. Wavelength selection and tuning is typically achieved by angular adjustment of a birefringent filter. In order to cover the entire wavelength range of Ti:sapphire, a change of the resonator mirrors is also required.

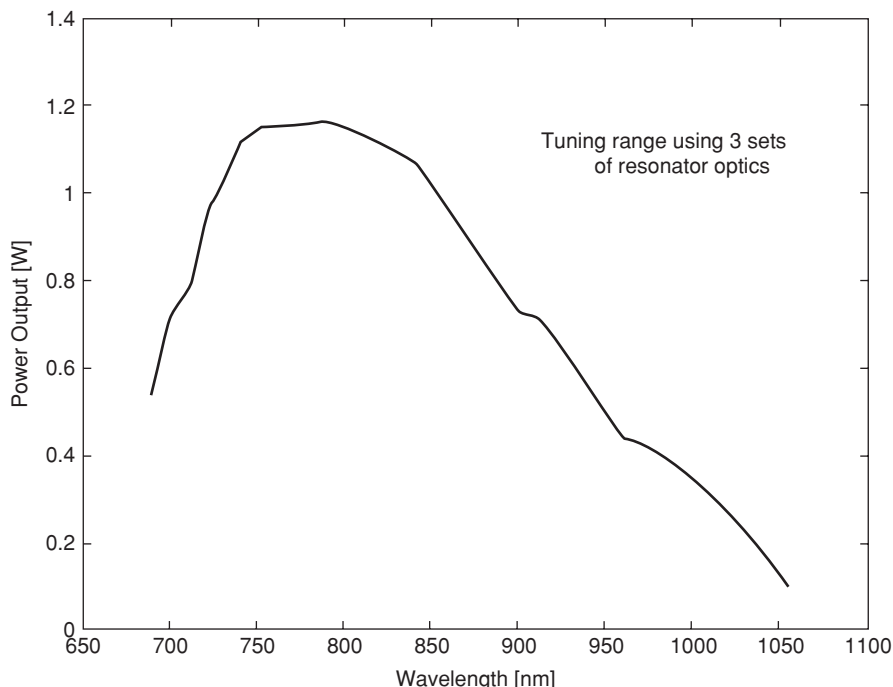


Fig. 2.27. Typical output power and spectral range of a Ti:sapphire laser pumped by a 5 W argon-ion laser (Schwartz Electro-Optics)

For pulsed solid-state lasers as pump source, output energies range from a few mJ at repetition rates of around 1 kHz, to 100 mJ per pulse at 20 pps.

Figure 2.28 displays the output of a Ti:sapphire laser pumped at 1 kHz by a frequency-doubled Nd:YLF laser which had an average output of 1.7 W at 527 nm. The pump pulses had a duration between 200 and 300 ns, whereas the Ti:sapphire laser yielded output pulses of 10–12 ns duration. This pulse shortening is characteristic of gain switched operation. The curves shown in Fig. 2.28 correspond to different sets of resonator mirrors.

With diode-pumped frequency-doubled Nd:YLF and Nd:YAG lasers as pump sources, very compact, all solid-state Ti:sapphire lasers can be designed [2.130–132]. The exceptionally broad gain band width of Ti:sapphire lasers can be exploited to generate extremely short pulses. The generation and amplification of mode-locked pulses is an important application of Ti:sapphire lasers and will be discussed in Chap. 9.

2.5.3 Cr:LiSAF

In the late 1980s, a family of fluorides was developed by Lawrence Livermore National Laboratory, which can serve as hosts for chromium. The crystals included $\text{Cr}^{3+}:\text{LiSrAlF}_6$ (LiSAF), which has a tuning range from 780 to 920 nm and an excited

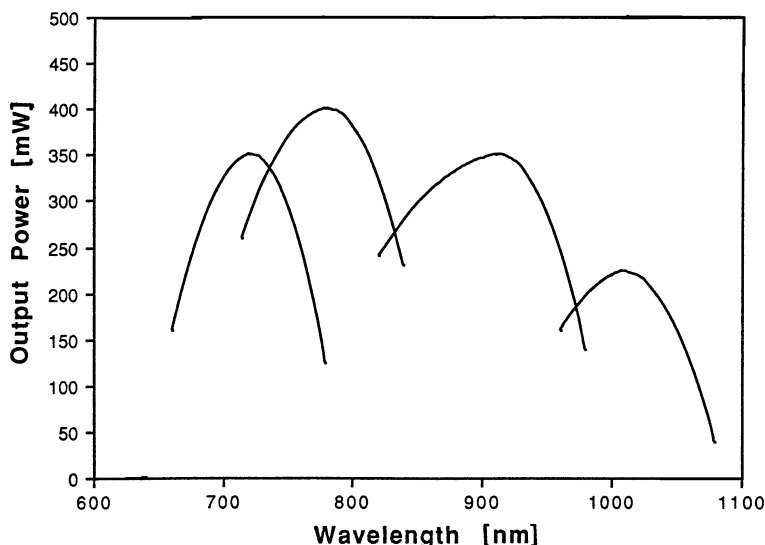


Fig. 2.28. Tuning range of a Ti:sapphire laser pumped by a Nd:YLF laser at 1 kHz [2.129]

lifetime of 67 μ s [2.133] and Cr³⁺:LiCaAlF₆ (LiCAF), which has a tuning range from 720 to 840 nm and a lifetime of 170 μ s [2.134]. Since the peak emission of LiCAF is four times larger than LiCAF, it generally performs better, and most of the recent laser work has concentrated on LiSAF.

The LiSAF host crystal is uniaxial and the Cr³⁺ emission has been shown to be strongly π -polarized ($E \parallel c$). The absorption and emission spectra are displayed in Fig. 2.29 [2.133]. The peak of the ${}^4T_2 \rightarrow {}^4A_2$ emission occurs at 830 nm and has a cross section of $4.8 \times 10^{-20} \text{ cm}^2$. Very large laser rods with diameters up to 25 mm have been fabricated from crystals grown by the Czochralski technique.

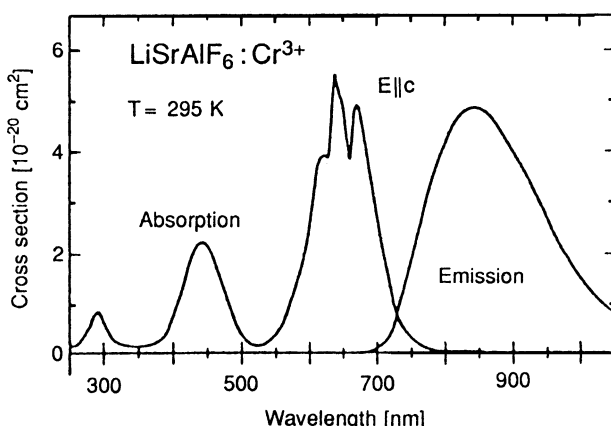


Fig. 2.29. Absorption and emission spectra of Cr:LiSAF [2.133]

Table 2.11. Comparison of relevant laser parameters for Cr:LiSAF and Ti:Sapphire

	Cr:LiSAF	Ti:Sapphire
Peak wavelength (nm)	850	790
Linewidth (nm)	180	230
Emission cross section (10^{-19} cm^2)	0.5	4.1
Fluorescence lifetime (μs)	67	3.2
Refractive index	1.41	1.76
Scattering loss (cm^{-1})	0.002	0

A comparison of important laser parameters of Cr:LiSAF with those of Ti:sapphire is shown in Table 2.11 [2.133, 134]. Peak emission of LiSAF is at a slightly longer wavelength as compared to Ti:sapphire, but there is a good overlap between the spectra. Actually, the output from mode-locked Ti:sapphire oscillators has been amplified by Cr:LiSAF amplifiers [2.135]. The gain bandwidth is narrower, but still comparable to Ti:sapphire. The major differences between the two crystals is the emission cross section, fluorescent lifetime, and the thermal and mechanical properties. While the gain of Cr:LiSAF is approximately one order of magnitude lower than that of Ti:sapphire, it has a long enough lifetime of 67 μs to permit efficient flashlamp pumping.

LiSAF is a rather soft and mechanically weak crystal with properties more related to glass than the far superior Ti:sapphire crystal. A comparison of the thermal and physical properties of LiSAF and glass is provided in Table 2.12 [2.136]. An important design consideration in using LiSAF crystals is the maintenance of the proper pH value of the cooling water for liquid-immersed laser rods. For example, at a pH value of 5, the material has a dissolution rate which is 100 times higher than that of YLF. However, at a pH value around 7, the dissolution rate is on the same order as YLF and phosphate glass.

Unlike Ti:sapphire, flashlamp pumping of Cr:LiSAF is fairly straight-forward due to the relatively long lifetime of the upper state level and the excellent overlap of the absorption bands with the emission of flashlamps. LiSAF can also be pumped with AlGaInP diodes at 670 nm [2.137, 138]. The product of emission cross section and upper state lifetime is sufficiently high ($\sigma \tau_f$) to facilitate a low cw laser threshold.

Table 2.12. Comparison of thermal and physical properties of LiSAF and glass

	Cr:LiSAF	Glass
Thermal shock resistance ($\text{W}/\text{m}^{1/2}$)	≈ 0.4	≈ 0.4
Fracture strength (kg/mm^2)	3.9	5
Thermal expansion coefficient ($\times 10^{-6}/^\circ\text{C}$)	22	11.4
Young's modulus (Gpa)	100	50
Microhardness (kg/mm^2)	197	≈ 500
Fracture toughness ($\text{MPam}^{1/2}$)	0.4	0.45
Thermal conductivity ($\text{W}/\text{m K}$)	3.09	0.62

Laser action has even been achieved by pumping highly doped crystals at the wings of the absorption profile at 752 nm with AlGaAs diodes [2.139].

Cr:LiSAF has found applications as a flashlamp or diode-pumped laser source with tunable output around 850 nm. The broadband emissions of Cr:LiSAF makes this crystal attractive for the generation and amplification of femtosecond mode-locked pulses. Of particular interest is a diode-pumped, all solid-state tunable source for femtosecond pulse generation [2.140–142]. As will be discussed in Chap. 9, systems have been developed which range from small diode-pumped Cr:LiSAF mode-locked oscillators to very large flashlamp-pumped amplifier stages with rod diameters up to 25 mm.

2.5.4 Tm:YAG

Thulium and thulium-sensitized holmium lasers have outputs in the 2 μm region, a wavelength of interest for coherent radar systems, remote sensing, and medical applications. The possibility of pumping Tm-doped crystals with readily available powerful GaAlAs laser diodes at 785 nm has stimulated interest in these materials. Representative crystals of this class of three-level lasers are Tm:YAG [2.145–147], Tm:YAP [2.151], Tm:YLF [2.143, 144] Ho:Tm:YAG [2.30], and Ho:Tm:YLF [2.152–154]. In the singly doped crystals, laser radiation is produced by the Tm³⁺ ion at 2 μm . In the doubly doped crystals, pump radiation is absorbed by the thulium ion, and by a cross-relaxation process energy is transferred to the holmium ion. Laser emission occurs at 2.1 μm between the ⁵I₇ and ⁵I₈ levels in holmium.

As an example of these tunable lasers in the 2 μm region, we will consider diode-pumped Tm:YAG. It seems to be the preferred crystal for a number of applications. Although Ho:Tm:YAG has a larger cross section as compared to Tm:YAG, it generally has poorer output performance because of increased losses introduced by up conversion from the upper laser level [2.146, 148]. However, impressive performance levels at room temperature have been obtained in Ho:Tm:YLF with output energies up to 125 mJ at single frequency [2.152]. This crystal has lower up conversion losses as compared to Ho:Tm:YAG. Also the extremely long lifetime of the upper laser level of 14 ms provides high energy storage capability for Q-switch operation at low repetition rates.

In the previous section we saw that tunability of solid-state lasers was achieved by the 3d electron of the transition metal ions Cr³⁺ and Ti³⁺. In Tm^{3+**:YAG}, the considerable phonon broadening and high multiplicity of the Stark levels of the 4f electron provides relative broad tunability around 2 μm .

The relevant energy levels and transitions of Tm:YAG are shown in Fig. 2.30. Pump radiation at 785 nm transfers Tm³⁺ ions from the ³H₆ ground state into the ³H₄ level of Tm. From the ³H₄ pump level the ions relax down to the upper laser level ³F₄. Laser action takes place between level ³F₄ and the lower laser level, which lies within the ³H₆ ground-state manifold. Output radiation is around 2 μm .

At high Tm concentrations, cross-relaxation between adjacent ions can occur, whereby the excitation is undergoing the transition ³H₄ \rightarrow ³F₄, while an unexcited ion simultaneously undergoes the transition ³H₆ \rightarrow ³F₄. This process leaves two

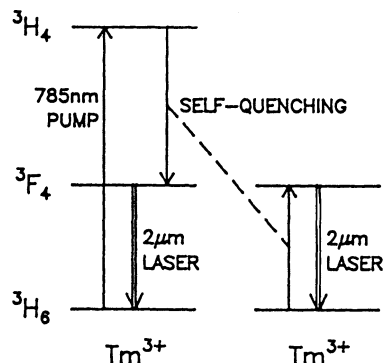


Fig. 2.30. Energy levels and pumping diagram for Tm:YAG [2.149]

Tm^{3+} ions in the upper laser level 3F_4 for every ion originally excited. In other words, two ions in the upper laser level are generated for every pump photon absorbed. At typical concentration levels of 3–12% Tm^{3+} , the quantum efficiency of pumping into the 3F_4 state is nearly two.

The fluorescence spectrum of Tm:YAG is shown in Fig. 2.31. The peak emission is at 2.02 μm and the bandwidth of fluorescence is about 400 nm. Tunability is typically from 1.87 to 2.16 μm. The absorption spectrum of Tm:YAG is centered at 785 nm and has a linewidth of 4 nm, which makes pumping attractive with GaAlAs diodes. Pertinent laser parameters are summarized in Table 2.13 [2.155]. Compared to Nd:YAG, the disadvantages of Tm:YAG are the higher threshold to overcome the residual population in the ground level and the two orders of magnitude smaller gain cross section. Since the lower laser level is in the ground-state manifold and therefore, partially populated, quasi-three-level lasers require stronger pump intensities or they require cooling to reduce the population in the lower laser level.

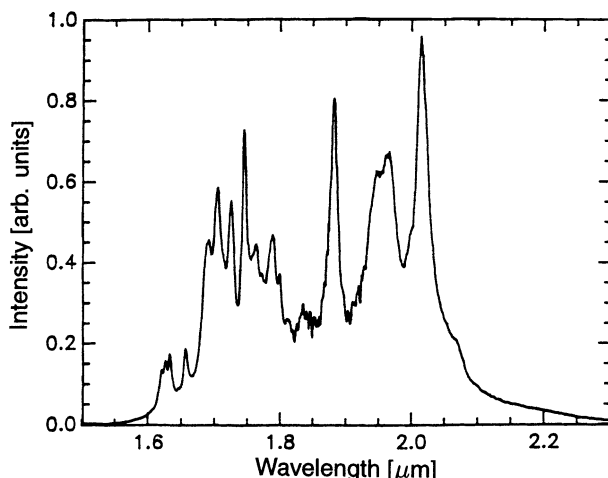


Fig. 2.31. Fluorescence spectrum for Tm:YAG [2.149]

Table 2.13. Material parameters of Tm:YAG
[2.149, 155]

Pump wavelength	780–785 nm
Peak laser wavelength	2.02 μm
Effective cross section at 25°C	$2 \times 10^{-21} \text{ cm}^2$
Fluorescence lifetime	10 ms
Tunability	1.87–2.16 μm

The rather dramatic improvement in laser performance when the Tm:YAG crystal is operated at reduced temperature is illustrated in Fig. 2.32. Also shown is the output dependence of Ho:Tm:YAG on temperature. Because of the more complete three-level nature of this material, the temperature dependence is even stronger than in Tm:YAG.

Instead of pumping Tm:YAG at the peak absorption line, sometimes “wing pumping” at 805 nm is employed. The lower absorption coefficient at that wavelength provides a longer pathlength in the crystal, which is advantageous in high power lasers for better heat removal and reduced thermal loading. Also, pump diode performance and reliability is improved because at the longer wavelength the aluminum concentration in GaAlAs is lower. In an end-pumped 3 mm diameter by 55 mm long Tm:YAG rod, a cw output of 115 W was achieved by pumping at 805 nm with 460 W of cw pump power [2.147]. The output was achieved by maintaining the crystal temperature at 3°C.

Side-pumping of a 3 mm diameter and 105 mm long, 3%-doped Tm:YAG rod produced 120 W cm power [2.145]. The active region of the Tm:YAG crystal was only 65 mm long. Diffusion-bonded, undoped end caps prevented absorption losses by the unpumped region of the laser rod. The 785 nm output from three diode arrays was coupled to the laser crystal through a compound parabolic concentrator. The maximum optical-to-optical conversion efficiency was 25%, and output vs input had a slope efficiency of 31%.

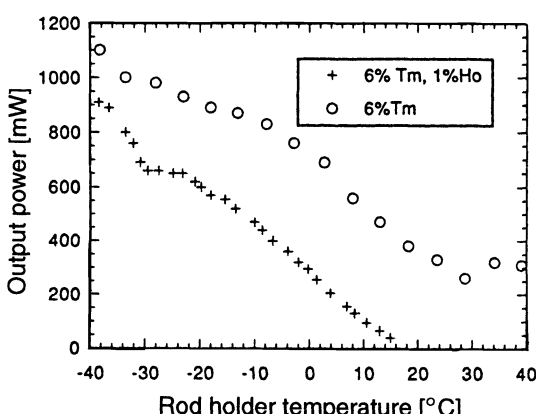


Fig. 2.32. Output power of Tm:YAG and Tm:Ho:YAG as a function of temperature [2.155]

Besides Tm:YAG, the crystal Tm:YLF has been frequently used to produce $2\mu\text{m}$ radiation [2.143, 144]. For example, a 3.5%-doped Tm:YLF slab, side-pumped by diode bars at 792 nm, generated 28 W of output at a pump power of 170 W. Threshold was 63 W and the slope efficiency was 25%.

2.6 Yb:YAG

Although Yb:YAG has been known for decades, interest was not very high in this material since it lacks any pump bands in the visible spectrum. The crystal has only a single absorption feature around 941 nm. With conventional pump sources such as flashlamps, the threshold is very high, which eliminated this material from any serious consideration. With the emergence of powerful InGaAs laser diodes that emit at 941 nm, the picture has changed completely and Yb:YAG has become an important laser material [2.156]. The relevant energy level diagram of Yb:YAG is very simple and consists of the $^2\text{F}_{7/2}$ lower level and $^2\text{F}_{5/2}$ excited state manifolds separated by about $10,000\text{ cm}^{-1}$. The laser wavelength is at $1.03\text{ }\mu\text{m}$, a representative emission spectrum for a 5.5 at.% doped sample is shown in Fig. 2.33.

The laser transition $^2\text{F}_{5/2}-^2\text{F}_{7/2}$ has a terminal level 612 cm^{-1} above the ground state (see Fig. 2.34). The thermal energy at room temperature is 200 cm^{-1} ; therefore, the terminal state is thermally populated making Yb:YAG a quasi-three level system. By comparison, the terminal laser level in Nd:YAG is about 2110 cm^{-1} above the ground state. Being a quasi-three-level laser, Yb:YAG absorbs at $1.03\text{ }\mu\text{m}$ unless it is pumped to inversion. At room temperature the thermal population of the lower laser level is about 5.5%. The absorbed pump power per volume needed to achieve

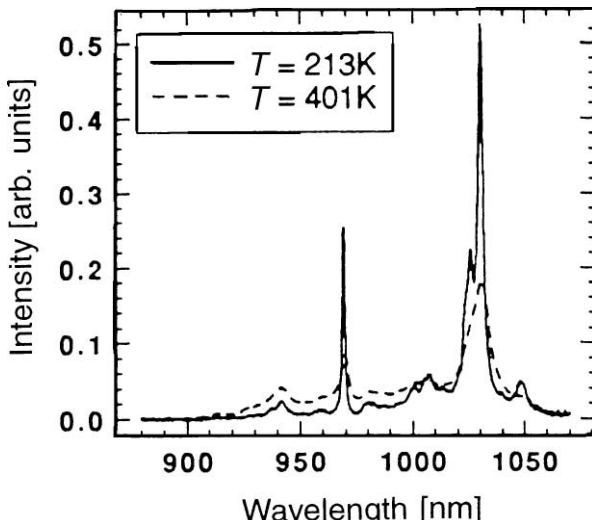


Fig. 2.33. Emission spectra of Yb:YAG with 5.5 at.% doping [2.157]

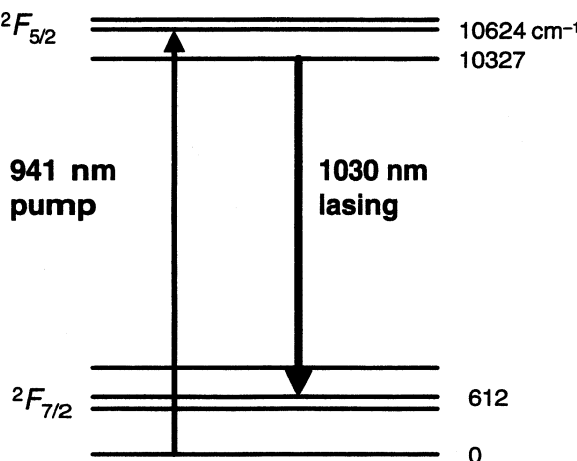


Fig. 2.34. Relevant energy levels in Yb:YAG

and maintain transparency at the laser wavelength is $I = f_a n_t h \nu_p / \tau_f$, where f_a is the fraction of the total ion density n_t occupying the lower laser level, $h \nu_p$ is the energy per pump photon, and τ_f is the lifetime of the upper level. With $f_a = 0.055$, $n_t = 1.38 \times 10^{20} \text{ cm}^{-3}$ at 1% doping, $h \nu_p = 2.11 \times 10^{-19} \text{ J}$, and $\tau_f = 0.95 \text{ ms}$, the absorbed pump power needed to reach inversion is 1.7 kW/cm³. Of course, a higher power density is required to overcome optical losses and reach laser threshold, and for an efficient operation the laser has to be pumped about five to six times above threshold. Typically, in this laser, small volumes of material are pumped on the order of 10 kW/cm³.

Yb:YAG performance is strongly dependent on temperature and can be improved by cooling the crystal, which reduces the thermal population and increases the stimulated emission cross section from $2.1 \times 10^{-20} \text{ cm}^2$ at room temperature to twice this value at 220 K.

Figure 2.35 illustrates the dependence of optical efficiency, i.e., the conversion of pump light into laser output, on temperature [2.158]. In this laser a thin disk, about 0.4-mm thick, is pumped with fiber-coupled laser diodes in a multiple-path arrangement. The Yb:YAG crystal is mounted on a heat sink which could be cooled to low temperature. Two different pump sources were evaluated. With the smaller diode array the efficiency increased from 45% at room temperature to 64% at -74°C. With the larger pump source the efficiency changes from 38% at room temperature to 55% at -65°C. At this low temperature the output was 100 W for the 183 W pump. At the more typical operating temperature of -9°C for this laser, a pump power of 225 W was needed to generate the same output. Clearly, laser efficiency and cost of the pump source can be traded for overall system efficiency which includes power and cost for refrigeration. Quite noticeable is the high optical-to-optical efficiency which can be achieved in these lasers.

The strong temperature dependence of Yb:YAG requires an aggressive thermal management to avoid high temperatures.

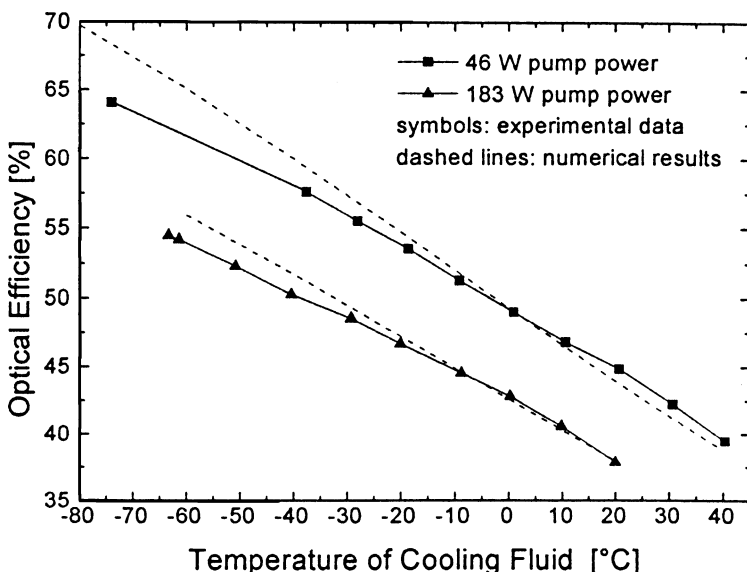


Fig. 2.35. Optical efficiency vs. temperature for Yb:YAG at two different pump powers [2.158]

In most of the large systems built to date the temperature of the crystal is maintained between -10°C and 20°C depending on the particular design and mode of operation. To maintain the laser crystal at such a temperature under intensive pump radiation requires, as a minimum, some kind of refrigeration.

Despite these obvious drawbacks, Yb:YAG has a number of redeeming features which motivated the development of very powerful systems. Pumping of Yb:YAG with an InGaAs pump source produces the smallest amount of crystal heating compared to any other major laser system. Actually the pump radiation in this material generates only about one-third of the heat compared to Nd:YAG. The fractional thermal loading, i.e., the ratio of heat generated to absorbed energy is around 11% for Yb:YAG pumped at 943 nm and 32% for Nd:YAG pumped at 808 nm. This substantially reduced thermal dissipation is the result of a very small energy difference between the photons of the pump and laser radiation. This quantum defect or Stokes shift is 9% in Yb:YAG versus 24% in Nd:YAG. The thermal load generated in a laser medium is of primary concern for high-power applications. The reduced thermal heat load can potentially lead to higher-average-power systems with better beam quality than possible with Nd:YAG. Other unique advantages of Yb:YAG are an absorption bandwidth of 18 nm for diode pumping, which is about 10 times broader than the 808 nm absorption in Nd:YAG. This significantly relaxes temperature control needed for the diode pump source. Yb:YAG has a long lifetime of $951\ \mu\text{s}$, which reduces the number of quasi-cw pump diodes required for a given energy per pulse output. As will be discussed in Chap. 6, since laser diodes are power limited, a long fluorescence time permits the application of a long pump pulse that, in turn, generates a high-energy output. Important materials parameters of Yb:YAG are listed in Table 2.14.

Table 2.14. Pertinent material parameters for Yb:YAG

Laser wavelength	1030 nm
Radiative lifetime at room temperature	951 μ s
Peak emission cross section	2.1×10^{-20} cm 2
Peak absorption wavelength	941 nm
Pump bandwidth at 941 nm	18 nm
Doping density (1% at.)	1.38×10^{20} cm 3

Besides overcoming the initial absorption of Yb:YAG that is determined by the quasi-three-level structure, a high pump intensity is also required because of the rather small cross section of Yb:YAG which results in a large saturation intensity of 9.7 kW/cm 2 and a saturation fluence of 9.2 J/cm 2 . For cw operation good extraction efficiency requires an intra-cavity intensity higher than the saturation density, and in pulsed operation the internal fluence has to exceed the saturation fluence.

The presence of only one excited-state manifold eliminates problems associated with excited-state absorption and up-conversion processes. Despite the quasi-three-level behavior of Yb:YAG, the obvious advantages of very low fractional heating, broad absorption at the InGaAs wavelength, long lifetime combined with high conductivity, and tensile strength of the host crystal have raised the prospect of high-power generation with good beam quality.

The major interest lies in large systems at the kilowatt level for industrial applications.

Different pump schemes, such as end- and side-pumping of a small rod, or face-pumping of a thin disk, have been tried with Yb:YAG lasers to meet the requirements of efficient thermal management and generation of high pump intensities. The various approaches all produced laser oscillators with output powers in excess of 1 kW.

In a side-pumped configuration, 1kW of cw power was obtained from an oscillator containing a 3 mm diameter and 30 mm long 1.5 at.% Yb:YAG crystal [2.159]. Threshold was at 1 kW, and with an optical-to-optical slope efficiency of 25% the maximum output was achieved at 5 kW pump input. The rod cooling temperature was held at 18°C. From the 0.21 cm 3 volume of the rod, follows a volumetric power density of 24 kW/cm 3 at the maximum input power. This power density is far in excess of the initial 1.7 kW/cm 3 pump investment required to bleach the crystal because of its quasi three-level nature. This explains why at very high output powers quasi-three-level lasers behave like four-level systems.

Different resonator mirrors were tested and output mirrors with reflectivities between 50 and 68% produced about the same maximum output. From these values and a rod cross-sectional area of 0.21 cm 2 follows a power density inside the crystal between 43 and 75 kW/cm 2 (see Sect. 3.3). This is about a factor four to seven times the saturation density for Yb:YAG and thus assures good extraction efficiency.

In the end-pumped configuration, the output radiation from a stack of diode bars is collimated and funneled into the front end of a 2 mm diameter and 60 mm long rod [2.160]. The crystal is doped at a low concentration of 0.44% such that the absorption path is long and heat removal can take place along the barrel of the

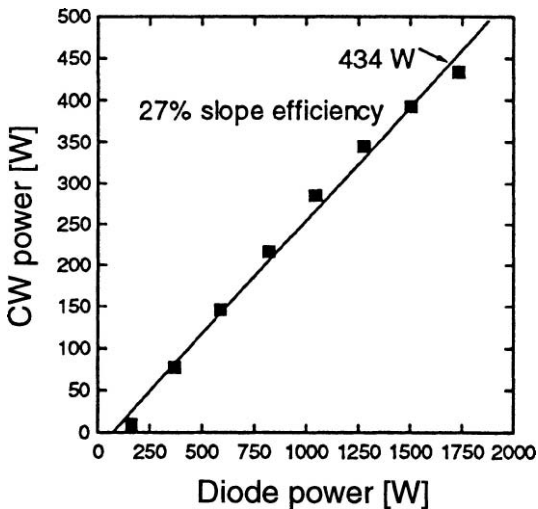


Fig. 2.36. cw output power as a function of diode power of an end-pumped Yb:YAG [2.160]

rod. The crystal temperature was maintained at 0°C with a water–alcohol mixtrue. Figure 2.36 illustrates the performance of the system, in which up to 434 W in cw mode was achieved.

In an extension of this work, two end-pumped 0.7%-doped Yb:YAG rods with undoped diffusion-bonded ends yielded 1080 W average power with 27.5% optical-to-optical efficiency[2.161].

Extremely small volumes, on the order of a few mm³, are pumped in the thin-disk approach [2.158, 162, 163]. In this design, disks with a thickness of typically (0.3–0.4) mm are pumped from the front in a multiple pass active mirror design. The disks, mounted on a cold finger, are cooled from the backside. The pump beam is typically 2.5–7 mm in diameter. The discs are heavily doped up to 11%. At a temperature of 1°C an output power of 264 W was measured for one particular setup. Electrical input power to the diodes was 2060 W which gives an electrical to optical efficiency of 12.8%.

A thin 8% Yb:YAG disk with one side mounted on a heat sink generated cw output power of 1070 W with 48% optical efficiency[2.164].

In general, the efficiency of quasi-three level Yb:YAG lasers is comparable to the overall efficiency obtained in large Nd:YAG systems; however, the much reduced heat load in Yb:YAG permits generation of comparable outputs in much smaller laser crystals.

A number of crystals have been doped with Yb, in particular apatite crystals, but YAG is favored for power scaling because it has excellent thermomechanical properties.

3. Laser Oscillator

In Chap. 1 we studied the processes which lead to optical amplification in laser materials. The laser oscillator is essentially a combination of two basic components: an optical amplifier and an optical resonator. The optical resonator, comprising two opposing plane-parallel or curved mirrors at right angles to the axis of the active material, performs the function of a highly selective feedback element by coupling back in phase a portion of the signal emerging from the amplifying medium.

Figure 3.1 shows the basic elements of a laser oscillator. The pump lamp inverts the electron population in the laser material, leading to energy storage in the upper laser level. If this energy is released to the optical beam by stimulated emission, amplification takes place. Having been triggered by some spontaneous radiation emitted along the axis of the laser, the system starts to oscillate if the feedback is sufficiently large to compensate for the internal losses of the system. The amount of feedback is determined by the reflectivity of the mirrors. Lowering the reflectivity of the mirrors is equivalent to decreasing the feedback factor. The mirror at the output end of the laser must be partially transparent for a fraction of the radiation to “leak out” or emerge from the oscillator.

An optical structure composed of two plane-parallel mirrors is called a Fabry-Pérot resonator. In Chap. 5 we will discuss the temporal and spatial mode structures which can exist in such a resonator. For the purpose of this discussion it is sufficient to know that the role of the resonator is to maintain an electromagnetic field configuration whose losses are replenished by the amplifying medium through induced emission. Thus, the resonator defines the spectral, directional, and spatial characteristics of the laser radiation, and the amplifying medium serves as the energy source.

In this chapter we will develop an analytical model of a laser oscillator that is based mainly on laser system parameters. A number of technical terms, which are briefly explained here, will be used. The arrangement of flashlamp and laser rod shown in Fig. 3.1 is referred to as side-pumped or transverse-pumped because the pump radiation strikes the laser rod from the side with respect to the direction of propagation of the laser radiation. The flashlamp is often water-cooled by inserting it into a flowtube or cooling jacket. Water or any other suitable coolant is pumped through the annulus between the lamp envelope and the flowtube inner diameter. The pump cavity can be elliptical in cross section or closely wrapped around the lamp and laser rod. The latter design of a pump cavity is called close-coupled.

Instead of a flashlamp as shown in Fig. 3.1, laser diode arrays can be placed along the length of the laser rod. A reflective pump cavity of the type employed for

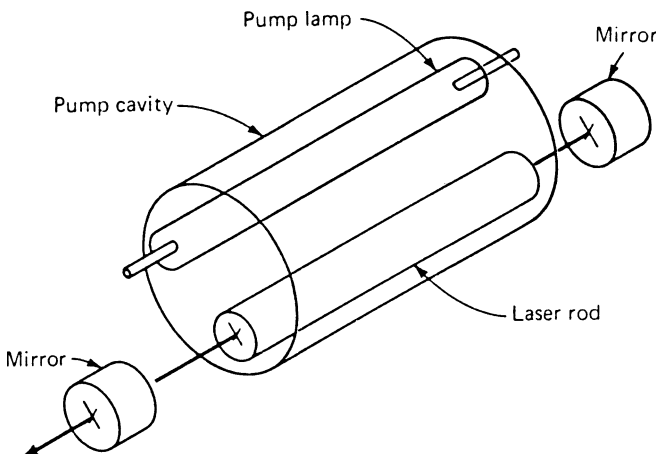


Fig. 3.1. Major components of an optically pumped solid-state laser oscillator

flashlamps is not necessary since the radiation output from laser diodes is directional. However, in some cases, focusing optics is inserted between the laser diodes and the laser crystal to shape and/or concentrate the pump beam. Since the output from laser diodes can be collimated and focused, contrary to flashlamp radiation, the pump radiation can also be introduced through the back mirror shown in Fig. 3.1. In this so-called end-pumped or longitudinal pump scheme, pump radiation and laser radiation propagate in the same direction.

The structure of the two mirrors reflecting the laser radiation is generally described as the laser resonator. However, in the literature, as well as in this book, the term cavity or laser cavity is also used. This is in contrast to the pump cavity which is the enclosure employed to contain the flashlamp radiation. The pump head is the structure and mechanical assembly that contains the laser crystal, pump source, cooling channels and electrical connections.

3.1 Operation at Threshold

We will calculate the threshold condition of a laser oscillator composed of two mirrors having the reflectivities R_1 and R_2 and an active material of length l . We assume a gain coefficient per unit length of g in the inverted laser material. In each passage through the material the intensity gains by a factor of $\exp(gl)$. At each reflection a fraction $1 - R_1$ or $1 - R_2$ of the energy is lost. Starting at one point, the radiation will suffer two reflections before it can pass the same point in the original direction.

(a) *Threshold condition:* The threshold condition is established by requiring that the photon density—after the radiation has traversed the laser material, been reflected by mirror with R_1 , and returned through the material to be reflected by mirror with

R_2 —be equal to the initial photon density. Then on every complete two-way passage of the radiation through the laser the loss will just equal the gain. We can express the threshold condition by

$$R_1 R_2 \exp(2gl) = 1. \quad (3.1)$$

The regenerative amplifier becomes unstable when the amplification per transit exceeds the losses. In this case oscillations will build up, starting from a small disturbance. Clearly, if the round-trip gain

$$G = R_1 R_2 \exp(2gl) \quad (3.2)$$

is larger than 1, radiation of the proper frequency will build up rapidly until it becomes so large that the stimulated transitions will deplete the upper level and reduce the value of g . The condition of steady state is reached if the gain per pass exactly balances the internal and external losses. This process, called gain saturation, will be discussed in Sect. 3.2. In an oscillator a number of loss mechanisms are responsible for attenuating the beam; the most important ones are reflection, scattering, and absorption losses caused by the various optical components. It is convenient to lump all losses which are proportional to the length of the gain medium, such as absorption and bulk scattering, into an absorption coefficient α . The condition for oscillation is then

$$R_1 R_2 \exp(g - \alpha)2l = 1. \quad (3.3)$$

Rearranging (3.3) yields

$$2gl = -\ln R_1 R_2 + 2\alpha l. \quad (3.4)$$

Losses such as scattering at interfaces and Fresnel reflections which are not dependent on the length of the gain medium can be thought of as leakage from the rear mirror. Hence the reduced reflectivity R_2 of the rear mirror $R_2 = 1 - \delta_M$ takes into account the miscellaneous losses. In practice, δ_M does not exceed a few percent. With the approximation

$$\ln(1 - \delta_M) \approx -\delta_M, \quad (3.5)$$

one can combine the optical losses in the resonator with the losses in the crystal

$$\delta = 2\alpha l + \delta_M, \quad (3.6)$$

where δ is the two-way loss in the resonator. With the aid of (3.5) and (3.6) we can express the threshold condition (3.3) in the following form:

$$2gl = \delta - \ln R_1 \approx T + \delta, \quad (3.7)$$

where $T = 1 - R_1$ is the transmission of the output mirror.

In (1.61) and (1.64) the decay time τ_c of the photon flux in the resonator was introduced. This time constant, determined by photons either scattered, absorbed, or emitted, can be related to the loss term of (3.7) and the quality factor Q of the resonator. Since τ_c represents the average lifetime of the photons in the resonator, it

can be expressed by the round-trip time of a photon in the resonator $t_r = 2L/c$ divided by the fractional loss ϵ per round trip

$$\tau_c = t_r/\epsilon = \frac{2L}{c(T + \delta)}, \quad (3.8)$$

where $\epsilon = T + \delta$ is the loss term in (3.7) and L is the length of the resonator. Resonators are characterized by the quality factor Q , which is defined as 2π times the ratio of stored energy E_{st} to dissipated energy E_d per period T_0 . The resonator Q defined in this way is $Q = 2\pi E_{st}/E_d$, where $E_d = E_{st}(1 - \exp(-T_0/\tau_c))$, from which we obtain

$$Q = 2\pi \left[1 - \exp\left(\frac{-T_0}{\tau_c}\right) \right]^{-1} \approx \frac{2\pi \tau_c}{T_0} = 2\pi v_0 \tau_c, \quad (3.9)$$

where $\omega_0 = 2\pi v_0 = 2\pi/T_0$. In a typical cw Nd:YAG laser, the transmission of the output mirror is around 10% and the combined losses about 5%. If we assume a resonator length of 50 cm, we obtain a photon lifetime of $\tau_c = 22$ ns and a Q factor for the resonator of $Q = 39 \times 10^6$. Compared to electronic resonance circuits, optical resonators have very high values of Q .

As will be further discussed in Sect. 5.2.3 the finite lifetime of the photons also determine the minimum bandwidth of the passive resonator according to the Fourier transform $\Delta\omega = 1/\tau_c$. With this relationship the quality factor in (3.9) can also be defined as $Q = v_0/\Delta\nu$. The laser parameters and conditions that lead to a low threshold will be examined next.

We turn to the rate equation (1.61), which gives the photon density in the amplifying medium. It is clear from this equation that for onset of laser emission the rate of change of the photon density must be equal to or greater than zero. Thus at laser threshold for sustained oscillation the condition

$$\frac{\partial\phi}{\partial t} \geq 0 \quad (3.10)$$

must be fulfilled, which enables us to obtain from (1.61) the required inversion density at threshold

$$n \geq \frac{1}{c\sigma\tau_c}. \quad (3.11)$$

In deriving this expression we have ignored the factor S , which denotes the small contribution from spontaneous emission to the induced emission.

According to (1.36) the gain coefficient g can be expressed by

$$g = n\sigma, \quad (3.12)$$

where n is the population inversion and σ is the stimulated emission cross section. The expression for threshold (3.11) is identical to (3.7) if we introduce τ_c from (3.8) and g from (3.12) into (3.11) and assume that the resonator mirrors are coated onto the ends of the laser rod, i.e., $L = l$. If we replace σ with (1.40) we may write the

threshold condition (3.11) in terms of fundamental laser parameters

$$n > \frac{\tau_f 8\pi v_0^2}{\tau_c c^3 g(v_s, v_0)}. \quad (3.13)$$

The lineshape factor $g(v_s, v_0)$ and therefore the stimulated emission cross section σ are largest at the center of the atomic line. Thus from (3.13) we can see qualitatively how the linewidth of the laser output is related to the linewidth of the atomic system. Self-sustained oscillation that develops from noise will occur in the neighborhood of the resonant frequency because only at a narrow spectral range at the peak will the amplification be large enough to offset losses. Consequently, the output of the laser will be sharply peaked, and its linewidth will be much narrower than the atomic linewidth.

It is also obvious from this equation that an increase of the inversion by stronger pumping will increase the laser linewidth because the threshold condition can now be met for values of $g(v_s, v_0)$ farther away from the center. As we will see in Chap. 5 the linewidth of an actual laser system is related to the linewidth of the active material, the level of pump power, and the properties of the optical resonator. The threshold condition at the center of the atomic line is obtained by introducing the peak values of the amplification curve into (3.13). If $g(v_s, v_0)$ has a Lorentzian shape with full width at half-maximum of $\Delta\nu$ centered about v_s , then $g(v_0) = 2/\pi\Delta\nu$ and

$$n > \frac{\tau_f 4\pi^2 \Delta\nu v_0^2}{\tau_c c^3}. \quad (3.14)$$

For a Gaussian lineshape, the right-hand expression of (3.14) has to be divided by $(\pi \ln 2)^{1/2}$. Again, we have assumed that the laser threshold will be reached first by a resonator mode whose resonant frequency lies closest to the center of the atomic line.

From (3.14) we can infer those factors favoring high gain and low threshold for a laser oscillator. In order to achieve a low-threshold inversion, the atomic linewidth $\Delta\nu$ of the laser material should be narrow. Furthermore, the incidental losses in the laser cavity and crystal should be minimized to increase the photon lifetime τ_c . It is to be noted that the critical inversion density for threshold depends only on a single resonator parameter, namely τ_c . A high reflectivity of the output mirror will increase τ_c and therefore decrease the laser threshold. However, this will also decrease the useful radiation coupled out from the laser. We will address the question of optimum output coupling in Sect. 3.4.

(b) Absorbed pump power at threshold: We will now calculate the pumping rate W_p , which is required to maintain the oscillator at threshold. For operation at or near threshold, the photon density ϕ is very small and can be ignored. Setting $\phi = 0$ in the rate equation (1.58) and assuming a steady-state condition of the inversion, $\partial n / \partial t = 0$, as is the case in a conventional operation of the laser oscillator, we obtain for a three-level system

$$\frac{n}{n_{\text{tot}}} = \frac{W_p \tau_f - g_2/g_1}{W_p \tau_f + 1} \quad (3.15)$$

and for a four-level system from (1.70)

$$\frac{n_2}{n_0} = W_p \tau_f. \quad (3.16)$$

For a four-level gain medium, the pumped population density n_2 is small compared to the total population. Therefore, the ground state population density n_0 can be considered as constant, and the pumped population density n_2 is proportional to the pump rate W_p or pump radiation intensity.

Other factors being equal, four-level laser systems have lower pump-power thresholds than three-level systems. In a four-level system an inversion is achieved for any finite pumping rate W_p . In a three-level system we have the requirement that the pumping rate W_p exceeds a minimum or threshold value given by

$$W_{p(\text{th})} = \frac{g_2}{\tau_f g_1} \quad (3.17)$$

before any inversion at all can be obtained. Whereas for a four-level material the spontaneous lifetime has no effect on obtaining threshold inversion, in a three-level material the pump rate required to reach threshold is inversely proportional to τ_f . Thus, for three-level oscillators only materials with long fluorescence lifetimes are of interest.

The reader is reminded again that (3.15) and (3.16) are valid only for a negligible photon flux ϕ . This situation occurs at operation near threshold; it will later be characterized as the regime of small-signal amplification. We will now calculate the minimum pump power which has to be absorbed in the pump bands of the crystal to maintain the threshold inversion. This will be accomplished by first calculating the fluorescence power at threshold, since near above threshold almost all the pump power supplied to the active material goes into spontaneous emission. The fluorescence power per unit volume of the laser transition in a four-level system is

$$\frac{P_f}{V} = \frac{h\nu n_{\text{th}}}{\tau_f}, \quad (3.18)$$

where $n_2 = n_{\text{th}}$ is the inversion at threshold.

In a three-level system at threshold, $n_2 \approx n_1 \approx n_{\text{tot}}/2$ and

$$\frac{P_f}{V} \approx \frac{h\nu n_{\text{tot}}}{2\tau_f}. \quad (3.19)$$

In order that the critical inversion is maintained, the loss by fluorescence from the upper laser level must be supplied by the pump energy. As a result we obtain for the absorbed pump power P_a needed to compensate for population loss of the laser level by spontaneous emission for a four-level laser

$$\frac{P_a}{V} = \frac{h\nu_p n_{\text{th}}}{\eta_Q \tau_f}, \quad (3.20)$$

where $h\nu_p$ is the photon energy at the pump wavelength and η_Q is the quantum efficiency as defined in (1.56). In a three-level system, one requires $n_2 \approx n_1 = n_{\text{tot}}/2$

to reach transparency, and therefore

$$\frac{P_a}{V} = \frac{\hbar v_p n_{\text{tot}}}{2\eta_Q \tau_f}, \quad (3.21)$$

3.2 Gain Saturation

For the radiation within the resonator to build up from the initial low level of spontaneous emission, the round-trip net gain must be greater than unity. As long as this is the case, the optical field grows exponentially. Once the rate of excitation by the pump source is insufficient to support continuous growth of the stimulated emission, the gain starts to saturate.

In a continuously pumped laser, the power circulating within the resonator stabilizes at a level at which the saturated gain just balances the total loss. The decrease of gain as a function of the circulating power in the resonator is determined by the saturation density I_s . This important parameter will be discussed in this section.

In the previous section we considered the conditions for laser threshold. Threshold was characterized by a steady-state population inversion, that is, $\partial n / \partial t = 0$ in the rate equations. In doing this we neglected the effect of stimulated emission by setting $\phi = 0$. This is a good assumption at threshold, where the induced transitions are small compared with the number of spontaneous processes.

As the threshold is exceeded, however, stimulated emission and photon density in the resonator build up. Far above threshold we have to consider a large photon density in the resonator. From (1.58) we can see that $\partial n / \partial t$ decreases for increasing photon density. Steady state is reached when the population inversion stabilizes at a point where the upward transitions supplied by the pump source equal the downward transitions caused by stimulated and spontaneous emission. With $\partial n / \partial t = 0$ one obtains, for the steady-state inversion population in the presence of a strong photon density ϕ ,

$$n = n_{\text{tot}} \left(W_p - \frac{\gamma - 1}{\tau_f} \right) \left(\gamma c \sigma \phi + W_p + \frac{1}{\tau_f} \right)^{-1}. \quad (3.22)$$

The photon density ϕ is given by the sum of two beams traveling in opposite directions through the laser material.

We will now express (3.22) in terms of operating parameters. From Section 1.3 we recall that the gain coefficient $g = -\alpha$ is defined by the product of stimulated emission, cross section, and inversion population. Furthermore, we will define a gain coefficient that the system would have at a certain pump level in the absence of stimulated emission. Setting $\phi = 0$ in (3.22) we obtain the small-signal gain coefficient

$$g_0 = \sigma n_{\text{tot}} [W_p \tau_f - (\gamma - 1)] (W_p \tau_f + 1)^{-1}, \quad (3.23)$$

which an active material has when pumped at a level above threshold and when lasing action is inhibited by blocking the optical beam or by removing one or both of the resonator mirrors. If feedback is restored, the photon density in the resonator will increase exponentially at the onset with g_0 . As soon as the photon density becomes

appreciable, the gain of the system is reduced according to

$$g = g_0 \left(1 + \frac{\gamma c \sigma \phi}{W_p + (1/\tau_f)} \right)^{-1}, \quad (3.24)$$

where g is the saturated gain coefficient. Equation (3.24) was obtained by introducing (3.23) into (3.22) and using $g = \sigma n$.

We can express ϕ by the power density I in the system. With $I = c\phi h\nu$ we obtain

$$g = \frac{g_0}{1 + I/I_s}, \quad (3.25)$$

where

$$I_s = \left(W_p + \frac{1}{\tau_f} \right) \frac{h\nu}{\gamma\sigma}. \quad (3.26)$$

The parameter I_s defines a flux in the active material at which the small-signal gain coefficient g_0 is reduced by one-half [3.1].

In a four-level system $W_p \ll 1/\tau_f$ and $\gamma = 1$, so (3.26) reduces to

$$I_s = \frac{h\nu}{\sigma\tau_f}. \quad (3.27)$$

For a three-level system the saturation flux is

$$I_s = \frac{h\nu[W_p + (1/\tau_{21})]}{\sigma[1 + (g_2/g_1)]}. \quad (3.28)$$

As we can see from (3.23) the small-signal gain depends only on the material parameters and the amount of pumping power delivered to the active material. The large-signal or saturated gain depends in addition on the power density in the resonator.

Gain saturation as a function of steady-state radiation intensity must be analyzed for lasers with homogeneous and inhomogeneous line broadening. Equation (3.25) is valid only for the former case, in which the gain decreases proportionately over the entire transition line. As we have seen in Chap. 2, a ruby laser has a homogeneously broadened bandwidth, whereas in Nd:glass the interaction of the active ion with the electrostatic field of the host leads to an inhomogeneous line. However, in solid-state materials such as Nd:glass, the cross-relaxation rate is very fast. The latter is associated with any process characteristic of the laser medium that affects the transfer of excitation within the atomic spectral line so as to prevent or minimize the departure of this line from the equilibrium distribution. It has been shown that in the case of a very fast cross-relaxation within the inhomogeneous line, the saturated gain is in agreement with that of a homogeneously broadened bandwidth [3.2].

3.3 Circulating Power

In a laser resonator the power density in the active medium increases up to the point where the saturated gain equals the total losses. This power density I is obtained from

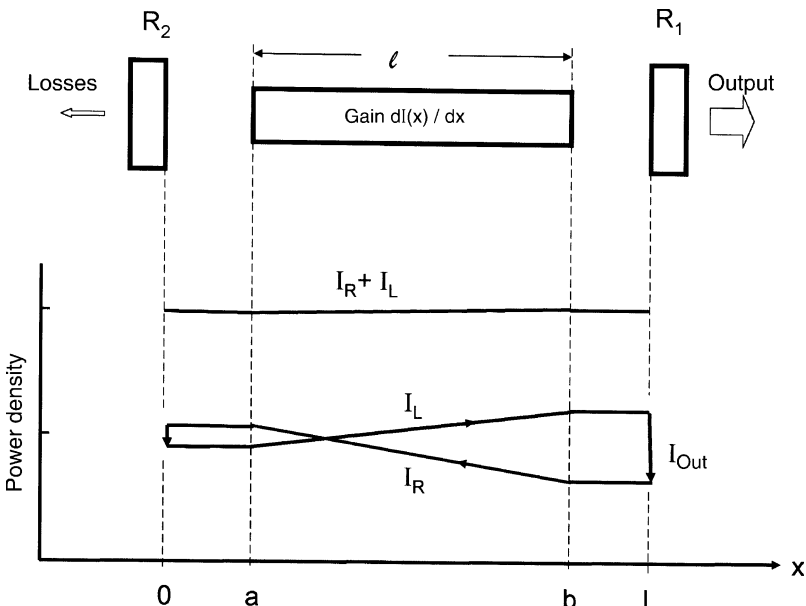


Fig. 3.2. Circulating power traveling from left to right (I_L) and right to left (I_R) in a laser oscillator

the threshold condition (3.7) and the expression for saturated gain (3.25),

$$I = I_s \left[\frac{2g_0l}{\delta - \ln R_1} - 1 \right]. \quad (3.29)$$

The first expression in brackets is a measure of how much the laser is pumped above threshold. From (3.29) it follows as one would expect $I = 0$ at threshold. If the gain medium is pumped above threshold, g_0 and I will increase, whereas the saturated gain coefficient g will stay constant according to (3.7). As I increases, so will the output power which is coupled out through mirror R_1 .

We will now relate the laser output to the power density in the resonator. The power density I in the laser resonator comprises the power densities of two oppositely traveling waves. One can think of a circulating power density I_{circ} , which is reflected back and forth between the two resonator mirrors. Figure 3.2 illustrates a standing wave laser resonator, where $I_L(x)$ and $I_R(x)$ are the intracavity one-way intensities of the left and right traveling resonator beams as a function of the intracavity location x . The rear reflector and output coupler are located at $x = 0$ and $x = L$, respectively. The rod faces are located at $x = a$ and $x = b$. Hence, the length of the active medium is $l = b - a$.

The beam moving in the $(+x)$ direction in Fig. 3.2 will experience an increase according to

$$\frac{dI_L(x)}{dx} = g(x)I_L(x). \quad (3.30)$$

If the gain coefficient $g(x)$ is replaced by the expression given in (3.25) we obtain

$$\frac{dI_L(x)}{dx} = \frac{g_0 I_L(x)}{1 + [I_L(x) + I_R(x)]/I_S}. \quad (3.31)$$

An identical equation, but with the sign reversed and $I_L(x)$ replaced by $I_R(x)$, is obtained for the wave traveling in the $(-x)$ direction. From (3.31) and the corresponding equation for $I_R(x)$ it follows that the product of the intensities of the two counterpropagating beams is constant, that is,

$$I_L(x)I_R(x) = \text{const.} \quad (3.32)$$

In most solid-state lasers, the internal losses are small and the reflectivity of the output mirror is high; in this case variations of $I_L(x)$ and $I_R(x)$ as a function of x are relatively small. If we treat these changes as a perturbation $I_L(x) + \Delta I$ and $I_R(x) + \Delta I$ in (3.32) we obtain, as an approximation,

$$I = I_L + I_R = \text{const}, \quad (3.33)$$

where I is the total power density in the resonator which is to a first-order independent of position along the resonator (see also Fig. 3.2).

The mean-field approach described above is only strictly valid for low losses δ and R close to unity, when the spatial variation of irradiance along the length of the gain medium is small. In this case the circulating power I_{circ} is to a good approximation equal to the average of the power densities of the counterpropagating beams

$$I_{\text{circ}} = (I_L + I_R)/2. \quad (3.34)$$

From Fig. 3.2 follows

$$I_{\text{out}} = (1 - R_1)I_L \quad (3.35a)$$

and

$$I_R = R_1 I_L. \quad (3.35b)$$

Introducing (3.35) into (3.33) yields

$$P_{\text{out}} = AI \left(\frac{1 - R}{1 + R} \right), \quad (3.36)$$

where R is now the reflectivity of the output mirror and A is the cross section of the gain medium. For values of R close to 1, (3.36) reduces to

$$P_{\text{out}} = AIT/2, \quad (3.37)$$

where T is the transmission of the output mirror.

3.4 Oscillator Performance Model

In this section we will develop a model for the laser oscillator. First we will discuss the various steps involved in the conversion process of electrical input to laser output.

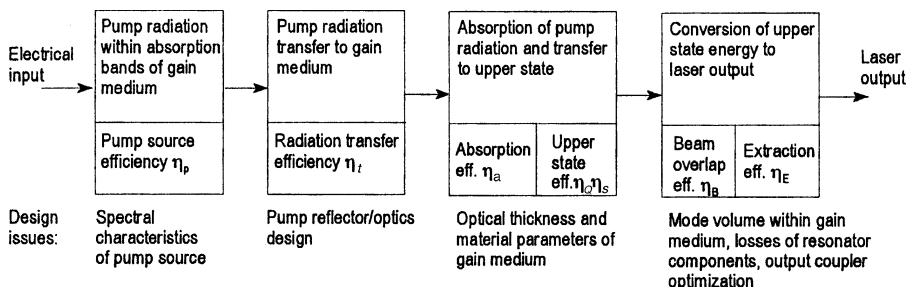


Fig. 3.3. Energy flow in a solid-state laser system

After that, we will relate these energy transfer mechanisms to parameters which are accessible to external measurements of the laser oscillator. The purpose of this section is to gain insight into the energy conversion mechanisms and therefore provide an understanding of the dependency and interrelationship of the various design parameters which may help in the optimization of the overall laser efficiency. In almost all applications of lasers, it is a major goal of the laser designer to achieve the desired output performance with the maximum system efficiency.

3.4.1 Conversion of Input to Output Energy

The flow of energy from electrical input to laser output radiation is illustrated schematically in Fig. 3.3. Also listed are the principal factors and design issues that influence the energy conversion process. There are different ways of partitioning this chain of transfer processes. This approach was chosen from an engineering point of view, which divides the conversion process into steps related to individual system components. As shown in Fig. 3.3, the energy transfer from electrical input to laser output can conveniently be expressed as a four-step process:

Conversion of Electrical Input Delivered to the Pump Source to Useful Pump Radiation

We define as useful radiation the emission from the pump source that falls within the absorption bands of the laser medium. The pump source efficiency η_p is therefore the fraction of electrical input power that is emitted as optical radiation within the absorption region of the gain medium. The output of a laser diode or a diode array represents all useful pump radiation, provided the spectral output is matched to the absorption band of the gain medium. Typical values of η_p for commercially available cw and quasi-cw diode arrays are 0.3–0.5.

For flashlamp or cw arc lamp-pumped systems, the pump source efficiency may be defined as

$$\eta_p = P_\lambda / P_{in} = \int_{\lambda_1}^{\lambda_2} P'_\lambda d\lambda / P_{in}, \quad (3.38)$$

where P_λ is the spectral output power of the lamp within the absorption bands of the gain material, P_{in} is the electrical power input, and P'_λ is the radiative power per unit wavelength emitted by the lamp, and the integral is taken over the wavelength range λ_1 to λ_2 , which is useful for pumping the upper laser level. The output characteristics of arc lamps and their dependency on operating parameters will be discussed in Sect. 6.1. The measurement of η_P for broadband sources is somewhat involved and requires either a calorimetric measurement of the power absorbed in a sample of the laser material or integration over the source emission spectrum and the absorption spectrum of the gain material. Typical values are $\eta_P = 0.04\text{--}0.08$. These numbers are typical for a 5- to 10-mm-thick laser material. The magnitude of η_P is dependent on the thickness of the active material because as the thickness increases, radiation at the wings of the absorption band will start to contribute more to the pumping action.

Transfer of the Useful Pump Radiation Emitted by the Pump Source to the Gain Medium

The transfer of flashlamp pump radiation to the laser medium is accomplished by means of a completely enclosed reflective chamber or pump cavity. The radiation transfer efficiency η_t can be defined as

$$P_e = \eta_t P_\lambda, \quad (3.39)$$

where P_λ is the useful pump radiation emitted by the source and P_e is the fraction of this radiation transferred into the laser material. The factor η_t is a combination of the capture efficiency, defined by the fraction of rays leaving the source and intersecting the laser rod, and the transmission efficiency. The former is based on the geometrical shape of the pump cavity, diameter and separation of the pump source, and laser rod. The latter is a function of the reflectivity of the walls of the pump cavity, reflection losses at the rod surface and coolant jacket, absorption losses in the coolant fluid, and radiation losses through the clearance holes at the side walls of the pump cavity. For close-coupled cavities, typical values are $\eta_t = 0.3\text{--}0.6$.

In diode-pumped lasers the radiation transfer is much simpler. In so-called end-pumped lasers, the transfer system usually consists of lenses for the collection and focusing of diode radiation into the laser crystal. Furthermore, in side-pumped systems, the laser diodes are mounted in close proximity to the laser crystal without the use of any intervening optics. If we express reflection losses and spill-over losses at the optics or active medium by the parameter R , we can write

$$\eta_t = (1 - R). \quad (3.40)$$

Since the laser crystal and optical components are all antireflection coated, the radiation transfer losses are very small in these systems. Values for the radiation transfer efficiency are typically $\eta_t = 0.85\text{--}0.98$.

Absorption of Pump Radiation by the Gain Medium and Transfer of Energy to the Upper Laser Level

This energy transfer can be divided into two processes. The first is the absorption of pump radiation into the pump bands of the gain medium expressed by η_a , and the second is the transfer of energy from the pump band to the upper laser level expressed by $\eta_Q\eta_S$.

The absorption efficiency is the ratio of power P_a absorbed to power P_e entering the laser medium

$$\eta_a = P_a / P_e. \quad (3.41)$$

The quantity η_a is a function of the path length and the spectral absorption coefficient of the laser medium integrated over the emission spectrum of the pump source. If the pump radiation is totally diffuse inside the laser rod, as is the case when the lateral surface is rough ground, a good approximation can be derived by expressing (3.41) in a different form

$$\eta_a = \frac{(dP_a/dV)V}{I_w F}, \quad (3.42a)$$

where dP_a/dV is the power absorbed per volume, I_w is the power density at the cylindrical surface of the rod, and F and V are the cylindrical rod surface area and volume of the rod, respectively.

The power absorbed per volume can also be expressed by $dP_a/dV = \alpha_0 I_{av}$, where α_0 is the absorption coefficient of the laser material averaged over the spectral emission range of the lamp and I_{av} is the average power density inside the rod. Radiation with an energy density W_{av} propagating at a velocity c has a power density of $I_{av} = cW_{av}$, where $c = c_0/n_0$ is the speed of light in the medium and n_0 is the refractive index. The energy density in the laser rod has a radial dependence due to absorption. The average value W_{av} can be closely approximated by taking the energy density W_s at the surface weighted by the factor $\exp(-\alpha_0 R)$, where R is the rod radius and α_0 is the absorption coefficient. From [3.3] it follows that this is a valid approximation over a large range of α_0 . From these considerations follows

$$dP_a/dV = \alpha_0 c W_s \exp(-\alpha_0 R). \quad (3.42b)$$

Owing to grinding the lateral surface of the rod, the pump radiation upon entering the rod will be diffused. For an enclosure with diffusely reflecting walls, we obtain from blackbody radiation theory a relationship between energy W_s inside the enclosure and the intensity I_w emitted by the walls

$$I_w = c W_s / 4. \quad (3.42c)$$

Introducing (3.42b, c) into (3.42a) yields our final result

$$\eta_a = 2\alpha_0 R \exp(-\alpha_0 R). \quad (3.43)$$

For diode-pumped lasers, the absorption efficiency can be approximated by

$$\eta_a = 1 - \exp(-\alpha_0 l), \quad (3.44)$$

where α_0 is the absorption coefficient of the laser crystal at the wavelength emitted by the laser diode and l is the path length in the crystal. Detailed data on η_a for both flashlamp and laser diode radiation can be found in Chap. 6.

The upper state efficiency may be defined as the ratio of the power emitted at the laser transition to the power absorbed into the pump bands. This efficiency is the product of two contributing factors, the quantum efficiency η_Q , which is defined as the number of photons contributing to laser emission divided by the number of pump photons, and η_S , the quantum defect efficiency. The latter is sometimes referred to as the Stokes factor, which represents the ratio of the photon energy emitted at the laser transition $h\nu_L$ to the energy of a pump photon $h\nu_p$, that is,

$$\eta_S = \left(\frac{h\nu_L}{h\nu_p} \right) = \frac{\lambda_p}{\lambda_L}, \quad (3.45)$$

where λ_p and λ_L are the wavelength of the pump transition and the laser wavelength, respectively. For Nd:YAG emitting at 1064 nm that is pumped by a laser diode array at 808 nm, we obtain $\eta_S = 0.76$.

In a flashlamp-pumped system, the value of η_S is an average value derived from considering the whole absorption spectrum of the laser.

Conversion of the Upper-State Energy to Laser Output

The efficiency of this process can be divided into the fractional spatial overlap of the resonator modes with the pumped region of the laser medium and the fraction of the energy stored in the upper laser level which can be extracted as output.

The beam overlap efficiency η_B is defined as the resonator mode volume divided by the pumped volume of the active material. A value of η_B less than 1 indicates that part of the inversion will decay by spontaneous, rather than stimulated, emission. In an oscillator η_B expresses the mode-matching efficiency, that is, the spatial overlap between the resonator modes and the gain distribution. In an amplifier η_B is a measure of the spatial overlap between the input beam and the gain distribution in the laser material.

This subject usually does not receive a lot of attention in laser literature, but a poor overlap of the gain region of the laser with the laser-beam profile is often the main reason that a particular laser performs below expectations. For example, the generally disappointing performance of slab lasers can often be traced to an insufficient utilization of the rectangular gain cross section by the laser beam. Likewise, the low overall efficiency of lasers with a TEM_{00} mode output is the result of a mode volume that occupies only a small fraction of the gain region of the laser rod. On the other hand, so-called end-pumped lasers, where the output from a laser diode pump is focused into the gain medium, achieve near-perfect overlap.

Instead of comparing the pump with the mode volume, it is often sufficient to compare the cross sections, if we assume that the radial distribution of the resonator mode does not change appreciably along the length of the active medium. For example, in a 50-cm-long resonator, with two curved mirrors of 5-m radius at each end, the TEM₀₀ mode changes only by 5% over the length of the resonator (Sect. 5.1.3).

The overlap between the resonator mode intensity distribution $I(r)$ and the gain distribution $g(r)$ is given by an overlap integral

$$\eta_B = \int g(r)I(r)2\pi r dr / \int g^2(r)2\pi r dr. \quad (3.46)$$

For two practical cases (3.46) can be easily evaluated. The first case is a uniformly pumped gain medium operated in a highly multimode resonator. If we assume a top hat distribution for both the gain region and resonator beam (i.e., independent of r), then η_B is simply the ratio of the overlapping cross sections, $\eta_B = w_m^2/w_p^2$, where πw_m^2 and πw_p^2 are the cross section of the resonator mode and the pump region, respectively. The efficiency η_B can at best equal unity.

Another simple case is found in some end-pumped lasers if a Gaussian pump beam and a Gaussian (TEM₀₀) resonator mode propagate coaxially inside the active medium. Introducing in (3.46) a normalized Gaussian resonator mode

$$I(r) = (2/\pi w_m^2) \exp[-2(r/w_m)^2], \quad (3.47)$$

and a similar expression for the pump beam yields

$$\eta_B = \frac{2w_m^2}{w_p^2 + w_m^2} \quad \text{for } w_p > w_m, \quad \text{and} \quad \eta_B = 1 \quad \text{for } w_p \leq w_m, \quad (3.48)$$

where w_p and w_m are the spot sizes for the pump beam and resonator mode profiles. for $w_m = w_p$, the TEM₀₀ mode and pump beam occupy the same volume and $\eta_B = 1$.

Values for η_B can range from as low as 0.1, for example, for a laser rod of 5-mm diameter operated inside a large radius mirror resonator containing a 1.5-mm aperture for fundamental mode control, to 0.95 for an end-pumped laser operating at TEM₀₀. Innovative resonator designs, employing unstable resonators, internal lenses, variable reflectivity mirrors, and so forth, can achieve TEM₀₀ mode operation typically at $\eta_B = 0.3\text{--}0.5$. Multimode lasers typically achieve $\eta_B = 0.8\text{--}0.9$. If a laser oscillator is followed by an amplifier, a telescope is usually inserted between these two stages in order to match the oscillator beam to the diameter of the amplifier and thereby optimize η_B .

The circulating power in an optical resonator is diminished by internal losses described by the round-trip loss δ (Sect. 3.1) and by radiation coupled out of the resonator. For reasons that will become apparent in the next section, we will define an extraction efficiency η_E which describes the fraction of total available upper state energy or power which appears at the output of the laser

$$\eta_E = P_{\text{out}}/P_{\text{avail.}} \quad (3.49)$$

Expressions for η_E will be given in Sect. 3.4.2 and in Chaps. 4 and 8 for the cw oscillator, laser amplifier, and Q-switch oscillator, respectively.

An indication of the reduction of available output power due to losses in resonator can be obtained from the coupling efficiency

$$\eta_c = T/(T + \delta). \quad (3.50)$$

As will be explained in the next section, the slope of the output versus input curve of a laser is directly proportional to this factor, whereas the overall system efficiency of a laser is directly proportional to η_E .

The conversion processes described so far are equally applicable to cw and pulsed lasers, provided that the power terms are replaced with energy, and integration over the pulse length is carried out where appropriate. The energy flow depicted in Fig. 3.3 can also be extended to laser amplifiers and Q-switched systems because the discussion of pump source efficiency, radiation transfer, and so forth is equally applicable to these systems. Even the definition for the extraction efficiency remains the same; however, the analytical expressions for η_E are different as will be discussed in Chap. 4 for the laser amplifier.

If the laser oscillator is Q-switched, additional loss mechanisms come into play, which are associated with energy storage at the upper laser level and with the transient behavior of the system during the switching process. The Q-switch process will be described in detail in Chap. 8. However, for completeness of the discussion on energy transfer mechanisms in a laser oscillator, we will briefly discuss the loss mechanisms associated with Q-switch operations.

In a Q-switched laser, a large upper state population is created in the laser medium, and stimulated emission is prevented during the pump cycle by the introduction of a high loss in the resonator. At the end of the pump pulse, the loss is removed (the resonator is switched to a high Q) and the stored energy in the gain medium is converted to optical radiation in the resonator from which it is coupled out by the output mirror.

There are losses prior to opening of the Q-switch, such as fluorescence losses and amplified spontaneous emission (ASE) losses that will depopulate the upper state stored energy. Also, not all of the stored energy available at the time of Q-switching is converted to optical radiation. For a Q-switched laser, the extraction efficiency η_E in Fig. 3.3 can be expressed as

$$\eta_E = \eta_{St} \eta_{ASE} \eta_{EQ}, \quad (3.51)$$

where η_{St} and η_{ASE} account for the fluorescence and ASE losses prior to the opening of the Q-switch, and η_{EQ} is the extraction efficiency of the Q-switch process.

Assuming a square pump pulse of duration t_p , the maximum upper state population reached at the end of the pump cycle is given by

$$n_2(t_p) = n_0 W_p \tau_f [1 - \exp(-t_p/\tau_f)]. \quad (3.52)$$

Since the total number of ions raised to the upper level during the pump pulse is $n_0 W_p t_p$, the fraction available at the time of Q-switching ($t = t_p$) is

$$\eta_{St} = \frac{[1 - \exp(-t_p/\tau_f)]}{t_p/\tau_f}. \quad (3.53)$$

The storage efficiency η_{St} is therefore the ratio of the energy stored in the upper laser level at the time of Q-switching to the total energy deposited in the upper laser level. From the expression for η_{St} it follows that for a pump pulse equal to the fluorescence lifetime ($t_p = \tau_f$) the storage efficiency is 0.63. Clearly, a short pump pulse increases the overall efficiency of a Q-switched laser. However, a shorter pump pulse puts an extra burden on the pump source because the pump has to operate at a higher peak power to deliver the same energy to the laser medium.

If the inversion reaches a critical value, the gain can be so high such that spontaneous emission after amplification (ASE) across the gain medium may be large enough to deplete the laser inversion. Furthermore, reflections from internal surfaces can increase the path length or allow multiple passes inside the gain section which will make it easier for this unwanted radiation to build up. In high-gain oscillators, multi-stage lasers, or in laser systems having large-gain regions, ASE coupled with parasitic oscillations present the limiting factor for energy storage.

We can define η_{ASE} as the fractional loss of the stored energy density to ASE and parasitic oscillations

$$\eta_{ASE} = 1 - E_{ASE}/E_{St}. \quad (3.54)$$

Minimizing reflections internal to the laser medium by AR coatings and providing a highly scattering, absorbing, or low-reflection (index matching) surface of the laser rod, coupled with good isolation between amplifier stages, will minimize ASE and parasitic losses. The occurrence of ASE can often be recognized in a laser oscillator or amplifier as a saturation in the laser output as the lamp input is increased (see also Sect. 4.4.1).

The fraction of the stored energy E_{St} available at the time of Q-switching to energy E_{EX} extracted by the Q-switch can be expressed as the Q-switch extraction efficiency

$$\eta_{EQ} = E_{EX}/E_{St}. \quad (3.55)$$

The fraction of initial inversion remaining in the gain medium after emission of a Q-switched pulse is a function of the initial threshold and final population inversion densities. These parameters are related via a transcendental equation, as shown in Chap. 8.

3.4.2 Laser Output

In this subsection, we will describe the basic relationships between externally measurable quantities, such as laser output, threshold, and slope efficiency, and internal systems and materials parameters.

After the pump source in a laser oscillator is turned on, the radiation flux in the resonator that builds up from noise will increase rapidly. As a result of the increasing flux, the gain coefficient decreases according to (3.25) and finally stabilizes at a value determined by (3.7). A fraction of the intracavity power is coupled out of the resonator and appears as useful laser output according to (3.36). If we combine (3.29) and (3.36), the laser output takes the form

$$P_{\text{out}} = A \left(\frac{1 - R}{1 + R} \right) I_S \left(\frac{2g_0 l}{\delta - \ln R} - 1 \right). \quad (3.56)$$

In this equation, I_S is a materials parameter, A and l are the cross section and length of the laser rod, respectively, and R is the reflectivity of the output coupler. These quantities are usually known, whereas the unsaturated gain coefficient g_0 and the resonator losses δ are not known. We will now relate g_0 to system parameters, and describe methods for the measurement of g_0 and the losses δ in an oscillator.

The Four-Level System

The population inversion in a four-level system as a function of pump rate is given by (3.16). Multiplying both sides of this equation by the stimulated emission cross section yields

$$g_0 = \sigma n_0 W_P \tau_f. \quad (3.57)$$

Now we recall from Chap. 1 that $W_P n_0$ gives the number of atoms transferred from the ground level to the upper laser level per unit time and volume, i.e., pump power density divided by photon energy. This can be expressed as

$$W_P n_0 = \eta_Q \eta_S \eta_B P_a / h \nu_L V, \quad (3.58)$$

where P_a is the total absorbed pump power and V is the volume of the gain medium. Not all of the atoms transferred from the ground level to the upper laser level contribute to gain, this is accounted for by η_Q . The Stokes factor η_S enters in (3.58) because the photon energy is expressed in emitted laser photons rather than pump photons, and the overlap efficiency η_B defined in (3.46) accounts for the fact that not all of the population inversion interacts with the photon density of the resonator modes.

If we introduce (3.58) into (3.57), we can express the small-signal gain coefficient in terms of absorbed pump power

$$g_0 = \sigma \tau_f \eta_Q \eta_S \eta_B P_{ab} / h \nu_L V. \quad (3.59)$$

The absorbed pump power in the laser material is related to the electrical input to the pump source by

$$P_{ab} = \eta_P \eta_t \eta_a P_{in}. \quad (3.60)$$

With (3.59) and (3.60) we can establish a simple relationship between the small-signal, single-pass gain and lamp input power

$$g_0 = \sigma \tau_f \eta P_{in} / h \nu_L V, \quad (3.61)$$

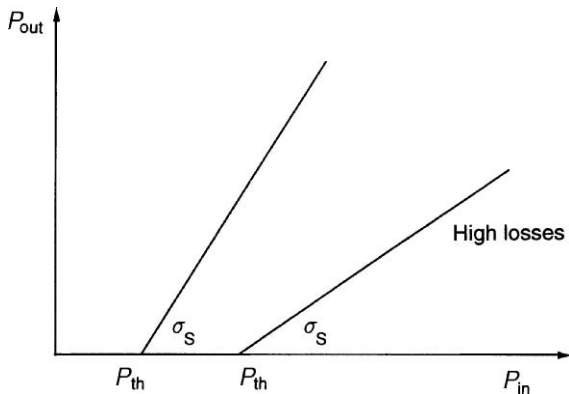


Fig. 3.4. Laser output versus pump input characterized by a threshold input power P_{th} and a slope efficiency σ_S

where, for convenience, we have combined all the efficiency factors into

$$\eta = \eta_p \eta_t \eta_a \eta_Q \eta_s \eta_B. \quad (3.62)$$

If we replace the small signal coefficient g_0 in (3.56) with the system and materials parameters given in (3.61) we obtain our final result

$$P_{\text{out}} = \sigma_S (P_{\text{in}} - P_{\text{th}}), \quad (3.63)$$

where σ_S is the slope efficiency of the output versus input curve, as shown in Fig. 3.4,

$$\sigma_S = \left(\frac{-\ln R}{\delta - \ln R} \right) \eta \approx \frac{T}{T + \delta} \eta. \quad (3.64)$$

The electrical input at threshold is

$$P_{\text{th}} = \left(\frac{\delta - \ln R}{2} \right) \frac{A h \nu_L}{\eta \sigma \tau_f} \approx \left(\frac{T + \delta}{2} \right) \frac{A h \nu_L}{\eta \sigma \tau_f}. \quad (3.65)$$

In deriving (3.64) and (3.65) we have made use of the approximation $2(1 - R)/(1 + R) = -\ln R$. Also for reflectivities of the output coupler of $R = 0.9$ or higher, the term $(-\ln R)$ can be replaced in most cases by the mirror transmission T with sufficient accuracy. In the laser literature, (3.65) is sometimes expressed in terms of pump photon energy; in this case $\eta_Q \eta_s$ have to be excluded from η since $h\nu_L = \eta_Q \eta_s h\nu_p$.

From (3.65) it follows that a laser material with a large product of the stimulated emission cross section and fluorescence lifetime ($\sigma \tau_f$) will have a low laser threshold. The slope efficiency σ_S is simply the product of all the efficiency factors discussed in Sect. 3.4.1. The input power P_{th} required to achieve laser threshold is inversely proportional to the same efficiency factors. Therefore, a decrease of any of the η terms will decrease the slope efficiency and increase the threshold, as shown in Fig. 3.4. In the expressions for σ_S and P_{th} we have left T and δ in explicit form, because these parameters are subject to optimization in a laser resonator. As expected, higher

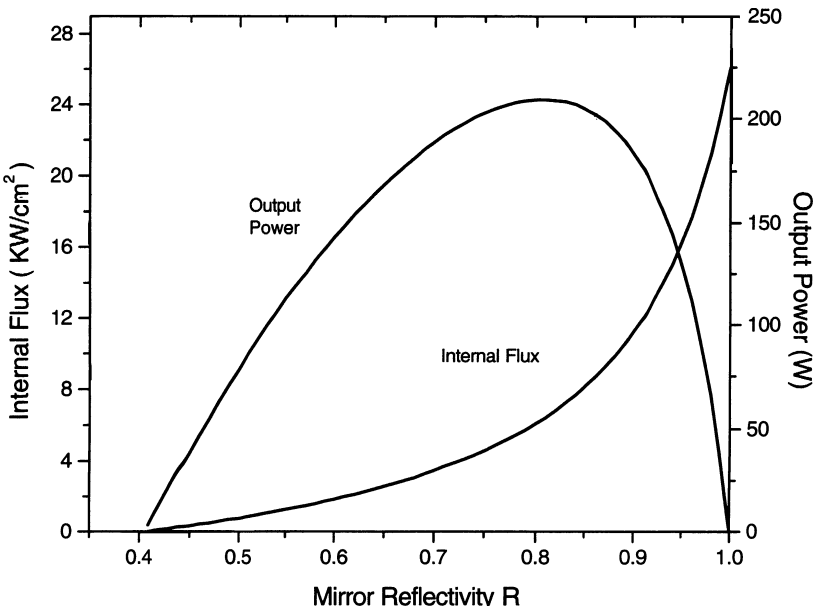


Fig. 3.5. Laser output power and total flux inside the resonator as a function of mirror reflectivity. Parameters: $I_5 = 2.9 \text{ kW/cm}^2$, $2g_0\ell = 1$, $\delta = 0.1$, $A = 0.4 \text{ cm}^2$

optical losses δ , caused by reflection, scattering, or absorption, increase the threshold input power and decrease the slope efficiency.

From (3.29) and (3.36) we can calculate the power density inside the resonator and the laser output as a function of output coupling. The general shape of I and P_{out} as a function of T is shown in Fig. 3.5. The power density I is maximum if all the radiation is contained in the resonator, that is, $R = 1$. At $2g_0\ell = \delta - \ln R$ the flux inside the resonator is zero. This occurs if the reflectivity of the output mirror is so low, namely $R_{\text{th}} = \exp(\delta - 2g_0\ell)$, that the laser just reaches threshold at the given input. The laser output P_{out} is zero for $R = 1$ and R_{th} . As shown in Fig. 3.5, the output reaches a maximum for a specific value of R .

Differentiation of (3.56) determines the output coupling R_{opt} , which maximizes P_{out} , i.e.,

$$-\ln R_{\text{opt}} = (\sqrt{2g_0\ell/\delta} - 1)\delta. \quad (3.66)$$

From this expression it can be seen that low-gain systems require a high reflectivity and vice versa. For cw-pumped Nd:YAG lasers the gain coefficient is typically on the order of $g_0 = (0.05-0.1) \text{ cm}^{-1}$ and the optimum output coupling ranges from 0.80 to 0.98. The lower number is typical for multi-hundred watt Nd:YAG lasers pumped with up to 10 kW of input power. The very high reflectivity is for very small systems. Pulsed-pumped systems operate at much higher pump powers and, correspondingly, have a higher gain coefficient. For example, a typical industrial Nd:YAG laser for

cutting sheet metal has a pulse length of 100 μs and an output energy of 2J per pulse. Assuming a 2% system efficiency, the pump pulse has a peak power of 1 MW. Gain coefficients for pulsed systems are on the order of (0.3–0.5) cm^{-1} , and the output mirror reflectivity ranges from 0.6 to 0.8. Pulsed systems that are also Q-switched have the highest gain coefficients, typically 1.5–2.5 cm^{-1} , and the output coupler reflectivity is between 0.4 and 0.6.

Introducing the expression for R_{opt} into (3.56) gives the laser output at the optimum output coupling

$$P_{\text{opt}} = g_0 l I_s A (1 - \sqrt{\delta/2g_0 l})^2. \quad (3.67)$$

If we use the definition for g_0 and I_s as given before, we can readily see that $g_0 I_s = n_2 h \nu / \tau_f$, which represents the total excited state power per unit volume. (A similar expression will be derived in Chap. 4 for the available energy in a laser amplifier.) Therefore, the maximum available power from the oscillator is

$$P_{\text{avail}} = g_0 l I_s A. \quad (3.68)$$

The optimum power output can be expressed as

$$P_{\text{opt}} = \eta_E P_{\text{avail}}, \quad (3.69)$$

where

$$\eta_E = (1 - \sqrt{\delta/2g_0 l})^2 \quad (3.70)$$

is the extraction efficiency already mentioned in Sect. 3.4.1. The behavior of η_E as a function of the loss-to-gain ratio $\delta/2g_0 l$ is depicted in Fig. 3.6. The detrimental effect

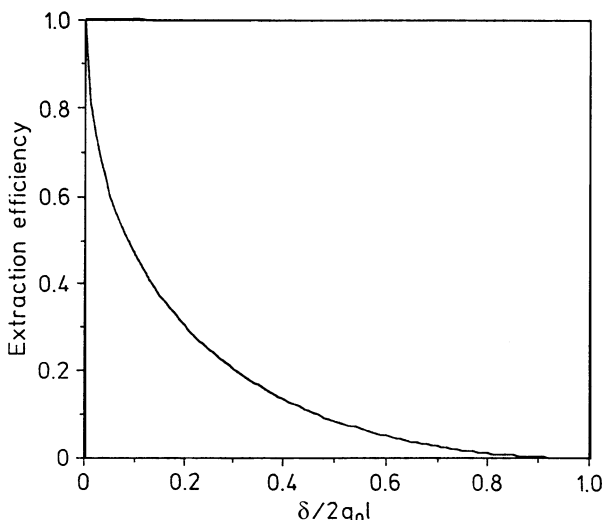


Fig. 3.6. Extraction efficiency η_E as a function of loss-to-gain ratios $\delta/2g_0 l$

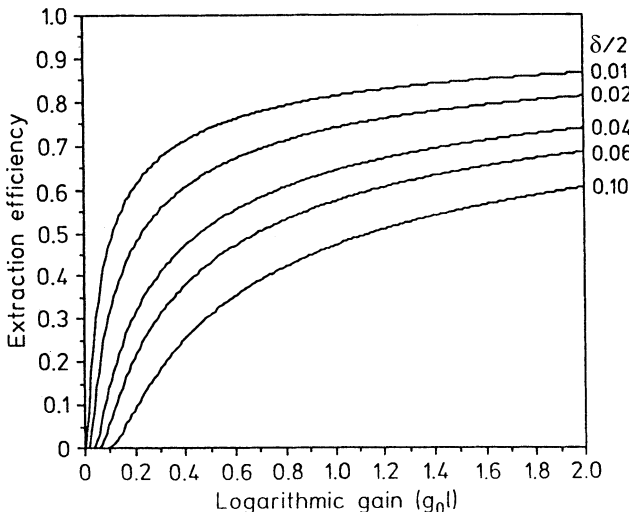


Fig. 3.7. Extraction efficiency for the optimized resonator as a function of the single-pass logarithmic gain. Parameter is the one-way resonator loss

of even a very small internal loss on the extraction efficiency is quite apparent. For example, in order to extract at least 50% of the power available in the laser material, the internal loss has to be less than 10% of the unsaturated gain. Achievement of a high extraction efficiency is particularly difficult in cw systems because the gain is relatively small, and unavoidable resonator losses can represent a significant fraction of the gain. In Fig. 3.7 the extraction efficiency for the optimized resonator is plotted for different values of δ and $g_0 l$.

The overall system efficiency of a solid-state laser is directly proportional to the extraction efficiency

$$\eta_{\text{sys}} = P_{\text{out}}/P_{\text{in}} = \eta_E \eta. \quad (3.71)$$

If one compares (3.71) with the expression for the slope efficiency of a laser given by (3.65), then the first term, namely the coupling efficiency, is replaced by the extraction efficiency η_E .

The sensitivity of the laser output to values of T that are either above or below T_{opt} is illustrated in Fig. 3.8. For resonators which are either over- or undercoupled, the reduction of power compared to that available to T_{opt} depends on how far the system is operated above threshold. For oscillators far above threshold, the curve has a broad maximum and excursions of $\pm 20\%$ from T_{opt} do not reduce the output by more than a few percent.

As we have seen, the resonator losses and the gain in the laser material play an important part in the optimization process of a laser system. Following a method first proposed by Findlay and Clay [3.4], the resonator losses can be determined by using

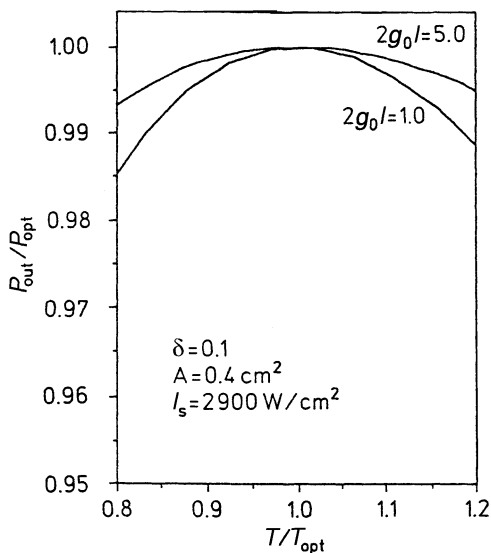


Fig. 3.8. Sensitivity of laser output for nonoptimal output coupling

output mirrors with different reflectivities and determining threshold power for lasing for each mirror. According to (3.7) we can write

$$-\ln R = 2g_0\ell - \delta. \quad (3.72)$$

Extrapolation of the straight-line plot of $-\ln R$ versus P_{th} , at $P_{\text{th}} = 0$, yields the round-trip resonator loss δ as shown in Fig. 3.9. With δ determined, the small signal gain g_0 as a function of input power can be plotted. From the slope of the straight

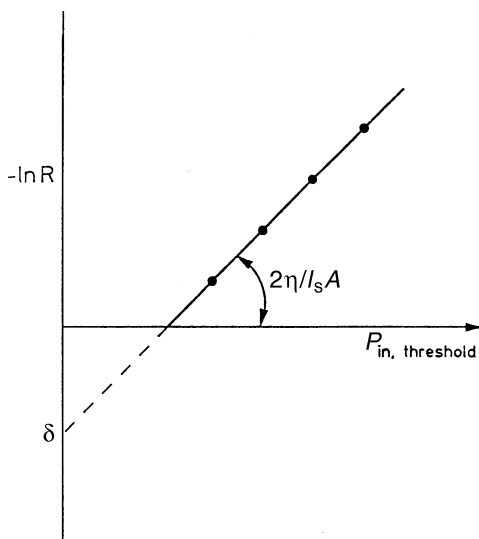


Fig. 3.9. Measurement of the resonator losses as well as the product of all the efficiency factors involved in the energy transfer mechanism of a laser

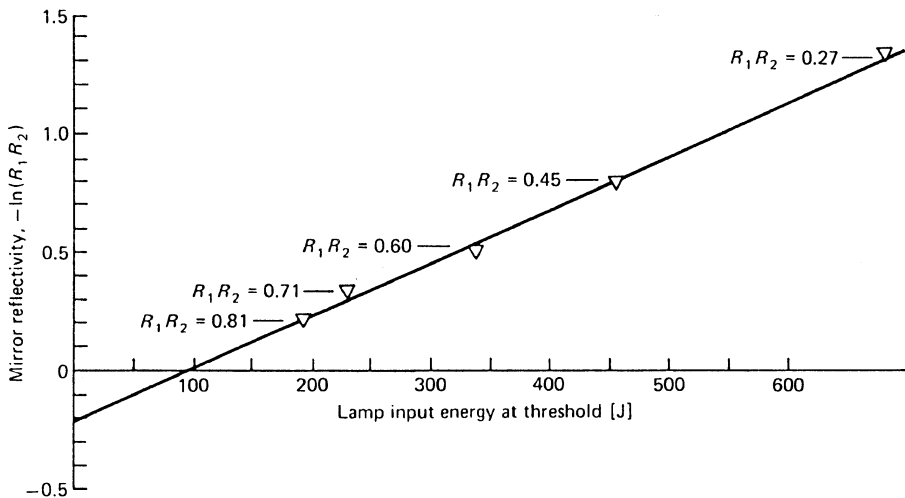


Fig. 3.10. Input energy for laser threshold of a Nd:Glass laser as a function of mirror reflectivity

line we can also calculate the efficiency factor η . With (3.61) and (3.27) we obtain $2g_0\ell = 2\eta P_{\text{in}}/I_S A$, and (3.72) can be written as

$$-\ln R = (2\eta/I_S A)P_{\text{in}} - \delta. \quad (3.73)$$

Figure 3.10 shows an example of the measurement of laser threshold as a function of mirror reflectivity in a Nd:Glass laser. The laser rod, 15 cm long and 1 cm in diameter, is pumped by two flashlamps in a double elliptical cylinder. The measurement reveals a loss in the resonator of $\delta = 0.21$. The slope of the straight line is $2\eta I_S A = 2.2 \text{ KJ}^{-1}$. With this value we obtain for the logarithmic small-signal gain $2g_0\ell = 2.2 E_{\text{in}} (\text{KJ})$.

The Quasi-Three-Level Laser

In Nd:YAG the laser transition at 1064 nm terminates on a Stark level at 2110 cm^{-1} , which is essentially thermally empty at room temperature, thus establishing Nd:YAG as a classic four level laser.

In several important diode laser pumped solid-state lasers, such as Yb:YAG and Nd:YAG operated at 946 nm, the laser transition terminates at a level close to the ground level and is therefore thermally populated. In Yb:YAG laser action terminates at the Stark level of the ground manifold at 612 cm^{-1} . For the 946-nm transition in Nd:YAG, the lower laser level is 852 cm^{-1} above the ground level. In both cases there is a significant lower laser level population at room temperature given by a Boltzmann distribution. Therefore these lasers have a quasi-three-level character at room temperature, and a fraction of the ground state population must be pumped to the upper level to achieve transparency.

In a four-level laser, threshold is achieved if the population at the upper level provides enough gain to overcome losses such as residual absorption and scattering, Fresnel losses, and output coupling loss. In a quasi-three-level laser, the thermal population at the lower laser level introduces an additional loss caused by a partial reabsorption of the laser radiation. In contrast to the losses described above, which are fixed and independent of the intensity, the lower laser level population acts as a saturable loss [3.5].

At or below threshold the reabsorption loss of a quasi-three-level laser has its maximum

$$\alpha_0 = \sigma f_l N_0, \quad (3.74)$$

where N_0 is the total dopant concentration, f_l is the fractional population at the lower laser level, and σ is the emission cross section.

For a quasi-three-level laser, the saturable loss term $\delta_s = 2\alpha_0 l$ has to be added to δ in (3.64) and (3.65). This additional loss term increases laser threshold and reduces slope efficiency. The dependence of the saturable absorption $\alpha(I)$ on the circulating intensity I is a function of the spatial distribution and overlap of the pump and laser beam. In a very general way we can express this dependence as follows

$$\alpha(I) = \frac{\alpha_0}{1 + I/I_s}, \quad (3.75)$$

where I_s is the saturation intensity given by [3.5]

$$I_s = \frac{h\nu}{(f_l + f_u)\sigma\tau} \quad (3.76)$$

In (3.76) f_u is the fraction of the upper manifold population in the upper laser level.

Near threshold the circulating intensity is zero and the loss is $\alpha(I) = \alpha_0$. As the circulating intensity increases, the transition saturates owing to absorption of the circulating power. At very large circulating intensity, the absorption coefficient $\alpha(I)$ goes to zero and the reabsorption loss δ_s becomes negligible. At that point the slope efficiency approaches that of a four-level laser.

If we use the 946-nm transition in Nd:YAG at room temperature as an example of a quasi-three-level laser we obtain the following values for the absorption coefficient at threshold and the saturation intensity. With $f_l = 0.0074$, $f_u = 0.6$, $N_0 = 1.5 \times 10^{20} \text{ cm}^{-3}$, $\tau = 230 \mu\text{s}$, and $\sigma = 4 \times 10^{-20} \text{ cm}^2$ follows from (3.74) and (3.76) a value of $\alpha_0 = 0.044 \text{ cm}^{-1}$ and $I_s = 38 \text{ Kw/cm}^2$.

The Three-Level System

The population inversion in a three-level system as a function of the pump rate is given by (3.15). If we multiply both sides of this equation by the stimulated emission cross section σ_{21} , we obtain

$$g_0 = \alpha_0 \frac{W_P \tau_{21} - (g_2/g_1)}{W_P \tau_{21} + 1}, \quad (3.77)$$

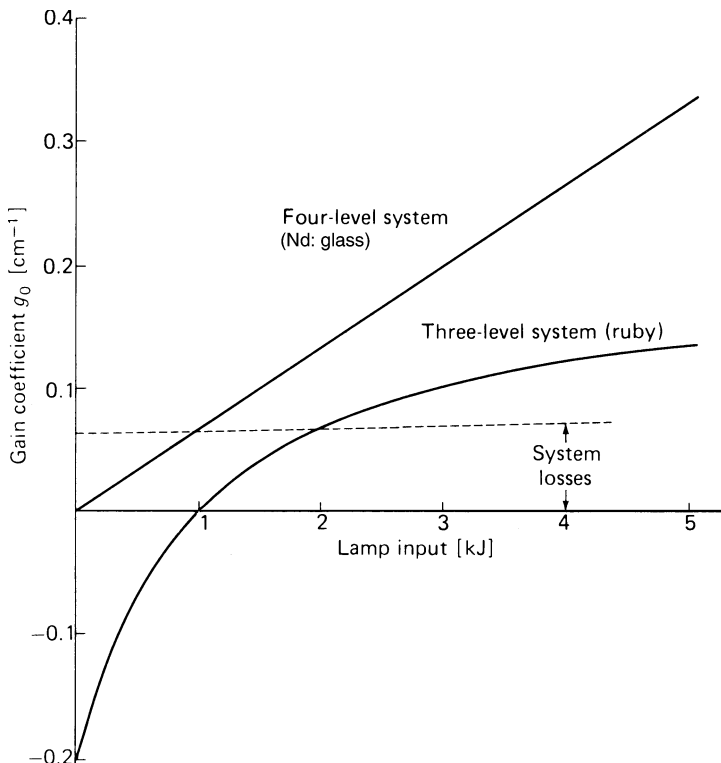


Fig. 3.11. Gain versus lamp input for a four-level and a three-level system

where $\alpha_0 = \sigma_{21} n_{\text{tot}}$ is the absorption coefficient of the material when all atoms exist in the ground state. In the absence of pumping, (3.77) simply becomes $g_0 = -\alpha_0$. In order to simplify our analysis, we assumed $g_2 = g_1$.

We assume now that the pump rate W_P is a linear function of lamp input P_{in} ,

$$W_P \tau_f = (\eta / A I_S) P_{\text{in}}. \quad (3.78)$$

Introducing (3.78) into (3.77) yields

$$g_0 = \alpha_0 \frac{(\eta / A I_S) P_{\text{in}} - 1}{(\eta / A I_S) P_{\text{in}} + 1}. \quad (3.79)$$

In a four-level system, the small-signal gain is directly proportional to the pump rate and therefore to the input power of the pump source. From (3.61) we obtain

$$g_0 = (\eta / A I_S) (P_{\text{in}} / l). \quad (3.80)$$

Equations (3.79) and (3.80) are plotted in Fig. 3.11. Since both lasers are assumed to be pulsed, the input power P_{in} has been replaced by the flashlamp input energy $E_{\text{in}} = P_{\text{in}} t_p$, where $t_p = 1$ ms is the pump pulse width. The other parameters are $(\eta / I_S A) = 10^{-6} \text{ W}^{-1}$, $\alpha_0 = 0.2 \text{ cm}^{-1}$, and $l = 15 \text{ cm}$.

3.5 Relaxation Oscillations

So far in this chapter we have considered only the steady-state behavior of the laser oscillator. Let us now consider some aspects of transient or dynamic behavior. Relaxation oscillations are by far the most predominant mechanisms causing fluctuations in the output of a solid-state laser. Instead of being a smooth pulse, the output of a pumped laser comprises characteristic spikes. In cw-pumped solid-state lasers the relaxation oscillations, rather than causing spiking of the output, manifest themselves as damped, sinusoidal oscillations with a well-defined decay time.

3.5.1 Theory

In many solid-state lasers the output is a highly irregular function of time. The output consists of individual bursts with random amplitude, duration, and separation. These lasers typically exhibit what is termed “spiking” in their output. We will explain the phenomena of the spike formation with the aid of Fig. 3.12. When the laser pump source is first turned on, there are a negligible number of photons in the cavity at the appropriate frequency. The pump radiation causes a linear buildup of excited ions and the population is inverted.

Although under steady-state oscillation conditions n_2 can never exceed $n_{2,\text{th}}$, under transient conditions the pump can raise n_2 above the threshold level because no laser oscillation has yet been built up and no radiation yet exists in the cavity to pull n_2 back down by means of stimulated emission.

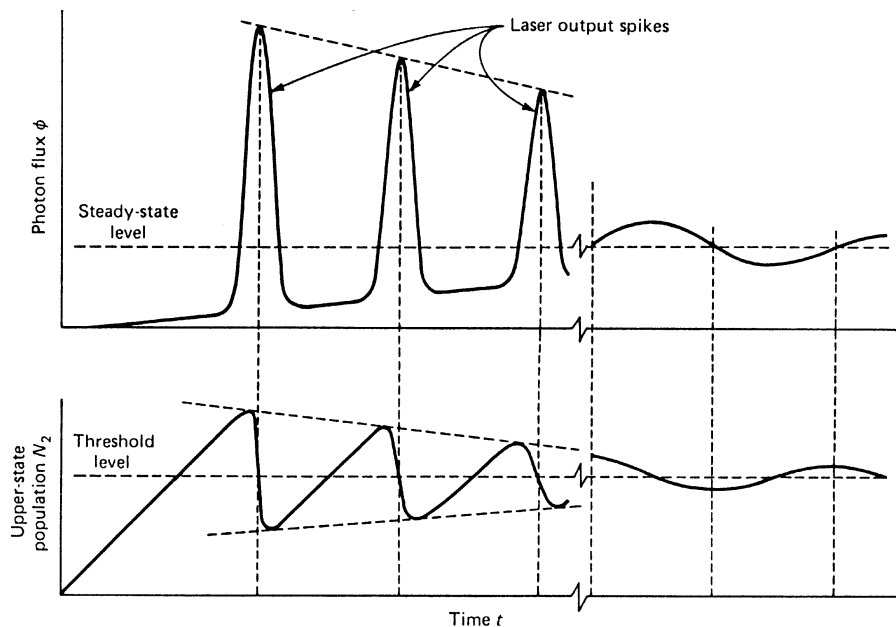


Fig. 3.12. Spiking behavior of a laser oscillator

The laser oscillation does not begin to build up, in fact, until after n_2 passes $n_{2,\text{th}}$, so that the net round-trip gain in the laser exceeds unity. Then, however, because n_2 is considerably in excess of $n_{2,\text{th}}$, the oscillation level will actually build up very rapidly to a value of the photon flux ϕ substantially in excess of the steady-state value for the particular pumping level.

But, when $\phi(t)$ becomes very large, the rate of depletion of the upper-level ions due to stimulated emission becomes correspondingly large, in fact, considerably larger than the pumping rate W_p . As a result, the upper-level population $n_2(t)$ passes through a maximum and begins to decrease rapidly, driven downward by the large radiation density. The population $n_2(t)$ is driven back below the threshold level $n_{2,\text{th}}$; the net gain in the laser cavity becomes less than unity, and so the existing oscillation in the laser cavity begins to die out.

To complete the cycle of this relaxation process, once the radiation level has decreased below the proper steady-state level, the stimulated emission rate again becomes small. At this point the pumping process can begin to build the population level n_2 back up toward and through the threshold value again. This causes the generation of another burst of laser action, and the system can again go through a repeat performance of the same or a very similar cycle.

Turning now to the rate equation, we can interpret these curves as follows: At the beginning of the pump pulse we can assume that the induced emission is negligible because of the low photon density. During this time we may neglect the term containing ϕ in (1.53) and write

$$\frac{dn}{dt} = W_p n_{\text{tot}}. \quad (3.81)$$

The population inversion therefore increases linearly with time before the development of a large spiking pulse. As the photon density builds up, the stimulated emission terms become important and for the short duration of one pulse the effect of the pumping can be neglected. Therefore, during the actual spiking pulse the rate equations can be written by neglecting both the pumping rate for the excess population and the cavity loss rate in (1.58) and (1.61):

$$\frac{dn}{dt} = -\gamma c \sigma n \phi, \quad \frac{d\phi}{dt} = +c \sigma n \phi. \quad (3.82)$$

The photon density thus grows with time and the population inversion decreases with time. The photon density reaches a peak when the decreasing inversion reaches the threshold value n_{th} . The inversion reaches a minimum at $\gamma n c \sigma \phi \approx W_p n_{\text{tot}}$. The cycle repeats itself, forming another spike. The inversion fluctuates in a zigzag fashion around the threshold value n_{th} . As time passes, the peaks become smaller and the curve becomes damped sinusoidal.

Solutions of the laser rate equations predict a train of regular and damped spikes at the output of the laser [3.6, 7]. Most lasers, however, show completely irregular, undamped spikes. This discrepancy between theory and experiment is due to the fact that the spiking behavior dies out very slowly in most solid-state lasers and therefore persists over the complete pump cycle. Furthermore, mechanical and thermal shocks and disturbances present in real lasers act to continually reexcite the spiking behavior

and keep it from damping out. Hence many lasers, especially the ruby laser, spike continuously without ever damping down to the steady state. Depending on the system parameters such as mode structure, resonator design, pump level, and so forth, the spiking may be highly irregular in appearance or it may be regular.

In cw-pumped lasers, such as Nd:YAG, the relaxation oscillations are much weaker and usually consist of damped sinusoidal oscillations around the steady-state value. These oscillations may be treated as perturbations of the steady-state population inversion and photon density given in the rate equations (1.58) and (1.61). Compared to the fluorescence time τ_f , the relaxation oscillations have a much shorter period; therefore the term including τ_f in the rate equations can be ignored (i.e., $\tau_f \rightarrow \infty$).

We now introduce a small perturbation Δn into the steady-state value of the population inversion n ; similarly, a perturbation $\Delta\phi$ is introduced into the steady state of the photon density ϕ . Thus we may write

$$n' = n + \Delta n \quad \text{and} \quad \phi' = \phi + \Delta\phi. \quad (3.83)$$

We now proceed to eliminate the population inversion n from (1.61). This is done by first differentiating the equation and then substituting $\partial n/\partial t$ from (1.58). The differential equation is then linearized by introducing n and ϕ from (3.83). Neglecting products of $(\Delta n \Delta\phi)$, we finally obtain

$$\frac{d^2(\Delta\phi)}{dt^2} + c\sigma\phi \frac{d(\Delta\phi)}{dt} + (\sigma c)^2 \phi n(\Delta\phi) = 0. \quad (3.84)$$

The solution of this equation gives the time variation of the photon density

$$\Delta\phi \approx \exp\left[\left(-\frac{\sigma c\phi}{2}\right)\right] t \sin[\sigma c(\phi n)^{1/2}t]. \quad (3.85)$$

The frequency $\omega_s = \sigma c(\phi n)^{1/2}$ and the decay time constant $\tau_R = 2/\sigma c\phi$ of this oscillation can be expressed in terms of laser parameters by noting that $I = c\phi h\nu$ and $n = 1/c\sigma\tau_c$. The latter expression follows from (1.61) for the steady-state condition, i.e., $\partial\phi/\partial t = 0$, and ignoring the initial noise level S . With the introduction of the intracavity power density I and the photon decay time τ_c we obtain

$$\omega_s = \sqrt{\frac{\sigma I}{\tau_c h\nu}} \quad \text{and} \quad \tau_R = \frac{2h\nu}{I\sigma}. \quad (3.86)$$

These expressions can be further simplified for the case of a four-level system by introducing the saturation power density I_s , leading to

$$\omega_s = \sqrt{\frac{I}{I_s \tau_f \tau_c}} \quad \text{and} \quad \tau_R = 2\tau_f \left(\frac{I_s}{I} \right). \quad (3.87)$$

Note that the greater the power density I and therefore the output power from the laser, the higher the oscillation frequency. The decay time τ_R will decrease for higher output power.

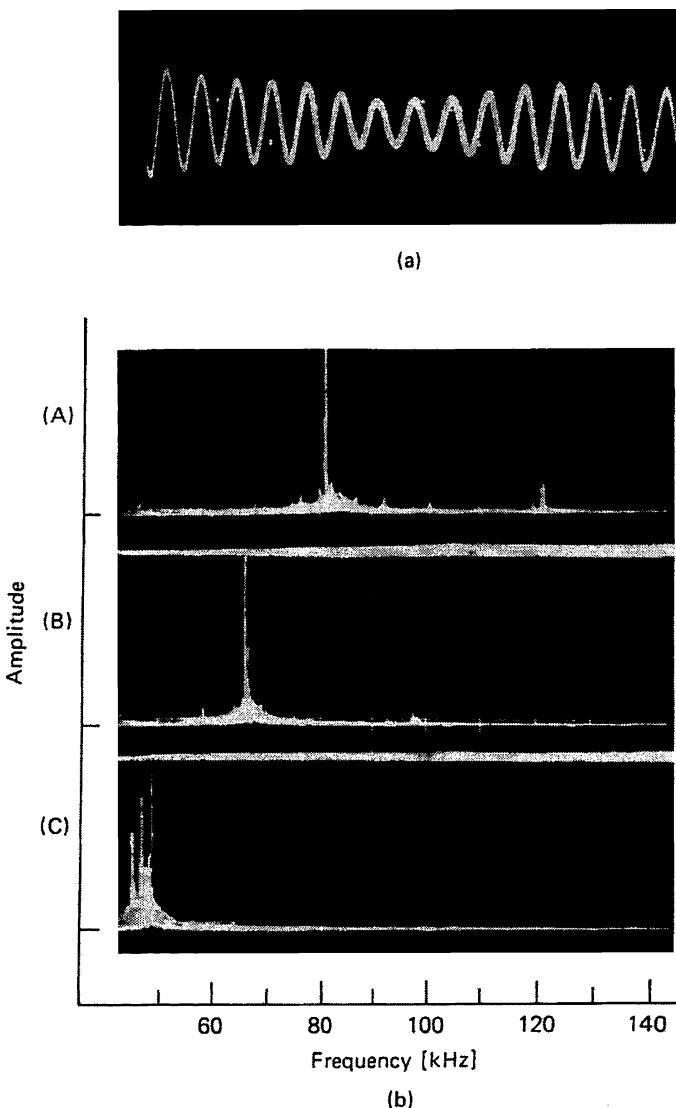


Fig. 3.13. Relaxation oscillation of a cw-pumped Nd:YAG laser. (a) Oscilloscope trace showing the temporal behavior of a relaxation oscillation: time scale, $20 \mu\text{s}/\text{div}$. (b) Frequency spectrum of relaxation oscillations at different output power levels: (A) 1.3 W, (B) 1.0 W, (C) 0.25 W

From these equations it follows that the damping time is proportional to the spontaneous lifetime. This is the reason that relaxation oscillations are observed mainly in solid-state lasers where the upper-state lifetime is relatively long.

Like most solid-state lasers, Nd:YAG exhibits relaxation oscillation. Figure 3.13 exhibits oscilloscope traces of the relaxation oscillations of a small cw-pumped Nd:YAG laser. The oscillation is a damped sine wave with only a small content

of harmonics. Figure 3.13b displays the spectrum of the relaxation oscillations as obtained by a spectrum analyzer. From (3.87) it follows that the resonant frequency is proportional to $(P_{\text{out}}^{1/2})$ of the laser. Figure 3.13b illustrates this dependence. With (3.87) we can calculate the center frequency ν_S and the time constant τ_R of the relaxation oscillations. With the laser operated at 1 W output, a mirror transmission of $T = 0.05$, and beam diameter of 0.12 cm, one obtains $I = 4.0 \times 10^3 \text{ W/cm}^2$; $l = 35 \text{ cm}$ is the length of the cavity and $\delta = 0.03$ are the combined cavity losses. With these values, and $I_S = 2900 \text{ W/cm}^2$ and $\tau_f = 230 \mu\text{s}$, it follows that $\tau_R = 333 \mu\text{s}$ and $\nu_S = 72 \text{ kHz}$. The measured center frequency of the relaxation oscillation is, according to Fig. 3.13b, about 68 kHz.

3.5.2 Spike Suppression

Relaxation oscillations are a fundamental property of the laser and are produced by the dynamic interaction between the radiation within the resonator and the energy stored in the active laser medium. Subsequently, relaxation oscillations can be stimulated by a variation in the optical losses of a particular resonator mode, or by a change of the gain in the laser medium.

The task of reducing relaxation oscillations requires eliminating the sources which start these oscillations and providing electronic feedback to attenuate the amplitude to the oscillations once they do occur.

Disturbances include mechanical vibrations of the resonator components and intensity noise of the pump source. In water-cooled arc lamp pumped lasers it is particularly difficult to reduce output fluctuations. Spatial and temporal instability of the lamp discharge combined with changes of the cooling conditions by the turbulent cooling flow introduces disturbances which promote the onset of relaxation oscillations. In these systems, active feedback systems designed to reduce amplitude fluctuations typically consisted of a beam splitter and photodiode at the output of the laser, and intracavity modulator, and an electronic drive circuit. The photodiode samples a fraction of the laser output and provides a feedback signal to the modulator, such as a Pockels cell or acousto-optic device. As the output of the laser increases above a certain value by the onset of a spike, the loss in the resonator is increased by the feedback circuit.

An enabling technology for designing low noise oscillators is the of diode-laser pump sources, in combination with conduction cooling and a monolithic resonator/gain medium design. Instabilities and fluctuations caused by the arc discharge are eliminated. Conductive cooling removes mechanical vibrations introduced by the water pump, and temporal optical disturbances in the laser rod by turbulent water flow are eliminated. A monolithic design drastically reduces mechanical instabilities and the laser operates in a single transverse and longitudinal mode. Extremely low-noise oscillators comprising conductively cooled, diode-pumped monolithic lasers with an active feedback loop that suppresses relaxation oscillations are described in [3.8–10]. In diode-pumped lasers, the feedback loop controls the drive current to the laser-diode source.

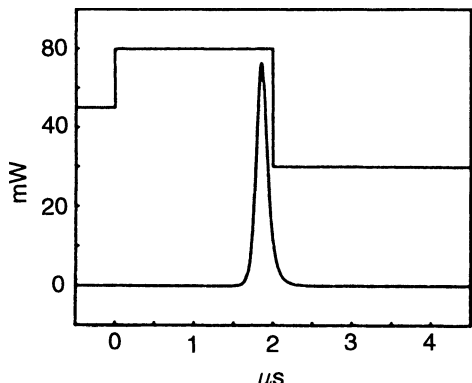


Fig. 3.14. Diode drive current (upper trace) and Nd:YAG laser output (lower trace) of a gain-switched system [3.12]

A more detailed discussion of the reduction of amplitude noise in diode-pumped lasers is provided in Sect. 5.3 in connection with linewidth control.

3.5.3 Gain Switching

In the previous subsection, we described techniques to suppress relaxation oscillations; in gain switching—the subject treated here—the phenomenon of spiking is exploited to produce a high peak power pulse. If a solid-state laser is pumped by another laser, it is possible to pump at such a fast pump rate that the population inversion and gain reach a level considerably above threshold before the laser oscillation has time to build up in the resonator. As the radiation increases in time, it will then deplete the upper-state population. The response of a laser to a very fast pump pulse which drives the inversion far above threshold is in the form of a relaxation oscillation depicted in Fig. 3.12 [3.11–13]. If the pump pulse is not only fast but also shorter than the width of the first peak of the relaxation oscillation, the radiation emitted from the system will consist of only the first spike. The population inversion will have been driven to a value below laser threshold after the first spike and it will not grow because there is no pump energy to replenish the population.

The use of gain-switching method to enhance the peak power of a diode-pumped monolithic Nd:YAG laser has been described in [3.12]. A single-longitudinal mode operation is established by pumping the oscillator at its threshold pump level of 1.5 mW of about 500 μs . The device is then gain-switched by increasing the diode drive current for several microseconds, which increases the power to 50 mW. This results in the emission of a relaxation oscillation from the Nd:YAG crystal. The gain-switching pulse is turned off at the end of the first relaxation oscillation. The emission of further relaxation pulses is thus avoided. This is sketched in Fig. 3.14. The drive current at $\tau = 0$ is switched from a value just above the threshold condition to a high value. After 2 μs the first relaxation oscillation has developed. At that point, the drive current to the pump source is turned off.

Both gain switching and Q-switching allow the generation of short pulses. Q-switched pulses are generated by storing energy in the upper state of the active medium by a pump pulse having a duration on the order of the upper-state lifetime. After the inversion and gain have been established, the loss in the resonator is suddenly switched off. In gain switching, energy is deposited very quickly in the upper state, i.e., gain is switched on before the radiation in the resonator has time to build up from noise.

From this discussion, it is clear why gain switching as compared to Q-switching is employed only in special cases in solid-state lasers. A Q-switch permits the transformation of a pump pulse of relatively low power and long duration into the emission of a very short pulse of high peak power. For example, in a Nd:YAG laser the flashlamp pump pulse is typically 200 μ s, and the Q-switch output pulse is on the order of 20 ns, which results in a time compression of 4 orders of magnitude. In gain switching, peak power and pulse width of the pump pulse and laser output are on the same order.

As an example of a gain-switched laser, we consider the pumping of Ti:Sapphire with a frequency-doubled Q-switched Nd:YAG laser. Ti:sapphire is difficult to pump with a flashlamp because the short upper-state lifetime of 3.2 μ s requires a pump pulse of similar pulse width. Therefore, a common pump source for a pulsed Ti:sapphire laser is a frequency-doubled, Q-switched Nd:YAG laser. In the specific example considered [3.13], the pulse width of 10 ns from the Nd:YAG laser pump is significantly shorter than the 3.2 μ s upper-state lifetime in Ti:sapphire, and the pump pulse is also significantly shorter than the power buildup time which may be on the order of 50–200 ns. Because of the short pump pulse, the inversion is initially driven far above threshold and the Ti:sapphire laser responds with the emission of a gain-switched pulse with a pulse width on the order of 10–40 ns depending on the intensity of the pump source.

3.6 Examples of Laser Oscillators

The Nd:YAG laser is by far the most widely used and most versatile solid-state laser. Pumping can be accomplished by means of flashlamps, cw arc lamps, or laser diodes, and the laser can be operated cw or pulsed thereby achieving pulse repetition rates from single shot to several hundred megahertz. In this section we will relate the performance characteristics of several of these systems to the oscillator model described in this chapter.

3.6.1 Lamp-Pumped cw Nd:YAG Laser

A type of laser which is widely used for materials processing consists of an Nd:YAG crystal 7.5 cm or 10 cm long and with a diameter of 6.2 mm pumped by two krypton-filled arc lamps. Electrical input to the lamp can be up to 12 kW. The optical resonator is typically composed of two dielectrically coated mirrors with a separation of 30–40 cm. Curvature of the mirrors and transmission of the output coupler is selected for optimum performance, that is, output power and beam quality. In Fig. 3.15 the output

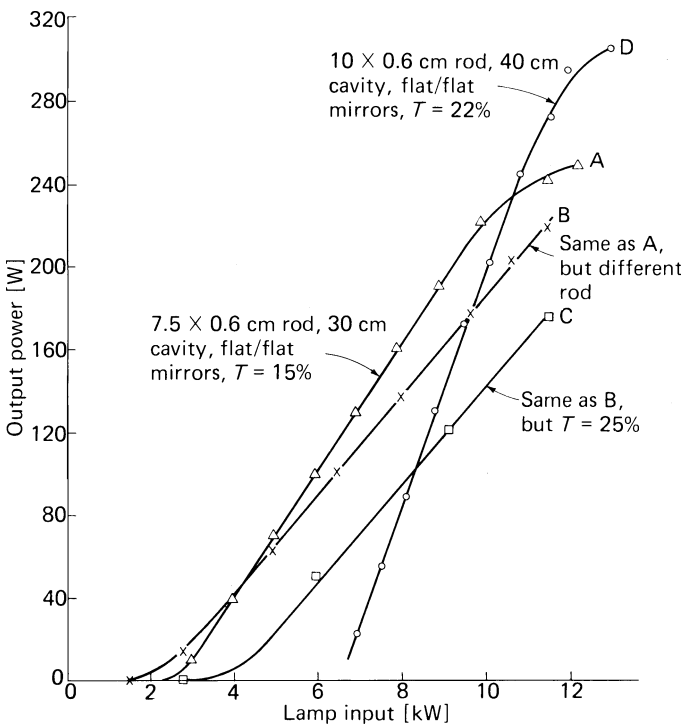


Fig. 3.15. Continuous output versus lamp input of a powerful Nd:YAG laser

versus input is plotted for a number of different laser crystals and mirror combinations. Curve A shows the output curve of a system that has slope efficiency of $\sigma_S = 3.1\%$ and an extrapolated threshold of $P_{th} = 2.5$ kW. The nonlinear portion of the curve close to threshold is due to the focusing action of the elliptical reflection. At first, only the center of the rod lases. The nonlinear behavior of the output curve at the high input end is due to thermal lensing within the laser rod. This lensing effect, caused by the thermal gradients in the the laser crystal, increases the resonator losses (see Chap. 7).

In Fig. 3.16 the lamp input power required to achieve laser threshold was measured for different mirror reflectivities for the laser system mentioned above. If one plots $\ln(1/R)$ versus P_{in} , one obtains a linear function according to (3.72). From this measurement follows a combined loss of $\delta = 0.075$ in the resonator. With this value and the slope efficiency measured for curve A in Fig. 3.15 one can calculate from (3.64) the efficiency factor $\eta = 4.6\%$. The same value can also be obtained from the slope of the curve in Fig. 3.16. Best agreement is obtained if one assumes a saturation power density of $I_S = 2.2$ kW/cm². This implies an effective emission cross section somewhere between the two values listed in Table 2.2. From the data of Fig. 3.16 one can plot the small-signal, single-pass gain and the gain coefficient as a function of lamp input power as shown in Fig. 3.17.

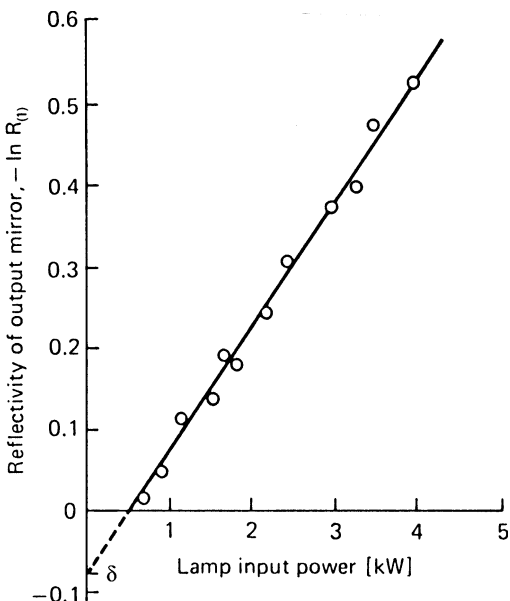


Fig. 3.16. Threshold power input as a function of mirror reflectivity

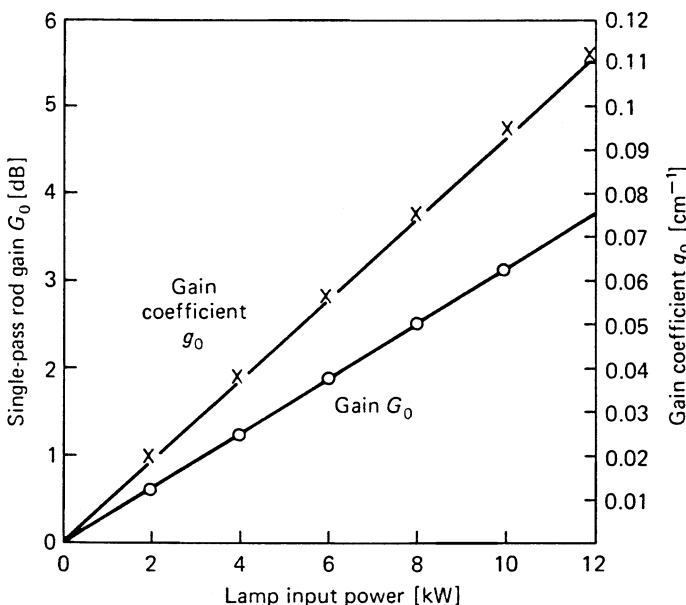


Fig. 3.17. Small-signal, single-pass rod gain and gain coefficient as function of lamp input

It is instructive to calculate the inversion density in the Nd:YAG crystal that has to be sustained to achieve the maximum small-signal gain coefficient of $g_0 = 0.11 \text{ cm}^{-1}$. Assuming a neodymium concentration of $1.38 \times 10^{20} \text{ cm}^{-3}$ and a stimulated emission cross section of $2.8 \times 10^{-19} \text{ cm}^2$, it follows from (3.12) that at maximum pump input only 0.28% of the total neodymium atoms are inverted. The small percentage of atoms at the upper laser level is due to the four-level nature of the transition and the large cross section of Nd:YAG.

For a mirror transmission of $T = 0.15$ the small-signal gain coefficient at threshold is about $g = 0.02 \text{ cm}^{-1}$, which results in an upper-state population density of $n_t = 10^{16} \text{ cm}^{-3}$. From this value and using (3.18) we can calculate the total fluorescence output of the laser at threshold. With $V = 2.3 \text{ cm}^3$, $\tau_f = 230 \mu\text{s}$, $h\nu = 1.86 \times 10^{-19} \text{ W s}$, one obtains $P_f = 130 \text{ W}$.

If δ and η have been determined for a particular laser crystal and resonator combination, the laser output at different input levels and mirror reflectivities can be calculated from (3.63) to (3.65). An example of such a calculation is shown in Fig. 3.18. The mirror reflectivity which gives the highest output power for the different

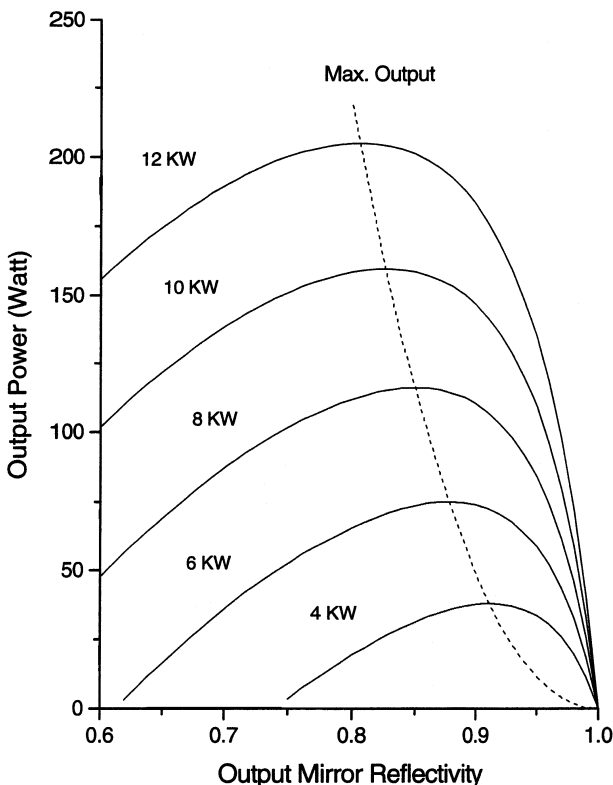


Fig. 3.18. Output power versus mirror reflectivity. Parameter is the lamp input power. Parameters: $\eta = 0.031$, $\delta = 0.075$, $I_S = 2.2 \text{ KW/cm}^2$

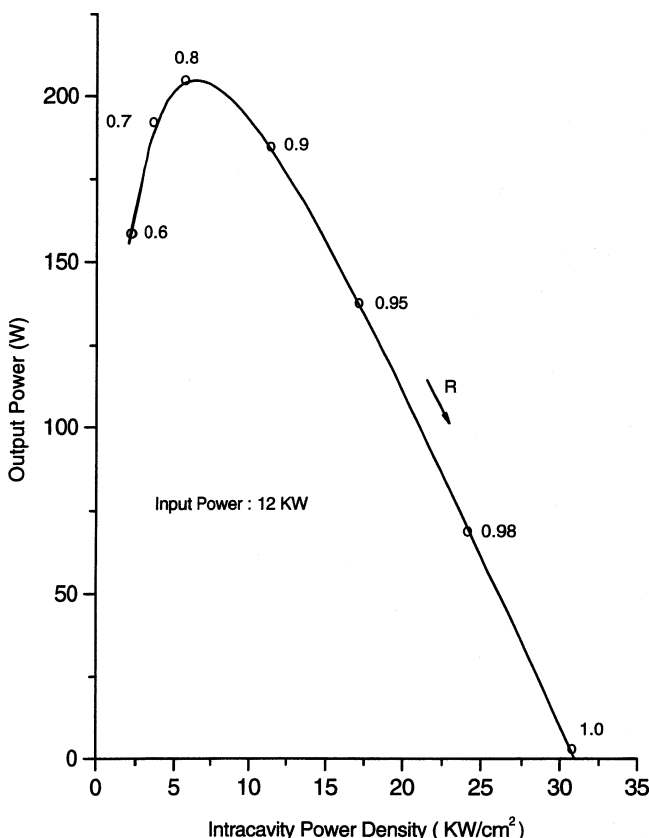


Fig. 3.19. Intracavity power density as a function of laser output power. Parameter is the reflectivity of the output coupler

input powers is located along the dashed curve. This curve has been obtained from (3.66) with (3.61) and (3.27). Figure 3.19 shows the intracavity power density as a function of laser output power for a fixed lamp input power of 12 kW. The parameter is the reflectivity of the front mirror. This curve is obtained from Fig. 3.18 (uppermost curve) and using (3.36). As we can see from this figure, the circulating power density in the resonator increases for the higher reflectivities despite the reduction of output power.

Figure 3.20 shows a photograph of a typical, commercially available, cw-pumped Nd:YAG laser. The laser head contains a single arc lamp. The mechanical shutter is used to stop laser oscillations for short periods of time without having to turn off the arc lamp. The purpose of the mode selector and Q-switch will be discussed in Chaps. 5 and 8. Bellows are employed between each optical element in the laser head in order to seal out dust and dirt particles from the optical surfaces. The laser head cover is sealed with a gasket in order to further reduce environmental contamination.

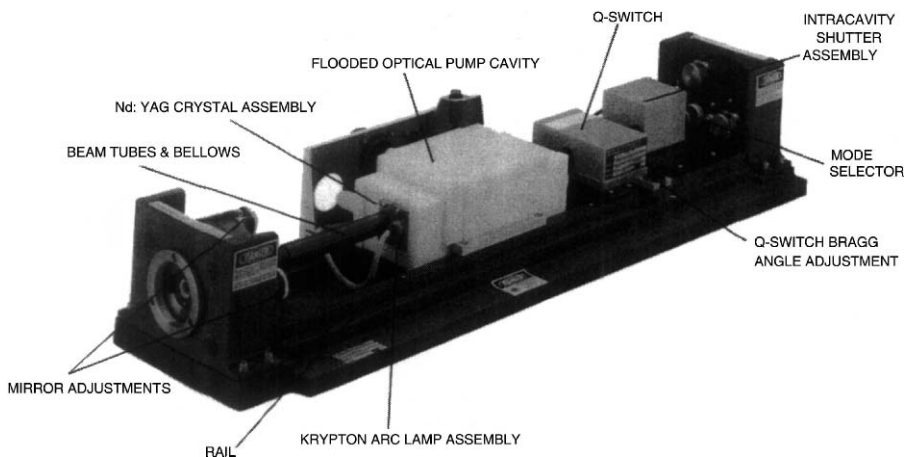


Fig. 3.20. Photograph of a commercial cw-pumped Nd:YAG laser (Quantronix, Series 100)

3.6.2 Diode Side-Pumped Nd:YAG Laser

As will be discussed in Chap. 6, diode-pumped systems can be divided into side-pumped and end-pumped systems. In the side-pumped geometry, the diode arrays are placed along the length of the laser rod or slab and pump the active material perpendicular to the direction of propagation of the laser resonator mode.

In the end-pumped geometry, the pump radiation is collimated and focused longitudinally into the laser material collinear with the resonator mode. These configurations take full advantage of the spectral as well as spatial properties of laser diodes. In this section, we will discuss examples of both classes of systems.

As an example of a side-pumped Nd:Laser oscillator, we will consider first a simple laboratory setup as illustrated in Fig. 3.21. A number of different laser materials were each side-pumped with a diode array close-coupled to the polished rod barrels

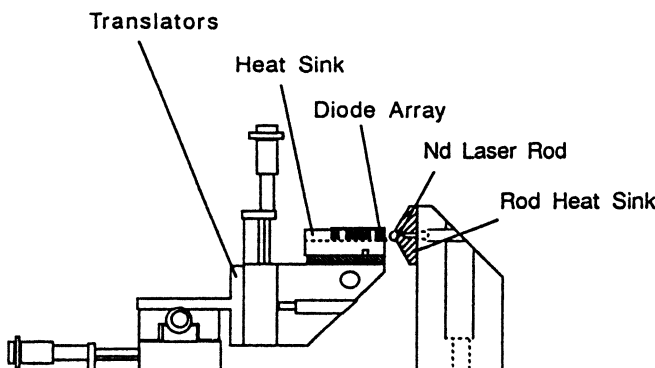


Fig. 3.21. Experimental setup of a solid-state laser side-pumped with a laser diode array

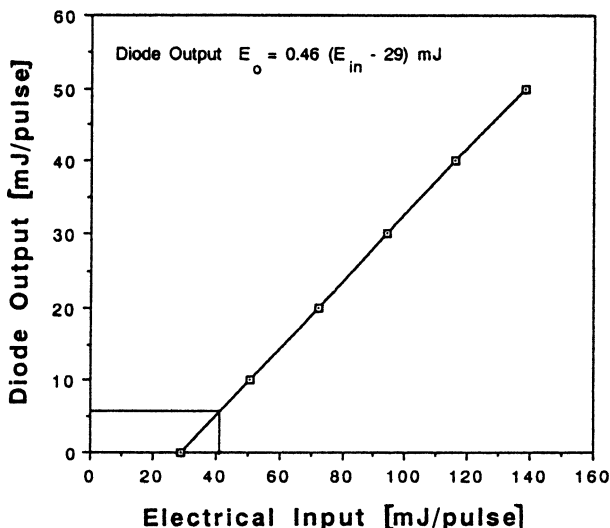


Fig. 3.22. Output energy vs. electrical input energy for a 1 cm by 5-bar laser diode array

without intervening optics. The pump array consisted of a stack of five 1-cm-pulsed GaAlAs laser bars each containing 40 laser subarrays. The diode array produced 50 mJ/pulse output with a 200- μ s pulse width at the maximum current rating of 80 A per pulse. At that current rating, the array had a linewidth of about 4 nm. Figure 3.22 shows the diode output as a function of electrical input. The diode-array output wavelength was temperature-tuned with a thermo-electric cooler between 805 and 812 nm. A translation stage was used to optimize the pump distribution in the laser rods which were mounted on a highly polished and silver-coated heat sink. The pump radiation emitted from the diode array has a divergence of 40° by 10° full width half maximum.

The polished cylindrical surface of the rod focuses the radiation toward the center, and radiation passing through the active material is reflected back also toward the center by the highly reflective back surface. The highest output was achieved with the smallest separation between the laser rods and the diode array, i.e., the front facet of the array was almost touching the laser rod. Larger separations produce high Fresnel losses owing to the very large angles of incidence at the laser rod surface.

The laser materials utilized in these experiments carried out in the author's lab (see also [3.14]) were a 3.5 mm diameter by 20 mm long, 1.1% doped Nd:YAG rod, a 3.5 mm diameter by 20 mm long, 1% doped Nd:BeL rod, and a 3 mm diameter by 20 mm long, 6% doped Nd:Phosphate Glass (Kigre Q-98) rod. The birefringent Nd:BeL rod was cut along the "y" axis to produce laser output at 1.07 μ m.

The 12-cm-long laser resonator consisted of a 50-cm-curvature concave total reflector, and a flat partially reflecting output coupler. Output from the lasers was multimode and matched the shape of the pumped area.

Figure 3.23 shows the calculated pump radiation distribution inside the Nd:YAG laser rod obtained from a ray trace analysis which takes into account the spectral and

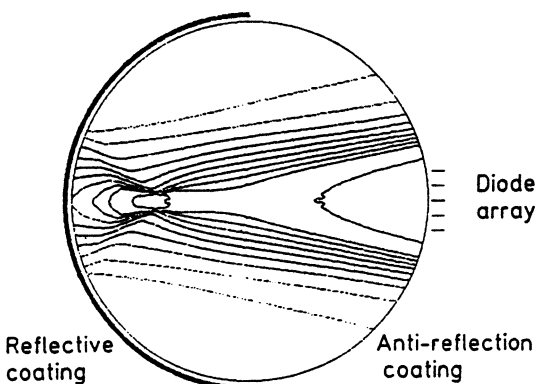


Fig. 3.23. Pump intensity distribution inside a Nd:YAG rod

spatial properties of the source and the spectral absorption by the laser material. The laser output beam had an almost rectangular shape, filling the area between the diode array and the back reflector. The hot spot located approximately between the center of the rod and the back reflector is the result of the focusing action of the cylindrical front and back surface. The pumped area of the 3.5-mm-diameter laser rod was about 70% of the total cross section or $A = 0.07 \text{ cm}^2$.

The output from the diode-array-pumped lasers is exhibited in Figs. 3.24 and 25. The laser output followed the current input to the diode with less than 10 μs buildup time and a small amount of relaxation oscillator. Therefore, for the purpose of analysis, the lasers were assumed to be in a steady-state regime.

Figure 3.24 shows the output energy from the lasers as a function of diode-array pump energy at 0.8 μm . The optical slope efficiencies are 54% for Nd:YAG, 42% for Nd:BeL, and 48% for Nd:Glass.

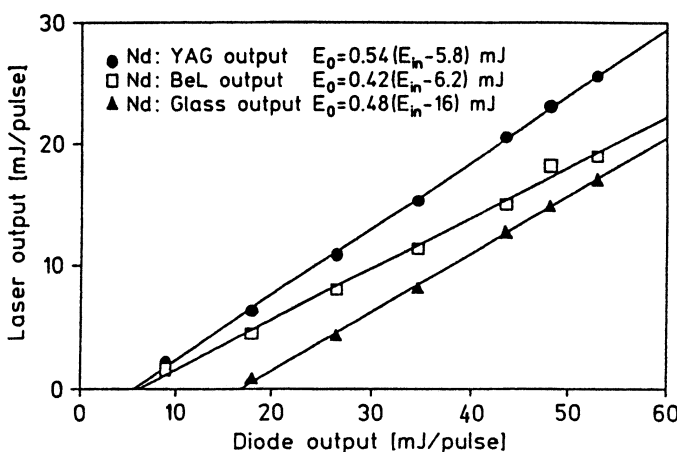


Fig. 3.24. Laser output energy vs. pump pulse energy

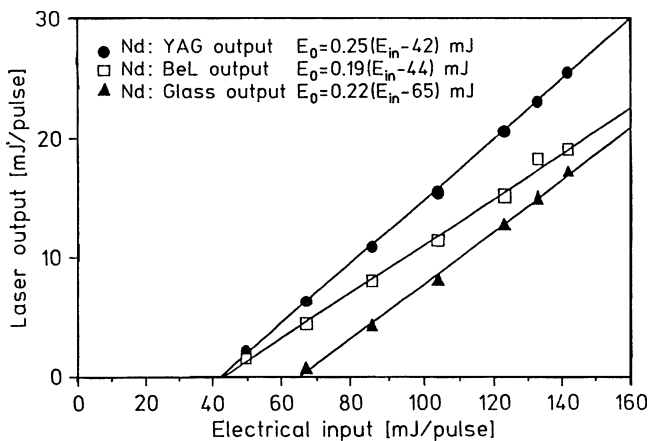


Fig. 3.25. Laser output energy vs. electrical input energy

Figure 3.25 depicts the output energy from the lasers as a function of electrical energy input to the diode array. The electrical slope efficiencies for the lasers are 25% for Nd:YAG, 19% for Nd:BeL, and 22% for Nd:Glass. The overall electrical “wallplug” efficiencies at maximum output for the three lasers are 18, 14, and 12%, respectively.

The electrical slope efficiencies of these curves are obviously the product of the slope efficiencies of the curves in Figs. 3.22 and 24. Furthermore, the threshold values in Fig. 3.25 are the sum of the diode laser threshold (which occurs at 29 mJ electrical input energy) and the solid-state laser thresholds. The optimum output coupling for each laser was experimentally determined and the results are shown in Fig. 3.26. Among the three materials, Nd:YAG has the largest stimulated emission

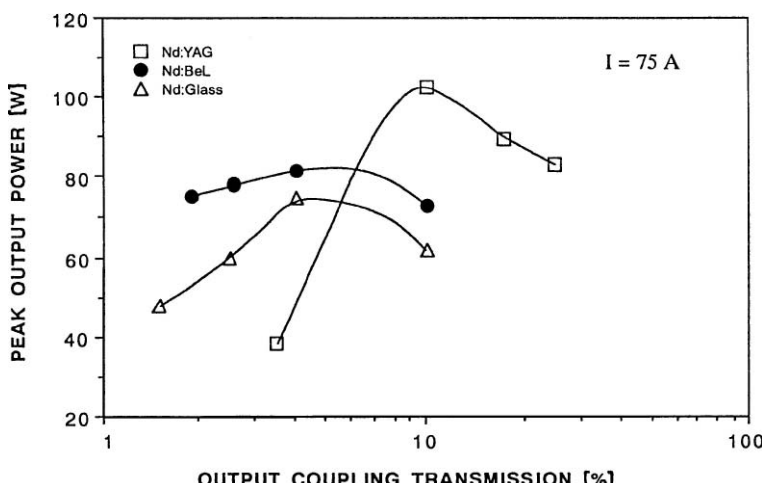


Fig. 3.26. Laser output vs. output coupling

Table 3.1. Energy transfer efficiencies of several laser oscillators

Transfer process	Nd:YAG	Nd:BeL	Nd:Glass
Diode slope efficiency (η_P)	0.46	0.46	0.46
Transfer efficiency (η_T)	0.99	0.89	0.95
Absorption efficiency (η_a)	0.91	0.94	0.94
Stokes shift (η_S)	0.76	0.76	0.76
Quantum efficiency (η_Q)	0.95	0.82	0.85
Coupling efficiency (η_C)	0.87	0.77	0.86
Beam overlap efficiency (η_B)	0.95	0.95	0.95
Optical slope efficiency (σ_S)	0.54	0.42	0.48
Electrical slope efficiency (σ_S)	0.25	0.19	0.22

cross section and therefore the highest gain coefficient. Therefore, for comparable resonator internal losses one would expect the highest output coupling for the Nd:YAG material according to (3.66).

From the experimental data presented in these figures, we can obtain a fairly accurate picture of the various steps involved in the conversion of electrical input power to laser output. Table 3.1 lists the numerical values for the various efficiencies for the three laser materials.

The diode slope efficiency η_P is experimentally determined by measuring the output with a power meter or calorimeter as function of electrical input. The transfer efficiency η_T is strictly a function of Fresnel losses of the cylindrical surface of the rods. In the case of the Nd:YAG rod, one-half of the barrel which is facing the diode array is antireflection (AR)-coated. The coating has less than 0.25% loss at 810 nm for normal incidence, but reflection losses are higher at larger angles. The 1% reflection loss is an average value obtained by considering all angles. The other two materials are not coated; therefore the reflection losses are higher.

The absorption efficiency η_a was calculated by employing a computer code specifically designed for diode pumping of materials ([3.15], see also Chap. 6 for details). In this work, the absorption of the laser diode radiation for a number of lasers is calculated versus path length in the laser material. From this reference follows that for the Nd:YAG laser, for example, about 70% of the incident radiation is absorbed in a 3-mm path length. This is about the average distance between the front surface and the back reflector of the 3.5-mm-diameter crystal. From the radiation incident on the back reflector, 30% was estimated to be lost owing to absorption and scattering and radiation being reflected into areas of the rod which are outside the gain region. Nd:BeL and Nd:Glass have a higher absorption coefficient for the diode radiation; therefore η_a is somewhat higher for these materials. Absorption efficiencies as a function of material thickness and laser pump wavelength for a number of Nd laser materials can be found in [3.16].

The Stokes shift is simply the ratio of the pump and laser wavelength, and the quantum efficiency is a materials parameter. The coupling efficiency η_C was determined by measuring the resonator losses according to the method described in Sect. 3.4.2. For Nd:YAG, the resonator round-trip loss was 1.5%, and for Nd:BeL and

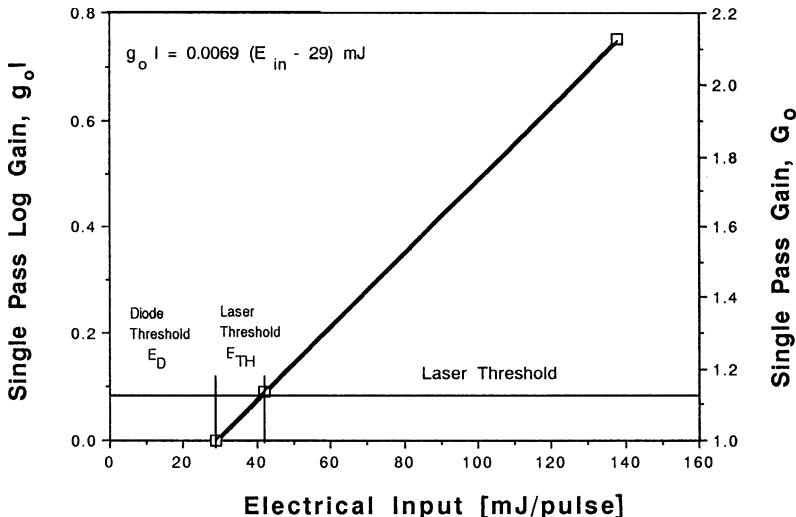


Fig. 3.27. Single-pass logarithmic gain as a function of electrical input energy

Nd:Glass, the loss was 1.8 and 1%, respectively. The output coupling for these three materials was 10% for Nd:YAG and 6% for Nd:BeL and Nd:Glass. The beam overlap efficiency takes into account pump radiation in areas which have not reached lasing threshold. It is the least known of all the parameters and was adjusted such that the product of the η terms agreed with the measured slope efficiencies. The optical slope efficiency $\sigma = \eta_T \eta_a \eta_S \eta_Q \eta_C \eta_B$ is the slope of the curves in Fig. 3.24 representing laser output vs. optical pump power, whereas the electrical slope efficiency is the slope of the laser output vs. electrical input curves which includes η_P .

We will now calculate a number of laser parameters from this data by using the Nd:YAG laser as an example. From the values in Table 3.1, one can calculate the gain of the laser as a function of input power. From (3.61) and with $A = 0.07 \text{ cm}^2$, $I_S = 2.9 \times 10^3 \text{ W/cm}^2$, and $\Delta t_P = 200 \mu\text{s}$ follows

$$g_0 l = 15 \times 10^{-3} E_D / \text{mJ}, \quad (3.88)$$

or if we want to express the gain in terms of electrical input power we have to introduce into (3.61) the diode characteristics $E_D = \eta_P(E_{in} - E_{THD})$. The laser gain vs. electrical input energy

$$g_0 l = 6.9 \times 10^{-3} (E_{in} - 29 \text{ mJ}) \quad (3.89)$$

is plotted in Fig. 3.27. Also indicated in this figure are the thresholds for the diode laser and solid-state laser. The maximum single-pass gain for the laser is $G_0 = \exp(g_0 l) = 2.1$. The laser output at this gain level is $E_{out} = 24 \text{ mJ}$, the available energy at the upper level follows from (3.68); with the values above one obtains $E_{avail} = 30 \text{ mJ}$. Therefore the extraction efficiency of the laser is $\eta_E = 0.80$. This value can also be obtained from (3.70). The optimum transmission of the laser is according to (3.66) $T_{opt} = 0.13$.

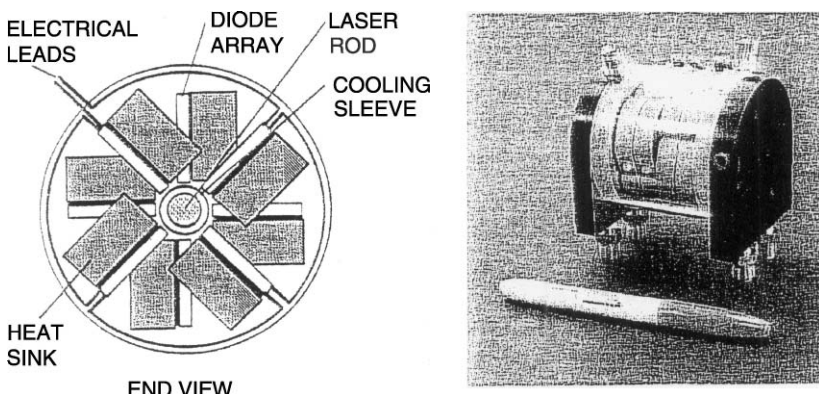


Fig. 3.28. Cross-section (*left*) and photograph (*right*) of diode-pumped Nd:YAG laser head

Putting this value into (3.65) gives a threshold input energy of $E_{\text{TH}} = 11 \text{ mJ}$. The values agree reasonably well with the measured data. The reader is reminded that these performance parameters are based on average values of the highly nonuniform and multimode beam profile.

The next example illustrates the performance of a relatively large diode array side-pumped oscillator. The system produces an energy per pulse of about 0.5 J at a repetition rate of 40 Hz. Critical design issues for this laser include heat removal from the diode arrays and laser rod, and the overlapping of the pump and resonator mode volumes. In side-pumped configurations, laser diode arrays are not required to be coherent, and pump power can be easily scaled with multiple arrays around the outside of the rod or along its axis. Instead of one diode-array pumping the laser crystal, this particular laser employs 16 diode-arrays located symmetrically around the rod. As shown in Fig. 3.28, the diode pumps are arranged in four rings, each consisting of four arrays. Since each array is 1 cm long, the total pumped length of the $6.6 \text{ cm} \times 0.63 \text{ cm}$ Nd:YAG crystal is 4 cm. This arrangement permits the incorporation of large water-cooled heat sinks required for heat dissipation, and it also provides for a very symmetrical pump profile. An eightfold symmetry is produced by rotating adjacent rings of diodes by 45° . A photograph of the extremely compact design is also shown in Fig. 3.28. The symmetrical arrangement of the pump sources around the rod produces a very uniform pump distribution, as illustrated in Fig. 3.29. The intensity profile displays the fluorescence output of the rod taken with a CCD camera. In Fig. 3.30, the output vs. optical pump input is plotted for long-pulse multimode and TEM₀₀ mode operation. Shown also is the output for Q-switch TEM₀₀ mode operation. The resonator configuration for the long pulse multimode operation is depicted in Fig. 3.31. The TEM₀₀ mode performance was achieved with a variable reflectivity mirror and a concave–convex resonator structure, which will be described in Chap. 5.

The multimode laser output can be expressed by

$$E_{\text{out}} = 0.5(E_{\text{opt}} - 180 \text{ mJ}), \quad (3.90)$$

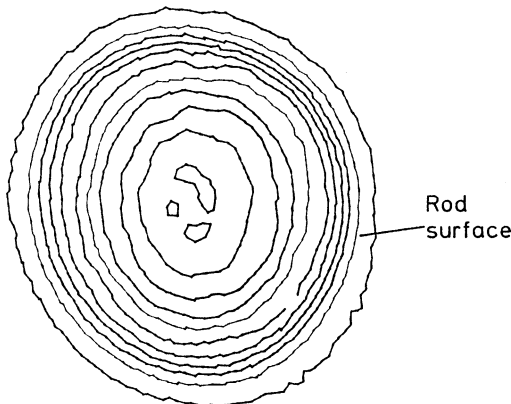


Fig. 3.29. Pump distribution of a 16-diode array side pumped Nd:YAG crystal (each line represents a 10% change in intensity)

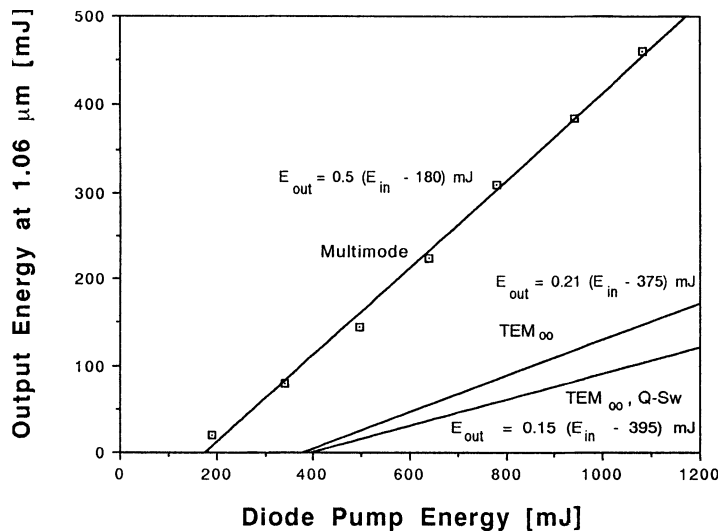


Fig. 3.30. Output vs. input energy for diode-pumped Nd:YAG oscillator

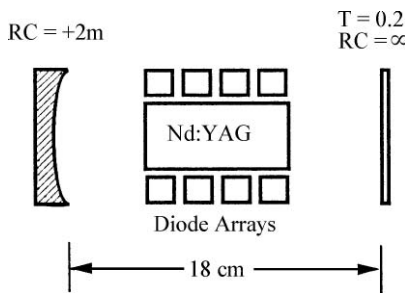


Fig. 3.31. Resonator configuration for multimode operation

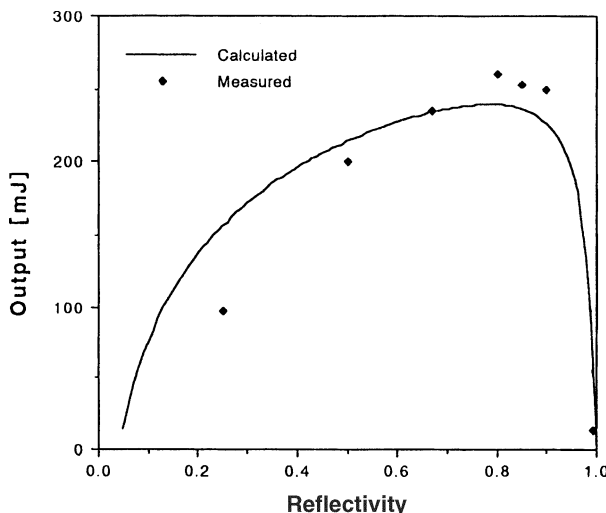


Fig. 3.32. Oscillator output vs. mirror reflectivity (calculated curve based on $T_{\text{opt}} = 0.2$, $g_{\text{OL}} = 1.4$, $\delta = 0.03$)

where E_{opt} is the optical pump energy from the 16 diode arrays. The electrical input energy E_{in} required to achieve E_{opt} is

$$E_{\text{opt}} = 0.5(E_{\text{in}} - 640 \text{ mJ}). \quad (3.91)$$

Combining these two output–input curves relates the laser output with the electrical input energy

$$E_{\text{out}} = 0.25(E_{\text{in}} - 1000 \text{ mJ}). \quad (3.92)$$

The slope efficiency of the laser is 25% and the overall electrical efficiency at the maximum output of 460 mJ per pulse is 16%. The optimum output coupling was experimentally determined. Figure 3.32 shows a plot of the laser output for different values of the reflectivity. The different efficiency factors of the system are listed in Table 3.2. The slope efficiency of the diode array was measured with a power meter.

Table 3.2. Energy transfer efficiencies of a large diode-pumped Nd:YAG oscillator

Transfer process	Multimode	Single mode
Diode slope efficiency (η_P)	0.50	0.50
Transfer efficiency (η_T)	0.95	0.95
Absorption efficiency (η_a)	0.90	0.90
Stokes shift (η_S)	0.76	0.76
Quantum efficiency (η_Q)	0.95	0.95
Coupling efficiency (η_C)	0.90	0.90
Beam overlap efficiency (η_B)	0.90	0.38
Electrical slope efficiency (σ_S)	0.25	0.10

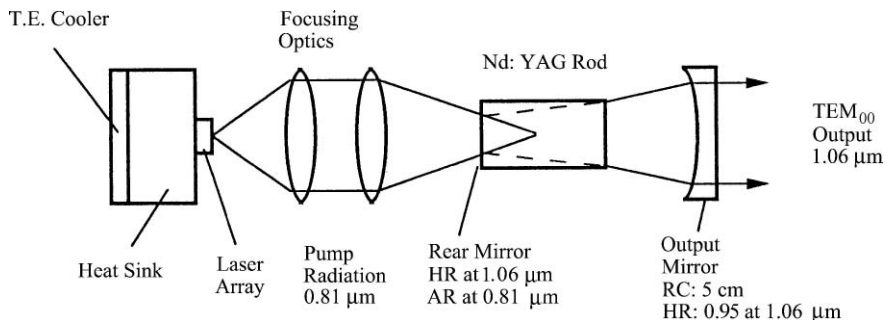


Fig. 3.33. End-pumped laser oscillator

The coupling of radiation to the rod is lower than in the previous example because in this system a water jacket and coolant are in the optical path of the pump radiation. The sapphire water jacket is AR-coated for the pump radiation. The absorbed pump radiation in the 6.3-mm diameter crystal was calculated as before from a computer code.

The output coupling follows from $T_{\text{opt}} = 0.20$ and the measured round-trip loss of $\delta = 2.2\%$. The gain/mode overlap efficiency η_B was estimated by comparing the beam profile with the pump distribution in the laser rod. The final value was adjusted for the product of the η terms to agree with the measured slope efficiency of 25%. For TEM_{00} mode operation, the major difference is a substantially reduced value for η_B as a result of a smaller beam. All other parameters remain unchanged.

3.6.3 End-Pumped Systems

In this so-called end-pumped configuration, the radiation from a single laser diode or diode bar is focused to a small spot on the end of a laser rod. With a suitable choice of focusing optics, the diode pump radiation can be adjusted to coincide with the diameter of the TEM_{00} resonator mode. The end pumping configuration thus allows the maximum use of the energy from the laser diodes.

Using this longitudinal pumping scheme, the fraction of the active laser volume excited by the diode laser radiation can be matched quite well to the TEM_{00} lasing volume. A solid-state laser pumped in this manner operates naturally in the fundamental spatial mode without intracavity apertures.

By way of illustrating the concept, we will consider the configuration illustrated in Fig. 3.33, which was originally proposed by Sipes [3.17]. The output from a diode array with 200 mW output at 808 nm is collimated and focused into a 1 cm long \times 0.5 cm diameter 1% Nd:YAG sample. The resonator configuration is plano-concave, with the pumped end of the Nd:YAG rod being coated for high reflection at 1.06 μm, and with an output coupler having a 5 cm radius of curvature and a reflectivity at 1.06 μm of 95%. The output from the laser was 80 mW.

In these early systems the radiation from the diode laser pump was collimated and focused into the laser crystal by means of simple spherical or cylindrical macro

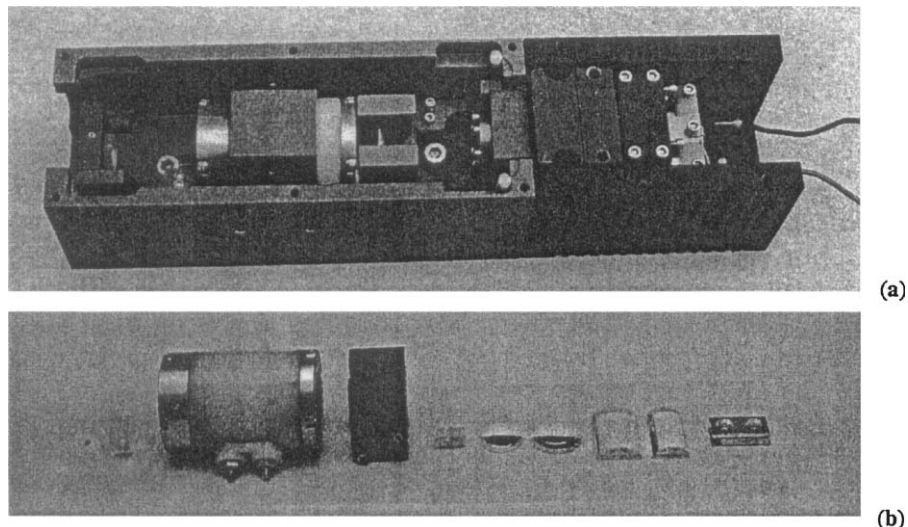


Fig. 3.34. Photograph of (a) assembled end-pumped laser and (b) disassembled optical components [Fibertek, Inc.]

lenses. Figure 3.34 displays a photograph of one of the very early end-pumped lasers.

The optical components shown separately are the laser diode array, two cylindrical and two spherical lenses, an Nd:YAG crystal, polarizer, Q-switch, and output coupler. The end mirror of the resonator is coated onto the laser crystal. The diode array comprises of three quasi-cw 1-cm bars. The three-bar stack had a maximum output energy of 27 mJ in a 200 μ s pulse. At that pulse energy, the laser output was 6.7 mJ in the TEM₀₀ mode and 8.4 mJ in multimode. The optical design of this laser is depicted in Fig. 6.90.

In modern end-pumped laser systems the radiation from diode bars is collimated by means of micro lens arrays, micro mirrors or fiberoptic bundles. Delivery of the pump radiation to the laser crystal is in most cases via an optical fiber. These technologies have dramatically increased the brightness that can be obtained from diode laser bars. (see Chap. 6). Current state-of-the-art high brightness pumps can maintain a well-collimated, circularized pump area over a distance long enough for complete beam absorption and excellent beam overlap.

The improvements in the brightness of pump beams have led to the development of powerful end-pumped lasers. High conversion efficiency and good beam quality are the characteristics of end-pumped lasers and many excellent systems are commercially available.

An example is the Nd:YVO₄ laser depicted in Fig. 3.35 that generates 35 W of output in a TEM₀₀ mode [3.18]. The two Nd:YVO₄ crystals are pumped by four diode bars with an output of 18 W each. The output from each bar is collected into a fiber bundles of 1.1 mm diameter. The outputs from the fibers are imaged through

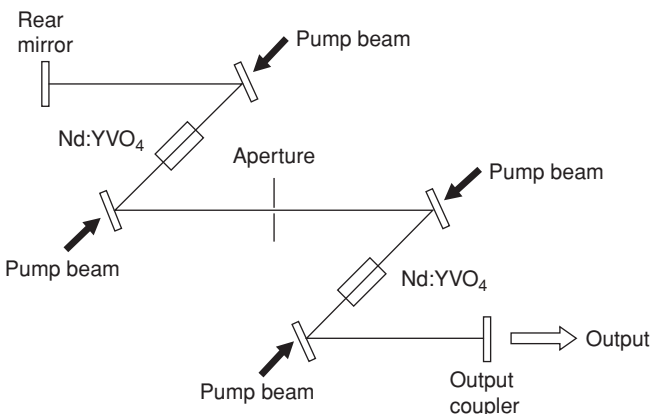


Fig. 3.35. Optical schematic of an Nd:YVO₄ laser end-pumped with four fiber-coupled diode bars [3.18]

dichroic folding mirrors into opposing faces of the two laser crystals. The 50-cm-long resonator consists of two Z-type resonators connected in series. From the 72 W output from the diode bars 54 W of pump power was incident on the two crystals to generate 35 W output. The laser output as a function of optical pump power incident on the crystal is plotted in Fig. 3.36 Total electrical input to the diode bars was 180 W. Table 3.3 summarizes the efficiencies in the transfer of energy from electrical input to laser output.

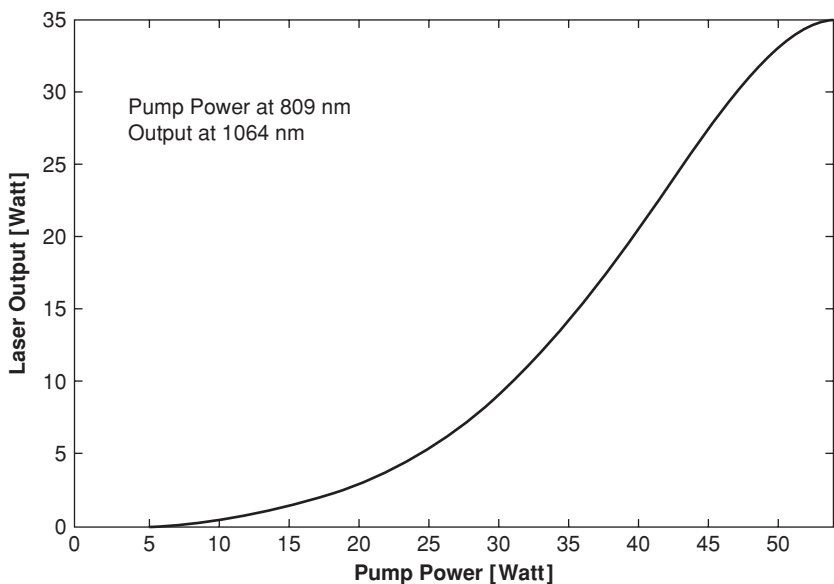


Fig. 3.36. Laser output as a function of pump power incident on the two Nd:YVO₄ crystals shown in the previous figure [3.18]

Table 3.3. Energy transfer efficiencies of the end-pumped laser depicted in Fig. 3.35

Diode laser efficiency	(η_D)	0.40
Transfer efficiency	(η_T)	0.75
Absorption efficiency	(η_A)	1.0
Stokes factor	(η_S)	0.76
Quantum efficiency	(η_Q)	0.94
Beam overlap and coupling efficiency	$(\eta_B \eta_C)$	0.90
System efficiency	(η_{SYST})	0.19

Laser diode end-pumped cw operation has been extended to a number of laser materials. Figure 3.37 compares the output from Nd:BeL, Nd:YAG, and Nd:YVO₄ [3.19]. The spectral differences of the materials studied have a considerable impact on laser threshold and slope efficiency. The comparative power curves of Fig. 3.37 were compiled on the basis of the optimized value of output coupler and diode pump wavelength for each crystal. Nd:YVO₄ clearly exhibits the lowest threshold despite its larger optical losses and short fluorescence lifetime (95 μs).

In recent years, end-pumped lasers have been constructed with many different Nd-doped laser materials, as well as Ho-, Tm-, Yb-, and Cr-doped crystals. Information regarding the latest developments can be found in the proceedings and technical digests of the various annual laser conferences. The performance of various

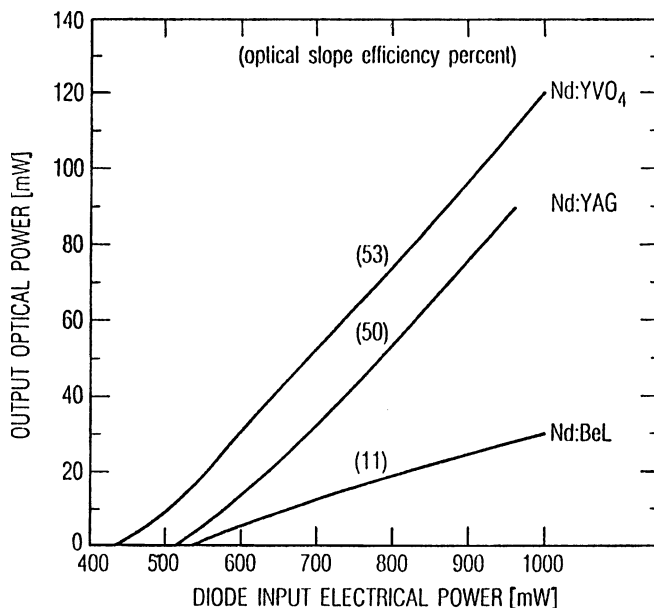


Fig. 3.37. Laser output as a function of pump laser diode electrical input. Optical slope efficiency percents are in parentheses. (YAG and YVO₄ at 97% and BeL at 99% output couplers) [3.19]

diode-pumped Nd lasers has been summarized in [3.20]. The following examples demonstrate the large range of pulse shapes and wavelengths, which can be generated with end-pumped solid-state lasers. Picosecond pulses have been generated in Nd:YAG [3.21] and Nd:YLF [3.22], and femtosecond pulses in Cr:LiSAF [3.23, 24]. End-pumped Nd:YAG lasers frequency doubled to 0.532 μm [3.25], Yb:YAG at 1.03 μm [3.26], and Tm:YAG at 2.0 μm [3.27] oscillators have all generated output powers in excess of 100 W.

In the diode-pumped lasers discussed so far, the active element is a thin slab or rod a few millimeters long. An extreme case of an end-pumped laser is the fiber laser made possible by the development of low loss rare earth fibers. Owing to the small cross section and long length of the active core, efficient operation with good beam quality can be achieved.

3.7 Ring Laser

In the oscillators that we have discussed so far, two counterpropagating traveling waves produce a standing wave in the resonator.

In an oscillator consisting of a ring-like resonator utilizing three or four mirrors and a nonreciprocal optical gate, a traveling wave can be generated. The optical gate provides a high loss for one of the two countercirculating traveling waves. The wave with the high loss is suppressed, and a unidirectional output from the laser is obtained. A typical laser cavity configuration of a traveling-wave oscillator is shown in Fig. 3.38. The system consists of a four-mirror rectangular resonator, a Brewster-extended laser rod, a $\lambda/2$ plate, and a Faraday rotator. Three mirrors are coated for maximum reflectivity at the laser wavelength and the fourth mirror is partially transparent. The unidirectional optical gate is formed by a half-wave plate and a Faraday rotator, consisting of a glass rod located within a solenoid-generated axial magnetic field.

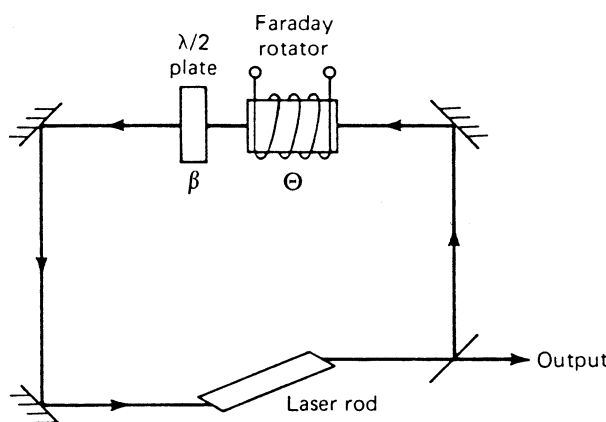


Fig. 3.38. Optical schematic of a traveling-wave oscillator [3.28]

The Faraday element, which should possess a high Verdet constant, rotates the plane of polarization (defined by the Brewster-ended rod) of the two circulating beams by a small angle $\pm\Theta$, the sign being dependent on the propagation direction and polarity of the magnetic field. The half-wave plate is orientated with one of its axes at an angle $\beta/2$ with respect to the polarization of the beams. The magnetic field is adjusted such that for the wave traveling in the clockwise direction, the half-wave plate rotates the plane of polarization by an angle β and the Faraday cell by an angle $+\Theta$ so that the total rotation is $\beta + \Theta$. The differential loss $\Delta\alpha$ between the counterrotating waves is then

$$\Delta\alpha = \sin^2(\beta + \Theta) - \sin^2(\beta - \Theta) \quad (3.93)$$

A typical Faraday rotator consists of a permanent magnet and a glass with a high Verdet constant. For maximum power output, the half-wave plate and the intensity of the magnetic field on the Faraday rotator are adjusted so that $\beta = \Theta$. Then the entire loss, proportional to $4\Theta^2$, is experienced only in the clockwise direction, leaving the wave in the counterclockwise direction unattenuated. As a result the laser will oscillate in a unidirectional wave.

Instead of the rectangular four-mirror cavity, a three-mirror cavity can be employed equally well. Also, the Brewster-ended rod can be replaced with a polarizer and a flat-ended rod. In some designs, rather than using a Faraday rotator, the traveling mode is produced by means of an asymmetric resonator [3.29]. Traveling-wave oscillators have generated interest mainly as a way to eliminate “spatial hole burning” (Sect. 5.2) caused by the standing-wave distribution of the intensity in a conventional oscillator. Since traveling-wave oscillators of the type depicted in Fig. 3.38 are more complicated to construct and require more optical components compared to standing-wave oscillators, these systems have not found any real applications in the past.

However, the interest in traveling-wave lasers has dramatically increased with the emergence of laser diodes as practical pumps for Nd:YAG lasers. The compact designs made possible with end-pumped diode-laser geometries have resulted in monolithic ring lasers where the functions of the elements shown in Fig. 3.38 are performed by a single Nd:YAG crystal. Unidirectional ring lasers contain three essential elements: a polarizer, a half-wave plate, and a Faraday rotator. The polarizer, half-wave plate equivalent, and the Faraday rotator are all embodied in the nonplanar ring Nd:YAG laser first proposed by Kane and Byer [3.30], and illustrated in Fig. 3.39. With a magnetic field H present in the direction shown, the YAG crystal itself acts as the Faraday rotator, the out-of-plane total internal reflection bounces (labeled A and C) act as the half-wave plate, and the output coupler (mirror D) acts as a partial polarizer. Polarization selection results from nonnormal incidence at the dielectrically coated output mirror.

The basic idea of a monolithic, diode-pumped unidirectional ring laser is to provide the equivalent of a discrete element design of a half-wave plate with a fast axis rotation angle which is half of the Faraday rotation angle. Since the Faraday rotation is small, the equivalent wave-plate rotation angle is also made small. The design of

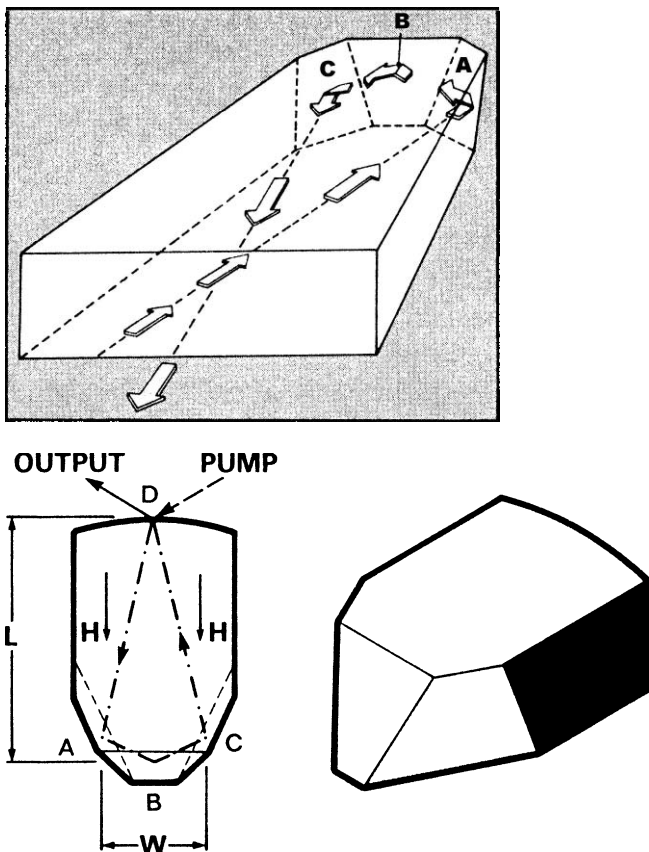


Fig. 3.39. Design of a monolithic ring Nd:YAG laser [3.30]

nonplanar ring oscillators incorporating the above concepts has matured considerably over the past years. A number of modified versions of the original monolithic ring laser have also been reported [3.31–34]. Compactness, single-mode operation combined with excellent frequency and amplitude stability due to the monolithic structure are the main practical advantages of this design.

Ring laser resonators have been extensively studied and developed primarily for single-frequency operation and mode-locked systems.

As we will discuss in Sect. 5.2.3, these devices are important as seed lasers for injection-seeded Nd:YAG oscillators.

The architecture of the monolithic ring laser precludes the use of intracavity elements such as those required for efficient second harmonic generation, Q-switching, or tuning of the single-frequency output. For these cases, a laser-diode pumped ring laser composed of discrete elements can be constructed [3.35, 36]. An intracavity frequency doubled Nd:YVO₄ ring laser which produced 8.5 W of output at 532 nm is described in [3.37].

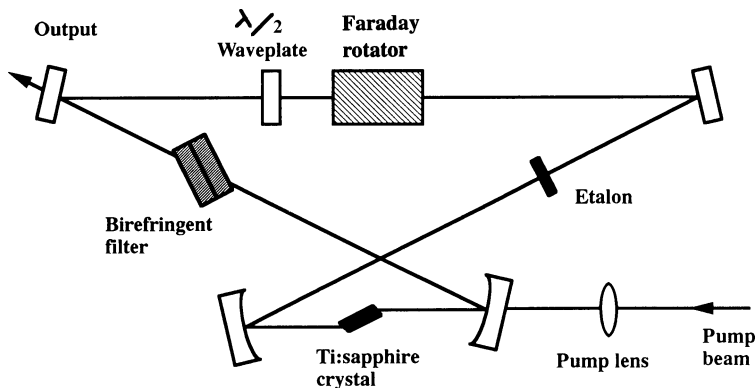


Fig. 3.40. The ring configuration for a cw Ti:sapphire laser cavity (courtesy of Schwartz Electro-Optics)

Figure 3.40 depicts a ring-configuration resonator for a cw Ti:Sapphire laser. The pump beam generated by an argon laser provides end-pumping of the Ti:Sapphire crystal. The Faraday rotator and $\lambda/2$ -waveplate combination assure unidirectional operation. A birefringent filter and an etalon, the remaining resonator components, are for wavelength selection and linewidth narrowing, respectively.

4. Laser Amplifier

The power or energy from an oscillator with specific spatial, temporal, or spectral properties can be increased by adding one or more amplifying stages to the laser system. The main function of the amplifier is to increase the brightness of the beam. Amplification of pulsed or cw power from an oscillator can be achieved using one of several techniques, including a master-oscillator power amplifier (MOPA) concept, a regenerative amplifier, a seeded or injection-locked power oscillator, and series connection of several gain modules within a common resonator.

The choice of the specific amplifier approach depends on the power level, spectral and temporal characteristics of the input signal, as well as the desired output energy or power. As will be discussed later in this chapter, for efficient energy extraction from a pulse amplifier, the energy density of the input signal must be close to the saturation density of the particular laser material. Therefore at very high energy levels, where the gain medium can be fully saturated, the MOPA architecture is normally used. This is the case, for example, in the amplification of Q-switch pulses from a laser oscillator.

If the power level from an oscillator is very low, many passes through an amplifier are required before a large fraction of the stored energy can be extracted. The low energy pulses from a mode-locked oscillator are typically amplified in a regenerative amplifier. The regenerative amplifier has a mirror at each end, like an oscillator, but is pumped below threshold. A pulse is coupled into the amplifier and makes many passes before being coupled out by an electro-optic Q-switch.

MOPA architectures also allow several passes through an individual amplifier, as will be explained in Sect. 4.1.3, but not as many as in a regenerative amplifier. In very powerful laser systems, such as those designed for inertial confinement fusion experiments, the different types of amplifiers are usually combined: A spectrally and temporally shaped pulse from an oscillator is first amplified in a regenerative amplifier, then makes several passes through a preamplifier stage before being further amplified in powerful single-pass amplifiers.

The injection seeded or locked oscillator can generate a powerful output in a narrow bandwidth. A low power pulse or cw signal from a spectrally narrow master oscillator is introduced into a powerful slave oscillator. The output power is determined by the slave oscillator, but the line width and frequency of the output matches the characteristics of the master oscillator. These types of systems are described in Chap. 5, since they are almost exclusively employed for the generation of narrow bandwidth radiation.

High power cw Nd:YAG lasers in the multihundred watt or kilowatt regime require several pump modules because of the size limitation of available crystals and issues

such as cooling and thermally induced stress and birefringence. The modules can all be operated inside a resonator forming a single oscillator, or they can be used in a MOPA configuration. In most cases it is more advantageous to employ the gain modules in series in a common resonator because this allows several passes of the radiation through each gain medium. However, at cw power levels of several kilowatts the MOPA configuration is sometimes preferred since the output coupling is so low with all the modules inside the resonator that the advantage of multiple passes no longer exists.

In the design of laser amplifiers the following aspects must be considered:

- Gain and energy extraction. When designing an amplifier, there is a trade-off between achieving high gain or high energy extraction.
- Feedback that may lead to parasitic oscillations.
- Potential surface or bulk damage. Excessive energy or power at the various optical elements of the amplifier, diffraction effects, or self-focusing can lead to optical damage.
- Wave front and pulse distortions introduced by the amplifier.

Gain and energy extraction in amplifiers employed in Q-switched or mode-locked systems is discussed in Sect. 4.1. Regenerative and cw amplifiers are treated in Sects. 4.2 and 4.3 respectively. Wave front or pulse-shaped distortions introduced by the amplifier stage are summarized in Sect. 4.4. In multiple-stage amplifier chains the stability of the system is of prime concern to the laser designer. Gain limitations and amplifier stability are discussed in Sect. 4.5. In high-power Q-switched or mode-locked amplifier systems, self-focusing leading to bulk damage is a phenomenon frequently observed. The issues of self-focusing are addressed in Sect. 4.6.

4.1 Single- and Multiple-Pass Pulse Amplifiers

The use of lasers as pulse amplifiers is of great interest in the design of high-energy, high-brightness radiation sources. In the pulse amplifiers described in this chapter the input Q-switched or mode-locked pulse is considerably shorter than the fluorescent lifetime of the active medium. Hence the effect of spontaneous emission and pumping rate on the population inversion during the amplification process can be neglected. Furthermore, energy is extracted from the amplifier, which was stored in the amplifying medium, prior to the arrival of the pulse.

The generation of high-energy pulses is based on the combination of a master oscillator and a power amplifier. For the purpose of illustrating the amplifier concept and principles we assume a straightforward system, as shown in Fig. 4.1. In this scheme an amplifier is driven by an oscillator which generates an initial laser pulse of moderate power and energy. In the power amplifier with a large volume of active material, stored energy is extracted during the passage of the oscillator pulse.

In an oscillator–amplifier system, pulse width, beam divergence, and spectral width are primarily determined by the oscillator, whereas pulse energy and power are

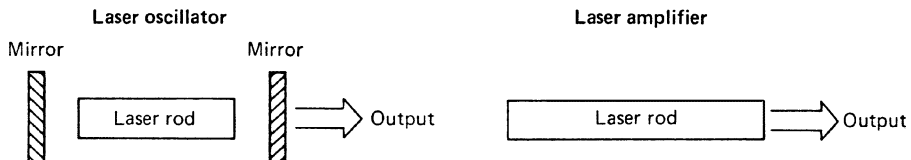


Fig. 4.1. Schematic diagram of a laser oscillator–amplifier configuration

determined by the amplifier. Operating an oscillator at relatively low-energy levels reduces beam divergence and spectral width. Therefore, from an oscillator–amplifier combination one can obtain either a higher energy than is achievable from an oscillator alone, or the same energy in a beam that has a smaller beam divergence and narrower linewidth. Generally speaking, the purpose of adding an amplifier to a laser oscillator is to increase the brightness B_r ($\text{W}/(\text{cm}^2 \text{ sr})$) of the output beam

$$B_r = \frac{P_{\text{out}}}{A\Omega}, \quad (4.1)$$

where P_{out} is the power of the output beam emitted from the area A and Ω is the solid-angle divergence of the beam. Multiple-stage amplifier systems can be built if higher amplifications are required.

4.1.1 Pulse Amplification

Of primary interest in the design of amplifiers is the gain, which can be achieved, and the energy, which can be extracted from the amplifier. The rod length in an amplifier is determined primarily by the desired gain, while the rod diameter, set by damage threshold considerations, is dependent on the output energy.

To a first approximation, we can assume the growth of input energy to be exponential, for the amount of stimulated emission is proportional to the exciting photon flux. It will be seen, however, that exponential amplification will occur only at low photon-flux levels. A deviation from the exponential gain regime in an amplifier occurs when an optical pulse traveling in the inverted medium becomes strong enough to change the population of the laser levels appreciably. The optical amplifier will exhibit saturation effects as a result of depletion of the inversion density by the driving signal. Taking an extreme case, we can see that if a high-intensity light pulse is incident on an amplifier, the stimulated emission can completely deplete the stored energy as it progresses. Then the gain can be expected to be linear with the length of the active medium rather than exponential.

The events during the amplifier action are assumed to be fast compared with the pumping rate W_p and the spontaneous emission time τ_f . Therefore $t_p \ll \tau_f$, W_p^{-1} , t_p being the width of the pulse which passes through the amplifying medium. Thus the amplification process is based on the energy stored in the upper laser level prior to the arrival of the input signal. As the input pulse passes through the amplifier, the ions are stimulated to release the stored energy. The amplification process can be described by the rate equations (1.58) and (1.61). If we ignore the effect of fluorescence and

pumping during the pulse duration, we obtain for the population inversion

$$\frac{\partial n}{\partial t} = -\gamma n c \sigma \phi. \quad (4.2)$$

The growth of a pulse traversing a medium with an inverted population is described by the nonlinear, time-dependent photon-transport equation, which accounts for the effect of the radiation on the active medium and vice versa,

$$\frac{\partial \phi}{\partial t} = cn\sigma\phi - \frac{\partial \phi}{\partial x} c. \quad (4.3)$$

The rate at which the photon density changes in a small volume of material is equal to the net difference between the generation of photons by the stimulated emission process and the flux of photons which flows out from that region. The latter process is described by the second term on the right of (4.3). This term that characterizes a traveling-wave process is absent in (1.61).

Consider the one-dimensional case of a beam of monochromatic radiation incident on the front surface of an amplifier rod of length l . The point at which the beam enters the gain medium is designated the reference point, $x = 0$. The two differential equations (4.2) and (4.3) must be solved for the inverted electron population n and the photon flux ϕ . Frantz and Nodvik [4.1] solved these nonlinear equations for various types of input pulse shapes.

If we take, for the input to the amplifier, a square pulse of duration t_p and initial photon density ϕ_0 , the solution for the photon density is

$$\frac{\phi(x, t)}{\phi_0} = \left\{ 1 - [1 - \exp(-\sigma nx)] \exp\left[-\gamma\sigma\phi_0c\left(t - \frac{x}{c}\right)\right] \right\}^{-1}, \quad (4.4)$$

where n is the inverted population density, assumed to be uniform throughout the laser material at $t = 0$. The energy gain for a light beam passing through a laser amplifier of length $x = l$ is given by

$$G = \frac{1}{\phi_0 t_p} \int_{-\infty}^{+\infty} \phi(l, t) dt. \quad (4.5)$$

After introducing (4.4) into (4.5) and integrating, we obtain

$$G = \frac{1}{c\gamma\sigma\phi_0 t_p} \ln\{1 + [\exp(\gamma\sigma\phi_0 t_p c) - 1] e^{n\sigma l}\}. \quad (4.6)$$

We shall cast this equation in a different form such that it contains directly measurable laser parameters. The input energy per unit area can be expressed as

$$E_{\text{in}} = c\phi_0 t_p h\nu. \quad (4.7)$$

A saturation fluence E_s can be defined by

$$E_s = \frac{h\nu}{\gamma\sigma} = \frac{J_{\text{st}}}{\gamma g_0}, \quad (4.8)$$

where $J_{st} = h\nu n$ is the stored energy per volume and $g_0 = n\sigma$ is the small-signal gain coefficient.

In a four-level system, $\gamma = 1$ and the total stored energy per unit volume in the amplifier is

$$J_{st} = g_0 E_s. \quad (4.9)$$

The extraction efficiency η_E is the energy extracted from the amplifier divided by the stored energy in the upper-laser level at the time of pulse arrival. With this definition, we can write

$$\eta_E = \frac{E_{out} - E_{in}}{g_0 l E_s}. \quad (4.10)$$

In this expression, E_{out} and E_{in} are the amplifier signal output and input fluence, respectively. In a four-level system, all the stored energy can theoretically be extracted by a signal. In a three-level system, $\gamma = 1 + g_2/g_1$ and only a fraction of the stored energy will be released because as the upper laser level is depleted, the lower-level density is building up.

Introducing (4.7) and (4.8) into (4.6), one obtains

$$G = \frac{E_s}{E_{in}} \ln \left\{ 1 + \left[\exp \left(\frac{E_{in}}{E_s} \right) - 1 \right] G_0 \right\}. \quad (4.11)$$

This expression represents a unique relationship between the gain G , the input pulse energy density E_{in} , the saturation parameter E_s , and the small-signal, single-pass gain $G_0 = \exp(g_0 l)$.

Equation (4.11), which is valid for rectangular input pulses, encompasses the regime from small-signal gain to complete saturation of the amplifier. The equation can be simplified for these extreme cases. Consider a low-input signal E_{in} such that $E_{in}/E_s \ll 1$ and furthermore $G_0 E_{in}/E_s \ll 1$, then (4.11) can be approximated to

$$G \approx G_0 \equiv \exp(g_0 l). \quad (4.12)$$

In this case, the “low-level gain” is exponential with amplifier length and no saturation effects occur. This, of course, holds only for rod lengths up to a value where the output energy density $G_0 E_{in}$ is small compared to E_s .

For high-level energy densities such that $E_{in}/E_s \gg 1$, (4.11) becomes

$$G \simeq 1 + \left(\frac{E_s}{E_{in}} \right) g_0 l. \quad (4.13)$$

Thus, the energy gain is linear with the length of the gain medium, implying that every excited state contributes its stimulated emission to the beam. Such a condition obviously represents the most efficient conversion of stored energy to beam energy, and for this reason amplifier designs that operate in saturation are used wherever practical, with the major limitation being the laser damage threshold.

We will now recast (4.11) into a form that makes it convenient to model the energy output and extraction efficiency for single- and multiple-amplifier stages operated either in a single- or double-pass configuration. With the notation indicated in

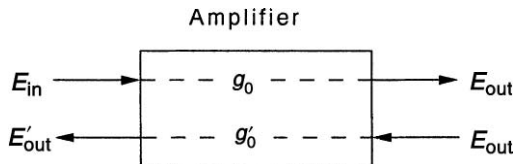


Fig. 4.2. Notation for the calculation of energy output fluence and extraction efficiency for one- and two-pass single or multiple amplifier stages

Fig. 4.2, E_{in} is now the input to the amplifier and E_{out} is the output fluence, and are related by

$$E_{out} = E_s \ln \left\{ 1 + \left[\exp \left(\frac{E_{in}}{E_s} \right) - 1 \right] \exp(g_0 l) \right\}. \quad (4.14)$$

The extraction efficiency is, according to (4.10),

$$\eta_E = (E_{out} - E_{in})/g_0 l E_s. \quad (4.15)$$

In a laser system which has multiple stages, these equations can be applied successively, whereby the output of one stage becomes the input for the next stage.

As already mentioned, efficient energy extraction from an amplifier requires that the input-fluence is comparable to the saturation-fluence of the laser transition. For this reason, amplifiers are often operated in a double-pass configuration; a mirror at the output returns the radiation a second time through the amplifier. A $\lambda/4$ waveplate is usually inserted between the amplifier and the mirror; this causes a 90° rotation of the polarization of the return beam. A polarizer in front of the amplifier separates the input from the output signal. In some situations, as shall be discussed in Sect. 10.4, the simple reflective mirror may be replaced by a phase conjugate mirror, in which case optical distortions in the amplifier chain will be reduced.

The output fluence E'_{out} from a two-pass amplifier can be calculated as follows:

$$E'_{out} = E_s \ln \left\{ 1 + \left[\exp(E_{out}/E_s) - 1 \right] \exp(g'_0 l) \right\}. \quad (4.16)$$

The input for the return pass is now E_{out} , which is obtained from (4.14) as the output of the first pass. The gain for the return pass is now lower because energy has been extracted from the gain medium on the first pass

$$g'_0 = (1 - \eta_E) g_0. \quad (4.17)$$

The extraction efficiency of the double-pass amplifier is

$$\eta'_E = (E'_{out} - E_{in})/g_0 l E_s. \quad (4.18)$$

The extraction efficiency calculated from (4.14)–(4.18) for one- and two-pass amplifiers, for different values of $g_0 l$ and normalized input fluences, are plotted in Fig. 4.3. The results show the increase in extraction efficiency with higher input energies, and the considerable improvement one can achieve with double-pass amplifiers. Equations (4.14)–(4.18) can be readily applied to multistage systems by writing a simple computer program which sequentially applies these equations to the different

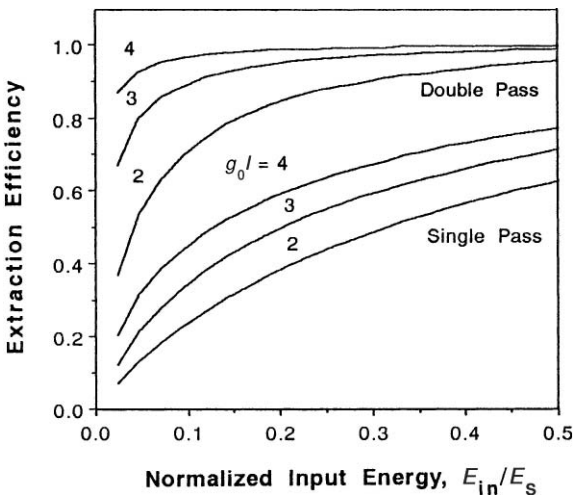


Fig. 4.3. Extraction efficiency for a one- and two-pass amplifier as a function of input intensity E_{in} and small signal logarithmic gain $g_0 l$. Input is normalized to saturation fluence E_s

amplifier stages. In Sect. 4.2, we will illustrate the results of such a modeling effort for a four-stage double pass amplifier chain.

It should be noted that the above equations assume a uniform gain coefficient and beam intensity profile. In most systems, both quantities will have a radially dependent profile. In this case, an effective gain coefficient can be calculated according to

$$g_{\text{eff}} = \frac{\int g_0(r) I_B(r) 2\pi r dr}{\int I_B(r) 2\pi r dr}, \quad (4.19)$$

where $g_0(r)$ is the radial gain distribution and $I_B(r)$ is the radial intensity profile of the beam.

Equation (4.11) permits one to calculate the gain of an amplifier as a function of the input energy density, provided that the small-signal gain or the energy stored in the amplifier is known.

In the design stage of an amplifier, these parameters have to be calculated based on the input energy, the volume of the active material, and the efficiency of the pump process. On an existing amplifier, the gain or stored energy can be determined by passing a small probe beam through the device or by operating the amplifier as an oscillator.

One of the significant points of (4.11) for the design of laser amplifiers lies in the fact that if one data point of an existing amplifier is known, the performance of the amplifier under different operating conditions can be calculated. Also, the effect on the performance of changes in design, such as amplifier length or diameter or the use of multiple stages in a system, can be studied with the aid of this equation. Before we discuss practical examples, it should be noted that in deriving (4.11) two assumptions

were made:

- 1) It was assumed that the pulse shape of the incident pulse was rectangular. However, it should be mentioned that despite this assumption, the above analysis holds, to a good approximation, for a symmetrical triangular-shaped pulse. This approximation becomes less valid in cases where amplified pulse shapes differ significantly from incident pulse shapes as a result of the higher gain experienced by the leading edge of the pulse. In such cases, more accurate gain equations, given in [4.2], should be used.
- 2) We have assumed a lossless amplifier. In real solid-state laser amplifiers there inevitably exist linear losses of radiation as a result of absorption and scattering caused by defects and impurities in the active medium. A linear loss limits the energy growth in the saturation regime. There the energy tends to grow linearly as a result of the amplification and to decrease exponentially as a result of loss.

Avizonis and Grotbeck [4.3] have derived an expression which describes the gain process in an amplifier without approximation. They obtained

$$\frac{dE(x)}{dx} = E_s g_0 \left[1 - \exp\left(\frac{-E(x)}{E_s}\right) \right] - \alpha E(x), \quad (4.20)$$

where $E(x)$ is the pulse energy at point x , α is the loss coefficient per unit length, and x is the amplifier length coordinate.

Equation (4.20) can be solved analytically only if a zero loss is assumed ($\alpha = 0$). In this case the result is identical to (4.11). From (4.20) follows that, in the presence of losses, gain in the saturating regime occurs only for pulse energies below a limiting value E_{\max} . For $\alpha \ll g_0$ this limiting value is

$$E_{\max} = \frac{g_0 E_s}{\alpha}. \quad (4.21)$$

Most laser materials such as Nd:glass and Nd:YAG have sufficiently small losses that they can be neglected in most cases in the design of amplifiers.

4.1.2 Nd:YAG Amplifiers

Amplified spontaneous emission (ASE) and parasitic oscillations due to the high gain of Nd:YAG effectively limit the energy storage density and therefore the useful energy which can be extracted from a given crystal. The small signal gain coefficient g_0 as a function of the stored energy density is $g_0 = J_{\text{st}}/E_s$ according to (4.9). Therefore, the small signal, single pass gain of an amplifier is given by

$$G_0 = \exp(J_{\text{st}}l/E_s). \quad (4.22)$$

With $\sigma = 2.8 \times 10^{-19} \text{ cm}^2$ for Nd:YAG we obtain for the saturation fluence a value of $E_s = 0.66 \text{ J/cm}^2$ from (4.8). If we want to extract 500 mJ from an Nd:YAG rod, 5 mm in diameter and 7.5 cm long, the minimum stored energy density has to be $J_{\text{st}} = 0.34 \text{ J/cm}^3$. The small signal single-pass gain in the rod will be $G_0 = 46$. Any small reflection at the output of the amplifier will cause spontaneous emission to

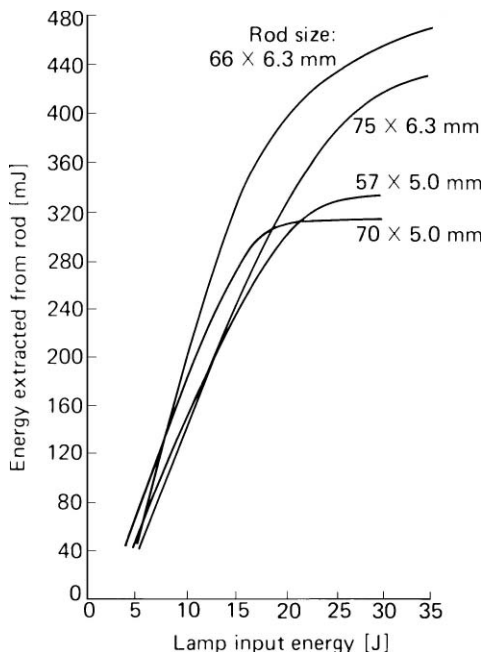


Fig. 4.4. Energy extraction from Nd:YAG amplifiers with different rod sizes [4.4]

travel through the gain medium a second time with a round trip gain of 2100. It is very difficult to keep an amplifier from prelasing with such a high gain. A Nd:glass amplifier with the same output and having the same dimensions would have a gain of only $G_0 = 1.5$.

Gain in laser materials is limited by the onset of parasitic oscillations which clamp the population inversion. In Nd:YAG, for example, a single-pass gain in excess of 30 is difficult to achieve. Parasitic oscillations, which will be discussed in more detail in Sect. 4.5, lead to a leveling off of the output energy versus the pump input energy curve in an Nd:YAG amplifier. Figure 4.4 shows plots of energy extracted from an Nd:YAG amplifier versus lamp input energy. As can be seen from these curves, the maximum energy which can be extracted from the different rods reaches a saturation level.

The data show that a long rod will provide a long path and therefore high gain for the spontaneous emission to build up, whereas in a relatively short rod of large diameter more total energy can be stored for the same total gain. Increasing the temperature of an Nd:YAG rod will reduce its gain and therefore more energy can be stored. For example, the extracted energy from an amplifier was increased from 770 to 926 mJ/cm² by raising the temperature from 26 to 96°C.

The relative performances of a laser rod when used as a normal-mode oscillator, as a Q-switched oscillator, and as a single-pass amplifier are displayed in Fig. 4.5. A 0.63 by 6.6 cm Nd:YAG laser rod in a silver-plated, single-ellipse, single-lamp pump cavity was used in all modes of operation. Normal-mode performance was achieved with two plane-parallel dielectric-coated mirrors. The pump pulse had a duration of approximately 100 μs at the half-power points. The Q-switched performance was

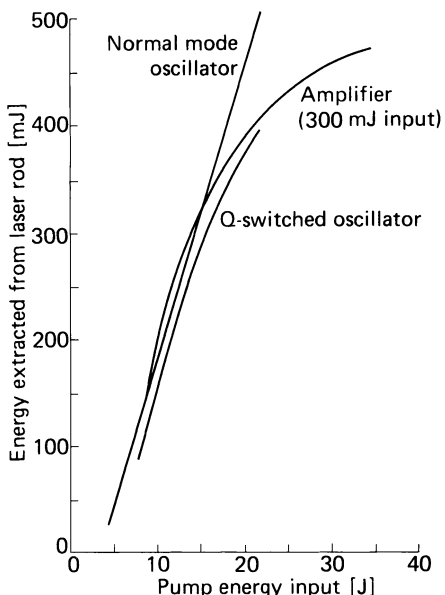


Fig. 4.5. Energy extraction from Nd:YAG operated as a normal mode and Q-switched oscillator, and amplifier of Q-switched pulses [4.4]

obtained with a rotating prism switch. The single-pass amplifier performance represents the energy extracted from the rod with a 300-mJ input from an oscillator. These data show that all modes of operation are approximately equivalent until the 320 mJ output level is reached. Above this level depopulation losses decrease the extractable energy.

If the Nd:YAG crystal is pumped with an input of 14 J, a total of 300 mJ can be extracted from the amplifier (top curve in Fig. 4.4). Since the signal input is 300 mJ, the amplifier has a saturated gain of $G = 2$ and a total output of 600 mJ. In order to extract 300 mJ from this rod, at least 0.15 J/cm^3 must be stored in the upper level. This corresponds to a small signal-pass gain of $G_0 = 4.4$ according to (4.22) or a small-signal gain coefficient of $g_0 = 0.23 \text{ cm}^{-1}$. The actually stored energy in the amplifier is higher than the extracted energy because of fluorescence losses and incomplete extraction of the energy by the input pulse. The efficiency of the energy extraction of an amplifier can be calculated from (4.10). If instead of the actual input pulse a low signal probe beam is passed through the amplifier, the small signal gain coefficient g_0 can be measured. With g_0 determined, all parameters in (4.10) are known and the extraction efficiency can be calculated.

For the amplifier discussed above the extraction efficiency as a function of input fluence is shown in Fig. 4.6. The change from an exponential (small signal) to a linear relationship (saturated gain) of input to output occurs for an input fluence of around 0.2 J/cm^2 . Extracton efficiency is maximized for $E_{\text{in}} > E_s$ which implies an input fluence of 1 J/cm^2 or higher for Nd:YAG.

In our next example, we will describe a modern, multistage Nd:YAG master-oscillator power-amplifier (MOPA) design, as depicted in Fig. 4.7. The laser produces an output in the TEM₀₀ mode of 750 mJ at 1.064 μm at a repetition rate of

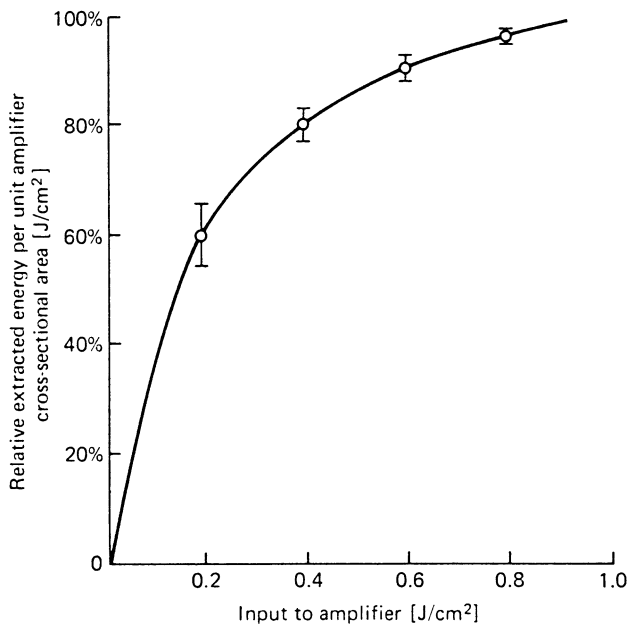


Fig. 4.6. Amplifier energy extraction as a function of oscillator energy density [4.4]

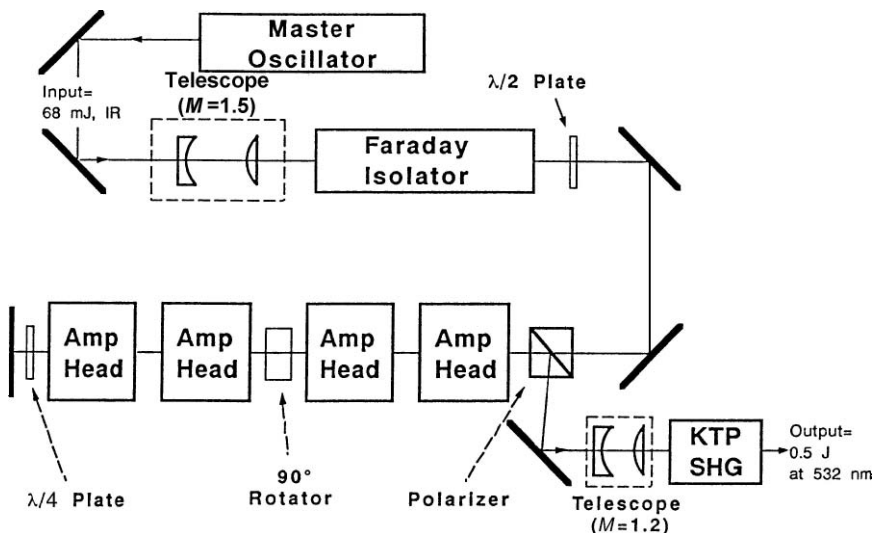


Fig. 4.7. Optical schematic of a high-power multistage Nd:YAG laser [4.5]

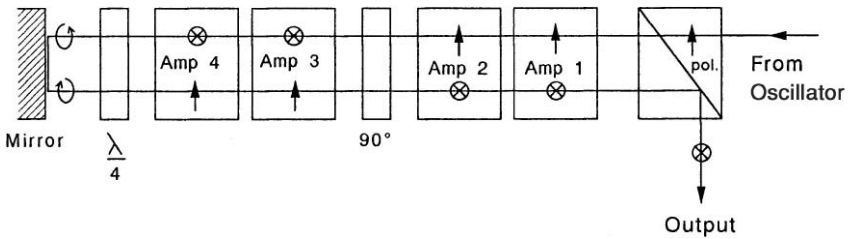


Fig. 4.8. Two-pass amplifier chain with polarization output coupling and birefringence compensation

40 Hz. A harmonic generator converts this output to 532 nm with 65% conversion efficiency.

The system features an oscillator and four amplifiers in a double-pass configuration. The linearly polarized output from the oscillator is expanded by a telescope to match the amplifier rods. A Faraday rotator and a $\lambda/2$ wave plate act as a one-way valve for the radiation, thereby isolating the oscillator from laser radiation and amplified spontaneous emission reflected back by the amplifier chain. The output from the oscillator passes through the four amplifiers and, after reflection by a mirror, the radiation passes through the amplifiers a second time. A quarter-wave plate introduces a 90° rotation of the polarized beam after reflection by the rear mirror; this allows the radiation to be coupled out by the polarizer located at the input of the amplifier chain. After a slight expansion, the output beam is passed through a KTP crystal for second-harmonic generation. Located between the two pairs of amplifiers is a 90° rotator which serves the purpose of minimizing thermally induced birefringence losses, as will be explained in Sect. 7.1.1. The changes in the polarization of the beam as it travels back and forth through the amplifier chain is illustrated in Fig. 4.8.

Each amplifier contains 16 linear diode arrays for side pumping of the Nd:YAG crystal. The optical pump energy for each amplifier is 900 mJ at 808 nm, or 4.5 kW at the pump pulse width of 200 μs . In each amplifier, the arrays are arranged in an eightfold symmetrical pattern around the 6.3 mm diameter and 6.5 cm long laser rod in order to produce a uniform excitation. The active length of the rod pumped by the arrays is 4 cm. The small-signal, single-pass gain of one amplifier as a function of pump energy is plotted in Fig. 4.9.

For low input signals, the gain increases exponentially with $g_0 l$ according to (4.12). The logarithmic gain $g_0 l$ is proportional to the pump energy, as derived in (3.61),

$$g_0 l = \eta' E_p, \quad (4.23)$$

where E_p is the optical pump energy from the diode arrays. The η terms for an amplifier operated in the energy storage mode are

$$\eta' = \eta_t \eta_a \eta_s \eta_Q \eta_B \eta_{Si} \eta_{ASE} / A E_S. \quad (4.24)$$

For this particular amplifier design, the numerical values are $\eta_t = 0.88$ for the transfer efficiency, $\eta_a = 0.85$ for the absorption of pump radiation in the 7.6 mm

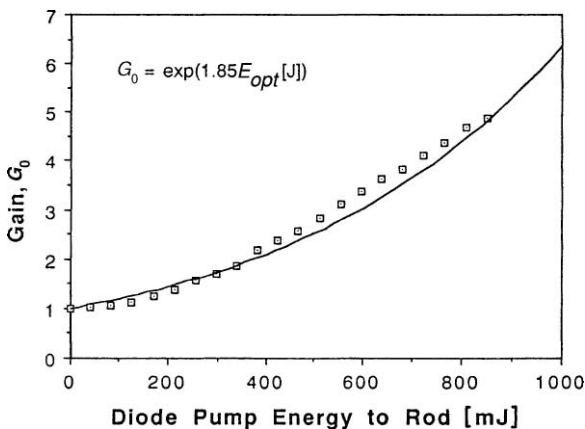


Fig. 4.9. Small signal, single-pass gain as a function of optical pump energy

diameter Nd:YAG crystal, $\eta_S = 0.76$ and $\eta_Q = 0.90$ for the Stokes shift and quantum efficiency, $\eta_B = 0.62$ for the overlap between the beam and gain region of the rod, and $\eta_{ASE} = 0.90$ and $\eta_{St} = 0.68$ for the storage efficiency. The latter is calculated from (3.53) for a pump pulse length of $t_p = 200 \mu\text{s}$ and a fluorescence lifetime of $\tau_f = 230 \mu\text{s}$ for Nd:YAG. With $A = 0.19 \text{ cm}^2$ and $E_S = 0.66 \text{ J/cm}^2$, one obtains $\eta' = 1.85$. The curve in Fig. 4.9 is based on this value of η' , i.e.,

$$E_{\text{out}}/E_{\text{in}} = \exp[1.85E_{\text{opt}}(J)]. \quad (4.25)$$

The energy output as a function of the signal input of one amplifier stage single pass and two amplifiers in a double-pass configuration is plotted in Fig. 4.10. The

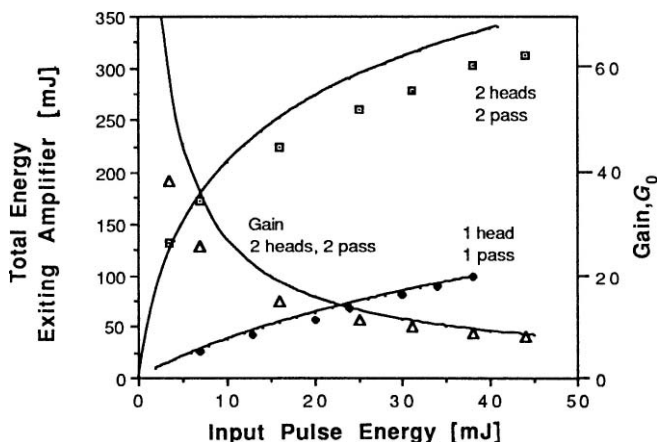


Fig. 4.10. Energy output as a function of signal input for a single-amplifier stage and a two-amplifier, double pass configuration. Also shown is the gain for the latter configuration

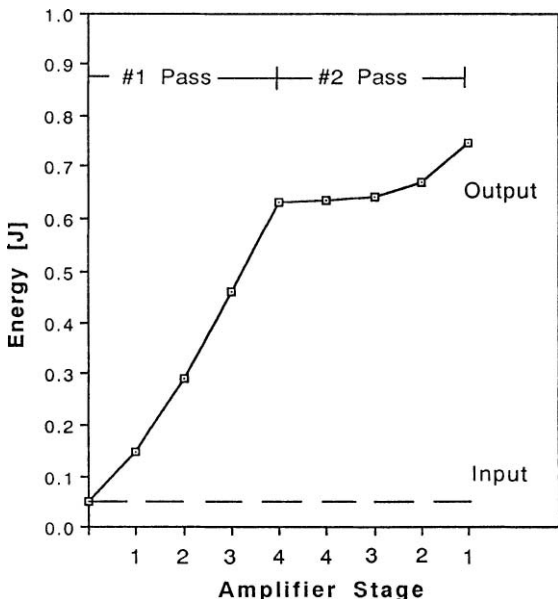


Fig. 4.11. Energy levels at successive stages in the amplifier chain. Points are measured values and curve is obtained from a computer model

amplifiers are operated at a fixed pump energy of 900 mJ each. Also plotted in this figure is the gain for the two-amplifier double-pass configuration. The amplifiers are highly saturated as can be seen from the nonlinear shape of the E_{out} versus E_{in} curve and the drop in gain at the higher input levels.

The increase in energy as the signal pulse travels forward and backward through the amplifier chain is plotted in Fig. 4.11. The figure shows the measured data points and a curve representing the values calculated from (4.14) to (4.18) with an input energy of 50 mJ, $A = 0.19 \text{ cm}^2$, $G_0 = 4.8$, and $E_s = 0.66 \text{ J/cm}^2$. Energy extraction from each stage for both passes is depicted in Fig. 4.12. The data indicate that the amplifiers are totally saturated and all the stored energy within the beam is extracted. As the input beam travels the first time through the amplifiers, successively more energy is extracted from each stage since the ratio of E_{in}/E_s increases. On the return pass, very little energy is removed from the last two stages because stored energy has already been depleted.

The logarithmic gain for the four stages having a 16-cm active length is $g_0 l = 6.0$. The double-pass configuration increases the extraction efficiency from 0.8 to 1.0. It should be noted that the small-signal gain obtained from Fig. 4.9 is measured over the cross-section of the beam. The gain and beam profile are both centrally peaked in this design and both have a Gaussian shape. In order to avoid diffraction effects, provide for adequate beam alignment tolerance, and accommodate a slightly expanding beam, the beam cross section at the $1/e^2$ intensity points is $A = 0.19 \text{ cm}^2$, whereas the rod cross section is 0.31 cm^2 .

Although the extraction is complete within the beam, stored energy is left at the outer regions of the rod. The beam fill factor takes into account this fact. Since both

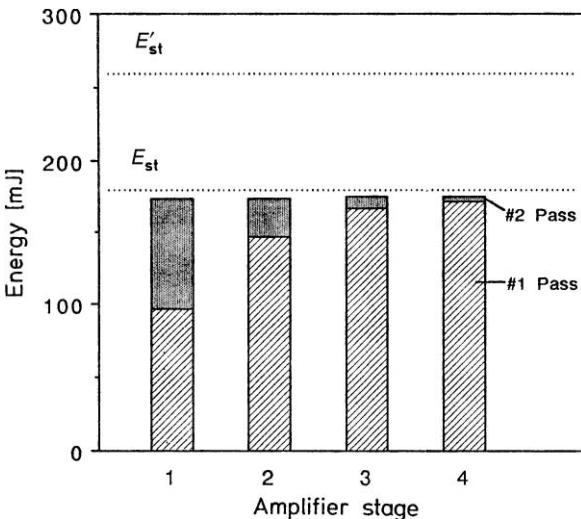


Fig. 4.12. Total energy extraction from each amplifier stage

gain and beam profiles are radially dependent, the beam fill factor cannot be calculated from the ratio of the areas, as would be the case with a uniform gain and beam profile. The beam overlap efficiency can be calculated provided the gain and beam profiles are known. These distributions were obtained from images taken with a CCD camera which recorded the profiles of the fluorescence and laser beam output. With the radial spot sizes of the Gaussian approximations given above, one obtains from (3.48) a value of $\eta_B = 0.62$ for the beam overlap efficiency.

According to (4.9) the total stored energy at the upper laser level is $E_{st} = g_0 l E_s A$. With $g_0 l = 1.55$, $E_s = 0.66 \text{ J/cm}^2$, and $A = 0.19 \text{ cm}^2$, one obtains $E_{st} = 170 \text{ mJ}$ of stored energy within the volume addressed by the beam. The stored energy in the full cross section of the rod is $E'_{st} = E_{st}/\eta_B = 260 \text{ mJ}$. The values for E_{st} and E'_{st} are indicated in Fig. 4.12.

The electrical system efficiency η_{sys} of the amplifier chain is the product of the laser diode efficiency η_p , the conversion efficiency of optical pump power to the upper laser level at the time of energy extraction, and the extraction efficiency of the stored energy into laser output, i.e.,

$$\eta_{sys} = \frac{E_{out} - E_{in}}{E_{EL}} = \eta_p \eta_l \eta_a \eta_s \eta_Q \eta_B \eta_E, \quad (4.26)$$

where

$$\eta_E = \eta_{St} \eta_{ASE} \eta_{EQ}. \quad (4.27)$$

Table 4.1 lists the individual efficiencies of the amplifier system.

Table 4.1. Energy conversion efficiency of the two-pass multistage Nd:YAG amplifier

Laser diode array electrical efficiency η_P	0.35
Conversion of optical pump energy to upper state energy	
transfer efficiency, $\eta_t = 0.88$	
absorption efficiency, $\eta_a = 0.85$	0.51
Stokes efficiency, $\eta_S = 0.75$	
quantum efficiency, $\eta_Q = 0.90$	
Conversion of upper state energy to laser output	
beam overlap efficiency, $\eta_B = 0.62$	
storage efficiency, $\eta_{St} = 0.68$	0.38
fractional loss, $\eta_{ASE} = 0.900$	
extraction efficiency, $\eta_{EQ} = 1.00$	
Amplifier efficiency, η_{sys}	0.068

4.1.3 Nd:Glass Amplifiers

An enormous database regarding the design of Nd:glass amplifiers exists since these systems have become the lasers of choice for inertial confinement fusion research. Motivated by requirements to drive inertial confinement fusion targets at ever higher powers and energies, very large Nd:glass laser systems have been designed, built, and operated at a number of laboratories throughout the world over the past 40 years.

During the 1960s and into the early 1970s, large glass laser systems consisted of pulsed oscillators followed by rod amplifiers. The introduction of face-pumped disk amplifiers relieved the inherent aperture constraint of rod amplifiers.

Initially the systems employed silicate glass as the host material for neodymium. The lower nonlinear refractive index and higher gain coefficient of phosphate glasses has provided a powerful incentive to build systems based upon these materials.

The architectural design of these master oscillator-pulse amplifier (MOPA) systems is based on an oscillator where a single pulse is produced and shaped, then amplified and multiplexed to feed a number of amplifier chains. The preamplifier stages consist of flashlamp-pumped Nd:glass rods, while at the higher power levels amplifier stages employ Nd:glass slabs pumped by flashlamps. The rectangular slabs are mounted at Brewster's angle to minimize Fresnel losses at the surfaces. The clear apertures of the power amplifiers increase stepwise down the chain to avoid optical damage as the beam energy grows. Located between the amplifier stages are spatial filters and Faraday isolators.

Spatial filters are important elements in a high-peak-power laser system and are required to serve three purposes: removal of small-scale spatial irregularities from the beam before they grow exponentially to significant power levels; reduction of the self-induced phase front distortion in the spatial envelope of the beam; and expansion of the beam to match the beam profile to amplifiers of different apertures. Laser oscillation in the chain is prevented by the appropriate placement along the chain of

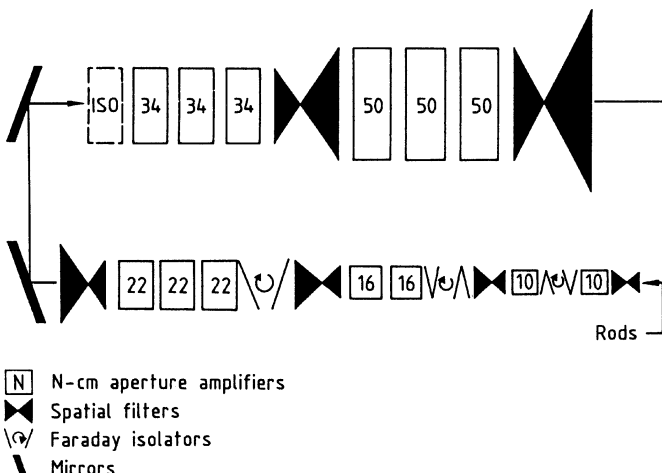


Fig. 4.13. Component layout of one beam line of the NOVA system (Lawrence Livermore National Laboratory)

Faraday rotators and polarizer plates. These devices prevent radiation from traveling upstream in the amplifier chain.

The system shown in Fig. 4.13. is an example of such a design. The figure shows one 10 kJ beam line of the NOVA glass laser system built at Lawrence Livermore Laboratory. The complete system has 10 such identical beam lines producing a total output energy in excess of 100 kJ in a 2.5 ns pulse [4.6]. The National Ignition Facility currently under development at Livermore National Laboratory will have 192 beamlines with about 10 kJ output from each aperture in a 3 ns pulse and at a wavelength after frequency tripling of 351 nm [4.7]. The oscillator generates a single pulse that seeds the entire NIF laser system. The preamplifiers provide the largest amount of amplification in the system >100 dB. Energy extraction takes place in the main amplifier chains which have apertures of 40 cm.

It is outside the scope of this book to address the complex issues surrounding the design, development, and operation of glass lasers employed in fusion target irradiation facilities. The reader interested in the design, modeling, and materials aspects of these lasers is referred to the extensive literature which covers the whole aspect of lasers for inertial confinement fusion in particular the annual reports issued by LLNL [4.8].

In this section we will proceed to provide several basic guidelines which are important in the design of Nd:glass oscillator-amplifier systems.

In order to calculate gain and energy extraction from a glass amplifier for a given input energy we have to know the saturation density E_s and the small signal gain G_0 according to (4.11).

The saturation fluence E_s of a laser glass depends inversely on the gain cross-section σ and can be written as

$$E_s = (hv/\sigma)\kappa. \quad (4.28)$$

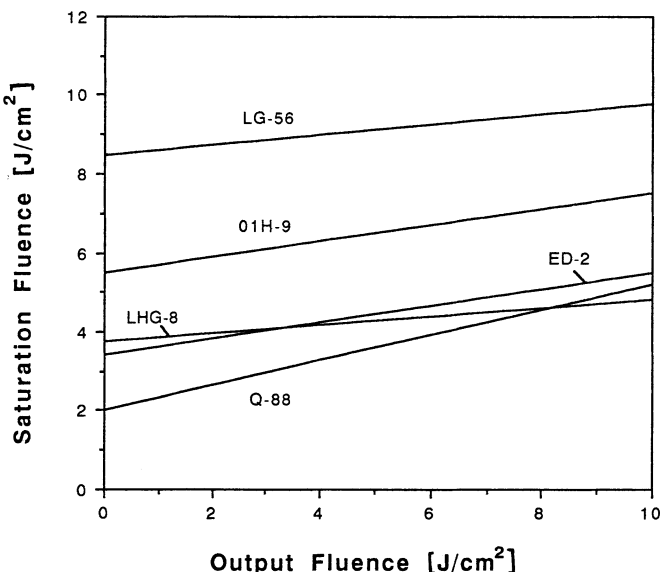


Fig. 4.14. Saturation versus output fluence for a number of silicate glasses (01H-9, LG-56, ED-2) and phosphate glasses (LHG-8, Q-88) [4.9]

The 1053 nm gain cross-section of phosphate glasses range from $3.0 \times 10^{-20} \text{ cm}^2$ and κ is a parameter which is dependent on the output fluence and the duration of the amplified laser pulse. Saturation fluence can depend on the pulse duration if it is less than the lifetime of the lower laser level (less than 1 ns for most glasses). The dependence of E_s on output fluence has been attributed to a hole-burning mechanism [4.9]. It is believed that the saturating pulse couples more strongly to one fraction of the inverted ions in the glass.

Figure 4.14 shows representative values of saturation fluence versus output fluences for several phosphate glasses. The increase of saturation fluence for a higher output fluence is quite pronounced. Pulselwidths for these measurements ranged from 1 to 50 ns.

The next step in the design of a glass amplifier is the calculation of the small signal gain. According to (4.9) we need to determine the stored energy density in the Nd:glass, which depends on the flashlamp operating parameters and energy output as well as on the pump cavity design and transfer efficiency.

We will first consider the gain and energy extraction of typical rod amplifiers since they are employed at the front end of each beam line of a high power Nd:glass laser system. As a general guideline one can expect that for a critically damped lamp pulse of about 300 μs typically 0.5–1.5% of the electrical lamp input will be converted to stored energy in the Nd:glass. The numerical value for the stored energy ranges from 0.2 to 0.8 J/cm^3 .

The performance of a rod amplifier is illustrated in Fig. 4.15 [4.10]. The Nd:glass rod is pumped by flashlamps with an arc length of 30 cm. At the maximum

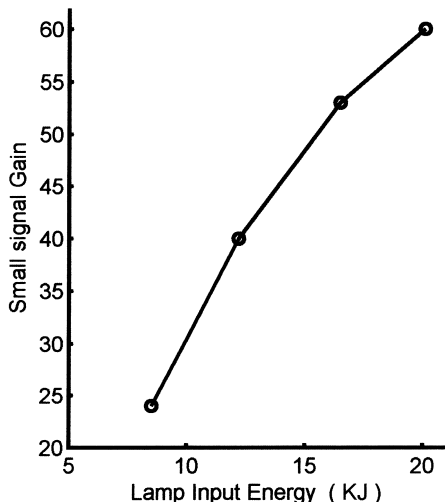


Fig. 4.15. Small signal gain of an Nd:glass amplifier. Clear aperture 2.5 cm, rod length 38 cm, Hoya laser glass LHG-7 [4.10]

pump-energy of 22.5 kJ a small signal gain of 59 was measured with a probe beam. From this measurement we calculate a small signal gain coefficient of $g_0 = 0.13 \text{ cm}^{-1}$ from (4.12). Since the saturation fluence for this Nd:glass is $E_s = 4.8 \text{ J/cm}^2$, We obtain from (4.9) a stored energy density of $J_{\text{st}} = 0.66 \text{ J/cm}^3$. The pump efficiency of this amplifier, defined as the ratio of stored energy to pump energy, is 0.5%.

The different operating regimes of rod and disk amplifiers can be illustrated by recasting (4.11) into a different form.

$$E_{\text{out}} = E_s \ln \left\{ 1 + \left[\exp\left(\frac{E_{\text{in}}}{E_s}\right) - 1 \right] \exp\left(\frac{J_{\text{st}}l}{E_s}\right) \right\}, \quad (4.29)$$

where the small signal gain coefficient is expressed in terms of stored energy density. We assume the same phosphate Nd:glass for both types of amplifiers with a saturation fluence of $E_s = 5 \text{ J/cm}^2$. For the rod amplifier having a length of 30 cm we assume a stored energy density of $J_{\text{st}} = 0.50 \text{ J/cm}^3$ or $g_0 = 0.1 \text{ cm}^{-1}$.

The disk amplifier is assumed to consist of four glass slabs, each 4 cm thick. The stored energy density is lower compared to the rod amplifier to avoid parasitic oscillations as will be explained in the next section. For the largest slabs of 80 cm by 40 cm of the NIF facility the stored energy density is $J_{\text{st}} = 0.25 \text{ J/cm}^3$, which gives a gain coefficient of $g_0 = 0.05 \text{ cm}^{-1}$. Figure 4.16 depicts the output versus input fluence for both amplifiers. The rod amplifier is operated at a input fluence well below 1 J/cm^2 , Whereas the input fluence to the disk amplifier is on the order of the saturation fluence.

The design of disk amplifiers is governed by the goal of simultaneously achieving high stored energy and efficient extraction. Both are essential to minimize the number and cost of amplifiers.

High-energy storage implies high gain, which can lead to amplified spontaneous emission owing to the large gain path across the slab dimension. Actually, the

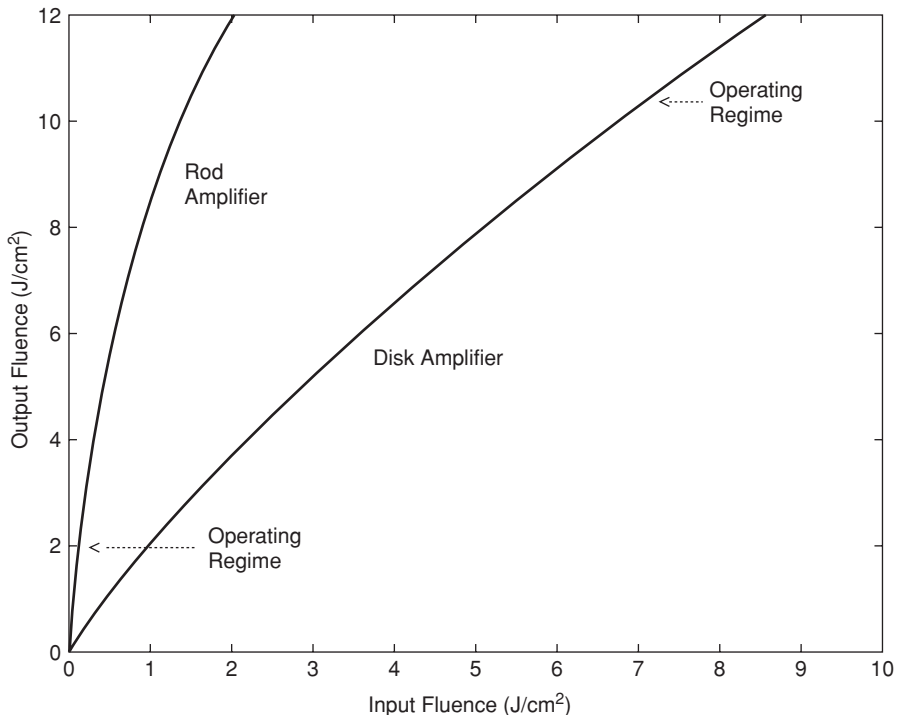


Fig. 4.16. Output vs. input fluence for a Nd:glass rod and disk amplifier

maximum energy storage that can be achieved in a large-aperture amplifier is determined by the onset of parasitic lasing, which is due to the formation of a laser resonator by Fresnel reflections at the interfaces of the gain medium. In general, many complex resonator configurations with multiple reflected beams can lase simultaneously. However, it has been shown that the lowest-loss path lies in a plane across the diameter of the disk. With D the diameter of the disk, parasitics will start if

$$\exp(g_0 D) = 1/R, \quad (4.30)$$

where g_0 is the small signal gain coefficient and R is the reflectivity of the edge of the disk.

In Nd:glass disks without special edge cladding the magnitude of the Fresnel reflections is on the order of 5%. The onset of parasitic lasing becomes a problem when the transfer gain approaches 20 or $g_0 D = 3$. Cladding the edge of the disks with index-matched absorbing glass results in a dramatic reduction of parasitic losses. A design parameter and upper limit for state-of-the-art edge cladded large-slab amplifiers is a product of $g_0 D = 4.2$. This value allows for a 1.5% reflection from the disk edge.

Efficient energy extraction requires operation of the amplifier at very high input fluence, as was discussed in Sect. 4.1. Extraction is particularly efficient at

a signal fluence higher than the saturation fluence of Nd:glass. The upper limit is surface and bulk damage in the glass due to optical inhomogeneities, inclusions, and bubbles and laser-induced damage caused by the nonlinear refractive index.

Actually, the principal limit on the performance of a high-power glass laser, such as employed in fusion research is small scale and whole beam self focusing caused by the intensity dependent refractive index. Both phenomena will be treated in Sect. 4.6.

We will illustrate the energy extraction and operating characteristics of disk amplifiers by comparing the measured data of two different amplifier stages of the NOVA beam line illustrated in Fig. 4.13 [4.6].

The three 22 cm slab amplifiers together have a small signal gain of $G_0 = 9.1$, from which follows a small signal gain coefficient of $g_0 = 0.18 \text{ cm}^{-1}$ for the combined optical path length of 12 cm. With this gain coefficient, parasitic oscillations can be suppressed since the product $g_0 D$ is below 4. The average input fluence to this stage is 0.27 J/cm^2 and the output fluence is 1.96 J/cm^2 across the 233 cm^2 of clear aperture area. This total extracted energy is 393 J from this stage, whereas the energy stored in the upper laser level is 5060 J. The energy extraction efficiency from this amplifier stage is about 8%. This efficiency is the product of the beam fill factor and the actual extraction of stored energy within the beam area. To avoid diffraction effects, the laser beam is smaller than the clear aperture of the amplifier. In this particular case the beam fill factor is 0.69. The input fluence, to this amplifier stage, is considerably below the saturation fluence; therefore, the energy extraction efficiency across the beam area is relatively low, i.e., 12%. With an emission cross section of $\sigma = 3.8 \times 10^{-20} \text{ cm}^2$ for the phosphate glass employed in this laser we obtain a saturation fluence of $E_s = 5.0 \text{ J/cm}^2$ from (4.8).

High-extraction efficiency requires a fluence level at or above the saturation level. At the amplifier stage with a 50 cm aperture the fluence levels are considerably higher compared to the smaller amplifiers. For the combined three amplifiers, shown in Fig. 4.13, the input fluence is 2.6 J/cm^2 and the output fluence is 9.70 J/cm^2 over a clear aperture area of 1330 cm^2 . Because of these high fluence levels, the energy extraction efficiency has risen to 0.54. The beam fill factor is 0.8, which means that about 43% of the total stored energy is extracted from the amplifier. The fluence at the output of this amplifier stage is about twice the saturation fluence, and is about as high as one can safely operate these systems before the potential for optical damage becomes too high. The fluence level at the output of this amplifier stage translates to a peak power of close to 4 GW/cm^2 for a 2.5 ns pulse. The total output at this pulse length is 12.9 kJ. The combined stored energy in all three amplifiers is 23 kJ, which results in a small signal gain of $G_0 = 7.5$. Consistent with the larger aperture the small gain coefficient has been reduced to $g_0 = 0.1 \text{ cm}^{-1}$ to avoid parasitics.

The measured output fluence levels listed above agree with the calculated values from (4.11) to within a few percent if one introduces the small signal gain, input fluence, and saturation fluence for each amplifier into this equation.

A few guidelines for the design of Nd:glass amplifiers can be summarized as follows:

1. The geometry of the pump chamber, flashlamp configuration, and reflectivity of the walls of the pump chamber will have a major influence on flashlamp life, energy storage efficiency, and gain uniformity.
2. The most important properties of the laser glass are the emission cross section, fluorescence lifetime, and nonlinear index of refraction. The emission cross section and fluorescence lifetime largely control the gain, energy storage and extraction efficiency of the laser glass. The nonlinear index strongly impacts beam quality, particularly ripple growth.
3. The Nd doping and fluorescence lifetime must be optimized to achieve maximum storage efficiency. The trade-off among high gain, good spatial gain uniformity, and efficient energy storage is quite complex, and is usually optimized with the use of sophisticated laser design computer codes.
4. Energy extraction from the amplifier is most efficient at high laser fluences, particularly fluences in excess of twice the saturation fluence. Having a glass with a high emission cross section is desirable because efficient extraction can be achieved at lower fluence, thereby reducing the chance of laser-induced damage to the optics.
5. A high-emission cross section is desirable as mentioned above, but it can lead to amplified spontaneous emission across the aperture, which tends to decrease the pumping efficiency. Therefore, the stored energy density has to be decreased for larger glass slabs, i.e., large amplifiers have low gain but because of their large volume the total energy storage is high.
6. Flashlamp pulse width and shape is critical in glass amplifiers because the lamp pulse is comparable to, or larger than, the fluorescence time of the gain storage medium. As a result, considerable depletion of the upper level can take place as a result of fluorescence.

The fluorescence time in Nd:glasses is between 200 and 300 μs . It is very difficult to obtain flashlamp pulses which are shorter than 300 μs without sacrificing lamp life to an intolerable value.

7. The main absorption bands for glass are between 0.6 and 0.9 μs . If one increases the electrical input to a flashlamp, then the higher current density will cause a blue shift of the radiation. As a result, the pump source becomes less efficient and one observes a gain foldover in the amplifier if one plots gain as a function of lamp input.

4.1.4 Multipass Amplifier Configurations

The multipass amplifiers described in this section require no active components; the radiation is directed through the gain medium several times by means of mirrors, lenses, or prisms. The counter propagating beams can be collinear as in a double-pass amplifier, they can be spatially off-set, or guided through the gain medium at slightly different angles. With several passes through a laser amplifier the output energy can

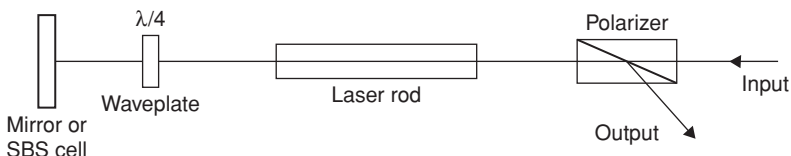


Fig. 4.17. Collinear double-pass amplifier

be increased and a compromise between high gain and high energy extraction can be achieved.

The most common arrangement is a double-pass amplifier, as shown in Fig. 4.17. After the first pass the amplified beam is returned by a high reflective mirror at normal incidence. After the second pass through the gain medium the quarter wave plate has rotated the polarization by 90° so that the return beam can be separated from the input beam with a thin-film polarizer or a Glan–Thompson prism.

A comparison of an amplifier operated single-pass and double-pass is described in [4.11]. The active medium is a Tm:Ho:YLF rod, 4 mm in diameter and 40 mm in length, pumped by GaAlAs diodes at 792 nm. At an input of 54 mJ from the oscillator, the output increased from 150 mJ in a single pass to 254 mJ in the double-pass configuration. Since such a dramatic improvement can be achieved with the addition of only two passive optical components, the double-pass architecture is employed quite frequently in the design of laser amplifiers.

The collinear double-pass design can also be extended to include several amplifier stages as was shown in Fig. 4.7. In such an arrangement the function of preamplifiers and power amplifiers are combined in the same pump modules.

Another version of a double-pass configuration is obtained if the high reflective mirror is replaced by an optical phase conjugate mirror. In Sect. 10.4, optical phase conjugation based on stimulated Brillouin scattering (SBS) will be discussed. Optical aberrations produced by an amplifier stage can be corrected by reflection of the beam off an SBS cell, and passing it back a second time through the amplifier. In this approach the beam is focused into a cell containing a particular gas or liquid. Stimulated Brillouin scattering involves the interaction of optical radiation and sound waves and produces a wave-front reversal of the backward scattered wave.

A multipass amplifier can also be designed with the various beams spatially offset or at slightly different angles at each pass. This approach is not particularly well suited for rod amplifiers because of geometrical constraints, but it is a very attractive approach for slab and disk geometries.

The rectangular geometry of a slab laser lends itself to a multipass arrangement with the beams traversing the gain element at small angles, as shown in Fig. 4.18. In this way the gain material can be addressed with a small beam of high intensity that is required for high energy extraction efficiency. The beams indicated in Fig. 4.18 can pass the slab straight through, or they can follow a zigzag pass perpendicular to the propagation direction by reflection at the top and bottom surface of the slab. The zigzag pass compensates for thermal distortions as explained in Chap. 7. The slab can be pumped from the sides, as indicated in Fig. 4.18, or from the top and bottom.

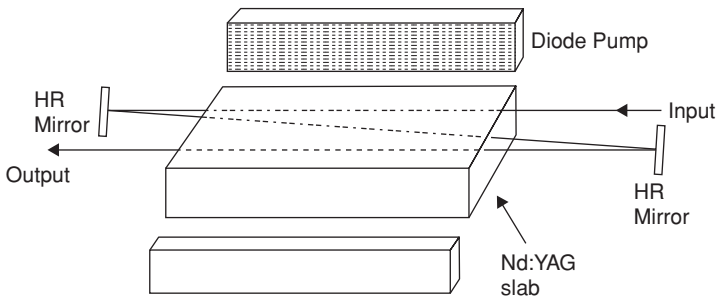


Fig. 4.18. Angular displacement of beams in a multipass slab amplifier

Descriptions of multipass slab amplifiers in a variety of active materials can be found in the following references: Nd:YAG [4.12, 13], Nd:YLF [4.14], Nd:YVO₄ [4.15], Yb:SFAP [4.16], Nd:glass [4.17], and Er:YLF [4.18].

In the Nd:YAG slab amplifier described in [4.16], three double passes through the gain material are achieved by combining the techniques discussed so far: direction reversal with a reflective mirror, a small angular change of the beam direction for the second double pass, and a reflection in the third double pass off a SBS cell. The amplifier produced 362 W of average power at 1 KHz repetition rate.

A thin disk laser either end- or front-pumped tolerates a wide range of incidence angles for the radiation to be amplified. Figure 4.19 depicts a Nd:YAG end-pumped amplifier where a quadruple pass through the gain material is achieved by a combination of an angular off-set and a polarization rotation and output coupling via a Glan–Thompson prism [4.19]. This particular amplifier designed for 946 nm radiation achieved a small signal gain of 3.3.

A design that allows many passes through a thin disk laser is schematically illustrated in Fig. 4.20. However, in this figure only mirrors are shown. Actually, the radiation needs to be refocused after each pass. Multipass relay imaging reproduces the

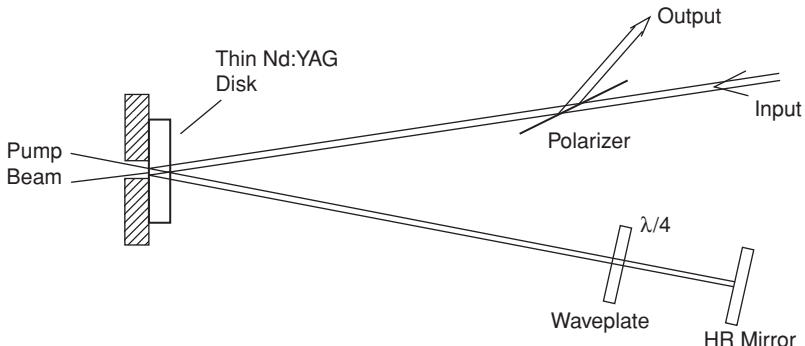


Fig. 4.19. Quadruple pass through a thin disk amplifier by combining a collinear pass with an angular displacement

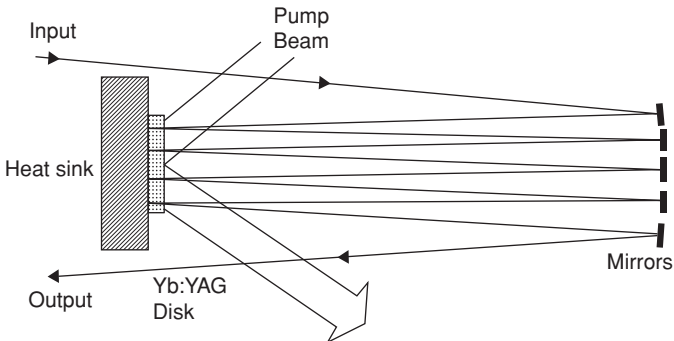


Fig. 4.20. Many passes through a Yb:YAG thin disk amplifier

laser beam on the active material from one pass to the next. The folding units can consist of a combination of lenses and mirrors or a parabolic mirror and prisms [4.20, 21]. In one design the beams are reflected 15° after each pass so that the laser beam is guided 24 times through the gain medium [4.20]. The number of passes is doubled to 48 passes by guiding the linearly polarized beam in the opposite direction again through the amplifier. A quarter wave plate and a thin-film polarizer separate the beams.

4.2 Regenerative Amplifiers

Very low level pulses are usually amplified in a regenerative amplifier. This amplifier is based on an electronically controlled optical switch (Pockels cell) and permits any number of amplification passes through the gain medium. The design and operation of these amplifiers is distinct from single- or double-pass amplifiers described in Sect. 4.1 or injection-seeded oscillators discussed in Sect. 5.2.4. In most cases regenerative amplifiers are designed to amplify single pulses from a cw mode-locked laser. An input pulse of only a few nanojoules is typically amplified to several millijoules providing a gain greater than 10^6 .

Figure 4.21 shows a schematic of diode-pumped Nd:YLF regenerative amplifier. The end-pumped Nd:YLF crystal is at one end of an astigmatically compensated three-mirror resonator. The other side of the resonator contains a thin-film polarizer, quarter-wave plate and a Pockels cell. These three components are characteristic for a regenerative amplifier. Another feature of this type of amplifier is the Faraday rotator, $\lambda/2$ plate and thin-film polarizer which separate the input and output beams. The operation of a regenerative amplifier can be explained by distinguishing three operating phases: pump phase, with Pockels cell voltage at zero; amplification phase, with Pockels cell switched to $\lambda/4$ retardation; cavity dump phase, Pockels cell voltage switched to $\lambda/2$ retardation or zero voltage.

Pump phase, with Pockels cell voltage at zero. The laser crystal can be either cw or pulsed pumped. During the pump phase, laser action is prevented by the $\lambda/4$ plate

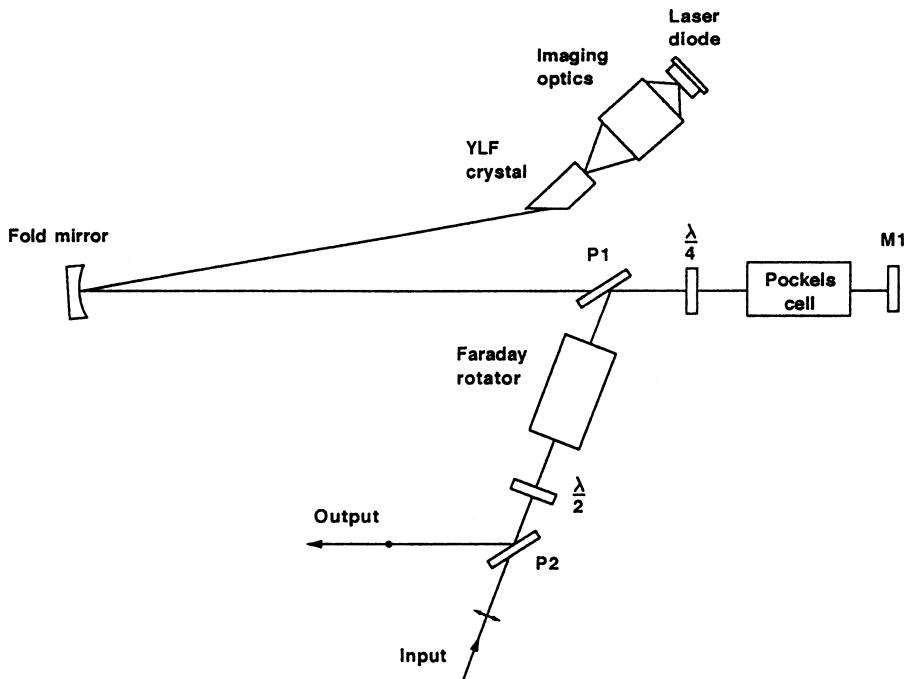


Fig. 4.21. Schematic of a diode-pumped Nd:YLF regenerative amplifier [4.22]

and rear-mirror combination, which causes a 90° rotation of the horizontally emitted radiation by the Brewster-cut laser rod.

A horizontally polarized pulse from a mode-locked oscillator will pass through the thin-film polarizer P2, experience a 45° rotation at the $\lambda/2$ plate and a further 45° rotation at the Faraday rotator. The now vertically polarized pulse is reflected by the thin-film polarizer P1 into the resonator. After reflection from the rear mirror M1 and passing through the $\lambda/4$ plate, the pulse will be horizontally polarized. Therefore, the pulse passes through the polarizer P1 and completes one round trip. On its second round trip, the pulse is rotated again now vertically polarized, it is reflected off the polarizer P1. The 45° rotation from the Faraday rotator is compensated by the $\lambda/2$ wave plate and therefore the vertically polarized pulse is directed to the output port of the amplifier by polarized P2.

The ratio of average power at the output with and without the pump source turned on is a measure of the small-signal double pass gain.

Amplification phase, with Pockels cell switched to $\lambda/4$ retardation. In order to trap a pulse in the resonator, a $\lambda/4$ voltage is applied to the Pockels cells as soon as a pulse has left the Pockels cell in the direction of the fold mirror. It takes about 5–8 ns to switch the voltage from zero to the level required for $\lambda/4$ rotation. Therefore, switching at this particular point provides the longest time period for the pulse to return or for a new pulse to arrive. With the $\lambda/4$ voltage applied to the Pockels cell,

the pulse returning from the gain medium no longer experiences a polarization rotation and therefore stays in the cavity.

Once the Pockels cell is switched to $\lambda/4$ voltage, pulses arriving from the oscillator also no longer experience a polarization rotation. Therefore, the pulses are ejected from the amplifier after being reflected by mirror M1.

The build-up time for the circulating pulse to reach maximum energy depends on the gain in the system and is characteristic of the Q-switch envelope of a cavity dumped pulse. The higher the gain, the shorter the build-up time. Typical time periods are from less than 100 ns for a very high gain system to a few hundred nanoseconds for smaller systems.

Cavity dump phase, Pockels cell voltage switched to $\lambda/2$ retardation or zero voltage. After many passes in the resonator, the energy of the pulse reaches a maximum because of gain saturation. At that point, the Pockels cell is switched to a $\lambda/2$ retardation voltage. Again as before, switching is started when the pulse is just leaving the Pockels cell. On its return, the pulse experiences now a 90° polarization rotation and the vertically polarized pulse is reflected by polarizers P1 and P2 to the output port of the amplifier.

Beside the single amplified pulse emitted by the amplifier, there are smaller pulses preceding and following the main pulse. As the circulating pulse inside the resonator increases in energy, a small fraction is reflected from the amplifier each time the pulse passes through P1. This is due to the finite extinction ratio of the polarizer and the limited contrast ratio of the Pockels cell. A small mis-alignment, or thermal effects leading to birefringence, or small voltage changes in the Pockels cell, will cause the pulse to have a small vertical polarization component. This leakage gives rise to a sequence of premature pulses separated by the round-trip time of the regenerative amplifier.

Another source of background noise is a second pulse trapped in the resonator. For equal resonator length of oscillator and regenerative amplifier, a new pulse arrives as one pulse is leaving the resonator. If the two resonators are not equal in length, there are always two pulses present inside the resonator separated by the difference in round-trip time. If this pulse is approaching the Pockels cell as it is switching, a small fraction of this pulse will also stay in the resonator and be amplified. The contrast ratio between the energy of the main pulse and the integrated background is on the order of 20:1 for most systems.

Performance of Regenerative Amplifiers. The energy that can be extracted from a regenerative amplifier is the most important consideration. Lowdermilk *et al.* [4.23, 24] derived analytical expressions which permit the calculation of the maximum fluence level in the resonator in terms of physical parameters of the gain medium and the resonator. Figure 4.22 summarizes the parameters which are needed to describe the output of a regenerative amplifier. The gain medium is characterized by the small-signal gain $G_0 = \exp(g_0 l)$, the saturation fluence I_s , and a gain recovery coefficient p . The amplifier performance depends on the gain recovery from lower-level relaxation between successive passes; therefore, the parameter p is a function of the time interval between passes and the lower-level relaxation time. For complete gain recovery, p corresponds to $p = 0.5$ and for no gain recovery between pulses $p = 1$. The parameter

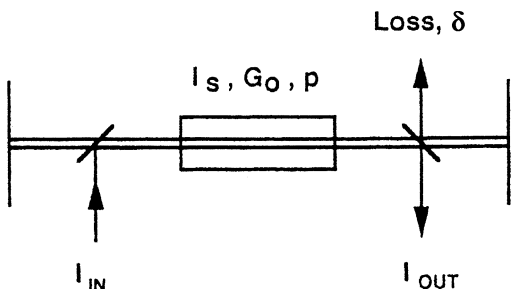


Fig. 4.22. Schematic representation of a regenerative amplifier

I_{in} is the input fluence of the seed pulse and I_0 is the fluence of the output pulse which is the same as the peak fluence in the resonator since the pulse is switched out as soon as it reaches maximum intensity. The total losses δ are represented by a single-pass transmission $T = \exp(-\delta)$.

With the parameters defined in Fig 4.22, it can be shown that the fluence increases with the number of passes according to [4.23].

$$I_{K+1} = T I_s \ln\{G_K [\exp(I_K/I_s) - 1] + 1\} \quad (4.31)$$

and the gain decreases after each pass according to

$$g_{K+1} = g_K - (p/I_s)[(I_{K+1}/T) - I_K]. \quad (4.32)$$

In these equations, uniform gain across the laser medium and complete spatial overlap of input and output pulse is assumed.

Equations (4.31, 32) can be iterated numerically to model multipass amplifiers. An analytical solution for the case in which changes of the gain are relatively small during each pass has also been derived in [4.23]. Gain saturation is reached when gain and losses are equal and the maximum fluence is

$$I_{\text{OUT}} = (I_s/p) \ln \left[T G_0 \left(\frac{1-T}{T(G_0-1)} \right)^{1-T} \right] + I_{\text{IN}}. \quad (4.33)$$

The function $(I_{\text{OUT}} - I_{\text{IN}})$ vs. G_0 has been plotted in Fig. 4.23 with the resonator losses L as parameter. The curves are for Nd:YAG for which $I_s = 0.66 \text{ J/cm}^2$ and $p = 0.72$ was chosen. The value of the saturation fluence $I_s = h\nu/\sigma$ is obtained from the values for the photon energy $h\nu$ and stimulated emission cross-section σ given in Table 2.4.

Figure 4.24 illustrates the increase of pulse energy during each pass in a regenerative Nd:YAG amplifier calculated from (4.31, 32). Input fluence for $K = 0$ was assumed to be $1.5 \times 10^{-7} \text{ J/cm}^2$. With a small-signal gain of $G_0 = 1.7$, pulse energy reaches a maximum at about 40 passes through the gain medium. The linear portion of the curve indicates exponential gain up to about 30 passes, after which gain saturation starts to have an effect. Fewer passes are required to reach gain saturation, and the maximum fluence is higher also, for the case in which a higher gain has been assumed.

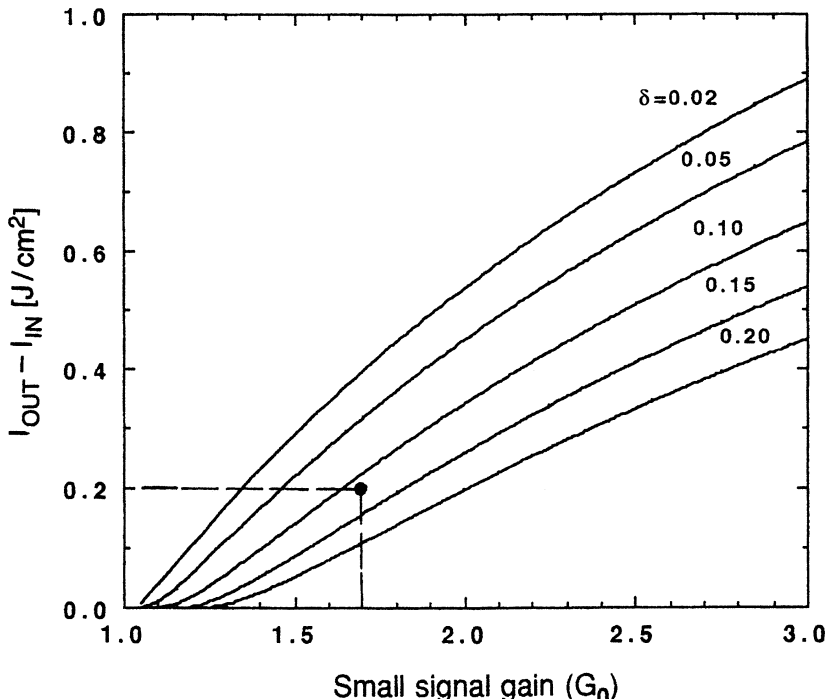


Fig. 4.23. Extracted energy from a regenerative amplifier as a function of small signal gain. Parameters are the resonator losses

Examples. An end-pumped Nd:YLF laser in a resonator configuration, as shown in Fig. 4.21, has produced 88 μJ , 11 ps pulses at a 1 kHz repetition rate [4.22]. The crystal was pumped by a 2 W cw laser diode and was operated at 1.047 μm . Output energies of up to 0.5 mJ have been obtained in another end-pumped configuration utilizing a 15 W cw diode array pump [4.25]. Side-pumping of Nd:YAG or Nd:YLF can produce even higher energy levels [4.26, 27].

As an example of a powerful all solid-state picosecond laser source, we will describe a regenerative amplifier of a system built in the author's laboratory [4.28]. The system produces 28 ps pulses at a repetition rate of 2 kHz and a pulse energy of 2.5 mJ. The schematic of the amplifier is sketched in Fig. 4.25. The resonator consists of a concave-convex mirror combination and two turning mirrors to reduce the physical length of the system. The resonator is designed according to the procedure described in Sect. 5.1.10. With an overall length of 1.5 m, mirror curvatures of $R_1 = 0.5$ m and $R_2 = -2.0$ m, and taking the thermal lensing of the laser rod into account, the resonator operates in a high stability zone. The resonator mode is largest close to the concave mirror, therefore all components are located as close as possible to this mirror. Side-pumping of laser rods creates a relatively large pump cross-section which needs to be matched by a large TEM_{00} resonator mode for good energy extraction efficiency. Furthermore, a large beam waist reduces the possibility of damage in the LiNbO_3 crystal.

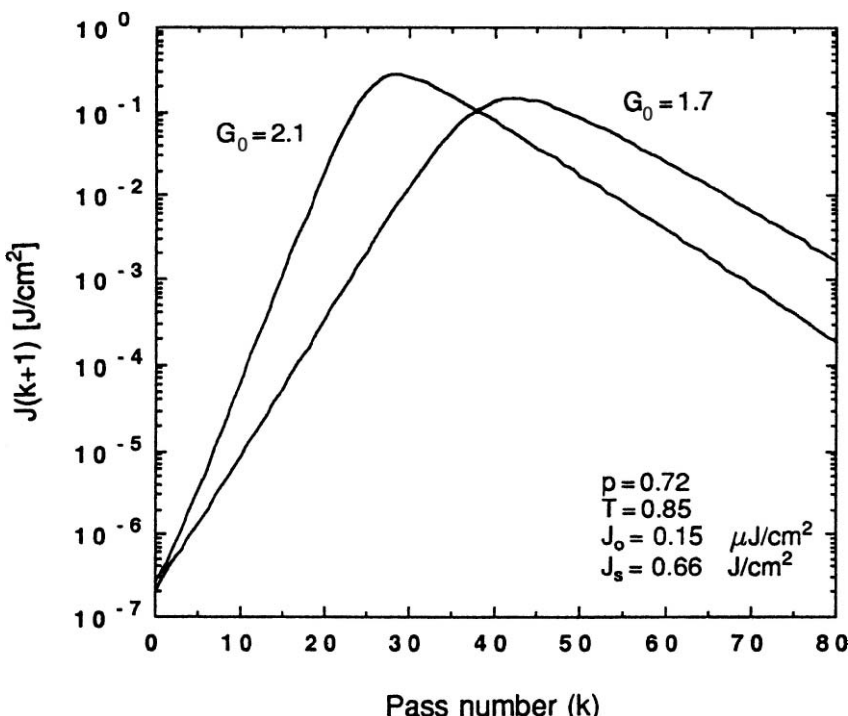


Fig. 4.24. Increase of energy in a regenerative amplifier versus number of passes

Input seed pulses were derived from an end-pumped acousto-optic mode-locked oscillator which generated 16 ps pulses with pulse energies of 1.5 nJ at a repetition rate of 100 MHz. The pump head of the regenerative amplifier contains a Nd:YAG rod, 4 mm in diameter and 68 mm long, which is pumped by 32 diode arrays arranged in a fourfold symmetry around the crystal. The arrays are pulsed for 100 μ s at a repetition rate of 2 kHz. Peak power from each array is 50 W or 1.6 kW total. At this 20% duty cycle, the average optical pump power is 320 W. The pump head, tested in a very short cavity as a long-pulse oscillator, produced 80 W of average multimode power. At a pump power of 1.6 kW, a single-pass small-signal gain of $G_0 = 1.7$ was measured for the regenerative amplifier configuration. Operation and switching sequence are identical to the device described previously. An acoustically damped LiNbO₃ Q-switch, with a switching time of 5 ns was employed in the amplifier. In this Q-switch, the acoustic modes which are excited by the piezoelectric effect are transmitted into a strongly attenuating material that is acoustically impedance matched to LiNbO₃. The Pockels cell is switched to $\lambda/4$ retardation at the end of the 100 μ s-long pump cycle. After about 100 ns, the circulating pulse has reached maximum energy, and the Pockels cell is switched to a $\lambda/2$ retardation.

Figure 4.26a,b shows oscilloscope traces of the circulating pulse inside the resonator up to the point of cavity dumping, as well as a pulse train for the case where

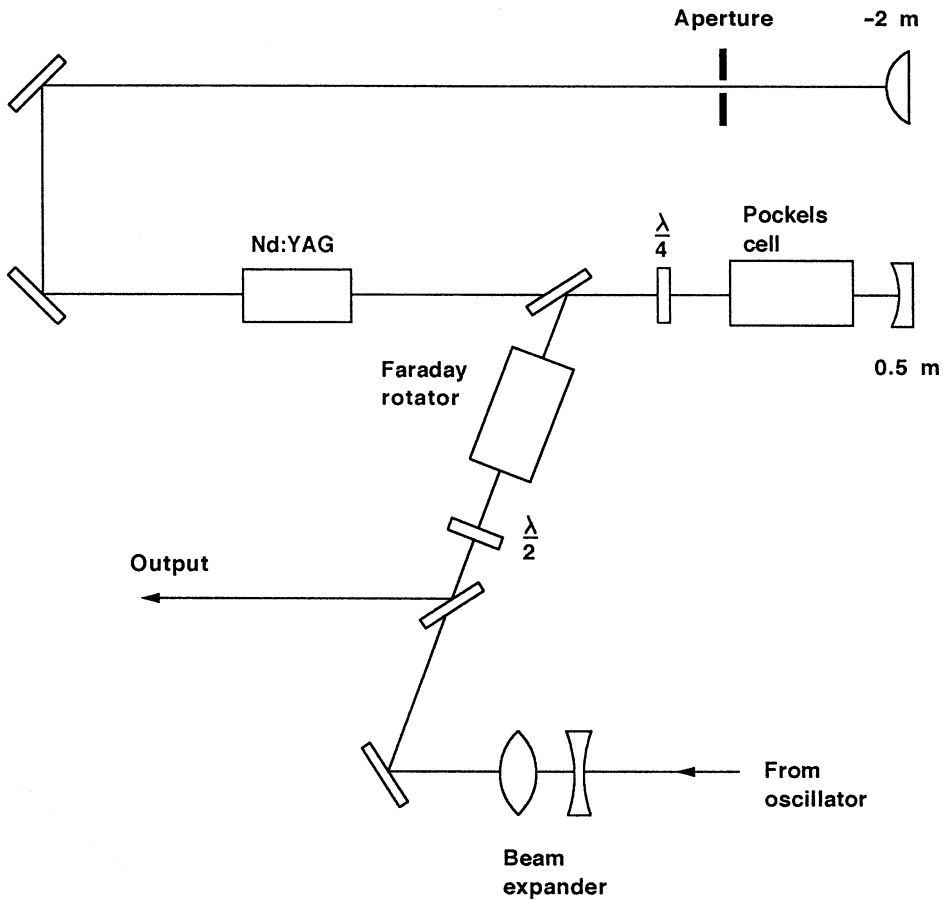


Fig. 4.25. High repetition rate laser diode pumped regenerative amplifier

the Pockels cell is not switched a second time to eject the pulse from the cavity. Both traces were obtained by monitoring the leakage through the near mirror. The output pulse emitted from the regenerative amplifier is displayed in Fig. 4.26c.

Figures 4.23 and 4.24 have been generated to model this particular regenerative amplifier. We will compare the predictions from the model with the experimental results. The model assumes uniform gain and a top-hat beam profile. The actual system had a fairly uniform gain profile in the center of the laser rod, but a Gaussian beam profile. The TEM₀₀ mode size was 2 mm at the $(1/e)^2$ points. A uniform beam with the same energy content as the Gaussian beam would have a beam width of 1.25 mm. This beam diameter was used in the comparison of the data. The measured small-signal gain and output fluence are indicated in Fig. 4.23. From this data follows a single-pass loss of 11% in the system. The high losses in the amplifier are mostly dynamic losses associated with heating of the Pockels cell, and incomplete opening and closing. The former is a result of the high average power, and the second loss

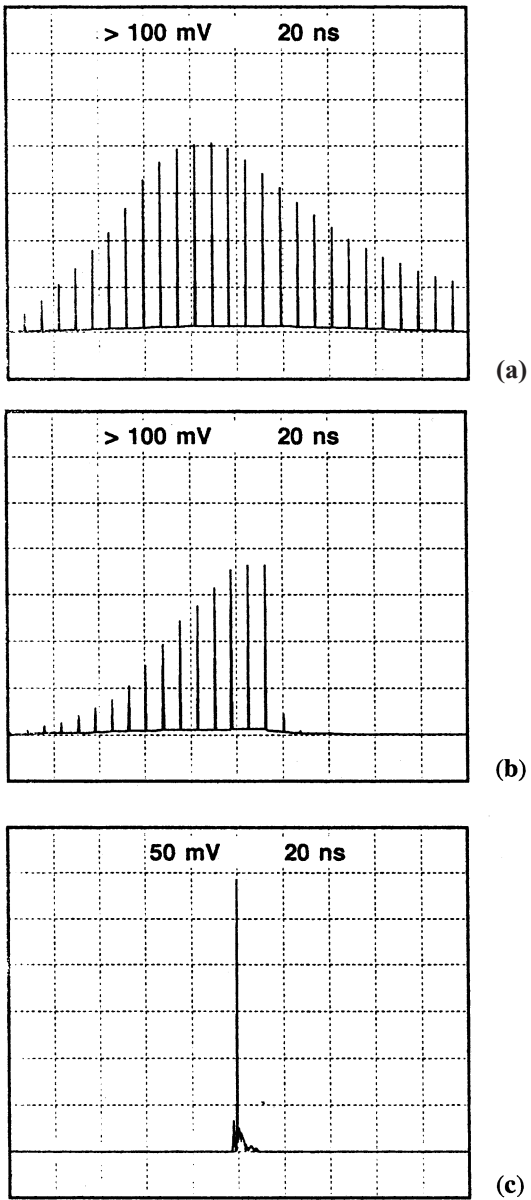


Fig. 4.26. (a) Circulating pulses of mode-locked laser if system is not cavity dumped. (b) Pulse train of mode-locked laser up to cavity dumping and (c) output pulse

factor is due to piezoelectric ringing in the crystal. The result in Fig. 4.24 indicates that 40 single passes or 200 ns are required in the 1.5-m-long resonator before the fluence reaches its maximum value. The actual measurements showed a time delay of 240 ns. Considering the simplifying assumptions made in the model, the experimental and theoretical data agree fairly well. More important is the ability of the model to

predict the performance of the amplifier if changes are made during the optimization process.

4.3 cw Amplifiers

In the past, with flashlamp-pumped Nd:YAG lasers, the gain that could be achieved was not high enough to consider an oscillator–amplifier architecture for cw systems. A large cw output was obtained by connecting several pump modules in series within the resonator. This is still the most common configuration today.

However, with diode-pumping, population inversions can be achieved that result in gain coefficients that make MOPA configurations attractive in certain situations. Particularly, since in very powerful lasers the gain is often so high that the benefit of putting all modules inside a resonator is diminished. In these systems the output coupling becomes so small that the circulating power is on average not making several passes through the gain medium. Therefore, other considerations become important.

In industrial applications a MOPA design allows easy scaling to higher power levels by adding more modules to the system. Also replacement and repair of individual modules is easier because it can be performed without major realignment of the system. Furthermore, beam distortions introduced by the laser rods have a smaller impact in an amplifier as compared to an oscillator. In scientific applications, a MOPA configuration allows scaling to high power while preserving the spatial and temporal coherence of a master oscillator.

If the input signal to the amplifier is long compared to the fluorescence time, the population inversion and gain reach a steady state determined by the intensity of the pump and the intensity of the laser beam. In Sect. 3.2 we derived an expression for the saturated gain in an oscillator under steady-state condition.

In the case of an amplifier, the gain depends on the coordinate z measured in the direction of the axis of the amplifier:

$$g(z) = \frac{g_0}{1 + I(z)/I_s}, \quad (4.34)$$

where g_0 is the small-signal gain, $g(z)$ is the gain at position z in the amplifier obtained at a signal level $I(z)$, and I_s is the saturation density defined as the signal power, which reduces the small-signal gain by a factor of one-half.

Whether operating in the energy storage or steady-state mode, the phenomenon of gain saturation is common to both time domains. In the case of pulses that are short compared to the fluorescence lifetime the amplification depends on the energy density, whereas in the case of long pulses of cw mode of operation the gain depends on power density.

Assuming that the inversion n does not change much over a photon transit time in the amplifier, the power density $I(z)$ builds up along z in the following manner:

$$\frac{dI}{dz} = \sigma n(z)I(z) = g(z)I(z). \quad (4.35)$$

For small signal levels $I(z) < I_s$, we obtain from (4.34, 35)

$$I_{\text{out}} = I_{\text{in}} \exp(g_0 l) \quad (4.36)$$

and at large signal levels $I(z) > I_s$

$$I_{\text{out}} = I_{\text{in}} + I_s g_0 l. \quad (4.37)$$

If one replaces fluence with power density, then the expression for the small signal gain and fully saturated gain are identical for short-pulse and cw amplification. A general relationship between small signal gain and saturated gain for steady-state amplification can be found if one introduces $g(z)$ from (4.34) into (4.35). Integration over the length of the amplifying medium and some algebra yields the following expression [4.29]:

$$\frac{I_{\text{in}}}{I_s} = \frac{\ln(G_0/G)}{G - 1}, \quad (4.38)$$

where $G_0 = \exp(g_0 l)$ is the small-signal, single-pass gain of the amplifier of length l and $G = I_{\text{out}}/I_{\text{in}}$ is the saturated gain. Equation (4.38), which is plotted in Fig. 4.27, permits one to calculate the power gain of solid-state lasers in the steady-state regime.

We assume a Nd:YAG amplifier containing a rod of 5 mm diameter and having a small signal gain of $G_0 = 10$. If the cw input to this amplifier is $P_{\text{in}} = 900$ W, the input intensity normalized to the saturation density for Nd:YAG is $I_{\text{in}}/I_s = 1.6$. With this number and G_0 , we obtain from Fig. 4.27 a power gain of $G/G_0 = 0.2$ or

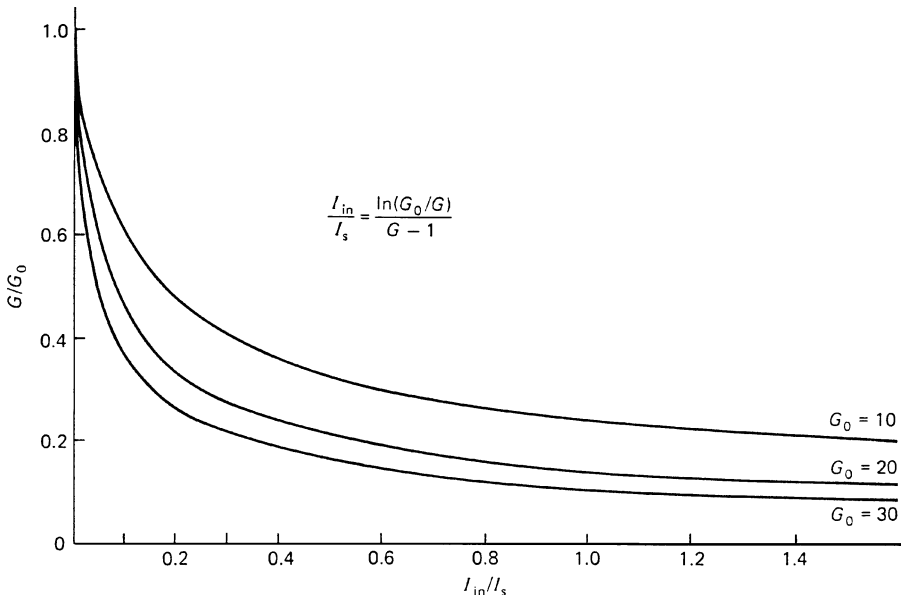


Fig. 4.27. Steady-state gain versus input power density in laser amplifiers. Parameters are the small-signal gain G_0 and the saturation power density I_s

$G = 2$. Therefore, the calculated output of this amplifier will be 1.8 kW of cw power. However, a nonuniform gain distribution, a fill factor less than unity, and losses caused by beam shaping and corrective optics that are required to improve beam quality at these high-power levels, usually result in an actual output that is considerably lower than the predicted value from (4.38).

In [4.30] a MOPA configuration is described that consists of two pump modules inside the resonator and two modules employed as amplifiers. The 400 W output from the oscillator was increased to 750 W by the amplifiers. The total electrical input to the diode-pumped Nd:YAG oscillator–amplifier system was 11.6 kW.

A Nd:YAG laser employing four pump modules within the oscillator followed by a four-stage amplifier generated cw output of 4.7 kW [4.31]. The diode laser bars in each module delivered 2 kW of optical pump power. With a rod diameter of 5 mm, the power density at the output of the last amplifier stage was approximately eight times the saturation density of Nd:YAG.

While the two systems described above have been designed for industrial applications, several cw Nd:YAG oscillator–amplifier systems have been built for scientific investigations, such as laser interferometry for the detection of gravitational waves. In these applications it is important that the spatial and temporal coherence from an extremely narrow bandwidth master oscillator is preserved. Once such system featuring two multiple pass slab amplifiers produced over 100 W cw in a narrow linewidth [4.13].

4.4 Signal Distortions

As an optical signal propagates through a laser amplifier, distortions will arise as the result of a number of physical processes. We can distinguish between spatial and temporal distortions.

4.4.1 Spatial Distortions

The development of high-power laser oscillator–amplifier systems has led to considerable interest in the quality of the output beam attainable from these devices. Beam distortions produced during amplification may lead either to an increase in divergence or to localized high energy densities, which can cause laser rod damage. We will consider the main phenomena producing a spacial distortion, which is analogous to a wavefront or intensity distortion.

Nonuniform Pumping. Because of the exponential absorption of pump light, the center of the rod is pumped less than the edges. Figure 4.28 shows the stored energy profile of several Nd:glass amplifier stages of the Omega system built at the University of Rochester [4.32]. The curves were obtained by measuring the small-signal gain with a narrow probe beam across the rod on five amplifier stages of increasing diameter. In order to provide a uniform gain profile as much as possible, the Nd concentration is decreased for increasing rod diameters.

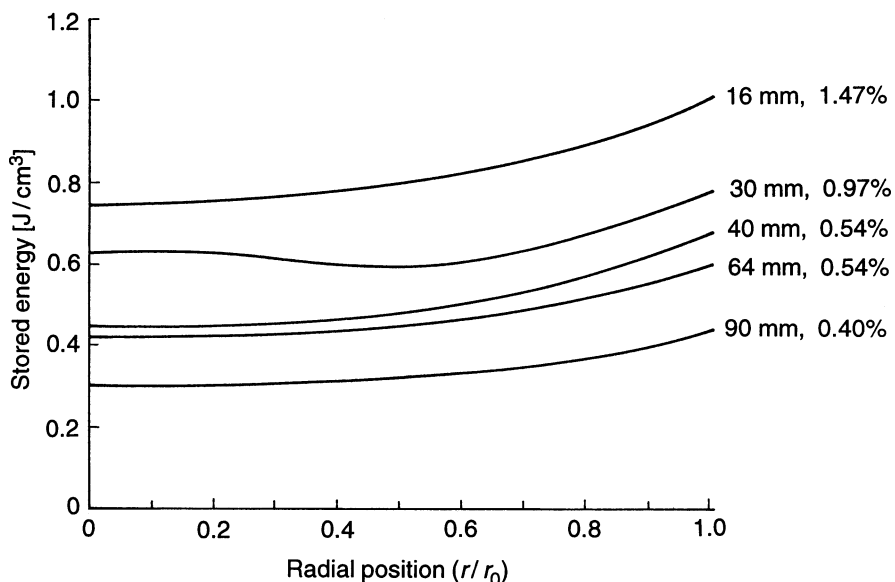


Fig. 4.28. Stored energy distribution in different Nd:glass rods [4.32]. Rod diameters and doping levels (wt. %) are indicated on the curves

Nonuniformities in the Active Material. Even laser rods of excellent optical quality contain a small amount of inherent stress, index of refraction variations, gradients in the active ion concentration, contaminants, inclusions, etc. These nonuniformities will significantly modify the energy distribution of an incoming signal. An initially smooth energy distribution will contain ripples after passing through a laser amplifier.

Gain Saturation. A beam propagating through an amplifier can experience a distortion of the spatial profile because of the saturation-induced change in the distribution of gain. The weaker portions of the signal are amplified relatively more than the stronger portions because they saturate the medium to a lesser degree.

The effect is most pronounced when the input fluence is about equal to the saturation fluence. For example, a Gaussian spatial profile can become more flat on top and the spot size can increase because of the stronger amplification of the wings. The beam profile is not changed if the amplification takes place in the small-signal region.

Diffraction Effects. Any limiting aperture in the amplifier section that removes energy at the edges of the beam will give rise to Fresnel rings. Diffraction effects are undesirable because they introduce strong intensity modulation in the beam that can produce spatial hot spots and lead to optical damage. Ideally, the beam injected into an amplifier should fill the cross section of the pumped volume to allow maximum extraction of energy, but at the same time should have an energy density profile that

minimizes diffraction effects. These two conflicting requirements lead to a trade-off between a high fill factor and minimizing diffraction effects.

A flat top or square beam has an ideal fill factor of unity but suffers from disastrous diffraction effects. A Gaussian beam with a spot size considerably smaller than the rod radius will show negligible diffraction rings, but the fill factor is very poor.

A reasonable compromise is a beam that is fairly flat in the central section and decreases rapidly towards the edges. The intensity of such a super-Gaussian beam is described by

$$I(r) = I_0 \exp[-2(r/w_0)^n], \quad (4.39)$$

where I_0 is the peak intensity at the center, w_0 is the spot size of the beam, and n determines the shape of the intensity distribution. For $n = 2$, one obtains the standard Gaussian beam shape, and for very large n the pulse shape approaches a square beam. With a value of n between 2 and infinity, a profile can be found that will result in a reasonable compromise between high energy extraction and small diffraction effects. Figure 4.29 depicts beam profiles for values of $n = 2, 4$, and infinity. For the two Gaussian profiles the limiting aperture is assumed 1.5 times the spot radius, w_0 .

Compared to a standard Gaussian profile it is obvious from Fig. 4.29 that a beam with a super-Gaussian profile will have a higher extraction efficiency. A high extraction efficiency requires a high input fluence. The maximum input fluence is

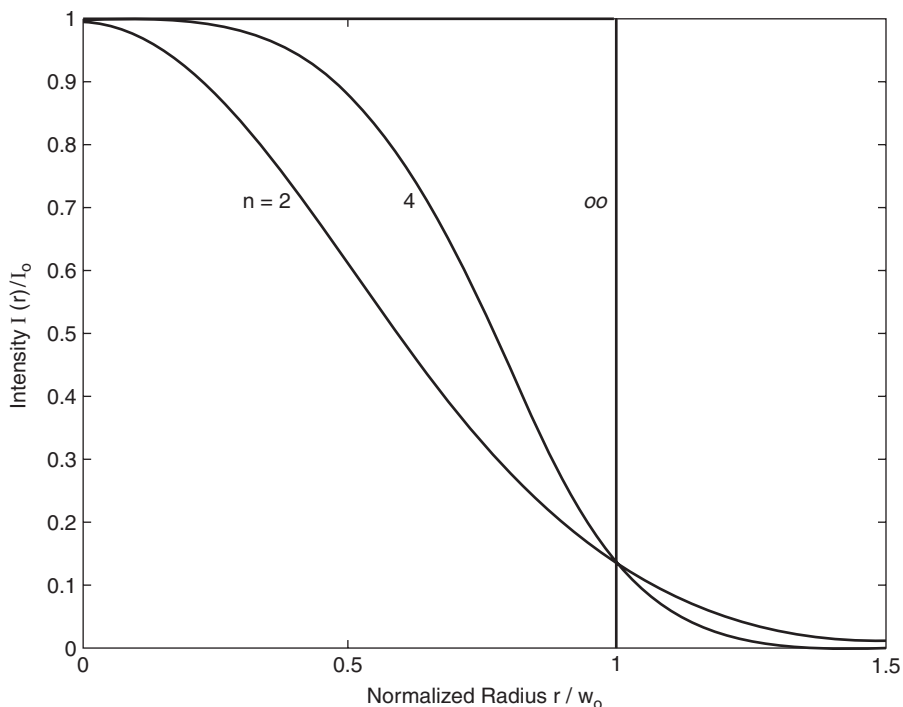


Fig. 4.29. Beam profiles for a Gaussian beam ($n = 2$), a super Gaussian beam ($n = 4$), and a flat top beam

determined by the damage threshold. A beam with a flat top can extract energy at peak intensities across the whole gain region. For any other beam profile the average intensity is below the peak intensity and the extracted energy is limited by the ratio of peak to average intensity.

Methods to reduce diffraction effects, in addition to tailoring the Gaussian beam profile to the limiting aperture, consist of using spatial filtering. A spatial filter consists of two positive lenses and a pinhole at the common focal plane. Spatial filtering in a amplifier chain is obtained if we match an aperture diameter to the first dark ring of the far-field pattern produced by the preceding stage. No modulation will appear in the regime of the Airy disc. In a more general sense, low-pass spatial filters in the amplifier chain filter the beam noise resulting from imperfection of the optics and diffraction. By choosing the pinhole diameter one can control which spatial frequencies are passed. The use of spatial filters in high peak power systems leads to the requirement that they be operated in vacuum, because the high intensities reached at the focal spot lead to optical breakdown in air.

Thermal Distortions. The nonuniform pumping which leads to a higher gain coefficient at the edges of a laser rod also causes a nonuniform temperature profile across the rod. The absorbed pump power raises the temperature of the surface of the rod above the temperature of the rod center. As a result, a negative thermal lens is created, which distorts the wavefront of the beam. Associated with the thermal gradients are stresses in the active material which lead to birefringence. Therefore, the thermal effect leads to strong optical aberrations which can be only partially compensated for by insertion of correcting elements. Thermal effects in laser rods are discussed in detail in Chap. 7.

Index Nonlinearity. When a powerful laser pulse propagates through an isotropic material, it induces changes in the refractive index. The manifestation of this nonlinearity are whole beam focusing and small-scale focusing that will be addressed in Sect. 4.6.

4.4.2 Temporal Distortions

Pulse-Shape Distortion. For a square pulse traversing an amplifier, the leading pulse edge sees a larger inverted population than does the trailing edge. This occurs simply because the leading edge stimulates the release of some of the stored energy and decreases the population inversion for the trailing edge. Thus, less energy is added to the final portions of a pulse than to the leading regions. The change of an arbitrary input pulse shape after propagation is described in [4.1]. If we consider for simplicity a square pulse, we can write for the power of the pulse

$$P(x, t) = P_{\text{in}} \left\{ 1 - [1 - \exp(-g_0 x)] \exp \left[- \left(\frac{t - x/c}{t_p} \right) \right] \frac{E_{\text{in}}}{E_s} \right\}^{-1}, \quad (4.40)$$

where g_0 is the small-signal gain coefficient, E_{in} and E_s are the input and saturation energy densities, respectively, and t_p is the length of the pulse. Note that the power

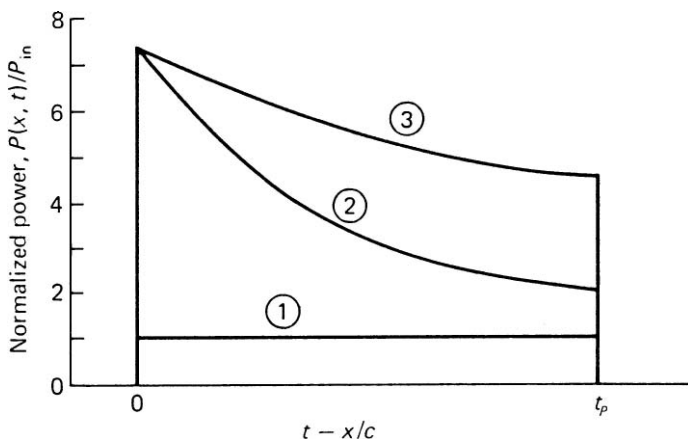


Fig. 4.30. Change of the pulse shape in an amplifier as a result of gain saturation. Curve 1 is the initially rectangular pulse, curves 2 and 3 are for $g_0 = 0.1 \text{ cm}^{-1}$, $l = 20 \text{ cm}$, $E_{in}/E_s = 0.5$, and $E_{in}/E_s = 0.1$, respectively

is dependent on time and location x within the amplifying medium and also on the input energy $E_{in} = P_{in}t_p$.

At the input of the amplifying medium ($x = 0$) we have $P(0, t) = P_{in}$. For the square-pulse case considered here we note that for any value of input, the gain at the leading edge of the pulse ($x = ct$) is exponential with distance through the amplifier. The trailing edge of the pulse is characterized by $t_p = t - x/c$. In Fig. 4.30 the change of a rectangular input pulse is shown. The pulse undergoes a sharpening of the leading edge and a reduction of its duration. Pulse-shape distortions for input pulses which have profiles other than rectangular are treated in [4.2]. The pulse-shape evolution depends appreciably on the rise time and shape of the leading edge of the input pulse. In general, one observes a forward shift of the peak as the pulse transverses the amplifying medium.

4.5 Depopulation Losses

One of the main considerations in the design of an amplifier or amplifier chain is its stability under the expected operating conditions. In a laser operating as an amplifier or as a Q-switched oscillator the active material acts as an energy storage device, and to a large extent its utility is determined by the amount of population inversion that can be achieved. As the inversion is increased in the active material, a number of different mechanisms begin to depopulate the upper level.

Depopulation can be caused by amplified stimulated emission (ASE). A process that will be enhanced by radiation from the pump source falling within the wavelength of the laser transition, or by an increase of the pathlength in the gain medium either by internal or external reflections.

Also, if sufficient feedback exists in an amplifier because of reflections from optical surfaces, the amplifier will start to lase prior to the arrival of the signal pulse. If the reflections are caused by surfaces which are normal to the beam direction, the amplifier will simply become an oscillator and prelasing will occur prior to Q-switching or the arrival of a signal pulse. Reflections which include the cylindrical surfaces of a rod will lead to parasitic modes, propagating at oblique angles with respect to the optical axis of the laser.

4.5.1 Amplified Spontaneous Emission

The level of population inversion which can be achieved in an amplifier is usually limited by depopulation losses which are caused by amplified spontaneous emission. The favorable condition for strong ASE is a high gain combined with a long path length in the active material. In these situations, spontaneous decay occurring near one end of a laser rod can be amplified to a significant level before leaving the active material at the other end. A threshold for ASE does not exist; however, the power emitted as fluorescence increases rapidly with gain. Therefore, as the pump power increases, ASE becomes the dominant decay mechanism for the laser amplifier. At that point, an intense emission within a solid angle Ω around the axis of the active material is observed from each end of the rod:

$$\Omega = A/l^2, \quad (4.41)$$

where l and A are the rod length and cross-sectional area, respectively. As a result of refraction at the end faces, the geometrical aperture angle of the rod is increased by n_0^2 , as shown in Fig. 4.31. No mirrors are required for ASE to occur; however, reflections from a mirror or internal reflections from the cylindrical surfaces of the rod will increase the pathlength for amplified spontaneous emission, which will lead to a further increase in intensity. This aspect will be treated in Sect. 4.5.2.

In high-gain, multistage amplifier systems ASE may become large enough to deplete the upper state inversion. ASE is particularly important in large Nd:glass systems employed in fusion experiments. An analytical expression for the fluorescence flux I_{ASE} from a laser rod as a function of small signal gain, which has been found very useful in estimating the severity of ASE, is given in (4.42) with the

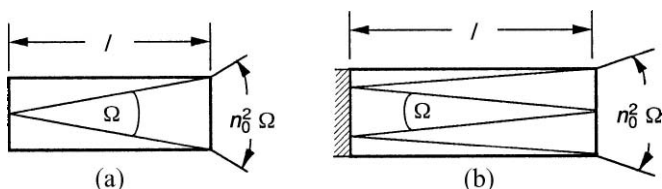


Fig. 4.31. Directionality and maximum pathlength for ASE in a laser rod (a) without a reflector and (b) with a reflector on one end

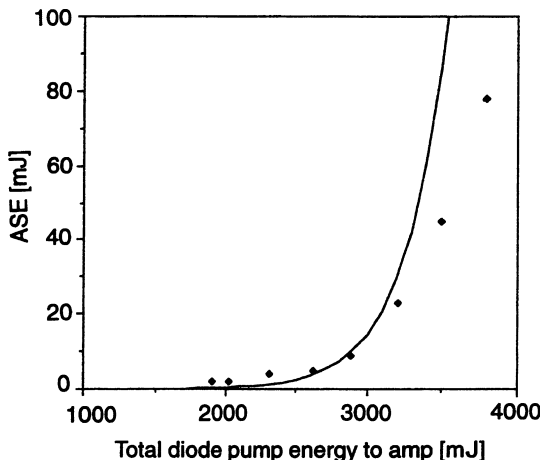


Fig. 4.32. ASE from a 4-stage double pass Nd:YAG amplifier chain. Dots are measured values and solid line represents calculated values from (4.42)

approximation $G_0 > 1$ [4.33]

$$\frac{I_{\text{ASE}}}{I_S} = \frac{\Omega}{4} \frac{G_0}{(\ln G_0)^{1/2}}, \quad (4.42)$$

where I_S is the saturation flux and G_0 is the small signal gain of the active medium. We will apply this formula to a multistage Nd:YAG amplifier and compare the calculated with the measured values of ASE.

In Fig. 4.32, the measured ASE from a four-stage, double-pass Nd:YAG amplifier chain is plotted as a function of diode-pump input. At an input of about 500 mJ into each amplifier ASE starts to become noticeable, and quickly increases in intensity to reach 75 mJ at an input of 900 mJ per amplifier. The detrimental effect of ASE can be seen in Fig. 4.33, which shows the output from the amplifier chain as a

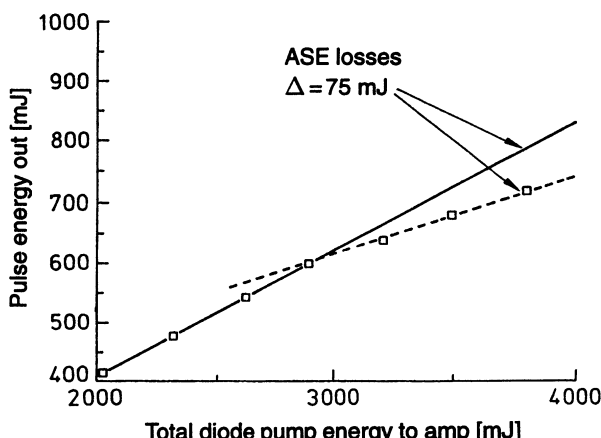


Fig. 4.33. Signal output versus pump input from a multistage Nd:YAG amplifier chain (onset of ASE shown in Fig. 4.32 accounts for drop in output energy)

function of pump input. As the amplified spontaneous emission increases, the slope of output versus input decreases and the difference can be accounted for by the loss due to ASE.

From (4.42) in conjunction with Fig. 4.9, which shows the gain versus pump input for one amplifier head, we can calculate the ASE from the amplifier chain. We have to recall that $\Omega = A/4l^2$ since the pathlength for ASE is doubled in a double-pass system, and $G_0 = (G'_0)^8$, where G'_0 is the small signal gain in one amplifier. With $A = 0.45 \text{ cm}^2$, $l = 50 \text{ cm}$, $I_S = 2.9 \times 10^3 \text{ W/cm}^2$, and $t_p = 200 \mu\text{s}$, one obtains the curve in Fig. 4.32 which closely matches the observed ASE output.

So far we discussed the amplification of fluorescence generated by the active material itself. It has been observed that flashlamp pump radiation, which is within the spectral region of the laser transition, will also be amplified and can lead to a reduction of stored energy in the laser material.

Gain saturation resulting from amplification of pump radiation in the active medium has been observed mainly in Nd:glass and Nd:YAG amplifiers [4.34]. In addition to the depumping process caused by the lamp radiation, fluorescence being emitted from the laser rod escaping out into the laser pump cavity can be reflected back into the laser rod and thereby stimulating further off-axis emission. Thus the presence of pump-cavity walls, which have a high effective reflectivity at the fluorescence wavelength, causes a transverse depumping action which depletes the energy available for on-axis stimulated emission. Elimination of these effects may require the use of optical filters in the pump cavity, cladding of the laser rod with a material which absorbs at the laser wavelength, or the addition of chemicals to the cooling fluid which serve the same purpose.

The influence of coolant properties upon the performance of a Nd:YAG laser amplifier is shown in Fig. 4.34. Two properties of the cooling fluid are of interest. These are the refractive index and the $1.06\text{-}\mu\text{m}$ absorption. The data is shown for a cored 2-cm-diameter by 10-cm-long Nd:YAG rod operated with water, FC-104, and air as cooling media [4.4]. FC-104 is a fluorcarbon flashlamp coolant which is no longer produced. All fluids were used with and without a $1.06\text{-}\mu\text{m}$ absorbing filter (samarium-doped glass) in the pump cavity which was located between the rod and lamp. The addition of a $1.06\text{-}\mu\text{m}$ absorbing filter when water was used as a coolant made little difference in amplifier performance. Water possesses an appreciable intrinsic absorption at $1.06 \mu\text{m}$. The performance obtained with FC-104, which is highly transparent at $1.06 \mu\text{m}$, was greatly affected by the use of $1.06\text{-}\mu\text{m}$ absorbing filters. The performance obtained with air cooling was also affected by the use of a $1.06\text{-}\mu\text{m}$ absorbing filter, but the change was not nearly as marked as the change noted with FC-104. The primary difference between air and FC-104 in this experiment is their respective refractive indices. FC-104 has a low refractive index of approximately 1.28, but this is still significantly higher than that of air. With air cooling, the reflection of fluorescence at the rod surface is so high that it exceeds the return from the pump reflector, thereby limiting the effectiveness of the samarium filter. The dependence of the saturation level on absorption in the pump cavity at $1.06 \mu\text{m}$, and on the refractive index of the material surrounding the rod, is attributed to the presence of amplified spontaneous emission from the rod, as well as the presence of significant reflections of $1.06 \mu\text{m}$ radiation from both the rod surfaces and pump

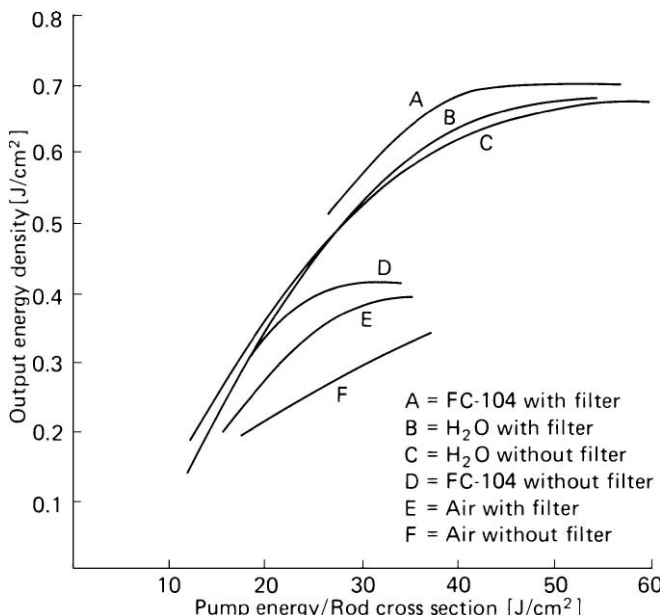


Fig. 4.34. Energy extraction density of YAG:Nd as a function of coolant properties [4.4]

reflectors. This energy storage limiting mechanism, although most pronounced in Nd:YAG rods, because of the high gain obtained in this material, is not unique to Nd:YAG lasers.

Gain limitations in Nd:glass rods, resulting from amplified pump radiation and reflection of spontaneous emission from the pump cavity walls back into the rod, have led to the development of samarium-clad Nd:glass rods. Cladding of the rod also suppresses internal reflection from the rod walls when the refractive indices of the rod and cladding are matched.

4.5.2 Prelasing and Parasitic Modes

Prelasing and parasitic modes are consequences of the interaction of a high-gain material with reflecting surfaces.

Prelasing

Laser action, occurring during the pump phase in an amplifier, results from the residual feedback of the various interfaces in the optical path. The condition for stable operation can be derived by considering the gain in an amplifier rod of length l pumped to an inversion level characterized by a gain coefficient g per unit length. Let the end faces of the rod exhibit residual reflectivities of R_1 and R_2 . Then spontaneous emission emanating from any given location in the rod, traveling normal to the rod end faces, will exhibit a loop gain after one round trip in the rod of approximately $R_1 R_2 \exp(2gl)$.

If this loop gain is greater than unity, oscillations will build up until the usable stored energy is depleted. The requirement for an amplifier is thus

$$R_1 R_2 \exp(2gl) < 1, \quad (4.43)$$

which sets an upper limit on rod length.

Parasitic Oscillations

Internal reflections at the boundaries of the active medium can drastically enhance the onset of ASE, particularly if these reflections lead to a closed path, that is, a ray that is reflected upon itself. In this case, we have a strong feedback mechanism and as soon as the gain in the laser medium exceeds the reflection losses parasitic oscillations will set in. For example, in rods with polished walls there can exist internal modes completely contained by total internal reflection. These are particularly troublesome.

One type of internal mode, the whisper mode, propagates circumferentially and has no longitudinal component. This mode can penetrate into the rod as far as r_0/n_0 , where n_0 is the index of refraction and r_0 is the rod radius. Another type of internal mode, the light-pipe mode, propagates down the rod in a zigzag fashion. The gain limitations due to internal radial modes are considerably improved in immersed rods particularly in the case of an index matching fluid, or rods with rough surfaces, grooves, or antireflection coatings. Longitudinal modes can be suppressed if the faces of the rod are either wedged or antireflection coated. Parasitic modes in laser disks have already been described in Sect. 4.1.3.

4.5.3 Reduction of Depopulation Losses

Amplified spontaneous emission (ASE), parasitic oscillations, or prelasing will decrease the energy available for laser radiation in an oscillator or amplifier. From the foregoing discussion follow a number of measures that can be implemented to minimize depopulation losses.

Reflections within the beam path of an amplifier can be avoided by applying antireflection coatings to optical surfaces and alignment of optical components at a slight angle to the beam axis. For example, the ends of laser rods are typically cut at an oblique angle to the rod axis or have surfaces cut at the Brewster angle. Edges of disks or slabs can be coated or cladded with absorbing layers for the laser radiation. Also, rough grinding of the cylindrical surface of a laser rod will eliminate total internal reflection that could set up parasitic oscillations.

Since ASE diverges more rapidly than laser emission, feedback between amplifiers can be reduced by increasing the separation between the amplifier stages or by insertion of a spatial filter. ASE can also propagate backwards into the oscillator, affect its performance, and potentially damage it. An optical isolator based on the Faraday effect can be inserted to decouple the oscillator from the amplifier.

In a double-pass amplifier the use of a SBS mirror instead of a highly reflective mirror is an effective means of suppressing ASE. Until the threshold is reached the

reflectance of the SBS mirror is essentially zero. As the SBS process is turned on by the incoming field, the energy stored in the laser rod is rapidly consumed by the laser emission.

In a flashlamp-pumped system harmful pump radiation that falls within the laser wavelength can be eliminated with a filter inside the pump cavity, a specially doped flashlamp envelope, cladding of the laser material, or additives in the coolant. Usually a combination of these measures will be effective in suppressing ASE or parasitic oscillations.

4.6 Self-Focusing

Self-focusing is a consequence of the dependence of the refractive index in dielectric materials on the light intensity. When an intense beam propagates through a laser medium its intensity profile generates a corresponding phase profile through the intensity-dependent refractive index. The phase shift resulting from the nonlinearity leads to whole beam self-focusing and small scale self-focusing. Whole beam self-focusing extends over the whole wave front and leads to a narrowing of the beam profile, small scale self-focusing increases the modulation depth between individual noise peaks and the average background intensity.

Changes in the refractive index can be described to first order by the equation

$$\Delta n_0(E) = n_0 + \Delta n_0 \quad (4.44)$$

with

$$\Delta n_0 = n_2 \langle E^2 \rangle = \gamma I, \quad (4.45)$$

where n_0 and n_2 are the linear and nonlinear refraction index, respectively, γ is the nonlinear refractive coefficient, E is the electric field strength, and I is the beam intensity. In the literature the nonlinear optical term is expressed by either n_2 or γ , the conversion is

$$\gamma [\text{cm}^2/\text{W}] = 4.19 \times 10^{-3} n_2 / n_0 [\text{esu}]. \quad (4.46)$$

From (4.45) it follows that a laser beam propagating in a transparent medium induces an increase in the index of refraction by an amount proportional to the beam intensity.

For optical glass a typical value of the nonlinear refractive coefficient is $\gamma = 4 \times 10^{-7} \text{ cm}^2/\text{GW}$. Thus at a power density of 2.5 GW/cm^2 the fractional index change is 1 ppm. Although a change of this magnitude seems small, it can dramatically affect beam quality and laser performance.

Since laser beams tend to be more intense at the center than at the edge, the beam is slowed at the center with respect to the edge and consequently converges. If the path through the medium is sufficiently long. The beam will be focused to a small filament by whole beam self-focusing and the medium will usually break down via avalanche ionization. This convergence is limited only by the dielectric break-down of the medium. Because of this intensity-induced index change, small beams (5 mm

or so) tend to collapse as a whole (whole-beam self-focusing), forming a damage track in the material when the intensity exceeds the damage level.

Small-scale self-focusing increases the contrast across the beam profile, and small intensity ripples or irregularities will grow quickly in amplitude and lead to individual damage tracks. Therefore, large beams tend to break up into a number of filaments.

A variety of physical mechanisms result in intensity-dependent contributions to the refractive index, such as electronic polarization, electrostriction, and thermal effects. The latter two mechanisms are responsible for stimulated Brillouin and Rayleigh scattering that form the basis for optical phase conjugation treated in Chap. 10. For short-pulse operation in solids, electronic polarization, also called the optical Kerr effect, which is caused by the nonlinear distortion of the electron orbits around the average position of the nuclei, usually dominates. The optical Kerr effect is utilized in Kerr lens mode-locking discussed in Chap. 9. Here we treat the negative aspects of this physical process as far as the design of lasers is concerned.

4.6.1 Whole-Beam Self-Focusing

Whole-beam self-focusing of laser radiation occurs when the focusing effect due to the intensity-dependent refractive index exceeds the spreading of the beam by diffraction. For a given value of n_2 , two parameters characterize the tendency of a medium to exhibit self-focusing. The first, the so-called critical power of self-focusing, is the power level that just compensates for diffraction spreading. The second is the focusing length that represents the distance at which an initially collimated beam will be brought to a catastrophic self-focus within the medium for power levels in excess of the critical power.

A first-order description of the phenomenon can be obtained by considering a circular beam of constant intensity entering a medium having an index nonlinearity Δn proportional to power density. We define the critical power P_{cr} to be that for which the angle for total internal reflection at the boundary equals the far-field diffraction angle. The critical angle for total internal reflection is

$$\cos \Theta_c = \frac{1}{1 + (\Delta n_0/n_0)}. \quad (4.47)$$

If we expand the cosine for small angles and the right-hand side of (4.47) for small $\Delta n_0/n_0$, we obtain

$$\Theta_c^2 = 2\Delta n_0/n_0. \quad (4.48)$$

The beam expands due to diffraction with a half-cone angle according to

$$\Theta_D \approx 1.22 \frac{\lambda_0}{n_0 D}, \quad (4.49)$$

where D is the beam diameter and λ_0 is the wavelength in vacuum. For $\Theta_c = \Theta_D$, and with

$$P = I(\pi/4)D^2 \quad (4.50)$$

one obtains from (4.45, 48, 49) the critical power

$$P_{\text{cr}} = a \frac{\lambda_0^2}{8\pi n_0 \gamma}, \quad (4.51)$$

where $a = (1.22 \pi)^2$

A more realistic approach defines the critical power at which a Gaussian beam eventually undergoes catastrophic self-focusing. Compared to a flat-top beam, a Gaussian beam has a lower beam divergence and higher peak intensity at the center. Therefore, one would expect self-focusing to occur at a much lower value of beam power compared to a plane wave. Indeed, numerical calculations show that the critical power for a Gaussian beam has a value for the factor a of 3.77–4 depending on the approximations [4.35, 36].

With the assumption that the shape of the amplitude profile is unchanged under self-focusing, one finds the following relation between power and self-focusing length; For a Gaussian profile whose spot size $w(z)$ changes by a scale factor $f(z) = w(z)/w_0$, the width of the beam varies with z according to [4.37].

$$f^2(z) = 1 - \left(\frac{P}{P_{\text{cr}}} - 1 \right) \left(\frac{\lambda z}{\pi w_0^2} \right)^2, \quad (4.52)$$

where w_0 is the beam waist radius at the entrance of the nonlinear material. For $P \ll P_{\text{cr}}$ this expression is identical to (5.5) and describes the divergence of the beam determined by diffraction. For a beam with $P = P_{\text{cr}}$ diffraction spreading is compensated for by self-focusing and $f(z) = 1$, for all z ; this is referred to as self-trapping of the beam. For larger powers $P > P_{\text{cr}}$ self-focusing overcomes diffraction and the beam is focused at a distance

$$z_f = \frac{\pi w_0^2}{\lambda_0} \left(\frac{P}{P_{\text{cr}}} - 1 \right)^{-1/2} \approx w_0 (2n_0 \gamma I_0)^{-1/2}. \quad (4.53)$$

As can be seen, the self-focusing length is inversely dependent on the square root of the total laser power. Equation (4.53) may be used even when the constant phase surface passing through $z = 0$ is curved, corresponding to a converging or diverging incident beam. One need only replace z_f by

$$z_f(R) = (1/z_f - 1/R)^{-1}, \quad (4.54)$$

where R is the radius of curvature of the incident phase surface ($R < 0$ for converging beams) and $z_f(R)$ is the new position of the self-focus.

Of course, (4.53) is only valid when the length of the medium is greater than z_f so that catastrophic self-focusing can occur. If the medium is shorter, it acts as a nonlinear lens. If the medium is so short that the beam profile does not change significantly, the equivalent focal length of the nonlinear lens is

$$f = \frac{w_0^2}{4\gamma I_0 l}, \quad (4.55)$$

Table 4.2. Linear and nonlinear refractive index and coefficient for various optical materials

Material	Refractive index n_0	Nonlinear refractive index n_2 (10^{-14} esu)	Nonlinear refractive coefficient γ (10^{-16} cm 2 /w)
BK-7	1.52	14.6	4.0
SiO ₂	1.48	7.4	2.1
LG-680	1.56	16.0	4.3
LSG-91H	1.55	15.8	4.3
LG760	1.51	10.2	2.8
LHG-5	1.53	12.8	3.5
YAG	1.83	30	6.9
Al ₂ O ₃	1.76	13	3.2
CaCO ₃	1.59	11	2.9
KTP/KTA	1.77	100	23.7
BBO	1.6	11	2.9
LiNbO ₃	2.2	48	9.1

where I_0 is the peak intensity and l is the length of the medium. This equation is the same as (9.18) which will be used in the section on Kerr lens mode-locking.

The laser designer is primarily interested in the threshold for self-focusing, since it is an effect he seeks to avoid rather than to study. Therefore, particular interest is attached to the values of n_2 for subnanosecond pulses in laser media. Several workers have measured the effective value of n_2 in various materials for pulses from 20 to 250 ps duration. It was reported that the results obtained were not very sensitive to pulse duration. Table 4.2 contains a summary of published values of n_2 and γ for several important optical materials [4.38, 39].

BK-7 and fused silica (SiO₂) are widely used for lenses and mirrors, the next four materials are Nd doped silicate and phosphate laser glasses, the host materials YAG and Al₂O₃ are used in a number of doped laser crystals, and the last group in Table 4.2 represent crystals employed in polarizers (calcite), harmonic generators and Q-switches.

4.6.2 Examples of Self-focusing in Nd:YAG Lasers

In the past, optical damage due to self-focusing was mainly an issue in large Nd:glass laser systems designed for inertial confinement fusion. Improvements of the damage threshold of optical coatings, and of the optical quality of crystals, in combination with advanced resonator designs and diode pumping, have considerably increased the beam brightness obtainable from solid-state lasers. As a result, modern Nd:YAG oscillators and amplifiers are operated at peak powers and fluence levels which can cause self-focusing. In diode-pumped system, catastrophic self-focusing can actually be observed under certain conditions, because optical breakdown manifests itself by generation of bright flashes in the laser crystal. In flashlamp-pumped lasers, these flashes are obscured by the pump light. Even in diode-pumped lasers it is not always possible to see these flashes, particularly if the ends of the laser rod are located deep inside the laser head.

In our lasers we have seen these bright light flashes to occur in both oscillator and amplifier stages. Close examination of the laser crystal reveals tiny damage tracks which are very difficult to see and do not seem to affect laser performance. After many hours of operation the Nd:YAG crystal will show gray tracks which eventually lead to a performance degradation. In glass, catastrophic self-focusing leads to a highly visible streak of bubbles. In Nd:YAG, because of the high melting temperature and high material strength, the bubbles tend to be very small. Also, we believe, because Nd:YAG is a single crystal, a certain amount of recrystallization and annealing may take place after each optical breakdown. The gray tracks are most likely caused by color centers which are created by absorption of UV radiation emitted during the electron avalanche process.

Arisholm [4.40] reported the occurrence of light flashes and associated damage tracks in a Nd:YAG oscillator rod and explained it as the result of catastrophic self-focusing. He also provided a simulation model which reproduces self-focusing of short spikes and computes the probability of an event consistent with the observed rate of flashes in his laser. Multi-longitudinal mode operation can lead to intensity peaks due to mode-beating. Such a spike can be powerful enough to produce intensity-induced self-focusing which then builds up on successive passes through the resonator. Eventually the reduction in beam cross-section during each round trip increases the power density to the point of optical breakdown.

The laser in which damage tracks and flashes were observed had a pulse energy of 45 mJ and a pulse width of 30 ns. Temporal pulse shapes and the occurrence of flashes were correlated, and it was observed that smooth pulses never caused beam collapse, whereas pulse shapes with superimposed spikes did frequently lead to catastrophic self focusing. The detection system was not fast enough to measure the width of individual spikes, but based on the bandwidth of the laser, spikes were assumed to have a width on the order of 40 ps. The peak intensity of the beam incident on the output mirror was calculated to be 90 MW/cm^2 and the $(1/e^2)$ beam radius was 1.5 mm. The average intensity in the resonator is not high enough to start self-focusing in the laser crystal. With a 10-cm-long Nd:YAG rod and a 2.5-cm-long LiNbO₃ crystal, and using the values for n_2 for both materials from Table 4.2, one obtains from (4.55) a combined focal length due to self-focusing of about $f = 25 \text{ m}$. For the intensity, a value of $I_0 = 270 \text{ MW/cm}^2$ has been introduced into (4.55) because in counter propagating beams, the return beam contributes twice as much to the refractive index change as the forward wave [4.41].

Because of multi-longitudinal mode operation, there can be random spikes of much higher intensity. Some of these spikes can be high enough to cause a collapse of the beam due to self-focusing. The simulation was run with different spike intensities and it revealed that a spike with an initial intensity about 12 times the mean intensity will cause catastrophic self-focusing. Assuming such a spike, the new focal length of the nonlinear lens, comprising the Nd:YAG rod and Pockels cell, is on the order of $f = 6 \text{ m}$. This value is obtained by introducing a value of $I_0 = 1.1 \text{ GW/cm}^2$ into (4.55), for a spike circulating in the resonator, the effect of counter-propagating fields can be ignored. The short spike is not likely to meet an equivalent spike circulating in the opposite direction through the nonlinear medium.

This new focal length is short enough to have a significant effect on a spike that propagates for many round trips. If the spike gets focused, the effect of the nonlinearity will grow for each round trip because the peak intensity increases. Because of the reduction in beam diameter, the spike reached a peak intensity around 40 GW/cm^2 at which point catastrophic self focusing occurred. The probability that the field in the resonator has a spike exceeding a certain value has been addressed also in [4.40]. It was assumed that the laser was running on more than 100 modes based on the spectral width. Interference between these modes can give rise to short spikes with high intensity. The intensity of a spike relative to the mean intensity is proportional to the number of modes interfering in phase. The analysis assumes lasing on multiple longitudinal modes with independent random phases and uniform probability distribution. If the number of modes is large, and the output is not dominated by a few modes, the probability that the average field $\langle E \rangle = \sigma$ has a spike exceeding a value $E = \beta\sigma$ during a round trip time t_r , of the resonator is given by [4.42]

$$P_t(\beta) = \frac{t_r}{\tau_c} \sqrt{\frac{4 \ln 2}{\pi}} \beta e^{-\beta^2}, \quad (4.56)$$

where τ_c is a correlation time of the signal. The laser has a spectral width of 20 GHz indicating a correlation time of about 50 ps. With $t_r/\tau_c = 150$ for the laser described above, the probability for a spike to occur with an intensity 12 times the average ($\beta = 3.5$) is $P_t(3.5) = 2.4 \times 10^{-3}$. Since the laser is operated at 20 Hz, one would expect to observe 2.9 spikes per minute. A number which was in agreement with observation.

In one of our diode-pumped MOPA high-brightness military lasers we observed initially a light flash about every second in the last amplifier stage. The system comprised an oscillator and two amplifier stages with Faraday rotators between stages for isolation. The system was folded by three corner cubes into a very small compact system. The complete laser system contained 47 individual pieces of optics such as laser rods, Porro prisms, waveplates, lenses, alignment wedges, polarizer, Faraday rotators, Q-switch, windows, etc. The complete optical train from the rear mirror of the oscillator to the exit window contained a total of 46 cm of Nd:YAG crystals, 42 cm of glass, and 6 cm of other crystalline material such as LiNbO₃, calcite, and BBO. The laser produced 1 J of output in a 16 ns long pulse from a 9 mm diameter aperture. The beam quality was $5 \times$ diffraction limited.

The bright light flashes emerging from the laser crystal in the last amplifier stage could be clearly seen, because the rod ends protruded from the laser head. The laser was run for many hours during initial alignment, system tests, and in performing nonlinear conversion experiments before the issue of self-focusing could be addressed. No measurable degradation in performance was observed during this time. Clearly the large amount of glass and crystalline material in this laser provides an ideal medium for self-focusing to occur. We believe catastrophic self-focusing was caused by a combination of temporal spikes forming in the oscillator as a result of longitudinal mode interference, and small ripples on the spatial beam profile due to diffraction effects.

Self focusing was eventually eliminated by incorporating several of the measures indicated in Sect. 4.6.4.

4.6.3 Small-Scale Self-Focusing

Actual laser beams do not have perfectly smooth envelopes as was assumed in treating whole-beam self-focusing. Experimentally it is found that beams containing amplitude irregularities on propagating in a nonlinear medium eventually break up into separate filaments. This nonlinearity of the refractive index gives rise to so-called small-scale ripple growth, in which case the amplitude of small perturbations grows exponentially with propagation distance.

Surface irregularities of optical components are the source of phase perturbations, which cause small-scale amplitude modulation. The intensity dependent refractive index provides the coupling mechanism between a weak ripple wave and a copropagating strong pump beam. Diffraction of the powerful laser beam by the phase-grating generated by the ripple wave will spill energy into the weak beam. As a result of the coupling between the amplitude noise and the laser radiation via the nonlinear index, the amplitude ripples grow exponentially.

A theory first suggested by Bespalov [4.43] treats self-focusing as an instability phenomenon wherein an initial perturbation (e.g., dust, refractive index inhomogeneities), no matter how small, grows to what are ultimately catastrophic proportions. Linear stability theory predicts that a small, one-dimensional intensity modulation of spatial wave number Λ , superimposed upon a uniform intensity background, will undergo approximately exponential growth with a gain coefficient g given by [4.44]

$$g = \Lambda \left(\gamma I - \frac{\Lambda^2 \lambda_0^2}{16\pi^2} \right)^{1/2}, \quad (4.57)$$

where λ_0 is in the wavelength in the medium and γ is the nonlinear refractive coefficient. For a range of Λ from 0 to $(4\pi/\lambda_0)(\gamma I)^{1/2}$, g is real and the ripples grow exponentially. The maximum growth rate occurs at

$$\Lambda_m = (2\pi/\lambda_0)(2\gamma I)^{1/2} \quad (4.58)$$

and has a value

$$g_m = (2\pi/\lambda_0)\gamma I. \quad (4.59)$$

An initial perturbation $\delta = |\delta E_0|/E_0$ of the fastest growing instability mode leads to self-focusing at a distance given by [4.45]

$$z_f = \frac{\ln(3/\delta)}{g_m}. \quad (4.60)$$

The validity of the linearized theory of small-scale self-focusing was verified by Bliss *et al.* [4.46] who used a shear plate interferometer to generate a perturbation of known amplitude and spatial frequency on an intense beam. It was found that the theory provided an accurate description of the modulation growth.

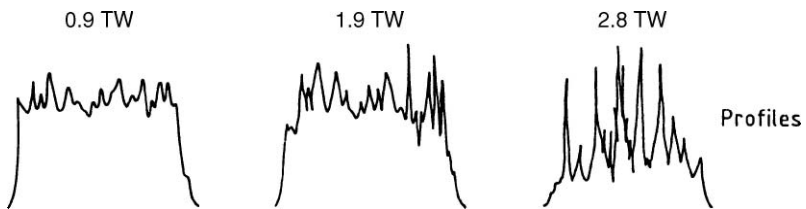


Fig. 4.35. Beam profiles of a large Nd:glass laser amplifier showing progressive modulation growth (small scale beam breakup) as the power is increased [4.47]

For a $1.06\text{-}\mu\text{m}$ laser beam with an intensity of 10 GW/cm^2 that is propagating through a section of glass with a nonlinear refractive coefficient of $\gamma = 2.8 \times 10^{-7}\text{ cm}^2/\text{GW}$ we obtain from (4.58, 59) a gain coefficient of $g_m = 0.17\text{ cm}^{-1}$ for a disturbance having a spatial wave number of $\Lambda = 140\text{ cm}^{-1}$. Assuming that the disturbance has a depth of modulation of 1% ($\delta = 0.01$), then according to (4.60) to the perturbation will focus at a distance of $z_f = 35\text{ cm}$.

Figure 4.35 illustrates the progressive growth of beam modulation as the power is increased in high-power glass lasers. The exponential growth of ripples in a high-peak-power system, if left uncontrolled, will quickly lead to component damage and beam degradation.

Integration of (4.59) over the length of the amplifier leads to the so called *B*-integral

$$B = \frac{2\pi}{\lambda_0} \int \gamma I(z) dz. \quad (4.61)$$

The value of the *B*-integral expresses the total nonlinear phase shift over the distance z added by the amplifier.

The amplitude of the ripples or intensity irregularities grow exponentially according to

$$G = \exp(B). \quad (4.62)$$

Growth of the amplitude noise depends on the value of the *B*-integral allowed between amplifier stages. A large value can quickly lead to optical damage and beam break up. Experience has shown that *B* needs to be less than about 2 to avoid unacceptable noise ripple growth [4.48, 49]. Therefore control of nonlinear ripple growth is an essential part of the design and operation of high power Nd:glass lasers. The selection of laser glasses with low nonlinear indices is an important design consideration.

4.6.4 Suppression of Self-Focusing

A number of steps can be taken to avoid the occurrence of self-focusing in a high power laser system. Self-focusing depends on the quality of the input beam, the amount of intensity fluctuations added by the amplifier, peak power, and the effectiveness of spatial filters in removing unwanted modulation.

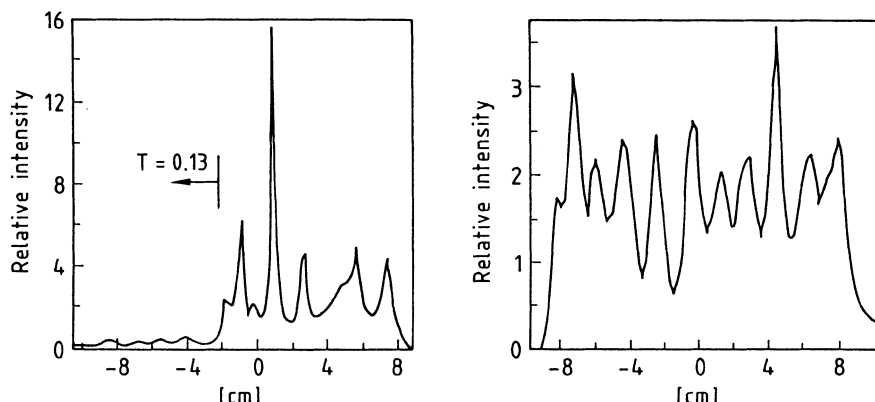


Fig. 4.36. Relative intensity of one beam line of the SHIVA system at 1.5 TW, before and after installation of the output spatial filter [4.50]

Ideally, the input beam to the amplifier system should have a smooth profile that is free of temporal intensity spikes or spatial irregularities and fluctuations. The most effective way of generating a smooth input pulse is the design of an injection-seeded oscillator operating at a single transverse and longitudinal mode. Mode-beating, causing spatial and temporal intensity fluctuations of the input beam, is eliminated in such an oscillator.

If single longitudinal mode operation cannot be implemented, a noticeable reduction of temporal spikes, caused by longitudinal mode-beating, can be achieved by insertion of a thin nonlinear crystal into the oscillator. The nonlinear crystal which acts as a dynamic limiter is chosen to convert only a few percent of the average intensity into the second harmonic, but represents a large nonlinear loss for high-peak intensities that can occur randomly.

As already discussed in Sect. 4.4.1, diffraction effects leading to intensity modulation of the pulse envelope have to be minimized by selecting the appropriate beam size and shape. Residual diffraction rings can be removed by a vacuum spatial filter.

As was already mentioned, spatial filters accomplish the task of removal of unwanted ripples, imaging, and beam magnification. A spatial filter is a low-pass filter, where the pin-hole diameter limits high spatial frequencies that can be passed. The spatial filter is designed to remove the most damaging ripples while passing most of the energy. Therefore ripples, rather than growing exponentially, are reset at each spatial filter. Figure 4.36 shows the relative intensity of one Shiva beam line before and after installation of a spatial filter at the output. As one can see from these densitometer scans, the intensity of the high-frequency spike was reduced by a factor of 4 by the low-pass filter.

Spatial filters are not only incorporated into large Nd:glass laser systems, but also in a number of commercial MOPA lasers.

Since n_2 depends on intensity, reducing the peak power by using a pulse as long as is consistent with the intended application is very helpful in suppressing

self-focusing. For example, to avoid component damage by self-focusing, amplification of femtosecond pulses to high energy levels is accomplished by increasing the pulse width at the input of the amplifier by many orders of magnitude, and compressing the pulse after the final amplifier. Pulse stretching and compression in chirped amplifiers will be discussed in Sect. 9.5.

Self-focusing is caused by a nonlinear refractive index that increases with beam intensity. A nonlinear phase shift introduced by a positive n_2 can be compensated by inserting a material into the amplifier section that has a real or effective negative n_2 . Several approaches have been proposed to generate such a compensating phase shift. For example, a negative nonlinear refractive index is present in semiconductors, such as GaAs, for wavelengths just longer than the absorption edge. This effect was used to suppress self-focusing in Nd:glass rods [4.51], and to cancel a positive phase shift in a chirped pulse amplifier system [4.52]. Also a negative phase shift through a cascade quadratic nonlinearity observed in BBO crystals, cut for type-I second harmonic conversion, has been investigated for eliminating self-focusing in a femtosecond Ti:sapphire laser [4.53].

5. Optical Resonator

The radiation emitted by most lasers contains several discrete optical frequencies, separated from each other by frequency differences which can be associated with different modes of the optical resonator. Each mode is defined by the variation of the electromagnetic field perpendicular and along the axis of the resonator.

It is common practice to distinguish two types of resonator modes: “Longitudinal” modes differ from one another only in their oscillation frequency; “transverse” modes differ from one another not only in their oscillation frequency, but also in their field distribution in a plane perpendicular to the direction of propagation. Corresponding to a given transverse mode are a number of longitudinal modes which have the same field distribution as the given transverse mode but which differ in frequency.

The symbols TEM_{mnq} and TEM_{plq} are used to describe the transverse and longitudinal mode structure of a wave inside the resonator for rectangular and cylindrical coordinates, respectively. The capital letters stand for “transverse electromagnetic waves” and the first two indices identify a particular transverse mode, whereas q describes a longitudinal mode. Because resonators that are used for typical lasers are long compared to the laser wavelength, they will, in general, have a large number of longitudinal modes. Therefore, the index q which specifies the number of modes along the axis of the cavity will be very high. The indices for the transverse modes, which specify the field variations in the plane normal to the axis, are very much lower and typically may be only the first few integers.

Although a resonator mode consists of a transverse and axial field distribution, it is useful to consider these two components separately because they are responsible for different aspects of laser performance. The spectral characteristics of a laser, such as line width and coherence length, are primarily determined by the longitudinal modes, whereas beam divergence, beam diameter, and energy distribution are governed by the transverse modes. In general, lasers are multimode oscillators unless specific efforts are made to limit the number of oscillating modes. The reason for this lies in the fact that a very large number of longitudinal resonator modes fall within the bandwidth exhibited by the laser transition, and a large number of transverse resonator modes can occupy the cross section of the active material.

5.1 Transverse Modes

It was the work of Fox and Li [5.1] that had the greatest impact on the development of the resonator theory. They utilized an integral equation technique to calculate the

field distributions in a resonator that are reproduced over many successive round trips. Their homogeneous Fredholm integral equation has eigen functions that describe the field dependence in the transverse direction, and the associated eigenvalues determine the diffraction loss and the phase shift of the field distribution during each transit.

A laser resonator will oscillate in what is called an eigen mode. This is the transverse intensity distribution that occurs when a round trip through the cavity ends with the same distribution (mode) with which it started, except for amplitude losses due to diffraction.

The theory of modes in optical resonators has been treated in [5.1–3]; comprehensive reviews of the subject can also be found in [5.4, 5].

5.1.1 Intensity Distribution

In an optical resonator, electromagnetic fields can exist whose distribution of amplitudes and phases reproduce themselves upon repeated reflections between the mirrors. These particular field configurations comprise the transverse electromagnetic modes of a passive resonator.

Transverse modes are defined by the designation TEM_{mn} for Cartesian coordinates. The integers m and n represent the number of nodes of zeros of intensity transverse to the beam axis in the vertical and horizontal directions. In cylindrical coordinates, the modes are labeled TEM_{pl} and are characterized by the number of radial nodes p and angular nodes l . The higher the values of m , n , p , and l , the higher the mode order. The lowest order mode is the TEM_{00} mode, which has a Gaussian intensity profile with its maximum on the beam axis. For modes with subscripts of 1 or more, intensity maxima occur that are off-axis in a symmetrical pattern. To determine the location and amplitudes of the peaks and nodes of the oscillation modes, it is necessary to employ higher order equations which involve either Hermite (H) or Laguerre (L) polynomials. The Hermite polynomials are used when working with rectangular coordinates, while Laguerre polynomials are more convenient when working with cylindrical coordinates.

In cylindrical coordinates, the radial intensity distribution of allowable circularly symmetric TEM_{pl} modes is given by the expression

$$I_{pl}(r, \phi, z) = I_0 \varrho^l [L_p^l(\varrho)]^2 (\cos^2 l\phi) \exp(-\varrho) \quad (5.1)$$

with $\varrho = 2r^2(z)/w^2(z)$, where z is the propagation direction of the beam and r, ϕ are the polar coordinates in a plane transverse to the beam direction. The radial intensity distributions are normalized to the spot size of a Gaussian profile; that is, $w(z)$ is the spot size of the Gaussian beam, defined as the radius at which the intensity of the TEM_{00} mode is $1/e^2$ of its peak value on the axis. L_p is the generalized Laguerre polynomial of order p and index l .

The intensity distribution given in (5.1) is the product of a radial part and an angular part. For modes with $l = 0$ (i.e., TEM_{p0}), the angular dependence drops out and the mode pattern contains p dark concentric rings, each ring corresponding to a zero of $L_p^0(\varrho)$. The radial intensity distribution decays because of the factor $\exp(-\varrho)$.

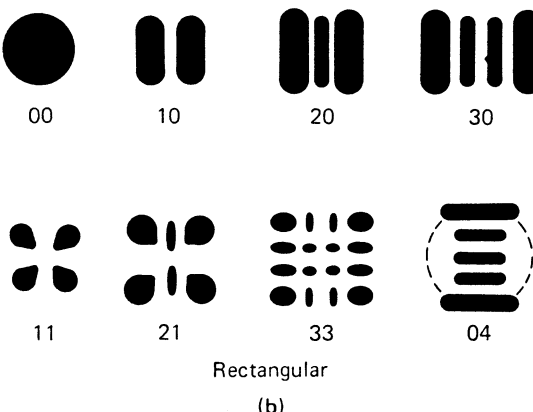
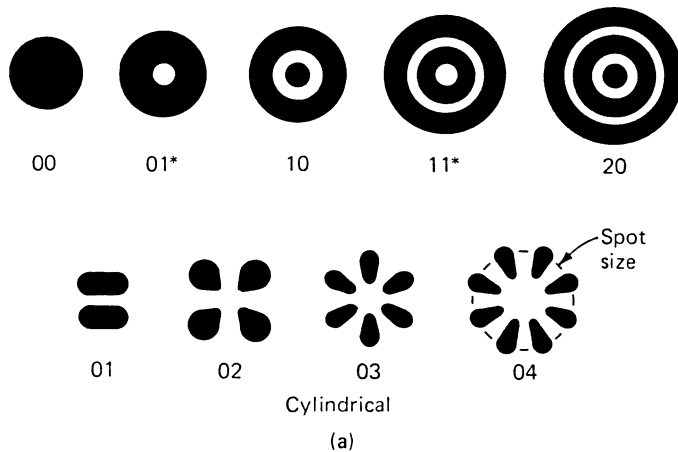


Fig. 5.1. Examples of (a) cylindrical and (b) rectangular transverse mode patterns. For cylindrical modes, the first subscript indicates the number of dark rings, whereas the second subscript indicates the number of dark bars across the pattern. For rectangular patterns, the two subscripts give the number of dark bars in the x - and y -directions [5.6]

The center of a pl mode will be bright if $l = 0$, but dark otherwise because of the factor ϱ^l . These modes, besides having p zeros in the radial direction, also have $2l$ nodes in azimuth.

The only change in a (pl) mode distribution comes through the dependence of the spot size $w(z)$ on the axial position z . However, the modes preserve the general shape of their electric field distributions for all values of z . As w increases with z , the transverse dimensions increase so that the sizes of the mode patterns stay in constant ratio to each other.

From (5.1) it is possible to determine any beam mode profile. Figure 5.1a depicts various cylindrical transverse intensity patterns as they would appear in the output

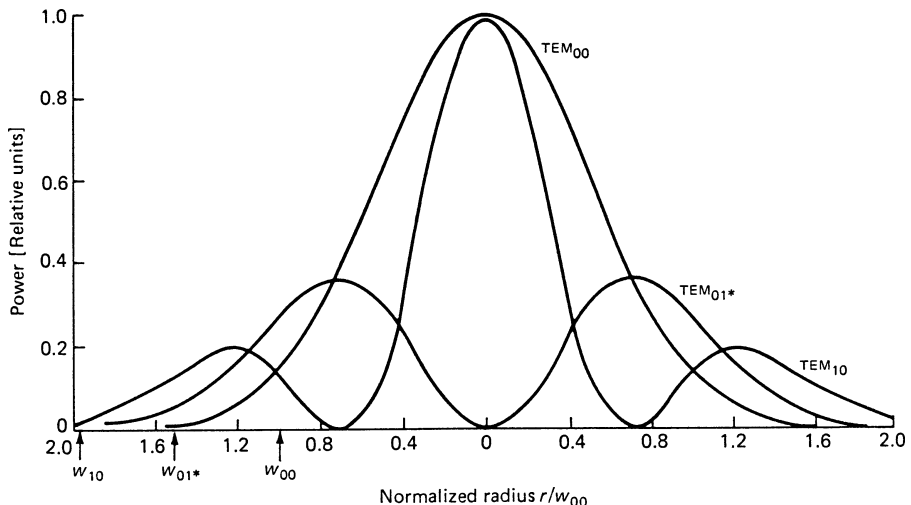


Fig. 5.2. Radial intensity distribution for TEM_{00} , TEM_{01^*} , and TEM_{10} modes. The radii are normalized to the beam radius w_{00} of the fundamental mode [5.7]

beam of a laser. Note that the area occupied by a mode increases with the mode number. A mode designation accompanied by an asterisk indicates a mode which is a linear superposition of two like modes, one rotated 90° about the axis relative to the other. For example, the TEM mode designated 01^* is made up of two TEM_{01} modes. This so-called “Donut” mode has a minimum at the center.

The intensity distribution of the modes shown in Fig. 5.1a can be calculated if we introduce the appropriate Laguerre polynomials into (5.1), that is,

$$L_0^l(\varrho) = 1, \quad L_1^0(\varrho) = 1 - \varrho, \quad L_2^0(\varrho) = 1 - 2\varrho + \frac{1}{2}\varrho^2.$$

A plot of the intensity distributions of the lowest order mode and the next two higher order transverse modes, that is, TEM_{00} , TEM_{01^*} , and TEM_{10} , is illustrated in Fig. 5.2.

In rectangular coordinates the intensity distributions of an (m, n) mode is given by

$$I_{mn}(x, y, z) = I_0 \left[H_m \left(\frac{x(2)^{1/2}}{w(z)} \right) \exp \left(\frac{-x^2}{w^2(z)} \right) \right]^2 \times \left[H_n \left(\frac{y(2)^{1/2}}{w(z)} \right) \exp \left(\frac{-y^2}{w^2(z)} \right) \right]^2. \quad (5.2)$$

As before, $w(z)$ is the spot size at which the transverse intensity decreases to $1/e^2$ of the peak intensity of the lowest order mode. The function $H_m(s)$ is the m th-order Hermite polynomial, for example, $H_0(s) = 1$, $H_1(s) = 2s$, and $H_2(s) = 4s^2 - 2$. At a given axial position z , the intensity distribution consists of the product of a function of x alone and a function of y alone. The intensity patterns of rectangular transverse modes are sketched in Fig. 5.1b. The m, n values of a single spatial mode can be

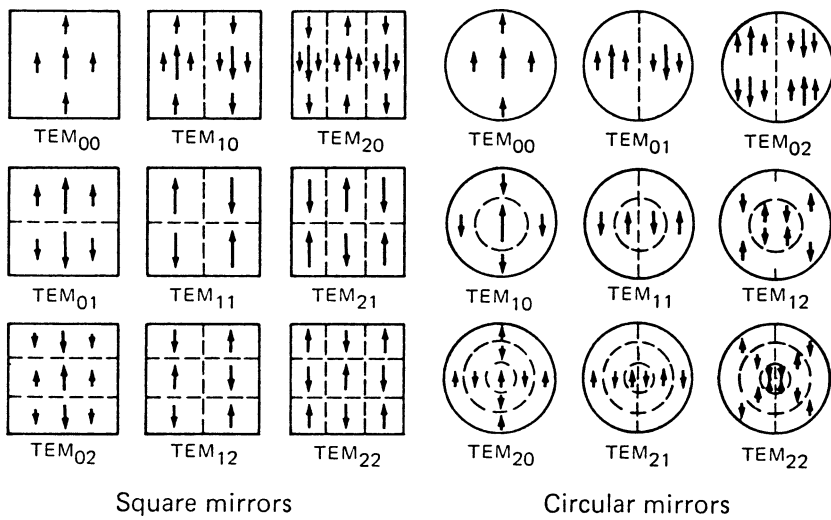


Fig. 5.3. Linearly polarized resonator mode configurations for square and circular mirrors [5.1]

determined by counting the number of dark bars crossing the pattern in the x - and y -directions. Note that the fundamental mode ($m = n = 0$) in this geometry is identical with the fundamental mode in the cylindrical geometry.

The transverse modes shown in Fig. 5.1 can exist as linearly polarized beams, as illustrated in Fig. 5.3. By combining two orthogonally polarized modes of the same order, it is possible to synthesize other polarization configurations; this is shown in Fig. 5.4 for the TEM₀₁ mode.

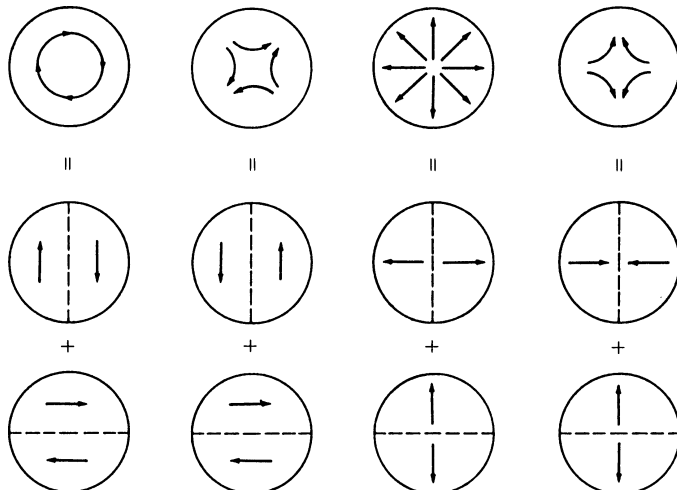


Fig. 5.4. Synthesis of different polarization configurations from the linearly polarized TEM₀₁ mode

5.1.2 Characteristics of a Gaussian Beam

A laser that operates in the fundamental or TEM₀₀ mode will emit a beam with a Gaussian intensity profile. Because of its importance it is discussed here in greater detail. The decrease of the field amplitude with distance r from the axis in a Gaussian beam is described by

$$E(r) = E_0 \exp\left(\frac{-r^2}{w^2}\right). \quad (5.3)$$

Thus, the distribution of power density is

$$I(r) = I_0 \exp\left(\frac{-2r^2}{w^2}\right). \quad (5.4)$$

The quantity w is the radial distance at which the field amplitude drops to $1/e$ of its value on the axis, and the power density is decreased to $1/e^2$ of its axial value. The parameter w is commonly called the “spot size” and $2w$ is the spot size diameter. The fraction of the total power of a Gaussian beam that is contained in a radial aperture of $r = w$ is 86.5%.

If a Gaussian beam is passed through a radial aperture of $3w$, then only $10^{-6}\%$ of the beam power is lost because of the obstruction. For our subsequent discussion, an “infinite aperture” will mean a radial aperture in excess of three spot sizes.

If we consider now a propagating Gaussian beam, we note that although the intensity distribution is Gaussian in every beam cross section, the width of the intensity profile changes along the axis. The Gaussian beam contracts to a minimum diameter $2w_0$ at the beam waist where the phase front is planar. If one measures z from this waist, the expansion laws for the beam assume a simple form. The spot size a distance z from the beam waist expands as a hyperbola, which has the form

$$w(z) = w_0 \left[1 + (z/z_R)^2\right]^{1/2}, \quad (5.5)$$

where

$$z_R = \pi w_0^2 / \lambda \quad (5.6)$$

is referred to as the Rayleigh range.

The Rayleigh range (the waist area divided by λ) is the distance from the waist for which the beam area has just doubled $w(z_R) = \sqrt{2}w_0$. An alternative term to the Rayleigh range that is also found in the literature is the confocal parameter $b = 2z_R$ or

$$b = 2(\pi w_0^2 / \lambda). \quad (5.7)$$

The distance within b can be considered the region over which the beam is approximately collimated. The asymptote of the hyperbola is inclined at an angle $\Theta/2$ with the axis, as shown in Fig. 5.5, and defines the far-field divergence angle of the emerging beam. The full divergence angle for the fundamental mode is given by

$$\Theta = \lim_{z \rightarrow \infty} \frac{2w(z)}{z} = \frac{2\lambda}{\pi w_0}. \quad (5.8)$$

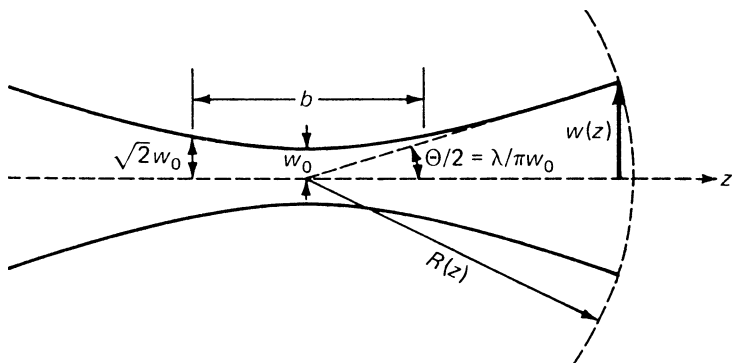


Fig. 5.5. Contour of a Gaussian beam near $z = 0$, i.e., in the vicinity of the confocal region $b = 2z_R$

From these considerations it follows that, at large distances, the spot size increases linearly with z and the beam diverges at a constant cone angle Θ . The most interesting point here is that the smaller the spot size w_0 at the beam waist, the greater the divergence.

At sufficiently large distances from the beam waist, the wave has a spherical wavefront appearing to emanate from a point on the beam axis at the waist. If $R(z)$ is the radius of curvature of the wavefront that intersects the axis at z , then

$$R(z) = z \left[1 + (z_R/z)^2 \right]. \quad (5.9)$$

The wavefront is plane for $z = 0$ and also $z = \infty$. From (5.8) follows also that the maximum curvature occurs for $z = z_R$. It is important to note that in a Gaussian beam the wavefront has the same phase across its entire surface. The $z > z_R$ regime corresponds to a spherical wave diverging from a point source at $z = 0$. The two regimes $z < z_R$ and $z > z_R$ define the near- and far-field region of the beam, respectively.

In dealing with Gaussian beams the relationship between peak power density and total power is used in several places in this book. A Gaussian beam with a peak power density I_0 at the center and a beam waist radius w_0 is characterized by

$$I(r) = I_0 \exp(-2r^2/w_0^2). \quad (5.10)$$

The total power P in the beam is obtained by integrating over the cross section

$$P = \int I(r) 2r\pi dr, \quad (5.11)$$

which leads to

$$P = \pi w_0^2 I_0 / 2. \quad (5.12)$$

For a Gaussian beam, the total power is half the peak intensity times the area defined by the beam radius w_0 .

The total power within a radius r from the axis of a Gaussian beam is obtained from (5.10)

$$P(r)/P = 1 - \exp(-2r^2/w_0^2) \quad (5.13)$$

In designing a laser for TEM₀₀ operation where the laser rod is the limiting aperture, it is usually sufficient for the rod radius to be $r = (1.5\text{--}2.0)w_0$. In this case between 98.9 and 99% of the TEM₀₀ beam power is propagated and the losses are 1.1% or less.

Before we leave the subject of Gaussian beams, we will briefly point out the difference in the definition of beam divergence for Gaussian beams and plane waves. A laser operating at the TEM₀₀ mode will have a beam divergence according to (5.8). For a plane wavefront incident upon a circular aperture of diameter D , the full cone angle of the central (Airy) disc, defined at the first minimum of the Fraunhofer diffraction pattern, is given by

$$\Theta_p = \frac{2.44\lambda}{D}. \quad (5.14)$$

The energy contained within this angle is about 84% of the total energy transmitted by the aperture. The half-cone angle of (5.14) is the Rayleigh criterion that defines the angular resolution of an optical instrument. If we assume for the Gaussian beam a diameter of $2w_0 = D$, a comparison of equations (5.8) and (5.14) indicates that the Gaussian beam has about half the beam divergence of the plane wave, whereby the Gaussian beam contains 86.5%, and the “top hat” beam 84% of the energy within the beam divergence given by these equations.

In laboratory work, a beam size is often obtained by measuring the diameter of the illuminated spot with a scale. This is not the spot size diameter $2w(z)$ as defined by (5.5). There is no obvious visual cue to the magnitude of the spot size in the appearance of the illuminated spot. Thus, “spot size” and “size of the illuminated spot” are totally different concepts. The former is a property of the laser cavity, the latter is a subjective estimate. To measure the spot size, the illuminated spot should be scanned with a photodetector behind a small pinhole. The resulting curve of intensity versus position of the pinhole will yield a Gaussian curve from which the spot size w_0 can be calculated.

Much faster results are obtained with electronic beam diagnostic instrumentation. These instruments consist of a CCD array camera, which samples the beam at the focal plane of a lens, a computer, and a beam analysis software. These instruments permit rapid 2-D or 3-D visualization of the beam profile and calculation of beam parameters.

5.1.3 Resonator Configurations

The most commonly used laser resonators are composed of two spherical or flat mirrors facing each other. We will first consider the generation of the lowest order mode by such a resonant structure. Once the parameters of the TEM₀₀ mode are known, all higher order modes simply scale from it in a known manner. Diffraction effects due to the finite size of the mirrors will be neglected in this section.

The Gaussian beam indicated in Fig. 5.6 has a wavefront curvature of R_1 at a distance L_1 from the beam waist. If we place a mirror at L_1 , whose radius of curvature equals that of the wavefront, then the mode shape is not altered. To proceed further, we can go along the z -axis to another point L_2 where the TEM₀₀ has a radius of

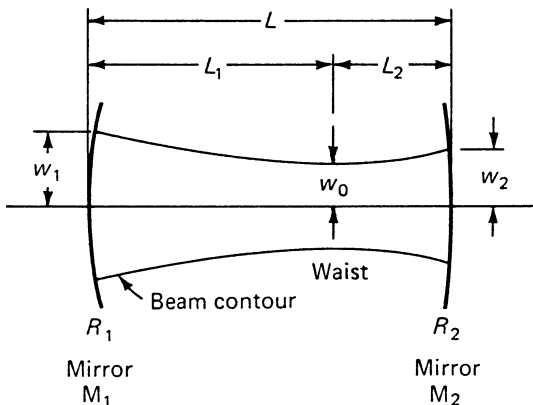


Fig. 5.6. Mode parameters of interest for a resonator with mirrors of unequal curvature

curvature \$R_2\$, and place there a mirror whose radius of curvature \$R_2\$ equals that of the spherical wavefront at \$L_2\$. Again the mode shape remains unaltered.

Therefore, to make a resonator, we simply insert two reflectors that match two of the spherical surfaces defined by (5.9). Alternatively, given two mirrors separated by a distance \$L\$, if the position of the plane \$z = 0\$ and the value of the parameter \$w_0\$ can be adjusted so that the mirror curvatures coincide with the wavefront surfaces, we will have found the resonator mode.

We will now list formulas, derived by Kogelnik and Li [5.4], which relate the mode parameters \$w_1, w_2, w_0, L_1\$, and \$L_2\$ to the resonator parameters \$R_1, R_2\$, and \$L\$. As illustrated in Fig. 5.6, \$w_1\$ and \$w_2\$ are the spot radii at mirrors \$M_1\$ and \$M_2\$, respectively; \$L_1\$ and \$L_2\$ are the distances of the beam waist described by \$w_0\$ from mirrors \$M_1\$ and \$M_2\$, respectively; and \$R_1\$ and \$R_2\$ are the curvatures of mirrors \$M_1\$ and \$M_2\$ that are separated by a distance \$L\$. Labeling conventions are that concave curvatures are positive.

The beam radii at the mirrors are given by

$$\begin{aligned} w_1^4 &= \left(\frac{\lambda R_1}{\pi} \right)^2 \frac{R_2 - L}{R_1 - L} \left(\frac{L}{R_1 + R_2 - L} \right), \\ w_2^4 &= \left(\frac{\lambda R_2}{\pi} \right)^2 \frac{R_1 - L}{R_2 - L} \left(\frac{L}{R_1 + R_2 - L} \right). \end{aligned} \quad (5.15)$$

The radius of the beam waist, which is formed either inside or outside the resonator, is given by

$$w_0^4 = \left(\frac{\lambda}{\pi} \right)^2 \frac{L(R_1 - L)(R_2 - L)(R_1 + R_2 - L)}{(R_1 + R_2 - 2L)^2}. \quad (5.16)$$

The distances \$L_1\$ and \$L_2\$ between the waist and the mirrors, measured positive (Fig. 5.6), are

$$L_1 = \frac{L(R_2 - L)}{R_1 + R_2 - 2L}, \quad L_2 = \frac{L(R_1 - L)}{R_1 + R_2 - 2L}. \quad (5.17)$$

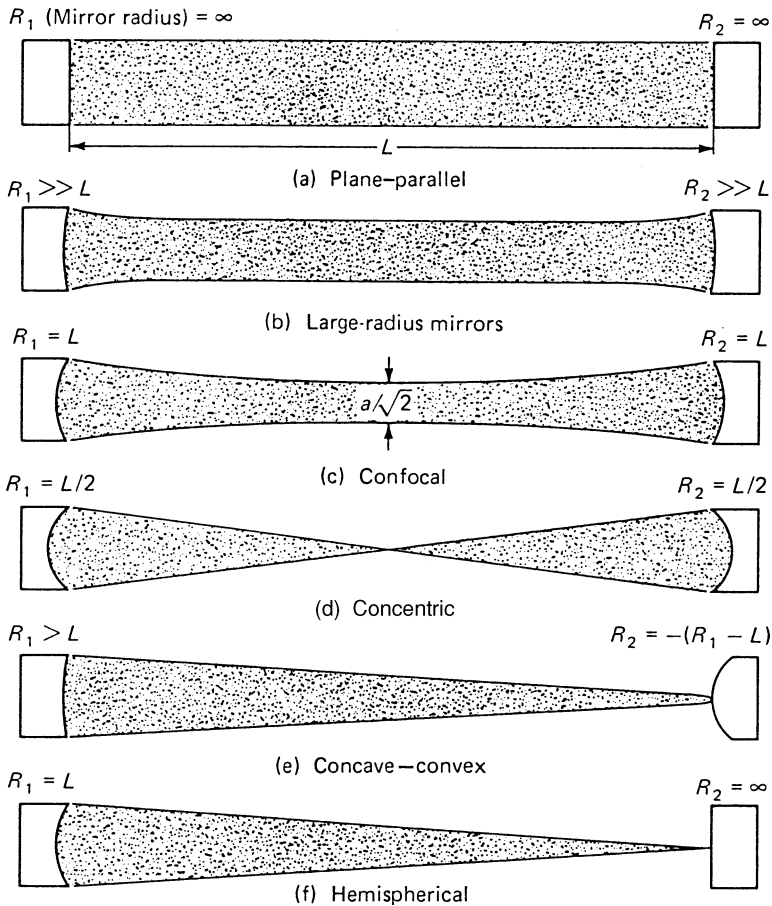


Fig. 5.7. Common resonator configurations (intracavity radiation pattern is shaded)

These equations treat the most general case of a resonator. There are many optical resonator configurations for which (5.15–5.17) are greatly simplified. Figure 5.7 shows some of the most commonly used geometries.

Mirrors of Equal Curvature

With $R_1 = R_2 = R$ we obtain, from (5.15),

$$w_{1,2}^2 = \frac{\lambda R}{\pi} \left(\frac{L}{2R - L} \right)^{1/2}. \quad (5.18)$$

The beam waist that occurs at the center of the resonator $L_1 = L_2 = L/2$ is

$$w_0^2 = \frac{\lambda}{2\pi} [L(2R - L)]^{1/2}. \quad (5.19)$$

If we further assume that the mirror radii are large compared to the resonator length $R \gg L$, the above formula simplifies to

$$w_{1,2}^2 = w_0^2 = \left(\frac{\lambda}{\pi}\right) \left(\frac{RL}{2}\right)^{1/2}. \quad (5.20)$$

As follows from (5.20), in a resonator comprising large-radius mirrors, the beam diameter changes very little as a function of distance.

A resonator comprising mirrors having a radius of curvature on the order of 2–10 m, that is, several times longer than the length of the resonator, is one of the most commonly employed configurations. Such a large-radius mirror resonator has a reasonable alignment stability and a good utilization of the active medium.

A special case of a symmetrical configuration is the concentric resonator that consists of two mirrors separated by twice their radius, that is, $R = L/2$. The corresponding beam consists of a mode whose dimensions are fairly large at each mirror and which focus down to a diffraction-limited point at the center of the resonator. A concentric resonator is rather sensitive to misalignment, and the small spot can lead to optical damage.

Another very important special case of a resonator with mirrors of equal curvature is the confocal resonator. For this resonator the mirror separation equals the curvature of the identical mirrors, that is, $R = L$. From (5.18) and (5.19) we obtain the simplified relations

$$w_{1,2} = \left(\frac{\lambda R}{\pi}\right)^{1/2} \quad \text{and} \quad w_0 = \frac{w_{1,2}}{(2)^{1/2}}. \quad (5.21)$$

The confocal configuration gives the smallest possible mode dimension for a resonator of given length. For this reason, confocal resonators are not often employed since they do not make efficient use of the active material.

Plano-Concave Resonator

For a resonator with one flat mirror ($R_1 = \infty$) and one curved mirror we obtain

$$w_1^2 = w_0^2 = \left(\frac{\lambda}{\pi}\right) [L(R_2 - L)]^{1/2} \quad \text{and} \quad w_2^2 = \left(\frac{\lambda}{\pi}\right) R_2 \left(\frac{L}{R_2 - L}\right)^{1/2}. \quad (5.22)$$

The beam waist w_0 occurs at the flat mirror (i.e., $L_1 = 0$ and $L_2 = L$ in Fig. 5.6). A special case of this resonator configuration is the hemispherical resonator. The hemispherical resonator consists of one spherical mirror and one flat mirror placed approximately at the center of curvature of the sphere. The resultant mode has a relatively large diameter at the spherical mirror and focuses to a diffraction-limited point at the plane mirror. In practice, one makes the mirror separation L slightly less than R_2 so that a value of w_1 is obtained that gives reasonably small diffraction losses.

In solid-state lasers, the small spot size can lead to optical damage at the mirror. A near-hemispherical resonator has the best alignment stability of any configuration; therefore it is often employed in low-power lasers such as HeNe lasers.

Concave–Convex Resonator

The pertinent beam parameters for concave–convex resonators can be calculated if we introduce a negative radius ($-R_2$) for the convex mirror into (5.15)–(5.17). A small-radius convex mirror in conjunction with a large-radius concave or plane mirror is a very common resonator in high-average-power solid-state lasers. As follows from the discussion in the next section, as a passive resonator such a configuration is unstable. However, in a resonator that contains a laser crystal, this configuration can be stable since the diverging properties of the convex mirror are counteracted by the focusing action of the laser rod. Since the convex mirror partially compensates for thermal lensing, a large mode volume can be achieved as will be shown in an example later in this chapter.

Plane–Parallel Resonator

The plane–parallel or flat–flat resonator, which can be considered a special case of the large-radius mirror configuration if ($R_1 = R_2 = \infty$), is extremely sensitive to perturbation. However, in an active resonator, that is, a resonator containing a laser crystal, this configuration can be quite useful. Heat extraction leads to thermal lensing in the active medium; this internal lens has the effect of transforming the plane–parallel resonator to a curved mirror configuration as explained later in this section. Therefore, the thermally induced lens in the laser material brings the flat–flat resonator into geometric stability.

Comment: Negative Lens Effect of the Output Mirror

In comparing calculated with measured mode sizes one should remember that the output mirror can change the characteristics of the emerging beam. The resonator mirrors are in most cases made from plano-concave blanks with the reflective coating on the concave surface. Such a mirror if used as the output coupler acts as a negative lens with a focal length of $f = -R/(n - 1)$. Since the radius of curvature R is usually on the order of several meters and n is about 1.5 the increase in beam divergence can in most cases be ignored.

5.1.4 Stability of Laser Resonators

For certain combinations of R_1 , R_2 , and L , the equations summarized in the previous subsection give nonphysical solutions (that is, imaginary spot sizes). This is the region where low-loss modes do not exist in the resonator.

Light rays that bounce back and forth between the spherical mirrors of a laser resonator experience a periodic focusing action. The effect on the rays is the same as in a periodic sequence of lenses. Rays passing through a stable sequence of lenses are periodically refocused. For unstable systems the rays become more and more dispersed the further they pass through the sequence. In an optical resonator operated in the stable region, the waves propagate between reflectors without spreading

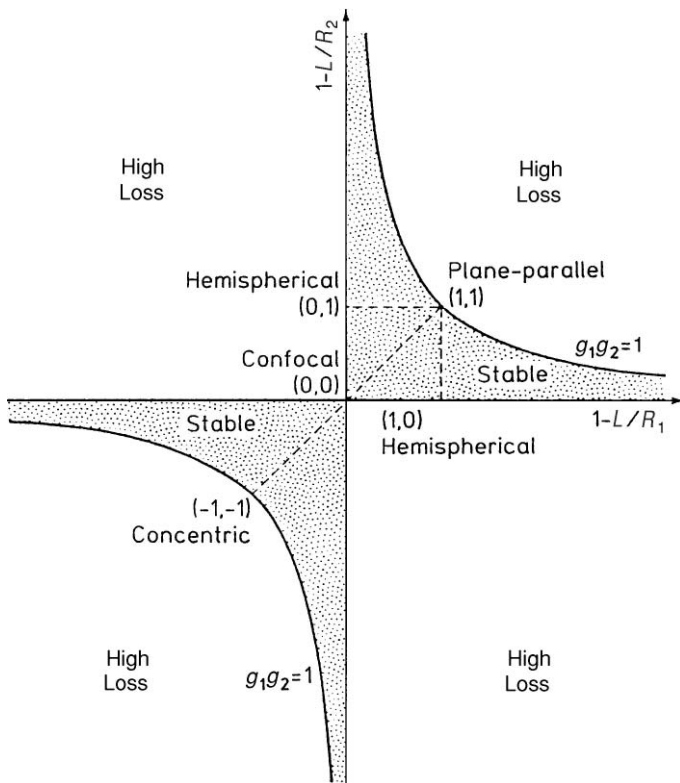


Fig. 5.8. Stability diagram for the passive laser resonator

appreciably. This fact can be expressed by a stability criterion [5.4]

$$0 < \left(1 - \frac{L}{R_1}\right) \left(1 - \frac{L}{R_2}\right) < 1. \quad (5.23)$$

To show graphically which type of resonator is stable and which is unstable, it is useful to plot a stability diagram on which each particular resonator geometry is represented by a point. This is shown in Fig. 5.8, where the parameters

$$g_1 = 1 - \frac{L}{R_1}, \quad g_2 = 1 - \frac{L}{R_2} \quad (5.24)$$

are drawn as the coordinate axes.

All cavity configurations are unstable unless they correspond to points located in the area enclosed by a branch of the hyperbola $g_1g_2 = 1$ and the coordinate axes. The origin of the diagram represents the confocal system.

The diagram is divided into positive and negative branches defining quadrants for which g_1g_2 is either positive or negative. The reason for this classification becomes clear when we discuss unstable resonators.

5.1.5 Diffraction Losses

In any real laser resonator some part of the laser beam will be lost either by spillover at the mirrors or by limiting apertures, such as the lateral boundaries of the active material. These losses will depend on the diameter of the laser beam in the plane of the aperture and the aperture radius. If we take a finite aperture of radius a within the resonator into account, the diffraction losses depend on four parameters, R_1 , R_2 , L , and a , which describe the resonator, and on three parameters λ , m , and n , characterizing the particular mode present in the resonator. Fortunately, the losses depend only on certain combinations of these parameters. These combinations are the so-called Fresnel number,

$$N = \frac{a^2}{\lambda L}, \quad (5.25)$$

and the quantities g_1 and g_2 , which were defined in (5.24). The parameter N can be thought of as the ratio of the acceptance angle (a/L) of one mirror as viewed from the center of the opposing mirror to the diffraction angle (λ/a) of the beam. That is to say, N corresponds to the number of Fresnel zones that fit within the mirror diameter viewed from the opposing mirror. The condition $N = 1$ defines a length $L = a^2/\lambda$ over which a plane wave of radius a will propagate before developing strong diffraction rings. Therefore a resonator with a Fresnel number much larger than 1 will experience minimal diffraction losses, and when N is smaller than 1 only a fraction of the beam will be intercepted by the mirrors and the losses will be high.

The fractional energy loss per transit because of diffraction effects for the lowest order mode (TEM₀₀) is shown in Fig. 5.9 for resonators with equally curved mirrors and apertures located in front of the mirrors ($g_1 = g_2 = g$, $a_1 = a_2 = a$). The plane-parallel and concentric resonator ($|g| = 1$) have the highest losses for a given aperture according to Fig. 5.9. This is not surprising because both resonator configurations have mode sizes which approach infinity at the limit. On the other hand, the confocal resonator ($g = 0$) has the smallest mode dimension for a given resonator length as discussed before. Therefore a given aperture will also cause the lowest diffraction losses. It can also be seen from Fig. 5.9 that the diffraction losses are very sensitive to changes in minor curvature, and losses decrease very rapidly for all resonator configurations as N increases.

Mode selection or discrimination of higher order modes, by choosing the appropriate Fresnel number, that is, intracavity aperture, is illustrated in Fig. 5.10. In this figure, the diffraction losses in a confocal resonator for a number of low-order modes are plotted versus the Fresnel number. For $N = 1$, only the TEM₀₀ and the TEM₀₁ modes have a power loss per transit of less than 1% per pass. All other modes have losses above 10%. A laser with this resonator would emit on only these two modes if the gain per pass were less than 10%. Single-mode emission would require a slightly smaller aperture to reduce the value of N just under 1. Going in the other direction, if the aperture is increased by about a factor of 1.4 in diameter to yield $F = 2$, then 10 modes from TEM₀₀ to TEM₀₅ have less than 1% loss per transit. This resonator would clearly have a multimode output.

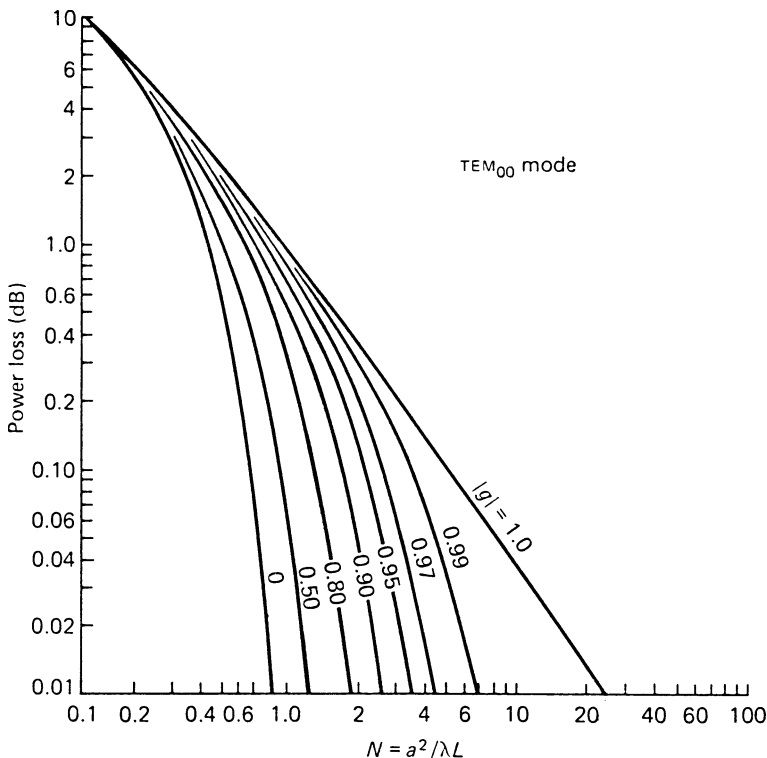


Fig. 5.9. Diffraction losses per transit for the TEM_{00} mode of various symmetrical and stable resonators [5.8]

5.1.6 Higher-Order Modes

The fundamental TEM_{00} mode has the smallest beam radius and divergence in the resonator. The beam radius of each mode increases with increasing mode number. Owing to the complicated beam patterns it is not possible to define the beam size by a $1/e$ drop in amplitude as is the case for the TEM_{00} mode. However, an idea of the relationship of beam divergence and mode structure can be obtained if one defines the spot size by a circle containing 90% of the energy for cylindrical modes, and for rectangular modes by a rectangle having dimensions of twice the standard deviation.

With these definitions we obtain for cylindrical modes [5.10]

$$w_{pl} = (2p + \ell + 1)^{1/2} w_0 \quad (5.26)$$

and for rectangular modes [5.11]

$$w_m = (2m + 1)^{1/2} w_0, \quad w_n = (2n + 1)^{1/2} w_0, \quad (5.27)$$

where p, ℓ, m, n have been defined in Sect. 5.1.1 and w_0 is the TEM_{00} mode radius.

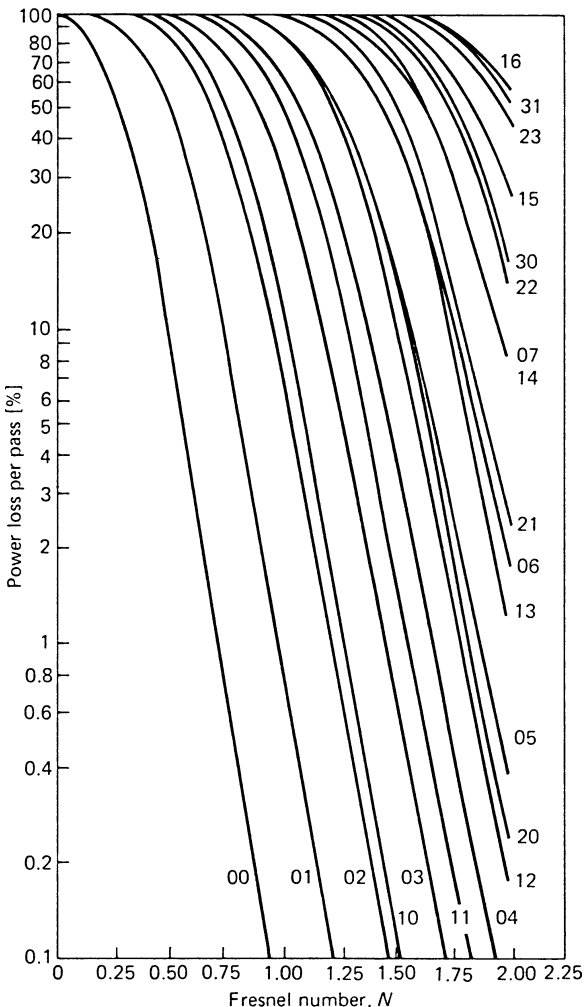


Fig. 5.10. Diffraction loss for various modes in a confocal resonator as a function of the Fresnel number [5.9]

The beam divergence of each higher order mode also increases according to the scaling law given by (5.26, 27). The increase of beam diameter and divergence of a multimode beam can be expressed by

$$\Theta = M\theta_0 \quad (5.28a)$$

and

$$D = MD_0, \quad (5.28b)$$

where the multimode beam divergence Θ and the beam diameter D are related to the fundamental mode beam parameters θ_0 and D_0 by a factor M .

It is not sufficient to characterize a laser beam only by its divergence because with a telescope it can always be reduced. The beam property that cannot be corrected by an optical system is the brightness, i.e., the beam intensity per unit solid angle. The brightness theorem states that the product of beam diameter and far-field angle is constant

$$\theta D = M^2 \theta_0 D_0, \quad (5.29)$$

where M^2 is a dimensionless beam-quality factor and θD is typically expressed as the beam-parameter product (mm mrad). A laser operating in the TEM₀₀ mode is characterized by $M^2 = 1$ and from (5.8) we obtain

$$\theta_0 D_0 = 4\lambda/\pi. \quad (5.30)$$

The value of M^2 expresses the degree by which the actual beam is “time diffraction limited” compared to an ideal TEM₀₀ beam.

For an Nd:YAG laser emitting at 1.064 μm this product is $\theta_0 D_0 = 1.35$ mm mrad. An Nd:YAG laser with a low-order mode output such as TEM₂₀ shown in Fig. 5.1 has a beam quality factor of $M^2 = 5$ or, in other words, the beam is five times diffraction-limited. The beam-parameter product is about 6.8 mm mrad.

Actually the output from a multimode laser rarely consists of a single higher order mode; typically the output comprises the incoherent superposition of several modes. Multimode beams composed of the superposition of modes with beam patterns, as shown in Fig. 5.1, have the property that the beam radius will retain a fixed ratio with respect to the Gaussian beam radius $w(z)$ over all distances. The multimode beam will therefore propagate with distance in the same form as described by (5.5) for a Gaussian beam [5.12]

$$W(z) = W_0[1 + (z/z_R)^2]^{1/2} \quad (5.31a)$$

where the Rayleigh range is now

$$z_R = \frac{\pi W_0^2}{M^2 \lambda} \quad (5.31b)$$

and $W(z)$, W_0 are multimode beam analogs to the spot sizes given in (5.5) for an ideal Gaussian beam. In the limit of a TEM₀₀ Gaussian beam $W(z) = w(z)$, $W_0 = w_0$, and $M^2 = 1$ and (5.31) reduces to (5.5).

Because the envelope of a multimode and TEM₀₀ beam change in the same ratio over distance, calculations of the propagation of a multimode beam through a resonator can first be performed for a Gaussian beam and then multiplied by $W_0/w_0 = M$ to obtain the multimode beam diameter at each point.

For lasers employed in industrial applications, the output beam is usually focused onto a workpiece. The beam quality factor M^2 determines the minimum spot size that can be achieved with a particular lens system. The spot size diameter d of a laser beam focused by a lens with focal length f is to a first approximation

$$d = f\theta, \quad (5.32)$$

where θ is the beam divergence of the laser beam. If we introduce the *f* number $F^\# = f/D$ into (5.32) we obtain

$$d = F^\# \theta D = F^\# M^2 \theta_0 D_0, \quad (5.33)$$

where D or D_0 is the diameter of the beam incident on the lens.

The focused spot size d is M^2 times larger than it would be for a TEM₀₀ Gaussian beam of the same diameter D . The intensity at the focal region is reduced by M^4 as compared to a TEM₀₀ beam.

Focusing the beam with a lens and measuring the diameter of the focal area and the beam diameter in front of the lens is a common way of determining M^2 . From (5.33) one obtains

$$d = 4M^2 \lambda f / \pi D \quad (5.34)$$

Since f and λ are known parameters, a measurement of d and D determines M^2 .

5.1.7 Mode Selection

In general, the spot size of the TEM₀₀ mode is relatively small. For example, a symmetric resonator with $R = 2$ m and $L = 1$ m has according to (5.19) a radius of the TEM₀₀ mode of $w_0 = 0.5$ mm at a wavelength of 1.06 μm. If the transverse dimension of the gain region of the active material is larger than the TEM₀₀ mode dimension, a laser oscillator will typically operate in an incoherent superposition of several modes.

Many applications of solid-state lasers require operation of the laser at the TEM₀₀ mode since this mode produces the smallest beam divergence, the highest power density, and hence the highest brightness. Furthermore, the radial profile of the TEM₀₀ mode is smooth. This property is particularly important at higher power levels, since multimode operation leads to the random occurrence of local maxima in intensity, so-called hot spots, which can exceed the damage threshold of the optical components in the resonator.

Operation at the TEM₀₀ mode requires some kind of mode control such as insertion of an aperture, expansion of the TEM₀₀ mode to fill the gain medium, or pumping only the volume occupied by the TEM₀₀ mode. In operating a laser outside the laboratory it is also important that the system is fairly robust with regard to small changes in pump input and mirror misalignment. Therefore the resonator needs to be located in the stability diagram in a region where the spot size is relatively insensitive to small changes of the resonator parameters.

A large amount of research has been devoted to the design of optical resonator configurations that maximize energy extraction from solid-state lasers at the TEM₀₀ mode. One finds that a resonator designed for TEM₀₀ mode operation will represent a compromise between the conflicting goals of large mode radius, insensitivity to perturbation, good mode discrimination, and compact resonator length.

In small- and medium-power lasers efficient TEM₀₀ mode output is achieved by concentrating the power from the diode laser pump source into a small gain region.

In lamp-pumped systems and high-power diode-pumped lasers, expansion of the TEM₀₀ by a suitable combination of the resonator parameters in combination with an intracavity aperture and operation of the resonator in a region that is less sensitive to perturbations are usually the options available for fundamental operation. Solid-state lasers with outputs in the multi-hundred watt or kilowatt regime have all multimode beams because the pump configurations required to achieve a high output power result in gain regions that are larger than the TEM₀₀ mode volume. Furthermore, severe thermally induced wavefront distortions exacerbate the problem of achieving diffraction-limited performance.

It should be pointed out that besides the mode-selecting techniques which are discussed here, it is important to have a perfectly aligned system with clean and damage-free optical surfaces. Slight misalignments, tilts, or imperfections (dust particles) of laser reflectors can cause changes in the mode character of the output, favoring higher order modes. For example, a particle or a damage spot located at the center of the beam can prevent oscillation in the TEM₀₀ mode and cause oscillation at the TEM₀₁ mode.

Insertion of an Intracavity Aperture. With a properly sized intracavity aperture higher order modes can be suppressed and the laser can be forced to operate at the TEM₀₀ mode but at the cost of substantially reduced output power and efficiency.

The diffraction losses caused by a given aperture and the transverse mode selectivity achievable with an aperture of radius a is illustrated in Fig. 5.11 [5.8]. In this figure the ratio of the loss of the TEM₁₀ mode to the loss of the TEM₀₀ mode is plotted as a function of the Fresnel number for a symmetrical resonator. Note that the mode selectivity is strongly dependent on the resonator geometry, and is greatest for a confocal resonator and smallest for the plane-parallel resonator. From Fig. 5.18 it follows that the resonator of lasers operating in the TEM₀₀ mode will have Fresnel numbers on the order of approximately 0.5–2.0. For Fresnel numbers much smaller

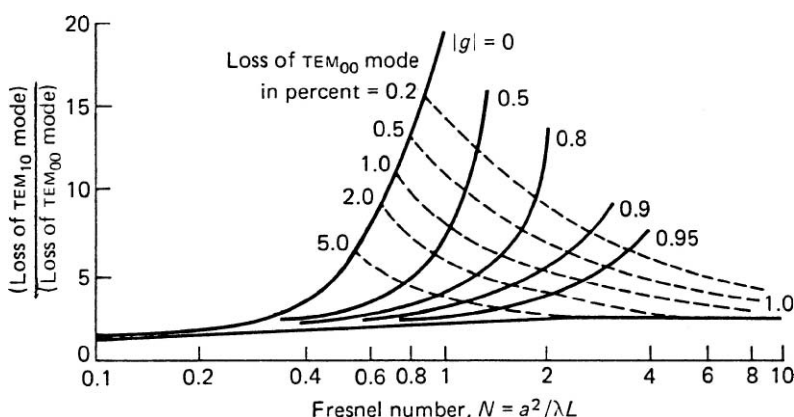


Fig. 5.11. Ratio of the losses per transit of the two lowest order modes for the symmetrical resonator. The dashed curves are contours of constant loss for the TEM₀₀ mode [5.8]

than these, the diffraction losses will become prohibitively high, and for much larger values of N mode discrimination will be insufficient.

These predictions are in agreement with the experimental observations. For example, typical Nd:YAG lasers have cavity lengths of 50–100 cm and TEM₀₀ operation typically requires the insertion of an aperture in the cavity with a diameter between 1 and 2 mm. Without an aperture, a 50-cm-long resonator with a 0.62-cm-diameter Nd:YAG rod as the limiting aperture will have a Fresnel number of 19.

To illustrate the effect of mode selection on the performance of a laser system, Fig. 5.12 presents mode patterns and radial intensity distribution from a cw-pumped Nd:YAG laser. Shown are the first six modes from the laser, which were obtained by successively increasing the mode-selecting aperture. Typical for these mode patterns is the fact that in a resonator containing a gain medium the minima of the higher order modes do not extent all the way to zero as they do in an empty resonator.

The resonator of the lamp-pumped Nd:YAG laser was composed of two 4-m-radius mirrors separated by 50 cm. The ends of the 3-mm-diameter Nd:YAG rod had concave surfaces of 5-m radius to compensate for thermal lensing. The mode patterns were taken in the far field (20 m away from the laser) by photographing the light striking a ground-glass surface through an infrared image intensifier. The radial intensity distribution of the transverse mode patterns was observed by sweeping the laser beam across a small-aperture detector using a rotating plane mirror and displaying the detector signal on an oscilloscope.

The system delivered a maximum of 8.5 W of multimode power. Mode selection was accomplished by insertion of different-sized apertures into the cavity. The various aperture sizes and the corresponding output powers, beam divergences, and mode structures are summarized in Table 5.1. From the measurement of the beam divergence follows that the TEM₀₀ mode has a diameter at the aperture of about 0.7 mm. The data show that the brightness of the laser output for higher modes decreases despite an increase in total power.

Increasing Mode Size. Because the TEM₀₀ mode has the smallest beam diameter of all the resonator modes, a number of techniques have been developed to increase the TEM₀₀ mode volume in the active material, which is normally considerably larger in diameter than the mode size. One obvious solution to increase the TEM₀₀ mode volume is to make the resonator as long as physical constraints permit, since for a given Fresnel number, the mode cross-sectional area increases proportional with length.

Another approach is to utilize resonators, such as the concentric and hemispherical configuration shown in Fig. 5.7. These resonators, owing to their focusing action, support large mode size differences along the axis. For example, in a hemispherical cavity the spot size in the limit can theoretically become zero at the flat mirror and grow to infinity for $L = R$. Location of the laser rod close to the curved mirror permits utilization of a large active volume. However, resonators with strong internal focusing suffer from several disadvantages which make them unattractive for most applications. In particular, since it is necessary to operate quite close to the edge of the optically stable region, the configurations are extremely sensitive to mechanical and optical perturbations.

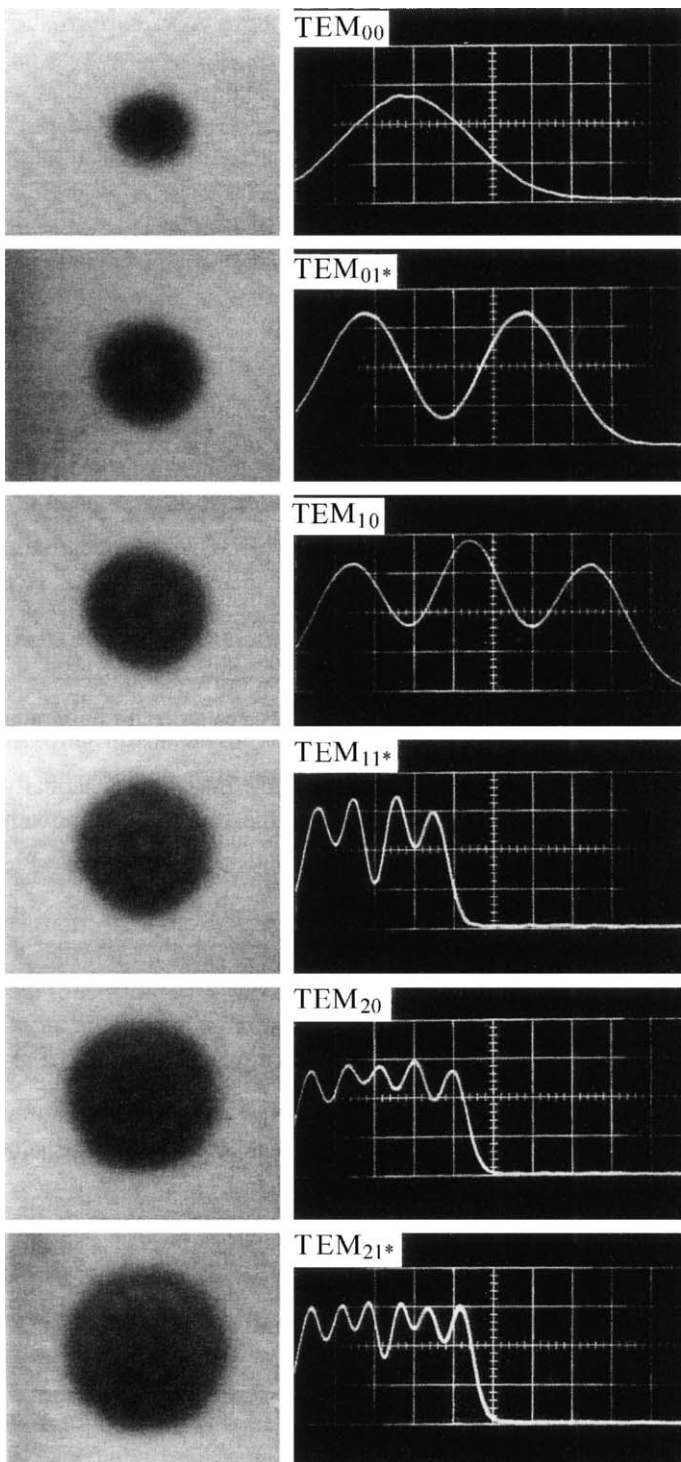


Fig. 5.12. Mode patterns and scans of the far-field beam intensity distribution of a cw-pumped Nd:YAG laser

Table 5.1. Performance of a cw-pumped Nd:YAG laser at different transverse modes

	TEM ₀₀	TEM _{01*}	TEM ₁₀	TEM _{11*}	TEM ₂₀	TEM _{21*}
Aperture size [mm]	1.4	1.6	1.8	2.0	2.2	2.3
Laser output power [W]	1.5	2.4	3.5	4.5	5.5	6.0
Beam divergence [mrad] ($1/e^2$ points)	1.9	2.3	2.8	3.1	3.4	3.6
Brightness [MW/cm ² sr]	28	18	20	18	15	15

It has long been recognized that by compensating the thermal lens induced in laser rods, one can increase the TEM₀₀ mode spot size and thus extract more energy in a diffraction-limited beam. Using a resonator with concave–convex mirrors or a resonator featuring an internal telescope are options for obtaining reliable operation with a large TEM₀₀ mode. In high-gain Q-switched lasers another option is the use of an unstable resonator. These various approaches will be discussed later in this chapter.

Spatial Match of Gain Region and TEM₀₀ Mode. In the end-pumped lasers discussed in Sects. 3.6.3, 6.2.3, and 7.3 a most elegant solution to the problem of mode selection can be implemented, namely a spatial match between the pump beam and the resonator TEM₀₀ mode. Because the beam characteristics of diode lasers allow for tight focusing of their output radiation into the active material, a near-perfect overlap between the pump or gain region and the TEM₀₀ mode volume can be achieved. Typically, the pump beam and resonator axis are oriented collinear within the active material. This way highly efficient TEM₀₀ mode operation can be achieved.

5.1.8 Active Resonator

In Sect. 5.1.3 we discussed the TEM₀₀ mode size in an empty resonator as a function of the mirror geometry. In this section we will analyze the changes that occur if a lasing medium is inserted into the resonator. In cw and high-average-power solid-state lasers the dominant effect that distorts the mode structure in a resonator is thermal lensing. Heat removed from the rod surface generates a thermal gradient. The thermally induced spatial variations of the refractive index causes the laser rod to act as a positive lens with a focal length that depends on the power dissipated as heat from the pump source.

As an introduction to the effect of thermal lensing on the resonator geometry we will first consider a thick lens. This is followed by considering a thick distributed lens that represents a laser rod. Finally at the end of the section the sensitivity of different active resonator configuration to mirror misalignment will be discussed.

Perturbation of the thermal lens of the laser rod leads mainly to changes in mode structure and beam divergence, whereas a misalignment of the resonator mirrors causes a lateral displacement and angular tilt of the output beam, which causes an increase of the diffraction losses and therefore a reduction of output power.

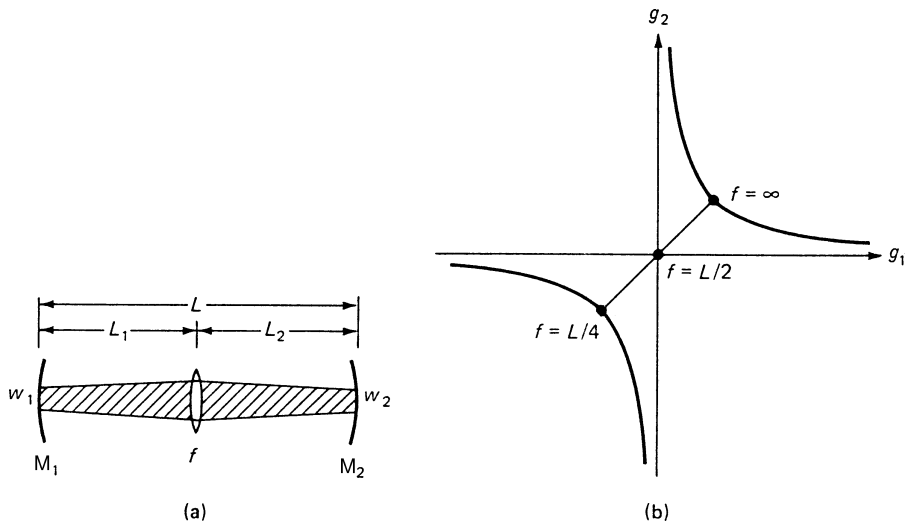


Fig. 5.13. (a) Geometry and (b) stability diagram of a resonator containing a thin positive lens

Resonator Containing a Thin Lens. The theory necessary to analyze resonators that contain optical elements other than the end mirrors has been developed by Kogelnik [5.13]. We will apply this theory to the case of a resonator containing an internal thin lens. To a first approximation, this lens can be thought of as representing the thermal lensing introduced by the laser rod.

Beam properties of resonators containing internal optical elements are described in terms of an equivalent resonator composed of only two mirrors. The pertinent parameters of a resonator equivalent to one with an internal thin lens are

$$g_1 = 1 - \frac{L_2}{f} - \frac{L_0}{R_1}, \quad g_2 = 1 - \frac{L_1}{f} - \frac{L_0}{R_2}, \quad (5.35)$$

where $L_0 = L_1 + L_2 - (L_1 L_2 / f)$ and f is the focal length of the internal lens; L_1 and L_2 are the spacings between mirrors M_1 , M_2 and the lens, as shown in Fig. 5.13a. The stability condition (5.23) remains unchanged.

For the subsequent discussions we find it convenient to express the spot sizes in terms of g_1 and g_2 . By combining R_1 , R_2 , and L with the relevant g_1 and g_2 parameters, (5.15) can be written

$$w_1^2 = \frac{\lambda L}{\pi} \left[\frac{g_2}{g_1(1 - g_1 g_2)} \right]^{1/2}, \quad (5.36a)$$

$$w_2^2 = \frac{\lambda L}{\pi} \left[\frac{g_1}{g_2(1 - g_1 g_2)} \right]^{1/2}. \quad (5.36b)$$

From (5.36) follows

$$w_1^2 / w_2^2 = g_2 / g_1. \quad (5.37)$$

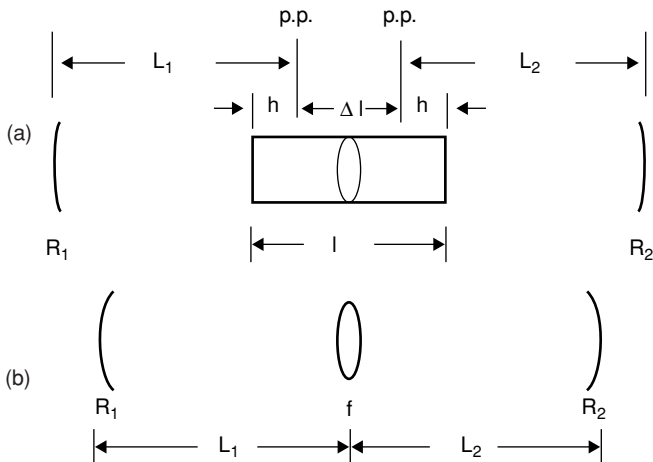


Fig. 5.14. Representation of a laser rod inside a resonator (a) and thin lens equivalent (b) Principal planes are denoted by p.p.

As an example we will consider a resonator with flat mirrors ($R_1 = R_2 = \infty$) and a thin lens in the center ($L_1 = L_2 = L/2$). From (5.35) and (5.36) we obtain

$$g = g_1 = g_2 = 1 - \frac{L}{2f}, \quad w_1^2 = w_2^2 = \left(\frac{\lambda L}{\pi}\right)(1 - g^2)^{-1/2}. \quad (5.38)$$

For $f = \infty$ the resonator configuration is plane-parallel; for $f = L/2$ we obtain the equivalent of a confocal resonator; and for $f = L/4$ the resonator corresponds to a concentric configuration.

The mode size in the resonator will grow to infinity as the mirror separation approaches four times the focal length of the laser rod. Figure 5.13b shows the location of a plane-parallel resonator with an internal lens of variable focal length in the stability diagram.

Resonator Containing a Laser Rod. A thermally stressed laser rod perturbs the mode configuration by acting as a thick distributed lens. In addition the rod increases the optical length of the resonator. In Fig. 5.14 the laser rod is approximated by a thin lens sandwiched between two pieces of material with refractive index n_0 . The distances from the mirrors are measured to the principal planes of the thick lens. In a laser rod the focal length is inversely proportional to the heat deposited. However, the position of the principal planes is independent of input power.

In Fig. 5.14a the distance of each principal plane from the end of the rod is

$$h = l/2n. \quad (5.39)$$

Since the location of the rod principal planes is independent of pump power, the rod can be treated as a thick lens, provided that the distances L_1 and L_2 are measured with reference to these planes. Since the distance between the principal planes is not

included in the equivalent thin lens resonator depicted in Fig. 5.14b, the equivalent resonator is shortened by the distance

$$\Delta l = l(1 - 1/n). \quad (5.40)$$

One has to remember that after the parameters of the resonator such as L_1 and L_2 and the spot sizes on the mirrors w_1 and w_2 have been calculated for specific values of the focal length f , the physical length of the resonator is actually

$$L_{\text{actual}} = L_1 + L_2 + l(1 - 1/n). \quad (5.41)$$

Of great interest to the laser designer is the mode size and sensitivity of the resonator to focal length changes that are the result of different pump powers. Time-varying thermal lensing manifests itself in changes of output power and beam divergence. Spot sizes of the TEM₀₀ mode inside a resonator containing an intractivity lens and sensitivity of the mode size to changes in focal length have been first studied in detail by Steffen et al. [5.14] and Chesler and Maydan [5.15]. Some of their conclusions are summarized below.

With the aid of (5.36b) we can plot curves for a fixed spot size w_2 in the stability diagram [5.14]:

$$(w_2\sqrt{\pi/\lambda L})^4 (g_2 - g_1 g_2^2) - g_1 = 0 \quad (5.42)$$

Figure 5.15 shows several curves for the normalized spot sizes $2w_2\sqrt{\pi/\lambda L}$. Inspections of these curves reveals that in the region for $g_1 > 1$, the spot size w_2 is less sensitive to variations of g_1 and g_2 compared to regions of small g_1 values. This is important because thermal lensing changes the g_1 and g_2 parameters as was shown in the previous section. In particular, the spot size is insensitive to variations of g_1 and g_2 at the extrema of the curves. The derivative dg_1/dg_2 of equaton (5.42) vanishes for

$$g_1 g_2 = 1/2 \quad (5.43)$$

Equation (5.43) represents a hyperbola that is indicated by a dashed line in Fig. 5.15. For g_1 to become larger than 1 requires R_1 to be negative. According to our convention a negative radius represents a convex mirror.

The spot sizes along the hyperbola for different values of g_2 are obtained by inserting (5.43) into (5.36).

$$w_1\sqrt{\pi/\lambda L} = g_1^{-1/2} \quad (5.44a)$$

and

$$w_2\sqrt{\pi/\lambda L} = (2g_1)^{1/2}. \quad (5.44b)$$

From (5.44) follows that for large values of g_1 the spot size will be large on mirror M₂ and small on mirror M₁. Therefore to obtain a large mode size inside the lasing medium, the distance L_2 between the mirror M₂ and the laser rod should be as short as possible. These were also the conclusions reached in [5.14, 15] by either considering changes of spot size or mirror radii as a function of focal length change.

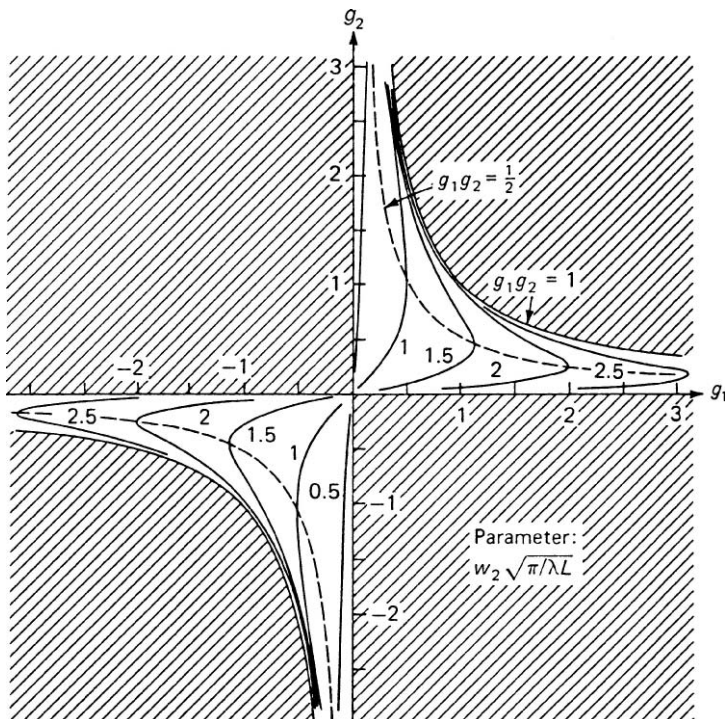


Fig. 5.15. Resonator stability diagram with curves for constant values of the normalized TEM₀₀ mode spot size $w_2(\pi/\lambda L)^{1/2}$ at one mirror

Because of the importance of the convex-concave resonator configuration, a more detailed analysis is provided later in this chapter.

Resonator Sensitivity to Mirror Misalignment. For a resonator to be aligned the mode axis must be normal to each of the two mirrors, which means the beam axis passes through the center of curvature of the mirrors. Figure 5.16 depicts a resonator composed of mirrors M₁ and M₂ with radii R₁ and R₂, respectively. The mirrors

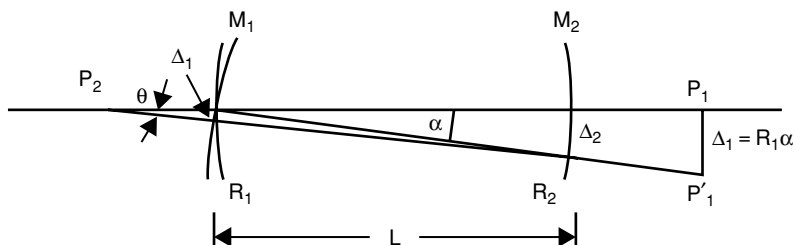


Fig. 5.16. Misalignment of mirror M₁

are separated a distance L and the center of curvature of mirror M_1 is at a point P_1 , and for mirror M_2 the center is at point P_2 . If mirror M_1 is tilted by an angle α , the center of curvature of mirror M_1 moves by $\Delta_1 = R_1\alpha$ to point P'_1 . The resonator axis is rotated by an angle θ and the center of the mode pattern is shifted by Δ_1 and Δ_2 at mirror M_1 and M_2 , respectively. From geometric considerations one obtains [5.16, 17]

$$\theta = \alpha \frac{1 - g_1}{1 - g_1 g_2} \quad (5.45a)$$

and

$$\Delta_1 = \frac{g_2 \alpha L}{1 - g_1 g_2}, \quad \Delta_2 = \frac{\alpha L}{1 - g_1 g_2}. \quad (5.45b)$$

Near the limit of stability ($g_1 g_2 = 1$) the beam steering and displacement of the mode pattern becomes large. Also the displacement increases with resonator length L . Any limiting aperture in the system such as the active medium or other optical components or apertures will cause diffraction losses that increase rapidly with increasing mirror tilt angle.

If we introduce the resonator parameters for g_1 and g_2 we can examine more closely a few typical resonator configurations. From (5.45) we obtain

$$\Delta_1 = \frac{R_1(R_2 - L)}{R_1 + R_2 - L} \alpha, \quad \Delta_2 = \frac{R_1 R_2}{R_1 + R_2 - L} \alpha. \quad (5.46)$$

The displacement of the mode axis and therefore the sensitivity of the resonator to mirror misalignment becomes larger for increasing mirror radii and also for resonators approaching the concentric configuration $R_1 + R_2 = L$.

For a resonator with large radius mirrors of equal radii $R_1 = R_2 = R$ we obtain from (5.46)

$$\Delta_1 = \Delta_2 = \frac{R\Theta}{2}. \quad (5.47)$$

Note that if one of the mirrors is slightly tilted, the entire mode is displaced parallel to the resonator axis.

For a confocal resonator ($R_1 = R_2 = L$) we have

$$\Delta_1 = 0 \quad \text{and} \quad \Delta_2 = L\Theta. \quad (5.48)$$

In this case the mirror being tilted represents the pivot point for the mode axis.

If the flat mirror of a hemispherical resonator ($R_1 \approx \infty, R_2 \approx L$) is tilted, we obtain

$$\Delta_1 = (R_2 - L)\Theta \approx 0, \quad \Delta_2 = L\Theta, \quad (5.49a)$$

which is similar to that of a confocal resonator. On the other hand, if the spherical

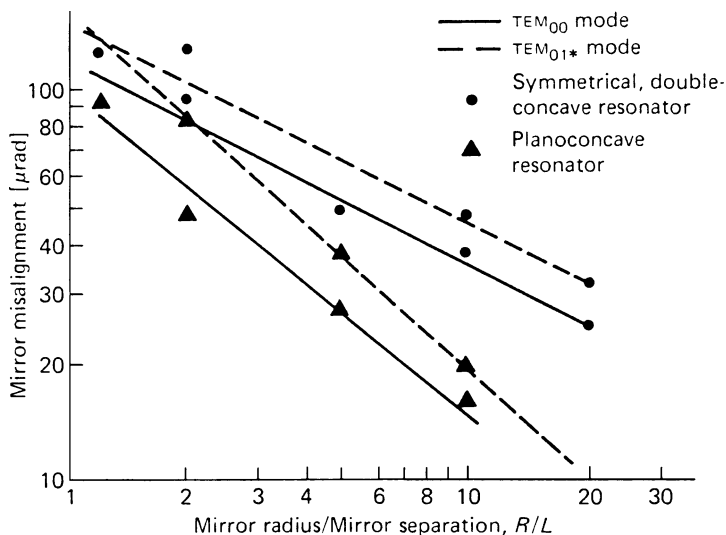


Fig. 5.17. Mirror misalignment in an argon laser which will produce a 10% drop in output power versus the normalized mirror radius. The curves show the characteristics for a symmetrical resonator with two curved mirrors and for a plano-concave resonator. Sensitivity is plotted for the TEM_{00} and TEM_{01^*} mode [5.7]

mirror is tilted ($R_1 \approx L$, $R_2 \approx \infty$), then

$$\Delta_1 \approx \Delta_2 \approx L\Theta. \quad (5.49b)$$

Comparing the sensitivity to angular tilt of the various resonator configurations, we note that, for example, a large-radius mirror resonator with $R = 10L$ is five times more sensitive to tilt than the confocal and hemispherical resonators.

In accordance with this theory, measurements performed on various lasers have shown that the alignment tolerances of a resonator with relatively short-radius mirrors is less stringent than those imposed with long-radius mirrors. Furthermore, a plano-concave resonator is more sensitive to misalignment than a resonator with two curved mirrors. Also, alignment tolerances become progressively less stringent for higher order modes. Figure 5.17 gives experimental results obtained with an argon laser [5.7]. Clearly, from these curves it follows that the higher-order mode is less sensitive to mirror misalignment and, furthermore, that the confocal resonator has the highest tolerance in terms of misalignment. Figure 5.18 shows the alignment tolerance of various types of resonators for a HeNe laser operating single mode [5.18]. Again, the confocal resonator is far more forgiving for mirror misalignment than the other types. As is apparent from this figure, the alignment tolerances for a concentric-type resonator ($L/R = 2$) and a resonator having large-radius mirrors is about the same.

Figure 5.19 shows the drop in output power of a pulsed Nd:YAG laser as a function of mirror misalignment for different mirror combinations [5.19]. As is to be expected, the resonator containing two curved mirrors is least sensitive to misalignment.

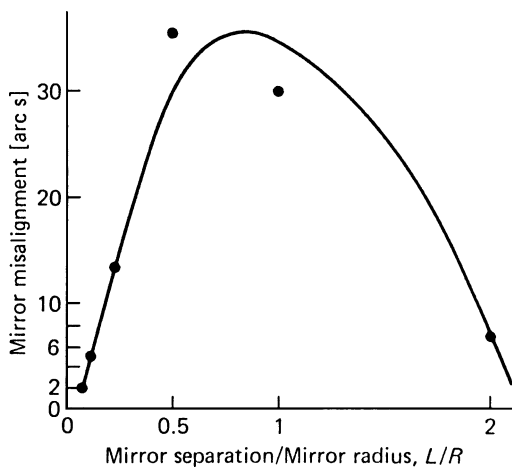


Fig. 5.18. Alignment tolerance of various types of resonators. Curve shows a reduction of output power by 50% of a He-Ne laser operated in a single transverse mode [5.18]

5.1.9 Examples of Resonator Designs

Almost all laser applications require a small beam divergence to obtain either a small spot size at the focal plane of a lens or a small illuminated area at a large range. A large

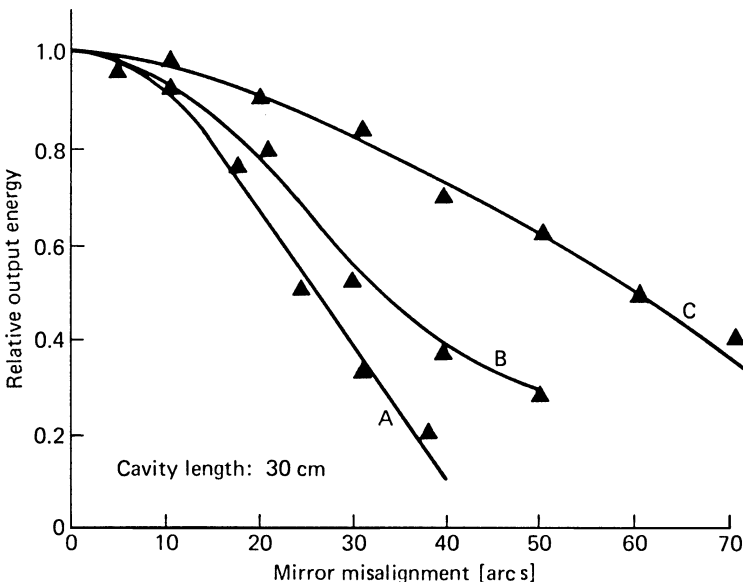


Fig. 5.19. Mirror misalignment sensitivity versus relative output power of an Nd:YAG laser. (A: two flat mirrors, B: one flat, one 10-m-radius mirror, C: two 10-m-radius mirrors). The mirror misalignment sensitivity to reduce the energy output by 10% was 12, 15, and 21 arc s, respectively. The laser, which was operated conventional mode, comprised a 5-mm by 50-mm Nd:YAG rod pumped by a single flashlamp. The cavity length was 30 cm and the front mirror was 70% reflective [5.19]

amount of research has been devoted to the design of optical resonator configurations that maximize energy extraction from the gain medium while producing a diffraction limited beam or at least a low-order mode beam.

We can establish the following criteria for the design of an efficient and practical laser system emitting a high-quality beam:

- The diameter of the TEM_{00} mode should be limited by the active material.
- The resonator should be dynamically stable, i.e., insensitive to pump-induced fluctuations of the rod's focal length.
- The resonator modes should be fairly insensitive to mechanical misalignments.

Lasers operating in the fundamental mode usually require the insertion of an aperture in the resonator to prevent oscillations of higher order modes. In this case, the efficiency of the laser is lower, compared with multimode operation, because of the small volume of active material involved in the laser action. Large-diameter TEM_{00} modes can be obtained using special resonator configurations, but if proper design criteria are not applied, the resonator becomes quite sensitive to small perturbations. Also, in solid-state lasers, thermal focusing of the rod greatly modifies the modes, and the pump-induced fluctuations of the focal length may strongly perturb the laser output, even preventing any practical or reliable use of the laser. Efficient exploitation of the rod volume of a solid-state laser operating in the fundamental mode requires the solution of two conflicting problems: The TEM_{00} mode volume in the rod has to be maximized, but the resonator should remain as insensitive as possible to focal length and alignment perturbations. Early solutions proposed compensation of the thermal lens by a convex mirror, or by negative lenses ground at the ends of the rod, that exactly eliminate the focusing effect of the rod. With these methods high power in a single-mode beam can be obtained; the compensation, however, is effective only for one particular value of the focal length. Large fundamental mode volume and good stability against thermal lens fluctuations have been achieved by a particular choice of mirror curvatures or by insertion of a telescope in the resonator.

In this section a number of resonators are discussed that are frequently employed in the design of solid-state lasers.

A near-hemispherical resonator provides a simple means of achieving a large mode size in the laser rod by moving the laser crystal toward the concave mirror until it becomes the limiting aperture. This resonator will be very sensitive to fluctuations in pump power and mechanical disturbances.

A birefringence-compensated resonator incorporates an important technique to improve beam quality and TEM_{00} mode power. As will be explained in Chap. 7, in a crystal such as Nd:YAG thermally induced lensing is associated with birefringence, which creates a thermal lens with two focal points. The beam emerging from two laser heads with a quartz rotator in between creates a thermal lens with one focal point. The combination of two laser heads with birefringence compensation can be implemented in any resonator configuration.

The concave-convex resonator is a very common configuration for achieving reasonable TEM_{00} mode size in the presence of thermal lensing. With a weakly focusing laser media the resonator is in the first quadrant of the resonator stability

diagram. Under strong focusing the resonator will be located in the third quadrant. In following certain design procedures the effects of pump fluctuations and mirror misalignment can be minimized. A disadvantage of this resonator is the small spot size at the convex mirror that can lead to optical damage.

Resonators with an internal telescope have a number of attractive features: they allow controllable adjustments to compensate thermal lensing under changing pump conditions and they avoid the disadvantage of the concave–convex mirror of having a small spot size on one of the mirrors. Particularly for Q-switched lasers a larger spot size is a big advantage because it reduces the danger of optical damage. The astigmatically compensated folded mirror resonator is important in the design of Ti:Sapphire lasers and for Kerr-lens mode locking.

The last resonator configuration discussed in this section is the crossed Porro prism, polarization coupled resonator. This is the most common resonator employed for military systems because it is the most robust design with regard to mechanical stability. In these resonators a portion of the circulating power is coupled out through a polarizer. This type of output coupling can also be implemented in any other resonator design. It has the advantage that the Q-switch for example can be located in the low-energy section of the resonator.

Near-Hemispherical Resonator. Spherical and hemispherical resonators have in common that they support large mode size differences in the resonator owing to their focusing action. For example, in a hemispherical cavity the spot size in the limit can theoretically become zero at the flat mirror and grow to infinity for $L = R$. Location of the laser rod close to the curved mirror permits utilization of a large active volume. An example of this type of resonator is indicated in Fig. 5.20 [5.20]. Mode selection in this resonator, which was employed in a cw Nd:YAG laser, is achieved by axially moving the laser rod until it becomes the limiting aperture for TEM₀₀ operation.

A simple resonator scheme, which can be used in cw experiments, is to operate the laser with two flat mirrors which are symmetrically moved farther apart until the TEM₀₀ mode power is optimized. The thermal lensing of the rod makes this resonator equivalent to a symmetrical system with strongly curved mirrors. As was discussed in Sect. 5.1.8, theoretically the mode size in the crystal will grow to infinity as the mirror separation approaches four times the focal length of the laser rod.

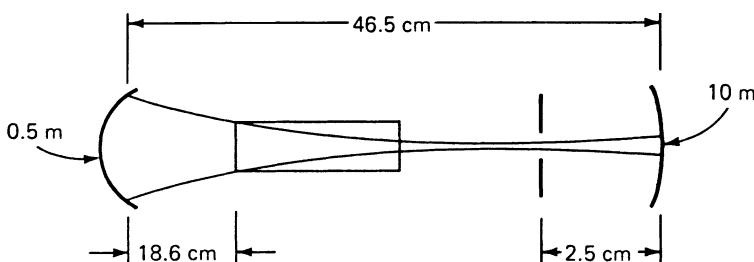


Fig. 5.20. Focusing resonator geometry

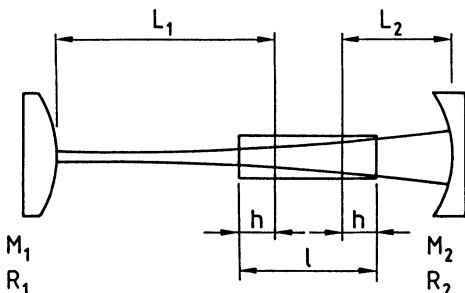


Fig. 5.21. Concave-convex resonator containing a Nd:YAG rod

Resonators with strong internal focusing suffer from several disadvantages which make them unattractive for most applications. In particular, since it is necessary to operate quite close to the edge of the optically stable region, the configurations are extremely sensitive to mechanical and optical perturbations.

Concave-Convex Resonator for a Weakly Focusing Laser Rod. In Sect. 5.1.8 we concluded that with a convex mirror at one end of the resonator one can achieve $g_1/g_2 > 1$ and independently set $g_1 g_2 = 0.5$. The first condition provides a large spot size w_2 on mirror M_2 , and the second condition minimizes the resonator sensitivity to changes of focal length. Another advantage of a concave resonator is its compactness in comparison with other resonators. Figure 5.21 illustrates a typical configuration consisting of a short-radius convex mirror at one end of the resonator, and a concave mirror at the other end of the laser rod close to it.

As an example we will calculate the parameters for a concave-convex resonator that has been used for a high repetition rate Nd:YAG laser. The laser rod, with a diameter of 5 mm, was measured to have a focal length of 6 m for a particular input. The length of the cavity was restricted to about 0.8 m. The optimum value of w_2 has been found empirically to be equal to one-half the laser rod radius. With the rod as close as possible to the output mirror, the following design parameters are obtained for the equivalent resonator (Fig. 5.21):

$$w_2 = 1.25 \text{ mm}, \quad f = 6 \text{ m}, \quad L_1 = 0.7 \text{ m}, \quad L_2 = 0.1 \text{ m}.$$

From (5.44b) we obtain a value of $g_1 = 2.9$, and from (5.43) follows $g_2 = 0.17$. The spot size on the concave mirror is obtained from (5.44a) and has a value of $w_1 = 0.31$ mm. The curvatures of the mirrors follow from (5.35). The radius of the convex mirror is $R = -0.41$ m and the concave mirror has a radius of $R = 1.1$ m. The physical length of the resonator will be 82.25 cm according to (5.41) for a 5-cm-long Nd:YAG crystal.

The design parameters for this particular laser cavity illustrate one disadvantage of the concave-convex resonator, namely, a very small spot size at the concave mirror. This small spot size, which could lead to mirror damage, effectively precludes the use of this resonator in high-power Q-switched lasers.

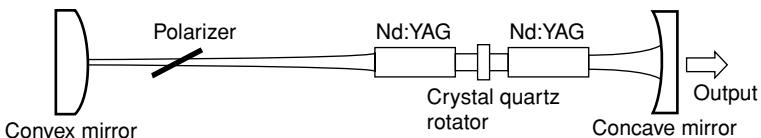


Fig. 5.22. Schematic of a birefringence-compensated resonator

Birefringence-Compensated Resonator. In a cubic crystal, such as Nd:YAG, the thermally induced stresses lead to the formation of a bifocal thermal lens. The focal length of the laser crystal is different for the radially and tangentially polarized electric fields (see Sect. 7.1 for a detailed explanation). The second focal point can be eliminated, thus leading to a better thermal compensation, if the pump head of an oscillator is separated into two smaller units and a 90° polarization rotator is placed between the laser rods. This eliminates bifocusing because the radial and tangential polarization components of the laser radiation are interchanged after the beam passes through both crystals. A two-pump head design also considerably increases the amount of polarized output that can be extracted from the laser. This is usually the main reason for this design approach.

Figure 5.22 shows an example of thermally compensated resonator designed to achieve high TEM_{00} mode output in a linearly polarized beam. The 90° quartz rotator eliminates bifocusing and the convex rear mirror of resonator compensates for the positive thermal lensing of the Nd:YAG crystals. Instead of using a convex resonator mirror, a negative lens is sometimes inserted between the two rods together with the quartz rotator. The resonator depicted in Fig. 5.22 contain also a Brewster plate to linearly polarize the laser output. Without the quartz rotator, the insertion of the polarizer generates a large depolarization loss for the TEM_{00} mode. Owing to stress birefringence the linearly polarized beam transmitted by the polarizer will be divided into two orthogonally polarized beams in the laser crystal. On its return path, the stress-induced orthogonally polarized portion of the beam will be rejected by the polarizer. The introduction of a 90° phase rotator between the two rods minimizes these losses because the birefringence induced by one rod is canceled in the other.

Concave-Convex Resonator for a Strongly Focusing Rod. Resonators known as dynamic stable, where the effect of changes in the rod focal length on the mode volume is minimized by an appropriate choice of the resonator geometry, have been briefly described in Sect. 5.1.8. Following this earlier work, a number of studies lead to a deeper understanding of the optical stability of the resonator, the TEM_{00} mode volume, and the misalignment sensitivity as a function of thermal lensing in the laser rod. A comprehensive analysis of resonators with an internal lens that represents the pumped laser rod can be found in [5.21–23]. The conclusion of these studies provide guidelines for the design of large mode volume, dynamically stable, and minimum misalignment sensitive resonators. In this subsection we will summarize some of the important findings presented in the above-cited references.

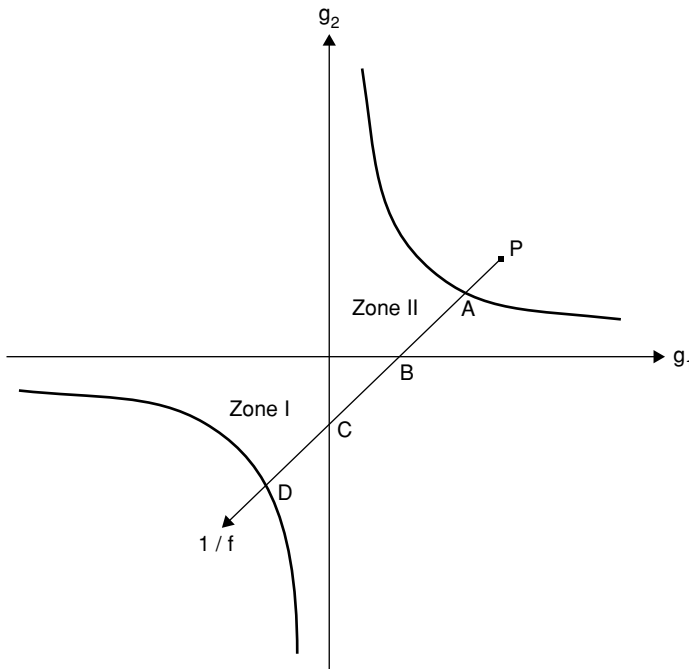


Fig. 5.23. Stability diagram of a resonator containing a laser rod with thermal lensing

As explained in Sect. 5.1.4 any stable resonator is represented by a point lying between the axes and the hyperbola $g_1 g_2 = 1$. In Fig. 5.23 we assume a resonator that is unstable in the absence of thermal lensing (point P). As the focal length changes from infinity to shorter length the point describing the resonator moves in a straight line through the diagram and crosses two stable zones defined by point A to D. Beyond point D the focal length is so short that the resonator is unstable again. The limits of the two stable regions as a function of the focal length f of the laser rod and the resonator parameter are as follows [5.21–23]:

$$\text{Point A} \quad 1/f = 1/(L_1 - R_1) + 1/(L_2 - R_2) \quad g_1 g_2 = 1 \quad (5.50\text{a})$$

$$\text{Point B} \quad 1/f = 1/L_1 + 1/(L_2 - R_2) \quad g_2 = 0 \quad (5.50\text{b})$$

$$\text{Point C} \quad 1/f = 1/L_2 + 1/(L_1 - R_1) \quad g_1 = 0 \quad (5.50\text{c})$$

$$\text{Point D} \quad 1/f = 1/L_1 + 1/L_2 \quad (-g_1)(-g_2) = 1 \quad (5.50\text{d})$$

where R_1, R_2 are the curvatures of the mirrors, and L_1, L_2 are the distances of the mirrors from the principal planes of the rod. At point A the spot sizes at both mirrors are infinite and at point D they are both zero. At points B and C the spot size at one mirror is zero and infinite at the other mirror. The two stability zones can be experimentally observed [5.23, 24]. The system lases over two separate ranges of pump input power. One range is at the low end and the other at the highest range of

input power. In each range the laser output quickly reaches a maximum as the pump power increases and then drops to zero. From (5.50) follows that the two zones have the same width namely

$$\Delta(1/f) = 1/(L_1 - R_1) - 1/L_1. \quad (5.51)$$

In Sect. 5.1.8 we assumed that the laser rod would be close to one mirror and therefore the beam diameter at the mirror and laser rod would be equal. The more general case is treated in [5.22]. By applying the rules of propagation for Gaussian beams, the spot size w_3 at a distance L_1 or L_2 from one of the mirrors is calculated. Therefore w_3 is the spot size at the lens (or inside the laser rod).

In both zones the spot size w_3 at the lens has a minimum w_{30} and goes to infinity at the stability boundaries. At the minimum the mode volume is relatively insensitive to small pump power fluctuations and the laser operates in the so-called dynamic stability condition. This is the operating regime already pointed out in Sect. 5.1.8. Of particular interest in designing a dynamically stable resonator is the width over which a spot size can be maintained in the presence of a changing focal length. It has been shown [5.22] that the spot size area and therefore the TEM_{00} volume is inversely proportional to the dioptric power of the laser

$$w_{30}^2 = \left(\frac{2\lambda}{\pi}\right) \frac{1}{\Delta(1/f)} \quad (5.52)$$

From (5.52) follows that a large dynamic range of focal length changes is associated with a small TEM_{00} beam. As will be explained in Chap. 7, the focal length of a cylindrical rod is inversely proportional to the input power

$$f = M/P_{\text{in}}, \quad (5.53)$$

where M contains all the material parameters of the laser crystal and an efficiency factor that relates the electrical input to the power dissipated as heat in the laser rod. From (5.52) and (5.53) follows immediately

$$\frac{\Delta P_{\text{in}}}{P_{\text{in}}} = \frac{2\lambda f}{\pi w_{30}^2}. \quad (5.54)$$

A large volume of the TEM_{00} mode inside the laser rod reduces the range over which the input power can be changed. For example, if an Nd:YAG rod at maximum input has a focal length of 0.5 m and the TEM_{00} mode radius is $w_{30} = 1$ mm we obtain $\Delta P_{\text{in}}/P_{\text{in}} = 0.34$. For a laser pump input of 1 kW the dynamic range over which input power can be changed without affecting the mode structure is ± 170 W.

The location of an active resonator within the stability diagram can be calculated with the aid of the equations provided in [5.22]. For convenience a number of new variables are introduced to describe the resonator containing a thick lens

$$u_1 = L_1 \left(1 - \frac{L_1}{R_1}\right), \quad u_2 = L_2 \left(1 - \frac{L_2}{R_2}\right), \quad x = \frac{1}{f} - \frac{1}{L_1} - \frac{1}{L_2}. \quad (5.55)$$

Using the above equations, g_1 and g_2 can be expressed as

$$g_1 = -\frac{L_2}{L_1}(1 + xu_1), \quad g_2 = -\frac{L_1}{L_2}(1 + xu_2). \quad (5.56)$$

By eliminating x in (5.56) a linear relationship between g_1 and g_2 is derived which describes changes of the resonator configuration as a function of the focal length of the internal lens.

$$g_2 = \left(\frac{L_1}{L_2}\right)^2 \frac{u_2}{u_1} g_1 + \frac{L_1}{L_2} \left(\frac{u_2}{u_1} - 1\right). \quad (5.57)$$

Equation (5.57) describes the straight line depicted in Fig. 5.23. Indicated in this figure is a line with a positive slope, depending on the resonator design negative slopes are possible as well.

The spot size w_3 at the lens is given by

$$w_3^2 = \frac{\lambda}{\pi} \frac{|2xu_1u_2 + u_1 + u_2|}{[(1 - g_1g_2)g_1g_2]^{1/2}}. \quad (5.58)$$

The minimum spot size inside the two stability zones expressed in terms of resonator parameters follows from (5.51, 52)

$$w_{30}^2 = \frac{2\lambda}{\pi} |u_1|, \quad |u_1| > |u_2|. \quad (5.59)$$

Mirror alignment tolerances play an important role in governing the practical design of resonator configurations. In particular, they can exert a large influence on the output power stability. Magni [5.22] treated in his analysis the mechanical stability of the resonator in terms of a misalignment sensitivity. Large diameter TEM₀₀ modes can become quite sensitive to small perturbations in the alignment. Two misalignment sensitivity factors can be defined for mirrors 1 and 2, respectively.

$$S_1 = d_1/w_0\alpha_1, \quad S_2 = d_2/w_0\alpha_2, \quad (5.60)$$

where d_1, d_2 is the displacement of the mode axis at the internal lens caused by a rotation of mirrors 1 and 2, and α_1, α_2 is the rotation angle of the mirrors. The expressions for S_1 and S_2 as a function of the resonator parameters lead to complicated algebraic expressions. The conclusions are that the two stability zones indicated in Fig. 5.23 can be clearly distinguished in terms of their different sensitivities to mirror misalignment. Stability regions indicated by zone I have a lower sensitivity to mirror misalignment compared to resonators located in zone II [5.22]. From these considerations follows that it is desirable to design resonators that fall within zone I, that is in the negative branch of the resonator stability diagram. The concave–convex resonator is one such configuration.

The analysis represented in [5.22] also revealed that the lowest sensitivity to mirror misalignment—that is the highest mechanical stability—is obtained for resonators in zone I that meet the condition

$$|u_1| = \gg |u_2|. \quad (5.61)$$

We will now apply the conclusions of the above analysis to the design of resonators where the influence of input power changes and mirror misalignment is minimized.

Maximum efficiency in a TEM_{00} mode system is obtained if the laser rod is the limiting aperture in the resonator. Earlier in this chapter we concluded that an aperture twice the diameter of the Gaussian beam diameter $2w_0$ is a good compromise to sustain TEM_{00} mode operation with acceptable losses. Based on this consideration we assume that three parameters of the laser are given, namely, the rod diameter and therefore w_0 , the minimum rod focal length f_m measured at the maximum input power, and the acceptable length L of the resonator. (We recall that the physical length of the resonator is longer by the factor $l(1 - 1/n)$, where l is the length of the laser rod.) We decide that the resonator configuration should be located in the zone I limited by points C and D. Therefore from the limit of the stability zone (5.50d) one obtains

$$1/L_1 + 1/L_2 = 1/f_m \quad (5.62)$$

Since w_{30} is a given, we have a relationship between L_1 , L_2 and R_1 from (5.55, 59) and with

$$L = L_1 + L_2 \quad (5.63)$$

we can determine L_1 , L_2 and R_1 . The radius R_2 of mirror 2 is still undetermined. R_2 can be freely chosen within the interval

$$L_1/L_2 R_1 \leq 1/R_2 \leq 1/L_2. \quad (5.64)$$

It is interesting to note that the spot size of the TEM_{00} mode inside the laser rod depends only on R_1 and L_1 . The free design parameter R_2 can therefore be chosen to optimize mechanical stability according to (5.61).

Figure 5.24 depicts a concave–convex resonator design [5.25] that meets the criteria developed in this section. The location of the resonator within the stability diagram as a function of thermal lensing is shown in Fig. 5.25. In the absence of thermal lensing ($f = \infty$) the resonator lies in an unstable region: $g_1 = 3$ and $g_2 = -0.25$. As the pump power increases, the boundary of the stable region is reached when the thermal lens has a focal length of 27 cm. The other boundary is reached at a focal length of 23 cm. The spot size within this stable region is calculated from (5.58) and is depicted in Fig. 5.26. The minimum spot size w_{30} follows

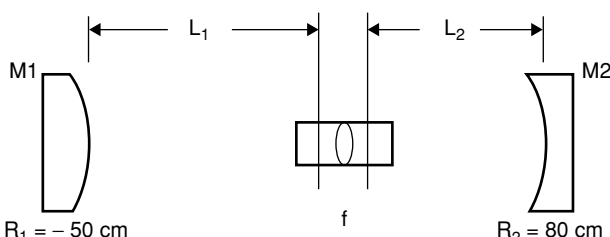


Fig. 5.24. Concave–convex resonator ($L_1 + L_2 = 100$ cm, $L_1 = 64.4$ cm)

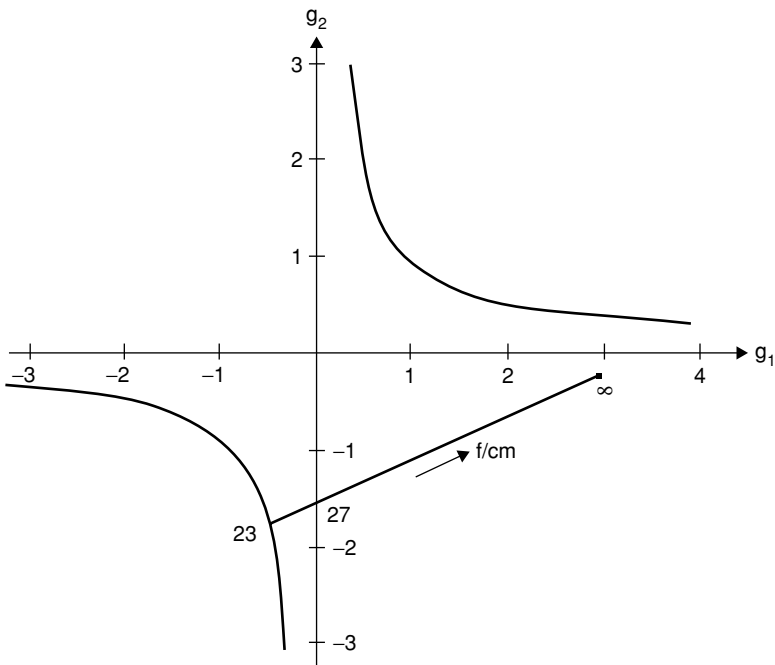


Fig. 5.25. Stability diagram for the resonator depicted in Fig. 5.24

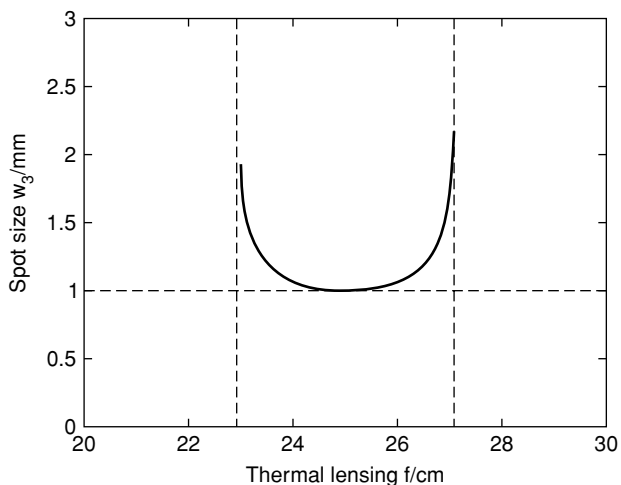


Fig. 5.26. Fundamental mode dimension inside the laser rod as a function of the focal length of the thermally induced lens

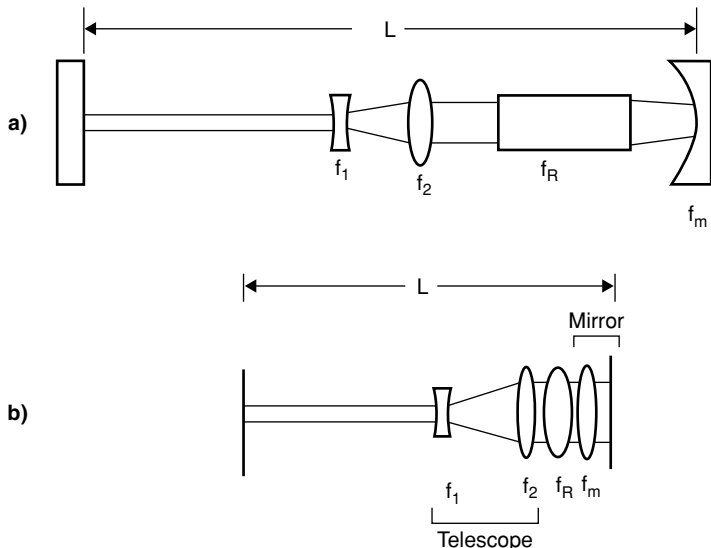


Fig. 5.27. Resonator with internal telescope, focusing laser rod, and curved mirror (a) and schematic of optical equivalent (b)

from (5.59). A laser system featuring such a resonator has very high threshold and a very steep slope efficiency. Since $u_1 = 147$ cm and $u_2 = 19.7$ cm the resonator located in zone I meets also the requirement for mechanical stability according to (5.61).

Resonator with Internal Telescope. A telescope inside a resonator allows controllable adjustments to compensate for thermal lensing under varying pump conditions. The telescope can also be used to reduce the warm-up time of a system. Typically it takes several minutes after a laser system is turned on before steady state is reached between the cooling system and the thermal profile in the laser medium. In military laser systems and in lasers employed for certain industrial applications where a fast turn-on time is required, the telescope can be dynamically adjusted via a stepping motor and computer control to provide a constant beam divergence during this transient period. In this case, a Galilean telescope is employed as shown in Fig. 5.27a with one lens mounted on a motor-driven translation stage. The magnification of the telescope is

$$M = -f_2/f_1, \quad (5.65)$$

where f_2 and f_1 are the focal lengths of the concave and convex lens, respectively. For small adjustments δ between the lenses, the focal length f_T for the defocused telescope is

$$f_T = f_2^2/\delta. \quad (5.66)$$

If the telescope is used in a multimode laser to provide for a quick turn-on time the magnification is typically very small. For example, a telescope consisting of two lenses, 2 cm apart, with $f_1 = -13$ cm and $f_2 = 15$ cm, is used in some laser systems. A change in the separation of the lenses ($f_1 + f_2 + \delta$) of a few millimeters will usually compensate for changes in the focusing power of the laser rod during turn-on time.

The use of an intracavity telescope for improved TEM₀₀ performance has been investigated in [5.26–28]. The insertion of a telescope has the advantage that it shortens the resonator, or results in larger spot sizes for the same resonator length. Two parameters can be chosen in the design of the telescope: the magnification and the amount of defocusing, i.e., the focal length.

In the analysis [5.26] it is assumed that the laser rod, telescope, and mirror M₂ are very close together, as shown in Fig. 5.27b. Therefore, the spot size w_2 of the TEM₀₀ mode at mirror M₂ and laser medium are approximately equal. The concave front mirror is represented by a flat mirror and a lens with focal length $f_m = R_2/2$. The focusing power of the laser medium is indicated by the lens with focal length f_R . Focal length and magnification of the telescope are calculated to compensate for thermal lensing in the dynamically stable region ($g_1 g_2 = 0.5$ (see Sect. 5.1.8), and to provide for a large mode size at mirror M₂. This is achieved if the various resonator parameters satisfy the following condition:

$$\frac{1}{2M^2L} = \frac{1}{f_T} + \frac{1}{f_R} + \frac{1}{f_m}. \quad (5.67)$$

The spot sizes at the mirrors are given by

$$w_1 = \sqrt{L\lambda/\pi}, \quad w_2 = \sqrt{2L\lambda/\pi} M. \quad (5.68)$$

These equations express the relationship between spot size, resonator length, telescope magnification, and defocusing. In arriving at a resonator design, it is assumed that f_R is known. This parameter is usually determined by passing a HeNe laser beam through the laser rod and measuring the beam waist at the desired pump level. The maximum spot size of the TEM₀₀ mode is determined by the radius of the laser rod, which is typically about 1.5 times larger than w_2 . With w_2 chosen, a trade-off can be made between M and L according to (5.68). A large magnification M leads to a short resonator length L that could result in an unacceptable small spot size w_1 at mirror M₁. Likewise, a small M may lead to an inconveniently long resonator.

After the trade-off has been made between resonator length L and magnification M , the curvature of the concave mirror can be selected. This determines the focal length of the telescope according to (5.67). The amount of defocusing required to achieve a particular f_T follows from (5.66).

It is interesting to compare the telescopic resonator with the concave-convex resonator discussed in Sect. 5.1.8. Both operate in the dynamically stable region ($g_1 g_2 = 0.5$). Therefore, the mode size w_2 has a range that is relatively insensitive to focal length changes f_R . If M is eliminated in (5.67) and (5.68), one obtains w_2 as a function of f_R . The shape of this curve is similar to Fig. 5.26.

In both resonator designs there is a large mode size on one end and a concentrated beam at the other end. The main limitation in both designs is the high

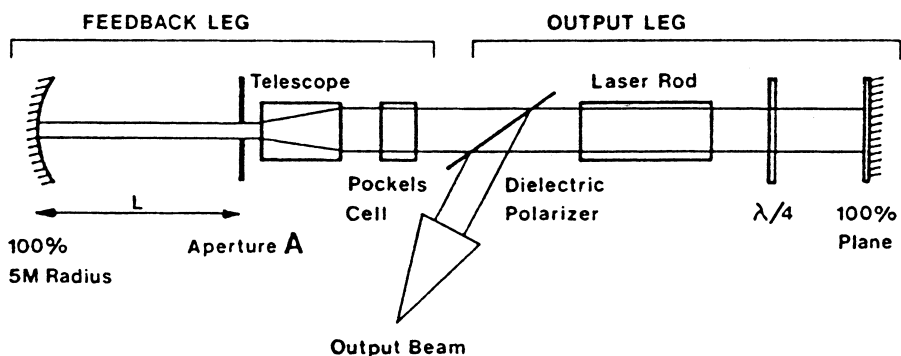


Fig. 5.28. Resonator with internal telescope

intensity, and therefore greater damage risk, caused by the small beam in one section of the resonator. If we compare the expressions for the spot sizes of the concave–convex mirror (5.44) with the telescopic resonator (5.68), we notice that g_1 is replaced by M^2 in the expression for the spot size w_2 . However, since w_1 does not depend on the magnification M , the telescopic resonator has a spot size at mirror M_1 that is larger by a factor M as compared to the concave–convex resonator. This is particularly important at the high power levels typical for Q-switched Nd:YAG lasers.

Figure 5.28 shows the optical schematic for a Q-switched laser featuring a resonator with an internal telescope. In this design polarization output coupling is used to further reduce the intensity in the section where the beam is small. This type of output coupling, discussed in more detail in the last example of this section, and in Sect. 8.6, is advantageous because vulnerable components, such as the Pockels cell, are in the low-intensity leg of the resonator. The difference in intensity between the two sections separated by the polarizer is determined by the amount of radiation coupled out of the cavity.

Astigmatically Compensated Folded-Mirror Resonator. The discussion of resonators has so far been restricted to devices having axial symmetry with respect to the beam axis. Resonators that contain inclined surfaces, such as Brewster-ended rods, polarizers, prisms, etc., lack axial symmetry. The effect of these asymmetric devices is to produce astigmatic beams, i.e., beams that have different spot sizes, wavefront curvatures, and beam waist positions in two orthogonal directions. For example, in the design of Ti:Sapphire lasers, Kerr-lens mode locking, or cavity dumping with a fast acousto-optic switch, or in intracavity frequency doubling, it is often necessary to have a highly concentrated beam inside the resonator. The requirement of a long resonator and small beam waist are best satisfied by a folded resonator commonly employed in dye lasers. A resonator configuration containing an internal focus can be designed with internal lenses. An equivalent resonator is a three-mirror design depicted in Fig. 5.29, which is preferable over a lens system because reflection losses can be kept much smaller.

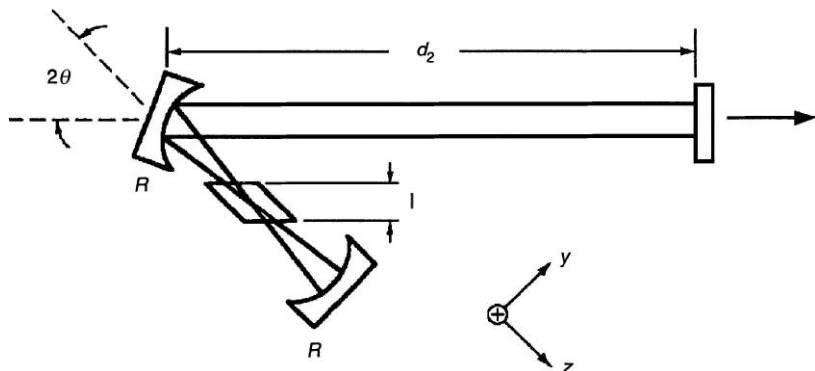


Fig. 5.29. Astigmatic compensation of a folded resonator containing an optical element at Brewster's angle

Such a folded resonator, because of the oblique angle of incidence of the center mirror, introduces astigmatism. Astigmatic beams have different spot sizes and beam-waist positions in two orthogonal directions. In highly focused resonators of this type, the adjustment of mirror spacing is critical as the cavity is stable only over a small range of values. In a highly astigmatic resonator, a condition can exist where the resonator is stable in only one coordinate unless steps are taken to minimize astigmatism.

The purpose of astigmatic compensation is to produce mode characteristics that are equal in x and y . For the case where an optical element between the two mirrors is at Brewster's angle, as shown in Fig. 5.29, the astigmatism of the mirror can be offset by those of the Brewster-ended element.

With the angle of incidence chosen to achieve astigmatic compensation, the beam-waist diameters in the x and y directions are approximately equal, and focal points for x and y are at the same location.

A mirror used at an oblique angle of incidence has two focal points [5.29]

$$f_x = (R/2)/\cos \Theta \quad \text{and} \quad f_y = (R/2)\cos \Theta \quad (5.69)$$

because it focuses sagittal (xz) and tangential (yz) ray bundles at different locations.

A Brewster-angle laser rod has two different effective distances l_x and l_y , which the rays have to traverse [5.29, 30]

$$l_x = l\sqrt{n^2 + 1/n^2} \quad \text{and} \quad l_y = l\sqrt{n^2 + 1/n^4}, \quad (5.70)$$

where l is the length and n is the refractive index of the laser rod.

It has been shown [5.29] that the astigmatism of the oblique angle of incidence mirror can be compensated for by the astigmatism of the Brewster-angle laser crystal at an included angle 2Θ by

$$\sin \Theta \tan \Theta = \frac{2l(n^2 - 1)(n^2 + 1)^{1/2}}{Rn^4}, \quad (5.71)$$

where R is the radius of curvature of the mirrors.

In practice, the laser rod, mode locking or nonlinear crystal, as well as the mirror curvatures, are chosen to achieve the proper operating conditions for the laser. With the parameters l , n , and R chosen, compensation is achieved by adjusting the tilt angle of the center mirror. As an example, we consider a diode end-pumped Nd:Glass laser with the pump beam directed through one of the curved mirrors. With a rod length of $l = 3$ mm, an index of refraction of $n = 1.503$, and a mirror with a radius of curvature of $R = 125$ mm, the center mirror has to be tilted by $\Theta = 8.35^\circ$ in order to achieve astigmatic compensation.

Instead of a three-mirror configuration, the folded mirrors are often used inside four-mirror designs, as illustrated in Figs. 3.40, 9.10, and 9.17.

Crossed Porro Prisms, Polarization-Coupled Resonator. Lasers employed in military systems, such as range finders and target designators, have to operate in a totally different environment compared to commercial or laboratory lasers. The design is dictated by the requirement that these lasers are insensitive to shock, vibration, and large temperature excursions. For these reasons, reliable operation under severe environmental conditions is more important than optimum system performance.

A temperature and alignment insensitive optical resonator is a key feature of military laser. As a result of decades of experience gained from fielded systems, a particular resonator-design concept and architecture has evolved, which is implemented in most military lasers.

The key feature of this design are as follows:

- Beam turning is accomplished with prisms rather than mirrors.
- The resonator is folded to reduce the overall length of the system.
- Alignment is performed by rotation of several refractive wedges.
- The output beam is obtained through polarization coupling.

The optical design of a typical military Q-switched laser which incorporates these features is exhibited in Fig. 5.30.

Mirrors attached to adjustable mirror mounts have proven not to be stable enough from a mechanical and thermal point of view for military applications. Instead, as

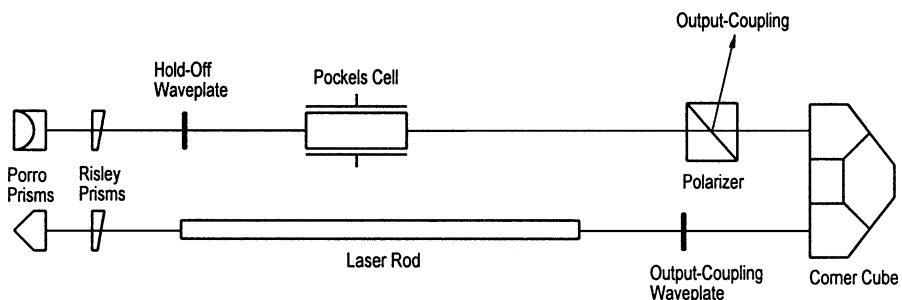


Fig. 5.30. Resonator using cross Porro prisms and polarization output coupling

shown in Fig. 5.30, fixed mounted Porro prisms and corner cubes are employed in the optical train. The self-aligning features of retro-reflectors provide the highest stability in the presence of harsh environmental conditions. Important for good beam quality are optically high-quality Porro prisms with less than 5- μm edge chips at the roof line, and an angular tolerance of no more than ± 5 arc s from the 90° roof angle. The prisms and corner cube are aligned in a test rig during assembly and either glued or mechanically locked in place.

The use of crossed Porro prisms for the resonator requires a different approach from standard designs for beam adjustment and output coupling. Fine adjustment of the beam is accomplished by rotation of refractive alignment wedges. The wedges consist typically of 5–10-mm-diameter and 3–5-mm-thick fused silica with a 1° wedge angle. A so-called *Risley pair* permits beam adjustment in the x – y directions. In resonators which use two fixed mounted reflective mirrors, one Risley pair is required in front of each mirror. Also, for boresighting the beam outside the laser, a Risley pair is often used. Aligning a laser with a Risley pair requires some practice. The best way to start is by orienting the pair with a HeNe laser such that the wedges are at 90° with respect to each other. If the prisms are then installed in the laser, a slight rotation of one prism around this starting position will move the beam in an arc which is orthogonal to the arc of the other prism. In this case, the alignment procedure is somewhat similar to a more conventional x – y mirror adjustment. Once alignment of the cavity is completed, the mounting rings of the prisms are locked in place by set screws. It was found that refractive alignment prisms, mounted in stainless steel holders and clamped down by set screws, are the most reliable method of achieving long-term alignment stability of the resonator in the presence of severe environmental conditions.

In the design illustrated in Fig. 5.30 which utilizes Porro prisms instead of reflective mirrors, only one wedge at each end of the resonator is required because of the self-aligning feature of these prisms in the other direction. Output coupling is achieved by a waveplate/polarizer combination. The amount of output coupling can be adjusted by rotation of the $\lambda/2$ waveplate. In principle, the waveplate is not necessary because the optimum output coupling could also be achieved by a rotation of the Porro prism located behind the laser rod. A Porro prism introduces a phase shift between the s and p components of light because of the total internal reflections. The prism-induced phase shift depends on the refractive index. An additional phase shift can be induced by changing the prism azimuth angle with respect to the plane of polarization. Therefore, in a Porro prism resonator the phase shift required for output coupling can be achieved with the proper combination of prism-induced phase shift and prism angle rotation. However, in most cases it is desirable to maintain the Porro prisms in a crossed fixed position to improve the alignment stability of the laser resonator.

Q-switching is accomplished with the Q-switch placed between the polarizer and waveplate–Porro prism combination. If, for example, the Q-switch is operated in the pulse-on mode, it needs to be located between two crossed polarizers. In this case, the waveplate–Porro prism combination is adjusted to transmit only radiation which is polarized orthogonally with respect to the transmission of the output coupling

polarizer. A high Q in the cavity is established if a $V_{1/2}$ voltage is applied to the Pockels cell which rotates the polarization 90° in the Q-switch. The phase retardation introduced by the Porro prism has to be compensated for by a rotation of the waveplate in such a way that the combination of both elements together with the output coupling polarizer produces the maximum extinction ratio in the resonator.

It should also be noted that in the design depicted in Fig. 5.30, the Q-switch is subjected to a lower intensity compared to other parts of the resonator, because a fraction of the radiation is coupled out before it reaches the Q-switch. This is important because LiNbO_3 , a common Q-switch crystal, has the lowest damage threshold of the optical components employed in the resonator.

In order to keep the laser systems short and compact, most military lasers are folded (Fig. 5.30). For the reasons discussed above, a corner cube rather than mirrors is used for bending the beam. In addition to the specific optical components discussed so far, a military laser requires the use of expansion matched materials for all optical mounts, a hermetically sealed enclosure to protect the optical components, and kinematic mounting of critical components to avoid stress-induced distortions.

5.1.10 Resonator Modeling and Software Packages

The equations provided in this chapter for the design of laser resonators are usually sufficient to characterize the most common configurations. Complicated resonator structures containing many optical elements can be evaluated with the aid of ABCD ray transfer matrices or by means of the Jones calculus if the state of polarization is critical.

The ABCD law based on geometrical optics allows to trace paraxial rays through a complicated sequence of lens-like elements. Each element is characterized by its ABCD matrix, and the transfer function of the whole system is obtained by multiplying all the matrices [5.4, 31, 32].

If a resonator contains a number of optical elements which change the polarization of the beam, such as waveplates, Porro prisms, corner cube reflectors, birefringent crystals, etc., the Jones calculus provides a powerful method for the evaluation of such a resonator [5.31]. The Jones calculus is a 2×2 matrix method in which the state of polarization is represented by a two-component vector and each optical element is represented by a 2×2 matrix. The polarization state of the transmitted beam is computed by multiplying all the matrices. The overall matrix is then multiplied with the vector representing the input beam.

An example of the application of the Jones matrix method to a resonator containing a birefringence laser crystal can be found in [5.33].

Beside the fundamental calculations and considerations presented in this subsection it is often necessary in the design of a complicated laser system to employ an optics analysis code. This is particularly the case in lasers which contain many optical elements and folded beam paths. One is normally interested in identifying potential problem areas that could lead to optical damage in high-peak power systems. Therefore, of particular interest is the beam profile within the resonator and throughout the

rest of the system, diffraction effects from limiting apertures, self-focusing caused by nonlinear refractive index changes in glass and crystals, back reflection from optical elements, etc.

In addition to the basic design tools mentioned above there are a number of commercially available software packages for optimizing resonator designs such as GLAD, PARAXIA, LASXAD, and ASAP [5.34]. Most of these software programs combine several simulation tools, such as finite element code for thermal analysis, ABCD matrix algorithm, and wave optics code, to provide analysis of the complex interactions in a resonator. An example of performing an opto/mechanical tolerance analysis with one of the codes listed above is presented in [5.35].

5.2 Longitudinal Modes

5.2.1 The Fabry-Perot Interferometer

The Fabry-Perot interferometer consists of two flat and parallel mirrors. Both mirrors have highly reflecting coatings. Another version, called an etalon, consists of a solid plate with its two faces published flat and parallel and in many cases also coated for high reflectivity. Fabry-Perot interferometers have narrow transmissions pass bands at discrete optical frequencies.

A basic understanding of the characteristics of a Fabry-Perot interferometer is important because a laser resonator is closely related to this device. Furthermore, Fabry-Perot etalons and interferometers are widely used for laser wavelength tuning, laser line width control, and as an instrument to measure line width.

In the device illustrated in Fig. 5.31 multiple reflections that occur between the surfaces cause the various waves to interfere at infinity (i.e. at the focus of a converging lens). For each member of either the reflected or the transmitted set of waves, the phase of the wave function differs from that of the preceding member by an amount which corresponds to a double traversal of the interferometer. This phase difference is

$$\varphi = 2\pi(2L/\lambda), \quad (5.72)$$

where L is the distance between the two reflecting surfaces and λ is the wavelength.

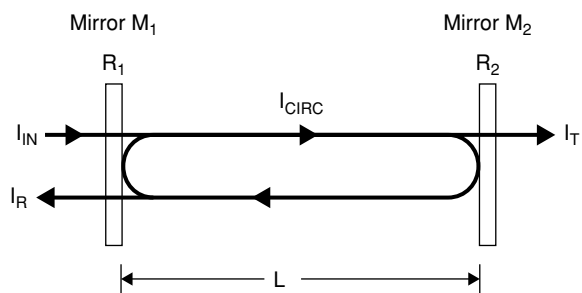


Fig. 5.31. Laser beam I_{IN} entering a Fabry-Perot interferometer

Each time the round-trip phase shift equals an integer of 2π , the resonance condition is reached and the maximum transmission through the device is obtained if

$$q = 2L/\lambda, \quad (5.73)$$

where q is an integer. Equation (5.73) corresponds to a spacing of the two mirrors of q half-wavelengths. Since solid-state lasers have a wavelength around 1 micron and L is typically on the order of tens of centimeters, q is a very large number. Each value of q corresponds to a different longitudinal mode of the interferometer having a frequency of

$$\nu = q(c/2L). \quad (5.74)$$

The frequency separation between modes follows from (5.74)

$$\Delta\nu = \frac{c}{2L}(q+1) - \frac{c}{2L}q = \frac{c}{2L}. \quad (5.75)$$

The frequency interval $\Delta\nu$ is called the free spectral range of the interferometer. The longitudinal modes form an equally spaced comb of resonant frequencies.

The transmitted power of a Fabry-Perot resonator is [5.36]

$$I_T = \frac{(1-R)^2}{1+R^2-2R\cos\varphi} I_{\text{in}}, \quad (5.76)$$

where for convenience we have assumed equal reflectivities for both mirrors $R_1 = R_2 = R$. If we assume negligible internal losses, the Fabry-Perot cavity transmits all of the incident power at the resonance.

$$I_T = I_{\text{in}}, \quad I_R = 0 \quad \text{for } \varphi = 2\pi q. \quad (5.77)$$

The reflected power from the Fabry-Perot cavity is

$$I_R = \frac{2R(1-\cos\varphi)}{1+R^2-2R\cos\varphi} I_{\text{in}}. \quad (5.78)$$

Maximum reflectivity occurs midway between the resonance peaks

$$I_{R\max} = \frac{4R}{(1+R)^2} I_{\text{in}}, \quad \text{for } \varphi = (2m+1)\pi, \quad (5.79)$$

where m is an integer. At the point of maximum reflectivity the fraction of power transmitted by the device is

$$I_{T\min} = \frac{(1-R)^2}{(1+R)^2} I_{\text{in}}. \quad (5.80)$$

In the absence of internal losses the sum of the transmitted and reflected power has to equal the incident power $I_T + I_R = I_{\text{in}}$.

The power reflected from the Fabry-Perot resonator is the superposition of two beams, namely the directly reflected beam $R_1 I_{\text{in}}$ from mirror M_1 and a fraction of

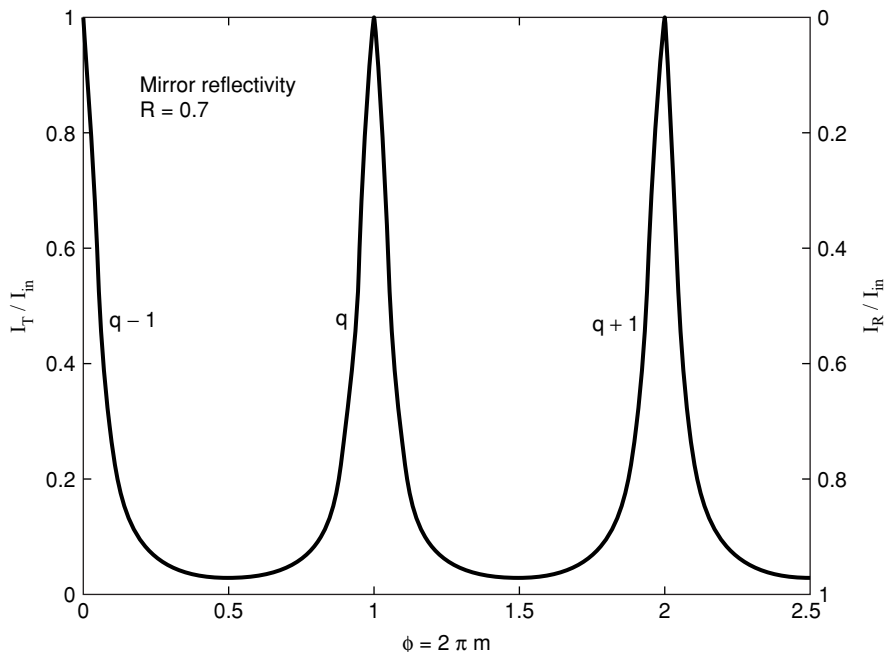


Fig. 5.32. Transmission and reflection from a Fabry-Perot interferometer as a function of the normalized frequency

the circulating power that is transmitted through the same mirror. At resonance these two beams destructively interfere and cancel each other, therefore reflectivity is zero and the transmission is maximized. At antiresonance the two beams are in phase and reflectivity is maximized.

In Fig. 5.32 the transmission I_T/I_{in} and reflectivity I_R/I_{in} are plotted as a function of the normalized frequency $q = v2L/c$, which is the ratio of the laser frequency divided by the round-trip frequency of the resonator. The phase angle in (5.76) is $\varphi = 2\pi mq$, where m assumes values from 0 to 1. If the laser wavelength v corresponds to an integer fraction of the round-trip frequency $c/2L$ of the resonator, then the resonance condition is met and $\varphi = 2\pi q$.

We define the ratio of the spacing between two adjacent passbands and the passband width as finesse $F = \Delta\nu/\delta\nu$. In transmission, the cavity acts as a narrowband transmission filter. The FWHM cavity line width is the frequency interval between the two points on either side of the transmission curve where the intensity falls to half of its maximum value. With (5.74) the line width is given by

$$\delta\nu = c/2LF \quad (5.81)$$

and the finesse is related to the mirror reflectivities

$$F = \pi \left[2 \arcsin \left(2 + \frac{4R}{(1-R)^2} \right)^{-1/2} \right]^{-1} \approx \frac{\pi R^{1/2}}{1-R}. \quad (5.82)$$

If the mirror reflectivities are different, then R is the geometric mean of the two reflectivities. The approximation in (5.82) is valid for high reflectivities.

The circulating power inside the Fabry-Perot cavity can be much larger than the power incident on the front mirror. For example, in order for the interferometer to transmit the total input power through the highly reflective mirror M_2 at resonance requires an intensity of the circulating beam of

$$I_{\text{cir}} = I_{\text{in}} / (1 - R). \quad (5.83)$$

For a Fabry-Perot interferometer with two 99% reflective mirrors, the circulating power at resonance is $100 \times I_{\text{in}}$.

The circulating power density as a function of phase angle is given by

$$I_{\text{cir}} = \frac{1 - R}{1 + R^2 - 2R \cos \varphi} I_{\text{in}}. \quad (5.84)$$

The peak intensity of the circulating power is reached at resonance ($\varphi = 2\pi q$) and was stated in (5.83). At antiresonance the circulating power is at a minimum

$$I_{\text{cir}} = \frac{1 - R}{(1 + R)^2} I_{\text{in}}. \quad (5.85)$$

The circulating power as a function of the normalized frequency is displayed in Fig. 5.33 for a mirror reflectivity of $R = 0.7$.

The Fabry-Perot interferometer is commonly used to measure the line width of the laser emission. The arrangement normally used to display the familiar Fabry-Perot

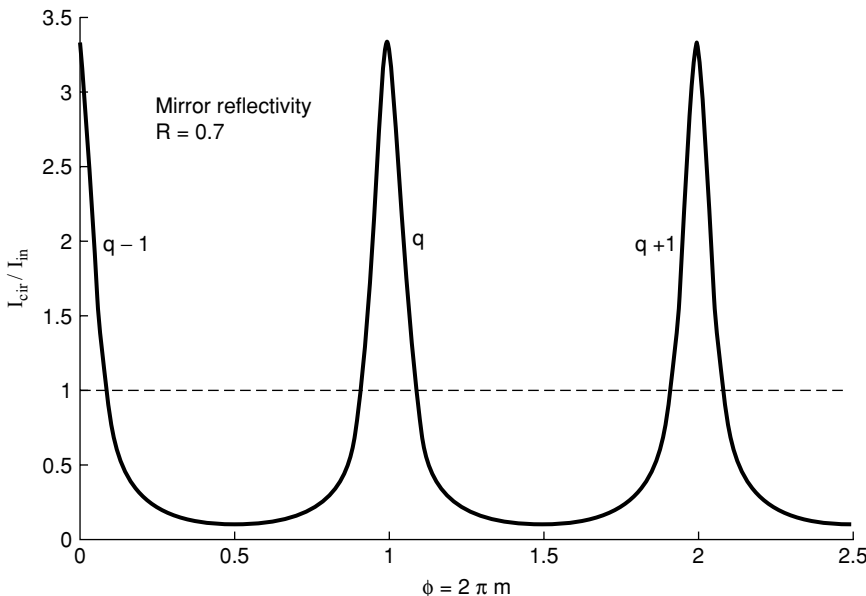


Fig. 5.33. Circulating power in a Fabry-Perot interferometer as a function of normalized frequency

rings consists of a short-focal-length negative lens, two mirrors with spacings of 5–40 mm, a long-focal-length positive lens, and a camera or screen. The first lens converts the parallel beam from the laser into a diverging cone of light.

The resonance of the interferometer cause an angularly selective transmission. The light transmitted by the interferometer is collected by a lens. Light beams leaving the interferometer inclined at the same angle with respect to the optical axis of the interferometer form a ring in the focal plane of the lens. The corresponding number of Fabry-Perot rings are displayed.

If the instrument is illuminated by a perfect monochromatic light source, one obtains a set of rings that correspond to directions for which constructive interference occurs. Since these interferometers are employed to measure the spectral characteristics of light beams, one is interested in the wavelength shift required to move the pattern from one ring to the next ring. This wavelength interval is called the free spectral range of the interferometer.

For an interferometer which consists of two dielectrically coated mirrors with a reflectivity of 90% and separated by 40 mm, we obtain a free spectral range of 3.75 GHz and a finesse of $F = 30$. The theoretical resolution of the instrument obtained from (5.81) is $\delta\nu = 125$ MHz. Comparing the width of the individual rings to their separation gives the line width of the laser.

5.2.2 Laser Resonator with Gain Medium

The spectral output from a laser is determined by the gain bandwidth of the active material and the properties of the Fabry-Perot-type resonator. Typically, many reflectivity peaks of the resonator are within the spectral width of the laser material leading to many longitudinal modes. According to (5.75) the separation of the longitudinal modes in a laser cavity is given by

$$\Delta\lambda = \frac{\lambda_0^2}{2L} \quad \text{or} \quad \Delta\nu = \frac{c}{2L}, \quad (5.86)$$

where L is the optical length of the resonator. For a resonator with $L = 50$ cm, adjacent longitudinal modes are separated by $\Delta\nu = 300$ MHz. For example, Nd:YAG lasers have a fluorescence line width of 120 GHz, and depending on the threshold and pump strength the gain bandwidth is on the order of 12 GHz. Therefore, about 40 longitudinal modes can oscillate within the resonator described above.

If the reflectivities of the two surfaces of a resonator are different, as in a laser cavity, the reflectivity R in (5.82) is the geometric mean reflectivity of the two mirrors: $R = (R_1 R_2)^{1/2}$. Typical values for a laser cavity are $R_1 = 0.8$ and $R_2 = 1.0$ and a resonator length of 50 cm. Introducing these numbers into (5.82) and (5.81), one obtains $F = 26.5$ and $\delta\nu = 11.3$ MHz for the finesse and the spectral width of the empty resonator (Fig. 5.34).

In the presence of several transverse modes, additional resonant frequencies occur in the laser cavity. The frequency separation of different TEM_{plq} modes in a laser

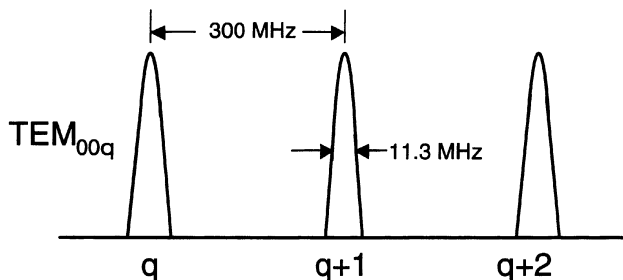


Fig. 5.34. Longitudinal modes in an empty resonator composed of an 80% and a 100% reflective mirror separated by 50 cm

resonator is given by [5.4]

$$\Delta\nu = \left(\frac{c}{2L}\right) \left[\Delta q + \left(\frac{1}{\pi}\right) \Delta(2p+l) \text{arc cos} \left(1 - \frac{L}{R}\right) \right], \quad (5.87)$$

where L is the length of the resonator and R is the radius of curvature for both mirrors. The term on the right containing Δq gives the frequency interval of the axial modes. The term with $\Delta(2p+l)$ describes the separation of the resonance frequencies of different transverse TEM_{pl} modes. Note that the resonant frequencies depend on $(2p+l)$ and not on p and l separately. Therefore, frequency degeneracies arise when $(2p+l)$ is equivalent for different modes. By replacing $(2p+l)$ with $(m+n)$, the cavity frequencies for transverse modes expressed in Cartesian coordinates are obtained. From (5.87) it follows that the frequency separation between transverse modes is not only a function of mirror separation, as is the case with the axial modes, but also depends on the curvature of the mirrors.

For a near plane-parallel or long-radius resonator ($L \ll R$), the second term within the brackets of (5.87) becomes small compared to Δq . In this case the resonant-mode spectrum is composed of the relatively large axial mode spacing $c/2L$, with each axial mode surrounded by a set of transverse-mode resonances, as shown in Fig. 5.35. For example, the 50-cm-long resonator mentioned before, if

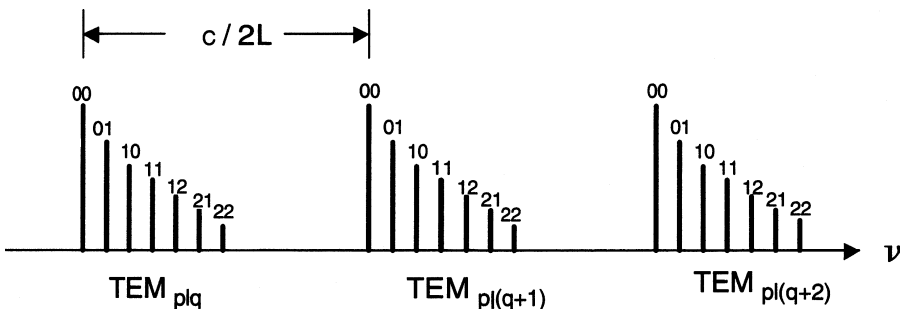


Fig. 5.35. Resonance frequency of a resonator containing higher order transverse modes

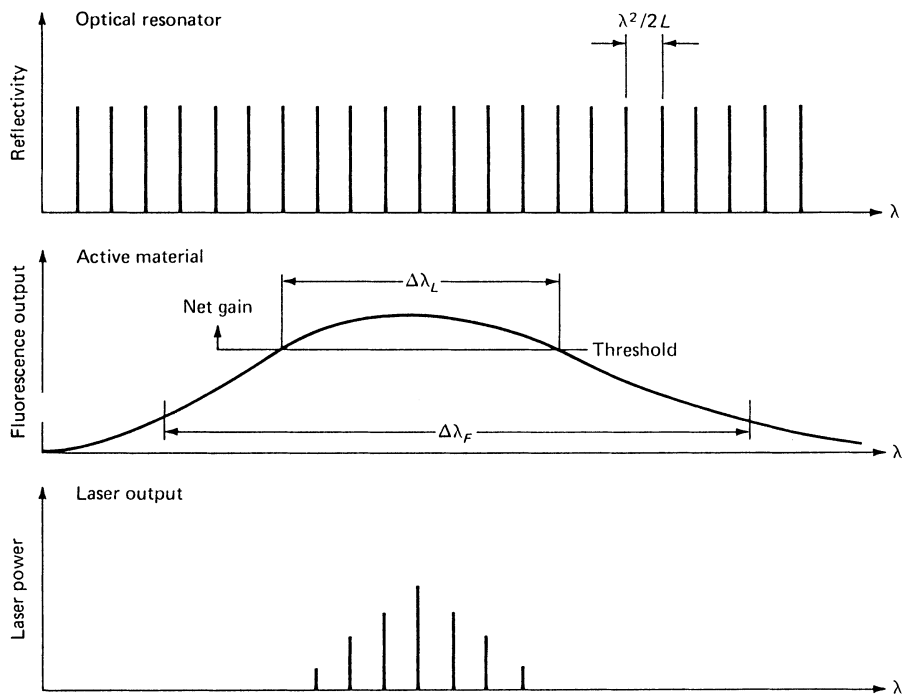


Fig. 5.36. Schematic diagram of spectral output of a laser without mode selection

terminated by two mirrors with 5-m curvatures, will have a resonance spectrum of $\Delta\nu/\text{MHz} = 300\Delta q + 43(2p + l)$. Because of these additional resonance frequencies, which occur with higher order transverse modes, techniques for narrowing the spectral output of a laser (to be discussed in Sect. 5.2.3) require operation at the TEM_{00} mode.

If a laser is operated without any mode-selecting elements in the resonator, then the spectral output will consist of a large number of discrete frequencies determined by the transverse and axial modes. The line width of the laser transition limits the number of modes that have sufficient gain to oscillate. The situation is diagrammed schematically in Fig. 5.36, which shows the resonance frequencies of an optical resonator and the fluorescence line of the active material. Laser emission occurs at those wavelengths at which the product of the gain of the laser transition and the reflectivity of the mirrors exceed unity. In the idealized example shown, the laser would oscillate at seven axial modes.

The beam emitted from a laser, which emits at a discrete number of integrally related wavelengths, is strongly modulated. The situation can be illustrated by considering the simplest case of two superimposed traveling waves whose wavelengths are specified by adjacent axial modes. This situation is shown schematically in Fig. 5.37. The two waves interfere with one another and produce traveling nodes that are found to be separated from one another in time by twice the cavity separation.

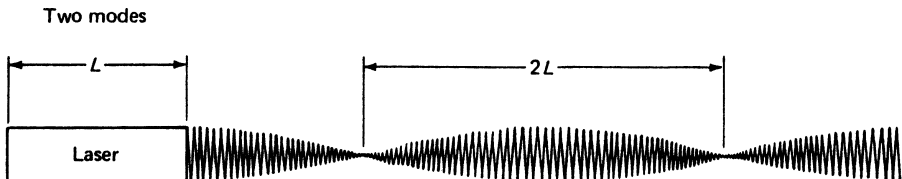


Fig. 5.37. Amplitude modulation of a laser beam due to emission of two adjacent longitudinal modes

The spectral characteristics of a laser are quite frequently described in terms of bandwidth, line width, number of axial modes, and coherence length. We will now outline the relationships among these quantities.

The temporal coherence of any spectral source is defined as the path length difference over which the radiation can still interfere with itself. Common techniques for measuring spectral bandwidth or coherence length of lasers include Fabry-Perot and Michelson interferometers and observation of beat frequencies.

In optics textbooks, coherence length is defined as the path length difference for which fringe visibility in a Michelson interferometer is reduced to $1/(2)^{1/2}$.

The fringe visibility of an interferometer is defined as [5.37]

$$V = \frac{I_{\max} - I_{\min}}{I_{\max} + I_{\min}}. \quad (5.88)$$

In our subsequent discussion we will assume that the intensities of the axial modes in the laser output are equal. In this case the power spectrum of the laser can be developed into a series of delta functions and one obtains

$$V = \left| \frac{\sin(N\pi\Delta l/2L)}{N \sin(\pi\Delta l/2L)} \right|, \quad (5.89)$$

where N is the number of axial modes.

The fringe visibility function has a periodicity of $2L$ and is equal or larger than $1/\sqrt{2}$ for path length differences of $\Delta l = l_C$

$$l_C = 2L/N, \quad N \geq 2. \quad (5.90)$$

As the number of integrally related modes increases, the region of constructive interference—which is inversely proportional to the number of oscillating modes—becomes narrower. If the laser emits N equally spaced axial modes, the bandwidth is

$$\Delta\nu = \frac{(N-1)c}{2L} \quad \text{or} \quad \Delta\lambda = \frac{(N-1)\lambda_0^2}{2L}, \quad N \geq 2. \quad (5.91)$$

Pulsed Nd:YAG lasers can be designed with a long coherence length by employing the cw monolithic Nd:YAG devices as seed lasers. An injection seeded Q-switched slave oscillator can produce a transform-limited line width, as will be explained later in this chapter. In such a system, the line width is determined by the pulse length. The

FWHM line width of a Gaussian-shaped pulse with no frequency chirp is

$$\Delta\nu = \frac{2 \ln 2}{\pi t_p}, \quad (5.92)$$

where t_p is the full width at the half-power points. A 20-ns transform limited Q-switch pulse with a Gaussian temporal profile will have a bandwidth of 22 MHz. The coherence length l_c for which fringe visibility has dropped to $1/\sqrt{2}$ is in this case

$$l_c = c/\pi \Delta\nu. \quad (5.93)$$

5.2.3 Longitudinal Mode Control

In contrast to transverse mode control, which is important for most laser applications, control of the longitudinal modes is generally required only for lasers employed in interferometric applications, coherent lidar, or holographic systems.

Depending on how stringent the requirements are for line width control, a number of approaches can be implemented: Line width narrowing can be achieved by insertion of one or several etalons into the resonator, true single longitudinal mode operation is obtained from monolithic ring lasers, and precise frequency control requires in addition to single line operation an external reference resonator. The various approaches will be discussed in the following sections.

Line Width Narrowing

A typical solid-state laser will emit radiation in a comb of discrete frequencies with an overall width of less than 10^{-4} of the laser frequency. Although such a narrow line width represents a rather monochromatic radiation source, the above-mentioned applications require greater spectral purity. Uncoated or dielectrically coated etalons are often employed as bandpass filters inside the laser resonator to reduce the gain bandwidth and thus the number of longitudinal modes.

The etalon is inserted at a small angle in the laser resonator. The tilt effectively decouples the internal transmission etalon from the resonator; that is, no other resonances will be formed with other surfaces in the main resonator. If the etalon is sufficiently misaligned, it acts simply as a bandpass transmission filter. The tilted etalon has no reflection loss for frequencies corresponding to its Fabry-Perot transmission maxima. At other frequencies the reflections from this mode selector are lost from the cavity, and thus constitute a frequency-dependent loss mechanism.

In Fig. 5.38 an etalon is depicted inclined at a small angle θ' with respect to the incident beam. Instead of (5.72) we can express the phase difference between reflected or transmitted rays as

$$\varphi = (2\pi/\lambda)2n_0d \cos\theta, \quad (5.94)$$

where n_0d is the optical thickness between the two reflecting surfaces and $\theta = \theta'/n_0$ is the angle between the beam direction and the surface normal inside the etalon. The

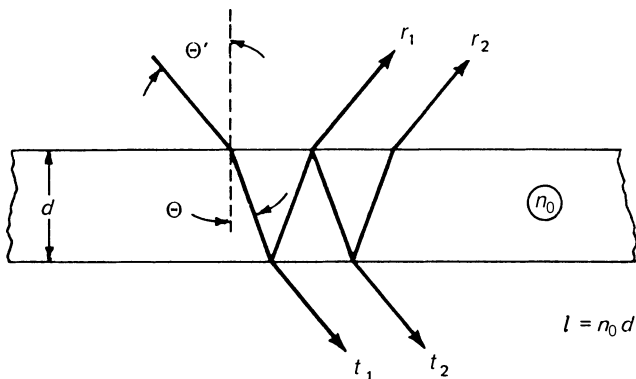


Fig. 5.38. Interference of a plane wave in a plane-parallel plate

transmission maxima can be tuned by changing the tilt angle. From (5.74) one obtains

$$\nu = q \frac{c}{2n_0 d \cos \Theta}. \quad (5.95)$$

The transmission peak will be shifted to higher frequencies if the tilt angle is increased. The separation of two passbands, called the free spectral range, is given by

$$\Delta\lambda = \frac{\lambda_0^2}{2n_0 d \cos \Theta} \quad \text{or} \quad \Delta\nu = \frac{c}{2n_0 d \cos \Theta}. \quad (5.96)$$

As follows from (5.96) an 8-mm-thick etalon with an index of refraction of $n = 1.45$ and inclined at 22° to the optical axis of the resonator will have a free spectral range of about 14 GHz. With reflective coatings of $R = 0.8$ on both sides, the finesse according to (5.82) is $F = 14$. The resulting spectral width of 1 GHz is considerably narrower than the 12 GHz gain bandwidth of a typical Nd:YAG laser. The laser output will be composed of longitudinal modes that fall inside the transmission band of the etalon, hence a narrowing of the laser line width is observed. The situation is schematically shown in Fig. 5.39.

By using several etalons of different thicknesses in cascade, it is possible to combine the narrow bandwidth and small free spectral range obtained from a thick etalon, with the wider bandwidth but also wider free spectral range of a thinner etalon. The stability, simplicity, low loss, and wide adaptability of the bandwidth and free spectral range make the tilted etalon a versatile mode selector.

If an etalon is used in place of an output mirror in a laser cavity, it is referred to as a resonant reflector. The operating region of a resonant reflector is at maximum reflectivity given by (5.79). In a high-power Q-switched oscillator a resonant reflector instead of a tilted etalon is sometimes used because of damage considerations. As shown in (5.83), the intensity inside the etalon is higher than in the resonator. The resonant reflector on the other hand has an internal intensity given by (5.85), which is lower compared to the power density in the laser cavity.

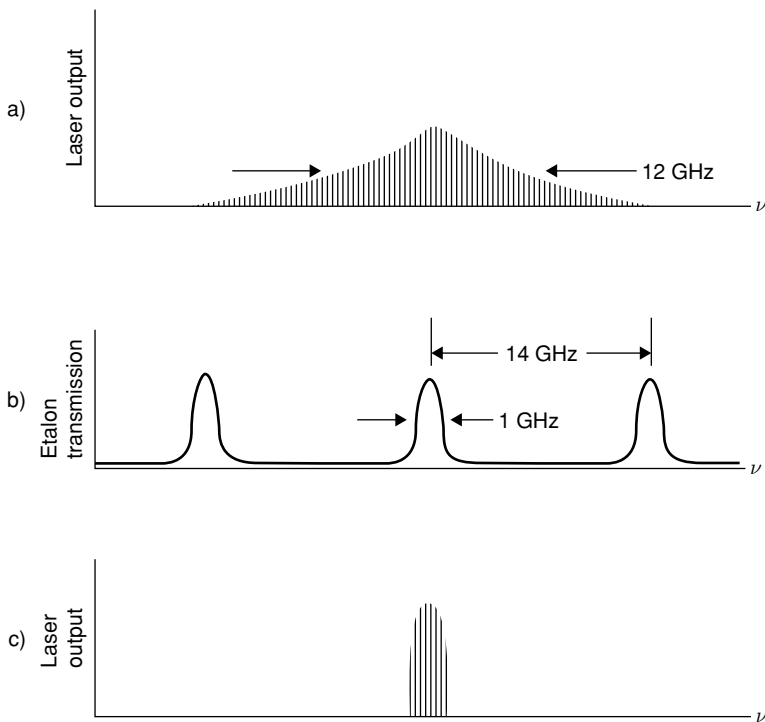


Fig. 5.39. Reduction of the laser line width with a tilted etalon. (a) Laser output consisting of many modes above threshold; (b) spectral characteristics of an etalon, (c) laser output with etalon

Single Mode Operation

While the insertion of etalons will narrow the line width of a laser, reliable single longitude mode output can only be achieved from a laser that meets the following design criteria: a very short resonator such that the axial modes are spread so far apart that only one mode has sufficient gain; elimination of spatial hole burning caused by the standing wave pattern in the resonator; mechanical stability of the resonator elements; and a stable, low-noise pump source. These desirable features are combined, for example, in the diode-pumped, monolithic ring laser illustrated in Fig. 5.40.

The laser resonator is only a few millimeters long, therefore axial modes are spaced sufficiently far apart for axial mode control. The ring laser configuration avoids spatial hole burning, and end-pumping provides a small gain volume for efficient and stable TEM_{00} mode operation. Furthermore, the monolithic design assures good mechanical stability of the resonator. Spatial hole burning is a descriptive term for the fact that along the axis of the resonator, “holes” in the inversion are burnt as a result of the standing wave nature of the mode. The fixed nodal planes on the other hand represent regions of untapped inversion which will preferentially contribute gain to other modes leading to mode-hopping. The tendency of a laser for mode-hopping can be eliminated

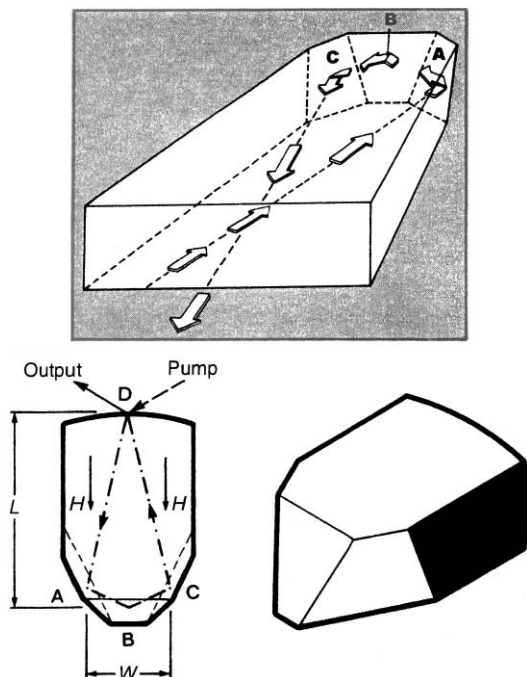


Fig. 5.40. Design of a monolithic ring Nd:YAG laser [5.40]

by providing relative motion between the atoms in the active material and the electric field of the resonator.

In gas lasers, spatial hole burning is all but prevented by the thermal motions of the atoms. In crystals, however, the amplitudes of the lattice vibrations are small compared to the light wavelength, and spatial averaging cannot take place.

In principle, spatial hole burning can be eliminated with traveling-wave ring structures [5.38–40], by generating circularly polarized light in the rod [5.41], with mechanical motion [5.42], or with electro-optic phase modulation [5.43].

Traveling-wave unidirectional ring lasers have been particularly successful in achieving narrow line width from a number of solid-state lasers. As was described in Sect. 3.2, a unidirectional ring laser contains three essential elements, a polarizer, a half-wave plate, and a Faraday rotator. Ring lasers can be constructed with discrete elements, or monolithic versions of traveling-wave ring oscillators have been developed pumped by laser diodes. The first such device was the monolithic isolated single-mode end-pumped ring laser (MISER) developed by Kane et al. [5.40].

The basic idea of a monolithic, diode-pumped unidirectional ring laser is to provide the equivalent of a discrete element design. The polarizer, half-wave plate equivalent, and the Faraday rotator are all embodied in the nonplanar ring Nd:YAG laser illustrated in Fig. 5.40. With a magnetic field H present in the direction shown, the YAG crystal itself acts as the Faraday rotator, the out-of-plane total internal reflection bounced (labeled A and C) acts as the half-wave plate, and the output coupler

(mirror D) acts as a partial polarizer. Polarization selection results from nonnormal incidence at the dielectrically coated output mirror.

The line width of the output of a laser operated in a single axial mode is usually many orders of magnitude narrower than the line width of the empty or passive resonator. The theoretical limit of the laser line width is determined by spontaneously emitted radiation which mixes with the wave already present in the resonator and produces phase fluctuations. The photons in the resonator all correspond to in-phase waves except for the spontaneous emission, which occurs at the same frequency but with a random phase. It is this phase jitter that causes the finite laser line width $\Delta\nu_L$, which is given by the Schalow–Townes limit [5.44]

$$\Delta\nu_L = \frac{2\pi h\nu(\Delta\nu_c)^2}{P_{\text{out}}}, \quad (5.97)$$

where $\Delta\nu_c$ is the line width of the passive resonator, $h\nu$ is the photon energy, and P_{out} is the laser output.

The limit can also be expressed as

$$\Delta\nu_L = \frac{\Delta\nu_c}{N_{\text{ph}}}, \quad (5.98)$$

which says that the theoretical minimum laser line width equals the line width of the empty resonator divided by the number of photons in the resonator. The above equation is derived if we note that the laser output power P_{out} equals the number of photons N_{ph} in the resonator times the energy per photon divided by the photon lifetime τ_c ,

$$P_{\text{out}} = \frac{N_{\text{ph}}h\nu}{\tau_c}. \quad (5.99)$$

Furthermore, from Chap. 3, we recall that in a resonator the loss mechanism, besides limiting the lifetime of the oscillation, causes a broadening of the resonance frequency. The width $\Delta\nu_c$ of the resonance curve, at which the intensity has fallen off to half the maximum value, is

$$\Delta\nu_c = (2\pi\tau_c)^{-1}. \quad (5.100)$$

Introducing (5.99) and (5.100) into (5.97) results in the expression (5.98).

We will now calculate the fundamental line width limits for such a laser and compare it with the values achieved in actual systems. The physical length of a minilaser is typically 5 mm and the refractive index is 1.82; therefore the optical length of the resonator is $2L = 1.82$ cm. Such a resonator has a longitudinal mode spacing of 16.7 GHz. Therefore in an Nd:YAG crystal, adjacent modes will have insufficient gain to reach laser threshold.

The output coupling and internal losses for such a monolithic laser are $\delta + T = 0.01$. These values result in a lifetime of the photons in the resonator of $\tau_c = 6$ ns or a line width of the empty resonator of $\Delta\nu_c = 26$ MHz. The theoretical limit for the laser line width at a typical output power of 1 mW is, according to (5.97), $\Delta\nu_L = 1$ Hz. In practice, the laser line width is determined by temperature fluctuations and

mechanical vibrations and instabilities which produce rapid changes in frequency. For example, the temperature-tuning coefficient for a monolithic Nd:YAG laser operating at 1064 nm is $3.1 \text{ GHz}/^\circ\text{C}$. The major contribution is the temperature dependence of the refractive index. The design of narrow line width laser oscillators requires extremely good temperature control. A state-of-the-art diode-pumped monolithic Nd:YAG laser has achieved a line width of 300 Hz during a 5-ms observation time, 10 kHz in time intervals of 300 ms, and the laser exhibited a long-term drift of 300 kHz/min [5.45].

5.2.4 Injection Seeding

A number of applications, such as remote sensing, laser radar, and high-resolution spectroscopy, require single-frequency Q-switched Nd:YAG lasers. Injection seeding is an attractive technique for achieving a narrow line width from a pulsed high-energy laser by transforming the low power of a highly coherent source into a powerful Q-switch pulse.

Injection seeding is accomplished by introducing radiation from a low-power (usually cw) stable single-frequency master oscillator into the high-power Q-switched laser cavity during the pulse buildup period. Both the injected single-mode radiation and spontaneous emission from the slave laser will be regeneratively amplified in the slave cavity. If the injected signal has enough power on a slave cavity resonance, the corresponding single axial mode will eventually saturate the homogeneously broadened gain medium and, in the absence of spatial hole burning, prevent development of any other axial modes from spontaneous emission.

The cw master oscillator provides a stable single-frequency TEM_{00} output for injection seeding. The seed laser then becomes the analog of the crystal oscillator in an RF transmitter. In [5.46, 47], an injection-seeding theory has been developed which treats the threshold for injection seeding and spectral purity of the laser output, as well as effects of position and angular alignment and frequency mismatch between the seed oscillator and power amplifier.

The most common master oscillator for injection seeding is a diode-pumped monolithic ring laser with a nonplanar optical cavity. We should point out here the difference between injection seeding and locking: Park et al. [5.46] have shown that Q-switched Nd:YAG laser operation in a single longitudinal mode can be achieved by seeding the Q-switched oscillator with low-level radiation from a single-frequency master oscillator. Single mode output is maintained as long as the difference between the frequencies of the two lasers is less than some limit determined by the axial mode spacing of the Q-switched slave cavity and the injected power. A consequence of the fact that the injected mode and the power oscillator mode do not have to be at exact resonance is that the line width and wavelength of the seeded power oscillator will not precisely match that of the injection source.

Injection locking entails locking both master and slave oscillators to a single reference cavity. Optimum locking requires that the resonant frequency of the injection laser and the power oscillator be exactly equal to each other. Injection locking requires stringent control of the laser resonator length. Locking of a master oscillator and reference cavity is described in Sect. 5.3.

Although injection seeding does not require the complexity of precise resonator control, some feedback signal is required to keep the modes within a certain range. The error signal for the servo system maintaining both resonators within the limits of effective injection seeding can be derived by monitoring the Q-switched pulse buildup time [5.48]. Employing this technique, the resonator length control is accomplished by detecting the pulse evolution time of the power oscillator and providing a feedback signal to the electronics that controls the position of one of the resonator mirrors. The time interval will be at a minimum when the seed and oscillator resonator are in resonance. By maintaining minimum pulse evolution time, the resonance condition for effective injection seeding is met.

Although injection seeding requires a feedback technique that is much less stringent compared to frequency locking, in certain situations such as a high noise or vibration environment, maintaining cavity length can still be a problem. In severe environments single mode operation can be maintained by employing a fast resonance detection technique [5.49, 50]. Sweeping the slave oscillator via a piezoelectrically mounted resonator mirror, a signal derived from the injection seed can be obtained that indicates when the slave cavity is resonant with the injected field. By detecting this signal with fast electronics, the Q-switch can be opened at the instant the slave cavity is at resonance and a single mode output is generated.

Several injection-seeded Nd:YAG lasers using this technique have been successfully built at our company for application in airborne radar systems.

Figure 5.41 illustrates the injection seeding technique that can convert the single line output from a cw seed laser into a powerful Q-switched pulse which is transform-limited (line width is limited only by the temporal width of the laser pulse) on a single shot basis. The long-term frequency drift is less than 50 MHz/h.

The injection seeding beam is introduced into the resonator cavity through reflection off the polarizing beam splitter. A Faraday rotator and polarizer combination provides the necessary isolation between the master laser and the Q-switched slave laser, both to protect the master laser from possible damage and to prevent destabilizing feedback into the master oscillator.

With the oscillator cavity of the slave laser in the low-Q condition, the injected pulse makes one round trip in the cavity and is then rejected by the polarizer. As the Q-switch opens, the injected pulse builds up rapidly in the cavity, extracting energy from the gain medium. If the original injected signal is of sufficient intensity, the laser mode that builds up will correspond to that of the injection source. Power gains of 10^9 can typically be achieved between the injection laser and the seeded oscillator output. A few milliwatt output of the injection laser is sufficient to obtain complete locking if the cavity resonance frequency is within 10% of the master oscillator frequency.

Active stabilization is required to ensure that the frequency detuning between the master and slave oscillators is within the tolerance for successful injection seeding. The frequency of the two cavities is maintained in coincidence by a feedback loop monitoring the buildup time of the oscillator pulse. If the master oscillator is properly injection-seeded, the Q-switch buildup time is considerably shorter as compared to a nonseeded resonator where the pulse has to build up from noise. Frequency adjustments between the two lasers is performed by temperature tuning of the monolithic

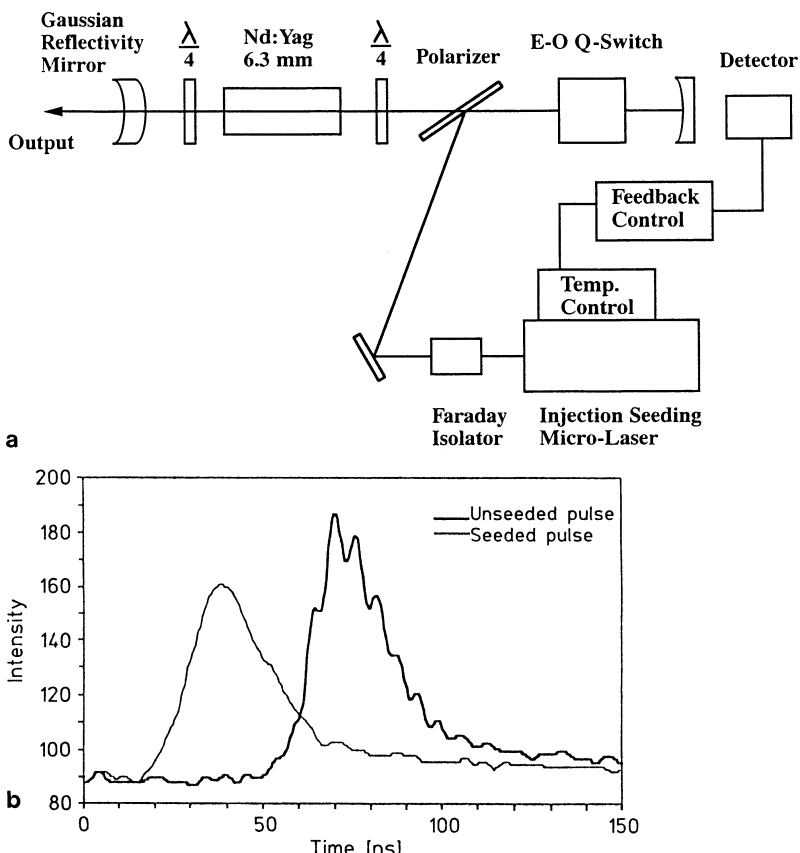


Fig. 5.41. Schematic of injection-seeded slave oscillator (a) and temporal pulse shape with and without seeding (b)

diode-pumped laser crystal in the master oscillator. Frequency sensitivity to temperature is about 3.1 GHz/K, and temperature stability of 0.01 K has been obtained using a proportional controller.

For single-frequency operation, it is necessary to avoid spatial hole burning in the laser rod. This is especially true in a high-gain system where unextracted energy gives rise to “post lasing” following the main Q-switched pulse. In order to avoid spatial hole burning, it is necessary to avoid the formation of a standing wave in the laser rod. To accomplish this, quarter-wave plates are inserted in the resonator at each end of the laser rod, as shown in Fig. 5.41.

The quarter-wave plates convert the forward and backward traveling waves in the rod to circular polarization. Superposition of the two circularly polarized waves which are spatially displaced with respect to each other by $\lambda/4$ produces an electric field pattern in the rod, which has the shape of a twisted ribbon with a spatial period of one optical wavelength [5.51]. Each polarization component of the electric field

forms a standing wave, but the 90° phase shift between the components assures that the total energy density in a mode is uniform along the rod. Thus, hole burning in the rod is prevented.

The resonator shown in Fig. 5.41 is an unstable resonator with a Gaussian output mirror. Proper injection seeding requires strong transverse mode discrimination in the slave oscillator. As will be discussed in Sect. 5.5, unstable resonators exhibit this characteristic.

The temporal shape of the output pulse of the laser with and without injection seeding is shown in Fig. 5.41b. The output of the laser is converted from a pulse characterized by beating between cavity modes in the uninjected condition to an output characterized by a single frequency and smooth temporal profile with the injection laser on. Pulse-to-pulse amplitude jitter is also virtually eliminated in the injection-seeded system.

The output from the diode-array-pumped slave oscillator is 50 mJ in a pulse with a smooth Gaussian time profile and a transform-limited line width. The output from this oscillator was amplified by a four-stage double-pass amplifier chain to 750 mJ/pulse.

5.3 Intensity and Frequency Control

In this section we will discuss intensity noise and frequency tuning as well as frequency stabilization of cw lasers.

5.3.1 Amplitude Fluctuations

Fluctuations may be broadly categorized as short-term or long-term. Long-term changes can be attributed to changes of parameters such as misalignment caused by thermal effects, contamination of optical surfaces, or degradation of the pump source.

Here we are concerned with short-term fluctuations with periods of less than a second. The sources of amplitude modulation of the laser output are mechanical vibrations of the optical components, thermal instabilities in the active material, variations in the pump intensity, mode beating and mode hopping, relaxation oscillations, and quantum noise. The latter two phenomena are inherent properties of the laser oscillator. Which of the fluctuations mentioned above are dominant in a particular situation depends on the operating mode of the laser and the frequency interval of interest.

The envelope of a Q-switched pulse can show amplitude modulation due to mode beating of axial modes. The envelope is smooth for operation at a single axial mode and appears to be smooth for a very large number of axial modes. In the latter case amplitude modulation due to mode beating is reduced as a result of averaging effects.

In cw lasers relaxation oscillations occurring in the 50–500 KHz range, depending on the particular system, dominate all other noise mechanisms. Any small perturbation having a frequency component at the vicinity of the resonance frequency of the relaxation oscillation will cause large oscillation in the output power. A potential source for the excitation of relaxation oscillations is mechanical vibrations. Obviously,

in order to reduce the modulation caused by relaxation oscillations, the mechanical laser structure must be extremely stable.

At the lower end of the megahertz region, parasitic noise is caused by mode competition of transverse modes, whereas mode hopping of longitudinal modes causes amplitude modulation at frequencies of several hundred megahertz. Different transverse modes occupy different regions of the laser rod; as a result of pumping nonuniformities, the gain varies for each transverse mode. Different axial modes are located at different points on the laser gain curve. Any disturbances of the laser system will encourage or discourage individual modes. Therefore, the mode pattern changes constantly. Mode selection eliminates output fluctuations associated with mode competition.

Output fluctuations at low frequencies can be traced to mechanical vibrations, acoustically transmitted noise, and noise in the pump source intensity.

The diode-pumped monolithic ring laser discussed before has not only an outstanding frequency stability but also is a ultra-low-intensity-noise laser. The monolithic resonator design drastically reduces mechanically and vibrationally induced instabilities, and the laser operates in a single transverse and longitudinal mode. This laser produces an output with a relatively small amplitude fluctuation except for the frequency spectrum in which relaxation oscillations occur. By adding an electronic feedback loop, residual intensity fluctuations, as well as the relaxation oscillations, can be reduced to a level close to the shot-noise-limited performance [5.52, 53].

The quantum or shot noise generated in a detector is a fundamental property and is due to the discrete nature of photon-electron generation. The value of shot noise for a detector irradiated by a Poisson-distributed stream of photons is given by

$$i_{\text{RMS}} = (2e\Delta f I)^{1/2}, \quad (5.101)$$

where I is the dc photo current in the detector, Δf is the electrical bandwidth, and e is the electron charge. Equation (5.101) expresses the limit of accuracy with which a current I can be measured at a fixed bandwidth Δf . Shot noise produces a white uniform noise floor at all frequencies.

In diode-pumped solid-state lasers, intensity noise suppression can be achieved with a feedback system which modulates the drive current to the diodes.

Figure 5.42 displays the schematic of such a feedback control system. A fraction of the radiation emitted by the laser is sampled by a photodiode. After amplification and phase shifting, the detected signal is used to change the drive current of the diode pump source. This causes a modulation of the laser radiation. The servo loop is ac-coupled to the power supply to avoid changes in the dc operation of the diode pump. If the feedback loop has the proper phase and gain with respect to the detected laser radiation, intensity fluctuations can be compensated. The feedback system has to be carefully designed in order to avoid noise amplification and to keep the control loop stable.

Figure 5.43 illustrates the reduction of intensity noise one can achieve with a carefully designed feedback control loop. Shown is the photo current noise power, as measured by a spectrum analyzer with a 10-kHz bandwidth, of a diode-pumped

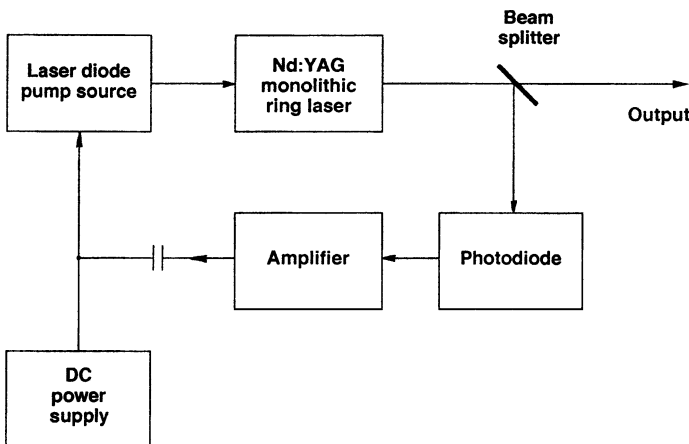


Fig. 5.42. Feedback control for the reduction of intensity noise in the laser output

Nd:YAG nonplanar ring laser in the free-running mode and with feedback control [5.53]. The peak in the noise spectrum at about 300 kHz of the free-running laser is caused by relaxation oscillations. It was observed that for frequencies below the relaxation oscillations, intensity noise in the laser output was mainly caused by noise in the pump-diode output. Radiation emitted from each of the individual stripes of the laser diode beat together, which results in the observed noise floor. At frequencies greater than 5 MHz, the output reaches the quantum-noise level.

With feedback control, there is a large reduction in the noise level for frequencies below 1 MHz. However, the intensity noise is increased between 1 and 5 MHz because of the excess noise generated by the feedback loop. Above 5 MHz, the laser noise is unaltered by the feedback loop. Also shown in Fig. 5.43 is the quantum-noise limit. Under feedback control, the spectral density of the output noise $\Delta P/P/\sqrt{\text{Hz}}$ was measured to be $3 \times 10^{-8} \sqrt{\text{Hz}}$ between 10 and 300 kHz, which is 6.1 dB above the quantum-noise limit.

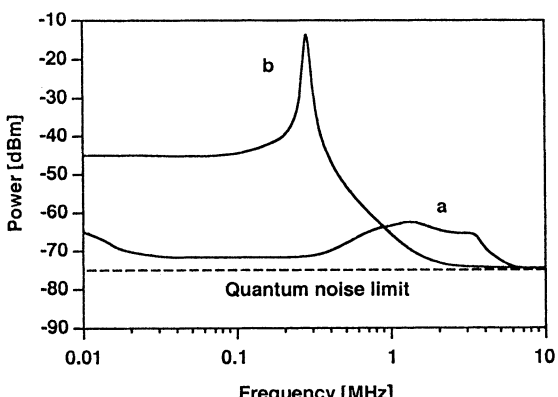


Fig. 5.43. Noise output of a monolithic cw Nd:YAG ring oscillator with (a) and without (b) feedback control [5.53]

5.3.2 Frequency Tuning

Frequency control requires a certain amount of tunability of the laser emissions, either to lock the frequency to a reference or to an incoming signal for coherent detection, or to provide an output signal at a specific wavelength for spectroscopic studies.

Depending on the range of tunability, we can distinguish between:

- *Broadband tunability*: This is achieved with tunable lasers (Sect. 2.5) in combination with wavelength-sensitive elements such as birefringent tuning plates, dispersive prisms, and gratings, as will be discussed in Sect. 5.6. The tuning range can be as large as 100 THz in the case of Ti:Sapphire.
- *Tuning over the gain bandwidth of a narrowband laser*: Small angular changes of an intracavity etalon, or cavity length adjustments with a piezoelectric transducer (PZT)-mounted resonator mirror provide some means of tuning the wavelength of Nd lasers. For example, rapid tuning within the line width of Nd:YAG, which is about 120 GHz, has been achieved with a combination of tilt-angle adjustment of an intracavity etalon and cavity-length adjustment via a PZT-controlled mirror. The etalon was mounted on a galvanometer which allowed a very precise and repeatable angular rotation. The tuning range, covering many longitudinal modes, was on the order of 50 GHz [5.54].
- *Tuning within a single longitudinal line of a resonator*: This is the topic of the present subsection. As we shall see, depending on the length of the resonator, and therefore the separation of longitudinal modes and the method of introducing a frequency shift, tuning has been achieved up into the GHz regime.

In certain applications, such as coherent LADAR systems, a stabilized single-frequency laser source is required, both as local oscillator for the detection system and as injection seeding source for a pulsed transmitter.

Miniature diode-pumped solid-state lasers, such as monolithic or microchip devices, are particularly attractive for this application because of their single-frequency operation. Furthermore, the short resonator of these devices supports a relatively large tuning range because longitudinal modes are widely separated. For example, a 2-mm-long monolithic resonator has a mode spacing of about 41 GHz in Nd:YAG. In monolithic lasers, the frequency can be tuned by thermal expansion or by mechanical stress applied to the crystal. Discrete-element miniature lasers can be tuned by insertion of an electro-optic modulator into the cavity or by cavity-length adjustments.

In monolithic lasers such as the microchip laser, or nonplanar ring laser, the resonator mirrors are coated directly on the Nd:YAG or Nd:YLF crystal, which precludes the introduction of traditional intracavity elements. However, varying the temperature of the crystal will change the resonator length, and therefore frequency-tune the laser emission. The sensitivity of the laser frequency to thermal changes can be calculated as follows. We assume a microchip laser consisting of a small disk of Nd:YAG polished flat and parallel on two sides, which is end-pumped by a laser diode.

The resonant frequency of the laser cavity changes with cavity length according to

$$\frac{d\nu}{\nu} = -\frac{dl_R}{l_R}, \quad (5.102)$$

where ν is the lasing frequency and $l_R = nl$ is the optical length of the resonator.

Temperature changes lead to a thermal expansion of the resonator and to thermal and stress-induced changes of the refractive index. To a first order, we can neglect stress-related index changes. Thermally induced length and refractive index changes of the microchip laser resonator can be expressed by

$$dl_R = nl \left(\alpha_e + \frac{1}{n} \frac{\delta n}{\delta T} \right) dT. \quad (5.103)$$

Introducing (5.103) into (5.102) yields

$$\frac{d\nu}{dT} = - \left(\alpha_e + \frac{1}{n} \frac{\delta n}{\delta T} \right) \nu. \quad (5.104)$$

With the materials parameters for Nd:YAG from Tables 2.2 and 2.3, one obtains $d\nu/dT = -3.25 \text{ GHz}/^\circ\text{C}$.

The actual tuning rate is the difference between the tuning rate of the resonator and the small temperature shift of the laser transition in Nd:YAG. Actual measured data of the thermal tuning coefficient in a monolithic Nd:YAG laser gave a value of $-2.5 \text{ GHz}/^\circ\text{C}$.

Temperature tuning results in a large tuning coefficient, but thermal control of the laser frequency is relatively slow with a time constant on the order of 1 s. Thermal tuning was employed to control two diode-pumped monolithic Nd:YAG ring oscillators to within 40 kHz [5.55].

From the standpoint of frequency control, the large thermal tuning coefficient is actually a disadvantage, because in order to maintain good frequency stability, these lasers require extremely precise temperature control. This is usually achieved by mounting these devices on TE coolers and environmental shielding from temperature fluctuations.

Instead of changing the temperature of the laser crystal by means of a TE cooler, pump power modulation has been successfully employed to cause rapid frequency tuning in miniature lasers. As the pump power increases, more thermal energy is deposited in the gain medium, raising its temperature and therefore changing the resonant frequency of the laser cavity. Modulation of the pump power has the undesirable effect of changing the laser output power. In implementing this technique, TE coolers maintain a fixed average temperature of the crystal. Around this temperature point, rapid thermal changes are induced by means of current modulation of the pump-laser diode. The thermal response is sufficiently fast, permitting phase locking of the laser.

Experiments have been described in which two 1-mm-long Nd:YAG microchip lasers operating at $1.32 \mu\text{m}$ have been frequency-locked to another [5.56, 57]. In the free-running mode, a frequency jitter of 250 kHz over a 15-s period was observed, which was reduced to 50 Hz in the frequency-locked case. At a modulation frequency

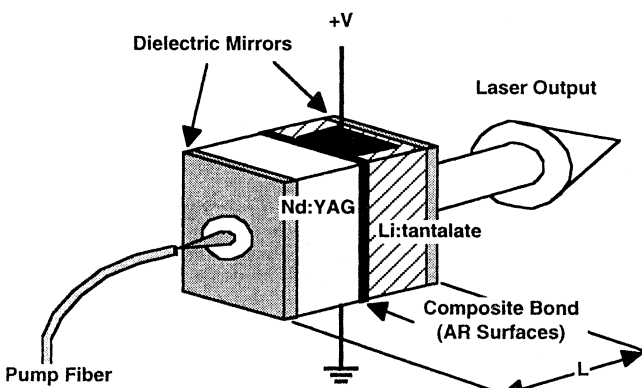


Fig. 5.44. Nd:YAG microchip laser with intracavity electro-optic modulator [5.62]

of 100 Hz, pump power changes of 1 mW produced an optical frequency change of 5.25 MHz.

Another technique for precisely tuning the laser frequency of a monolithic laser is based on stress-induced changes in the resonator. In these designs, stress is applied to the laser crystal by using a piezoelectric transducer. This results in a stress-induced birefringence of the refractive index, and a strain-related distortion or elongation of the resonator. In a disk-shaped Nd:YAG monolithic laser with a thickness of 1 mm, a frequency range of 76.5 GHz could be scanned by applying stress transverse to the beam axis [5.58]. Bonding a thin plate of piezoelectric material to a monolithic Nd:YAG ring laser permitted piezoelectric tuning over a range of 100 MHz with a speed fast enough to achieve phase locking of two lasers [5.59]. Tuning could be accomplished over several tens of MHz in a few microseconds. Frequency stability over 1 ms was better than 500 Hz.

In the case of discrete-element microcavity lasers, frequency tuning has been achieved by cavity length modulation or by incorporating an electro-optic modulator into the resonator. In the former design, an air gap between the two pieces forming a ring resonator was adjusted by a piezoelectric transducer. Cavity length tuning was achieved over a frequency range of 13.5 GHz at a speed on the order of milliseconds [5.60].

Intracavity electro-optic modulation of diode-pumped linear Nd:YAG and Nd:YVO₄ microcavity lasers have been demonstrated [5.61–63]. Figure 5.44 illustrates an Nd:YAG microchip laser with a rapid frequency tuning capability. A composite laser cavity is formed by bonding a lithium tantalate wafer to an Nd:YAG crystal. Both wafers have a combined thickness of 1 mm. A high voltage applied parallel to the *c*-axis of the LiTaO₃ crystal modulated the laser output over a tuning range of 1.5 GHz [5.62].

5.3.3 Frequency Locking

Frequency stability is degraded by mechanical vibrations, acoustic noise, and ambient temperature variations. The most stringent requirement for absolute frequency

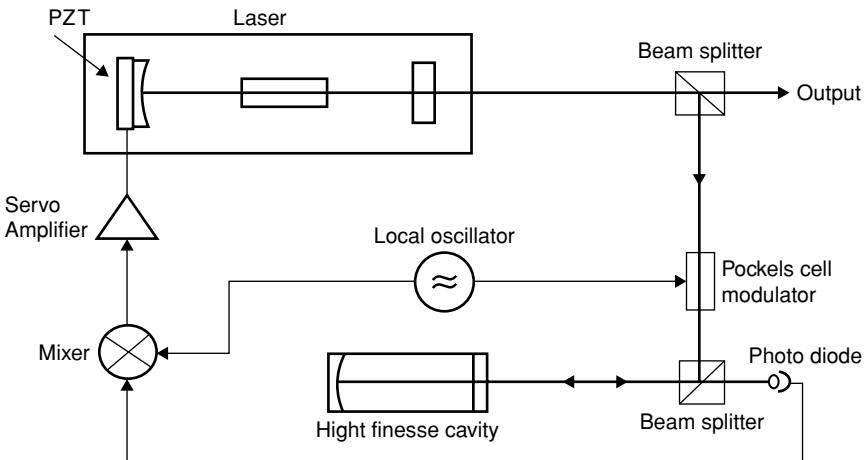


Fig. 5.45. Basic schematic for locking a laser to a reference cavity

controls is imposed on scientific lasers developed for gravitational-wave detectors.

Absolute frequency stability can be achieved by locking the output of the laser to a high finesse reference Fabry-Perot cavity employing the Pound-Drever-Hall (PDH) servo system [5.64]. Figure 5.45 shows a basic PDH setup. A fraction of the laser output is directed into a highly stable reference Fabry-Perot cavity. The reflected beam from the reference cavity is detected by a photodiode. A servo system detects an error signal and adjusts the length of the laser resonator via a piezoelectric transducer. An error signal that is proportional to the deviation of the frequency between the two cavities is not sufficient because there is an ambiguity whether the laser resonator length needs to be shortened or lengthened.

In the PDH technique, the laser beam is rf phase modulated and by optical heterodyne detection of the sidebands that are produced by the rf phase modulation, an error signal is obtained that is positive or negative depending whether the frequency needs to be adjusted up or down. As shown in Fig. 5.45 a Pockels cell modulates the phase of the laser beam typically between 10 and 20 MHz. After the beam has passed through the Pockels cell, its electric field is

$$E = E_0 \exp i(\omega t + \beta \sin \Omega t), \quad (5.105)$$

where β is the modulation depth and Ω is the frequency of the local oscillator.

If the modulation depth is small only two sidebands are produced and there are three different beams incident on the reference cavity: a carrier with frequency ω and two sidebands with frequencies $\omega \pm \Omega$. The reflected radiation from the reference cavity is incident on a photodetector and the electrical signal is directed into a mixer. The mixer compares the modulation signal generated by the local oscillator with the output of the photodetector. The sign of the mixer's output is different on either side of the resonance, and it is zero when the system is in resonance. A servo-amplifier provides the input to a piezoelectric transducer that adjusts the cavity length. At

resonance, the phase φ is a multiple of 2π , near resonance $\varphi \approx 2\pi N + 4\pi\delta L/\lambda$, where δL is some small deviation in the cavity length from resonance and N is an integer. Shot noise is the mechanism that limits the error signal.

In Fig. 5.45 the laser frequency is adjusted by a change of the resonator length. Many of the frequency stable lasers rely on the high intrinsic stability of an Nd:YAG nonplanar ring oscillator (NPRO) that does not have external mirrors.

In a monolithic laser such as the MISER illustrated in Fig. 5.40 the frequency can be adjusted by a PZT glued on top of the laser crystal. A voltage applied to the PZT deforms the crystal and in this manner changes the optical path length of the oscillator [5.65–69]. Another technique of frequency control in an NPRO is to control the power of the laser diode pump source which causes thermally induced changes to the optical path length in the laser crystal [5.70]. In addition, the long-term drift is usually controlled by temperature changes to the laser.

Employing NPRO in combination with high finesse reference cavities and PHD feedback control, lasers have been stabilized to sub-hertz levels.

5.4 Hardware Design

In the construction of a resonator for a laser oscillator, the important considerations are the mechanical stability and the quality of the optical components, protection of the optical train from the environment, and protection of the operator from radiation hazards.

Laser Support Structure. The key requirement of a laser resonator is that all optical components be accurately and rigidly fixed relative to each other, that the structure be insensitive to temperature variations, and that there be a provision for making angular adjustments of the beam.

General research involving lasers is usually carried out with the components mounted on an optical table, since this provides maximum flexibility for the experimental setup. The optical components of commercial lasers are usually mounted on a baseplate or on support structures made from aluminum extrusions. In the latter case, adjustment of the axial position of optical components can be provided by sliding carriages. Commercial lasers are also fully enclosed by a housing for protection against the environment and for eye-safety reasons.

In most cases the optical surfaces are additionally protected by enclosing the whole optical train with tubes or bellows. Enclosures may range from a mere safety cover to a rubber-sealed dust-proof cover, all the way to a hermetically sealed cover which will maintain a positive pressure on the inside.

In military systems weight and size constraints lead to densely packaged structures with aluminum as the material of choice. Often, the whole support structure is machined from one solid block of metal and the optical beam is folded to achieve a compact design.

For complex designs, a solid-model-based mechanical design and analysis capability is indispensable. The most widely used software is Pro/Engineer, a 3D

parametric solid modeling CAD system. It allows laser systems to be virtually built, assembled, and analyzed prior to fabrication. This capability produces an accurate virtual representation of the laser system, allowing the designer to focus on technical intents and requirements rather than drawing accuracy. Such virtual representations provide the foundation for both engineering and manufacturing reviews prior to fabrication. Maintaining focus on product integrity is partially enhanced by the automated drafting process of the Pro/Engineer system. Detail drawing views, dimensions, and bill-of-materials are automatically created directly from the model, eliminating the traditional drafting errors inherent in 2D CAD systems. Changes in the model are automatically reflected in the detail drawings as well. Substantial quality enhancements, as well as error reduction, is achieved by the automated component interference checks of assemblies. The model checks for interfering components and identifies those requiring modification prior to fabrication. This solid modeling capability can be integrated with an analysis capability. Interactive analysis capabilities include stress, deflection, thermal and modal. Analysis capabilities also include mass properties.

Mirror Mounts. The requirements for a good mirror mount are an independent, orthogonal, and backlash-free tilt with sufficient resolution and good thermal and mechanical stability. Commercial mirror mounts meeting these requirements usually employ a two-axis gimbal suspension, a three-point suspension using a torsion spring, two independent hinge points formed by leaf springs, or a metal diaphragm. Rotation is achieved by micrometers or differential screws.

Adjustable mirror mounts are, in general, not used in military laser systems because these components do not provide the required long-term stability in the presence of temperature excursions, shock, and vibration. Instead of mirrors, these systems employ crossed Porro prisms or retro reflectors. Beam alignment is accomplished by insertion of two thin prisms (Risley prism) into the beam. The prisms which can be independently rotated will deflect the beam over a small cone angle. After alignment is completed, the prisms are locked in place. Output coupling from such a resonator is by means of a polarizer and Q-switch.

Optical Surfaces. The polished surfaces of components, such as mirrors, laser rod, windows, lenses, and doubling crystal, used in a laser resonator must meet certain requirements in terms of surface quality, flatness, parallelism, and curvature. The quality of an optical surface is specified by the scratch and dig standards (MIL-13830A). According to this standard, surface quality is expressed by two numbers. The first number gives the apparent width of a scratch in microns and the second number indicates the maximum bubble and dig diameter in $10\text{-}\mu\text{s}$ steps. Components used in optical resonators should have an optical surface quality of about 15/5. As a comparison, commercially available lenses of standard quality have an 80/50 surface.

Mirror blanks for the resonator are either plano-concave, plano-plano, or in special cases plano-convex, made from schlierengrade fused quartz or BSC 2. Standard curvatures are flat, 10, 5, 3, 2, 1, 0.5, and 0.25 m radius of curvature. The surface finish should be $\lambda/10$ or better. Standard mirror blanks have diameters of 25, 12.5,

and 6.2 mm, and thicknesses of 6.2 and 10 mm. A parallelism of 1 arc s or better and a flatness of at least $\lambda/20$ are required for plane-parallel blanks to be used for etalons.

Coatings. Evaporated dielectric films are essential parts of the resonator optics, and their properties are important for the performance of the laser. A typical laser requires a highly reflective and a partially reflective mirror coating and several antireflection coatings on the laser rod, Q-switch crystal, windows, lenses, etc.

Dielectric thin films are produced by evaporation and condensation of transparent materials in a vacuum. The dielectric thin film must adhere well to the substrate. It should be hard, impervious to cleaning, have low loss, and should exhibit a high damage threshold. Commercially available coatings are either hard coatings which will meet MIL-C-675A or semihard coatings which will pass the Scotch-tape adherence test per MIL-M-13508B.

The simplest antireflection coating is a single quarter-wave film. The reflectivity of a single dielectric layer of index n_1 , which has an optical thickness of $\lambda/4$, is, at normal incidence,

$$R = \left(\frac{n_s - n_1^2}{n_s + n_1^2} \right)^2, \quad (5.106)$$

where n_s is the refractive index of the substrate. Zero reflection is achieved when $n_1 = (n_s)^{1/2}$.

The lowest refractive index available as stable film is MgF₂ with $n_1 = 1.38$, a value which results in a perfect antireflection coating for a substrate with $n_s = 1.90$. For $n_s = 1.80$, 1.70, and 1.5 the residual reflectance from a $\lambda/4$ MgF₂ coating is ≈ 0.1 , 0.3, and 1.4%, respectively. From Table 5.2 it follows that MgF₂ is an excellent match for sapphire and Nd:YAG. In cases where the reflection from a single-layer antireflection coating is still too high, two or more dielectric layers must be applied.

A substrate having two layers with index values of n_1 and n_2 of optical thickness $\lambda/4$ will have a total reflectance of

$$R = \left(\frac{n_2^2 - n_1^2 n_s}{n_2^2 + n_1^2 n_s} \right)^2. \quad (5.107)$$

Table 5.2. Substrate characteristics

	Index of refraction	Reflectivity percent	Reflectivity with single-layer MgF ₂
Fused quartz (0.63 μm)	1.46	3.5	1.5
BSC-2 (0.63 μm)	1.52	4.2	1.4
Sapphire (0.69 μm)	1.76	7.6	0.15
Nd:YAG (1.06 μm)	1.82	8.4	0.1

Table 5.3. Thin-film materials

Chemical formula	Material	Index of refraction
MgF ₂	Magnesium fluoride	1.38
ThF ₄	Thorium fluoride	1.50
CeO ₂	Cerium oxide	2.3
ZrO ₂	Zirconium oxide	2.1
SiO ₂	Quartz	1.45
ZnS	Zinc sulfide	2.35
TiO ₂	Titanium oxide	2.28

Zero reflection can be obtained if $(n_2/n_1)^2 = n_s$. If coating materials with the proper ratio n_2/n_1 are not available for a particular substrate, thicknesses which deviate from $\lambda/4$ must be used to achieve zero reflection from glass. Because the region of low reflectance of this type of coating is rather small, the coating is sometimes called “V”-coating. A very hard and durable two-layer coating frequently employed on glass substrates is the system ZrO₂–MgF₂.

High reflectivity, multilayer dielectric films can be tailored to give specific reflectivity versus wavelength characteristics by the appropriate choice of the number of layers, layer thickness, and index of refraction of the materials. The simplest design of a multilayer coating is a stack of alternating films of equal optical thickness, corresponding to $\lambda/4$, but of two different refractive indices. It is most efficient to start and end with a high-index layer so that the structure will have an odd number of layers. We obtain

$$R_{\max} = \left(\frac{n_1^{l+1} - n_2^{l-1} n_s}{n_1^{l+1} + n_2^{l-1} n_s} \right)^2, \quad (5.108)$$

where n_1 is for the high-index material, n_2 is for the low-index material, and l is the odd number of $\lambda/4$ films.

Table 5.3 lists some of the most common thin-film materials used for solid-state laser optics. Titanium oxide, cerium oxide, and zinc sulfide are used mainly as the high-index materials; magnesium fluoride and silicon dioxide are used for the low-index materials.

As follows from (5.108), the reflectance increases with increasing number of $\lambda/4$ films in discrete steps. The number of layers employed depends on the material combination and the desired reflectance value. Normally, it does not exceed 21 because scatter and absorption losses increase with the number of layers.

For commercially available mirror coatings, the maximum reflectance ranges between 99.5 and 99.8%. Scattering and absorption losses combined are in the order of 0.5–0.2%. Typical thin-film combination are ZnS–MgF₂, ZnS–ThF₄, CeO₂–MgF₂, TiO₂–SiO₂, and ZrO₂–SiO₂. The first system is very soft and must be handled with great care; the second coating is more durable and can be cleaned with alcohol and lens tissue; the last two coatings are extremely hard and durable.

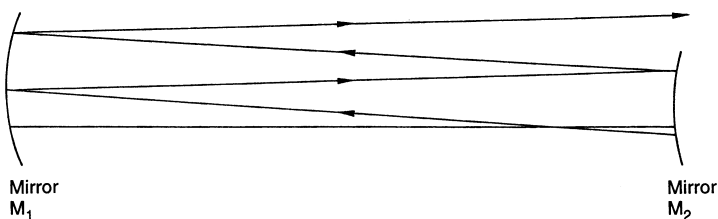


Fig. 5.46. Light ray in an unstable resonator

Properties of optical coatings and designs, as well as a description of the various thin-film techniques can be found in the book by Macleod [5.71].

5.5 Unstable Resonators

As was discussed in Sect. 5.1, in a stable resonator the radiation is confined between the surfaces of the resonator mirrors. In order to produce a diffraction-limited output beam from a stable resonator, the Fresnel number must be on the order of unity or smaller (Sect. 5.1.5), otherwise sufficient discrimination against higher order modes cannot be achieved. For practical resonator lengths, this usually limits the diameter of the TEM_{00} mode to a few millimeters or less.

If the resonator parameters g_1 and g_2 lie outside the shaded regions defined in Fig. 5.8, one obtains an unstable resonator. In these configurations, rays are no longer confined between the mirrors. A ray in an “unconfining” or unstable resonator diverges away from the axis, as shown in Fig. 5.46, and eventually radiation will spill around the edges of one or both mirrors. This fact can, however, be used to advantage if these walk-off losses are turned into useful output coupling.

Figure 5.47 illustrates the spherical waves bouncing between the mirrors of an unstable resonator. In this so-called confocal configuration, the concave mirror’s focal point coincides with the back focal point of the smaller convex mirror. Thus we see that P_1 is the common focus. Light traveling to the left is collimated and may conveniently be coupled out by providing an unobstructed aperture around mirror M_1 .

The unstable resonator corresponds to a divergent periodic focusing system, whereby the beam expands on repeated bounces to fill the entire cross-section of at least one of the laser mirrors. The unstable resonator has a much higher order mode discrimination, as compared to its stable counterpart, and therefore a nearly diffraction-limited output beam from a large diameter gain medium can be obtained. In the near field, the output from an unstable resonator usually has an annular intensity pattern. As we have seen, stable resonator modes are well approximated by Gaussian–Laguerre or Hermite–Gaussian functions. Unstable resonator modes do not have a simple functional form; their intensity distributions must be generated numerically.

The unstable resonator first described by Siegman [5.72] has been studied extensively both theoretically and experimentally. Excellent reviews are found in [5.73, 74].

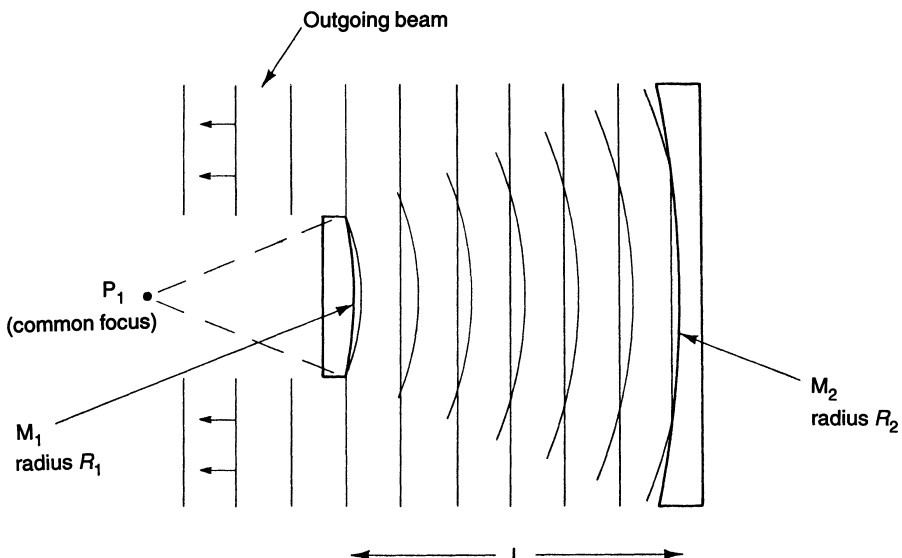


Fig. 5.47. Confocal unstable resonator

The most useful property of an unstable resonator is the attainment of a large fundamental mode volume and good spatial mode selection at high Fresnel numbers. In other words, unstable resonators can produce output beams of low divergence in a short resonator structure which has a large cross section.

Immediately following its invention, the significance of the unstable resonator was recognized for the extraction of diffraction-limited energy from large volume gas lasers. However, it took many years for unstable resonators to be applied to solid-state laser system. There are a number of reasons for this slow acceptance. The laser medium must be of high optical quality for an unstable resonator to be effective. This requirement has limited applications of unstable resonators primarily to gas lasers, because the time- and power-dependent thermal distortions occurring in solid-state lasers made this type of resonator unattractive. In addition, the output coupler of an unstable resonator, having the dimensions of a few millimeters in typical solid-state lasers, is much more expensive and difficult to fabricate in comparison to a partially transmitting mirror required for a stable resonator.

Furthermore, the misalignment tolerance of an unstable resonator is smaller compared to its stable counterpart and the advantage of a large mode volume is achieved at a sacrifice of mode quality because of aperture-generated Fresnel fringes. The output from a solid-state laser is often passed through amplifier stages, or the oscillator may be followed by a harmonic generator. The near-field beam pattern of an unstable resonator which consists of a doughnut-shaped beam with diffraction rings and a hot spot in the center is not very attractive in these applications.

About 10 years after its discovery, Byer and coworkers [5.75] applied the unstable resonator concept for the first time to a Q-switched Nd:YAG oscillator/amplifier

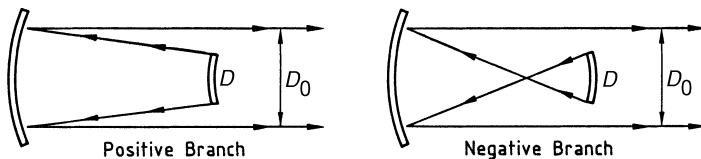


Fig. 5.48. Positive- and negative-branch confocal unstable resonators

system. They did achieve a marked improvement in Nd:YAG output energy in a diffraction-limited mode.

However, only recently has the unstable resonator found applications in commercial lasers, mainly as a result of the availability of the variable reflectivity output mirror which provides a smooth and uniform output beam from an unstable resonator. Output coupling via such a mirror provides an elegant solution in overcoming the beam profile issue. Whether an unstable resonator has an advantage over a stable resonator for a particular system depends on the gain of the laser. As we will discuss later, gain, mode volume, and sensitivity to misalignment are closely related in unstable resonators. (In a stable resonator, only mode volume and alignment stability are directly related as we have seen from the discussions in Sect. 5.1.9.) Generally speaking, only in a high-gain laser can a large mode size be realized in an unstable resonator at a reasonable misalignment tolerance.

The most useful form of an unstable resonator is the confocal unstable resonator. A primary advantage of this configuration is that it automatically produces a collimated output beam; this also means that the final pass of the beam through the gain medium is collimated.

Confocal configurations can be divided into positive-branch resonators which correspond to the case $g_1 g_2 > 1$, and negative-branch resonators for which $g_1 g_2 < 0$ (see Fig. 5.8). Confocal unstable resonators of the positive or negative branches are shown in Fig. 5.48. These configurations are defined by the following relationships:

$$2L = R_1 + R_2 \quad \text{or} \quad L = f_1 + f_2, \quad (5.109)$$

where L is the optical length of the resonator, and R_1, R_2 and f_1, f_2 are the radii and focal lengths of the two mirrors, respectively. For concave mirrors, the sign for R and f is positive, and for convex mirrors it is negative.

5.5.1 Confocal Positive-Branch Unstable Resonator

The confocal positive-branch unstable resonator is the most widely used form of the unstable resonator for solid-state lasers because it does not have an intracavity focal point that could lead to air breakdown or could cause damage to optical components.

Referring to Fig. 5.48 the annular output beam has an outer diameter of D_0 and inner diameter D , where D is also the diameter of the output coupler.

The resonator magnification

$$m = D_0/D \quad (5.110)$$

is the amount that the feedback beam is magnified when it travels one round trip in the resonator and becomes the output beam.

The magnification in the transverse beam dimensions results in a decrease of intensity by a factor $1/m^2$ in each round trip, with radiation spilling out around the edges of the output mirror. A beam reflected between the mirrors will, after one round-trip, lose a fraction T of its energy.

The geometrical output coupling is related to the magnification by

$$T = 1 - \frac{1}{m^2}. \quad (5.111)$$

The output coupling of an unstable resonator is determined by the magnification instead of the transmission of the output mirror as is the case in stable resonators.

If we insert a gain medium between the mirrors, the loss in energy has to be made up by the gain of the laser. According to the laser threshold condition (see Sect. 3.1), we obtain

$$2gl = \delta + \ln m^2. \quad (5.112)$$

Ignoring internal resonator losses δ for a moment, the round-trip gain of the laser has to be

$$G = \exp(2gl) \geq m^2. \quad (5.113)$$

For a confocal resonator, the mirror radii are given by

$$R_1 = \frac{-2L}{m-1} \quad \text{and} \quad R_2 = \frac{2mL}{m-1}, \quad (5.114)$$

where L is the length of the resonator and R_1 and R_2 are the output and back-cavity mirror curvatures. Note that the output mirror has a negative curvature and thus is convex, while the rear mirror has a positive curvature and is concave.

Actually, the relationship between m and the output coupling T for confocal unstable resonators is such that T is less than the geometrically predicted value $(1 - 1/m^2)$. This is because the intensity distribution, according to wave optics, tends to be more concentrated toward the beam axis than that predicted by geometrical optics.

The equivalent Fresnel number of a resonator characterizes the destructive or constructive interference of the mode at the center of the feedback mirror because of the outcoupling aperture. For a positive-branch, confocal resonator, the equivalent Fresnel number is

$$N_{\text{eq}} = \frac{(m-1)(D_0/2)^2}{2L\lambda}, \quad (5.115)$$

where D_0 is the diameter of the output mirror and L is the resonator length. Plots of the mode eigenvalue magnitudes versus N_{eq} show local maxima near half-integer N_{eq} 's.

Physically, the half-integer equivalent Fresnel numbers correspond to Fresnel diffraction peaks centered on the output coupler which leads to increased feedback

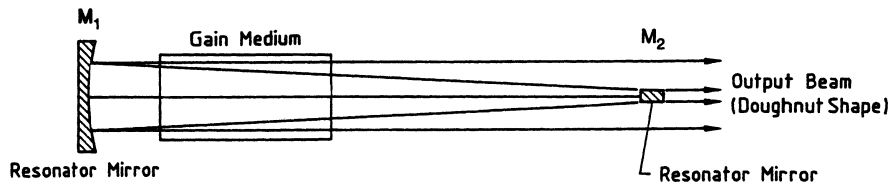


Fig. 5.49. Small-mirror out-coupling scheme in a confocal, positive-branch unstable resonator

into the resonator. Resonators should be designed to operate at half-integer equivalent Fresnel numbers (N_{eq}) to obtain best mode selectivity.

As a final step one has to take into account the effect of the focal length f of the active medium. One usually chooses an available mirror curvature R and calculates the rod focal length at the desired input power required to achieve an effective mirror curvature R_{eff} . If the mirror to rod distance is less than the rod focal length, then

$$\frac{1}{f} + \frac{1}{R_{\text{eff}}} = \frac{1}{R}. \quad (5.116)$$

Essentially the focusing effect of the laser rod is compensated for by increasing the radius of curvature of the mirror.

The design of such a resonator is an iterative process. It starts with some knowledge of the optimum output coupling T or the saturated gain coefficient g obtained from operating the laser with a stable resonator. From either of these two parameters, we obtain from (5.111) or (5.112) the magnification m . Selecting a value of 0.5, 1.5, 2.5, ... for N_{eq} from (5.115) provides a relationship between D_0 and L . With (5.109), (5.110), and (5.114) the pertinent resonator design parameters such as D , D_0 , L , R_1 , and R_2 can be calculated. The effect of thermal lensing is then accounted for by adjusting the radius of curvature according to (5.116). There are basically two types of output couplers possible with solid-state lasers, the dot mirror and the radially variable reflectivity mirror.

The design depicted in Fig. 5.49 consists of a concave mirror M_1 and a convex output mirror M_2 , both of which are totally reflecting. The dot mirror M_2 is a small circular dielectrically coated area of radius d centered on a glass substrate. The disadvantage of a dot mirror, namely the generation of an annular output beam containing diffraction rings and a hot spot in the center, can be eliminated by employing a partially transparent output coupler with a radially variable reflectivity profile. In such a mirror, reflectivity decreases radially from a peak in the center down to zero over a distance comparable to the diameter of the laser rod. The output is a smooth Gaussian-shaped beam. Design procedures for such mirrors are described in Sect. 5.5.3.

Illustrated in Fig. 5.50 is a diode-pumped Nd:YAG slab laser with a positive-branch, confocal unstable resonator in a folded configuration. The output coupler is a dielectrically coated mirror with a variable reflectivity profile. The resonator in Fig. 5.50 has a magnification $M = 1.38$ and a cavity length of 58 cm. The laser

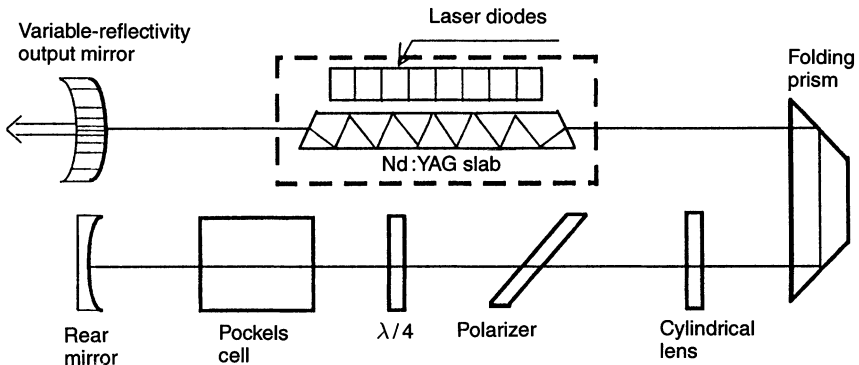


Fig. 5.50. Diode-pumped Nd:YAG slab laser with positive-branch unstable resonator and variable reflectivity output coupler [5.76]

generated 100 mJ of Q-switched output at a repetition rate of 100 Hz with a near diffraction-limited beam [5.76].

5.5.2 Negative-Branch Unstable Resonator

Because of the presence of an intracavity focal point, the negative-branch resonator has been neglected in practical laser applications. Despite the potential problem of air breakdown this resonator merits consideration owing to its unique feature of relatively large misalignment tolerances.

It was found [5.77] that a Q-switched Nd:YAG laser featuring a negative-branch unstable resonator was not significantly degraded with a mirror misalignment angle of as much as a few milliradians. Also system air breakdown was not experienced for Q-switched pulses on the order of 170 mJ and 12 ns pulse length. Therefore, for small solid-state lasers, typical of range finders and target designators with peak powers not exceeding 5–10 MW, it is conceivable that a negative-branch unstable resonator could be employed.

The design parameters for a negative-branch resonator of the type shown in Fig. 5.51 are

$$R_1 = 2L/(m + 1) \quad \text{and} \quad R_2 = 2mL/(m + 1), \quad (5.117)$$

where L is the confocal resonator length and m is the optical magnification defined before.

A variation of the negative-branch unstable resonator was described by Gobbi et al. [5.78]. The design is based on the proper choice for the size of the field-limiting aperture d located at the common focal plane of the mirror. If the aperture is chosen such that a plane wave incident on it is focused by mirror M_1 to an Airy disk having the same diameter d , then this results in the removal of the hot spot inside the cavity and in a smoothing of the spatial profile.

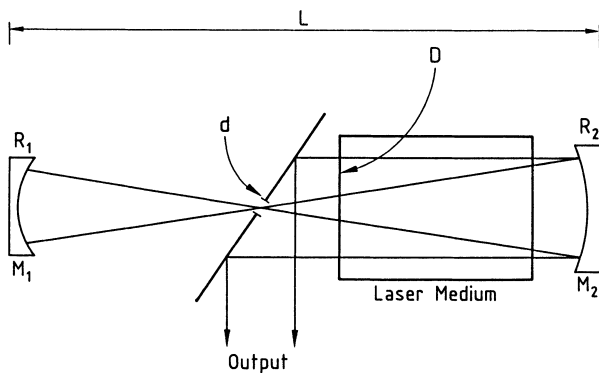


Fig. 5.51. Arrangement of a typical negative-branch unstable resonator

If the aperture diameter d is chosen such that

$$d = 2(0.61\lambda f_1)^{1/2}, \quad (5.118)$$

where $f_1 = R_1/2$, then only the Airy disk is allowed to propagate beyond the aperture, and on reflection from the mirror M_2 , it is magnified, collimated, and ready to start another similar cycle.

The radius at which the beam has zero amplitude is not determined by the geometrical magnification m , but an effective magnification imposed by diffraction.

$$m_{\text{eff}} = 1.5m = -1.5f_2/f_1 \quad f_2 = R_2/2. \quad (5.119)$$

The diameter of the collimated beam passing through the laser is

$$D = |m_{\text{eff}}|d. \quad (5.120)$$

By adding the constraint on the aperture size that it match the Airy disk, the usual hot spot in the focal plane is completely removed by diffraction. Actually the combination of aperture d and mirror M_1 acts on the resonator field as a low-pass spatial filter. This accounts for the smoothness of the field profile.

The disadvantage of this design is the limited value of D which can be achieved in practical systems. In order to fill a large active volume with diameter D , for example a slab laser, either m_{eff} or d has to be large (5.120). In order for d to be large, it follows from (5.118) that f_1 has to be large, which in turn leads to a long resonator. A large m_{eff} requires a very high-gain material, for example, a Q-switched Nd:YAG oscillator. A beam diameter of $D = 4.8$ mm inside the laser rod requires a resonator of 125 cm in length and a magnification of $m = 4$. In order to achieve the high gain required for this design the laser was pumped 2.5 times above threshold.

An interesting feature of the design illustrated in Fig. 5.52 is the beam extraction from the resonator. Beam extraction was achieved by means of a polarization coupling scheme, employing a polarizer and a quarter wave plate.

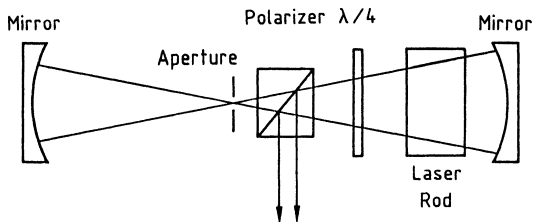


Fig. 5.52. Negative-branch unstable resonator with polarization output coupling

5.5.3 Variable Reflectivity Output Couplers

One of the major disadvantages of an unstable resonator, namely the generation of an annular output beam containing diffraction rings and a hot spot in the center, can be eliminated by employing a partially transparent output coupler with a radially variable reflectivity profile.

In such a mirror, reflectivity decreases radially from a peak in the center down to zero over a distance comparable to the diameter of the laser rod. Such a resonator is, in principle at least, capable of sustaining a single transverse mode of a very large volume and with a smooth, uniform spatial profile. Whether a large volume can be realized in a practical system depends on the gain of the system. As will be discussed at the end of the section, only in a high-gain laser can a large mode size be utilized. Otherwise alignment stability becomes a very critical issue and the laser has only a very small tolerance for mirror misalignment caused by environmental conditions.

It clearly seems that if an unstable resonator is to be used in a solid-state laser, a Gaussian-type reflectivity output coupler is a very elegant solution in overcoming the beam profile issue. The merits of such a design in providing a smooth output profile in an unstable resonator have long been recognized. Various solutions have been proposed for the fabrication of variable reflectivity profiles. Among these have been birefringent elements [5.79–80] and a radially variable Fabry-Perot interferometer [5.81]. However, advances in thin-film manufacturing technology have made it possible to produce mirrors with a Gaussian reflectivity profile by deposition of multilayer dielectric films of variable thickness on a transparent substrate [5.82–87]. This represents a real breakthrough in terms of a practical implementation of unstable resonators, and a number of commercially available Nd:YAG lasers incorporate such mirrors.

The reflectivity of a mirror having a Gaussian-type reflectivity profile such as shown in Fig. 5.53a can be described as follows:

$$R(r) = R_{\max} \exp[-2(r/w_m)^n], \quad (5.121)$$

where r is the radial coordinate, R_{\max} is the peak reflectivity at the center, w_m is the mirror spot size or radial distance at which the reflectivity falls to $1/e^2$ of its peak value, and n is the order of the Gaussian profile. Most mirrors have a Gaussian profile for which $n = 2$; super-Gaussian profiles are obtained for $n > 2$. By adjusting the maximum reflectivity (R_{\max}), the width (w_m), and the order of the Gaussian (n),

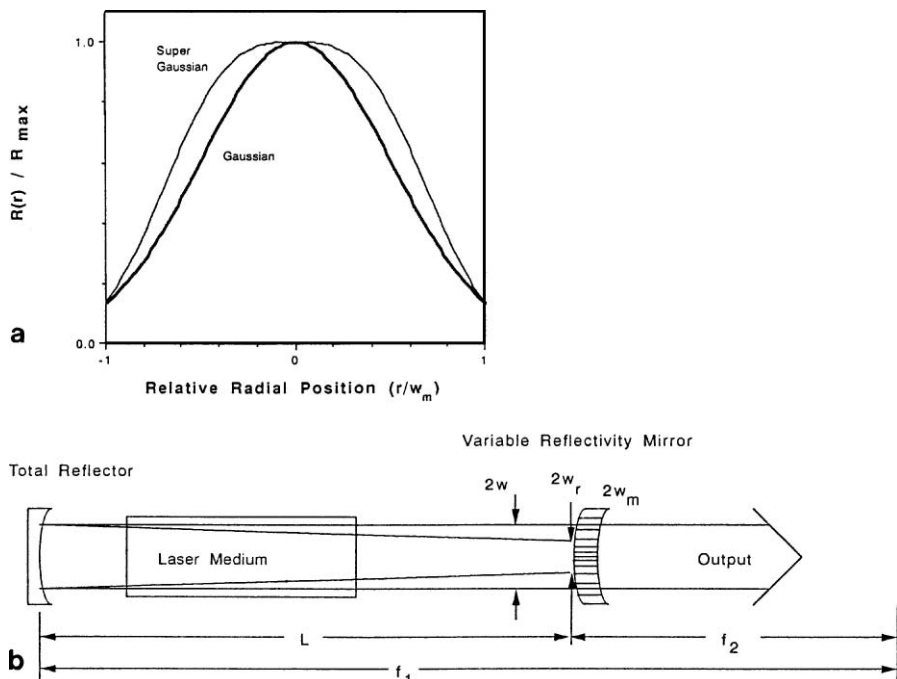


Fig. 5.53. Mirror with a Gaussian and super-Gaussian reflectivity profile (a) and unstable resonator employing such a mirror (b)

the output energy for a given oscillator design with a specific magnification can be optimized while maintaining a smooth output beam profile.

In the following discussion, we will address the design issues concerning Gaussian mirrors of order 2 ($n = 2$). Super-Gaussian mirrors which can provide a higher beam fill factor as compared to Gaussian mirrors have been treated in [5.88]. Figure 5.53b illustrates the concept of the variable reflectivity unstable resonator.

Upon reflection at a Gaussian mirror, a Gaussian beam is transformed into another Gaussian beam with a smaller spot size

$$\frac{1}{(w_r)^2} = \frac{1}{w^2} + \frac{1}{w_m^2}, \quad (5.122)$$

where w is the spot size of the incident beam and w_r is the spot size of the reflected beam.

For an unstable resonator containing a variable reflectivity output coupler, the magnification m is the ratio between the beam sizes of the incident and reflected beam, given by

$$m = \frac{w}{w_r} = [1 + (w/w_m)^2]^{1/2}. \quad (5.123)$$

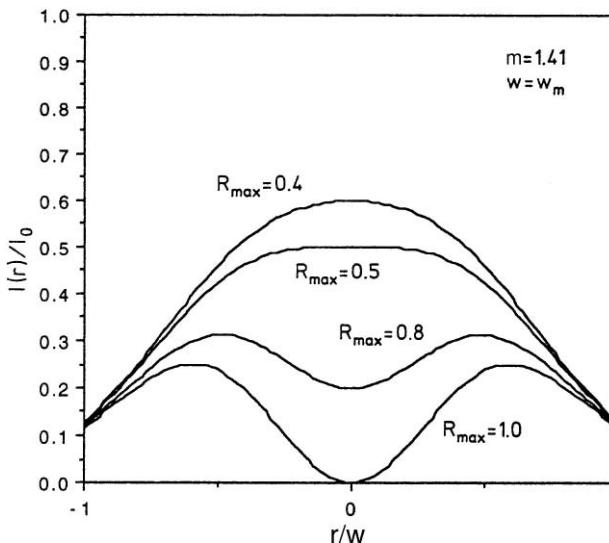


Fig. 5.54. Profile of the output beam for various peak reflectivities of the mirror

The effective output coupling from a resonator containing a variable reflectivity mirror depends on the average reflectivity of the mirror, which is a function of the profile of the incident beam. For a Gaussian beam (TEM₀₀ mode) the effective average reflectivity is

$$R_{\text{eff},00} = R_{\max}/m^2. \quad (5.124)$$

For the next higher order mode (TEM₀₁), the effective reflectivity can be shown to be

$$R_{\text{eff},01} = R_{\max}/m^4. \quad (5.125)$$

Mode discrimination is achieved because the effective mirror reflectivity for the TEM₀₁ mode is reduced by (1/m²) as compared to the TEM₀₀ mode.

Though the reflected beam is Gaussian, the same is not true for the transmitted beam I_{out} . The spatial profile of the transmitted beam is the product of the incident Gaussian beam and the transmission profile of the mirror

$$I_{\text{out}}(r) = \left\{ 1 - R_{\max} \exp[-2(r/w_m)^2] \right\} I_0 \exp[-2(r/w)^2]. \quad (5.126)$$

Figure 5.54 shows a plot of the profile of the output beam for various peak reflectivities of the mirror. As the curve illustrates, if R_{\max} is greater than a certain value, a dip occurs in the center of the output beam. In these situations, the mirror transmission increases with radius faster than the beam intensity decreases. The condition for which the central dip of the mirror just begins to occur is given by

$$R_{\max} \leq 1/m^2. \quad (5.127)$$

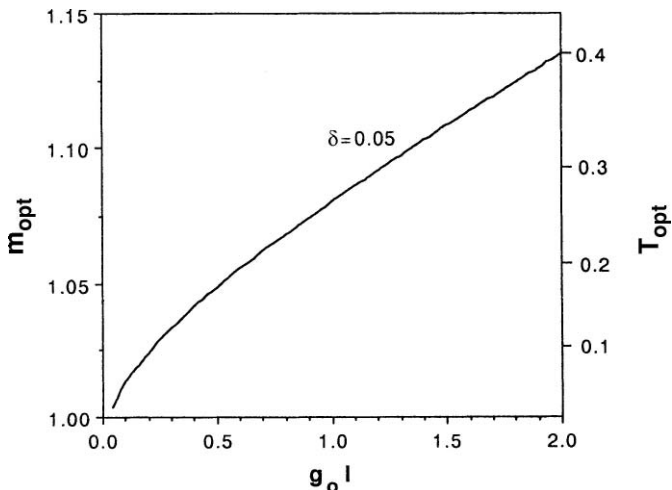


Fig. 5.55. Relationship of logarithmic gain $g_0 l$, T_{opt} , and m_{opt} . Parameter is the resonator loss δ

From (5.124 and 127) we obtain the condition that in order to have a filled-in output beam without a dip in it, the effective reflectivity must be less than

$$R_{\text{eff}} = 1/m^4. \quad (5.128)$$

The output coupling for this resonator is then

$$T = 1 - 1/m^4. \quad (5.129)$$

Since the optimum output coupling T_{opt} of an oscillator is related to the logarithmic gain and losses according to (3.66) we can plot m_{opt} as a function of these quantities as shown in Fig. 5.55.

Design Procedure. We assume that the oscillator was operated with a stable resonator and T_{opt} was determined. Alternatively, the laser can be operated as an amplifier and with a small probe beam, the gain and losses can be measured; in this case T_{opt} has to be calculated from (3.66). With T_{opt} known, we obtain from (5.129) the value of m . The spot size radius w of the Gaussian beam is usually selected to be half the radius of the laser rod r_d in order to avoid diffraction effects, i.e., $w/r_d = 0.50$. With this assumption, the mirror spot size w_M follows then from (5.123). Therefore, the mirror parameters R_{max} from (5.127), and w_M have been specified. The mirror radii and mirror separation follow from (5.109, 114) for the confocal unstable resonator. Thermal lensing of the laser rod can be accounted for by changing the curvature of one of the mirrors according to (5.116).

As an example, we use a diode-array-pumped Nd:YAG laser rod for which the following parameters have been measured with a $1.06 \mu\text{m}$ probe beam: logarithmic gain $g_0 l = 1.5$, internal losses $\delta = 0.05$, thermal lensing $f = 6 \text{ m}$. From these parameters it follows that, based on the discussion above, $T_{\text{opt}} = 0.34$, $R_{\text{eff}} = 0.66$, $m = 1.11$, and

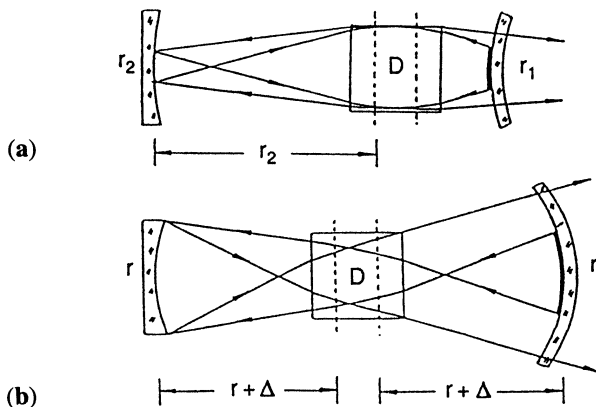


Fig. 5.56. Rod imaging (a) and near-concentric (b) unstable resonators containing a laser rod with optical power D [5.94]

$R_{\max} = 0.81$. The laser rod has a diameter of 5 mm. For good extraction efficiency, we select a diameter of the fundamental mode of half the rod diameter, or $w = 1.25$ mm. The spot radius for the mirror is therefore from (5.123) $w_M = w/(m^2 - 1)^{1/2} = 2.6$ mm. The focal length of the uniform reflectivity mirror was chosen $f_1 = 5$ m, which determines the focal length of the Gaussian mirror, $f_2 = -4.5$ m. Resonator length is $L = 0.5$ m. The focal length of mirror M_1 is increased according to (5.116) to compensate for thermal lensing: one obtains $f'_1 = 7.7$ m.

The operation of multi-hundred watt Nd:YAG lasers which incorporated positive- or negative-branch unstable resonators was first reported in [5.89–91]. Two unstable-resonator designs have been described which are particularly suitable for high-power solid-state lasers, because in these designs, the influence of thermal-rod lensing on the resonator properties is minimized. Both configurations, the rod-imaging negative branch [5.92], and the near-concentric positive [5.93, 94] branch unstable resonators, employ graded reflectivity mirrors.

As already mentioned, a negative-branch unstable resonator contains a focal point inside the cavity. A special case is the rod-imaging resonator shown in Fig. 5.56a. In this resonator, the rear mirror images the principal plane of the rod onto itself. In this case, it can be shown that the g parameter of the rear mirror does not depend on the focal length of the rod thermal lens.

If both principal planes of the thermal lens are imaged onto themselves by the mirrors, one obtains a stable concentric resonator. A near-concentric unstable resonator is formed if both mirrors are moved a small distance further apart from this position (Fig. 5.56b). It has been shown that this resonator is less sensitive to rod focal length changes as compared to other configurations. Theoretical and experimental investigations of these resonator concepts, as well as design procedures, can be found in [5.94].

In our laboratory, we tested a high-power diode-pumped, Nd:YAG laser with both of these unstable resonator configurations in an attempt to optimize system performance [5.95]. The dual-head laser contained an Nd:YAG rod of 10 mm diameter

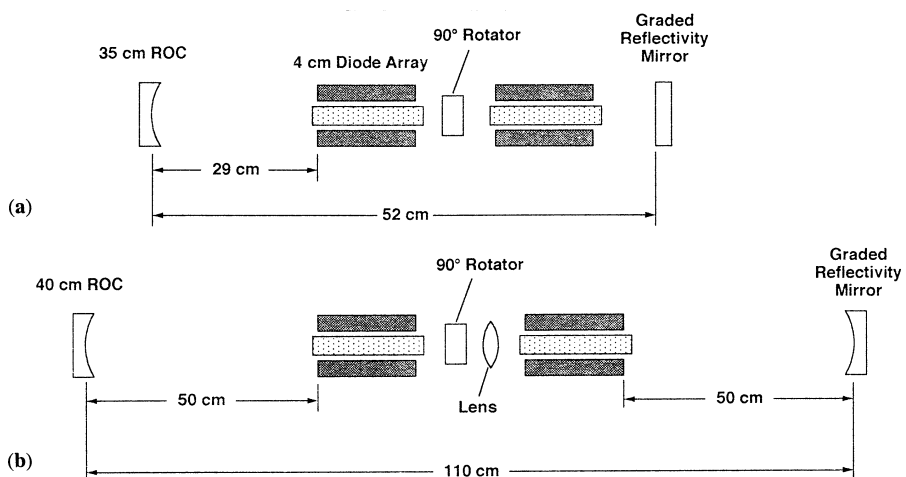


Fig. 5.57. Rod imaging (a) and symmetric near-concentric (b) unstable resonators

and a length of 69 mm. Each head is pumped by a fivefold symmetric stack of laser diodes emitting at 810 nm. The heads are pumped with 250- μ s-long pulses at a repetition rate of 200 Hz at a combined optical average pump power of 3.2 kW. With a close-coupled flat/flat resonator and an 80% reflective output coupler, a maximum of 425 W average output was obtained from the dual-head oscillator. The laser heads were placed close together in all experiments. At a combined maximum input pump power of 3.2 kW, this arrangement behaves as one rod with a refractive power of 3.3 diopters.

The rod-imaging unstable resonator was formed by a concave rear mirror and a flat graded reflectivity output coupler. As shown in Fig. 5.57a, a 90° quartz rotator is placed between the laser rods to compensate for birefringence. The best result from this setup was an output power of 250 W at a beam parameter product of 9.6 mm mrad [defined as beam diameter times full angle]. In a symmetric near-concentric unstable resonator configuration with a 10-mm separation from the concentric position, the best performance was at an output of 220 W at a beam divergence of 5.5 mm mrad. The super-Gaussian mirror had a central reflectivity of 87%, a spot radius of 2.5 mm, and a super-Gaussian exponent of 9. In order to match the desired beam diameter to the available variable reflectivity mirrors, the refractive power of the rods was increased by placing a lens between the rods, as shown in Fig. 5.58b. For a given mirror spot size, this leads to a larger intracavity beam inside the rod and to a beam cross section reduction at the mirrors.

On the basis of these experiments, we came to the following conclusions. The laser output power is about the same for both resonator configurations. The near-concentric unstable resonator was about twice as long in comparison to the rod-imaging design, but it produced a lower beam divergence. Consistent with theory, the near-concentric resonator was more tolerant to changes in thermal lensing of the rod (i.e., pump input power), as compared to the rod-imaging resonator. Both designs are considerably less

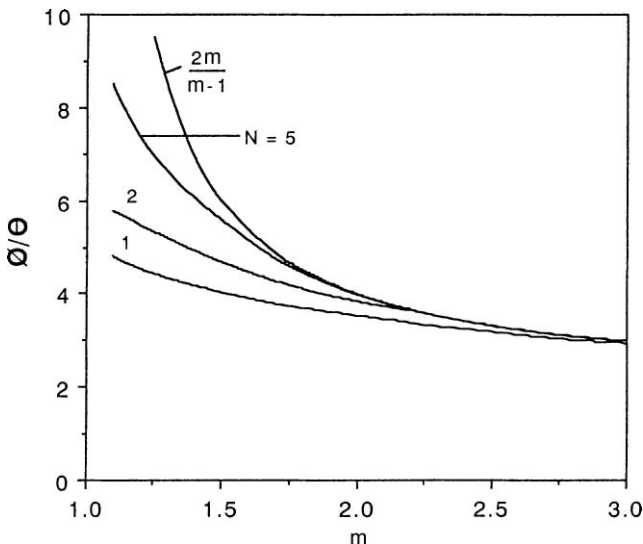


Fig. 5.58. Ratio of the fundamental mode beam-steering angle ϕ to the mirror misalignment angle θ for different values of the magnification m . Parameter is the equivalent Fresnel number N [5.82]

sensitive to pump input changes compared to a positive-branch confocal configuration. The advantages of lower beam divergence and higher tolerance to pump input changes of the near-concentric unstable resonator have to be traded-off against the much shorter rod-imaging resonator.

5.5.4 Gain, Mode Size, and Alignment Sensitivity

Whether a large mode size in a resonator can be realized in practical situations depends upon the resonator's sensitivity to mirror tilt and thermal lensing. The former determines the laser's susceptibility to the effects of temperature variations, structural changes, and shock and vibration, whereas the latter determines the laser's tolerance to changes in the operating parameters such as repetition rate or laser output. For stable resonators, these issues have been addressed in Sects. 5.1.8, 9. Here we will discuss the sensitivity of the unstable resonator to mirror tilt. The principal effect of a small tilt of a resonator mirror is to steer the output beam. We consider the case of a tilted primary mirror because its sensitivity is greater than the sensitivity to feedback-mirror tilts. If the primary mirror is tilted by θ with respect to its aligned position, the propagation of the output beam is then tilted by an angle ϕ . The relationship between the mirror tilt angle θ and the beam angle ϕ has been treated in [5.96] for the confocal resonator using a hard aperture output coupler.

For the positive-branch confocal resonator, the alignment sensitivity is

$$\frac{\phi}{\theta} = \frac{2m}{m-1} \quad (5.130)$$

and for the negative-branch confocal resonator

$$\frac{\phi}{\theta} = \frac{2m}{m+1}. \quad (5.131)$$

The major conclusions we can draw from these results are as follows:

- (a) A confocal positive-branch resonator is more sensitive to mirror misalignment compared to a negative-branch resonator; this is particularly the case for values of m less than 2;
- (b) In a low-gain laser, the value of m will be small, and therefore in such lasers, the unstable resonator will be very sensitive to mirror misalignment.

We will now turn our attention to the Gaussian mirror unstable resonator. McCarthy et al. [5.82] have presented an analytical solution to the problem of the misaligned optical resonator with a Gaussian mirror. The misalignment is introduced by tilting the uniform mirror by an angle θ . The Gaussian beam propagates then along an axis making an angle ϕ relative to its original propagation direction. As before, the quantity ϕ/θ characterizes the resonator sensitivity to misalignment.

The ratio ϕ/θ as a function of the resonator magnification m is plotted in Fig. 5.58. Parameter is the equivalent Fresnel number of the Gaussian mirror which is defined as

$$N = w_M^2/\lambda L. \quad (5.132)$$

For large values of N and magnifications larger than 2, the alignment sensitivity approaches the value given in (5.130), which is based on purely geometrical considerations. As we recall from our previous discussion, the gain of the laser determines the magnification m , whereas high extraction of the energy stored in the volume of the laser rod requires a large beam size, and therefore a large w_M and N .

It is apparent from the curves in Fig. 5.58 that for large Fresnel numbers in combination with small values of m , the resonator becomes extremely sensitive to misalignment. Unfortunately, most solid-state lasers have a small gain which results in a rather low m value. For the example chosen in the last section, one obtains $w_M = 2.6$ mm, and $L = 0.5$ m which gives $N = 13$ for the Nd wavelength. On the basis of the data presented in Fig. 5.58, this is not a very robust resonator to say the least. This was verified in actual experiments; alignment was difficult to obtain and could be maintained only under laboratory conditions.

Actually, the analysis presented in [5.82] concludes that for values of m much less than 2, the unstable resonator has about the same misalignment sensitivity as a plane–plane resonator. Therefore, only in high-gain materials such as Nd:YAG with the pump beam tightly focused to achieve high inversion, will it be possible to achieve magnifications high enough such that a large beam diameter can be utilized.

Also in certain gas lasers, where the gain is high, and therefore $m > 2$, the resonator sensitivity is independent of mode size. In this regime, one can take full advantage of the unstable resonator in creating a large fundamental mode volume.

In low-gain systems, an unstable resonator has to be designed with a Fresnel number close to 1 for good alignment stability. This, of course, defeats the purpose of using an unstable resonator since with such a low Fresnel number, a stable resonator can provide the same performance.

5.6 Wavelength Selection

Vibronic lasers such as alexandrite, Ti:Sapphire, and Cr:GSGG have very broad gain curves. In the operation of these lasers it is necessary to use a wavelength selection technique to (a) restrict laser action to a specified wavelength and (b) tune the laser output. Several different methods are available (in principle) for providing the wavelength selection and tuning. These include (a) use of a prism inside the resonator, (b) utilization of an adjustable optical grating within the laser, (c) use of intracavity etalons, or (d) use of one or more thin birefringent plates within the laser that are tilted at Brewster's angle.

The technique most commonly employed for the wavelength selection of tunable lasers is the birefringent filter [5.97]. In its simplest form, the birefringent filter consists of a single thin birefringent crystal located inside the laser (Fig. 5.59). For simplicity, we assume that the birefringent axes lie in the plane of the crystal, and that the crystal is tilted at Brewster's angle.

The crystal and birefringent axes and the incident light are shown in more detail in Fig. 5.60. In this figure, α is the incidence angle between the incoming laser beam and the normal to crystal plane, and ϕ is the angle between the plane of incidence and the crystal optic axis. The phase difference δ between the ordinary and extraordinary rays emerging from the crystal is given by

$$\delta = \frac{2\pi h(n_0 - n_e) \sin^2 \theta}{\lambda \sin \alpha}, \quad (5.133)$$

where λ is the laser wavelength in vacuum.

An alternate representation of the single-stage tuning element is given in Fig. 5.59. The input and output partial polarizers represent the front and back surfaces of the quartz crystal situated at Brewster's angle. In addition, the crystal is assumed to be rotated to $\theta = 45^\circ$ in this figure.

Wavelength selection occurs with the birefringent filter because of the two different crystal indices of refraction. When the laser light has a wavelength corresponding to an integral number of full-wave retardations, the laser operates as if the filter were

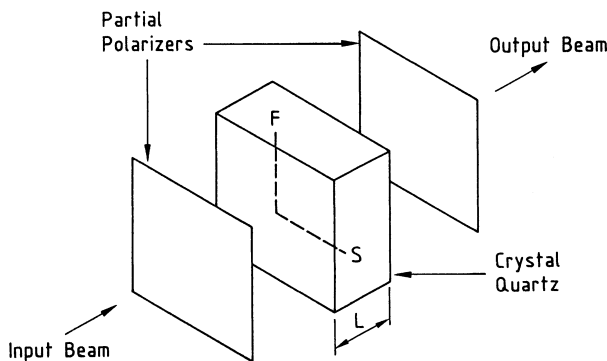


Fig. 5.59. Single-crystal wavelength selector

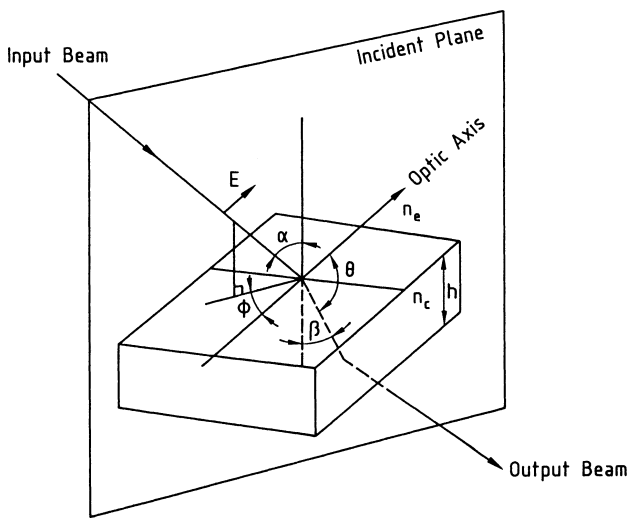


Fig. 5.60. Schematic of typical single-plate birefringent filter

not present. At any other wavelength, however, the laser mode polarization is modified by the filter and suffers losses at the Brewster surfaces.

Tunability of the laser is achieved by rotating the birefringent crystal in its own plane. This changes the included angle ϕ between crystal optic axis and the laser axes and, hence, the effective principal refractive indices of the crystal.

The amplitude transmittance of the single-stage filter of Fig. 5.59 has been calculated in [5.97]. For a quartz crystal rotated to $\phi = 45^\circ$ and tilted to Brewster's angle, the transmittance at unwanted wavelengths is about 82%. This may or may not provide adequate suppression of unwanted wavelengths for certain lasers.

One way to lower the filter transmittance in the rejection band is to use a stack of identical crystal plates that are similarly aligned, as shown in Fig. 5.61 [5.98]. If one uses a stack of 10 quartz plates, the resulting transmittance in the rejection band is about 15%, which is certainly small enough to suppress unwanted laser frequencies.

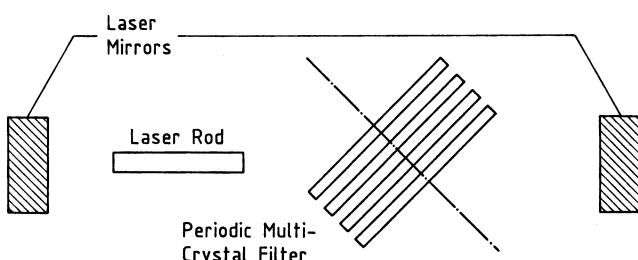


Fig. 5.61. Four-crystal wavelength selector

Another technique for lowering the filter transmittance in the rejection band is to include more Brewster's angle surfaces in the laser. This reduces the value of T_0 for the filter at the cost of increasing the width of the central passband slightly.

Still another approach for narrowing the width of the central passband of the filter is to use several crystals in series whose thicknesses vary by integer ratios. One such filter, consisting of three crystals whose thicknesses are in the ratio 1:4:16, has been analyzed in [5.99]. The central passband of this filter is considerably narrower than those of the previously discussed designs. The disadvantage of this approach, however, is that numerous (unwanted) transmission spikes are now present, the largest of which has an amplitude of about 75%.

It is obvious from these results that there are virtually an unlimited number of designs that can be tried, with corresponding tradeoffs in central passband width, stopband transmittance, presence of spikes in the stopband, and complexity of the birefringent filter. For all of these birefringent filter designs, tuning is continuous and easily implemented through rotation of the multiple crystals.

6. Optical Pump Systems

An efficient pump system utilizes a radiation source having a spectral output that closely matches the absorption bands of the gain medium, transfers the radiation with minimum losses from the source to the absorbing laser material, and creates an inversion which spatially matches the mode volume of the resonator mode. In this chapter we will review the most common pump sources and radiation transport systems employed in solid-state lasers.

6.1 Pump Sources

A number of different radiation sources have been employed over the years to pump solid-state lasers; today only flashlamps, cw arc lamps, and laser diodes depicted in Figs. 6.1 and 6.2 are of practical interest. Pump sources for solid-state lasers range in size and power from tiny laser diodes at the 1 W level, pumping a microchip laser, to flashlamp-pumped lasers employed in inertial confinement fusion research, which occupy large buildings and provide tens of megajoules of pump radiation.

In the past, tungsten–halogen lamps have been a very popular source for many Nd:YAG lasers because of their low cost and simple power supply design. However, because of the low efficiency, this pump source has been replaced by cw arc lamps or laser diodes. In a vortex lamp the arc is stabilized by a gas jet which requires a closed-cycle gas recirculation system. Several early Nd:YAG lasers have been pumped with this very powerful radiation source. Mercury arc lamps have been employed to pump small cw ruby lasers. Before the emergence of laser diodes, alkali-metal lamps, as well as the sun, have been considered as pump sources for space-based systems. LEDs are the precursors to laser-diode pumping and several laboratory devices have been built with these sources. Chemical energy stored in photo flash bulbs has been utilized in the design of single-shot Nd:YAG lasers. In classified programs, the use of radiation from explosive devices has been pursued as a pump source for solid-state lasers. readers interested in details of the earlier pump sources may refer previous editions of this book.

If we compare the spectral characteristics of the various pump sources, we find that on one side we have monochromatic pump sources, such as laser diodes, and at the other extreme blackbody radiators, such as filament lamps. The discharge lamps operated at low current densities represent a compromise between a monochromatic source and a blackbody radiator. Radiation from an arc discharge lamp is made up of both line and continuum components.

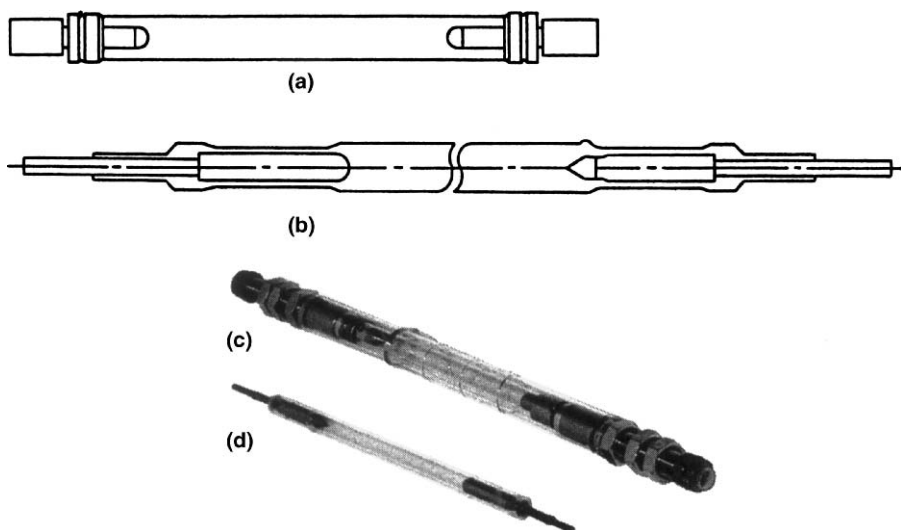


Fig. 6.1. Outline drawing of (a) a flashlamp and (b) a cw krypton arc lamp and photograph of an arc lamp (c) with and (d) without cooling jacket

The dramatic improvement in laser efficiency which can be achieved by replacing a blackbody pump source with a more efficient emitter can be illustrated in the following example: A 6-mm-thick sample of Nd:YAG absorbs about 3% of the radiation from a blackbody source at 2800 K. Therefore, a standard 1 kW tungsten–iodine filament lamp generates about 30 W of useful radiation for pumping a 6-mm-diameter Nd:YAG laser rod. A krypton arc lamp has a radiation efficiency of 45% and a fractional utilization of the radiation by Nd:YAG of 20% for the same sample thickness as above. Therefore, 9% of electrical input is available as potential pump radiation. This reduces the required electrical input to 330 W for the above case. A typical diode laser array will produce 30 W of radiation at 808 nm at an electrical input of about 70 W. All of the optical output of the diode laser is within the absorption bands of Nd:YAG.

This comparison addresses only the spectral characteristics of the various pump sources. Coherent pump sources, such as laser diodes, because of their spatial characteristics, permit concentration of pump radiation into the active medium with little losses, whereas only a fraction of the omnidirectional radiation from a lamp pump source can be directed into the active medium. The result is an overall electrical efficiency for a tungsten lamp pumped laser of about 0.5%, which increases for arc lamp pumped systems to about 2–3% and diode-pumped lasers achieve around 10–15%.

The electronics required to operate the pump source of the laser is loosely referred to as the power supply or power conditioning system. However, most lasers contain a number of auxiliary electronic subsystems. Furthermore, in most lasers, the vital system functions are controlled and monitored via digital electronics. Generally, the electronics of solid-state lasers can be divided into the following subsystems:

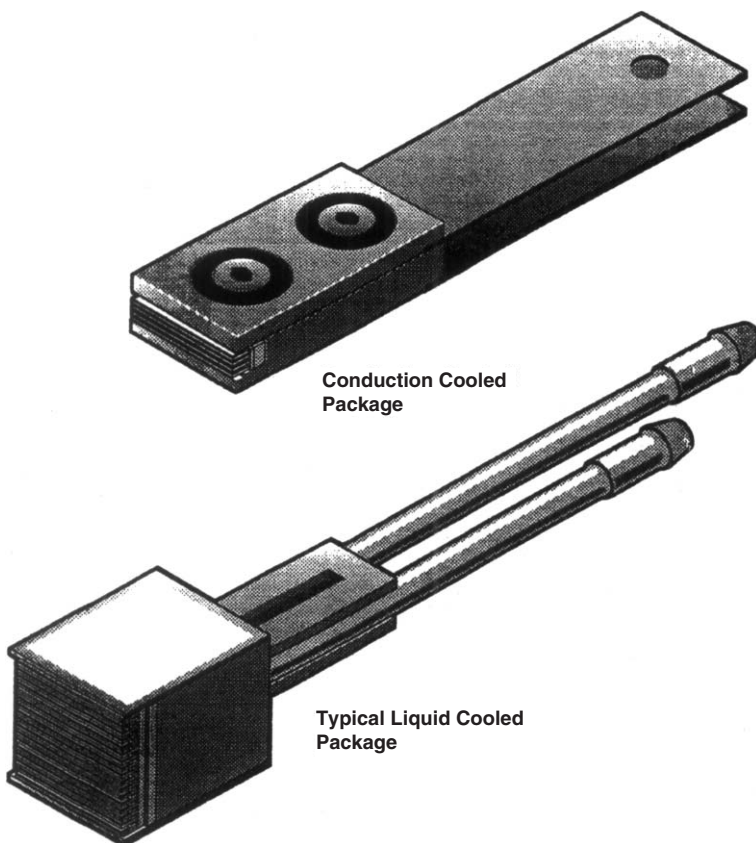


Fig. 6.2. Two-dimensional diode laser arrays. Stocked 1-cm bars (a) conduction-cooled and (b) internally water-cooled

- *Power conditioning.* This unit converts ac line voltage or power from a battery to the appropriate dc level required for operation of arc lamps or laser-diode arrays.
- *Energy storage.* Capacitors are required for pulsed arc lamps and diode arrays to store the energy transferred to the pump during each pulse.
- *Switching or trigger circuit.* In the case of diode arrays, energy is transferred from a capacitor bank via a semiconductor switch. Flashlamps behave electrically like switches which are turned on by a high-voltage trigger pulse.
- *Auxiliary subsystems.* Besides subsystems which provide energy to the pump source, a number of electronic subsystems are usually required in a laser, such as Q-switch electronics, heaters for second-harmonic generators, mechanical shutters, motor driven translation stages, piezoelectrically driven mirrors, fans, coolers, etc.
- *System microcontroller.* With the exception of laboratory setups, most lasers contain a microcontroller which is employed for controlling and monitoring

all electrical, electromechanical, and thermal subsystems. The output from the microcontroller usually consists of a display indicating the health and status of the laser system. Housekeeping functions which are displayed may contain interlock data, such as temperature and coolant flow, optical data, such as pulse energy and pulse timing, and electrical data, such as voltage and current levels.

- *Timing control board.* This unit typically comprises synchronous clocks, logic devices, gate arrays, and drive components to supply the necessary timing signals for control of the pump source and Q-switch driver.

In this section, we are concerned only with the electronics associated with operating the pump source of the laser.

6.1.1 Flashlamps

Lamp Design and Construction

Flashlamps used for laser pumping are essentially long arc devices designed so that the plasma completely fills the tube. A flashlamp consists of a linear quartz tube, two electrodes which are sealed into the envelope, and a gas fill. Standard linear lamps have wall thicknesses of 1–2 mm, bore diameters between 3 and 19 mm, and lengths from 5 cm to 1 m.

Flashlamps are typically filled with gas at a fill pressure of 300–700 Torr at room temperature. Xenon is generally chosen as the gas fill for flashlamps because it yields a higher radiation output for a given electrical input energy than other gases. However, in a few special cases, such as small, low-energy lamps employed to pump Nd:YAG lasers, the low-atomic-weight gas krypton provides a better spectral match to the absorption bands of Nd:YAG.

The anode in flashlamps consists of pure tungsten or often thoriated tungsten because the alloy is easier to machine. The cathode comprises a compressed pellet of porous tungsten impregnated with barium calcium aluminate. This pellet is attached onto a tungsten heat sink. The surface area of the tip must be large enough to handle the peak current while the shape of the tip positions the arc during the trigger pulse. During the lamp operation, barium is transported to the cathode surface where it forms a monolayer with a work function of about 2 eV versus 4.5 eV for pure tungsten. A lower work function improves electron emission for a given temperature. For the same reason, a cathode material with a low work function makes it easier to trigger the lamp. Since in a standard lamp the cathode is more emissive than the anode, flashlamps are polarized and will pass current in only one direction without damage.

There are several designs in commercial use for sealing the electrodes to the body of a flashlamp. The most common type of lamp seal is the tungsten-rod seal. Figure 6.1b illustrates the design which is in this case applied to a cw arc lamp. The tungsten-rod seal uses an intermediate highly doped borosilica glass to seal the electrode to the fused quartz envelope. The glass balances the thermal stresses between fused silica, which has an extremely low coefficient of thermal expansion, and tungsten, which has a large coefficient.

A variation of the rod seal is the ribbon seal, which is made by encapsulating a thin molybdenum foil with quartz. The quartz is shrunk down around the foil. The main application for this lamp is for low peak and average current operation.

Beside the rod seal, another common flashlamp design utilizes an end-cap seal as illustrated in Fig. 6.1a. This seal, which is soldered onto the quartz envelope, uses a copper rod, one end of which is brazed to an electrode and the other end welded to a nickel cup. The seal is made with a low-temperature indium solder between the copper-plated nickel cup and the platinum-coated end of the quartz envelope. The solder seal must be operated below the softening point of the solder, which is about 180°C. A unique feature of this type of quartz-to-metal seal is that the diameter of this seal joint can be as large as the quartz tubing itself. This permits a large cross section for the electrodes and thus an excellent path for dissipation of heat from the electrodes. In some cases the copper stem is water-cooled internally. The lamp is filled at room temperature through the hollow copper stem. When the filling is finished, the copper tube is crushed to seal in the gas. Thus, there is no "tip-off" on this lamp and little residual stress due to formation of the seal.

The tungsten-rod seal, on the other hand, can be operated at much higher temperatures. Since the heat removal through the small-diameter tungsten stem is not very large, the quartz tubing is shrunk into close proximity to the electrode to aid cooling of the electrode in radial directions. An advantage of the rod-seal construction is that during evacuation the lamps can be baked out at 1000°C, and during the filling process the electrodes can be induction-heated to a bright red for their final outgassing. The lamps are then backfilled to the appropriate gas pressure and tipped off. The tungsten-rod seal permits the fabrication of high-purity contaminant-free lamps having long shelf lives.

The envelope and the electrode-seal area of flashtubes are normally cooled by free or forced air, water, or water-alcohol mixtures. Liquid cooling permits operation of the lamps at a maximum inner-tube wall surface loading of 300 W/cm² of average power. Free-air convection cooling is limited to handling about 5 W/cm² of dissipation; forcing air across the flashtube envelope increases this value up to 40 W/cm². Liquid-cooled linear flashlamps are also available with outer quartz jackets, which permit cooling of the lamps with a highly turbulent flow.

Optical Characteristics

The radiation output of a gas discharge lamp is composed of several different components, each corresponding to a different light-emission mechanism. The relative importance of each of these mechanisms depends strongly on the current density in the lamp, and so the low- and high-power optical output spectra are markedly different. The total radiation is made up of both line and continuum components. The line radiation corresponds to discrete transitions between the bound energy states of the gas atoms and ions (bound-bound transitions). The continuum is made up primarily of recombination radiation from gas ions capturing electrons into bound states (free-bound transitions) and of bremsstrahlung radiation from electrons accelerated during

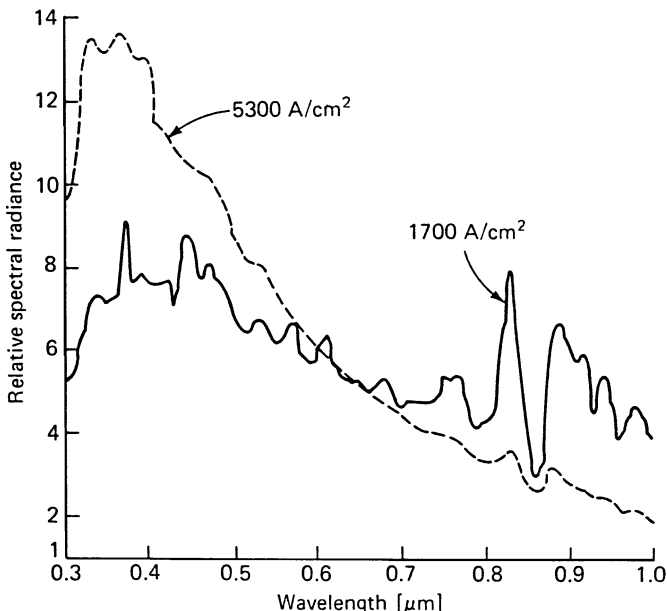


Fig. 6.3. Spectral emission of a xenon flash tube (EG&G, model FX-47A) operated at high current densities. Lamp fill pressure is 0.4 atm. The spectrum at the two current densities can be approximated by blackbodies at 7000 and 9400 K, respectively [6.1]

collisions with ions (free–free transitions). The spectral distribution of the emitted light depends in complex ways on electron and ion densities and temperatures.

In the continuous-power, wall-stabilized noble gas arc, current densities are such that there is a high number of bound–bound transitions and therefore the radiation spectrum is characteristic of the fill gas and is broadened by increases in pressure.

In high current density, pulsed laser applications, the spectral output of the lamp is dominated by continuum radiation, and the line structure is seen as a relatively minor element. Between these two cases, a pulsed-power region can exist where the pulsed-power level is such that discrete line radiation is still emitted and is superimposed on a strong background continuum.

In Fig. 6.3 the spectral emission of a xenon flashtube is plotted for two current densities. As a result of the high current densities, the line structure is in this case masked by a strong continuum. From Fig. 6.3 it also follows that a high current density shifts the spectral output toward the shorter wavelenghts. One can relate the radiation characteristics of a flashlamp $R(\lambda, T)$ to the characteristics of a blackbody. The departure of any practical light source from the blackbody characteristic is accounted for in the emissivity $\varepsilon(\lambda, T)$, which varies between zero and one and is both wavelength and temperature dependent; thus $R(\lambda, T) = \varepsilon(\lambda, T)B(\lambda, T)$. In a flashlamp, $\varepsilon(\lambda, T)$ depends strongly on temperature and wavelength. If we assume local thermodynamic equilibrium in the plasma, the blackbody characteristic $B(\lambda, T)$ becomes the blackbody curve corresponding to the electron temperature in the plasma.

In general, the emissivity of the flashlamps radiation at longer wavelengths is greater than the emissivity at shorter wavelengths. An increase in power density will result in a large increase in emissivity (and radiation) at short wavelengths, but only in small changes at longer wavelengths where the emissivity is already close to unity.

The xenon lamp is a relatively efficient device as it converts 40–60% of the electrical input energy into radiation in the 0.2–1.0 μm region. As noted in Chap. 2, principal pump bands of Nd:YAG are located from 0.73 to 0.76 μm and 0.79 to 0.82 μm . The xenon spectrum has no major line radiation in these bands, so pumping is primarily due to continuum radiation.

However, some strong krypton lines fall within the Nd:YAG pump bands. Investigations have shown that krypton flashlamps are more efficient than xenon lamps at low power densities for pumping Nd:YAG lasers [6.2–5]. There are indications that a crossover occurs in the pumping efficiency of krypton and xenon at high peak power densities, corresponding to that power density at which the xenon continuum becomes more efficient than the krypton line structure. This crossover occurs at a power density of approximately $2 \times 10^5 \text{ W/cm}^3$.

In general, the pumping efficiency of Nd:YAG of both xenon and krypton increases as the pressure is increased. In the range of 450–3000 Torr no maxima are found [6.6]. The limitation to further increases appears to be the fact that high-pressure lamps are difficult to trigger. The effect of an increase in gas fill pressure is to reduce the mean free path of the electrons and atoms in the discharge, and thus to increase their collision frequency. This leads to the production of more excited species in the discharge and the emission of more useful line radiation.

The transmission properties of the flashlamp envelope will influence the spectral output. Usually the envelope is fused silica, which transmits light between 0.2 and 4 μm . Figure 6.4 shows the UV transmission of doped and undoped fused silica. Germisil and Heliosil, manufactured from fused silica containing a slight admixture of titanium, are sometimes employed as lamp or flow-tube envelope material to prevent

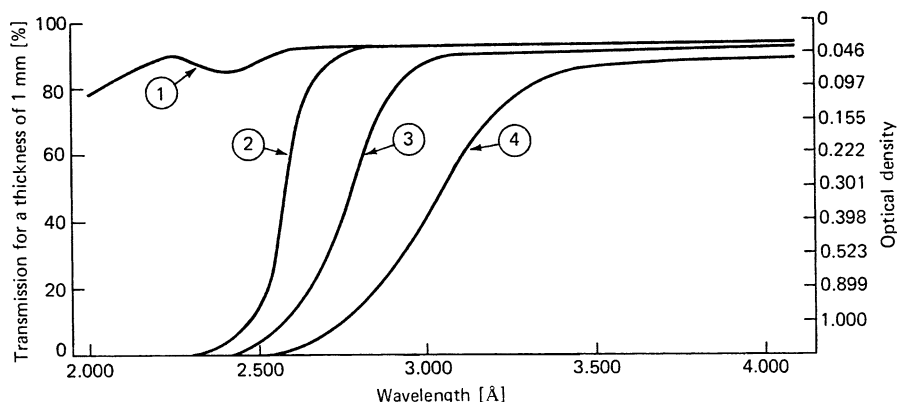


Fig. 6.4. Ultraviolet transmission (for 1-mm thickness) of different types of fused quartz. (1) Pursil, (2) Germisil, (3) Heliosil I, and (4) Heliosil II

the production of ozone in the air, or prevent breakdown of the flashlamp coolant, or inhibit the formation of color centers in certain solid-state laser materials.

Lamps with cerium-doped quartz envelopes have also been designed. Quartz doped with 6% cerium oxide will absorb radiation below 0.31 μm and will fluoresce at wavelengths between 0.4 and 0.65 μm . Spectral data from these lamps show that a 50-mm \times 4-mm bore lamp with 450 Torr of pressure operated at 10 J has a 15% greater output over the spectral range of 0.4–0.65 μm compared to a lamp with an undoped envelope.

In the design of pumping geometries for high-power laser systems, it is important to know how opaque the flashtube is to its own radiation. The optical transmission of a xenon flashtube has been measured at wavelengths from 0.25 to 1.0 μm and at currents up to 4000 A/cm² [6.7, 8]. From the experimental data plotted in Fig. 6.5 it follows that the absorption increases with current and wavelength. Above about 0.5 μm and a current of 4000 A/cm², a discharge tube 1 cm in diameter is nearly opaque. At shorter wavelengths and lower currents, the discharge is fairly transparent. From Fig. 6.5 it also follows that the absorption coefficient varies linearly with the square of the current density [6.9]. Thus in a large-bore flashlamp driven at high current densities, a large percentage of the radiation emanating from the plasma core is absorbed before it reaches the lamp surface. Hence the bulk of the radiation comes from a thin sheath near the lamp surface with a corresponding reduction in lamp efficiency.

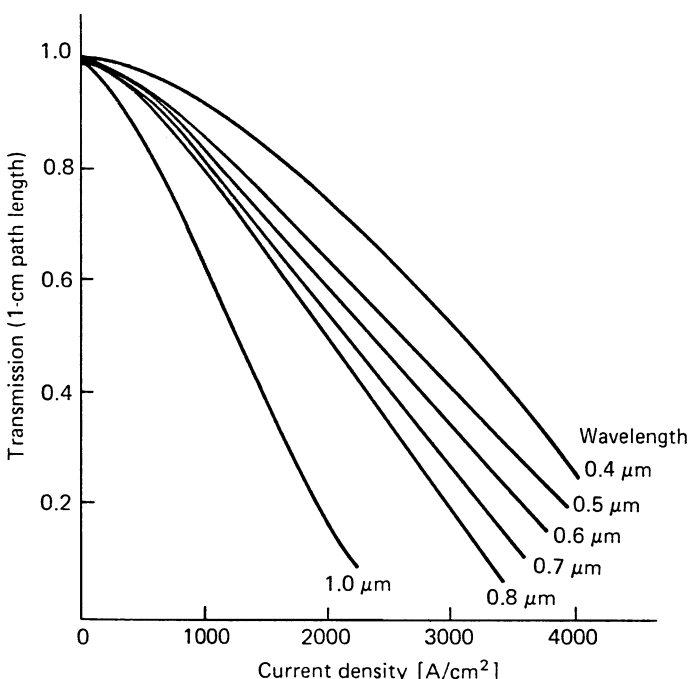


Fig. 6.5. Spectral transmission of the xenon plasma in a flashlamp as a function of current density [6.8]

Electrical Characteristics

The impedance characteristics of a flashlamp determine the efficiency with which energy is transferred from the capacitor bank to the lamp. The impedance of the arc is a function of time and current density. Most triggering systems initiate the arc as a thin streamer which grows in diameter until it fills the whole tube. The expansion period is fast, of the order of 5–50 µs for tubes of bore diameter up to 1.3 cm. During the growth of the arc, lamp resistance is a decreasing function of time (Fig. 6.6). The decreasing resistance arises in part from the increasing ionization of the gas and from the radial expansion of the plasma. After the arc stabilizes, the voltage–current relationship is described by [6.10, 11–13].

$$V = K_0 i^{1/2}, \quad (6.1)$$

where $K_0 = kl/d$ and describes the impedance characteristics of the particular lamp. The constant k is dependent only on such parameters as gas type and gas pressure, and l and d are the length and diameter of the flashlamp bore, respectively. K_0 or k is essentially the only parameter needed to describe the high-current electrical characteristics of a given flashlamp. This parameter is usually supplied by the manufacturers

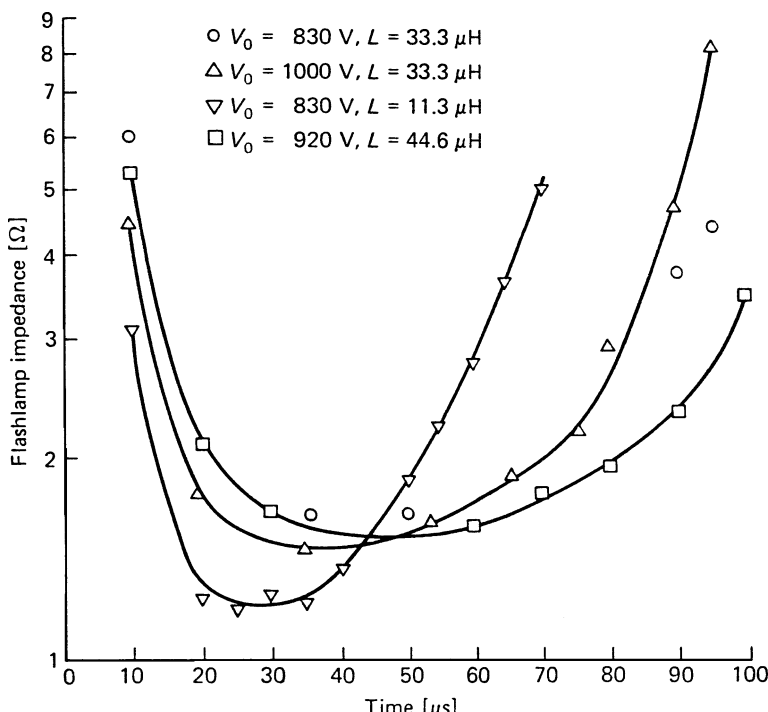


Fig. 6.6. Time dependence of flashlamp impedance for several input energies and series inductance values. The 60-mm-long and 3-mm-diameter flashlamp was filled with 450 Torr of xenon. The discharge circuit consisted of a 19-µF capacitor and one inductor which was varied from 11.3 to 44.6 µH [6.6]

of the flashlamps. K_0 is found simply by flashing the lamp at some reasonable loading, while measuring the voltage and current. The resistance of the flashlamp for the high-current regime with the plasma filling the bore of the tube is obtained from

$$V \cong R_L(i)i = \left(\frac{\varrho(i)l}{A} \right) i, \quad (6.2)$$

where $\varrho(i)$ is the specific resistivity of the xenon or krypton plasma and is a function of the current density. A is the cross-sectional area of the lamp. In (6.2) the voltage drop at the electrodes, which is of the order of 20 V, has been neglected. In operating regions of interest, the flashlamp resistivity for xenon at 450 Torr is related to current density j by [6.11]

$$\varrho(i) = \frac{1.13}{j^{1/2}}. \quad (6.3)$$

This relationship is valid for current densities of approximately 400–10,000 A/cm² [6.14]. The lamp resistance R_L is obtained by introducing (6.3) into (6.2)

$$R_L(i) = 1.27 \left(\frac{l}{d} \right) i^{-1/2}. \quad (6.4)$$

Comparing (6.2) with (6.1), we obtain an expression for the flashlamp parameter K_0

$$K_0 = 1.27 \frac{l}{d}. \quad (6.5)$$

The value of 1.27 holds for 450-Torr xenon lamps. It has been found from many flashlamp experiments that (6.5) can be generalized for other pressures and expressed as

$$K_0 = 1.27 \left(\frac{P}{450} \right)^{0.2} \frac{l}{d}, \quad (6.6)$$

where P is the flashlamp pressure in torr. The parameter K_0 obtained for krypton has been found to be about the same as that for xenon.

Tube Failure

The flashtube end of life can occur in either of two modes, and we can distinguish between catastrophic and nondestructive failures. The factors which contribute to catastrophic failure are explosion of the walls due to the shock wave in the gas when the lamp is fired or overheating of the lamp envelope or seal and subsequent breakage due to excessive thermal loading of the lamp. The first failure mode is a function of pulse energy and pulse duration, whereas the second catastrophic-failure mode is determined by the average power dissipated in the lamp. When the flashtube is operated well below the rated maximum pulse energy and average power, the lamp usually does not fail abruptly. Rather, the tube will continue to flash with a gradual decrease in light output, which will eventually fall below a level necessary for the

particular application. In the latter mode of failure, the reduced light output is caused by the erosion of the flashtube electrodes and the quartz walls and by the gradual buildup of light-absorbing deposits within the flashtube envelope.

Flashtube Explosion. When a high-voltage trigger pulse is applied between the electrodes of a flashtube, the gas breaks down generally near the axis of the tube and a conducting filament is established. As energy is released into the channel, heating of the ambient gas causes the filament to expand radially, forming cylindrical shock waves. The shock front and its associated plasma travel radially from the tube axis to its wall. The radial velocity of the plasma discharge and the shock amplitude are proportional to the input energy. The velocity was measured to vary from about 90 to 900 m/s for inputs from 60 to 600 J into a 5-cm-long flashlamp with 6-mm bore diameter [6.15]. The cylindrical shock wave and the associated plasma heat cause stress on the inside of the tube wall, which is axial in tension toward the electrodes. If the energy discharged exceeds the explosion limit for the lamp, the shock wave will be sufficiently intense to rupture the lamp walls and consequently destroy the lamp.

If the lamp is operated somewhat below the explosion point, catastrophic failure of the lamp is preceded by the formation of hairline cracks and a milky deposit. The microcracks, originating around minute flaws in the quartz envelope, will expand with each flash, eventually resulting in lamp failure. As a result of the high temperature of the expanding plasma, a steep temperature gradient is created near the tube surface when the plasma impinges upon the tube wall. Therefore, in addition to the progressive appearance of cracking and crazing of the inside wall, there is an associated silica deposit from evaporation and deposition [6.16].

Dugdale et al. [6.17] have investigated the effect of pulse heating on glass and ceramic surfaces. If the energy Q_0 per unit area is delivered to a material surface in time t_p , a rise surface temperature ΔT takes place, given by

$$\Delta T = a Q_0 (\pi K c_p \varrho t_p)^{-1/2}, \quad (6.7)$$

where K is the thermal conductivity, c_p is the specific heat, and ϱ is the density of the material; a is a constant between 1 and 2 depending on the heat pulse waveform ($a = 1.08$ for an exponential waveform). We can relate the pulse energy per unit area to the total flashlamp electrical input energy E_0 by writing

$$Q_0 = \frac{k_1 E_0}{\pi d l}, \quad (6.8)$$

where the parameter k_1 depends on the type of gas and fill pressure used. During the heat pulse, the temperature rise is confined to a depth Δx below the surface, given by

$$\Delta x = 2 \left(\frac{K t_p \varrho}{c_p} \right)^{1/2}. \quad (6.9)$$

The depth lies in the range of 10^{-4} to 10^{-2} cm for glasses and ceramics subjected to heat pulses of duration 10^{-6} to 10^{-3} s. The restraint imposed by the unheated

substrate may cause stresses σ_T to develop in the hot surface layer of magnitudes up to

$$\sigma_T = \frac{\varepsilon \alpha \Delta T}{1 - \mu}, \quad (6.10)$$

where α is the thermal expansion of the material, μ is Poisson's ratio, and ε is the Young's modulus of elasticity. The temperature gradient ΔT , which will cause thermal shock damage of the envelope, is obtained by equating σ_T with the rupture stress σ in (6.10). From (6.7, 8, 10) follows the lamp input pulse energy, which will generate stresses that exceed those of the wall material. Therefore, the explosion energy E_{ex} of thin-walled flashtubes, defined as the minimum input energy sufficient to crack the lamp catastrophically, is

$$E_{ex} = k_2 l d t_p^{1/2}, \quad (6.11)$$

where k_2 depends on the type of gas and fill pressure as well as on the physical and thermal properties of the lamp envelope. The explosion energy is directly related to the inside-wall surface area of the lamp and to the square root of the pulse duration. If l and d are measured in centimeters and t_p is in seconds, and if a critically damped single-mesh discharge circuit is assumed, then it has been found empirically that for xenon-filled quartz flashtubes [6.1, 18]

$$E_{ex} = (1.2 \times 10^4) l d t_p^{1/2}. \quad (6.12)$$

This relation is useful for lamps with $0.5 \leq d \leq 1.5$ cm and xenon fill pressures of 300–450 Torr, where t_p is defined as the time between the one-third peak light output points for a damped sinusoidal waveform and the one-half light output points for quasi-rectangular waveform [6.19]. E_{ex} , as calculated above, is a “free air” value, which assumes that no radiation which leaves the lamp is reflected back to be reabsorbed. In an actual laser pumping cavity a certain fraction of the radiated energy—depending on the reflectivity of the cavity, its diameter, and its focal properties—is returned to the flashtube. This markedly increases the erosion and wear accompanying each discharge. In fact, the flashtube often acts as if it were being loaded with as much as 30% more energy than is actually being dissipated in the tube. Single-pulse explosion energy as a function of pulse duration is shown in Fig. 6.7 for quartz-envelope xenon flashlamps of different bore diameters [6.20]. For a flashlamp with a specific bore size and arc length, the explosion point is a function of lamp input energy and pulse duration.

Having determined the ultimate limit for the tube, the question of the life that the tube will have in a given application has to be addressed. It has been shown that lamp life can be related to the fraction of explosion energy at which the lamp is operated. The life in flashes for a xenon-filled quartz-envelope flashlamp as a function of the single-shot explosion energy is empirically given by [6.21]

$$N \cong \left(\frac{E_{ex}}{E_0} \right)^{8.5}. \quad (6.13)$$

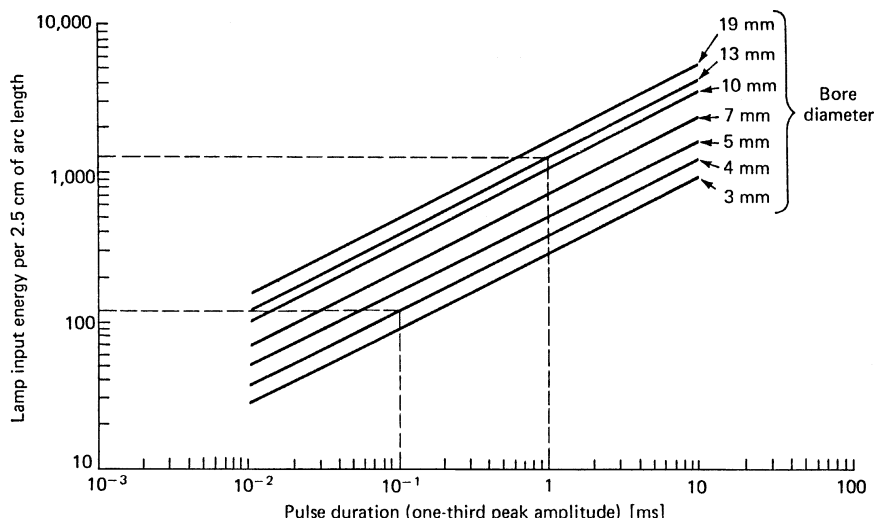


Fig. 6.7. Explosion energy of linear flashlamps ($J/2.5\text{ cm}$) as a function of pulse duration and bore diameter. The wall thickness of the lamp is 1 mm, except for the 19-mm-bore lamp which has a wall thickness of 1.5 mm [6.20]

The extremely strong dependence of flashlamp lifetime on the total input energy is a great incentive to underrate the lamp.

In Fig. 6.8, life expectancy as a function of lamp input is shown assuming that the interpulse interval is sufficiently long to permit the tube to cool between pulses [6.21].

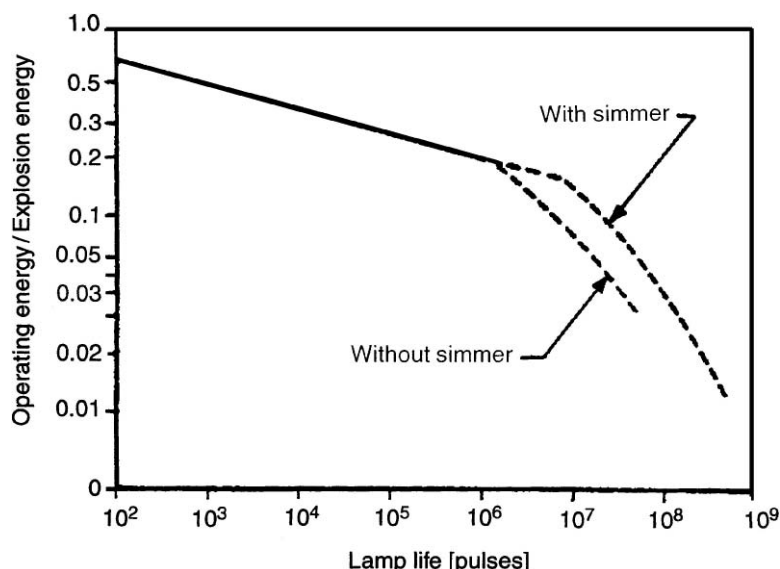


Fig. 6.8. Lamp life as a function energy [6.21]

The lifetime expressed by (6.13) is defined as the number of shots at which the light output is reduced by 50% of initial value. The life expectancy of a flashlamp begins to deteriorate rapidly when peak current exceeds 60% of explosion current. Above 60%, the lamp's life is usually limited to less than 100 discharges, even if all other parameters are optimized. At the 80% level, explosion can occur on any discharge. Most flashlamps, with the exception of lamps installed in single-shot lasers, such as employed in inertial confinement fusion, are operated at only a small fraction of the explosion energy. In this case, cathode degradation is the primary failure mode. The two dotted lines in Fig. 6.8 indicate where cathode end of life begins to occur. As explained below, lamp life is considerably improved by operation in the simmer mode, which keeps the lamp continuously ionized at a low current level. Because of the increased lamp life most lamps are nowadays operated in the simmer mode.

Excessive Thermal Wall Loading. Cooling of the end seals and the lamp envelope has to be adequate. The amount of average power a flashlamp can handle is determined by the quartz wall area available to dissipate the heat. The envelope of a flashlamp is under stress which is caused by the temperature and pressure differences between the inner and outer walls and by the acoustical shock wave. The combined stress permissible at the envelope determines the power dissipation per unit area. The total electrical input power of a gas discharge lamp is divided between the heat dissipated by the electrodes, the quartz walls, and the emitted radiation. Typically 30–50% of the lamp input power is dissipated as heat by the quartz envelope [6.22]. Under high-average-power operating conditions the inner wall is close to the melting temperature of quartz, whereas the liquid-cooled outer wall surface is close to room temperature. As will be discussed in Sect. 6.1.2, the maximum heat which can be dissipated through the liquid-cooled quartz envelope of a lamp is $300\text{--}400 \text{ W/cm}^2$ depending on the wall thickness.

In flashlamps a temperature rise from 300 to 12,000 K is experienced during the pulse, which will produce a 36-fold increase in gas pressure. As a result of the additional stresses caused by the pressure increase and the shock wave, flashlamps are operated considerably below the thermal limit. Conservative numbers assuring good life expectancy are $50\text{--}100 \text{ W/cm}^2$ for water-cooled lamps.

Nondestructive Failure. Operated well below the explosion limit, flashlamp lifetime is limited by electrode erosion, with the subsequent formation of opaque deposits on the lamp jacket near the lamp electrodes, or by outgassing or tube leakage. Of these, cathode sputtering caused by the bombardment of the xenon ions onto the negative lamp electrode is the most significant. The emitted hot-cathode material deposits on the relatively cool lamp walls and effectively attenuates the amount of radiation released by the plasma. It was observed that the optimum cathode temperature is the most critical parameter in reducing wall deposits. If the temperature is too low, tungsten will sputter onto the walls causing darkening. If the temperature is too high, barium will evaporate and deposit onto the envelope.

Tube blackening, which occurs in a new tube after a few shots, is a sign of electrode impurity. The greatest hazard to a lamp during its final stages of processing is the

introduction of water vapor from the atmosphere [6.23]. If the water vapor is not entirely removed from the lamp, tungsten will react readily with water vapor traces to form WO_2 and atomic hydrogen. The tungsten oxide vaporizes from the electrode and condenses on the cooler parts of the envelope. This reaction often accounts for premature blackening of the envelope walls. Besides darkening of the envelope, the useful life of a flashlamp is limited by erratic triggering and the eventual inability to reignite; this indicates that a significant outgassing or tube leakage has occurred.

In all these cases where the input energy is a small fraction of the explosion energy, the above-listed secondary effects dominate and the life of a lamp is largely determined by the lamp process control and the precautions taken during manufacture. For lamps which are operated in this regime, the useful lamp life, rather than being determined by a mechanical failure, is determined by the reduction of lamp radiation below a useful level. The term "lamp life" is used loosely, since no definite standards exist with regard to the determination of the end of lamp usefulness. Lamp manufacturers usually state lamp life as the number of shots after which lamp intensity drops to 50% of its initial value. The life expectancy is usually stated for a particular set of operating parameters and for a lamp operated in free air. In laser applications, lamp life is usually defined to end when the laser output has degraded a certain amount, for example 10%, or when the lamp fails to trigger at a specified voltage.

Continued improvements in flashlamp design and fabrication techniques have resulted in ever increasing flashlamp life. Careful attention to the operational aspects of flashlamps have also contributed substantially to longer lifetimes. As illustrated in Fig. 6.8 lamp life is greatly increased by maintaining a low current discharge in the lamp between pulses. This simmer mode minimizes cathode sputtering, and arc formation is more controlled and associated with a smaller shockwave as compared to a high voltage trigger pulse.

About 20 years ago, nominal lifetime for flashlamps employed in industrial lasers was on the order of 10–20 million shots. Optimization of the tungsten matrix and improvements in the design of the geometry of the cathode and the surrounding quartz envelope has extended flashlamp lifetime into the 10^8 region. Today state-of-the-art flashlamps can operate up to several hundred million shots.

Examples of Typical Operating Conditions

In selecting a particular lamp the following steps are usually followed:

- A flashlamp arc length and bore diameter is chosen that matches the rod size.
- The explosion energy for the lamp chosen is calculated.
- An input energy is selected that is consistent with the desired lamp life. If the lamp input required to achieve a certain laser output is not consistent with a desired minimum lamp life, the application of a multiple-lamp pump cavity has to be considered.
- The average power loading of the lamp is calculated and compared with the limit specified by the lamp manufacturer.

- In designing the pulse-forming network, care must be taken to avoid fast current rise times and/or reverse currents. To obtain the expected life, manufacturers recommend that the rise time of the flashlamp current be greater than 120 μ s for lamps discharging more than a few hundred joules. Both electrode erosion and wall vaporization are accelerated by fast-rising peak currents.

First we will consider a typical small linear flashlamp used in military equipment such as target designators or laser illuminators. These systems operate typically at a flashlamp input of 10 J with pulse repetition rates of 20 pps. The lasers typically use 63-mm-long Nd:YAG laser rods of 6.3 mm diameter and have a *Q*-switched output of 100–200 mJ. A 4-mm-diameter and 60-mm-long lamp operated at 10 J input and a pulse width of 300 μ s is operated at only 2% of the explosion energy. The wall loading of the liquid-cooled lamp operated at 10 pps is 15 W/cm². From the extensive data which exist for this type of lamp operated in a closed coupled laser cavity, it follows that the useful lamp life (10% drop in laser performance) is in excess of 10⁷ shots.

An example of a large lamp employed to pump Nd:glass laser rods is the FX-67B-6.5 made by EG & G. This lamp is 16.5 cm long and has a bore diameter of 13 mm. The lamp has an explosion point of 8450 J for a 1-ms-long pulse. The maximum long-term average power input for the water-cooled lamp is specified by the lamp manufacturer at 10 kW. This corresponds to an effective thermal wall loading of about 60 W/cm². If the lamp is operated at an input energy of 2000 J, a flashlamp life of 150×10^3 shots can be expected before the light output is decreased to 50% of its initial value. For a laser operated essentially on a single-shot basis in a research environment, this is not an unreasonable lamplife.

Extremely long lifetimes can be obtained with carefully selected operating parameters and lamp design. For example, Under a special lamp-improvement program which included refinement of the cathode tungsten matrix, careful cathode temperature control, ultrapure quartz envelopes, and backing the anode in high vacuum and at a high temperature, lifetimes of up to one billion shots were observed [6.24].

The lamps filled with 760 Torr of xenon had a 6-mm bore and a length of 10 cm. One group of lamps was operated at 15 J input in a 180- μ s-long pulse. The other lamps were fired at 45 J per pulse at the same pulse length. From Fig. 6.7 follows an explosion energy of 1200 J for this lamp and pulse length. This means the lamps were operated at only 1.3% or 3.8% of the explosion energy. From the lamps tested at the 15 J level, most reached half a billion shots and some exceeded one billion. At the 45 J input level most lamps failed between 10⁸ and a half billion shots.

Additional literature on flashlamp performance can be found in [6.25–28].

Power Supply for Flashlamps

The major components of a power supply employed in a flashlamp-pumped laser are a charging power supply, capacitive energy storage, a pulse-shaping device, and a flashlamp trigger unit. A pulse-forming network (PFN) combines the function of

energy storage and pulse shaping. A flashlamp pulse can be initiated and controlled essentially in three different ways:

- a) *The flashlamp serves as a switch.* In this case, energy is stored in a PFN which is directly connected to the flashlamp. The flashlamp is ignited by a trigger circuit which then discharges the energy stored in the capacitor of the PFN into the flashlamp. Pulse duration and pulse shape are determined by the PFN. The lamp extinguishes after the capacitor is discharged. Simplicity is the major advantage of this design, which requires no high-voltage and current-switching elements.
- b) *Discharge controlled by a separate on-switch.* In this technique the PFN is connected to the flashlamp via a switch such as an SCR, or a gas, or mercury-filled tube. These switches can be turned on, but not off. The pulse shape is determined by the PFN, as before, and the switch, as well as the flashlamp, is turned off once the capacitor is discharged. There are several reasons why such a switch is advantageous. For example, under high-repetition-rate operation the PFN can be recharged while the flashlamp is still ionized. The switch prevents firing of the lamp in cases where the voltage of the capacitor bank is higher than the ignition voltage of the flashlamp. And foremost, a separate switching device permits operation of the flashlamp in the so-called simmer mode, which is a low-level continuous ionization. This mode of operation increases lamp life, allows monitoring of the lamp status, and provides for a more reliable performance.

SCRs have also been used as on-switches in situations where the flashlamp energy is directly supplied by a three-phase powerline. This is possible in applications, such as materials processing, which require relatively long pulse width and modest peak currents. An isolation transformer contains a bridge rectifier comprising phase-controlled SCRs. The combination of the rectified ac waveform and the firing point of the SCRs provide control of flashlamp pulse length and energy. The lamp extinguishes when the rectified half-wave voltage reaches zero.

- c) *Pulse shape controlled by an on-off switch.* The availability of high-voltage and current semiconductor switches such as GTOs (gate turn-off SCR), MOSFETs, and IGBT (insulated gate bipolar transistor) makes it possible to design very compact and flexible flashlamp charging units if the lamp operating parameters are within the capabilities of these devices. In such a charging unit, a fraction of the energy stored in electrolytic capacitors is transferred to the flashlamp at each pulse. The externally controlled switch determines the pulse width, which in this case can be varied over a wide range. Very large energy storage banks, or flashlamps pumped with very short pulses, often require high voltages and currents which are beyond the ratings of these switching devices.

Charging Unit

The function of the charging unit is to charge the energy storage capacitor to a selected voltage within a specified time, which depends on the desired repetition rate of the laser. The capacitor-charging source usually consists of a transformer followed by

a rectifier bridge, a switching element in the primary of the transformer, a current-limiting element, a voltage sensor, and control electronics. The transformer and the rectifier bridge provide the required dc voltage for the energy-storage capacitor. In order to be able to vary this voltage and therefore to obtain a variable output energy from the laser, a semiconductor switch is usually included in the primary circuit of the transformer. This control element, which can be either a triac, a solid-state relay, or a pair of inverse parallel SCRs, is turned on at the beginning of the charge cycle and turned off when a preset voltage is reached at the capacitor. Control signals are derived from the capacitor voltage as in conventional dc supply designs. The charging of a capacitor presents a problem insofar as the discharged capacitor constitutes a short circuit. Without a current-limiting device in the power supply, the short-circuit current is limited only by the resistance of the transformer windings. To protect the rectifier diodes and other components in the circuit, current-limiting circuits are required. Ideally, one would like a constant current supply, in which case the capacitor-charging current would be constant over the entire charging cycle. The charging current in this case would be

$$I = CV/t, \quad (6.14)$$

where C is the capacitance of the capacitor, V is the final charging voltage, and t is the charging time. Figure 6.9 depicts a number of circuits which are frequently employed to limit the short-circuit current into a capacitive load. The most straightforward way to charge capacitors is resistance-limited charging from a constant-voltage source, as shown in Fig. 6.9a. The least amount of power dissipated in the current-limiting resistor is equal to that stored and discharged in the capacitor if three or more time constants are used in charging. For shorter charging times, even more power is wasted in the resistor. For low-power, low-repetition-rate systems the heating losses usually can be tolerated. Since capacitor charging to high-energy levels, or at high-repetition rates, causes appreciable power losses when charging through a resistor, attempts have been made to produce power supplies without the resistor, but retaining the resistor's function of limiting initial capacitor-charging currents to safe values.

Figure 6.9b displays current limitation by an inductor in the primary of the transformer. During initial charging, when the secondary of the transformer is shorted by the discharged capacitor, the peak current is limited by the inductive reactance. The inrush current equals the primary voltage divided by the reactance. As a refinement of this technique, the inductance can be built into the transformer as primary leakage (Fig. 6.9c).

At repetition rates approaching the power-line frequency, it becomes difficult to achieve repeatable output voltage from charge to charge because of the limited number of current pulses within the charging period. For these cases it becomes necessary to use resonant charging (Fig. 6.9d). Glascoe [6.29] gave a complete analysis of the circuit. Current will flow from the dc source for the first half-cycle of the resonant frequency, charging the capacitor to twice the source voltage. The peak current drawn from the supply depends on the inductor, the resonant frequency of the LC circuit, and the voltage to which the capacitor is charged.

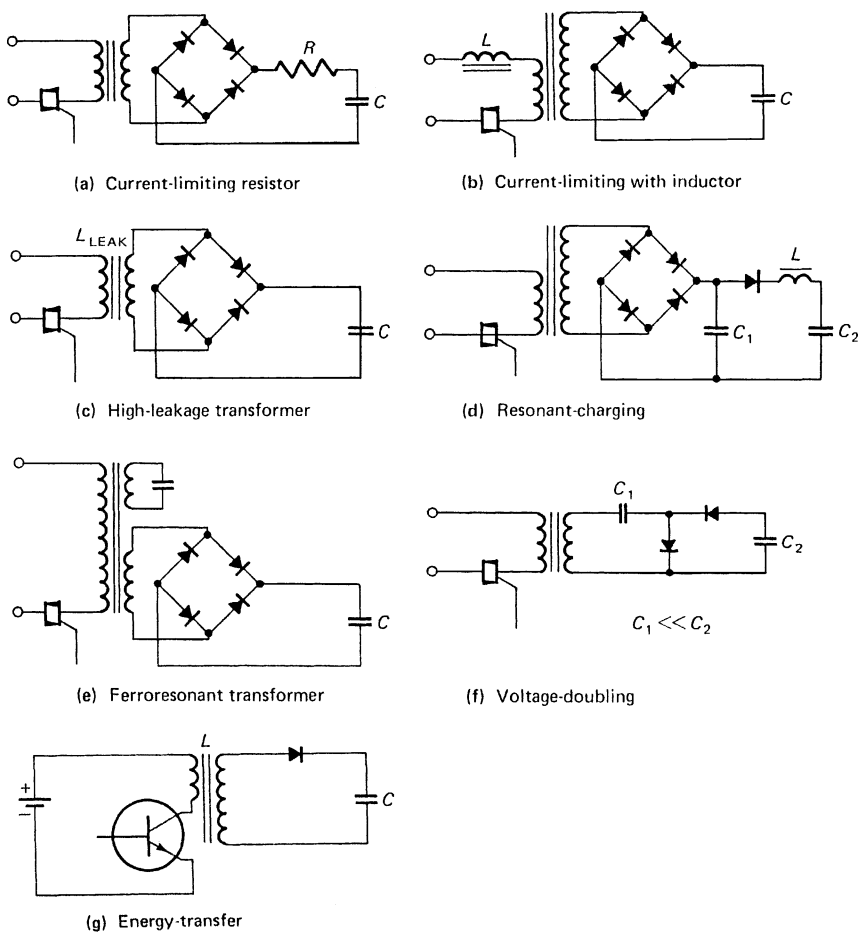


Fig. 6.9. (a-g) Power supply charging circuits for pulsed lasers

The capacitance C_1 shown in Fig. 6.9d is a filter to aid voltage regulation and is usually 10 times the bank capacitance C_2 . The constant-voltage and short circuit current characteristics of ferroresonant line regulator transformers have been used to approximate a constant-current source for capacitor charging. Figure 6.9e shows the typical ferroresonant transformer with its associated components. The current-limiting characteristic of the ferroresonant transformer is attained through the use of a magnetic shunt and a resonant tank circuit. In addition to resistive and inductive current limitations, the short-circuit current can be reduced by repetitively transferring a small amount of energy to the energy storage capacitor. In the voltage-doubling circuit depicted in Fig. 6.9f, the small capacitor C_1 transfers its charge to the main capacitor C_2 during each cycle of the ac line. A circuit in which magnetically stored energy is transferred to a capacitor is shown in Fig. 6.9g.

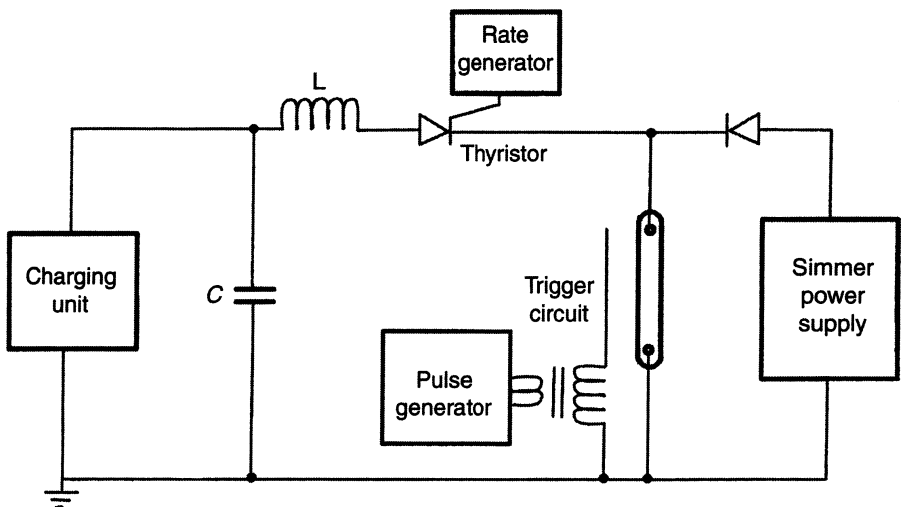


Fig. 6.10. Typical power supply employed for the operation of flashlamps

In the following, we will describe a few typical power supplies employed in pumping solid-state lasers.

Figure 6.10 illustrates a circuit, which is widely used for flashlamp-pumped solid-state lasers. For clarity we will assume for the moment that the simmer power supply and the thyristor have been removed and the flashlamp is directly connected to the inductor. The energy delivered to the lamp is stored in the capacitor C . The discharge of the stored energy into the flashlamp is initiated by a high-voltage trigger pulse generated by a pulse generator and a step up transformer. The trigger pulse applied to a wire wrapped around the tube envelope creates an ionized spark streamer between the electrodes. The energy stored in the capacitor is discharged through the inductor L into the lamp. The pulse duration and pulse shapes are determined by the time constant of the LC circuit. The lamp extinguishes after the capacitor is discharged. Simplicity is the major advantage of this operation, which requires no high voltage and current-switching device since the flashlamp serves as a switch.

It has been found that the lifetime of a flashlamp can be significantly increased and pump efficiency can be improved if the lamp is preionized.

The improvement is mainly due to a decrease in cathode sputtering, a more uniform arc formation, and an associated smaller shock wave. In the so-called simmer mode a low-current discharge is maintained between the high-current pulses. The simmer mode of operation requires a switching element between the flashlamp and the PFN. The flashlamp is initially ignited as described before by a trigger pulse on the order of 20 kV. A low-current discharge of a few hundred milliamperes is maintained in the lamp by the simmer supply shown in Fig. 6.10. The energy storage capacitor is discharged via a switch such as an SCR, thyristor, a gas, mercury-filled tube. The pulse shape is determined by the PFN, as before, and the switch, as well as the flashlamp are turned off once the capacitor is discharged.

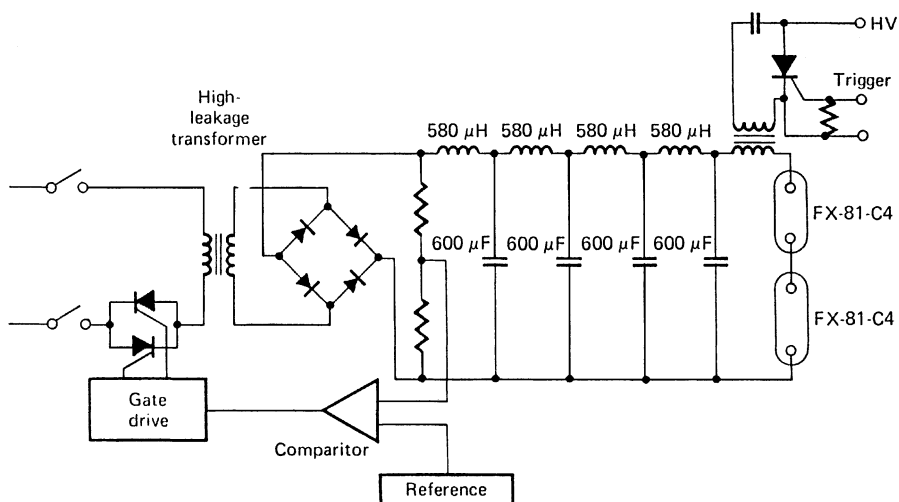


Fig. 6.11. Power supply featuring a high-leakage transformer

Figure 6.11 shows a power supply which can charge a 1-kJ capacitor bank at a repetition rate of 10 pps. The unit features a high-reactance current-limiting transformer, with two inverse parallel SCRs as a switching element in the primary, and a full-wave rectifier bridge. Since this power supply is for a Nd:YAG laser welder, long pulses of the order of 5 ms are required. As we will see in the next subsection, this requires a multiple-mesh network. The trigger circuit, which we will discuss in more detail later, consists essentially of a trigger transformer with a capacitor and a SCR in the primary. When the capacitor is discharged, a high voltage is generated at the secondary, which breaks down the lamp. The power supply is designed to operate two linear flashlamps (FX81-C4). Each lamp has a bore of 10 mm and a length of 10 cm. This power supply can also be built as a three-phase supply. In this case, three separate transformers and voltage-rectifier bridges are connected in parallel at the dc output end.

For high repetition rates a resonant charging supply is best used. Figure 6.12 shows the simplified schematic of a power supply which is employed to pump a Nd:YAG laser at repetition rates of up to 50 pps. The laser is pumped by a single linear flashlamp with 5-mm bore diameter and 50-mm arc length at a maximum of 20 J. The dc section of the power supply represents a variable voltage source. In the primary circuit of the transformer is an inductor for current limitation and a triac for voltage control. The stepped-up voltage is rectified by a full-wave bridge and filtered by means of a bank of 950- μ F electrolytic capacitors. The dc output voltage is controlled by a circuit which senses the voltage and generates trigger pulses to the gate of the triac. The resonant charging device consists of a hold-off diode, a 50- μ F energy storage capacitor, and a 350-mH inductor. The flashtube trigger is generated by switching the energy from a small storage capacitor into the trigger transformer primary. The secondary of this transformer is connected in series with the PFN (series injection triggering). When a

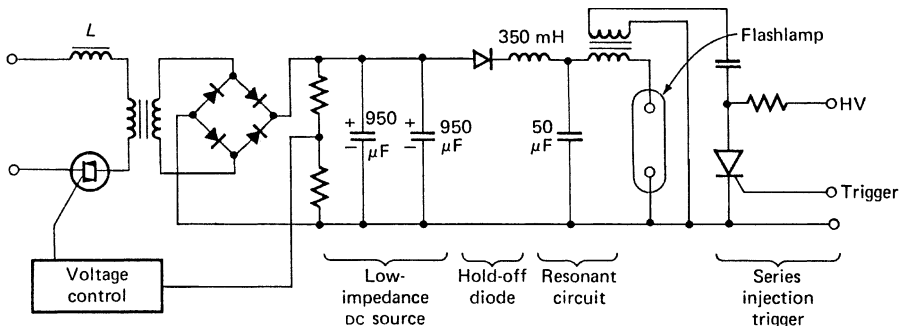


Fig. 6.12. Resonant charging of the energy storage capacitor in a high-repetition-rate system

flashlamp is operated at high repetition rates, the recovery characteristic of the lamp must be taken into account. After cessation of current flow, the lamp remains ionized for a time on the order of a few milliseconds.

A type of power supply often employed in Nd:YAG and Nd:glass lasers, mainly for materials processing applications, is illustrated in Fig. 6.13. In application such as spot welding, the desired laser pulse is relatively long on the order of 0.5–2 ms. This often reduces the flashlamp voltage to below 2 kV, which makes it possible to use controllable on-off switches such as GTOs, MOSFETs, and IGBTs. Such a device has the advantage that the flashlamp pulse width is continuously variable. Also, the energy can be stored in electrolytic capacitors, which results in a very compact and flexible flashlamp driver unit.

Figure 6.13 depicts a schematic diagram of a flashlamp charging unit which contains an IGBT as switching element. The high-voltage supply on the righthand side of Fig. 6.13 charges a small capacitor C_1 to a sufficiently high voltage, about 8–15 kV, until the flashlamp is ignited. Once the flashlamp is conducting, the simmer supply takes over through diodes D_1 and D_2 , and the trigger unit, no longer needed, is turned off by the automatic controller. Diode D_1 protects the left part of the circuit from the high-voltage trigger pulse, and diode D_2 protects the simmer supply from the high

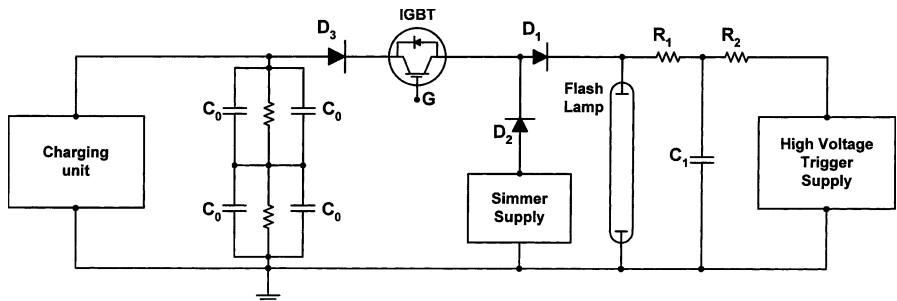


Fig. 6.13. Power supply with programmable pulse width control and electrolytic capacitor energy storage [6.30]

voltage when the IGBT is conducting. Since IGBTs have a backward conducting “free wheel” diode built-in, diode D_3 prevents that the simmer supply current is diverted to charge the capacitor bank C_0 .

In most cases, strings of diodes, rather than single devices, will be needed for D_1 – D_3 to meet the high-voltage requirements. A constant current power supply charges a capacitor bank comprising electrolytic capacitors. The capacitor bank stores at least 10 times the energy discharged into the flashlamp at each pulse. This is important because electrolytic capacitors are specified for a maximum ripple current. Electrolytic capacitors provide the most compact and economical means of storing electric energy. Firing time and pulse width of each flashlamp pulse is controlled by a trigger input delivered to the gate of the IGBT from a control unit.

We found that in high-current and high-voltage applications, IGBTs tend to have a smaller voltage drop during the pulse as compared to MOSFETs. The typical saturation voltage across the IGBTs is between 3.5 and 5 V. Currently the most powerful IGBT (Toshiba ST 1000 EX21) has maximum ratings of 2500 V for the collector-emitter voltage and 2000 A forward current under pulsed conditions. The collector-emitter saturation voltage is 5 V.

Power supplies used for military-type Nd:YAG lasers, such as rangefinders, target designators, or illuminators, mostly operate from batteries or on-board dc power lines. Figure 6.14 sketches a simplified schematic of the power supply of an airborne target designator, which operates from 28 V dc. The unit, which consists of a dc-to-ac converter, a step up transformer, a high-voltage rectifier, a PFN, and a parallel trigger circuit, is capable of charging the capacitor to an energy of 20 J at a repetition rate of 10 pps. The flashlamp (ILC L-213) has a bore of 4 mm and an arc length of 50 mm. Current is limited by an inductor on the high-voltage dc side of the unit.

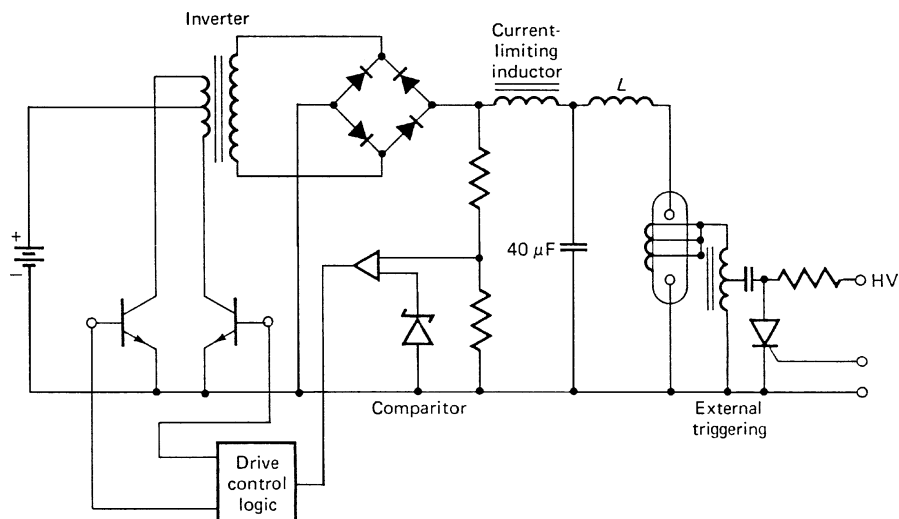


Fig. 6.14. Power supply employing a dc-to-ac inverter

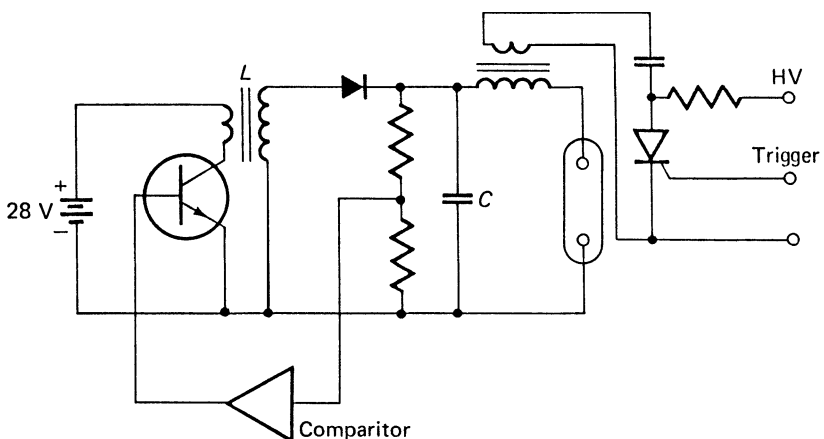


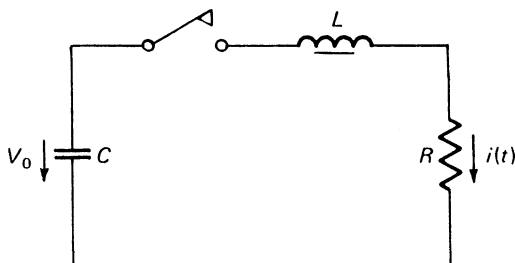
Fig. 6.15. Battery-operated power supply with energy transfer from the inductor L to the PFN capacitor C

A feature of this power supply is the fact that the repetition rate of the dc-to-ac converter progressively increases from 1 kHz to about 5 kHz during the charge cycle in order to keep the peak-to-peak rms current drawn from the battery at a low value. This is achieved by a current-sensing network which feeds a signal to the logic circuit, which in turn controls the switching frequency of the transistors in the dc-to-ac converter. At full capacitor charge, a voltage sensor turns off the driving signals to the transistors. A schematic diagram of another type of power supply used in small military systems is shown in Fig. 6.15. The system operates on the principle of a flyback dc-to-ac converter. The transistor is turned on for a short period of time to allow current flow in the primary of the inductor. When the transistor is turned off, the magnetic energy stored in the inductor is transferred to the energy storage capacitor; at the same time the voltage rises from 28 V to approximately 800 V. The device is short circuit protected since the inductive voltage kickback charges the capacitor after the transistor has turned off. The transistor is operated typically at a repetition rate of 1–10 kHz in order to keep the inductor small. For a 10-pps system this allows between 100 and 1000 transfers of energy from the inductor to the capacitor.

Further references on the design of power supplies employed to operate flashlamps can be found in [6.19, 31–33]. The special problems which arise in power supplies designed to charge capacitor banks with stored energies in the MJ range have been discussed in [6.34].

Pulse-Forming Network

Flashlamps are usually operated from a single- or multiple-mesh LC network. The network stores the discharge energy and delivers it to the lamp in the desired current pulse shape. In most situations, the lamp input energy E_0 , the pulse width t_p , and the lamp dimensions have been determined before the PFN is designed. The

**Fig. 6.16.** Single-mesh discharge circuit

above-mentioned parameters completely describe the network's capacitance and inductance as well as the charging voltage and peak current. To familiarize the reader with the design of flashlamp energy-storage networks, we will consider first the elementary model of a pulse discharge circuit (Fig. 6.16). The capacitor C is charged to an initial voltage V_0 . At time $t = 0$ the switch S is closed and the energy stored in the capacitor is delivered to the load. We assume for the moment that the load is a linear resistor R . In this case the circuit is described by the second-order differential equation

$$L \frac{d^2q}{dt^2} + R \frac{dq}{dt} + \frac{q}{C} = 0, \quad (6.15)$$

where q is the charge on the capacitor. With the initial charge on the capacitor $q(0) = CV_0$ and the initial current $dq/dt(0) = 0$, the voltage across R is given by

$$v(t) = V_0(\alpha/\beta)\{\exp[-(\alpha - \beta)t] - \exp[-(\alpha + \beta)t]\}, \quad (6.16)$$

where $\alpha = R/2L$ and $\beta = (R^2/4L^2 - 1/LC)^{1/2}$.

Depending on the relative values of R , L , and C , the voltage or current waveform across R may be as follows:

Critically Damped. In this case, $\beta = 0$ and

$$R = 2\left(\frac{L}{C}\right)^{1/2}. \quad (6.17)$$

The capacitor voltage decays exponentially from V_0 to zero. If we define the rise time t_r as the time required for the voltage or current at R to rise from zero to its maximum value, we obtain

$$t_r = (LC)^{1/2}. \quad (6.18)$$

The rise time measured between the 10 and 90% points of the voltage is $0.57t_r$. The discharge current as a function of time is

$$\frac{i(t)}{i_p} = e\left(\frac{t}{t_r}\right) \exp\left(-\frac{t}{t_r}\right), \quad (6.19)$$

where the peak discharge current is

$$i_p = \frac{2V_0}{Re}. \quad (6.20)$$

Overdamped. The waveform is similar to the critically damped pulse, except that the peak current is reduced and the time required to reach zero is extended. The overdamped case (β real) is defined by

$$R > 2 \left(\frac{L}{C} \right)^{1/2}. \quad (6.21)$$

Underdamped. The resulting pulse shape is characterized by strongly damped oscillations (β imaginary). The frequency of the oscillation depends mostly on L and C , whereas the decaying amplitude is a function of only R . Oscillations and the associated current and voltage reversal in the discharge circuit occur if

$$R < 2 \left(\frac{L}{C} \right)^{1/2}. \quad (6.22)$$

Nonlinear Load. As we have seen in Sect. 6.1, the flashlamp resistance is nonlinear and can be described by $R_L(i)$ given in (6.4) or by the lamp impedance parameter K_0 defined in (6.1). The design of single-mesh circuits for driving flashlamps has been considered in [6.12, 35]. In order to apply the results published in the literature, we must make the following substitutions and normalizations:

$$Z_0 = \left(\frac{L}{C} \right)^{1/2}, \quad \tau = \frac{t}{T}, \quad T = (LC)^{1/2}, \quad i = \frac{IV_0}{Z_0}. \quad (6.23)$$

In addition, a damping factor α is defined, which determines the pulse shape of the current pulse:

$$\alpha = K_0(V_0 Z_0)^{-1/2}. \quad (6.24)$$

Solutions of the nonlinear differential equation of the lamp current for various values of α have been reported in [6.12, 13]. The current waveform for different values of α is shown in Figs. 6.17 and 6.18. As can be seen from these curves, $\alpha = 0.8$ corresponds to the critically damped case. The current pulse duration t_p at the 10% points is approximately $3T$; during this time about 97% of the energy has been delivered. If we substitute

$$\alpha = 0.8 \quad \text{and} \quad t_p = 3T = 3(LC)^{1/2} \quad (6.25)$$

for a critically damped pulse into (6.23, 24), then we can determine for a given lamp type the relationship between energy input, pulse duration, pulse shape, inductance, capacitance, and operating voltage.

The energy initially stored in the capacitor is

$$E_0 = \frac{1}{2} CV_0^2. \quad (6.26)$$

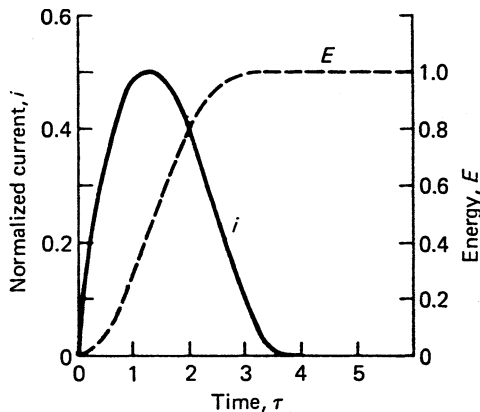


Fig. 6.17. Normalized current and energy of a critically damped flashlamp discharge circuit. Pulse shape factor $\alpha = 0.8$

The relation is used to eliminate V_0 from (6.24). With $\alpha = 0.8$ we obtain from (6.24) the value of the capacitor

$$C^3 = 0.09 \frac{E_0 t_p^2}{K_0^4}. \quad (6.27)$$

The inductance can be calculated from (6.25)

$$L = \frac{t_p^2}{9C}. \quad (6.28)$$

We now have a set of three equations (6.26–28) which, given the specifications of the flashlamp parameter K_0 , the desired input energy E_0 , and the pulse width t_p , provide

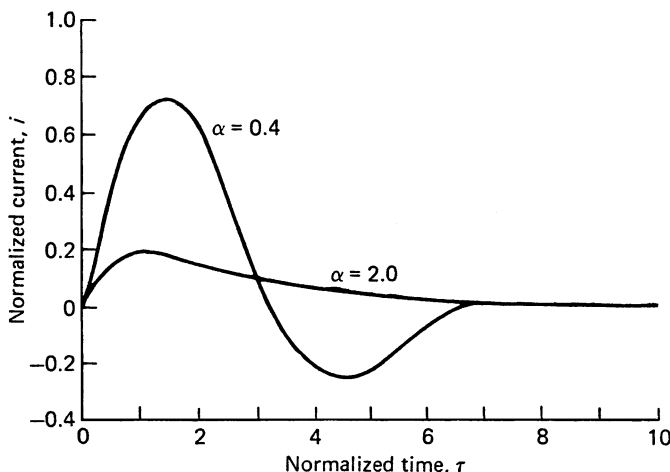


Fig. 6.18. Overdamped and underdamped current waveforms of a lamp discharge circuit

explicit values of C , L , and V_0 . If the lamp parameter K_0 is not specified by the lamp manufacturer, it can be calculated from (6.5). From Fig. 6.17 also follows the peak current for a critically damped current pulse

$$i_p = 0.5 \frac{V_0}{Z_0}. \quad (6.29)$$

The rise time to reach this peak value is

$$t_r = 1.25(LC)^{1/2} \cong 0.4t_p. \quad (6.30)$$

Differences between these solutions and those for the linear LC circuit are readily apparent. For a given Z_0 , V_0 , and peak current, the solution of the nonlinear equation is more heavily damped than that of the linear case. The damping parameter α is dependent on V_0 , the initial capacitor voltage. This is consistent with the experience that a discharge circuit, critically damped at one voltage, begins to ring as the voltage is increased.

Multiple-Mesh Networks: For pump pulses with a more rectangular pulse shape, multiple-mesh networks are used. These consist of two or more LC networks in series. Switching an open-ended charged transmission line into a resistor equal to its characteristic impedance yields a rectangular pulse across the resistor. The width of the pulse equals twice the propagation time of the line. This same technique can be applied to a lumped parameter line. The principal advantage of the lumped-parameter delay line as an energy-storage PFN is its nearly constant output over the length of the pulse. This property is especially useful in producing long normal-mode laser pulses of constant power.

Most PFNs employ the “E” -type circuit of a lumped constant transmission line. In this configuration, all capacitors are of equal value and the inductance values per mesh are nearly identical (Fig. 6.19). Following are the approximate equations of a lumped-type “E” transmission line terminated by its characteristic impedance [6.29]. The characteristic impedance of the network is

$$Z_n = \left(\frac{L_T}{C_T} \right)^{1/2}, \quad (6.31)$$

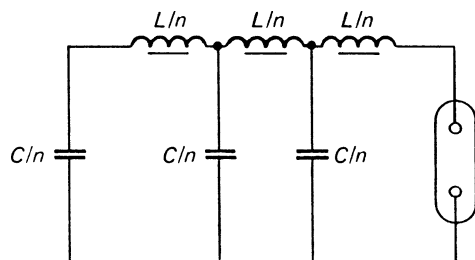


Fig. 6.19. Multiple-mesh network

where L_T and C_T are the total inductance and total capacitance. The pulse width at the 70% point is

$$t_p = 2(L_T C_T)^{1/2}. \quad (6.32)$$

With the pulse duration known, the total capacitance follows from

$$C_T = \frac{t_p}{2Z_n}, \quad (6.33)$$

and the total inductance is

$$L_T = \frac{t_p Z_n}{2}. \quad (6.34)$$

In order to deliver the required energy, the capacitors of the network must be charged to a voltage

$$V = \left(\frac{2E}{C_T} \right)^{1/2}. \quad (6.35)$$

The peak current during the discharge from the pulse-forming network is given by

$$i_p = \frac{V_0}{2Z_n}. \quad (6.36)$$

From (6.33, 34) it follows that the values of L_t and C_t are determined by the desired pulse width and the lamp impedance $R = Z_n$. The desired lamp energy input determines the charging voltage.

Once L_T , C_T , and V_0 are calculated, the desired rise time determines the number of circuit meshes in the network. Experiments have shown that current rise times of less than 50 μs for lamps pumped up to the 100-J level and rise times of 200 μs for lamps pumped in the kilojoule regime can cause severe electrode sputtering and crazing of the flashtube. The number of sections chosen to make up the PFN is determined by first considering the rise time and then a convenient number of components. If n is the number of meshes, then the rise time from the 10% to the 80% level is

$$t_r = \frac{t_p}{2n}, \quad (6.37)$$

and the fall time (80–10%) is

$$t_f = 3t_r. \quad (6.38)$$

The capacitance and inductance per mesh are

$$C_M = \frac{C_T}{n} \quad \text{and} \quad L_M = \frac{L_T}{n}. \quad (6.39)$$

Network Components: Inductors for PFNs are usually air-core coils, except for small systems where an iron core may be used. Besides inductance, other parameters of interest are the operating voltage and the rms current, which determine insulation

and wire size. Energy storage capacitors ranging from 1 to 10 kV and energy levels from 10 to 5000 J are commonly used. Because space is usually at a premium, energy storage capacitors are customarily designed with a higher dielectric stress than is usually employed for conventional dc capacitors. These low-inductance capacitors are designed for quick charge and discharge. The capacitor's dc life may be entirely different from its pulse discharge lifetime. Large discharge capacitors with storage energies in the kilojoule range are usually castor oil-impregnated paper dielectric capacitors. These capacitors are designed for energy densities of 0.04–0.07 J/cm³ and 30–65 J/kg. In pulse discharge capacitors using high-strength dielectric materials, such as polyester or polypropylene film, energy densities of up to 0.5 J/cm³ and 270 J/kg can be achieved. These capacitors, which are used mostly in military-type systems, have storage energies of up to a few hundred joules. Capacitor lifetime is determined by the charging voltage, the percentage of voltage reversal, and the operating temperature. In most practical situations, where a critically damped or overdamped pulse is generated and operation occurs below the peak rated voltage and at temperatures under 50°C, the capacitor life is not a serious consideration compared to other component failures.

In Figs. 6.20–6.23 typical current waveshapes are shown which are obtained from single- and multiple-mesh networks for various types of lamps. One usually finds that the final selection of the elements of a discharge circuit depends on commercially available components rather than on the exact calculated values. Furthermore, a laser system is in most cases operated over a range of input energies, and theoretically the optimum network would have to be slightly different for each input level.

We will illustrate the procedure for calculating a multiple-mesh network for the pulse shape shown in Fig. 6.20. A 5-ms-long current pulse is desired for two linear lamps connected in series and pumped at a total energy input of 1 kJ. Each of the lamps (EGG-FX81-4) has an arc length of 10 cm and a bore of 1 cm. From (6.4) it follows that with $l = 10$ cm and $D = 1$ cm, there is a resistance of $R_L = 0.5 \Omega$ for each lamp if we assume a peak current of $i_p = 650$ A. As we will see, the design of a PFN is an iterative process. First, a peak current is assumed, which permits one to calculate the

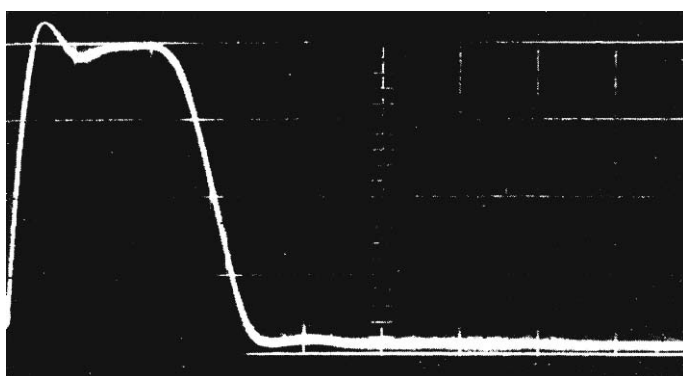


Fig. 6.20. Current waveform obtained from circuit shown in Fig. 6.11 at lamp input energy of 1 kJ and a bank voltage of 900 V. (Horizontal) 2 ms/div; (vertical) 100 A/div

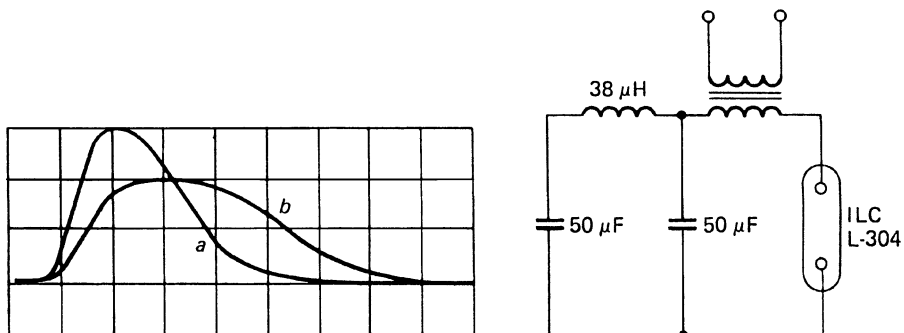


Fig. 6.21. Current pulse obtained from (a) a single-mesh and (b) double-mesh network for 25-J input (ILC lamp model L-304). (Horizontal) 50 μ s/div; (vertical) 200 A/div

lamp impedance. With this parameter known the network can be designed. However, at the end of the analysis the peak current has to be rechecked. With $Z_0 = 1 \Omega$ for the total lamp resistance, it follows from (6.33–35) that $C_T = 2500 \mu\text{F}$, $V = 900 \text{ V}$, and $L_T = 2.5 \text{ mH}$. Recalculating the peak current, we find from (6.36) a value of 450 A, which means the values of C_T and L_T must be recalculated using another assumed i_p . To obtain a fairly flat 5-ms-long pulse, a four-mesh network, each section containing a 600- μF capacitor and a 580- μH inductor, is chosen. The PFN is shown in Fig. 6.11 and the current waveform is illustrated in Fig. 6.20. The measured rise time of the current pulse, which is about 0.6 ms, follows from (6.37).

Figure 6.21 exhibits the current pulse of a single- and a double-mesh network. Each section consists of a 50- μF capacitor and a 38- μH inductor. For the single-mesh network the inductance is actually the saturated inductance of the trigger transformer. The flashlamp is 50 mm long and has a bore of 3 mm (ILC L-304). Total input energy is 25 J. The current pulse into a 75-mm-long, 4-mm-bore flashlamp generated by a three-mesh network is shown in Fig. 6.22. Each section of the network contains a 33- μH inductor and a 120- μF capacitor. The total stored energy is 300 J. Figure 6.23 depicts the current waveform generated by a single-mesh network. The load is a

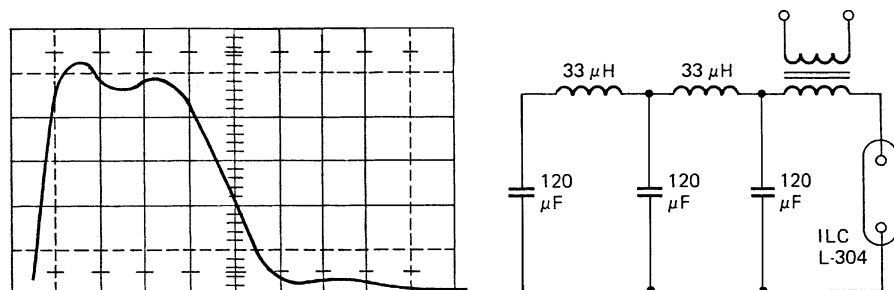


Fig. 6.22. Current pulse obtained from a three-mesh network. Input energy 300 J into ILC lamp model L-305. (Horizontal) 100 μ s/div; (vertical) 200 A/div

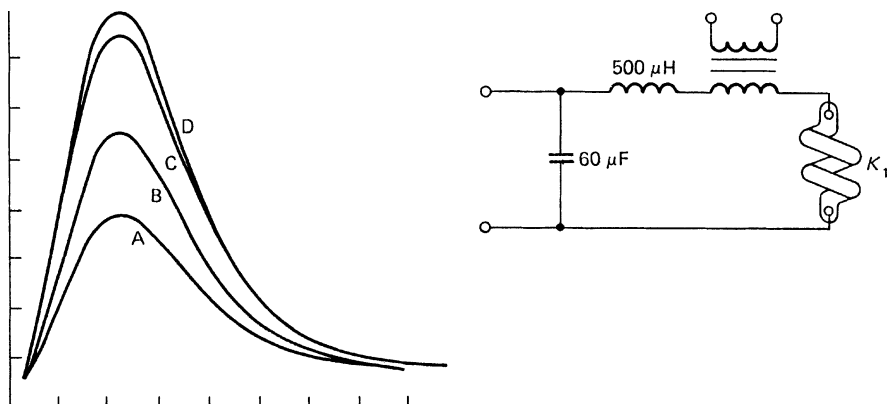


Fig. 6.23. Current waveform generated by different charging voltages: (A) 5 kV; (B) 7 kV; (C) 9 kV; (D) 9.5 kV. (Horizontal) 200 $\mu\text{s}/\text{div}$; (vertical) 100 A/div

helical flashlamp with a tube inside diameter of 8 mm and a total arc length of 72 cm. The lamp impedance parameter for this lamp was measured to be $K_0 = 150 \Omega \text{ A}^{1/2}$. The values for the discharge circuit are obtained if one introduces $t_p = 500 \mu\text{s}$ and $E_0 = 2700 \text{ J}$ into (6.26–28). The pulses shown in Fig. 6.23 correspond to different charging voltages of 5, 7, 9, and 9.5 kV. As can be seen from this figure, despite the large range in bank voltage, input energy, and peak current, the pulses are all approximately critically damped and have pulse widths of about 500 μs .

Trigger Circuit

The discharge of the stored energy into the flashlamp is generally initiated by a high-voltage trigger pulse. The function of the trigger signal is to create an ionized spark streamer between the two electrodes so that the main discharge can occur. The initial spark streamer is formed by the creation of a voltage gradient of sufficient magnitude to ionize the gas column. The concept of a voltage gradient is important here, since it implies the existence of a stable voltage reference surface in close proximity to the flashlamp. Regardless of the triggering method used, reliable triggering cannot be achieved without this reference. Usually, an equipotential condition on the outside wall of the tube is achieved through the use of a wire wrapped around the flashlamp or by the proximity of the metal parts of the pump cavity. The ignition process can be explained by assuming that areas of the inside glass wall behave as small electrodes capacitively coupled to the reference plane. When the trigger voltage is applied, a discharge takes place between the cathode and the nearby part of the inside wall; this part will then be almost at cathode potential. Next, a discharge takes place between this part of the glass wall and a more remote area still at high potential, and so on until the anode is reached [6.36].

The two most common methods of triggering flashlamps are external and series injection triggering. Other techniques are the simmer and pseudosimmer triggers.

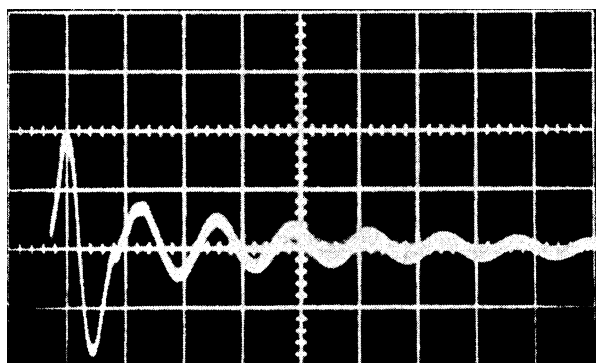


Fig. 6.24. Typical flashlamp trigger pulse. (Horizontal) 10 $\mu\text{s}/\text{div}$; (vertical) 10 kV/cm

In the external trigger device a wire is wrapped around the flashlamp between the electrodes and connected to the secondary of a high-voltage transformer. A high voltage is generated by discharging a capacitor through the primary of the transformer. The switching element can be a SCR, for example. The trigger voltages of flashtubes are between 5 and 10 kV. Figure 6.14 shows an example of external triggering. The waveform of a typical flashlamp trigger pulse is given in Fig. 6.24. The pulse shown was generated by discharging a 33- μF capacitor at a voltage of 500 V through the primary of a trigger transformer (EGG model TR132) with a turns ratio of 53:1.

Sometimes it is undesirable to have a wire wrapped around the flashlamp. For example, the possibility of accidental voltage breakdown to the surrounding pump cavity is greatly increased by the presence of a trigger wire. In such applications, a triggering scheme which does not require an external trigger wire is highly desirable. In the series injection method, a pulse is generated in a transformer whose secondary winding is in series with the flashlamp. The high-voltage pulse causes initial ionization of the plasma. The large lamp current which follows saturates the transformer so that its inductance is low. Each method has its own particular advantages. External triggering provides greater design flexibility, because the secondary winding is not in the main discharge circuit. External triggering is the simplest, lightest, and most commonly used technique. Series triggering, on the other hand, is the choice when no exposed high-voltage leads are permitted. When a series trigger circuit is used, the secondary of the trigger transformer is part of the lamp discharge circuit; therefore, the resistance of the secondary winding should be much less than the flashlamp resistance. This makes the series injection trigger transformer relatively bulky and heavy.

On the other hand, series triggering produces generally better pulse-to-pulse uniformity and reproducibility than does external triggering. Also, in some cases longer flashtube life and more efficient pumping have been observed. These observations may possibly be explained by the fact that when a lamp is series-triggered, the core of the trigger transformer is not saturated and initial current flow is limited by the unsaturated inductance of the transformer. It appears that the reduced current growth rate during the arc-expansion phase results in a more uniform arc formation and an

associated smaller shock wave. An extension of this reasoning has led to the development of the so-called simmer and pseudosimmer triggering schemes. In these schemes a low-current discharge is maintained in the lamp between pulses. This keep-alive discharge is accomplished by employing a low-current dc power supply in parallel with the main supply. A typical circuit is shown in Fig. 6.10.

The simmer mode of operation requires a switching element between the lamp and the PFN. The lamp is initially ignited by an external trigger circuit or by the open-circuit voltage of 20 kV of the high-voltage simmer power supply. At steady state the voltage drop across the lamp is between 500 V and 1 kV. Using this technique, considerable improvements in system performance can be achieved, including the following:

- 1) Increased flashlamp life: An order-of-magnitude improvement in lamp life can be achieved in employing a keep-alive discharge [6.21]. Improvement is mainly due to a drastic decrease in cathode sputtering which is caused to a large degree by the high-voltage surge across the lamp in standard trigger schemes.
- 2) Reduced coolant degradation: Ethylene-glycol/water mixtures possess the temperature characteristics required for military equipment, but they tend to degrade from UV irradiation. A major source of this radiation is the high-voltage ignition which is eliminated in the simmer mode.
- 3) Reduced EMI/RFI radiation: A difficult requirement, particularly in military laser systems, is the reduction of broadband RF radiation. For example, a laser operating at 10 pps presents three major electric-field noise sources, the flashlamp igniter pulse, flashlamp current pulse, and Pockels-cell switching pulse. The first, and often the largest, source of this type of noise is eliminated in the simmer mode.
- 4) Increased efficiency: It has been demonstrated that in some cases the simmer mode can provide increases in Kr and Xe flashlamps' pumping efficiency for lamps operated with a pulse length of 50–200 μ s and pulse energy levels of 5–20 J.
- 5) Lamp status control: By monitoring the keep-alive current, a broken flashlamp or a short circuit can be detected before the energy storage capacitor is discharged. This is particularly important in large systems or in systems employing many flashlamps.

The major disadvantage of this mode of flashlamp operation is the added electronics and the power consumption of the continuous discharge. Small 7.5-cm-long linear lamps are operated at about 30 mA dc and consume between 5 and 10 W. To reduce the power consumption of the simmer mode, a pseudosimmer was devised that combines the advantage of the light-weight external trigger transformer with the improvements achieved in a simmer-mode system. Figure 6.25 shows a schematic block diagram of the circuit which has been used in small Nd:YAG systems. The lamp is ignited with an external trigger transformer. Lamp current initially flows through a limiting resistor, which is in parallel with the pulse-forming inductor and the SCR. Current flow through the inductor is prevented by the SCR. After an appropriate time delay, the SCR is turned on and the high-current pulse is initiated.

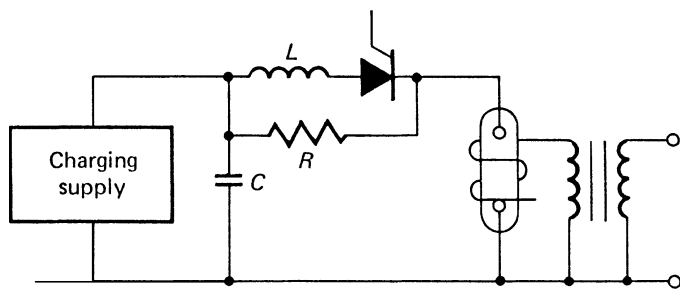


Fig. 6.25. Power supply with pseudosimmer discharge

6.1.2 Continuous Arc Lamps

For continuous pumping of Nd:YAG lasers, the use of halogen cycle tungsten filament lamps, noble gas arc lamps, and alkali vapor lamps has been explored. Since the discovery of the Nd:YAG laser in 1964, there has been a continual effort to find more effective means of pumping this material. One of the early devices used for pumping of the Nd:YAG laser was the tungsten-halogen filament lamp. The pump lamps considered next were the inert gases, which are rich in line structure in the near-infrared. Xenon has the highest overall conversion efficiency and is commonly used in arc lamps. However, the infrared line spectra of xenon misses all of the Nd:YAG pump bands, which are located at 0.73 to 0.76, 0.79 to 0.82, 0.86 to 0.89, and 0.57 to 0.60 μm . It has been observed [6.22, 6.37, 6.38] that the line spectrum from krypton is a better match to Nd:YAG than the line spectrum of xenon, since two of its strongest emission lines (7600 and 8110 \AA) are strongly absorbed by the laser crystal (Fig. 6.26).

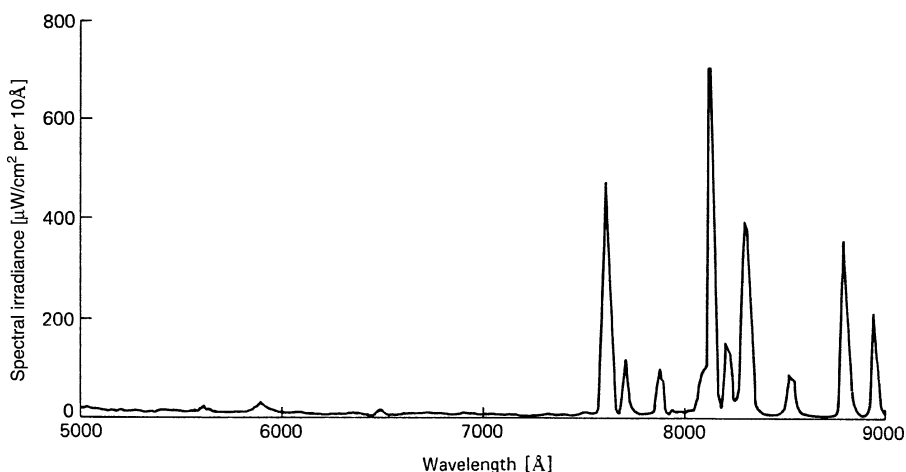


Fig. 6.26. Emission spectrum of a typical cw-pumped krypton arc lamp (6-mm bore, 50-mm arc length, 4-atm fill pressure, 1.3-kW input power) (ILC Bulletin 3533)

The laser output from a krypton-filled lamp is about twice that obtained from a xenon arc lamp operated at the same input power.

Mechanical Design

Continuous arc lamps are similar in design to linear flashlamps, with the exception that the cathode has a pointed tip for arc stability (see Fig. 6.1b–d). In the type of lamp employing a soft solder seal, additional cooling is provided to the tungsten anode cap by means of a water channel that forces some of the cooling flow through the copper cylinder and into close proximity to the tungsten. In the tungsten rod seal lamps the entire heat must be dissipated through the quartz envelope. In order to reduce thermal stresses in the walls, these lamps are often fabricated from 0.5-mm-thick tubing rather than the standard 1-mm thickness.

Cooling of the lamps is accomplished by circulating water in a flow tube surrounding the quartz envelope of the lamps. Often the flow tube will be made out of Germisil to absorb the ultraviolet content of the lamps. The design of the electrode holders and the flow tube must be such that localized boiling of the water is avoided.

Thermal Considerations

The maximum input power of a cw-pumped arc lamp is determined by the permissible stresses in the quartz envelope. The stresses are caused by the temperature gradient between the inner surface of the wall and the outer surface, and by the internal gas pressure during operation of the lamp. Since thermal considerations are of utmost importance in the operation of cw lamps, we will take a closer look at the mechanisms that generate heat at the electrodes and the lamp envelope.

At both electrodes, heat is generated by bombardment from either electrons or ions, conduction of heat from the plasma, and absorption of radiation. The kinetic energy of electrons incident on the anode is very high compared to that of ions impinging on the cathode. Therefore, the anode heats up much more than the cathode. The anode also conducts more heat from the plasma, since the area of the anode that is in contact with the plasma is larger than in the case of the pointed cathode. As far as absorption of radiation is concerned, both electrodes will absorb about the same amount of power. Polished tungsten has a reflectivity of about 60% in the visible region. Because of the emission of electrons from the cathode surface, this electrode is cooled to a certain extent. The heat removed by this process is given by

$$P = \frac{\Delta E I}{e}, \quad (6.40)$$

where ΔE is the work function, I is the current, and e is the electron charge. With $\Delta E = 2$ eV, $I = 30$ A, and $e = 1.6 \times 10^{-19}$ A, the heat removed from the cathode is 60 W in a typical lamp.

The total electrical input power of a gas discharge lamp is divided among the heat dissipated by the electrodes, the quartz walls, and the emitted radiation. Generally, it can be assumed that 10–20% of the electrical input power is dissipated as heat

through the electrodes and 30–50% is dissipated through the envelope [6.39]. The thermal loading of the tube envelope is due to the loss of kinetic energy of electrons, ions, and molecules by collision with the wall of the tube. The thermal gradient in the envelope is

$$\Delta T = \frac{Qd}{K}, \quad (6.41)$$

where Q is the dissipated power density, d is the wall thickness, and K is the thermal conductivity. Allowing a maximum temperature difference of $\Delta T = 1800^\circ\text{C}$ for fused quartz between the inner and outer wall surface, then with $K = 0.017 \text{ W}/(\text{°C cm})$ follows for the maximum power which can be dissipated through the quartz wall a value of $Q = 300 \text{ W/cm}^2$ for a 1-mm-thick envelope. In thinner walls thermal loadings as high as 400 W/cm^2 are achieved. Absorption of radiation in a quartz envelope is negligible. However, vaporization of electrode material leads to a gradual darkening of the lamp envelope. The deposits absorb radiation, hence, the wall-temperature gradient increases during the life of the lamps. The pressure of the fill gas when hot increases by up to a factor of 10. The operating pressure depends on the cold fill pressure of the lamp, the temperature of the plasma, and the volume of dead space behind the electrodes. Thermal and pressure stresses occurring in arc lamps can be calculated using equations given by Thouret [6.40]. Calculations carried out on cw arc lamps [6.25] have shown that the inner wall is under compression, whereas the outer wall is under tension and the total stress is largest on the outside of the quartz envelope. The rupture stress of quartz is 500 kg/cm^2 . Most lamps in commercial applications are operated at about 20–30% of the ultimate tensile strength of quartz.

Electrical Characteristics

Continuous arc lamps are ignited just like flashlamps. For example, a series injection trigger transformer supplying a 30-kV spike will lower the lamp impedance to a level that is within the range of a 300-V dc supply. The operating parameters and impedance depend on current density, arc length, bore size, and fill pressure. Typical krypton arc lamps are operated between 80 and 150 V and 20–50 A. Characteristic impedance values are between 2 and 10Ω . Figure 6.27 shows typical current–voltage curves for several arc lamps filled at 4 atm of krypton. The discharge voltage and dynamic resistance increases with the increase in gas pressure.

Optical Characteristics

At current densities obtainable in standard krypton arc lamps the plasma is optically thin. Calorimetric measurements of the total optical output power in the spectral region $0.3\text{--}1.2 \mu\text{m}$ reveal a radiation efficiency of about 40% for most Kr arc lamps. Figure 6.28 shows the dependence of the radiation efficiency on lamp input power and bore diameter. It has been found that the useful light output of krypton arc lamps for pumping Nd:YAG lasers increases with bore size, fill pressure, and input power. For example, the conversion efficiency of a lamp filled with 8 atm of Kr is about

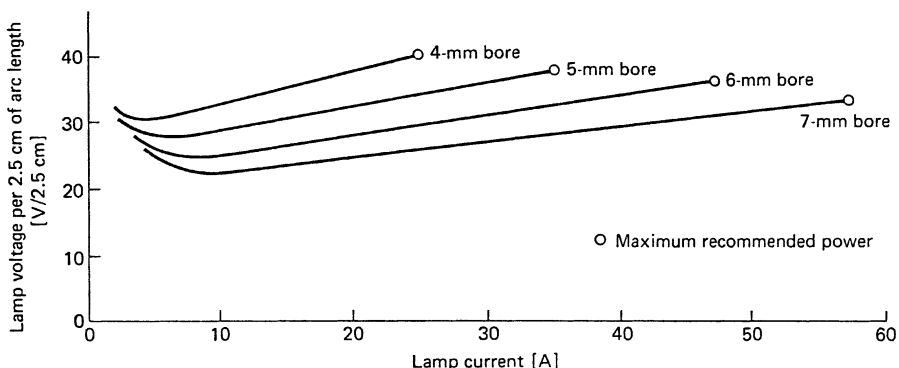


Fig. 6.27. Voltage versus current for different krypton arc lamps (ILC Bulletin 3533)

1.2–1.5 times as high as that of a lamp filled at 2 atm, depending on the electrical input [6.41]. A summary of the spectral data of a representative Kr arc lamp is given in Table 6.1. Note the large fraction of radiation between 0.7 and 0.9 μm .

Combining the absorption spectra of Nd:YAG with the emission spectra of the krypton lamp, the spectral utilization as a function of sample thickness has been calculated. The result is shown in Fig. 6.29. The curve illustrates rather dramatically kind of improvement one can achieve by increasing the diameter of a Nd:YAG laser rod in a pumping cavity.

Lamp Life and Operating Characteristics

The main degradation mechanism in these lamps is the accumulation of wall deposits. The deposits arise from evaporation and sputtering from the electrodes and from the residual gaseous and high-vapor-pressure impurities left in the lamp after fabrication.

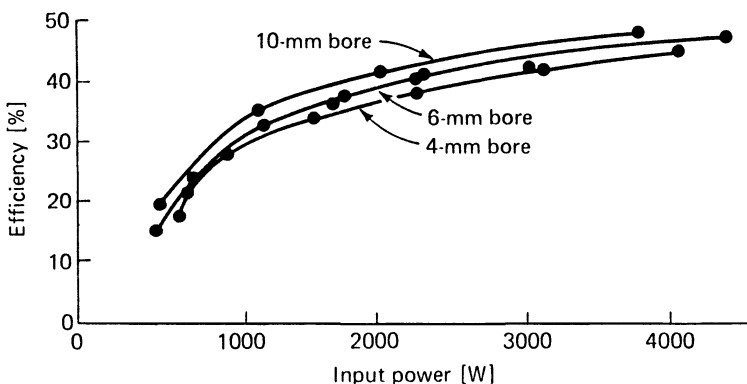


Fig. 6.28. Krypton arc lamp radiative efficiency as a function of input power; 4-, 6-, and 10-mm bore, 75-mm arc length, 4 atm of Kr fill pressure [6.39]

Table 6.1. Spectral data for cw krypton arc lamps

Quantity	Definition	Numerical data ^a
Radiation efficiency	Radiation output/electrical input	0.45
Spectral output	Fraction of radiation in spectral lines	0.40
	Fraction of radiation in continuum	0.60
Spectral power distribution	Fraction of total radiation below 0.7 μm	0.10
	Fraction of total radiation between 0.7 and 0.9 μm	0.60
	Fraction of total radiation between 0.9 and 1.4 μm	0.30

^a Data are typical for lamps having a 6–13-mm bore, 7.5–25-cm arc length, 2–3-atm fill pressure, operated at 6–16 kW.

The black deposit that builds up eventually completely attenuates the radiative output of the lamp. The underlying quartz becomes overheated, and catastrophic failure of the lamp occurs from excessive thermal stresses developing in the envelope walls. Black anode wall deposits are greatly reduced by the use of an internally water-cooled anode structure.

Krypton arc lamps are available from 5 to 20-cm arc length, with bore diameters from 3 to 10 mm, and are designed to handle electrical input powers of up to 15 kW [6.25]. Design parameters and performance data of typical lamps used in commercial lasers are summarized in Table 6.2. Some of the lamps listed are operated far below the manufacturer's maximum rating in order to obtain good lamp life. Typical overall efficiencies obtainable in krypton-pumped Nd:YAG lasers are between 2 and 3%. For

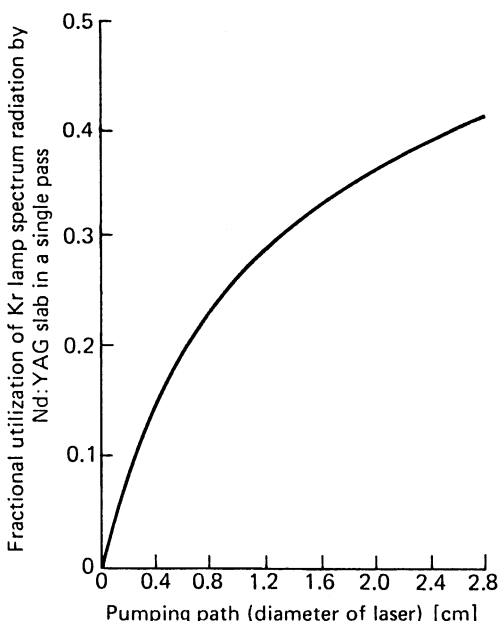
**Fig. 6.29.** Fractional utilization of krypton lamp output by Nd:YAG

Table 6.2. Typical operating parameters of cw-pumped krypton arc lamps

Model number	FK-125-C2.75 EG&G	FK-111-C3 EG&G	5Kr2 ILC
Arc length	70 mm	75 mm	50 mm
Bore diameter	5 mm	7 mm	5mm
Fill pressure	2 atm	2 atm	4 atm
Typical input power	3 kW	6 kW	2.5 kW
Lifetime	400–600 h	40–60 h	150–200 h
Wall loading (40% of electrical input)	110 W/cm ²	145 W/cm ²	128 W/cm ²
Coolant flow rate	120 cm ³ /s	120 cm ³ /s	60 cm ³ /s
Electrical characteristics	100 V 30 A	112 V 56 A	84 V 30 A
Current density	150 A/cm ²	140 A/cm ²	150 A/cm ²

example, at output levels of 100 and 250 W, 2.9% and 2.1% efficiencies were achieved with krypton lamps filled to 4 atm [6.38, 42]. Efficiencies of 3.3% have been attained at input power levels of 3 kW with a 6-mm bore and 50-mm-long lamp filled at 8 atm of krypton [6.39].

Operation of Arc Lamps

Continuous arc lamps are ignited just like flashlamps. For example, a series injection trigger transformer supplying a 30-kV spike will lower the lamp impedance to a level that is within the range of a 300-V dc supply. The operating parameters and impedance depend on current density, arc length, bore size, and fill pressure. Typical krypton arc lamps are operated between 80 and 150 V and 20–50 A.

A trigger circuit is required to start the lamps, and in some cases when the lamps are filled at high pressure an additional high-voltage boost must be provided. A simplified schematic of a power supply which is employed in a large number of krypton arc pumped Nd:YAG lasers is shown in Fig. 6.30. The input is applied to a three-phase isolation transformer. Each output of the secondary of the 6-kV power transformer is connected to the center of three pairs of series connected SCRs. This is the conventional three-phase bridge rectifier configuration, with the exception that the rectifiers are SCRs. The control unit senses the analog input from a current-sampling resistor, compares it with a reference voltage, and generates phase-controlled pulses which fire the SCRs. Control of the SCR conductance time provides regulation of the supply. The unit operates as a variable time switch for each leg of the three-phase ac input. The output of a rectifier is applied to a L/C filter network for ripple elimination. The ignitor provides the high-voltage pulse to start the lamp. This is done by discharging a capacitor with SCR through the primary of a trigger transformer. The transformer steps up this voltage to over 30 kV, which is sufficient to ignite the lamp. For reliable lamp starting, the voltage of the main power supply must be boosted to about 600 V to 1 kV during the trigger phase. This is most conveniently done by

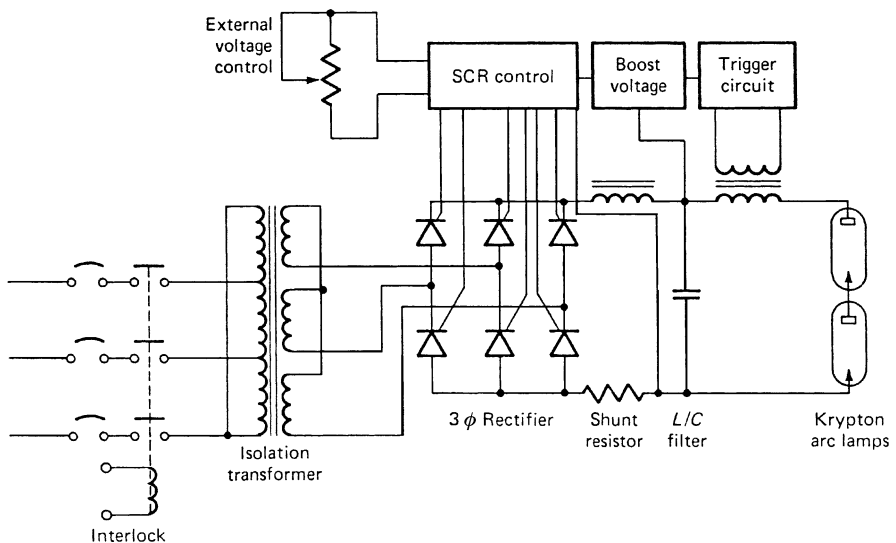


Fig. 6.30. Phase-controlled power supply for use with krypton arc lamps

charging the filter capacitor to this voltage with a small, low-current, high-voltage supply. Power supplies of the type shown in Fig. 6.30 have been built for lamp inputs of up to 20 kW.

6.1.3 Laser Diodes

The most efficient pump source for solid-state lasers is the diode laser. Although the advantage of pumping solid-state lasers with monochromatic pump sources has been recognized very early, the low power output, low packaging density, and extremely high cost of diode lasers prevented any serious application for laser pumping until the mid-1980s. At that time, linear laser diode arrays, based on aluminum gallium arsenide (AlGaAs) quantum well technology, became available with output powers of 10 W/cm at room temperature, and with efficiencies on the order of 30% [6.43]. During the last two decades significant progress has been made in developing monolithic, linear laser-diode arrays which have become the building blocks for solid-state laser pumps. Output power, slope efficiency, laser threshold, and wavelength control have all been dramatically improved due to a combination of new structures and advanced growth techniques. In particular, epitaxial growth based on MOCVD allows close control of material composition, layer thickness, and device geometry.

Today, the output from 1 cm single cw diode bars is typically around 50 W/cm with efficiencies between 40 and 50%. Historical overviews of diode laser-pumped solid-state lasers can be found in [6.44] and in earlier editions of this book. The major attributes of diode pumping can be summarized as follows:

- *Increased system efficiency.* Compared to traditional broadband flashlamps or continuous arc lamps, a laser diode pump source has a very narrow emission

bandwidth. Although flashlamps have a radiation efficiency (40–60%) comparable to diode lasers, only a small fraction of the radiation is absorbed by the laser crystal. In contrast, the wavelength of a diode laser can be chosen to fall completely within an absorption band of a particular solid-state laser. For example, 808 nm for Nd:YAG, or 941 nm for pumping a Yb:YAG laser.

- *Improved beam quality.* A concomitant advantage derived from the spectral match between the diode laser emission and the long-wavelength Nd absorption band is a reduction in the amount of heat which is deposited in the laser material. This reduces thermo-optic effects and therefore leads to better beam quality. In addition, the directionality of diode radiation allows designs with good spatial overlap between pump radiation and low-order modes in the resonator, which in turn leads to a high-brightness laser output.
- *Enabling technology for compact and versatile laser systems.* The directionality of the diode output and the small emitting area, as compared to lamp pump sources, made it possible to design whole new classes of solid-state lasers, such as end-pumped systems, microchip lasers, and fiber lasers. The flexibility of shaping and transferring the output beam from the pump source to the laser medium provides a great opportunity for the invention of new pump configurations and design architectures. An almost endless variety of optical coupling schemes has been reported.
- *Enabling technology for new laser materials.* The most prominent laser materials which are pumped with diode pump sources can also be pumped with flashlamps. However, a number of very useful materials such as Nd:YVO₄, Yb:YAG, and Tm:YAG have reached prominence only as a result of diode pumps.
- *Increased component lifetime.* System lifetime and reliability is higher in laser diode pumped solid-state lasers as compared to flashlamp-based systems. Laser-diode arrays exhibit lifetimes on the order of 10⁴ h in cw operation and 10⁹ shots in the pulsed mode. Flashlamp life is on the order of 10⁸ shots, and about 500 h for cw operation.
- *Benign operating features.* The absence of high-voltage pulses, high temperatures, and UV radiation encountered with arc lamps lead to much more benign operating features of laser-diode-pumped systems. Furthermore, the high pump flux combined with a substantial UV content in lamp-pumped systems causes material degradation in the pump cavity and in the coolant, which lead to systems degradation and contribute to maintenance requirements. Such problems are virtually eliminated with laser-diode-pump sources.
- *Increased pulse repetition rate.* Besides low repetition rate and cw operation covered also by flashlamps and cw arc lamps, quasi-cw laser diodes permit, in addition, pulsed operation of solid-state lasers in the regime from a few hundred hertz to a few kilohertz.

The degree of penetration of diode-pumped Nd lasers in commercial markets has been governed by the cost per average watt of pump power. Because laser diodes are inherently constant power sources, they are most economically exploited in continuous pumped lasers, such as cw or high repetition rate free running or Q-switched systems.

The unit cost per watt of pump power has declined sufficiently in recent years and most solid-state lasers with output powers up to 50 W are now beginning to dominate commercial industrial lasers. The cost reduction was mainly the result of increasing the power output from a 1-cm bar from the initial 10 W to over 50 W, and a higher production volume. For larger systems, the diode pumps are the major cost driver and the initial high costs have to be weighted against savings in the life cycle costs of the system, such as reduced electrical power consumption and lower maintenance costs.

The most costly application is the use of diode laser pump sources to produce high energy, low-duty factor pulses as required in military applications, such as range finders or target designators. However, in these applications either size and weight, efficiency, beam quality, or low maintenance are the overriding considerations.

In this subsection the following topics will be discussed: Internal structure of laser diodes, packaging configurations, spatial and spectral beam characteristics, input vs. output power, lifetime issues, and thermal control.

Internal Structure of Laser-Diodes

The most basic form of a diode laser consists of a semiconductor in which one part is doped with electron donors to form n-type material and the other part is doped with electron acceptors (holes) to produce p-type material. Application of a negative voltage to the n-material and a positive voltage to the p-material drives electrons and holes into the junction region between the n- and p-doped material. This is called forward biasing the pn junction. In the junction electron-hole recombination takes place. In this process, electrons from a higher-energy state (conduction band) transfer to a lower-energy state (valence band) and this releases energy in the form of photons. In order to produce stimulated emission in the junction area, population inversion and optical feedback is required. Passing a high current through the junction area provides a population inversion. A Fabry–Perot resonator, formed by cleaving the chip along parallel crystal planes, provides optical feedback. Gain in laser diodes is very high; therefore, only a small length of active material is needed. Typical edge emitting laser chips have active layers about 500 μm long. In order to increase efficiency and output power, actual laser diodes contain a number of different layers with the active region sandwiched in between.

Semiconductor laser technology has produced an amazing variety of new device structures in the past decade. Overviews of this technology made possible by sophisticated growth techniques such as metallorganic chemical-vapor deposition (MOCVD) and molecular beam epitaxy (MBE) can be found in [6.43]. Most techniques differ in the way confinement is achieved regarding the width and depth of the gain region and mode volume of the optical radiation. We will illustrate the key design features of diode lasers by describing the single quantum well separate confinement heterostructure (SQW-SCH) because it is a widely employed design for solid-state laser pumps.

Figure 6.31 shows the dimensions of a typical 1-cm monolithic linear array (top) and a cross section of the device (bottom) that is made up of a stack of several semiconductor layers with varying thickness and doping levels. The thickest layer on

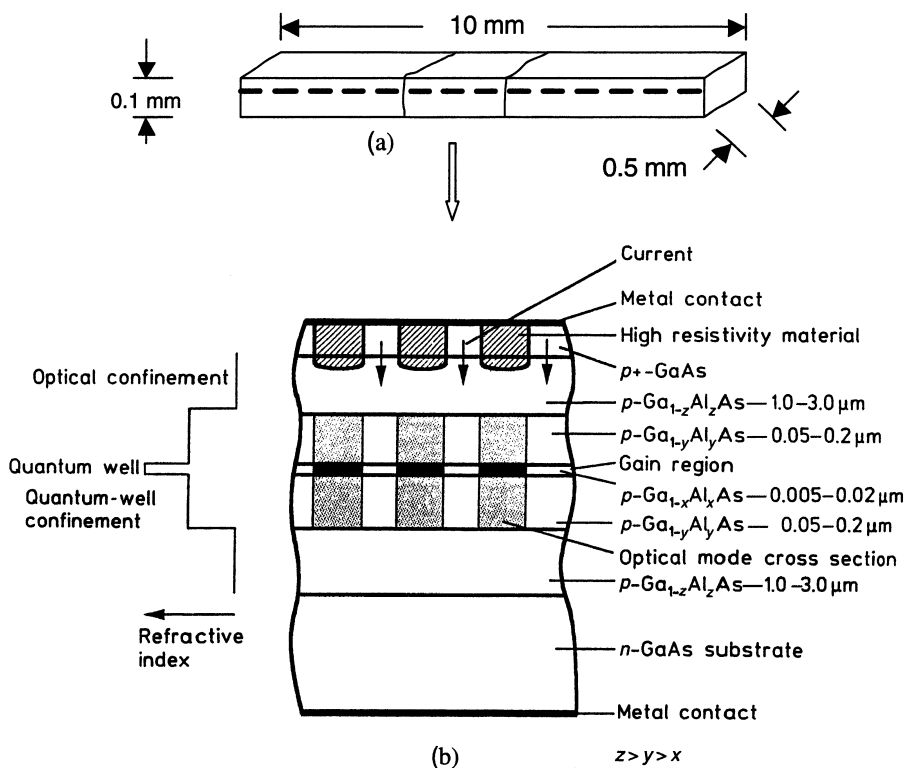


Fig. 6.31. Gain-guided, single quantum-well separate confinement heterostructure stripe laser [6.43]. (a) Typical dimensions of a 1-cm bar and (b) detail of internal structure (thickness of layers is greatly exaggerated)

the bottom is the n-GaAs substrate onto which the other layers are deposited. The top layer is p-GaAs. Sandwiched between several other layers is the very thin active region of the pn junction. The top and bottom surfaces of the whole stack are coated with metallic contacts for electrical connection to the drive electronics. The active region is divided into many parallel and narrow stripes by restricting the current in the lateral direction. The width of the active region has to be restricted to avoid the onset of amplified spontaneous emission which would propagate in off-axis directions and compete with the laser beam for the available population inversion. In the gain-guided design illustrated in Fig. 6.31a a particular emitter width is achieved by deposition of a region of high-resistivity material beneath the contact area. Therefore, the current is channeled through narrow low-resistance areas of the p-GaAs surface layer (white rectangular area in Fig. 6.31(b)). Electrical current injected through the forward-biased pn junction creates the population inversion and gain in the active region. The distribution of the charge carriers injected in the active region, and therefore the gain distribution, is determined by the width of the current channel. The voltage across the junction is on the order of 2 V for GaAs/AlGaAs materials, and the slope efficiency

is about 1 W/A. Laser emission, which is between 790 and 860 nm for GaAs/AlGaAs laser diodes, is perpendicular to the planar front facet of the laser diode bar shown in Fig. 6.31.

A 1-cm bar contains 10–50 independent laser emitters, all radiating in the same direction perpendicular to the planar front of the structure. The width of each emitter (white rectangle in Fig. 6.31b) is between 50 and 200 μm . The spacing between adjacent emitters ranges from 200 μm to 1 mm. In the so-called broad area emitters, each emitter consists of a single stripe. In other designs the total width is subdivided in subarrays of 10–20 closely spaced narrow-stripe emitters for better lateral mode control. The width of, and spacing between, individual emitters is dictated by the average power, peak power, or duty cycle requirements and the type of cooling applied to the bar.

Radiation in the vertical direction of the pn junction is confined by a wave guide structure comprising several layers of differently doped materials. The active layer shown in Fig. 6.31 is sandwiched between two pairs of layers having a different concentration of aluminum. The main purpose of the innermost pair of layers is to confine the carriers to the active region, whereas the purpose of the outer layers is to confine the optical beam. In a conventional double-heterostructure pn junction the active region has a thickness of around 0.1–0.3 μm . The quantum-well active region illustrated in Fig. 6.31b is an order of magnitude thinner. Extremely high gains on the order of $3\text{--}5 \times 10^4 \text{ cm}^{-1}$ and low thresholds can be achieved in such a thin layer.

A quantum well is a thin layer of semiconductor located between two layers with a larger bandgap. Electrons in the quantum-well layer lack the energy to escape and cannot tunnel through the thicker surrounding layers. The quantum-well layer in Fig. 6.31b has a composition of gallium and aluminum indicated by x , which defines the emission wavelength. A higher aluminum concentration increases the bandgap and shifts the output toward shorter wavelength. The quantum-well structure is sandwiched between two thick layers of a composition which contains a higher concentration of aluminum ($y > x$). The higher aluminum concentration increases the bandgap, thereby defining the quantum well, and the large thickness of the layer prevents tunneling of the carriers out of the quantum well. Instead of a single quantum-well active layer, several quantum wells can be sandwiched one above the other to generate multiple quantum-well stacks.

The thin active region incorporating a quantum-well active layer structure provides low threshold and high electrical-to-optical efficiency. However, such a very small emitting surface poses one problem since the power from a diode laser is limited by the peak flux at the output facet. One can increase the output from these devices by spreading the beam over an area that is larger than the active layer or gain region. The standard approach is to deposit layers next to the active layer, each of which has a slightly lower refractive index than the active layer, thus making a wave guide of the active layer. In the separate carrier and optical confinement heterostructure (SCH) design shown in Fig. 6.31b, the refractive index boundary is abrupt, at the layer boundary. Alternatively, the refractive indices of the surrounding layers may be graded, forming a graded-index and separate carrier and optical confinement heterostructure (GRINSCH).

In the single quantum-well structure depicted in Fig. 6.31b, the effective aperture of the laser output is 0.1–0.4 μm vertical to the pn junction, which is about a factor 20 larger than the gain region. This substantially reduces the energy density at the output facet and enhances reliability by minimizing catastrophic facet damage.

Each small white rectangle in Fig. 6.31b indicates the gain region, whereas the large rectangle surrounding it represents the optical aperture of one emitter. The drawing exaggerates the vertical dimension by several orders of magnitude. The emitting aperture is, in reality, a wide and very narrow horizontal line with a width up to 200 μm and a thickness of no more than 1 μm .

As described above, the beam cross section of a single emitter is given by the width of the current channel in the plane of the pn junction and by the waveguide structure in the vertical direction. The front and rear facets, separated by about 500 μm , define the length of the Fabry–Perot resonator. The facets, which provide optical feedback and output coupling, are created by cleaving the bars from the processed semiconductor wafer. Cleaving along directions dictated by the crystal structure generates extremely planar and parallel surfaces. The facets are dielectrically coated to provide a high reflectivity at the rear facet and an appropriate output transmission at the front facet.

Diode Pump Source Configuration

Depending on the output-power requirement of the laser and the particular pump configuration chosen, one can select a diode pump source from a large number of standard commercial designs.

The smallest device is a single emitter diode laser with an output of about 1 W. However, the basic building block for diode-pumped solid-state lasers is the 1-cm bar, which can be incorporated into a laser as a single component or as part of a vertical or horizontal stack that combines many bars in a single pump module with a common heat sink and electrical connection.

Vertical stacks consist of 1 cm bars mounted on top of each other with thin spaces in between for heat conduction. Individual bars or vertical stacks can also be mounted side by side to form horizontal stacks with a common heat sink.

Modules with long and narrow emitting surfaces consisting of individual bars or small vertical stacks mounted side by side are most suitable for pumping laser rods. Large square or rectangular pump modules are designed primarily for pumping slabs. Bars and stacks emit radiation from an extended surface. The ability to focus pump radiation to a small spot is very critical for end-pumped laser configurations. For end-pumping a laser a small circular beam is required. For these applications fiber-coupled bars or stacks are offered commercially.

Depending on the number of bars and the type of cooling employed, several kilowatts of cw output and tens of kilowatts of peak power in quasi-cw mode can be obtained from two-dimensional arrays.

Commercial high-power diode pumps are available for the wavelength range of 790–860 nm and 940–980 nm, whereby the main interest is for pump sources around 808 nm for Nd:YAG and Nd:YVO₄ and at 940 nm to pump Yb:YAG lasers.

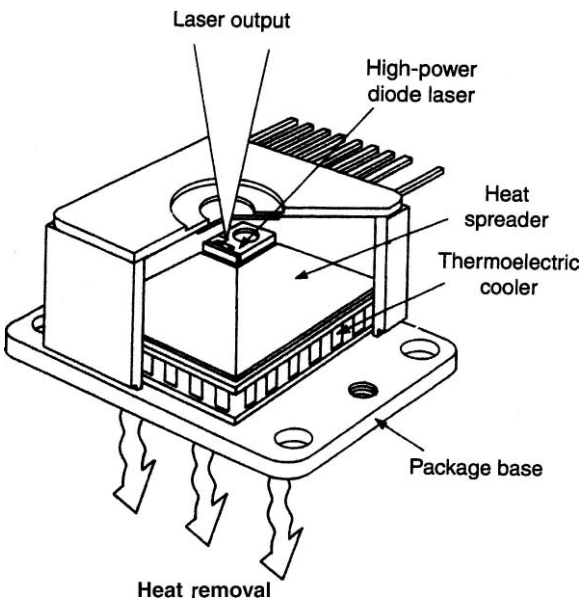


Fig. 6.32. Diode laser mounted on thermoelectric cooler (SDL, Inc.)

Single Emitter. The device consists of a single active junction region or output facet with a width ranging from 50 to 200 μm , and produces an output power up to 2 W. The brightest high-power single emitters generate more than 1 W of cw power that can be coupled into a 60- μm fiber. The single emitter package illustrated in Fig. 6.32 has a total output of 2 W in cw mode. The output is emitted from an area of $200 \times 1.0 \mu\text{m}$ with a beam divergence of 40° by 10° . The device can be coupled to an optical fiber or mounted on a thermoelectric cooler. In the latter configuration shown in Fig. 6.32 the array is mounted on a pyramidal heat sink that connects to a thermoelectric cooler. Heat dissipates through the base, while the radiation emerges from the top. The thermoelectric cooler permits temperature tuning of the output to match the absorption lines of the solid-state laser. In a GaAlAs diode laser, the wavelength changes with temperature according to $0.3 \text{ nm}/^\circ\text{C}$.

The maximum safe power density at the facet of a laser diode is about $10 \text{ mW}/\mu\text{m}^2$ or $1 \text{ MW}/\text{cm}^2$. Therefore, a 100- μm -wide and 1- μm -thick emitter will generate 1 W of output consistent with a long lifetime.

Linear Arrays. The key to generating high powers from diode lasers has been the development of 1-cm bars as illustrated in Figs. 6.31a and 6.33. The active element of a bar is a monolithic semiconductor chip containing multiple individual laser emitters. The chip is bonded to an alloy submount. An insulated wire bond plate is soldered to the submount behind the laser diode array. Electrically the individual diodes in the array are all connected in parallel to a wire bond plate. The bonding of the bar to the submount is made through the thinner p-doped

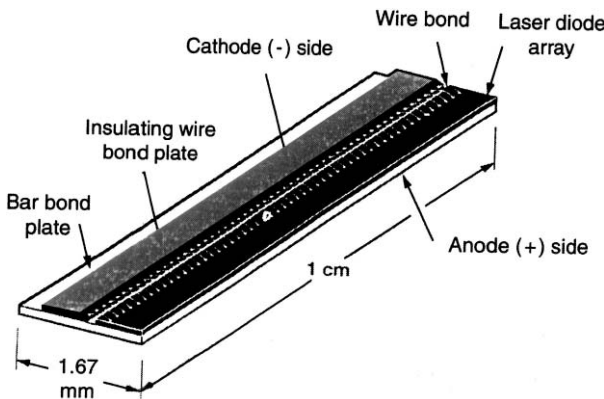


Fig. 6.33. Basic structure of a 1-cm bar

side to minimize the thermal resistance between the gain medium and the heat sink.

In the finished device, the very thin submount is soldered onto a much larger copper heat sink, which also provides for the electrical connection. In the fabrication of laser bars, 10–50 independent laser emitters are serially repeated on a single substrate to form a monolithic bar structure. Practical processing considerations limit the length of such bars to 1 cm.

The spacing between adjacent emitters may range for cw devices from 200 μm to 1 mm. The spacing of emitters, or pitch, determines the fill factor for the device and is governed by thermal considerations.

The output from a conductively cooled cw 1-cm bar is between 20 and 40 W. The emitting area is 10 mm by 1 μm . Spectral width is 2–3 nm. For a 40 W device, threshold current is around 14 A, and 50 A at full output, which relates to an efficiency of 45%. Beam divergence (FWHM) is typically $10 \times 35^\circ$.

For cw bars mounted on internally water-cooled microchannel heat sinks, the industry standard is 50 W per bar and a lifetime exceeding 5000 hours. At reduced lifetime, individual 1-cm bars mounted on microchannel heat sinks have produced output powers in excess of 250 W, both at 808 nm and 980 nm.

The use of diode lasers for pumping pulsed neodymium lasers requires a pulse length on the order of several hundred microseconds. One limit of the output of diode lasers is the temperature of the junction and the associated thermal runaway condition that raises the local temperature of the facet to the melting temperature. Because of the small volume of material involved, this temperature rise occurs in less than 1 μs . Therefore, the power limit of diodes in the long-pulse mode is the same as for cw operation. Thus, long-pulse operation ($\gg 1 \mu\text{s}$) is called quasi-cw operation. The peak power obtained from a 1-cm bar can be increased over the cw value by increasing the number of single emitters; this is achieved by increasing the fill factor. Of course, the duty cycle has to be limited such that the average power from the bar is about the same as for a cw bar.

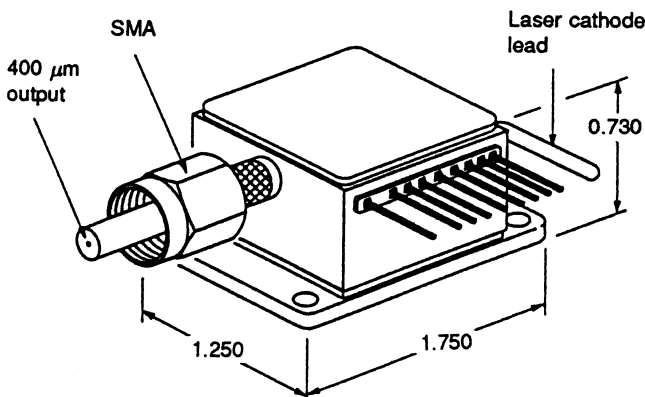


Fig. 6.34. Fiber-coupled laser diode bar

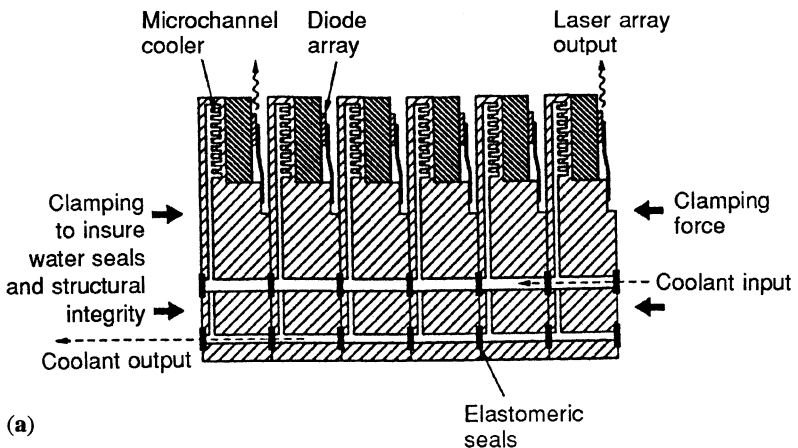
Operated in the quasi-cw mode, a single bar typically generates 60 W peak power, or 12 mJ in a 200 μs long pulse, although devices up to 100 W are available at reduced lifetime. Depending on cooling conditions, duty cycles on the order of 30% are possible. Micro lenses can be mounted in front of a bar to concentrate pump radiation into a fiber. Output up to 30 W are available from single fibers ranging in diameter from 200 to 400 μm . Fiber-coupled diode bars are the standard pump configuration for end-pumped lasers. Also, the ability to mount the pump source away from the laser onto a heat dissipating structure is a big advantage. Fig. 6.34 displays the package of a single 20 W cw bar coupled to a 400 μm fiber with 16 W available at the end of the fiber.

Two-Dimensional Array. In multibar pump modules, a number of 1-cm bars are stacked vertically and/or horizontally to form two-dimensional arrays. The bars must be positioned as close together as possible to maximize brightness. The key issue is the efficient removal of waste heat from the individual bars. Several techniques known as “rack and stack,” “bars in a groove,” and “microchannel cooled devices” have evolved with regard to assembly and cooling of multibar pump modules.

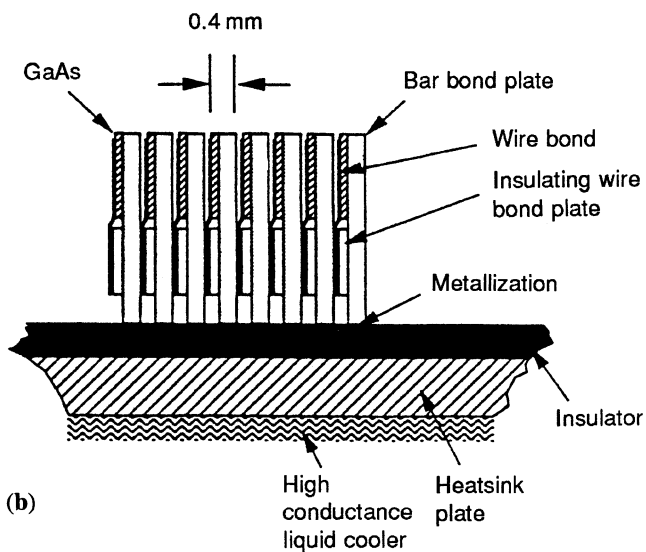
In the so-called rack-and-stack assembly technique, laser diode bars are first mounted on individual submounts which are then stacked to produce two-dimensional array [6.45]. The spacing (pitch) between adjacent bars depends on the average output power and on the cooling method.

For quasi-cw arrays one common design approach uses thin copper heat sink spacers between the bars. The assembly of sandwiched bars and spacers is soldered onto a common heat sink.

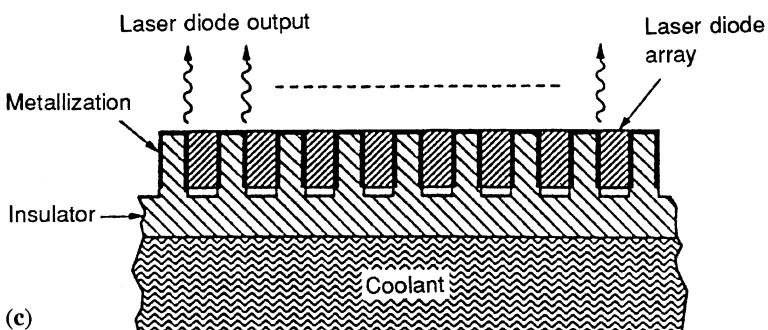
Heat from each bar is extracted from the back of the copper spacers through the common heat sink. Example of back-plane cooled stacked arrays are shown in Figs. 6.2a and 6.35b. This internally conductively cooled diode stack has to be attached via two mounting holes to a larger cold plate or water-cooled heat sink. Electrically the bars are connected in series, the two large copper leads extending from the back



(a)



(b)



(c)

Fig. 6.35. Cooling techniques for multibar arrays. (a) Microchannel cooling of each bar. (b) Bars pre-assembled and mounted on a common heat sink. (c) Bars directly mounted onto a common heat sink

of the device in Fig. 6.2(a) are for connection to a power supply. The thickness of the copper heat spreader, and therefore the stacking density, depends on the duty cycle of operation. Higher average power operation requires thicker heat sinks. For low-duty-cycle operation around 3%, the bars can be densely packaged with only 0.4-mm space in between; this allows a power density of 1.5 kW/cm^2 . At a 6% duty cycle, the spacing increases to 0.8 mm and 800 W/cm^2 can be achieved. Operation of a 10 stack array, with $200 \mu\text{s}$ pulses at 100 Hz, produces typically a peak power of 600 W at 40% efficiency.

In the “bar in the groove” approach (illustrated in Fig. 6.35c) the laser diode bars are inserted into individual parallel grooves machined into a block of beryllium oxide. The latter material is a thermally conductive, but electrically insulating material. The bars are soldered to the side walls of the grooves which produces a monolithic device. Electrical interconnections are achieved by conductively coating the side walls of the grooves [6.46, 47].

Multibar arrays for cw or high-duty cycle-pulsed operation require active cooling close to the junction of the individual emitters. This can be achieved by using microchannel cooling technology whereby each diode bar has its own liquid heat exchange submount [6.48]. In one approach as shown in Fig. 6.35(a) individual bars are separated by cooling plates approximately 1 mm thick, through which cooling water is channeled. The space inside these hollow plates is divided into flow channels by thin cooling fins separated by a few hundred microns, thereby maximizing the metal surface area in contact with the cooling water. Compared to the conductively cooled heat sink spacers, the thermal resistance for the internally liquid-cooled heat sinks is greatly reduced.

Two-dimensional arrays are created by stacking individual bar/cooler assemblies. Using this approach, bars can be stacked with a 2-mm bar-to-bar pitch. Figures 6.2b and 6.36 depict internally liquid-cooled two-dimensional arrays. In a microchannel cooled pump module each bar can be operated up to 50 W; this is the same as in a

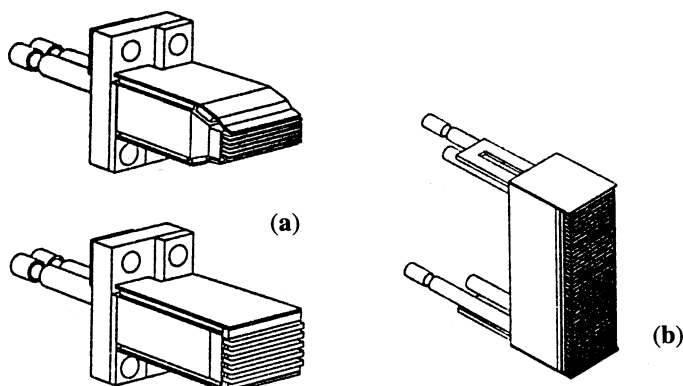


Fig. 6.36. Packaging configurations of diode arrays. High-duty-cycle liquid-cooled arrays for (a) rod pumping and (b) slab pumping

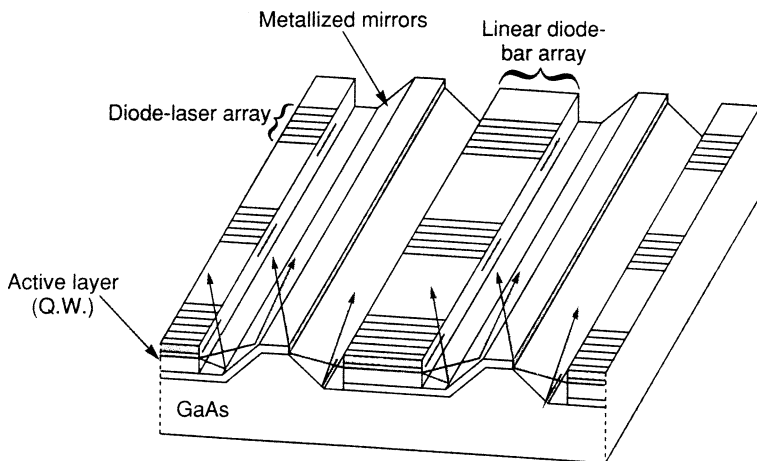


Fig. 6.37. Diode-laser array with integrated 45° mirrors

single bar. A 2×10 array composed of two stacks of 10 bars each can produce 1 kW of cw power from a total emitting surface of only 4 cm^2 .

Pulsed arrays can be operated up to 30% duty cycle with internal active cooling. The most powerful multibar pump modules generate peak powers in excess of 30 kW and cw powers of several kilowatts.

Figure 6.36 illustrates different packaging configurations of diode arrays. The two-dimensional arrays employed in rod pumping (Fig. 6.36a) have typically an emitting area of $1 \text{ cm} \times 0.3 \text{ cm}$ or $1 \text{ cm} \times 0.5 \text{ cm}$. The arrays can be symmetrically arranged around the laser rod. Pumping of slabs requires large area pump sources such as the $1 \text{ cm} \times 3 \text{ cm}$ depicted in Fig. 6.36b.

Surface Emitters. The basic method for stacking up linear arrays to create two-dimensional arrays requires a large number of fabrication processes. An intuitively appealing alternative approach is to fabricate two-dimensional arrays directly at the wafer stage, thereby substantially reducing the manufacturing complexity.

Figure 6.37 exhibits an example of a monolithic structure, in which a mirror at a 45° angle to the active layer deflects laser radiation from the chip surface, rather than the edge. The mirrors are etched into the substrate in these monolithic, surface emitting, quantum-well diode-laser arrays [6.49]. Instead of using integrated mirrors, the diode radiation can be deflected with a distributed-Bragg reflector [6.50], or the resonator can be rotated 90° in the so-called vertical cavity laser [6.51].

Spatial Profile

The output beam emerging from the facet of a diode laser is in the form of a light cone that is oval in cross section, as illustrated in Fig. 6.38. In the vertical direction with respect to the pn junction, the beam is diffraction limited and has a divergence

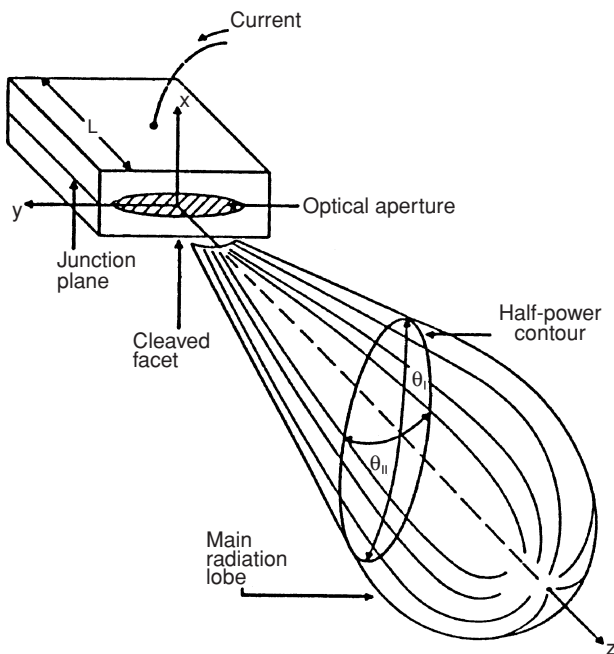


Fig. 6.38. Radiation pattern from a laser diode [6.52]

of about 40° FWHM. The Gaussian beam appears to emerge from a $1 \mu\text{m}$ aperture. If one introduces in (5.8) a wavelength of $\lambda = 0.8 \mu\text{m}$ and a spot size radius for a Gaussian beam of $0.5 \mu\text{m}$, the beam divergence at the $1/e^2$ points is $\theta = 57^\circ$.

Collimation of such a highly divergent beam requires optics with a numerical aperture of $\text{NA} = \sin(\theta/2) = 0.5$ or higher. Optical systems with such a high numerical aperture are said to be fast. From this it follows that the direction of the output beam from a laser diode in the vertical direction of the emitting stripe is termed the fast axis.

In the plane parallel to the pn junction, the beam divergence is much smaller and is about 10° FWHM. However, considering the width of the emitter, which is between 50 and $200 \mu\text{m}$, this is many times diffraction limited. For example, a Gaussian beam emerging from an aperture of $150 \mu\text{m}$ would have a divergence of 0.4° at the $1/e^2$ points. The output consists of many high-order spatial modes, termed lateral modes in the literature. The number of lateral modes depends on the design of the emitter (i.e., broad area or subdivided into narrow stripes), cavity length, and various material parameters.

Depending on the design of the emitter architecture, the shape of the beam can vary from a flat-top beam with round edges to a beam with two lobes. The former is typical of broad area emitters, whereas the latter is the result of coupling between the fields in a narrow stripe emitter [6.53, 54]. Compared to the vertical direction, the smaller divergence of the beam in the plane of the pn junction allows the use of optics

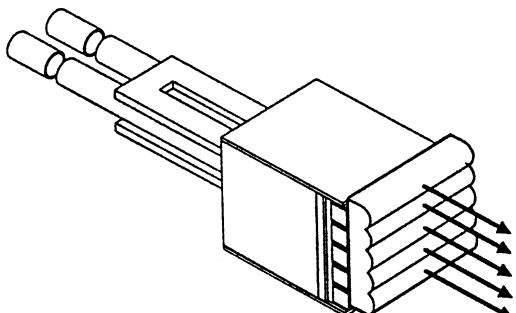


Fig. 6.39. Five bar diode array with individual micro lenses to reduce beam divergence of the fast axis

with a smaller numerical aperture. Therefore, the beam in this direction is referred to as the slow axis.

Reformatting the highly astigmatic pump beam emitted from a line source into a circular beam, which is required for end-pumped lasers, is a challenging task. End-pumped lasers require focusing of the pump radiation to a small spot size for mode matching or for coupling into an optical fiber. In Sect. 6.2.3 a number of different optical schemes that accomplish this task will be discussed.

If it is necessary to concentrate pump radiation into a narrow region of a small slab or cylindrical laser rod, it is often sufficient to reduce the faster diverging angle of the beam by mounting a tiny micro lens close to the emitting surface of the laser bar. For example, in the commercial device illustrated in Fig. 6.39 the 10×40 beam divergence of each laser bar is reduced in this manner to $10^\circ \times 1^\circ$.

Spectral Properties

The spectral properties of laser-diode arrays that are most critical for the pumping of solid-state lasers are the center wavelength and the spectral width of the emission and the wavelength shift with temperature.

The wavelength of a laser diode is inversely proportional to the energy difference ΔE between the conduction and valence band

$$\lambda = hc / \Delta E, \quad (6.42)$$

where h is the Planck's constant and c is the speed of light. The bandgap depends on the crystalline structure and chemical composition of the semiconductor. A binary compound such as GaAs has a fixed wavelength. Adding a third element, by substituting a fraction of gallium with aluminum in GaAs, changes the bandgap.

In a compound semiconductor, such as GaAlAs, the wavelength of the emitted light can be tailored over a wide range by changing the ratio of aluminum and gallium. Adding aluminum increases the bandgap, producing lasers with shorter wavelengths. Most commercial GaAlAs lasers have wavelengths of 750–850 nm. Neodymium ions have substantial absorption in the vicinity of 808 nm, which is the emission

wavelength of diode lasers with $\text{Ga}_{0.91}\text{Al}_{0.09}\text{As}$ active regions. As far as the pumping of neodymium lasers is concerned, the output wavelength can be tailored to the peak absorption by adjustments of the aluminum concentrations according to [6.55]

$$\Delta E = 1.424 + 1.247x \text{ (eV)}, \quad (6.43)$$

where x is the aluminum concentration.

Compositional changes and temperature gradients within an array lead to a broader spectral output for the whole array as compared to a single device. A typical spectral width of a single bar or small stacked array is on the order of 2.5–3.5 nm. State-of-the-art performance is about 2.2 nm for a 10 bar array. The bandwidth of the Nd:YAG absorption line at 808 nm is 2 nm for an absorption coefficient larger than 3.8 cm^{-1} . Similarly, in Nd:YLF, the absorption line is about 2 nm wide for absorption coefficients larger than 2 cm^{-1} . The excellent spectral overlap between the absorption line of Nd:YAG at 808 nm and the emission of a two-dimensional array of GaAlAs laser diodes is illustrated in Fig. 6.40.

In diode-pumped lasers that have only a short absorption path, it is important to have a narrow spectral emission from the diode array in order to absorb most of the pump radiation. In optically thick materials, such as large diode-pumped lasers with rod or slab dimensions on the order of 10–15 mm, spectral width becomes less

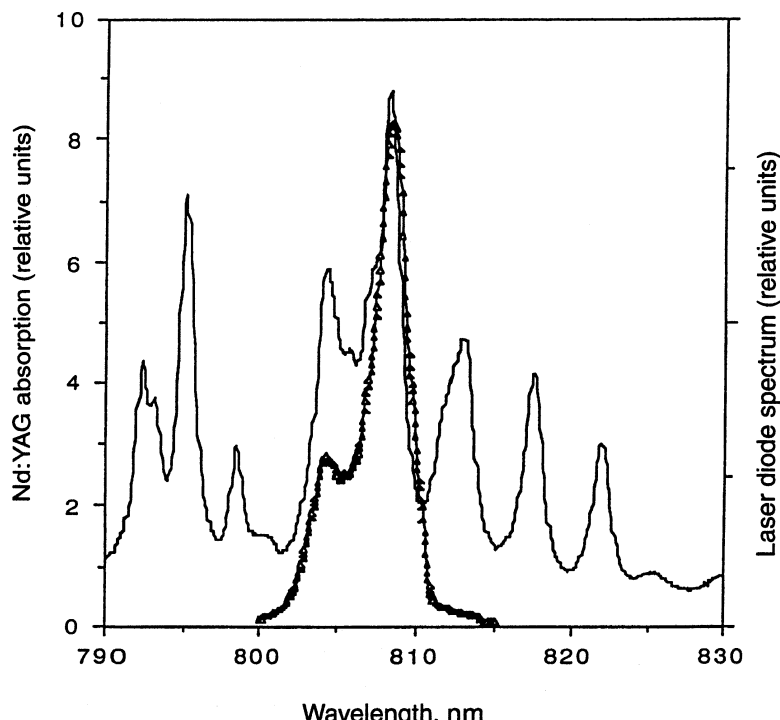


Fig. 6.40. Spectral overlap between Nd:YAG absorption and emission spectrum of a 10 bar array [6.56]

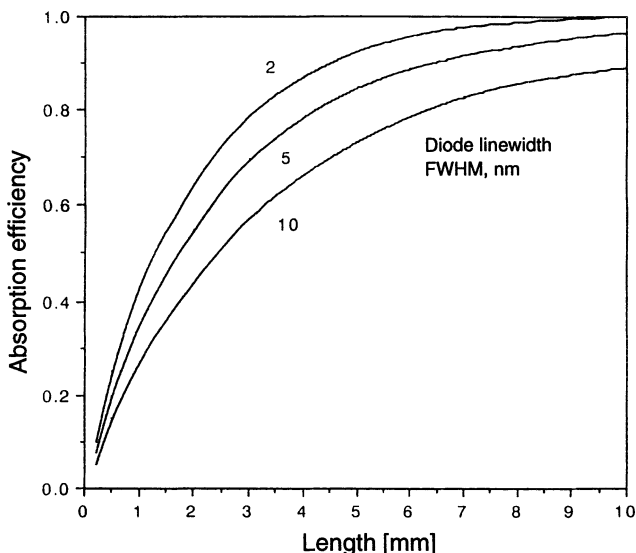


Fig. 6.41. Absorption efficiency of Nd:YAG as a function of absorption length for a pump wavelength of 808 nm [6.57]

important because eventually all the pump radiation gets absorbed. In Fig. 6.41 the absorption of diode-pumped radiation for Nd:YAG is plotted versus optical thickness with spectral width as a parameter.

In a GaAlAs structure the peak emission changes $0.3 \text{ nm}/^\circ\text{C}$. Therefore, the material composition has to be chosen such that the desired wavelength is achieved at the operating temperature of the junction. Figure 6.42a displays the spectral output from a diode array as the repetition rate is increased from 10 to 100 Hz. The output shifts slightly from 807 to 810 nm as a result of the increased junction temperature at the higher repetition rate. In Fig. 6.42b, the wavelength shift of a diode array is plotted versus change in drive current.

The average temperature changes as a result of varying operating conditions of cw or high repetition rate diode pump sources can often be mitigated by temperature controlling the heat sink. In pulsed diode bars, the temperature rise during the pulse causes a change of the center wavelength, known as chirp, and a reduction of efficiency and output power, known as sag. This effect becomes particularly noticeable if a laser crystal with a narrow absorption width is pumped with a relatively long pump pulse. The transient temperature rise is determined by the heat sink properties. A model that describes thermal effects in high peak power laser diode bars can be found in [6.58].

The most common pumps for the wavelength region of 790–860 nm are the GaAlAs-based laser diodes because of their availability and high state of development. Lasers that can be pumped with GaAlAs diodes include neodymium-doped solid-state laser materials and Tm:YAG as listed in Table 6.3.

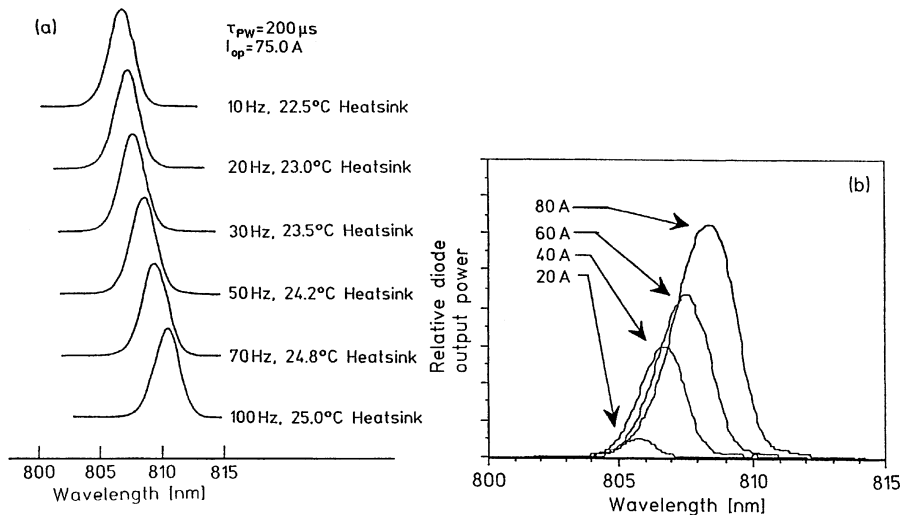


Fig. 6.42. (a) Diode array linewidth vs. repetition rate and (b) wavelength shift vs. drive current

In GaAlAs diodes, aluminum has been identified as being the main source of device degradation over time [6.59, 60]. In the late 1990s, an aluminum-free material composition for 808-nm laser diodes based on indium-gallium-arsenide-phosphate (InGaAsP) quantum wells has been introduced [6.61]. Aluminum-free InGaAsP laser diodes are optically more robust than the 808 nm GaAlAs devices.

For pumping Yb:YAG or ytterbium-sensitized lasers, such as Er:Yb:glass, pump sources for the wavelength region of 940–980 nm are needed. For this wavelength region, so-called strained-layer super lattice lasers based upon InGaAs active layers on GaAs substrates [6.62–64] have been developed.

Traditional diode lasers are restricted to materials that can be lattice-matched to GaAs or InP substrates because unmatched materials are prone to defects and quickly degrade. However, it was discovered that very thin layers—below a critical

Table 6.3. Important lasers and diode pump sources

Laser material	Pump wavelength [nm]	Semiconductor laser material
Nd:YAG	808	GaAlAs, InGaAsP
Nd:YLF	798, 792	GaAlAs
Nd:YVO ₄	809	GaAlAs, InGaAsP
Tm:YAG	805 (wing) 785 (peak)	GaAlAs GaAlAs
Yb:YAG	941	InGaAs
Er:glass	980	InGaAs
Cr:LiSAF	670 (peak) 760 (wing)	AlGaInP GaAlAs

thickness of a few tens of nanometers—can accommodate the strain of a small lattice mismatch. This discovery led to the development of a single, thin strained layer used as a quantum well, which has an emission wavelength not achievable with GaAlAs or InGaAsP laser diodes.

On the short-wavelength end of available diode pump sources are the visible AlGaInP diode lasers operating in the 640–680-nm region. These devices have been used to pump chromium-doped lasers, such as Cr:LiCaAlF₆ (LiCAF) and Cr:LiSrAlF₆ (LiSAF).

Input versus Output Characteristics

The optical losses in the diode structure determine the threshold current i_s that has to be exceeded before amplification can take place. A diode laser that is operating above threshold will exhibit a linear relationship between output power and electrical current as shown in Fig. 6.43. The optical output power as a function of current input can be expressed by

$$P_{\text{out}} = \eta_d (\Delta E/e)(i - i_s), \quad (6.44)$$

where η_d is the differential quantum efficiency characterized by the number of photons emitted per injected electrons, ΔE is the bandgap of the recombination region, and e is the electron charge.

The slope efficiency σ_s , determined from the slope of the output power versus input current, follows from (6.44)

$$\sigma_s = \eta_d (\Delta E/e). \quad (6.45)$$

Figure 6.43 depicts the output power versus current for a 10 W cw bar. The device has a slope efficiency of $\sigma_s = 1 \text{ W/A}$ and with $\Delta E = 1.5 \text{ eV}$ there follows from (6.45) a differential quantum efficiency of $\eta_d = 0.66$. The applied forward voltage for diode

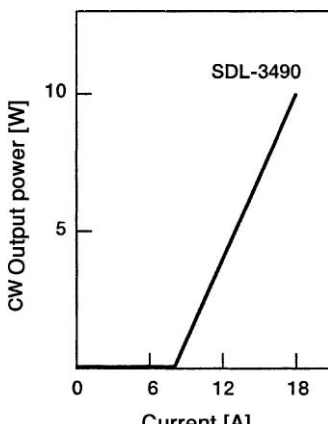


Fig. 6.43. The cw output power versus input current for a 1-cm bar

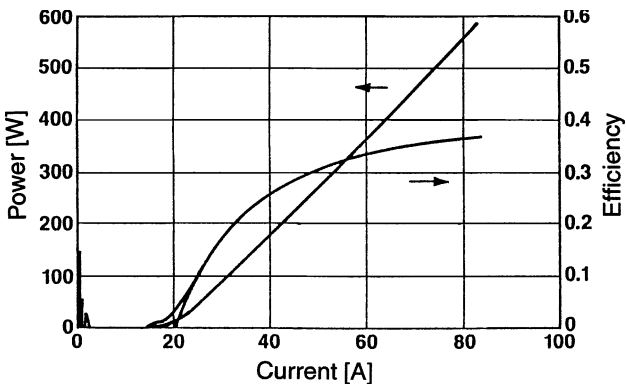


Fig. 6.44. Performance of a quasi-cw 10 bar array (Spectra Diode Laboratories)

lasers is

$$V_0 = (\Delta E/e) + i R_d, \quad (6.46)$$

where R_d is the series resistance of the diode due to the resistivity of the epilayers and the resistivity of the metal contacts. For typical devices the voltage drop across the junction is 1.5 V and one obtains $V_0 = 1.5V + i R_d$.

The energy conversion efficiency of the diode laser, defined as the ratio of optical output power to electrical input power, which we call the pump efficiency η_p , follows from the above equations

$$\eta_p = \frac{\sigma_s(i - i_s)}{i[(\Delta E/e) + i R_d]}. \quad (6.47)$$

The device characterized in Fig. 6.43 has an overall efficiency of $\eta_p = 0.32$ at the maximum output based on a series resistance of $R_d = 0.015 \Omega$ and $\Delta E/e = 1.5$ V.

If bars are stacked into two-dimensional arrays, the bars are connected electrically in series to avoid high currents and the associated resistive losses. This is illustrated in Fig. 6.44. The drive current for this 10 bar stack is identical to the current of a single bar. The nonlinear behavior of the overall efficiency with increasing current occurs because the ohmic losses in the material increase as the square of the current (see (6.47)), whereas the output power is linear in the current.

Thermal Management

Diode-array pumping offers dramatic improvements in efficiency of solid-state laser systems. However, the need to maintain the operating temperature within a relatively narrow range requires a more elaborate thermal management system as compared to flashlamp pumped lasers. The small area combined with the high output power of a semiconductor laser can lead to heat fluxes as high as 1 kW/cm^2 at the junction. Because the junction must stay below 50°C for efficient operation, low thermal impedance packaging is a key consideration.

Thermal resistance, temperature drops, and coolant flow rates will be dependent on the exact cooling geometry selected. For example, in a back plane cooled diode array, heat is conducted away from the individual bars by a submount which is typically made from copper or beryllia. This conduction path is characterized by a finite thermal resistance. The resistance depends on the thickness of the mount and therefore on the spacing of the bars in the array. A rough calculation of the resistance is obtained from

$$R_{\text{th}} = \frac{\Delta T}{Q} = \frac{l}{kA}, \quad (6.48)$$

where R_{th} is the thermal resistance [$^{\circ}\text{C}/\text{W}$], l and A are the length and area of the one cm-wide laser bar submount, and k is the submount conductivity ($\approx 3 \text{ W/cm } ^{\circ}\text{C}$). For a 1.7-mm-long by 0.4-mm-thick copper submount, the thermal resistance is $1.4 \text{ } ^{\circ}\text{C}/\text{W}$.

The most efficient thermal management strategy revolves around microchannel cooling technology, in which the heat producing pn junctions are mounted on internally liquid cooled heat sinks. Different liquid cooled heat sinks have been designed with the aim to improve heat transfer between the cooling fluid and metal surfaces, or to reduce the complexity of the device.

In a typical device, each bar is bonded to an individual 1.8–2-mm-thick heat sink containing many microchannels with cross-sectional area of 10^{-4} – 10^{-5} cm^2 . Heat transfer can be further improved by incorporation of small microfins within the flow channels.

In the impingement cooler design, heat is removed from the pn junction by a turbulent water flow through tiny holes that strike a thin impingement plate beneath the diode bar. The impingement plate has a roughened inner surface to enhance heat transfer.

In another design, the large parts count of individual coolers is circumvented by allowing several bars to be mounted simultaneously to a micro channel cooled monolithic substrate. The micro channels are produced in this case in silicon wafers [6.65].

Compared to the conductively cooled heat sink spacers mounted to a single common back plane, the thermal resistance for the internally liquid cooled heat sinks is much reduced. Typical values are $0.3 \text{ } ^{\circ}\text{C}/\text{W}$.

In end-pumped systems, the diode wavelength is usually temperature tuned to the peak absorption line of the laser and maintained at that wavelength by controlling the array temperature with a thermoelectric cooler. This approach works well for small lasers, and systems including thermoelectric coolers can work over a large range of ambient temperatures.

In large systems, the power consumption of thermoelectric coolers is usually prohibitive. For these systems, a liquid cooling loop with a refrigeration stage can be employed, which maintains the temperature of the coolant independent of the environment. However, the coefficient of performance for refrigerators is typically no greater than one. Therefore, the electrical input power requirement for the refrigeration unit is equal to the heat load to be controlled.

In the controlled environment of an industrial or laboratory space, refrigeration is usually not necessary, and a liquid-to-air, or in case an external cooling water supply is available, a water-to-water, heat exchanger is often sufficient. In such a cooling system

there will be a variation of the cooling fluid temperature depending on the ambient condition. At ambient temperatures much below the operating temperature of the laser diodes, the flow is thermostatically controlled. At higher ambient temperatures, and maximum coolant flow, the diode temperature will vary according to the ambient changes. Provided that diode-array wavelength, spectral width, and optical thickness of the solid-state laser material are properly chosen, a fairly large tolerance for temperature fluctuations can be achieved. Actually, temperature-insensitive performance closely matching the athermal behavior of lamp-pumped systems can be obtained.

Primarily for military applications where large temperature excursions are encountered, diode arrays have been developed that can operate at high junction temperatures. Thus the need for refrigerated cooling loops is eliminated.

Diode arrays can be operated now at junction temperatures as high as 75°C, which is higher than ambient in most situations. A simple liquid-to-air cooling system provides the most efficient thermal control system for the laser because the power consumption of only a pump and possibly a fan is added to the total electrical requirements. There is a slight reduction of the diode operating efficiency (about 0.2%/C) at elevated temperatures. However, this reduction in diode efficiency is small compared to the power penalty one would have to pay for a refrigeration cooler.

Diode-pumped systems have been designed with constant output power and beam quality over a -30° to $+50^\circ\text{C}$ temperature range without employing a refrigeration stage. This is only possible in very large diode-pumped systems with absorption lengths of the pump light on the order of 10–20 mm. Because the laser material is optically thick, the tolerances for the emission wavelength and spectral width is much relaxed. In this case, it is actually advantageous to increase the spectral width of the diode in order to provide a more uniform pump distribution throughout the active material. The benefit of a large pathlength in the laser material is revealed dramatically in Fig. 6.45. The data plotted shows that for a diode bandwidth of 15 nm

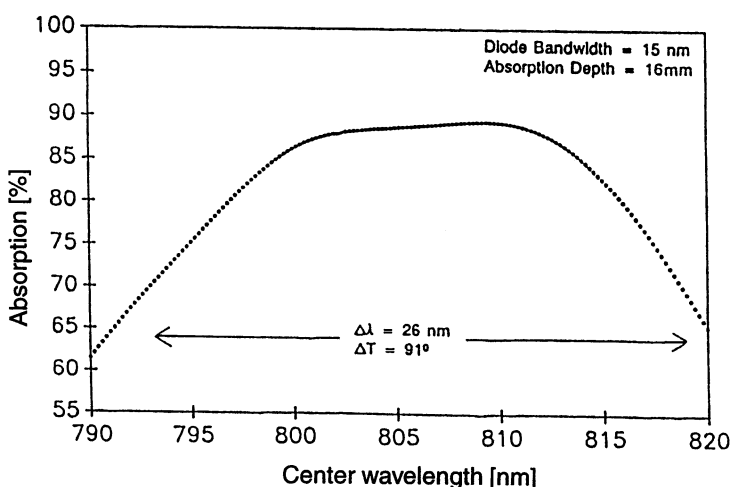


Fig. 6.45. Calculated total absorption in Nd:YAG for a 15-nm pump width and a 16-mm optical path

Table 6.4. Power dissipation from a diode array pumped solid-state laser

System output	160 W
Diode array	1300 W
Laser crystal	160 W
Electronics/other components	380 W
Total electrical input	2000 W

and an absorption depth of 16 mm (8 mm double pass), the absorbed energy (and to a first approximation the laser output energy) can be held to within $\pm 10\%$ even though the center wavelength of the diode output varies by 26 nm. This 26 nm change in central frequency corresponds to a change in diode temperature of 86°C .

The power dissipation of the various subsystems of a pulsed diode-pumped laser is listed in Table 6.4. The system has a repetition rate of 200 Hz and an output pulse energy of 0.8 J/pulse. By far the greatest heat dissipation occurs in the diode pump arrays, and accounts for approximately 65% of the system input power. The solid-state laser medium itself dissipates heat at a rate approximately equal to the output power from the laser system. The electronics dissipate on the order of 19% of the input power.

The use of liquid cooling is at present the simplest and most cost-effective method for heat removal from diode-pumped laser systems. However, expected material improvements can significantly reduce the heat dissipation and temperature-control requirements of the diodes. These improvements include increases in the efficiency of the diode arrays and the development of new solid-state laser materials in which the sensitivity to pump wavelength and linewidth is reduced. With continuing improvements, the need for liquid cooling can be eliminated in many applications altogether. For burst mode operation, the possibility exists for the implementation of cooling by latent heat of fusion of low-melting-temperature substances such as paraffin. For space-based operation, radiative cooling can be implemented in many systems using heat pipes for thermal transfer from the dissipative elements to low-temperature radiators.

Diode-Laser Lifetime

We will distinguish between catastrophic failures and normal degradation during operation. Laser diodes, like all semiconductors, are very susceptible to damage by electrostatic discharges or high-voltage transients. Therefore handling of these components requires electric discharge control such as wearing wrist straps and grounded work surfaces. Also great care has to go into power supply and driver design to protect this very expensive pump source from transients, current surges, and high voltage. Operation at excessive currents will lead to catastrophic mirror facet damage. Also, insufficient cooling combined with high currents can melt the solder joints or vaporize the wire bonds within the diode structure.

Under proper operating conditions laser diodes degrade in a fairly predictable manner which results in a decrease in output over time. The higher the operating

current and/or the operating temperature, the faster the degradation. The decrease in output over time can be caused by structural defects, which spread through the laser diode forming light absorbing clusters. Dark lines or spots in the output beam are a manifestation of this damage. The degradation of AlGaAs laser diodes, the most common pump source, is usually attributed to oxidation and migration of aluminum under high-power operation. Structural defects can also be caused by thermal stress due to different thermal expansion coefficients of semiconductor and heat sink material.

Facet damage due to the environment or high-radiation flux is another source of degradation, so is diffusion of solder into the semiconductor lattice over time caused by the high-current density. After screening of the laser diodes during a burn-in period performed by the manufacturer has eliminated early failures due to production problems, very long operational lifetimes can be achieved.

Useful service lifetime of 40 and 50 W cw bars is typically specified at 10–20,000 h or 2 years of operation. At that point, output has usually decreased by 20%. This is the wear-out phase of the diodes caused by a general degradation of the facet coatings and semiconductor material. In most cases, the diode bars are operated at the same output power level, and the degradation is compensated for by increasing the nominal diode current.

Operation below the maximum specified output power greatly extends lifetime. In most commercial laser systems requiring long life of the pump source, diode arrays are operated typically at 75% of their rated power levels. The lifetime of the diode pump is also a question of economics. A larger pump source containing more diodes will not only increase the cost of the system, but also increase the lifetime of the device. Lifetime impacts the cost effectiveness of an application in two ways: First, failure of the pump source results in the direct replacement cost. In production line applications, there may also be a significant expense due to an unscheduled down-time required for replacement and system realignment.

Degradation of 100 W quasi-cw laser diode bars was evaluated by NASA as part of a complete laser system life test. The bars were operated at 500 Hz at a pump pulse of 200 μ s. The output for most bars decayed about 20% between 5 and 7 billion shots [6.66].

Our own experience shows that, depending on the operating conditions, lifetime in quasi-cw diode stacks can range from 150 million to 15 billion shots. For example, one of our Nd:YAG systems contains four internally liquid cooled arrays, each composed of 8-bar stacks. The arrays operated at 20% duty cycle are pulsed at a repetition rate of 2 kHz with a pulse width of 100 μ s. The peak power from each 1-cm bar is limited to 45 W, and the system is operated for long periods of time without being turned off. Typically, the system is run in 8-h shifts. The diode pump source, as well as the rest of the system, operated maintenance free for about 2000 h. During this time the diodes accumulated a total of 15 billion shots. After 10 billion shots, the laser power dropped below the level required for the application and the user increased diode current until units failed catastrophically at 15 billion shots.

The other extreme, in terms of operating condition, is encountered in our systems installed in helicopters. The 1-cm bars are operated at 60 W and the system is subjected to many turn-on and turn-off cycles during each mission. Each system contains

96 five-stack bars operated at a pulse width of 200 μs and a repetition rate of 40 Hz. The low-duty cycle arrays are mounted on water-cooled heat sinks at 40°C. The arrays typically show a 20% drop in output after 1000 h of operation which represents about 150 million shots. This might not seem impressive in an industrial application, but 1000 h of maintenance-free operation is totally acceptable in a helicopter. In six systems built to date, no catastrophic pump source failures occurred, and the diodes are replaced every 18–24 months during regular maintenance.

Newer devices, for example, a 8-bar array with peak power at 480 W, operated at a high heat sink temperature of 65°C and many turn-on and turn-off cycles, achieve lifetimes over 2×10^8 pulses.

Operation of Laser-Diode Arrays

In comparison to arc lamps, the electrical operating conditions of laser diodes are much more benign. The operating voltages are low and a trigger circuit is not required.

CW Diode Arrays. Essentially, only a low-voltage dc power supply of the appropriate voltage and current range is required to operate the cw devices. Despite the very straightforward electronics, there are several challenges for operating laser diodes efficiently and reliably. The series resistance of laser diodes is very low; therefore, the internal resistance of the power supply must be minimized for efficient energy transfer.

Secondly, compared to flashlamps, laser diodes are electrically much more vulnerable. Therefore, overvoltage, reverse bias, and current protection are essential features in the design of power sources.

The diode array must be protected from several electrical fault modes both during operation and during installation, repair, and in the “off” mode. The most serious electrical “threat” to diode arrays is the possibility of electrostatic buildup across the diode-array junction. Static charge can build up to a level sufficient to cause electrical breakdown across the diode junction, inducing permanent damage. Thus, the diode array must be shorted or connected across a low resistance at all times. When in use, a 100- Ω resistor is sufficient to prevent static buildup without affecting electrical efficiency of the diodes.

Diodes are high-power devices that are not easily damaged by high currents. Diode drivers must be designed to deliver only slightly more than the design operating current for the arrays. The possibility of a high current being applied to the diode arrays is avoided by limiting the output current of the diode driver power supply. This can be accomplished with a current-limiting power supply.

Arrays have to be protected against reverse voltage bias using a diode across the input to the arrays. This device also protects against reverse voltage transients and static buildup. Excess transient forward bias must be eliminated by careful design of the array driver.

Pulsed-Diode Arrays. The power supply a diode-pumped solid-state laser is the subsystem where most of the weight and volume savings occur compared to a

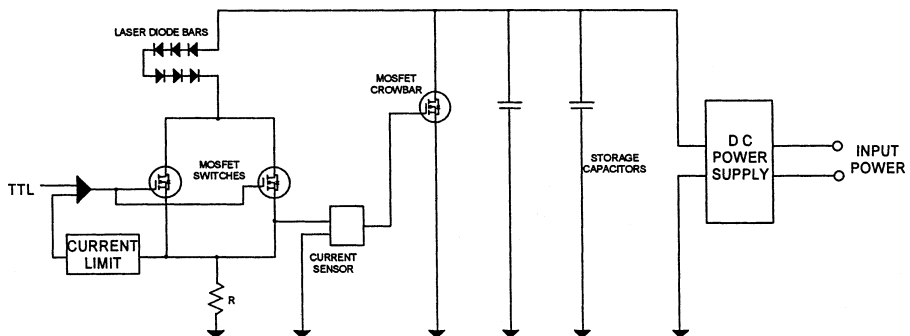


Fig. 6.46. Schematic diagram of a typical laser-diode-array driver

flashlamp-based laser. High efficiency of a diode-pumped laser, low-voltage operation of the diodes, and the use of electrolytic capacitors for energy storage allow the design of very small and compact power supplies. In a pulsed diode-pumped solid-state laser system, the diode array drivers replace the pulse forming network in a conventional flashlamp-pumped laser system. The diode-array driver is a low-voltage switching network which supplies a constant-current pulse to the diode arrays. The low-voltage requirements for the diode arrays allow the use of power MOSFET's as switching elements. Electrical energy stored in electrolytic capacitors is transferred to the diode arrays on each laser pulse. Figure 6.46 depicts a schematic diagram of a typical diode-array driver. The inherent simplicity of the device is responsible for the high reliability and efficiency.

A power conditioning unit converts line power or battery power to the appropriate dc voltage which is typically on the order of 20–200 V, depending on how many diode bars are connected in series. In order to avoid current surges from the DC power supply during the nominally 200 μ s-long pump pulse, energy is stored in electrolytic capacitors. Connected parallel to the capacitors is a string of laser-diode bars, one or several MOSFETs, and a small series resistor for current sensing. The function of the MOSFET is to generate the desired current waveform by switching the diode current on and off, and by providing current control by means of a current sensing feedback loop. The MOSFET's are switched on and off by input pulses from a timing circuit.

In addition, a diode-array driver includes fault protection to protect the diode arrays against damage caused by catastrophic failure of an array or the driver itself. Fault protection is based on a fast crowbar circuit that senses excess current, duty cycle, or temperature. The crowbar circuit can shunt the output of the driver within one pulse in order to remove the power from the diode arrays. This circuitry protects the diodes from several rare but potentially catastrophic system faults. The first mode of failure is for the MOSFET not to switch off. When this happens, all of the energy stored in the capacitor is dumped into the diode arrays. This condition usually results in diode failure, since the stored energy is many times that delivered in a single pulse. Without the crowbar circuit, the heat dissipated when this failure occurs is enough to

melt the solder used to attach the bars to the heat sink. A second fault mode arises from accidentally applying an excessively long trigger pulse to the diode drivers. This can occur during setup and test. Under this condition, the diode driver senses the product of the pulse length and repetition rate. If it exceeds the preset duty-cycle, the driver is shut down, again protecting the diode arrays. The value of fault protection cannot be overemphasized.

Besides protecting the diode arrays electrically from damage due to excessive voltage and currents, another key feature of a well-designed diode driver is a high transfer efficiency of the stored energy to the laser diode arrays. This is not a trivial task due to the very low impedance of laser diode arrays. A high efficiency can be obtained by operating individual diode bars in series, reducing circuit losses to an absolute minimum, and by selecting a large energy storage capacitor.

The impact of the unavoidable circuit losses on efficiency is minimized by connecting as many diode arrays in series as possible. The fraction of diode impedance to the total resistance of the capacitor discharge circuit has to be as close as possible to one. The maximum number of diodes which can be connected in series is set by the limits of the standoff voltage of the diode arrays. Diode drivers have been reliably operated up to 80 bars in series without breakdown.

In addition, MOSFETs and capacitors have to be selected for low internal resistance, and current leads and wires have to be kept as short as possible. Constant current to the laser diodes is maintained by regulating the internal impedance of the MOSFET. A large voltage droop during the discharge cycle is undesirable, because the excessive voltage must be dropped across the power MOSFET, which results in a low driver efficiency at the beginning of the pulse. A small voltage droop requires a large capacitance, which stores many times the energy extracted during one pulse. The size of the capacitor is a trade-off between efficiency and physical size constraints of the power supply.

To illustrate some of the criteria in designing diode drivers, we will use, as an example, a diode-pumped Nd:YAG laser which produces 200 mJ in a Q-switched pulse. The laser is pumped by 16 diode arrays, each containing five 1-cm bars. All arrays and bars are electrically connected in series to increase impedance from $0.026\ \Omega$ for each bar to $R_D = 2.09\ \Omega$. Each bar has a 60-W optical output and requires a 70-A pulse. The voltage drop across each bar is 1.83 V. With the bars electrically connected in series, a voltage of 146.4 V is required across the diode arrays.

In series with the diode resistance R_D is the internal resistance, R_M of the MOSFET, and a resistor R_L representing circuit losses due to wires, leads, and the current sampling resistor. In Fig. 6.46, two MOSFETs are configured in parallel in order to achieve at least a 50% current derating from manufacturer specifications for improved reliability and lifetime, and also to decrease the internal resistance of this switch.

Typical series resistance of a MOSFET is $0.2\ \Omega$ with two in a parallel configuration, series resistance is reduced to a minimum of $R_M = 0.1\ \Omega$ for the fully forward-biased condition. The wires, connectors, and the series resistance of the energy storage capacitors accounted for a total series resistance of $0.04\ \Omega$. The current sensing resistor R represents an additional impedance of $0.01\ \Omega$. Therefore the discharge side of the energy storage capacitor contains an additional resistive loss of $R_L = 0.05\ \Omega$.

The combined impedance of the discharge circuit at the end of the pulse is $R = R_D + R_M + R_L = 2.24 \Omega$, which requires a voltage at the capacitor of $V_2 = 156.8 \text{ V}$. If we design for a 10% voltage drop during the pulse, then the voltage at the capacitor is $V_1 = 174.2 \text{ V}$ at the beginning of the discharge cycle, and the initial impedance of the MOSFET is $R_i = 0.35 \Omega$ in order to limit the desired drive current to $I_D = 70 \text{ A}$. Total impedance at the beginning of the discharge cycle is therefore $R_T = 2.49 \Omega$.

Based on the RC time constant of the circuit and the allowable voltage drop during the pulse, the capacitance of the energy storage capacitor follows from $C = -t_p/R_{AV} \ln(1 - \Delta V/V_1)$. With $t_p = 200 \mu\text{s}$, $R_{AV} = 2.36 \Omega$, $\Delta V/V_1 = 0.1$, one obtain $803 \mu\text{F}$. The energy delivered to the diodes is $E_D = R_D I_D^2 t_p = 2.05 \text{ J}$, and the energy extracted from the capacitor is $E_{EX} = C(V_1^2 - V_2^2)/2 = 2.31 \text{ J}$. The efficiency of the diode driver is therefore $\eta = 0.88$.

Actually, this overall efficiency can be viewed as the average of the efficiency at the beginning and the end of the discharge cycle. In this particular case, efficiency starts at 84% and increase to 93% at the end of the current pulse. The energy transfer efficiency can also be expressed by

$$\eta = \frac{R_D}{R_D + R_M + R_L} \left(1 - \frac{\Delta V}{2V_1} \right) \quad (6.49)$$

The first term on the right is the limit of efficiency determined by circuit losses, whereas the second term is due to the dissipation of excess energy stored in the capacitor by the MOSFET in order to maintain a constant current. In our example, circuit losses limit efficiency to 93%, and voltage droop limits efficiency to 95%.

6.2 Pump Radiation Transfer Methods

The efficiency in the transfer of radiation from the source to the laser element determines, to a large extent, the overall efficiency of the laser system. The optical design, besides providing good coupling between the source and the absorbing active material, is also responsible for the pump power distribution in the laser element which influences the uniformity, divergence, and optical distortions of the output beam.

In the development of solid-state lasers, many different optical design have been employed to transfer the radiation from a light source to the active material. Laser device architectures differ mainly by the orientation of the pump radiation relative to the direction of propagation of the laser beam and relative to the geometric form of the gain medium. They also differ in the direction in which waste heat is removed, and in the resulting direction of the thermal gradients with respects to the pump and laser beam direction.

Depending on the shape of the active material and type of pump source used, one can broadly divide pumping geometries into systems in which the active material is side-, edge-, end-, or face-pumped. Figure 6.47 illustrates the major pump configurations of solid-state lasers. In a side-pumped laser, the pump radiation strikes the active medium perpendicular to the laser beam. The most common configuration for

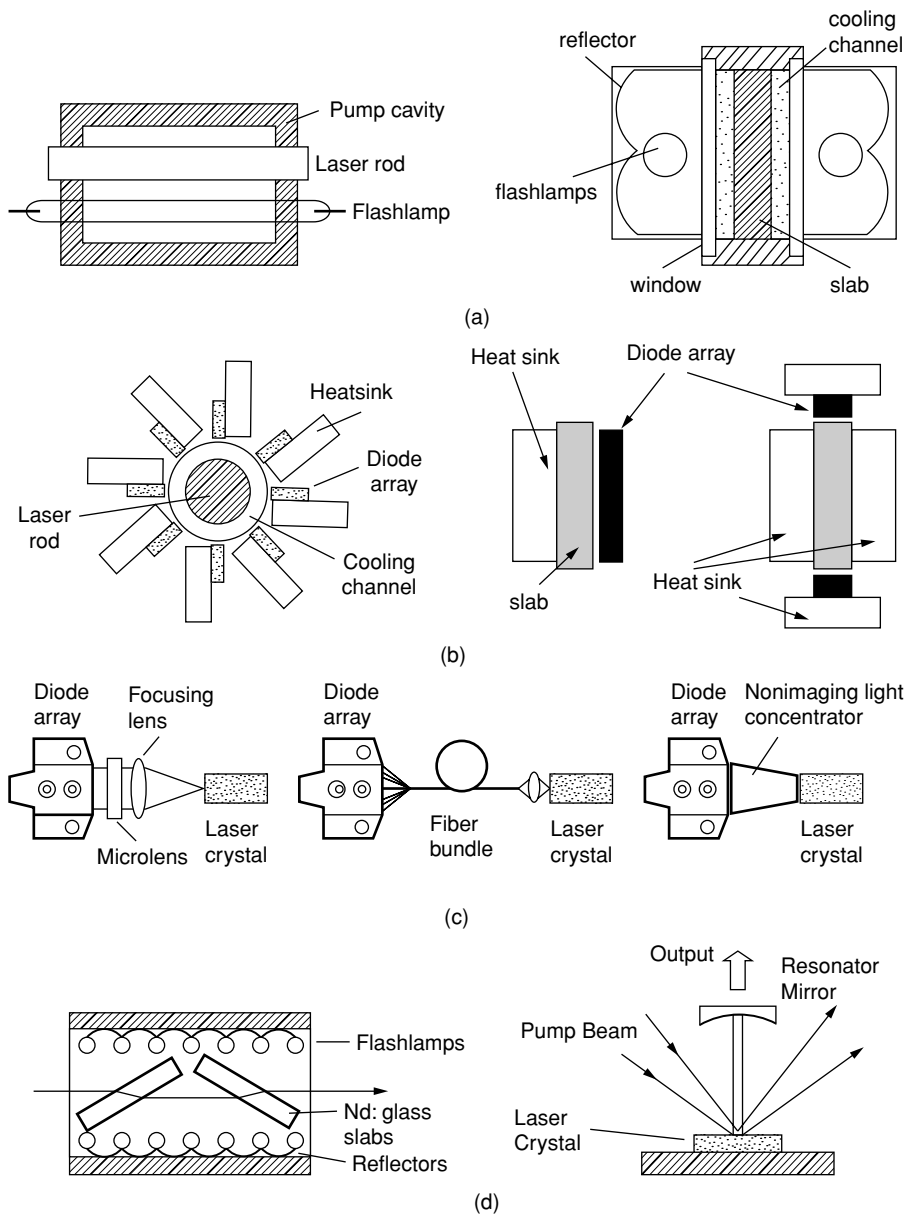


Fig. 6.47. Major pump configurations a) side pumping with flashlamps, b) side-and edge pumping with laser diodes, c) end pumped lasers, d) face pumping with flashlamps or laser diodes.

a flashlamp or arc lamp pumped laser is a cylindrical rod and lamp inside a highly reflective enclosure as shown in Fig. 6.47a.

If in a side-pumped laser, the pump sources are laser diodes; the laser rod is symmetrically surrounded by the diode pumps. In its most basic form, no other

optical components or reflectors are needed as indicated in Fig. 6.47b. Similar to laser rods, flashlamp pumped slabs as shown on the right side of Fig. 6.47a, also need a reflective housing to direct the radiation toward the active medium. In case of diode pumping, slab lasers can result in a very simple geometry as shown in the middle of Fig. 6.47b. A laser slab is sandwiched between a diode array and a heat sink. In another very common design, the slab is pumped and water-cooled from both sides. The edge pump design on the right side of Fig. 6.47b is particularly suitable for conductively cooled slabs. Heat is removed from the large surface areas and the slab is pumped through the edges. The optic axis of the laser beam is for all designs shown in Fig. 6.47b perpendicular to the plane of the paper. In contrast to flashlamps, the directed radiation emitted by a laser-diode array permits shaping and focusing of the pump beam to accommodate a large variety of pump schemes.

While in side-pumped configurations laser diodes are used very much as lamp replacements, end pumping designs fully exploit the directional radiation properties of laser diodes. In end-pumped lasers, pump radiation is introduced longitudinally into the active material, i.e., colinear with the resonator axis. The output from a small array, single bar, or stack of bars is transferred into the laser medium by an optical imaging system, a fiber optic bundle or a nonimaging concentrator as indicated in Fig. 6.47c.

Because end pumping requires only a small active medium it has enabled the wide spread use of Nd:YVO₄ which is difficult to grow in large crystals.

In a disk amplifier, very large Nd:glass slabs are set at Brewster's angle and the pump radiation is incident through the disk faces as shown on the left side of Fig. 6.47d. In a thin disk laser, depicted on the right side of Fig. 6.47d, the laser beam enters through the front face and is reflected at the backside. The diode pump beam also enters through the front face at a small angle. This design has been developed specifically for pumping Yb:YAG lasers.

6.2.1 Side-Pumping with Lamps

In a lamp-pumped laser system, the pump source and the laser rod are surrounded by highly reflective walls. We can distinguish between polished metal, i.e., highly specular reflectors, or diffuse reflectors made from ceramic materials.

The polished metal enclosures are usually shaped in form of long cylinders having an elliptical cross section with the laser rod and pump lamp at each focus. The elliptic configuration is based on the geometrical theorem that rays originating from one focus of an ellipse are reflected into the other focus. Therefore, an elliptical cylinder transfers energy from a linear source placed at one focal line to a linear absorber placed along the second focal line. The elliptical cylinder is closed by two plane-parallel and highly reflecting end plates. This makes the cylinder optically infinitely long.

If two pump sources are required, the cross section of the focusing pump chamber consists of two intersecting ellipses with the laser rod at the common focus. Cross sections of single and double elliptical pump cavities are shown in Fig. 6.48.

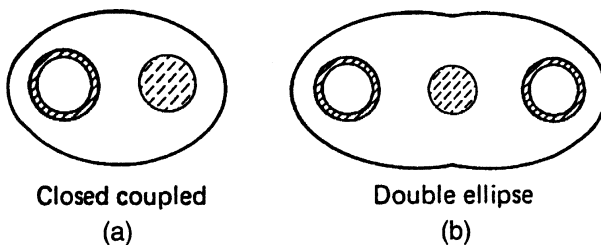


Fig. 6.48. (a) Single and (b) double elliptical pump cavity

Another very common pump cavity uses diffuse reflectors made from a white ceramic material or powder packed barium sulfate. Typical cross sections of diffuse reflecting pump cavities are illustrated in Fig. 6.49. The reflector can simply be a circular tube or oval shaped as shown.

Of course, the pump cavities illustrated in Fig. 6.49 can also be fabricated with polished metal reflectors. For a practical reason, and as we will see, also from a performance point of view, the laser rod and lamp are mounted in most system very closely together. In these very compact close coupled pump cavities the difference in performance between an elliptical and an oval shaped cross section, as illustrated by Figs. 6.48a and 6.49b, is often not very large.

Generally speaking, pump chambers based on focusing geometries, such as an elliptical cylinder, are more efficient compared to diffuse reflecting cavities, but require more maintenance because the metal surfaces will tarnish over time and need to be repolished. Ceramic reflectors are more durable, they do not tarnish, and are not subject to corrosion.

Both designs illustrated in Figs. 6.48 and 6.49 can be implemented in so-called wet or dry pump cavities. In the wet cavity design, which is the most common, the pump cavity is flooded with cooling water for heat removal from the lamp, laser rod, and the reflectors. In a wet cavity, a specular or diffuse reflector becomes an insert which surrounds the lamp and laser rod, and the whole assembly is contained in a water-filled housing.

In a dry cavity, the laser rod and flashlamp are surrounded by flow tubes. Water is channeled in the annulus between the rod or lamp and the inside wall of the flow tube.

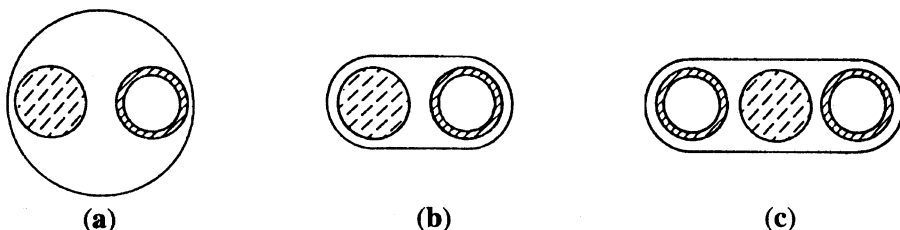


Fig. 6.49. Nonfocusing pump cavities; (a) circular cylinder, (b) single, and (c) double-lamp closed-coupled configuration

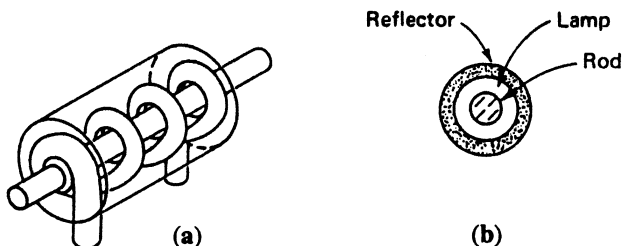


Fig. 6.50. Diffuse reflecting cavities. (a) Helical flash tube and (b) coaxial flash tube cylinder

Variations of diffuse reflecting pump cavities are shown in Fig. 6.50. These designs are mostly interesting for historical reasons. In Fig. 6.50a, a helical flashlamp surrounds a laser rod and both elements are enclosed by a ceramic reflector made from two half shells for easy installation. This was actually the design of the first ruby laser, and was also the most common design of these systems in the 1960s. Occasionally, rods have been pumped by hollow lamps which were surrounded by a diffuse reflecting surface [6.67–69] as shown in Fig. 6.50b.

Elliptical Pump Cavities

An elliptical cylinder can have a cross section with a large or small eccentricity. In the former case, the laser rod and lamp are separated by a fairly large distance, and in the second case they are close together. If the elliptical cylinder closely surrounds the lamp and rod, then one speaks of a close-coupled elliptical geometry (see Fig. 6.48a). This geometry usually results in the most efficient cavity and it has the further advantage that it minimizes the weight and size of the laser heads. Since the energy delivered to a discharge lamp is limited, schemes to focus the energy from several lamps onto a single crystal are attractive. Figure 6.48b shows two partial elliptical cylinders having one common axis at which the crystal is placed. Multilamp close-coupled cavities provide a higher degree of pumping uniformity in the laser rod than single-lamp designs.

The fraction of pump energy that is transferred from the source to the laser rod can be expressed by

$$\eta_t = \eta_{tg} \times \eta_{to}, \quad (6.50)$$

where η_{tg} is the geometrical cavity transfer coefficient. It is the calculated fraction of rays leaving the source which reach the laser material either directly or after reflection from the walls. The parameter η_{to} expresses the optical efficiency of the cavity and essentially includes all the losses in the system. This parameter can be expressed as

$$\eta_{to} = R_w(1 - R_r)(1 - \delta)[1 - (A_n/A_{tot})], \quad (6.51)$$

where R_w is the reflectivity of the cavity walls at the pump bands, R_r is the reflection at the laser-rod surface or at the glass envelopes of the cooling jackets and Fresnel losses of any filters inserted in the cavity, δ is the absorption loss in the optical

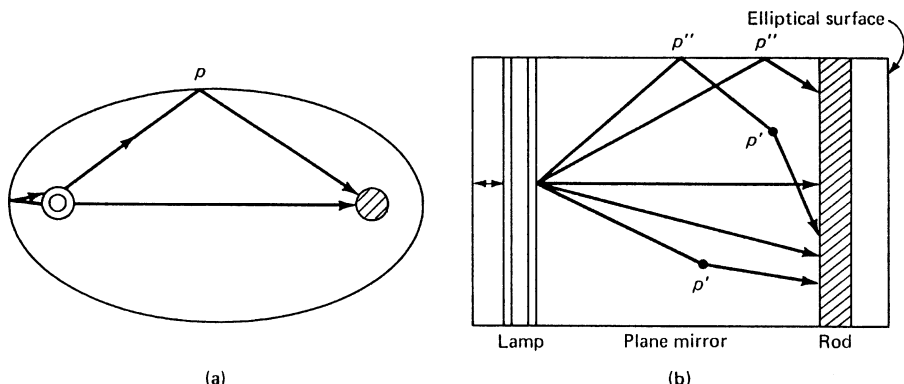


Fig. 6.51. Trajectories of photons emitted from the pump source. (a) Cross section and (b) top view of elliptical pump cavity

medium between the lamp and the laser rod such as coolant liquid, filters, etcetera, and (A_n/A_{tot}) is the ratio of the nonreflecting area of the cavity A_n to the total inside area A_{tot} . This factor accounts for losses due to openings in the reflector which are required, for example, to insert the laser rod and pump lamp. Equations (6.50) and (6.51) are rough approximations based on the assumption that all the lamp radiation undergoes just one reflection. If one were to include direct radiation and multiple reflections from the cavity walls, these equations would have to be developed in series expressions.

The pump source is usually assumed to be a cylindrical radiator having a Lambertian radiation pattern. This implies that it appears as a source having constant brightness across its diameter when viewed from any point. In Fig. 6.51 trajectories of photons that originate from a volume element dv of the source are shown. In Fig. 6.51a the rays leave normal to the surface of the source and therefore remain in a cross-sectional plane. Figure 6.51b depicts trajectories of photons that leave the source at an angle with respect to a cross-sectional plane of the ellipse. In this case the photons can be reflected off the end-plate reflectors as well as undergo a reflection at the elliptical cylinder. In an elliptical pump cavity, all rays emanating from one point of the source are transformed into parallel lines at the laser rod. Each line corresponds to rays leaving the source inclined at the same angle with respect to the major axis of the ellipse, but at different angles with respect to the cross-sectional plane.

Image formation, in its usual sense, is meaningless for the elliptical cylinder since rays emanating in different directions from a point at the source converge after reflection from the cavity at altogether different points. In a pump cavity, all that is actually desired is the transfer of radiant energy from the source to the laser rod. From the foregoing considerations, it is obvious that the condition of an infinitely long elliptical pump cavity can be satisfied by enclosing the ends of the cylinder with highly reflective plane mirrors. Therefore, in the analysis of this arrangement the two-dimensional case can be treated by considering the light distribution in a plane perpendicular to the longitudinal axes of the cylinder.

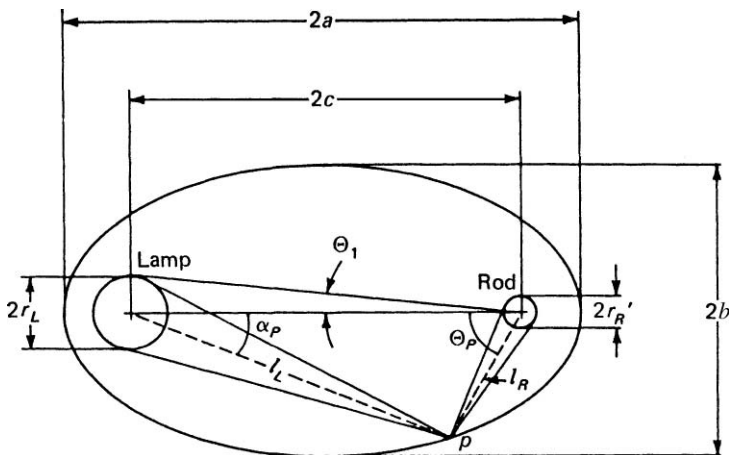


Fig. 6.52. Cross section of elliptical pump cavity. Eccentricity $e = c/a$; focal point separation $c = (a^2 - b^2)^{1/2}$

In the theoretical expressions obtained for the efficiency of elliptical configurations, the pump system is usually characterized by the ratio of the rod and lamp radii r_R/r_L , the ratio of the lamp radius to the semimajor axis of the ellipse r_L/a , and the eccentricity $e = c/a$, where $2c$ is the focal separation. Consider any point P on the surface of the cavity with a distance l_R from the crystal and distance l_L from the lamp as shown in Fig. 6.52. Suppose that the lamp has a radius r_L , then, as a consequence of the preservation of angles, upon reflection the image will have the radius $r'_L = r_L l_R / l_L$. This means that the portion of the elliptical reflector nearer the lamp forms a magnified image at the laser rod, while the portion near the crystal forms a reduced image of the lamp. A point P , with corresponding angles α_p and Θ_p measured from the lamp and rod axis, respectively, may be defined dividing these two regions. At this point, the ellipse generates an image of the lamp which exactly fills the crystal diameter. We must allow for this effect of magnification and demagnification when determining how much energy is captured by the crystal. From the properties of an ellipse, and noting that at P , $l_R/l_L = r_R/r_L$, we obtain

$$\cos \alpha_p = \frac{1}{e} \left[1 - \frac{1 - e^2}{2} \left(1 + \frac{r_R}{r_L} \right) \right] \quad (6.52)$$

and

$$\sin \Theta_p = \left(\frac{r_L}{r_R} \right) \sin \alpha_p. \quad (6.53)$$

The geometrical cavity transfer coefficient can be calculated by considering what fraction of the energy radiated by the lamp into an angle $\Delta\alpha$ is trapped by the crystal.

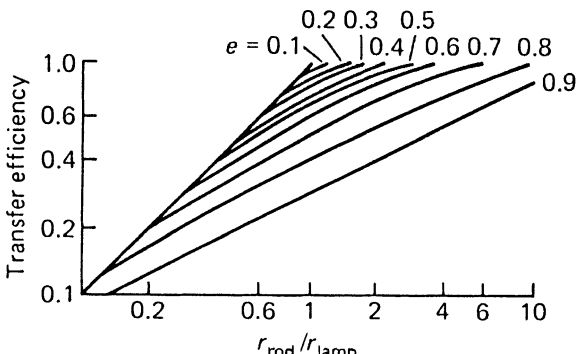


Fig. 6.53. Dependence of transfer efficiency of an elliptical reflector on the quantity $r_{\text{R}}/r_{\text{L}}$ and eccentricity e [6.72]

Integration over all angles leads to [6.70, 71]

$$\eta_{\text{tg}} = \frac{1}{\pi} \left[\alpha_p + \left(\frac{r_{\text{R}}}{r_{\text{L}}} \right) \Theta_p \right]. \quad (6.54)$$

This expression is plotted in Fig. 6.53. A certain portion of the reflecting surface behind the lamp is screened from the crystal by the lamp itself. In flashlamps, which resemble a blackbody source, the radiation reflected back into the lamp will be absorbed. On the other hand, the plasma in cw arc lamps is optically thin, and the reflected pump radiation is transmitted through the plasma. If we assume the radiation reflected back to the pump source to be lost, we must reduce the angle Θ_p in the above formula by Θ_1 , where

$$\sin \Theta_1 = \frac{r_{\text{L}}}{4ae} \quad (6.55)$$

and

$$\eta'_{\text{tg}} = \frac{1}{\pi} \left[\alpha_p + \left(\frac{r_{\text{R}}}{r_{\text{L}}} \right) (\Theta_p - \Theta_1) \right]. \quad (6.56)$$

It is seen from Fig. 6.53 that the efficiency increases with an increase in the ratio $r_{\text{R}}/r_{\text{L}}$ and with a decrease in the eccentricity e . This result stems from the fact that the magnification of the pump source increases with the eccentricity of the ellipse. A superior efficiency is therefore obtained for an almost circular cavity and as small a pump source as possible.

It should be noted that in these calculations the crystal is assumed to absorb the radiation which falls upon it; no second traverses of light through the crystal are considered. Furthermore, no allowance was made for the reflection loss at the cavity walls or losses due to Fresnel reflection at the surface of the laser rod. Multiple reflections can become significant if the absorption coefficient of the crystal is small compared to the inverse of the crystal diameter.

The analytical methods developed for the design of pumping configurations imply idealized systems in which reflection and refraction losses are usually ignored and only a single reflection from the walls is considered. In order to analyze pumping

systems with fewer idealizations, statistical sampling methods, such as the Monte Carlo method, have been employed. The Monte Carlo method consists essentially of tracing, in detail, the progress of large numbers of randomly selected rays over many events (i.e., absorptions, reflections, and refractions) throughout the pumping cavity. The average transfer efficiency of these rays can then be taken as representative of all possible rays in the cavity. Monte Carlo calculations for a variety of geometrical configurations were reported in [6.72–75]. For the single elliptical pump cavity, the adverse effect of a small value of the quantity r_R/r_L was confirmed. The analysis also showed the efficiency to be strongly dependent on the reflector reflectance. On the other hand, the calculated efficiency values appear to be less dependent on the eccentricity than indicated by the results of earlier work, in which multiple passes were ignored.

Multiple-elliptical laser pump cavities generally consist of a number of partial-elliptical cylinders having a common axis at which the crystal is placed. The results of calculations performed to obtain the efficiency of various multiple cavities with varying sources and crystal diameters show that, for equal diameters of the source and the crystal, the single-elliptical cavity has the highest efficiency. However, a cavity with two or more partial-elliptical cavities will allow higher input power, at some sacrifice in overall efficiency, if a high-power output laser is required. If the diameters of the source and crystal are different, these conclusions must be modified. It should also be pointed out that the multi-ellipse cavity results in more uniform pumping of the laser crystal.

Referring back to the case of a single-elliptical cylinder, (6.54) gives the efficiency for the case when the lamp does not block radiation. For multielliptical pump cavities one obtains the expression

$$\eta_{tg} = \frac{1}{\pi} \left[(\alpha_p - \alpha_2) + \left(\frac{r_R}{r_L} \right) \Theta_p \right]. \quad (6.57)$$

Here, α_p has been reduced by an angle α_2 which represents that portion of the reflecting wall that was cut away. Light falling in this region is assumed to be lost. For a double-elliptical pumping cavity,

$$\cos \alpha_2 = \frac{2e}{1 + e^2}. \quad (6.58)$$

Equation (6.57) is plotted in Fig. 6.54.

Figure 6.55 shows the reflection characteristics of a double-elliptical cavity.

Empirical Data. Theoretical considerations of the efficiency of pump cavities are of utility primarily in their qualitative aspects and in their illustration of the gross features of the energy transfer in the various reflector configurations. Even under very idealized assumptions, calculation of the amount of energy absorbed in the laser rod is very tedious since the spectral properties of the pumping source, the absorption spectrum of the laser material, and all possible path lengths of the elementary rays through the laser rod, determined by the specific reflector configuration, must be taken

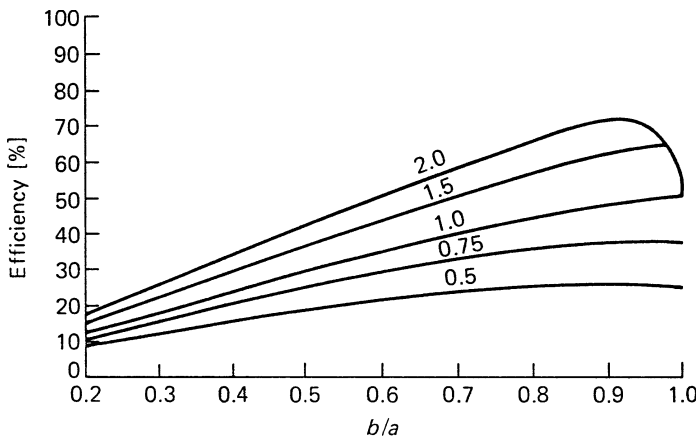


Fig. 6.54. Efficiency of a double-elliptical cavity. Parameters are for r_R/r_L [6.71]

into consideration. Not even the most thorough computations can take into account the effect of mechanical imperfections in the fabrication of the reflectors, optical obstructions caused by seams and gaps, aberrations by flow tubes, losses due to holes and apertures in the end plates, etc.

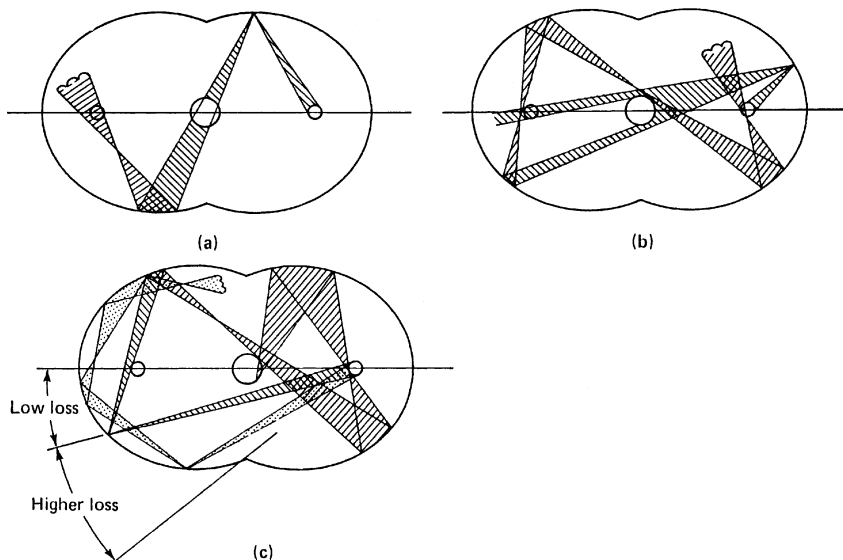


Fig. 6.55. Reflection characteristic of double-elliptical cavities. (a) Radiation focused on the rod but not absorbed is focused back upon the second lamp. (b) Radiation which misses the rod on the first pass is intercepted after a few reflections by one of the lamps or the laser rod. (c) Direct radiation that passes close to the laser rod will eventually be intercepted by one of the pump lamps or the laser rod. Direct radiation which enter the second ellipse far away from the rod is essentially lost

Summarizing the experimental work carried out on pump-cavity design, we may draw the following conclusions:

- For maximum efficiency a closed coupled elliptical cylinder is optimum. In a small elliptical cavity the fraction of direct radiation is high, and most of the pump radiation is incident on the rod after a single reflection on the cavity walls. Therefore, in this geometry, a reflectivity of less than unity, imperfections in the geometry, and obstruction of the light path are less detrimental to the efficiency than is the case in a large elliptical cylinder. Another strong argument for making elliptical cavities as small as possible is the increased probability of the lost radiation being redirected to the laser rod if the ratio of cavity volume to laser rod volume is small.
- In agreement with theory, the highest efficiency in an elliptical cylinder is obtained for a large r_R/r_L ratio. However, lamp-life considerations demand that in most cases a ratio of one is chosen.
- A high reflectivity is extremely important, whereas mechanical tolerances of the elliptical shape are not very critical in small ellipses. This is not surprising because in a close-coupled ellipse the cross sections of lamp and rod are fairly large with respect to the dimensions of the ellipse, which reduces the requirement for accurate imaging.
- The length of elliptical-cylinder cavities should be as large as possible in relation to the diameter, but the laser rod, pump lamp, and cavity should all be the same length.
- Multiple cylindrical ellipse cavities may be utilized to increase the number of pump lamps and to produce symmetrical pumping. If the cavity size is kept small, this can be achieved with a minimum sacrifice in efficiency.

Diffuse Reflecting Pump Cavities

The transfer efficiency of laser pumping cavities that have diffusely reflecting walls can be estimated if we assume that the light inside the cavity is isotropic. Since all surfaces will be equally illuminated, the light absorption at each surface will be the product of the area and the fractional absorption. Since all radiation must eventually be absorbed somewhere, the proportion of light absorbed at a surface area S_1 having a fractional absorption A_1 will be [6.74]

$$\eta = \frac{S_1 A_1}{\sum_{i=1}^n S_i A_i}, \quad (6.59)$$

where the summation covers the entire internal surface of the cavity. If S_1 is the exposed surface area of the laser crystal and A_1 is the effective absorption over this surface, the transfer efficiency of the laser configuration is given by

$$\eta = \frac{S_1 A_1}{S_1 A_1 + S_2 A_2 + S_3 A_3 + S_4}, \quad (6.60)$$

where S_2 and A_2 are the diffusely reflective wall area and absorption coefficient of the cavity, S_3 is the surface area of the lamps, and A_3 is the absorption of pump radiation

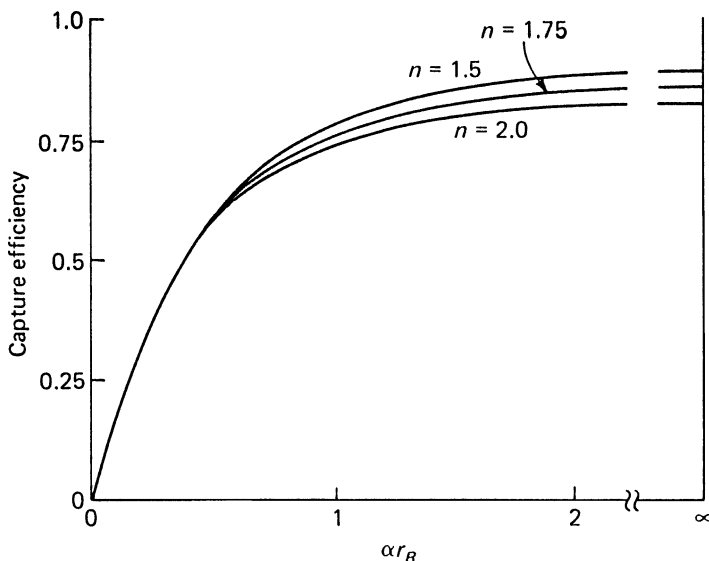


Fig. 6.56. Capture efficiency of a cylindrical laser rod exposed to isotropic light. The parameters n , r , and α are the refractive index, radius, and absorption coefficient of the rod [6.74]

by the lamp. S_4 is the area covered by holes in the cavity wall; these surfaces are treated with unit absorption, i.e., $A_4 = 1$.

An important parameter in the formula for transfer efficiency is A_1 , the fraction of photons which strike the laser-rod surface and are absorbed by the laser material. This parameter, which has been called the capture efficiency, depends on the absorption coefficient, the refractive index, and the radius of the laser rod.

Figure 6.56 shows the capture efficiency A_1 of a cylindrical crystal exposed to isotropic light. Radiation incident on the rod which is not absorbed is either reflected off the surface or passes through the laser material. For large values of αr_R the capture efficiency is limited only by Fresnel reflection losses on the crystal surface. Using this grossly simplified analysis, no significant discrepancy between it and the Monte-Carlo calculation is usually found.

With the aid of (6.60) and Fig. 6.56, we will calculate the transfer efficiency of the diffusely reflecting cavities shown in Figs. 6.64 and 6.50a. Both cavities are 10 cm long and contain a 1-cm-diameter ruby crystal. In the first case, the crystal is pumped by a linear flashlamp and, in the second case, by a helical flashlamp. For ruby with an index of refraction of 1.76 and an average absorption coefficient in the pump bands of 1.0 cm^{-1} , we obtain a capture efficiency of $A_1 = 0.60$ from Fig. 6.56; the surface area is $S_1 = 31.4 \text{ cm}^2$. For both lamps we assume that 10% of the pump radiation is reflected back to the lamp and is reabsorbed by the plasma; that is, $A_3 = 0.1$. The linear lamp is of the same size as the laser rod ($S_3 = 31.4 \text{ cm}^2$). The helical lamp is approximated by an annular region of isotropically radiating material with an inner diameter of 1.8 cm. The reflectivity of the diffusely reflecting walls is assumed to be 95%. The cavity diameter is 4 cm, from which we obtain $S_2 = 150 \text{ cm}^2$, if we

include the end walls. The area covered by holes and apertures is about $S_4 = 0.1S_2$. Introducing these parameters into (6.60), we obtain $\eta = 0.42$ and $\eta' = 0.40$ for the linear and helical lamp-pumped ruby system.

Pump-Light Distribution in the Laser Rod

The pump-light distribution over the cross section of the active material is the result of a combination of three effects: the properties of the pump cavity, refractive focusing occurring in the rod itself, and nonuniform absorption of pump radiation. How dominant these individual effects are depends on the pumping geometry, i.e., focusing or diffuse reflecting, on the treatment of the cylindrical surface of the rod, i.e., rough or polished, and on the optical thickness, i.e., the product of absorption coefficient and radius.

We can superficially distinguish between strongly focused, uniform, and peripheral pump light distributions. A nonuniform distribution of pump energy in the active medium leads to a nonuniform temperature and gain coefficient distribution. Saturation effects, threshold energy, and possible laser rod damage depend on the gain distribution across the rod. The distribution of pump light in a cylindrical laser rod will be considered for two cases of practical interest: a strongly focusing elliptical cylinder and a diffuse reflecting cavity.

Considering first the case of a laser rod in a diffuse reflecting cavity, we find that if a laser rod with a polished surface is exposed to isotropic pump radiation, appreciable focusing results from the refraction of the pump light at the cylindrical surface. Rays which strike the rod periphery tangentially will pass the center of the rod at a radius [6.76]

$$r_i = \frac{r_R}{n}. \quad (6.61)$$

Furthermore, all radiation incident on the surface passes through a core bound by the diameter $2r_i$. The pump light intensity in this region is higher than in the boundary region $r_R \geq r \geq r_i$. The focusing action from the refraction of pump light at the surface of a polished rod is modified by absorption [6.72, 77]. The pump intensity as a function of path length x in the rod is given by

$$\frac{I(v)}{I_0(v)} = \exp[-\alpha(v)x]. \quad (6.62)$$

Pump radiation propagating to the center of the rod is attenuated by absorption at the periphery. The compensating effects of refractive focusing and pump light absorption can be seen in Fig. 6.57a. Plotted is the relative energy density within a Nd:glass rod situated in an isotropic field as a function of normalized radius for a number of absorption values [6.72]. It is seen that for an optically thin rod, refractive focusing is predominant and the pump density is highest in the central region ($r \ll 0.63r_R$) of the rod. On the other hand, in rods which are optically dense, the pump intensity is highest at the periphery.

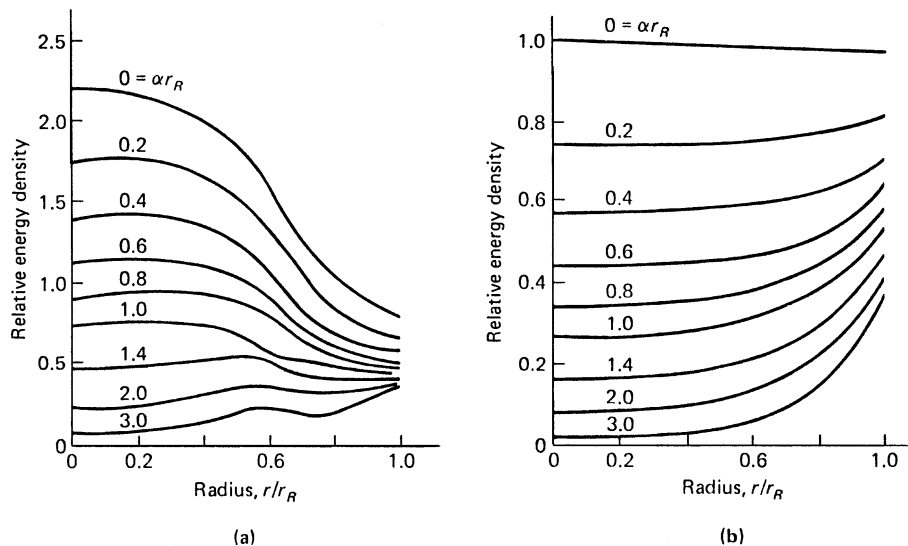


Fig. 6.57. Relative energy density within a Nd:glass rod situated in an isotropic field as a function of normalized radius for different absorption values. (a) With polished and (b) with frosted lateral surface [6.72]

Several solutions exist to improve the pumping uniformity of laser rods located in diffuse cavities. The internal focusing effect can be reduced by roughening the surface of the rod, immersing the rod in a liquid (ideally an index-matching fluid), and cladding the rod. In the latter case the active core is surrounded by a transparent layer, such as sapphire for ruby rods and glass for Nd:glass rods. This makes the collecting cross section larger than the absorbing cross section.

Figure 6.57b shows the pump-light distribution in a rod with a frosted lateral surface. No focusing effect is observed and the rod exhibits a peripheral pump light distribution which is strictly determined by absorption. At low absorption values αr_R a fairly uniform pump light distribution is obtained in the laser material. Generally, the most uniform pump distribution is obtained in a laser rod which has a roughened side wall, is optically thin, and is pumped by a helical flashlamp.

If the laser rod is in a focusing pump cavity, the light source is imaged on the laser rod. When the region of maximum energy density in free space is smaller than the cross section of the laser rod, a highly illuminated core results, whose diameter is no longer given by the outside diameter of the rod but by the image-forming properties of the pump system and the index of refraction of the active material.

Figure 6.58 shows the reflection of different light cones emerging from a circular light source of an elliptical reflector. Reflection at point P_a gives the beam of greatest diameter, perpendicular to the major axis. Reflection at P_e gives the beam of least diameter parallel to the major axis. The three cones which are reflected at points P_a and P_e define the region through which the total flux of the light source passes. This oval region has a long axis (ϱ_a) parallel to the minor axis of the ellipse and a short

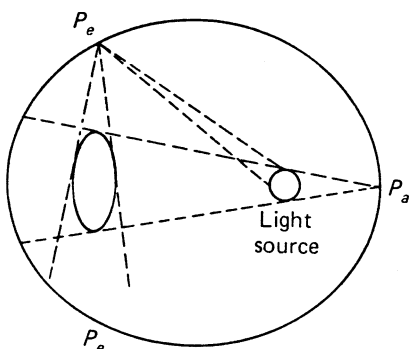


Fig. 6.58. Reflections of different light cones emerging from a circular light source located inside an elliptical reflector

axis (ϱ_b) parallel to the major axis of the ellipse. We have [6.78]

$$\varrho_a = r_1 \frac{a/e + 1}{a/e - 1} \quad \text{and} \quad \varrho_b = r_1 \frac{(a/e)^2 - 1}{(a/e)^2 + 1}, \quad (6.63)$$

where r_1 is the radius of the light source. Note that ϱ_a and ϱ_b are the boundaries in free space, inside a laser rod these dimensions are reduced by the ratio $1/n$.

From these considerations it follows that, while the emission of the light source is axially symmetrical, the energy density distribution at the site of the laser is no longer axially symmetrical in an elliptical cavity. There is a preferred axis perpendicular to the long axis of the ellipse. The region of maximum energy density is of interest for laser operation, since it is here that the material first reaches the threshold inversion. The focusing action is strongest in a laser rod with a polished surface located in an elliptical pumping cavity.

Figure 6.59 exhibits the result of a Monte Carlo calculation carried out to determine the pump radiation distribution in a ruby rod pumped by a xenon flashlamp in a single-elliptical cavity. Indicated in Fig. 6.59 are the areas of the ruby crystal which reach threshold as a function of time. The pump nonuniformity in the crystal is again a combination of the focusing action of the ellipse and direct radiation from the pump source.

In order for strong focusing to occur, it is necessary that the rod be fairly transparent to the pump radiation. Standard-doped ruby, Nd:glass, and Nd:YAG rods of up to 1 cm diameter are sufficiently transparent for strong focusing effects. With three-level systems, where a substantial change in the ground-state population will occur during pumping, a rod that is initially opaque may become transparent in the course of the pump pulse. The pump radiation can “bleach” the rod, so to speak, or “burn” its way in. The bleaching of ruby rods can be very substantial when the rods are used as storage devices (amplifiers, Q-switched lasers). Here, no regeneration is present during the pump phase of the laser cycle and the ground state can be almost completely depleted.

One of the consequences of focusing is that the threshold for oscillation is lowered in the focal region. Concentration of pump light at the center of the rod can be desirable

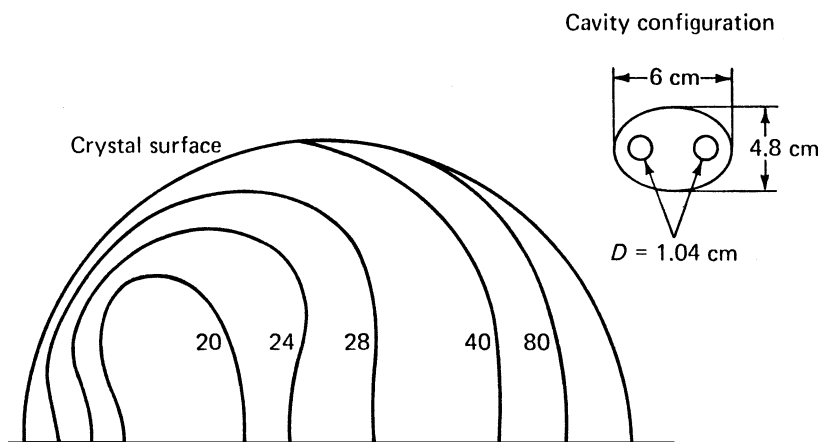


Fig. 6.59. Area of ruby crystal that has reached the threshold condition for lasing as a function of time (arbitrary units) in a single elliptical pump cavity

in systems which operate at the TEM_{00} mode, since operation in this mode requires maximum gain in the center.

If the lateral surface of the rod is frosted, then the pump radiation entering the rod remains diffuse; in this case radiation from the entire surface arrives at each point within the rod. Frosting of the lateral surface of the rod provides for a considerably more uniform gain distribution, and a larger cross section of the rod is utilized. However, an asymmetric gain distribution remains, since the rod is pumped from one side. To eliminate this asymmetry, a dual flashtube and close-coupled geometry can be utilized. This configuration provides for a relatively uniform gain distribution. If the laser rod is surrounded by a flow tube for water cooling, the glass tube can also be ground to achieve a homogeneous pump light distribution in the laser rod [6.79].

Mechanical Design and Materials

Figure 6.47a depicts a drawing of a generic pump head comprising a laser rod and a flashlamp or arc lamp surrounded by either a specular or diffuse reflector. The whole assembly is contained in a water-cooled enclosure which also contains provisions for mounting and sealing the optical components and for electrical connection to the pump source. The laser designer has a number of choices in designing such a pump head:

- elliptical pump cavity or diffuse reflectors
- single or double lamp system
- wet or dry pump cavity
- metal or polymer pump cavity enclosure

Table 6.5. Energy transfer in a cw krypton arc lamp, pumped Nd:YAG laser

Heat dissipation of lamps	55%
Heat dissipation of pump reflectors	30%
Power absorbed by coolant and flow tubes	7%
Heat dissipation by rod	5%
Laser output	2%
Fluorescence output	0.4%
Optical losses	0.6%
Power absorbed by laser rod	8%
Electrical input to lamps	100%

In addition, human engineering aspects have to be considered, such as ease of lamp replacement.

The mechanical design of a pump cavity is determined mainly by two considerations: (1) the geometry chosen for efficient energy transfer from the pump source to the laser material and (2) the provisions required for extracting the heat generated by the pump source. Optically pumped lasers have efficiencies of a few percent: therefore, almost all the electrical energy supplied to the lamp will have to be removed as heat from the pump cavity.

Table 6.5 summarizes the energy balance in a gold-plated double-elliptical pump cavity which contained an Nd:YAG rod pumped by two cw krypton arc lamps [6.80]. In a pump cavity the electrical input power supplied to the lamp is dissipated as heat by the lamp envelope and electrodes or emitted as radiation, and a portion of the radiation will be absorbed by the metal surfaces of the pump cavity. The radiation reflected from the walls will either be absorbed by the lasing medium or will return to the lamp. The light that is absorbed by the lamp will add energy to the radiation process in the same way as the electrical power does, and the returned light will be radiated with the same efficiency as the power supplied electrically. One consequence of the reabsorption is that a lamp, when enclosed in the pumping cavity, is operated under a higher thermal loading, resulting in shorter lamplife than when operated in the open for the same electrical input power. The heat dissipated by the laser rod assembly listed in Table 6.5 contains not only heat rejected by the laser crystal, but also energy absorbed by the flow tube and cooling water. The pump power absorbed by the laser rod causes stimulated emission and fluorescence at the laser wavelength and other main emission bands. The remainder is dissipated as heat by the laser material.

Reflector Design. Elliptical pump cavities are made from a base material, such as copper or aluminum, which is polished to a mirror surface and gold or silver plated. Silver plating gives optimum broadband reflectance, but requires an overcoat process which delays oxidation and extends cavity life.

Close coupled pump cavities can also be fabricated from glass or quartz with dichroic thin-film coatings on the inner or outer surfaces. These coatings are designed

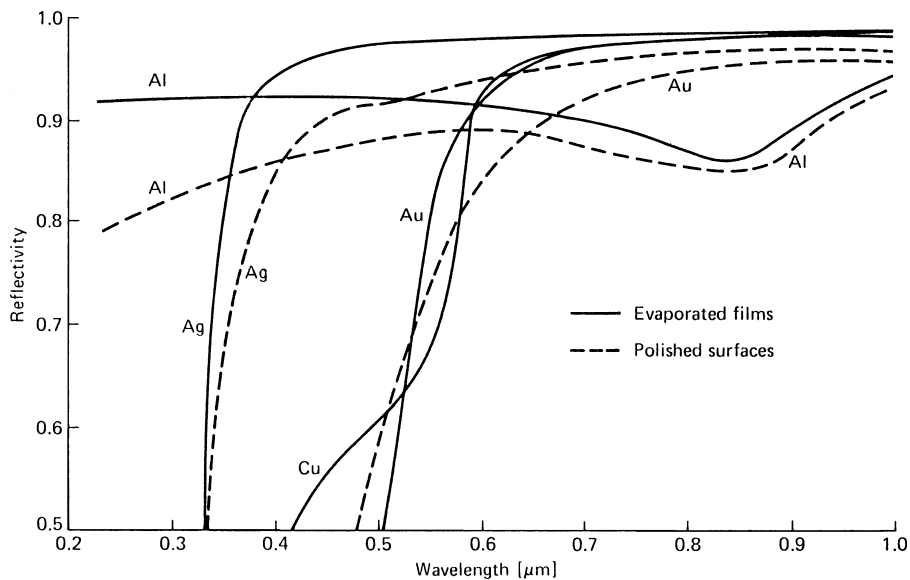


Fig. 6.60. Reflectivity versus wavelength for metals commonly used in the design of laser pump cavities

to reflect useful pump radiation and transmit radiation that is outside the absorption bands of the laser medium. The transmitted radiation is absorbed by the metal walls of the housing of the pump cavity.

The polished metal surfaces will tarnish after some use as a result of chemical reactions with the environment in combination with the high pump flux. As part of a maintenance procedure the mirror surfaces are stripped, precision-polished, and replated. The metals most commonly employed to obtain specular-reflecting surfaces in laser cavities are aluminum, silver, and gold. The reflectance versus wavelength of these materials is shown in Fig. 6.60. The cavity walls must have a high reflectivity at the absorption bands of the laser material. Compared to silver, aluminum has a higher reflectivity for wavelengths shorter than about $0.35\text{ }\mu\text{m}$, whereas for all longer wavelengths the reflectivity of silver is higher. Maintaining the high reflectivity of silver presents a real problem. During the aging of silver in air, a layer of silver sulfide forms on the surface, causing the reflectance to drop. This tarnishing may be prevented by coating the silver with a thin protective layer of a transparent material, such as SiO_2 . Alternatively, if the silver reflectors are immersed in an inert cooling fluid or operated in a dry nitrogen atmosphere, they will maintain their high reflectance for long periods of time.

As can be seen from Fig. 6.60, aluminum has a minimum in its reflectance curve in the near-infrared. Therefore, both silver and gold have higher reflectances in the main pump bands of neodymium lasers. For cw-pumped Nd:YAG lasers, where most of the pumping occurs in the wavelength region between 0.7 and $0.9\text{ }\mu\text{m}$, gold is used exclusively because, in contrast to silver, it does not tarnish. In high-power

pumped-pulsed neodymium lasers, a considerable amount of the flashlamp radiation is in the Nd pump bands located around 0.53 and 0.58 μm . In these systems silver-coated reflectors are usually employed.

In focusing geometries the base material for the reflector is either aluminum or copper. Aluminum is usually employed for light-weight systems. Aluminum reflectors in Nd:YAG lasers require silver plating for pulsed-pumped systems and gold plating for cw-pumped systems. Usually, aluminum is plated with nickel first. Nickel provides a hard surface which polishes very easily. After polishing, a flash of either silver or gold is applied. If weight considerations are not too stringent, a better choice for the reflector base material is copper, since copper has a lower thermal expansion, higher thermal conductivity compared to aluminum, and nickel plating on copper is much more durable than on aluminum. Kanigen-plated copper can easily be polished to very good tolerances. Both aluminum and copper must be nickel-plated before polishing if a good surface is to be obtained. A thin layer of gold or silver is electroplated or evaporated onto the surface after the polishing process.

Diffuse reflectors are usually fabricated from a white ceramic material, cast aluminum oxide (Al_2O_3) or powder packed barium sulfate. Diffuse reflectors made of ceramic materials are chemically inert and are not subject to corrosion as are metal coatings. However, unless the ceramic material has a high degree of purity it can turn yellow, thus diminishing reflectivity. Even minute amounts of iron oxide will cause the ceramics to turn yellow under the high pump fluxes.

The radiation reflected by a ceramic reflector corresponds closely to a Lambertian distribution following a cosine function with the radiation distributed evenly in all directions.

Cooling Issues. We distinguish between dry and wet cavity designs. In the former, the laser rod and lamp are liquid-cooled by circulating the coolant in flow tubes that surround these elements. The inside of the pumping chamber itself is dry. However, in most cases the body of the reflector contains cooling chambers through which the coolant fluid passes.

In the so-called flooded cavity approach, the whole inside of the pump cavity with either metal or diffuse reflectors is immersed in cooling fluid. The absence of flow tubes and separate cooling chambers for the reflector makes this type of cavity very compact and simple in design. For example, only one inlet and outlet are required for the cooling loop, whereas in an elliptical cavity with flow tubes, one pair of coolant ports with the associated fittings, tubing, and so on, is required for each reflector half, lamp, and laser rod. Also, in the flooded cavity design, lamp and laser rod can be brought very close together, and no reflection losses from additional glass surfaces are encountered.

Most liquid-cooled military-type Nd:YAG lasers and most commercial cw-pumped Nd:YAG lasers feature this design because of its compactness and simplicity. Figure 6.61 shows a photograph of a liquid-immersed pump cavity used for a high-repetition-rate military Nd:YAG laser. The cavity is sealed by one large O-ring in the top cover. The reflector inserts are machined from aluminum which is nickel-plated,

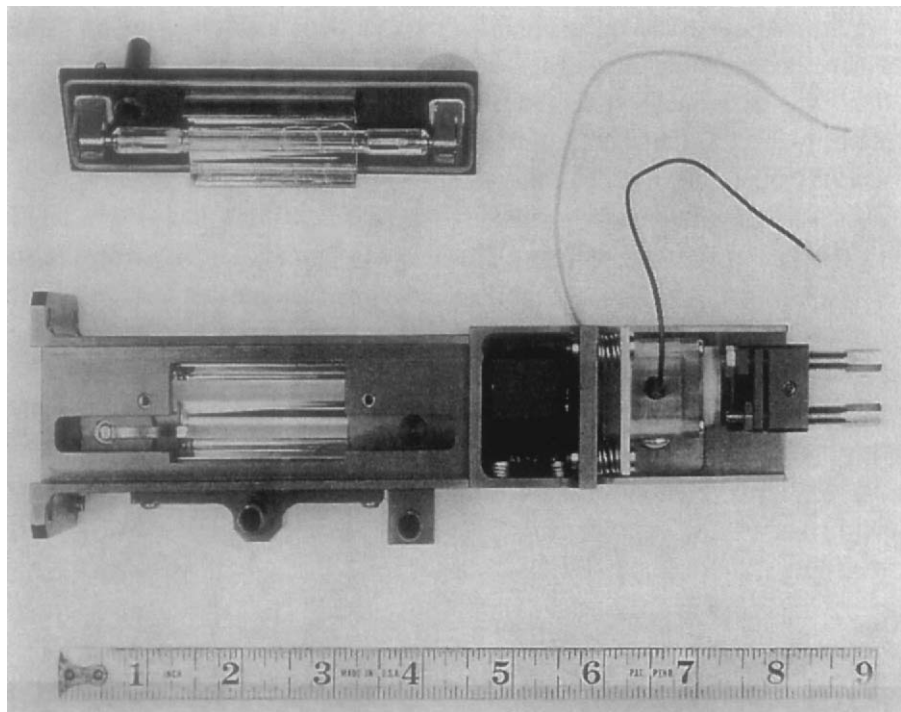


Fig. 6.61. Laser head of a military Nd:YAG laser

polished, and silver-plated. The housing is machined from aluminum that is hard-anodized to prevent corrosion.

Figure 6.62 illustrates an exploded view of a double-elliptical pump cylinder using immersion cooling. The laser head is machined from a solid block of acrylic. This material alleviates the problem of arcing and eliminates the need to electrically insulate the electrodes from the laser head. The reflector inserts are machined from copper and are gold-plated.

Great care has to be taken in the design of liquid-immersed cavities to achieve symmetrical high-velocity flow along the lamp and laser rod. Otherwise, the different cross sections and pockets in the cavity result in low velocity and, in extreme cases, stagnant areas in the cooling loop. Note that in the design depicted in Fig. 6.63 the lamps and laser rod are surrounded by flow tubes to provide symmetrical and highly turbulent flow. Diffuse-reflecting pump cavities are usually liquid-immersed.

Figure 6.64 presents a laser head employed to pump laser rods up to 15 cm in length by a single linear flashlamp. Lamp and rod are contained in a diffuse reflector consisting of barium sulfate which is compressed between two quartz tubes. Inside, the pumping chamber is filled with water. The body of the laser head is made from acrylic.

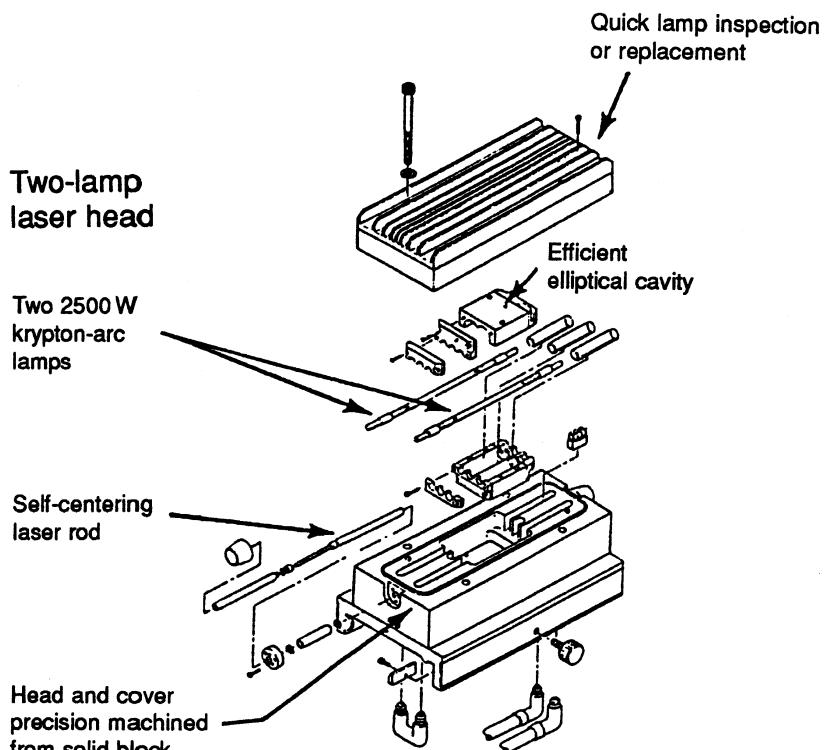


Fig. 6.62. Exploded view of a single- and double-elliptical pump cavity of a cw-pumped Nd:YAG laser

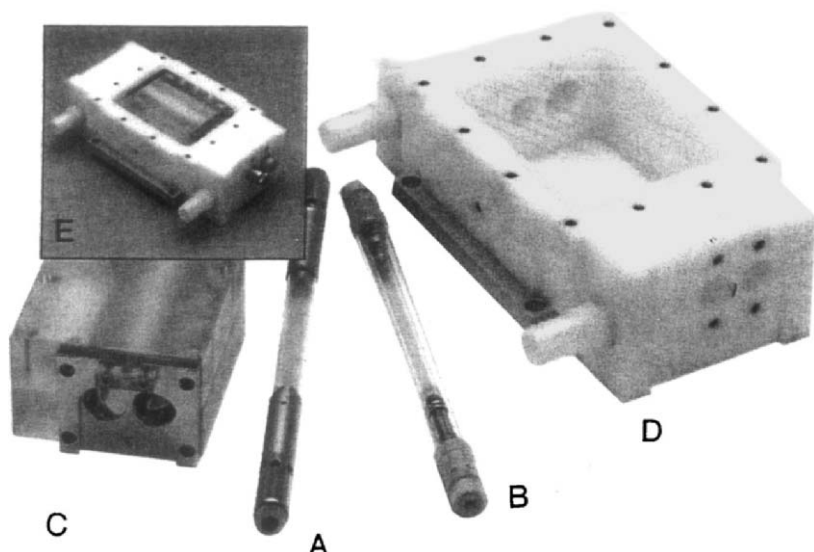


Fig. 6.63. Commercial cw-pumped Nd:YAG laser featuring a flooded pump cavity design. The photo shows the laser rod assembly (A), krypton arc lamp assembly (B), single elliptical reflector (C), and pump housing (D). The insert (E) shows the assembled pump head with top removed (Quantronix Corp. Model 114)

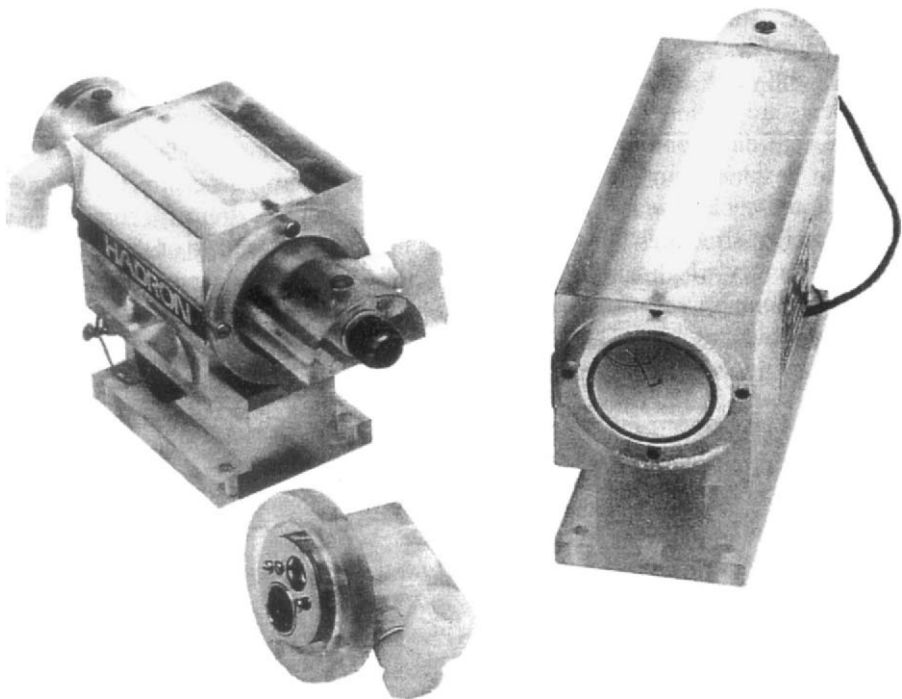


Fig. 6.64. Example of a diffuse-reflecting pump cavity

A dry pump cavity usually consists of two parts that separate along the plane of the major axis. The end-plate reflectors, in addition to serving their optical function, can be used to mount and register the elliptical sections and to provide precision mounts for the laser rod assembly, as shown in Fig. 6.65. The rod assembly, consisting of the laser rod mounted in rod holders (Fig. 6.66a) can slide into precision-bored holes in these end plates. O-rings around the rod holder will seal this unit from the cavity.

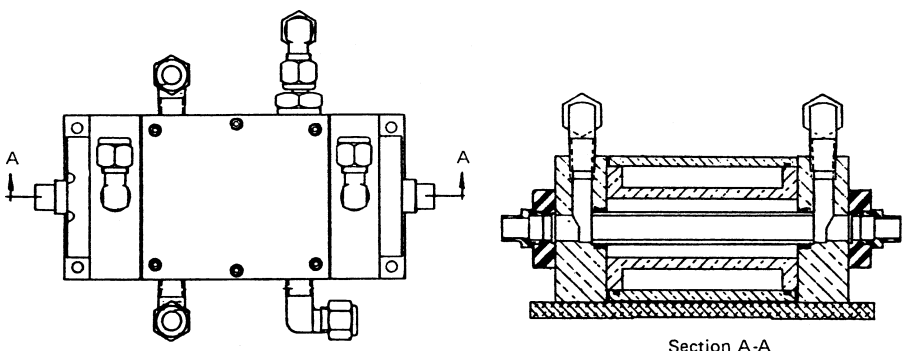


Fig. 6.65. Outside configuration of a double-elliptical pump cavity

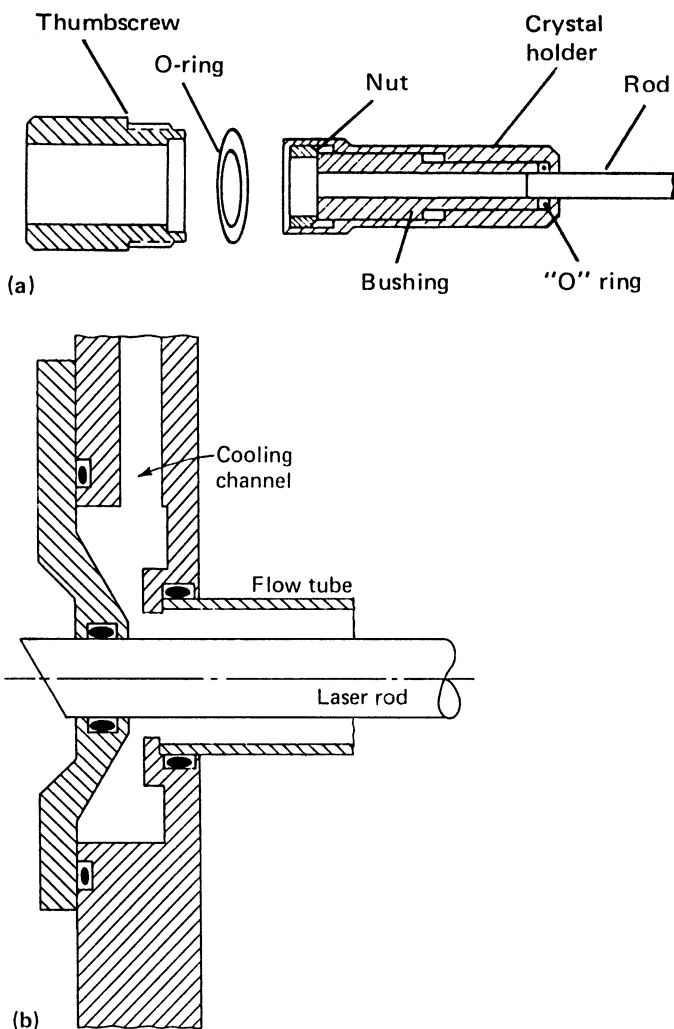


Fig. 6.66. Laser rod mounting techniques (a) with and (b) without separate rod holder

Figure 6.66b shows an example of a large Brewster-angle ruby rod installed in the end plate of an elliptical cavity without the use of rod holders. The drawing also shows the cooling channel and plenum chamber employed to force the cooling water into the annular cooling path defined by the ruby rod and the flow tube.

An O-ring seal, if properly designed, is very reliable and does not present a problem. Seal areas within the pump cavity are considerably more critical because organic materials exposed to the pump radiation will quickly deteriorate. If O-rings made from an organic material are used to seal the laser rod, flow tubes, or lamps, they should be well shielded from radiation. Figure 6.66 displays several examples of

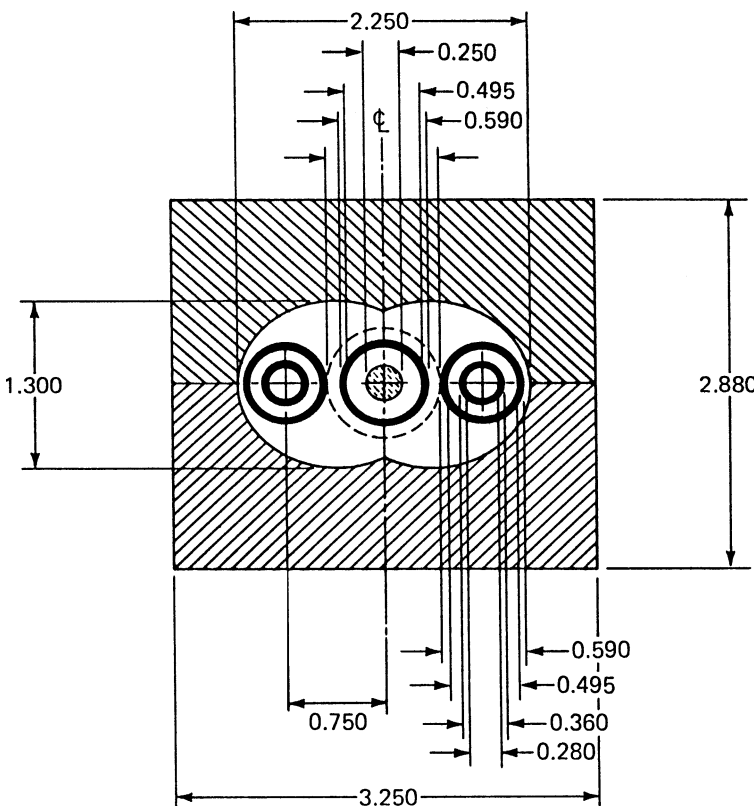


Fig. 6.67. Cross section of a double-elliptical pump cavity. Dimensions are in inches

O-ring locations which provide maximum protection from pump light. White silicon O-rings are usually found to be best suited for laser applications.

Figure 6.67 Shows the cross section of a dry pump cavity with flow tubes for the laser rod and arc lamp. The enclosure is water-cooled also. A dry cavity design featuring flow tubes is usually employed only in elliptical pump cavities. It allows easy replacement of the flash lamp or arc lamp and it protects the reflective surfaces from corrosion or deposits from the cooling water. It also allows the addition of special dyes in the water to absorb unwanted radiation from the lamps.

Most industrial and commercial laser systems are operated indoors, above the freezing point of water. Military lasers and laser systems operated outdoors require ethylene glycol/water mixtures as cooling fluid. In both cases, attention has to be paid to the proper conditioning of the cooling fluid to minimize corrosion.

A typical laser cooling loop usually consists of surfaces composed of dissimilar materials which can cause galvanic corrosion, which will eventually degrade the laser performance. The potential for galvanic corrosion increases as the separation of dissimilar materials on the galvanic-metal series becomes greater. Two metals

commonly found in laser systems, aluminum and copper, are widely separated in the galvanic series. Aluminum is usually used in the design of the laser head, and copper is employed mostly in the heat exchanger of the cooling unit. Because aluminum and copper serve as anode and cathode, respectively, electrons can readily flow in aqueous solutions from anode to cathode, causing increased corrosion activity. Corrosion rates are particularly accelerated when the surface area of the aluminum anode is much smaller than the copper cathode.

Corrosion can be minimized by increasing the pH of the cooling fluid in conjunction with the use of a corrosion inhibitor. The optimum value of the pH is in most cases an alkaline condition with a pH between 9 and 11. Control of pH can be achieved by buffering the solution.

In designing a close-coupled single-elliptical cylinder, the following procedure can be followed: First, the smallest separation of rod and pump source is determined according to

$$2c = s_1 + \frac{d_r + d_L}{2}, \quad (6.64)$$

where d_r and d_L are the clearances required for the rod and lamp assembly, respectively. These two dimensions are normally several times larger than the physical diameter of the rod and lamp in order to allow space for flow tubes, O-rings, rod and lamp supports, rod holders, lamp terminals, cooling channels, etc. s_1 is the separation between the rod and lamp assembly; it is a safety factor to allow for tolerance buildup.

After the separation of the focal points has been determined, we can calculate the major axis of the ellipse:

$$2a = s_1 + 2s_2 + d_r + d_L, \quad (6.65)$$

where s_2 is the clearance of the rod and lamp assembly from the elliptical surfaces. We see from (6.64, 65) that in the extreme, $s_1 = s_2 = 0$, $a = 2c$, and the eccentricity of the ellipse is $e = 0.5$. In practical cases, e will be somewhat lower.

The minor axis of the ellipse follows from

$$b = (a^2 - c^2)^{1/2}. \quad (6.66)$$

Spectral transmission. Since the reflectivity of the metal surfaces as well as the transmission of the cooling fluid in the cavity are wavelength dependent, the spectrum of the pump light incident on the laser rod is different from the source emission spectrum. Ideally, in the transmission of the radiation from the source to the laser rod, one would like to have minimum optical losses in the pump bands of the laser material as well as total absorption of all pump energy in spectral regions which do not contribute to the laser output. In this way the thermal heat load and the associated optical distortions in the active material would be kept at a minimum. Particularly undesirable is the ultraviolet content of the pump light, because it causes solarization in most materials. Furthermore, ultraviolet radiation leads to rapid deterioration of any organic materials in the pump cavity, such as silicon O-rings. Also undesirable is the formation of ozone by the ultraviolet radiation, because it leads to corrosion

of metal parts in the cavity. Pump radiation, which has a longer wavelength than the stimulated emission, does not contribute to the laser output but does heat up the laser crystal and leads to optical distortions. The intensity and spectral content of the pump radiation reaching the laser rod depend on the reflectivity of the cavity walls, spectral filters placed inside the pump cavity, and the cooling medium.

The purpose of spectral filters placed inside the pump cavity is to provide adequate absorption of the intense ultraviolet radiation from xenon flashlamps. One way to accomplish this is to surround the laser rod or flashlamp with a tube made of Nonex, Pyrex, titanium-doped quartz, samarium-doped glass ED-5 and ED-6, or colored filter glass with a sharp cutoff. Instead of a tube as filter, a flat plate can be inserted, for example, in an elliptical-pump cylinder separating the rod and lamp. Other approaches include the use of ultraviolet-free lamps which are manufactured by employing an ultraviolet-absorbing or reflecting envelope. In glass rods, ultraviolet radiation can be prevented from reaching the active material by cladding the rod with samarium-doped glass.

The spectral properties of the cooling fluid can be utilized to remove some of the unwanted pump radiation. Water, if used as a coolant, is very effective in absorbing radiation at wavelengths longer than 1.3 μm. Where absorption of ultraviolet radiation by the laser material must be held to a minimum, potassium chromate, potassium dichromate, or sodium nitrite can be added to the cooling water.

The efficiency of Nd:glass and Nd:YAG lasers pumped by xenon flashlamps can be improved by circulating fluorescent dyes around the laser rod [6.81–83]. The dyes absorb in the spectral region in which the Nd ions do not absorb, and become fluorescent at one of the pump bands of Nd³⁺. Rhodamine 6G dissolved in ethanol was identified as the best dye, giving better than 50% improvement in the laser output.

Pump Geometries for Slab Lasers

The planar pump and cooling geometry achieved with a slab provides the possibility for one-dimensional heat flow. The design of flashlamp-pumped slab lasers has been extensively studied, and the potential advantages and deficiencies of such systems will be discussed in Chap. 7.

In Fig. 6.68 a single lamp is placed along the axis of the slab on each side. Appropriate reflectors are employed to distribute the pump light evenly over the slab surface area. Uniform pumping and cooling of the optical surfaces is absolutely crucial for good performance of this type of laser. The planar pump and cooling geometry achieved with a slab provides the possibility for one-dimensional heat flow, and simplifies heat removal from the laser medium and pump arrays. The purpose of the cusp-shaped reflectors is explained in Sect. 6.2.4.

As will be explained in Chap. 7, the thermal gradient caused by cooling the large top and bottom surface in Fig. 6.68 causes a cylindrical lens effect which can be eliminated by a zigzag path through the slab. This is accomplished with the beam undergoing total internal reflections at the top and bottom surfaces. The primary advantages of the zigzag slab are the minimization of stress-induced birefringence and thermally induced focusing by optical propagation along a zigzag path.

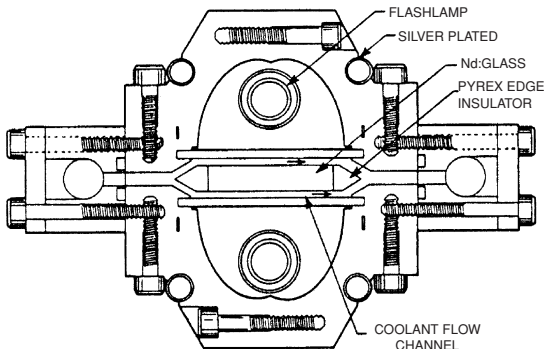


Fig. 6.68. Cross section of a typical slab laser pump cavity [6.84]

The surface and angular tolerances required to achieve typical design goals make slabs more expensive to fabricate than rods. In practice, edge effects and thermally induced stresses degrade their performance from that predicted. The slab geometry also supports a large number of parasitic modes that can limit the useful stored energy. Special coatings to suppress these parasitics, or to provide thermal coupling to the cooling system without spoiling the total internal reflections, can add to the cost and design complexity of slabs. The advantages given above and possible approaches to dealing with the disadvantages will be discussed in more detail below.

The first step in a slab-based design is a careful analysis of the trade-offs possible using different slab geometries and an analysis of fabrication issues, including coatings, that will be necessary for optimum performance. A choice between odd-bounce and even-bounce configurations will be the first decision that will have to be made. For even bounce slabs, the entrance and exit faces are parallel. This simplifies fabrication and reduces the cost of the slab compared to a odd-bounce slab with opposing faces. However, for one-sided conduction cooling, as implemented often in diode-pumped slabs the geometry of the odd-bounce slab gives symmetric thermal gradients at the two ends of the slab, which are better compensated by the zigzag path.

Flatness tolerances on the TIR surfaces of the slabs are an important factor in determining the wavefront distortion of the beam after passing through the slab. Since there will be several bounces per pass, it is important that the flatness of the area intercepted at each bounce be $< \lambda/5$. However, it is not necessary that the overall surface be this flat as long as the two surfaces are sufficiently parallel.

The combination of relatively high-localized gain regions due to strong pump absorption coupled with the highly symmetric geometry of the slab can cause amplified spontaneous emission (ASE) and parasitic oscillations which limit the useful stored energy. Coating or roughening the sides of the slab helps to suppress modes that propagate along the relatively high-gain region parallel to and near the pump face. In addition, it has been shown that breaking the symmetry of the slab by slightly canting the parallel surfaces can significantly reduce the number of parasitic modes.

6.2.2 Side-Pumping with Diodes

In contrast to flashlamps, the emission from laser diodes is highly directional; therefore, many arrangements are possible for transferring the pump radiation to the solid-state laser material. Since the output beams of laser diodes can be shaped and focused, a major consideration is the design of a pump geometry which maximizes the overlap of the pumped volume with the volume occupied by a low-order resonator mode. The optimization of the overlap is referred to as mode-matching.

In side-pumping the diode arrays are placed along the length of the gain material and pumping is transverse to the direction of the laser beam. Scalability to higher power is the advantage of this design approach. As more power is required, more diode arrays can be added along and around a laser rod or slab. There are several approaches to couple the radiation emitted by the diode lasers to the rod:

- (a) *Direct coupling.* From a design standpoint this is by far the most desirable approach. However, this arrangement does not allow for much flexibility in shaping the pump radiation inside the laser medium.
- (b) *Intervening optics between source and absorber.* In this case, the pump distribution can be peaked at the center of the rod allowing for a better match with the resonator modes. Optical coupling can be achieved by using imaging optics such as lenses or elliptical and parabolic mirrors or by nonimaging optics such as reflective or refractive flux concentrators.
- (c) *Fiber optic coupling.* Because of the coupling losses combined with the increased manufacturing cost of fiber-coupled diode arrays, this technique is not very attractive for side-pumping.

Whether or not to use intervening optics between the arrays and the laser medium depends mainly on the desired beam diameter and optical density of the active medium.

The excellent spectral match of the diode output and the absorption of the solid-state material, in conjunction with a high spatial overlap between pump radiation and resonator mode volume, are responsible for the high overall efficiencies that can be achieved in diode-pumped lasers. Figure 6.69 illustrates the energy flow in a typical Nd:YAG laser, pumped with a 20-W diode bar at 808 nm. Laser diodes have efficiencies of $\eta_p = 0.3\text{--}0.45$, with quasi-cw diodes at the upper range since they are more efficient pump sources as compared to cw diodes. Transfer of diode radiation and absorption by the lasing medium is expressed by the transfer and absorption efficiencies that in most systems are around $\eta_t \eta_a = 0.7\text{--}0.8$. In end-pumped configurations, diode radiation is, in most cases, not all collected by the optical system and reflection losses further diminish pump radiation. On the other hand, the diode radiation is almost completely absorbed in the longitudinally pumped active medium. In side-pumped configurations, transfer efficiency is close to one, but absorption of the pump radiation is often incomplete because a portion of the diode output is transmitted through a small rod or thin slab.

The absorbed pump radiation produces heat in the crystal. The fractional thermal loading, that is, the ratio of heat generated to absorbed power, is 32% in Nd:YAG

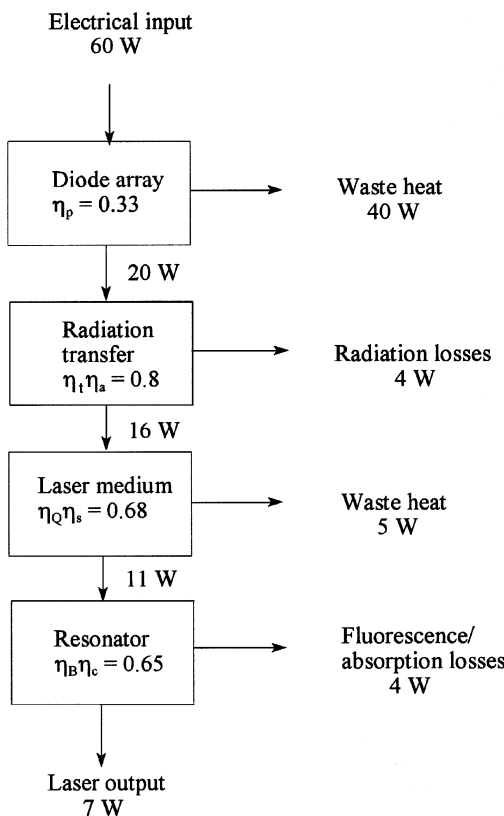


Fig. 6.69. Energy flow in a typical diode-pumped Nd:YAG laser (efficiencies are defined in Sect. 3.4.1)

pumped at 808 nm. These losses are accounted for by the Stokes shift and quantum efficiency $\eta_s \eta_Q = 0.68$. Mode-matching and optical losses in the resonator are expressed by the beam overlap and coupling efficiency which typically are $\eta_B \eta_c = 0.6\text{--}0.8$. The generic laser postulated in Fig. 6.69 has an overall efficiency of 11.6% and an optical-to-optical efficiency of 35%. In reviewing the energy-flow diagram, it is clear that the laser designer has control only over Steps 2 and 4, namely the design of the pump radiation transfer, pump geometry, and mode volume.

Traditional Rod Geometry

Some of the more important pumping configurations that have evolved in an effort to optimize the performance of solid-state lasers will be discussed next.

The most basic side-pumped arrangement is illustrated in Fig. 6.70. This high power amplifier head contains no coupling optics or reflective surface for recycling the pump radiation. The pump radiation is assumed to be absorbed in a single path through the 9-mm diameter Nd:YAG rod. The laser rod is surrounded by eight stacked arrays, each containing six bars. Since the bars are 1 cm long, and each bar produces

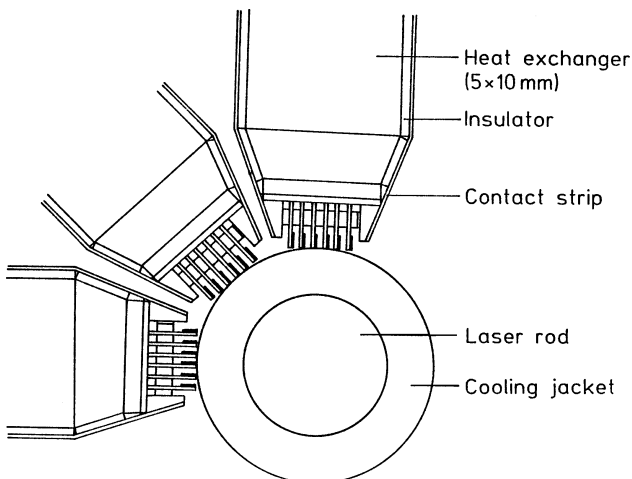


Fig. 6.70. Arrangement of stacked diode array bars around a laser rod

12 mJ in a 200 μ s pump pulse, the rod can be pumped at 576 mJ per centimeter rod length.

A photograph of a pump head without transfer optics for the pump beam is shown in Fig. 6.71. The design contains four rings of stacked diode arrays. In this closely coupled cavity, 4 cm of the 5-cm-long rod are pumped by the diode arrays.

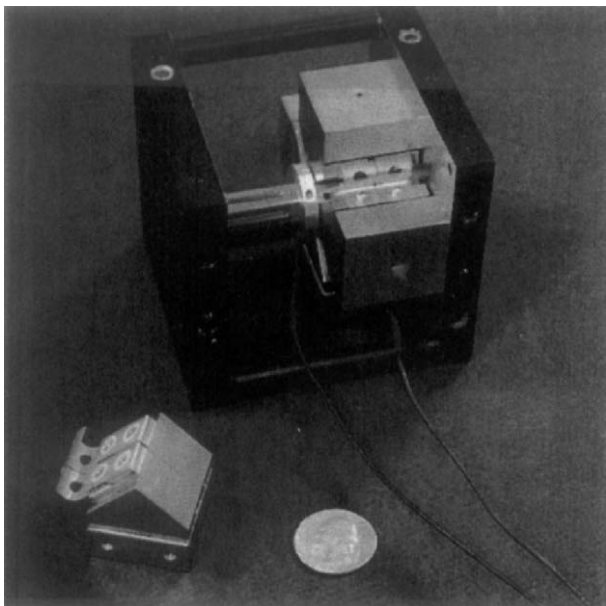


Fig. 6.71. Photograph of diode-array-pumped laser head (background) and stacked diode array bars mounted on copper heat sink (foreground)

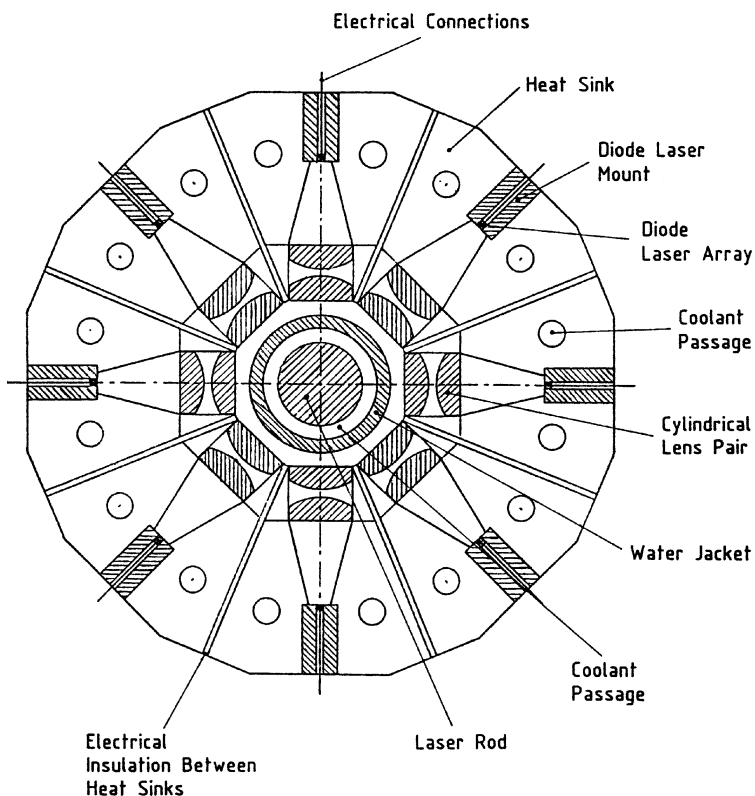


Fig. 6.72. Side pumping of a laser rod in a symmetrical pump configuration

Actually in three-level, or quasi three level lasers, such as Er:glass, Tm:YLF, or Yb:YAG, such a long section of unpumped region of the laser rod could not be tolerated. In these lasers, just a few millimeters of unpumped length will introduce absorption losses. The length of the laser rod can be extended by a crystal holder with the unpumped length being the "O" rings set as short as possible. This rod holder assembly is then inserted into the larger support structure of the pump chamber. A very elegant method of avoiding absorption is the approach where undoped sections are thermally fused to each end of the laser crystal.

In Fig. 6.72 the pumping cavity consists of a number of linear arrays symmetrically located around the rod. The arrays are mounted on long heat-sink structures and contain cylindrical optics. The output apertures of the diode bars are imaged near the center of the rod by using a symmetrical doublet of plano-convex cylindrical lenses.

The optics allow the diode arrays to stand-off from the laser crystal to create the necessary space for incorporation of large heat sinks.

The design illustrated in Fig. 6.73 also employs lenses in the path of the pump beam for beam shaping and stand-off, in addition the pump cavity has a highly reflective surface for the enhancement of pump beam absorption. The laser rod is conductively

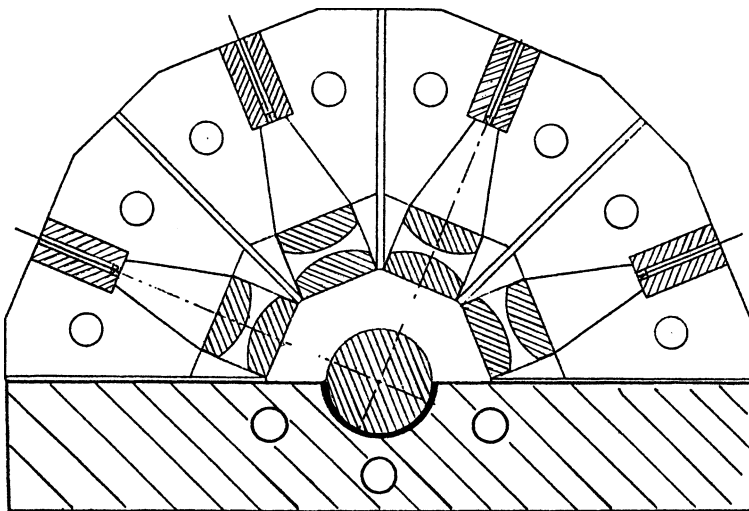


Fig. 6.73. Side-pumping of a cylindrical laser rod employing a hemispherical pump geometry

cooled by a copper heat sink and the rod surface in contact with the heat sink has a gold coating that returns the pump light for a second pass through the rod.

For optimization of the pump distribution within the gain medium, a ray trace program is very useful. Figure 6.74 presents the result of such a calculation for the pump arrangement of Fig. 6.73. The code calculates the spatial pump distribution in the laser material as a function of spectral absorption, and the spectral and spatial properties of the radiation source as modified by the optical surfaces between the

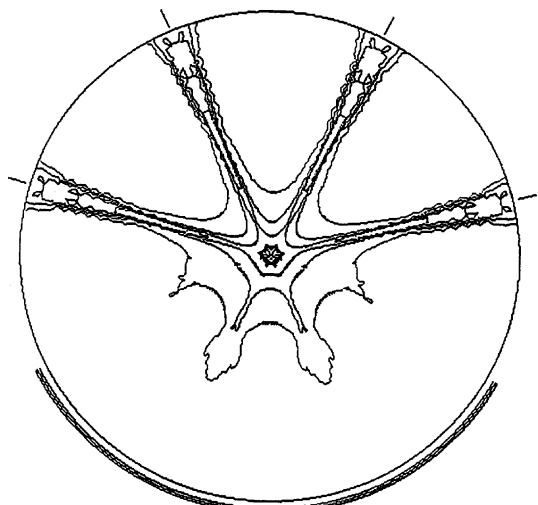


Fig. 6.74. Contour plot of pump intensity distribution

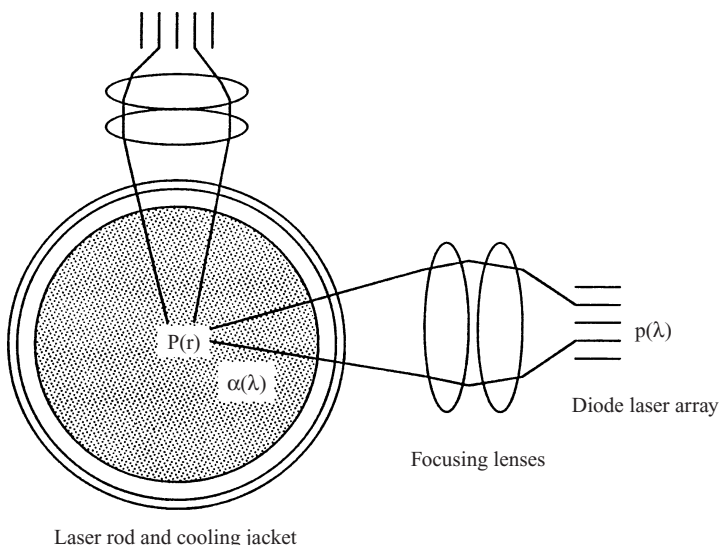


Fig. 6.75. Analysis of side-pumped laser rods

source and absorber. The strong concentration of pump radiation at the center of the rod was responsible for the good TEM_{00} performance of the laser.

An example of such a program called CRADLE [6.85] solves the general problem of radiation transport in a side-pumped laser rod using ray tracing with integration over the diode-array pump system. As schematically illustrated in Fig. 6.75, this code calculates the spatial pump distribution $p(r)$ in the laser material as a function of spectral absorption $\alpha(\lambda)$ and the spectral and spatial properties of the radiation source $p(\lambda)$ as modified by the optical surfaces between the source and absorber.

In Fig. 6.76 the cylindrical lens doublet shown in the previous examples has been replaced by a glass rod. The inside surfaces of the copper spacers opposite each diode array have a gold coating to reflect the pump radiation back to the laser rod for a second pass.

Figure 6.77 illustrates diode array and heat sink mounting details of an assembly employing focusing optics and a TE cooler for temperature control. The figure shows several 1-cm diode bars, forming a small 2-dimensional array, which are mounted and bonded to a common copper tungsten heat sink. Two such arrays are soldered to copper heat-sink blocks which, in turn, are coupled to TE coolers and liquid-cooled heat exchangers. The entire unit consisting of the diode array, coupling optics, and heat sink is positioned and mounted around the laser rod.

In the design illustrated in Figs. 6.70 and 6.72, the pump radiation is absorbed in a single pass through the laser material. If the laser medium is optically thick such an approach is acceptable. With a reflective coating opposite each diode array, as shown in Figs. 6.73 and 6.76 a longer absorption path is created. A number of pump cavities have been designed with the laser rod completely surrounded by a reflective cylinder with narrow slots for introducing the pump radiation.

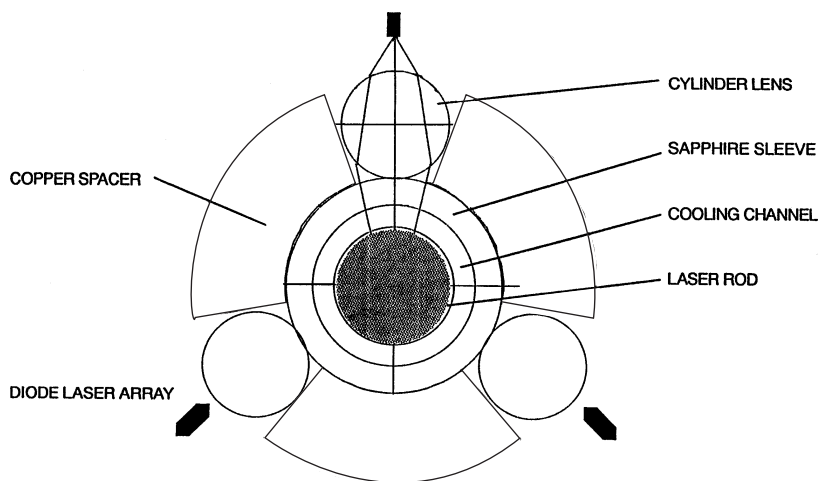


Fig. 6.76. Cross-section of diode-pumped laser head using cylindrical lenses

The basic concept is illustrated in Fig. 6.78, which shows a laser rod water-cooled in a diffuse reflecting cooling sleeve and side-pumped by three close-coupled cw diode arrays through narrow slots in the reflective surface. Each bar is radiating directly through such a narrow opening in the pump chamber reflector.

The cooling sleeve can have a silver, gold, or dielectric coating [6.86, 87] or the rod flow tube assembly can be surrounded by a diffuse reflector [6.88–90]. A close-coupled diffuse reflecting pump chamber generates a near uniform pump distribution. A lens system [6.86, 87, 89] or a nonimaging compound parabolic concentrator [6.88] can be used to compress the radiation through narrow slots in the walls of the

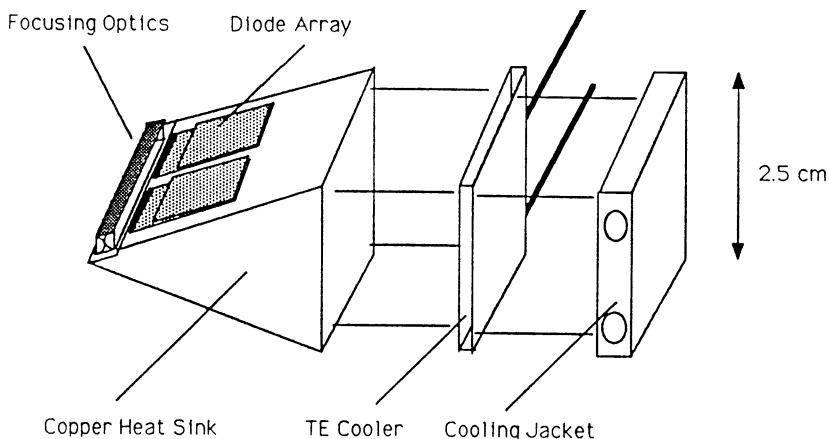


Fig. 6.77. Diode arrays and heat sink mounting and assembly details

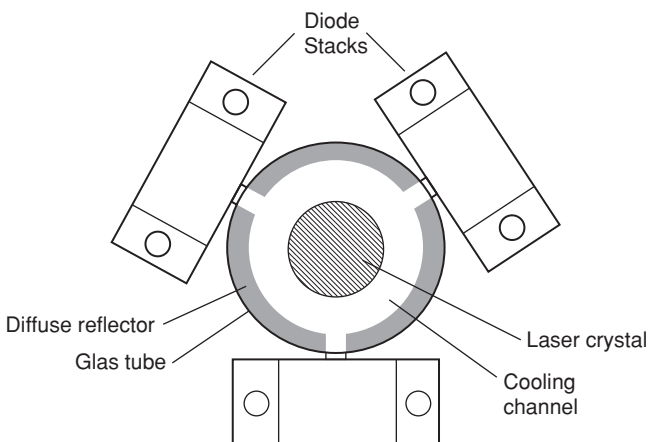


Fig. 6.78. Diode-pumped laser rod in a highly reflective pump chamber

reflective pump chamber. In the design described in [6.88] only 4% of the walls of the pump chamber are lost by the openings, which results in very efficient recycling of the pump radiation. If the emitter surfaces are brought in close contact with the slots of the reflective walls, the optical transport system can be eliminated [6.90].

Examples of the construction of pump heads for water-cooled side-pumped cylindrical rods are shown in the photograph Fig. 6.79.

The light-emitting surface of laser diodes cannot come directly in contact with liquid coolants, therefore laser diodes need to be conductively cooled. The design of cooled pump heads for diode-pumped lasers requires an entirely different approach compared to flashlamp-based systems.

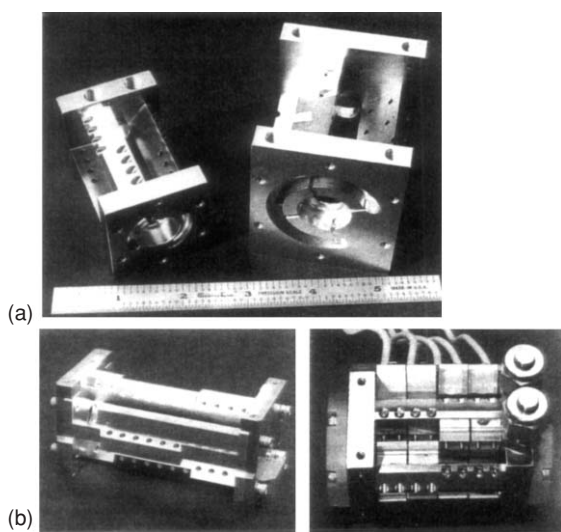


Fig. 6.79. (a, b) Liquid-cooled laser heads for diode-pumped Nd:YAG lasers. (c) Assembled pump head containing 16 diode arrays

In smaller lasers, the heat generated by the diode array and laser crystal can be conducted to a mounting structure and carried away by air cooling. In intermediate systems, water cooling of the common mounting structure is usually necessary. Large systems require a liquid-immersed laser rod or slab and a highly efficient liquid coolant flow as close as possible to the junction of the laser diode.

The laser-diode arrays are directly mounted on liquid-cooled heat sinks. After many iterations, extremely compact and lightweight structures have emerged which take full advantage of the high packaging density which can be achieved with diode arrays. Figure 6.79a,b displays a design composed of two end plates, which includes manifolds, and four triangular connecting bars. The laser crystal is inserted into a sapphire sleeve. Cover plates screwed to the end plates, seal and secure the rod. The diode arrays are mounted in a symmetrical pattern around the rod to produce uniform excitation. The flat areas of the triangular bars provide the mounting surface for the diodes and the thermal interface.

To carry off heat from the diodes and laser rod, liquid flows into the pump head through a fitting that screws into a part in the end plate. Directed by the manifolds, the coolant flows back and forth through passages in the triangular structures, and also through the annulus between the rod surface and sapphire sleeve. Eventually, the coolant exits the pump head through a second fitting on the end plate. With the diode arrays mounted on the internally water-cooled bars, the coolant, as it moves through the structure, is close to the heat source, thus facilitating heat transfer. For maximum heat transfer, a thin layer of indium is applied between the mounting surface and the diode arrays.

The monolithic structure comprising the four bars and two end plates is machined from a single piece of tellurium copper. Because of the monolithic design, only six “O” rings are required. One pair each for sealing the laser rod and flow tube, and one pair for the two end plates which seal the manifolds.

Figure 6.79c presents a photo of an assembled pump head for a side-pumped Nd:YAG rod pumped by 16 diode arrays. Each array is 1 cm long, and the devices are arranged in four pairs symmetrically around the rod. The adjacent 4 pairs are off-set 45° in order to achieve an eightfold symmetry around the laser crystal. The active pump area is 4 cm long and the complete assembly, including the end plates, has a length of 7 cm.

Each diode array contains 5 bars, i.e., the laser crystal is pumped by 80 bars at a pulse energy of 800 mJ in a 200- μ s-long pulse. Electrical input is 2 J per pulse, which at a repetition rate of 100 Hz amounts to about 120 W of heat which has to be carried away by the laser head.

Side-Pumped Slab Laser

Slab lasers are usually pumped by large densely packed two-dimensional arrays. In a slab laser, the face of the crystal and the emitting surface of the laser diodes are in close proximity and generally no intervening optic is used. Single-sided conductive cooling and diode pumping of the slab (Fig. 6.80) allows the simplest and most compact construction of the pump head. The slab is pumped from one face, and the opposite face is bonded to a copper heat sink containing a reflective coating to return

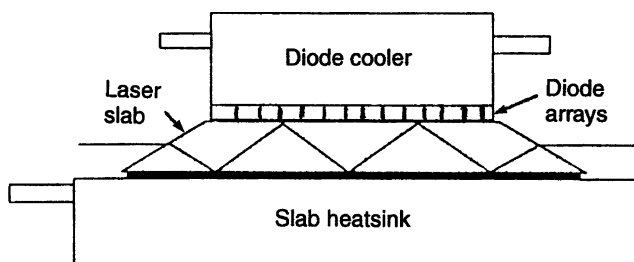


Fig. 6.80. Side-pumped conductively cooled slab laser

unused pump radiation back into the slab for a second pass. An antireflection coating on the pump face is used to reduce coupling losses (the diode array is not in contact with the active material). Liquid cooling is employed to remove heat from the crystal and diode heat sink. The purpose of the zigzag optical path shown in Fig. 6.80 is to mitigate the effects of thermal lensing caused by thermal gradients in the slab, as will be explained in Chap. 7.

The slab sides are frosted to prevent internal reflections which could cause parasitic oscillations. The Brewster angle at the ends of the slab eliminates the need for coatings. It also simplifies the resonator layout because with the combination of a zigzag path and Brewster ends, the beam leaves the slab parallel to its major axis.

The slab bounce angle and coatings are designed to preserve total internal reflection within the slab. Apertures are usually placed at each end of the slab to protect the slab edges against energy spillover, which can cause damage.

Depending on the way heat is extracted from the slab we can distinguish the three design configurations illustrated in Fig. 6.81. If the slab is water-cooled, pumping and

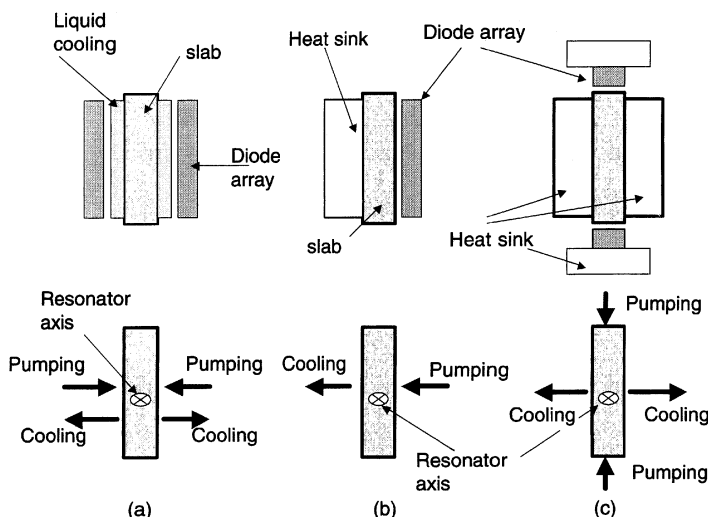


Fig. 6.81. Cross section of (a) liquid-cooled slab, (b) one-sided conductively cooled, and (c) two-sided conductively cooled slab

heat extraction can occur through the broad faces of the rectangular slab as shown in Fig. 6.81a. Space and military applications require conductively cooled slabs. One approach, shown in Fig. 6.81b, is to conductively cool one face of the slab and pump through the opposite side. More powerful lasers can be built by conduction cooling of both large surface areas of the slab. Pump radiation is introduced through the two narrow sides of the slab as shown in Fig. 6.81c. Therefore, this pumping geometry is termed edge-pumping [6.91]. The concentration of pump radiation, which is possible with diode sources, makes this approach feasible. In all three cases depicted in Fig. 6.81 pump radiation enters into the slab transverse to the resonator axis and the laser output is extracted from the ends of the slab. Also the plane of the zigzag beam is collinear with the direction of the thermal gradients in the slab.

A photograph and details of a side-pumped and conductively cooled slab laser are shown in Fig. 6.82. The zigzag slab Nd:YAG laser is air-cooled and battery-powered. At a repetition rate of 10 pps, the system produces 270 mJ per pulse at the frequency doubled wavelength of 532 nm. The slotted compartment shown in the photograph houses the pump module consisting of the Nd:YAG slab, diode arrays, heat sink, and cooling fans. The zigzag slab is pumped by twelve 18 bar arrays with a total optical output of 2.6 J at a pulselength of 200 μ s.

A cross section of the pump module is shown in Fig. 6.82(b). The slab was bonded to a thermal expansion-matched heat sink which is clamped to the bridge assembly. This clamping method was employed to reduce mounting and thermal cycling stresses in the laser crystal. Zigzag slab lasers can be scaled to the kilowatt level employing diode arrays. The large face area available in a slab geometry allows stacking of a sufficient number of diode arrays to achieve a high-output power. The large flat surfaces eliminate the need for intervening optics between the pump source and the laser crystal. This facilitates scaling to large systems.

The pump module of high-power diode laser is shown in Fig. 6.83. A $20 \times 2 \times 0.7$ cm Nd:YAG slab is pumped by 14 diode arrays on each side. Each array comprises 16 bars with a peak output of 50 W at a 30% duty cycle. The total optical pump power to the slab is 6.72 kW at an electrical input of 15 kW. The system was designed for a pulse repetition rate 2 kHz and a pump pulse length of 150 μ s. The pump head generated 740 W of average Q-switched power in a $7 \times$ diffraction limited beam. Peak power was 1 MW.

Figure 6.84 shows the cross section of a commercial Nd:YAG laser made by Fanuc that generates an average output of 3.3 kW in a single slab. The slab is pumped by closely coupled arrays of quasi cw laser diodes. The arrays are arranged such that they pump one half of the slab on either side. The surface opposite each array is highly reflective to increase pump absorption. The slab is 200 mm long, 25 mm wide, and 6 mm thick. The optical-to-optical conversion efficiency is 35% and the output efficiency is 13%.

The slabs illustrated in Fig. 6.81 can range in size from very large structures with a thickness of up to 8 mm to very thin planar wave guide lasers with a thickness of only a few hundred microns. For example, in [6.94] a planar wave guide laser is described with a 200- μ m-thick Nd:YAG core and a 400- μ m-thick diffusion bonded cladding. The 60-mm-long and 11-mm-wide slab is sealed in a gold plated water-cooled chamber. A 10 bar diode array with as much as 450 W of cw power radiating

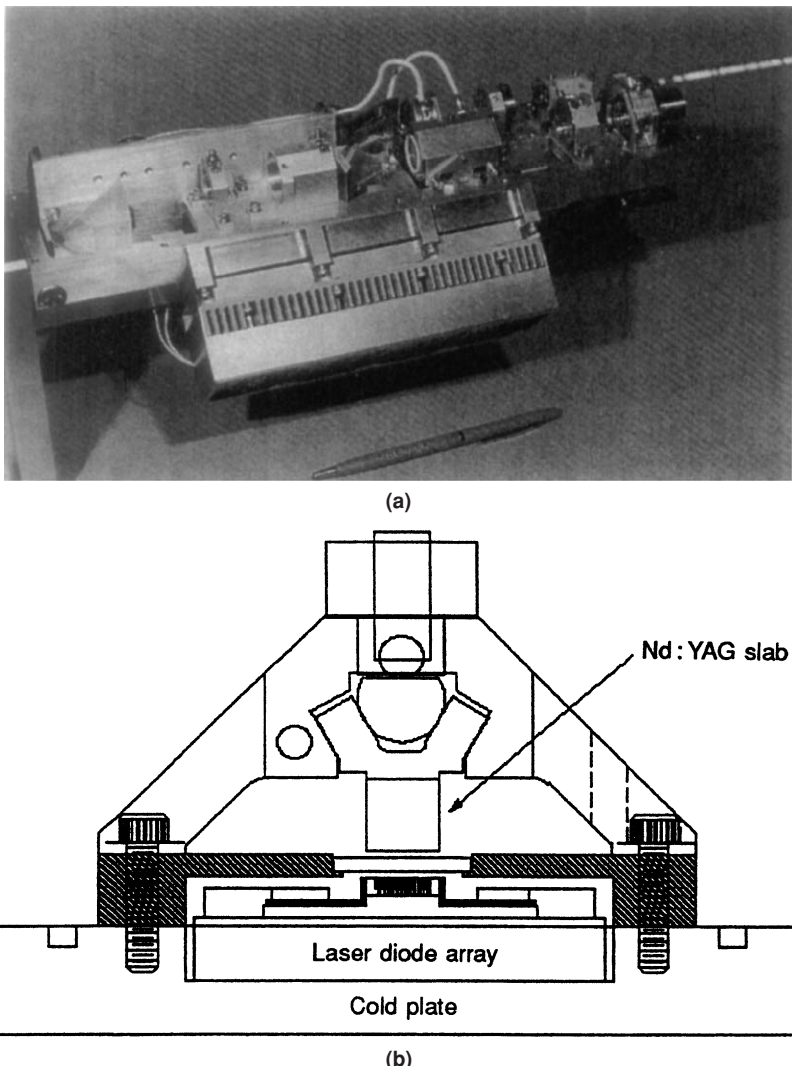


Fig. 6.82. (a) Photograph of an air-cooled and battery-operated zigzag slab Nd:YAG laser and (b) cross section of pump module [6.92]

through slots in the pump chamber produces a multimode output of 150 W. The low pump absorption during one pass through the optically thin slab is solved by incorporating the slab into a highly reflective pump chamber.

Pump Configurations Based on Internal Reflections of the Laser Beam

Besides the classical side-pumped configurations discussed in this section, there is an almost unlimited number of pump-configuration variations possible. Most of the

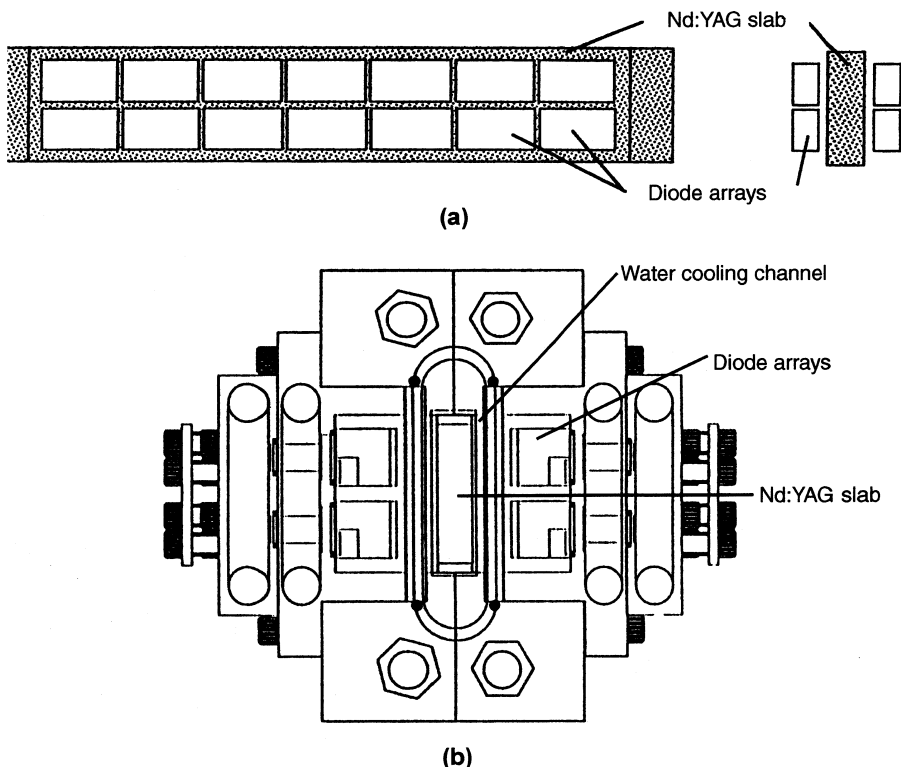


Fig. 6.83. High-power diode-pumped Nd:YAG slab laser; (a) the arrangement of the diode arrays and (b) a cross section of the pump head are depicted [6.93]

more unusual design configurations utilize internal reflections of the laser beam. In Fig. 6.85 designs are illustrated which contain one, or many internal reflections of the laser beam. An extension of this concept is the monolithic ring laser which was discussed in Sect. 5.2.3.

In the design shown in Fig. 6.85a side-pumping through a polished face of the gain medium is used to obtain high gain. The resonator mode makes a single grazing-incidence total internal reflection at the pump face, thus remaining in the region of the highest gain throughout its passage through the slab.

Micro lenses at each bar of a multibar stack collimate the output in the fast axis of the diodes.

The grazing incidence design results in a high inversion density localized in a shallow region below the pumping face. By utilizing total internal reflection from the pump face, the laser beam experiences very high gain. The total internal reflection also provides spatial averaging of the gain nonuniformity caused by the exponential absorption of the pump radiation. This design concept has been applied to a number of small lasers, such as Nd:YVO₄, Er:YAG, Nd:YAG, and Cr:LiSAF [6.95,97–99].

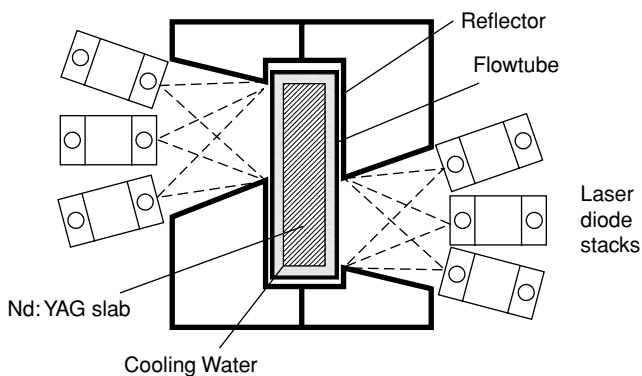


Fig. 6.84. Commercial Nd:YAG slab laser pumped by stacked arrays of laser diodes (Fanuc Corp.)

The one bounce design, shown in Fig. 6.85a, can be extended to include several bounces [6.100]. For example, by placing another diode laser bar at the other side of the crystal slab the system can be expanded to accommodate pumping with two diode bars. Figure 6.85b exhibits a miniature slab laser with a folded zigzag path of the laser

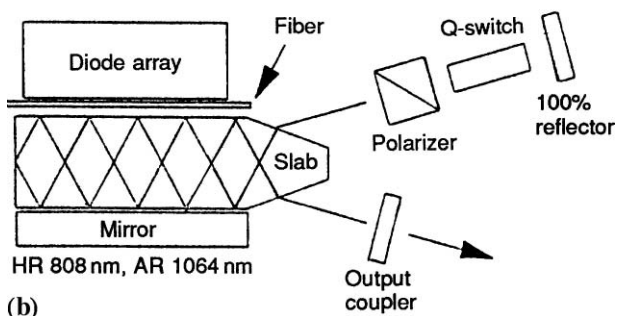
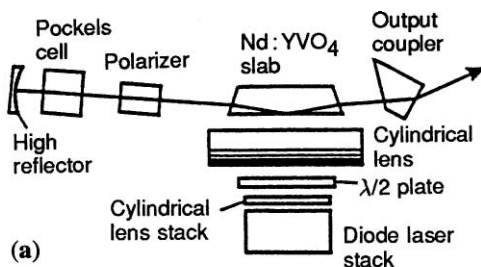


Fig. 6.85. Pump configurations based on internal reflections of the laser beam. (a) Slab with grazing angle at the pump face [6.95] and (b) slab with folded zigzag path [6.96]

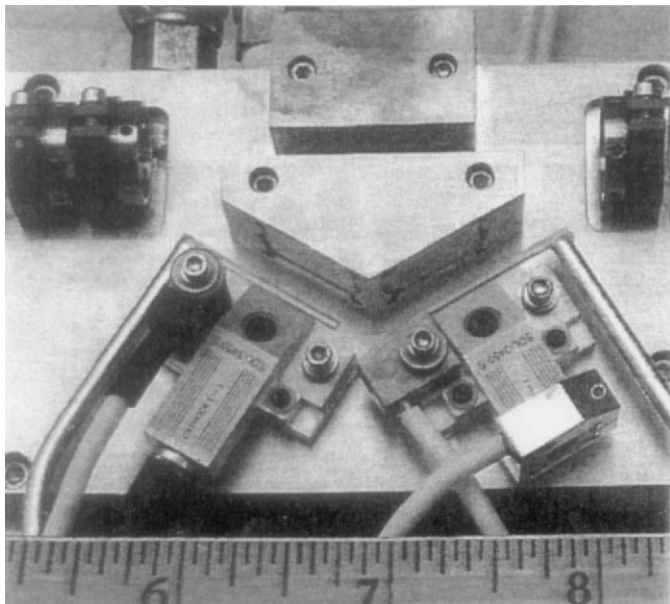


Fig. 6.86. Conductively cooled side-pumped ND:YLF laser

beam. The entrance and exit faces are cut at Brewster's angle. The beam path in this particular Nd:YAG slab consisted of five bounces. The pump radiation is collimated in the plane of the zigzag path by a fiber lens to maximize the overlap between pump beam and resonator mode. Many more design variations have been conceived around these basic schemes and almost every month, a new configuration is reported in the literature.

Figure are 6.86 shows a laser that is based on a variation of the single bounce grazing angle design. In this laser, pump beams from two 15 W cw laser diode arrays arranged in a "V" shaped configuration overlap at the laser crystal. The two diode arrays and a small slab Nd:YLF crystal are mounted on a copper block that is water-cooled. The triangular structure between the diodes and laser crystal contains cylindrical optics for collimation and focusing of the pump radiation. The pump face of the Nd:YLF crystal was antireflection coated for the 798-nm pump beam. The surfaces for transmission of the laser beam were antireflection coated for 1053 nm radiation, and had a tilt angle of 5° to minimize parasitic self-lasing effects in this high gain system. The laser produces 6 W of average power at a repetition rate of 15 kHz in a high quality beam.

6.2.3 End-Pumped Lasers

In the end-pumped technique, which is unique to laser diode pump sources, the pump beam is circularized, and focused into the gain medium coaxial with the resonator

beam. The gain medium must be long enough to absorb all, or at least a large fraction, of the pump radiation.

Spatial Overlap of Pump and Laser Beam

For the optimum design of an end-pumped laser, one of the most important parameter that determines the laser efficiency and the output power is the spatial overlap between the pump and the laser beam. The influence of the pump and laser mode size on the laser threshold and slope efficiency has been the subject of many theoretical studies. Early models assumed a TEM_{00} Gaussian pump beam whose spot size variation in the medium is negligible [6.101, 102]. With this very simplifying assumption the overlap integral can be evaluated in closed form. The result of these investigations indicated that for a given laser beam radius, the lowest threshold is achieved with the smallest pump beam waist allowed by diffraction.

In most end-pumped systems the pump radiation is delivered by a multimode optical fiber delivery system and the radiation is strongly focused into the laser medium. Therefore, the assumptions made in these earlier studies are not realistic for most end-pumped lasers.

In later modeling efforts, the beam divergence [6.103–107] and beam quality [6.105–107] has been taken into account. In these cases the overlap integral has to be computed numerically. The conclusions of these studies indicate that a ratio of the average pump beam waist to laser mode close to unity is about optimum for most situations.

As an example of a model developed for the optimization of fiber-coupled end-pumped solid-state lasers, we will briefly summarize some of the key features of the work presented by Pavel et al. [6.107]. In this work, it is assumed that the pump beam emerges from an optical fiber and is focused into the active medium as illustrated in Fig. 6.87. The spatial distribution of the pump volume $r_p(r, z)$ and the resonator mode $\varphi(r, z)$ are taken into account by calculating the overlap integrals that average the upper laser level population within the resonator mode.

The parameters calculated in this analysis are the mode-matching efficiency η_B and a normalized threshold pump power F_{th} as a function of the ratio of multimode pump beam waist to laser Gaussian spot size $a = (W_{\text{Po}}/w_m)$ and the position z_0 of the pump beam waist from the front face. Both parameters are then introduced into (3.63 and 3.64) for input–output calculations. In the expression for the efficiency factors (3.62) the value for η_B is entered, and in (3.65) the term A/η_B is replaced by $(\pi w_m^2)F_{\text{th}}$, where w_m is the spot size of the laser beam. Since the authors considered the optical-to-optical conversion efficiency, the other two terms contained in (3.62), namely pump and optical transfer efficiency, need not to be included.

The normalized spatial distribution $\int \varphi(r, z) dV = 1$ of the laser photons in the resonator is assumed to have a TEM_{00} Gaussian distribution with a spot size w_m constant over the length L of the active medium

$$\varphi(r, z) = \frac{2}{\pi w_m^2 L} \exp \left(-2r^2/w_m^2 \right). \quad (6.67)$$

where w_m is the Gaussian laser beam spot size.

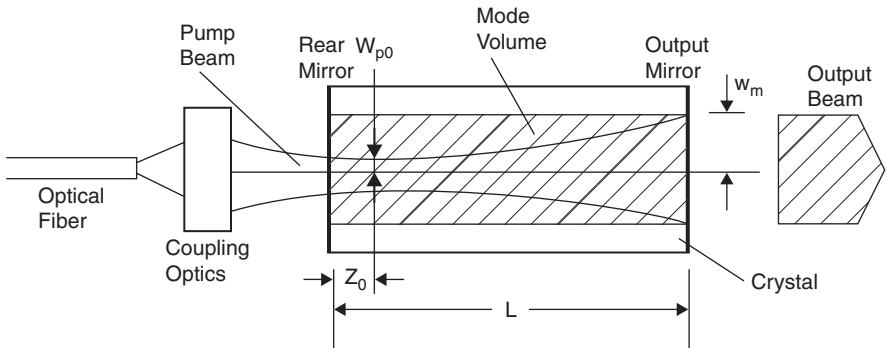


Fig. 6.87. Model of an end-pumped solid-state laser with pump beam waist at z_0 and radius $W_{p0} = aw_m$

For the fiber-coupled pump beam, the spatial distribution $r_P(r, z)$ is described by

$$r_P(r, z) = C \exp(-\alpha z) \exp(-2r^2/W_P^2(z)), \quad (6.68)$$

where α is the absorption coefficient at the pump wavelength and the constant C must be determined from the normalization condition

$$\int r_P(r, z) dV = 1. \quad (6.69)$$

The expression for the pump beam spot size $W_P(z)$ is the same as given in (5.31) for a multimode beam characterized by M^2 , except for the inclusion of the refractive index n_0 of the laser crystal, and also the pump beam waist W_{p0} is assumed a distance z_0 from the entrance of the crystal

$$W_P(z) = W_{p0} \left[1 + \left\{ \frac{M^2 \lambda_P}{n_0 \pi W_{p0}^2} (z - z_0) \right\}^2 \right]^{1/2}. \quad (6.70)$$

Near threshold the mode matching efficiency η_B follows from

$$\eta_B = \frac{\left[\int r_P(r, z) \varphi_0(r, z) dV \right]^2}{\int r_P(r, z) \varphi_0^2(r, z) dV}. \quad (6.71)$$

And the normalized threshold pump power is given by

$$F_{th} = \left[\int r_P(r, z) \varphi_0(r, z) dV \right]^{-1}. \quad (6.72)$$

Both overlap integrals have to be computed numerically. The solutions are three dimensional plots of η_m or F_{th} as a function of a and z_0 . The optimum values for a and z_0 correspond to the peak of the mode matching efficiency $\eta_m(a, z_0)$ or the minimum of the function $F_{th}(a, z_0)$.

From the input parameters of this analysis, namely laser beam spot size w_m , a pump beam characterized by M^2 , and an absorption coefficient α , one obtains the

ratio of pump beam waist to laser spot size a , and the distance z_0 of the pump beam waist from the entrance face of the crystal that give the lowest threshold F_{th} . The results for η_B and F_{th} can be introduced into (3.64) and (3.65) to obtain the threshold power and slope efficiency of the particular laser.

The general conclusions from this analysis are as follows: If the pump beam approaches the TEM₀₀ mode ($M^2 = 1$) the smallest pump beam is best. For $M^2 > 1$ an optimum waist ratio exist which increases with increasing M^2 values. Also if the absorption coefficient increases, the optimum focusing position moves closer to the entrance face of the crystal.

In [6.107] the analysis was applied to the calculation of the optimum pump beam characteristics for a 10-mm-long Nd:YAG crystal pumped with a fiber-coupled cw diode array. The 250-μm core fiber had a beam quality of $M \approx 110$ (0.22 rad half-angle). The laser beam was assumed to be 400 μm in diameter and almost constant over the pump area. The optimum condition was found for a pump beam with a waist of 212 μm, focused 0.3 mm behind the entrance face. This gives a ratio of pump beam to laser beam waist of 0.53. The average pump beam radius is 347 μm. From this follows a ratio of 0.92 for the ratio of average pump beam to laser beam radius.

This is the same conclusion as derived by another investigation that considered thermal effects as an important factor in scaling diode end-pumped lasers to high power [6.108, 109]. These studies concluded that the optimum ratio of an average pump size radius and laser beam radius is an increasing function of pump power. For a Nd:YAG crystal, pumped at 10 W input power this optimum was close to unity.

While diode end-pumping has produced some of the best conversion efficiencies for high quality TEM₀₀ mode beams, it is power limited by thermally induced lensing and thermal fracture damage. Thermal lensing ultimately destabilizes the laser output as the pump power is increased. While for small end-pumped lasers a pump beam less or equal to the spot size of the fundamental mode seems optimum, for high power end-pumped lasers such as Nd:YVO₄ producing over 20 W of output, it was found that a pump beam larger than the fundamental mode is actually preferable.

When the pump light is focused into the small area of an end-pumped laser, it causes intense local heating that induces a refractive index gradient, i.e., thermal lensing. In addition, expansion of the crystal material causes bulging of the facets. As will be explained in Chap. 7, the gradient of the refractive index change and bulging is largest at the boundaries of the pump beam. A laser mode that is smaller than the pump beam will avoid this transition region and experiences lower beam distortions. Clearly, this is a trade-off because if the pump beam is larger than the laser mode, part of the inversion will decay by spontaneous rather than stimulated emission and the system efficiency will decrease.

Purely thermal considerations lead to the conclusion that to further reduce distortions in powerful end-pumped lasers, a pump beam that is flat is better than a Gaussian profile because it creates a larger central region of relatively small distortions. Also, a lower doping and correspondingly longer crystal is advantageous because heat dissipation is distributed over a larger volume, thereby reducing thermal lensing and bulging of the front face. This requires high brightness pumps which will keep the pump beam focused over a long section in the gain material. As explained in

Chap. 7, diffusion-bonded end caps of undoped crystal material substantially reduce the thermal load at the front face of an end-pumped laser.

For high power end-pumped lasers with output power on the order of 100 W, Nd:YAG is usually preferred over Nd:YVO₄ because it has stronger thermomechanical properties.

Optical Transport System

The practical realization of a complete spatial overlap between the longitudinal pump beam and the laser mode depends very much on the degree with which the strongly astigmatic and highly divergent radiation emanating from the pump source can be reshaped into a beam with circular symmetry and a small beam waist. Focusing the output from a 1-cm bar or a stack of bars into a laser crystal requires collimation of the emitted radiation, compensation of astigmatism, and finally focusing the beam to a circular spot.

Common techniques of coupling radiation from laser diode bars into the gain medium of an end-pumped laser typically involve one of the following methods:

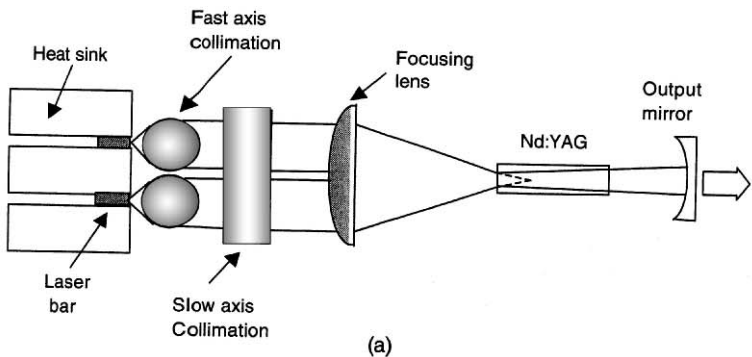
- Two orthogonally mounted microlens arrays for collimation of the output from each emitter followed by a focusing lens (Fig. 6.88a).
- A single cylindrical microlens array for collimation of the fast axes of the bars and a macrolens for focusing (Fig. 6.88b).
- A single cylindrical microlens array for collimation of the fast axes of the bars and a fiber bundle to circularize the beam followed by focusing optics (Fig. 6.88c).
- A nonimaging light concentrator (Fig. 6.88d).
- A macrolens system (Fig. 6.90).

A single laser bar or a stack of bars represent a pump source with an overall cross section of up to a few centimeters squared, which consists of a multitude of independent emitters. The smallest focused spot size from a single bar or two-dimensional bar can be achieved if the radiation from each emitter is individually collimated and corrected for astigmatism. This is usually done with microlenses or fiber bundles. After collimation, the multitude of beamlets are focused with a bulk lens or lens assembly into the gain medium. This approach requires extreme precision in positioning and aligning the optical components with the emitters.

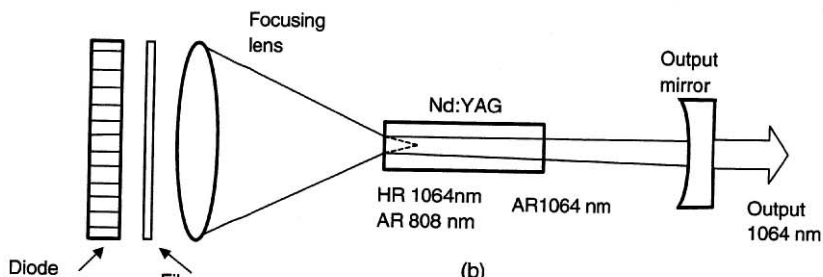
Designs based on ordinary macrolens assemblies or nonimaging light concentrators treat the radiation emerging from a stack of bars as coming from a large extended source. The designs are relatively simple but the minimum spot size which can be achieved is at least an order of magnitude larger than can be obtained by collimating the output from each emitter.

A compromise between the above mentioned approaches are designs whereby the fast axis of each bar is collimated with a cylindrical microlens and the emerging beams are focused with a conventional lens or nonimaging light concentrator.

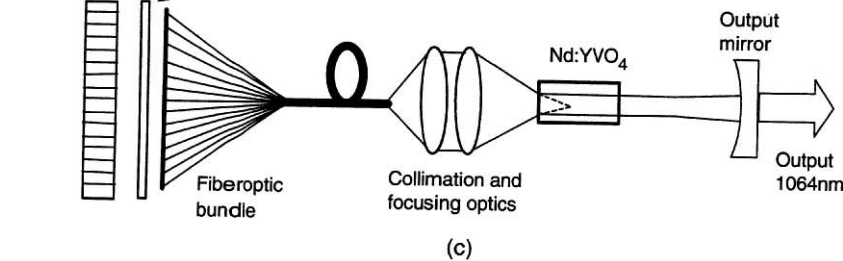
Figure 6.88 shows end-pumped lasers which are pumped from one side only. In the folded cavity designs illustrated in Fig. 3.35 and Fig. 6.91 laser and pump beam are separated by a mirror. Such a design allows the crystals to be pumped from both ends.



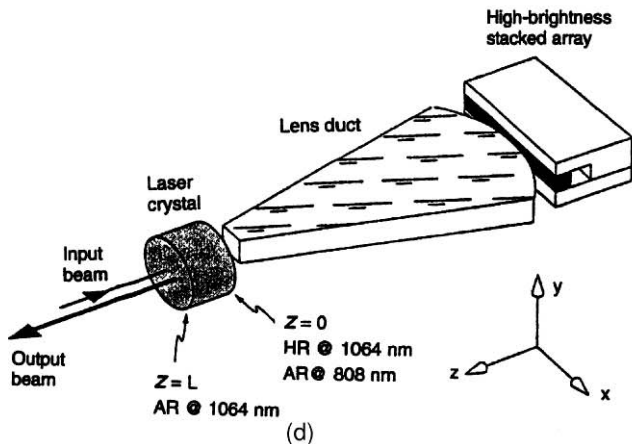
(a)



(b)



(c)



(d)

Fig. 6.88. Focusing of pump radiation into an end-pumped laser (a) with two cylindrical microlens arrays and a focusing lens, (b) a single microlens array and a focusing lens, (c) a microlens array followed by a fiber bundle and focusing optics, and (d) a nonimaging light concentrator [6.110]

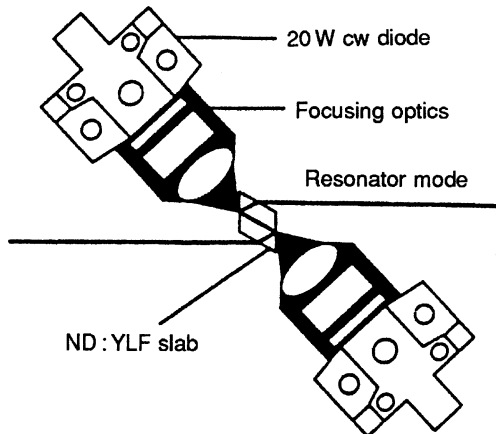


Fig. 6.89. End pumping of a small Nd:YLF slab from both sides utilizing internal reflection of the laser beam [6.111]

Another approach is shown in Fig. 6.89. The rhombic-shaped slab can be pumped from both sides without the use of external mirrors [6.111]. In this case, an internal reflection of the laser beam provides the separation from the pump beam.

Besides the collimation and focusing of pump radiation into a small spot within the crystal, other critical areas of end pumping are the coatings and proper heat sinking and cooling of the crystal. The latter issue will be discussed in Chap. 7.

Producing an antireflection coating for the pump beam and a highly reflective coating for the laser radiation at the crystal entrance facet requires complex designs and sophisticated fabrication procedures. The pump radiation causes intense local heating which results in a slight bulging of the facet, the coating must withstand high power as well as the thermal mechanical strain without cracking or de-lamination. As explained in Chap. 7, an undoped end cap considerably reduces the thermal stress at the entrance facet of an end-pumped laser. This also removes some of the more severe constraints imposed on the coatings.

Cylindrical Microlenses. Although the radiance from each emitter aperture is quite high, the average radiance over the entire length of a 1-cm bar is much lower because of the dead space between emitters. The brightness from a bar can be greatly increased if the radiation from each emitter surface is collimated individually. This is a technical challenge because it requires collimating the radiation from many small emitters with different beam characteristics in each axis. For this reason, the collimation has to be performed in separate steps for the fast and slow axis.

A very effective method of collimating the output from a single bar or a stack of bars is by means of two orthogonally oriented arrays of microlenses. The first set of lenses are typically cylindrical microlenses similar to short pieces of optical fibers. Each lens is oriented along the length of a bar close to the facets of the emitters. These fiber lenses, mounted in a rigid holder assembly, collimate the fast axis of each bar

within the stacked array. The number of microlenses required is thus given by the number of bars in the array. These fiber lenses are 1 cm long and have a maximum diameter determined by the pitch of the array (typically 0.4–1 mm). The distance from the facets is determined by the back focal length which is, for a microlens with a circular cross section and uniform refractive index, $D(2 - n_0)/4(n_0 - 1)$. For a fiber lens with a diameter $D = 800 \mu\text{m}$, made from fused silica with $n_0 = 1.50$, the distance between the microlens and the facet is therefore 200 μm .

Instead of simple step-index fibers with a circular cross section, lenses with non-circular cross section (aspherics) or graded index (GRIN) lenses can be used to reduce spherical aberration. Aspheric lenses can be fabricated in large volume from drawing of a shaped-glass preform.

A common commercial bar containing “wide stripe” laser diodes has 24 emitters with a width of 200 μm , each at a 400 μm center-to-center pitch. The output from each emitter diverges about 40° in the fast axis determined by the 1- μm thickness of the emitting surface. An ideal microlens would have a large acceptance angle, i.e., a 0.7 numerical aperture or higher, to capture most of the radiation into a diffraction limited beam.

For collimation of the radiation from a diode stack it is also common practice to make microlens arrays monolithic rather than from discrete segments of optical fibers. Monolithic arrays consist of a glass plate in which parallel curved surfaces that optically act the same way as individual fiber lenses are shaped (see Fig. 6.39).

Mounted in front of the cylindrical microlens is a monolithic array of orthogonally oriented small cylindrical microlenses which collimate the radiation in the slow axis from each of the 100–200- μm -wide emitters. Since the divergence in the slow axis is typically 10°, the numerical aperture of these lenses is around 0.1.

The number of microlenses is given in this case by the number of emitters in each bar. The diameter of the microlenses cannot exceed the spacing between adjacent emitters (0.2–1 mm). Because of the stand-off distance from the facets, which is largely determined by the intervening microlens required to collimate the fast axis, the back focal length of the second lens array must be significantly larger than the lens diameter. This rules out microlenses with a circular cross section since these optical elements have a very short back focal length. Either aspheric or plano-convex cylindrical microlenses are normally used for the collimation of the slow axis of the emitters.

As an example, we consider a typical 1-cm cw bar which contains 20 emitters each 100 μm wide and spaced 400 μm apart. If we assume a 5-bar internally cooled stack with a pitch of 1 mm, a collimator could be designed that consists of five horizontal cylindrical microlenses with a circular diameter of 800 μm and a back focal length of 200 μm .

In front of these lenses are 5 monolithic arrays, each containing 20 plano-convex microlenses with a diameter of 500 μm and a back focal length of 2.5 mm and with their axis vertically oriented with respect to the first set of lenses.

With this approach the output from a stacked bar can be focused to a spot with a diameter of a few hundred micrometers. Manufacturing and alignment

tolerances will induce positioning errors between the individual emitters and lenses which will affect the collimation. The major positioning errors are planarity, curvature (smile), and periodicity between the array of emitters and lenses. Imperfection between the planarity between diodes and laser arrays implies that not every emitter will be in the focal plane of the lenses causing an increase of the divergence of the beam. Smile as well as a variation in periodicity will produce off-axis beam side lobes.

If larger spot sizes can be tolerated, a compromise between complexity and performance can be reached if only one array of microlenses is employed followed by an ordinary lens system. In a typical design, a set of fiber lenses reduces the beam divergence of the fast axis of each bar to match the divergence of the slow axis and a bulk lens focuses the beam into the active medium. Figure 6.88b illustrates such an approach.

Macrolens Approach. In the absence of microlenses or fiber-optic bundles one can attempt to focus the radiation from a single bar or stacked bar array with conventional optics. As already mentioned, the power density at the focal point will be far below that which can be achieved with micro-optics. To illustrate this point and to provide a comparison the following example is given.

Figure 6.90 depicts an imaging optical system for focusing pump radiation from a stack of three 1-cm bars into an Nd:YAG crystal. The optic consists of two cylindrical lenses, L1 and L2, with 12.7 and 19 mm focal length, respectively, followed by a

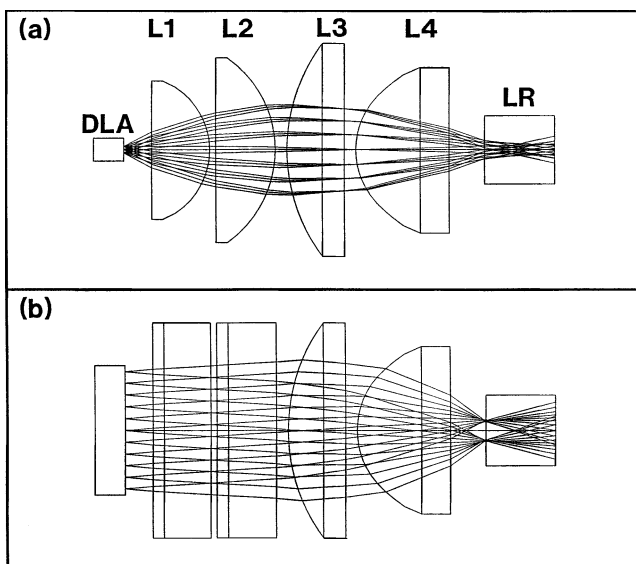


Fig. 6.90. Optical system for end-pumping a Nd:YAG crystal with a stack of three 1-cm laser diode bars. Ray tracing plot (a) parallel and (b) perpendicular to the bars [6.113]

30-mm focal length plano-convex lens L3 and a 12-mm focal length aspheric L4. The rays traced in the plane perpendicular to the bars span a total angular field of 60° at the source and those traced in the plane parallel to the bars cover a total field of 10° . The corresponding width at the pump end of the laser rod is ≈ 2 mm.

In order to at least approximately match such a large pump profile with the resonator mode, a near hemispherical resonator was chosen. The resonator length was adjusted until the TEM_{00} mode at the curved mirror and the front surface of the Nd:YAG was expanded to 1.8 mm. At the flat output coupler the $1/e^2$ beam diameter was 120 μm . The expansion of the mode at the pump end of the resonator is achieved at the expense of alignment stability. A photograph of the system is shown in Fig. 3.34.

Fiber Coupling. Using fiber optics to deliver the diode output to the laser crystal has a number of advantages: the beam at the fiber output has a circular distribution and the ability to remove heat from the diode remote from the optical components of the laser is an attractive feature. Also the pump source can be replaced relatively easily without disturbing the alignment of the laser. Typically one of the following three techniques is implemented in coupling the output from a diode bar or stacked bar into an optical fiber.

The first approach is identical to the technique already described for end-pumping a laser. Two sets of microlenses and a condenser lens are used for focusing the radiation into a multimode fiber with a diameter of 200–400 μm . In another design, the output from a diode bar is first collimated using a fiber lens and subsequently imaged with a combination of lenses into a two-mirror beam-shaping device. With this focusing scheme the output from a 1-cm bar has been focused into a circular spot of less than 200 μm [6.112].

In the third approach a fiber bundle is employed to transform a line source, which a single 1-cm bar represents, into a circular beam. A microlens reduces the divergence of the fast axis of the emitters before the radiation is collected by a flat bundle of fibers (see Fig. 6.88c). The line-to-bundle converting fiber-optic coupler consists of a large number of small fibers spread out in a linear array which faces the emitting diodes of the laser bar. At the other end, the fibers are arranged into a round fiber bundle.

The technique of using a fiber-optic bundle to circularize the output from a 1-cm diode bar is implemented in the laser illustrated in Fig. 6.91. The figure depicts an Nd:YVO₄ laser crystal pumped from both ends by two fiber-coupled 20-W diode bars. For separation of the pump and resonator beam, two dichroic beam splitters are inserted into the optical train, which results in a z-configuration of the optical resonator. The radiation from each bar is coupled into a flat fiber bundle by a microlens, which reduces the divergence in the fast axis of the diode output. At the pump end, the fibers form a round bundle and a collimating and focusing lens transfer the pump radiation into the crystal through a dichroic fold mirror. The high efficiency that can be achieved with diode end-pumping solid-state lasers is illustrated in Fig. 6.91b. With a fiber coupling efficiency of 85% and some reduction in the rated power level of the diode to preserve lifetime, each side of the Nd:YVO₄ crystal is pumped with

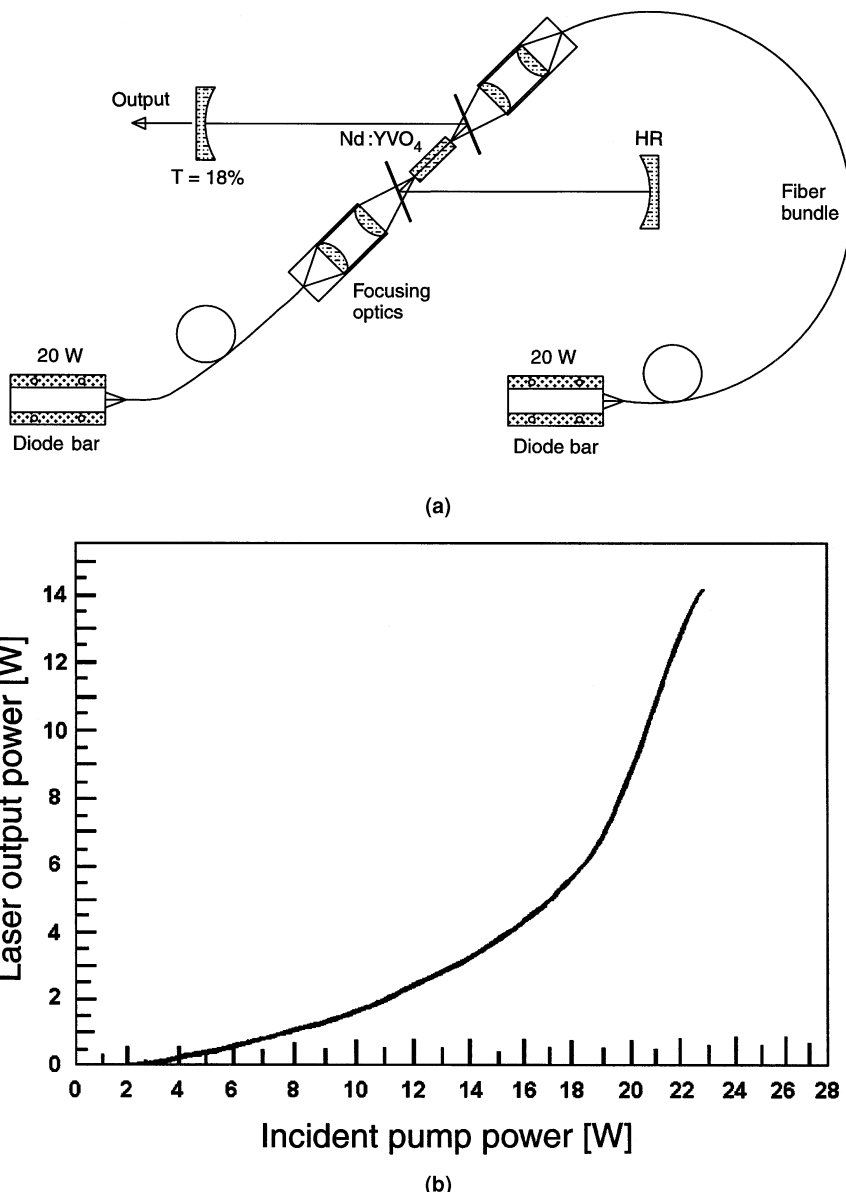


Fig. 6.91. (a) Optical schematic of an Nd:YVO₄ laser pumped with fiber-coupled diode bars (Spectra-Physics Lasers, Inc.) and (b) laser output versus optical pump power incident on the crystal

13 W. Pump radiation at the crystal is converted with over 50% conversion efficiency into a polarized TEM₀₀ mode.

Maximum output of the system is 13 W. An Nd:YAG laser used in the same configuration produced 11 W of polarized cw output.

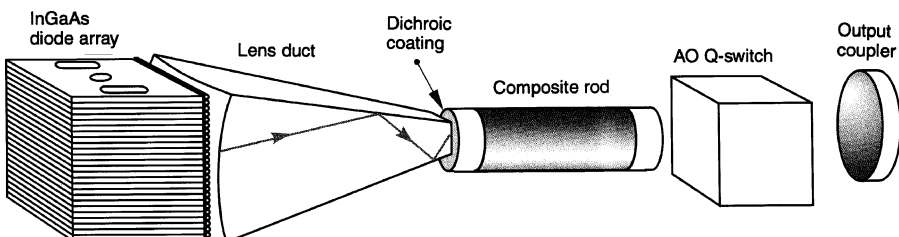


Fig. 6.92. End-pumping with a nonimaging light concentrator [6.114]

Nonimaging Light Concentrators. Figure 6.92 illustrates an end-pumping technique based on a nonimaging device. In this approach the output from a stack of bars is first collimated in the fast axis by cylindrical microlenses mounted in front of each bar. The collimated radiation is directed into a lens duct that combines focusing at its curved input face and total internal reflection at the planar faces to channel the diode pump radiation to the laser rod. Powerful Nd:YAG, Tm:YAG, and Yb:YAG lasers have been pumped with this technique and outputs in excess of 100 W have been reached in these lasers. A slightly different version of a light concentrator that has parallel walls in the vertical direction is shown in Fig. 6.88c. The stack width is reduced from 10 to 1.5 mm in the horizontal dimension and this resulted in an output aperture of the device of $1.5 \times 1.5 \text{ mm}^2$ [6.110].

Concentrators are an attractive solution for large stacks because they are relatively easy to fabricate. The degree of concentration is governed by the radiance theorem stating that the radiance of the light distribution produced by an imaging system cannot be greater than the original source radiance.

6.2.4 Face-Pumped Disks

The purpose of face-pumped disk amplifiers is to provide a uniform gain distribution over a very large cross-section. For example, in the laser system designed for the National Ignition Facility (NIF) slabs with dimensions of about $80 \times 46 \times 4 \text{ cm}$ are used to provide a 40 cm^2 clear aperture. This is about the practical limit imposed by amplified spontaneous emission (ASE) that depumps the laser slabs and limits gain.

As shown in Fig. 6.93, in a face-pumped amplifier the rectangular slabs, made from neodymium-doped phosphate glass, are oriented at Brewster's angle with respect to the beam to eliminate reflection losses. The slab faces have a high quality optical finish to minimize scattering losses. The edges are cladded with an absorbing glass to prevent internal parasitic oscillation.

Flashlamps are used for pumping, with lamp radiation incident on the disk faces and transverse to the beam direction. Thus, the disks are said to be face-pumped. Nd:glass amplifiers containing glass disks have mainly been developed at laboratories engaged in laser fusion studies. Generally, an even number of disks is used in an amplifier since beam translation occurs due to refraction in a single disk. Beam

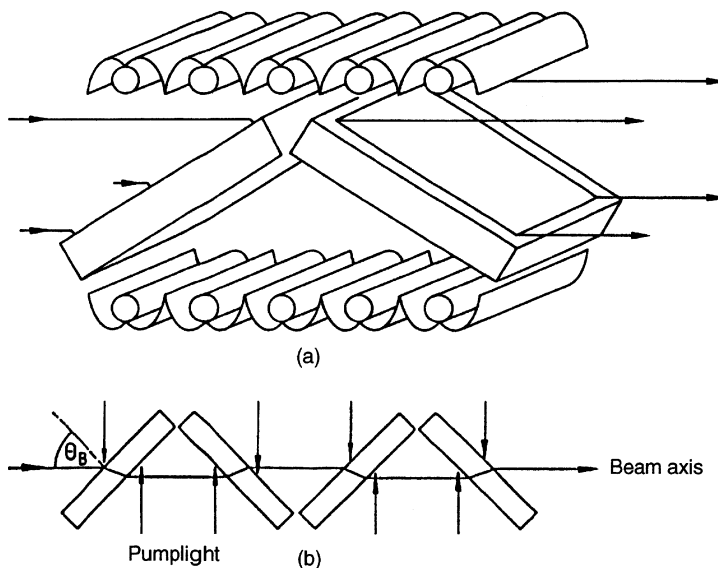


Fig. 6.93. Schematic diagram of (a) a disk amplifier and (b) alternate arrangement of disks (Lawrence Livermore National Laboratory)

steering can be minimized if the disks are placed in an alternate rather than parallel arrangement, as shown in Fig. 6.93b.

In face pumping, as opposed to pumping through the sides of a slab, the pump radiation can be evenly distributed over the cross section of the laser beam. Pumping in this way yields uniform gain over the aperture for a laser beam, but more important, the slab heating is uniform laterally, thus allowing transverse temperature gradients to be minimized. Such temperature gradients give rise to distortion in the slab just as in the rod geometry.

The cusp-shaped reflectors shown in Fig. 6.93 direct radiation to the slabs and shield each flashlamp from the radiation from adjacent lamps. The design of the flashlmap reflector housing requires a careful design to provide uniform illumination of the slabs as well as having good coupling efficiency. Figure 6.94 shows several reflector geometries that have been used for pumping slab lasers. The figure illustrates cusp-, and "V"-shaped, and semicircular reflectors (Fig. 6.94a–c), surrounding a single lamp, as well as a "V"-shaped reflector in combination with a diffuser to spread out direct radiation and thus provide a more uniform pump intensity profile (Fig. 6.94d).

Flashlamp reflector shapes have been studied extensively to improve disk amplifier efficiency [6.115–117]. The double-cusp reflector shown in Figs. 6.93 and 6.94a are optimum in preventing first-pass self absorption of the flashlamp radiation. In a flat or round reflector, without the sharp ridge in the middle, the radiation falling on the area right behind the flashlamp is reflected back into the plasma.

In some designs, a blast shield between the flashlamps and laser slab is installed to prevent acoustic waves generated by the flashlamps from propagating into the beam

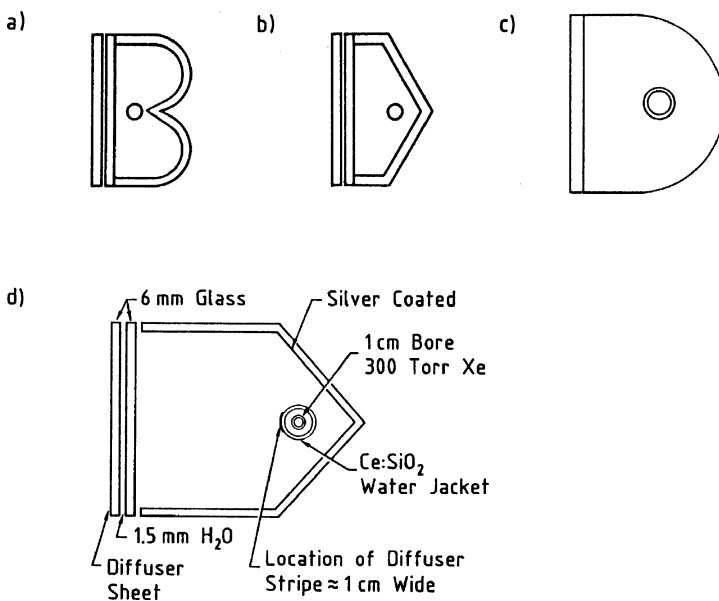


Fig. 6.94. Typical face-pumped Nd:glass disk laser amplifier geometry

path causing wave front distortions, to provide a contamination barrier between the flashlamp cavity and the beam path, and to define a channel for flowing cooling gas around the lamps.

Even with gas cooling it takes several hours after each shot before the average slab temperature recovers to within ambient temperature. The slabs are pumped by a large number of flashlamps to make the distribution of pump light as uniform as possible. An uneven temperature rise in the lateral direction produced by waste heat deposited in the slab during each pump cycle leads to wave front distortions in the laser beam.

Table 6.6 lists the results of an energy-transfer analysis performed on a large Nd:glass disk amplifier. About 1% of the total electrical input is available as stored

Table 6.6. Energy transfer in an Nd:glass disk amplifier [6.118]

Circuit losses	8%
Lamp heat	50%
Heating of pump cavity walls	30%
Ultraviolet absorption	7%
Heating of glass disks	2%
Fluorescence decay	2%
<i>Useful laser energy</i>	1%
Electrical input to lamps	100%

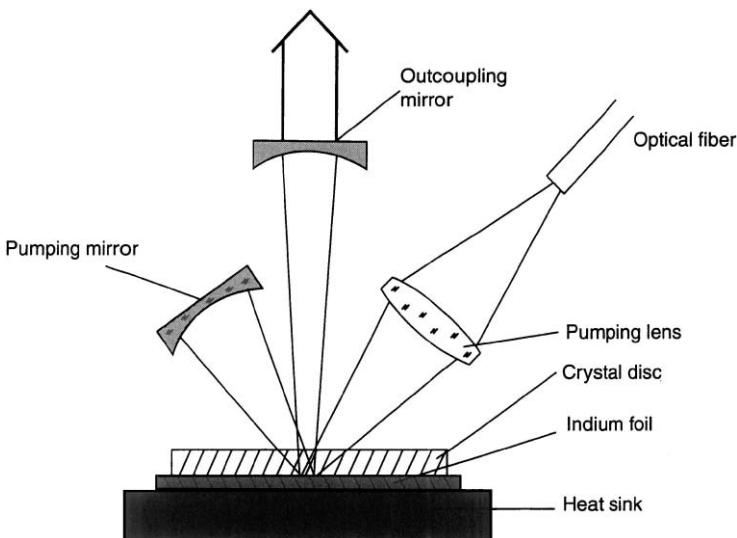


Fig. 6.95. Thin-disk-pumping geometry of a Yb:YAG laser [6.119]

energy at the laser level. Of course, only a fraction of this energy can be extracted during the amplification of a laser pulse.

The other extreme of a face-pumped laser, in terms of size, is the thin-disk approach employed for pumping Yb:YAG. As illustrated in Fig. 6.95 a disk about 300 μm thick is pumped in a small spot of a few millimeters in diameter at a small angle about the normal of the disk face. The 941-nm pump radiation reflected back from the disk is refocused by a mirror for a second path through the crystal. The backside of the disk, which is in contact with a heat sink, is coated to form one of the resonator mirrors. The other resonator mirror is the curved output coupler shown in Fig. 6.95.

In the thin-disk laser, waste heat generated in the disk is extracted through the back high-reflectivity mirror and to an actively cooled submount that holds the laser disk. The key feature of the thin-disk design approach is that this cooling geometry constrains resulting thermal gradients to lie essentially parallel to the laser resonator axis. Consequently, thermal focusing by the gain disk is greatly reduced, facilitating the achievement of high beam quality.

The crystal Yb:YAG is particularly well suited for the thin disk geometry because of its high absorption of the 941-nm pump radiation. The performance of Yb:YAG is strongly dependent on temperature because Yb:YAG is a quasi-three-level material with a substantial population of the lower laser level at room temperature.

For this reason the temperature rise across the disk has to be minimized. Since the thin disk is mounted with one face on a heat sink, a reduced crystal thickness yields a lower thermal gradient and effective temperature in the crystal. However, if the disk is made very thin, the pump radiation cannot be fully absorbed during a single pass because the dopant concentration cannot be made sufficiently high.

If the number of passes of pump radiation is increased, the crystal thickness can be reduced without changing the amount of absorbed pump power. But the shorter cooling path will reduce the disk temperature. The laser design requires a careful balance of crystal thickness, dopant concentration, number of passes of the pump radiation through the disk and heat sink temperature. The design shown in Fig. 6.95 has one return mirror that allows for four absorption passes through the thin disk. Efficient laser operation requires cryogenic cooling in this case. For operation at higher temperatures a more elaborate multipass scheme is required.

In [6.120] a pump geometry is described that allows 16 passes through the thin disk. The pump radiation is almost completely absorbed in a 220- μm thick disk and the heat sink temperature could be raised to 15°C and still achieve highly efficient operation. The optical design consists of a parabolic mirror and roof prism combination. A beam parallel to the optical axis of the parabolic mirror focuses the off-axis radiation and directs it to the thin disk. The reflected pump radiation returns to the parabolic mirror where it is collimated and directed by roof prism to another spot on the parabolic mirror. Eight reflections on the parabolic mirror correspond to 16 absorption passes in the active medium. At a pump power of 65 W and a heat sink temperature of 15°C, the laser output was 38 W corresponding to an optical efficiency close to 58%.

7. Thermo-Optic Effects

The optical pumping process in a solid-state laser material is associated with the generation of heat for a number of reasons:

- (a) The energy difference of the photons between the pump band and the upper laser level is lost as heat to the host lattice; similarly, the energy difference between the lower laser level and the ground state is thermalized. The difference between the pump and laser photon energies, termed quantum defect heating, is the major source of heating in solid-state lasers.
- (b) In addition, nonradiative relaxation from the upper laser level to the ground state, owing to concentration quenching, and nonradiative relaxation from the pump band to the ground state will generate heat in the active medium.
- (c) In flashlamp-pumped systems, the broad spectral distribution of the pump source causes a certain amount of background absorption by the laser host material, particularly in the ultraviolet and infrared regions of the lamp spectrum. Absorption of lamp radiation by impurity atoms and color centers can further increase heating.

The temperature gradients setup in the gain material as a result of heating can lead to stress fracture, which represents the ultimate limit in average power obtainable from a laser material. Below the stress fracture limit thermal lensing and birefringence adversely affect the output beam quality. Also, as a result of thermal lensing, the operating point of the resonator within the stability diagram becomes a function of input power. Therefore the output beam quality and mode structure are power-dependent because the thermal lens can only be compensated for a fixed input power level.

Efficient heat removal and the reduction of the thermal effects that are caused by the temperature gradients across the active area of the laser medium usually dominate design considerations for high-average-power systems.

The ability to predict the amount of heat generated in a laser material is important to obtain an indication of the thermo-optic effects that can be expected in a particular rod or slab laser. In the laser literature several parameters have been introduced to quantify the amount of heat dissipated by the active material. The fractional thermal loading η_h is defined as the ratio of heat produced to absorbed pump power or energy. A different way to quantify heat generation is expressed by the parameter χ , defined as the ratio of heat deposited to energy stored in the upper laser level.

The theoretical lower limit of η_h for Nd:YAG lasing at 1.06 μm and pumped with a laser diode pump source at 808 nm is $\eta_h = 1 - \lambda_p/\lambda_L = 0.24$, where $\eta_S = \lambda_p/\lambda_L$

is the Stokes factor discussed in Sect. 3.4.1 and λ_p and λ_L are the wavelengths of the pump and laser beam, respectively.

A Yb:YAG crystal lasers at 1.03 μm and can be diode-pumped at 943 nm. Owing to the smaller difference between pump and laser photon energy the theoretical thermal loading is only $\eta_h = 0.09$.

In flashlamps and cw krypton arc lamps optical excitation is less efficient compared to laser diode pumping because of the comparatively high content of short wavelength radiation in the spectrum. Therefore the difference between pump and laser photon energies is larger and results in sizeable quantum defect heating.

In actual lasers there are also a number of nonradiative decay processes that generate heat but do not contribute to laser output.

Concentration quenching reduces the inversion density and manifests itself by a rapid reduction of the fluorescence lifetime for doping levels above 1% in Nd:YAG. It causes a nonradiative decay of excited ions from the upper laser level to the ground state. A summary of published data is presented in [7.1].

Another source of heat generation is created by nonradiative sites. So-called “dark neodymium ions” or “dead sites” are ions that absorb pump photons but do not contribute to inversion. This leads to a pump quantum efficiency of less than unity [7.2].

The fraction of absorbed pump radiation converted into heat was measured to be around 30–32% for different Nd:YAG lasers pumped at 808 nm [7.3]. Estimated values of η_h derived from thermal measurements also suggest a value of $\eta_h = 0.32$ for Nd:YAG and $\eta_h = 0.11$ for Yb:YAG pumped at 943 nm [7.4].

In Sect. 3.4.2 we have combined the losses due to nonradiative processes in the quantum efficiency η_Q . For Nd:YAG we use $\eta_Q = 0.9$ (see Fig. 6.69), which gives a heat load of $\eta_h = 1 - \eta_Q \eta_s = 0.32$ for diode pumping, consistent with the measured value.

The parameter χ is usually determined by measuring the small-signal gain with a probe beam at the end of the pump pulse. The stored energy is then calculated from the gain, and the heat deposited is deduced from the observed temperature rise of the material. In the energy storage mode the value of χ depends on the pump pulse length because of the fluorescence losses (see (3.53)). Operated in the energy storage mode, a value of $\chi = 1.1$ was measured for a 200- μs -long pump pulse [7.5].

In flashlamp-pumped lasers, the quantum defect heating is larger as already mentioned, and in addition to the nonradiative processes described above there is additional heating because of the background absorption of the pump radiation by the host, and additional absorption because of impurity atoms and color centers. Measured values for χ range from 2.9 to 3.3 for Nd:YAG and from 1.6 to 3.0 for Nd:phosphate glass doped at 3–6% neodymium [7.6,7].

Comparing the value of χ measured for flashlamp and diode pumping of an Nd:YAG laser suggests that diode pumping produces only one third of the heat in the crystal compared to flashlamp-pumped systems.

From the magnitude of η_h and χ one can obtain an estimate of the amount of heat generated in the laser material relative to the output of the laser system. Absorbed power in the laser element is channeled into heat, stimulated emission, and

fluorescence. In the presence of a strongly saturating stimulated emission the fluorescence becomes insignificant. Only the excited ions that are outside the volume occupied by the resonator modes will relax as fluorescence to the ground state.

For example, from the definition of η_h it follows that the ratio of heat to inversion power density available for extraction is $\eta_h/(1 - \eta_h)$. If we account for the resonator losses expressed by the coupling efficiency η_c and for the less than unity overlap of the gain region with the resonator modes expressed by η_B (see Sect. 3.4.1) we obtain, for the ratio of heat load to output power,

$$\frac{P_h}{P_{\text{out}}} = \frac{\eta_h}{\eta_c \eta_B (1 - \eta_h)}. \quad (7.1)$$

This expression is a lower limit because it does not include the portion of the resonator losses which appear as heat in the active medium as a result of absorption of intracavity laser radiation by the laser material.

Typical examples of heating generated in the laser process are provided in Sect. 6.2. In the laser-diode-pumped systems analyzed in Fig. 6.69 an output of 7 W is associated with 5 W of heating due to the quantum defect and nonradiative processes. This is expressed by $\eta_h = 0.32$. In addition, a fraction of the absorption losses also contribute to the heating of the laser crystal. Let us assume that the 7 W output is produced by a 5-cm-long Nd:YAG rod with an absorption coefficient of 10^{-3} cm^{-1} . If the resonator has an output coupler with a reflectivity of 90%, then the intracavity power is 133 W, which produces about 0.7 W of absorption losses in the Nd:YAG rod. Therefore, in the example given in Fig. 6.69, the total heat load for the crystal is around 5.7 W. With this number a ratio of $P_h/P_{\text{out}} = 0.81$ is obtained for the laser postulated in Fig. 6.69.

In general, one can assume a ratio of

$$P_h/P_{\text{out}} = 0.8-1.1 \quad (7.2)$$

for a diode-pumped Nd:YAG laser, depending on the crystal quality and the overlap of the resonator and pump region. In flashlamp- or krypton arc lamp-pumped Nd:YAG lasers the thermal load of the crystal is about three times higher

$$P_h/P_{\text{out}} = 2.5-3.3. \quad (7.3)$$

In the example of the energy flow in an arc lamp system summarized in Table 6.5, the measured ratio of heat load to laser output was about 2.5 for a highly multimode beam. Any measures to improve the beam quality will invariably result in a reduced overlap between resonator mode and pump region and, therefore, the ratio of heat load to laser output will increase.

In this context it is of interest to point out that the thermal load in an Nd:YAG crystal is different under lasing and nonlasing conditions. This is easily observed in cw or repetitively pumped lasers if the lasing action is interrupted by blocking the beam in the resonator. After lasing is reestablished, the beam divergence will show a transient behavior until the thermal load, and therefore thermal lensing, has reached its final value.

The fraction of the absorbed pump power that is converted into heat was determined by Fan [7.4] to be $\eta_h = 0.37\text{--}0.43$ without stimulated emission, and a value of $\eta_h = 0.32$ was estimated under lasing conditions. The reason for this difference is that the absorbed pump power which is converted into heat depends on whether the upper-state population is extracted by lasing action or depleted by fluorescence. The latter has about a 10% branching ratio into nonradiative decay that contributes to the heat load. Far above threshold, where the upper-state population is extracted by stimulated emission and fluorescence is negligible, thermal loading is decreased.

7.1 Cylindrical Geometry

The combination of volumetric heating of the laser material by the absorbed pump radiation and surface cooling required for heat extraction leads to a nonuniform temperature distribution in the rod. This results in a distortion of the laser beam due to a temperature- and stress-dependent variation of the index of refraction. The thermal effects which occur in the laser material are thermal lensing and thermal stress-induced birefringence.

An additional issue associated with thermal loading is stress fracture of the laser material. Stress fracture occurs when the stress induced by temperature gradients in the laser material exceeds the tensile strength of the material. The stress-fracture limit is given in terms of the maximum power per unit length dissipated as heat in the laser medium.

7.1.1 Temperature Distribution

We will first consider the steady-state condition that exists in a cw laser or in a high repetition rate system where the time interval between pulses is short compared to the thermal time constant of the laser rod.

In a single-shot laser the transit thermal profile in the laser rod is a combination of a fast heating process during the pump pulse and a slow thermal decay during the cooling phase. Heat transport in a laser rod has typically a much longer time constant than the pump pulse of a few hundred microseconds or less. Since laser action occurs only during the pump pulse, or in case of Q-switching toward the end, heat transport can be neglected. In single-shot operation, optical distortions are the result of thermal gradients generated by nonuniform absorption of the pump radiation.

In a low repetition rate laser the thermal profile has a component caused by heating during the pump pulse and a residual thermal component that is the result of thermal energy remaining in the laser rod from previous pump pulses.

Steady-State Condition

We consider the case where the heat generated within the laser rod by pump-light absorption is removed by a coolant flowing along the cylindrical rod surface. With the assumption of uniform internal heat generation and cooling along the cylindrical

surface of an infinitely long rod, the heat flow is strictly radial, and end effects and the small variation of coolant temperature in the axial direction can be neglected. The radial temperature distribution in a cylindrical rod with the thermal conductivity K , in which heat is uniformly generated at a rate Q per unit volume, is obtained from the one-dimensional heat conduction equation [7.8]

$$\frac{d^2T}{dr^2} + \left(\frac{1}{r}\right) \left(\frac{dT}{dr}\right) + \frac{Q}{K} = 0. \quad (7.4)$$

The solution of this differential equation gives the steady-state temperature at any point along a radius of length r . With the boundary condition $T(r_0)$ for $r = r_0$, where $T(r_0)$ is the temperature at the rod surface and r_0 is the radius of the rod, it follows that

$$T(r) = T(r_0) + \left(\frac{Q}{4K}\right) (r_0^2 - r^2). \quad (7.5)$$

The temperature profile is parabolic, with the highest temperature at the center of the rod. The temperature gradients inside the rod are not a function of the surface temperature $T(r_0)$ of the rod. The heat generated per unit volume can be expressed as

$$Q = \frac{P_h}{\pi r_0^2 l}, \quad (7.6)$$

where P_h is the total heat dissipated by the rod and l is the length of the rod. The temperature difference between the rod surface and the center is

$$T(0) - T(r_0) = \frac{P_h}{4\pi Kl}. \quad (7.7)$$

The transfer of heat between the rod and the flowing liquid creates a temperature difference between the rod surface and the coolant. A steady state will be reached when the internal dissipation P_h is equal to the heat removed from the surface by the coolant

$$P_h = 2\pi r_0 l h [T(r_0) - T_F], \quad (7.8)$$

where h is the surface heat transfer coefficient and T_F is the coolant temperature. With $A = 2\pi r_0 l$ being the surface area of the rod, it follows that

$$T(r_0) - T_F = \frac{P_h}{Ah}. \quad (7.9)$$

Combining (7.7) and (7.9) one obtains, for the temperature at the center of the rod,

$$T(0) = T_F + P_h \left(\frac{1}{4\pi Kl} + \frac{1}{Ah} \right). \quad (7.10)$$

Thus, from the geometry, and the appropriate system and material parameters, the thermal profile of the crystal can be determined, except that h must be evaluated.

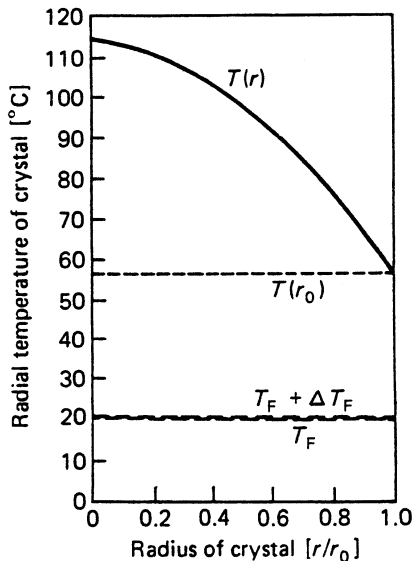


Fig. 7.1. Radial temperature distribution within an Nd:YAG crystal as a function of radius. T_F is the temperature of coolant entering the flowtube assembly, ΔT_F is the axial temperature gradient, and $T(r_0)$ is the rod surface temperature [7.9]

The convective heat transfer coefficient h is a function of the coolant flow rate, the physical properties of the coolant and laser rod, and the pumping cavity geometry.

The boundary conditions for the heat transfer coefficient are a thermally insulated laser rod ($h = 0$) or unrestricted heat flow from the rod surface to a heat sink ($h = \infty$). For cases of practical interest the heat transfer coefficient is typically around $h = 0.5\text{--}2 \text{ W cm}^{-2} \text{ C}^{-1}$.

If we assume water as the coolant, and a turbulent flow in an annular space formed by a laser rod inside a flowtube, we can greatly simplify the rather cumbersome general expressions for h [7.9, 10].

$$h = 10.47 \times 10^{-3} \frac{(D_2/D_1)^{0.53}}{(D_2 - D_1)(D_2 + D_1)^{0.8}} f_r^{0.8} \quad (\text{W/cm K}), \quad (7.11)$$

where D_1 and D_2 are the diameter of the rod and the inner diameter of the coolant jacket in cm, respectively, and f_r is the flow rate in cm^3/s . For example, for a rod of diameter $D_1 = 0.3 \text{ cm}$ and an inner diameter $D_2 = 0.8 \text{ cm}$ of the flowtube, we obtain $h = 1.8 \text{ W/cm}^2 \text{ K}$ for a water flow of $150 \text{ cm}^3/\text{s}$.

Figure 7.1 shows as an example the radial temperature profile in an Nd:YAG rod calculated from (7.10). The laser, which delivered between 200 and 250 W of output, was pumped at 12 kW of input power. The following parameters have been used in the numerical calculations of the temperature profile in the crystal: rod length $l = 7.5 \text{ cm}$; rod radius $r_0 = 0.32 \text{ cm}$; flowtube inside radius $r_F = 0.7 \text{ cm}$; power dissipated by the Nd:YAG rod $P_h = 600 \text{ W}$; flow rate of the coolant $f_r = 142 \text{ cm}^3/\text{s}$; heat transfer coefficient $h = 0.58 \text{ W/cm}^2 \text{ K}$; and fluid temperature entering the cavity $T_F = 20^\circ\text{C}$. As can be seen from this figure, the maximum temperature of the crystal occurring at the center is 114°C . The large temperature gradient of 57°C between the center of the crystal and the surface is responsible for the high stresses present in the material.

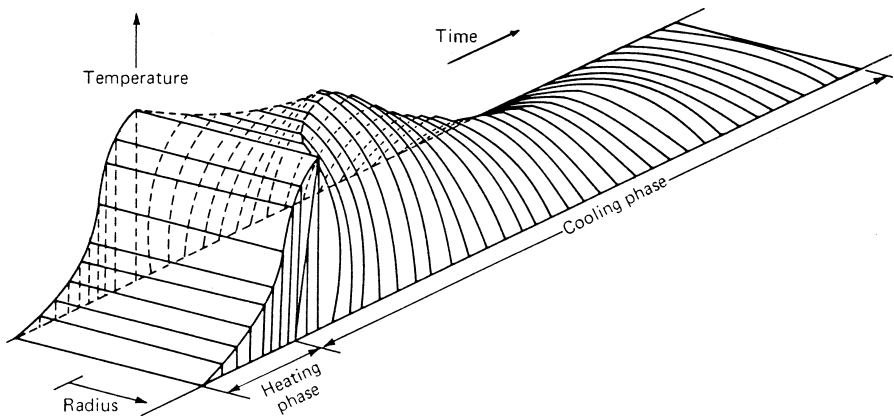


Fig. 7.2. Thermal relaxation of a single input pulse in a cylindrical laser rod

Single-Shot Operation

If a laser rod is pumped by a single pump pulse, a transient thermal profile will be established, which is the result of a fast heating process followed by a slow recovery of the rod to thermal equilibrium. Figure 7.2 sketches the transient temperature distribution in an optically pumped cylindrical laser rod. During the flashlamp pulse, energy is absorbed by the laser, crystal. At the end of the pump pulse, the temperature of the rod increases uniformly by ΔT above the coolant temperature if we assume uniform absorption of pump radiation. Since only the surface of the rod is in contact with the coolant, a radial heat flow develops at the end of the pump pulse. The initially uniform temperature distribution changes to a parabolic temperature profile which decays with a certain time constant. Since lasing action occurs during or at the end of the pump cycle, the optical distortion in a single-shot laser arises from the thermal gradients produced during the pump cycle and not from heat flow as a result of cooling.

If the temperature of the laser rod increases uniformly over the rod cross section, the bulk temperature rise at the end of the pump pulse is given by

$$\Delta T = \frac{Q}{cV\varrho}, \quad (7.12)$$

where Q is the thermal energy deposited in the rod, c is the specific heat, V is the volume, and ϱ is the density of the laser material. The bulk temperature rise as a function of time depends on the shape of the flashlamp pulse. The energy deposited in the rod is

$$Q = \int_0^{\infty} P(t) dt, \quad (7.13)$$

where $P(t)$ is the pulse shape of the pump power. The time dependence of the

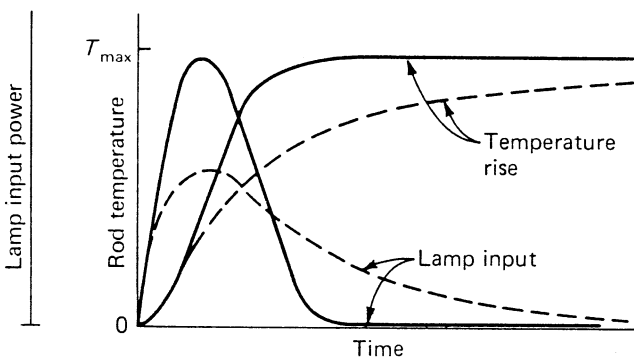


Fig. 7.3. Temperature rise in a laser rod for different lamp input pulse shapes

temperature during the pump pulse can be obtained from

$$T(t) = \frac{1}{cVQ} \int_0^t P(t) dt. \quad (7.14)$$

In Fig. 7.3 the temperature rise for several common pulse shapes is illustrated. Measurements have shown that the temperature increases without any observable delay with respect to the energy deposited in the rod. In air-cooled laser heads, a considerable amount of rod heating can take place after the pump pulse because of conductive and convective heat transfer from the hot flashlamp. In liquid-cooled systems, most of this long IR radiation is absorbed and carried away by the coolant.

If the temperature rises uniformly in the active material, thermal effects in an oscillator are limited to a frequency shift of the emitted radiation and an increase in optical length of the resonator. Nonuniform pumping will also lead to thermal lensing and birefringence. If one assumes a pump-induced thermal profile $T(r)$ at a given time during the pump cycle, then thermal lensing for this particular instant in time can be calculated, as was discussed for the cw case.

The temperature profiles are usually inferred from an interferometric measurement of the optical path-length changes. If we ignore changes in refractive index resulting from thermal stress, then optical path length and temperature changes are related according to

$$\Delta(n_0l_0) = n_0l_0(\alpha_l + \alpha_n)\Delta T, \quad (7.15)$$

where n_0l_0 is the undistorted optical length, $\alpha_l = (1/l_0)(dl/dT)$ is the thermal coefficient of linear expansion, and $\alpha_n = (1/n_0)(dn/dT)$ is the thermal coefficient of refractive index.

Most measurements reveal that the optical path-length change is actually concave and the rod behaves like a negative lens. The implication is that the absorption of pump energy is higher at the outer edge of the rod than in the center. Figure 7.4 shows an example of a concave temperature profile calculated from the fringe pattern of an

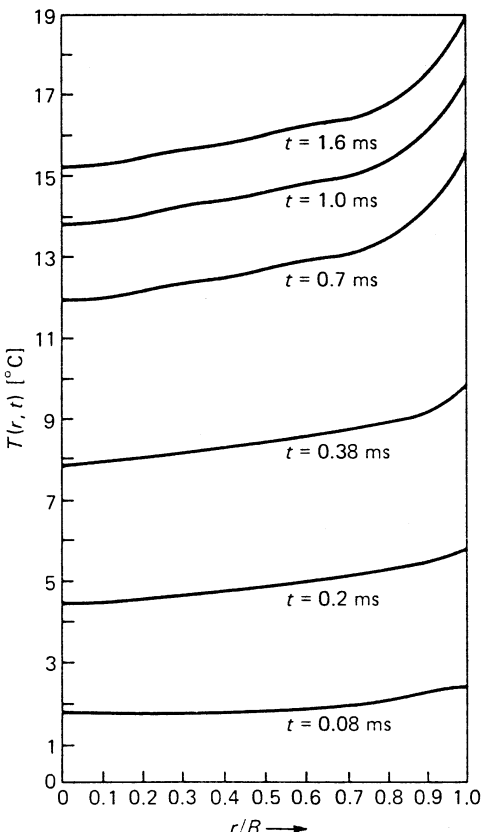


Fig. 7.4. Temperature rise in a 7.5-cm-long and 1.0-cm-diameter Nd:Glass rod pumped by a 15-cm-long helical flashlamp operated at 11500 J input [7.11]

interferometric measurement [7.11]. The total path-length change in the center of this rod was nine wavelengths.

The transient temperature distribution in a laser rod affects energy output and beam divergence of the laser. Calculations treating the thermal relaxation of a cylindrical laser rod which is suddenly heated by a pump pulse can be found in [7.12, 13]. A general theory describing the transient thermal profile in a pulse-pumped rod for a large variety of operating parameters has been presented by Koechner [7.14]. The calculations were performed by solving the heat diffusion equation for a cylindrical rod for radial heat flow. The general solution of this equation is given by Carslaw and Jaeger [7.8] for an infinite circular cylinder.

The general expression of the radial temperature profile $T(r, t)$ in a solid rod as a function of time can be expressed in a series of Bessel functions of the first kind and zero-, first-, and second-order (J_0, J_1, J_2)

$$\frac{T(r, t)}{\Delta T} = \sum J_{0,1,2} \left(\frac{t}{\tau}, \frac{r}{r_0}, \frac{\Delta t}{\tau}, M, g, A \right), \quad (7.16)$$

where ΔT is the initial temperature rise, t/τ is the normalized time, r/r_0 is the

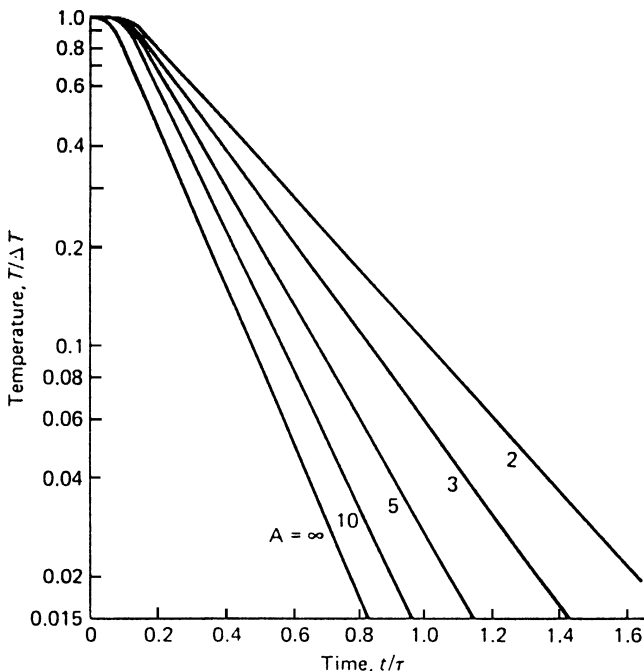


Fig. 7.5. Temperature decay in the center of an optically pumped laser rod versus time. Initial temperature rise is uniform throughout the rod ($g = 0$). Parameter is the cooling factor A [7.14]

normalized rod radius, $\Delta t/\tau$ is the normalized pulse repetition rate (Δt is the pulse interval time), M is the number of consecutive pulses ($M \rightarrow \infty$ at steady state), g specifies the temperature distribution in the rod at the end of the first pump pulse, and A is a cooling parameter which specifies the cooling condition of the rod. Figures 7.5–6 illustrate some of the results of an analysis of (7.16). Shown are thermal distributions in laser rods for a variety of system parameters. Since all quantities are normalized, the results are applicable to any laser host, rod size, cooling flow, pump energy, etc. In order to be able to apply the results to practical cases, we have to discuss briefly the normalization parameters τ , ΔT , and A . The thermal time constant of the rod is

$$\tau = r_0^2/k, \quad (7.17)$$

where r_0 is the rod radius and k is the thermal diffusivity, which is related to the materials parameters by

$$k = K/c\gamma, \quad (7.18)$$

where K is the thermal conductivity, γ is the mass density, and c is the specific heat. The initial temperature distribution at the end of the pump cycle is approximated by a parabolic function

$$T(r, 0) = \Delta T \left[1 + g \left(\frac{r}{r_0} \right)^2 \right], \quad (7.19)$$

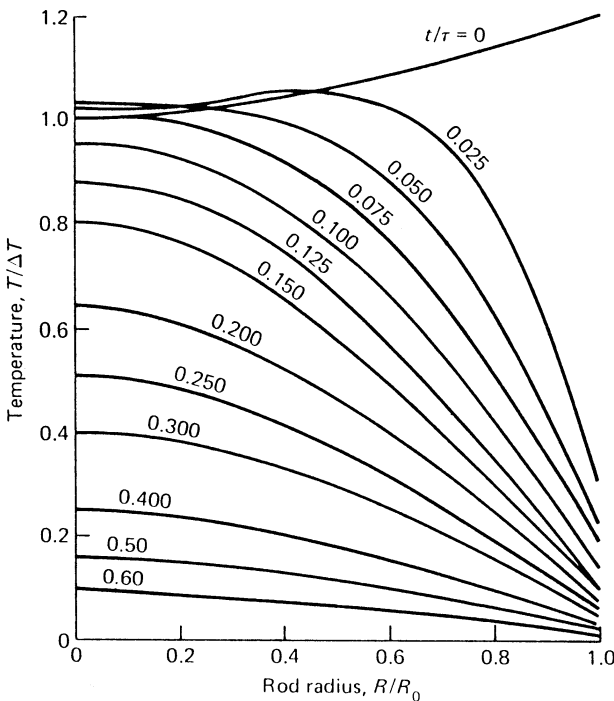


Fig. 7.6. Temperature profile of a solid laser rod for single-shot operation. Pumping coefficient $g = 0.2$, cooling factor $A = 10$ [7.14]

where ΔT is the temperature rise in the center of the rod and g is a measure of the pumping nonuniformity; for example, $g = 0$ indicates a uniform pump distribution across the rod, $g > 0$ represents a pumping nonuniformity leading to a negative lensing effect, and focusing of pump radiation in the rod can be expressed by $g < 0$. The amount of heat deposited in the laser rod is given by

$$Q = 2\pi l_0 c \gamma \int_0^{r_0} T(r, 0) r dr. \quad (7.20)$$

From (7.19, 20) it follows that the temperature rise ΔT in the center of the rod at the end of the first pump cycle is

$$\Delta T = \frac{Q}{V c \gamma (1 + g/2)}. \quad (7.21)$$

The cooling condition of the rod is specified by a dimensionless parameter

$$A = r_0 h / K, \quad (7.22)$$

where h is the surface heat transfer coefficient.

Figure 7.5 illustrates the thermal relaxation of a cylindrical laser rod pumped by an isolated pulse. The temperature is plotted for the center of the rod as a function

of normalized time. The value $A = \infty$ represents the case of infinitely good thermal contact between the laser crystal and the cooling fluid; that is, the boundary surface of the rod is held at a constant temperature during the heat removal process. With this idealized assumption, the decay of thermal effects depends only on the thermal diffusivity and rod diameter. A thermal relaxation time

$$\tau' = r_0^2 / 4k \quad (7.23)$$

can be defined at which the temperature in the center of the rod has decayed to $1/e$ of the initial value ΔT .

In actual cases, however, it is the temperature of the coolant fluid which is constant and the surface of the rod which varies in temperature. As a result of this assumption, the temperature decay in a rod depends on the material parameters and the conduction of heat across the flow boundary. This condition is expressed by a finite value of A . For most liquid-cooled laser rods the value of the rod-surface cooling parameter A is between 2 and 10. Therefore, in practical situations the thermal relaxation processes are considerably slower than in the case where a zero thermal impedance between the rod surface and the cooling fluid is assumed.

Figure 7.6 shows the temperature profile in a solid rod as a function of time for a cooling factor of $A = 10$. It is assumed that the initial temperature distribution at the end of the pump pulse ($t/\tau = 0$) is parabolic, with the temperature of the cylindrical surface 20% higher than in the center of the rod ($g = 0.2$). As one can see from this figure, at the water-cooled cylindrical surface the temperature decreases very rapidly, causing large temperature gradients. The temperature in the center changes very little for about 0.075 time constants. Actually, the temperature in the center shows a slight increase owing to heat flow toward the center immediately after the flashlamp pulse.

The thermal relaxation in a laser rod can be determined experimentally by measuring the thermally induced birefringence or lensing or by observing an interference fringe pattern. Figure 7.7 shows the temperature decay in a ruby rod, 1 cm in diameter and 12 cm long [7.15]. The temperature was calculated from the interference pattern which was recorded with a movie camera. According to (7.17), the thermal

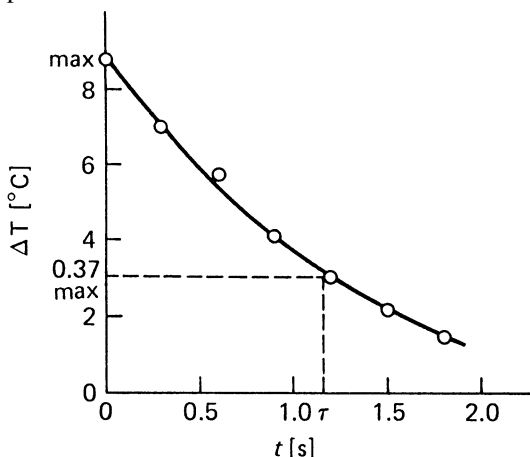


Fig. 7.7. Temperature difference ΔT between center and edge of a ruby rod after the pump pulse [7.15]

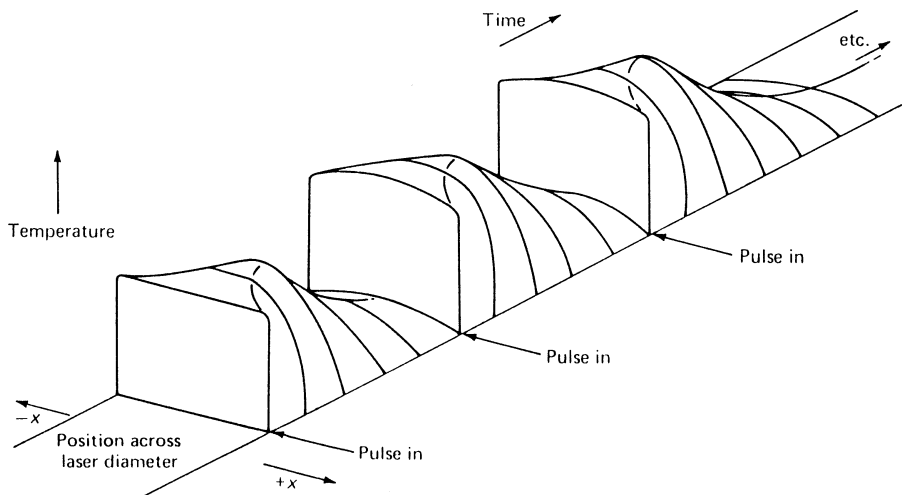


Fig. 7.8. Thermal profile in a laser rod when pump intervals are near the thermal relaxation time

time constant of this rod is about 2s. The temperature in the center of the rod has decayed to 0.37 of the initial value after 1.1 s. Comparing this data with Fig. 7.5 reveals a cooling parameter of this water-cooled rod of $A = 2$ or a surface heat transfer coefficient of $h = 1.68 \text{ W/cm}^2 \text{ K}$.

Repetitively Pulsed Lasers

In the previous subsection we discussed pump-induced thermal distortions which occur for single-shot lasers operated either in normal pulse or Q-switched operation. In this regime, the pump intervals are long with respect to the thermal relaxation of the laser rod, and the active material has returned to ambient temperature before the onset of the next pump pulse. If the laser is operated at a repetition rate at which there exists a residual temperature distribution from the previous pulse, a temperature buildup inside the material will occur. The residual temperature will accumulate for subsequent pulses until a steady-state condition is reached. Figure 7.8 displays the temperature profile of a laser operated at a fairly low repetition rate. The residual temperature has not completely decayed between pulses, and the initial uniform temperature rise caused by the pump source is modified to a slightly parabolic temperature profile.

Figure 7.9 shows a thermal buildup at a pulse interval smaller than the thermal relaxation time. Under these conditions, the laser rod will soon establish a steady-state operating condition where the radial flow of heat out of the rod will be equal to the total heat being put into the rod. During the transition period the cylindrical rod passes through several regions of radial thermal profiles as a steady-state equilibrium is approached. In the extreme case, when the pulse interval time becomes negligibly small as compared to the thermal relaxation time, the thermal profile in the laser rod

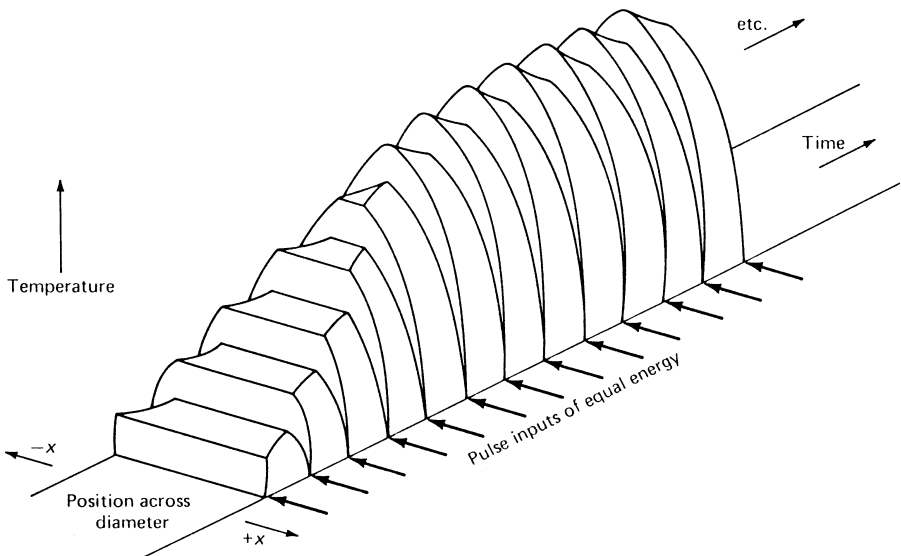


Fig. 7.9. Thermal buildup when the pulse interval time is less than the thermal relaxation time

approaches the cw condition. In this mode of operation the thermal effects depend only on the average input power.

Figure 7.10 exhibits temperature profiles at the end of each pump pulse for different repetition rates. As one can see from this figure, the initially concave temperature profile is changed to a convex profile. The absolute temperature as well as the temperature gradient at each point of the rod cross section increase for the higher repetition rates. Again, $A = 10$ and $g = 0.2$ were chosen in (7.16) for the cooling factor and the pumping coefficient, respectively. After the first pulse, the outside of the rod is at a higher temperature than the center as a result of the assumed nonuniform pump light absorption. In Fig. 7.10a the negative focusing effect created by nonuniform pumping is partially compensated by the interpulse cooling process. In Figs. 7.10b and c the initial diverging condition of the rod changes to a strongly focusing condition after quasi-steady state is reached.

If a laser is repetitively pumped, the thermal buildup in the rod depends on the ratio of the pulse interval time to the thermal time constant. In Fig. 7.11 the temperature buildup at the center of a cylindrical rod is plotted as a function of number of pump pulses. The parameter is the ratio $\Delta t/\tau$. The values for the temperature buildup are obtained at the end of each pump pulse. During the pulse interval time the temperature decreases, of course. The cooling factor was chosen $A = 10$ and the pumping coefficient $g = 0$. In the case of $\Delta t = \tau$, any distortion introduced by the pumping process has a chance to relax out before the onset of the next pump pulse. If the pulse interval time Δt is shorter than the thermal relaxation time τ , a temperature buildup occurs. For example, for $\Delta t/\tau = 0.2$, the incremental temperature rise at the center of the rod is more than twice as high as compared to the single-pulse operation.

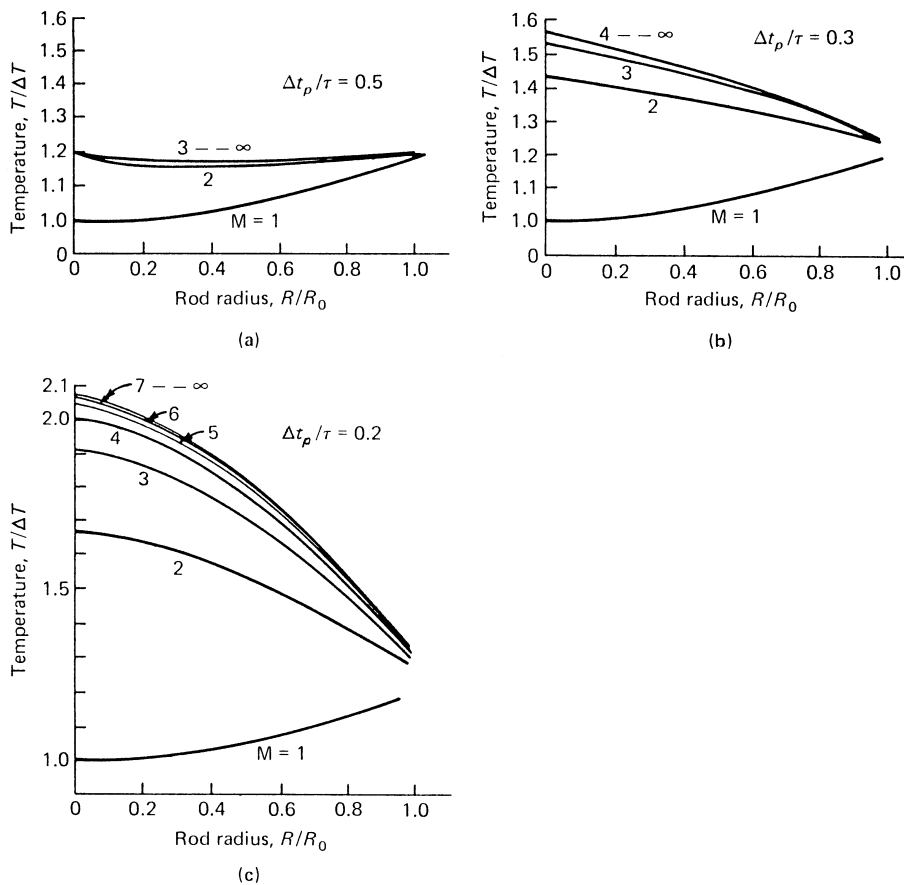


Fig. 7.10. Thermal profile in a repetitively pumped laser rod at the end of each pump cycle. Parameter is the normalized repetition rate. Δt is the pulse interval time and τ is the thermal time constant. M is the number of consecutive pulses. Cooling factor is $A = 10$ and pumping coefficient is $g = 0.2$ [7.14]

7.1.2 Thermal Stresses

The temperature gradients generate mechanical stresses in the laser rod since the hotter inside area is constrained from expansion by the cooler outer zone. The stresses in a cylindrical rod, caused by a temperature distribution $T(r)$, can be calculated from the equations given in [7.16]. Equations (7.24–26) describe the radial σ_r , tangential σ_ϕ , and axial σ_z stress in an isotropic rod with free ends and a temperature distribution according to (7.5),

$$\sigma_r(r) = QS(r^2 - r_0^2) \quad (7.24)$$

$$\sigma_\phi(r) = QS(3r^2 - r_0^2) \quad (7.25)$$

$$\sigma_z(z) = 2QS(2r^2 - r_0^2), \quad (7.26)$$

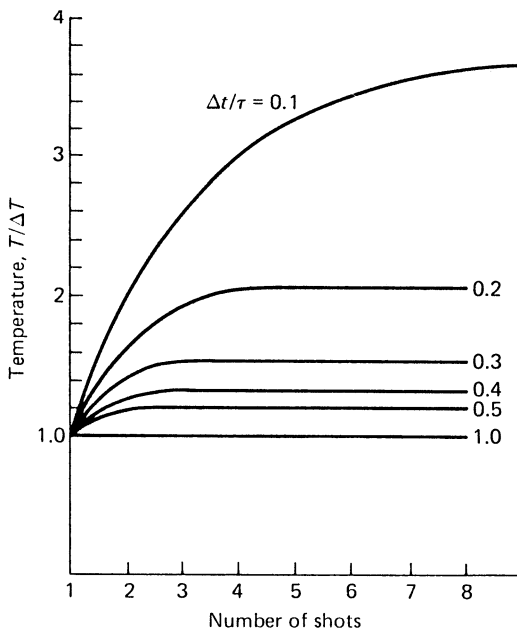


Fig. 7.11. Temperature buildup in the center of a repetitively pumped laser rod versus number of shots. Parameter is the normalized repetition rate. Cooling factor $A = 10$ and pumping coefficient $g = 0$ [7.14]

where the factor $S = \alpha E[16K(1 - \nu)]^{-1}$ contains the material parameters, E is Young's modulus, ν is Poisson's ratio, and α is the thermal coefficient of expansion. The stress components, σ_r , σ_ϕ , σ_z represent compression of the material when they are negative and tension when they are positive. We notice that the stress distributions also have a parabolic dependence on r . The center of the rod is under compression. The radial component of the stress goes to zero at the rod surface, but the tangential and axial components are in tension on the rod surface by virtue of the larger bulk expansion in the rod's center compared to the circumference.

Figure 7.12 gives the stresses as a function of radius inside the Nd:YAG rod whose temperature profile was shown in Fig. 7.1. From these curves it follows that the highest stresses occur at the center and at the surface. Since the tensile strength of Nd:YAG is 1800–2100 kg/cm², the rod is stressed about 70% of its ultimate strength. As the power dissipation is increased, the tension on the rod surface increases and may exceed the tensile strength of the rod, thereby causing fracture. It is of interest to determine at what power level this will occur. Using (7.25) we find, for the hoop stress,

$$\sigma_\phi = \frac{\alpha E}{8\pi K(1 - \nu)} \frac{P_h}{l}. \quad (7.27)$$

The total surface stress σ_{\max} is the vector sum of σ_ϕ and σ_z , i.e., $\sigma_{\max} = 2^{1/2}\sigma_\phi$.

We note from (7.27) that the tension on the surface of a laser rod depends on the physical constants of the laser material and on the power dissipated per unit length of the material, but does not depend on the cross section of the rod. Upon substitution

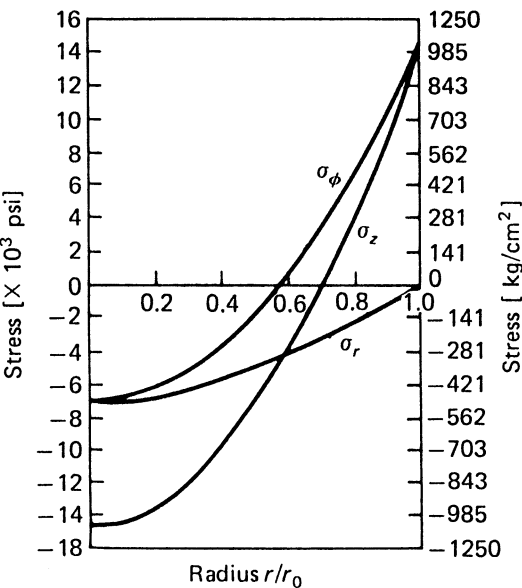


Fig. 7.12. Radial (σ_r), tangential (σ_ϕ), and axial (σ_z) stress components within an Nd:YAG crystal as a function of radius [7.9]

of σ_{\max} with the value of the tensile strength of Nd:YAG, we find that with 150 W dissipated as heat per centimeter length of Nd:YAG rod, the tension on the surface of the rod equals the tensile strength of the material. The actual rupture stress of a laser rod is very much a function of the surface finish of the rod, and can vary by almost a factor of 3 in Nd:YAG [7.17].

Stress Fracture Limit

The mechanical properties of the laser host material determine the maximum surface stress that can be tolerated prior to fracture. If there were no other constraints, such as stress-induced focusing and birefringence, the thermal loading and thus average output power of a rod laser could be increased until stress fracture occurred. If σ_{\max} is the maximum surface stress at which fracture occurs, then we can rewrite (7.27) as follows:

$$\frac{P_h}{l} = 8\pi R_s, \quad (7.28)$$

where

$$R_s = \frac{K(1-\nu)}{\alpha E} \sigma_{\max} \quad (7.29)$$

is a “thermal shock parameter.” A larger R_s indicates a higher permissible thermal loading before fracture occurs. Table 7.1 lists typical values for a number of laser materials if we assume a standard surface treatment.

Table 7.1. Thermal shock parameter for different materials

Material	Glass	GSGG	YAG	Al_2O_3
Thermal shock parameter R_s [W/cm]	1	6.5	7.9	100

7.1.3 Photoelastic Effects

The stresses calculated in the previous subsection generate thermal strains in the rod, which, in turn, produce refractive index variations via the photoelastic effect. The refractive index of a medium is specified by the indicatrix that, in its most general case, is an ellipsoid. A change of refractive index due to strain is given by a small change in shape, size, and orientation of the indicatrix [7.18]. The change is specified by small changes in the coefficients B_{ij} of the perturbed indicatrix.

$$\Delta B_{ij} = p_{ijkl} \varepsilon_{kl} \quad (i, j, k, l = 1, 2, 3), \quad (7.30)$$

where p_{ijkl} is a fourth-rank tensor giving the photoelastic effect. The elements of this tensor are the elasto-optical coefficients. ε_{kl} is a second-rank strain tensor.

Working with a fourth-rank tensor is inconvenient so using a matrix notation [7.19], i.e. 1 = xx , 2 = yy , 3 = zz , 4 = zy , 5 = zx , 6 = yx , Eq. (7.30) is changed to

$$\Delta B_m = p_{mn} \varepsilon_n \quad (m, n = 1, 2, \dots, 6). \quad (7.31)$$

For many crystals, the elasto-optical coefficients p_{mn} which express the change in the indicatrix proportional to the strain are tabulated. The 36 coefficients are much reduced for most laser materials of interest. For example in an isotropic material such as Nd:Glass the stress optic tensor must be invariant under spatial rotation and under inversion. This restricts the number of nonzero independent stress optic coefficients to two. A cubic crystal such as Nd:YAG has three independent p_{mn} coefficients.

We will confine our calculation to the case of an Nd:YAG laser rod. The method, however, is applicable to any material if the proper photoelastic matrix is used. Since Nd:YAG is a cubic crystal, the indicatrix is a sphere. Under stress the indicatrix becomes an ellipsoid. Nd:YAG rods are grown with the cylindrical axes along the [111] direction. The light propagates in this direction, and thus the change of the refractive index along the [111] is of interest.

Since the transverse stresses are in the radial and tangential directions—relative to the coordinate system shown in Fig. 7.13—the local indicatrix also orients its axis in these directions. In a cylindrical coordinate system the photoelastic changes in the refractive index for the r and ϕ polarizations are given by [7.19]

$$\Delta n_r = -\frac{1}{2} n_0^3 \Delta B_r \quad (7.32)$$

and

$$\Delta n_\phi = -\frac{1}{2} n_0^3 \Delta B_\phi. \quad (7.33)$$

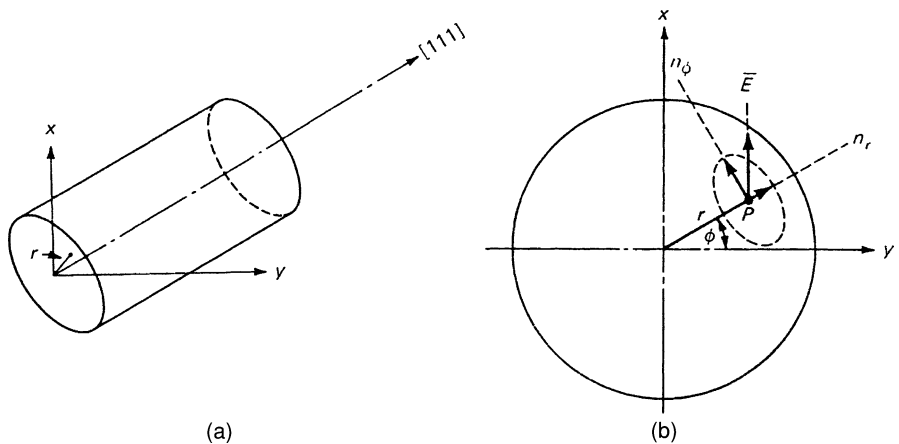


Fig. 7.13. (a) Crystal orientation for an Nd:YAG rod and (b) orientation of the indicatrix of the thermally stressed Nd:YAG rod in a plane perpendicular to the rod axis

A considerable amount of tensor calculation is required to determine the coefficients ΔB_r and ΔB_ϕ in a plane perpendicular to the [111] direction of the Nd:YAG crystal. The technique used in these calculations consists of introducing the elasto-optic coefficients for Nd:YAG into the matrix form p_{mn} of the photoelastic tensor. The published values of these coefficients are given in a [100]-oriented Cartesian coordinate frame: $p_{11} = -0.029$; $p_{12} = +0.0091$; and $p_{14} = -0.0615$. The strain tensor is obtained from the stresses calculated in (7.24)–(7.26). After a coordinate transformation to bring p_{mn} and ε_{kl} into the same coordinate system, the tensor operation according to (7.30) can be performed. Introducing the expression for ΔB_r and ΔB_ϕ into (7.32), (7.33), the refractive index changes are given by [7.20, 21]

$$\Delta n_r = -\frac{1}{2} n_0^3 \frac{\alpha Q}{K} C_r r^2, \quad (7.34)$$

$$\Delta n_\phi = -\frac{1}{2} n_0^3 \frac{\alpha Q}{K} C_\phi r^2, \quad (7.35)$$

where C_r and C_ϕ are functions of the elasto-optical coefficients of Nd:YAG,

$$C_r = \frac{(17\nu - 7)p_{11} + (31\nu - 17)p_{12} + 8(\nu + 1)p_{44}}{48(\nu - 1)},$$

$$C_\phi = \frac{(10\nu - 6)p_{11} + 2(11\nu - 5)p_{12}}{32(\nu - 1)}.$$

The induced birefringence is determined from (7.34) and (7.35)

$$\Delta n_r - \Delta n_\phi = n_0^3 \frac{\alpha Q}{K} C_B r^2, \quad (7.36)$$

where

$$C_B = \frac{1 + \nu}{48(1 - \nu)}(p_{11} - p_{12} + 4p_{44}).$$

Inserting the values of the photoelastic coefficients and the material parameters of Nd:YAG, $\alpha = 7.5 \times 10^{-6}/^\circ\text{C}$, $K = 0.14 \text{ W/cm}^\circ\text{C}$, $\nu = 0.25$, $n_0 = 1.82$ into (7.34–36), one obtains $C_r = 0.017$, $C_\phi = -0.0025$, $C_B = -0.0099$, and

$$\Delta n_r = (-2.8 \times 10^{-6})Qr^2, \quad (7.37\text{a})$$

$$\Delta n_\phi = (+0.4 \times 10^{-6})Qr^2, \quad (7.37\text{b})$$

$$\Delta n_r - \Delta n_\phi = (-3.2 \times 10^{-6})Qr^2, \quad (7.37\text{c})$$

where Q has the dimension of watts per cubic centimeter and r is measured in centimeters.

7.1.4 Thermal Lensing

Having explored the stresses in the laser rod, we now turn to the optical distortions which are a result of both temperature gradients and stresses. The change of the refractive index can be separated into a temperature- and a stress-dependent variation. Hence

$$n(r) = n_0 + \Delta n(r)_T + \Delta n(r)_\varepsilon, \quad (7.38)$$

where $n(r)$ is the radial variation of the refractive index, n_0 is the refractive index at the center of the rod, and $\Delta n(r)_T$ and $\Delta n(r)_\varepsilon$ are the temperature- and stress-dependent changes of the refractive index, respectively.

The temperature-dependent change of the refractive index can be expressed as

$$\Delta n(r)_T = [T(r) - T(0)] \left(\frac{dn}{dT} \right). \quad (7.39)$$

With the aid of (7.5) and (7.7) we obtain

$$\Delta n(r)_T = -\frac{Q}{4K} \frac{dn}{dT} r^2. \quad (7.40)$$

As can be seen from (7.34), (7.35), and (7.40) the refractive index in a laser rod shows a quadratic variation with radius r . An optical beam propagating along the rod axis suffers a quadratic spatial phase variation. This perturbation is equivalent to the effect of a spherical lens. The focal length of a lens-like medium, where the refractive index is assumed to vary according to

$$n(r) = n_0 \left(1 - \frac{2r^2}{q^2} \right) \quad (7.41)$$

is given by

$$f \cong \frac{q^2}{4n_0}. \quad (7.42)$$

This expression is an approximation where it was assumed that the focal length is very long in comparison to the rod length. The distance f is measured from the principal plane of the rod to the focal point.

The total variation of the refractive index is obtained by introducing (7.34), (7.35), and (7.40) into (7.38):

$$n(r) = n_0 \left[1 - \frac{Q}{2K} \left(\frac{1}{2n_0} \frac{dn}{dT} + n_0^2 \alpha C_{r,\phi} \right) r^2 \right]. \quad (7.43)$$

As was discussed in the previous subsection, the change of refractive index due to thermal strain is dependent on the polarization of light; therefore the photo-elastic coefficient $C_{r,\phi}$ has two values, one for the radial and one for the tangential component of the polarized light. Comparing (7.43) with (7.41) yields

$$f' = \frac{K}{Ql} \left(\frac{1}{2} \frac{dn}{dT} + \alpha C_{r,\phi} n_0^3 \right)^{-1}. \quad (7.44)$$

In our final expression for the focal length of an Nd:YAG rod, we will include the contributions caused by end effects. Perturbations of the principal thermal distortion pattern occur in laser rods near the ends, where the free surface alters the stress character. The so-called end effects account for the physical distortion of the flatness of the rod ends. Self-equilibrating stresses causing a distortion of flatness were found to occur within a region of approximately one diameter from the ends of Nd:glass and one radius from the ends of Nd:YAG. The deviation from flatness of the rod ends is obtained from

$$l(r) = \alpha l_0 [T(r) - T(0)], \quad (7.45)$$

where l_0 is the length of the end section of the rod over which expansion occurs. With $l_0 = r_0$ and (7.5) we obtain

$$l(r) = \alpha r_0 \frac{Q}{4K} (r_0^2 - r^2) \quad (7.46)$$

The focal length of the rod caused by an end-face curvature is obtained from the thick-lens formula of geometric optics

$$f'' = \frac{R}{2(n_0 - 1)}, \quad (7.47)$$

where the radius of the end-face curvature is $R = -(d^2 l / dr^2)^{-1}$. From these expressions follows the focal length of the rod caused by a physical distortion of the flat ends

$$f'' = K [\alpha Q r_0 (n_0 - 1)]^{-1}. \quad (7.48)$$

The combined effects of the temperature- and stress-dependent variation of the refractive index and the distortion of the end-face curvature of the rod lead to the following

expression for the focal length

$$f = \frac{KA}{P_h} \left(\frac{1}{2} \frac{dn}{dT} + \alpha C_{r,\phi} n_0^3 + \frac{\alpha r_0(n_0 - 1)}{l} \right)^{-1}, \quad (7.49)$$

where A is the rod cross-sectional area and P_h is the total heat dissipated in the rod. If one introduces the appropriate materials parameters for Nd:YAG into (7.49) then one finds that the temperature-dependent variation of the refractive index constitutes the major contribution of the thermal lensing. The stress-dependent variation of the refractive index modifies the focal length about 20%. The effect of end-face curvature caused by an elongation of the rod is less than 6% [7.22].

Ignoring the end effects, we notice that the focal length is proportional to a material constant and the cross section A of the rod and is inversely proportional to the power P_h dissipated as heat in the rod. At first, it may be surprising that the length of the rod does not enter the equations. However, in a longer rod, for example, the reduction in power dissipation per unit length is offset by a longer path length.

We see from (7.49) that we have little flexibility in influencing the focal length. The material constants are determined when we choose the laser material: the dissipated power P_h is determined by the application (even though we may be able to reduce the heat load by avoiding unusable pump radiation); thus the only remaining design parameter is the rod cross section. The focal length can be increased by increasing A , but this is usually not a practical way of solving the problem, since a larger crystal reduces pump power density and therefore leads to lower gain.

According to (7.49), the focal length of a cylindrical laser rod, where heat is generated uniformly within the bulk material, can be written as

$$f = M_{r,\phi} P_{\text{in}}^{-1}, \quad (7.50)$$

where M contains all the material parameters of the laser rod and an efficiency factor η which relates the electrical input power to the power dissipated as heat in the rod ($P_h = \eta P_{\text{in}}$).

We can introduce a laser-rod sensitivity defined as

$$\frac{d(1/f)}{dP_{\text{in}}} = M_{r,\phi}^{-1}. \quad (7.51)$$

The sensitivity factor describes how much the optical power $1/f$ of a laser rod changes with input power. For an Nd:YAG rod 0.63 cm in diameter, and assuming that 5% of the electrical input power to the lamp is dissipated as heat, we obtain a change of focusing power of 0.5×10^{-3} diopters per watt of lamp input variation.

Returning now to (7.49), we can see that the rod acts as a bifocal lens with different focal lengths for radiation with radial and tangential polarization. Since a linear polarized wave or a nonpolarized wave incident on the crystal will always have components in radial and tangential directions, two focal points are obtained. For Nd:YAG one finds a theoretical value of $f_\phi/f_r = 1.2$. A difference in focal length for different polarizations means that a resonator designed to compensate for the lensing of the radial polarization cannot also compensate for the lensing of tangentially polarized light.

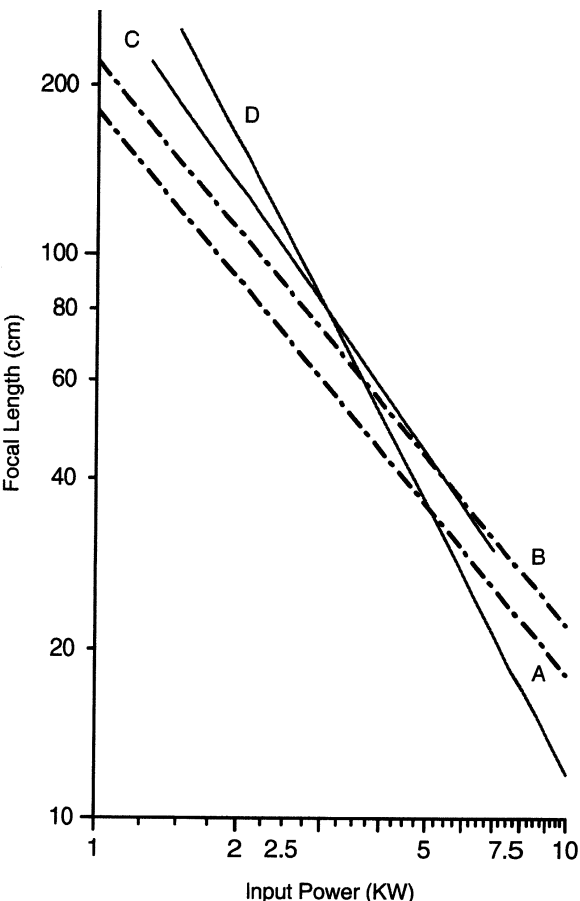


Fig. 7.14. Thermally induced back focal length as a function of lamp input power for Nd:YAG rods. Shown are calculated curves for (A) the radially and (B) tangentially polarized beam components, and (C, D) measurements of average focal length for different rods and pump cavities [7.23]

In Fig. 7.14 theoretical and measured thermally induced back focal lengths of various laser rods are plotted as a function of lamp input. Experimentally, the focal length was determined by projecting an HeNe laser beam through the rod and measuring the position of the beam diameter minimum. The measured curves have been observed for the same rod size in different pump cavities. The focal length changes faster than predicted, probably as a result of nonuniform pumping. The calculations for the theoretical back focal length assumed that 5% of the electrical input power will be dissipated as heat in a 7.5×0.63 cm diameter crystal. The value of M for the radially polarized beam (A) is $M_r = 18 \times 10^4$ W cm, and $M_\phi = 22 \times 10^4$ W cm for the tangentially polarized beam (B).

7.1.5 Stress Birefringence

We will now investigate the influence of thermally induced birefringence on the performance of a solid-state laser. Taking Nd:YAG as an example, it was shown in (7.34)

and (7.35) that the principal axes of the induced birefringence are radially and tangentially directed at each point in the rod cross section and that the magnitude of the birefringence increases quadratically with radius r . As a consequence, a linearly polarized beam passing through the laser rod will experience a substantial depolarization. We refer to Fig. 7.13, where we have chosen a point $P(r, \phi)$ in a plane perpendicular to the rod axes. At this point we have a radial refractive index component n_r , which is inclined at an angle ϕ with respect to the y -axis and a tangential component n_ϕ perpendicular to n_r . Assume that \bar{E} is the polarization vector for incident radiation. Radiation incident at point P must be resolved into two components, one parallel to n_r and the other parallel to n_ϕ . Since $\Delta n_r \neq \Delta n_\phi$, there will be a phase difference between the two components and the light will emerge elliptically polarized. This will occur for all points of the rod cross section with the exception for points located along the x - and y -axis in Fig. 7.13. Radiation incident along the y -axis will see only one refractive index, n_ϕ , while along the x -axis, n_r will be the only refractive index.

Birefringence effects in pumped laser rods can be studied in a polariscopic arrangement in which the expanded and collimated light beam from an HeNe laser serves as an illuminator for the observation of the rod between crossed polarizers. Because of thermally induced birefringence, the probe light suffers depolarization and is partially transmitted by the analyzer. The transmitted light forms the so-called isogyres, which display the geometrical loci of constant phase difference. Photographs of conoscopic patterns for various pump powers of an Nd:LaSOAP rod between crossed polarizers are shown in Fig. 7.15.

The isogyre pattern exhibits a cross and ring structure, where the arms of the cross are parallel and orthogonal to the incident polarization. As mentioned before, the crosses correspond to those regions of the crystal where an induced (radial or tangential) axis is along a polarizer axis, so that the induced birefringence results only in a phase delay and not in a polarization rotation. The dark rings correspond to an integral number of full waves of retardation.

A number of operations of solid-state lasers, for example, electro-optical Q-switching, frequency doubling, and external modulation of the beam, require a linearly polarized beam. An optically isotropic material, such as Nd:YAG, must be forced to emit a linearly polarized beam by the introduction of a polarizer in the resonator. In the absence of birefringence, no loss in output power would be expected. However, the thermally induced birefringence causes a significant decrease in output power and a marked change in beam shape.

For a system with an intracavity polarizer, the effect of depolarization involves two phenomena: coupling of power into the orthogonal state of polarization followed by subsequent removal of that component by the polarizer and modification of the main beam by the depolarization process leading to a distortion of beam shape. When a birefringent crystal is placed between a polarizer and an analyzer that are parallel, the transmitted intensity is given by [7.18]

$$\frac{I_{\text{out}}}{I_{\text{in}}} = 1 - \sin^2(2\phi) \sin^2\left(\frac{\varphi}{2}\right), \quad (7.52)$$

where ϕ is the angle between the polarizer and one of the principal birefringence axes

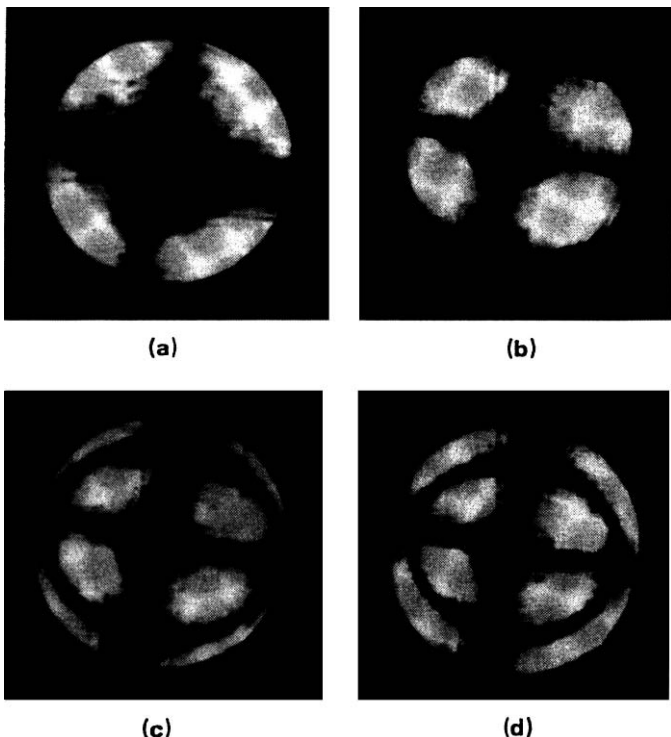


Fig. 7.15. Thermal stresses in a 7.5-cm-long and 0.63-cm-diameter Nd:LaSOAP crystal. The rod was pumped at a repetition rate of 40 pps by a single xenon flashlamp in an elliptical pump cavity. Input power (a) 115 W, (b) 450 W, (c) 590 W, and (d) 880 W [7.23]

and φ is the polarization phase shift of the light emerging from the crystal. The index difference, $\Delta n_\phi - \Delta n_r$, leads to a phase difference

$$\varphi = \frac{2\pi}{\lambda} l(\Delta n_\phi - \Delta n_r). \quad (7.53)$$

To illustrate the magnitude of stress birefringence in an Nd:YAG rod, the difference in optical path length normalized to the wavelength

$$\frac{\Delta l}{\lambda} = \frac{l(\Delta n_\phi - \Delta n_r)}{\lambda} \quad (7.54)$$

is plotted in Fig. 7.16 as a function of pump power. The following constants were used: $P_h = 0.05 P_{in}$, $l = 7.5$ cm, $r_0 = 0.31$ cm, and $\lambda = 1.06 \times 10^{-4}$ cm. As can be seen from this figure, at maximum lamp input power of 12 kW, the path-length difference is approximately six wavelengths.

Assuming a plane wave, we can calculate the total transmitted intensity from (7.52) and (7.53) by integrating over the cross-sectional area of the rod. The following

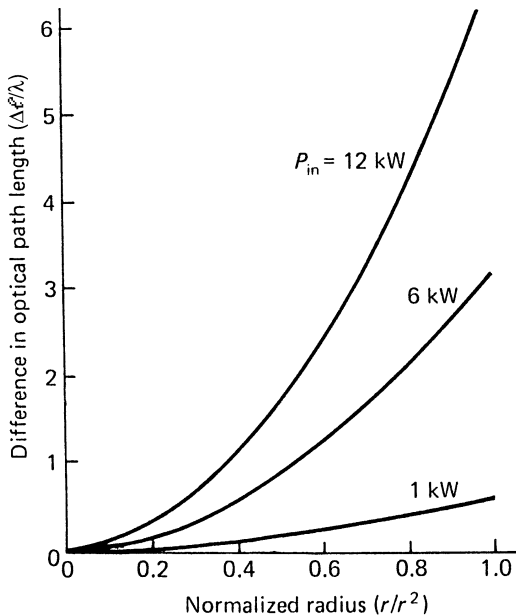


Fig. 7.16. Differences in optical path length as a function of normalized rod radius in an Nd:YAG rod. Parameter is the lamp input power

integral must be evaluated

$$\left(\frac{I_{\text{out}}}{I_{\text{in}}} \right)_T = \left(\frac{1}{\pi r_0^2} \right) \int_{\phi=0}^{2\pi} \int_{r=0}^{r_0} \left[1 - \sin^2(2\phi) \sin^2 \frac{\varphi}{2} \right] r dr d\phi. \quad (7.55)$$

with $\varphi = C_T P_h (r/r_0)^2$ where $C_T = 2n_0^3 \alpha C_B / \lambda K$. Integration of (7.55) yields

$$\frac{I_{\text{out}}}{I_{\text{in}}} = \frac{3}{4} + \frac{\sin(C_T P_h)}{4C_T P_h}. \quad (7.56)$$

A laser resonator containing a polarizing element is optically equivalent to a laser rod of twice the actual length located between a polarizer and analyzer. Subtracting $I_{\text{out}}/I_{\text{in}}$ from unity and multiplying the phase difference φ by a factor of 2 yields the fraction of the intracavity power which is polarized orthogonal to the polarizer. This beam, caused entirely by birefringence, will actually be ejected from the cavity and represents the depolarization loss of the resonator

$$\delta_{\text{depol}} = 0.25 [1 - \text{sinc}(2C_T P_h)]. \quad (7.57)$$

This loss is plotted in Fig. 7.17, where the same constants as for Fig. 7.16 have been used. Note that this curve represents the round-trip loss in the cavity for a plane-parallel beam which was used as an approximation for a highly multimode laser beam.

Also shown is the depolarization loss for a TEM_{00} mode for which it was assumed that the beam radius w is $w = r_0/2$. A similar calculation as the one carried out for

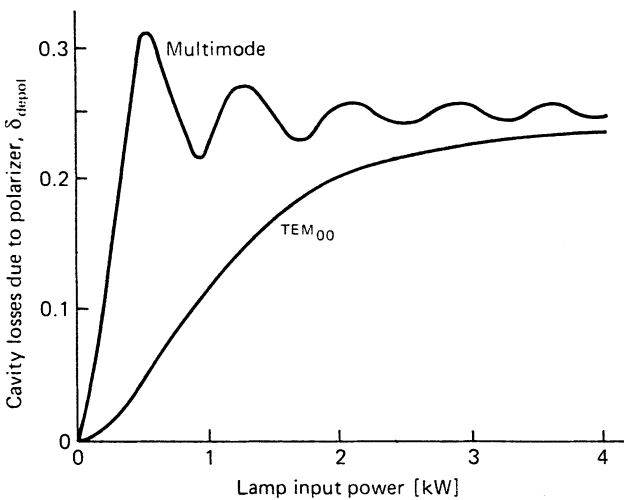


Fig. 7.17. Calculated resonator loss caused by the combination of thermally induced birefringence in an Nd:YAG rod and an intracavity polarizer

a plane wave yields the loss factor

$$\delta_{\text{depol}} = 0.25 \left(1 + \frac{16}{C_T^2 P_h^2} \right)^{-1}. \quad (7.58)$$

For the same lamp input power the losses for the TEM₀₀ mode are less than for a highly multimode beam. This is expected since the energy in the TEM₀₀ mode is concentrated nearer the center of the rod, where the induced birefringence is smaller.

The interaction of a linearly polarized beam with a birefringent laser rod and a polarizer not only leads to a substantial loss in power, but also a severe distortion of the beam shape. Figure 7.18 shows the output beam shape obtained from a cw-pumped Nd:YAG laser with and without an intracavity polarizer. The output is obtained in the form of a cross with a bright center. As discussed before, the depolarization losses are smallest in the rod center and in directions parallel and orthogonal to the preferred direction of the polarizer. Areas of high depolarization losses are removed from the cavity by the polarizer and are, therefore, missing in the output beam.

The $\sin(2\phi)$ dependence of birefringence on the azimuth angle ϕ is very nicely illustrated in Fig. 7.19. The plane of polarization is assumed to be in the y -direction and, consistent with observation, the largest depolarization occurs at 45° with respect to this direction.

7.1.6 Compensation of Optical Distortions

From the foregoing analysis we have seen that a long cylindrical laser rod with uniform internal heat deposition develops a quadratic radial temperature profile. This leads directly to a quadratic radial refractive index profile which causes the laser rod

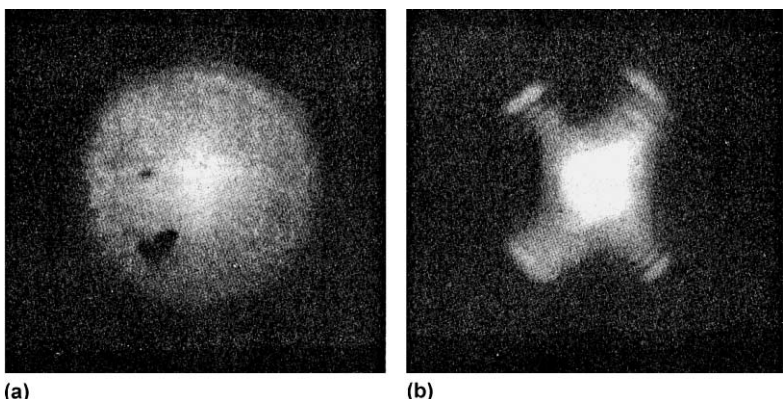


Fig. 7.18. Output beam pattern for a high-power cw Nd:YAG laser (a) without and (b) with a Brewster plate in the cavity

to act as a lens with variable focal length. The optical power of the thermal lens is proportional to pump power.

The thermal gradients lead also to a quadratic strain distribution. In a crystal such as Nd:YAG, the strain effects are different in the radial and azimuthal directions and give rise, through the photoelastic effect, to thermally induced birefringence. The thermal and stress dependence of the refractive index produce thermally induced bifocusing.

For linearly polarized beams, birefringence also leads to depolarization losses, because a linearly polarized beam will be elliptically polarized after passing through the rod.

Deviations from a radially uniform pump distribution causes nonspherical optical aberrations in the rod. In the ideal case of a perfectly uniform pumped rod, the

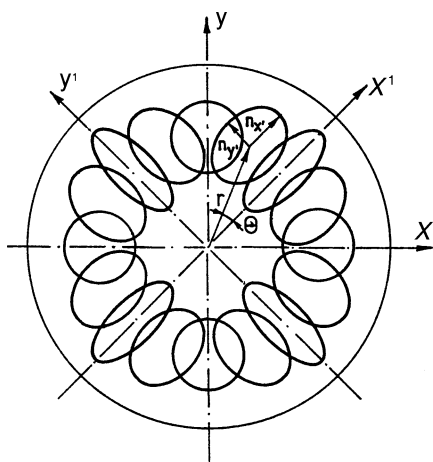


Fig. 7.19. Orientation of the indicatrix of a thermally stressed rod [7.24]

thermal lens is spherical. In most cases the thermal lens is aspheric because pumping is stronger in the center of the rod compared to the outer regions. Also depending on the arrangement of the pump sources around the laser rod the thermal lens may not be radially symmetric.

The upper limit on the input power is determined by the fracture strength of the laser material.

Since the thermally induced optical distortions of the TEM_{00} wavefront are the main reason for limiting the output, the major objective in obtaining a high-quality beam is to minimize the thermal load of the rod and to compensate existing distortions in the resonator. The basic problem facing the resonator designer is to provide a compensation scheme of the optical distortion that can tolerate fluctuations in the rod focusing that are due to varying pumping conditions.

Compensation of Thermal Lensing

Complete compensation of the thermal aberrations produced by a laser rod is difficult because the focal length changes with pump power, nonuniform pumping leads to nonspherical aberrations, and the thermal lens is bifocal.

Compensation of the Average Spherical Component. In order to get an idea about the amount of compensation needed, usually a collimated HeNe laser beam is passed through the pumped rod and the average focal length is measured as a function of pump power. The objective of a first-order compensation is to negate the positive lensing of the rod with a diverging optical component. The most common approaches are the insertion of a negative lens in the resonator, or a resonator featuring an internal telescope, or a design where one of the mirrors has a convex surface. The latter two approaches have been discussed in Sect. 5.1.9.

A first order dynamic compensation, which accommodates variations in pump power can be achieved with a movable optical element. For example, a low-magnification Galilean telescope can be inserted into the resonator, whereby the relative position of the two lenses is adjusted with a motor drive. In another approach, dynamic compensation was achieved with a negative lens in front of the concave rear mirror of the resonator. By adjusting the spacing between these elements, the effective radius of curvature of the rear mirror is altered, thus creating a variable-radius mirror [7.25]. Movement was accomplished by placing the rear mirror on a motorized translation stage. Dynamic compensation of thermal lensing, by means of a microprocessor-controlled translation of an optical element, is sometimes required in military systems in order to provide a minimum beam divergence on a first-shot basis, i.e. zero warm-up time.

Compensation of Nonspherical Aberrations. Clearly the approaches mentioned above rely on a radially symmetric wavefront distortion. Therefore, uniform pumping is important in compensating phase aberrations.

In many pump configurations, with flashlamps as well as diode pump sources, pump radiation is more intense at the center than at the periphery of the rod. The

focal length of a given area in the rod is inversely proportional to the intensity of the absorbed pumped radiation. Therefore, in the case of on-axis focusing of pump light, the focal length at the center of the rod is shorter than at the edges. Or expressed differently, the thermally induced refractive index profile contains terms that are higher than quadratic. A negative lens will remove the quadratic term; however higher order effects cannot be compensated.

Essentially two approaches are possible: dynamic correction of thermally induced wavefront distortions by means of phase conjugation, or static correction with an aspheric correction plate.

In an amplifier, wavefront distortions can be eliminated with an optical phase conjugated mirror as discussed in Sect. 10.5. This approach requires an injection-seeded, narrow bandwidth oscillator with a diffraction limited output, and a double pass amplifier. The oscillator typically has a low power output because only aberrations in the amplifier are corrected. Compared to spherical diverging lenses, optical phase conjugation does provide complete correction of wavefront distortions over a large dynamic range.

Thermally induced phase-front distortions can also be corrected with an aspheric optical element in the beam path. Appropriate phase profiles can be generated with currently available techniques such as diamond turning, microlithography, and ion etching. Just like optical phase conjugation, such an element can correct for spherical, as well as nonspherical, aberrations. However, a correction can be achieved for only one set of operating conditions. Since static correction requires a thermal aberration profile that is stable over time, this method is particularly well suited to diode pumping. In one of our lasers, intended for a space-based application, a diamond-turned CaF₂ aspheric lens was able to perform a high degree of correction [7.26]. The very compact diode-pumped oscillator-amplifier system generated 46 W of average power in the Q-switched mode within a $1.3 \times$ diffraction limited beam. The phase corrector was a single antireflection-coated CaF₂ plano-concave plate which was inserted into the amplifier chain. The optical phase profile of the amplifier was measured by monitoring the interference of a probe beam that propagated through the amplifier and a reference path of a Mach-Zehnder interferometer. The phase profile was circularly symmetric, and the predominant aberration was a high-order spherical aberration, which resulted in a stronger focus in the center of the rod compared to the outer region. The interference pattern was quantified with fringe analysis software. This provided the information needed for the fabrication of the optical element. Calcium fluoride was chosen because it can easily be diamond turned and is a very robust material.

Elimination of Bifocusing. The variable focal length creates zones of stable TEM₀₀ mode operation as discussed in Sect. 5.1.9. Birefringence splits the cavity mode into two components that propagate along the radial and tangential axes. Stable TEM₀₀ mode operation can be achieved only in the pump-power range in which the stability zones for the two polarization axes overlap. As the TEM₀₀ mode radius, and therefore output power, increases, the overlap zones become narrower. The separation of the resonator stability zones by the two polarization modes makes it difficult to obtain an optimum spot size that maximizes beam overlap efficiency.

A greater reduction of thermally induced optical distortions can be achieved if thermal lensing compensation is combined with bifocusing compensation.

Compensation of Thermal Birefringence

In this case bifocusing is eliminated and depolarization losses are minimized in resonators containing polarized beams. The most common technique consists of placing a 90° quartz rotator between two identical rods to exchange the radial and tangential polarization between rods. In case of a single-rod oscillator the same effect can be achieved by placing a Faraday rotator between the rod and rear mirror. However, full compensation requires the insertion of additional optical elements as discussed later. In a polarization coupled resonator containing a Porro prism, the displacement provided by the Porro prism places the second pass in a symmetrically opposite section of the laser rod to the first pass and this allows to achieve compensation.

90° Polarization Rotation. The basic approach has already been described in Sect. 5.1.9. This compensation scheme relies on the fact that two passes occur in the laser rod, and by modifying the polarization state of the beam between the two passes it is possible to remove any thermally induced depolarization effects that occur in the first pass with an equal and opposite effect in the second pass. The objective of birefringence compensation is to achieve equal phase retardation at each point of the rod's cross section for radially and tangentially polarized radiation. This can be accomplished by rotating the polarizations, either between two identical laser rods or in the same rod on successive passes, such that the radial and tangential components of the polarizations are exchanged.

The most important factor in this approach is that the two laser rods are identically pumped and the beam traveling through the rods experiences the same environment.

A laser beam entering the first rod having a linear polarization will experience a phase retardation between the radial and tangential electric field. The beam leaving the rod will be elliptically polarized. Before the beam enters the second rod, radial and tangential components of the polarization state are exchanged by a 90° rotator. Therefore, the phase shift between the radial and tangential polarization in the second rod has the opposite sign compared with the phase shift in the first rod.

In a two-rod system, the 90° polarization rotator is usually crystalline quartz cut perpendicular to the optic axis. In a single-rod oscillator a Faraday rotator is required between the rod and rear mirror.

An unpolarized beam entering the first rod will be focused to two different focal points corresponding to the radial and tangential component of the electric field. The compensation scheme discussed above leads to a thermally induced lens with a single focal length.

In the example shown in Fig. 5.22 the main purpose of birefringence compensation is to reduce depolarization losses in a resonator containing a linear polarized beam.

In the laser depicted in Fig. 7.20 the emphasis is on removing bifocusing such that an optimum TEM_{00} mode spot size could be selected for maximum output [7.27]. In

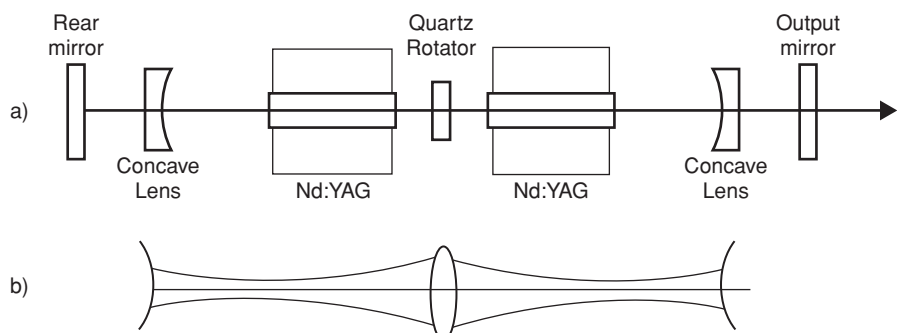


Fig. 7.20. Optical schematic of a bifocusing compensated TEM_{00} mode laser (a) and equivalent optical resonator (b)

each laser head a 3-mm Nd:YAG rod was side-pumped in a fourfold symmetry by twelve 5-bar stacked diode arrays at an average power of 550 W and a peak power of 2.75 KW. Pulse repetition rate was 1 KHz. The output from the diode arrays was focused into a diffuse reflecting pump cavity which provided a uniform pump beam distribution inside the laser rods.

To maximize the beam overlap efficiency and minimize diffraction effects at the laser rods, the diameter of the TEM_{00} mode inside the laser rods was chosen as 2.2 mm. Two negative lenses with 50-mm focal length compensated for spherical lensing. The largest spot size was inside the laser rods, and the minimum spot sizes occurred at the resonator mirrors. An equivalent resonator is depicted in Fig. 7.20b. The large spot size in the laser rods maximizes the overlap efficiency, and the small spot sizes at the mirrors provide discrimination against higher order modes. From this laser an unpolarized TEM_{00} mode output of 208 W was obtained.

In the work described above it was observed, but not explained, that the range of stable pump-power was larger than expected from a stability analysis. Actually this observation is consistent with the result of an analysis published by Eggleston [7.28] on periodic resonators. In these resonators the power range for stable operations is proportional to the number of periods, provided that the focal power and spot size for TEM_{00} mode are the same in both rods. Therefore, in a symmetric two-rod resonator, the output power is twice that of a single-rod system, and the power range for stable operation is also twice that of a single-rod resonator. The wider dynamic operating range of a dual-rod system compared to a resonator containing a single long laser rod is an additional advantage of this bifocusing compensation scheme.

Birefringence compensation using a polarization rotator can also be employed between two identical amplifier stages. Figure 7.21 illustrates the improvement one can achieve with this compensation technique. Shown is the measured depolarization of two flashlamp-pumped Nd:YAG amplifiers as a function of average pump power. The Q-switched average output power is also indicated. The two amplifiers are arranged in a double-pass configuration with polarization output coupling similar to the diode-pumped system illustrated in Fig. 4.7. However, instead of an ordinary mirror

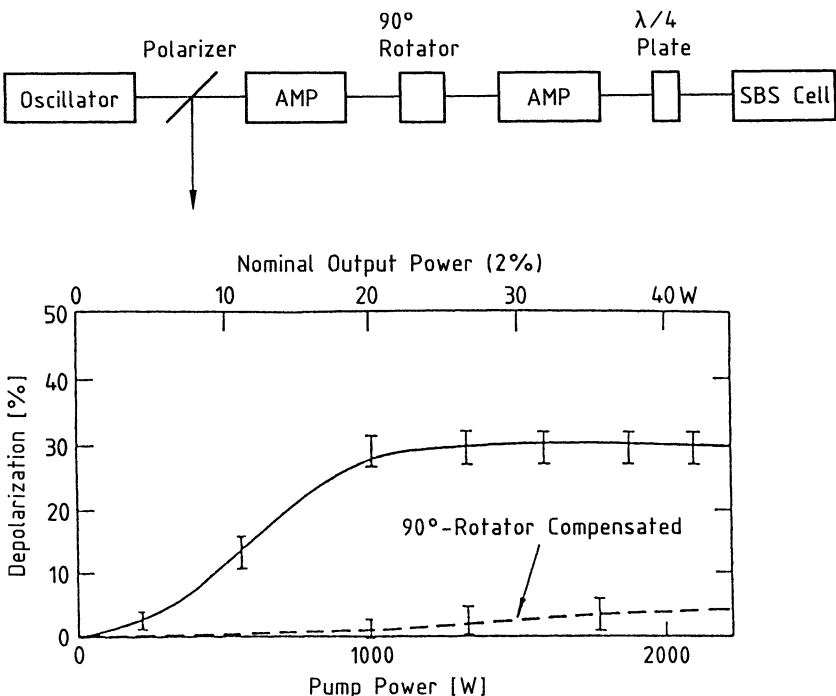


Fig. 7.21. Depolarization losses in a double-pass Nd:YAG amplifier chain with and without birefringence compensation by means of a 90° polarization rotator [7.29]

at the output of the second amplifier, a phase-conjugate mirror based on stimulated Brillouin scattering (SBS) is employed to compensate for optical distortions produced in the amplifier rods. (See Sect. 10.5 for details on SBS). A 90° polarization rotator placed between the two amplifiers compensates for birefringence and greatly reduces the total depolarization.

If the laser system uses only a single amplifier, a Faraday rotator with a 45° rotation, placed between the amplifier and the back mirror or SBS cell, is equivalent to a 90° rotator located between two identical amplifier stages (Fig. 10.50).

In a laser resonator containing a single rod, the phase difference between the radially and tangentially polarized rays can be compensated by a 45° Faraday rotator placed between the rod and rear mirror. On each round trip, the light passes through the 45° Faraday rotator, thereby undergoing a 90° rotation of the plane of polarization. In the resonator depicted in Fig. 7.22 birefringence compensation, employing a Faraday rotator, is combined with the added feature of four passes through the active medium before the radiation reaches the output coupler [7.25, 30]. In a low-gain laser this can be advantageous in certain situations. In the scheme illustrated in Fig. 7.22, linearly polarized radiation traveling to the right through the polarizer, laser rod, and Faraday rotator will be orthogonally polarized on its return path. Therefore, the radiation will be rejected by the polarizer and directed toward the reentrant mirror. On its

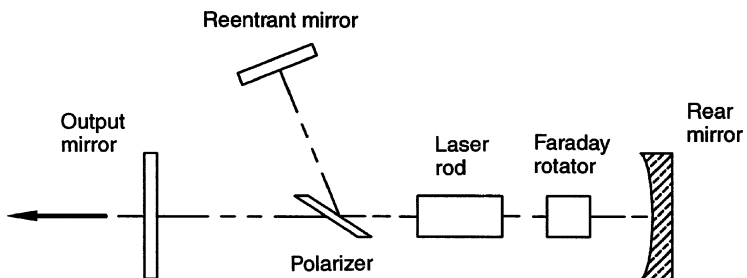


Fig. 7.22. Reentrant resonator with birefringence compensation [7.25]

second round trip through the laser rod and Faraday rotator, the radiation will pass the polarizer and reach the output coupler.

90° Polarization Rotation Plus Imaging Telescope. A further refinement of the concept of rotating the radial and tangential polarization between two identical and symmetrically loaded rods has been proposed in [7.31]. A necessary condition for complete birefringence compensation, with the technique described above, is the propagation of each ray through exactly the same position in each rod. Because of thermal focusing, the rays do not propagate parallel to the optical axis, and therefore do not retrace identical sections in each rod. This is mainly an issue at high pump powers when thermal focusing is severe. According to theoretical and experimental investigations described in [7.31–33], a much improved compensation for birefringence and bifocusing can be achieved if an optical imaging system is added to the polarization rotator. In this approach, the beam in the first rod is imaged into the second rod. Figure 7.23 shows one implementation of the concept. A telescope with magnification one images the facing principal planes of both rods onto each other and a 90° quartz rotator exchanges the radial and tangential polarization states between the rods.

The imaging performed by the telescope assures that the transverse coordinates remain unaltered.

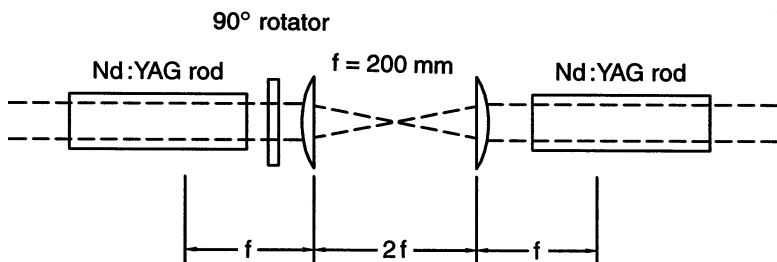


Fig. 7.23. Birefringence compensation with a polarization rotator and a telescope imaging the principal planes of both rods [7.31]

Porro Prism Resonator. Birefringence compensation by double-pass retracing of a ray through the thermally aberrated rod can also be achieved with two optically passive elements, namely a Porro prism and a waveplate [7.34]. A ray which travels on one side of the laser rod on the first pass is reflected by the Porro prism about the plane of symmetry, so that it travels down the opposite side of the rod on the second pass at the same radial distance. The phase difference between the radial and tangential polarization state in a thermally stressed rod is only a function of radius and independent of the azimuth angle. Because of this rotational symmetry, the birefringence that a given ray experiences on the two passes through the laser rod has the same magnitude. By modifying the polarization state of the beam between the two passes it is possible to remove any thermally induced depolarizing effects that occur in the first pass with equal and opposite effects in the return pass. With a normal mirror providing reflection after one pass, only a Faraday rotator is able to achieve this. However, if a Porro prism is used, the displacement provided by the Porro places the second pass in a different portion of the laser rod to the first pass, and this allows the use of completely passive components to achieve compensation. The result is a zero-phase retardation upon emergence from the laser rod. The incorporation of a waveplate with the appropriate orientation and phase retardation in front of the Porro prism produces the desired result (see Sect. 8.3 for details).

Reduction of Optical Distortions

The aforementioned techniques deal with the issue of minimizing optical losses in the presence of thermally induced stress birefringence. Other measures for achieving high TEM₀₀ mode output are more fundamental and address the origin of thermal distortions.

Changing from an arc lamp pumped system to diode pumping drastically reduces the thermal distortions in the laser crystal. For the same output power, a diode pump source generates only about one-third the amount of heat in an Nd:YAG crystal compared to an arc lamp.

If the TEM₀₀ output beam has to be linearly polarized, a naturally birefringent crystal such as Nd:YLF can be advantageous in particular situations. The natural birefringence in Nd:YLF is much larger than the thermally induced birefringence. However, Nd:YLF is a softer laser material, and the thermal fracture limit is a factor 8 lower than that for Nd:YAG.

Also, instead of using a cylindrical rod, a rectangular slab with an internal zigzag path minimizes wavefront distortions in the resonator. As explained in Sect. 7.2, such a structure provides a high degree of self-compensation of optical beam distortions.

7.2 Slab and Disk Geometries

Practical limitations arise in the operation of any solid-rod laser owing to the thermal gradients required to dissipate heat from the rod. As was discussed in Sect. 7.1, the thermally loaded cylindrical laser medium exhibits optical distortions that include

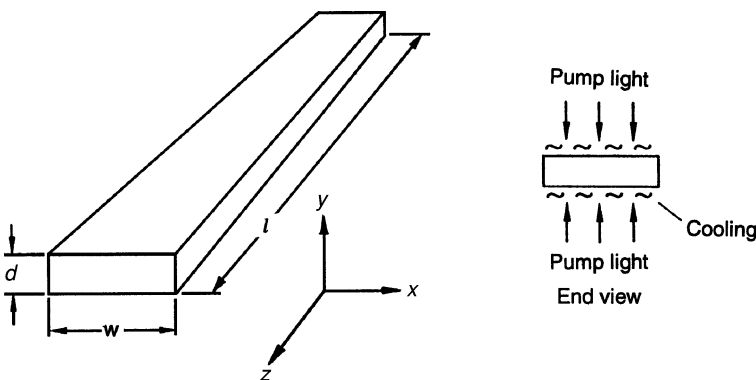


Fig. 7.24. Geometry of a rectangular-slab laser

thermal focusing, stress-induced biaxial focusing, and stress-induced birefringence. These thermally induced effects severely degrade the optical quality of the laser beam and eventually limit the laser output power, either because of an unacceptably poor beam pattern or because of thermal stress-induced breakage of the rod.

The limitations imposed by the rod geometry have long been recognized and a number of designs have emerged, such as slab and disk geometries, in an attempt to reduce the effect of thermal gradients on beam quality.

7.2.1 Rectangular-Slab Laser

The rectangular-slab laser provides a larger cooling surface and essentially a one-dimensional temperature gradient across the thickness of the slab. Figure 7.24 shows the geometry of a rectangular-slab laser. The z -axis coincides with the optical axis of the slab.

The slab has thickness d and width w . The upper and lower surfaces are maintained at a constant temperature by water cooling, and the sides are uncooled. Provided the slab is uniformly pumped through the top and bottom surfaces, the thermal gradients are negligible in the x - and z -directions and the thermal analysis is reduced to a one-dimensional case, that is, temperature and stress are a function of y only. This, of course, is only true for an infinitely large plate in x and z , and uniform pumping and cooling. Under these conditions we find that the temperature assumes a parabolic profile (Fig. 7.25a).

The maximum temperature that occurs between the surface and the center of the slab ($y = d/2$) is given by

$$\Delta T = \frac{d^2}{8K} Q, \quad (7.59)$$

where Q is the heat deposition, d is the thickness, and K is the thermal conductivity of the slab. For example, a heat deposition of 2 W/cm^3 , in a 1-cm-thick glass slab

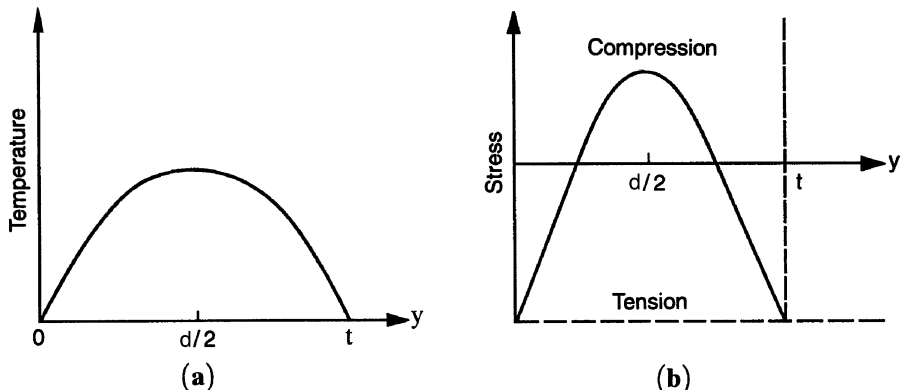


Fig. 7.25. (a) Temperature profile and (b) stress in a rectangular slab

($K = 0.01 \text{ W/cm K}$) will create a temperature difference between the cooled surfaces and the center of 25°C .

The temperature rise causes stress in the slab according to

$$\sigma_{\max} = \frac{2\alpha E}{3(1-\nu)} \Delta T = \frac{\alpha E d^2}{12(1-\nu)K} Q, \quad (7.60)$$

where σ_{\max} is the surface stress for the slab. The surfaces are in tension and the center is under compression as shown in Fig. 7.25b.

If we introduce the “thermal-shock parameter” from Sect. 7.1 we can calculate the maximum temperature difference allowed between the surface and the center before thermal fracture occurs; this is

$$\Delta T_{\max} = \frac{3R_s}{2K}. \quad (7.61)$$

With $R_s = 1 \text{ W/cm}$ for Nd:glass, one obtains

$$\Delta T_{\max} = 150^\circ\text{C}.$$

Stress fracture at the surface limits the total thermal power absorbed by the slab per unit of face area. For slabs of finite width w , the power per unit length at the stress fracture limit is given by

$$\frac{P_h}{l} = 12\sigma_{\max} \frac{(1-\nu)K}{\alpha E} \left(\frac{w}{d}\right), \quad (7.62)$$

where w/d is the aspect ratio of a finite slab. It is interesting to compare the surface stress of a rod and slab for the same thermal power absorbed per unit length. From (7.27) and (7.62) it follows that

$$\frac{(P_h/l)_{\text{rod}}}{(P_h/l)_{\text{slab}}} = \frac{2\pi}{3} \left(\frac{d}{w}\right). \quad (7.63)$$

Thus, for a superior power handling capability relative to a rod, the aspect ratio of the slab must be greater than 2.

The temperature and stress profile leads to a birefringent cylindrical lens. The focal lengths of the birefringent lens are [7.35]

$$f_x = \frac{1}{2l(S_0 - S_1)}, \quad f_y = \frac{1}{2l(S_0 - S_2)}, \quad (7.64)$$

for x and y polarized light, respectively. The parameter S_0 is the contribution from thermal focusing, that is,

$$S_0 = \frac{dn}{dT} \left(\frac{Q}{2K} \right), \quad (7.65)$$

and the parameters S_1 and S_2 are related to stress-induced focusing

$$S_1 = \frac{Q\alpha E}{2(1-\nu)K} (B_{\perp} + B_{\parallel}), \quad S_2 = \frac{Q\alpha E}{(1-\nu)K} B_{\perp}, \quad (7.66)$$

where B_{\parallel} and B_{\perp} are the stress optic coefficients for stress applied parallel and perpendicular to the polarization axis.

From (7.64) follows that for incident radiations polarized along either the x - or y -direction the stress-induced depolarization is zero.

For an isotropic material such as Nd:glass the values of B_{\parallel} and B_{\perp} can be written as [7.35].

$$B_{\parallel} = (1/E)(p_{11} - 2\nu p_{12}) \quad (7.67)$$

$$B_{\perp} = (1/E)[p_{12} - \nu(p_{11} + p_{12})] \quad (7.68)$$

Comparing the focal length of a rod (7.44) with the focal length of a slab (7.64) and considering only thermal focusing, then the slab has twice the focal power of a rod. In [7.35] it has been shown that if the stress-induced focusing is included, the slab still shows about twice the focal power compared to a rod.

In a slab, however, for incident radiation polarized along either the x - or y -direction, the stress-induced depolarization is zero. In a rectangular rod, the main axes of the resulting index ellipse are oriented parallel to the x - and y -axes of the rod, and a beam polarized along either one of these axes can propagate in a direction parallel to the z -axis without being depolarized. This is, as mentioned earlier, in contrast to the situation in a cylindrical rod, where a plane-polarized beam does suffer depolarization because the direction of the main axes of the index ellipsoid vary from point to point within the cross section of the rod. The advantage of the rectangular geometry is obtained at some cost: The focal lengths are shorter than for the cylindrical rod, and cylindrical rather than spherical compensating optics are needed. The idea of the zigzag path in a slab, which will be discussed in Sect. 7.2.2 is to eliminate to a first-order focusing in a slab.

Thin-Slab Lasers

In a rectangular slab the temperature gradients and stress scale with d^2 as follows from (7.59, 60). Therefore a thin slab with a large aspect ratio (width/thickness) would be advantageous from a thermal point of view. However, there is a lower limit to the thickness d where the pump radiation is no longer effectively absorbed in a single pass. To overcome this limitation, a thin slab can be mounted in a highly reflective pump chamber allowing multiple passes of the pump radiation through the slab. In Sect. 6.2.2 reflective pump chambers containing cylindrical rods have been described.

In the work described in [7.36, 37] a thin slab of Nd:Glass or Nd:YAG is sandwiched between two highly reflective coated quartz plates with slots etched into the mirrored surfaces for injection of the pump radiation from the laser diode bars. The planar pumping chamber allows multiple passes through the active medium. Water flows between the slab and the mirrors. Mounting and sealing very fragile thin slabs is a practical engineering challenge. The Nd:YAG had a 200- μm -thick active core with 400 μm undoped YAG cladding on each side. The 11-mm-wide and 60-mm-long slab laser produced over 150 W of output power. The Nd:Glass slabs ranged in thickness from 0.5 to 1 mm. Below a thickness of about 0.5 mm, wall reflections effectively make a thin slab into a planar wave guide.

7.2.2 Slab Laser with Zigzag Optical Path

In the previous section we considered propagation straight through an infinite slab. Because of the rectilinear pumping and cooling geometry of the lasing medium, thermal gradients and thermally induced stresses are present only in the y -direction. Therefore, for light polarized in either the x - or y -direction, stress-induced bi-axial focusing and depolarization losses are eliminated. However, the slab still behaves as a thin cylindrical lens with a focal length shorter by a factor of 2 relative to that of a rod.

The cylindrical focusing in the slab can be eliminated by choosing propagation along a zigzag optical path. In the zigzag geometry, the optical beam does not travel parallel to the z -axis, as was the case for the straight-through optical path. Instead the beam traverses the slab at an angle with respect to the x - z plane, using total internal reflection from the slab y faces. This geometry is depicted in Fig. 7.26.

The laser beam is introduced into the slab with suitable entrance/exit optics, usually through surfaces at Brewster's angle, as shown in Fig. 7.26b. In order to maintain total internal reflection for the desired path length the two opposing faces have to be highly polished and have to be fabricated with a high degree of parallelism. The same two optical faces are also employed for pumping and cooling of the slab.

In the ideal case, this geometry results in a one-dimensional temperature gradient perpendicular to the faces and a thermal stress parallel to the faces. Since the thermal profile is symmetrical relative to the center plane of the slab, the thermal stress averaged from one slab surface to the other is zero. Thus, for a beam traversing from one slab surface to the other, the stress-optic distortion is compensated for to a high degree. Also, since all parts of a beam wavefront pass through the same temperature gradients in a surface-to-surface transit, no distortion results from the variation of

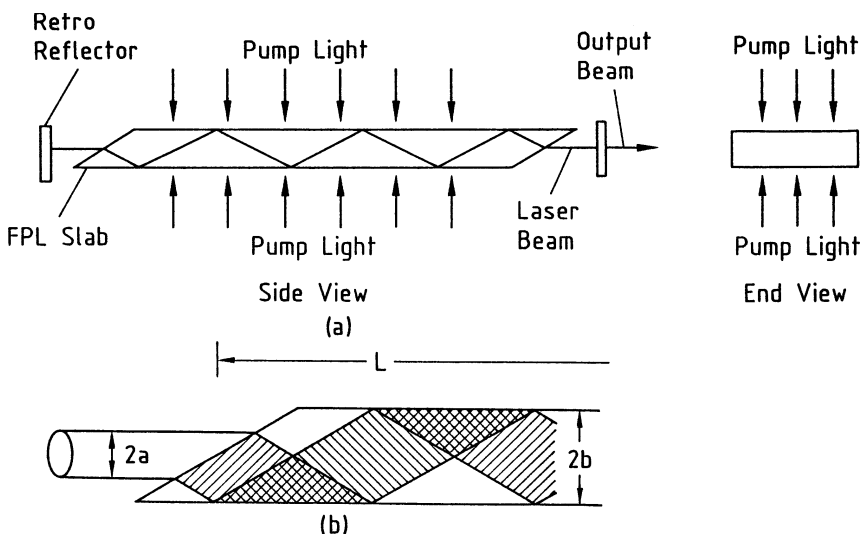


Fig. 7.26. Schematic of a zigzag laser with Brewster angle faces; (a) schematic and (b) detail of Brewster angle entrance. The coordinate system is the same as chosen in Fig. 7.24

refractive index with temperature. Thus, in this geometry, thermal distortion effects are fully compensated for within the host material in the ideal case.

The advantage of this configuration is the combination of two ideas: the elimination of stress-induced birefringence by virtue of the rectangular geometry and the elimination of thermal and stress-induced focusing by optical propagation along a zigzag path. The concept of a slab-laser geometry with a zigzag optical path confined in the slab by total internal reflection was first proposed by Martin and Chernoch [7.38, 39]. Figure 7.27 shows two different designs of a zig-zag slab laser [7.40]. In Fig. 7.27a a multitude of flashlamps are oriented transverse to the optical axis of the slab, and in Fig. 7.27b a single lamp is placed along the axis of the slab on each side. Appropriate reflectors are employed to distribute the pump light evenly over the slab surface area. Uniform pumping and cooling of the optical surfaces is absolutely crucial for good performance of a zig-zag slab laser, as will be discussed below.

A detailed model for calculating temperature and stress distributions in an infinitely long slab (plain strain approximation) has been described in [7.35]. Despite the inherent advantages, at least on a conceptual level, of a zigzag slab to overcome the thermal limitations of rod lasers, a number of practical engineering issues have to be solved before the potential advantages of the zigzag slab laser over the rod geometry can be realized. Distortions can only be eliminated in a slab of infinite extent, which is uniformly pumped and cooled. In practice, the slab laser approximates only an ideal infinite slab. For a slab of finite width and length, pump- or cooling-induced gradients across the slab width (normal to the plane of reflection), as well as end effects, give rise to distortions and unavoidable temperature nonuniformities. Residual thermal gradients and thermally induced strain have in some cases resulted in beam qualities considerably below expectations.

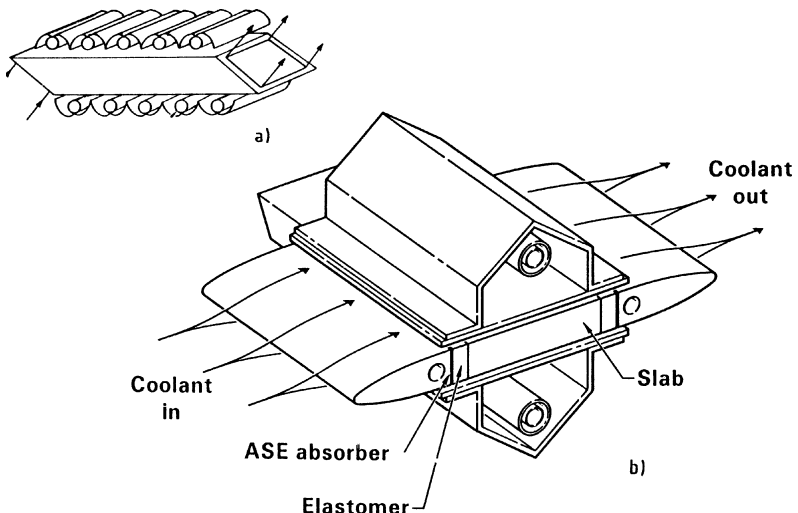


Fig. 7.27. Different designs of zigzag slab lasers, multiple flashlamp (a) and single flashlamp (b) configuration [7.40]

Gradients in the x -direction, i.e., transverse to the beam direction, are highly undesirable because there is no compensation (see Fig. 7.24 for definition of coordinates). The major sources of thermal gradients in the x -direction are nonuniform illumination of the slab by the pump source and cooling of the slab at the edges. In order to approach an infinitely large slab, the edges need to be thermally insulated from the coolant flow. This is the purpose of the wedge-shaped flow diverter shown in Fig. 7.27b. In an infinitely large slab, thermal gradients and therefore heat flow occur only in the y -direction.

Thermal gradients in the z -direction are mainly encountered in the transition region between pumped and unpumped regions at the ends of the slab.

In order to reduce end effects, a smooth temperature profile in the transition region is usually attempted. Figure 7.28 illustrates a particular design whereby a

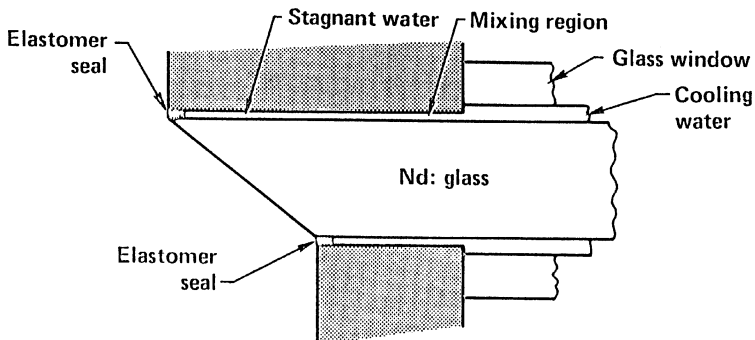


Fig. 7.28. Cooling and sealing of the ends of a slab laser [7.40]

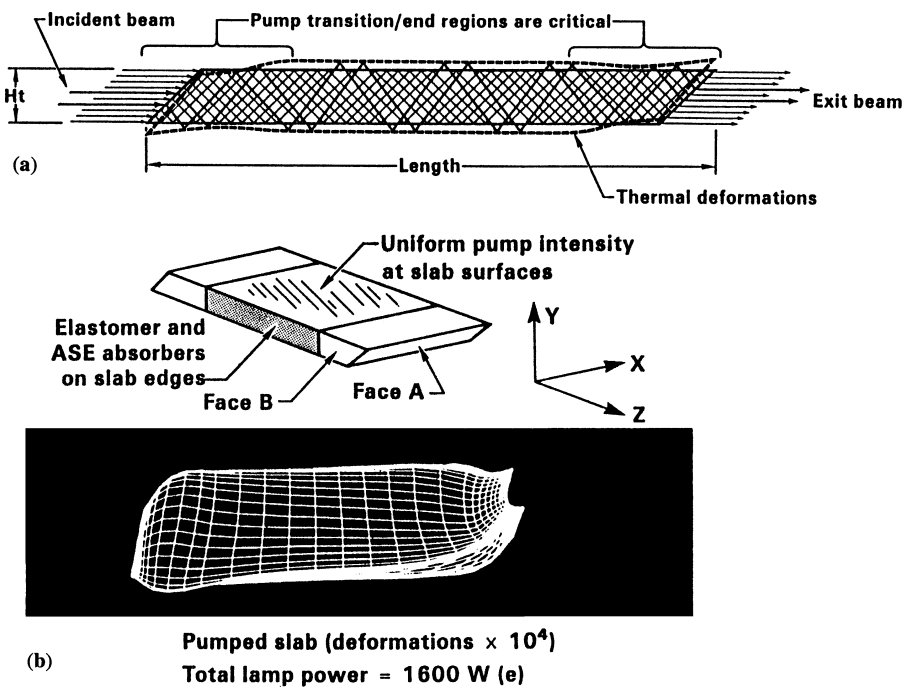


Fig. 7.29. Deformations in a thermally loaded slab laser (a) beam trajectories, (b) 3-D deformations computed in pumped glass slabs [7.40]

plenum provides for the mixing of flowing with stagnant water to produce a gradually decreasing surface heat transfer coefficient.

The severeness of surface deformation, and bulging of the entrance and exit faces of a slab under thermal loading, is illustrated in Fig. 7.29. These deformations in conjunction with index gradients lead to focusing effects of the slab laser.

Despite the inherent advantages, at least on a conceptual level, of a zig-zag slab to overcome the thermal limitations of rod lasers, the acceptance of these systems has been slow. The reason for this is cost considerations in combination with a number of practical engineering issues which have to be solved before the potential advantages of the zig-zag slab laser over the rod geometry can be realized.

- (a) *Low efficiency.* The awkward rectangular beam geometry which requires conversion to a circular beam in most applications, combined with the fact that the full width of the slab can usually not be used because of distortions at the edges, results in a poor utilization of the pumped volume. Therefore zigzag slab lasers exhibit rather modest efficiencies.
- (b) *Residual distortions.* Deformation of the ends and pump faces of the slab due to thermal strain have resulted in beam qualities considerably below expectations.
- (c) *High fabrication cost.* The high optical fabrication costs of the slab, combined with the very demanding and therefore expensive laser head design caused

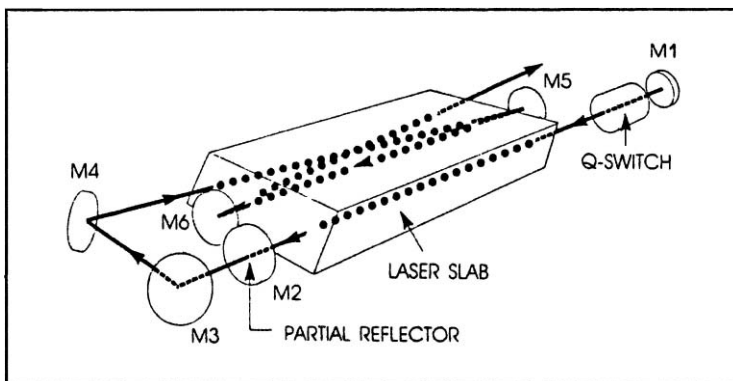


Fig. 7.30. Example of a multipass zigzag slab laser. Shown is an oscillator and a 3-pass amplifier

by the complicated mechanical mounting and sealing geometry, and stringent pumping and cooling requirements have also prevented wider application of this technology.

For the last 20 years, continued engineering improvements have been made to overcome some of the problems encountered in the earlier systems. Efforts have been directed to improve sealing and stress-free mounting of slabs and to reduce edge effects. In order to avoid perturbation of the total internal reflections by "O" ring seals due to coupling of evanescent waves into the seals, side faces of slabs are coated over the whole length with a thin layer of SiO_2 [7.41, 42] or Teflon [7.43]. A uniform thermal loading profile is achieved by thermally insulating the edges with thin insulating and compliant material at the contact areas. To avoid thermal distortions due to the long unpumped Brewster tips, sealing and mounting have been changed to allow pumping and cooling up to the very end of the slab.

In addition to these structural changes, major performance improvements have been realized as a result of a thermally superior slab material, improved resonator designs, and the use of more efficient pump sources.

Earlier work on slab lasers concentrated on Nd:Glass slabs pumped with flash-lamps. Besides the designs depicted in Fig. 6.68, systems were developed using large slabs with oscillator and several-pass amplifiers contained in one unit, as shown in Fig. 7.30 [7.44].

In recent years, design efforts have concentrated mainly on systems utilizing Nd:YAG slabs. Improvements in the growth technology of Nd:YAG boules has made it possible to fabricate Nd:YAG slabs up to 20 cm in length and 2.5 cm wide. The superior thermal properties of this crystal, compared to glass, has led to dramatic performance improvements and also opened the door for conductively cooled slabs in combination with diode pumping. Nd:YAG flashlamp and diode pumped zigzag slab lasers have been built with output power in the multi-kilowatt regime. Also, small conductively cooled diode-pumped slab lasers have found applications in many military and space-borne systems.

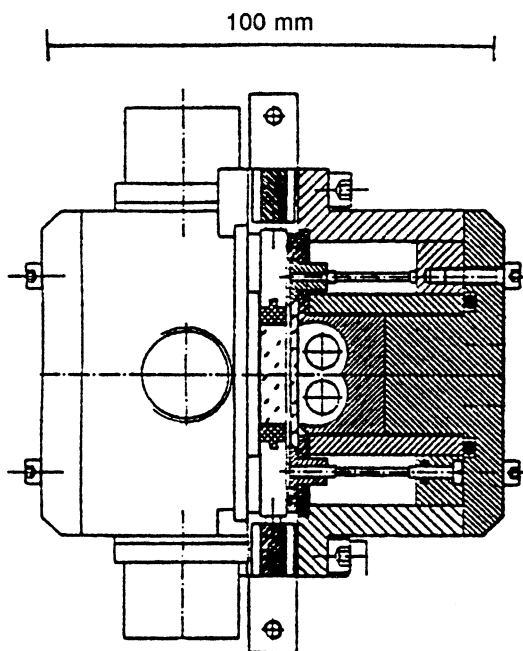


Fig. 7.31. Cross-sectional view of a flashlamp-pumped Nd:YAG slab laser head [7.42]

Figure 7.31 exhibits an example of a zigzag slab design which contains a $0.7 \text{ cm} \times 2.6 \text{ cm} \times 19.1 \text{ cm}$ Nd:YAG slab pumped symmetrically by four krypton arc lamps in a gold-plated reflector [7.42]. The sides are cooled transversely with water at a flow rate of 23 l/min each. The faces of the slab are protected with a $2.2\text{-}\mu\text{m}$ -thick quartz layer to avoid coupling of the laser radiation into the O-ring seals. Top and bottom are thermally insulated by a $200\text{-}\mu\text{m}$ -thick silicone layer. The laser was operated in the long-pulse mode with pump pulses of 4 ms duration and a repetition rate of 22 Hz . A system comprising three slab-pump heads in an oscillator-amplifier configuration produced a maximum of 2.3 kW output. Overall efficiency of the system was 4.3% . The laser had a beam divergence about an order of magnitude lower than a comparable rod system, which was mainly the result of a negative-branch unstable resonator design, which also contained gradient reflective mirrors. At an output of 1.5 kW , the laser had a beam diameter times divergence product of 16mm-mrad (FWHM).

A single oscillator containing an Nd:YAG slab of $1 \text{ cm} \times 2.5 \text{ cm} \times 15.2 \text{ cm}$ pumped by four krypton flashlamps produced an output of 700 W with a beam divergence of $17 \times 8 \text{ mrad}$ [7.45]. The overall efficiency for this system was 2.4% when operated at a $5\text{--}7 \text{ Hz}$ repetition rate and at a pulselwidth of $1\text{--}10 \text{ ms}$. Large Nd:YAG diode-pumped zigzag slab lasers are illustrated in Figs. 6.83 and 6.84.

Diode-array-pumped and conductively cooled Nd:YAG slab lasers for low and medium power output are very attractive for a number of applications and have received considerable attention in recent years. In these lasers, one face of the slab is thermally bonded to a metal heat sink. Pump radiation enters the slab through the

opposite face. At the slab-heat sink interface, a SiO_2 coating preserves total internal reflections, and a gold coating reflects the pump light twice through the slab.

Conductively cooled slabs permit great flexibility in thermal management. Heat from the laser diodes and heat sink can be dissipated into the air via a fin structure and a small fan, or the laser can be attached to a larger structure which provides a thermal sink. An obvious option is liquid cooling. In this case, the liquid is passed through channels in the heat sink and laser diode mounting structure, and does not come into contact with optical surfaces. This greatly simplifies the design. Waste heat can also be absorbed by a phase change material in cases where the laser is operated only intermittently.

A photograph of a compact zigzag slab Nd:YAG laser which is air-cooled and battery-powered is depicted in Fig. 6.82 along with a cross section of the pump module [7.46].

The zigzag slab is pumped by twelve 18-bar arrays with a total optical output of 2.6 J at a pulselength of 200 μs . The slab is designed for 13 bounces and near-normal incidence AR-coated input faces. This type of slab geometry allows both S and P polarizations to be transmitted without loss. The slab dimensions are 138 mm \times 9.5 mm \times 8 mm. The narrow side of the slab, mounted to the heat sink, was coated with a high reflection coating at 808 nm to allow two passes of the pump light through the slab.

One of the engineering difficulties of conduction-cooled laser crystals is stress-free mounting of the slab onto the heat sink. If the slab or the heat sink have even a very slight bow, stress is introduced after the two components are contacted. The application of slight uniform pressure along the length of the slab is not a trivial task. A cross section of the pump module is shown in Fig. 6.82b. The slab was bonded to a thermal expansion-matched heat sink which is clamped to the bridge assembly. This clamping method was employed to reduce mounting and thermal cycling stresses in the laser crystal. A samarium-doped glass window isolates the laser diodes from the Nd:YAG slab. The window protects the slab from possible laser diode bar failure, minimizes contamination near the laser diode facets, and helps suppress parasitic modes in the zigzag slab. The bridge assembly and laser diode arrays are mounted to a common cold plate, where heat is removed by forced convection. Four small fans are used to remove excess heat and regulate the laser diode temperature.

Typical applications for this kind of system are for space applications, range finders, target designators, and airborne lasers for altimetry, as well as medical lasers and small industrial systems.

Other examples of small conductively cooled diode-pumped slab lasers can be found in [7.47]. In this work with only a single diode array, 2mJ pulses with a duration of 4 ns, at repetition rates up to 90 Hz have been obtained.

Edge-Pumped Zigzag Laser

In the zigzag slab lasers discussed so far, the thickness of the slab is a trade-off between efficient pump absorption and efficient heat extraction. Efficient pump absorption

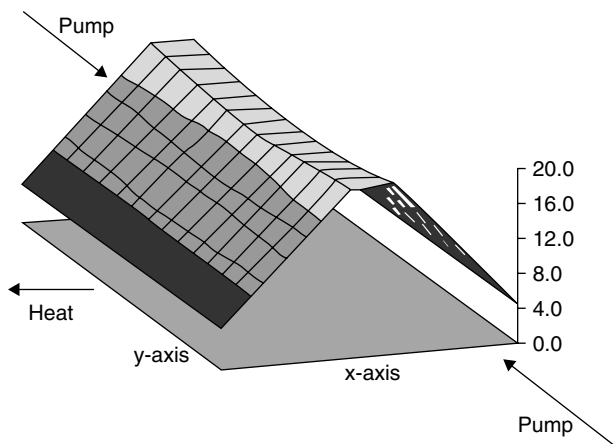


Fig. 7.32. Temperature profile in an edge-pumped Nd:YVO₄ slab. Scale shows temperature in °C

requires a large thickness, whereas thermal gradients and stress are minimized in a thin slab. One approach to solve this dilemma is a thin slab mounted in a highly reflective pumping chamber which allows multiple passes as described in the previous section.

The edge-pumped slab geometry illustrated in Fig. 6.81c and described in [7.48, 49] decouples the cooling and pumping interfaces. As before, the cooling is through the large slab faces and the laser beam follows a zigzag path between these faces by multiple total internal reflecting. However, the pump radiation is incident through the narrow sides, normal to the plane of cooling and the plane of laser beam propagation.

For slabs pumped through the large faces, the pump absorption is a function of the slab thickness; in the edge-pumped geometry the pump absorption is a function of the slab width. Very important in this geometry is a relatively uniform pump absorption along the width, since optical distortions of the crystal in this direction are not compensated by the zigzag path.

Because of the exponential absorption of pump radiation, achieving perfectly uniform pump absorption is not possible. A two-sided pumping geometry results in a symmetric absorbed pump power profile with the lowest point in the center of the slab and the maximum absorbed power at the edges.

The pump nonuniformity can be minimized by the optimum choice of the product (αw), where α is the absorption coefficient and w is the width of the slab. This product is proportional to the Nd concentration n and the slab width, since $\alpha = n\sigma$, where σ is the effective absorption cross section.

Figure 7.32 shows the calculated temperature distribution in an Nd:YVO₄ slab with a cross section of 3 × 3 mm and a length of 20 mm pumped with 40 W at 808 nm from each edge [7.50]. An absorption coefficient of 10 cm⁻¹ was assumed at 808 nm. Heat is extracted symmetrically outward from the center along the x -axis to the

conductively cooled large faces of the slab. As expected the temperature profile in the y -direction peaks at the pumped surfaces. The maximum temperature rise in the slab is 20°C above the heat sink temperature. The temperature gradient in the x -direction is averaged by the zigzag path in the slab. To first order, only the temperature gradient in the y -direction caused by nonuniform pump absorption need to be compensated. The thermal profile illustrated in Fig. 7.32 generated a noncompensated thermal lens in the y -axis of 50 cm, and in the x -axis the residual thermal lens had a focal length larger than 500 cm.

The edge-pumped and conductively cooled Nd:YAG slab laser described in [7.49] with dimensions $1.5 \times 1.8 \times 59$ mm produced 104 W multimode power for 340 W of pump power. The effective thermal lens had a focal length of about 50 cm, in both the zigzag and nonzigzag plane.

A big advantage of the edge-pumped geometry is the possibility of conduction cooling both large faces of the slab. As illustrated in Fig. 6.81, slabs pumped and cooled through the large faces are either liquid-cooled or can be conductively cooled on one side only.

7.2.3 Disk Amplifiers and Lasers

This section addresses thermal-optic issues of large Nd:Glass disk and active mirror amplifiers as well as Yb:YAG thin disk lasers employed in industrial systems.

Large-Disk Amplifiers

Solid-state glass-disk amplifiers were considered very early in the development of high-brightness pulsed laser systems in order to solve problems of cooling, large aperture size, gain uniformity, and pumping efficiency. In a disk laser amplifier (see Fig. 6.93) pump radiation is distributed uniformly over the faces of the slab. Pump-induced slab heating is uniform laterally, thus allowing transverse temperature gradients to be minimized. Such temperature gradients give rise to distortion in the slab just as in the rod geometry. In contrast to the rod geometry, however, the transverse gradients in the slab geometry arise only from spurious effects in pumping and cooling, whereas in the rod geometry, transverse temperature gradients arise from the principal cooling mechanism.

In a disk laser amplifier the surfaces are set at Brewster's angle, as shown in Fig. 6.93. The slab faces have a high-quality optical finish to minimize scattering loss. The beam is linearly polarized in the p -plane to avoid reflection losses. Flash-lamp radiation is incident on the disk faces. Nd:Glass amplifiers containing face-pumped glass disks were first built in the late 1960s at General Electric, University of Rochester, Los Alamos Laboratory, and at the Naval Research Laboratory. Over the years this type of amplifier has been highly developed at laboratories engaged in laser fusion studies, and particularly at the Lawrence Livermore National Laboratory [7.51–53].

A thorough treatment of all optical, mechanical, and electrical aspects of disk laser amplifiers can be found in the Lawrence Livermore National Laboratory Laser

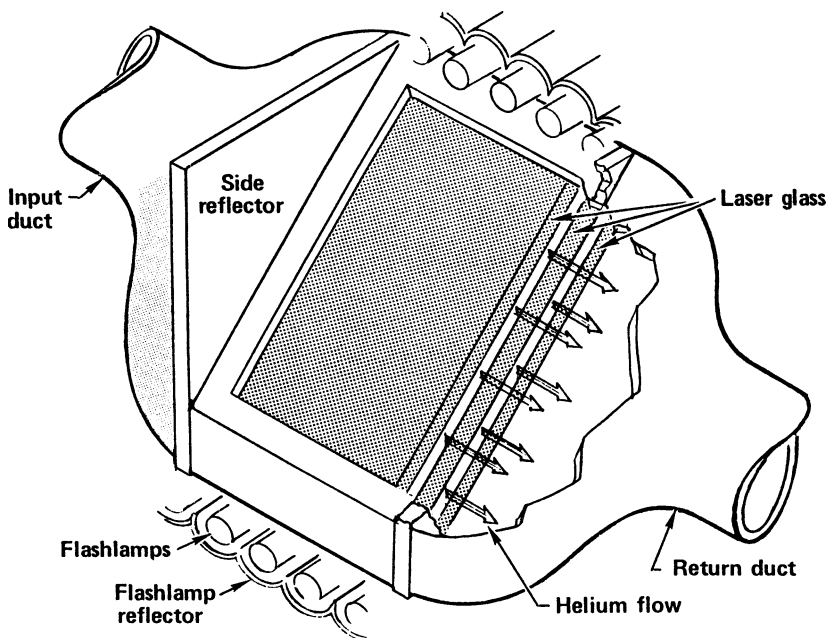


Fig. 7.33. Concept of a gas-cooled disk amplifier module designed for high-average-power operation

Program Annual Reports. Also the book by Brown [7.54] provides a detailed discussion of the various engineering issues related to disk lasers. In the earlier designs, the disks were elliptical in shape and mounted in a cylindrical pump geometry. The design was later changed to a rectangular pump-geometry because of the greater pump efficiency. Disk amplifiers with Nd:Glass slabs 74 cm long have been built and operated.

Generally, an even number of disks is used in an amplifier since beam translation occurs because of refraction in a single disk. Nonlinear beam steering in disks can be minimized if the disks are placed in an alternate rather than parallel arrangement. The entire periphery of each disk is generally surrounded by a metal frame. A blast shield is normally placed between the flashlamp array and the disks; this makes it possible to completely encase the disk assembly. It also protects the disks in case of a flashlamp explosion.

The Brewster's angle disk lasers have been primarily developed for very high peak-power and single-shot operation, with the slabs and coolant all approaching thermal equilibrium in the interval between pulses. To operate the Brewster's angle slab laser at high average power requires adequate cooling as, for example, with forced convection over the faces. In addition, since the laser beam must pass through the coolant, the problem of thermal distortion in the coolant must be dealt with. This operating mode requires that the slabs be sufficiently thin so that the cooling time is several times less than the laser repetition period. Figure 7.33 shows a configuration

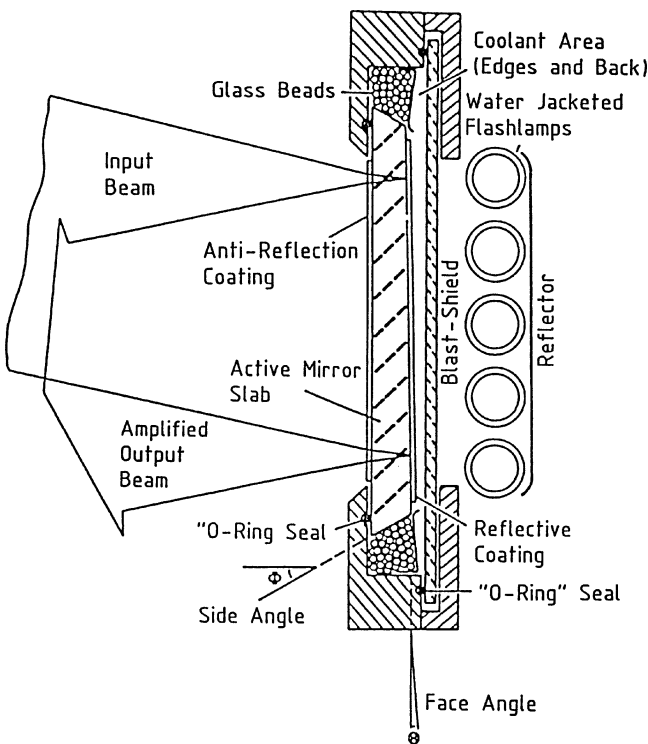


Fig. 7.34. Schematic of active mirror amplifier design [7.57, 58]

of a gas-cooled disk module which could potentially be developed for high-average-power operation, particularly if the Nd:Glass slabs are replaced with crystalline laser host materials [7.55].

Active Mirror Amplifier

The active mirror concept was invented at General Electric [7.56] and extensively developed at the Laboratory for Laser Energetics, University of Rochester [7.57, 58]. In this approach, a single circular or rectangular disk is pumped and cooled from the backside, and laser radiation to be amplified enters from the front, as shown in Fig. 7.34. The front face of the disk has an antireflection coating for the laser radiation, whereas the backside has a thin-film coating which is highly reflective for the laser radiation, and transparent for the flashlamp pump radiation. The laser radiation passes twice through the disk thus improving extraction efficiency. The advantage of this type of amplifier is that it can be pumped uniformly and efficiently; the disadvantage is that the slab can be pumped only through one face, and this unsymmetrical pumping leads to some thermal distortion. Originally designed for Nd:Glass systems requiring large apertures such as needed for fusion research, the concept of an active mirror

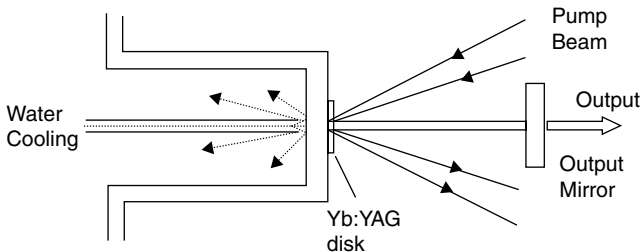


Fig. 7.35. Thin Yb:YAG disk mounted on an internally cooled heat sink

design has also been applied to crystalline hosts such as Nd:Cr:GSGG [7.59] and Yb:YAG [7.60].

Thin-Disk Laser

In the thin-disk laser developed at the University Stuttgart, a Yb:YAG disk a few hundred micrometers thick is attached to a water-cooled heat sink. The pump and laser beams are incident from the front and are reflected at the back surface as indicated in Fig. 6.95. Since heat is extracted from the disk through the back face, the thermal gradients approach a longitudinal cooling geometry. Heat flux is one-dimensional and longitudinal to the laser beam, which minimizes thermal distortions.

Figure 7.35 depicts a 200- μm -thick disk mounted on an internally cooled heat sink. The laser spot is about 3 mm in diameter. The disk is made thin to reduce the thermal gradient within the crystal. Such a thin disk requires many passes through the crystal for efficient energy extraction as also mentioned in Sect. 6.2.4, but the smaller temperature drop compared to a thicker disk allows the cooling water to be at room temperature. At an output power of 1 kW the Yb:YAG disk reaches a temperature of 140°C, with the cooling water inlet temperature at 25°C.

Despite the longitudinal temperature gradients in the disk, there is some beam distortion arising from a bending and bulging of the disk as illustrated in Fig. 7.36. The result of thermal modeling a thin Nd:YAG disk has been published in [7.61].

The bend is the result of a larger thermal expansion on the pumped side of the crystal compared to the side attached to the heat sink. The bulging stems from the finite pump beam diameter causing a concentration of energy deposition at the center of the

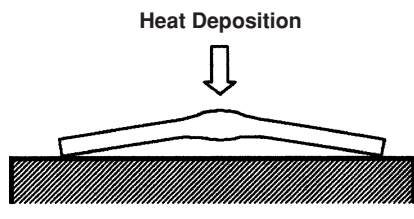


Fig. 7.36. Deformation of a face-pumped disk with back surface cooling

disk. The physical distortion can be minimized by mounting the thin disk between a thick sapphire window and heat sink. As shown in [7.61], by clamping down on the sapphire window, the applied pressure substantially reduces the deformation, leading to a reduced thermal lensing effect.

7.3 End-Pumped Configurations

For cylindrical rods and rectangular slab configurations which are pumped from the side, analytical solutions generally assume uniform heating in an infinitely long rod or slab structure. End effects are treated separately as a distortion of the two-dimensional temperature distribution.

In contrast to side-pumped systems, heat deposition in end-pumped lasers is very inhomogeneous. The very localized heat deposition leads to highly nonuniform and complex temperature and stress profiles. Besides the temperature and stress-dependent variations of the refractive index, the contribution of end bulging to the formation of a thermal lens can be substantial in end-pumped lasers.

Thermal lensing effects and aberrations are particularly strong at the pump face of end-pumped solid-state lasers. Inhomogeneous local heating and nonuniform temperature distribution in the laser crystal lead to a degradation of the beam quality owing to the highly aberrated nature of the thermal lens.

With the availability of high-power diode lasers, end pumping, or longitudinal pumping, of laser crystals has become a very important technology. End-pumped lasers are described in Chaps. 3, 6, and 9. Here, we are concerned with the thermal aspects of end pumping.

7.3.1 Thermal Gradients and Stress

The most common end-pumped configuration is a cylindrically shaped crystal, wrapped in indium foil and press-fitted into a copper block. The heat deposited is radially removed by the water-cooled heat sink. The end surfaces of the crystal are in contact with air.

The attraction of this arrangement is the relative simplicity of its implementation, but owing to the predominantly radial heat flow, it has the disadvantage of strong thermal lensing. Figure 7.37 shows the calculated temperature distribution in a conductively cooled end-pumped laser rod [7.62]. An end-pumped laser rod has a temperature profile across the pumped region which is a function of the distribution of pump radiation. For example for a “top hat” pump beam the temperature distribution is parabolic inside the beam. From the edge of the pumped region, the temperature decays logarithmically to the cooled cylindrical surface of the rod. Along the axis of the rod, the temperature profile will decay exponentially because of the exponential absorption of pump radiation. Temperature and stress profiles and thermal lensing in end-pumped lasers, employing different pump and rod geometries, and cooling techniques, have been described in the literature. The fraction of pump power which is converted to heat inside the laser material acts as heat source.

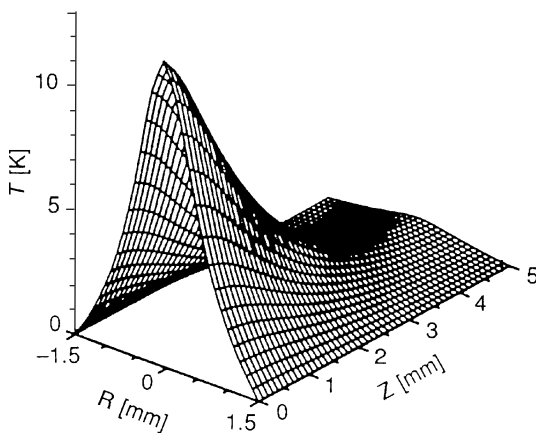


Fig. 7.37. Temperature distribution in an end-pumped laser rod [7.62]

Different cooling arrangements and rod shapes lead to different boundary conditions. The major distinctions are convective or conductive cooling at the rod surface and face-cooled thin disks or edge-cooled long cylinders.

With the temperature at the radial surface of a cylindrical rod clamped, which is typical of a crystal mounted in a temperature-controlled copper heat sink, thermal profiles have been calculated in [7.62–64]. For the boundary condition of a convective heat transfer to the surrounding medium which is typical of a water-cooled crystal, models have been developed and are represented in [7.65, 66]. End-pumped thin disks, either edge- or face-cooled, were treated in [7.67]. Most models have been developed to treat Nd:YAG crystals. A finite-element analysis of temperature, stress, and strain distributions, which includes, besides Nd:YAG, also Nd:GSGG and Nd:YLF, can be found in [7.68]. Another important boundary condition is the radial profile of the pump beam. In the above-mentioned models, top hat profiles were analyzed in [7.64, 67] and Gaussian pump beams have been assumed in [7.62, 63, 68]. A specific investigation of pump-beam profiles and their effect on thermal distortion is found in [7.66].

For most crystalline laser materials, the stress contributions to the refractive index are small. For example, in Sect. 7.1.4, we calculated that in Nd:YAG, the temperature-dependent change of the refractive index represents 74% of the optical distortion. Therefore, most theoretical models consider only the temperature effect on the index of refraction. However, stress components of the refractive index are included in the treatment reported in [7.64, 68].

The large thermal gradients and associated stresses in an end-pumped laser are illustrated in Figs. 7.38a and 7.39a. Shown are the temperature and stress distributions calculated by finite-element analysis for an Nd:YAG crystal [7.69]. In this analysis, a 15 W pump beam from a diode array was assumed to be focused onto an Nd:YAG rod of 4.75 mm radius. The pump beam, which enters the laser crystal from the left along the z -axis in Figs. 7.38 and 7.39, has a Gaussian intensity distribution and a spot-size radius of 0.5 mm in the x -direction. It was assumed that 32% of the incident pump radiation is converted to heat. In the case considered here, the

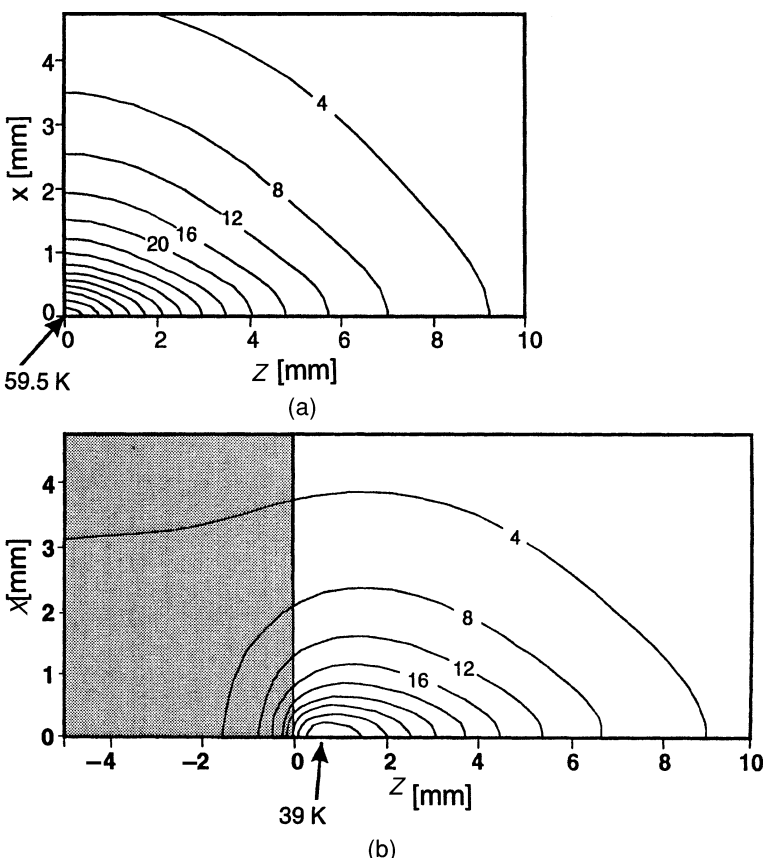


Fig. 7.38. Modeled temperature profiles of an end-pumped Nd:YAG rod (a) with uniform doping and (b) with a 5-mm-long undoped end cap. The maximum values and their locations are indicated by arrows. The temperature difference between two isotherms is 4 K [7.69]

absorption length is much larger than the pump spot size. For the 1.3 at.%-doped rod an absorption coefficient of 4.5 cm^{-1} was assumed. Therefore, 90% of the pump radiation is absorbed in a 5-mm-long path length.

Figure 7.38a illustrates the temperature distribution in one-half of the cross section of the rod. The isotherms represent the temperature difference from the heat sink surrounding the cylindrical surface of the rod. The temperature reaches a maximum of 59.5 K at the center of the pumped surface. The temperature gradients lead to thermal stress. The corresponding stresses in the Nd:YAG rod are indicated in Fig. 7.39a. Positive values of the isobars indicate tensile stresses, and negative values show areas under compression. The core of the crystal is in compression, while the outer regions are in tension. The highest stress occurs on the face of the end-pumped rod, but in contrast to the temperature profile, not at the center, but at the edge of the pump beam (about $2\omega_p$ from the center). The heat generated by the pump radiation causes an axial

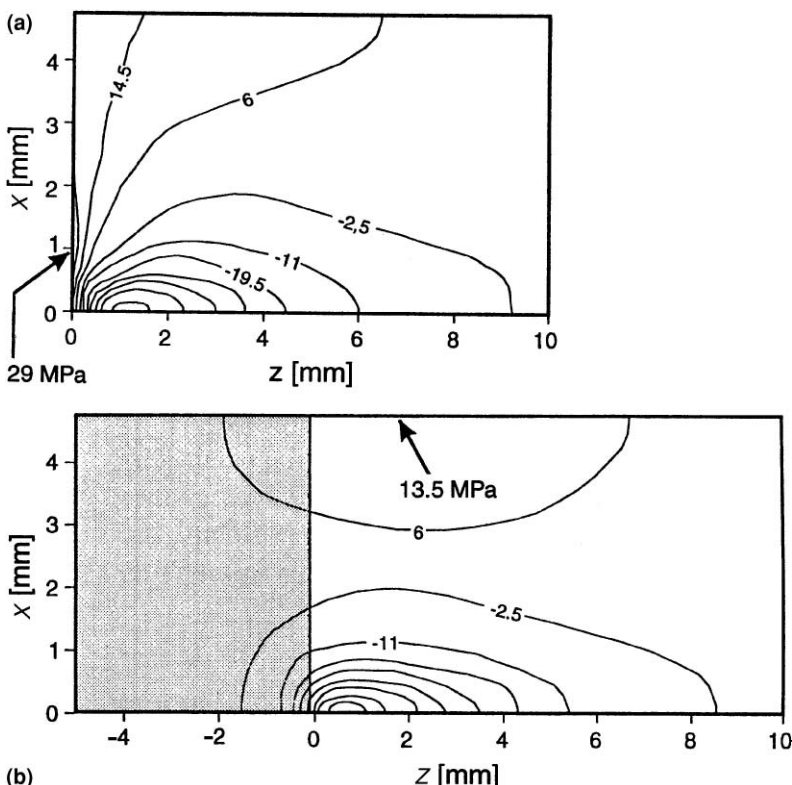


Fig. 7.39. Distribution of the stresses (megapascals) generated by the temperature gradients illustrated in Fig. 7.38 (a) for the uniformly doped crystal and (b) the rod with an undoped end cap [7.69]

expansion of the rod, that is, the front face begins to bulge as the crystal heats up. In the example above, the bending of the pumped surface resulted in a dioptic power of 1.4 m^{-1} . The axial expansion of the rod leads to the high tensile stress at the pump face, as indicated in Fig 7.39a.

The above-mentioned example illustrates a number of characteristic features of end-pumped systems. In order to maximize gain, and to match the TEM_{00} resonator mode, the pump beam is tightly focused, which leads to high-pump-power irradiance incident on the end of the laser rod. As a result, the input face is under a high thermal load. The thermal stress, which leads to strong thermal lensing, is often high enough to cause fracture of the end face of the laser rod.

The thermal management of end-pumped lasers can be greatly improved by the use of composite rods. Laser crystals, such as Nd:YAG, Nd:YVO₄, and Yb:YAG, have become available with sections of undoped host material on one or both ends. These end caps are diffusion-bonded to the doped laser crystal. Composite rods are proven to provide a very effective way to reduce temperature and stresses at the face of end-pumped lasers. This is illustrated in Figs. 7.38b and 7.39b that show the result of

an analysis carried out for an Nd:YAG rod with a 5-mm-long undoped YAG section at the pumped front end. The other parameters are the same as for the uniformly doped crystal. Because the undoped region is transparent to the impinging pump radiation, there is no thermal load generated at the rod pump face.

The diffusion bond provides uninhibited heat flow from the doped to the undoped region. A large temperature reduction of about 35% is achieved for the composite rod, where a significant part of heat flow occurs into the undoped end cap. The undoped end cap prevents the doped pump face from expanding along its axis; therefore no surface deformation takes place at this interface. This leads to strong compressive stresses (as shown in Fig. 7.39b) instead of tensile stresses, as was the case for the unrestrained surface (Fig. 7.39a). Since the Nd:YAG crystal, like most materials, is much stronger under compression than under tension, the undoped end cap increases the stress fracture limit and thereby the maximum thermal loading that can be tolerated by the end-pumped laser.

Besides increasing the average power capability of the laser, as a result of better thermal management, a composite rod has a number of other advantages. In end-pumped lasers, a dichroic coating is generally applied to the pump face, i.e., the coating is highly reflecting for the laser wavelength at 1.06 μm and highly transmitting for the pump wavelength at 808 nm. The durability of this coating can be affected by the considerable mechanical and thermal stress present at this surface. In a composite rod, the coating temperature is spatially uniform and surface deformation and associated stresses are absent.

Another advantage of undoped end caps is associated with cooling the ends of the laser rod. In a water-cooled end-pumped crystal, the last few millimeters of a rod cannot be effectively cooled by circulating water because of the space required for o-ring seals. The nonabsorbing end sections of a composite laser rod solve this thermal management problem.

Diffusion bonding is a heat treatment to redistribute surface energy and restore crystallographic order within the crystal. Diffusion bonding of an Nd:YAG crystal with undoped YAG involves precision polishing, assembly by optical contacting, and heat treatment. Surface flatness and roughness determine the ability to optical contacting. YAG crystals are heat-treated between 1200 and 1600°C, well below the melting point of 1920°C [7.70].

7.3.2 Thermal Lensing

An important parameter for the design of the optical resonator is the amount of thermal lensing caused by the temperature distribution in an end-pumped laser crystal. In a first approximation, the thermally induced lens can be described by considering only the temperature-dependent part of the refractive index. Also assuming only radial heat flow in a rod that is in contact with a thermal heat sink of fixed temperature, an analytical solution for the focal length of the thermal lens was derived in [7.63]. A Gaussian pump beam incident on the crystal has been assumed

$$I(r, z) = I_0 \exp(-2r^2/w_p^2) \exp(-\alpha_0 z), \quad (7.69)$$

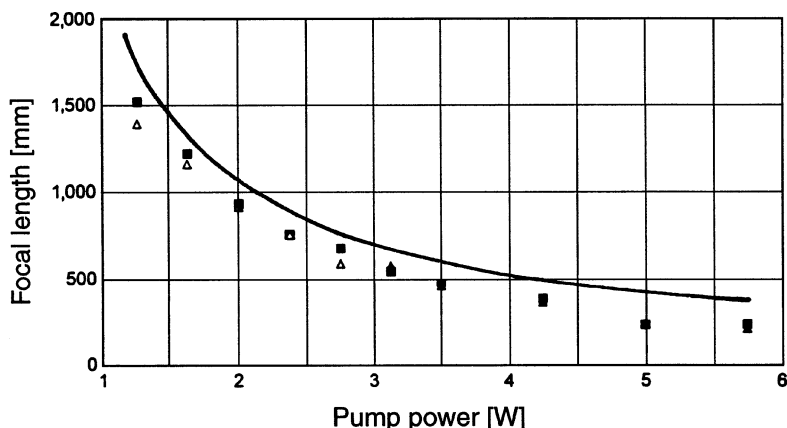


Fig. 7.40. Thermal lensing in an end-pumped Nd:YAG laser. Measured values are from [7.71]

where α_0 is the absorption coefficient and w_p is the $(1/e^2)$ Gaussian radius of the pump beam. With P_h , the fraction of the pump power that results in heating, the effective focal length for the entire rod can be expressed by

$$f = \frac{\pi K w_p^2}{P_h(dn/dT)} \left(\frac{1}{1 - \exp(-\alpha_0 l)} \right), \quad (7.70)$$

where K is the thermal conductivity of the laser material and dn/dT is the change of refractive index with temperature. From (7.70) it follows that the effective focal length depends on the square of the pump-beam radius w_p . Therefore, it is desirable to use the largest pump-beam radius consistent with resonator-mode match.

The dependence of thermal lensing on pump power is illustrated in Fig. 7.40. An end-pumped Nd:YAG rod with a length of 20 mm and a radius of 4.8 mm was pumped with a fiber-coupled laser diode array. The output from the fiber bundle was imaged onto the crystal surface into a pump spot with radius $w_p = 340 \mu\text{m}$. Figure 7.40 displays the measured thermal lens and the calculated values according to (7.70). In using this equation, we assume that 32% of the pump power results in heating. The material parameters required for Nd:YAG are $dn/dT = 7.3 \times 10^{-6} \text{ K}^{-1}$, $\alpha_0 = 4.1 \text{ cm}^{-1}$, and $K = 0.13 \text{ W/cm K}$.

Equation (7.70) is an approximation for low and medium pump intensities. At high pump levels, the contribution of end bulging to thermal lensing is substantial and in Nd:YVO₄ can be as high as the thermal index variations [7.72]. As discussed above, end bulging due to thermal deformation can be prevented by diffusion bonding of an undoped end cap at the pump side of the laser. Another approach to reduce bulging is the application of mechanical stress to the crystal to compensate for thermally induced deformation. In this approach a thin crystal is compressed between a sapphire window and a copper heat sink. Pump and resonator beam enter through the sapphire window. At an applied pressure on the order of 700 MPa a marked reduction of thermal lensing was observed [7.73].

Also by using the sapphire window just as a heat sink without applying a large pressure, a markedly reduced surface deformation has been measured in Nd:YAG [7.69]. In general, surface deformation is much more pronounced in Nd:YVO₄ as compared to Nd:YAG [7.72, 74].

The total amount of thermal lensing is not only strongly affected by the cooling method and choice of crystal, but is also a function of the shape of the pump beam. In [7.74] it was shown that a gaussian beam has thermal lensing that is a factor of 2 stronger than a top hat intensity distribution.

7.3.3 Thermal Fracture Limit

In end-pumped lasers a large amount of thermal energy is accumulated near the pump region and the maximum laser output power is limited by thermal fracture of the laser crystal. In an edge-cooled end-pumped laser, just as in side-pumped lasers, the center is in compression and the outer regions are under tension. Stress fracture typically starts at the periphery because the tensile strength of most materials is much lower than the rupture strength under compression.

Models to analyze the scaling limits of diode end-pumped Nd:YAG lasers have been reported in [7.64, 67]. Compared to vanadate crystals, YAG has a three times higher stress fracture limit and a higher thermal conductivity. This is the reason that the highest output power from end-pumped lasers have been obtained from lasers with YAG as the host crystal. As discussed in Sect. 6.2.3 output power in excess of 100 W have been achieved in end-pumped Nd:YAG, Tm:YAG, and Yb:YAG lasers.

For the development of compact and efficient end-pumped lasers, Nd:YVO₄ is the most attractive material owing to its high pump absorption coefficient, large pump wavelength tolerance, and large stimulated emission cross section. A number of studies have focused on power scaling of Nd:YVO₄ lasers [7.75, 7.76]. The investigation revealed that the fraction limited pump power in vanadate crystals is strongly related to the Nd³⁺ concentration.

Pump absorption increases linearly with dopant concentration. A high level of absorption results in an increase of the temperature gradients and consequently a great amount of stress is produced within the crystal. Also the fractional thermal loading increases with higher dopant concentration because of fluorescence quenching. Table 7.2 lists the fractional thermal loading in Nd:YVO₄ corresponding to different Nd³⁺ concentrations under lasing and nonlasing conditions [7.75, 77–79].

Table 7.2. Fractional thermal loading of Nd:YVO₄ crystals [7.75]

	Nd ³⁺ concentration		
	0.5%	1%	2%
η_h (lasing)	0.24	0.28	0.36
η_h (nonlasing)	0.36	0.49	0.59

Lowering the dopant concentration extends the fracture limited input power. On the other hand, power conversion efficiency is generally greater for higher concentrations. A higher dopant concentration and therefore a stronger absorption of the pump radiation allow the use of a shorter crystal. Because of the large divergence of the pump beam, higher beam overlap efficiency can be achieved in a shorter crystal, which in turn leads to a higher slope efficiency for TEM₀₀ mode operation. To assure a high absorption of the pump beam, the length of the crystal is usually chosen to satisfy the condition $\alpha l = 4\text{--}5$, where l is the crystal length and α is the absorption coefficient for the pump wavelength.

For an edge-cooled Nd:YVO₄ crystal mounted in a copper heat sink, Peng et al. [7.75] have performed a finite-element analysis to evaluate the maximum permissible pump power as a function of Nd³⁺ concentration, crystal dimensions, and pump beam size. The maximum pump power was defined as operation at 80% of the stress fracture limit. The number for the maximum tensile strength was obtained from an experiment in which a crystal was pumped beyond the fracture limit. Fracture occurred at 22 W with a pump beam radius of 0.2 mm and 1% doping. From these data the tensile strength of Nd:YVO₄ was calculated to be 53 MPa. For a crystal size of 3 × 3 × 5 mm and a given pump beam radius of 0.4 mm it was found that the maximum pump power decreased from 30 W for a doping concentration of 0.5% to 15 W for a concentration of 2%. For a fracture limited pump power of 36 W the doping concentration was calculated to be 0.25%.

These results seemed to be confirmed by comparing the calculations with the performance of actual systems. An end-pumped Nd:YVO₄ laser with a Nd³⁺ concentration of 0.3 at.% pumped from both sides produced a TEM₀₀ output of 25 W for 52 W incident pump power [7.80], and a two-crystal laser with each crystal pumped at one end and having an Nd³⁺ concentration of 0.3 at.% produced 30 W of TEM₀₀ for 48 W incident pump power [7.81].

In the above-mentioned finite-element analysis the dependence of the pump radius and crystal size on the fracture limited pump power was also evaluated. The pump beam radius had a much smaller effect on the maximum pump power compared to the dopant concentration. The maximum pump power was calculated to increase from 30 W to 35 W as the radius of the pump beam increases from 0.4 mm to 1 mm. The analysis also showed that the smaller the rod diameter the larger the fracture limited pump power. The reason is that the shorter thermal path in a smaller crystal reduces the temperature gradient and stress inside the crystal.

Diffusion bonding undoped end caps to an Nd:YNO₄ crystal reduces the stresses at the pump face as was discussed for the case for Nd:YAG. An increase of the maximum pump power of a factor 1.5 was reported in [7.82] for a composite rod compared to a conventional rod.

The thermal shock parameter R introduced in (7.29), which depends on mechanical and thermal properties of the laser medium, indicated the permissible loading before a fracture occurs. Actually the maximum pump power is proportional to R . A thermal shock parameter for end-pumped lasers was introduced by Chen [7.76]

$$R = K \sigma_{\max} / \alpha E, \quad (7.71)$$

where K is the thermal conductivity, σ_{\max} is the maximum tensile strength, α is the thermal expansion coefficient, and E is Young's modulus. With the exception of the term $(1 - \nu)$ this is the same equation as presented in (7.29). For Nd:YVO₄ if one introduces the appropriate values of $K = 0.051 \text{ W/cm K}$, $\alpha = 4.43 \times 10^{-6} \text{ K}^{-1}$, $E = 133 \text{ GPa}$, and $\sigma_{\max} = 53 \text{ MPa}$ into (7.71), then one obtains $R = 4.6 \text{ W/cm}$. Comparing this number with the shock parameters listed in Table 7.1 and using the Poisson ratio of $\nu = 0.33$ for Nd:YVO₄ we find that Nd:YVO₄ has a thermal shock parameter 39% that of Nd:YAG.

7.4 Thermal Management

Most solid-state lasers are liquid-cooled with either the heat dissipated into the surrounding air in a liquid-to-air heat exchanger or the waste heat transferred to an external cooling loop in a liquid-to-liquid heat exchanger. In smaller diode-pumped lasers, thermal energy can be removed from the pump source and laser medium by conduction followed by dissipation into the surroundings by forced air cooling.

Besides these traditional cooling techniques a number of more exotic thermal management systems have been used or are contemplated for special military solid-state lasers.

For short burst operation, heat from the laser can be transferred by conduction to a fin-type radiator where the spaces between the fins are filled with a phase transition material. Usually paraffin or special waxes with melting temperatures between 50 and 90°C are employed. The waste heat from the laser is absorbed in this case by melting the phase transition material.

In the above-mentioned cooling system the latent heat of melting is exploited. Spray cooling is another phase change process using the latent heat of vaporization. With this method large amounts of heat can be removed from a surface, in spray cooling a dense spray of liquid droplets is deposited on a surface through an atomizer nozzle. Such a thermal management system is contemplated for a 100 kW diode-pumped solid-state military laser. If one assumes a 50% efficient diode pump source and 20% optical-to-optical efficiency of the laser, then 500 kW have to be dissipated from the heat sinks of the diode arrays.

In the heat capacity laser, another concept for a military-type laser (already proposed by the author in the 1970s), the laser medium is not actively cooled and heats up during operation. Rapid cooling occurs between bursts of pulses. For example, 10 × 10 × 2 cm plates of Nd:GGG crystals are pumped at 808 nm. The waste heat is absorbed by the laser crystals and the temperature rises after each pulse until a critical point is reached, either determined by a drop in gain below threshold or by the thermal limit of the laser medium.

7.4.1 Liquid Cooling

In flashlamp or arc lamp pumped systems, the primary purpose of the liquid is to remove the heat generated in the laser material, pump source, and laser cavity.

Sometimes the coolant serves additional functions, such as index matching, thereby reducing internal reflections which could lead to depumping modes, or as a filter to remove undesirable pump radiation. The coolant is forced under pressure to flow over the rod and lamp surfaces. These elements are located either inside flowtubes or in cooling chambers machined out of the main body of the laser head. The temperature difference between the part to be cooled and the liquid is a function of the velocity and the cooling properties of the flowing liquid. At low velocities, the flow is laminar and most of the temperature drop is due to pure conduction across a stationary boundary layer at the liquid interface. For higher velocities, the flow becomes turbulent, leading to a more efficient heat transfer process with a subsequent lower temperature drop. Turbulent flow requires a greater pressure differential for the same volume flow, but the necessary differential usually is still small compared to the total pressure difference associated with the complete cooling system.

The temperature increase of the coolant, as it passes through the laser cavity, is given by

$$\Delta T = \frac{Q}{c_p m} = \frac{Q}{c_p f_v \rho}, \quad (7.72)$$

where Q is the extracted heat, c_p , m , and ρ is the specific heat, mass flow rate, and density of the coolant, respectively, and f_v is the volumetric flow rate.

Water is preferably used as a coolant for solid-state lasers, with the exception of military lasers which have to operate over an extremely wide temperature range. A standard specification for airborne military systems is MIL-E-5400K, class 1, which requires operation of electronic equipment over the range of -54°C to $+55^{\circ}\text{C}$.

The major difficulty in finding coolants for use in systems which have to be stored and operated at freezing temperatures is the strong ultraviolet radiation within the laser cavity. This causes most of the fluids, which would otherwise have suitable optical and physical parameters, to decompose. Extensive tests have indicated that under these conditions, ethylene glycol water mixtures are the best choice for laser coolants exposed to low temperatures. Properties of water and a glycol–water mixture are given in Table 7.3.

Table 7.3. Room-temperature properties of various coolants

Parameter	Water	Ethylene glycol 50%, water 50%
Specific heat [cal/g $^{\circ}\text{C}$]	1.0	0.79
Viscosity (poise) [g/cm s]	1×10^{-2}	3.0×10^{-2}
Thermal conductivity [cal/cm s K]	1.36×10^{-3}	1.01×10^{-3}
Density [g/cm 3]	1.0	1.06
Prandtl number N_{Pr} –	7.4	23.5
Volumetric thermal expansion coefficient [$^{\circ}\text{C}^{-1}$]	0.643×10^{-4}	5.7×10^{-4}
Boiling point [$^{\circ}\text{C}$]	100	110
Freezing point [$^{\circ}\text{C}$]	0	-36

From purely heat transfer considerations, water is by far the best fluid. As compared to the other coolants, it has the highest specific heat and thermal conductivity and the lowest viscosity. If we express the mass flow rate by the volumetric flow $f_v = m/\varrho$, where ϱ is the density of the fluid, then after introducing appropriate parameters from Table 7.3 into (7.72), we obtain the temperature rise in water:

$$\Delta T [^{\circ}\text{C}] = \frac{0.24 P [\text{kW}]}{f_v [\text{litr/s}]}, \quad (7.73)$$

where P is the heat carried away by the water.

As a comparison if an ethylene glycol–water mixture is employed as a coolant, we obtain a temperature rise

$$\Delta T [^{\circ}\text{C}] = \frac{0.29 P [\text{kW}]}{f_v [\text{litr/s}]}. \quad (7.74)$$

Besides the higher temperature rise for that same flow rate, it is also important to note that the higher viscosity of the glycol–water mixture compared to water will result in a much higher pressure drop in the cooling channels and supply lines.

Water has the additional advantage over all other coolants that it is chemically stable under intensive ultraviolet radiation. Water–alcohol mixtures have C–H bonds which break if the energy from the UV radiation exceeds the bond energy. The coolants become acidic, precipitates develop, and the optical transmission decreases. The degradation of these coolants can be related to their UV cutoff wavelength, which shifts toward longer wavelengths as the coolant degrades [7.83]. Dissociation followed by complete carbonization of the coolant have led to the development of UV-free flashlamps. The envelope of these lamps is usually made from UV-absorbing titanium-doped quartz. Even though most military systems employ flashlamps with UV-absorbing quartz envelopes, the amount of UV remaining may still cause coolant degradation. Once an ethylene glycol and water mixture has been exposed to UV radiation, it continues to build up acidity even when not in use. Stainless steel plumbing has been used with ethylene glycol and water systems to preclude corrosive buildups.

In large diode-pumped systems, the laser medium, either in the shape of a rod or slab, is liquid-cooled in the same way as a lamp-pumped laser. However, a diode-pumped laser represents a much more benign environment because of the absence of ultraviolet radiation. The heat sinks of the diode pump sources are internally water-cooled. If the diode arrays have microchannels for cooling, a larger pressure head will be required to move the coolant through the small passageways as compared to a standard water-cooled heat sink.

In conductively cooled slab or end-pumped lasers only the heat sinks of pump and laser medium need to be liquid-cooled. In this case, the cooling fluid is not in the optical path. This further relaxes the requirement on the cleanliness and transparency of the coolant.

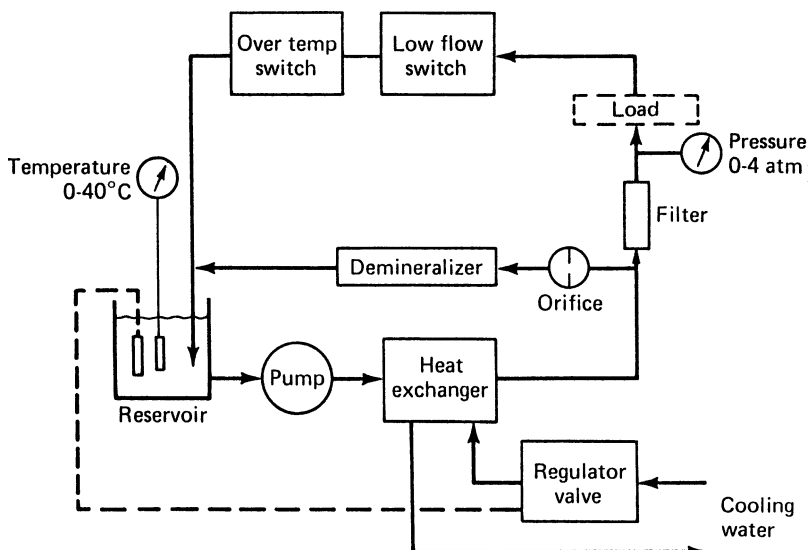


Fig. 7.41. Schematic of a water cooler containing a water-to-water heat exchanger

Cooling Equipment

With the exception of lasers cooled directly by tap water, a closed-loop cooling system is usually employed which consists in its most basic form of at least a liquid pump, a heat exchanger, and a reservoir. Commercially available coolers contain, in addition to these components, a particle filter, a demineralizer, gauges, and sensors for monitoring flow, temperature, and pressure. If common tap water is used, periodic cleaning is necessary to remove deposition of organic and mineral deposits. In closed-loop systems, if demineralization and filtering are employed, the need to clean surfaces exposed to the cooling fluid is essentially eliminated.

The heat exchanger removes heat from the closed-loop system by thermal coupling to an outside heat sink. This can be accomplished in several ways: In a liquid-to-air heat exchanger the coolant is passed through an array of fins through which air is blown by a fan similar to a car radiator. In a liquid-to-liquid heat exchanger the heat generated within the closed loop is exhausted to external water. Figure 7.41 shows the plumbing diagram of a typical cooler with a liquid-to-liquid heat exchanger. The water flows from the reservoir to a centrifugal pump, through a heat exchanger, into the laser head, and back again into the reservoir. This sequence of components minimizes the static pressure in the laser head. The temperature of the closed-loop water is regulated by a control valve in the external supply line. The valve probe is located in the reservoir. As the temperature at the reservoir increases, the valve is opened, thereby allowing more external cooling water to flow through the heat exchanger. The system contains an in-line honeycomb filter to remove particulate matter and a bypass demineralizer which will maintain low electrical conductivity in the water and minimize corrosion.

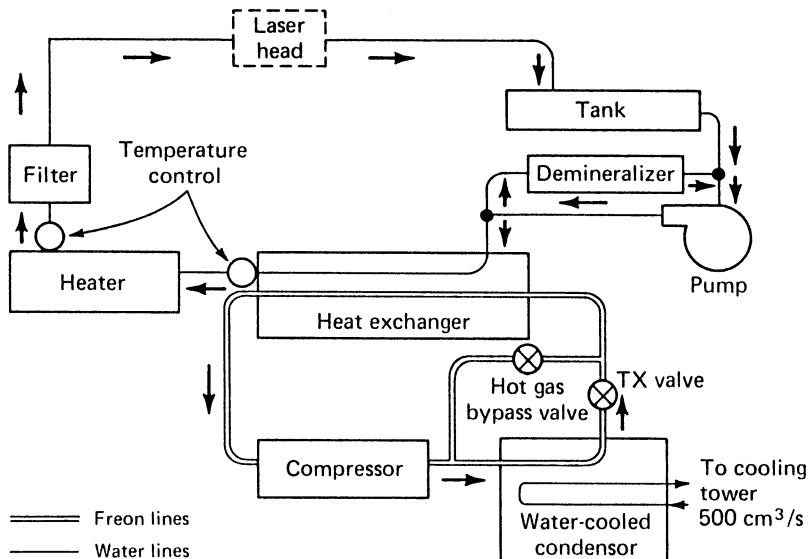


Fig. 7.42. Schematic of a water cooler employing a refrigeration unit

The return line is monitored by a low-flow interlock and an over-temperature switch. If flow falls below a preset value or the discharge temperature exceeds a certain limit, the interlock turns off the power supply. The system also contains gauges to display temperature in the return line and the discharge pressure.

In both types of coolers we have discussed so far, the temperature of the closed loop can be regulated only over a relatively narrow temperature range. Furthermore, the temperature of the cooling loop is always above ambient air temperature or the temperature of the external cooling water. Figure 7.42 shows a diagram of a cooler which maintains the cooling water at a precise, reproducible temperature which is independent of the ambient air or water temperature. This cooler contains a thermostatically controlled refrigeration stage between the heat exchanger and the external water supply. Freon is cycled in a closed loop between the heat exchanger and a water-cooled condenser by means of a compressor. Any changes in the heat dissipation of the load, or temperature variations in the external lines, are compensated by a hot gas bypass valve which regulates the amount of refrigeration. Smaller units contain air-cooled condensers, thus eliminating the need for an external water source.

7.4.2 Conduction Cooling

In a number of diode-pumped lasers the active medium is mounted directly to a heat sink. Typical examples are conductively cooled slab lasers and end-pumped lasers described in Chap. 6 and Sect. 7.3.

Good conduction cooling of the laser element requires intimate thermal contact between the laser medium and the heat sink. The laser rod can be mechanically

clamped, soldered, or bonded to the heat sink. If the laser crystal is mechanically clamped to a heat sink, a temperature gradient across the rod-clamp interface will develop.

$$\Delta T = P/hA, \quad (7.75)$$

where P is the total power dissipated through the contact area A , and h is the surface heat transfer coefficient discussed at the beginning of this chapter.

Usually a thin layer of indium foil is applied between the crystal and copper heat sink. For such a boundary condition a heat transfer coefficient of $h = 1.5 \text{ W/cm}^2 \text{ K}$ is typically assumed. By comparison convection to stagnant air would result in values of $h = 5\text{--}25 \cdot 10^{-3} \text{ W/cm}^2 \text{ K}$.

If the crystals and heat sink are bonded together, a compliant material such as silver-filled epoxy adhesive will accommodate the different thermal expansion coefficients.

Niobium has a thermal coefficient of expansion that closely matches that of Nd:YAG. In this case the laser crystal can be soldered to the heat sink with indium solder after the contact surfaces are gold-plated.

Besides the temperature drop across the contact area there is a temperature differential between the front and back sides of the heat sink.

$$\Delta T = Pd/KA, \quad (7.76)$$

where d is the thickness and K is the thermal conductivity of the heat sink, respectively.

Heat is removed from the system by either air or water cooling the backside of the heat sink.

7.4.3 Air/Gas Cooling

Diode-pumped low-average-power lasers are often cooled by forced air. Air flow is generated by employing miniature axial or centrifugal blowers or fans which have been designed for air cooling of electronic equipment. The air flow required for cooling the laser head is calculated from the dissipated heat and the maximum temperature difference along the air stream. For standard air (20°C , 1 atm) we obtain

$$\Delta T [\text{ }^\circ\text{C}] = 49 \frac{P [\text{W}]}{f_v [\text{ltr/min}]}, \quad (7.77)$$

where f_v is the air flow and ΔT is the temperature difference between the inlet air and the exhausted air. The numerical factor contains the thermal properties of air. The air flow which can be obtained from a given fan depends on the static pressure the fan must work against. Small fans which are used for cooling lasers usually provide an air flow of 300–600 l/min at a static pressure of 30 torr. Allowing a temperature rise of 10°C of the exhausted air, heat removal capacity will be in the 60–120 W range. Figure 6.82 shows an example of an air-cooled diode-pumped Nd:YAG laser. Three small axial fans generate an air flow which passes over the heat sink to dissipate the heat from the diode arrays and the laser crystal.

In lasers with high-power dissipation, difficulties arise if one attempts to force low-pressure air into a small cavity while maintaining a high heat transfer coefficient. As the density of air is increased, for instance by a factor of 20, the pressure drop required to move the same mass flow of air through the cavity is reduced to 1/20th and the pump power required is reduced to 1/400th.

Many years ago a cooling system has been employed very successfully in small military laser systems which was based on the use of compressed dry nitrogen as the coolant medium to transfer the heat generated in the laser cavity to the ambient air. The compressed nitrogen was circulated through the laser pumping cavity by means of an axial flow blower. Nitrogen exhausted from the cavity was then ducted through fins of a heat exchanger, where it gave up the energy picked up in the laser cavity. The cooled nitrogen was then ducted back through the cavity again to complete the nitrogen cooling loop. A fan provided the required air flow through the heat exchanger. The unit was charged to a pressure of 20 atm; with dry nitrogen at this high pressure the heat transfer capability of compressed nitrogen is about half that of water-glycol mixtures.

More recently, gas cooling of diode pumped ytterbium-strontium-fluorapatite (Yb:S-FAP) crystals has been considered by Lawrence Livermore Laboratory for an advanced inertial confinement fusion laser. Helium in a highly turbulent flow has been chosen as the heat transfer medium because it has a high thermal conductivity and causes only insignificant optical distortions [7.84].

8. Q-Switching

A mode of laser operation extensively employed for the generation of high pulse power is known as Q-switching. It has been so designated because the optical Q of the resonant cavity is altered when this technique is used [8.1, 2]. As was discussed in Chap. 3, the quality factor Q is defined as the ratio of the energy stored in the cavity to the energy loss per cycle. Consequently, the higher the quality factor, the lower the losses.

In the technique of Q-switching, energy is stored in the amplifying medium by optical pumping, while the cavity Q is lowered to prevent the onset of laser emission. Although the energy stored and the gain in the active medium are high, the cavity losses are also high, lasing action is prohibited, and the population inversion reaches a level far above the threshold for normal lasing action. The time for which the energy may be stored is on the order of τ_f , the lifetime of the upper level of the laser transition. When a high cavity Q is restored, the stored energy is suddenly released in the form of a very short pulse of light. Because of the high gain created by the stored energy in the active material, the excess excitation is discharged in an extremely short time. The peak power of the resulting pulse exceeds that obtainable from an ordinary long pulse by several orders of magnitude.

Figure 8.1 shows a typical time sequence of the generation of a Q-switched pulse. Lasing action is disabled in the cavity by a low Q of the cavity. Toward the end of the flashlamp pulse, when the inversion has reached its peak value, the Q of the resonator is switched to some high value. At this point a photon flux starts to build up in the cavity and a Q-switch pulse is emitted. As illustrated in Fig. 8.1, the emission of the Q-switched laser pulse does not occur until after an appreciable delay, during which time the radiation density builds up exponentially from noise.

8.1 Q-Switch Theory

A number of important features of a Q-switched pulse, such as energy content, peak power, pulse width, rise and fall times, and pulse formation time, can be obtained from the rate equations discussed in Chap. 1. In all cases of interest the Q-switched pulse duration is so short that we can neglect both spontaneous emission and optical pumping in writing the rate equations.

From (1.61, 1.58), it follows that

$$\frac{\partial \phi}{\partial t} = \phi \left(c\sigma n \frac{l}{L} - \frac{\varepsilon}{\tau_r} \right) \quad (8.1)$$

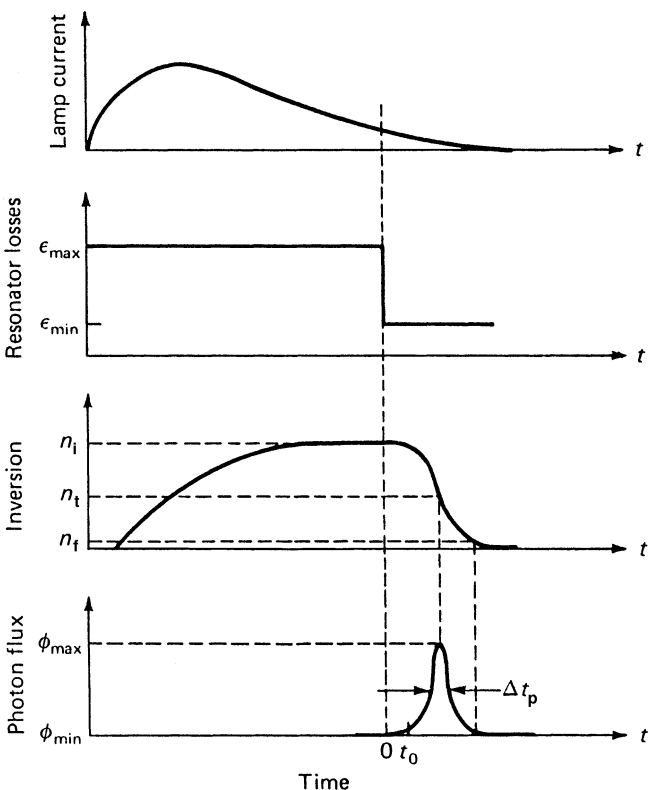


Fig. 8.1. Development of a Q-switched laser pulse. The flashlamp output, resonator loss, population inversion, and photon flux as a function of time are shown.

and

$$\frac{\partial n}{\partial t} = -\gamma n \phi \sigma c. \quad (8.2)$$

In (8.1) we expressed the photon lifetime τ_c by the round-trip time t_r and the fractional loss ε per round trip according to (3.8). Also, a distinction is made between the length of the active material l and the length of the resonator L . Q-switching is accomplished by making ε an explicit function of time (e.g., rotating mirror or Pockels cell Q-switch) or a function of the photon density (e.g., saturable absorber Q-switch). The losses in a cavity can be represented by

$$\varepsilon = -\ln R + \delta + \zeta(t), \quad (8.3)$$

where the first term represents the output coupling losses determined by the mirror reflectivity R , the second term contains all the incidental losses such as scattering, diffraction, and absorption, and $\zeta(t)$ represents the cavity loss introduced by the Q-switch. For a particular explicit form of $\zeta(t, \phi)$, the coupled rate equations can be solved numerically with the boundary condition $\zeta(t < 0) = \zeta_{\max}; \zeta(t \geq 0) = 0$. In

many instances Q-switches are so fast that no significant change of population inversion takes place during the switching process; in these cases ζ can be approximated by a step function.

8.1.1 Fast Q-Switch

In the ideal case, where the transition from low Q to high Q is made instantaneously, the solution to the rate equations is particularly simple. In this case we assume that at $t = 0$ the laser has an initial population inversion n_i , and the radiation in the cavity has some small but finite photon density ϕ_i . Initially, the photon density is low while the laser is being pumped and the cavity losses are $\varepsilon_{\max} = -\ln R + \delta + \zeta_{\max}$ as illustrated in Fig. 8.1. The losses are suddenly reduced to $\varepsilon_{\min} = -\ln R + \delta$. The photon density rises from ϕ_i , reaches a peak ϕ_{\max} many orders of magnitude higher than ϕ_i , and then declines to zero. The population inversion is a monotone decreasing function of time starting at the initial inversion n_i and ending at the final inversion n_f . We note that the value for n_f is below the threshold inversion n_t for normal lasing operation. At n_t the photon flux is maximum and the rate of change of the inversion dn/dt is still large and negative, and n falls below the threshold value n_t and finally reaches the value n_f . If n_i is not too far above n_t , that is, the initial gain is close to threshold, then the final inversion n_f is about the same amount below threshold as n_i is above and the output pulse is symmetric. On the other hand, if the active material is pumped considerably above threshold, the gain drops quickly in a few cavity transit times t_r to where it equalizes the losses. After the maximum peak power is reached at n_t , there are enough photons left inside the laser cavity to erase the remaining population excess and drive it quickly to zero. In this case the major portion of the decay proceeds with a characteristic time constant τ_c , which is the cavity time constant.

The equations describing the operation of rapidly Q-switched lasers involve the simultaneous solution of two coupled differential equations for the time rate of change of the internal photon density in the resonator, (8.1), and the population inversion density in the active medium, (8.2). We can express the output energy of the Q-switched laser as follows [8.3]:

$$E_{\text{out}} = \frac{h\nu A}{2\sigma\gamma} \ln\left(\frac{1}{R}\right) \ln\left(\frac{n_i}{n_f}\right), \quad (8.4)$$

where $h\nu$ is the laser photon energy and A is the effective beam cross-sectional area. The initial and final population inversion densities, n_i and n_f , are related by the transcendental equation

$$n_i - n_f = n_t \ln\left(\frac{n_i}{n_f}\right), \quad (8.5)$$

where n_t is the population inversion density at threshold, that is,

$$n_t = \frac{1}{2\sigma l} \left(\ln \frac{1}{R} + \delta \right). \quad (8.6)$$

The pulse width of the Q-switch pulse can also be expressed as a function of the inversion levels, n_i , n_f , n_t ,

$$t_p = t_r \frac{n_i - n_f}{n_i - n_t [1 + \ln(n_i/n_t)]}. \quad (8.7)$$

The equations for pulse energy, pulse width, and therefore peak power are expressed in terms of the initial and final population inversion densities, which depend not only on the particular choice of output coupler, but are also related via a transcendental equation.

An analytical solution has been reported in [8.4], which reveals that key parameters such as optimum reflectivity, output energy, extraction efficiency, pulse width, and peak power can all be expressed as a function of a single dimensionless variable

$$z = 2g_0l/\delta = \ln G_0^2/\delta, \quad (8.8)$$

where $2g_0l$ is the logarithmic small-signal gain and δ is the round-trip loss.

It is interesting to note that in Chap. 3 we derived expressions for T_{opt} , P_{opt} , and η_E for normal mode operation of the oscillator which were also functions of the parameter z . We will summarize the results of [8.4] because the equations presented in this work are particularly useful to the laser designer. The following expression for the optimum reflectivity was derived

$$R_{\text{opt}} = \exp \left[-\delta \left(\frac{z - 1 - \ln z}{\ln z} \right) \right]. \quad (8.9)$$

The energy output for an optimized system is

$$E_{\text{out}} = E_{\text{sc}}(z - 1 - \ln z), \quad (8.10)$$

where E_{sc} is a scale factor with the dimension of energy which contains a number of constants

$$E_{\text{sc}} = Ah\nu\delta/2\sigma\gamma,$$

where A is the beam cross section, $h\nu$ is the photon energy, σ is the stimulated emission cross section, δ is the round-trip loss, and γ is one for a four-level laser. The FWHM pulse width versus z is obtained from

$$t_p = \frac{t_r}{\delta} \left(\frac{\ln z}{z[1 - a(1 - \ln a)]} \right), \quad (8.11)$$

where t_r is the cavity round-trip time and $a = (z - 1)/(z \ln z)$.

In the limit of large z , the output energy approaches the total useful stored energy in the gain medium

$$E_{\text{st}} = \frac{Ah\nu\delta}{2\sigma\gamma} z = \frac{Vh\nu n_i}{\gamma}. \quad (8.12)$$

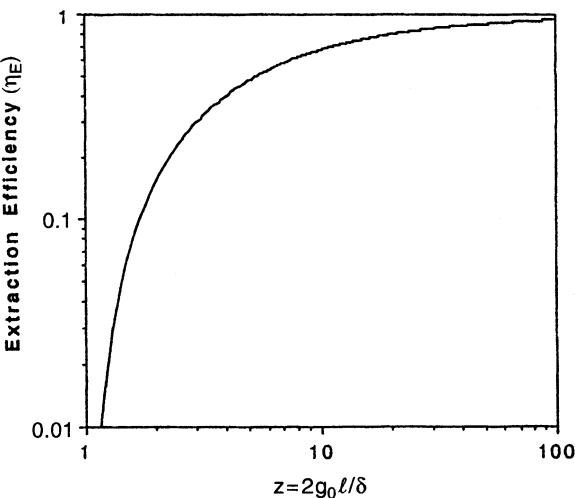


Fig. 8.2. Q-switch extraction efficiency as a function of z .

With (8.10) and (8.12) one can define an energy extraction efficiency

$$\eta_E = 1 - \left(\frac{1 + \ln z}{z} \right), \quad (8.13)$$

which is plotted in Fig. 8.2. As one would expect, a high gain-to-loss ratio leads to a high Q-switch extraction efficiency. For a ratio of logarithmic gain to loss of about 10, an extraction efficiency of 70% is achieved. For higher factors of z , the extraction efficiency increases only very slowly.

The reader is reminded that the shape of the curve for η_E is similar to the results obtained for the free-running laser discussed in Chap. 3, (see Fig. 3.7), which also depends only on the ratio of $2g_0l/\delta$. It is also important to remember that besides the Q-switch extraction efficiency expressed by (8.13), the total energy extraction from a Q-switched laser also depends on the fluorescence losses and ASE depopulation losses prior to opening of the Q-switch. The overall efficiency of the Q-switch process has been defined in Sect. 3.4.1 as the product of the Q-switch extraction efficiency, storage efficiency, and depopulation efficiency.

Laser-design trade-offs and performance projections and system optimization can be accomplished quickly with the help of (8.8)–(8.13). For example, we consider the design parameters for a Q-switched Nd:YAG laser with a desired multimode output of 100 mJ. The laser crystal has a diameter of 5 mm and the laser resonator is 30 cm long. Assuming a 5% round-trip cavity loss ($\delta = 0.05$), and with $h\nu = 1.86 \times 10^{-19}$ J and $\sigma = 2.8 \times 10^{-19}$ cm², we calculate $E_{sc} = 3.2 \times 10^{-3}$ J. This requires a ratio of $E_{out}/E_{sc} = 30.8$ in order to achieve the desired output energy. From (8.10), one therefore obtains a value $2g_0l/\delta = 35.4$, or a single-pass power gain of the rod of $G = \exp(g_0l) = 2.4$. Extraction efficiency follows from (8.13) to be around 87% for $z = 35.4$ and the optimum output coupler has a reflectivity of $R = 0.65$ according to

(8.9). Since the cavity transit round-trip time for the given resonator length is about 2 ns, the expected pulse width from the laser is $t_p = 11$ ns according to (8.11). The peak power of the Q-switch pulse follows from the parameters already calculated and is $P_p = E_{\text{out}}/t_p = 9$ MW.

8.1.2 Slow Q-Switching

Instead of a step function, we will now consider the case of a resonator loss that varies in time. A form of Q-switch used in the past is a rotating prism driven by a highspeed motor. A typical spinning rate is 24,000 rpm. At this rate of rotation it takes about 40 ns to sweep over an angle of 0.1 mrad. In this case the cavity loss introduced by Q-switch can be expressed by $\zeta(t) = a \cos \omega t$ in (8.3).

In a slow Q-switch the development of a Q-switch pulse depends on the ratio of pulse build-up time t_D to the switching time. This is illustrated in Fig. 8.3 for three extreme cases. In Fig. 8.3a, the pulse build-up time is longer than the switching time of the Q-switch. The photon flux starts to increase exponentially at $t = 0$, and at the time ϕ_{\max} is reached and a pulse is emitted, the Q-switch has already passed the point of ϵ_{\min} . The pulse energy is relatively small because the cavity losses are not at a minimum at the time of maximum photon density. In Fig. 8.3b, Q-switch operation is optimized. The Q-switch is emitted when the cavity losses are minimum, i.e., pulse build-up time and switching times are equal. In Fig. 8.3c, the opening time of the Q-switch is much slower than the pulse build-up time. This leads to the emission of several Q-switched pulses. We note that the first pulse is larger than the second and occurs at a larger value of Δn ; the second pulse occurs near the minimum loss level and is much lower in energy. We can explain the occurrence of multiple pulsing as follows: At $t = 0$, the resonator losses are low enough for the photon density to grow exponentially. After 200 ns the photon density has built up to its maximum level and a pulse is emitted. After the pulse is emitted the inversion reaches the

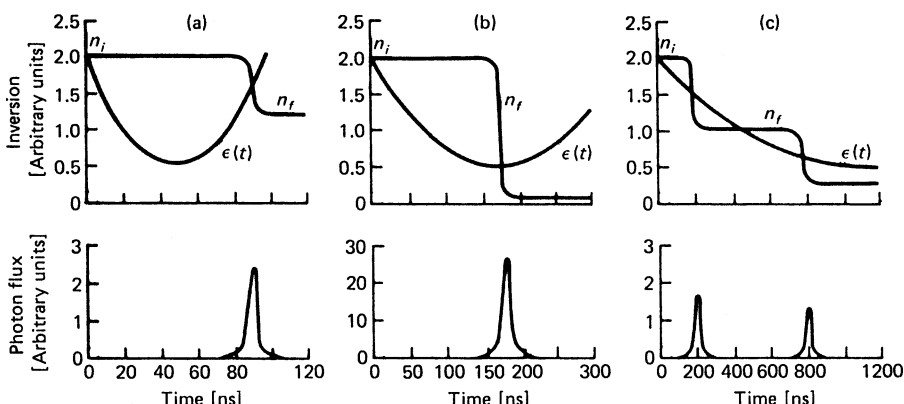


Fig. 8.3. Inversion, cavity losses, and pulse development as a function of time in a slow Q-switched system [8.5]

level n_f . Because n_f is below threshold, the photon density ϕ is very small and a steady state is reached until the slowly changing loss rate term ε decreases enough so that the condition for photon density buildup occurs. The cycle then starts over, but because it now begins with a lower initial value of the inversion a small pulse is produced.

It should be noted that for this multiple pulsing to occur, the first pulse must be emitted at the point of a relatively high loss rate so that another pulse can build up and be emitted when the resonator loss is lower and probably near its minimum.

Multiple pulsing can be avoided either by shortening the switching time of the Q-switch (higher rotational speed) or by increasing the pulse delay time, for example, by increasing the cavity length. From the foregoing consideration it follows that in a laser with fixed pumping level and mirror separation, maximum output is obtained only at one particular speed.

8.1.3 Continuously Pumped, Repetitively Q-Switched Systems

A very important class of laser systems, employed extensively, in micromachining applications, is the cw-pumped, repetitively Q-switched Nd:YAG laser. In these laser systems the population inversion undergoes a cyclic variation, as shown in Fig. 8.4. Between Q-switches the population inversion rises from a value n_f to a value n_i . The buildup of the inversion under the influence of a continuous pumping rate and spontaneous decay is described as a function of time by

$$n(t) = n_\infty - (n_\infty - n_f) \exp\left(-\frac{t}{\tau_f}\right), \quad (8.14)$$

where n_∞ is the asymptotic value of the population inversion, which is approached as t becomes large compared to the spontaneous decay time τ_f . The value n_∞ , which depends on the pump input power, is reached only at repetition rates small compared

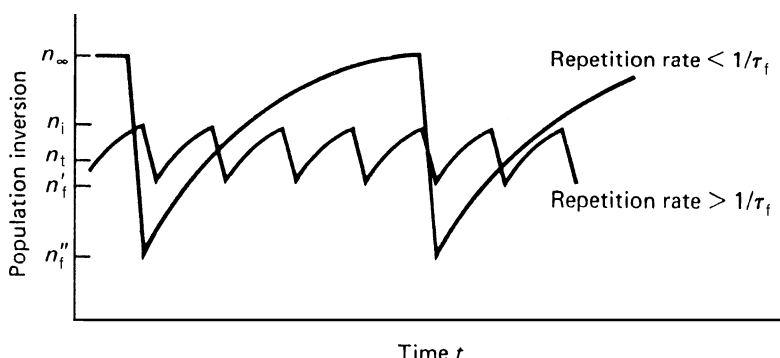


Fig. 8.4. Population inversion versus time in a continuously pumped Q-switched laser; Inversion for two different repetition rates is shown. At repetition rates less than $1/\tau_f$, the inversion approaches the asymptotic value n_∞

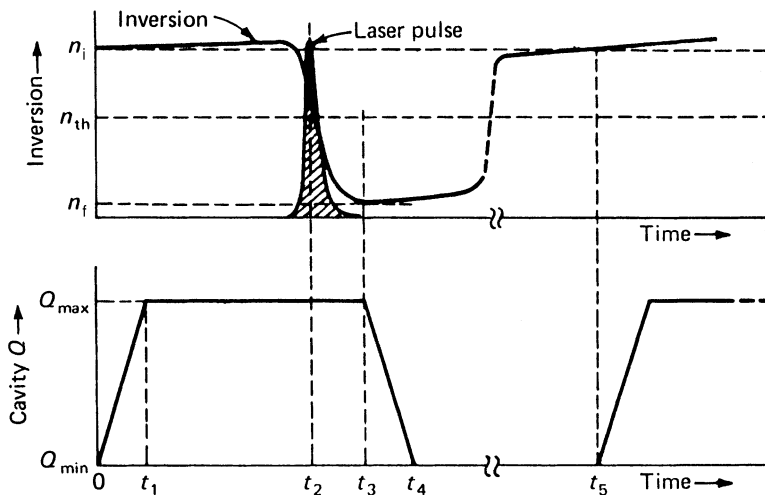


Fig. 8.5. Development of a Q-switched pulse in a cw-pumped system [8.6]

to $1/\tau_f$. For repetition rates larger than $1/\tau_f$, the curves representing the buildup of the population are shorter segments of the same exponential curve followed for the lower repetition rates.

During the emission of a Q-switched pulse, the inversion changes from n_i to n_f . Figure 8.5 shows the development of the Q-switched pulse on an expanded time scale. At $t = 0$, the cavity Q factor starts to increase until it reaches its maximum value Q_{\max} at $t = t_1$. Pulse formation ensues until the full pulse output is achieved at $t = t_2$. Stimulated emission ceases at $t = t_3$; at this time continued pumping causes the inversion to start to increase. At the point where the inversion begins to increase, $t = t_3$, the cavity Q begins to decrease, reaching its minimum value at $t = t_4$. During the time period t_3-t_5 , the inversion is allowed to build up to its initial value n_i .

The theory of Q-switch operation, summarized at the beginning of this chapter for the case of single Q-switched pulses, can also be applied to the case of repetitive Q-switches, with some modifications that take into account the effects of continuous pumping. Equations (8.1) and (8.2) are applicable; however, we will set $\gamma = 1$ and $n = n_2$ because all repetitively Q-switched lasers of practical use are four-level systems. The inversion levels n_f and n_i are connected by (8.5). During the low- Q portion of the cycle, the inversion n_2 is described by the differential equation

$$\frac{dn_2}{dt} = W_p(n_{\text{tot}} - n_2) - \frac{n_2}{\tau_f}. \quad (8.15)$$

With the assumption that $n_2 \ll n_{\text{tot}}$ and with

$$n_\infty = W_p \tau_f n_{\text{tot}} \quad (8.16)$$

we obtain (8.14) as a solution. For repetitive Q-switching at a repetition rate f , the maximum time available for the inversion to build up between pulses is $1/f$. Therefore,

$$n_i = n_\infty - (n_\infty - n_f) \exp\left(-\frac{1}{\tau_f f}\right) \quad (8.17)$$

in order for the inversion to return to its original value after each Q-switch cycle.

During each cycle a total energy $(n_i - n_f)$ enters the coherent electromagnetic field. Of this a fraction, $T/(T + \delta)$, appears as laser output. Therefore, the Q-switched average power P_{av} at a repetition rate f is given by

$$P_{av} = \frac{Tf}{T + \delta} (n_i - n_f) h\nu V. \quad (8.18)$$

From the average power and pulse repetition rate follows the energy per pulse, and with the pulse width calculated from (8.7) one obtains the peak power of each pulse. It is convenient to calculate the ratios P_p/P_{cw} and P_{av}/P_{cw} , where P_p is the Q-switched peak power and P_{cw} is the cw power from the laser at the same pumping level. For cw operation the time derivatives in (8.1) and (8.2) are zero, and we have

$$P_{cw} = \frac{T}{T + \delta} \left(\frac{n_\infty - n_t}{\tau_f} \right) h\nu V. \quad (8.19)$$

Because of the transcendental functions expressed by (8.5), (8.7), and (8.17), the ratios P_p/P_{cw} and P_{av}/P_{cw} cannot be expressed in closed form. The result of numerical calculations is shown in Figs. 8.6 and 8.7.

In Fig. 8.6 the ratio of Q-switched peak power output to the maximum cw output is plotted versus repetition rate for an Nd:YAG laser. For repetition rates below approximately 800 Hz ($\tau_f f \approx 0.20$), the peak power is independent of the repetition rate. At these low repetition rates there is sufficient time between pulses for the inversion to reach the maximum value n_∞ . In the transition region between 0.8 and 3 kHz, peak power starts to decrease as the repetition rate is increased. Above 3 kHz, the peak power decreases very rapidly for higher repetition rates.

Figure 8.7 shows the ratio of Q-switched average power to cw power as a function of repetition rate. Above a repetition rate of approximately 10 kHz, the Q-switch average power approaches the cw power. At low repetition rates the average power is proportional to the repetition rate. In Fig. 8.8 the experimentally determined peak power, average power pulse width, and pulse buildup time are plotted as a function of repetition rate for an Nd:YAG laser. In accordance with theory, for higher repetition rates the pulse width and the pulse buildup time increase as a result of the reduction of gain.

In the following sections we will describe and compare different Q-switch techniques.

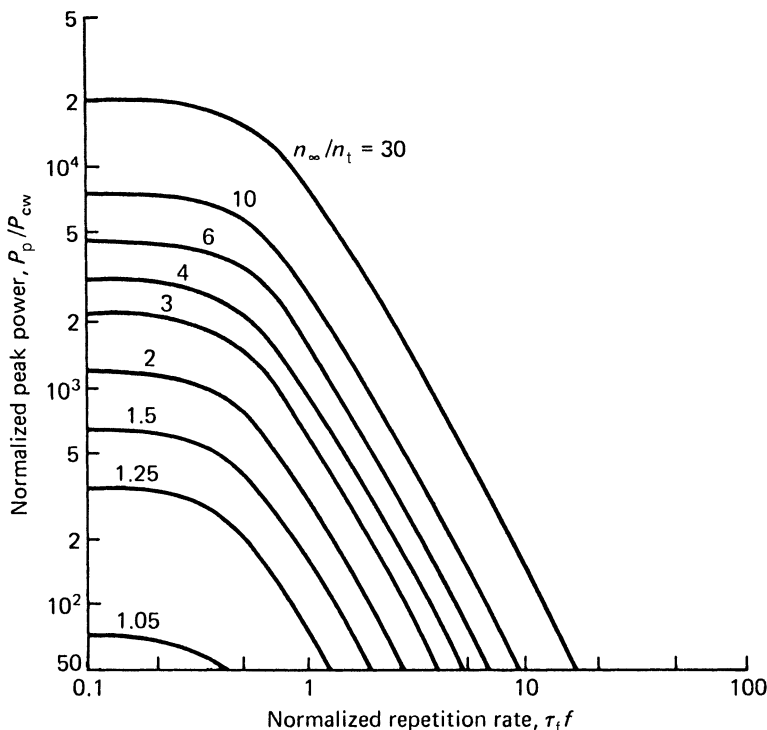


Fig. 8.6. Ratio of peak power to cw power as a function of the repetition rate for a typical cw-pumped Nd:YAG laser. The parameter n_∞/n_t expresses the fractional inversion above threshold [8.7]

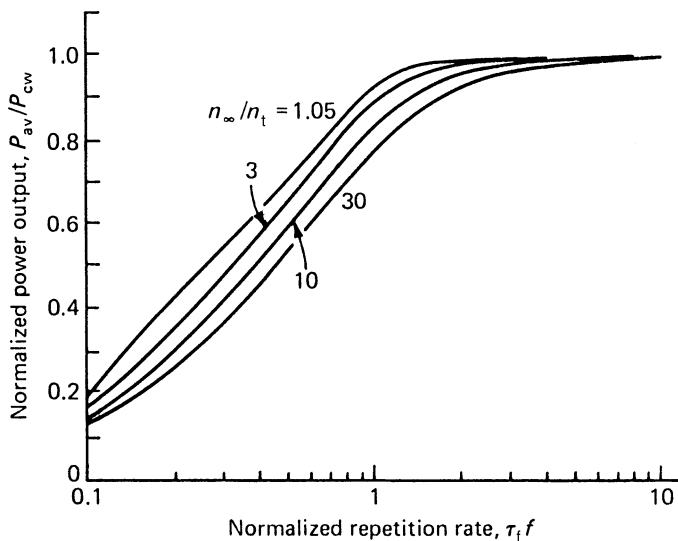


Fig. 8.7. Ratio of Q-switched average power to maximum cw power as a function of normalized repetition rate f [8.7]

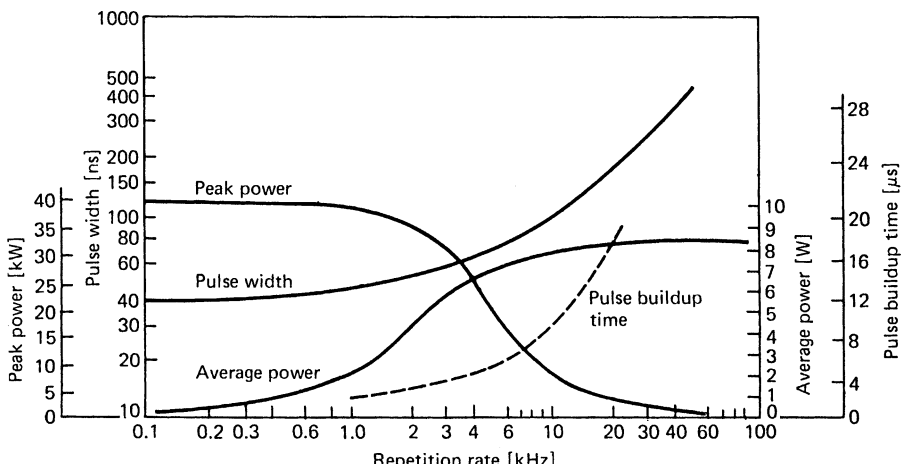


Fig. 8.8. Performance of a cw-pumped Nd:YAG laser system. The peak power, average power, pulse buildup time, and pulse width as a function of repetition rate are plotted

8.2 Mechanical Q-Switches

Q-switches have been designed based upon rotational, oscillatory, or translational motion of optical components. What these techniques have in common is that they inhibit laser action during the pump cycle by either blocking the light path, causing a mirror misalignment, or reducing the reflectivity of one of the resonator mirrors. Near the end of the pump pulse, when maximum energy has been stored in the laser rod, a high Q-condition is established and a Q-switch pulse is emitted from the laser.

The first mechanical Q-switch consisted of nothing more than a rotating disc containing an aperture [8.8]. This method was soon abandoned in favor of rotating mirrors or prisms, which allow much faster switching times [8.9]. In some cases one of the resonator mirrors was attached to one end of a torsional rod driven at its mechanical resonance frequency [8.10]. Minute translations of one mirror have been utilized to change the Q of the cavity. One technique consists of replacing the output mirror of the laser oscillator by a two-plate Fabry–Perot resonator. By modulating the spacing between the two plates, for example, with a piezoelectric transducer, the device can be shifted from a transmission peak to a reflection peak [8.11]. Another technique makes use of frustrated total internal reflection [8.12]. In a FTIR device, a piezoelectric transducer changes the spacing between a roof prism and a second prism. If the two prisms are brought to within a fraction of a wavelength to the surface of the internally reflecting roof prism, the total internal reflection is destroyed. Consequently, the radiation incident on the roof prism is transmitted rather than totally reflected.

The spinning reflector technique for the generation of Q-switched pulses, as shown in Fig. 8.9, involves simply rotating one of the two resonant cavity reflectors so that

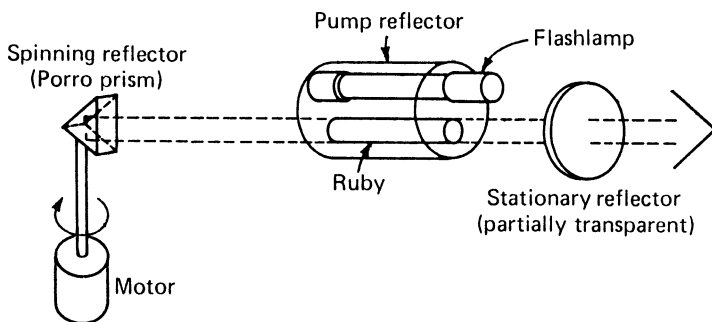


Fig. 8.9. Diagram of a ruby laser employing a spinning prism Q-switch

parallelism of the reflectors occurs for only a brief instant in time. If a plane mirror is employed as the rotating element, the axis of rotation must be aligned to within a fraction of a milliradian parallel to the face of the opposing reflector. This difficulty can be overcome by using a roof prism as the rotating element. If the roof of the prism is perpendicular to the axis of rotation, then the retroreflecting nature of the prism assures alignment in one direction, while the rotation of the prism brings it into alignment in the other direction.

Rotating-mirror devices are simple and inexpensive. They are insensitive to polarization and therefore birefringence effects. Hence, more energy from the laser can be extracted under certain conditions as compared to electro-optic Q-switches. However, the mechanical Q-switches suffer from the tendency to emit multiple pulses. Also, the devices are very noisy and they require frequent maintenance because of the relatively short lifetime of the bearings. Because of these disadvantages the rotating prism Q-switch has been replaced for visible and near infrared lasers by the acousto-optic Q-switch in cw-pumped lasers, and by electro-optic or passive Q-switches in pulsed lasers. However, for Q-switching mid-infrared lasers mechanical devices are still in use. For example 3- μm erbium lasers are frequently Q-switched with rotating prisms [8.13, 14] or with FTIR devices [8.15, 16]. The major disadvantage of Pockels cells is the high switching voltage required at these longer wavelengths.

8.3 Electro-Optical Q-Switches

Very fast electronically controlled optical shutters can be designed by exploiting the electro-optic effect in crystals or liquids. The key element in such a shutter is an electro-optic element that becomes birefringent under the influence of an external field. Birefringence in a medium is characterized by two orthogonal directions called the “fast” and “slow” axes, which have different indices of refraction. An optical beam, initially plane-polarized at 45° to these axes and directed normal to their plane, will split into two orthogonal components, traveling along the same path but at different velocities. Hence, the electro-optic effect causes a phase difference between the two beams. After traversing the medium, the combination of the two components results,

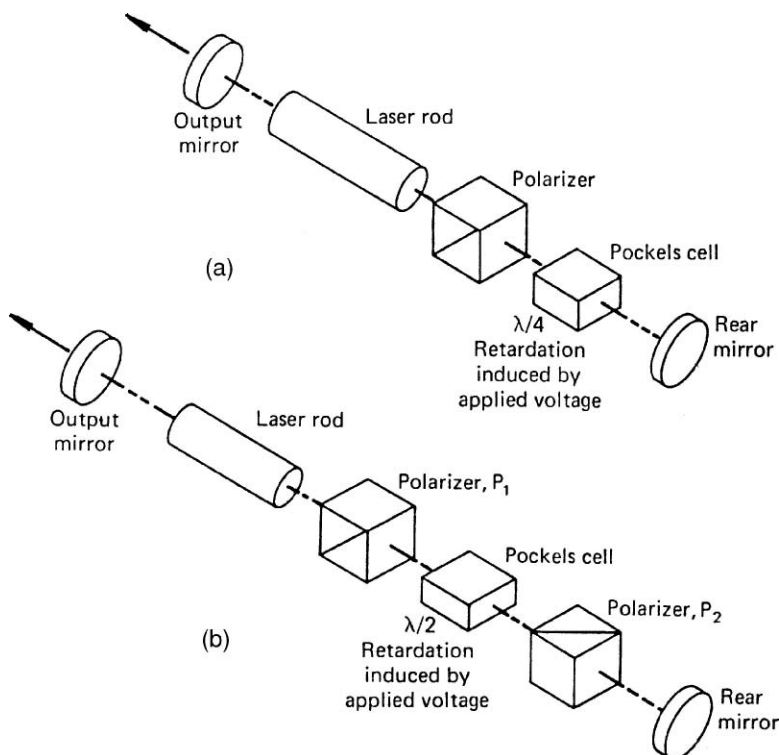


Fig. 8.10. Electro-optic Q-switch operated at (a) quarter-wave and (b) half-wave retardation voltage

depending on the voltage applied, in either an elliptical, circular, or linearly polarized beam. For Q-switch operation only two particular voltages leading to a quarter-wave and half-wave retardation are of interest. In the first case, the incident linearly polarized light is circularly polarized after passing the cell, and in the second case the output beam is linearly polarized; however, the plane of polarization has been rotated 90°.

The two most common arrangements for Q-switching are shown in Fig. 8.10. In Fig. 8.10a the electro-optic cell is located between a polarizer and the rear mirror.

The inclusion of the polarizer is not essential if the laser radiation is polarized, for example, in Nd:YLF. The sequence of operation is as follows: During the pump pulse, a voltage $V_{1/4}$ is applied to the electro-optic cell such that the linearly polarized light passed through the polarizer is circularly polarized. After being reflected at the mirror, the radiation again passes through the electro-optic cell and undergoes another $\lambda/4$ retardation, becoming linearly polarized but at 90° to its original direction. This radiation is ejected from the laser cavity by the polarizer, thus preventing optical feedback. Toward the end of the pump pulse the voltage on the cell is switched off, permitting the polarizer-cell combination to pass a linearly polarized beam without loss. Oscillation within the cavity will build up, and after a short delay a Q-switch pulse will be emitted from the cavity.

In the arrangement of Fig. 8.10b an electric voltage must first be applied to the cell to transmit the beam. In this so-called pulse-on Q-switch, the cell is located between two crossed polarizers. As before, polarizer P_1 , located between the laser rod and the cell, is not required if the active medium emits a polarized beam. During the pump pulse, with no voltage applied to the cell, the cavity Q is at a minimum due to the crossed polarizers. At the end of the pump pulse, a voltage $V_{1/2}$ is applied to the cell, which causes a 90° rotation of the incoming beam. The light is therefore transmitted by the second polarizer P_2 . Upon reflection at the mirror the light passes again through polarizer P_2 and the cell, where it experiences another 90° rotation. Light traveling toward the polarizer P_1 has experienced a 180° rotation and is therefore transmitted through P_1 .

There are a number of reasons why it is advantageous to place the Q-switch assembly in front of the rear mirror rather than between the gain medium and the output coupler. First, there is a certain amount of leakage through the Q-switch/polarizer assembly since the extinction ratio is not infinite. A better hold-off of laser radiation, i.e., a lower Q of the resonator, can be achieved if the high reflectivity mirror is blocked by the Q-switch rather than the low reflectivity output coupler. Second, the occurrence of amplified spontaneous emission (ASE) is reduced for the same reason as mentioned above. The feedback loop for potential ASE has a lower reflectivity if the high reflectivity rear mirror is blocked. Third, the peak power in the section between the gain medium and the rear mirror is lower than between the laser crystal and the output coupler, because the circulating power has made only one pass through the gain medium before a fraction is emitted through the output coupler. Since Q-switch assemblies usually have a lower damage threshold than other components, it is advantageous to place these more vulnerable components in the section of the resonator experiencing the lowest peak power.

Two types of electro-optic effects have been used in laser Q-switches: the Pockels effect, which occurs in crystals that lack a center of point symmetry, and the Kerr effect, which occurs in certain liquids. Kerr cells have only been used in the early days of laser technology because they require a voltage that is 5–10 times higher than is required for Pockels cells. The Pockels cell contains an electro-optic crystal in which a refractive index change is produced by an externally applied electric field. Crystals are classified into 32-point groups according to their structure. Only 20-point groups, namely those that lack a center of symmetry, exhibit a nonvanishing electro-optic effect.

The index change produced by an externally applied field is described in each case by a 6×3 matrix of electro-optic coefficients. The number of coefficients is greatly reduced by the structural characteristics of crystals. The most commonly used electro-optic materials have only a few distinct coefficients. The location of a coefficient in the matrix array interrelates the crystal orientation, the applied field direction, and the polarization and direction of the optical beam. The magnitude of each coefficient determines the strength of the electro-optic effect for each geometry.

The basic requirements for a crystal to be useful as an electro-optic Q-switch are a good optical quality combined with a high laser damage threshold and a large electro-optic coefficient for light propagating parallel to the optic axis. The latter requirement

is important because the two-phase-shifted orthogonal components of the beam travel along the same path only if the direction of the light beam is either parallel or normal to the optical axis of the crystal. For other directions the fast and slow axes of the beam include a small angle. Two crystals that meet these criteria and are widely employed in electro-optical Q-switches are potassium dihydrogen phosphate (KDP) and lithium niobate (LiNbO_3).

8.3.1 KDP and KD*P Pockels Cells

KDP (KH_2PO_4) and its isomorph KD*P (KD_2PO_4) are grown at room temperature from a water solution that yields large distortion-free single crystals. The attributes of this family of crystals are their high damage threshold and excellent optical quality combined with a large electro-optic coefficient. Crystals with cross sections up to 100 mm have been produced. A disadvantage is the fact that the crystals are fairly soft and hygroscopic and must be protected from the environment by enclosing them in cells that are hermetically sealed or filled with an index-matching fluid. In order to avoid walk-off between the fast and slow beam axes, the electric field has to be applied longitudinally in the same direction as the beam propagation axis and the optical axis of the crystal. The electric field is applied to the crystal by means of a pair of electrodes that contain openings for passage of the laser beam.

Potassium dihydrogen phosphate (KH_2PO_4) or KDP and the deuterated form, which is (KD_2PO_4) or KD*P, are widely used crystals for Pockels cell Q-switches. The latter is usually preferred because of its larger electro-optic coefficient. The dependence of the index of refraction on the electric field can be described in terms of a change in orientation and dimensions of the index ellipsoid. The crystals are uniaxial, that is, in the absence of an electric field the index ellipsoid is an ellipse of revolution about the optic (z) axis. As indicated in Fig. 8.11 the index ellipsoid projects as a circle on a plane perpendicular to the optic axis. The circle indicates that the crystal is not birefringent in the direction of the optic axis. When an electric field is applied parallel to the crystal optic axis, the cross section of the ellipsoid becomes an ellipse with axes x' and y' , making a 45° angle with the x and y crystallographic axes. This angle is independent of the magnitude of the electric field. The length of the ellipse axes in the x' and y' directions are proportional to the reciprocals of the indices of refraction in these two directions.

We will now express the phase shift between the orthogonal components corresponding to a wave polarized in the x' and y' directions. Changes of the refractive index Δn are related by the electro-optic tensor r_{ij} of rank 3 to the applied field

$$\Delta \left(\frac{1}{n_i^2} \right) = \sum_{j=1}^3 r_{ij} E_j, \quad (8.20)$$

where $i = 1, \dots, 6$ and $j = 1, \dots, 3$.

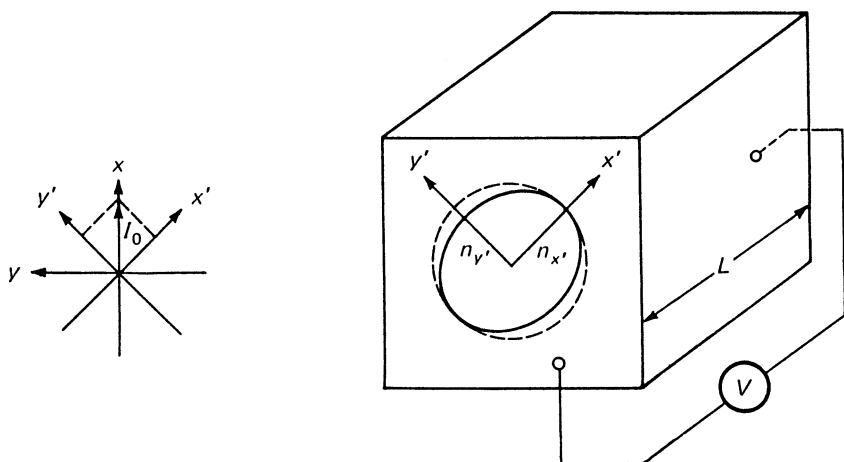


Fig. 8.11. Change of the index ellipsoid in a KDP crystal when an electric field is applied parallel to the z -axis, I_0 is an incident wave polarized in the x direction, x and y are the crystallographic axes, and x' and y' are the electrically induced axes

Generally there exist 18 linear electro-optic coefficients r_{ij} . However, in crystals of high symmetry, many of these vanish. For phosphates of the KDP family, r_{63} is the only independent electro-optic coefficient that describes the changes in the ellipsoid when a longitudinal field is applied to the crystal. The change of refractive index in the x' and y' directions is [8.17]

$$n_{x'} = n_0 + \frac{1}{2}n_0^3 r_{63} E_z, \quad n_{y'} = n_0 - \frac{1}{2}n_0^3 r_{63} E_z, \quad (8.21)$$

where n_0 is the ordinary index of refraction and E_z is the electric field in the z direction. The difference in the index of refraction for the two orthogonal components is then

$$\Delta n_0 = n_0^3 r_{63} E_z. \quad (8.22)$$

For a crystal of length l , this leads to a path-length difference $\Delta n_0 l$ and a phase difference of $\Delta\varphi = (2\pi/\lambda)\Delta n_0 l$.

The phase difference $\Delta\varphi$ in a crystal of length l is related to the voltage $V_z = E_z l$ applied across the faces by

$$\Delta\varphi = \frac{2\pi}{\lambda} n_0^3 r_{63} V_z. \quad (8.23)$$

It should be noted that $\Delta\varphi$ is a linear function of voltage and is independent of the crystal dimensions. If linearly polarized light is propagated through the crystal with the direction of polarization parallel to the x - or y -axis, as shown in Fig. 8.11, the components of this vector parallel to the electrically induced axes x' and y' will suffer a relative phase shift $\Delta\varphi$. In general, orthogonal components undergoing a relative phase shift produce elliptically polarized waves. Thus, the application of a voltage in

this configuration changes linearly polarized light to elliptically polarized light. If the light then passes through a polarizer, the resulting light intensity will be a function of the ellipticity and therefore the voltage applied to the crystal. A simple derivation shows that, with the analyzer axis oriented at right angles to the input polarization direction, the voltage and the transmitted light intensity I are related by [8.18].

$$I = I_0 \sin^2 \frac{\Delta\varphi}{2}, \quad (8.24)$$

where I_0 is the input light intensity.

For Q-switch operation, two particular values of phase shift are of interest: these are the $\lambda/4$ and $\lambda/2$ wave retardations that correspond to a phase shift of $\pi/2$ and π . With linearly polarized light being applied, for example, in the x direction, as shown in Fig. 8.11, the output from the crystal is circularly polarized if $\Delta\varphi = \pi/2$. For $\Delta\varphi = \pi$, the output beam is linearly polarized, but the plane of polarization has been rotated 90° .

From (8.23) it follows that the voltage required to produce a retardation of π is

$$V_{\lambda/2} = \frac{\lambda}{2n_0^3 r_{63}}. \quad (8.25)$$

KD*P has an index of refraction of $n_0 = 1.51$ and an electro-optic constant $r_{63} = 26.4 \times 10^{-6} \mu\text{m/V}$. With these values we calculate a voltage of $V_{\lambda/2} = 5.8 \text{ kV}$ at $1.06 \mu\text{m}$ in order to produce a half-wave retardation. Deviations from this voltage will change the transmission $T = I/I_0$ of the Pockels cell according to

$$T = \sin^2 \left(\frac{\pi}{2} \frac{V}{V_{\lambda/2}} \right). \quad (8.26)$$

This equation is obtained by combining (8.23–25).

A number of crystals which have been used in Q-switches and electro-optic modulators are listed in Table 8.1. The most widely used crystal is the deuterated form of KH_2PO_4 (KDP), which is KD_2PO_4 (KD*P) because it possesses a low half-wave voltage. The crystal CD*A has actually a lower value, but this advantage is offset by a high loss tangent. KD*P and its isomorphs have been characterized in great detail; their properties are reviewed in [8.19–22].

Although the crystals are water-soluble and fragile, they can be handled, cut, and polished without difficulty. The crystals have a high optical transmission in the range of 0.22 – $1.6 \mu\text{m}$, and they possess relatively large electro-optic coefficients.

All crystals listed in Table 8.1 are hygroscopic and must be protected from atmospheric water. This protection is typically provided by enclosing the crystal in a cell which is hermetically sealed or filled with index-matching fluid. As a result, six surfaces are encountered by a laser beam on a single transit through the cell. Transmission losses can be reduced by the use of antireflection coatings on the cell windows. While hard, damage-resistant AR coatings cannot be applied to KDP and its isomorphs, losses at the crystal itself can be very much reduced by the use of an index-matching liquid.

Transmission of typical electro-optic shutters with liquid-immersed crystals and AR-coated windows is about 90%. The electric field is usually applied to the crystal

Table 8.1. Electro-optic parameters of 42 m-type crystals

Material	Index of refraction at 0.55 μm	Electro-optic constant, τ_{63} ($\mu\text{m}/\text{V} \times 10^{-6}$)	Typical half-wave voltage (kV) at 0.55 μm
Ammonium dihydrogen phosphate (ADP)	1.53	8.5	9.2
Potassium dihydrogen phosphate (KDP)	1.51	10.5	7.5
Deuterated KDP	1.51	26.4	3.0
Rubidium dihydrogen phosphate (RDP)	1.51	15.5	5.1
Ammonium dihydrogen arsenate (ADA)	1.58	9.2	7.2
Potassium dihydrogen arsenate (KDA)	1.57	10.9	6.5
Rubidium dihydrogen arsenate (RDA)	1.56	14.8	4.9
Cesium dihydrogen arsenate (CDA)	1.57	18.6	3.8
Deuterated CDA	1.57	36.6	2.0

by means of a pair of metal electrodes containing apertures which are either bonded or evaporated onto the square ends of the crystal or simply held in place by compression. The main drawback of end-plate electrodes is their geometry, which gives rise to a nonuniform electric field across the clear aperture. The field strength across the aperture varies from a maximum around the inner edge of the rings to a minimum at the geometric center. Fringing necessitates operation at considerably higher voltages than if the field were uniformly applied. Partial compensation is attained by making the crystal dimension roughly 30% greater than the clear aperture diameter.

A considerable improvement in fringe uniformity can be achieved by using cylindrical band electrodes applied to the end of the barrel of cylindrical-shaped crystals. Band electrodes allow an optical transmission uniformity to within a few percent across the clear aperture. This represents a substantial improvement compared to standard cells containing rectangular crystals and end-plate electrodes.

The electro-optic coefficient of KDP is strongly temperature-dependent. As a consequence, the quarter wave voltage at 1.06 μm increases by approximately 80 V/°C with temperature [8.23]. If large temperature excursions are expected, the voltage of the Pockels cell needs to be adjusted by a feedback loop to provide a stable output energy. Temperature changes of the crystal may be the result of ambient temperatures variations, or they may be caused by absorption losses in the crystal.

The thermally induced nonuniformity of the refractive index caused by the absorption of laser radiation produces birefringence, which can degrade the performance of the Q-switch. The result is a decrease of the transmission of the electro-optic Q-switch when the Q-switch is open. The depolarized component of the intracavity radiation is ejected from the resonator by the polarizer. Also a deviation from the exact quarter wave voltage has the same effect.

In high-average-power Q-switched Nd:YAG lasers, thermally induced birefringence in the Q-switch crystal can be a problem. Similar to the cancellation of thermally induced depolarization in a laser rod, the problem can be solved with two Pockels cells and a polarization rotator inserted between the two electro-optic crystals [8.24].

KDP Pockels cells can also be designed with the electric field perpendicular to the direction of the beam. For this geometry, the half-wave voltage depends on the ratio of thickness to length of the crystal, which has the advantage that by proper choice of the crystal geometry a considerably lower voltage is required as compared to longitudinally applied fields. However in KDP crystals with a transverse field, the propagation direction is at an angle other than normal or parallel to the optic axis. Therefore the extraordinary and ordinary ray propagate in different directions through the crystal. To compensate for this walk-off as well as for temperature effects, two crystals of suitable orientation are usually employed. Because of the need to compensate for the angular and temperature dependence of birefringence in KDP-type crystals, transverse field devices have not become popular as Q-switches in this class of materials.

8.3.2 LiNbO₃ Pockels Cells

Lithium niobate is grown from the melt; it is hard and nonhygroscopic. The crystals can be antireflection-coated and do not need a special protection from the environment. Also, the quarter and half-wave voltages are about a factor of 2 lower compared to KD*P. In LiNbO₃, the electric field is applied perpendicularly to the beam propagation and optical axis of the crystal. As we will see, this has the advantage of reducing the required voltage by the width to length ratio of the crystal. A drawback of LiNbO₃ is that the crystal is available only in relatively small sizes, with cross sections of about 10 mm, and the laser damage threshold is considerably below that of KD*P.

In an arrangement as shown in Fig. 8.12 light propagates along the *c*-axis of the crystal. If the light is polarized parallel to the *a*-axis and an electric field is applied parallel to the *a* axis, the half-wave retardation is [8.25]

$$V_{\lambda/2} = \frac{\lambda d}{2r_{22}n_0^3 l}, \quad (8.27)$$

where *l* is the length of the crystal in the *c* direction, *d* is the distance between the electrodes along the *a*-axis, and *r*₂₂ is the electro-optic coefficient.

The half-wave voltage is directly proportional to the distance between the electrodes and inversely proportional to the path length. At a wavelength of $\lambda = 1.064 \mu\text{m}$, the linear electro-optic coefficient is $r_{22} = 5.61 \times 10^{-6} \mu\text{m/V}$ and the refractive index of the ordinary ray is $n_0 = 2.237$ in LiNbO₃. The theoretical half-wave voltage obtained from (8.27) for a typical crystal size of 9 mm \times 9 mm \times 25 mm is 3.0 kV. The high refractive index of LiNbO₃ and the geometrical factor *d/l* are responsible for the lower voltage requirements of LiNbO₃ as compared to KD*P.

The above mentioned half-wave voltage is the value for a dc bias voltage; for pulsed Q-switch operation a slightly higher voltage is usually required. In pulsed

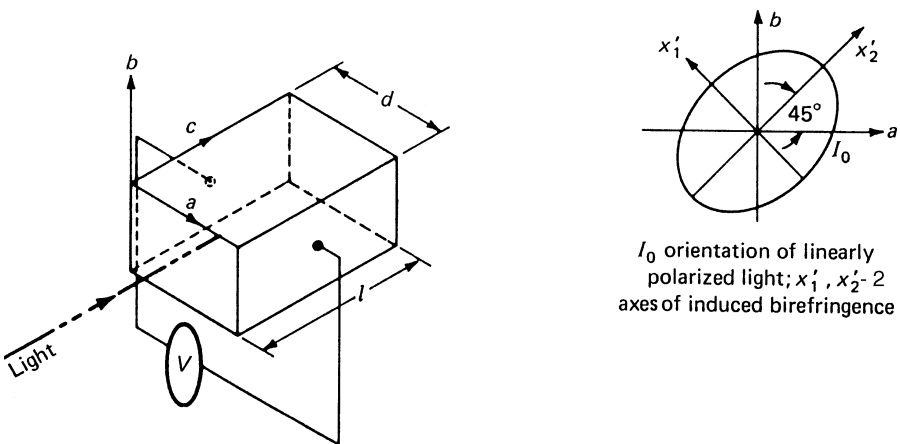


Fig. 8.12. Electro-optic Q-switch employing an LiNbO_3 crystal

operations, the value of r_{22} is smaller than for dc operation, which is explained by the fact that for static fields the electro-optic effect is equal to the sum of the intrinsic electro-optic effect and that induced by the piezo-optic effect [8.26]. $r_{22} = r'_{22} + p_{2k}d_{2k}$, where p_{2k} and d_{2k} are the elasto-optic and piezoelectric constants of the crystal. When the bias voltage is turned on or off rapidly, the piezo-optic effect is absent, since deformation of the crystal cannot occur during the fast switching times typical for Q-switch operation.

Output energies of up to 250 mJ are typically obtained from Nd:YAG oscillators containing LiNbO_3 Q-switches. The energy extraction is limited by the high gain of this material, which leads to prelasing and subsequently to a depopulation of the inversion. The width of the Q-switched pulses is usually between 10 and 25 ns, and the pulse buildup time is between 50 and 100 ns in typical systems. Generally speaking, the build-up time of the Q-switched pulse is about an order of magnitude larger than the pulse duration, and the Q-switch opening time is shorter than the pulse build-up time.

According to (8.7) the pulse width of a Q-switched laser is a function of the resonator length (t_r) and the gain in the material (n_i). The shortest Q-switch pulses are obtained in very short resonators with the gain medium pumped far above threshold. Small end-pumped Q-switched lasers have generated pulses on the order of a few nanoseconds or less.

For some applications it is desirable to generate relatively long Q-switch pulses. By combining a long resonator with operation close to threshold, pulses as long as 150 ns have been generated. Employing a feedback loop to control the switching of a Pockels cell, pulse durations of up to 1.4 μs have been obtained from Q-switched Nd:YAG lasers [8.27, 28]. The principle of electro-optical feedback control is depicted in Fig. 8.13. The resonator incorporates a Pockels cell as a Q-switching element. Negative feedback to the circulating power is applied by means of the photo-detector-derived voltage on the Pockels cell. In this way the stored energy in the laser rod is released at a controlled rate.

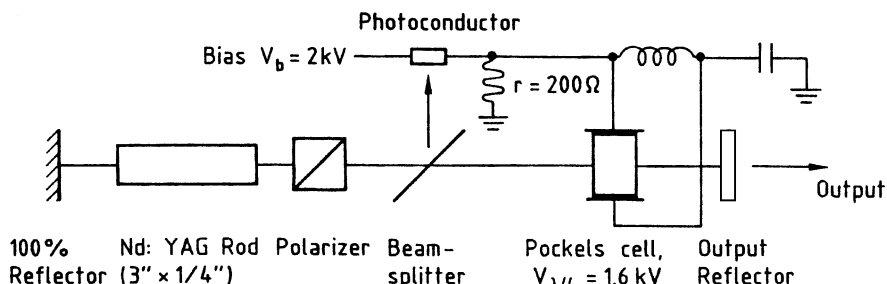


Fig. 8.13. Electro-optic feedback control for stretching of Q-switched pulses [8.27]

In diode-pumped solid-state lasers a fairly rectangular pump pulse is usually generated and the optimum time for Q-switching occurs right at the end of the pump pulse. In flashlamp-pumped systems, the pump pulse can have a relatively long decay time. In this case the maximum extraction energy is obtained if the Q-switch is opened prior to the end of the pump pulse. At the tail end of a slowly decreasing pump pulse, population inversion decreases because the diminishing pump power cannot keep up with the increase of spontaneous emission losses.

The electro-optic coefficients of LiNbO₃ are less sensitive to temperature changes as compared to KDP. This is particularly important because LiNbO₃ is used in most military rangefinders and target designators which involves operation over a large temperature range. These systems generate between 100 and 250 mJ of output energy and the power density at the Q-switch is on the order of 50 MW/cm². Pulse width is 10–20 ns. In these applications crystal temperature may reach 70°C.

The quarter-wave voltage of LiNbO₃ is proportional to the laser wavelength according to (8.27). Therefore, very high voltages are required to Q-switch erbium lasers which emit radiation at around 3 μm. LiNbO₃ Pockels cells have been successfully used for Q-switching Er:YAG [8.29] and Er:Cr:YSGG [8.15]. However, rapidly switching high voltages produced substantial electromagnetic interference in these lasers.

8.3.3 Prelasing and Postlasing

Theoretically, an infinite loss is introduced into the cavity by a Pockels cell operated at a proper $\lambda/4$ or $\lambda/2$ voltage. In practice, field strength nonuniformities, inhomogeneities in the crystal, birefringence introduced by mechanically clamping the crystal, and nonperfect polarizers limit the extinction ratio of an electro-optic Q-switch to about a hundred. The extinction ratio is defined as the ratio of the maximum to the minimum transmitted intensity obtained between crossed polarizers as the applied voltage is varied through a half-wave voltage.

If the gain of the laser exceeds the loss produced by the Q-switch, normal lasing will occur before the instant of Q-switching. This phenomenon, which is termed “prelasing,” is due to the Pockels cell and polarizer combination not acting as a perfect shutter, so that there is still some feedback from the resonator mirror. Prelasing is most

likely to occur just prior to the time of Q-switching since the population inversion, the stored energy, and the gain are largest at that time.

Because of the high gain of Nd:YAG, depopulation of the stored energy by prelasing is a particular problem with this material. Tests have also shown that prelasing may be a major cause of damage to the Pockels cell crystal or polarizers. Prelasing, if it occurs, allows a pulse buildup from a “seed” pulse in a small region of the laser rod. In the area of the laser rod where prelasing occurs, the Q-switched pulse develops more rapidly compared to the rest of the pulse, which must develop from spontaneous emission. As a result, a very high peak power density will occur in this small part of the rod.

Appropriate design precautions must be undertaken to ensure that prelasing does not occur. The first major requirement is to operate the Q-switch at its optimum extinction ratio. This requires that the correct dc bias voltage is applied and that the Pockels cell crystal and polarizers are aligned properly. Typically the optic *c*-axis of the Pockels cell crystal must be parallel to the laser beam direction to within 10 arc min or less. Alignment of the *c*-axis is best performed by centering the optic-axis figure (the Maltese cross pattern) on the resonator optical axis. This is done by illuminating the crystal with a diffuse light source and observing the crystal between crossed polarizers. A pattern of a cross surrounded by a series of circles appears. The line connecting the center of the cross to the point at which the observation is made is exactly parallel to the *c*-axis. Furthermore, to establish the proper condition for Q-switching, the crystal must be aligned so that either the *a*- or *b*-axis is parallel to the polarization direction of the laser (LiNbO_3 crystals and longitudinal field KD^*P). Figure 8.14 shows the extinction ratio versus bias voltage for a 9 mm × 9 mm × 25 mm LiNbO_3 crystal.

The main Q-switched pulse may be followed by one or more pulses of lower amplitude (postlasing). The second pulse may occur from several hundred nanoseconds to several tens of microseconds after the main pulse. Postlasing results from piezo-optic effects in the electro-optic crystal. The piezoelectric action of the applied voltage compresses the crystal, and when that voltage is removed the crystal remains compressed for some time. This compression generates a retardation of the optical wave by means of a strain-birefringence effect, thus creating a loss in the cavity which becomes smaller with time as the compression relaxes. Figure 8.15a shows a waveform picture of the voltage conventionally applied to a Pockels cell, and Fig. 8.15b shows the loss versus time for an actual Pockels cell switch. It was found [8.31] that the loss drops to about 25% and then decays to zero in approximately 400 ns. If the resulting decay time of the loss is longer than the output pulse buildup time, the main laser pulse will be emitted before the loss reaches its minimum. Thus some energy will remain in the rod after the first output pulse. This residual energy may produce a second pulse when the cavity loss reaches its minimum. By creating this time-dependent loss, the elasto-optic effect seriously affects the efficiency of a Q-switched laser.

At low input energy levels there is a long time delay between the switching time and the time the output pulse actually appears, as shown in Fig. 8.15c and thus there is negligible loss in efficiency. However, at higher input energy levels the time

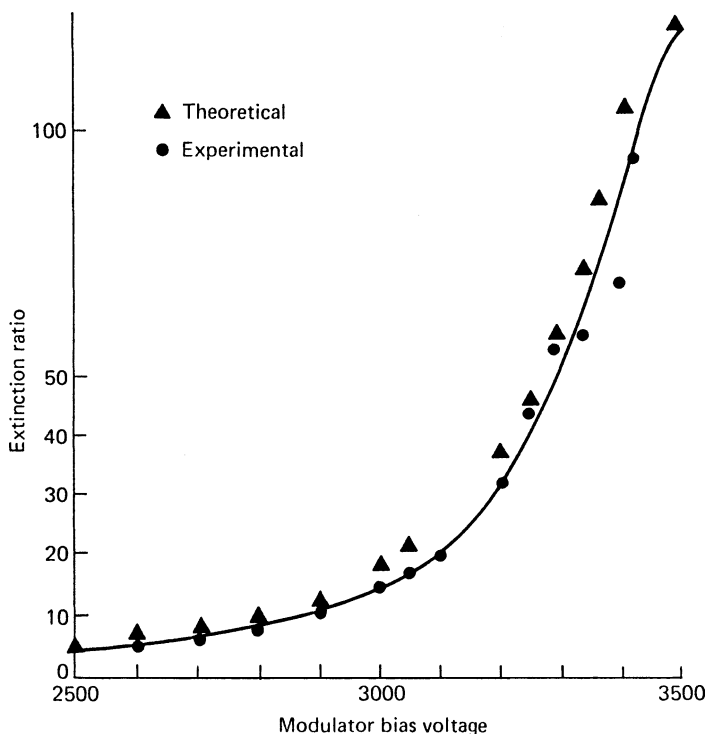


Fig. 8.14. Extinction ratio versus applied voltage of a LiNbO₃ Pockels cell-calcite prism assembly [8.30]

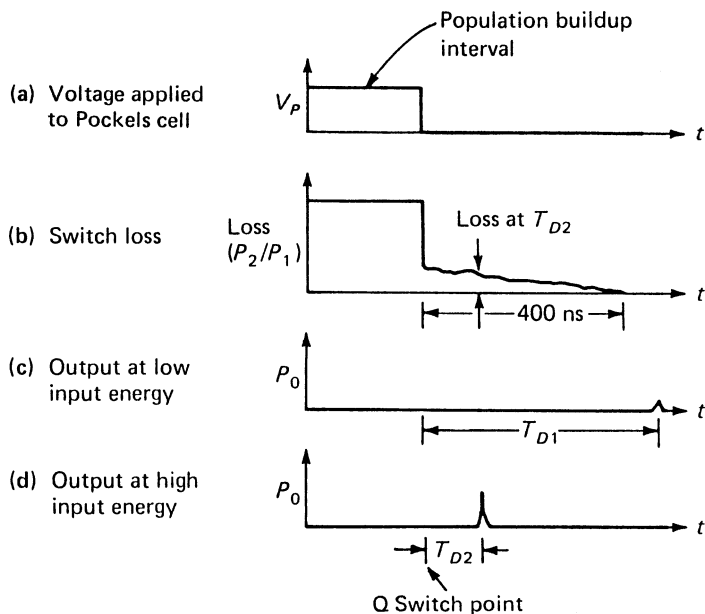


Fig. 8.15. Piezo-optic effect in LiNbO₃ [8.31]

delay T_D becomes shorter and thus the laser suffers a considerable output loss due to the switch loss, as shown in Fig. 8.15d. This, besides prelasing, accounts for the roll-off in output efficiency in the Q-switched laser at higher input energy levels.

The elasto-optic effect, which is quite pronounced in LiNbO₃ but is also observed in KD*P, can be minimized by switching the bias voltage to a negative value rather than to zero.

KTP, a crystal which is used extensively as an efficient nonlinear-optical crystal, has also been explored as a Q-switch because piezoelectric effects have not been observed in this material [8.32].

8.3.4 Depolarization Losses

In low-repetition-rate systems, or at low input powers, depolarization losses can be ignored, but in higher-average-power systems depolarization losses become significant.

The polarizer, required for Q-switch operation employing a Pockels cell, rejects any radiation not polarized in the proper plane of polarization. This can lead to large depolarization losses in the presence of thermally-induced birefringence, as may occur in high-repetition-rate systems.

Basically the same techniques as discussed in Sect. 7.1.6 can be employed in order to reduce depolarization losses in electro-optic Q-switched resonators. In large Q-switched oscillators, two laser heads with a 90° phase rotator inserted between the laser rods are sometimes used. In an oscillator containing a single laser head, a Faraday rotator inserted between the laser rod and rear mirror can be employed. Smaller Q-switched oscillators, in particular military lasers, employ mostly a waveplate-Porro prism combination for birefringence compensation. This approach will be discussed in more detail at the end of this section.

Also several techniques have been developed in conjunction with Pockels cell Q-switches which act on both polarizations. In general, the techniques are based on the use of a calcite polarizer in the resonator which separates the two orthogonally polarized beams.

Figure 8.16 shows a calcite polarizer which separates the two orthogonal polarization components into two parallel beams. A quarter-wave plate is inserted into one of the beams, before both beams are passed through a large aperture Pockels cell. A roof prism returns the beams back to the Pockels cell/polarizer assembly [8.33].

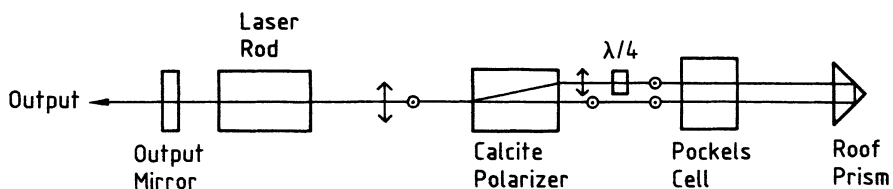


Fig. 8.16. Polarization insensitive Q-switch based on spatial separation of orthogonally polarized beams [8.33]

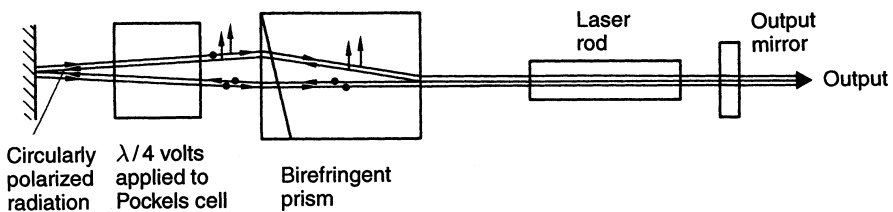


Fig. 8.17. Polarization insensitive Q-switch based on angular separation of orthogonally polarized beams [8.34]

A design which exploits directional differences between the two orthogonal beam components after passing through a birefringent prism has been proposed in [8.34]. A schematic diagram of the laser is shown in Fig. 8.17. The resonator contains a birefringent prism that replaces the linear polarizer commonly used in Q-switched lasers. After passing through the birefringent prism, radiation is split up into two orthogonally polarized components, the extraordinary (e) and the ordinary (o) rays, that propagate in two slightly different directions. When these two rays are reflected by the back mirror, a further separation of the two rays will occur. In this case the losses in the cavity will be very high and laser action will be suppressed. However, if a quarter-wave voltage is applied to the Pockels cell, the e and o rays returning to the prism will be interchanged. In this case, the walk off occurring in the first pass will be canceled by an equal and opposite walk off during the return pass, hence the beam returning to the laser rod will have low losses, allowing a Q-switched pulse to develop.

A very common resonator in military systems is a polarization coupled design such as depicted in Fig. 8.18. The resonator typically contains one or two Porro prisms to take advantage of the alignment insensitivity of these components. If such a laser is operated at high average power, the depolarization caused by thermally induced birefringence will drastically distort the output beam profile. An output beam resembling a Maltese cross will be obtained from a thermally stressed laser rod. However, in such a resonator, a birefringence compensation technique is possible by adding to the Porro prism a waveplate with the proper phase retardation and orientation.

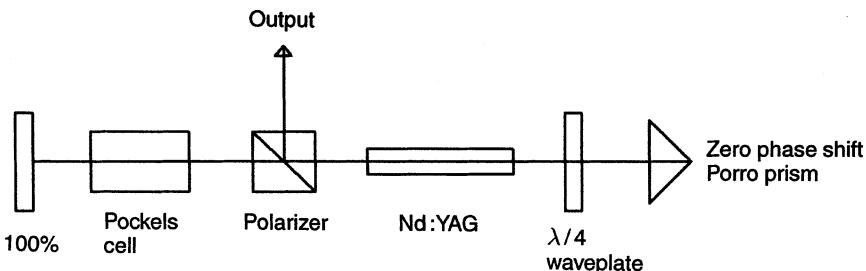


Fig. 8.18. Polarization output coupled resonator with birefringence compensation

Like the compensation with a Faraday rotator between the rear mirror and laser rod, or the placement of a 90° rotator between two laser rods, this technique relies on the fact that two passes occur in the thermally stressed laser rod before the beam is passed through the linear polarizer. However, there is a difference with regard to the above mentioned techniques. The phase difference between radial and tangential rays caused by birefringence is not cancelled by two passes of each ray through the same region of the laser rod, but by passing through two different, but symmetrically located points in each half of the rod. Each half being defined by the Porro prism bisecting plane. If the prism is oriented with its roof edge bisecting the rod axis, then each ray passing through one part in the rod returns at the opposite side of the bisecting plane through a section which is symmetrically opposite and at the same radial distance from the rod center. In a uniformly pumped laser rod, birefringence is radially symmetric and the amount of phase distortion depends only on the radius.

By changing the polarization state of the beam between the two passes, it is possible to cancel the relative phase difference between the tangential and radial components of polarization that occur in the first pass with equal and opposite phase changes in the return pass. The appropriate change of polarization between the two passes can be accomplished with a waveplate or optical rotator in front of the Porro prism [8.35, 36]. For example, the combination of a zero-phase-shift Porro prism and a quarter-waveplate with an orientation of 45° between its fast axis and the prism apex can accomplish this task. Any thermally induced depolarization effects that occur in the first pass are removed in the return path.

A Porro prism with zero phase shift (Fig. 8.18) is not a common optical component. As has been explained in Sect. 5.1.9. Porro prisms introduce a phase shift to a linearly polarized beam which depends on the refractive index and the angle between the plane of polarization and the roof edge. A Porro prism which does not introduce a phase shift requires dielectric coatings on the totally reflecting prism surfaces. Another combination, which results in a cancellation of the thermally induced depolarization, is a half-waveplate and a π -shift Porro prism at a relative orientation of 22.5°. Again the Porro prism requires dielectric coatings on the internally reflecting surfaces. The combination of a quarter- or half-waveplate and a Porro prism are only special cases of many possible combinations. They are of interest because these waveplates are readily available; however, the use of either of these waveplates requires a specially dielectrically coated Porro prism. By use of the Jones matrix method, a waveplate with a suitable phase change and orientation can be found for any uncoated Porro prism in order to achieve birefringence compensation. In [8.35, 36] curves are provided for waveplate-phase angle and Porro prism refractive index combinations, which permit the compensation of thermally induced depolarization in a laser rod.

The output coupling of the resonator, depicted in Fig. 8.18, can be optimized by a rotation of the Porro prism/waveplate combination while maintaining the relative angular position between these two components. As already mentioned, a change of the angle between the plane of polarization and the roof edge introduces a phase change in the return beam. However, in most situations it is found that it is more convenient to add a second waveplate to the resonator for control of the output coupling. Also, the 100% mirror shown in Fig. 8.18 can be replaced by a second Porro prism to add

alignment stability in two directions. In addition, space constraints drive the design very often to a folded configuration, shown, for example in Fig. 5.30.

8.3.5 Drivers for Electro-Optic Q-Switches

Switching a Pockels cell to obtain a quarter-wave retardation has the advantage that it requires only half the voltage of a half-wave retardation device. But the voltage has to be applied to the crystal for the duration of the pump pulse (i.e., about 240 μs for Nd:YAG). In the case of a half-wave retardation, the voltage is applied to the crystal only during the pulse build-up time at the end of the pump cycle (typically about 100 ns). As far as the electronics is concerned, for $\lambda/4$ switching a fast turn-off of the high voltage is critical and, for $\lambda/2$ switching a fast rise-time of the high voltage pulse is important to minimize resonator losses.

Operation of an electro-optically Q-switched laser requires fast switching of voltages in the multi-kilovolt regime. The driver for the Pockels cell must be a high-speed, high-voltage switch that also must deliver a sizeable current. The cell has a few tens of picofarads capacitance which is charged (or discharged) to several kilovolts in a few nanoseconds. The resulting current is of the order of 10–20 A. Common switching techniques include the use of MOSFETs, SCRs, and avalanche transistors.

A typical circuit is based on a Marx bank, in which a number of capacitors are charged in parallel and then connected in series by means of semiconductor switches. The advantage of the Marx bank circuit is that the voltage requirement of the power supply is only a fraction of the voltage generated at the crystal. Figure 8.19 illustrates such a design. The capacitors C_1 to C_n are all charged through resistors R_1 and R_n to about 1 kV. A string of transistors is connected in parallel to each capacitor and associated diode D. The transistors are operated close to their avalanche breakdown voltage. As soon as one transistor is triggered, all the transistors are switched on, which connects all capacitors in series and a large negative voltage appears on the Pockels cell. Typically four to six strings of avalanche transistors are employed to generate voltages in the 2.5–6 kV range starting with 0.8–1 kV at the power supply.

The circuit illustrated in Fig. 8.19 is typical for producing a half-way voltage in the Pockels cell. In this case the high voltage is applied for only a very short time at the end of the pump cycle. If a high voltage power supply is available, a Marx bank is not needed and the switching circuit is simplified. Figure 8.20 shows a string of avalanche transistors (Q1–Q10) that will switch a high voltage applied to the Pockels cell quickly to zero. This circuit is intended for quarter wave operation of the Q-switch.

8.4 Acousto-Optic Q-Switches

In acousto-optic Q-switches, an ultrasonic wave is launched into a block of transparent optical material, usually fused silica. By switching on the acoustic field, a fraction of the energy of the main beam is diffracted out of the resonator, thus introducing a

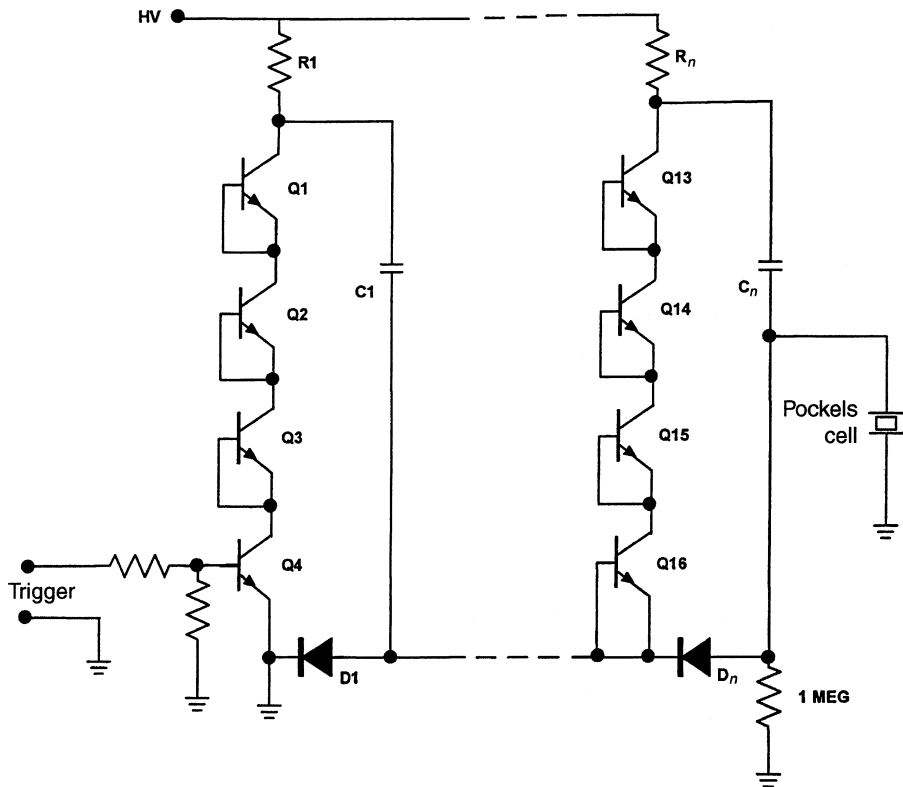


Fig. 8.19. Circuit diagram of Pockels cell drive electronics employing avalanche transistors

loss mechanism that prevents laser action. When the acoustic field is switched off, full transmission through the Q-switch cell is restored and a laser pulse is created.

The acousto-optic Q-switch is the device of choice for repetitively Q-switching cw lasers. The low-gain characteristics of cw-pumped solid-state lasers do not require very high extinction ratios, but do demand an exceptionally low insertion loss. Since high optical quality fused silica with antireflection coatings can be used as the active medium in the acousto-optical Q-switch, the overall insertion loss of the inactive Q-switch can be reduced to less than 0.5% per pass. The low-insertion loss of the acousto-optic Q-switch offers the convenience of converting from Q-switched to cw operation simply by removing the RF drive power.

An acousto-optic Q-switch is activated by the application of RF power to a transducer that is attached to the transparent medium. The resulting acoustic wave gives rise to a sinusoidal modulation of the density of the medium. The index of refraction is coupled to these periodic variations of the density and strain via the photoelastic effect. Considering only the one-dimensional case for an acoustic wave traveling in the y direction, we can write

$$n(y, t) = n_0 + \Delta n_0 \sin(w_s t - k_s y), \quad (8.28)$$

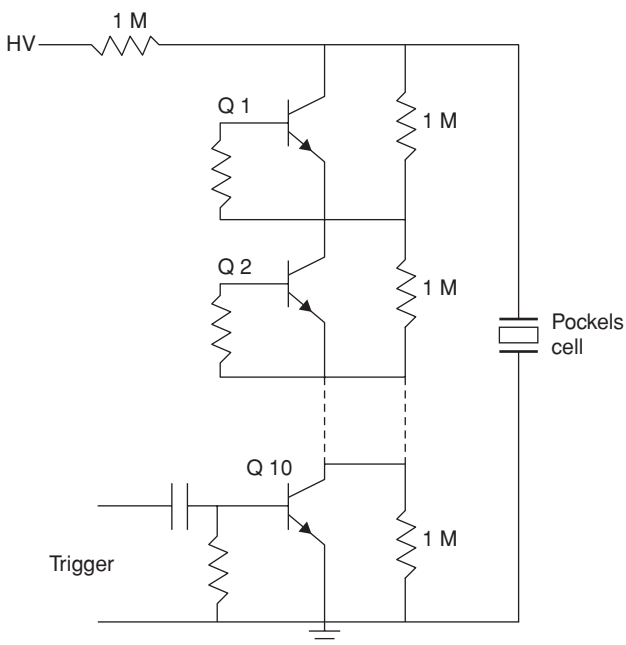


Fig. 8.20. Quarter-wave switching circuit for a Pockels cell

where n_0 is the average refractive index of the medium, Δn_0 is the amplitude of the index change, and $w_s = 2\pi v_s$ and $k_s = 2\pi/\lambda_s$ are the angular frequency and the wave vector of the sound wave which travels with the sound velocity $v_s = \nu_s \lambda_s$ through the medium.

8.4.1 Bragg Reflection

The refractive index change described by (8.28) forms a traveling-wave phase grating across the width of the optical beam. The grating has a period equal to the acoustic wavelength and an amplitude proportional to the sound amplitude. A portion of the optical beam which passes through the region occupied by the acoustic wave is diffracted by this phase grating. Acousto-optic Q-switches are operated at ultrasonic frequencies in the tens of megahertz, and the beam interaction length is on the order of several centimeters. In this so-called Bragg regime, the grating acts as a thick phase grating. The diffracted beam is primarily confined to a single direction and has a maximum at the Bragg angle. The condition for Bragg scattering to occur is $l\lambda \gg \lambda_s^2$, where l is the interaction length and λ and λ_s are the optical and acoustical wavelengths in the medium, respectively.

In the case of a short interaction length or long acoustical wavelength the acousto-optic cell becomes a thin phase grating and the light beam is diffracted into many orders. This is the regime of Raman-Nath scattering. Because of the higher RF power requirements, acousto-optic Q-switches are not used in this regime.

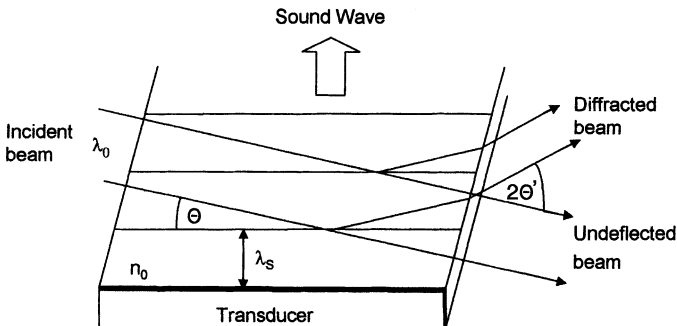


Fig. 8.21. Geometry for Bragg reflection

Figure 8.21 displays the geometry for Bragg reflection. The incident beam appears to be reflected from the acoustic wavefronts as if they were mirrors. This phenomenon is called acoustic Bragg reflection in analogy to the selective reflection of X-rays by the lattice of crystals first observed by Bragg. Conservation of energy and momentum of the photon–phonon interaction leads to the condition

$$\sin \Theta = \lambda / 2\lambda_s, \quad (8.29)$$

where Θ is the angle of incidence between the optical beam and the acoustic wave, and $\lambda = \lambda_0/n_0$ is the optical wavelength in the diffracting medium. We can derive the Bragg condition (8.29) with the aid of Fig. 8.22 if we assume for the moment that there is no motion of the sound wave. Rays A and B are reflected by two successive acoustic wavefronts. The rays differ in pathlength by the distance $2s$. In order for the rays to be in phase and reinforce we require $2s = \lambda$. From Fig. 8.22 we also obtain the relationship $\sin \Theta = s/\lambda_s$. Elimination of s in these two equations yields the Bragg condition. The beam observed at the Bragg angle arrives from reflections at successive acoustic wavefronts. The rays from each wavefront add in phase and the total intensity is, therefore, N times the intensity of a single reflection.

The difference in direction of the diffracted and incident beam inside the medium is twice the Bragg angle, that is, $2 \sin \theta$ or 2Θ , since the angle is very small. Reflection at the external boundary of the device will increase the angle by n_0 , accordingly we obtain

$$2\Theta' = \lambda_0/\lambda_s. \quad (8.30)$$

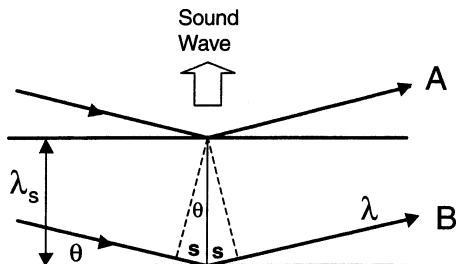


Fig. 8.22. Reflection of rays A and B by two successive acoustic wavefronts

The external angular separation of the two beams is equal in radians to the ratio of the optical to acoustic wavelengths.

A typical acousto-optic Q-switch uses fused silica as the ultrasonic medium and an RF frequency to the transducer for launching an acoustic wave of $v_s = 50$ MHz. The velocity of sound in fused silica is $v_s = 5.95$ km/s. With these numbers and $\lambda_0 = 1.06 \mu\text{m}$, we obtain $\lambda_s = 119 \mu\text{m}$ and $2\theta' = 8.9$ mr.

Although of no particular consequence for Q-switch operation, it is worth mentioning that the diffracted beam is frequency shifted. The diffracted beam may be thought of as having been Doppler-shifted during diffraction from the acoustic traveling wave. It has the frequency ($\nu \pm v_s$) depending on whether the optical beam is incident in front of the oncoming acoustic wave (see Fig. 8.21) or from behind the receding wave.

We will now calculate the partitioning of the power between the incoming and diffracted beam as a function of acoustic power and material parameters. A rigorous treatment of the subject that requires the solution of two coupled traveling wave equations can be found in [8.37, 38].

The total electric field $E(x, t)$ is taken as the sum of two waves along the distance x . The diffracted wave grows at a rate [8.39]

$$\frac{dE_1(x)}{dx} = \frac{1}{2} E_2 \frac{d\varphi}{dx} \quad (8.31)$$

and the undeflected beam decreases at a corresponding rate

$$\frac{dE_2(x)}{dx} = -\frac{1}{2} E_1 \frac{d\varphi}{dx}, \quad (8.32)$$

where E_1 and E_2 are the electric field strength of the diffracted and undeflected beam, respectively, and $d\varphi$ is the phase excursion of the beam over an incremental length x given by

$$d\varphi = \beta_0 \frac{\Delta n_0}{n_0} dx, \quad (8.33)$$

where β_0 is the propagation constant $\beta_0 = 2\pi/\lambda_0$ in free space. Equations (8.31) and (8.32) have the solution

$$E_1 = E_3 \sin(\Delta\varphi/2) \quad (8.34)$$

and

$$E_2 = E_3 \cos(\Delta\varphi/2), \quad (8.35)$$

where E_3 is the amplitude of the wave entering the crystal.

The diffracted power P_1 as a function of the incident power P_3 follows from (8.34)

$$P_1/P_3 = \sin^2(\Delta\varphi/2) \quad (8.36)$$

and the reduction of power of the undeflected beam is obtained from (8.35)

$$P_2/P_3 = \cos^2(\Delta\varphi/2), \quad (8.37)$$

where $\Delta\varphi$ is the total phase shift the beam experienced over the interaction length l ,

$$\Delta\varphi = l\beta_0\Delta n_0. \quad (8.38)$$

The sum of the powers of the undeflected and diffracted beams remains constant $P_1 + P_2 = P_3$. Now we have to connect a change of Δn_0 with the acoustic power P_{ac} in the medium.

The change of refractive index as a function of strain s is given by [8.18]

$$\Delta n_0 = \frac{n_0^3 p_{ij}}{2} s, \quad (8.39)$$

where p_{ij} is the elasto-optic coefficient in the medium, and the strain s is related to the acoustic power P_{ac} by [8.37]

$$s = \left[\frac{2P_{ac}}{\rho_0 v_s^3 l w} \right]^{1/2}. \quad (8.40)$$

In the above equation v_s is the velocity of sound in the medium, ρ_0 is the mass density, and l and w are the length and width of the transducer that launches the acoustic wave into the medium. Introducing (8.38–40) into (8.36) yields

$$\frac{P_1}{P_3} = \sin^2 \left[\frac{\pi}{\lambda} \left(\frac{l P_{ac} M_{ac}}{2w} \right)^{1/2} \right]. \quad (8.41)$$

The quantity M_{ac} is a material constant that determines the inherent efficiency of diffraction and is called the figure of merit

$$M_{ac} = n_0^6 p_{ij}^2 / \rho_0 v_s^3. \quad (8.42)$$

It is apparent from (8.41) that the amount of diffracted power depends on the material parameters expressed by M_{ac} , the ratio of length to width of the interaction path and the acoustical power P_{ac} . In a given material, for example fused silica, the value of the photoelastic coefficient p_{ij} in (8.42) depends on the plane of polarization of the light beam with respect to the ultrasonic propagation direction and on the type of ultrasonic wave, that is, longitudinal or shear wave. With shear wave generation the particle motion is transverse to the direction of the acoustic wave propagation direction. In this case the dynamic optical loss is independent of polarization in isotropic materials such as fused quartz.

Table 8.2 lists the pertinent material parameters for an acousto-optic Q-switch fabricated from fused silica. The p coefficients and velocity of sound in fused silica are from [8.40, 41]. The figure of merit M_{ac} follows from (8.42) with $n_0 = 1.45$ at $1.06 \mu\text{m}$ and $\rho_0 = 2.2 \text{ g/cm}^3$. The acoustic power requirement for 1% diffraction has been calculated from (8.41) for $l/w = 10$ and $\lambda = 1.06 \mu\text{m}$. The dimension of P_{ac} in (8.41) is erg/s ($1 \text{ erg/s} = 10^{-7} \text{ W}$).

8.4.2 Device Characteristics

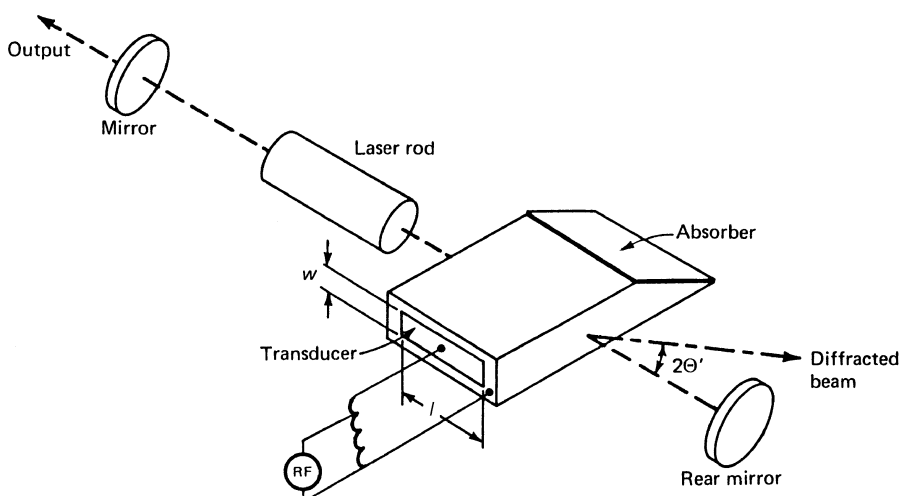
Figure 8.23 shows an optical schematic of a cw-pumped laser that contains an acousto-optic Q-switch. The Q-switch consists of a fused silica block to which a crystalline

Table 8.2. Material parameters of acousto-optic Q-switches employing fused silica

Acoustic wave	p Coefficient	Polarization of optical beam with respect to acoustic wave vector	Velocity of sound $\times 10^5$ (cm/s)	Figure of merit $M_{ac} \times 10^{-18}$ (s ³ /g)	Acoustical power $P_{ac}(\text{W})$ for 1% diffraction ($l/w = 10$)
Shear wave	$p_{44} = 0.075$	Independent	3.76	0.45	0.51
Longitudinal	$p_{11} = 0.121$	Parallel	5.95	0.30	0.77
Longitudinal	$p_{12} = 0.270$	Perpendicular	5.95	1.46	0.16

quartz or an LiNbO_3 transducer is bonded. Both the transducer and the fused silica interface contain vacuum-deposited electrodes to allow for electrical connections. An inductive impedance-matching network couples the signal of the RF generator to the quartz transducer. The ultrasonic wave is launched into the Q-switch block by the piezoelectric transducer that converts electrical energy into ultrasonic energy. The laser is returned to the high Q-state by switching off the driving voltage to the transducer. With no ultrasonic wave propagating through it, the fused silica block returns to its usual state of high optical transmission and a Q-switch pulse is emitted. The width of the transducer is typically 3 mm, which is about twice the beam diameter for most TEM_{00} -mode Nd:YAG lasers. The length of the Bragg cell and the transducer is around 50 mm. From (8.41) it follows that a large length-to-width ratio reduces the acoustic power requirement for a given diffraction ratio P_1/P_3 .

Virtually all acousto-optic Q-switches are single-pass devices, i.e., the acoustic wave generated by the transducer is absorbed after traveling across the interaction region. The absorber, consisting of a piece of lead attached to the tapered end of the

**Fig. 8.23.** Acousto-optic Q-switch employed in a cw-pumped Nd:YAG laser

quartz block, prevents reflected acoustical waves from interfering with the incident light beam.

Although the figure of merit M_{ac} of fused quartz is quite low, its optical high-quality, low optical absorption, and high damage threshold make it superior to other, more efficient acousto-optic materials, such as lithium niobate (LiNbO_3), lead molybdate (PbMoO_4), tellurium dioxide (TeO_2), and dense flint glass. These materials are usually employed in low-power light modulators and optical scanners.

By properly choosing the parameters of the acousto-optic device, a large enough fraction of the laser beam can be deflected out of the resonator to provide an energy loss that inhibits laser action. The frequency of the RF generator determines the diffraction angle according to (8.30), whereas the magnitude of the diffracted power is controlled by the RF power according to (8.41). The frequency of the RF signal driving the transducer is typically in the 40–50 MHz range. For these frequencies we obtain, with the values from Table 8.2 for both shear wave and longitudinal wave Q-switches, scattering angles in fused quartz between 14.1 and 7.1 mr. These angles are large enough to deflect the diffracted beam out of the resonator.

The amount of acoustical power required to achieve a certain diffraction efficiency can be calculated from (8.41). Unpolarized lasers are usually Q-switched with shear-wave devices, whereas for polarized laser radiation longitudinal modulators are employed. A longitudinal Q-switch in which the large p_{12} coefficient is utilized requires substantially lower RF powers compared to a shear wave device.

For the practical case of a shear wave Bragg cell having a length of $l = 50$ mm and a width of $w = 3$ mm, we find from (8.41) that in order to deflect 35% of the laser beam out of the resonator an acoustic power of 11.7 W is required. Since the Q-switch diffracts radiation in both directions the total insertion loss per round trip is $\delta = (P_1/P_3)(2 - P_1/P_3)$, where (P_1/P_3) is the fraction of radiation diffracted out of the resonator in one pass. For the example above, one obtains a round trip insertion loss of 58%, which is large enough to prevent laser action in most cw lasers. The conversion efficiency of RF power delivered to the transducer to acoustic power is on the order of 25–30%; therefore, at least 40 W of RF power have to be delivered to the transducer. If the laser output is polarized, a Bragg cell with a longitudinal wave can be utilized, and in this case only 12 W of RF power is required to achieve the same insertion loss.

The Q-switch must be able to switch from the high-loss to the low-loss state in less than the time required for the laser pulse to build up if maximum output energy is to be achieved. The turn-off time of an acousto-optical Q-switch is determined by the transit time of the sound wave across the beam diameter. Depending on the type of interaction, the transit time of the acoustic wave across a 1-mm diameter beam is between 266 and 168 ns. The relatively slow transit-time is not a serious drawback since the Q-switch pulse evolution time in most cw-pumped systems is considerably larger. Performance of an acousto-optic Q-switched, cw-pumped Nd:YAG laser is shown in Fig. 8.8. An acousto-optic Q-switch allows laser operation with a continuously adjustable pulse repetition rate, shown is the range from 100 Hz to about 40 KHz.

As already mentioned, an acousto-optic device is the most widely used Q-switch for cw-pumped Nd lasers. From (8.41) it follows that the modulation depth is inversely

proportional to the wavelength. Therefore, for longer wavelengths the modulation depth decreases, which has to be compensated for by a drastic increase in acoustic drive power since modulation depth increases only with the square root of P_{ac} . This makes the use of acousto-optic devices difficult for Q-switching mid-infrared lasers. In [8.42] an acousto-optic Q-switched Er:YSGG laser with an output at 2.79 μm and which uses a TeO₂ crystal as the interaction medium, is described.

Despite these difficulties several erbium lasers have been Q-switched with acousto-optic Q-switches. By using a linearly polarized beam for maximum diffraction efficiency and TeO₂ as the Q-switch medium, an efficient acousto-optic Q-switch for a Er:YSGG laser at 2.79 μm has been reported in [8.42]. Pulse energies of 27 mJ with durations of 125 ns have been obtained from a 90-mm-long and 4-mm-diameter rod. Linear polarization was achieved with a Si plate orientated at Brewster angle.

8.5 Passive Q-Switches

A passive Q-switch consists of an optical element, such as a cell filled with organic dye or a doped crystal, which has a transmission characteristic as shown in Fig. 8.24. The material becomes more transparent as the fluence increases, and at high fluence levels the material “saturates” or “bleaches,” resulting in a high transmission. The bleaching process in a saturable absorber is based on saturation of a spectral transition. If such a material with high absorption at the laser wavelength is placed inside the laser resonator, it will initially prevent laser oscillation. As the gain increases during a pump pulse and exceeds the round-trip losses, the intracavity power density increases dramatically causing the passive Q-switch to saturate. Under this condition the losses are low and a Q-switch pulse builds up.

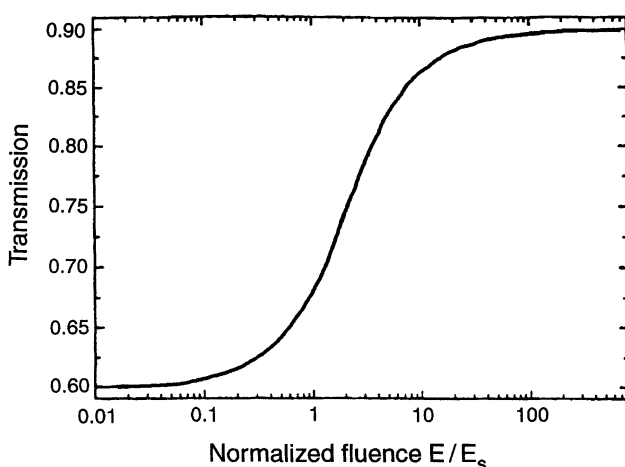


Fig. 8.24. Nonlinear transmission of a saturable absorber versus fluence normalized to the saturation fluence E_s of the absorber

Since the passive Q-switch is switched by the laser radiation itself, it requires no high voltage, fast electro-optic driver, or RF generator. As an alternative to active methods, the passive Q-switch offers the advantage of an exceptionally simple design, which leads to very small, robust, and low-cost systems. The major drawbacks of a passive Q-switch are the lack of a precision external trigger capability and a lower output compared to electro-optic or acousto-optic Q-switched lasers. The latter is due to the residual absorption of the saturated passive Q-switch which represents a rather high insertion loss.

Originally, saturable absorbers were based on different organic dyes, either dissolved in an organic solution or impregnated in thin films of cellulose acetate. The poor durability of dye-cell Q-switches, caused by the degradation of the light sensitive organic dye, and the low thermal limits of plastic materials severely restricted the applications of passive Q-switches in the past. The emergence of crystals doped with absorbing ions or containing color centers has greatly improved the durability and reliability of passive Q-switches.

The first new material to appear was the F_2^- :LiF color center crystal. The color centers are induced in the crystal by irradiation with gamma, electron, or neutron sources. Today, the most common material employed as a passive Q-switch is Cr⁴⁺: YAG. The Cr⁴⁺ ions provide the high absorption cross section of the laser wavelength and the YAG crystal provides the desirable chemical, thermal, and mechanical properties required for long life.

A material exhibiting saturable absorption can be represented by a simple energy-level scheme such as that shown in Fig. 8.25. For the moment we will consider only levels 1–3. Absorption at the wavelength of interest occurs at the 1–3 transition. We assume that the 3–2 transition is fast. For a material to be suitable as a passive Q-switch, the ground-state absorption cross section has to be large and, simultaneously, the upper state lifetime (level 2) has to be long enough to enable considerable depletion of the ground state by the laser radiation. When the absorber is inserted into the laser cavity, it will look opaque to the laser radiation until the photon flux is large enough to depopulate the ground level. If the upper state is sufficiently populated the absorber

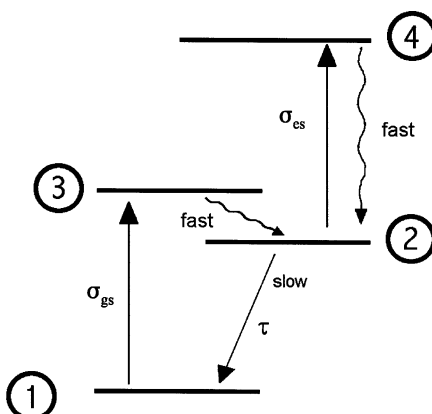


Fig. 8.25. Energy levels of a saturable absorber with excited-state absorption (σ_{gs} and σ_{es} are the ground-state and excited-state absorption cross sections, respectively, and τ is the upper state lifetime)

becomes transparent to the laser radiation, a situation that is similar to a three-level laser material pumped to a zero inversion level.

Solutions of the rate equation lead to an absorption coefficient which is intensity dependent [8.43]

$$\alpha_0(E) = \frac{\alpha_0}{1 + E_i/E_s}, \quad (8.43)$$

where α_0 is the small-signal absorption coefficient and E_s is a saturation fluence

$$E_s = h\nu/\sigma_{\text{gs}}, \quad (8.44)$$

where σ_{gs} is the absorption cross section for the 1–3 transition.

Important characteristics of a saturable absorber are the initial transmission T_0 , the fluence E_s at which saturation becomes appreciable, and the residual absorption which results in a T_{max} of the fully bleached absorber.

The small signal transmission of the absorber is

$$T_0 = \exp(-\alpha_0 l_s) = \exp(-n_g \sigma_{\text{gs}} l_s), \quad (8.45)$$

where l_s is the thickness of the bleachable crystal and n_g is the ground state density. In order to calculate the transmission as a function of fluence, the photon flux and population density must be considered as a function of position within the absorbing medium.

Similar to the situation which occurs in pulse amplifiers (Sect. 4.1), differential equations for the population density and photon flux have to be solved. The solution is the Frantz–Nodvik equation, which is identical to (4.11) except that gain G , G_0 is replaced by transmission T_i , T_0 . Therefore, the energy transmission T_i of an ideal saturable absorber as a function of input fluence E_i is given by

$$T_i = \frac{E_s}{E_i} \ln[1 + (e^{E_i/E_s} - 1)T_0]. \quad (8.46)$$

Equation (8.46) reduces to $T_i = T_0$, for $E_i < E_s$, and $T_i = 1$, for $E_i > E_s$.

In practical saturable absorbers, the transmission never reaches 100%; the reason being photon absorption by the excited atoms. A passive Q-switch requires a material which exhibits saturation of the ground-state absorption. However, most materials also exhibit absorption from an excited state. This is illustrated in Fig. 8.25 by the transition from the upper state (level 2) to some higher level 4 which has an energy level corresponding to the laser transition. As the ground state is depleted, absorption takes place increasingly between levels 2 and 4. Excited-state absorption (ESA) results in a residual loss in the resonator when the ground-state absorption has been saturated. The 2–4 transition does not saturate because of the fast relaxation of level 4. A saturable absorber is useful for Q-switching only as long as $\sigma_{\text{gs}} > \sigma_{\text{es}}$, where σ_{es} is the cross section for ESA.

A saturable absorber with ESA can be described by a four-level model [8.43, 44]. In this case, maximum transmission T_{\max} is given by

$$T_{\max} = \exp(-n_g \sigma_{\text{es}} l_s). \quad (8.47)$$

In [8.44] an approximation in closed form, which gives the shape of the transmission versus fluence curve in the presence of ESA, has been derived. For a nonideal absorber the transmission T_n can be approximated by

$$T_n = T_0 + \frac{T_i - T_0}{1 - T_0} (T_{\max} - T_0), \quad (8.48)$$

where T_i is the transmission of an ideal absorber given by (8.46) and T_0 and T_{\max} are the lower and upper limits of the transmission.

In Fig. 8.24, T_n is plotted for the case of $T_0 = 60\%$ and $T_{\max} = 90\%$. For a given saturable absorber one needs to know the cross sections σ_{gs} and σ_{es} , the ground-state concentration n_g , and the thickness l_s of the material. With these quantities known one can calculate T_0 , T_{\max} , and E_s and plot a transmission versus energy density curve as determined by (8.48).

Because of the importance of Cr⁴⁺:YAG as a passive Q-switch material, we will briefly review the properties of this material. In order to produce Cr⁴⁺:YAG, a small fraction of chromium ions in YAG are induced to change valence from the normal Cr³⁺ to Cr⁴⁺ with the addition of charge compensating impurities such as Mg²⁺ or Ca²⁺. The crystal Cr⁴⁺: YAG has broad absorption bands centered at 410, 480, 640, and 1050 nm. Published values for the cross section of the ground state vary greatly [8.44, 45]. The most recent measurements indicate $\sigma_{\text{gs}} = 7 \times 10^{-18} \text{ cm}^2$ and $\sigma_{\text{es}} = 2 \times 10^{-18} \text{ cm}^2$ for the excited-state absorption at the Nd:YAG wavelength [8.44]. The excited-state lifetime (level 2 in Fig. 8.25) is 4.1 μs and the lifetime of the higher excited state (level 4) is 0.5 ns. With $h\nu = 1.87 \times 10^{-19} \text{ J}$ at 1.06 μm and the above value for σ_{gs} one obtains a saturation fluence of $E_s = 27 \text{ mJ/cm}^2$ for Cr⁴⁺:YAG.

Commercially available Cr⁴⁺:YAG passive Q-switches are specified by the low-power transmission at the laser wavelength. Typical transmission values range from 30 to 50%, and the crystal thickness is usually between 1 and 5 mm. Values of the small signal absorption coefficient α_0 vary from 3 to 6 cm⁻¹. For example, for $\alpha_0 = 4 \text{ cm}^{-1}$ and $l_s = 2 \text{ mm}$ the low-power transmission is $T_0 = 45\%$.

Figure 8.26 illustrates the transmission of a 2.65-mm-thick sample of Cr⁴⁺: YAG. The transmission starts at about $T_0 = 53.5\%$ for low power, increases linearly, and then saturates at about $T_{\max} = 84\%$ for high fluence [8.46]. From (8.45) follows a Cr⁴⁺ ion density of $n_g = 3.4 \times 10^{17} \text{ cm}^{-3}$ for this sample.

For a given pump power, i.e. gain in the laser medium, there is an optimal choice of output coupler reflectivity and unsaturated absorber transmission. A design procedure that permits the optimization of a passively Q-switched laser has been developed by Degnan [8.47] by applying the Lagrange multiplier method in analogy to his analysis of actively Q-switched lasers. Figure 8.27, which is adapted from [8.47], shows that the design procedure permits the optimum choice of the unsaturated

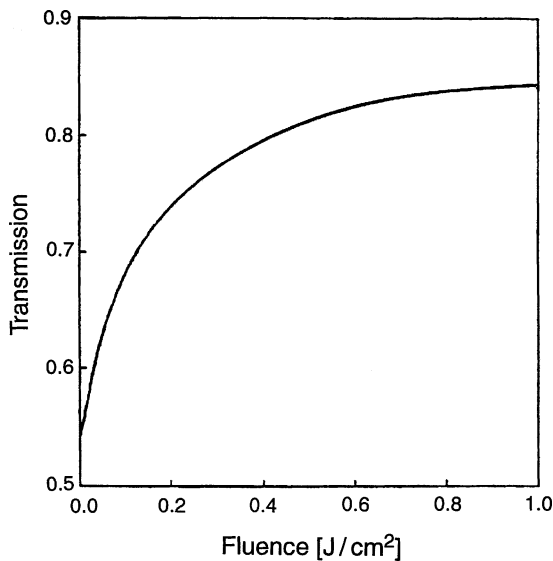


Fig. 8.26. Transmission versus fluence for a 2.65-mm-thick Cr⁴⁺:YAG absorber [8.46]

Q-switch transmission T_0 and the output mirror reflectivity R for a given gain G_0 . The above quantities are normalized as follows:

$$x = \frac{1}{\delta} \ln \left(\frac{1}{R} \right) \quad y = \frac{-\ln T_0}{\ln G_0} \quad z = \frac{\ln G_0^2}{\delta}, \quad (8.49)$$

where

$$\delta = \delta_R + 2\sigma_{es} n_g l_s. \quad (8.50)$$

The terms in (8.50) are the combined roundtrip loss in the resonator caused by dissipative losses δ_R and the residual absorption in the fully saturated Q-switch.

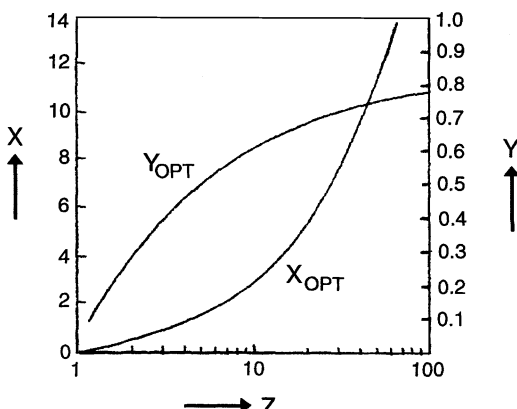


Fig. 8.27. Dependence of the optimum mirror reflectivity x and absorber transmission y on laser gain z . All parameters are normalized according to (8.49)

The variable z is the same that has been used in the analysis of the actively Q-switched case (see Eq. (8.8)).

The optimization of a passively Q-switched laser can proceed along the following path: First one determines the single pass, small-signal gain G_0 , and optical losses δ_R according to the procedure outlined in Sect. 3.4.2. From the manufacturer data which usually provides the optical density of T_0 of the crystal, one can calculate n_g and therefore δ . With G_0 and δ known, the parameter z can be calculated and with it x_{opt} and y_{opt} follow from Fig. 8.27.

Rearranging (8.49) one obtains

$$R_{\text{opt}} = \exp(-x_{\text{opt}}\delta) \quad T_{\text{opt}} = \exp(-y_{\text{opt}} \ln G_0). \quad (8.51)$$

Building upon the work reported in [8.47] the analysis of passive Q-switched lasers has been expanded to include ESA in the saturable absorber [8.48, 49].

Passive Q-switching of pulsed and cw-pumped Nd:lasers employing Cr⁴⁺:YAG are described in [8.46, 48, 50–52]. In a passively Q-switched, cw-pumped laser, once a certain threshold is reached, peak power and pulse width do not change further, but the repetition rate increases approximately linearly with pump input power [8.53].

According to (8.11) the pulse width of a Q-switched laser is directly proportional to the cavity round trip time and therefore to the resonator length. Passive Q-switches permit the design of lasers with very short resonators because the Q-switch and laser crystal can be closely packaged. For example, diode-pumped microchip lasers have resonators typically less than 1 mm in length. These lasers, consisting of a Nd:YAG crystal bonded to a thin piece of Cr⁴⁺:YAG and with reflective coatings applied to the outside surfaces, have produced Q-switch pulses well below a nanosecond [8.54–56].

For passive Q-switching of lasers other than Nd-doped crystals, particularly lasers emitting at 1.5 μm and 2 μm, different saturable absorbers are required. Passive Q-switching of erbium-doped lasers emitting at 1.5 μm has been achieved with CaF₂ [8.57, 58]. For passive Q-switching of 2-μm lasers, such as Tm:YAG or Tm:Cr:YAG lasers, the crystal Ho:YLF has been used as an effective saturable absorber [8.59].

In the passive Q-switches discussed so far, the *transmission* increases with intensity. A different kind of passive Q-switch is the semiconductor saturable absorber mirror. In such a mirror *reflectivity* increases with intensity. As will be explained in more detail in Sect. 9.2.4, a semiconductor saturable absorber consists of an InGaAs/GaAs multiple quantum well absorber layer with appropriate coatings applied to both surfaces. This device is mostly employed for passive mode-locking; however, it can also be used for passively Q-switching lasers.

The layout of a diode-pumped Nd:YVO₄ microchip laser containing a semiconductor saturable absorber mirror (SESAM) Q-switch is illustrated in Fig. 8.28. The 3% doped Nd:YVO₄ crystal, with a thickness of 200 μm and an absorption length of about 100 μm, is sandwiched between a 10% output coupler and the saturable absorber mirror. At an incident pump power of 460 mW pulses with a duration of 56 ps and a peak power of 1.1 kW were obtained. The pulse repetition rate was 85 kHz [8.60].

The compactness which can be achieved with a passive Q-switched laser is illustrated in the following example. For a space-borne high-resolution lidar system

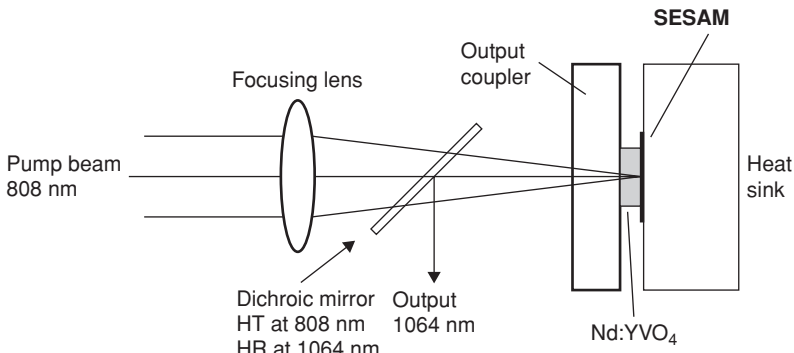


Fig. 8.28. Layout of a passively Q-switched Nd:YVO₄ microchip laser [8.60]

an extremely small, conduction-cooled laser transmitter was required having pulse width of less than 2 ns [8.52]. The optical layout is sketched in Fig. 8.29a. The laser uses a single 100 W quasi-cw diode bar to pump a ten bounce zigzag Nd:YAG slab of 13 mm length and 1×0.75 mm² cross-section.

The passive Q-switch permits the design of a resonator which is only a few centimeters in physical length. The optical length of the resonator comprising a flat and curved mirror is 6.75 cm, which results in a roundtrip time of $t_r = 0.45$ ns. The laser produces a TEM beam with an output energy of 0.85 mJ per pulse and a pulse length of 1.4 ns at a repetition rate of 100 Hz (see Fig. 8.29b). The pump radiation from the diode array is collimated with a cylindrical lens to confine the radiation into a 500-μm-wide region within the slab. With this arrangement a small pump mode volume can be realized which well overlaps the resonator fundamental mode. Pumping for 200 μs produces 20 mJ of pump power. The single pass, small-signal gain was measured to be about $G_0 = 8$. The AR-coated Cr⁴⁺:YAG crystal has a thickness of 2 mm and an optical density of 0.5 or $T_0 = 0.32$ in the unsaturated state. With the value of T_0 and with σ_{gs} for Cr⁴⁺:YAG, we can calculate the ground-state population density

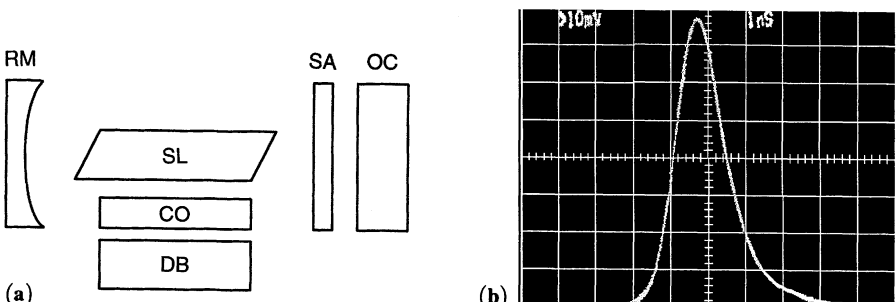


Fig. 8.29. (a) Optical schematic of a passively Q-switched Nd:YAG oscillator. SL, Nd:YAG slab; DB, diode bar; CO, coupling optics; OC, output coupler; RM, rear mirror; SA, saturable absorber. (b) Oscilloscope trace of the Q-switched output pulse (horizontal: 1 ns/div) [8.52]

n_g from (8.45). Introducing n_g and σ_{gs} into (8.47) gives the saturated transmission $T_{\max} = 0.72$. This results in a roundtrip loss of about $\delta = 0.6$, if one includes 4% losses in the crystal slab. Typical of passive Q-switched lasers, the insertion loss is dominated by the residual absorption in the Q-switch caused by undepleted ground-state population density and excited-state absorption. As follows from (8.45) and (8.47), the ratio of excited-state to ground-state absorption cross section is fixed for a given saturable absorber $\ln T_{\max}/\ln T_0 = \sigma_{es}/\sigma_{gs}$.

The output beam has a diameter of about 0.5 mm, which gives a fluence of 0.45 J/cm². Since the output coupler has a reflectivity of $R = 20\%$, the fluence within the saturable absorber is about 0.67 J/cm². This is 25 times above the saturation level for Cr⁴⁺:YAG and according to the curves of Figs. 8.24 and 8.26, it is close to the maximum transmission for this material.

Generally, a good agreement is obtained between the calculated and measured values of pulse width, optimum mirror reflectivity, and Q-switch transmission. With the above values for G_0 and δ , one obtains $z = 6.9$ from (8.8). The pulse width calculated from (8.11) is 1.1 ns for this laser. This compares well with the measured pulse width of 1.4 ns. From (8.49) follows $x_{\text{opt}} = 2.0$ and $y_{\text{opt}} = 0.56$. The optimum values for unsaturated transmission and output coupler reflectivity are therefore $R_{\text{opt}} = 30\%$ and $T_{\text{opt}} = 31\%$.

The Cr⁴⁺:YAG crystal selected for this laser had an optical density T_0 at the unsaturated state, which comes very close to the optimum predicted value. The reflectivity of the output mirror was deliberately chosen to be lower than the calculated value R_{opt} .

Energy output versus mirror reflectivity is not a strongly peaked function, and it is sometimes desirable to select a lower reflectivity for the output mirror rather than the optimum value in order to make the laser more robust from the point of view of optical damage and multiple pulsing. A lower reflectivity of the output coupler reduces the fluence in the cavity which reduces the likelihood of optical coating damage. Multiple Q-switched output pulses occur if the unsaturated transmission of the absorber and/or the output mirror reflectivity is too high. In this case, Q-switching occurs early in the pump pulse. With the proper values and ratio of output coupling to absorption in the Q-switch, a single pulse can be generated which should occur near the end of the pump pulse.

8.6 Cavity Dumping

A means for generating extremely short Q-switched laser pulses involves Q-switching the laser with 100% mirrors on both ends of the cavity and then, at the peak of the circulating power, rapidly switching the output mirror from 100 to 0% reflection. This leads to a rapid dumping of the entire optical energy from within the cavity. One of the advantages of this technique is the production of Q-switched pulses whose width is primarily a function of the oscillator cavity length, rather than the gain characteristics of the laser medium. Specifically, the laser pulse width at the half-power points will be equivalent to the roundtrip transit time in the cavity, with the

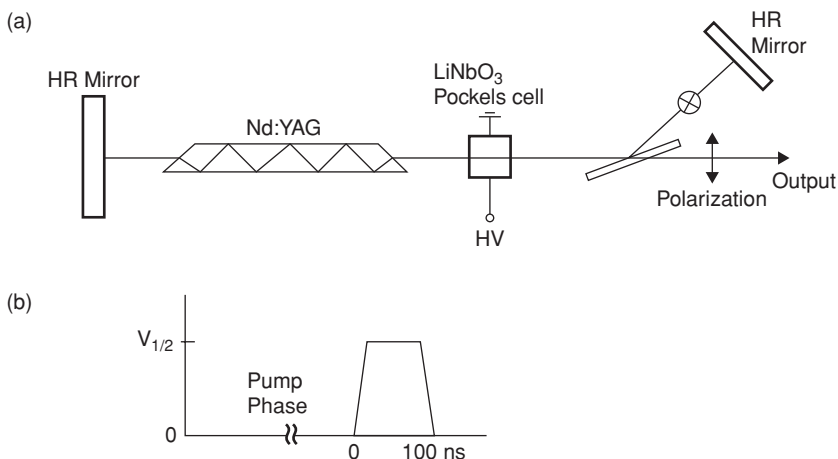


Fig. 8.30. (a) Optical schematic of a cavity dumped Nd:YAG laser and (b) voltage at the Pockels cell

condition that the Q-switch employed be switched within this same time period. Thus, based on typical cavity dimensions, pulse widths in the range of 2–5 ns are feasible for oscillators whose pulse widths are of the order of 10–20 ns in the normal Q-switch mode.

Figure 8.30 shows the layout of a Nd:YAG slab laser designed to generate short pulses by cavity dumping. During the 200- μ s-long pump pulse, the horizontally polarized beam is transmitted by a thin film or calcite polarizer thereby preventing optical feedback. Upon reaching peak energy storage in the Nd:YAG crystal, the Pockels cell is biased to its half-wave retardation voltage. The vertically polarized radiation is now reflected by the polarizer to the high reflectivity mirror, and a high Q is established in the resonator.

When the power in the cavity reaches its peak value, the bias is removed from the Pockels cell in a time period of about 2 ns. The cavity energy then literally drains out of the cavity in the time required for the radiation to travel one round trip in the optical cavity. The combination of the polarizer, Pockels cell, and 100% mirror comprises what amounts to a high-speed voltage-variable mirror whose reflectivity is changed from 0 during the pumping cycle to 100% during the pulse buildup, and back to 0 during the cavity dumping phase.

Cavity dumping is also possible in a continuously pumped laser. As is the case for repetitively Q-switching, a continuous train of pulses is emitted. However, energy accumulation and storage between output pulses are primarily in the optical field for cavity dumping, and primarily in the population inversion for Q-switching.

The finite buildup time of the field inside the laser cavity and the time required to repump the inversion set an upper limit to the repetition rate available from Q-switched lasers. This maximum value of repetition rate for Q-switched Nd:YAG lasers is of the order of 50–100 kHz. Cavity dumping of continuously pumped lasers is a way

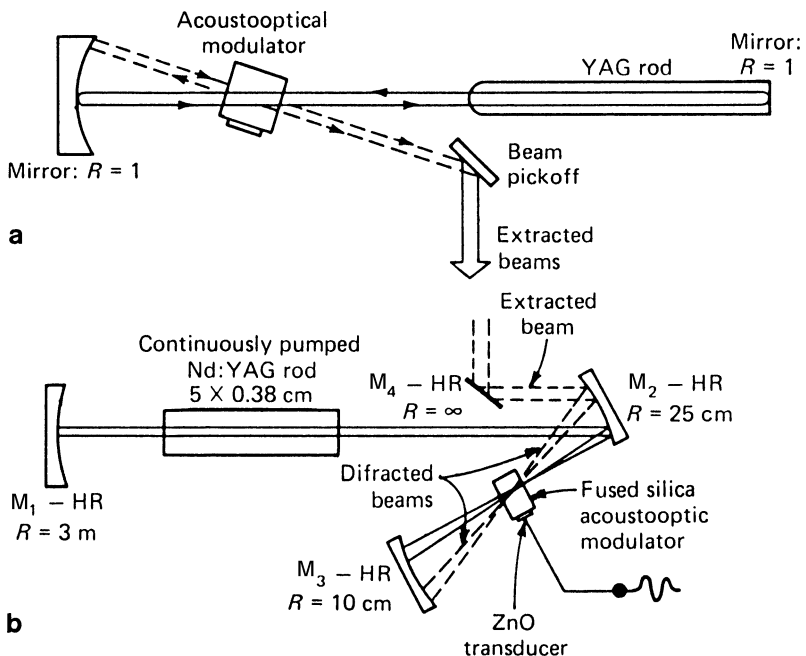


Fig. 8.31. Common arrangements for cavity dumping of cw-pumped solid-state lasers. The broken lines indicate the beams which are diffracted by the modulator

to obtain pulsed output at higher repetition rates than are available by Q-switching. Repetition rates from 125 kHz up to several megahertz for cavity dumping have been achieved with cw-pumped Nd:YAG lasers.

Figure 8.31 exhibits two common arrangements employed for cavity dumping of cw-pumped solid-state lasers [8.61, 62]. Essentially all systems of this type employ acousto-optic modulators as the switching element. In order to obtain fast switching action, the incident beam must be focused to a narrow waist inside the modulator. The two oscillator designs differ in the way the optical beam is focused into the modulator.

In Fig. 8.31a the modulator is located at a beam waist created by a concave mirror and by the thermal lens properties of the laser rod. The acoustic wave in the fused silica causes Bragg scattering of the forward- and backward-traveling light beam in the resonator. The two diffracted beams which are obtained from the cavity-dumped oscillator are initially traveling in opposite directions; therefore, their frequencies are shifted to a value of $\omega + \Omega$ and $\omega - \Omega$, where ω is the frequency of the incident beam and Ω is the frequency of the acoustic wave. The two diffracted beams are extracted from the cavity as a single beam and deflected out of the system by a mirror. In Fig. 8.31b the cavity is formed by three high-reflectivity mirrors M_1 , M_2 , and M_3 . The mirror curvature and the distance between M_2 and M_3 are chosen such that the light beam between M_2 and M_3 is focused to a small diameter at

the center of curvature of M_3 . The modulator is inserted at the waist of the optical beam.

Acousto-optic modulators employed for cavity dumping differ from their counterparts used in Q-switch applications in several respects:

- 1) Compared to Q-switching, the cavity-dump mode requires much faster switching speeds. The rise time in an acousto-optic modulator is approximately given by the beam diameter divided by the velocity of the acoustic wave. In order to obtain rise times around 5 ns, a value which is required for efficient cavity dumping, the incident beam must be focused to a diameter of approximately 50 μm .
- 2) For efficient operation in the cavity-dump mode, it is important that essentially all the circulating power be diffracted into the first diffraction order. In a Bragg device the diffraction efficiency increases with the rf carrier frequency and therefore modulators employed in cavity dumpers operate at considerably higher frequencies, i.e., 200–500 MHz as compared to acousto-optic Q-switches.
- 3) In order to generate an output pulse in the cavity-dump mode, a short rf pulse is applied to the modulator, whereas in an acoustooptic Q-switch the rf carrier is turned off for the generation of an output pulse.
- 4) The cavity is never kept below threshold condition as in the Q-switched mode of operation. If the cavity is dumped of all its energy, the field has to build itself from the noise level. Repetitive cavity dumping was observed to become unstable in this case. If the repetition rate is lowered, the laser material is pumped higher above threshold between pulses and, therefore a larger fraction of the stored energy is extracted from the system (see Sect. 8.1). The lower limit of the dumping repetition rate is reached when the internal laser energy decreases to one photon immediately after dumping. The upper limit of the cavity dumping repetition rate is set by the switching speed of the modulator. Repetition rates as high as 10 MHz have been reported. From a cw-pumped Nd:YAG laser capable of 10 W of cw power, peak powers of 570 W with a pulse duration of 25 ns have been obtained at a 2 MHz repetition rate [8.63].

The technique of cavity dumping is also employed in regenerative systems. In a regenerative laser a pulse is injected into a laser resonator containing an amplifier. The pulse passes several times through the same amplifier medium and is then switched out. Figure 8.32a shows an optical schematic of a laser which employs this technique [8.64]. The figure illustrates a diode-pumped Nd:YAG crystal located between two highly reflective mirrors, a Pockels cell Q-switch, and a polarizer. The Nd:YAG crystal is cw-pumped and repetitively cavity dumped at a 10 kHz repetition rate. During the 100 μs pump time, the Pockels cell is operated at zero wave retardation. This is the low Q-condition because radiation is transmitted out of the resonator through the polarizer. At the end of the pump pulse, the injection laser seeds a 8-ns pulse into the resonator through the rear reflector. At the same time, the Pockels cell is switched to 1/4 wave retardation which establishes the high Q-condition. Radiation is building up between the two highly reflective mirrors. The injected pulse is regeneratively amplified in the cavity for about 360 ns or 120 passes. The Q-switch is then returned

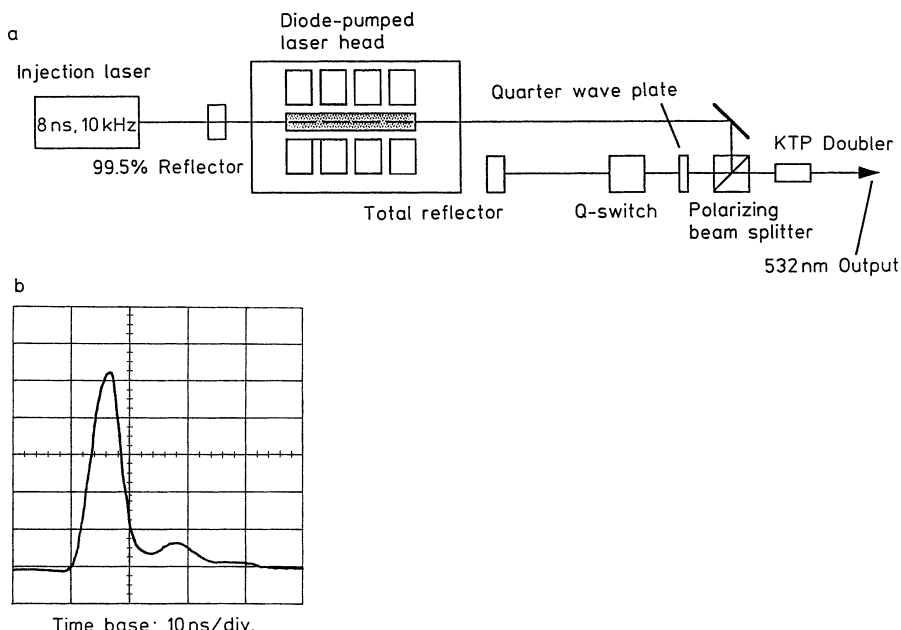


Fig. 8.32. Cavity dumping of an injection seeded laser. (a) Optical schematic of laser system and (b) output pulse shape

to zero wave retardation which dumps the amplified pulse through the polarizer. The KTP crystal converts the wavelength to 532 nm and shortens the pulse to about 5 ns. The sequence is repeated at a 10 kHz pulse repetition frequency. Figure 8.32b displays the output pulse at 532 nm.

An analysis of the extraction efficiency of cavity-dumped regenerative lasers can be found in [8.65]. The results are quite similar to the Q-switched case, and the extraction efficiency depends only on the amplifier gain and resonator losses.

9. Mode Locking

With the exception of very small lasers having extremely short resonators, the typical pulse width obtained from a Q-switched laser is on the order of 10–20 ns for most systems. With the cavity dumping technique, the pulse width can be reduced to a minimum of 1–2 ns. The limitation here is the length of the cavity, which determines the pulse length. Ultrashort pulses with pulse widths in the picosecond or femtosecond regime are obtained from solid-state lasers by mode locking. Employing this technique, which phase-locks the longitudinal modes of the laser, the pulse width is inversely related to the bandwidth of the laser emission.

The output from laser oscillators is subject to strong fluctuations which originate from the interference of longitudinal resonator modes with random phase relations. By establishing a fixed-phase relationship among the longitudinal modes a powerful well-defined single pulse circulating in the resonator can be generated. Mode locking requires a mechanism that results in a lower loss for a more intensive radiation peak compared to the average intensity in the resonator. In passive mode locking the radiation itself, in combination with a real or effective saturable absorber, generates a periodic modulation that leads to a fixed relationship of the longitudinal modes. Real absorbers are materials with a finite number of absorption centers such as organic dyes or semiconductors. Effective saturable absorbers utilize the nonlinear index of refraction in optical materials together with a spatially dependent loss mechanism. In active mode-locking, an acousto-optic modulator provides a phase or frequency modulation exactly at the frequency separation of adjacent modes that leads to a higher gain for a train of mode-locked pulses compared to cw operation.

Utilizing organic dyes as saturable absorbers, mode locking was first observed in solid-state lasers in the mid-1960s. For about 10 years, the systems of choice for picosecond pulses were flashlamp-pumped ruby, Nd:glass, and Nd:YAG lasers employing saturable absorbers. Employing a dye cell as the mode-locking element has the major drawback of poor shot-to-shot reproducibility. In pulsed solid-state lasers, the presence of a saturable dye absorber will result not only in mode locked, but also in Q-switched operation. For each flashlamp pump pulse, a short burst of mode-locked pulses is generated with a duration of a typical Q-switched pulse, i.e., a few tens of nanoseconds. For each flashlamp pulse, the mode-locked pulses build up from noise. Because of the statistical randomness of this process, large variations in the shot-to-shot output from the laser are observed. The problem of poor output reproducibility is exacerbated by the instability of the dye solutions which degrade with time and decompose when exposed to light.

As a result of the difficulty in obtaining reliable and consistent mode-locked output pulses, emphasis shifted away from pulsed mode-locked solid-state lasers to mode-locked organic dye lasers. The large gain-bandwidth product of dye lasers in combination with novel mode-locking techniques made the generation of pulses as short as tens of femtoseconds possible. Therefore, despite the inherent disadvantages of handling and maintaining dye solutions, the dye laser became the workhorse for ultrafast studies during the 1980s.

At about the same time, tunable solid-state laser materials were developed. Tunable lasers, notably Ti:sapphire, have a gain-bandwidth product equal or greater than organic dyes and are therefore ideally suited for the generation of femtosecond pulses. Motivated by the availability of broadband lasers, novel passive mode-locking techniques, such as additive pulse mode locking and Kerr-lens mode locking, have been developed.

In particular, the argon-pumped Ti:sapphire laser that is passively mode-locked via Kerr-lens modulation has become the standard for femtosecond research. In an all solid-state laser version, the argon laser is replaced by a frequency doubled Nd:YAG laser. More recently, mode locking with semiconductor saturable absorbers has emerged as a very important technique. For example, diode-pumped solid-state lasers, such as Cr:LiSAF, passively mode locked with semiconductor saturable absorbers have led to compact and robust systems with pulses in the femtosecond regime.

The progress of actively mode-locked solid-state lasers was equally dramatic. These were initially developed to mode lock krypton arc or tungsten lamp cw pumped Nd:YAG lasers by inserting either electro-optic or acousto-optic modulators into the resonator. In contrast to passive mode locking, the method of phase or amplitude modulation has not changed much over the years, but the bulky and inefficient lamp-pumped solid-state lasers have been replaced by extremely compact and efficient diode-pumped lasers. Very stable and reliable trains of mode-locked pulses can be generated with these lasers. Individual pulses from these continuously mode-locked lasers can be selected to provide a seed pulse for further amplification.

Today, laser-diode end-pumped Nd:YLF or Nd:YAG lasers that are actively mode-locked with an acousto-optic modulator provide output pulses with pulsewidths on the order of 10–20 ps. Such systems having a high degree of reliability and long-term reproducibility are offered commercially from a number of companies.

9.1 Pulse Formation

In a free-running laser, both longitudinal and transverse modes oscillate simultaneously without fixed mode-to-mode amplitude and phase relationships. The resulting laser output is a time-averaged statistical mean value. Restricting oscillation of the laser to the TEM_{00} mode for the moment, we recall from Chap. 5 that in a typical laser cavity there are perhaps a few hundred axial modes which fall within the frequency region where the gain of the laser medium exceeds the losses of the resonator.

As an example for illustrating the formation of a mode-locked pulse, we consider a passively mode-locked laser containing as nonlinear element a bleachable dye

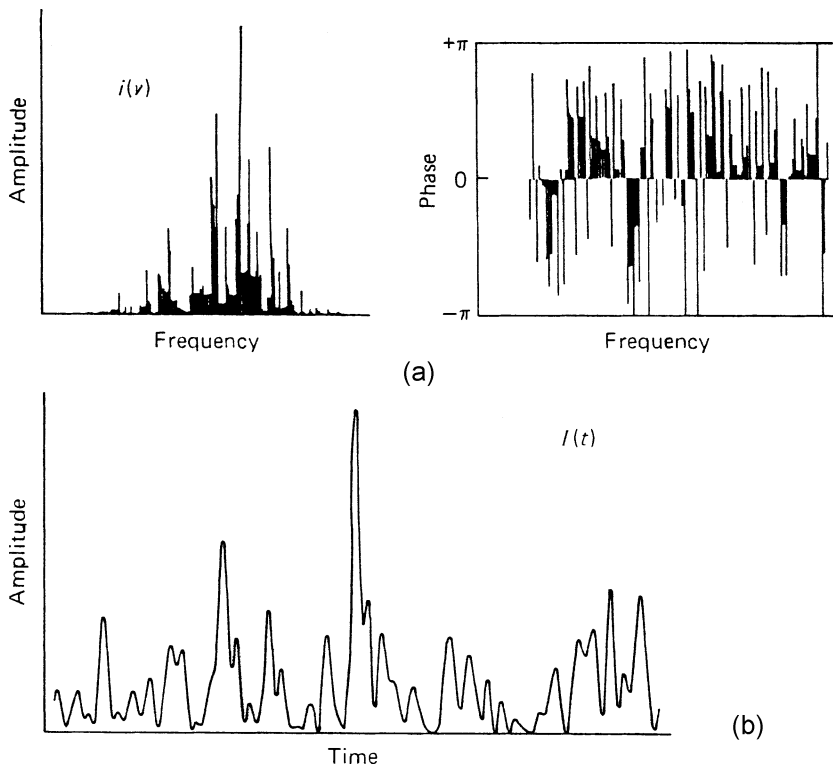


Fig. 9.1. Signal of a non-mode-locked laser. (a) In the frequency domain the intensities $i(\nu)$ of the modes have a Rayleigh distribution about the Gaussian mean and the phases are randomly distributed. (b) In the time domain the intensity has the characteristic of thermal noise

absorber. In order for the passive mode-locking process to start spontaneously from the mode beating fluctuations of a free-running laser, the nonlinear element must create an amplitude instability so that an intensive fluctuation experiences lower losses compared to less intensive parts of the radiation. A further requirement is that the reaction time of the nonlinear element be as short as the fluctuation itself in order to lock all the modes oscillating in the resonator.

In Fig. 9.1 the spectral and temporal structure of the radiation inside a laser cavity are shown for a non-mode-locked laser. In the frequency domain, the radiation consists of a large number of discrete spectral lines spaced by the axial mode interval $c/2L$. Each mode oscillates independent of the others, and the phases are randomly distributed in the range $-\pi$ to $+\pi$. In the time domain, the field consists of an intensity distribution which has the characteristic of thermal noise.

If the oscillating modes are forced to maintain a fixed-phase relationship to each other, the output as a function of time will vary in a well-defined manner. The laser is then said to be “mode-locked” or “phase-locked.” Figure 9.2 shows the output signal of an ideally mode-locked laser. The spectral intensities have a Gaussian distribution,

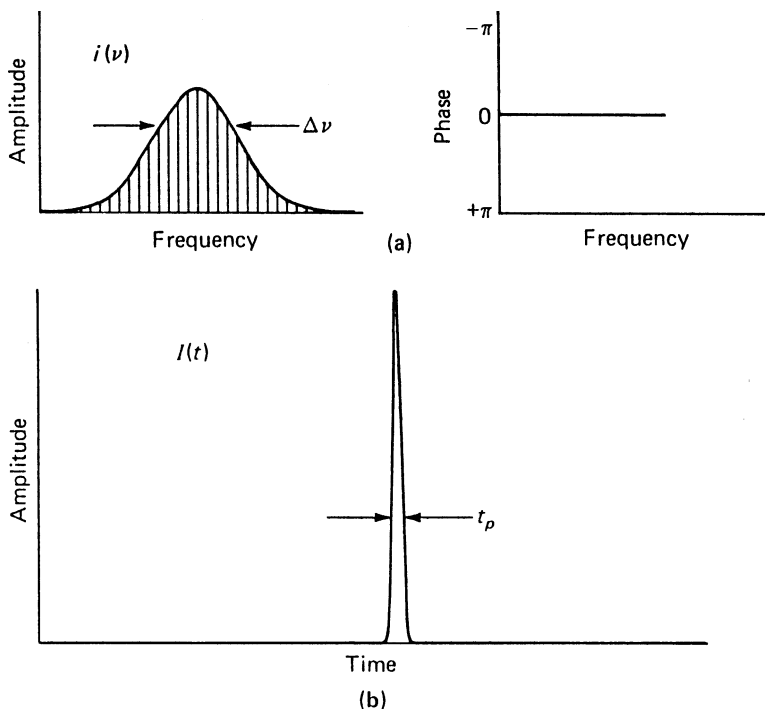


Fig. 9.2. Signal structure of an ideally mode-locked laser. (a) The spectral intensities have a Gaussian distribution, while the spectral phases are identically zero. (b) In the time domain the signal is a transform-limited Gaussian pulse

while the spectral phases are identically zero. In the time domain the signal is a single Gaussian pulse. As can be seen from this figure, mode locking corresponds to correlating the spectral amplitudes and phases. When all the initial randomness has been removed, the correlation of the modes is complete and the radiation is localized in space in the form of a single pulse.

Because the intensity profiles $I(t)$ shown in Figs. 9.1b and 2b circulate around inside the cavity with a repetition rate determined by the round-trip transit time, these signals will repeat themselves and appear in the laser output at a rate of $c/2L$. Therefore, mode locking results in a train of pulses whose repetition period is twice the cavity transit time, i.e.

$$\text{PRF} = 1/t_r = c/2L \quad (9.1)$$

where PRF is the pulse repetition frequency, t_r is the separation of individual pulses, and L is the resonator length.

If we make some simplifying assumptions, we can obtain a general idea of the pulse width and peak power of the mode-locked pulses. In Chap. 5 we have shown that laser oscillations can take place at a number of longitudinal modes if the gain bandwidth $\Delta\nu$ is larger than the mode spacing $c/2L$. We consider a laser that is

restricted to a single transverse mode but that is oscillating at $N = 2m + 1$ longitudinal modes. The mode at the center of the gain bandwidth curve has a frequency ω_0 . Above and below this frequency are $\pm m$ additional modes, whereby adjacent modes have an angular frequency separation $(2\pi/t_r)$ where t_r is the round trip time in the resonator $t_r = 2L/c$.

The electric field resulting from multimode oscillations can be expressed at some arbitrary plane $z = 0$ as follows:

$$E(t) = \sum_{n=-m}^m E_n \exp i \left(\omega_0 + n \frac{2\pi}{t_r} \right) t + \varphi_n, \quad (9.2)$$

where E_n and φ_n are the electric field and phase of the n th mode. Normally each of these modes oscillates independently of the other modes, and the amplitudes and phases of different longitudinal modes vary randomly with time. This causes the intensity of the laser output to fluctuate and show a spiking behavior. This is the situation illustrated in Fig. 9.1. In the middle of this figure we see one spike exceeding the other random fluctuations.

Given a uniform probability distribution of the independent phases of the longitudinal modes, there is a finite probability that occasionally a larger pulse will be generated. In Sect. 4.6.2 we calculated the probability of the occurrence of high-intensity spikes as a result of the random interference of several modes. In Q-switched lasers this is an important issue because these occasional spikes can lead to self-focusing and laser damage. In mode locking the more intense spike experiences lower losses because of the nonlinear saturable absorber and this will lead to the initiation of the mode-locking process.

In a mode-locked laser, all the phases of the modes are equal. For simplicity we can assume the phase of the center mode to be zero, therefore $\varphi_n = 0$. We also assume equal field strength for all the modes $E_n = E_0$. The total electric field at any point can then be written as

$$E(t) = E_0 \sum_{n=-m}^m \exp i \left(\omega_0 + n \frac{2\pi}{t_r} \right) t. \quad (9.3)$$

The summation can be expressed in a finite series that has a value of

$$E(t) = E_0 \left[\frac{1 - \exp i N(2\pi/t_r)t}{1 - \exp i(2\pi/t_r)t} \right] \exp i \omega_0 t. \quad (9.4)$$

The electric field $E(t)$ consists of a sinusoidal carrier of frequency ω_0 , whose amplitude changes with the time according to the expression in brackets.

The intensity is the product of E with its complex conjugate E^* :

$$I(t) = E(t)E^*(t) = E_0^2 \frac{\sin^2(N\pi t/t_r)}{\sin^2(\pi t/t_r)}. \quad (9.5)$$

Figure 9.3 shows an example of five mode-locked pulses in a 15 cm optically long resonator. With $N = 5$ and $t_r = 1$ ns, we obtain from (9.5) a train of pulses with a PRF = 1 GHz and a width at the half power point of $t_p = 177$ ps.

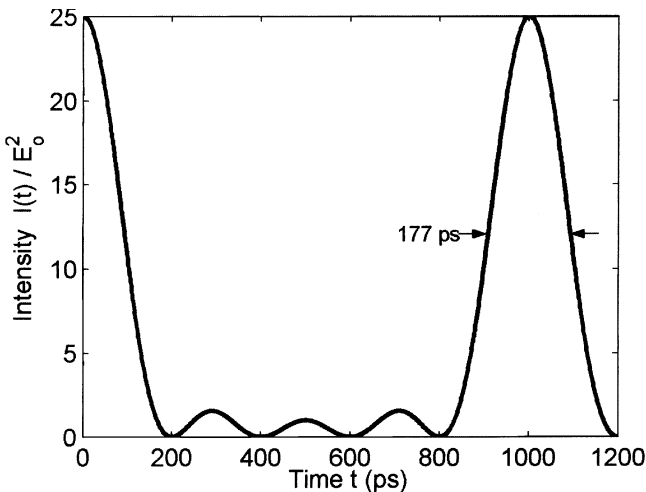


Fig. 9.3. Mode locking of five longitudinal modes in a 15-cm long resonator

The series of short pulses can also be understood in terms of a pulse that propagates back and forth between the two mirrors. The pulse maxima occur at those times when the denominator in (9.5) vanishes. With $t = t_r$, it follows as expected a separation of two successive pulses that is equal to the round trip time t_r . The time difference between the peak and the base of the pulse amplitude follows from (9.5) when the numerator becomes zero. With $(N\pi t/t_r) = \pi$, we obtain $t = t_r/N$. This time is also approximately equal to the full width, half power points t_p of the pulse

$$t_p \approx \frac{t_r}{N} \approx \frac{1}{\Delta v}, \quad (9.6)$$

where Δv is the gain bandwidth of the laser that is equal to the number of modes N times the frequency interval ($1/t_r$) between modes (see Fig. 9.2a). This assumes, of course, a perfectly mode-locked laser, i.e., all modes within the gain-bandwidth are locked.

Equation (9.6) expresses the well-known result from Fourier's theorem that the narrower the pulse width, the larger the bandwidth required to generate the pulse. From (9.6) follows also the interesting fact that the pulse width of the mode-locked pulses roughly equal the cavity round trip time divided by the number of phase-locked modes.

The shortest pulse obtainable for a given spectral bandwidth is said to be transform limited. Equation (9.6) is an approximation. The exact solution for the pulse width/bandwidth product for phase-locked modes of equal intensities has to be found numerically since (9.5) is a transcendental equation:

$$t_p \Delta v = 0.886. \quad (9.7)$$

In the example given above we assumed five longitudinal modes equally spaced at 1 GHz. With $\Delta v = 5$ GHz, the FWHM pulse width indicated in Fig. 9.3 follows from

(9.7). The maximum value for $I(t)$ is obtained from (9.5) by taking the limit of $I(t)$ as the argument $(\pi t/t_p)$ of the sine function in the denominator approaches zero. In this case the sine functions can be replaced by their arguments and

$$I_{\max} = N^2 E_0^2. \quad (9.8)$$

By comparison the total intensity of modes oscillating with random phases is equal to N times the intensity of the individual modes:

$$I = N E_0^2. \quad (9.9)$$

In the previous analysis we assumed that the amplitudes of the mode-locked pulses are all equal. A more realistic intensity distribution is shown in Fig. 9.2, where the longitudinal mode intensities are within the envelope of a Gaussian shaped gain curve that is typical for an inhomogeneously broadened line width of the laser medium. If the intensity of the modes follows a Gaussian function it has been shown that the resulting mode-locked pulse has also a Gaussian shape. Instead of (9.7) the pulse width/bandwidth product is in this case given by

$$t_p \Delta \nu = 0.44. \quad (9.10)$$

Short mode-locked pulses require a large spectral bandwidth. A problem of obtaining transform limited performance can be due to dispersion occurring in optical elements within the resonator. Dispersion introduces a frequency chirp that increases pulse length. We will briefly discuss the increase of the pulse width/bandwidth product for a Gaussian pulse in the presence of frequency chirp.

The most general Gaussian optical pulse is given by

$$E(t) = \left(\frac{E_0}{2} \right) \exp(-\alpha t^2) \exp[j(\omega + \beta t)t]. \quad (9.11)$$

The term α determines the Gaussian envelope of the pulse, and the term $j\beta t$ is a linear frequency shift during the pulse (chirp). From (9.11) follows for the pulse width at the half-intensity points

$$t_p = \left(\frac{2 \ln 2}{\alpha} \right)^{1/2}. \quad (9.12)$$

The bandwidth taken at the half-power points of the pulse spectrum is given by [9.1]

$$\Delta \nu = \frac{1}{\pi} \left[\left(\frac{\alpha^2 + \beta^2}{\alpha} \right) 2 \ln 2 \right]^{1/2}. \quad (9.13)$$

From the above equations follows the pulse width/bandwidth product

$$t_p \Delta \nu = \left(\frac{2 \ln 2}{\pi} \right) \left[1 + \left(\frac{\beta}{\alpha} \right)^2 \right]^{1/2}. \quad (9.14)$$

The shortest pulse width is obtained for $\beta = 0$ (i.e., no frequency chirp), that is, the result stated in (9.10).

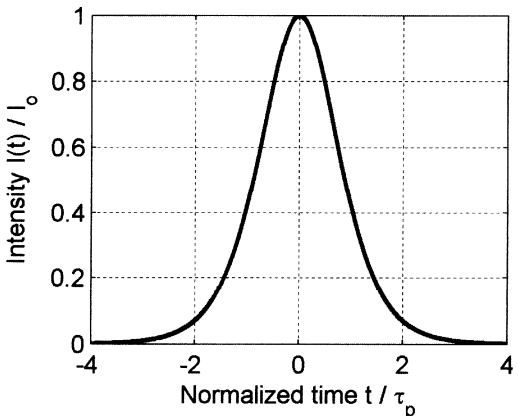


Fig. 9.4. Pulse envelope described by the hyperbolic secant function

Before leaving this subject, we have to mention one other important pulse shape, namely the hyperbolic secant function. The steady-state solution of the differential equation describing the pulse envelope $I(t)$ of a cw mode-locked pulse is a function of the form [9.2]

$$I(t) = I_0 \operatorname{sech}^2(t/\tau_p). \quad (9.15)$$

For $t = \tau_p$, the intensity is $I(t)/I_0 = 0.42$. The FWHM pulse width t_p of a sech^2 pulse is $t_p = 1.76\tau_p$, and a transform-limited sech^2 pulse has a pulse width/bandwidth product of

$$t_p \Delta\nu = 0.315. \quad (9.16)$$

A pulse shape according to (9.15) is illustrated in Fig. 9.4.

Mode-locked lasers can have very high peak powers. From (9.8) and (9.9) follows that the peak power of the mode-locked pulses is N times the average power

$$P_p = N P_{av}. \quad (9.17)$$

Typical output-pulse formats from pulsed and cw mode-locked lasers are illustrated in Fig. 9.5. The output of a flashlamp-pumped, mode-locked solid-state laser consists of a burst of pulses with amplitudes which fit underneath the envelope of a Q-switched pulse. A cw mode-locked laser produces a train of pulses with equal amplitude. In both cases the consecutive pulses are separated by the cavity round-trip time.

A modern diode end-pumped Nd:YAG laser, cw mode-locked with an acousto-optic modulator, produces pulses of about 20 ps in duration and has an average output power of about 200 mW. If we assume a resonator length of $L = 1.2$ m, we obtain from (9.1), a pulse separation of $t_r = 8$ ns or a PRF of 125 MHz. The pulse width of 20 ps in combination with (9.6) indicates that about 400 longitudinal modes are phase locked together ($N = 400$). From (9.17) follows a peak power of 80 W.

The homogeneously broadened line in Nd:YAG is $\Delta\nu = 120$ GHz. Therefore, the ultimate limit in short-pulse generation in Nd:YAG is according to (9.16) about 2.6 ps.

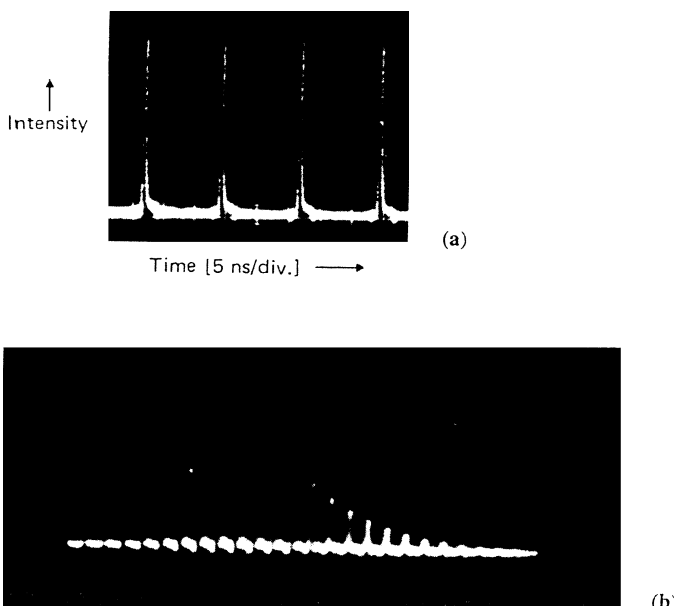


Fig. 9.5. Output pulses from a (a) cw mode-locked and (b) pulsed mode-locked laser

Passively cw mode-locked Nd:YAG have approached this limit. The modulation index one can achieve in active mode locking is not large enough to support phase locking over a very large bandwidth. Therefore, actively mode-locked lasers emit longer pulses compared to cw passively mode-locked systems.

The generation of mode-locked pulses from a laser requires that the longitudinal modes be coupled together. This is achieved experimentally by placing inside the laser cavity either an externally driven loss or phase modulator, or a passive device which exhibits saturable absorption. Details of the generation of mode-locked pulses with active and passive devices will be discussed in the following sections. Literature on the theory of mode-locked lasers with extensive references can be found in [9.2–6].

9.2 Passive Mode Locking

Originally the nonlinear absorption of saturable absorbers was employed for simultaneously Q-switching and mode-locking of pulsed solid-state lasers. The saturable absorbers consisted of organic dyes that absorb at the laser wavelength. At sufficient intense laser radiation, the ground state of the dye becomes depleted, which decreases the losses in the resonator for increasing pulse intensity.

In pulsed mode-locked solid-state lasers, pulse shortening down to the limit set by the gain-bandwidth is prevented because of the early saturation of the absorber, which is a result of the simultaneously occurring Q-switching process. Shorter pulses

and a much more reproducible performance are obtained if the transient behavior due to Q-switching is eliminated.

In passive cw mode locking, components or effects are utilized that exhibit a saturable absorber like behavior, i.e., a loss that decreases as the intensity in the resonator increases. The first successful technique for passive mode locking of cw lasers, termed coupled cavity or resonant passive mode locking, makes use of an external nonlinear coupled resonator that is responsible for the mode-locking process. In the most common technique an intensity-dependent phase shift in a fiber produces constructive interference of the pulse in the main resonator, with the reinjected pulse from the coupled resonator at the peak of the pulse, and destructive interference in the wings. Because of relative resonator length fluctuations there is a need for active resonator length stabilization to within a fraction of a wavelength. Coupled cavity techniques have been quickly supplanted by intracavity saturable techniques based on the Kerr effect or absorption bleaching in semiconductors.

Kerr lens mode locking (KLM) represented a real breakthrough in providing a relatively simple means for generating ultrashort pulses from solid-state lasers. In Kerr lens mode locking, strong self-focusing of the laser beam combined with an aperture is used to produce self amplitude modulation, i.e., the equivalent of a fast saturable absorber. Despite the great success of KLM there are some significant drawbacks for practical applications of these ultrafast lasers. First, the resonator is typically operated near one end of its stability range, where the Kerr lens induced change of the beam diameter is large enough to sustain mode locking. This results in a requirement for critical resonator alignment where mirrors and the laser crystal have to be positioned to an accuracy of several hundred microns. Second, Kerr lens mode locking requires a starting mechanism.

Today, most commercial passive mode locked cw lasers incorporate an intracavity semiconductor saturable absorber mirror (SESAM) to start and sustain stable mode locking. The nonlinear element comprises a thin multilayer quantum well structure monolithically embedded between two reflective surfaces forming a Fabry–Perot resonator. Absorbed energy from the pulse causes carrier recombination in the quantum wells that leads eventually to absorption bleaching. The combination of the saturable absorber and mirror surfaces causes the reflectivity of the device to increase with increasing intensity. The advantage of a SESAM lies in the inherent simplicity, the device essentially replaces the rear mirror of the laser resonator.

9.2.1 Liquid Dye Saturable Absorber

The distinction between an organic dye suitable for simultaneous mode locking and Q-switching, as opposed to only Q-switching the laser, is the recovery time of the absorber. If the relaxation time of the upper-state population of the dye is on the order of the cavity round trip, that is, a few nanoseconds, passive Q-switching will occur, as described in Chap. 8. With a dye having a recovery time comparable to the duration of mode-locked pulses, that is, a few picoseconds, simultaneous mode locking and Q-switching can be achieved. A typical example of a mode-locked laser utilizing a saturable absorber is illustrated in Fig. 9.6.

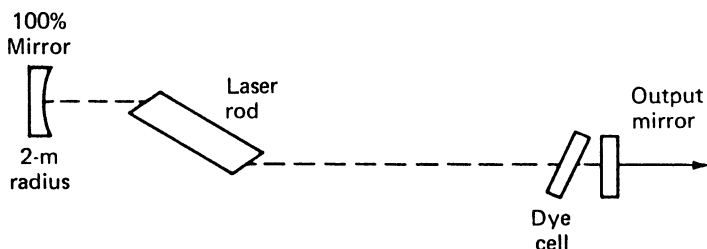


Fig. 9.6. Mode locking with a liquid dye saturable absorber

One major requirement in the resonator design of a mode-locked system is the complete elimination of reflections that can occur from components located between the two cavity mirrors. This is accomplished by employing laser rods with Brewster's angle at the ends, placing the dye cell at Brewster's angle in the resonator, and by using cavity mirrors which are wedged. Reflection from an optical surface that is parallel to the cavity mirrors will create a secondary resonator. The mode-locked pulse will be split into several pulses that will circulate inside the resonators with different round-trip times. The result is a very erratic output usually consisting of several superpositioned pulse trains or containing subsidiary pulses in the train. With all optical surfaces inside the resonator, either at Brewster angle or antireflection-coated and tilted away from the resonator axis, coupled resonator structures can be avoided and the occurrence of satellite pulses is minimized. Similar attention must be paid to avoid back-reflection into the cavity from external components.

Despite the relatively simple construction of a passively mode-locked laser oscillator, the output will be very unpredictable unless dye concentration, optical pumping intensity, and resonator alignment are carefully adjusted. Furthermore, mixing and handling the dye solution and maintaining proper dye concentration proved cumbersome. As a result of the inherent shortcomings of pulsed passive mode locking, this technology has been superseded by cw mode-locking.

Although systems based on dye cells are no longer used, the formation of a mode-locked pulse can be best illustrated with the simple arrangements of Fig. 9.6.

As mentioned in Chapter 8, a saturable absorber has a decreasing loss for increasing pulse intensities. In order for the passive mode-locking process to start spontaneously from the mode-beating fluctuations of a free-running laser, the nonlinear element must create an amplitude instability so that an intensive fluctuation experiences lower losses compared to less intensive parts of the radiation. A further requirement is that the reaction time of the nonlinear element be as short as the fluctuation itself in order to lock all the modes oscillating in the resonator.

A computer simulation of the evolution of a mode-locked pulse train from noise is shown in Fig. 9.7. This figure shows the transformation of irregular pulses into a single mode-locked pulse. The simultaneous Q-switched and mode-locked pulse evolution from noise can be divided into several stages.

In Fig. 9.7a–c the noiselike fluctuations are linearly amplified; however, a smoothening and broadening of the pulse structure can be seen. The chaotic sequence

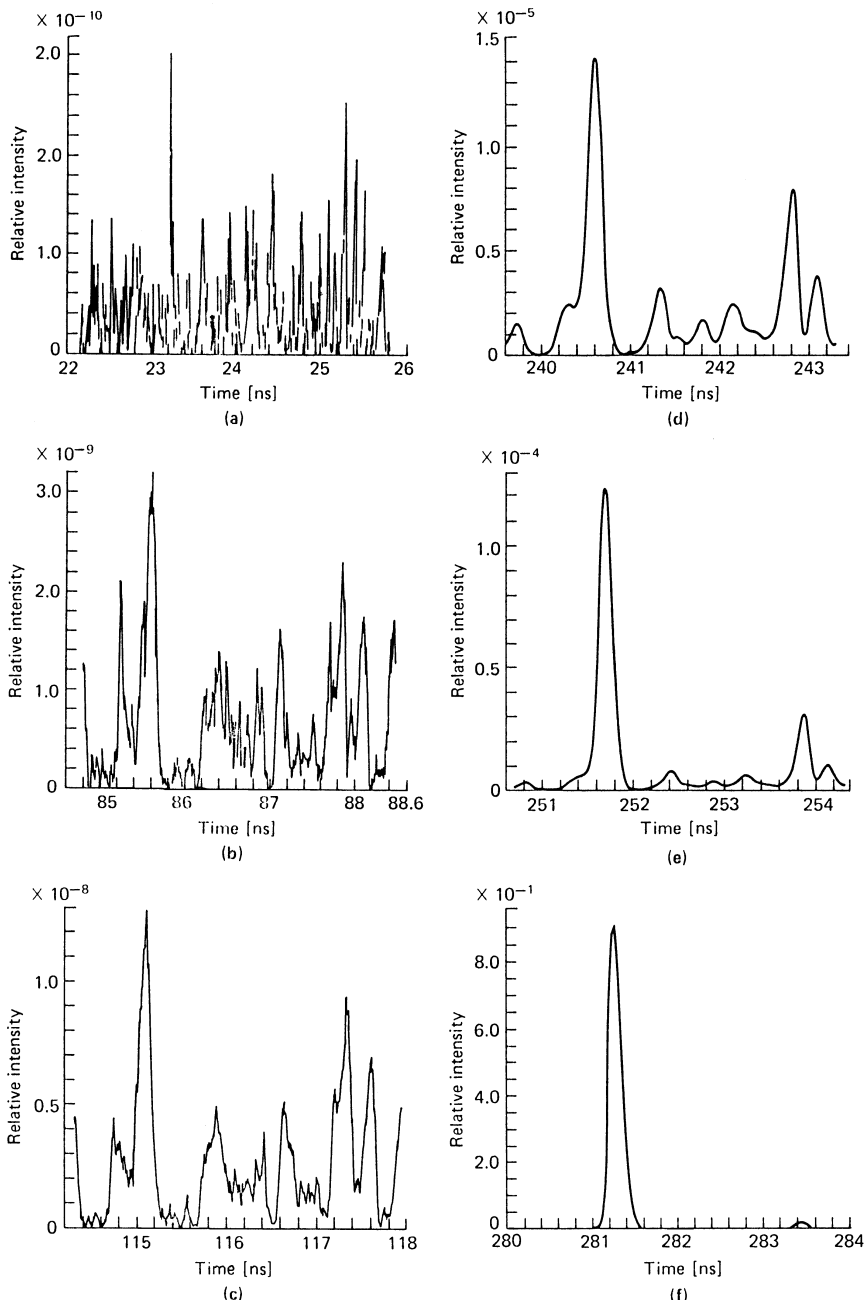


Fig. 9.7. Computer simulation of the evaluation of a mode-locked pulse from noise: (a–c) regime of linear amplification and linear dye absorption, (d–e) nonlinear absorption in the dye cell, and (f) regime of nonlinear amplification, dye completely bleached [9.7]

of fluctuations shown in Fig. 9.7a represents the laser radiation in the early stage of pulse generation. As the pump process continues, the gain increases above threshold and the noiselike signal is amplified. During the linear amplification a natural mode selection takes place because the frequency-dependent gain favors cavity modes in the center of the fluorescence line. As a result of the spectral narrowing caused by the amplification process, a smoothening and broadening of the amplitude fluctuations occurs, as shown in Fig. 9.7b and c.

The following numbers are typical for the linear amplification process in Nd:glass. A large number of longitudinal modes is initially excited. For a typical cavity length of ~ 1 m, one calculates $\sim 4 \times 10^4$ cavity modes in Nd:glass with $\Delta\nu \approx 7500$ GHz. Assuming a typical pulse build-up time of $10\ \mu\text{s}$, the linear stage comprises ≈ 1500 round trips. The light intensity rises by many orders of magnitude to approximately $10^7\ \text{W/cm}^2$.

In Fig. 9.7d and e the peak-to-peak excursions of the fluctuations have increased and, in particular, the amplitude of the strongest pulse has been selectively emphasized. In this second phase of pulse evolution, the gain is still linear but the absorption of the dye cell becomes nonlinear because the intensity peaks in the laser cavity approach values of the saturation intensity I_S of the dye. In the nonlinear regime of the mode-locked laser we note two significant processes acting together.

First, there is a selection of one peak fluctuation or at least a small number. The most intense fluctuations at the end of the linear amplification phase preferentially bleach the dye and grow quickly in intensity. The large number of smaller fluctuations, on the contrary, encounter larger absorption in the dye cell and are effectively suppressed.

The second effect is a narrowing of the existing pulses in time, which broadens the frequency spectrum. The shapes of the pulses are affected by the nonlinearity of the dye because the wings of the pulse are more strongly absorbed than the peak. The second phase ends when the absorbing transition in the dye cell is completely saturated. Under favorable conditions the final transmission is close to one; that is, the dye is transparent.

In Fig. 9.7f the background pulses have been completely suppressed. The final phase of the pulse evolution occurs when the intensity is sufficiently high for complete saturation of the absorber transition to take place and for the amplification to be nonlinear. This is the regime of high-peak power. During the nonlinear stage the pulse intensity quickly rises within ≈ 50 cavity round trips to a value of several gigawatts per square centimeter. Successive passages of the high-intensity radiation pulse through the resonator result in a pulse train appearing at the laser output. Finally, the population inversion is depleted and the pulse decays.

9.2.2 Coupled-Cavity Mode Locking

In this technique, mode locking is induced by feeding back into the laser part of its output after it has been nonlinearly modulated in an external cavity. In most cases, the external cavity contains an optical fiber in which a nonlinearity is produced via the intensity-dependent index of refraction. Mode locking employing a coupled cavity

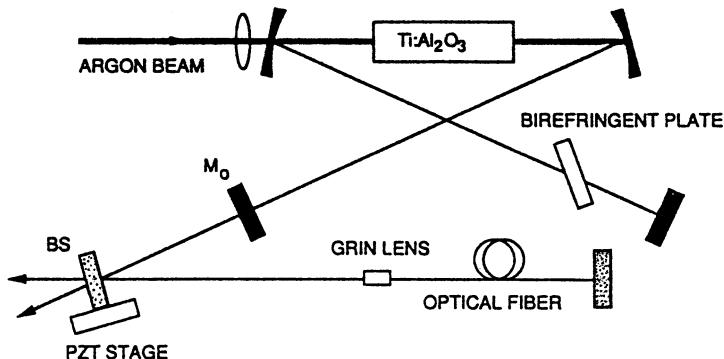


Fig. 9.8. Additive pulse mode locking using an optical fiber in an external cavity [9.9]

with a fiber was first demonstrated in the soliton laser [9.8]. Later, the technique was mainly used to enhance the performance of actively mode-locked lasers. Goodberlet et al. [9.9] extended the technique to achieve self-starting, passive APM in a tunable $\text{Ti:Al}_2\text{O}_3$ laser. Figure 9.8a illustrates the basic setup which we will use to illustrate the principle of APM.

The main laser cavity consists of a four-mirror arrangement and an argon laser pumped $\text{Ti:Al}_2\text{O}_3$ crystal cut at Brewster angle. The wavelength can be adjusted with a birefringent plate. The output mirror M_0 had a 15% transmission. A beam splitter (BS) directed half of the output energy via a GRIN lens into a 5 μm core diameter fiber. The optical beam is reflected back to the main resonator with a mirror that is attached to the end of the fiber. For a given fiber length, the time of flight of a pulse in the external cavity has to be adjusted to be an integral multiple of the round trip time of the main laser cavity. This ensures that pulses that are reinjected from the external cavity are synchronized with the pulses in the main cavity. When a pulse from the main laser is coupled into the external optical fiber, it experiences an intensity-dependent phase shift and will interferometrically recombine with the pulse in the main laser cavity at the output mirror M_0 .

When the relative phases are set appropriately, the peak of the pulse constructively interferes, while the wings of the pulse destructively interfere. This technique has been termed additive pulse mode locking (APM) because the pulse-shaping mechanism depends on the coherent addition of pulses that are fed back from the external cavity to pulses in the main laser cavity. The disadvantage of coupled cavity mode locking employing optical fibers is the requirement for interferometric stabilization of the cavities.

For this reason, interest has focused on cw passive mode-locking concepts which do not require this amount of precision and complexity.

In an other embodiment of coupled-cavity mode locking, an amplitude nonlinearity in the coupled resonator such as absorption bleaching in a semiconductor reflector introduces an intensity dependent reflectivity into the main resonator. The technique of using a saturable semiconductor reflective mirror inside a low Q coupled cavity was termed resonant passive mode locking (RPM). This technique does not require

active cavity length control; however, it does introduce small optical frequency shifts which continuously compensate for any relative cavity length fluctuations between the coupled cavities.

An extension of this technique, which leads to a simpler device architecture and eliminates the problem of frequency fluctuations, is mode locking via a SESAM, which is discussed in Sect. 9.2.4.

9.2.3 Kerr Lens Mode Locking

The field of ultrafast pulse generation has been revolutionized by the development of Kerr lens mode locking. The Kerr effect produces intensity-dependent changes of the refractive index. It is generally an undesirable effect because it can lead to self focusing and filament formation in intense beams, as explained in Sect. 4.6. In Kerr lens mode locking, strong self-focusing of the laser beam combined with either a hard aperture or a “soft” gain aperture is used to produce a self amplitude modulation that is equivalent to a fast saturable absorber-like action.

In contrast to the absorption in bleachable dyes, the nonresonant Kerr effect is extremely fast, wavelength-independent, and allows the generation of a continuous train of mode-locked pulses from a cw-pumped laser. For a Gaussian beam, the Kerr effect focuses the radiation toward the center, and essentially an intensity-dependent graded-index lens is formed. The action of a fast saturable absorber can be achieved if an aperture is introduced in the resonator at a position where the mode size decreases for increased intensity.

The transformation of the power-dependent change in the spatial profile of the beam into an amplitude modulation is illustrated in Fig. 9.9. Transmission through the aperture is higher for an intense beam, as compared to a low-power beam. This technique, which provides an extremely simple means for ultrashort pulse generation in tunable lasers, has been termed Kerr lens mode locking (KLM).

The laser crystal acts as a lens with a focal length that changes with the intracavity intensity. With the assumption of a parabolic index variation and a focal length much longer than the Kerr medium we obtain, to a first approximation, (see also Sect. 4.6.1.)

$$f = \frac{w^2}{4\gamma I_{0l}}, \quad (9.18)$$

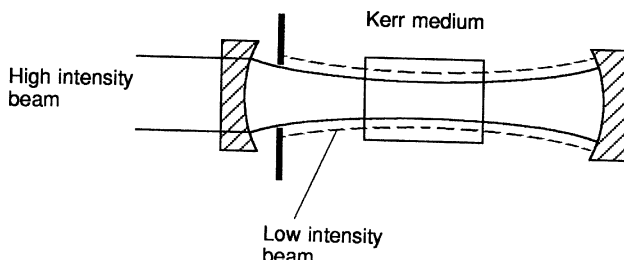


Fig. 9.9. Intensity-dependent amplitude modulation of the resonator mode

where w is the beam waist, γ is the nonlinear refractive coefficient, I_0 is the peak intensity, and l is the length of the Kerr medium.

Assuming a waist radius w of 50 μm in a 4-mm long Ti:Al₂O₃ crystal, and a peak power of 150 kW we obtain, with $\gamma = 3.45 \times 10^{-16} \text{ cm}^2/\text{W}$, a focal length of $f = 24 \text{ cm}$.

As was discussed in Section 4.6 beam focusing due to the Kerr effect can lead to catastrophic beam collapse with the beam breaking up into filaments. The critical power level at which beam collapse will set in for a Gaussian beam is usually defined by (see also Eq. 4.51)

$$P_{\text{cr}} = \frac{a\lambda_0^2}{8\pi n_0 \gamma}, \quad (9.19)$$

where the factor a can take on values between 3.77 and 4 depending on which analytical approach or numerical method was used [9.10].

For the materials and wavelengths of interest, one finds $P_{\text{cr}} = 2\text{--}3 \text{ MW}$. For example, $P_{\text{cr}} = 2.6 \text{ MW}$ for Al₂O₃ and BK7 glass at 0.8 μm. In KLM lasers, the peak power has to be large enough to produce a strong nonlinearity, but needs to be well below the critical power for beam collapse.

Returning to Fig. 9.9, for a hard aperture of radius r_0 , the rate of change in transmission T with respect to the beam waist w for a Gaussian beam is given by

$$dT/dw = (-4r_0^2/w^3) \exp(-2r_0^2/w^2). \quad (9.20)$$

If one assumes that the aperture size is close to the mode size $r_0 \approx w$, one obtains $\delta T \approx -(1/2w)\delta w$. The limiting aperture introduces a loss discrimination for low power (cw) and high peak power (mode locked) operation which is proportional to mode size changes $dP \sim (-1/w)dw$.

Since the mode size w is power-dependent due to the Kerr effect, the resonator losses are expressed as

$$\delta = \delta_0 - \left(\frac{1}{w} \right) \frac{dw}{dP} P = \delta_0 + sP, \quad (9.21)$$

where δ_0 are the fixed losses and P is intracavity power. The parameter s , also called the Kerr lens sensitivity, is important for analyzing and designing KLM resonators. The parameter s describes the relative spot size variation of the laser beam at an aperture, usually placed in front of one of the mirrors, with respect to the circulating intracavity power. It is defined as [9.11].

$$s = \left(\frac{1}{w} \frac{dw}{d(P/P_{\text{cr}})} \right), \quad (9.22)$$

where w is the spot size at a particular position inside the resonator. The second term is the slope of the spot size versus power taken at $P = 0$. The power is normalized to the critical power for catastrophic self-focusing.

A typical resonator, used for KLM of a Ti:Al₂O₃ crystal pumped by an argon laser, consists of two plane mirrors and two focusing mirrors. The crystal is at the

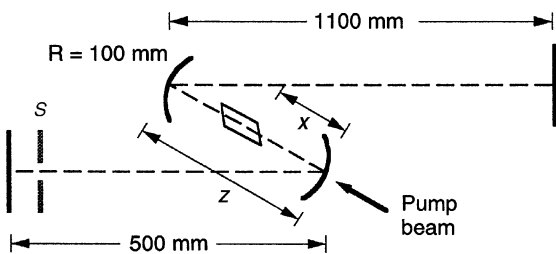


Fig. 9.10. Typical resonator used for Kerr lens mode-locking (KLM)

beam waist as shown in Fig. 9.10. An aperture is usually located close to one of the flat mirrors. As will be explained later, the spot size variation s , at the aperture as a function of the circulating power, critically depends on the position x of the Kerr medium around the focus of the beam, and on the separation z of the two focusing mirrors.

We will first consider the properties of the empty resonator illustrated in Fig. 9.10. The equivalent resonator consists of two flat mirrors with two internal lenses essentially forming a telescope with a magnification of one, as shown in Fig. 9.11. For a slightly misadjusted telescope, the lens spacing is $z = 2f - \Delta z$, where Δz measures the misadjustment. The focal length of the lens assembly is then $f_{\text{ef}} = f^2/\Delta z$, where f is the focal length of the individual lenses. The distances from the resonator mirrors and the principal planes of the lenses are L_1 and L_2 . The g parameters for a resonator comprising two flat mirrors and an internal telescope are (see also Sect. 5.1.8)

$$g_1 = 1 - (L_2/f_{\text{ef}}) \quad \text{and} \quad g_2 = 1 - (L_1/f_{\text{ef}}) \quad (9.23)$$

or

$$g_1 = 1 - (L_2 \Delta z/f^2) \quad \text{and} \quad g_2 = 1 - (L_1 \Delta z/f^2). \quad (9.24)$$

The operating region of the passive resonator is depicted in the stability diagram (Fig. 9.12). For $\Delta z = 0$, the lenses are in focus and the resonator configuration becomes

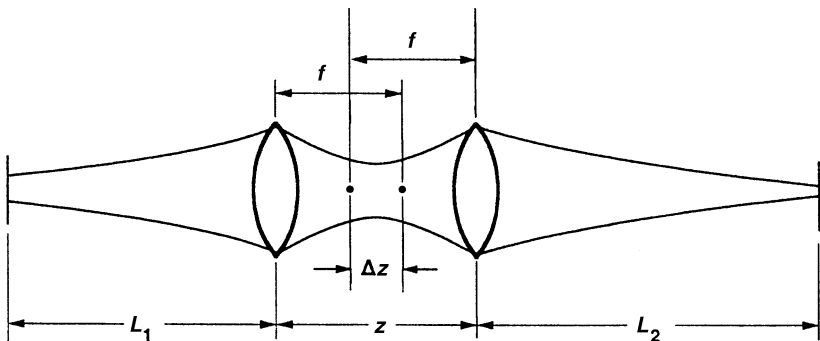


Fig. 9.11. Equivalent empty resonator of the arrangement shown in Fig. 9.10 ($f = 50 \text{ mm}$, $L_1 = 500 \text{ mm}$, $L_2 = 1100 \text{ mm}$)

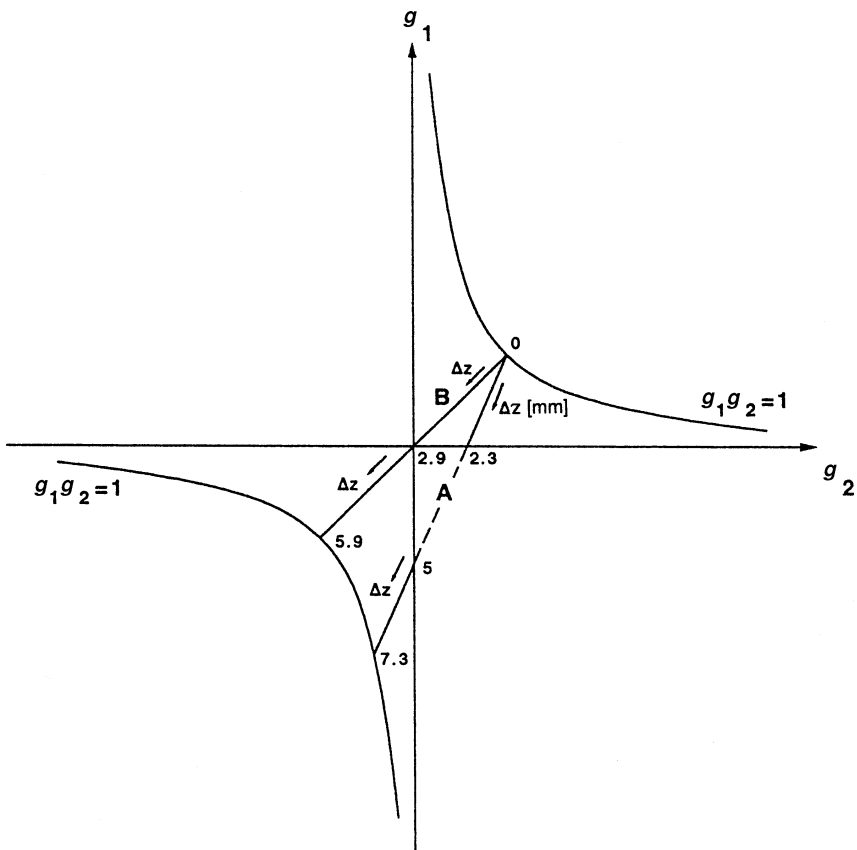


Fig. 9.12. Stability diagram for the resonator shown in Fig. 9.11

plane-parallel. As the lenses are moved closer together, a stability limit is reached for $g_2 = 0$. As both g -parameters become negative, a second zone of stable operation is reached. As Δz becomes larger, a point is reached for $g_1 g_2 = 1$, where the lens assembly focuses the beam onto one of the flat mirrors, that is, the spot size becomes zero at the mirror. If the two legs of the resonator are of unequal length, $L_1 \neq L_2$, two stability regions exist, as indicated by curve A in Fig. 9.12. Curve B gives the stability range of a resonator with $L_1 = L_2 = 850$ mm. The two stability regions are joined and the resonator changes from plane-parallel, confocal, to concentric for increasing values of Δz (or decreasing mirror separation z).

A particularly useful and practical design procedure for KLM lasers can be found in [9.12–14.] The authors introduced a nonlinear ABCD ray matrix to treat the Gaussian beam propagation in a Kerr medium. The dependence of the spot size w on the power P is given in closed form by a set of equations. From these equations contour plots can be generated of the spot size variation s as a function of x and z for a given spot size and power of the input pump beam. The results of these calculations provide guidelines for the design of KLM resonators.

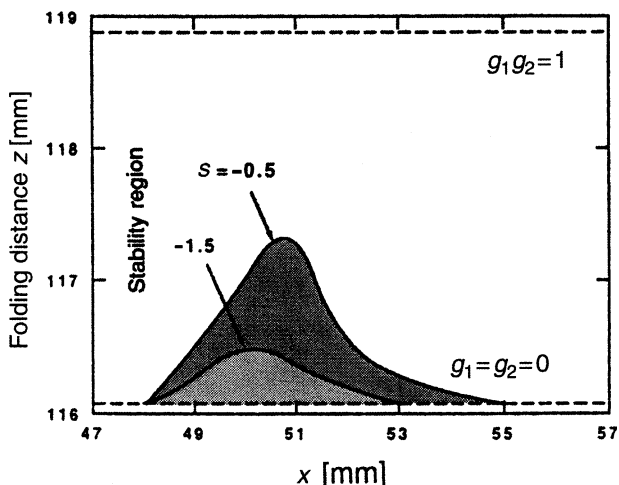


Fig. 9.13. Contour plot of Kerr sensitivity for a resonator with $R = 100$ mm, $L_1 = L_2 = 850$ mm, and a 25-mm long Ti:sapphire crystal [9.14]

An example of such a contour plot is shown in Fig. 9.13. Plotted is the Kerr lens sensitivity s for the resonator depicted in Fig. 9.14 with $L_1 = L_2 = 850$ mm, $l = 25$ mm, and $f = 50$ mm. Compared to the empty resonator discussed above, the introduction of the laser crystal increases the optical length and also makes the resonator rotational unsymmetrical because the ends of the crystal are cut at Brewster angle. The plot is for the tangential plane of the resonator because s is larger in this plane as compared to the sagittal plane. The curves for s are bound by the stability limits of the resonator, i.e., $g_1g_2 = 1$ and $g_1 = g_2 = 0$. Experiments performed on an actual system revealed that for reliable mode locking a value of $|s| \geq 0.5$ was necessary. This restricts the operating regime of the laser system to very small areas within the allowed stability regions. It was found experimentally [9.14] that the region for the large mirror separation z was more stable as compared to the smaller separation. In the stability diagram, the more stable operation corresponds to a configuration located in the first quadrant.

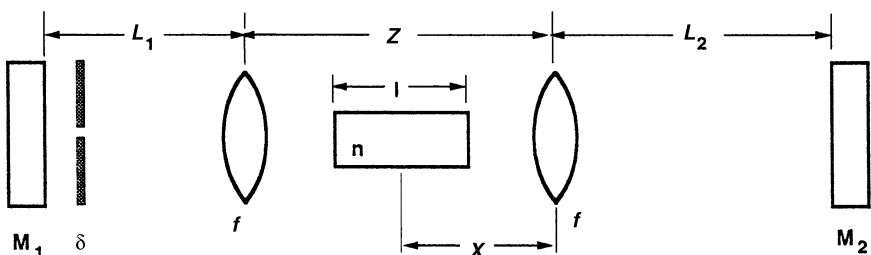


Fig. 9.14. Equivalent resonator of the design depicted in Fig. 9.10

From calculations based on a nonlinear ABCD matrix follows that s can be expressed as a function of the resonator parameters [9.13]. The analysis revealed that the maximum value of s depends on the resonator configuration according to

$$|s|_{\max} = \frac{1}{4\sqrt{g_1 g_2 (1 - g_1 g_2)}}. \quad (9.25)$$

From (9.25) follows that a large s is obtained only as the resonator approaches the stability limit with g_1 or $g_2 = 0$ or $g_1 g_2 = 1$. It was found that the best compromise between a large s and a reasonable stable performance is achieved for a symmetric resonator $L_1 = L_2$ and operation close to $g_1 g_2 = 0$.

For this configuration, which is equivalent to a confocal resonator, the tolerance for stable operation is about ± 0.6 mm in the z -direction, with the resonator operated about 0.5–1 mm from the stability limit.

From the results illustrated in Fig. 9.13 it is evident that the operating range of the KLM resonator is restricted to a small area close to the stability limit. Therefore, the alignment of a KLM resonator is very critical, and the tolerance in length adjustments are fractions of a millimeter. Of course this also means that the resonator is very susceptible to environmental effects, and the operating point has to be a comprise between a large Kerr lens sensitivity s and stable and reliable performance.

The operation of a KLM laser is a tradeoff between output power, stability, and tolerance to the exact position of the components. An analytical treatment of nonlinear resonators has shown that for a given pump power and pump spot size, the most critical parameters are

- (a) the distance z of the two focusing mirrors,
- (b) the location x of the Kerr medium with respect to the mirrors, and
- (c) the spot size variation s at the aperture.

As already mentioned because of the Brewster angle design, resonators employed for mode locking are not rotationally symmetric. This is illustrated in Fig. 9.15, which shows the change in beam size in two orthogonal directions at the flat mirror for a similar resonator configuration as depicted in Fig. 9.10. Since the spot size changes essentially in only one direction, a slit rather than a round aperture is usually employed for the adjustment of the proper loss modulation.

The Kerr nonlinearity is usually not strong enough for the cw mode-locking process to self-start. In order to initiate KLM, usually a strong fluctuation must be induced by either perturbing the cavity or by adding another nonlinearity to the system. The simplest method to start KLM in a laboratory setup is to slightly tap one of the resonator mirrors. Disturbing the cavity mirrors will sweep the frequencies of competing longitudinal modes, and strong amplitude modulation due to mode beating will occur. The most intense mode-beating pulse will be strong enough to initiate mode locking.

Several methods for the self-starting of KLM that are practical enough to be implemented on commercial lasers have been developed. A simple approach for starting KLM is to mount one of the resonator mirrors on a PZT and introduce a vibration on the order of a few micrometers at a frequency of tens of hertz.

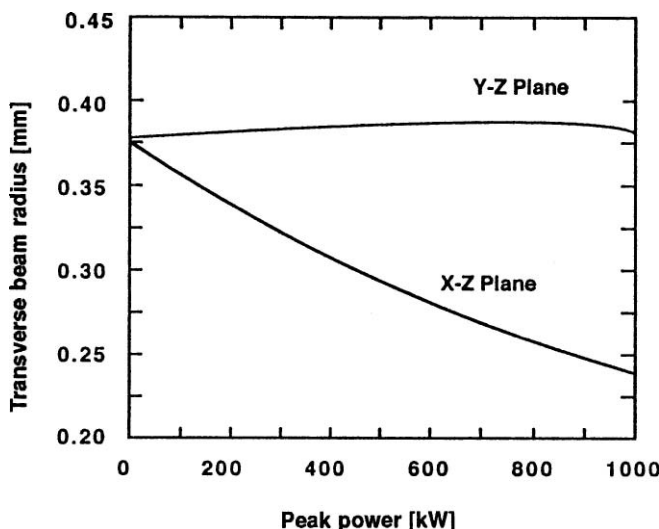


Fig. 9.15. Spot sizes as a function of intracavity peak power for two orthogonal directions [9.15]

In synchronous pumping, the Kerr material is pumped from a source that produces already mode-locked pulses. For example, a Ti:Al₂O₃ crystal can be pumped with a frequency-doubled Nd:YAG laser which is actively mode locked.

Also SESAM (discussed in the next section) have been employed to start and maintain reliable Kerr lens mode locking.

The purpose of this discussion was to acquaint the reader with the basic issues related to KLM resonator design and to provide an idea about the dimensional tolerances which have to be observed in aligning these systems. Specific resonator designs can be analyzed by following the formulas developed in the referenced papers. The design usually starts with the assumption of a pump beam which has a certain spot size and power in the Kerr medium (defined by γ and P_{cr}). From this a nonlinear matrix is developed, which combined with the linear matrix of the passive elements of the resonator describes the behavior of the system.

Another issue crucial for reliable mode-locking performance is the absence of spurious reflections, as demonstrated experimentally [9.16] and studied theoretically [9.17]. These studies revealed that even a very small fraction on the order of 10^{-5} of the output power fed back into the resonator can seriously impair mode locking. It was reported that even the back face of a high reflectivity mirror may adversely affect mode locking.

The Kerr-lens medium can be the laser crystal itself or a separate element such as a piece of glass. Also, the resonator can include a hard aperture, as discussed so far, or a soft aperture provided by the spatial profile of the gain in the laser crystal. Particularly in longitudinally pumped lasers, the gain has a Gaussian profile with the peak at the center where the pump intensity is highest. Therefore, a smaller beam will experience higher gain.

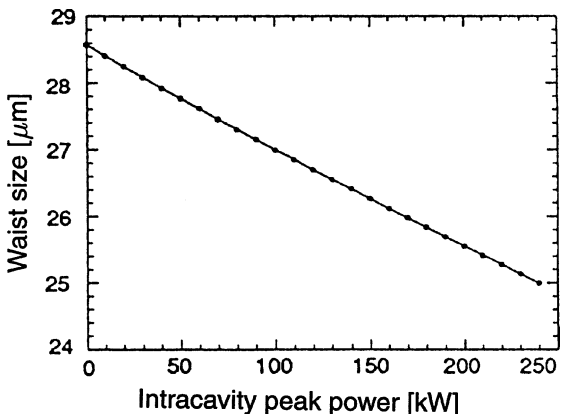


Fig. 9.16. Beam-waist radius as a function of peak power [9.18]

In effect, the radial decrease in gain is equivalent to a radial increase in loss, i.e., an aperture distributed throughout the gain medium. Therefore, the term soft aperturing or gain aperturing is used for this mode of operation.

Gain aperturing is mainly observed in Ti:Al₂O₃ lasers because this material has a much higher saturation intensity, as compared to Nd:YAG or Nd:YLF. The higher gain that a smaller mode experiences is limited by gain saturation. The latter effect causes defocusing, which increases the beam cross section, thereby canceling nonlinear effects.

In Fig. 9.16 the beam waist at the center of a Ti:Al₂O₃ crystal is plotted. The calculations were performed for a 100 fs pulse width, 3 W intracavity average power, and a 80 MHz pulse repetition rate. The beam radius decreases with a slope of approximately $-1.5 \times 10^{-5} \mu\text{m}/\text{W}$. Introducing this value into (9.22), and normalizing to the spot size w and critical power P_{cr} , gives $s = -1.36$.

The simplest embodiment of Kerr-lens mode locking utilizes the nonlinear index of the laser crystal as the Kerr medium and the soft aperture formed by the gain profile within the lasing material. Kerr-lens mode locking was actually first observed by Spence et al. [9.19], in an argon pumped Ti:Al₂O₃ laser which did not contain any additional passive or active element in the resonator. Therefore, the laser was called *self-mode locking*. Figure 9.17 illustrates the simplicity of the set-up in which self-mode locking was observed.

Because the KLM mechanism simulates an intracavity saturable absorber, no cavity length control is required for this type of mode locking. KLM uses the nonlinearity of the whole laser crystal (bulk effect).

Subsequent to its demonstration using Ti:sapphire, Kerr-lens mode locking has been demonstrated in a number of different materials, such as Cr:LiSAF, Cr:LiCAF, Nd:glass, Nd:YAG, Nd:YLF, and Cr:forsterite.

Kerr-lens mode locking is the preferred method for the generation of femtosecond pulses in the laboratory. Pulses on the order of a few tens of femtoseconds have been obtained from solid-state tunable lasers. The ultimate limit of pulse duration for Ti:sapphire is somewhere in the range of ~ 3 fs, or about 1 cycle of light at 800 nm.

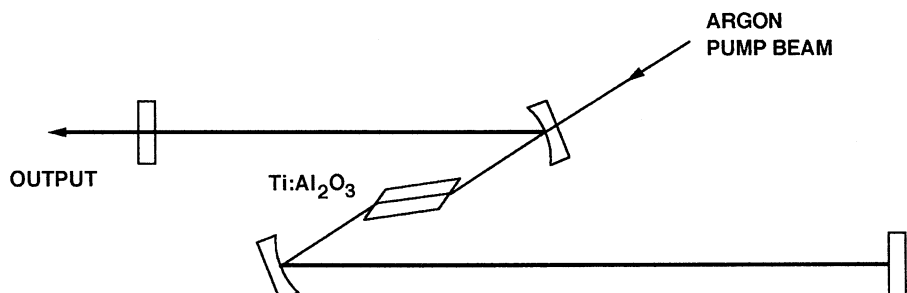


Fig. 9.17. Schematic diagram of the resonator configuration for a self-mode-locked Ti:sapphire laser

Some of the engineering aspects of femtosecond lasers such as self-starting of the KLM process, dispersion compensation of the resonator, and elimination of spurious reflections will be discussed in Sect. 9.5. The reader interested in analytical models describing the KLM effect is referred to [9.12, 13, 20–24].

9.2.4 Semiconductor Saturable Absorber Mirror (SESAM)

In the early 1990s a nonlinear reflector that was based on absorption bleaching in a semiconductor successfully mode locked a Nd:YLF laser [9.25, 26]. The advantage of mode locking with a nonlinear mirror is its simplicity compared to the previously described techniques. Such a nonlinear mirror simply replaces the rear reflector of a laser resonator in order to achieve mode locking.

A SESAM is a semiconductor saturable absorber monolithically embedded between two reflective surfaces. Bandgap engineering and modern semiconductor growth technology has allowed the design of saturable absorbers with accurate control of absorption wavelength, saturation intensity and fluence, and recovery time. In these devices, reflectivity increases with increasing beam intensity.

We will first consider a saturable absorber layer on top of a highly reflective surface as illustrated in Fig. 9.18a. The typical saturation behavior of such a device is shown in Fig. 9.18b and c. Initially the pulses are formed by noise fluctuations. This process is determined by the cw intensity I incident on the absorber. The absorber is barely bleached and $I \ll I_{\text{sat}}$, where $I_{\text{sat}} = h\nu/\sigma_A\tau$. The parameter σ_A is the absorber cross-section and τ is the absorber recovery time. The absorption coefficient α of the material is given by $\alpha = \sigma_A N_D$, where N_D is the density of states in the semiconductor.

The slope dR/dI at around $I = 0$ determines the mode-locking build-up time, which is inversely proportional to the slope, since a small intensity fluctuation will introduce a larger reflectivity change of the saturable absorber if the slope is larger.

After a pulse has developed, the loss reduction per round trip is now due to bleaching of the saturable absorber by the pulse energy rather than by the cw intensity. The saturation fluence E_{sat} is given by $E_{\text{sat}} = h\nu/\sigma_A$. Under steady-state mode-locking conditions the pulse energy density on the saturable absorber is typically three to five times the saturation fluence.

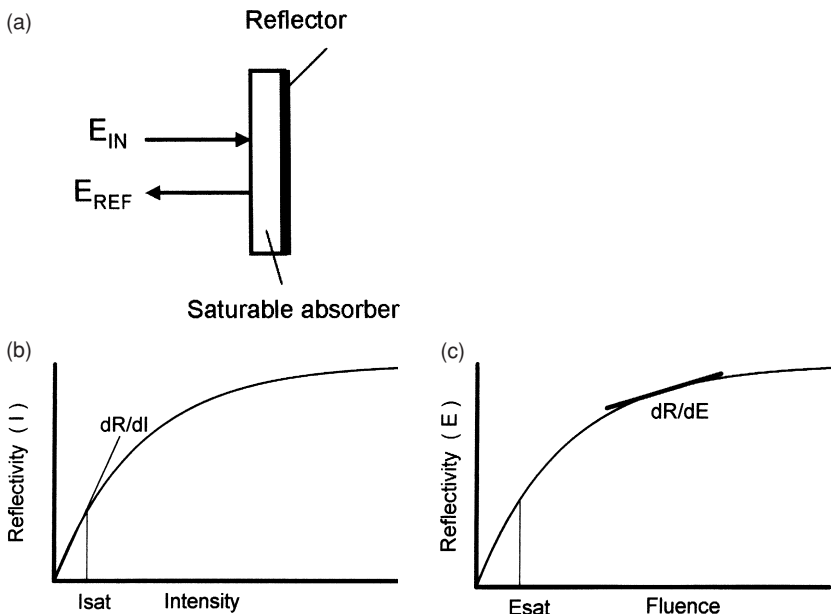


Fig. 9.18. (a) Saturable absorber with back mirror, (b) mode-locked pulse build up at low intensity, and (c) fully developed mode-locked pulse with nonlinear absorber in saturation

The saturable absorbers are III-V semiconductors that exhibit carrier trapping into point defects formed by the excess group V atoms incorporated during the growth process. Typically the saturable absorber is a low temperature ($\sim 380^{\circ}\text{C}$) molecular beam epitaxy (MBE) grown multiple quantum well (MQW) structure comprising GaAs barrier layers and InGaAs quantum wells. The low temperature growth reduces the carrier lifetime to 25 ps. The bandgap of the MQW absorber layer is chosen close to the laser wavelength.

If the device illustrated in Fig. 9.18a is employed as the rear mirror of a laser resonator several problems are encountered: The semiconductor saturable absorber has too low a saturation intensity, the insertion loss is too high, and the device cannot withstand the high intracavity peak intensity.

The addition of a reflector on top of the saturable absorber determines the amount of radiation that can penetrate and bleach the absorber. Therefore, the top reflector provides protection from the high intracavity fluence and significantly reduces the insertion loss. The nonsaturable or fixed loss of a saturable absorber needs to be small, because the gain is low in a typical cw pumped laser. The top reflector also increases dramatically the effective saturation fluence of the device. For a InGaAs-GaAs saturable absorber, the saturation fluence is typically $60 \mu\text{J}/\text{cm}^2$. With a high reflectivity top mirror, the effective fluence can be increased by two orders of magnitude.

Of course, the top reflector significantly reduces the net reflectivity change, but the nonlinearity is still large enough to mode lock solid-state lasers. The bottom reflector, MQW nonlinear absorber, and the top reflector together with the GaAs

substrate form a monolithic device. In such a device, the absorption wavelength is controlled by the design of the band gap, the response time is a function of the growth temperature, and the saturation is determined by the reflectivity of the top reflector, the absorber thickness, and the chosen spot size of the beam incident on the SESAM. The fixed losses depend on the absorber thickness and the reflectivity of the top mirror. The two reflectors with the nonlinear absorber in between form a Fabry–Perot resonator. The optical length of the Fabry–Perot is chosen such that the laser wavelength is at the reflectivity maximum. From the discussion of Sect. 5.2.1 follows that in a high finesse Fabry–Perot the peaks for high transmissions are spectrally very narrow, whereas the range of high reflectivity is rather broad. This is important because the range of high reflectivity has to extent over the gain-bandwidth of the laser. Also a Fabry–Perot resonator operated at maximum reflectivity (anti-resonance) has a lower intensity inside the device than the incident intensity. If a Fabry–Perot is designed for maximum transmission (resonance) the intensity is higher inside compared to the incident intensity. Considering the relatively low damage threshold of the semiconductor the use of the Fabry–Perot in the antiresonance condition is very important.

The following example of one of the earliest devices will illustrate typical design and performance parameters of a SESAM [9.25, 26]. The device consists of a GaAs substrate, a multilayer reflective coating, a GaAs/InGaAs quantum well saturable absorber, and on top another reflective coating (see Fig. 9.19). The MQW has 50 layer pairs of GaAs barriers and $In_xGa_{1-x}As$ quantum wells (with $x = 0.29$). The InGaAs quantum wells have a thickness of 6 nm. The total optical thickness of the Fabry–Perot structure is 4 μm . From (5.79) follows that the maximum reflectivity in a Fabry–Perot resonator occurs at a phase difference between transmitted and reflected rays of

$$\varphi = (2m + 1)\pi. \quad (9.26)$$

This phase expressed as path length difference is given in (5.72). In the device illustrated in Fig. 9.19a, the bottom reflective layers introduce an additional phase shift of π . Therefore, instead of (5.72) we have

$$\varphi = \left(\frac{2\pi}{\lambda} \right) 2nd + \pi, \quad (9.27)$$

where nd is the optical thickness of the resonator. If we eliminate φ from (9.26, 27) we obtain

$$nd = m(\lambda/2). \quad (9.28)$$

With an optical thickness of $nd = 4 \mu\text{m}$ and a eighth order Fabry–Perot ($m = 8$), the center of the reflectivity is at 1 μm .

The short resonator provides for a spectral range that is much larger than the gain bandwidth of most solid-state lasers. This particular SESAM was designed for mode locking a Nd:YLF laser at 1047 nm. The free spectral range, or in this case the width

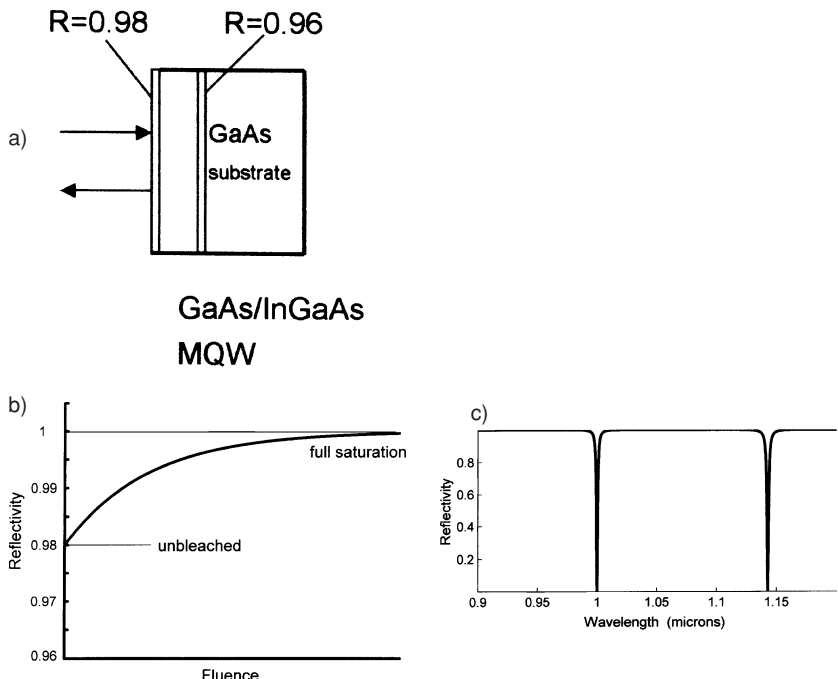


Fig. 9.19. (a) Design of a SESAM for mode locking a Nd:YLF laser, (b) dynamic range of reflectivity as a function of pulse energy density, and (c) spectral range of reflectivity

of the reflectivity maximum, is given by (5.75) or $\Delta\lambda = \lambda_0^2/2nd$. With $nd = 4 \mu\text{m}$ and $\lambda_0 = 1047 \text{ nm}$ the range of high reflectivity is $\Delta\lambda = 137 \text{ nm}$ (see Fig. 9.19b). This is much wider than the gain bandwidth of the Nd:YLF laser, which is on the order of 0.7 nm. The finesse of the Fabry–Perot is obtained from (5.82), with the reflectivities indicated in Fig. 9.19a we obtain $F = 103$. For R we used the geometric mean of the two reflectivities.

At cw power, the reflectivity of the SESAM is 98%, which is the reflectivity of the top mirror. Individual noise spikes bleach the saturable absorber and experience a slightly larger reflectivity. Once the intensity bleaches completely the saturable absorber, the Fabry–Perot resonator becomes a highly reflective mirror with a reflectivity close to 100%. (see Fig. 9.19c).

Figure 9.20 shows the optical schematic of the mode-locked Nd:YLF laser utilizing a SESAM. The laser produced cw mode-locked pulses with a duration of 3.5 ps at a repetition rate of 220 MHz. The average power was 700 mW. From the foregoing data follows that the carrier lifetime of 69 ps in the SESAM is much shorter than the pulse separation of 4.5 ns but longer than the 3.5 ps pulse duration. Depending on the reflectivity and structure of the top and bottom reflectors and the design of the quantum-well saturable absorber, many different configurations have been explored and SESAMs have been successfully used to passively mode lock solid-state lasers.

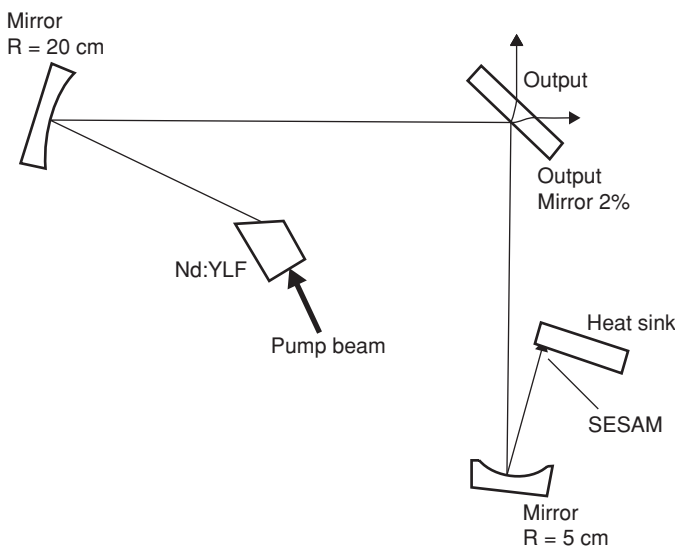


Fig. 9.20. Resonator design of a mode-locked Nd:YLF laser employing a SESAM [9.25]

For example, a SESAM has generated pulses as short as 6.5 fs from a Ti:sapphire laser [9.27]. Over 10 W average power from a diode-pumped, and SESAM mode-locked cw Nd:YAG laser was obtained with pulses of 16 ps in duration [9.28]. Originally femtosecond lasers required many optical components and large setups on optical tables. An example of a highly compact SESAM mode-locked cw diode pumped Cr:LiSAF laser is described in [9.29]. The laser generates pulses with a 113 fs pulse width at an average power of 20 mW. Comprehensive overviews of SESAMs for pulse generation in solid-state lasers can be found in [9.26, 29, 30].

9.3 Active Mode Locking

By placing inside a laser cavity either a frequency modulator (FM) or an amplitude modulator (AM) driven at exactly the frequency separation of the axial modes, one can cause the laser to generate a train of mode-locked pulses with a pulse repetition rate of $v_m = c/2L$. Active mode locking, performed on cw-pumped lasers such as the Nd:YAG system, is achieved by inserting into the resonator an electrooptic or acousto-optic modulator, as will be discussed in Sect. 9.3.1.

A cw actively mode-locked laser generates a train of equal pulses at a repetition rate typically in the range of 80–250 MHz with pulse energies in the nanojoules range. If more energy per pulse is required, one pulse is selected from the train and directed to a regenerative amplifier. However, one can also obtain more powerful mode-locked pulses from a single oscillator by combining mode locking with Q-switching and cavity dumping. This approach will be discussed in Sect. 9.3.2.

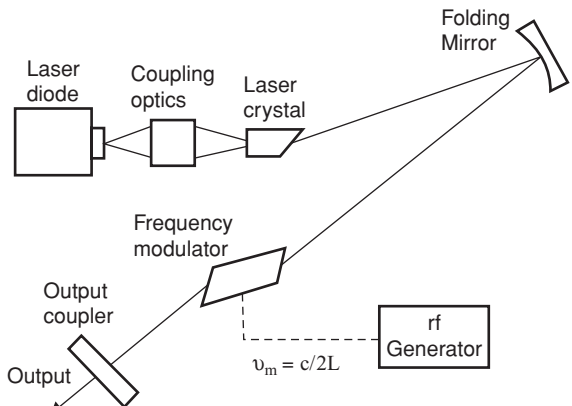


Fig. 9.21. Typical end-pumped and actively mode-locked Nd laser [9.31]

9.3.1 cw Mode Locking

Figure 9.21 shows the optical schematic of a typical actively mode-locked laser comprising an end-pumped laser crystal and an acousto-optic modulator within a three mirror folded resonator [9.31]. Although the system architectures look identical, we have to distinguish between AM and FM modulation.

AM Modulation. From a frequency-domain viewpoint, introducing a time-varying transmission $T(t)$ through an amplitude modulator inside the laser resonator creates sidebands on each oscillating axial mode that overlap with adjoining axial modes. The operation can be described by assuming that the mode with the frequency ν_0 , nearest the peak of the laser gain profile, will begin to oscillate first. If a loss modulator operating at a frequency ν_m is inserted into the resonator, the carrier frequency ν_0 will develop sidebands at $\pm\nu_m$. If the modulating frequency is chosen to be commensurate with the axial mode frequency separation $\nu_m = c/2L$, the coincidence of the upper ($\nu_0 + \nu_m$) and the lower ($\nu_0 - \nu_m$) sidebands with the adjacent axial mode resonances will couple the $\nu_0 - \nu_m$, ν_0 , and $\nu_0 + \nu_m$ modes with a well-defined amplitude and phase. As the $\nu_0 + \nu_m$ and $\nu_0 - \nu_m$ oscillations pass through the modulator, they will also become modulated and their sidebands will couple the $\nu_0 \pm 2\nu_m$ modes to the previous three modes. This process will continue until all axial modes falling within the laser linewidth are coupled.

Viewed in the time domain, the same intracavity modulating element, with its modulation period equal to the round-trip transit time $2L/c$, can reshape the internal circulating field distribution repeatedly on each successive round trip inside the cavity. For example, radiation incident at the modulator during a certain part of the modulation cycle will be again incident at the same point of the next cycle after one round trip in the laser resonator. Radiation suffering a loss at one time will again suffer a loss on the next round trip. Thus, all the radiation in the resonator will experience loss except the radiation which passes through the modulator when the modulator loss is zero

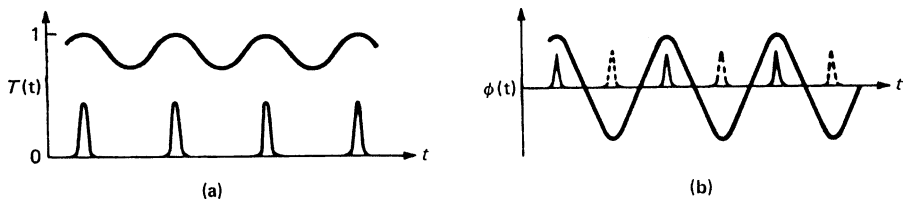


Fig. 9.22. Mode-coupling behavior in the case of (a) AM mode locking and (b) FM mode locking

(Fig. 9.22a). Radiation will tend to build up in narrow pulses in these low-loss time positions. In a general way, we can see that these pulses will have a width given by the reciprocal of the gain bandwidth since wider pulses will experience more loss in the modulator, and narrower pulses will experience less gain because their frequency spectrum will be wider than the gain bandwidth.

By following a single mode-locked pulse through one round trip around the laser cavity a comprehensive analysis of active mode locking has been developed [9.32–34]. For steady-state mode locking the pulse shape should be unchanged after a complete round-trip. The self-consistent solution carried out for a Gaussian pulse leads to a simple expression that shows the dependence of the mode-locked pulse width on the spectral linewidth, modulation frequency, depth of modulation, and saturated gain.

For an acousto-optic AM operating in the Bragg regime, as well as for electro-optic AMs, the round trip amplitude transmission is

$$T(t) \approx \cos^2(\delta_{\text{AM}} \sin \omega_m t), \quad (9.29)$$

where δ_{AM} is the modulation depth and $\omega_m = 2\pi v_m$ is the angular frequency of the modulation. In the ideal mode-locking case, the pulse passes through the modulator at the instant of maximum transmission. This occurs twice in every period of the modulation signal ω_m and, hence, one drives these modulators at a modulation frequency equal to half the axial mode-spacing of the laser. Expanding (9.29) at the transmission maximum gives, for the round-trip modulation function,

$$T(t) = \exp(-\delta_{\text{AM}} \omega_m^2 t^2), \quad (9.30)$$

which results in a pulse width for the AM mode-locked laser of

$$t_p(\text{AM}) = \mu \frac{(gl)^{1/4}}{(\delta_{\text{AM}} \omega_m \Delta v)^{1/2}}, \quad (9.31)$$

where $\mu = 0.53$ for Bragg deflection and $\mu = 0.45$ for Raman–Nath modulation, g is the saturated gain coefficient at the line center, Δv is the gain bandwidth of the laser, and l is the length of the active medium. The AM mode-locked pulses have no frequency “chirp”, that is, $\beta = 0$ in (9.14).

The pulse width/bandwidth product for AM is

$$t_p(\text{AM}) \times \Delta v(\text{AM}) = 0.440. \quad (9.32)$$

From (9.31) it follows that the pulse duration of cw AM mode-locked lasers is inversely related to the product of the modulation depth and modulation frequency, $t_p(\text{AM}) \sim (\delta_{\text{AM}} v_m)^{-1/2}$. It follows that pulse duration can be shortened by increasing the modulation depth or the frequency of the mode locker. The pulse width is also inversely proportional to the gain bandwidth $\Delta\nu$. Therefore, Nd:glass and Nd:YLF produce shorter pulses as compared to Nd:YAG.

As is the case with passive mode-locked systems, etalon effects due to intracavity elements will reduce the bandwidth of the system and broaden the mode-locked pulses. In a cw-pumped Nd:YAG laser, even a weak etalon effect due to the modulator or rod surfaces can decrease the effective value of $\Delta\nu$ by a large amount. Therefore, one of the most important considerations in a practical mode-locking system is the elimination of residual reflections and optical interference effects in the laser cavity.

On the other hand, it is possible to use a tilted etalon inside a mode-locked laser to deliberately lengthen the pulse width. With uncoated quartz etalons of thickness between 1 and 10 mm, good control of the pulse width can be achieved.

FM Modulation. Light passing through an electro-optic phase modulator will be up- or down-shifted in frequency unless it passes through at the time when the intracavity phase modulator $\delta(t)$ is stationary at either of its extrema. The recirculating energy passing through the phase modulator at any other time receives a Doppler shift proportional to $d\delta/dt$, and the repeated Doppler shifts on successive passes through the modulator eventually push this energy outside the frequency band over which gain is available from the laser medium. The interaction of the spectrally widened circulating power with the narrow laser linewidth leads to a reduction in gain for most frequency components. Thus, the effect of the phase modulator is similar to the loss modulator, and the previous discussion of loss modulation also applies here. As shown in Fig. 9.22b, the existence of two phase extrema per period creates a phase uncertainty in the mode-locked pulse position since the pulse can occur at either of two equally probable phases relative to the modulating signal. The quadratic variation of $\delta(t)$ about the pulse arrival time also produces a frequency “chirp” within the short mode-locked pulses.

In the FM case, the internal FM introduces a sinusoidally varying phase perturbation such that the round-trip transmission through the modulator is given approximately by

$$T(t) \approx \exp(\pm j\delta_{\text{FM}}\omega_m^2 t^2), \quad (9.33)$$

where δ_{FM} is the peak phase retardation through the modulator. The \pm sign corresponds to the two possible phase positions at which the pulse can pass through the modulator, as mentioned earlier. With these parameters the pulse width of phase mode-locked pulses is given by [9.33]

$$t_p(\text{FM}) = 0.54 \left(\frac{gl}{\delta_{\text{FM}}} \right)^{1/4} \frac{1}{(v_m \Delta\nu)^{1/2}}. \quad (9.34)$$

The time-bandwidth product is given by

$$t_p(\text{FM}) \times \Delta\nu(\text{FM}) = 0.626. \quad (9.35)$$

In an electro-optic phase modulator the phase retardation is proportional to the modulating voltage; hence $\delta_{\text{FM}} \propto P_{\text{in}}^{1/2}$, where P_{in} is the drive power into the modulator. Therefore, we obtain from (9.34) the following expression for the pulse width: $t_p(\text{FM}) \propto P_{\text{in}}^{-1/8}$, which indicates that the pulses shorten very slowly with increased modulator drive. More effective in shortening the pulses is an increase of the modulation frequency. Since $v_m = c/2L$, the pulse width will be proportional to the square root of the cavity length.

In order to calculate the pulse width from (9.34), we can calculate the saturated gain coefficient g by equating the loop gain with the loss in the resonator

$$2gl \approx \ln\left(\frac{1}{R}\right), \quad (9.36)$$

where R is the effective reflectivity of the output mirror and includes all losses. For a typical Nd:YAG laser with 10% round-trip loss, that is, $R = 0.9$, a resonator length of 60 cm, and a linewidth of 120 GHz, the pulse length is given by $t_p(\text{FM}) = 39(1/\delta_{\text{FM}})^{1/4}$. For $\delta_{\text{FM}} = 1$ rad, which is easily obtainable, pulses of 39 ps can be generated.

The mode-locked pulses obtained through FM modulation show a linear frequency shift

$$\beta_{\text{FM}} = \pi^2 \left(\frac{\delta_{\text{FM}}}{4gl} \right)^{1/2} \Delta\nu v_m, \quad (9.37)$$

where β_{FM} is as defined in (9.11).

It has been observed that actively mode-locked, diode-pumped, solid-state lasers generate pulses with durations considerably shorter than predicted by (9.31 and 34). The shorter pulse width is attributed to spatial hole burning. Diode-pumped lasers are typically end-pumped with the gain medium at one end of the resonator. This causes pulse self-overlap near the end mirror which creates a population grating that inhomogeneously broadens the gain. Inhomogeneous broadening, caused by spatial hole burning, results in shorter pulses and larger time-bandwidth products, as discussed in [9.35].

9.3.2 Transient Active Mode Locking

Techniques such as simultaneous mode locking and Q-switching or cavity dumping can substantially increase the pulse energy from a mode-locked laser. In the case of a Q-switched and mode-locked laser, a burst of mode-locked pulses is emitted which are contained within the envelope of a 100–200 ns Q-switch pulse. If the laser is cavity-dumped, a single mode-locked pulse is emitted from the oscillator.

Schematic diagrams of such systems are shown in Figs. 9.23 and 24. As compared to cw mode locking, the resonator now contains a Q-switch as an additional element. In order to understand the operation of the two systems depicted in these figures, it is important to consider first the build-up time required for the development of transform limited pulses.

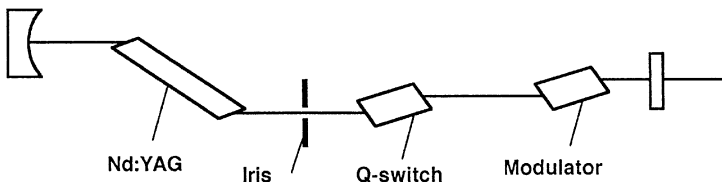


Fig. 9.23. Mode-locked and Q-switched laser

In a typical Q-switched laser, radiation builds up from noise within a few round trips. For mode-locked pulses to reach their transform-limited pulse width, several thousand round trips are required. The time needed to approach the steady-state pulse length is dependent on the modulator depth δ_m and frequency ν_m of the mode locker, the saturated gain gl , and the linewidth $\Delta\nu$ of the gain medium. Kuizenga [9.36, 37] has shown that after M round trips, the pulse width is given by

$$t_{\text{tr}} = \frac{t_p}{[\tanh(M/M_0)]^{1/2}}, \quad (9.38)$$

where

$$M_0 = \frac{1}{4\sqrt{gl}\delta_m} \frac{\Delta\nu}{\nu_m}. \quad (9.39)$$

The transient pulse width t_{tr} is within 5% of the steady-state value t_p after $M > 1.52M_0$ round trips or

$$M > \frac{0.38}{\sqrt{gl}\delta_m} \frac{\Delta\nu}{\nu_m}. \quad (9.40)$$

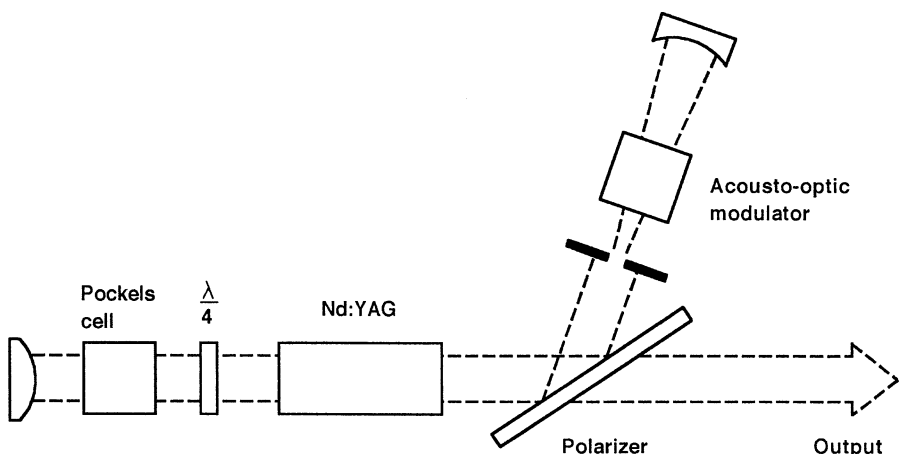


Fig. 9.24. Optical schematic of a mode-locked, Q-switched, and cavity-dumped Nd:YAG laser

Since $\Delta\nu/\nu_m$ is a very large number, and the other parameters are less than one, it takes many round trips for the mode-locked pulses to develop.

For a typical diode-pumped Nd:YAG laser, one obtains the following parameters: $\Delta\nu = 120$ GHz, $gl = 0.4$, $\delta_m = 0.5$ and $\nu_m = 80$ MHz. Therefore, according to (9.40), a minimum of 1802 round trips are required for the pulses to reach steady state. With a round-trip time of 10 ns, the time required for the pulses to develop is on the order of 18 μ s. However, the limiting time constant for repetitive Q-switching is not the time needed to reach a steady state for the mode-locked pulse, but the time required for relaxation oscillations to die out. Each pump cycle produces transient dynamics, which strongly perturb the steady-state level in the laser; therefore, the coupling between the population inversion and the intracavity radiation results in oscillations of both quantities until a steady-state is established. This usually takes 0.5–2 ms before spike-free cw mode locking is established. Therefore, the following timing sequence is followed in the system depicted in Figure 9.23 for obtaining simultaneous mode locking and Q-switching.

First, the Nd:crystal is quasi-cw pumped at full pump level for about 0.5–1 ms. The rf signal to the acousto-optic Q-switch is adjusted such that the laser is just above threshold. The rf signal to the mode locker is also switched on together with the pump. Mode-locked pulses develop during this phase in competition with strong fluctuations from relaxation oscillations. After the relaxation oscillations have died out, the Q-switch is rapidly turned-off. Because of the high gain, the mode-locked pulse is amplified by many orders of magnitude. During the Q-switch process, mode-locked pulses are emitted within a bell-shaped envelope which has a width of about 100–200 ns. The time separation between pulses corresponds to the resonator length, i.e. $2L/c$. If one assumes a pulse separation of typically 10 ns, then a burst of 10–20 mode-locked pulses is obtained, with the strongest pulse at the center. The pump cycle is repeated at a rate of tens of hertz.

The system depicted in Fig. 9.24 emits only one mode-locked pulse during each pump cycle. The resonator is formed by two highly reflective mirrors and a polarizing beam splitter. The active elements in the resonator are the laser crystal, a Pockels cell, and an acousto-optic modulator. Without a voltage applied to the Pockels cell, the resonator has a low Q because radiation leaks out through the beam splitter. Likewise, with a $\lambda/4$ voltage applied to the Pockels cell, radiation is reflected between the two resonator mirrors and the Q of the cavity is high.

Mode locking is established in the resonator similar to the technique described previously. Together, with the pump pulse, rf power is applied to the mode locker, and a bias voltage is applied to the Pockels cell to increase the Q of the resonator just enough for the laser to exceed threshold. The bias voltage to the Pockels cell is usually generated by applying a $\lambda/4$ voltage to electrode 1 and a voltage close to $\lambda/4$ to electrode 2. Operation of the laser slightly above threshold establishes mode locking. After the appropriate build-up time and waiting period for relaxation oscillations to dampen out, the voltage on electrode 2 of the Pockels cell is switched to zero. The mode-locked pulse circulates between the mirrors and the power quickly increases by several orders of magnitude. A photo diode is used to monitor the amplitude of the pulse circulating in the resonator. Once the pulse has reached its maximum amplitude,

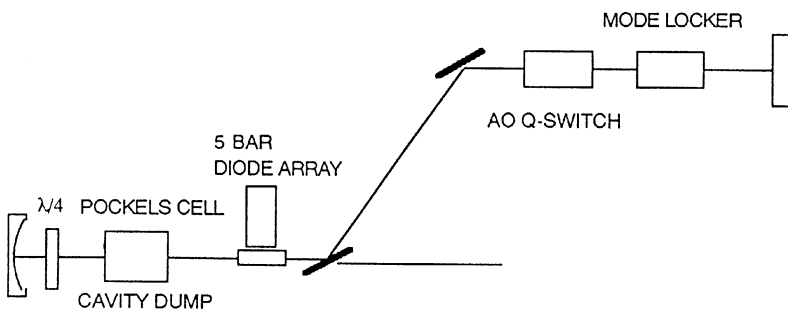


Fig. 9.25. Q-switched, mode-locked, and cavity-dumped diode-pumped Nd:YAG laser

the voltage on electrode 1 of the Pockels cell is quickly switched to zero and the pulse is coupled out through the polarizer.

Cavity dumping of a mode-locked pulse is an elegant method for producing a single short pulse on the order of 100 ps. However, the requirement of switching high voltages within nanoseconds is not a trivial task. Furthermore, fast and clean switching of the Pockels cell is complicated by the piezoelectric effect in materials such as LiNbO₃, which causes ringing, i.e. partial opening and closing of the switch. To minimize the switching problem, the function of the Pockels cell in Fig. 9.24 is sometimes divided into two switches, as shown in Fig. 9.25. Here the acousto-optic mode locker and Q-switch develop a strong mode-locked pulse in a two-step process, as described before. Once the mode-locked pulse has reached maximum intensity, the Pockels cell rotates the polarization and the pulse is coupled out through the thin-film polarizer. This system, developed in the author's laboratory, produced single output pulses at 20 Hz with a pulse length of 95 ps and an energy of 1 mJ [9.38]. The laser rod was a 3.5 mm diameter by 25 mm long Nd:YAG crystal side-pumped diode arrays. The combined output of the two arrays was 300 mJ in a 600-μs-long pulse. The laser resonator consisted of a 3-m concave reflector and a flat reflector spaced 86.6 cm apart. Two thin-film polarizers were used, one acting as the output coupler for the cavity-dumped pulse. The rf drive frequency to the acousto-optic mode locker is 80 MHz and the cavity round-trip time is 6.25 ns. Cavity dumping was accomplished using a KD*P Pockels cell and a quarter-wave plate. The 600-μs-long pump pulse was required to allow the mode-locked pulse to approach steady state and to allow the relaxation oscillations to dampen. After about 500 μs, stable mode locking was established, the acousto-optic Q-switch was turned off, allowing the circulating pulse to build up in approximately 80 ns. The Pockels cell was then switched from $\lambda/4$ voltage to zero, thus dumping the pulse through a thin-film polarizer. Fig 9.26 depicts an oscilloscope trace of the pulse build-up after the acousto-optic Q-switch is turned off. Also shown is the single output pulse of the laser.

Although Q-switching and cavity dumping in combination with mode locking appears to be a simple method for obtaining a single, powerful mode-locked pulse from a single oscillator, the technique is not easy to implement. The major problem is the presence of relaxation oscillations caused by the transient nature of the pulse evolution.

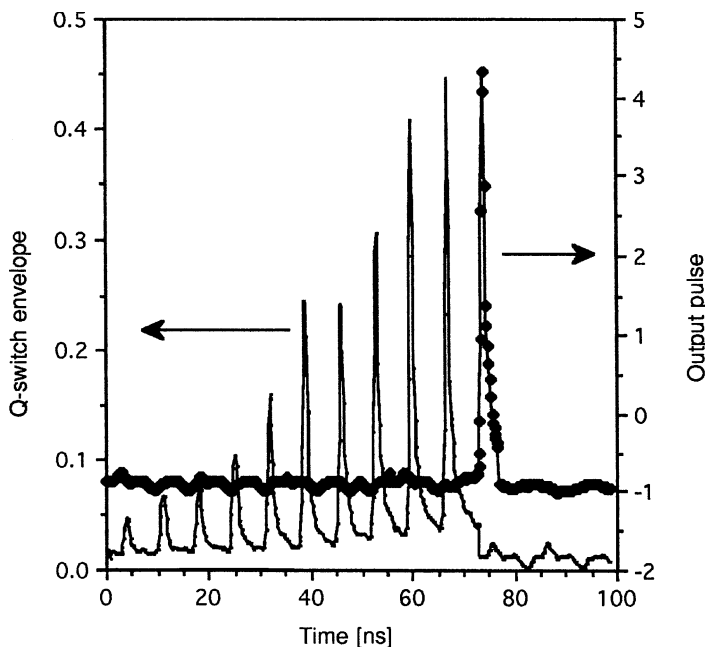


Fig. 9.26. Q-switch build-up envelope and cavity-dumped output pulse

An alternative approach of generating single, powerful mode-locked pulses is by means of a cw mode-locked oscillator, followed by a pulse slicer and a regenerative amplifier. Shorter pulses, and generally a more reliable performance, can be achieved with the latter approach. Further examples of transient mode locking can be found in [9.39–41].

9.4 Picosecond Lasers

Today, diode-pumped cw Nd:YAG or Nd:YLF lasers, mode-locked with an acousto-optic modulator, are the standard sources for the production of picosecond pulses. A typical end-pumped and actively mode-locked neodymium laser is shown in Fig. 9.21. The output from a GaAlAs diode array is focused onto the end of the laser crystal. Spot sizes of the pump beam range from 50 μm to a few hundred micrometers. A common resonator configuration for diode-pumped actively mode-locked lasers is a three-mirror arrangement. A folded cavity geometry provides a beam waist at both the laser crystal and the modulator, as well as astigmatic compensation. In commercial mode-locked lasers, the resonator is usually folded a few times to decrease the overall length of the system. The length of the cavity is usually a compromise between the need for short pulses, which requires a short resonator and a high-modulation frequency and the ability to slice out a single pulse with a Pockels cell.

Typical of end-pumped lasers is the highly reflective coating applied to the back face of the crystal (Fig. 9.21) to form one of the resonator mirrors. Small thermal or vibrational changes in the pump radiation readily induce relaxation oscillations in mode-locked systems. These relaxation oscillations cause fluctuations in amplitude, accompanied by damped oscillations at frequencies in the 30–150 kHz range. Therefore, careful alignment and isolation is required for clean mode-locking. The modulator is usually placed close to the front mirror at the beam waist created by the folding mirror. The resonator length is typically on the order of 1 m or longer to provide a sufficiently large separation between pulses for pulse selection by an external switching device. Actively mode-locked lasers are very sensitive to cavity length detuning. In practice, cavity length changes on the order of 1 μm can cause serious degradation in pulse quality. Therefore, active length stabilization of the resonator by a feedback loop is needed to maintain long-term stability of mode locking.

Active mode locking of a laser can be achieved by using a tunable rf oscillator and adjusting the modulator frequency to agree with the cavity length; or, alternatively, selecting a fixed frequency and adjusting the mirror spacing.

9.4.1 AM Mode Locking

Amplitude modulation for modelocking cw lasers is usually performed with an acousto-optic modulator. These devices are different from the modulators employed for Q-switching lasers because they are operated at resonance. The modulator material, such as a quartz block, has parallel faces and the sound wave is reflected back and forth in the material. The length of the quartz cell is cut such that the length is equal to an integer number of half-wavelength of the sound wave. In such a standing-wave pattern, the diffraction loss of the optical beam will be modulated at twice the frequency of the sound wave since the diffraction loss reaches a maximum wherever the standing-wave pattern has a maximum. The transducer of the acousto-optic modulator is therefore driven at an rf frequency of $v_{\text{rf}} = c/4L$. Operation of the modulator at resonance requires considerably less rf power compared to a traveling-wave device. For Q-switching of lasers, this approach is not feasible because the high Q of the acoustic resonance prevents fast switching.

Acousto-optic mode-locking requires a precise match of the drive rf with one of the acoustic resonances of the modulator and also with the frequency spacing of the cavity modes. Since an acousto-optic mode locker operates at a fixed frequency, exact synchronism between the modulation frequency and the cavity length is achieved by mounting one of the resonator mirrors on a piezoelectric translator for cavity-length adjustment. A second feedback loop is usually required to maintain synchronism between the rf drive frequency and the resonance frequency of the high-Q modulator. This is achieved by sampling the rf reflected back from the modulator by means of a directional coupler. This reflected rf power provides an error signal for slight frequency adjustments caused by a shift of the modulator's resonance due to thermal effects.

Usually, fused quartz is used as the Bragg deflector in mode lockers because of its excellent optical quality, which ensures a low-insertion loss. A transducer, such as

Table 9.1. Modulation depth and rf power requirements for typical mode lockers

Frequency (MHz)	Modulation depth (δ_{AM})	Drive power (W)	Corresponding resonator length (cm)
38	0.8	5	197.4
120	0.63	1	62.5

LiNbO_3 , is bonded to the quartz block and launches an acoustic wave into the substrate. Such mode lockers are driven by an rf generator anywhere from 40 to 120 MHz and at power ranges from 1 to 5 W. For example, two commercially available units at the low and high ends of the frequency range have the performance characteristics, as listed in Table 9.1.

The modulation depth δ_m is usually determined experimentally by measuring the one-way diffraction efficiency ε of the device according to the relationship

$$\varepsilon = 0.5[1 - J_0(2\delta_m)], \quad (9.41)$$

where $J_0(x)$ is the zero-order Bessel function of x .

In cases where a modulation frequency considerably higher than about 100 MHz is desired, or in cases where a very large modulation depth is required, a material other than quartz has to be chosen. As was discussed in Sect. 9.3.1, a higher modulation frequency or a larger depth of modulation decreases the duration of a mode-locked pulse. Therefore, the generation of mode-locked pulses with a duration of 20 ps or less requires a departure from the standard transducer-fused quartz Bragg cell. Since the acoustic losses rapidly increase in fused quartz for acoustic frequencies above 100 MHz, sapphire has been chosen for Bragg cells operating around 500 MHz. Pulses with less than 10 ps in duration have been obtained with a ZnO-sapphire acousto-optic modulator at this frequency [9.42].

A technique which will substantially increase the modulation depth is the use of the transducer itself as the optical loss modulator. In conventional acousto-optic modulators, a piezoelectric transducer is used to launch an acoustic wave into the Bragg deflector. In a so-called *piezoelectrically induced strain optics modulator*, the piezoelectric material itself is selected as the deflection medium. Operated at resonance, a very efficient refractive-index grating can be created in the bulk of the piezoelectric material. The shortest actively mode-locked pulses are generated with this type of mode locker which usually employs GaP or LiNbO_3 as Bragg material [9.43, 44]. Actually, the shortest pulses reported from an actively mode-locked diode-pumped Nd:YLF laser, with 6.2 ps duration, has been achieved with a GaP acousto-optics mode locker [9.45]. Since both gallium phosphide (GaP) and lithium niobate (LiNbO_3) have large strain-optic coefficients, a very efficient refractive index grating can be created in the bulk piezoelectric transducer itself. This technology has, of course, its own difficulties. The optical quality of the material is inferior to fused quartz, and impedance matching the rf generator to a thick transducer creates considerable difficulties.

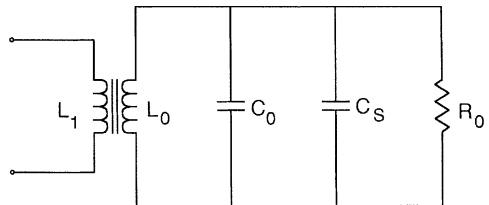


Fig. 9.27. Equivalent rf circuit for a piezoelectric transducer with impedance matching transformer

Figure 9.27. depicts the equivalent rf circuit for a piezoelectric transducer. The two conductively coated surfaces of the transducer with the piezoelectric crystal in between represent a capacitor C_0 . Stray capacitance associated with the package and electrical leads is accounted for by C_s , whereas R_0 accounts for the dielectric losses. Connecting an inductance L_0 parallel to the transducer creates a resonance circuit with a resonance frequency $1/\nu_R = 2\pi\sqrt{L_0(C_0 + C_s)}$ and a quality factor $Q = 2\pi\nu_R L_0 / R_0$. The electrical resonance frequency ν_R has to correspond to the acoustic standing-wave resonance of the transducer, which is controlled by the thickness of the transducer crystal. As we recall from the previous discussion, the laser light is loss modulated at twice the rf drive frequency ν_R owing to the acoustic standing wave in the mode-locker substrate. The inductance L_0 is actually the secondary winding of a transformer required to match the impedance of the transducer circuit to a $50\ \Omega$ coaxial transmission line. The transducer can be made very thin if it is used to launch an acoustic wave into a Bragg cell, such as a quartz block. In this case, C_0 is large compared to the stray capacitance C_s .

If a transducer is employed in a dual role of launching the acoustic wave and modulating the optical beam, it has to be fairly thick for the laser beam to pass through. This reduces C_0 , and in order to achieve resonance at ν_R , a very large inductance has to be matched to the transducer. A small C_0 makes it very difficult to efficiently couple the rf signal into the transducer because the stray capacitance provides a parallel loss path to the transducer.

Optimum mode locking is achieved by adjusting the cavity length such that its resonant frequency matches the frequency of the mode locker. This is usually accomplished by fixing the frequency of the mode locker and tuning the resonator length to match the mode locker's frequency. The cavity length is tuned by translating one mirror mounted on a piezoelectric translator.

Figure 9.28 shows feedback control of a laser mode locked with an acousto-optic Bragg cell. The mode locker is driven by an rf generator whose output frequency is divided by 2. Manually, the cavity length is adjusted until a region of stable mode locking is achieved. This is accomplished by adjusting the reference voltage of a differential operational amplifier, which then provides a dc voltage to the piezoelectric transducer. At that point, the feedback loop is closed. The train of mode-locked pulses is detected by a photodiode. Appropriate filtering of the photodiode output provides a sine wave that corresponds to the resonator round-trip repetition frequency. The phase of this waveform is compared with the waveform of the rf generator in a phase detector. A deviation or drift between these two frequencies produces an error signal directed to the differential amplifier, which in turn provides a dc voltage to the piezoelectric translation stage.

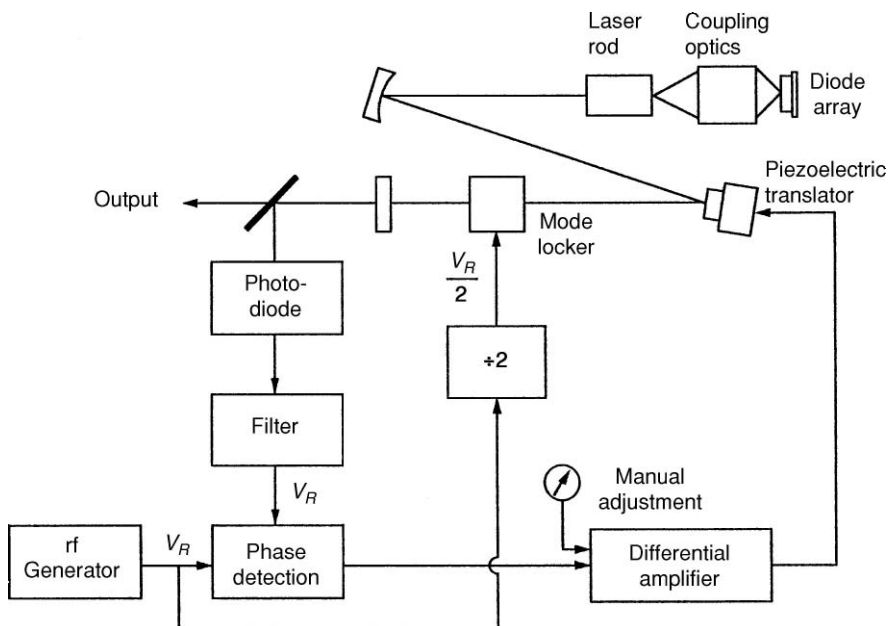


Fig. 9.28. Feedback control of an acousto-optic mode-locked lasers

9.4.2 FM Mode Locking

To achieve FM mode-locking, an intracavity electro-optic phase modulator is driven at the cavity resonance frequency. Electrically, the modulator consists of a pair of electrodes between which the crystal is placed. An inductive loop and a tuning capacitor are shunted across these electrodes and are used to achieve the desired resonant frequency.

Lithium niobate is usually the crystal employed in electro-optic modulators. With the electric field applied transversely to the optical beam, the r_{33} electro-optic coefficient can be utilized, and one obtains

$$\Delta n_z = \frac{-1}{2} r_{33}(n^e)^3 E_z, \quad (9.42)$$

where n^e is the extraordinary index of refraction. The light propagates in the x direction, and the beam is polarized in the z direction in the same direction as the applied electric field.

The total phase change in the crystal is $\delta_{FM} = 2\pi \Delta nl/\lambda_0$, where l is the length of the crystal in the x direction. If a voltage $V = V_0 \cos \omega_m t$ is applied across the crystal in the z direction, the peak single-pass phase retardation of the modulator is

$$\delta_{FM} = \frac{\pi r_{33}(n^e)^3 V_0 l}{\lambda_0 d}, \quad (9.43)$$

where d is the dimension of the crystal in the z direction.

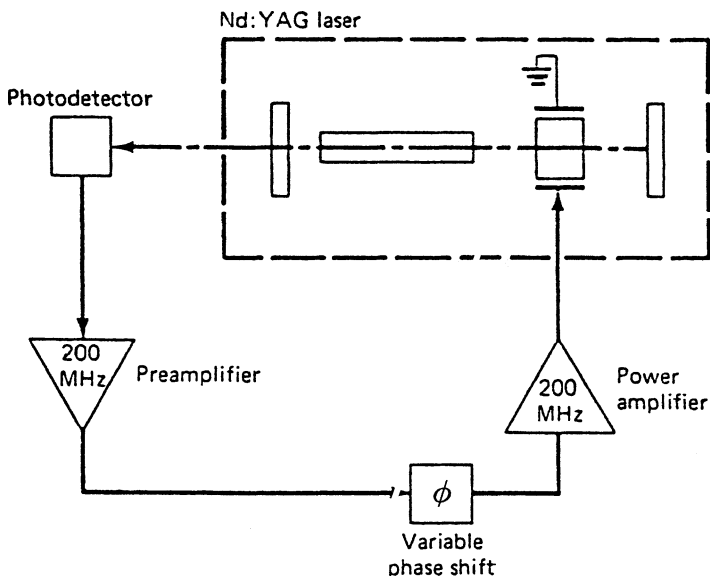


Fig. 9.29. Direct drive mode-locking system

For LiNbO_3 , the material parameters are $n^e = 2.16$ at $1.06 \mu\text{m}$ and $r_{33} = 30.8 \times 10^{-10} \text{ m/V}$. Typically, a phase retardation of about $\delta_{FM} = 1 \text{ rad}$ is achieved with 300 V across a $5 \times 5 \times 20 \text{ mm}$ crystal. At a frequency of a few hundred megahertz, this requires an rf power of a few watts.

We will illustrate the performance of an FM mode-locked Nd:YLF laser that has an optical design, similar as shown in Fig. 9.21. The Brewster cut LiNbO_3 FM had dimensions of $15 \times 6 \times 2 \text{ mm}$ and was driven by 1 W of rf power at a frequency of 200 MHz . The Nd:YLF rod was pumped by a 3-W cw laser diode. The output from the $500 \times 1 \mu\text{m}$ diode-emitting aperture was focused to a $300 \mu\text{m}$ spot at the laser crystal. The mode-locked oscillator generated 14 ps pulses at an output power of 830 mW at an output wavelength of $1.047 \mu\text{m}$.

In the case of an FM mode-locked laser, a simple mode-locking system can be built by allowing the laser to determine its own drive frequency, as shown in Fig. 9.29. This can be accomplished by using a high-speed photodetector to sense the first beat frequency $c/2L$ of the oscillator. This signal is amplified, phase-shifted a variable amount, and then applied to the intracavity modulator. The adjustable phase shifter compensates for the delay in the feedback loop. When the phase of the electric signal on the modulator and the signal derived from the laser equal an integer times π , the loop goes into regeneration and the laser is mode locked. The resultant mode-locking system is a closed-loop oscillator using the laser cavity as the basic reference. Such a system will automatically track changes in cavity length.

In a phase-modulation system there is an ambiguity in the phase relationship between the laser pulse train and the modulator driving signal, as the pulses may pass through the modulator at either of the two extreme voltage points. Because of this phase ambiguity, two possible pulse trains can be obtained: one at 0° phase with

respect to the modulator drive and one at 180° . The laser will always operate with only one of these pulse trains running at a time, because to do otherwise would result in a larger net loss in the laser cavity. However, small perturbations to the laser can cause random shifting from one phase to the other, the phase change requiring several microseconds. An automatic phase-modulating mode-locked system, which operates by synchronizing the modulator drive signal to the first-order mode beat of the laser, suffers from sporadic loss of lock as the laser hops from one stable phase to the other.

In a phase-modulated laser one can avoid this failure mode, which occurs due to a spontaneous switch of 180° in the phase of the output pulse train, by utilizing the second-order beat frequency. A mode-locking control system that has proven to be quite stable is shown in schematic form in Fig. 9.30 [9.46]. The oscillator is phase modulated at the fundamental beat frequency of 200 MHz by a modulator driven from a voltage-controlled oscillator (VCO). A photodetector mounted behind the rear mirror of the oscillator samples a portion of the beam. A bandpass filter selects the second harmonic of the cavity beat frequency. The resultant amplified 400-MHz signal is compared in a phase detector with a 400-MHz comparison signal derived by multiplying the output of the VCO by 2. The phase-detected output is amplified and used to control the VCO. Initial mode locking is performed manually by adjusting the bias of the VCO.

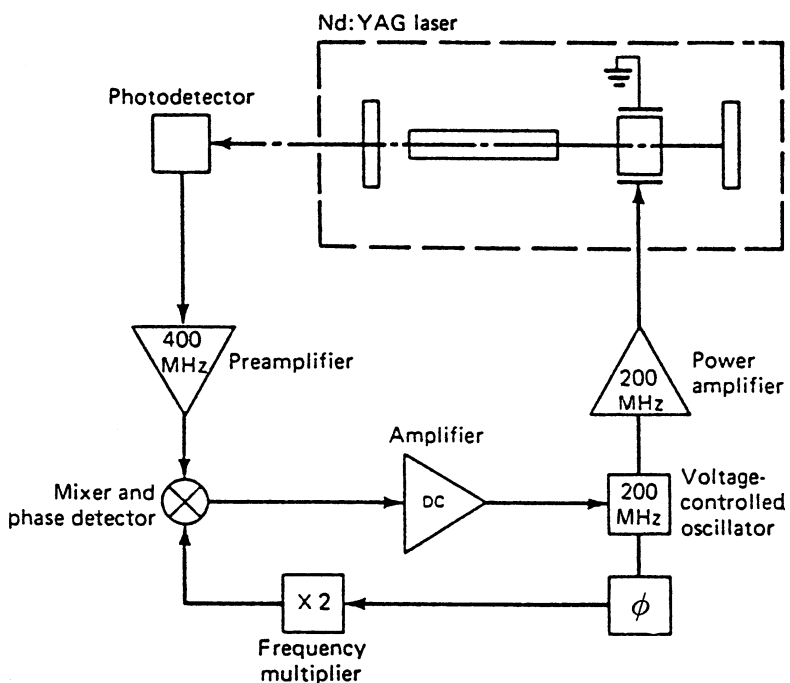


Fig. 9.30. Automatic closed-loop mode locking system

Information about diode-pumped, actively mode-locked lasers employing AM and FM modulation in a number of Nd materials such as Nd:YAG, Nd:YLF, Nd:glass, and Nd:YVO₄ can be found in [9.31, 47–51].

9.5 Femtosecond Lasers

The minimum pulse duration of a mode-locked laser is determined by the net gain bandwidth of the laser material, group velocity dispersion, and properties of the saturable absorber. The goal of an all solid-state laser source for ultrafast pulse generation has motivated research efforts worldwide. Kerr-lens mode locking (KLM) has revolutionized femtosecond pulse generation in solid-state materials because the KLM technique produces the shortest pulses and is relatively simple to implement.

9.5.1 Laser Materials

The laser most actively explored for ultrashort pulse generation is Ti:A1₂O₃. This laser has the largest gain bandwidth and is therefore capable of producing the shortest pulses; it also provides the widest wavelength tunability. Typically, the Ti:Ai₂O₃ crystal is pumped by a cw argon laser. The future trend will be to replace the argon laser with a diode-pumped, frequency-doubled Nd:YAG laser in order to create an all-solid-state source.

With regard to providing a compact, reliable femtosecond source, Cr:LiSAF (Cr:LiSrAlF₆) is an intriguing material because it can be pumped directly by laser diodes. Compared to Ti:A1₂O₃ systems, Cr:LiSAF does not have as wide a tuning range, but the much longer upper-state lifetime (67 μs) and a broad absorption band centered at 640 nm permit pumping with red AlGaInP diodes. Diode-pumped Cr:LiSAF lasers are currently the most compact femtosecond pulse sources.

A third material which has a broad gain bandwidth is Cr:forsterite. This laser can be pumped with the output from a diode-pumped Nd:YAG laser to produce femtosecond pulses at around 1.3 μm. Table 9.2 lists key parameters of these three important materials for femtosecond pulse generation in solid-state lasers.

Table 9.2. Spectroscopic properties of broadband solid-state laser materials

	Ti:sapphire	Cr:LiSAF	Cr:forsterite
Peak emission cross section (×10 ⁻²⁰ cm ²)	30	4.8	14.4
Emission peak (nm)	790	850	1240
Gain bandwidth (nm)	230	180	170
Upper state lifetime (μs)	3.2	67	2.7
Nonlinear coefficient γ (×10 ⁻¹⁶ cm ² /W)	3.2	1.5	2.0

9.5.2 Dispersion Compensation

For ultrashort pulse generation, the round-trip time t_r in the resonator for all frequency components of the mode-locked pulse must be frequency independent, i.e., $t_r(v) = d\varphi/dv = \text{constant}$, where φ is the phase change after one round trip. Otherwise, frequency components that experience a cumulative phase shift no longer add constructively and are attenuated. This limits the bandwidth of the pulse and leads to pulse width broadening. The frequency-dependent phase shift of the pulse during one round trip can be expressed in a Taylor series about the center frequency v_0 ,

$$\frac{d\varphi}{dv} = \varphi'(v_0) + \varphi''(v_0)\Delta v + \frac{1}{2}\varphi'''(v_0)\Delta v^2, \quad (9.44)$$

where φ' , φ'' , and φ''' are the derivatives of the phase with respect to frequency. When φ'' is nonzero, the pulse will have a linear frequency chirp, while a nonzero third-order dispersion will induce a quadratic chirp on the pulse.

Dispersion in the laser crystal due to the wavelength dependence of the refractive index will result in temporal spreading of the pulse. Crystals such as Ti-sapphire exhibit normal or positive dispersion which means that longer wavelengths travel faster than shorter ones.

The change of group velocity with frequency is usually expressed by

$$\frac{dv_g}{dv} = -v_g^2\beta'', \quad (9.45)$$

where β'' is the group dispersion of the medium. Materials in the visible region of the spectrum have positive or normal dispersion, i.e. $\beta'' > 0$. Therefore, in a laser crystal, v_g decreases with increasing frequency causing a red-shift of the pulse.

The importance of controlling the round-trip group velocity dispersion in femtosecond lasers was soon recognized. Positive group velocity dispersion in the laser crystal can be compensated for by optical components that intentionally introduce negative dispersion into the resonator. The most common technique is a pair of prisms inside the laser cavity. A more recently developed technique for dispersion compensation is based on chirped mirrors which can be used in addition to the prisms or as a replacement.

Prism Pair. The prisms depicted in Fig. 9.31 represent a dispersive delay line that intentionally introduces negative dispersion into the resonator. Although the glasses of the prisms have normal dispersion, the geometry of the ray path can be arranged such that the blue components of the pulse traverses the two prisms in a shorter time than do the red components.

The first prism spatially disperses the pulse, causing the long wavelength component to travel through more glass in the second prism than the shorter wavelength components. The net effect is to create “anomalous” dispersion to counteract normal dispersion in the Ti:sapphire crystal. The spatial off-set of the different frequency components caused by the prisms is neutralized by placing the prism pair at one end of the cavity so that the pulse retraces its path through the prism.

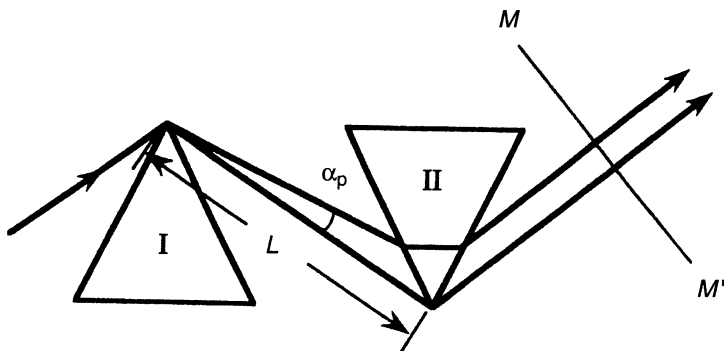


Fig. 9.31. Dispersive delay line employing a prism pair

Although a number of prism arrangements can be devised, usually two prisms are used at minimum deviation and Brewster angle incidence at each surface. In Fig. 9.31 the entrance face of prism II is parallel to the exit face of prism I and the exit face of prism II is parallel to the entrance of prism I. The prisms are cut so that the angle of minimum deviation is also the Brewster angle. The plane MM' normal to the rays is a plane of symmetry.

A detailed description of the design of dispersive delay lines based on prism pairs can be found in [9.52, 53]. Referring to Fig. 9.31, it can be shown that the optical path that contributes to dispersion is

$$l = 2L \cos \alpha_p. \quad (9.46)$$

Group-velocity dispersion is the second derivative of the pathlength with respect to wavelength. From [9.52] we obtain

$$\frac{d^2l}{d\lambda^2} = 4L \left\{ \left[\frac{d^2n_0}{d\lambda^2} + \left(2n_0 - \frac{1}{n_0^3} \right) \left(\frac{dn_0}{d\lambda} \right)^2 \right] \sin \alpha_p - 2 \left(\frac{dn_0}{d\lambda} \right)^2 \cos \alpha_p \right\}. \quad (9.47)$$

The second part of (9.47) is responsible for negative dispersion; therefore the first part has to be made as small as possible. The term $L \sin \alpha_p$ expresses the distance of the beam from the apex of the first prism. This term is minimized by placing the beam as close to the apex as possible. In actual systems, the incident beam is adjusted to pass at least one beam diameter inside the apex of the first prism. We introduce $L \sin \beta = 4w$, where w is the beam radius, and with $\cos \beta \approx 1$ and $2n_0 \gg 1/n_0^3$ we obtain

$$\frac{d^2l}{d\lambda^2} = 16w \left[\frac{d^2n_0}{d\lambda^2} + 2n_0 \left(\frac{dn_0}{d\lambda} \right)^2 \right] - 8L \left(\frac{dn_0}{d\lambda} \right)^2. \quad (9.48)$$

For sufficiently large prism separation L , the right-hand side of (9.48) can be made negative, as illustrated by the following example. We assume a Ti:sapphire laser, with two SF10 glass prisms for dispersion compensation. With $n_0 = 1.711$,

$dn_0/d\lambda = -0.0496 \mu\text{m}^{-1}$, $d^2n_0/d\lambda^2 = 0.1755 \mu\text{m}^{-2}$ at 800 nm, and a beam radius of $w = 1 \text{ mm}$,

$$\frac{d^2l}{d\lambda^2} = [0.294 - 0.0197L \text{ (cm)}]10^{-8} \quad [1/\text{cm}]. \quad (9.49)$$

Therefore, for a prism separation larger than about 15 cm, negative group-velocity dispersion is obtained.

Chirped or Dispersive Mirrors. Both names are used depending whether the emphasis is on the design of the mirrors or their function. Group delay dispersion compensation arises from the wavelength dependence of the penetration depth of the incident optical field in multilayer coatings [9.54].

The design utilizes a structure consisting of many alternating layers of SiO_2 and TiO_2 with optical thickness close to a quarter wavelength for the selected center wavelength. A monotonic variation of the multilayer period throughout the deposition process (chirped coatings) results in a penetration depth, and thus group delay, that varies monotonically with wavelength. The multilayer period is slightly increased near the substrate to produce a group delay that increases with wavelength, i.e., negative dispersion. Undesirable resonance features are eliminated by a chirp in the thickness of the high index layer in addition to the chirp of the center wavelength of the Bragg mirror (double-chirped mirrors) [9.55]. Figure 9.32 illustrates the general structure of a double-chirped mirror designed for the control of group-delay dispersion.

The dispersive mirrors designed for Ti:sapphire passive mode-locked lasers are highly reflective and exhibit a negative dispersion over the wavelength range of 710–900 nm. Dispersive mirrors have the advantage over a prism pair of allowing a shorter resonator length, but the range of adjustability is more limited.

Generally speaking, in the design of the femtosecond lasers, dispersion effects have to be minimized. A small positive dispersion in the resonator requires a short laser crystal. As the pulse width approaches a few tens of femtoseconds, third-order dispersion from the prism pair and the laser crystal become critical. Minimizing the optical path length in the prisms will reduce third-order dispersion.

Chirped mirrors can be designed for compensating third-order dispersion. In prism pairs third-order dispersion is determined by the materials parameters and operating

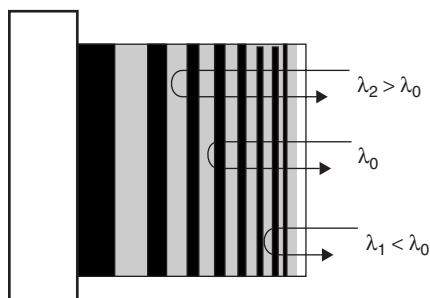


Fig. 9.32. General structure of a double-chirped mirror designed for dispersion control

wavelength. Chirped mirrors are sometimes used in combination with a prism pair to reduce third-order dispersion.

Soliton Mode-Locked Regime. Experimental results, supported by theoretical analysis, have actually shown that the shortest pulses are not obtained for an overall zero dispersion in the cavity, but for the case of a slight negative group-velocity dispersion [9.56].

Femtosecond pulse generation relies on a net negative dispersion because of the self-phase modulation caused by the optical Kerr effect in the laser medium. In soliton-like pulse shaping, the frequency chirp induced by the positive nonlinearity is balanced by negative group velocity dispersion from prism pairs or chirped mirrors.

Besides modifying the spatial profile of the beam leading to a self-induced quadratic index gradient, the Kerr effect also causes a phase shift among the frequency components as the pulse propagates through the crystal. The time-varying phase shift $\varphi(t)$ or phase modulation produced by the pulse itself can be expressed by

$$\Delta\varphi(t) = (2\pi/\lambda)\gamma I(t)l, \quad (9.50)$$

where $I(t)$ is the intensity and l is the length of the Kerr medium. Since the Kerr effect always leads to an increase of n_0 for increasing intensity, the rising edge of the pulse experiences a medium which is getting optically denser, i.e., $dn_0/dt > 0$. The increasing index of refraction at the rising edge of the pulse delays the individual oscillations of the electric field, which is equivalent of red-shifting of the leading edge.

The interplay between negative dispersion and Kerr-induced self-phase modulation, referred to as soliton like shaping, appears to be the dominant pulse forming mechanism that determines the steady-state pulse duration [9.3].

9.5.3 Examples of Kerr Lens or SESAM Mode-Locked Femtosecond Lasers

Passive mode locking produces shorter pulses compared to active mode locking because the nonlinearity continues to increase as the peak intensity of the pulse increases and the pulse is shortened. In active mode locking, the modulator response is independent of the pulse duration.

Today, passive mode locking via the Kerr-lens effect or by means of a SESAM is the preferred way for femtosecond-pulse generation. The laser crystals most frequently employed are Ti:A₁₂O₃, Cr:LiSAF, and Cr:forsterite. Usually a cw argon laser is used to pump Ti:A₁₂O₃. However, all three crystals can be pumped by solid-state laser sources. A diode-pumped Nd:YAG laser can be employed to pump Cr:forsterite, a doubled Nd:YAG can pump Ti:A₁₂O₃, and Cr:LiSAF can be pumped directly with laser diodes.

A more recent entry into the class of femtosecond lasers is the Yb:YAG laser. It does not produce particularly ultrashort pulses, but can emit a train of sub-picosecond

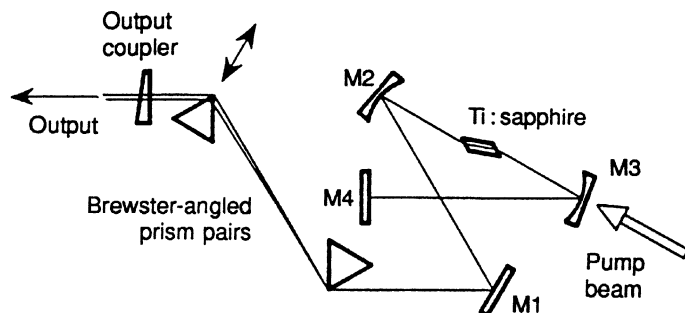


Fig. 9.33. Femtosecond Ti:sapphire laser

mode-locked pulses at very high average power and it can also be pumped directly with laser diodes.

Ti:Sapphire. Since the discovery of the self-mode-locked Ti:sapphire laser, there has been rapid progress in the generation of stable femtosecond lasers. Figure 9.33 depicts the schematic of a typical Kerr lens mode-locked Ti:sapphire laser. Because of its excellent performance, this type of laser has become the dominant source for generating ultrashort pulses. The Ti:sapphire crystal is pumped by either an argon-ion laser emitting around 514 nm, or a diode-pumped solid-state laser generating output at 532 nm. The Ti:sapphire absorbs 532 nm radiation more efficiently therefore 4–5 W of pump power is typically used from a solid-state laser, while 6–8 W of pump radiation from an argon-ion laser is required. A lens focuses the pump light into the Ti:sapphire crystal which provides gain and serves as the nonlinear material for mode locking.

The resonator is a standard folded design with two flat mirrors and two curved mirrors that have typically a 100-mm radius of curvature to produce a beam waist inside the laser crystal. The two prisms compensate for group velocity dispersion in the laser crystal. Mode locking is achieved either by soft aperturing, afforded by the spatial gain profile in the Ti:sapphire crystal, or by adjusting a slit or knife edge close to one of the mirrors. By translating the prisms along their symmetry axis dispersion compensation can be optimized. As is usual with this type of laser, mode locking does not self-start. A slight tap on one of the curved mirrors or motion of one of the prisms initiates the mode locking.

With a configuration as shown in Fig. 9.33, pulses of 15 fs in duration over a tuning range of 790–850 nm have been generated [9.3, 57]. At an absorbed pump power of 3 W in the 4-mm-long crystal, the peak power per pulse was 200 kW. The average output power was 200 mW. The pulse width stated above represents about five optical cycles and the pulse is shorter than 5 μm in space. The frequency-doubled Nd:YLF pump laser was actively mode locked to provide picosecond seed pulses in order to get the KLM operation started.

In ultrashort pulse generation, third-order dispersion in the resonator is the primary factor that determines the minimum pulse width than can be achieved. The

dominant contribution to third-order dispersion is mainly from the prisms employed to correct for second-order dispersion. For this reason, ultrafast femtosecond lasers have only very short Ti:A₁O₃ crystals, typically a few millimeters long to minimize the need for negative dispersion compensation. In addition, the prisms are made of materials, such as fused quartz or CaF₂, that have low positive third-order dispersion.

The shortest mode-locked pulses are obtained by replacing the flat mirrors in Fig. 9.33 with chirped mirrors that correct for third-order dispersion. Typically more than two chirped mirrors are needed to provide sufficient third-order dispersion compensation.

A Kerr-lens mode-locked Ti:sapphire laser with a 2-mm-long crystal featuring a prism pair and dispersive mirrors produced pulses of 5.4 fs duration at repetition rates of 90 MHz and at an average power of 200 mW [9.58]. The pulses are shorter than two cycles of light. To start mode-locked operation one of the mirrors had to be moved slightly.

As a further refinement, a SESAM can be added to the resonator for reliable starting of the mode-locking process. A SESAM-assisted Kerr-lens mode-locked Ti:sapphire laser containing seven broadband dispersive mirrors and a prism pair produced also a pulse width about two wavelengths long [9.59]. The dispersive mirrors together with a pair of fused silica prisms compensate for intracavity dispersion. The resonator contains two 100-mm-radius folding mirrors and a 2.3-mm-long 0.25% Ti:A₁O₃ crystal. Repetition rate of the laser is 100 MHz.

Figure 9.34 shows an optical schematic of a commercial femtosecond Ti:sapphire laser that employs only broadband dispersive mirrors for the compensation of intracavity group-delay dispersion [9.60]. The elimination of prisms permits a very compact design that is also less sensitive to cavity alignment, thereby improving reproducibility and stability of the output pulses. With a 5-W pump beam at 532 nm, the average mode-locked output is 300 mW. Pulses are on the order of 20 fs and peak power is above 200 kW. The pulse repetition rate depending on resonator length is typically 75 MHz.

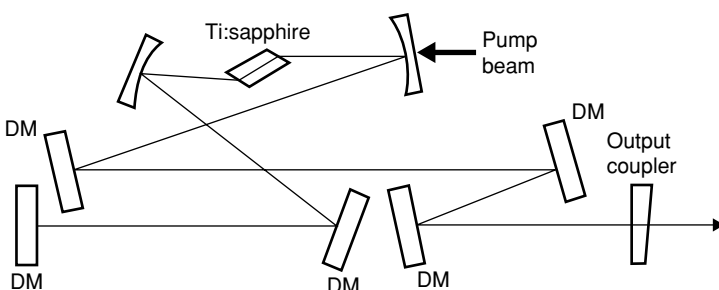


Fig. 9.34. Optical schematic of a KLM mode-locked Ti:sapphire laser using dispersive mirrors (DM) for compensation of intracavity group delay dispersion

Design information such as the parametric dependence of the mode locking on mode radius, reduction of amplitude fluctuations, and optimization of intracavity dispersions can be found in [9.61–63].

Cr:LiSAF. This laser crystal is particularly interesting from an engineering point of view because it can be directly pumped by diode lasers, which opens the possibility for the design of a low cost and compact femtosecond laser system. The absorption band of Cr:LiSAF is around 670 nm. Diode laser pumping is a challenge because the AlGaInP pump sources available at this short wavelength have a lower brightness compared to their counterparts at 800 nm. The advantage of eliminating the expensive pump source required for Ti:sapphire lasers was quickly recognized and a number of diode-pumped femtosecond Cr:LiSAF lasers have been developed shortly after this crystal became available [9.64–66].

Today, Cr:LiSAF and Cr:LiSGAF lasers have produced output powers up to 500 mW [9.67] and pulse durations as short as 45 fs [9.68] and 10 fs [9.69]. As a result of careful modeling of the low threshold performance and intracavity dispersion characteristics, a significant reduction in size and complexity of a low power SESAM mode-locked laser has been reported [9.70]. The laser with a footprint not larger than a sheet of paper produces 113 fs pulses at a repetition rate of 300 MHz and with an average power of about 20 mW. The total electrical input power is less than 500 mW. An optical schematic of the system is shown in Fig. 9.35.

The compactness was achieved by using a three rather than the usual four mirror resonator and by eliminating one of the dispersion-compensating prisms from the highly asymmetric resonator. The 5.5% Cr:LiSAF crystal was pumped with a 50-mW diode emitting at 660 nm and a 60-mW diode at 690 nm. By utilizing a SESAM, the gain medium and mode-locking element are separated, thus allowing reliable and efficient mode locking at a low intracavity power density.

A Kerr-lens mode-locked Cr:LiSAF laser end pumped from both sides by a 350 mW and 500 mW diode laser produced pulses with a minimum duration of 10 fs. The output wavelength was centered at 850 nm. The z -type resonator contained

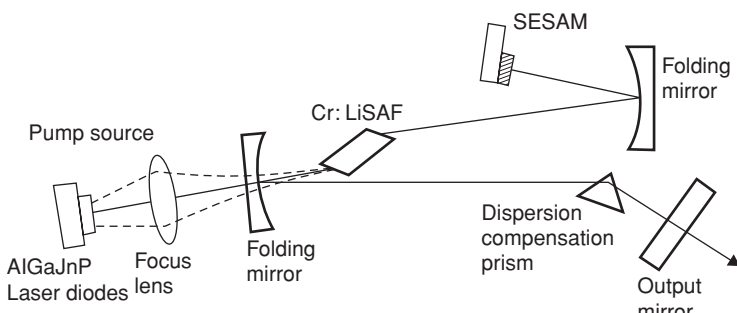


Fig. 9.35. Schematic of a diode-pumped SESAM mode-locked Cr:LiSAF laser

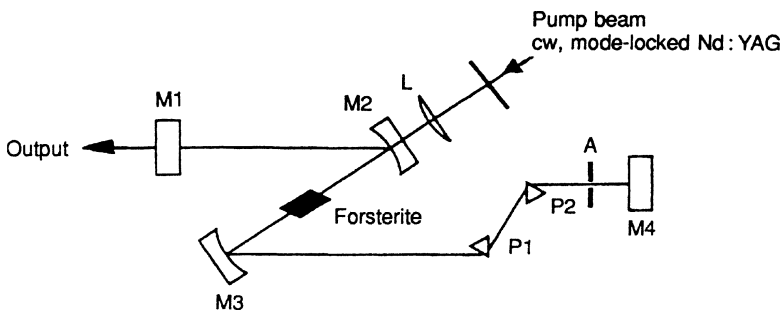


Fig. 9.36. Synchronously pumped KLM Cr:forsterite laser

a 5-mm-long 1.5% Cr:LiSAF crystal, two curved and two flat mirrors, and a prism pair for dispersion compensation [9.69].

Cr:Forsterite. This crystal, which can be pumped with the output of a Nd:YAG laser at 1.06 μm , has a wavelength tunability near 1250 nm. Self-mode locking can be achieved in this material with initiation via active mode locking, regeneratively mode locking, or just by tapping one end mirror or moving a prism [9.71–74].

Figure 9.36 exhibits the schematic of a synchronously pumped KLM Cr:forsterite laser [9.75]. Pulses from an actively mode-locked Nd:YAG laser provide the starting mechanism for self-mode-locked operation. The 12-mm-long Cr:forsterite crystal was placed between two 100-mm radius mirrors, in a standard Z-fold resonator. A prism pair provided dispersion compensation. The laser produced a train of pulses at 82 MHz with a maximum power of 45 mW for 3.9 W of absorbed pump power. The transform limited pulses had a duration of 50 fs.

Yb:YAG. While the emphasis of the lasers discussed so far has been on achieving an ultrashort pulse width, or in designing a very compact and portable femtosecond source, the work with Yb:YAG is aimed at achieving very high average powers. In [9.76] a SESAM mode-locked Yb:YAG laser is described that generated 60 W of average power with 720 fs pulses at a repetition rate of 34 MHz and at a wavelength of 1030 nm. The Yb:YAG crystal was pumped at 940 nm with diode bars at a combined output up to 370 W.

Yb:KGW. The yttrium tungstate laser $\text{Yb:KGd(WO}_4)_2$ is another solid-state laser that can be directly pumped by laser diodes, thus reducing cost and complexity of the laser pumps required for Ti:sapphire and forsterite femtosecond systems. This crystal has a high emission cross section, broad emission spectrum from 1020 to 1060 nm, and can be pumped with diode lasers at 940 or 980 nm. Diode-pumped Yb:KGW lasers have been developed for the generation of femtosecond pulses at an output wavelength of 1048 nm.

Problems associated with the poor thermal properties and quality of the crystal presented a challenge in engineering a viable laser system. However, elimination of

crystal defects, optimization of doping concentration and careful thermal management have led to lasers producing 500-ps pulses at 7 KHz repetition rate and 4 W average power in oscillator–amplifier systems.

9.5.4 Chirped Pulse Amplifiers

The femtosecond oscillators described in the previous subsection generate a train of pulses at a repetition rate of around 100 MHz and with an average power of a few hundred milliwatts. Therefore, the energy of each mode-locked pulse is on the order of a few nanojoules. These pulses have been amplified by as much as a factor of 10^{10} , or up to the joule level, by regenerative amplification followed by a chain of power amplifiers. The chirped-pulse amplification technique was developed to reduce the enormous peak powers in these amplifiers, which would otherwise limit the output energy because of intensity-dependent pulse distortions and damage of the amplifier components.

In a chirped pulse amplifier system, the output pulses from a mode-locked oscillator are stretched by a diffraction grating. A high-speed switch selects a single pulse from the train of pulses from the oscillator. The pulse energy is then amplified in a regenerative amplifier, and after a number of round trips, the switching unit deflects the pulse out of the cavity for further amplification in single- or double-pass amplifiers. At the end of the amplifier chain a second diffraction grating compresses the pulse close to its original pulse length.

Chirped-pulse amplification was first developed for radar and later adapted to the optical regime [9.77]. It is now a powerful technique by which the energy of femtosecond pulses can be increased to produce peak powers in the terawatt regime.

The technique of chirped-pulse amplification uses the dispersion of gratings to expand the pulse width at the input of the amplifier chain by many orders of magnitude and thereby reduces peak power. The chirp process is then reversed after the final amplifier, dispersion is now employed to compress the pulse to near its original duration.

Similar to a prism pair discussed in Sect. 9.5.2, in a pair of diffraction gratings different wavelengths have different path lengths through the system because they diffract from the gratings at slightly different angles. Diffraction gratings have a much larger dispersion compared to prisms and therefore they produce a considerably higher group delay dispersion. On the other hand, insertion losses are higher compared to prisms. For this reason, gratings are not used for intracavity dispersion compensation.

Depending on the arrangement of the two diffraction gratings, positive or negative group velocity dispersion can be obtained.

Typically, pulses are stretched with a dispersive delay line consisting of a pair of gratings arranged to provide positive group-velocity dispersion and compressed with a grating pair which provides negative group-velocity dispersion.

Figure 9.37a illustrates the diffraction gratings arranged to provide positive group delay dispersion, which causes an expansion of the input pulse. By chirping, that is, distributing the frequency content of the pulse in time, a short duration pulse can be expanded to a significantly longer duration. In the pulse expander the transit

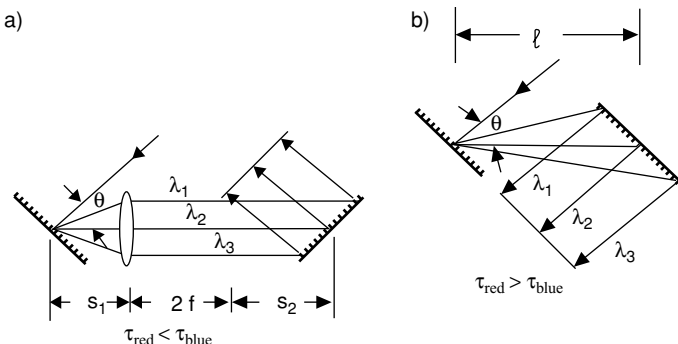


Fig. 9.37. Diffraction gratings arranged for (a) pulse expansion and (b) pulse compression. The optical path for $\lambda_1 < \lambda_2 < \lambda_3$ is shown

time is shorter for the long wavelength. The pulse compressor, Fig. 9.37b, introduces negative group delay dispersion by creating a longer path length for the longer wavelength.

To first order, these arrangements produce a linear delay of frequency with respect to time whose magnitude is proportional to the separation of the gratings and whose sign is opposite—positive for the expander and negative for the compressor.

The group-velocity delay introduced by the first grating pair is compensated by the second pair of gratings if

$$l = 2f - s_1 - s_2. \quad (9.51)$$

And the angle of incidence θ is the same in the pulse expander and compressor.

In an actual system, the optical material of the amplifier chain located between the two grating pairs produces a positive delay. The dispersion occurring in the gratings and amplifier chain have to be balanced to give equal delay for each frequency component of the pulse after amplification and thus create a transform limited pulse.

The gain media that are most commonly employed for chirped amplification are Nd:glass [9.78], Ti:sapphire [9.79, 80], and Cr:LiSAF [9.81, 82]. The performance of Cr:LiSAF lasers is somewhere between Nd:glass and Ti:sapphire. Nd:glass systems produce longer but more energetic pulses than Ti:sapphire lasers. In Nd:glass, the gain bandwidth supports only pulses of several hundred femtoseconds, more than an order of magnitude longer than the pulses from Ti:sapphire lasers. However, the large aperture disk amplifiers available for Nd:glass permit the generation of extremely high peak intensities. With 46-cm aperture Nd:glass amplifiers peak powers above one petawatt have been achieved [9.78].

Scaling of Ti:sapphire chirped pulse amplifier systems have been limited by the availability of large aperture crystals, but up to several hundred terawatts have been produced in these lasers [9.79].

The gratings, typically separated by 1–2 m to provide a large dispersion, can stretch and compress pulses by over three orders of magnitude.

For example, a Cr:LiSAF flashlamp-pumped laser system consisting of a regenerative amplifier and three additional double-pass amplifiers produced 90 fs pulses at a peak power of 8 TW. The 1 nJ input pulse is almost stretched 2000 times to 170 ps before injection into the regenerative amplifier [9.81]. Similarly, a multistage Ti:sapphire laser chain produced 95 fs pulses at an energy of 0.45 J per pulse. In this case, the pulses are stretched to 500 ps before they enter the amplifier chain [9.83].

10. Nonlinear Devices

Nonlinear optical devices, such as harmonic generators and parametric oscillators, provide a means of extending the frequency range of available laser sources. In 1961, Franken and coworkers detected ultraviolet light at twice the frequency of a ruby laser when the beam was propagated through a quartz crystal [10.1]. This experiment marked the beginning of an intense investigation into the realm of the nonlinear optical properties of matter.

Frequency conversion is a useful technique for extending the utility of high-power lasers. It utilizes the nonlinear optical response of an optical medium in intense radiation fields to generate new frequencies. It includes both elastic (optical-energy-conserving) processes, such as harmonic generation, and inelastic processes (which deposit some energy in the medium), such as stimulated Raman or Brillouin scattering.

There are several commonly used elastic processes. Frequency doubling generates a single harmonic from a high-power source. The closely related processes of sum- and difference-frequency generation also produce a single new wavelength but require two input wavelengths. These processes have been used to generate high-power radiation in all spectral regions, from the ultraviolet to the far-infrared. Optical parametric oscillators and amplifiers generate two waves of lower frequency from a pump source. They are capable of generating a range of wavelengths from a single frequency source, in some cases spanning the entire visible and near-infrared regions.

As far as inelastic processes are concerned, the Raman process can be utilized in solid-state lasers for the generation of additional spectral output lines. The strongest interaction is for the output shifted toward a longer wavelength (first Stokes shift), but at sufficiently high-pump intensities additional lines at longer, as well as shorter, wavelengths with respect to the pump wavelength will appear (Stokes and anti-Stokes lines).

Although it produces a small wavelength shift, stimulated Brillouin scattering is mainly of interest for the realization of phase-conjugating mirrors. The application of phase conjugation, or wave front reversal, via stimulated Brillouin scattering, offers the possibility of minimizing thermally induced optical distortions which occur in solid-state laser amplifiers.

10.1 Nonlinear Optical Effects

Nonlinear optical effects are analyzed by considering the response of the dielectric material at the atomic level to the electric fields of an intense light beam. The propagation

of a wave through a material produces changes in the spatial and temporal distribution of electrical charges as the electrons and atoms react to the electromagnetic field of the wave. The main effect of the forces exerted by the field on the charged particles is a displacement of the valence electrons from their normal orbits. This perturbation creates electric dipoles whose macroscopic manifestation is the polarization. For small field strengths this polarization is proportional to the electric field. In the nonlinear case, the reradiation comes from dipoles whose amplitudes do not faithfully reproduce the sinusoidal electric field that generates them. As a result, the distorted reradiated wave contains additional frequencies from that of the original wave.

On a microscopic scale, the nonlinear optical effect is rather small even at relatively high-intensity levels, as the following example illustrates. We will compare the applied electric field strength of a high-intensity beam to the atomic electric field which binds the electrons to the nucleus. The magnitude of the atomic field strength is approximately equal to $E_{\text{at}} = e/4\pi\epsilon_0 r^2$, where e is the charge of an electron, ϵ_0 is the permittivity of free space, and r is the radius of the electron orbit. With $r = 10^{-8}$ cm, one obtains $E_{\text{at}} = 10^9$ V/cm. A laser beam with a power density of $I = 100\text{MW}/\text{cm}^2$ generates an electric field strength in the material of about $E = 10^5$ V/cm according to $I = n_0 E^2 (\mu_0/\epsilon_0)^{-1/2}$, where n_0 is the refractive index and $(\mu_0/\epsilon_0)^{1/2}$ is the impedance of free space. To observe such a small effect, which is on the order of 10^{-4} , it is important that the waves add coherently on a macroscopic scale. This requires that the phase velocities of the generated waves and the incident wave are matched.

In a given material, the magnitude of the induced polarization per unit volume \mathbf{P} will depend on the magnitude of the applied electric field \mathbf{E} . We can therefore expand \mathbf{P} in a series of powers of \mathbf{E} and write

$$\mathbf{P} = \epsilon_0 \chi^{(1)} \mathbf{E} + \epsilon_0 \chi^{(2)} \mathbf{EE} + \epsilon_0 \chi^{(3)} \mathbf{EEE} + \dots, \quad (10.1)$$

where ϵ_0 is the permittivity of free space and $\chi^{(1)}$ is the linear susceptibility representing the linear response of the material. The two lowest order nonlinear responses are accounted for by the second- and third-order nonlinear susceptibilities $\chi^{(2)}$ and $\chi^{(3)}$. The expression of the polarization in anisotropy materials is rather complicated, for the induced polarization depends not only on the magnitude of the electric vector but also on the magnitude and direction of all vectors that characterize the electromagnetic field. Normally $\chi^{(1)} \gg \chi^{(2)} \gg \chi^{(3)}$ and therefore the nonlinear effects will be negligible unless the electric field strength is very high.

The linear term in (10.1) represents three separate equations, one for each value of the i th Cartesian coordinate of \mathbf{P} , that is,

$$\mathbf{P}_i = \epsilon_0 \chi_{ij} \mathbf{E}_j \quad (i, j = 1, 2, 3). \quad (10.2)$$

The linear polarization tensor, which is rank 2, has an array of nine coefficients. The linear susceptibility, related to the refractive index through $\chi = n_0^2 - 1$ and to the dielectric constant $\epsilon = \epsilon_0(1 + \chi)$, is responsible for the linear optical properties of the medium such as refraction, dispersion, absorption, and birefringence. In the linear regime optical properties are independent of light intensity and the wavelength of radiation does not change.

The nonlinear optical susceptibilities of second and third order which describe three- and four-wave mixing processes, respectively, give rise to a large variety of optical phenomena since each electric field can have a different frequency, propagation vector, polarization, and relative phase. Therefore \mathbf{P} can contain many different product terms of the various interacting fields. In the following overview only interactions that are utilized in the nonlinear devices described in the remainder of this chapter are described.

The subject of nonlinear optics has been treated in several books [10.2–6] and tutorial review articles [10.7].

10.1.1 Second-Order Nonlinearities

The second-order susceptibility $\chi^{(2)}$ is responsible for second harmonic generation, sum and difference frequency generation, and optical parametric amplification. Sections 10.2 and 10.3 describe devices based on these nonlinear phenomena. The above-mentioned second-order nonlinear effects are produced by two waves, which interact to produce a third wave. Conservation of momentum and photon energy is always required in these processes. The optical fields of the three waves are coupled to one another through the second-order susceptibility. The coupling provides the mechanism for the exchange of energy among the interacting fields. The second-order nonlinear susceptibility in a Cartesian coordinate system can be written as

$$\mathbf{P}_j = \varepsilon_0 \chi_{ijk}^{(2)} \mathbf{E}_j \mathbf{E}_k, \quad i, j, k = 1, 2, 3. \quad (10.3)$$

The tensor $\chi_{ijk}^{(2)}$ in general has 27 independent coefficients. By taking into account symmetry conditions, the second-order susceptibility can be expressed by a two-dimensional 3×6 tensor, commonly known as the d -tensor. The nonlinear coefficients ranging from d_{11} to d_{36} will be frequently used throughout this chapter.

Most nonlinear crystals are described by only a few d -coefficients. For example, the nonlinear crystal KDP has only three nonvanishing terms (d_{14}, d_{25}, d_{36}). Furthermore, for those crystals of main interest there is usually one predominant coefficient associated with a beam propagation direction which yields maximum harmonic power. In centrosymmetric crystals the $\chi^{(2)}$ tensor is actually zero; therefore second-order nonlinear processes are only possible in crystals that lack inversion symmetry. Using the d -coefficients, the nonlinear polarization is given by

$$\mathbf{P} = \varepsilon_0 d \mathbf{E} \mathbf{E}, \quad (10.4)$$

where d has the dimension of meter per volt.

Sum and Difference Frequency Generation

Two waves of comparable intensity and frequency ω_1 and ω_2 are initially present, and a wave at the third frequency ω_3 is created through the nonlinear interaction

$$\mathbf{P}(\omega_3) = \varepsilon_0 \chi^{(2)} \mathbf{E}(\omega_1) \mathbf{E}(\omega_2), \quad (10.5)$$

where $\omega_3 = \omega_1 + \omega_2$. Similarly, a wave at the difference frequency $\omega_3 - \omega_2 = \omega_1$ may be generated ($\omega_3 > \omega_2 > \omega_1$). Sum frequency generation is described in Sect. 10.2.5. A very common technique to produce the third harmonic of a neodymium laser is, first, the generation of the second harmonic and then sum frequency generation by mixing the second harmonic (ω_2) with the unconverted portion of the fundamental beam (ω_1).

Second Harmonic Generation

This is a special case of frequency mixing with the initial waves having a common frequency, i.e., $\omega = \omega_1 = \omega_2$ and $\omega_3 = 2\omega$ in (10.5). The generation of a second harmonic can be readily shown if we describe the applied field by $E = E_0 \sin(\omega t)$. The induced polarization, according to (10.1), takes the form

$$\mathbf{P} = \varepsilon_0 [\chi^{(1)} \mathbf{E} \sin(\omega t) + \chi^{(2)} \mathbf{E}^2 \sin^2(\omega t) + \dots], \quad (10.6a)$$

which can be written as

$$\mathbf{P} = \varepsilon_0 [\chi^{(1)} \mathbf{E} \sin(\omega t) + 1/2 \chi^{(2)} \mathbf{E}^2 (1 - \cos 2\omega t) + \dots]. \quad (10.6b)$$

In the last expression, the presence of the second term shows that a wave having twice the frequency of the fundamental can be formed in a nonlinear medium. Second harmonic generation is described in Sect. 10.2.

Parametric Amplification

Parametric amplification refers to the growth of two waves in the presence of a strong input wave, which will be referred to as the pump. Energy and momentum are conserved if $\omega_3 = \omega_2 + \omega_1$, where ω_3 is the frequency of the input pump beam and ω_2 and ω_1 are the frequencies of the resulting signal and idler beams. Parametric oscillators are described in Sect. 10.3.

10.1.2 Third-Order Nonlinearities

Third-order optical nonlinearities involve the nonlinear susceptibility tensor $\chi^{(3)}$ in (10.1). This term governs third harmonic generation, optical Kerr effect, Raman effect, and Brillouin scattering. In general, $\chi^{(3)}$ will couple together four frequency components, that is, three fields interact to produce a fourth field,

$$\mathbf{P}(\omega_4) = \varepsilon_0 \chi^{(3)} \mathbf{E}(\omega_3) \mathbf{E}(\omega_2) \mathbf{E}(\omega_1), \quad (10.7)$$

where $\omega_4 = \omega_3 + \omega_2 + \omega_1$. In the above equation $\chi^{(3)}$ is a four-rank tensor with 81 elements, because an array of 3×27 coefficients couple a single component of the polarization \mathbf{P} to three independent components of three electric field vectors.

The third-order optical nonlinearity is thus a four-photon process. There can be up to three different input laser frequencies, but several of the frequencies can also be the same. In a lossless medium the susceptibility coefficients of $\chi^{(3)}$ are real. In

this case, the primary nonlinear optical effects are the generation of new frequency components and the intensity-dependent change in the refractive index (Kerr effect). In third-order interactions involving absorption, the imaginary part of $\chi^{(3)}$ describes Raman and Brillouin scattering.

Third Harmonic Generation

The third harmonic generated by an intense beam at frequency ω can be described by (10.7) with $\omega = \omega_1 = \omega_2 = \omega_3$ and $\omega_4 = 3\omega$. The expression of a sinusoidal electric field raised to the third power will include a term $\sin^3(\omega t) = 3/4 \sin(\omega t) - 1/4 \sin(3\omega t)$, which illustrates the creation of a third harmonic. The possibility of third harmonic generation exists in principle, although it suffers from practical drawbacks. Typical values of $\chi^{(3)}$ are orders of magnitude smaller than $\chi^{(2)}$ coefficients found in nonlinear crystals. Therefore the preferred method of third harmonic generation is the utilization of two second-order effects. (Second harmonic generation, followed by sum frequency mixing to generate the third harmonic, is explained in Sect. 10.2.5.)

Optical Kerr Effect

The third-order nonlinearity can lead to an intensity-dependent refractive index known as the optical Kerr effect. With $\omega_2 = -\omega_1$, (10.7) transforms to

$$\mathbf{P}(\omega) = [\chi^{(3)} \mathbf{E}_{av}^2] \mathbf{E}(\omega), \quad (10.8)$$

where \mathbf{E}_{av} is the average electric field strength. The tensor $\chi^{(3)}$ describes the effect of an intense light beam upon the propagation path of the beam. The self-induced effect manifests itself as an intensity-dependent contribution to the index of refraction

$$n_2 = n_0 + (12\pi/n_0)\chi^{(3)}\mathbf{E}_{av}^2. \quad (10.9)$$

The effect of an intensity-dependent refractive index is exploited in Kerr lens mode locking (KLM), which is described in Sect. 9.2.3. In high-intensity beams the nonlinear refractive index can be the source of optical damage because it can lead to self-focusing and small-scale ripple growth. Both phenomena are discussed in Sect. 4.6.

Stimulated Raman Scattering

This nonlinear process involves the interaction of a laser beam with the molecular vibrations in gases or liquids. In the presence of a strong external electric field, the charge distribution of a diatomic molecule is polarized. The molecule acquires a dipole that can interact with the driving field. The external field exerts a force on the molecule proportional to E^2 . This implies that there must be two input photons driving the interaction. Therefore two electric fields in (10.7) have the same frequency and represent the pump beam ω_p which drives the interaction to provide amplification at $\omega_p - \omega_0$, where ω_0 is the frequency of the molecular vibration wave. In accordance

with (10.7) three waves produce a fourth wave via the third-order polarization, and energy at the pump frequency can be transferred to the signal frequency $\omega_p - \omega_0$. In addition, nonlinear mixing processes create additional frequency components at $\omega_p - j\omega_0$ and $\omega_p + j\omega_0$, where $j = 1, 2, 3 \dots$. Raman lasers employed to shift the wavelength of solid-state lasers are described in Sect. 10.4.

Stimulated Brillouin Scattering

In this process an optical beam interacts with an acoustic wave in the medium. The acoustic wave is associated with the propagation of pressure in the medium, leading to periodic density fluctuations. Electrostriction provides the coupling mechanism between the acoustic wave and electromagnetic wave, that is, a local compression of the medium in response to the strength of the electromagnetic field. An incident laser beam can scatter with the periodic index variations associated with a propagating acoustic wave. The interaction is stimulated because the acoustic and scattered waves can grow as the pump beam is depleted. The acousto-optic interaction with the laser pump beam depends on the intensity of the pump, just as in stimulated Raman scattering; therefore, the polarizability is a function of E^2 . The four-wave mixing process is characterized by two electromagnetic fields with the same frequency ω_p interacting with an acoustic wave of frequency ω_a to produce a fourth wave at $\omega_p - \omega_a$. The frequency of the acoustic wave is determined by the conservation of energy and momentum. The stimulated wave is usually radiated backward toward the incoming pump beam. The acoustical frequency for a backward wave is $\omega_a = 2\omega_p(n_0 v_a/c)$, where v_a is the speed of sound in the medium. Since v_a is very small compared to the speed of light in the medium c/n_0 , the frequency shift is very small.

Acoustic waves occur at frequencies orders of magnitude smaller than molecular vibrations. Brillouin scattering is therefore frequency-shifted from the incident radiation by a much smaller amount as compared to Raman scattering. From an engineering point of view, interest in Brillouin scattering is not related to the frequency shift which occurs in the interaction, but in the phase-conjugate reflection of the pump beam. Brillouin scattering is the mechanism for phase conjugation discussed in Sect. 10.5.

10.2 Harmonic Generation

In this section we will review the basic theory and discuss system parameters and material properties that affect harmonic generation.

Harmonic generation is achieved by sum frequency mixing in birefringent crystals which possess a second-order nonlinear optical susceptibility. In the sum frequency mixing process, two input waves, at frequencies ω_1 and ω_2 , interact in a nonlinear medium to produce a third wave at $\omega_3 = \omega_1 + \omega_2$ via the second-order nonlinear polarization. This process is described mathematically by three coupled differential equations that are obtained from Maxwell's equations. To simplify our analytical treatment we assume absorption losses in the nonlinear crystal to be negligible.

The combination of Maxwell's equations for a lossless, nonlinear dielectric medium leads to the following wave equation [10 8]:

$$\nabla^2 E + \mu_0 \varepsilon \frac{\partial^2 E}{\partial t^2} = -\mu_0 \frac{\partial^2 P_{NL}}{\partial t^2} \quad (10.10)$$

The nonlinear source term on the right side of (10.10) is the nonlinear polarization P_{NL} . The polarization P consists of a linear and a nonlinear term

$$P = \varepsilon_0 \chi_L E + P_{NL}, \quad (10.11)$$

where

$$P_{NL} = 2d_{ijk} E_j E_k. \quad (10.12)$$

For $P_{NL} = 0$, Eq. (10.10) is a homogeneous equation describing propagation of a wave in a linear medium.

We limit our discussion to three monochromatic plane waves of frequencies ω_1 , ω_2 , and ω_3 propagating in the z -direction. The electric field of each wave is expressed as the product of a complex amplitude and exponent summed with the complex conjugate of that product. The addition of the complex conjugate keeps the electric field real. The corresponding fields of the traveling plane waves are

$$E_i(z, t) = \frac{1}{2}[E_{1i}(z) \exp i(\omega_1 t - k_1 z) + \text{c.c.}], \quad (10.13a)$$

$$E_k(z, t) = \frac{1}{2}[E_{2k}(z) \exp i(\omega_2 t - k_2 z) + \text{c.c.}], \quad (10.13b)$$

$$E_j(z, t) = \frac{1}{2}[E_{3j}(z) \exp i(\omega_3 t - k_3 z) + \text{c.c.}], \quad (10.13c)$$

where i, j, k are Cartesian coordinates that are either x or y , k_1, k_2, k_3 are the propagation constants of the three waves, and c.c. denotes the complex conjugate.

For these traveling waves we obtain from the wave equation three coupled, first-order nonlinear differential equations

$$\frac{dE_1}{dz} = -i\omega_1 \sqrt{\mu_0/\varepsilon_1} d_{ijk} E_3 E_2^* \exp(-i\Delta kz), \quad (10.14a)$$

$$\frac{dE_2}{dz} = -i\omega_2 \sqrt{\mu_0/\varepsilon_2} d_{kij} E_1^* E_3 \exp(-i\Delta kz), \quad (10.14b)$$

$$\frac{dE_3}{dz} = -i\omega_3 \sqrt{\mu_0/\varepsilon_3} d_{jik} E_1 E_2 \exp(i\Delta kz). \quad (10.14c)$$

The difference of the propagation constants, i.e., the phase mismatch is expressed by

$$\Delta k = k_3 - k_1 - k_2. \quad (10.15)$$

Equations (10.14), which are solved by integration over the length $z = L$ of the nonlinear medium, provide the basis for our discussion of second and third harmonic generation. We note from (10.14) that the waves at frequencies ω_1 and ω_2 are decaying as they propagate through the crystal, whereas the wave at ω_3 is increasing in amplitude.

10.2.1 Basic Theory of Second Harmonic Generation

Second harmonic generation is the degenerate case of three-wave interaction where two of the waves have equal frequencies $\omega_1 = \omega_2 = \omega$ and $\omega_3 = 2\omega$. Therefore E_1 and E_2 in (10.14) are the electric fields of the same fundamental beam. Since $E_1 = E_2 = E_\omega$ and $E_3 = E_{2\omega}$, Equations (10.14a) and (10.14b) are identical and (10.14) reduces to two coupled differential equations

$$\frac{dE_\omega}{dz} = i\omega\sqrt{\mu_0/\varepsilon_\omega}d_{ijk}E_{2\omega}E_\omega^* \exp(-i\Delta kz), \quad (10.16a)$$

$$\frac{dE_{2\omega}}{dz} = -i2\omega(1/2)\sqrt{\mu_0/\varepsilon_{2\omega}}d_{ijk}E_\omega^2 \exp(i\Delta kz). \quad (10.16b)$$

The factor of $(1/2)$ has to be included in (10.16b) to account for the degeneracy $\omega_2 = \omega_1$. For efficient energy transfer it is necessary that the interacting waves remain in phase. With $k_3 = k_{2\omega}$, $k_1 = k_2 = k_\omega$ and $\Delta k = 0$ in (10.15) we obtain from (10.15)

$$k_{2\omega} = k_\omega + k_\omega \quad (10.17)$$

Since $k_\omega = 2\pi n_\omega/\lambda_0$ and $k_{2\omega} = 4\pi n_{2\omega}/\lambda_0$ from the above condition (10.17) follows $n_\omega = n_{2\omega}$. Therefore the phase mismatch expressed by (10.15) can be written in the case of frequency doubling as follows

$$\Delta k = \frac{4\pi}{\lambda_0}(n_\omega - n_{2\omega}), \quad (10.18)$$

where λ_0 is the wavelength at the fundamental wave in vacuum.

Before discussing the exact solution of (10.16) we will consider two special cases which are usually treated in textbooks [10.9], namely (a) frequency conversion at low efficiency and (b) conversion under perfect phase matching conditions.

Second Harmonic Conversion at Low Efficiency

In this case we can make the assumption that the fundamental beam is not depleted, and therefore $dE_\omega/dz = 0$ in (10.16a) and only Eq. (10.16b) has to be considered. By observing the tensor properties of d_{ijk} , integration of (10.16b) yields

$$I_{2\omega} = C^2 L^2 I_\omega^2 \frac{\sin^2(\Delta k L/2)}{(\Delta k L/2)^2}, \quad (10.19a)$$

where

$$C^2 = \frac{8\pi^2 d_{\text{eff}}^2}{\varepsilon_0 c \lambda_0^2 n_0^3}, \quad (10.19b)$$

L is the length of the nonlinear crystal, n_0 is the refractive index at the fundamental wavelength λ_0 , and d_{eff} is the effective nonlinear coefficient of the tensor d_{ijk} for a particular nonlinear crystal

$$d_{ijk} = \varepsilon_0 d_{\text{eff}}. \quad (10.20)$$

The unit of d_{eff} in (10.19b) is m/V. Some authors include ϵ_0 in the nonlinear coefficient in this case the unit of d_{ijk} is As/V² and $d_{ijk} [\text{As}/\text{V}^2] = 8.855 \times 10^{-12} d_{\text{eff}} [\text{m}/\text{V}]$. Introducing the appropriate constants into (10.19b) we obtain

$$C = 5.46 \frac{d_{\text{eff}}}{\lambda_0 n_0^{3/2}}, \quad (10.21)$$

where the unit of d_{eff} is pm/V, λ_0 is measured in μm , and the unit of C is $\text{GW}^{-1/2}$. In deriving (10.19a) we used the conversion of electric field strength E to intensity I

$$I = n_0 E^2 / 2Z_0, \quad (10.22)$$

where Z_0 is the plane wave impedance in vacuum $Z_0 = (\mu_0 / \epsilon_0)^{1/2} = 120\pi [\text{V}/\text{A}]$.

The conversion efficiency for frequency doubling follows from (10.19a)

$$\eta = C^2 L^2 I_\omega \text{sinc}^2(\Delta k L / 2). \quad (10.23)$$

The second harmonic power generation is strongly dependent on the phase mismatch expressed by the sinc^2 function, as is illustrated in Fig. 10.1. In this case, a variation of Δk was obtained by changing the crystal temperature. The harmonic power is at maximum when $\Delta k = 0$, that is, at the exact phase matching temperature. For a fixed Δk , second harmonic power as a function of distance l along the crystal grows or

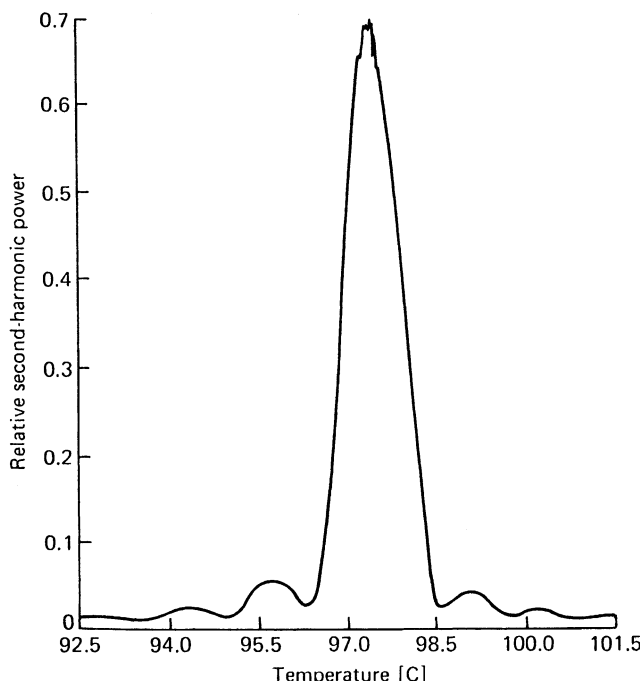


Fig. 10.1. Second-harmonic generation as a function of temperature in a $\text{Ba}_2\text{NaNb}_5\text{O}_{15}$ crystal employed to frequency-double a Nd:YAG laser.

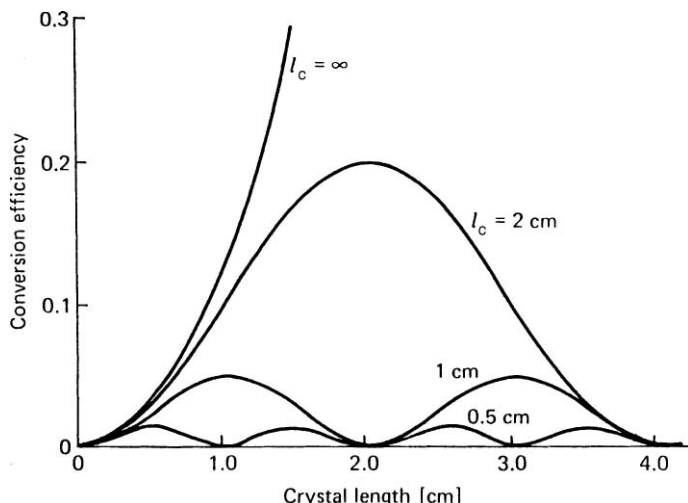


Fig. 10.2. Second-harmonic power conversion efficiency as a function of distance l from the entrance surface of a CDA crystal. Parameter is the coherence length l_c ($C = 1.1\text{ GW}^{-1/2}$; $\lambda = 1.06\text{ }\mu\text{m}$; $I = 100\text{ MW/cm}^2$).

decays with a period of $\Delta k l / 2 = \pi$. Half of this distance has been termed coherence length l_c . It is the distance from the entrance face of the crystal to the point at which the second harmonic power will be at its maximum value. This parameter is not to be confused with the coherence length l_c the laser beam, which was defined in Chap. 5. For normal incidence the coherence length is given by

$$l_c = \pi / \Delta k. \quad (10.24)$$

If one expresses the phase mismatch Δk in terms of coherence length in (10.23) one obtains

$$\eta = C^2 L^2 I_\omega \operatorname{sinc}^2(\pi L / 2l_c) \quad (10.25)$$

The oscillatory behavior of (10.25) is shown in Fig. 10.2 for several values of l_c . In the ideal case of perfect phase matching conditions, i.e., $\Delta k = 0$ or $l_c = \infty$, the second harmonic conversion efficiency is proportional to the square of the crystal length. This is of course only true for small signals or low conversion efficiencies.

If the crystal is not perfectly phase-matched the highest second harmonic power we can expect to generate will be the signal obtained after the beam propagates one coherence length, independent of the length of the crystal.

The decrease in harmonic power, for example, between l_c and $2l_c$, is explained by a reversal of the power flow. Power at the second harmonic is coupled back into the input beam. Thus we find that in a lossless medium the power oscillates back and forth between the harmonic and the fundamental wave.

In almost all practical cases the coherence length is limited by the divergence and the line width of the laser beam and by angular and thermal deviations of the crystal from the phase matching angle and temperature.

Following the work of Eimerl [10.10], the subsequent calculations of nonlinear conversion can be substantially simplified if one combines the various parameters of (10.23). The terms in front of the sinc function can be combined in the so-called drive η_0

$$\eta_0 = C^2 L^2 I_\omega. \quad (10.26)$$

The terms in the argument of the sinc function are combined in the dephasing δ

$$\delta = \Delta k L / 2. \quad (10.27)$$

With the definition of the drive and dephasing factors we can restate (10.23) as follows

$$\eta = \eta_0 \operatorname{sinc}^2 \delta. \quad (10.28)$$

Frequency Doubling Assuming Perfect Phase Matching Conditions

When the fundamental and second harmonic waves propagate through the nonlinear crystal with exactly equal phase velocities, the propagation vector mismatch is zero. With the assumption of $\Delta k = 0$, Eqs. (10.16a, b) are greatly simplified and can be integrated to yield

$$\eta = \tanh^2 \sqrt{\eta_0}. \quad (10.29)$$

This equation predicts that the conversion efficiency asymptotically approaches one as the drive becomes very large (see uppermost curve in Fig. 10.3). For small η_0 one obtains $\eta = \eta_0$, which also follows from (10.28) for $\Delta k = 0$. Equation (10.29) takes the depletion of the fundamental beam into account, but dephasing as it occurs in real systems is ignored.

Harmonic Generation with Pump Depletion and Dephasing

Most modern laser systems generate high peak powers with good beam quality and incorporate nonlinear crystals of high optical quality which leads to conversion efficiencies typically between 50 and 80%. In this case depletion of the fundamental beam as well as phase mismatch has to be considered to adequately describe the experimental results. Armstrong et al. [10.8] have solved the coupled nonlinear differential equations (10.16) for arbitrary Δk and intensities. We will use the solution in a format which is particular useful for numerical calculations [10.10]

$$\eta = \eta_m s n^2 [\sqrt{\eta_0 / \eta_m}, \eta_m^2], \quad (10.30a)$$

where

$$\eta_m = 1 + (\delta^2 / 2\eta_0) - \sqrt{[1 + (\delta^2 / 2\eta_0)]^2 - 1}. \quad (10.30b)$$

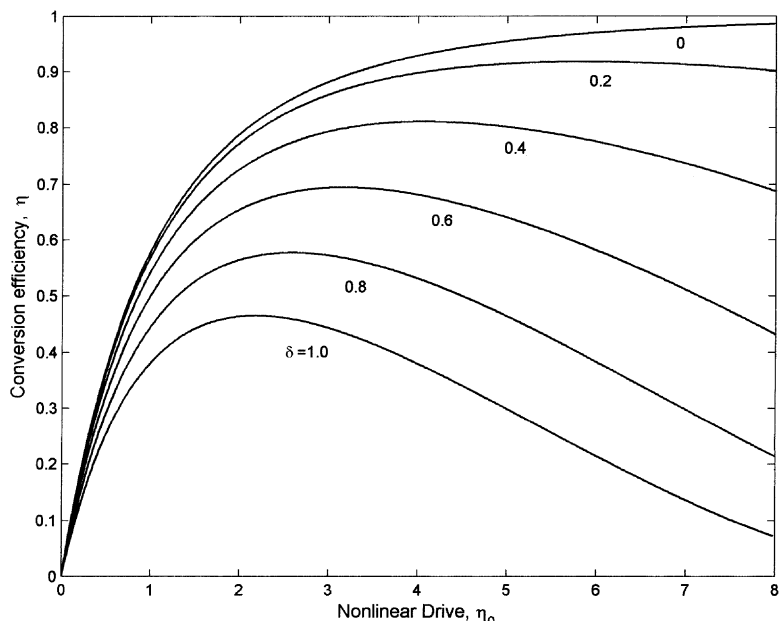


Fig. 10.3. Plane wave conversion efficiency as a function of the nonlinear drive. Parameter is the dephasing δ

The expression for the conversion efficiency contains the Jacobi elliptic function $\text{sn}(u, m)$. This is a periodic function with argument u and a period determined by the modulus m . For $m = 0$, the elliptic function reduces to the sine function $\text{sn}(u, 0) = \sin u$, and for $m = 1$ the period is infinite $\text{sn}(u, 1) = \tanh u$. Since the highest value $\text{sn}^2(u, m)$ can reach is 1, the term η_m in front of the Jacobi function determines the maximum efficiency that can be achieved at the optimum nonlinear drive.

Math packages such as MATLAB or MATHEMATICA include the $\text{sn}(u, m)$ function and therefore the expression can easily be evaluated for specific system parameters. The conversion efficiency in (10.30) is a function of only two parameters: the phase mismatch between the two beams expressed by the dephasing factor δ , and the nonlinear drive η_0 which is proportional to the input beam intensity. Figure 10.3 shows a plot of second harmonic conversion efficiency as a function of the nonlinear drive with the dephasing factor as parameter. When perfect phase matching is achieved ($\delta = 0$), the transfer of energy from the input wave to the second harmonic is maximized and the curve is identical to the one obtained from (10.29). When the drive η_0 is small relative to unity, the slope of the curves is the same as given by the no-depletion expression (10.28).

When both fundamental wave depletion and dephasing are considered, second harmonic efficiency rises with increasing drive until an optimum value is reached. Back-conversion is the reason for the reduction of the conversion efficiency after a peak value has been reached. When the phases are not perfectly matched, power is cycled between the fundamental and harmonic waves. The efficiency peaks and then oscillates between the peak and zero in a non-sinusoidal fashion. Mathematically

this is expressed in (10.30) by a rapid rise of efficiency for small values of η_0 (i.e., low intensities or short crystal length), until the terms containing δ dominate and the efficiency decreases.

We note also from Fig. 10.3 that second harmonic generation becomes increasingly more sensitive to dephasing δ as the drive η_0 increases. This explains why focusing a beam beyond the optimum spot size does not lead to a further increase in efficiency. Focusing the beam into the nonlinear crystal increases intensity as well as beam divergence and therefore dephasing. At one point the adverse effect of dephasing on the efficiency dominate over any benefits gained from a further increase in intensity.

In comparing the results of (10.30) with the approximations of (10.28) and (10.29) we note that the exact solution predicts that for a fixed crystal length and phase mismatch there is an optimum pump energy at which the conversion efficiency is maximized. The approximations predict no such optimum. Furthermore the conversion efficiencies calculated from (10.30) are considerably below the values obtained from the approximations. For example, if we consider harmonic generation with a drive of $\eta_0 = 1$ and dephasing $\delta = 1$, we obtain from (10.30) a conversion efficiency of $\eta = 0.38$. The approximation (10.28) which ignores depletion of the fundamental beam yields $\eta = 0.71$, and the approximation that does not take phase mismatch into account (10.29) gives a value for the efficiency of $\eta = 0.62$.

Figure 10.4 shows the same result as Fig. 10.3 but on an expanded scale for the region of greatest interest for most laser systems.

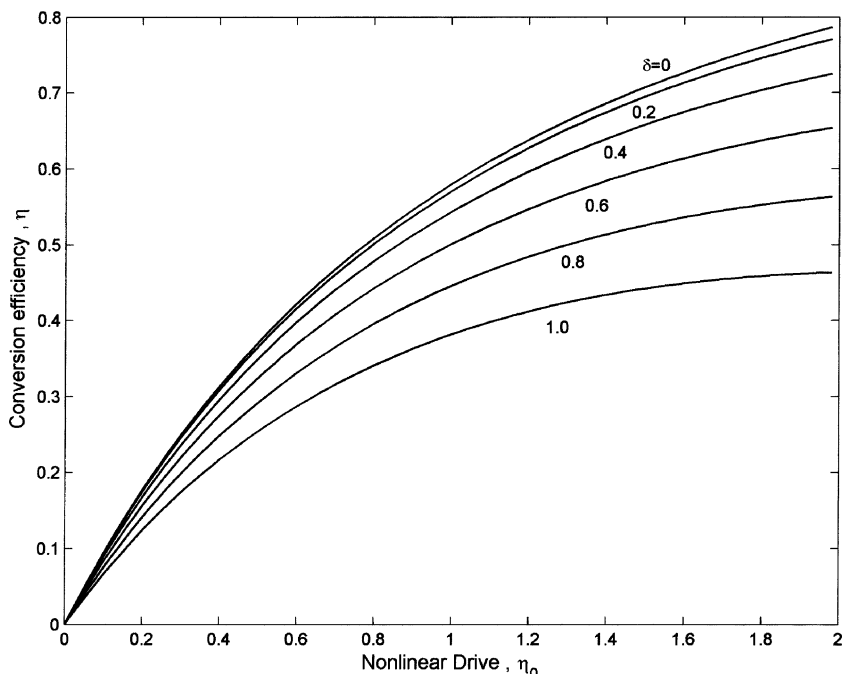


Fig. 10.4. Conversion efficiency vs. nonlinear drive on an expanded scale with dephasing as parameter

Before we can relate the results of (10.30) to real situations we have to express dephasing in terms of systems parameters.

Second harmonic conversion depends on parameters that are related to the laser source, such as power density, beam divergence, and spectral line width, and parameters associated with the harmonic generator, such as the value of the nonlinear coefficient, crystal length, and angular, thermal, and spectral sensitivity to deviations from the exact phase matching angle.

The most critical *laser parameters* are power density and beam divergence. In general, one finds that Nd-doped crystals have sufficiently narrow line widths for efficient harmonic generation. In these lasers attention is focused mainly on obtaining a diffraction limited beam, i.e., TEM₀₀ mode operation. Nd:Glass lasers and tunable lasers require in addition a reduction of the spectral line width.

The most important intrinsic *crystal parameters* are the nonlinear coefficient and the angular sensitivity to the phase match condition. In the technique of index matching, the dependence of the refractive index of the extraordinary ray on the propagation direction in birefringent crystals is exploited to match the phase velocity of the fundamental and second harmonic waves.

In principle, by adjusting the crystal orientation we can achieve $\Delta k = 0$ for plane waves. However, real beams have a curved wavefront that can be thought of as a bundle of rays with different slope angles and intensities. Consequently, it is impossible to achieve perfect phase matching for all rays simultaneously.

In the phenomenological model described here the fundamental beam is characterized by an average intensity and an average beam angle. Half of this beam angle multiplied by the crystal's sensitivity to angular deviations from the phase match condition defines the phase mismatch

$$\Delta k = (\beta_\theta / n_0)(\theta/2), \quad (10.31)$$

where θ is the FWHM beam divergence of the fundamental beam measured *outside* the crystal, (β_θ / n_0) is the angular sensitivity, and n_0 is the refractive index. The parameter β_θ is the angular sensitivity of the wave-vector mismatch caused by a deviation of the beam from the phase-matched direction *inside* the crystal. For the special case of a noncritically phase-matched crystal, the dependence of Δk on $\theta/2$ becomes a second-order effect, as will be discussed in the next section. The beam divergence of a diffraction-limited or a multimode beam as a function of diameter, wavelength, and beam quality factor M can be calculated from the equations provided in Chap. 5.

Numerical calculations based on (10.30) can be carried out if we know the relevant parameters that describe the nonlinear medium and the input laser beam. The nonlinear crystal is characterized by the nonlinear parameter C , the angular sensitivity (β_θ / n_0) , and length L , and the fundamental beam is described by the intensity I_ω and divergence θ . These five parameters are needed to calculate the drive η_0 and dephasing δ .

Although (10.30) is considerably more accurate compared to the approximations (10.28) and (10.29), second harmonic generation efficiency is still somewhat overstated because the input and output electromagnetic fields have been assumed to be plane waves, i.e., the input beam is flat in time and spatial extent. Real beams are nonuniform in both space and time, and the spatial and temporal wings convert with different efficiencies than do the peaks.

Instead of characterizing the fundamental beam by an average intensity and beam angle, a more accurate calculation can be based on a detailed numerical model that includes the effects of diffraction and beam nonuniformity. This requires calculation of the harmonic conversion according to (10.30) for rays having different intensities and slope angles and integration over the cross section of the beam.

For example, one can divide the beam into strips oriented along the angular sensitive direction of the crystal. Each strip has a different intensity and deviates by a different angle from the exact phase match condition. Conversion efficiency is calculated for each strip with subsequent integration over the angular extent of the beam.

A number of important conclusions can be drawn from Fig. 10.3.

- Tighter focusing of the fundamental beam into the nonlinear crystal will increase beam intensity and beam divergence; consequently, both the nonlinear drive and dephasing will increase. For a given crystal length and laser input power there is an optimum spot size that maximizes the conversion efficiency. Beyond this point tighter focusing will not result in a higher efficiency because any further increase in intensity is counteracted by the adverse effect of a larger dephasing factor δ .
- At a fixed input intensity and beam divergence there is an optimum length of the nonlinear material. As the length is increased both the drive and dephasing will increase. The drive varies quadratically with crystal length whereas the dephasing varies linearly. The optimum crystal length is a tradeoff between drive and dephasing. Conversion efficiency as a function of crystal length in KTP for different input beams is illustrated in Fig. 10.5. Efficiency increases rapidly

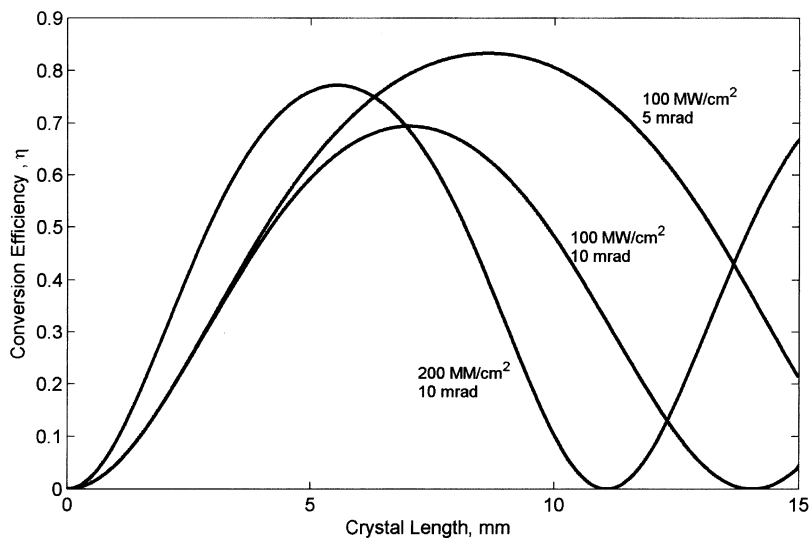


Fig. 10.5. Conversion efficiency in KTP as a function of crystal length for different values of beam intensities and beam angles

for very short lengths because both the drive and dephasing are small. After an optimum length is reached, dephasing, which is proportioned to length, starts to dominate over a further increase in drive, and the conversion decreases.

- (c) A telescope inserted in front of the nonlinear crystal has the same effect as a length change since the drive (i.e., intensity) will change quadratically with the telescope magnification, and dephasing (i.e., beam divergence) will change linearly.

We will consider second harmonic generation of a 1.06- μm beam with an 8-mm-long KTP crystal. The input beam has an intensity $I_\omega = 200 \text{ MW/cm}^2$ and a diameter of 350- μm and is three times diffraction-limited ($M = 3$). KTP has a nonlinear coefficient of $C = 6.9 \text{ GW}^{-1/2}$ and an angular sensitivity $(\beta_\theta/n_0) = 0.32 \text{ cm}^{-1} \text{ mrad}^{-1}$. From these values follows a beam divergence of $\theta = 11.6 \text{ mrad}$ and from (10.26, 27, 31) we obtain $\eta_0 = 6.1$ and $\delta = 0.74$. Figure 10.3 gives a conversion efficiency of $\eta = 0.46$ for these parameters. From Fig. 10.3 we can see that the crystal is operated at an intensity that is too high since the operating point is well beyond the optimum. For example, a shorter crystal with a length of 5 mm will result in a drive of $\eta_0 = 2.38$ and dephasing of $\delta = 0.46$. These parameters yield an efficiency of $\eta = 0.74$, that is near the optimum. The same improvement in efficiency can be obtained by adding a telescope with magnification $m = 1.6$ in front of the 8-mm-long crystal. The upcollimating telescope will reduce the intensity and dephasing.

KDP crystals have a lower nonlinear coefficient compared to KTP and for efficient conversion they require exposure to very high intensities. A typical example would be a 1.5-cm-long crystal inserted into a 1.06- μm beam having an intensity of $I_\omega = 1 \text{ GW/cm}^2$. Assuming a beam of 4-cm diameter that is two times diffraction-limited, and using the nonlinear constant $C = 0.97 \text{ GW}^{-1/2}$ and angular sensitivity $(\beta_\theta/n_0) = 1.73 \text{ cm}^{-1} \text{ mrad}^{-1}$ for KDP, we calculate a drive of $\eta_0 = 2.1$ and a dephasing of $\delta = 0.04$. With these values a second harmonic conversion efficiency of $\eta = 0.80$ is obtained from Fig. 10.3.

Figure 10.6 shows experimental data and predicted performance for a harmonic generator comprising an 8-mm-long KTP crystal. The fundamental beam was generated by a Q-switched diode-pumped Nd:YAG laser at 1064 nm. The laser generated a pulse energy of up to 40mJ in a 12-ns pulse. At the maximum output intensity of 175 MW/cm^2 the conversion efficiency approached 80%. The beam having a diameter of 1.5 mm was weekly focused into the crystal, which resulted in a beam divergence of 5 mr. If one introduces these parameters together with the data for KTP from the previous example, one obtains the theoretical curve in Fig. 10.6. The theoretical doubling efficiency calculated from (10.30) gives quite acceptable agreement with the experimental values.

10.2.2 Phase Matching

With typical dispersion values in the visible region, the coherence length in most crystals is limited to about 10 μm . For this reason the intensity of second harmonic

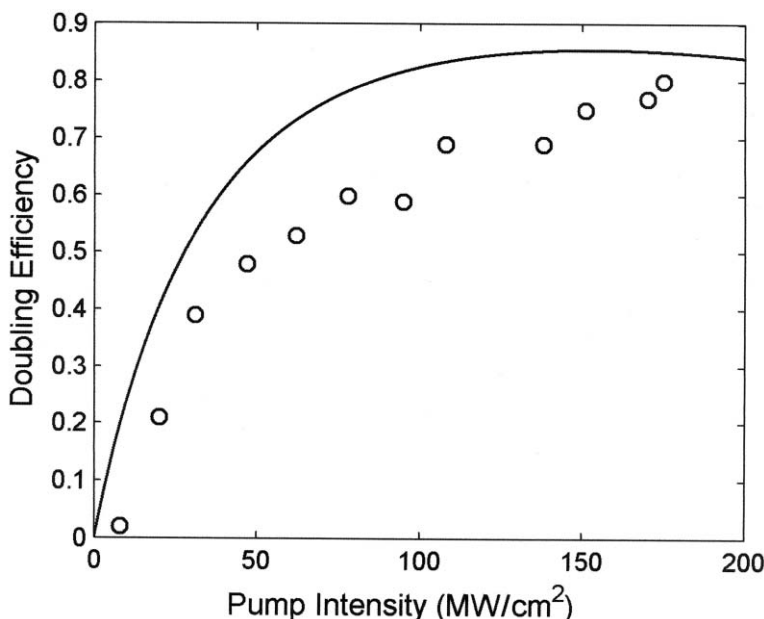


Fig. 10.6. Second harmonic conversion efficiency versus power density for a KTP crystal pumped by a Q-switched Nd:YAG laser at 1060 nm

power is small. Only if the refractive indices of the fundamental and second harmonic wave (i.e., n_ω and $n_{2\omega}$) can be made essentially equal can one expect high conversion efficiencies.

An effective method of providing equal-phase velocities for the fundamental and second harmonic waves in the nonlinear medium utilizes the fact the dispersion can be offset by using the natural birefringence of uniaxial or biaxial crystals. These crystals have two refractive indices for a given direction of propagation, corresponding to two orthogonally polarized beams; by an appropriate choice of polarization and direction of propagation it is often possible to obtain $\Delta k = 0$. This is termed phase matching or index matching.

We will illustrate the method of index matching in uniaxial crystals because of its relative simplicity. The reader interested in a review of phase matching in biaxial crystals is referred to reference [10.11]. For a general introduction to crystal optics the following references are recommended [10.12–14].

Uniaxial crystals, which include KDP and its isomorphs, BBO, and LiNbO₃ have an indicatrix which is an ellipsoid of revolution, with the optic axis being the axis of rotation, as shown in Fig. 10.7. The two directions of polarization and the indices for these directions are found by drawing a line through the center of the ellipsoid in the direction of beam propagation (line OP in Fig. 10.7), the intersection of a plane perpendicular to OP with the ellipsoid is an ellipse. The two axes of this ellipse are parallel to the two directions of polarization, and the length of each semi-axis is equal to the refractive index in that direction.

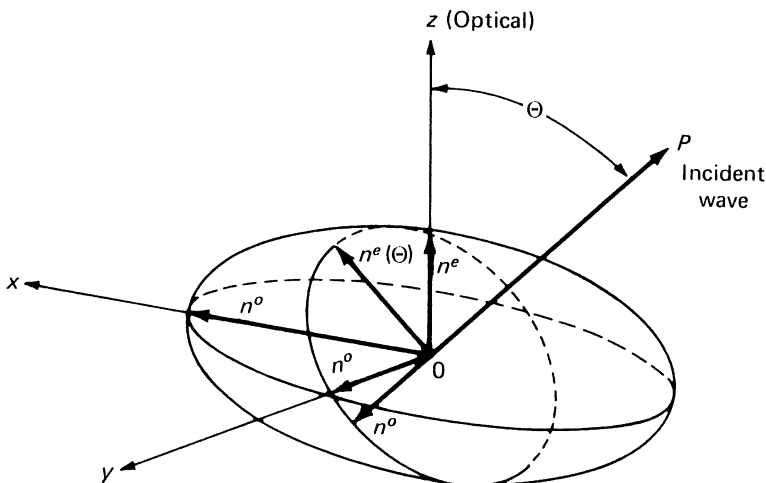


Fig. 10.7. Indicatrix ellipsoid of a uniaxial crystal. Also shown is a cross section perpendicular to the light propagation direction P

We now examine how the indices of refraction vary when the direction of propagation is changed. We notice that for the direction of polarization perpendicular to the optic axis, known as the ordinary direction, the refractive index is independent of the direction of propagation. For the other direction of polarization, called the extraordinary direction, the index changes between the value of the ordinary index n^o when OP is parallel to z and the extraordinary index n^e when OP is perpendicular to z . The dependence of n^e on the angle between the propagation direction and the optic axis is given by the index ellipsoid equation

$$[n^e(\theta)]^{-2} = (n^o)^{-2} \cos^2 \theta + (n^e)^{-2} \sin^2 \theta, \quad (10.32)$$

where the superscripts “o” and “e” refer to the ordinary and the extraordinary rays.

Changing the point of view, we look now at the shape of the wavefronts for these two rays instead of their direction and polarization. Assuming that the input is a monochromatic point source at O , the expanding wavefront for the o-ray is spherical, whereas the spreading wavefront for the e-ray is an ellipsoid. This property of crystals is described by the index surface, which has the property that the distance of the surface from the origin along the direction of the wave vector is the refractive index. For a uniaxial crystal this surface has two sheets—a sphere for ordinary waves polarized perpendicular to the optic axis with index n^o , and an ellipsoid for extraordinary waves with index $n^e(\theta)$. By definition the optic axis is that direction at which the o- and e-rays propagate with the same velocity. If the value of $n^e - n^o$ is larger than zero, the birefringence is said to be positive, and for $n^e - n^o$ smaller than zero the birefringence is negative; the corresponding crystals are called positive or negative uniaxial. Figure 10.7 shows a cross section of the index surface of a negative uniaxial crystal (for the moment we consider only the solid lines n_o and n_e). The complete surfaces are

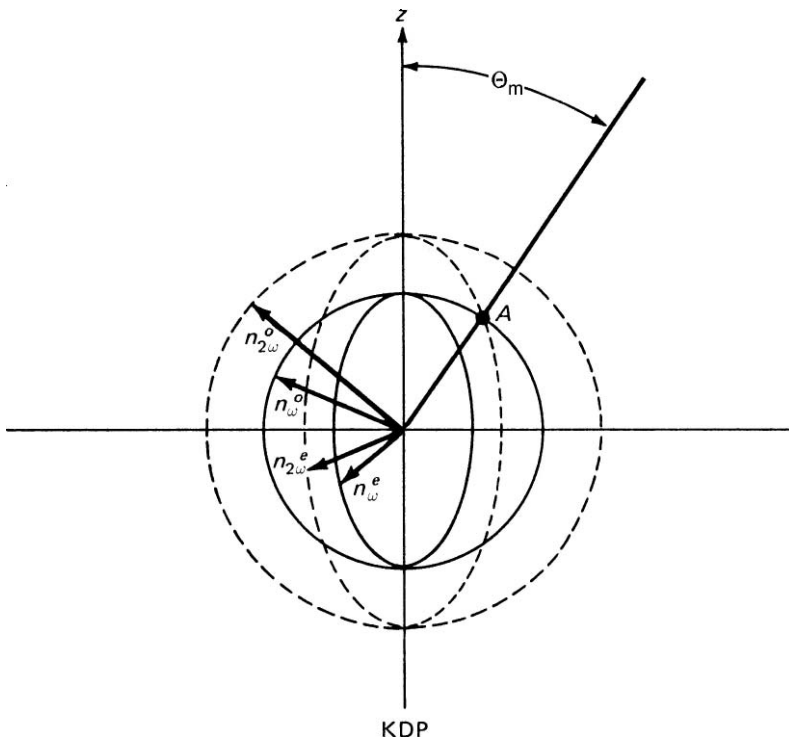


Fig. 10.8. Cross section of the index surface of a negative uniaxial crystal for two different wavelengths

generated by rotating the given sections about the z -axis. The wavefront velocity v and the refractive index n_0 are related by $v = c/n_0$, where c is the velocity of light in vacuum.

Both refractive indices n^o and n^e are a function of wavelength. Figures 10.8 and 10.9 illustrate how the dependence of the refractive index on beam direction, wavelength, and polarization can be utilized to achieve angle-tuned phase matching. The dashed lines in these figures show the cross section of the index surfaces $n_{2\omega}$ at the harmonic frequency. As can be seen, the negative uniaxial crystal has sufficient birefringence to offset dispersion, and the matching condition can be satisfied for a beam deviating from the z -axis by the angle θ_m .

The directions for phase-matched second harmonic generation are obtained by considering the intersection of the index surfaces at the fundamental and harmonic frequencies. As was mentioned earlier, frequency doubling may be considered as a special case, where two incident waves with electric fields E_m and E_n are identical wave forms. In a negative uniaxial crystal there are two loci where the index surfaces intersect and $\Delta k(\theta) = 0$ depending on the two possible orientations for the linear polarization vectors of the incident beams. In the type I process the two input waves have the same polarization and in the type II process the waves are orthogonally polarized.

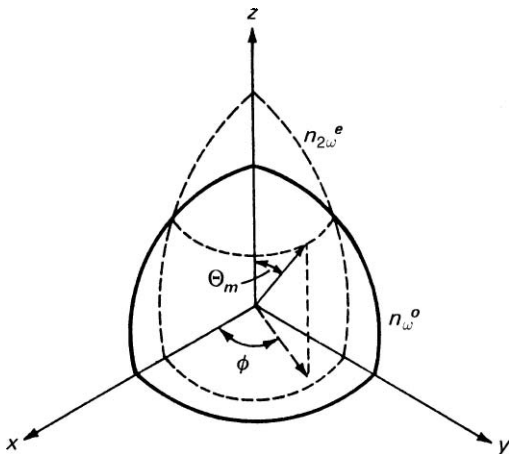


Fig. 10.9. Direction for phase-matched second harmonic generation (type I) in a uniaxial crystal, where θ_m is the phase matching angle measured from z , and ϕ is the azimuth angle measured from x .

Type I Phase Matching

Phase matching can occur in a symmetrical cone at θ_m about the optic axis, where two o-rays at ω are matched to an e-ray at 2ω .

$$n_{2\omega}^e(\theta_m) = n_\omega^o \quad (10.33)$$

The phase-matching angle θ_m is obtained by combining (10.32) and (10.33)

$$\sin^2 \theta_m = \frac{(n_\omega^o)^{-2} - (n_{2\omega}^e)^{-2}}{(n_{2\omega}^e)^{-2} - (n_{2\omega}^e)^{-2}}. \quad (10.34)$$

Owing to its application in large Nd:Glass lasers, the nonlinear crystal KDP has been analyzed in great detail. We will use KDP as an example to illustrate phase matching.

For frequency doubling of $1.05\text{-}\mu\text{m}$ radiation, the beam propagation vector is at $\theta_m = 41^\circ$ with respect to the optical axis of the KDP crystal, and the azimuth angle is at $\phi = 45^\circ$ in type I phase matching. The fundamental beam is polarized perpendicular to the optical axis (ordinary direction) and the frequency doubled beam is polarized parallel to the optical axis of the crystal (extraordinary direction). The orientation of the beam propagation vector, polarization, and crystal axes is illustrated in Fig. 10.10a for the case of KDP.

The harmonic power is not independent of the azimuth angle of the phase-matched direction (Fig. 10.9). In general, d_{eff} is a combination of one or several coefficients of $\chi^{(2)}$, and the angles θ and ϕ , which define the direction of the wave propagation vector. For example, for KDP and its isomorphs and type I index matching, one obtains [10.16]

$$d_{\text{eff}} = d_{36} \sin 2\phi \sin \theta_m \quad (10.35)$$

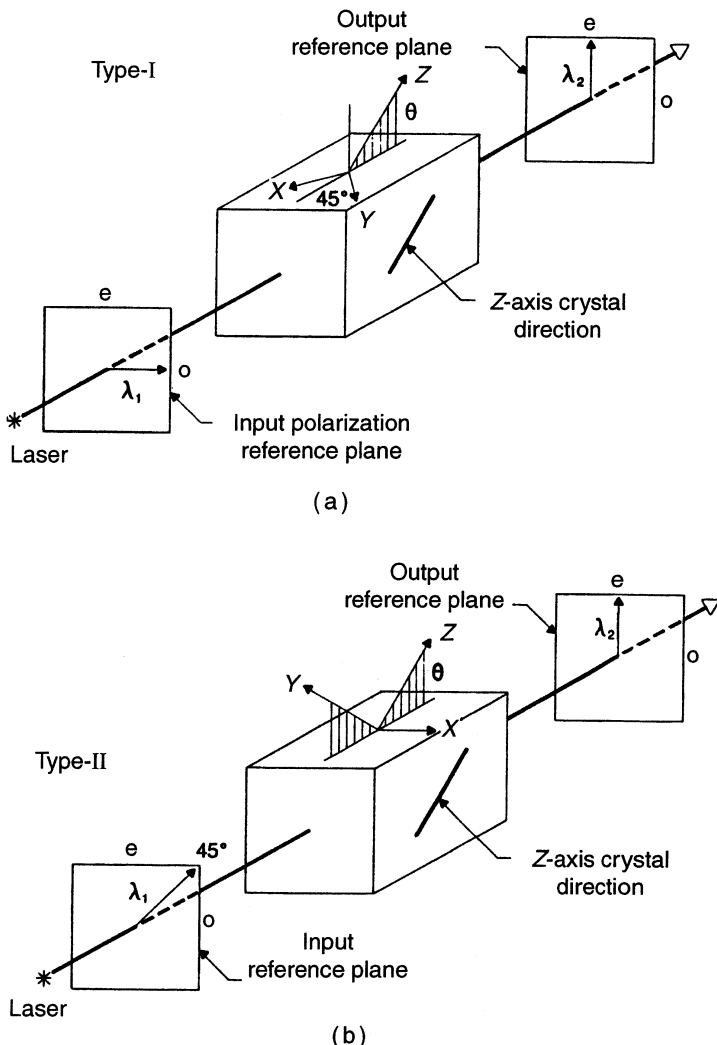


Fig. 10.10. Crystal and electric vector orientation for harmonic generation in KDP and its isomorphs for (a) type I and (b) type II phase matching [10.15]

Type II Phase Matching

In this case phase matching occurs in a cone at θ_m about the optic axis where an o-ray and an e-ray at ω are matched to an e-ray at 2ω . For negative uniaxial crystals

$$n_{2\omega}^e(\theta_m) = (1/2)[n_\omega^e(\theta_m) + n_\omega^o]. \quad (10.36)$$

Solution of (10.36) may be obtained numerically. For KDP, the angle between the beam direction and the crystal axis is $\theta_m = 59^\circ$ and $\phi = 90^\circ$ with respect to the x-axis.

A single linearly polarized fundamental beam incident on the crystal may be equally divided into o- and e-rays by orienting the polarization vector at 45° with respect to the x -axis. The polarization vector of the harmonic beam is rotated 45° from the fundamental beam with the polarization parallel to the optical axis (see Fig. 10.10b). For type II phase matching in KDP one obtains [10.16]

$$d_{\text{eff}} = (1/2)(d_{36} + d_{14}) \cos 2\phi \sin 2\theta_m \quad (10.37)$$

Comparing type I and type II phase matching, we find that type I is more favorable when θ_m is near 90° , whereas type II leads to a higher d_{eff} when θ_m lies near 45° .

Parameters Affecting the Phase Matching Condition

Owing to the dependence of the refractive indices on angle, temperature, and wavelength, any change of these parameters will cause a deviation from the exact phase matching condition. The sensitivity of second harmonic conversion to these parameters is obtained by treating Δk in (10.18) as a function of angle, temperature, and wavelength, i.e., $\Delta k = \Delta k(\theta, T, \lambda)$. Values of the angular, thermal, and spectral sensitivity of important nonlinear crystals are summarized in Subsect. 10.2.3.

With the exception of tunable lasers and Nd:Glass lasers, the line width of most solid-state lasers is sufficiently narrow for efficient harmonic conversion. It should be noted, however, that the sensitivity of the phase matching angle to laser line width increases dramatically at shorter wavelengths and can become an issue in frequency quadrupling of infrared lasers. In Nd:Glass lasers, the spectral line width is narrowed by employing Nd:YLF oscillators to drive the Nd:Glass amplifier chains.

Thermal loading of the nonlinear crystal caused by absorption of the fundamental or harmonic beam or by multiphoton absorption processes can result in a phase mismatch. Absorption in the crystal will lead to thermal gradients as well as thermally induced stresses. Heating of the nonlinear crystal caused by residual absorption is particularly a problem in doubling of high-power cw beams. Temperature changes of the doubling crystal may also be the result of ambient temperature variations. An example of the temperature tuning range of $\text{Ba}_2\text{NaNb}_5\text{O}_{15}$ is shown in Fig. 10.1. Because of its importance, angular sensitivity will be discussed in greater detail below.

Angular Sensitivity. Dephasing depends on the deviation of the beam direction from the phase matching angle that is caused by the divergence of the input beam or by an imperfect crystal orientation.

For type I phase matching we can derive an analytical expression for the angular sensitivity. Introducing (10.33) into (10.18) gives the following expression for the phase mismatch

$$\Delta k = \frac{4\pi}{\lambda_0} [n_\omega^o - n_{2\omega}^e(\theta)]. \quad (10.38)$$

For a direction close to the perfect phase matching direction θ_m we can express the difference of the refractive indices as follows

$$n_\omega^o - n_{2\omega}^e(\theta) = \frac{\partial[n_\omega^o - n_{2\omega}^e(\theta)]}{\partial\theta}(\theta - \theta_m) \quad (10.39)$$

The dependence of $n_{2\omega}^e$ on the angular direction in the crystal is given in (10.32). To simplify the calculation, Eq. (10.32) can be approximated as follows:

$$n_{2\omega}^e(\theta) = n_{2\omega}^o - (n_{2\omega}^o - n_{2\omega}^e) \sin^2 \theta. \quad (10.40)$$

Introducing (10.40) into (10.39) yields

$$n_\omega^o - n_{2\omega}^e(\theta) = \partial\theta(n_{2\omega}^o - n_{2\omega}^e) \sin 2\theta_m, \quad (10.41)$$

where we note that $\partial n_\omega^o / \partial\theta = 0$ and $\partial n_{2\omega}^o = \partial\theta = 0$.

With the result of (10.41) we can express the wave vector mismatch defined in (10.38) as follows:

$$\Delta k = \beta_\theta \delta\theta, \quad (10.42)$$

where

$$\beta_\theta = \frac{4\pi}{\lambda_0}(n_{2\omega}^o - n_{2\omega}^e) \sin 2\theta_m. \quad (10.43)$$

In the above expression β_θ is the angular sensitivity of the nonlinear crystal and $\delta\theta$ is the deviation of a ray from the phase matching direction inside the crystal. We will equate this angle with the expansion half angle of a multimode beam inside the crystal

$$\theta/2 = (\lambda_0/\pi n_0 w_0)M. \quad (10.44)$$

This is the same equation as presented in Chap. 5, except for the inclusion of n_0 since beam divergence is measured inside the crystal. If we define the beam divergence outside the crystal, as is customary, the refractive index n_0 in (10.44) is removed and included in the angular sensitivity (β_θ/n_0) as was done in (10.31).

The angular sensitivity is inversely proportional to the so-called angular acceptance angle of the crystal. The angle $\Delta\theta$ describes the angular bandwidth at full width and half maximum (FWHM). In other words, it is the full acceptance angle over which the crystal can be tilted before the second harmonic power decreases to less than half. If the angular tuning range is stated for an internal angle, the value has to be multiplied by the refractive index of the crystal to convert it to an external angle.

Figure 10.11 illustrates the angular tuning range for a barium borate crystal. The curve is obtained from the expression (10.19a) for low conversion efficiency $I_{2w} \sim \text{sinc}^2(\Delta k L/2)$, and $\Delta k = (\beta_\theta/n_0)\delta\theta$ given in (10.42), where $\delta\theta$ is measured external to the crystal. The values of BBO are $\beta_\theta/n_0 = 6.6 \text{ (mrad cm)}^{-1}$ and $L = 0.7 \text{ cm}$. Experimental data can be found in [10.18].

From (10.19a) it follows that the conversion efficiency will be reduced to one-half of its peak value for

$$\Delta k L/2 = 1.39. \quad (10.45)$$

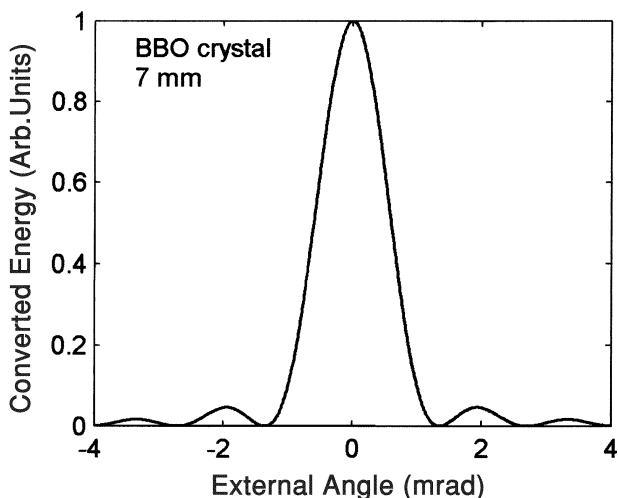


Fig. 10.11. Angular dependence of harmonic power generation in BBO at low conversion efficiency for a 7-mm-long crystal

If we eliminate Δk in (10.42) with the aid of (10.45) we obtain an expression for the acceptance angle of the crystal

$$\Delta\theta = \frac{5.56}{(\beta_\theta/n_0)L}. \quad (10.46)$$

In the literature, values for β_θ or β_θ/n_0 are published depending whether the angular deviation from the phase matching condition is measured inside or outside the crystal.

Critical and Noncritical Phase Matching

If phase matching can be accomplished at an angle of 90° with respect to the optical axis ($\theta_m = 90^\circ$) we can make the approximation $\sin 2(90^\circ + \delta\theta) \approx 2\delta\theta$ in (10.43). Instead of Δk being linear with $\delta\theta$, the dependence of Δk on beam divergence or angular misalignment is now a much smaller quadratic term

$$\Delta k = \beta'_\theta (\delta\theta)^2, \quad (10.47)$$

where

$$\beta'_\theta = (8\pi/\lambda_0)(n_{2\omega}^o - n_{2\omega}^e).$$

Another important advantage of phase matching at $\theta_m = 90^\circ$ is the absence of walk-off caused by double refraction. If phase matching is accomplished at an angle other than 90° with respect to the optic axis, the direction of power flow (Poynting vector) of the fundamental and second harmonics will not be completely collinear but occur at a small angle. For a negative uniaxial crystal and type I phase matching,

this angle is given by [10.17]

$$\tan \rho = \frac{(n_\omega^0)^2}{2} \left[\frac{1}{(n_{2\omega}^e)^2} - \frac{1}{(n_{2\omega}^0)^2} \right] \sin 2\theta. \quad (10.48)$$

The angle ρ has the effect of limiting the effective crystal length over which harmonic generation can take place. The distance at which the fundamental and harmonic beam just separate is called the aperture length l_a . For Gaussian beams the aperture length is

$$l_a = \sqrt{\pi} w_0 / \rho \quad (10.49)$$

where w_0 is the fundamental beam radius.

Because of this beam walk-off and the much smaller angular tolerance, phase matching at angles other than one of the principal axes of the crystal is called critical phase matching. The difference between critical and noncritical phase matching can be illustrated by comparing two uniaxial crystals. Phase matching in KDP type I for second harmonic generation at 1.064- μm requires an angle of $\theta_m = 41^\circ$ between the beam direction and optic axis. Provided that n_ω^0 and $n_{2\omega}^e$ are nearly equal and $d(n_\omega^0 - n_{2\omega}^e)/dT \neq 0$, noncritical phase matching can be achieved by temperature-tuning the crystal for type I phase matching in uniaxial crystals. One example is LiNbO₃. Second harmonic generation in LiNbO₃ occurs at $\theta_m = 90^\circ$ for 1.064- μm radiation, provided the crystal is at a temperature of 107°C (for a crystal doped with 5% MgO). As a result of the noncritical phase matching, LiNbO₃ has a much larger angular tolerance, and the beam divergence introduces a phase shift Δk that is over an order of magnitude smaller in LiNbO₃ as compared to KDP (see next section).

10.2.3 Properties of Nonlinear Crystals

Table 10.1 lists phase matching parameters and properties of several important nonlinear materials for 1064 to 532 nm conversion [10.16, 19–25]. Frequency doubling of neodymium lasers is one of the major applications of harmonic generation.

From purely theoretical considerations it would seem that the crystal with the highest nonlinear coefficient would be the most desirable material to use in a doubling experiment. However, for a nonlinear crystal to be of practical use, damage threshold, optical quality, chemical stability, and hardness are of equal importance. For example, despite the lower nonlinear coefficient of KDP compared to the other materials discussed in this section, conversion efficiencies as high as 80% have been obtained from these crystals. Since a high conversion efficiency is actually the result of material properties as well as pump source characteristics, the high peak power, narrow spectral bandwidth, small beam divergence, and clean spatial and temporal beam profiles obtained from Nd:Glass lasers employed in fusion research make possible such high harmonic conversions even in crystals with modest nonlinearity. Another example is Barium sodium niobate (Ba₂NaNb₅O₁₅) featured in Fig. 10.1, which has a nonlinear coefficient 38 times larger than KDP. The material showed great

Table 10.1. Phase matching parameters for 1064 to 532 nm conversion

	Crystal				
	KDP	KTP ^a	BBO	LBO ^a	LiNbO ₃ ^b
Phase matching parameters					
Type	I	II	I	I	I
Angle[°]	41.2	24.3	22.8	11	90
Temperature [°C]	25	25	25	25	107
Efficiency parameters					
Eff. nonlinear coefficient $d_{\text{eff}}[\text{pm/V}]$	0.37	3.18	1.94	1.16	4.7
External angular sensitivity $\beta_{\theta}/n_0[(\text{mrad cm})^{-1}]$	1.73	0.35	6.6	0.65	0.12
Walk-off angle[°]	1.60	0.26	3.19	0.35	0
Bandwidth (FWHM)					
Angular $L\Delta\theta [\text{m rad cm}]$	3.2	15.9	0.84	8.5	46.3
Thermal $L\Delta T [\text{°C cm}]$	6.7	25	55	8.4	0.7
Spectral $L\Delta\lambda [\text{nm cm}]$	0.66	0.56	0.66	0.75	0.23
Material parameters					
Refractive index n°	1.49	1.74, 1.75	1.65	1.56, 1.56	2.23
n^e	1.46	1.84	1.54	1.61	2.15
Absorption [%/cm]	0.5	0.5	0.5	0.5	0.2
Damage threshold [GW/cm ²]	8	1	1.5	2.5	0.2

^aBiaxial crystal.^bDoped with 5% MgO.

promise initially but index variations introduced during the growth process could not be eliminated and production was dropped.

At the present time, the leading candidate material for nonlinear experiments with solid-state lasers is KTP since the crystal has a large nonlinear coefficient, high damage threshold, and a large angular and temperature acceptance range. Its major drawbacks are the limited size (about 1–2 cm³) and the high cost associated with the difficult growth process. KDP is superior to any other nonlinear crystal with regard to availability in large sizes combined with an excellent optical quality. Crystals with cross sections of 30 cm² have been produced. Crystals grown from the melt such as LiNbO₃ or KTP are generally hard, chemically stable, and can easily be polished and coated. Solution-grown crystals such as KDP and its isomorphs are soft and hygroscopic. These crystals need to be protected from the atmosphere.

From Table 10.1 it follows that KDP has the lowest nonlinear coefficient of the crystals listed but the highest damage threshold; the reverse is true for LiNbO₃. The other crystals KDP, LBQ, and BBO are in between these two extremes. Damage threshold is the parameter where the published values show large variations because the result of a measurement depends on pulse duration, beam quality, spot size, and whether surface or bulk damage is considered. For Q-switch pulses in the 10- to 20-ns range, typical damage threshold are about 400–500 MW/cm² for the crystals listed, except LiNbO₃ which has a much lower threshold. The values in the GW/cm² range listed in Table 10.1 are for subnanosecond pulses.

An idea of a crystal's sensitivity to a departure in angle, temperature, and wavelength from the ideal phase matching condition can be gleaned from the respective bandwidth data. However, it should be pointed out that the bandwidth is defined at the low conversion limit (10.19a). As we have seen from the results displayed in Fig. 10.3, second harmonic generation becomes increasingly more sensitive to changes in Δk as the intensity increases, i.e., the bandwidth decreases at high efficiencies. For example, at a nonlinear drive of $\eta_0 = 3$, the efficiency drops one half from 0.9 to 0.45 for a change in dephasing of $\delta = 1.0$. The change of δ required to reduce efficiency by one half in the low conversion limit is, according to (10.45), a factor $\delta = 1.39$.

A more useful parameter for efficiency calculations is therefore the angular sensitivity also listed in Table 10.1. As was explained earlier, in a 90° phase matching condition the effect of beam divergence on the interaction length is minimized. This explains the large acceptance angle of LiNbO_3 .

If birefringence is a slow function of temperature, then the crystal has a wide central peak, making it easier to maintain peak output in the presence of small temperature fluctuations. In this regard, KTP and BBO outperform other crystals. Crystals which have a birefringence that is not strongly dependent on wavelength allow efficient doubling of laser beams that have a broad spectral bandwidth.

KDP and Its Isomorphs. The crystals of this family have proven to be an important group of useful second harmonic generators. The most prominent member of this group of nonlinear crystals is potassium dihydrogen phosphate, KH_2PO_4 (symbol KDP). Because of the availability of large aperture harmonic crystal assemblies, KDP is the material of choice for the large Nd:Glass lasers employed in fusion research. Other related crystals are potassium dideuterium phosphate, KD_2PO_4 (symbol KD*P); cesium dihydrogen arsenate (CDA) and cesium dideuterium arsenate, CsD_2AsO_4 (symbol CD*A); and ammonium dihydrogen phosphate, $\text{NH}_4\text{H}_2\text{PO}_4$ (symbol ADP). The crystals which are all negative uniaxial are grown at room temperature from a water solution which makes large, distortion-free, single crystals available. Transparency exists from about 0.22 to 1.6 μm .

Deuteration increases the infrared limit to about 1.9 μm . The greatest attributes of this family of crystals are their resistance to laser damage and their high optical quality. Opposing these advantages are several disadvantages. The materials have fairly low refractive indices, typically 1.50–1.55, and therefore they have small nonlinear coefficients. All of the KDP isomorphs are water-soluble and have a maximum safe operating temperature of about 100°C . The crystals are sensitive to thermal shock, and should be heated slowly at a rate of less than about $5^\circ\text{C}/\text{min}$.

ADP and KDP were the first crystals used for the demonstration of phase-matched second harmonic generation. Some of the other isomorphs have been used because the temperature dependence of their refractive index allows noncritical phase matching for particular interactions. For example, CDA and CD*A 90° phase-match the important 1.06- μm transition of Nd:YAG and Nd:Glass. With the exception of KDP, the isomorphs have been replaced by the other crystals mentioned in Table 10.1. Calculations of various basic properties of KDP related to the generation of the second, third, and fourth harmonics of 1- μm laser radiation for five different conversion processes

can be found in [10.19]. Figure 10.10 shows the crystal and electric vector orientation for harmonic generation in KDP and its isomorphs.

Potassium Titanyl Phosphate (KTP)

The crystal KTiOPO_4 (KTP) is a unique nonlinear optical material that is being widely used for second harmonic generation of Nd lasers emitting around $1 \mu\text{m}$. KTP is also very attractive for various sum and difference frequency and optical parametric applications over its entire transparency range from 0.35 to $4.0 \mu\text{m}$. Although a few specific characteristics of other materials are better, KTP has a combination of properties that make it unique for second-order nonlinear optical applications, and second harmonic generation of Nd lasers. In particular, the crystal has large nonlinear coefficients; and the adequate birefringence in the $y-z$ and the $x-z$ planes allows phase matching of the more efficient type II process over a large wavelength range. It has wide acceptance angles, an unusually large temperature bandwidth, relatively good thermal properties, and a high damage threshold. KTP is the best nonlinear material for Nd:lasers to emerge in recent years. The major drawback is the difficult growth process required to produce these crystals, which leads to high cost and small-size crystals.

KTP decomposes on melting ($\approx 1150^\circ\text{C}$) and hence normal melt processes cannot be used to grow this material. However, single crystals of KTP can be grown by both hydrothermal and flux techniques. Currently crystals up to 20 mm in length are commercially available. KTP crystallizes in the orthorhombic point group $\text{mm}2$. The crystal structure, refractive indices, and phase matching parameters have been reported in [10.16, 22].

Figure 10.12 shows the transmission curve for KTP. The material is transparent from $0.35 \mu\text{m}$ to about $4.0 \mu\text{m}$. The optical spectrum is structure-free except for traces of OH^- absorption bands observed at 2.8 and $3.5 \mu\text{m}$.

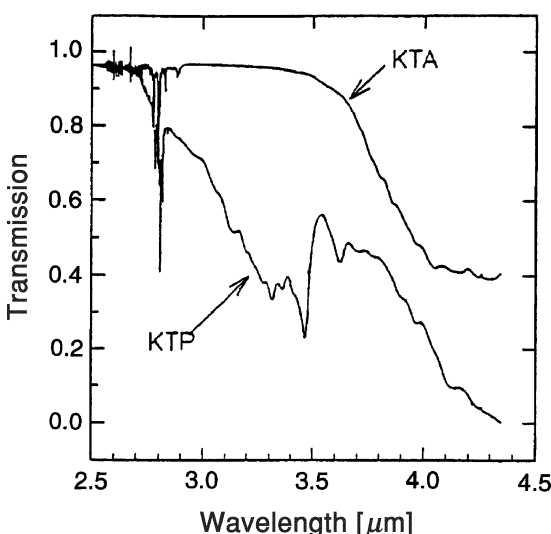


Fig. 10.12. Optical transmission of KTP and KTA [10.20]

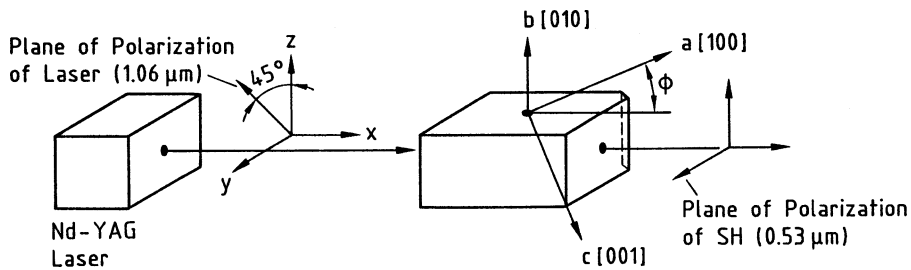


Fig. 10.13. Orientation of KTP for type-II interaction at $1.06 \mu\text{m}$. $\phi = 26^\circ$ for hydrothermally and $\phi = 21^\circ$ for flux-grown material [10.21]

Figure 10.13 shows the crystal orientation for the phase match condition of the type II interaction at $1.06 \mu\text{m}$. It should be noted that the phase match angle ϕ measured from the x -axis in the xy plane is different for flux and hydrothermally grown crystals. The phase match direction in KTP for second harmonic generation of $1.06\text{-}\mu\text{m}$ radiation results in a walk-off angle of 4.5 mrad between the fundamental and second harmonic beam.

Frequency-doubling efficiencies in excess of 65% are now routinely obtained from KTP pumped by high-quality laser beams. However, KTP suffers from gradual photochemical degradation (gray tracking) which is cumulative with exposure to a combination of second harmonic and fundamental radiation. This degradation leads to increased absorption in the crystal, which can eventually cause crystal failure. The photochemical effect is reversed by operating the KTP at an elevated temperature. Crystals operating at flux levels of 150MW/cm^2 and temperatures of 80°C have shown lifetimes in excess of 20 million pulses with $>60\%$ conversion efficiency. However, there have been failures owing to bulk damage in crystals operated at 65°C and lower. (see also Sect. 11.3.4).

Potassium Titanyl Arsenate (KTA)

KTA is isomorphic with KTP, but has lower absorption losses in the $3\text{--}6 \mu\text{m}$ region (see Fig. 10.12). It has about the same nonlinear coefficients and high damage threshold of KTP. Since KTA does not phase-match a $1.06\text{-}\mu\text{m}$ laser for second harmonic generation, the main attraction of this material is for applications in optical parametric oscillators. Properties of this material can be found in [10.23].

Lithium Triborate (LBO)

LiB_3O_5 (LBO) is a nonlinear optical crystal characterized by good UV transparency, a high optical-damage threshold, and a moderate nonlinear optical coefficient [10.24–26]. These properties, along with its mechanical hardness, chemical stability, and nonhygroscopicity, make LBO an attractive alternative to KTP. A number of laser systems have been reported that employ LBO for frequency doubling of pulsed as

well as cw-pumped intracavity-doubled Nd lasers. For example, up to 105 W in the green has been reported with a pulsed laser (see Sect. 10.2.6).

At a temperature of 148°C, LBO can be noncritically phase-matched at 1064 nm for second harmonic generation. In this case the acceptance angular bandwidth is 52 mr cm ($\theta = 90^\circ$, $\Phi = 0$). This large acceptance angle combined with the high damage threshold permits tight focusing of the fundamental beam in intracavity frequency-doubled systems.

For second harmonic generation of low- and medium-power Nd lasers KTP is generally preferred owing to its larger nonlinear coefficient. For second harmonic conversion at high peak powers or high average powers LBO has the advantage of a higher damage threshold.

Beta-Barium Borate. The material $\beta\text{-BaB}_2\text{O}_4$ (BBO) is a nonlinear optical crystal which possesses excellent properties for nonlinear frequency conversion in a spectral range that extends from the ultraviolet to the mid-infrared. This material has a moderately large nonlinear coefficient, a large temperature tolerance, low absorption, and a very high damage threshold. The principal shortcoming with BBO is the low angular tolerance of 0.8 mr cm, which requires a diffraction-limited beam for efficient frequency doubling.

BBO is of particular interest for frequency doubling into the blue region. The transmission band for BBO extends to 200 nm in the UV so that single or multiphoton absorption is not a problem with this material. BBO has been used to double the output of a Ti:Sapphire laser with efficiencies up to 60%. Relevant data can be found in [10.16, 24, 27].

Lithium Niobate (LiNbO_3). This material is nonhygroscopic and hard, taking a good polish readily. The uniaxial crystal, belonging to the trigonal point group $3m$, has a large nonlinear coefficient relative to KDP. The crystals of lithium niobate are transparent in the region of 0.42–4.2 μm . Temperature sensitivity of birefringence is such that, by varying the temperature, phase matching can be achieved at 90° to the optical axis.

Unfortunately, LiNbO_3 is particularly susceptible to photorefractive damage from visible or UV radiation. This optical-index damage is reversible if the ambient temperature of the crystal is increased to about 170°C, which is above the annealing temperature for the photorefractive damage. Doping of LiNbO_3 with 5% of MgO reduces photorefractive damage and permits noncritical phase matching at a somewhat lower temperature, namely 107°C [10.28].

Despite the high nonlinear coefficient, and the ease of handling and polishing, the need for operation at elevated temperatures combined with a relatively low damage threshold have severely limited practical applications for this material.

The emergence of periodically poled LiNbO_3 (PPLN), which will be discussed in Sect. 10.3, has attracted renewed interest in this material. In PPLN, the largest nonlinear index of LiNbO_3 can be utilized. This allows efficient nonlinear conversion at modest power levels which are well below the damage threshold.

Cesium Borate (CBO)

Besides BBO and LBO there are two other members of the borates that are important for harmonic generation with solid-state lasers, namely CsB_3O_5 (CBO) and $\text{CsLiB}_6\text{O}_{10}$ (CLBO). The latter two crystals are mainly of interest for UV and deep UV production. Acceptance of these crystals was hampered in the past by the availability of high-quality crystals. It has been reported that a new modified crystal growth process improved the quality of borate crystals [10.29]. Both CBO and CLBO are hygroscopic and are usually operated at elevated temperatures between 100 and 140°C .

In [10.30], third harmonic generation at 355 nm by use of a type II CBO crystal is described. The output at the third harmonic was 3 W obtained at a repetition rate of 31 KHz. Conversion efficiency from the fundamental to the third harmonic reached 30%. The same reference contains also the nonlinear characteristics of a number of borate crystals for the generation of 355-nm radiation. At a phase matching angle of 40.2° for type II conversion, CBO yields a nonlinear coefficient of $d_{\text{eff}} = 1.15 \text{ pm/V}$. The acceptance angular bandwidth of type II is larger compared to the other borates.

Cesium Lithium Borate (CLBO)

Generation of short-wavelength UV radiation with solid-state lasers is of interest for photolithography and for writing gratings into fibers. Borate crystals have a UV cutoff wavelength between 160 and 190 nm. The shortest wavelength and the most powerful output in the UV regime has been obtained with the nonlinear crystal $\text{CsLiB}_6\text{O}_{10}$ (CLBO). It is the primary candidate for the generation of deep UV radiation.

By mixing the third harmonic of an Nd:YLF laser with the output from a Ti:Sapphire laser using two CLBO crystals an output of 1.5 W at 196 nm was obtained. [10.31]. Phase matching properties for the generation of 241 nm and 196 nm radiation with CLBO are also listed in this reference. With CLBO as the nonlinear crystal over 20 W at 266 nm was generated by frequency-doubling a green laser Q-switched at 10 KHz [10.32]. The 15-mm-long CLBO crystal was cut for type I conversion and heated to 140°C to prevent hygroscopic deterioration. Fourth and fifth harmonic generation in CLBO with 28% and 7% conversion efficiency, respectively, have been obtained from a repetitively Q-switched Nd:YAG laser [10.33]. The average power was 2.5 W at 266 nm and 0.6 W at 213 nm. The fifth harmonic was generated by sum frequency mixing of the fourth harmonic with the fundamental wavelength. Experiments carried out with CLBO and BBO revealed that the conversion efficiency was limited in both cases by thermal effects caused by UV absorption. However, CLBO had almost a factor 3 lower absorption.

In another system CLBO was used to produce radiation at 236 nm which is the fourth harmonic of a 946 nm Nd:YAG laser [10.34]. The crystal was operated at noncritical phase matching, which occurs at -15°C for these wavelengths. In this case, the crystal was mounted in a vacuum-tight housing to prevent deterioration. For

fourth harmonic generation of a 1064-nm Nd:YAG laser, BBO has a slightly larger nonlinear coefficient; however, at shorter wavelength than 266 nm CLBO has a larger nonlinearity.

10.2.4 Intracavity Frequency Doubling

In the previous section we discussed frequency doubling by placing a nonlinear crystal in the output beam of the laser system. Frequency-doubling a cw-pumped laser system in this manner results in an unacceptably low harmonic power because large conversion efficiencies require power densities which are not available from a cw-pumped laser. One obvious solution to this problem is to place the nonlinear crystal inside the laser resonator, where the intracavity power is approximately a factor $(1 + R)/(1 - R)$ larger than the output power. The power is coupled out of the resonator at the second harmonic wavelength by replacing the output mirror with transmission T by one which is 100% reflective at the fundamental and totally transmitting at the second harmonic. Functionally, the second harmonic crystal acts as an output coupler in a manner analogous to the transmitting mirror of a normal laser. Normally the transmitting mirror couples out power at the laser frequency, whereas the nonlinear crystal inside the laser couples out power at twice the laser frequency. Because advantage is taken of the high power density inside the laser cavity, it is only necessary to achieve a conversion efficiency equal to the optimum mirror transmission to convert completely the available output at the fundamental to the harmonic. For example, for a cw-pumped Nd:YAG laser with an optimum output coupling of $T = 0.1$, an intracavity conversion efficiency of 10% will produce an external conversion of 100%, in the sense that the total 0.53- μm power generated in both directions by the nonlinear crystal is equal to the maximum 1.06- μm power, which could be extracted from the cavity without the nonlinear crystal.

There are several disadvantages associated with intracavity doubling. A nonlinear crystal of poor optical quality will drastically degrade the performance of the laser. Amplitude fluctuations are strongly magnified by the combination of the nonlinear process and the gain of the active material. The harmonic power is generated in two directions, which requires an additional dichroic mirror for combining the two beams. The other alternative to intracavity doubling of a cw laser is external doubling with a strongly focused beam. However, crystal acceptance angles are frequently too narrow to permit tight focusing of the beam onto the crystal. For pulsed-pumped operation, on the other hand, the fraction of intracavity power that is coupled out is so high that there is little advantage in placing the crystal inside the laser.

The choice of nonlinear materials for intracavity frequency doubling of the Nd:YAG, Nd:YLF, and Nd : YVO₄ lasers are KTP, BBO, LBO, and PPLN. Compared to pulsed-pumped systems, in internally frequency-doubled cw lasers the average power is usually high and the peak power low. Therefore, a high nonlinear coefficient, small absorption losses, and good optical quality are the determining factors for the selection of a particular crystal. In order to increase the conversion efficiency of cw-pumped systems, the power density can be increased by employing an acousto-optic Q-switch or mode locker in the resonator.

Simplification of the basic intracavity doubling design is achieved by using a gain medium that also functions as the nonlinear material. Combining both gain and nonlinearity into a single crystal is appealing from a device point of view. The most attractive nonlinear gain medium is Nd:YAB, which is a dilute form of the stoichiometric neodymium compound neodymium aluminum borate (NAB). Diode-pumped Nd:YAB lasers with output powers over 1 W in the green as well as tunable output in the green/yellow spectrum have been demonstrated [10.35]. The tunable laser employed a birefringent filter for wavelength selection. Since the thermally sensitive phase matching process takes place in the presence of pump-related thermal gradients, accurate temperature control is required.

Cavity Configuration

There are several factors which affect the choice of a laser cavity configuration. In order to achieve efficient harmonic generation it is important to obtain a high power density inside the nonlinear crystal. Concurrently, the intracavity beam must be large enough inside the laser medium to utilize the maximum volume which can contribute to TEM₀₀ mode oscillation. This generally requires that the beam cross-sectional area must be larger inside the laser medium than inside the nonlinear crystal.

Intracavity harmonic generation produces a beam of harmonic power in both directions. Only the harmonic wave emitted toward the output mirror is emitted; the harmonic beam traveling in the opposite direction is mostly absorbed by the laser medium. In order to capture both beams a dichroic mirror that reflects the second harmonic and transmits the fundamental can be inserted between the doubling crystal and the laser rod. If the dichroic coating is applied directly to the surface of the doubling crystal facing the laser crystal the need for an additional mirror is eliminated.

The more common approach for combining the frequency-doubled beams and for providing a large mode volume in the laser medium and tight focusing in the nonlinear crystal is accomplished with L-, V-, or Z-shaped resonators. One example of an L-shaped resonator configuration is illustrated in Fig. 10.14. The 45° dichroic mirror is

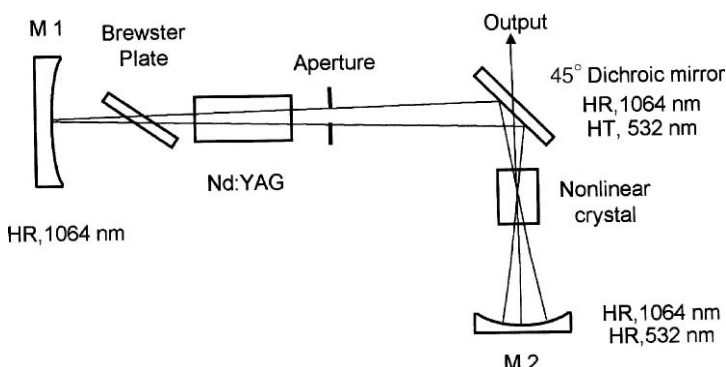


Fig. 10.14. Three-mirror L-shaped resonator configuration

designed to reflect the 1064-nm beam and transmit the orthogonally polarized 532-nm beam. Mirror M_2 is highly reflective for both wavelengths. The resonator is typically designed to obtain an adequate TEM_{00} mode volume in the laser medium and a small waist at the nonlinear crystal. This is achieved by a short-radius mirror M_2 close to the nonlinear crystal and a large-radius mirror M_1 behind the laser medium. Designs have been published with a beam diameter of 1.8 mm inside the laser rod and spot size of 25 μm inside the nonlinear crystal. More typical is a ratio of about 10 between the two diameters. If the angle between the two legs of the resonator is less than 90° a V-shaped configuration is obtained.

In long resonators the phase shifts due to dispersion between the 1.06- and 0.53- μm beams in the air path between the doubling crystal and the dielectric coating of mirror M_2 must be adjusted so that they are in phase as they reenter the doubling crystal after reflection from M_2 . This is accomplished by providing a translation adjustment for the mirror M_2 to move it toward or away from the doubling crystal, such that the net phase shift between the two waves is a multiple of 2π . The computed phase shift, based on the measured 1.06- to 0.53- μm dispersion of air of $3.6 \times 10^{-6} \mu\text{m}^{-1}$, is approximately 29.0°/cm. For doubling of the 1.06- μm line of Nd:YAG, this requires a mirror movement of no more than 3.28 cm [10.36], and the accuracy required to correct for the phase shift is of the order of millimeters.

As the pump power in a laser is changed, the focal length of the thermal lens formed by the laser crystal varies. This changes the spot size of the beam throughout the resonator. In particular the spot size in the nonlinear crystal can decrease to a point which causes damage. A resonator that minimizes changes of the beam size inside the nonlinear crystal despite large changes of thermal lensing is the Z-shaped resonator illustrated in Fig. 10.15. The resonator consists of four mirrors, whereby the two concave mirrors represent a telescope which relays the image of the hard aperture at one end of the laser rod into the nonlinear crystal. This is the same type of optical relay described in Chap. 4 that is commonly used in large Nd:Glass amplifiers.

Depending on the magnification the relay optics also transforms the larger spot size in the laser crystal to the smaller beam inside the laser crystal. Typical magnifications determined by the ratio of the mirror radius range between 2 and 2.5. The resonator shown in Fig. 10.15 contains also a Q-switch for power enhancement. With resonators of the type illustrated in Fig. 10.15 and including an acoustic-optic Q-switch, harmonic power in excess of 100 W have been generated [10.37, 38].

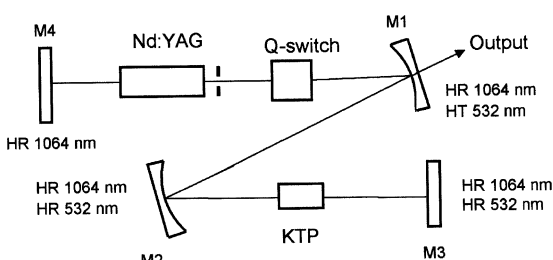


Fig. 10.15. Resonator Z-configuration for high power generation

An analysis of optical second harmonic generation internal to the laser cavity has been presented in [10.39, 40]. The steady-state condition for intracavity doubling can be determined if we equate the round-trip saturated gain of the laser to the sum of the linear and nonlinear losses

$$\frac{2g_0l}{1 + I/I_s} = \delta + \kappa I, \quad (10.50)$$

where g_0 is the unsaturated gain coefficient, l is the length of the laser medium, I is the power density in the laser rod, and I_s is the saturation power density of the active material. All linear losses occurring at the fundamental frequency are lumped together into the parameter δ ; the quantity κI is the nonlinear loss. If we express the saturated gain coefficient g by the small signal gain coefficient $g_0/(1 + I/I_s)$ in (3.7), we see that κI in (10.50) is equivalent to the transmission T of a normal laser.

The nonlinear coupling factor κ , defined by

$$I(2\omega) = \kappa I^2(\omega), \quad (10.51a)$$

is related to the nonlinear factor C defined in (10.19b)

$$\kappa = (I_{NC}/I_L)l^2C^2, \quad (10.51b)$$

where I_{NC}/I_L accounts for the different power densities in the laser medium (I_L) and nonlinear crystal (I_{NC}), and l is the crystal length.

The maximum second harmonic power as a function of κ is obtained from (10.50) by differentiating and $dI/d\kappa = 0$.

$$\kappa_{max} = \delta/I_s. \quad (10.52)$$

The magnitude of the nonlinearity required for optimum second harmonic production is proportional to the loss, inversely proportional to the saturation density, and independent of the gain. Thus, for a given loss, optimum coupling is achieved for all values of gain and, hence, all power levels. As we recall from Chap. 3, in a laser operating at the fundamental wavelength the optimum output coupling of the front mirror is gain-dependent. The usefulness of (10.52) stems from the fact that by introducing the material parameters for a particular crystal into (10.52) and combining with (10.19b), the optimum length of the nonlinear crystal is obtained.

For example, $Ba_2NaNb_5O_{15}$ has a nonlinear factor of $C = 38 \text{ GW}^{-1/2}$. With $I_s = 2.9 \text{ KW/cm}^2$ for Nd:YAG, and assuming a round-trip loss of $\delta = 0.02$ and a power-density enhancement of $I_{NC}/I_C = 50$, we obtain an optimum crystal length of $l = 0.5 \text{ cm}$ from (10.52, 53).

From the theory presented in [10.40], it follows that if the insertion loss of the second harmonic crystal is small compared to the total internal loss, the value of κ is the same for fundamental and second harmonic output coupling. Also, the maximum second harmonic power equals the fundamental power obtainable from the same laser.

In most systems, the second harmonic power is considerably below the output power which can be achieved at the fundamental wavelength. Insertion losses of the

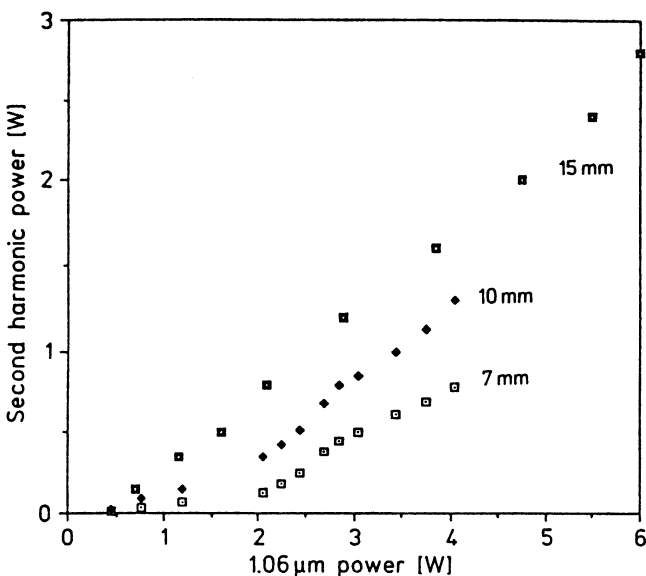


Fig. 10.16. Comparison of fundamental and second harmonic output from a cw-pumped intracavity frequency-doubled Nd:YAG laser for different KTP crystal lengths

nonlinear crystal, or any other additional intracavity element, are often the reason for the poor performance, or in the case of Nd:YAG, thermally induced depolarization losses can have a major effect. In low-gain lasers employed for intracavity harmonic generation, even small insertion losses are very detrimental to the system performance. The effect of intracavity losses on the laser performance has been analyzed in detail in [10.39]. For example, in a laser with a round-trip gain coefficient of $2g_0l = 0.2$, the output drops 20% if the internal loss is increased from 2 to 3%. Furthermore, availability of crystals and damage considerations lead often to nonoptimum conditions as far as crystal length and pump-power density are concerned.

As an example, the performance of a typical intracavity-doubled Nd:YAG laser is illustrated in Fig. 10.16. The output at the harmonic wavelength is compared to the TEM₀₀ output available at 1.064 μm from the same laser. The Nd:YAG laser employed in these experiments was cw-pumped by diode arrays and intracavity-doubled with KTP. After measuring the output at 1.064 μm, a KTP crystal was inserted in the folded resonator and the output coupler was replaced with a mirror of high reflectivity at 1.064 and 0.53 μm. For the short crystals, the nonlinear coupling factor κ is too small and far from optimum. A higher output at 532 nm would require tighter focusing of the beam. However, this makes alignment very critical and sacrifices mechanical and thermal stability of the laser. A longer nonlinear crystal is therefore a better solution. However, a 15-mm-long crystal is about the longest crystal available for KTP.

It is commonly observed that the output from a continuously pumped, intracavity-doubled laser is much less stable than the output obtained from the same laser without

the nonlinear crystal in the resonator. Typically, one observes large amplitude fluctuations of the harmonic power consisting of a series of random spikes superimposed upon the cw background. The nature of these severe power instabilities, termed the green problem, is caused by the nonlinear interaction of the longitudinal modes in the harmonic generator and has been analyzed in [10.41]. A typical laser resonator contains a large number of longitudinal modes, each with a well-defined polarization and a gain and loss that is time-dependent since it is a function of the instantaneous mode intensity.

In a multimode laser two nonlinear processes occur simultaneously in the harmonic generator, namely frequency doubling and sum frequency generation. Frequency doubling converts an individual mode to the harmonic, whereas in sum frequency generation two separate modes interact to produce a harmonic. The dynamics of intracavity doubled lasers can be modeled by a set of rate equations, one for each longitudinal mode. Solutions of these nonlinear equations show instability and chaotic behavior. Hole burning has been considered in [10.42] as an additional contributor to instabilities because it forces the laser to jump to different modes.

From the analysis in [10.41] it follows that the amplitude fluctuations should disappear if the laser is restricted to operate in a single longitudinal mode. This is consistent with the observation that a laser containing etalons or a birefringent filter for mode selection does not exhibit chaotic behavior.

The birefringent filter is typically formed by a combination of the birefringent nonlinear crystal such as KTP and a polarizer or by a combination of the nonlinear crystal and a laser crystal such as Nd:YVO₄ which has a polarized output. For example, in [10.43] a single longitudinal mode laser is described that consists of an end-pumped Nd:YAG crystal, a Brewster plate, and a KTP crystal with its axis at 45° to the axis of the Brewster plate. In KTP the linearly polarized fundamental beam is split into an ordinary and extraordinary component because phase matching does not occur at 90° with respect to the optical axis. The radiation leaves the crystal elliptically polarized. After one round trip there is a certain phase difference between the ordinary and extraordinary ray. When this phase difference is an integral of π the wave still has p-plane polarization and the loss passing through the Brewster plate will be zero. Mode selection is provided because the phase shift depends on the wavelength, which is different for different modes.

If one uses an Nd:YVO₄ crystal instead of Nd:YAG, the Brewster plate can be eliminated because of the polarized output from the laser crystal. In this case the combination of the Nd:YVO₄ laser crystal and the KTP nonlinear crystal acts as a birefringent filter. Such a laser end-pumped with fiber-coupled laser diodes produced stable output of 3.2 W [10.44]. The problem with birefringent filters is the fact that they need to be temperature-controlled. For example, the above-mentioned system required temperature control of the two crystals to within 0.1°C to obtain stable single-mode output.

The coupling of orthogonal linearly polarized modes through the sum frequency generation process can be eliminated by modifying the polarization of the laser modes in the doubling crystal. The instabilities caused by coupling of modes with different polarizations are effectively suppressed by inserting a quarter wave plate in the

resonator for the fundamental wavelength [10.45]. The modes will be linearly polarized parallel to the axis of the quarter waveplate which reduces the likelihood of chaotic fluctuations.

Actually, the thermally induced birefringence in an Nd:YAG crystal was found sufficient to eliminate chaotic amplitude fluctuation of the laser by proper rotation of the Nd:YAG and KTP crystal [10.46]. Again as in the system mentioned above, modes which are linearly polarized in a specific direction have lower losses as compared to orthogonally polarized modes.

In the so-called twisted mode approach hole burning and mode hopping are avoided by placing the Nd:YAG crystal between two quarter waveplates. With the beam polarized by a Brewster plate, the laser polarization vector within the crystal rotates with a period equal to the laser wavelength. Unlike the traditional standing wave cavity where the gain exhibits nodes and antinodes, in this case the gain is constant along the beam axis.

A steady-state solution derived in [10.46] predicts that the stability of an intracavity frequency-doubled laser increases with round-trip time and the number of oscillating modes. It was indeed demonstrated experimentally [10.47] that output fluctuations and random behavior in cw frequency-doubled systems can be greatly reduced by a long resonator. The measurements were performed with a lamp-pumped Nd:YLF laser, introcavity frequency-doubled with LBO, which provided as much as 13.5 W in a 1.9 m long resonator. The instabilities arising from orthogonally polarized modes were eliminated in this laser by temperature tuning the crystal at 142°C. This provides type I noncritical phase matching and therefore the fundamental beam remains linearly polarized as it propagates through the crystal.

Most of the approaches mentioned above require the insertion of additional elements in the resonator or very accurate temperature stabilization. For this reason, a number of commercial lasers employ a long resonator as a means to achieve stable second harmonic output.

The highest average harmonic output is obtained if intracavity frequency doubling is combined with repetitive Q-switching. In a typical system the resonator contains an acoustic-optic Q-switch in addition to the harmonic generator as indicated in Fig. 10.15. The pulse repetition rate is in the KHz range. Owing to the higher gain and larger spot sizes compared to cw systems the resonator is less sensitive to adjustments and perturbations. Repetitively Q-switched and internally doubled lasers with high harmonic outputs are described in [10.37, 38, 48, 49].

The harmonic power extracted from the laser can be related to the pumping rate above threshold and to the coupling coefficient if one considers the effects of pump depletion and pulse stretching [10.50]. In a regular Q-switched laser the transmission of the output mirror is higher compared to cw operation because of the high gain. Similarly the coupling factor κ is higher in case of a repetitively Q-switched and internally doubled laser.

Intracavity harmonic generation can also be combined with mode locking [10.51, 52]. Since the harmonic conversion efficiency is highest at the peak of the mode-locked pulses, the harmonic conversion process tends to flatten and broaden the pulses, opposing the modulator's efforts to sharpen the pulses.

10.2.5 Third Harmonic Generation

Efficient conversion of the output of a laser to the third harmonic is an example of sum frequency generation via the process of three-wave mixing. The interaction of two input waves at frequencies ω and 2ω in a nonlinear medium produces a third wave at the sum frequency 3ω as a result of second-order nonlinear polarization.

The sum frequency generation is governed by three factors: (a) the nonlinear drive, i.e., the intensity of the input beams, (b) the phase mismatch between the three interacting waves, and (c) the ratio of the intensities of the two input beams.

A third harmonic converter consists of two crystals—the first crystal is a second harmonic generator (doubler) and produces at its output radiation at ω and 2ω . In the sum frequency mixing process of the second crystal (tripler) unconverted fundamental radiation of the first stage is mixed with the second harmonic to produce the third harmonic. In this arrangement, the total output of the frequency doubler becomes the input to the sum frequency stage.

Besides the nonlinear drive and dephasing, the two parameters that also determine the efficiency of frequency doubling, third harmonic generation places an additional constraint on the laser system since for efficient tripling the ratio of ω and 2ω photons incident on the sum frequency mixing crystal is very important.

The mix of ω and 2ω photons will be expressed as the ratio of second harmonic intensity to total intensity at the entrance to the sum frequency stage.

$$M = \frac{I_{2\omega}}{I_\omega + I_{2\omega}}. \quad (10.53)$$

The optimum situation is achieved if, for three photons at the fundamental frequency ω entering the first crystal, two photons are converted to create a photon at 2ω , and the third photon at ω is combined in the second crystal with the 2ω photon to produce one 3ω photon. This situation is depicted in Fig. 10.17 for type I/type II and type II/type II cascaded third harmonic generation.

In a nonabsorbing doubling crystal, the parameter M is also equivalent to the conversion efficiency of the doubler. Therefore, the mix of equal ω and 2ω photons at the exit of the doubling crystal requires $M = 2/3$. Given this photon ratio, in a nonabsorbing and perfectly matched crystal, a complete conversion of the fundamental beam to the third harmonic is theoretically possible.

Complete conversion as indicated in Fig. 10.17 occurs only for the experimentally unrealizable condition of perfect phase matching and photon mix over the whole cross section and pulse duration of the beam. In actual systems one can only hope to approach these conditions as close as possible. If conversion is incomplete then the output of the sum frequency stage contains, besides the third harmonic, residual outputs at the fundamental and second harmonic as indicated by I_ω' and $I_{2\omega}'$ in Fig. 10.18.

Third harmonic generation can be analyzed starting with the general equations (10.14) governing frequency mixing for plane waves in a nonabsorbing medium.

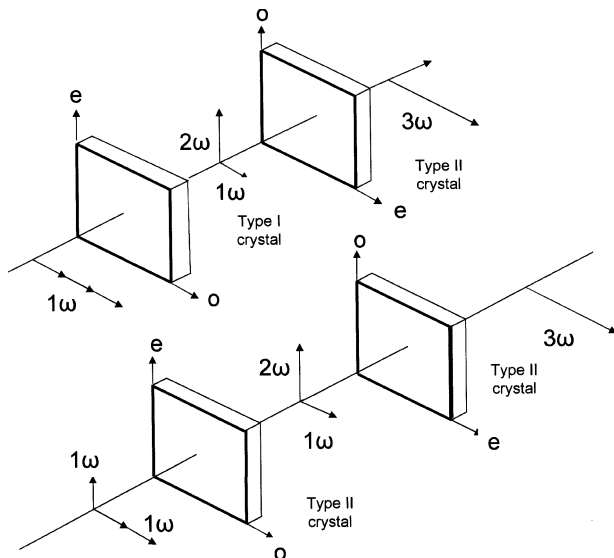


Fig. 10.17. Cascaded third harmonic generation with (a) type I/type II and (b) type II/type II phase matching

With $\omega_1 = \omega$, $\omega_2 = 2\omega$, $\omega_3 = 3\omega$, and $E_1 = E_\omega$, $E_2 = E_{2\omega}$, $E_3 = E_{3\omega}$, we can rewrite (10.14).

$$\frac{dE_\omega}{dz} = -i\omega\sqrt{\mu_0/\varepsilon_\omega} d_{ijk} E_{3\omega} E_{2\omega}^* \exp(-i\Delta kz) \quad (10.54a)$$

$$\frac{dE_{2\omega}}{dz} = -2i\omega\sqrt{\mu_0/\varepsilon_{2\omega}} d_{kij} E_\omega^* E_{3\omega} \exp(-i\Delta kz) \quad (10.54b)$$

$$\frac{dE_{3\omega}}{dz} = -3i\omega\sqrt{\mu_0/\varepsilon_{3\omega}} d_{jik} E_\omega E_{2\omega} \exp(i\Delta kz) \quad (10.54c)$$

Since we have omitted terms that relate to absorption losses in the nonlinear crystal, equations (10.54) can be solved analytically [10.8, 10], and the overall efficiency of

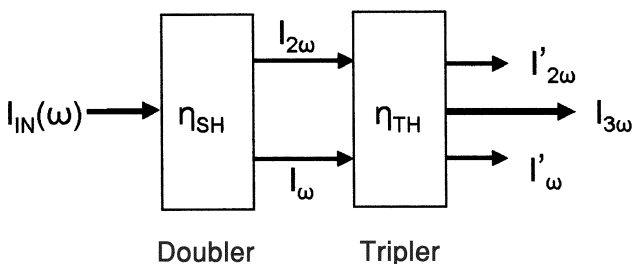


Fig. 10.18. Cascaded third harmonic generation with a second harmonic generator followed by a sum frequency stage

third harmonic generation can be calculated.

$$\eta_{\text{TH}} = \frac{I_{3\omega}}{I_\omega + I_{2\omega}}. \quad (10.55)$$

In (10.55) $I_{3\omega}$ is the output at the third harmonic and $I_\omega + I_{2\omega}$ is the input to the tripler, that is, the same as the total input $I_{\text{in}}(\omega)$ from the laser driving the two stages since we are assuming a lossless conversion process (see Fig. 10.18).

Integration of the coupled differential equations (10.54) for the case of perfect phase matching ($\Delta k = 0$) leads to the following expression for the efficiency of third harmonic conversion [10.10].

$$\begin{aligned} \eta_{\text{TH}} &= \eta_m s n^2[(\eta_0/\eta_m)^{1/2}, m], \\ \text{where } \eta_0 &= 9M^2(1-M)C^2L^2I_{\text{in}}(\omega) \\ \text{and } \eta_m &= (3/2)M, \quad m = M/2(1-M) \quad \text{for } M \leq 0.67 \\ \eta_m &= 3(1-M), \quad m = 2(1-M)/M \quad \text{for } M \geq 0.67. \end{aligned} \quad (10.56)$$

Not surprising, the expression for η_{TH} has the same form as obtained for frequency doubling since both frequency doubling and tripling are based on sum frequency mixing. Equation (10.56) contains the Jacobi elliptic function with argument $\sqrt{\eta_0/\eta_m}$ and modulus m . The nonlinear drive η_0 , modulus m , and the maximum efficiency η_m are all functions of the mixing ratio M between ω and 2ω photons. The other parameters of (10.56) are the crystal length L , the nonlinear factor C defined in (10.21), and $I_{\text{in}}(\omega) = I_\omega + I_{2\omega}$, which is the total combined beam intensity at the entrance of the tripling stage.

Figure 10.19 illustrates the overall efficiency of third harmonic generation for two different intensity ratios of the two beams entering the sum frequency stage. Illustrated is third harmonic generation of a 1064-nm fundamental beam mixed with the second harmonic entering a KDP crystal that is used in the sum frequency stage. The nonlinear crystal is characterized by $C = 0.97 \text{ GW}^{-1/2}$ and $L = 1 \text{ cm}$. The maximum conversion efficiency is achieved for $M = 0.67$ which represents the ideal 1:1 mix of ω and 2ω photons. For $M = 0.40$ the conversion efficiency in the doubler is too low, leading to an excess of ω photon at the entrance of the sum frequency stage. Fig. 10.19 can be applied to different crystals by scaling the input intensity according to $C^2 L^2 I_{\text{in}}(\omega)$.

For the ideal 1:1 mix of ω and 2ω photons we obtain with $M = 0.67$, a modulus of $m = 1$ and a maximum efficiency $\eta_m = 1$ from (10.56). This reduces the expression of (10.56) to

$$\eta_{\text{TH}} = \tanh^2 \sqrt{2C^2 L^2 I_{\text{in}}(\omega)}. \quad (10.57)$$

In this case the photons of both beams are depleted at the same rate and the result is similar to the perfect phase matching condition of second harmonic generation. The efficiency saturates at 100% as the input intensity increases. For other mixing ratios, after the waves have propagated a distance in the crystal, the number of photons in one of the waves depletes to zero, and the energy transfer reverses. The energy is then cycled between the waves, and in a nonabsorbing crystal, the conversion efficiency

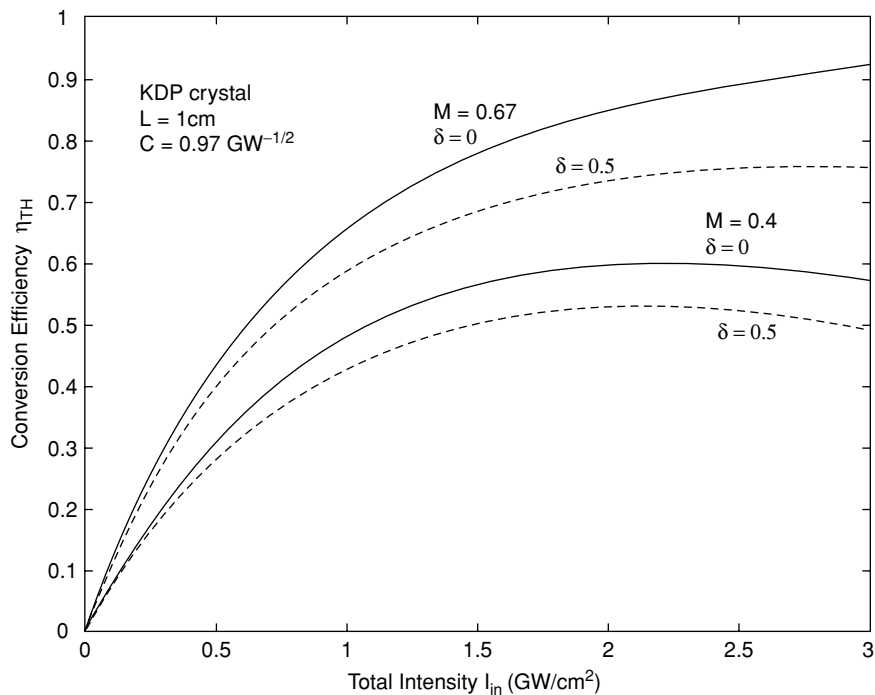


Fig. 10.19. Efficiency of third harmonic generation of a 1064 nm beam in a 10-mm-long KDP crystal. M is the ratio of the intensity of the green beam to total beam intensity entering the tripler. In a nonabsorbing crystal, M is the conversion efficiency of the doubler

oscillates as a function of the input intensity with a period determined by the modulus of the Jacobi function.

If one includes nonperfect phase matching in (10.56) the modulus m and maximum efficiency η_m include expressions for the dephasing δ . For the case $M \leq 0.67$ we obtain (if $\delta > 0$ minus sign, if $\delta = 0$ plus sign)

$$m = [2 - \sigma + \varepsilon \mp \sqrt{(\sigma - \varepsilon)^2 + 4\varepsilon}]^2 / 4(1 - \sigma) \quad (10.58a)$$

$$\text{and } \eta_m = (3/4)M[2 - \sigma + \varepsilon \mp \sqrt{(\sigma - \varepsilon)^2 + 4\varepsilon}], \quad (10.58b)$$

$$\text{where } \sigma = (3M - 2)/M, \quad \varepsilon = 3\delta^2(1 - M)/\eta_0.$$

The nonlinear drive η_0 has been defined in (10.56) and dephasing δ in (10.27).

In (10.58) the conversion efficiency of the sum frequency process is described by only three parameters: the nonlinear drive η_0 , phase mismatch δ , and the ratio of intensities M of the two waves being mixed.

The detrimental effect of dephasing on the overall efficiency of third harmonic generation is illustrated by the dashed curves in Fig. 10.19. A dephasing of $\delta = 0.5$ was assumed in calculating third harmonic generation for the two cases previously described. The reduction of the conversion efficiency caused by a phase mismatch between the interacting waves can be clearly seen.

Third harmonic generation is very important for frequency up-conversion of high-energy Nd:Glass lasers employed in fusion research. In these lasers the frequency converters are constructed from two potassium dihydrogen phosphate (KDP) crystals arranged in tandem. Since the diffraction-limited, high-intensity beams typically generate a second harmonic output with an efficiency around 80%, a number of schemes have been devised to detune the first stage in order to achieve the optimum 67% conversion. The desired intensity mix at the output of the doubler can be achieved by controlling the length of the doubling crystal by adjusting the propagation direction of the fundamental beam relative to the phase matching direction (angular tilt) or by a polarization mismatch [10.53, 54]. For example, in the latter approach the polarization vector of the fundamental beam is at 35° with respect to the “o” direction of the KDP crystal instead of the usual 45° as depicted in Fig. 10.10b.

10.2.6 Examples of Harmonic Generation

Examples of several different types of laser systems which incorporate harmonic generators will illustrate the technology. Figure 10.20 depicts a typical three-mirror internally frequency-doubled laser configuration. Employing a KTP crystal, harmonic generation with an output power of 3.9 W at 532 nm by intracavity frequency doubling in an Nd:YAG laser oscillator acousto-optically Q-switched at 10 kHz has been demonstrated [10.55]. The laser head contained a 25 mm by 3 mm Nd:YAG crystal side-pumped by six 1-cm-long diode arrays which were arranged symmetrically around the rod in two sets of three arrays each. The optical pump power at 807 nm was 60 W. At the fundamental output, the laser oscillator produced 12 W multimode and 5.5 W TEM₀₀ Q-switched average power. The optimal fundamental power was obtained with a 96% reflecting mirror.

A hemispherical laser cavity was employed to obtain TEM₀₀ operation with reasonable extraction efficiency while at the same time giving a tight beam waist for intracavity doubling. Using a type II doubling crystal, the intracavity flux incident upon the crystal was maximized by placing it at the waist of the cavity mode. The length of the KTP crystal was 15 mm. To improve the doubling efficiency, and to obtain a unidirectional output, the cavity was folded with a dichroic mirror, and the 1.06-μm output coupler used to obtain optimum fundamental output was replaced with a high reflector at 1.06 and 0.532 μm.

Figure 10.20a illustrates the optical schematic of the folded resonator-configuration. The performance of the acousto-optically Q-switched laser is depicted in Fig. 10.20b, which exhibits the average power produced at 1.06 μm (for optimum coupling) and at 0.532 μm when the output coupler is replaced by a total reflector at 1.06 and 0.532 μm.

Figure 10.21 shows the schematic of an end-pumped intracavity frequency doubled and Q-switched Nd:YAG laser [10.56]. The system uses the same type of three-mirror L-shaped resonator, as shown in the previous figure. Also, the average output in the green is about the same as in the previous example. However, because of the more efficient pump arrangement, only 30 W of optical pump power is required, compared to 60 W for the side-pumped laser. In the design depicted in Fig. 10.20, the Nd:YAG

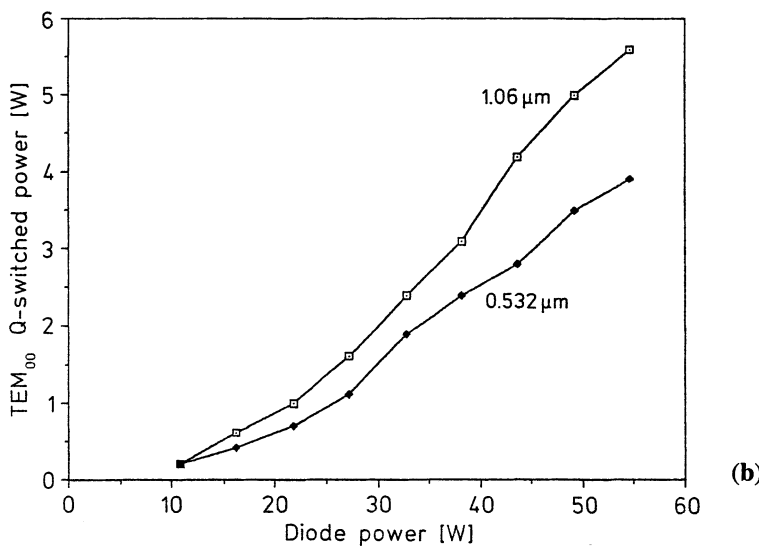
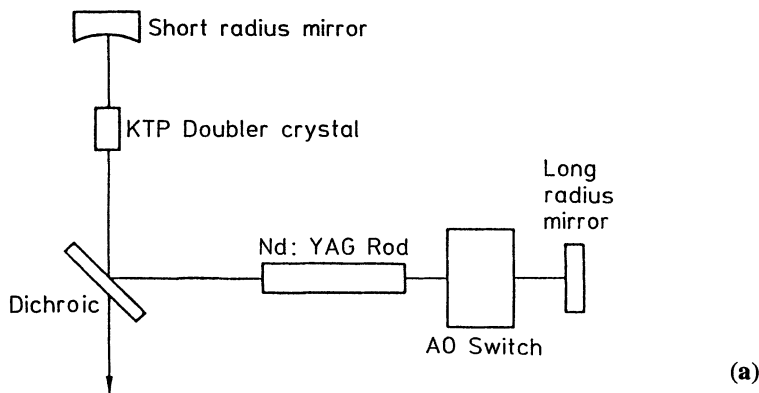


Fig. 10.20. Optical schematic (a) and fundamental and second harmonic average output power from a repetitively Q-switched cw-pumped Nd:YAG laser (b)

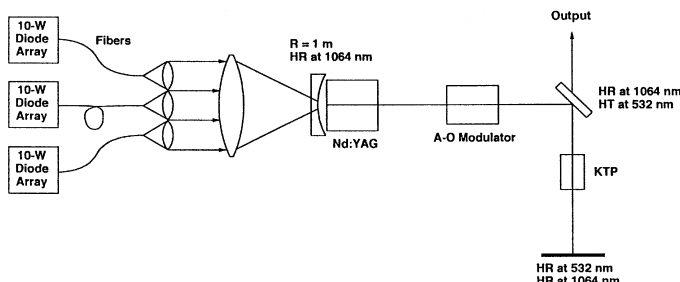


Fig. 10.21. Schematic of an end-pumped Q-switched and internally frequency-doubled cw-pumped Nd:YAG laser [10.56]

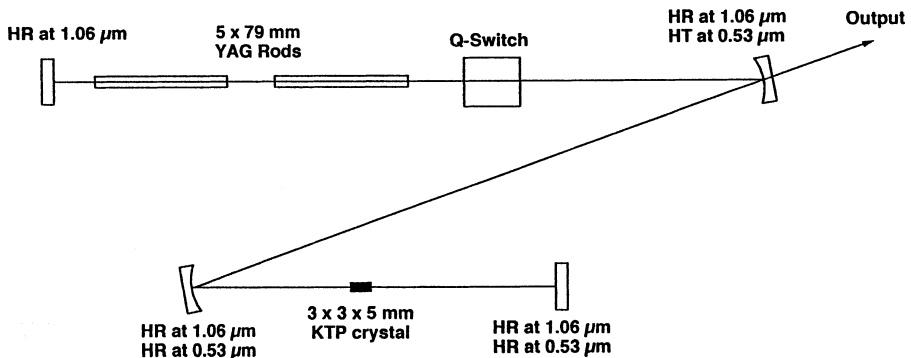


Fig. 10.22. High-power second harmonic generation in an internally frequency-doubled Nd:YAG laser featuring a “Z” resonator with relay optics [10.38]

crystal is pumped with the combined output of three fiber-coupled diode laser arrays. The fiber output of each pump was first collimated and then focused with a single lens onto one end of the Nd:YAG rod. The laser produced 3.5 W average power in the green at a repetition rate of 50 kHz in a nearly diffraction-limited beam.

At the high end of intracavity second harmonic generation, one finds krypton arc lamp and diode-pumped Nd:YAG lasers, AO Q-switched and intracavity doubled with KTP or LBO, which have generated in excess of 100 W at the harmonic [10.37, 38, 48, 49].

An illustration of such a high-average-power second harmonic generation system is given in Fig. 10.22 [10.38]. This design features a Z-shaped resonator, containing two laser heads, a Q-switch, and a KTP crystal. The laser was repetitively Q-switched with an acousto-optic device at repetition rates ranging from 4 to 25 kHz. The laser operated in high-order multitransverse mode. An interesting feature of the design is an optical relay system formed by the two curved mirrors between the Nd:YAG rod and the KTP crystal. One plane of this optical relay is at the end face of the YAG rod closest to the KTP crystal and the other plane is in the center of the KTP crystal. As explained in Sect. 10.2.4, the purpose of the relay optics is to keep the spot size in the KTP crystal as constant as possible, despite large changes of thermal lensing in the rods. The optical relay images the hard aperture of the laser rod into the KTP crystal, and therefore the multimode spot size in the KTP is fairly constant over a large range of pump power. The hard aperture at the rod was 4.9 mm, the relay optics was adjusted for a magnification of 2.5, and therefore a multimode spot size in the KTP crystal of about 2 mm was created. Particularly at these high power levels, a well-controlled and fairly large spot size in the nonlinear crystal is very important in order to avoid material damage.

The system produced 106 W of average power at 0.532 μm when Q-switched at 17 kHz. The laser was also operated at 1.32 μm with a different set of optics. In this case, 23 W at 0.659 μm has been generated. The nonlinear crystal for doubling both

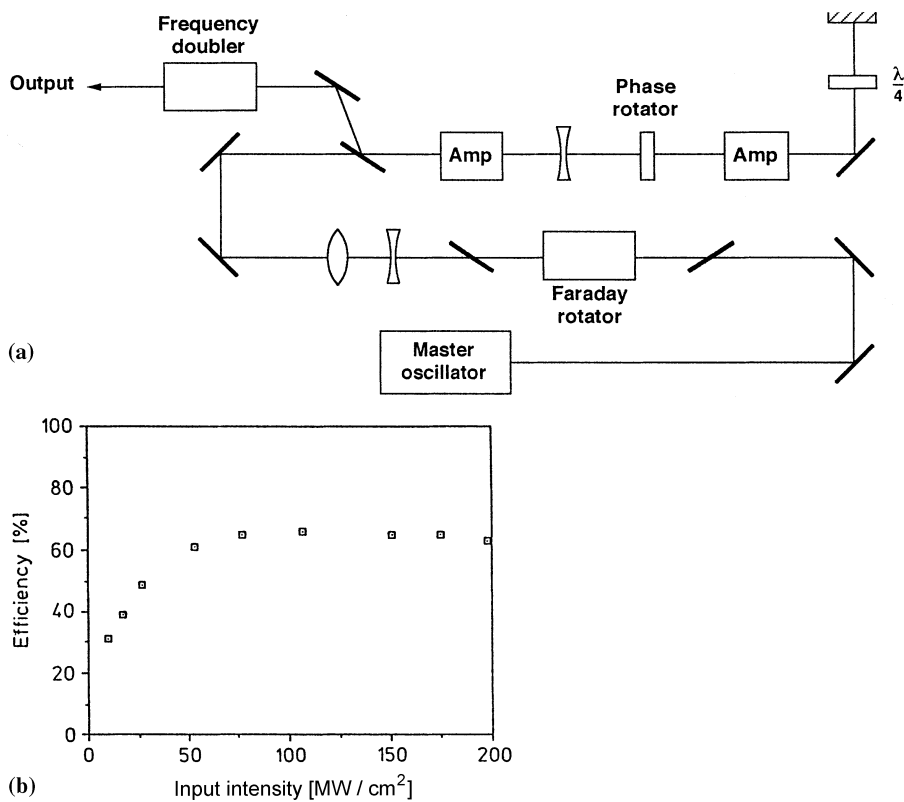


Fig. 10.23. High average power Q-switched and externally frequency doubled, MOPA system. Optical schematic (a) and conversion efficiency vs. pump intensity at the KTP crystal (b)

wavelengths was KTP. For $0.532\text{ }\mu\text{m}$ generation, the crystal was cut such that critical phase matching was obtained at the usual $x-y$ plane, at $\theta = 90^\circ$ and $\phi = 23.5^\circ$. The cut used for $0.694\text{ }\mu\text{m}$ generation was such that phase matching in the $x-z$ plane was achieved at $\phi = 0^\circ$ and $\theta = 60^\circ$.

Output of up to 40 W average power from an externally frequency-doubled, diode-pumped Nd:YAG oscillator amplifier system has been obtained. The system architecture is shown schematically in Fig. 10.23a [10.57]. The oscillator was Q-switched at a repetition rate of 100 Hz. The output from the amplifiers was 0.7 J per pulse at $1.064\text{ }\mu\text{m}$ in a $2\times$; diffraction-limited beam. At $0.532\text{ }\mu\text{m}$, the energy per pulse was 400 mJ in a 17-ns pulse. Each laser head contains an Nd:YAG rod side-pumped with 5-bar laser diode arrays operated at 60 W/bar. In the oscillator, 80 bars pump a 5-mm-diameter rod, whereas in the amplifiers 160 bars are used each to pump the 9-mm rods.

Thermal lensing and birefringence of the amplifier is compensated with a lens and a 90° phase rotator. The output is doubled to the green with a 1-cm-long KTP

Table 10.2. Frequency conversion efficiencies achieved on the Argus laser

Wavelength [nm]	Conversion efficiency[%]	Maximum energy generated [J]	Output power [GW]
532	83	346	495
355	55	41	68
266	51	50	83

crystal heated to 100°C. As shown in Fig. 10.23b, near 60% conversion efficiency was achieved.

The requirement for generation of short wavelengths from inertial-confinement-fusion lasers has prompted the development of large-aperture harmonic converters for doubling, tripling, and quadrupling of the Nd:Glass laser output. As an example, we will consider conversion experiments originally carried out on the now dismantled Argus laser at the Lawrence Livermore National Laboratory [10.58]. Argus was an image-relayed, spatially filtered laser system capable of delivering up to 1 kJ output energy in a 600-ps pulse. Frequency conversion experiments were performed with a beam of 10-cm diameter and beam divergence of about 100 μrad. Table 10.2 summarizes the results for second, third, and fourth harmonic generation. Doubling efficiency as a function of input intensity for type I phase matching in a 2.29-cm-long KDP crystal is illustrated in Fig. 10.24. At intensities above 2.8 GW/cm² the crystal is overdriven and reconversion of 532 nm radiation to 1064 nm photons takes place as discussed earlier in this chapter. The plot shows, also the sensitivity of the conversion process on crystal alignment.

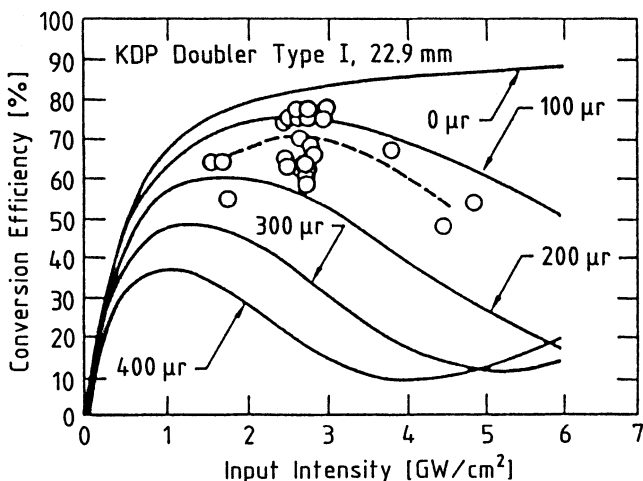


Fig. 10.24. Frequency-doubling efficiency as a function of input power [10.58]

10.3 Optical Parametric Oscillators

As was mentioned at the beginning of this chapter, two beams with different frequencies incident on a nonlinear crystal will generate a traveling polarization wave at the difference frequency. Provided the polarization wave travels at the same velocity as a freely propagating electromagnetic wave, cumulative growth will result. For reasons that will soon become clear, the two incident beams are termed “pump” and “signal” waves having a frequency of ν_p and ν_s , and the resulting third wave is termed an “idler” wave with frequency ν_i . Under proper conditions, the idler wave can mix with the pump beam to produce a traveling polarization wave at the signal frequency, phased such that growth of the signal wave results. The process continues with the signal and idler waves both growing, and the pump wave decaying as a function of distance in the crystal.

Since each pump photon with energy $h\nu_p$ is generating a photon at the signal ($h\nu_s$) and idler frequency ($h\nu_i$), energy conservation requires that

$$\frac{1}{\lambda_p} = \frac{1}{\lambda_s} + \frac{1}{\lambda_i}. \quad (10.59)$$

In order to achieve significant parametric amplification, it is required that at each of the three frequencies the generated polarization waves travel at the same velocity as a freely propagating electromagnetic wave. This will be the case if the refractive indices of the material are such that the k vectors satisfy the momentum-matching condition $k_p = k_s + k_i$. For collinearly propagating waves this may be written as

$$\frac{n_p}{\lambda_p} - \frac{n_s}{\lambda_s} - \frac{n_i}{\lambda_i} = 0, \quad (10.60)$$

where n_s , n_i , and n_p are the refractive indices at the signal, idler, and pump frequency, respectively.

Since the three indices of refraction depend on the wavelength, the direction of propagation in the crystal, and on the polarization of the waves, it is generally possible, by using birefringence and dispersion, to find conditions under which (10.60) is satisfied.

Tunability is a fundamental characteristic of all parametric devices. With the pump providing input at the fixed wavelength λ_p , small changes of the refractive index around the phase matching condition will change the signal and idler wavelengths such that a new phase matching condition is achieved. Tuning is possible by making use of the angular dependence of the birefringence of anisotropic crystals.

Figure 10.25 illustrates different configurations that make use of the parametric interaction process of three waves. The simplest device is a nonresonant configuration, namely an optical parametric amplifier (OPA), exhibited in Fig. 10.25(a). In this case, a pump beam and a signal beam are present at the input. If the output of a Q-switched laser is focused into the crystal and if the intensity of the pump is sufficiently high, and phase matching conditions are met, gain is obtained for the signal wave and at the

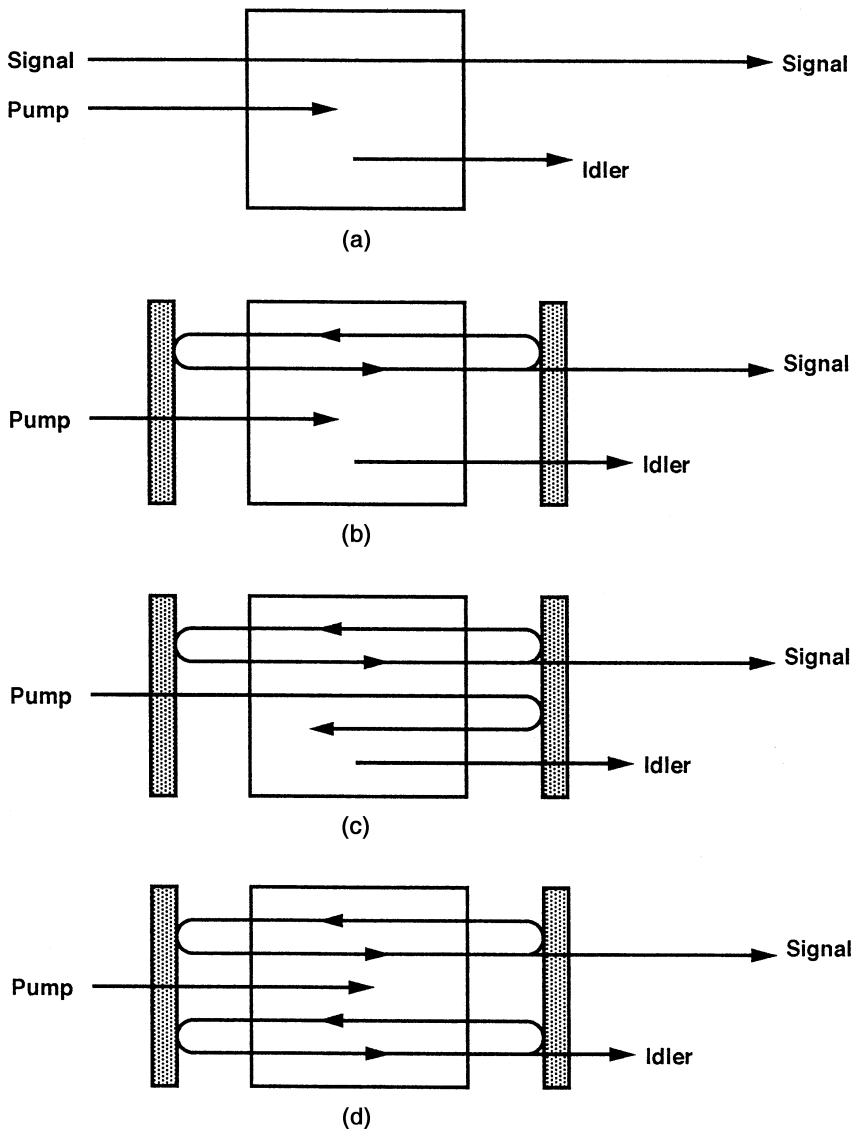


Fig. 10.25. Configurations for parametric interactions: (a) optical parametric amplifier (OPA); (b) singly resonant optical parametric oscillator (SRO); (c) singly resonant oscillator with pump beam reflected; (d) doubly resonant OPO (DRO)

same time an idler wave is generated. Typically, an OPA is used if the signal obtained from an optical parametric oscillator (OPO) is too weak and further amplification is desired.

The most common optical parametric device is the singly resonant oscillator depicted in Figs. 10.25b and c. In this device, the crystal is located inside a resonator that

provides feedback at either the signal or idler frequency. In the example illustrated, the pump beam enters through a mirror that is highly transmitting at the pump wavelength and highly reflective for the signal wavelength. In Fig. 10.25b the opposite mirror, which is the output coupler, has typically 80–95% reflectivity for the signal wavelength, and high transmission for the idler and pump beam. Only the signal wavelength is resonant in the cavity, and a small fraction is coupled out through the front mirror. In the configuration in Fig. 10.25c the pump beam is reflected at the output mirror and makes one return pass through the crystal. Since the input mirror through which the pump enters is highly transmissive for this wavelength, no resonance condition is set up for the pump wavelength. However, threshold is lowered, because on the return path the pump beam provides gain for the resonant signal wave.

Figure 10.25d depicts a doubly resonant oscillator (DRO), which provides feedback at both the signal and idler wavelengths. The double-resonance condition, in which both the signal and the idler waves are simultaneously resonant within the optical cavity, lowers the threshold significantly. However, this advantage of a DRO is offset by a reduction in stability and tunability. Maintaining the doubly resonant condition in a common resonator requires that the pump be single frequency and stable, and that the OPO cavity length be actively controlled to maintain the resonance condition.

Since the gain of a parametric device depends on power density, the design of a cw OPO presents a particular challenge. In the past, the design of cw OPOs was based on the use of doubly resonant oscillator configurations because of the lower pump power requirements. The need for active stabilization and single frequency pump lasers has placed major limitations on the utility of doubly resonant OPOs for practical devices outside the laboratory.

In recent years the increased availability of new nonlinear materials and high-power laser pump sources of high spatial and spectral beam quality have led to great advances in the development of singly resonant cw OPOs. Today, essentially all cw OPOs are singly resonant devices.

The first successful operation of an optical parametric oscillator was achieved by Giordmaine and Miller [10.59] in 1965. Their oscillator employed lithium niobate as the nonlinear material and used a 530-nm pump signal derived by frequency-doubling the 1.06- μm output of an Nd:CaWO₄ laser.

Since then considerable effort has been expended in understanding and improving the device performance, and numerous nonlinear materials were evaluated for possible use in practical devices. While the process of optical parametric conversion is conceptually simple and elegant, many difficulties have been encountered in realizing practical systems. Among the most serious has been optical damage to the nonlinear crystal, caused by the high electric fields necessary for nonlinear conversion. Typical damage thresholds for nonlinear materials are in the same range as the intensities required for efficient conversion. Another limitation for achieving high parametric conversion has been the poor beam quality of the pump sources themselves.

In recent times, however, these two problems have been overcome. First, new nonlinear crystals with high damage thresholds became available (for example, KTP, BBO, LBO) and a new class of nonlinear materials has been developed, namely

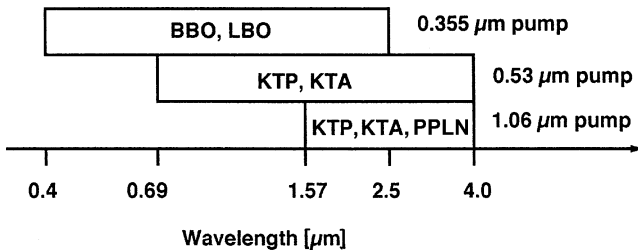


Fig. 10.26. Wavelength coverage of Nd:YAG or Nd:YLF pumped OPOs

periodically poled crystals such as LiNbO_3 , that allow quasi phase matching, which has a number of advantages over birefringence phase matching, as will be explained in Sect. 10.3.3.

Second, diode pumping has provided a new generation of efficient high-power solid-state lasers with single-transverse-mode outputs and a high degree of pulse-to-pulse stability. The introduction of these new nonlinear materials in conjunction with diode-pumped solid-state lasers have resulted in a fairly mature technology, and pulsed or cw-pumped singly resonant OPOs are now common devices used to extend the spectral range of solid-state lasers.

As an example, Fig. 10.26 depicts the wavelength coverage of Nd:YAG or Nd:YLF laser pumped OPOs employing the above-mentioned nonlinear crystals. The optical parametric oscillator has been the subject of many papers and review articles; detailed discussions of the theory and summaries of earlier work on OPOs can be found in [10.60–62].

10.3.1 Performance Modeling

Of greatest interest for the design of parametric devices are simple models which describe gain, threshold, phase matching, and conversion efficiency as a function of device and input parameters.

For the amplifier depicted in Fig. 10.25a, a parametric gain coefficient for the amplification of the signal wave can be defined [10.62]

$$g = \sqrt{\kappa I_p}, \quad (10.61)$$

where I_p is the pump flux and κ is a coupling constant

$$\kappa = \frac{8\pi^2 d_{\text{eff}}^2}{\lambda_s \lambda_i n_s n_i n_p \varepsilon_0 c}. \quad (10.62)$$

The effective nonlinear coefficient d_{eff} connects the pump, signal, and idler fields. The parameters n_p , n_s , n_i and λ_s and λ_i are the refractive indices of the three waves, and the wavelengths of the signal and idler wave, respectively.

The single-pass power gain of the parametric amplifier in the high-gain limit can be approximated by

$$G = \frac{1}{4} \exp(2gl), \quad (10.63)$$

where l is the length of the crystal.

A phase mismatch between the waves can be expressed by

$$\Delta k = k_p - k_s - k_i, \quad (10.64)$$

where $k_j = 2\pi n_j / \lambda_j$, with $j = p, s, i$, are the propagation constants of the three waves.

In the presence of phase mismatch, the gain coefficient is reduced according to

$$g_{\text{eff}} = \left[g^2 - \left(\frac{1}{2} \Delta k \right)^2 \right]^{1/2}. \quad (10.65)$$

The reduction of gain resulting from momentum or phase mismatch is clearly evident. Maximum gain is achieved for $\Delta k l = 0$. Typical values for the coupling constant are on the order of $\kappa = 10^{-8} / \text{W}$, as will be discussed later. Therefore, a power density of at least 100 MW/cm^2 is required to obtain a gain coefficient of $g = 1 \text{ cm}^{-1}$ and a modest power gain of $G = 1.8$ in a 1-cm-long crystal. At a 1- μm wavelength, the propagation constant is $k \approx 10^5 / \text{cm}$ in a material with a $n = 1.7$ refractive index. In order to minimize the effect of phase mismatch, we require from (10.65) that $\Delta k / 2 \ll g$. This means that the propagation constants have to be phase-matched to better than $10^{-5} / \text{cm}$.

From these very basic considerations, one can already draw several conclusions which govern the design of parametric devices. The optimum configuration of a parametric converter depends critically on the pump intensity in the nonlinear crystal. There is a strong incentive to operate at the highest attainable levels for a given pump source. However, the practical and acceptable pump intensity depends strongly on the optical damage threshold of the crystal and its coatings. The importance of a high nonlinear coefficient d_{eff} is also clearly evident from these equations, as is the detrimental effect of phase mismatch.

Singly-Resonant OPO. The singly-resonant OPO is the most common configuration owing to the ease of mirror and resonator design, good conversion efficiency, frequency, and power output stability. These advantages more than offset the disadvantage of increased threshold relative to the DRO. The pump wave makes a single pass through the nonlinear crystal. The generated signal and idle waves increase during the single pass in the pump-wave direction. Following reflection and backward trip in the resonator, the signal wave travels again with the pump wave and is amplified.

Threshold condition for steady-state operation for a singly-resonant OPO is given by

$$g^2 l^2 = 2\sqrt{1 - R_s}(1 - \delta), \quad (10.66)$$

where R_s , the reflectivity of the output coupler for the signal wave, and δ are combined reflection and absorption losses.

Threshold Condition. Singly-resonant OPOs are usually pumped with the output from a Q-switched Nd:YAG laser at either the fundamental or a harmonic of $1.06\text{ }\mu\text{m}$, depending on the desired output wavelength and nonlinear material. The signal wave is amplified from an initial noise power, as it makes m cavity transits. A model which calculates the threshold pump intensity of a pulsed singly-resonant oscillator has been described by Brosnan and Byer [10.61]. The model assumes that only the signal wave is resonated, whereas the idler wave is free to accept the profile of its driving polarization. The pump flux required to reach threshold is given by

$$I_{\text{th}} = \frac{1.12}{\kappa g_s l_{\text{eff}}^2} \left(\frac{L}{t_p c} \ln \frac{P_s}{P_n} + 2\alpha l + \ln \frac{1}{\sqrt{R}} + \ln 2 \right)^2. \quad (10.67)$$

The pump flux I_{th} on the left-hand side of this equation relates to gain [see (10.61)], and the right-hand side represents loss terms.

The coupling constant κ has been previously defined, and g_s is the signal spatial mode coupling coefficient defined as

$$g_s = \frac{1}{1 + (w_s/w_p)^2}. \quad (10.68)$$

The signal spot size w_s for a Gaussian beam is always smaller than the pump beam w_p because of the nonlinear conversion process. The effective parametric gain length l_{eff} is determined by the walk-off length

$$l_{\text{eff}} = \frac{\sqrt{\pi} w_p}{2\rho}, \quad (10.69)$$

where ρ is the double refraction walk-off angle. The walk-off length is closely related to the aperture length introduced in (10.49). In short crystals, or under noncritically phase-matched conditions, the effective length can equal the crystal length l , i.e., $l_{\text{eff}} = l$. From (10.69) follows that walk-off has a greater influence on a small beam. The pump spot size dependence of parametric gain for critically phase-matched interactions is well known [10.63]. Actually for maximum efficiency, the beam diameter must be increased until the effective walk-off length is equal to the crystal length.

The first term in the bracket of (10.67) represents the loss of the pump beam due to the buildup time required to increase signal power from the noise level P_n to a signal level P_s defined as threshold. It was found that best agreement between the model and experimental data was obtained if threshold signal power P_s was defined as an increase of 10^{14} over the noise floor, or $\ln(P_s/P_n) = 33$. The logarithmic term is divided by the number of round trips it takes to reach P_s . The quantity L is the cavity length, t_p is the $(1/e^2)$ intensity full width of the pump pulse and c is the velocity of light. If more round trips ($t_p c/L$) are allowed for the noise to build up to the signal level, then the pump-power density to reach threshold is lowered. In practice, this means a long pump pulse and a short OPO cavity lower the threshold.

The second term in (10.67) describes the absorption losses in the crystal where α is the absorption coefficient and l is the crystal length. The next term is the cavity output coupling loss, determined by the reflectivity R of the output mirror. The final term is due to SRO operation.

Inspection of (10.67) reveals that a high d_{eff} and long l_{eff} are the key to a low threshold for a parametric oscillator. The threshold input power is inversely proportional to the square of these terms. A long pump pulse and short cavity also tend to decrease the threshold somewhat as was already mentioned.

The model assumes a collimated Gaussian beam with a uniform wavefront. A transverse phase variation in the pump beam, caused by the laser or by intervening optics, acts as an effective phase mismatch in the presence of beam walk-off. If the beam has a transverse phase variation, and propagates at the walk-off angle with respect to the resonator axis, the generated signal wave sees a pump beam with a changing phase. As a result, threshold can be noticeably increased.

Singly-Resonant OPO with Return Pump Beam. The threshold in a singly-resonant OPO can be reduced by reflecting the pump radiation for a second pass through the crystal. This creates signal gain on both the forward and backward passes through the crystal. The changes in the OPO design are minimal; it only requires that the coating of the output mirror has to reflect both the resonated signal wave and the pump wave. If we let γ be the ratio of backward to forward pump intensity inside the crystal, then the threshold condition is as follows:

$$I_{\text{th}} = \frac{1.12}{\kappa g_s l_{\text{eff}}^2 (1 + \gamma)^2} \left(\frac{L}{t_p c} \ln \frac{P_s}{P_n} + 2\alpha l + \ln \frac{1}{\sqrt{R}} + \ln 4 \right)^2. \quad (10.70)$$

The reduction in threshold can be clearly seen from this equation. It should also be noted that in this scheme the fluence of the forward and backward pump beams are superimposed in the crystal, which leads to higher power densities compared to the previous case, and therefore damage considerations are important.

We found the model describing singly-resonant OPOs to be of adequate accuracy for design purposes, particularly in view of the fact that different qualities of nonlinear crystals can easily change threshold by a factor of 2.

We use (10.70) to calculate the threshold of an OPO build in our laboratory. The OPO contains a 15-mm-long KTP crystal as the nonlinear material which is pumped by a Q-switched Nd:YAG laser at 1.064 μm . The maximum output energy of the pump laser was 10 mJ, produced in a 50 ns pulse. This OPO is not used for generating a tunable output, but for providing an eye-safe wavelength at 1.6 μm [10.64–66]. The crystal was positioned to achieve type II noncritical phase matching for a pump wavelength of 1.06 μm (Nd:YAG) and a signal wavelength near 1.6 μm ; the idler wavelength was therefore near 3.2 μm . Noncritical phase matching maximizes the effective nonlinear coefficient and essentially eliminates walk-off. The crystal was positioned inside an optical cavity formed by a pair of plane-parallel mirrors, as shown in Fig. 10.27. The input mirror, through which the pump enters, was antireflection-coated at the pump wavelength (1.06 μm) and highly reflecting at

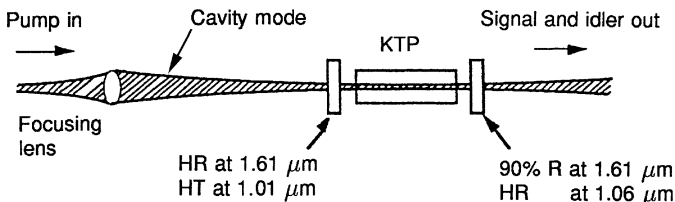


Fig. 10.27. Plane-parallel resonator for optical parametric oscillator, showing mode matching of focused pump beam to OPO cavity mode

the signal wavelength ($1.6 \mu\text{m}$) while the output mirror was highly reflecting at the pump wavelength and 10% transmitting at the signal wavelength. The laser output was focused by a 100-cm focal length lens, carefully positioned so as to mode-match the waist of the pump to the cavity mode of the OPO resonator.

In this noncritically phase-matched configuration, the wavelengths are $\lambda_s = 1.61 \mu\text{m}$, $\lambda_i = 3.2 \mu\text{m}$, $\lambda_p = 1.06 \mu\text{m}$ and the respective indices of refraction are $n_s = 1.7348$, $n_i = 1.7793$, and $n_p = 1.7474$. One can approximate the effective nonlinear coefficient for both type II doubling and this OPO by use of [10.16]

$$d_{\text{eff}} \approx (d_{24} - d_{15}) \sin 2\phi \sin 2\theta - (d_{15} \sin^2 \phi + d_{24} \cos^2 \phi \sin \theta), \quad (10.71)$$

which reduces to $|d_{\text{eff}}| = 0.15d_{15} + 0.84d_{24}$ for $\theta = 90^\circ$ and $\phi = 23^\circ$. With the values of $d_{24} = 3.64 \text{ pm/V}$ and $d_{15} = 1.91 \text{ pm/V}$ [10.67], one obtains $d_{\text{eff}} \approx 3.3 \text{ pm/V}$. Using these parameters, we calculate from (10.62) $\kappa = 1.2 \times 10^{-8} \text{ W}^{-1}$.

In order to calculate the threshold of an SRO with pump reflection according to (10.70), we need the following system parameters: because of the noncritical phase matching condition, l_{eff} is as long as the physical length of the crystal, i.e., $l_{\text{eff}} = 1.5 \text{ cm}$, the round-trip loss is about $2\alpha l = 0.01$, the optical length of the OPO resonator is $L = 5 \text{ cm}$, output reflectivity is $R = 0.9$, pump length is $t_p = 50 \text{ ns}$. At threshold, we can make the following approximation: the ratio of backward to forward pump intensity is $\gamma \approx 1$, and the mode sizes are about equal at this low-power level with $w_s \approx w_p$, one obtains for the mode-coupling coefficient $g_s = 1/2$. Introducing these parameters into (10.70) yields a value for the threshold power density of $I_{\text{th}} = 52 \text{ MW/cm}^2$.

The performance of this OPO is illustrated in Figs. 10.28 and 29. In the experiment, a confocal configuration was also evaluated and its performance is displayed. In the confocal design, the plane mirrors were replaced with a pair of 5-cm concave mirrors with identical coatings to those used in the plane-parallel cavity. The use of this cavity allows the pump to be more tightly focused while still maintaining good matching of the pump, to reduce the pump energy threshold for the device. This matching proved critical to successful operation of the OPO. Any mismatch between the pump mode and the TEM_{00} mode of the OPO cavity will cause a reduction in gain for optical parametric oscillation and a subsequent increase in threshold. For this reason, a single-transverse-mode pump is essential for obtaining high OPO efficiency. The OPO employing a plane-parallel resonator reached threshold at a pump energy of 1.5 mJ, with a maximum output energy of 2.5 mJ obtained at 10 mJ pump energy.

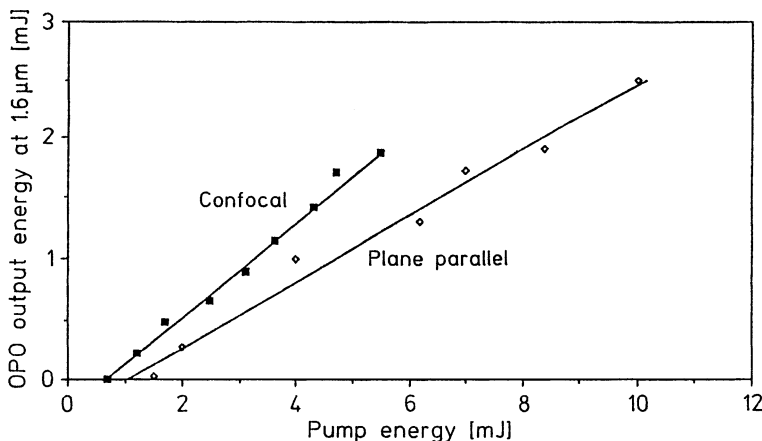


Fig. 10.28. Signal (1.6 μm) energy vs. pump energy for confocal and plane-parallel OPO resonator configurations

This corresponds to an energy conversion efficiency of 25%. Since the 25-ns duration signal pulse is only half as long as the pump pulse, the power conversion efficiency of the OPO is 50%.

Higher conversion efficiencies were observed with the confocal resonator than with the plane-parallel resonator, because of the lower threshold energy required in

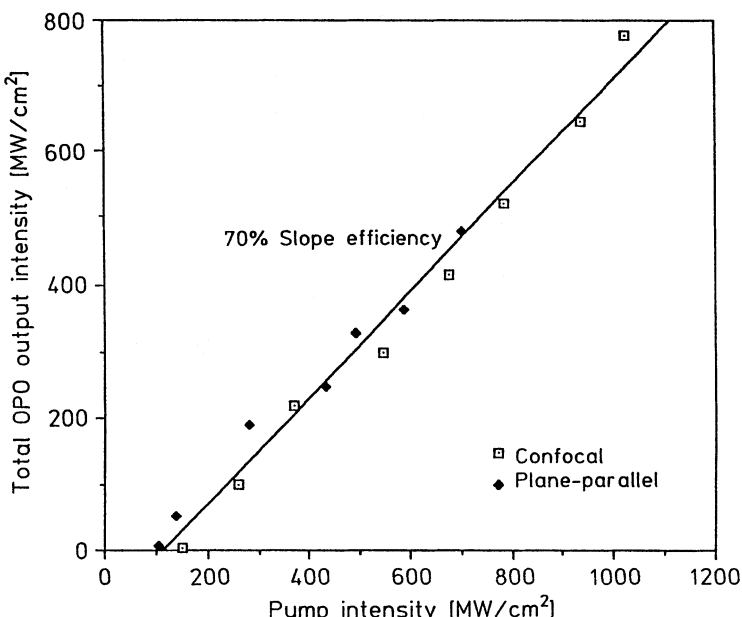


Fig. 10.29. Total OPO output intensity vs. pump intensity

the former configuration. Threshold energy is reduced because the pump is focused more tightly into the KTP crystal to obtain optimum matching for the confocal resonator. The threshold pump energy of this device was only 0.8 mJ, considerably lower than that of the plane-parallel configuration. A maximum output energy at 1.6 μm of 1.8 mJ was obtained for 5.5 mJ input pump energy. This corresponds to an energy-conversion efficiency of 33%. In the confocal configuration, the power conversion efficiency of 1.06 μm pump to 1.61 μm signal exceeds 50%, and the overall power conversion efficiency of the OPO, to both signal and idler outputs, exceeds 70%.

Optical parametric oscillation is intensity-dependent, so the pump intensity is a more meaningful parameter for gauging OPO performance than is pump energy. In Fig. 10.29, total output intensity is plotted vs. pump intensity. From the data presented in this figure follows that both resonator configurations produce similar results. Compared to the measured threshold, the theoretical value is a factor 2 lower. Crystal quality and its influence on the actual interaction length and resonator losses are probably the major reason for the discrepancy.

Saturation and Pump Beam Depletion

When the Q-switched pump pulse is incident on the nonlinear crystal, the signal and idler waves are amplified from the initial noise level. The number of round trips in the optical cavity necessary to amplify the signal and idler waves, multiplied by the cavity round-trip time, determines the delay in achieving threshold. This buildup time, required to achieve parametric oscillation, causes a temporal compression of the OPO output with respect to the pump pulse. Above threshold, after a short transition period during which a steady-state condition is established, the pump power is limited at the threshold value. Any pump input power above threshold is divided into power at the signal and idler beams. Since $v_3 = v_1 + v_2$, it follows that for each input pump photon above threshold, one photon at the signal and idler wavelengths is generated.

In other words energy of the pump beam is depleted, and in a lossless system, the depleted energy goes into the signal and idler beams.

The oscilloscope trace in Fig. 10.30, taken from the OPO described earlier, shows the dynamics of signal generation very nicely. The dashed curve is the input pump pulse. The two solid curves display the signal pulse and the depleted pump pulse at the output of the OPO. During the early part of the pump pulse, there is a transient period during which the oscillation builds up from noise. After the transient period, the pump beam is clamped at its threshold value until the pump power falls below threshold.

The onset of depletion to full limiting occurs quite rapidly. The fast-falling part of the pump beam has a time constant characteristic of the rise time of the signal wave. The buildup time required to achieve parametric oscillation causes a temporal compression of the OPO output with respect to the pump pulse. It is also clear from these considerations that the pump power must remain on long enough to allow the fields to build up to the threshold value. This leads to the consideration of a minimum pump fluence as well as flux.

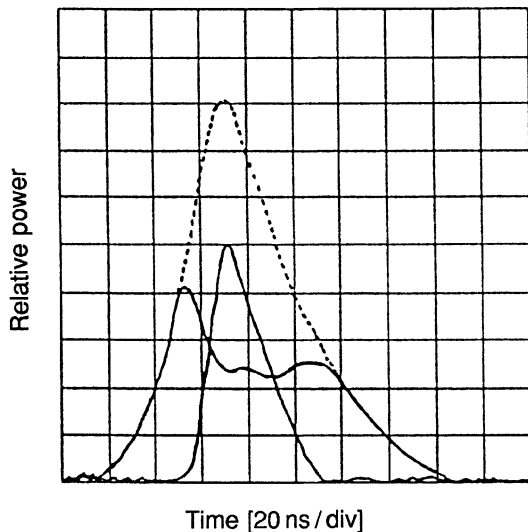


Fig. 10.30. Oscilloscope trace showing the depleted pump and the generated OPO output at 1.61 μm (solid curves) and the input pump (dashed curve)

Conversion Efficiency: In the plane-wave approximation, the conversion efficiency of an SRO for the ideal case of perfect phase matching and zero losses is given by [10.68]

$$\eta_{\text{par}} = \sin^2 gl, \quad (10.72)$$

where g and l have been defined in (10.61, 63).

Using this expression, total conversion of the pump can be achieved in theory. As the point of total conversion is exceeded, power starts to couple back into the pump field at the expense of the signal and idler fields, and the conversion efficiency decreases.

In practice, Gaussian beams are employed rather than plane waves. In this case, as in the case of frequency doubling, the maximum theoretical conversion efficiency is reduced. Although the center of the beam may be achieving total conversion, the intensity in the wings is considerably lower than the optimum. As one increases the pump power to convert the wings, the center exceeds the optimum and some back conversion occurs, resulting in an overall decrease in the conversion efficiency.

Theoretical conversion efficiencies for a plane wave and a Gaussian pump beam are plotted in Fig. 10.31 as a function of pump intensity above threshold. For a phase-matched uniform plane wave, the conversion can be 100% and occurs for $I/I_{\text{th}} = (\pi/2)^2$, where I and I_{th} are the input and threshold pump intensities, respectively. For a phase mismatch of $\Delta kl = \pi/2$, efficiency is around 75% for the plane-wave pump beam. Using a Gaussian pump beam, maximum efficiency is about 71% and occurs for $I/I_{\text{th}} \approx 6.5$.

The dependence of the conversion efficiency on pump power is illustrated in Fig. 10.32. Plotted is experimental data from several OPO experiments carried out with KTP as the nonlinear crystal and an Nd:YAG laser pump at 1.064 μm. The solid curve

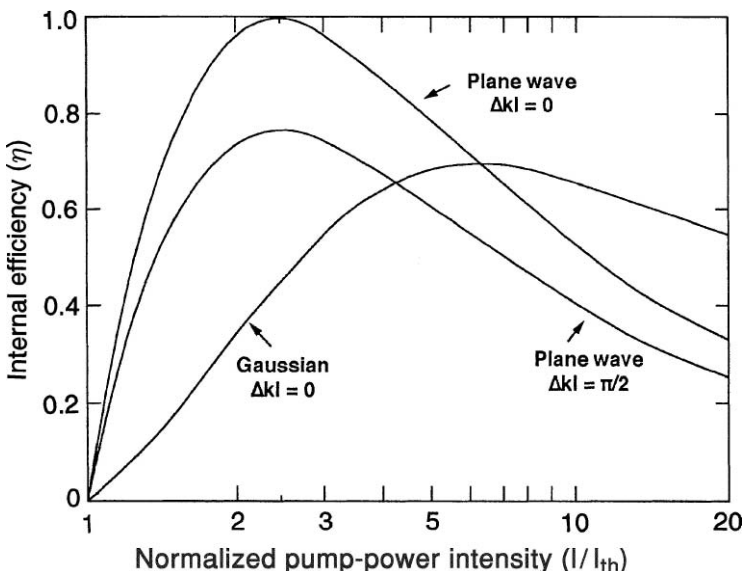


Fig. 10.31. Theoretical conversion efficiencies for a phase-matched plane wave and Gaussian pump beam and a plane-wave beam with a phase mismatch of $\pi/2$

was obtained by integrating the equations for plane wave OPOs over the spatial profile of the Gaussian beam, as described in [10.68].

One can derive a generic relationship between the factor by which pump power exceeds threshold power, and the OPO conversion efficiency. While there is some spread in the data, the general agreement is surprisingly good. The general “rule of

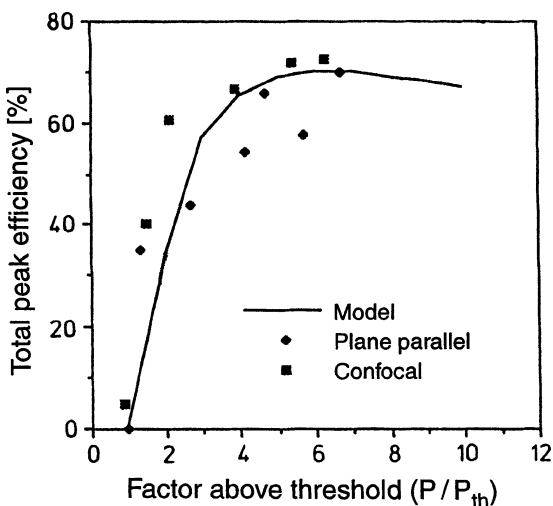


Fig. 10.32. Efficiency of an OPO vs. factor above threshold

thumb" for design of an efficient OPO is to pump at least four times above threshold for maximum efficiency. Thus one can calculate the threshold for a given OPO, then multiply this value by a factor 4 to determine the required pump intensity.

The conversion efficiency in (10.72) is defined as the ratio of the sum of signal and idler power to pump power. The energy or power between the signal and idler beams is divided according to the ratio of the photon energies, that is,

$$\frac{h\nu_s}{h\nu_i} = \frac{\lambda_i}{\lambda_s}. \quad (10.73)$$

From this follows the ratio of the energy of the signal compared to the total energy converted by the OPO

$$\frac{h\nu_s}{h\nu_s + h\nu_i} = \frac{1}{1 + \lambda_s/\lambda_i}. \quad (10.74)$$

Phase Matching

In order to achieve significant gain in the parametric device, the pump, signal, and idler waves have to be phase-matched according to (10.60). In a medium without dispersion, all waves propagate with the same velocity, hence $\Delta k = 0$. In reality, Δk is not zero for different wavelengths, and just as in harmonic generation, dispersion is compensated for by birefringence. The index of refraction at a given wavelength is a function of the direction of propagation in the crystal as well as orientation of polarization.

When the signal and idler waves are both ordinary rays, one has type I phase matching. When either one is an ordinary ray, it is referred to as type II phase matching.

In a uniaxial crystal, if the signal and idler are ordinary rays (type I) with indices of refraction n_s and n_i , then the index of refraction for the pump wave necessary to achieve phase matching is

$$n_p = (\lambda_p/\lambda_s)n_s = (\lambda_p/\lambda_i)n_i. \quad (10.75)$$

In uniaxial crystals, the index of refraction n_o for an extraordinary wave propagating at an angle θ to the optic axis is given by

$$\frac{1}{n_0(\theta)^2} = \frac{\cos^2 \theta}{(n^o)^2} + \frac{\sin^2 \theta}{(n^e)^2}, \quad (10.76)$$

where n^o and n^e are the ordinary and extraordinary indices of refraction, respectively. The index n_0 is thus limited by n^o and n^e . If n_p falls between n^o and n^e , then an angle θ_m exists for which $n_0 = n_p$. Propagation with $\Delta k = 0$ results, and all three waves travel at the phase matching angle θ_m with respect to the optical axis.

Phase matching with a propagation direction normal to the optic axis (90° phase matching) is preferred if possible. In that direction, the double refraction angle is zero and the nonlinear interaction is not limited by the effective gain length but by the crystal's physical length. Non- 90° phase matching does, however, allow angle tuning.

Line Width Control and Wavelength Tuning. The gain line width of an OPO is set by crystal dispersion; therefore the device has a rather broad line width, limited only by the phase-matching bandwidth of the crystal. Small dispersion and birefringence leads to relatively large bandwidths and tuning ranges, vice versa. In [10.62], a simple relationship is given for the bandwidth $\delta\nu$ (in wave numbers) and birefringence Δn ,

$$\delta\nu[\text{cm}^{-1}] \approx \frac{1}{\Delta nl[\text{cm}]}, \quad (10.77)$$

where l is the crystal length. Crystals with small birefringence have larger bandwidth than crystals with large birefringence.

The line widths of OPOs are generally too broad for spectroscopic applications. Line width control can be achieved by using highly dispersive resonators which contain etalons, diffraction gratings, or resonant reflectors [10.61]. A more recent development is line width control by means of injection seeding of the OPO [10.69]. Similar to the technique described for line width control of a laser oscillator, a cw beam is injected into the pulsed SRO cavity. The length of the oscillator cavity is adjusted so that it is resonant at the injected frequency. When the pump is then applied, the desired mode starts from the level of the injected signal, whereas the competing modes begin from spontaneous emission. Provided the injected power level is sufficiently high, the injected signal will be the first to build up to a high power level and will deplete the pump.

Tuning curves for parametric oscillators can be determined by solving the phase matching equations (10.59,60) for signal and idler frequencies at a given pump frequency as a function of the tuning variable. The most common tuning methods are varying the direction of propagation with respect to the crystal axes or by changing the crystal temperature. To carry out the calculations, the indices of refraction must be known over the entire tuning range. For most nonlinear crystals of interest, the indices can be obtained from the Sellmeier equations.

We will consider KTP pumped by an Nd:YAG laser at 1.06 μm , as an illustration of the type of calculation which has to be performed to determine the tuning range and appropriate phase matching angle for an optical parametric oscillator [10.70].

Potassium titanyl phosphate (KTP) belongs to the orthorombic crystal system, and therefore is optically biaxial (having two optical axes). The mutually orthogonal principal axes of the index ellipsoid are defined such that $n_x < n_y < n_z$, and the optical axes lie in the x - z plane (at 18° to the z -axis in KTP [10.71] (Fig. 10.33)).

The indices of refraction for any propagation direction are given by the index ellipsoid defined by

$$k_x^2/(n_{\omega j}^{-2} - n_{x,\omega j}^{-2}) + k_y^2/(n_{\omega j}^{-2} - n_{y,\omega j}^{-2}) + k_z^2/(n_{\omega j}^{-2} - n_{z,\omega j}^{-2}) = 0, \quad j = p, s, i, \quad (10.78)$$

where $k_x = \sin\theta \cos\phi$, $k_y = \sin\theta \sin\phi$, $k_z = \cos\theta$; θ is the angle to the z -axis and ϕ is the angle to the x -axis in the x - y plane. The subscript “j” refers to either the pump, signal, or idler frequency. Equation (10.78) must be solved to determine the

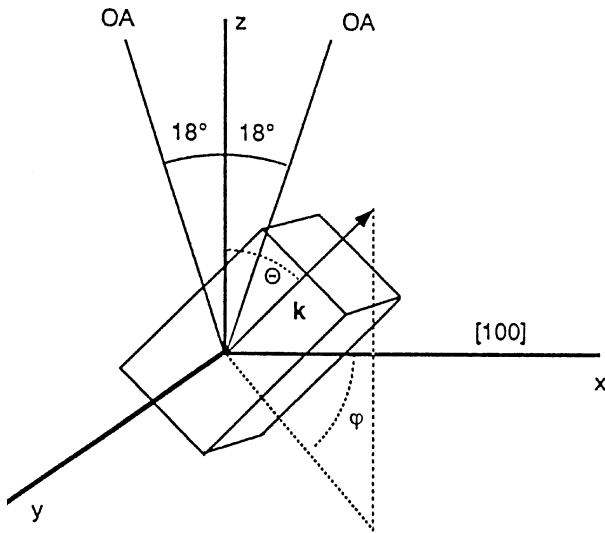


Fig. 10.33. KTP phase-matching angles

refractive indices ($n_{\omega j1}, n_{\omega j2}$) for the two eigen-polarizations perpendicular to the propagation direction for each wavelength. The equations can be solved numerically using the technique described in [10.71, 72]. In our work, this has been done using a spreadsheet (Excel) program.

The indices of refraction are obtained from the appropriate Sellmeier equation [10.67, 73]

$$\begin{aligned} n_x^2 &= 3.0065 + \frac{0.03901}{\lambda^2 - 0.04251} - 0.01327\lambda^2, \\ n_y^2 &= 3.0333 + \frac{0.04154}{\lambda^2 - 0.04547} - 0.01408\lambda^2, \\ n_z^2 &= 3.3134 + \frac{0.05694}{\lambda^2 - 0.05658} - 0.01682\lambda^2, \end{aligned} \quad (10.79)$$

where λ is in micrometers.

The phase matching condition for optical parametric conversion in KTP is given by [10.71, 72]

$$\omega_p n_{\omega p1} = \omega_s n_{\omega s2} + w_i n_{\omega i2} \quad (\text{type I}) \quad (10.80)$$

or

$$\omega_p n_{\omega p1} = \omega_s n_{\omega s1} + w_i n_{\omega i2} \quad (\text{type IIa}) \quad (10.81)$$

or

$$\omega_p n_{\omega p1} = \omega_s n_{\omega s2} + w_i n_{\omega i1} \quad (\text{type IIb}). \quad (10.82)$$

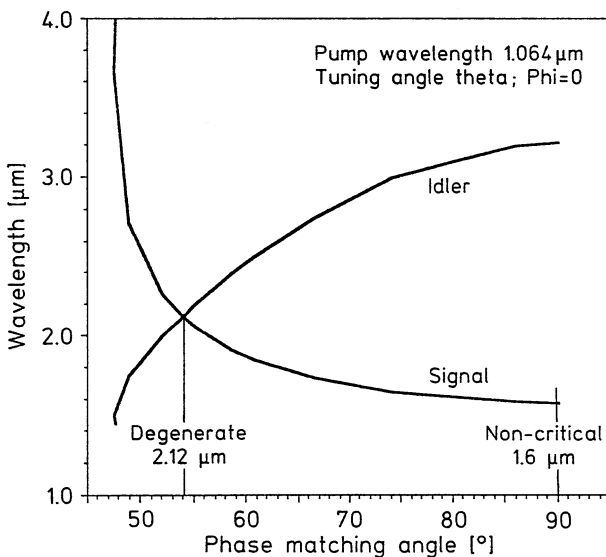


Fig. 10.34. Tuning range of an OPO pumped by a $1.064\text{ }\mu\text{m}$ Nd laser and employing a type II KTP crystal

In KTP, type I interactions have very low nonlinear coefficients, and therefore are not useful. For propagation in the $x-z$ plane ($\phi = 0$) in KTP, type II interactions correspond to type II phase matching in a positive uniaxial crystal (e.g., $\omega_p n_p^o = \omega_s n_s^o + \omega_i n_i^e$), where “o” and “e” represent the ordinary and extraordinary rays, respectively.

Figure 10.34 exhibits the calculated phase matching angles for a KTP optical parametric converter pumped at $1.064\text{ }\mu\text{m}$. The two curves correspond to the signal and idler wavelengths for type II phase matching with $\phi = 0$. The polarization of the pump wave is along the y -axis (o-wave) of the crystal as is that of the signal wave. The idler wave is polarized in the $x-z$ plane (e-wave). The degenerate point at $2.12\text{ }\mu\text{m}$ corresponds to a phase matching angle of $\theta = 54^\circ$.

10.3.2 Crystals

The nonlinear crystals used for parametric oscillators must be transparent and have low loss at the pump as well as the signal and idler wavelengths. Very important for reliable OPO operation is a high damage threshold, and a large ratio of optical damage threshold to pump threshold. Table 10.3 lists a number of nonlinear materials for use in OPOs. The critical parameters for OPO crystals are slightly different to those for doubling where one requires broad angular acceptance, low-temperature sensitivity, and broad-frequency acceptance. In OPOs, absence of these qualities merely leads to broad linewidth output from the OPO owing to the inherent tunability of the OPO. For example, exceeding the acceptance angle prevents phase matching at one pair of signal and idler wavelengths; however, the OPO will tune these wavelengths until phase matching is recovered, producing an output of broader line width.

Table 10.3. Common crystals employed in OPOs

	LBO	BBO	KTP	KTa	AgGaS ₂	LiNbO ₃	PPLN
$d_{\text{eff}} [\text{pm/V}]$	1.16	1.94	3.64	4.47	13.5	5.1	17.2
Transparency [μm]	0.16–2.6	0.19–2.5	0.4–3.5	0.4–4.0	0.5–12	0.5–5	0.5–5
Damage threshold [GW/cm ²]	2.5	1.5	0.5	0.5	0.03	0.2	0.2
Typical length [cm]	0.5–1	0.5–1	1–2	1–2	2–4	2–5	2–6

Listed in Table 10.3 is also the maximum crystal size currently available from commercial sources. A minimum crystal length of at least 1 cm is usually required for the achievement of a high conversion efficiency, and a sufficient crystal cross section is important to keep the pump intensity substantially below the damage threshold. For example, when pumping at the joule level, one typically needs to expand the pump beam to lower the pump intensity. In this case, operation at 100 MW/cm², with a typical pulse length of 20 ns, requires a beam diameter of 0.8 cm. Thus, one requires a crystal size on the order of 1 cm³. The use of a larger pump-beam diameter also reduces the effect of walk-off; for example, the walk-off angle in a mid-IR KTP OPO is 2.6°, which reduces the effective interaction length to 4 mm for a 200-μm pump beam diameter. However, if the pump-beam diameter is increased to 8 mm, the interaction length is dramatically increased to 160 mm, so that walk-off is negligible over the typical 15-mm-long crystals employed in practice.

Most of the materials listed in Table 10.3 have already been described in Sect. 10.2.3. For OPOs operating in the UV, visible, or near-infrared, BBO and LBO are the preferred materials because of the transparency range which extends to very short wavelengths. As an example, Fig. 10.35 displays tuning curves for OPOs using BBO

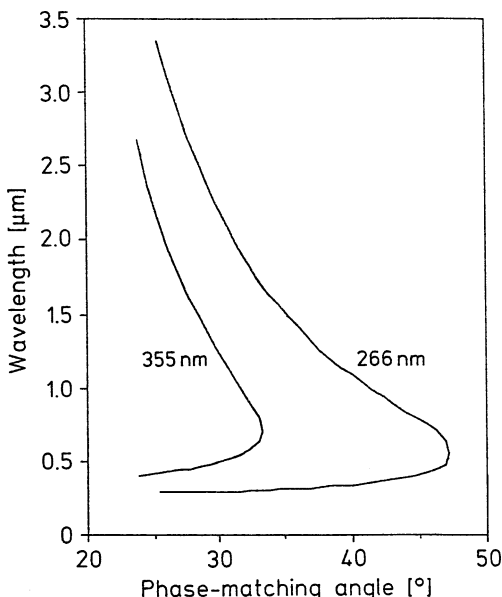


Fig. 10.35. Tuning curves for BBO in a type I configuration pumped at the wavelength of 266 and 355 nm [10.75]

in a type I configuration pumped at the tripled or quadrupled output from an Nd laser [10.74,75]

KTP is the material of choice for the design of OPOs pumped with Nd lasers at 1.064 μm [10.64–66, 76–78]. This material has already been described in the previous sections. It has been observed that the damage threshold of KTP when used in an OPO can be considerably lower compared to second harmonic generation [10.79]

Potassium titanyl arsenate (KTA) is a new nonlinear material which is isomorphic with KTP. Substitution of arsenic for phosphorous extends the transparency range further into the infrared. However, the major difference between the two materials is the considerably lower absorption losses in the 3–5 μm region of KTA, as illustrated in Fig. 10.12. Usually, the wavelength beyond 3 μm is the idler wavelength when a KTA or a KTP OPO is pumped by an Nd:YAG or an Nd:YLF laser. For example, a pump wavelength of 1.06 μm and signal wavelength of 1.54 μm produce an idler wavelength at 3.44 μm. Since KTA does not have any appreciable absorption at the idler wavelength, this material has fewer problems associated with thermal lensing and heating of the crystal in high-average-power OPOs. In terms of damage threshold and nonlinear coefficient, the materials are quite similar although d_{eff} is somewhat higher in KTA. With a 1.064-μm pump beam from an Nd:YAG laser, noncritical phase matching produces a signal at 1.538 μm in KTA, whereas in KTP the signal output is at 1.574 μm. OPOs featuring KTA crystals are described in [10.79–81].

Although silver gallium selenide (AgGaSe_2) has a low damage threshold, it is of interest for the design of low-power OPOs because its transparency reaches far into the infrared. Optical parametric oscillators using AgGaSe_2 have been pumped by Nd:YAG lasers to produce output from 6 to 14 μm. This tuning range was achieved in a two-stage OPO system, with an Nd:YAG laser pumping a noncritically phase-matched KTP OPO at fixed wavelength of 1.57 μm, which was used to pump a AgGaSe_2 OPO [10.82]. Also continuously tunable output from 6.7 to 9.8 μm was achieved by directly pumping a AgGaSe_2 OPO with a Q-switched pulse from an Nd:YAG laser [10.83].

Another crystal that is used to produce output in the mid-infrared region is ZnGeP_2 . The crystal has a transparency range from 2 to 8.4 μm; therefore, pump sources such as Ho:YAG or Tm:Ho:YAG lasers are required, which emit at or above 2 μm. ZnGeP_2 has a higher thermal conductivity and nonlinear coefficient compared to AgGaSe_2 . Disadvantages are the increasing losses above 8 μm and the fact that none of the common Nd-based laser sources can be used to pump this material.

LiNbO_3 is a nonlinear crystal which has been employed widely in the past. Unfortunately, it has a much lower damage threshold compared to newer materials such as KTP and KTA which cover the same wavelength regime. However, recently a different version of this material, namely periodically poled LiNbO_3 (PPLN), has become available. PPLN has a very large nonlinear coefficient, and therefore it is well suited for low-peak-power OPOs in the near- and mid-infrared. Because of the unique concept underlying PPLN, it will be described in more detail below.

10.3.3 Quasi Phase Matching

In this subsection we will briefly review the concept of quasi phase matching (QPM), and summarize the properties of periodically poled LiNbO₃ (PPLN). Although QPM is applicable to any nonlinear process, the subject is covered here because of the importance of PPLN and its application in OPOs for the generation of mid-infrared radiation.

PPLN is the first commercially available crystal in which efficient nonlinear conversion processes, such as harmonic generation or parametric interactions, are not based on birefringence phase matching but on a periodic structure engineered into the crystal. We will briefly explain this technique, termed quasi phase matching, by referring to Sect. 10.2.1. An in-depth treatment of this subject can be found in [10.84–86].

As illustrated in Fig. 10.2 and expressed by (10.19), in a phase-matched condition $\Delta k = 0$ the harmonic power increases with the square of the interaction length ℓ . In the situation of a fixed phase mismatch Δk , energy flows back and forth sinusoidally between the fundamental and harmonic beams with a period of $\Delta k \ell / 2 = \pi$ as the waves propagate through the crystal. Half of this period is the coherence length ℓ_c given by (10.24), which is the maximum distance over which the second harmonic can grow. In a non-phase-matched condition, this distance is on the order of 2–20 μm for conversion processes of interest. The objective of birefringence phase matching is to make this distance as long as possible by taking advantage of the wavelength and polarization dependence of the refractive indices in a crystal. By arranging proper balance between dispersion and birefringence the technique of phase matching increases ℓ_c by a factor of 10³.

Even before the concept of birefringence phase matching was invented, it was proposed that a periodic structure in the crystal which corrects the phase of the propagating beams each time it reaches π would enable continued energy flow from the fundamental to the harmonic beam [10.8]. An implementation of this concept is a crystal where the sign of the nonlinear coefficient is reversed after each distance ℓ_c . In this case the relative phase between the waves is inverted after the conversion has reached its maximum. Therefore, on the average the proper phase relationship between the beams is maintained and the second harmonic power, increases with the square of crystal length similar to the birefringence phase matching case. The nonlinear coefficient d_Q for QPM is, however, reduced as compared to the phase-matched interaction according to [10.84]

$$d_Q = \frac{2}{\pi} d_{\text{eff}}. \quad (10.83)$$

A phase reversal is equivalent of slicing a crystal in thin wafers and stacking the wafers by rotating alternate wafers by 180°. The periodicity \wedge of this structure is twice that of ℓ_c , i.e.,

$$\wedge = 2\ell_c. \quad (10.84)$$

Because of the micrometer-size thickness of alternating layers, the practical realization of QPM had to wait until it was possible to engineer a periodic phase reversal into a monolithic crystal. Only recently has the technique of periodically reversed polarization domains in ferroelectric crystals, combined with advances in lithography, made it possible to realize this concept. A reversal of the ferroelectric domains corresponds to a sign reversal of the nonlinear coefficient. In this process, standard lithography produces a patterned electrode with a period between 5 and 30 μm on the surface of a ferroelectric crystal such as LiNbO₃. A high-voltage pulse is applied to the crystal which is sandwiched between the patterned electrode and a uniform electrode. The high electric field strength of the voltage pulse permanently reverses the sign of the nonlinear coefficient in a pattern determined by the electrode structure.

This electric-field-poling technique is employed to reproducibly manufacture PPLN suitable for applications in infrared parametric oscillators and second harmonic generation.

We will now derive an expression for the QPM condition in OPOs for periodically poled crystals. Parametric conversion requires energy conservation and momentum matching conditions, as given by (10.59 and 60). A momentum mismatch expressed as a phase mismatch between the pump, signal, and idler waves has been defined in (10.64). In the frequency domain, a periodic structure can be represented by a grating wave vector

$$k_g = 2\pi/\lambda_g, \quad (10.85)$$

where λ_g is the period of the grating.

In the presence of a grating structure in the crystal, the equation for phase mismatch (10.64) includes as an additional term the grating wave vector k_g [10.85]

$$\Delta k = k_p - k_s - k_i - k_g, \quad (10.86)$$

the first three terms being the conventional phase matching condition. It is assumed that all wave vectors are collinear with the grating vector.

The objective of high parametric conversion is to eliminate the phase mismatch caused by dispersion by selecting the appropriate crystal orientation, temperature, and polarization such that $\Delta k = 0$ is achieved. The grating vector in (10.86) provides an additional adjustable parameter that is independent of inherent material properties.

Differences of the three wave vectors k_p , k_s , and k_i can be compensated by an appropriate choice of the grating vector k_g such that $\Delta k = 0$ can be achieved. Introducing (10.85) into (10.86) and with $\Delta k = 0$ the grating period under QPM conditions is given by

$$\lambda_g = \frac{2\pi}{k_p - k_s - k_i}. \quad (10.87)$$

Equation (10.87) can also be expressed by

$$\frac{1}{\lambda_g} = \frac{n_p}{\lambda_p} - \frac{n_s}{\lambda_s} - \frac{n_i}{\lambda_i}. \quad (10.88)$$

This equation is the equivalent of (10.60), which was derived for the birefringence phase matching case. If one substitutes Δk in (10.18) with k_g from (10.85), then one obtains the following condition for harmonic generation:

$$\Lambda_g = \frac{\lambda_1}{2(n_{2\omega} - n_{1\omega})}. \quad (10.89)$$

The fact that the domain thickness is a free parameter which can be customized for a particular nonlinear process offers significant advantages over birefringent phase matching. For example, QPM permits wavelength selection over the entire transmission window of the crystal, it allows utilization of the largest nonlinear coefficient, and it eliminates problems associated with walk-off since all interactions are noncritical.

For example, LiNbO₃ interactions with all waves polarized parallel to the crystal optic axis utilize the largest nonlinear coefficient $d_{33} = 27 \text{ pm/V}$. PPLN permits non-critical phase matching with this coefficient. Birefringent phase matching requiring orthogonally polarized beams can only be accomplished with the smaller coefficient $d_{31} = 4.3 \text{ pm/V}$. Therefore, PPLN has a parametric gain enhancement over single-domain material of $(2d_{33}/\pi d_{31})^2 \approx 16$.

The grating period of PPLN for a particular OPO can be calculated from (10.88), with the indices of refraction obtained from the Sellmeier equation. For example, if it is desired to shift the wavelength of an Nd: YAG laser with output at $\lambda_p = 1.064 \mu\text{m}$ to the eye-safe region of $\lambda_s = 1.540 \mu\text{m}$, then one obtains from (10.59) an idler wavelength of $\lambda_i = 3.442 \mu\text{m}$. The next step is the determination of the indices of refraction at these wavelengths. The most recent coefficients of the Sellmeier equation for the extraordinary index of refraction have been published in [10.87]. At an operating temperature of 120°C we obtain $n_p = 2.160$, $n_s = 2.142$, and $n_i = 2.085$. Introducing these values into (10.88) yields $\Lambda_g = 29.8 \mu\text{m}$.

PPLN is commercially available as 1-mm-thick crystals, with lengths ranging from 20 to 60 mm, and a width depending on the number of different gratings desired. For example, a width of 11 mm may contain up to eight separate grating periods. Translation of the crystal normal to the beam moves a different grating into the beam, which shifts the signal and idler waves to a new wavelength band. Fine tuning can be accomplished by changing the temperature.

LiNbO₃ has a relatively low damage threshold in comparison to, for example, KTP. Also, PPLN, like single-domain LiNbO₃, has to be heated to eliminate photorefractive effects. Although photorefractive damage is mainly caused at shorter wavelengths, it can be a problem also in infrared OPOs because a certain amount of visible radiation is generated in these devices by second harmonic and sum frequency processes.

Pulsed and cw optical parametric oscillators using PPLN, and pumped by Nd: YAG lasers, have been operated over the wavelength range from 1.4 to 4 μm and with outputs from cw [10.86, 88] to Q-switched pulses in the nanosecond regime [10.89–91] up to femtosecond pulses [10.92, 93]. Tuning has been accomplished by translation of the PPLN crystal or by temperature changes or by both.

Peak powers and pulse energies are limited by the small aperture of available crystals and the relatively low damage threshold of this material. Therefore, PPLN has become the crystal of choice for OPOs pumped by cw or high-repetition-rate

Nd:YAG lasers producing up to several watts of mid-infrared radiation. These lasers have pulse energies and peak powers that are relatively low and provide a natural match for PPLN. In addition, the high-gain and noncritical phase matching permit the design of highly efficient OPOs.

Although PPLN is used mainly in OPOs for infrared interactions, the five times higher nonlinear coefficient compared to KTP allows efficient single-pass cw frequency doubling external to the resonator [10.94]. The efficiency obtained is comparable to the performance of intracavity doubling but without the complications associated with output fluctuations discussed in Sect. 10.2.4. Since dispersion is larger at shorter wavelengths, the period of the domain structure must be reduced according to (10.89). This poses a fabrication problem since the domain period for frequency doubling a Nd:YAG laser is only $6.5\text{ }\mu\text{m}$ for a PPLN crystal operated at 200°C . As mentioned earlier, suppression of photorefractive damage requires operation of a PPLN at a fairly high temperature. However, it seems that PPLN is more resistant to photorefractive damage compared to ordinary LiNbO_3 [10.95].

As already pointed out in Sect. 10.2.3, LiNbO_3 crystals doped with MgO show improved photorefractive damage resistance at visible wavelengths [10.96].

Although not available commercially, other ferroelectric crystals such as KTP, RTA rubidium titanyl arsenate), and LiTaO_3 (lithium tantalate) have been periodically poled, and promising results have been achieved with these materials in harmonic generators and OPOs [10.97–100]. Since these crystals have high damage thresholds they hold promise for efficient nonlinear interactions at higher pulse energies compared to PPLN.

It is anticipated that the research for new and improved periodically poled crystals remains very active in the future because QPM has a number of advantages over birefringence phase matching. Since QPM allows noncritically phase-matching beams can be tightly focused. New nonlinear materials which have a low birefringence such as LiTaO_3 can be used as nonlinear material. This is particularly important at shorter wavelengths where the dispersion increases more dramatically than birefringence. Also QPM allows the largest nonlinear coefficient to be used and provides the ability to phase-match over the full transparency range of crystal.

10.3.4 Design and Performance

As mentioned at the beginning of this section, the advent of new nonlinear materials such as KTP, KTA, BBO, LBO, and PPLN in combination with the high beam quality obtained from diode-pumped lasers has led to the practical realization of pulsed or cw-tunable radiation sources with output in the UV, visible, and IR region of the spectrum. The most mature OPO technology exists for the generation of radiation in the $1.5\text{--}4\text{ }\mu\text{m}$ region utilizing Nd:YAG lasers as pump sources.

Figure 10.36 illustrates the generation of mid-infrared radiation using PPLN employed in an intracavity OPO pumped by Nd:YAG laser emitting at $1.064\text{ }\mu\text{m}$ [10.101].

The fundamental pump laser was quasi-cw-pumped and repetitively Q-switched from 30 to 100 kHz. The output of the intracavity OPO consisted of a signal wave

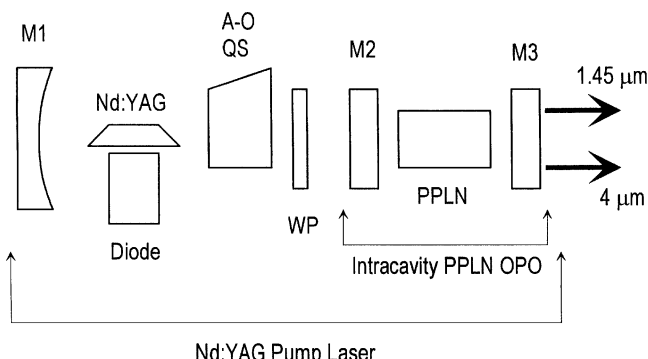


Fig. 10.36. Generation of mid-infrared radiation using PPLN employed in an intracavity OPO pumped by an Nd:YAG laser

near $1.45\text{ }\mu\text{m}$ and an idler wave near $4\text{ }\mu\text{m}$. For applications that require high repetition rate or cw output, achieving high pump intensity often poses difficulty for the system architecture. One way to overcome this difficulty, yet still maintain the high pump intensity, is to use the intracavity configuration, which is employed frequently in second harmonic generation. Intracavity parametric conversion utilizes the high intracavity intensity available inside an optical resonator. The one way intracavity power density is enhanced by a factor $1/(1 - R)$ over the output beam intensity, where R is the reflectivity of the output coupler.

The energy transfer in a Q-switched intracavity OPO consists of three steps: First, energy is stored in the upper laser level with the Q-switch turned off. When the laser cavity is Q-switched, pump radiation for the OPO builds up. When the pump intensity exceeds the OPO threshold, the signal and idler fields build up and the energy is transferred from the pump field to the signal and idler beam. A fraction of the signal and idler radiation leaves the cavity as useful output. The OPO acts as a nonlinear output coupler for the laser.

The layout of the intracavity OPO is shown in Fig. 10.36. It consists of a Nd:YAG, 1064 nm fundamental pump laser, and an intracavity PPLN OPO resonator. The Nd:YAG laser was a side-pumped slab design. An acousto-optic Q-switch was placed inside the pump laser resonator to provide repeated Q-switching. A half wave plate at 1064 nm was positioned between the Q-switch and PPLN OPO to provide the correct polarization of the pump laser for the quasi phase matching of the PPLN. The PPLN crystal had eight grating periods. The wavelength indicated in Fig. 10.36 was achieved with a period of $28.2\text{ }\mu\text{m}$. The PPLN crystal kept at 116°C was 19-mm long and had a thickness of 0.5 mm. Mirror M_1 had a radius of curvature of 20 cm and produced a beam waist at the PPLN crystal. The intracavity OPO was formed by mirrors M_2 and M_3 , where mirror M_3 served also as one resonator mirror of the pump laser resonator. Mirror M_2 had a AR coating for 1064 nm and a high reflectivity coating for $1.45\text{ }\mu\text{m}$ and $4\text{ }\mu\text{m}$. Mirror M_3 had a high reflectivity at 1064 nm, and 10% transmission at $1.45\text{ }\mu\text{m}$ and high transmission for the idler at $4\text{ }\mu\text{m}$. The OPO is therefore singly resonant.

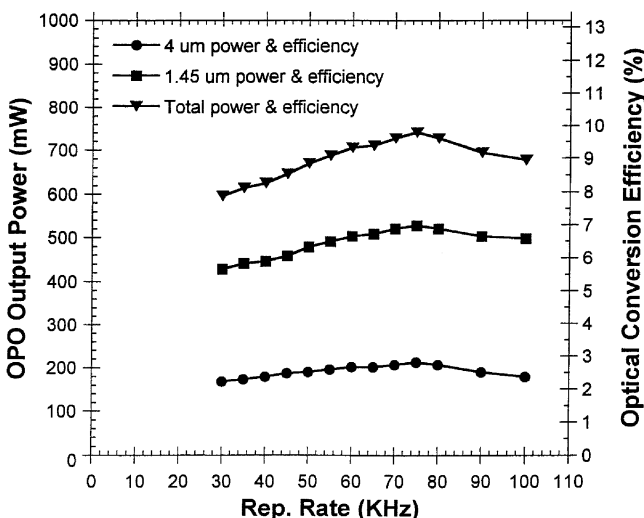


Fig. 10.37. Average power (left scale) and optical conversion efficiencies (right scale) of an intracavity-pumped PPLN OPO as function of the Q-switching repetition rate

Figure 10.37 shows the average power performance (left scale) and the optical conversion efficiency (right scale) of the intracavity PPLN OPO as function of the Q-switching repetition rate. The optical conversion efficiency of the intracavity PPLN OPO is defined as the ratio of the OPO average power to the average diode pump power.

Three sets of data are shown, representing the average output powers and optical conversion efficiencies at $1.45\text{ }\mu\text{m}$, $4\text{ }\mu\text{m}$, and the total, respectively. The best power performance appeared to be near 75 KHz, at which the average powers of $1.45\text{ }\mu\text{m}$ and $4\text{ }\mu\text{m}$ lasers were 528 mW and 212 mW, respectively, and the total output power was 740 mW.

Other examples of intracavity-pumped OPOs for the generation of $1.5\text{- or }2\text{-}\mu\text{m}$ radiation can be found in [10.102, 103].

The wavelength coverage of OPOs has been extended as far as $10\text{ }\mu\text{m}$. For example, tunable output from 3.7 to $10.2\text{ }\mu\text{m}$ was achieved with a system comprising an Nd:YAG laser and two OPOs in series. The first OPO contained a PPLN crystal and was pumped by the Nd:YAG laser that provided tunable radiation over the range 2.3 – $3.7\text{ }\mu\text{m}$. This output was the pump source for an OPO containing a zinc germanium phosphide (ZnGeP_2) crystal [10.104]. In another system a ZnGeP_2 was pumped by a Ho:YAG laser at $2.09\text{ }\mu\text{m}$ to yield tunable output in the 3 – $5\text{ }\mu\text{m}$ region. [10.105].

Tunable output in the visible spectral region can be achieved in two ways. One approach is to use a UV pump source such as a frequency tripled or quadrupled Nd:YAG laser. An alternative approach is the frequency conversion of the signal or idler wavelength of a near-infrared OPO. An example of each approach is illustrated below.

Optical parametric oscillation in the UV, visible, and near-infrared region has been demonstrated in BBO and LBO which have been pumped with Q-switched, frequency

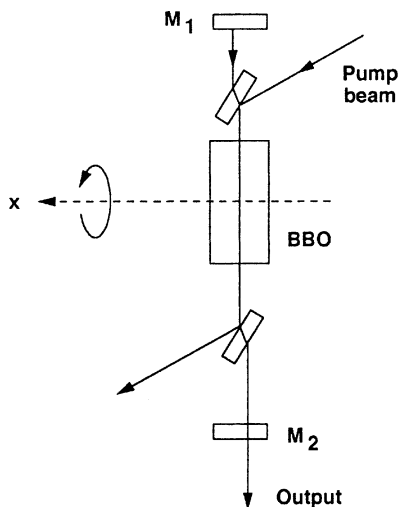


Fig. 10.38. Optical parametric oscillator featuring a BBO crystal pumped by the fourth harmonic of a Nd:YAG laser [10.110]

tripled [10.106–109] and quadrupled [10.110] Nd:YAG lasers. An example of such a device is the singly resonant OPO, shown in Fig. 10.38 [10.110]. A 20.5-mm-long BBO crystal pumped by a Q-switched and quadrupled Nd:YAG laser with output at 266 nm provided tunable output from 0.33 to 1.37 μm with different sets of mirrors. The BBO crystal was cut for type I phase matching at 39.1°. The optical cavity length was 7.5 cm, which allowed about 20 round-trip passes through the crystal during the 9-ns-long pump pulse. Threshold was obtained at 4.5 mJ or 23 MW/cm².

Optical damage of the mirrors is a major consideration in the design of OPOs. In a singly-resonant OPO, trichroic dielectric mirrors are required which are highly transmissive at the pump and idler wavelengths and highly reflective at the signal wavelength. In addition, the mirrors must have a high damage threshold. With a pump wavelength in the ultraviolet, demands on mirror coatings are particularly severe. An interesting feature of this OPO is the introduction of the pump beam into the OPO resonator by means of a separate set of mirrors oriented at Brewster's angle. The advantage of this design is the fact that the resonator mirrors M₁ and M₂ of the OPO do not have to transmit the intense UV pump beam.

Figure 10.39 illustrates a configuration of an intracavity-doubled OPO designed to produce output in the UV/blue wavelength region [10.111]. The device generates radiation between 760 and 1040 nm, which is internally doubled to produce tunable output from 380 to 520 nm. The OPO employs a 15-mm-long KTP crystal, antireflection-coated at 911 nm, cut for normal incidence at $\phi = 0^\circ$ and $\theta = 69^\circ$. The angles correspond to type II phase matching for a signal wavelength of 911 nm.

The pump source is a diode-pumped Nd:YAG laser which is frequency-doubled by a 1-cm-long KTP crystal. The waist of the pump beam is positioned at the center of the 5-cm-long OPO cavity.

The 532-nm pulse enters the OPO cavity through a flat dichroic turning mirror (M₁; highly reflecting at 800–950 nm and highly transmitting at 440–540 nm). The

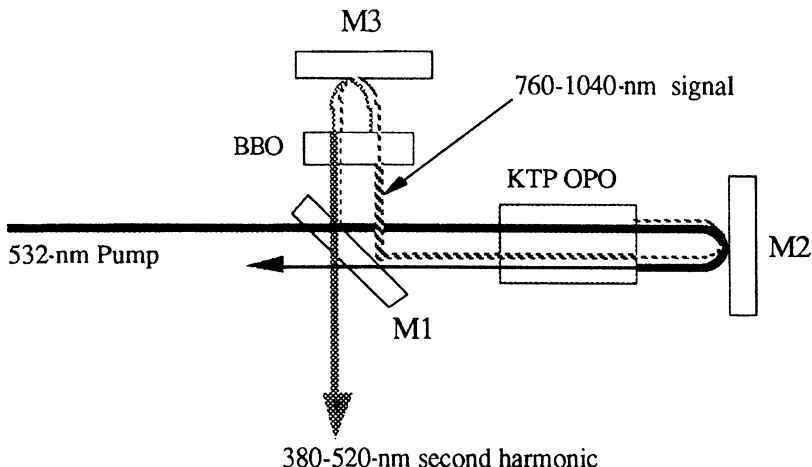


Fig. 10.39. Layout of intracavity OPO, showing the different pump wavelengths involved: the 532-nm pump, the 760–1040-nm signal, and the 380–520-nm intracavity-doubled signal [10.111]

532-nm pulse passes through the OPO crystal and is reflected off the flat rear cavity mirror (M_2 ; highly reflecting at 532 nm and 880–950 nm), to leave the cavity through mirror M_1 after making a second pass through the OPO crystal.

All mirrors have minimal reflectivity at the idler wavelength, making the OPO singly resonant. The intracavity 911-nm flux is reflected by the turning mirror (M_1) to pass through a 3-mm-long BBO type I doubling crystal. The final cavity mirror (M_3) is highly reflective at both 880–950 nm and 410–480 nm, which allows the doubled output to be extracted through the turning mirror (M_1) after making another pass through the doubling crystal. The use of two-pass nonlinear generation in both the doubler and the OPO significantly improves the conversion efficiency of these processes. The advantage of this configuration is that the KTP crystal is not exposed to the blue-UV flux, which could cause damage problems.

The output energies obtained at the various wavelengths are shown in Fig. 10.40, plotted as a function of the electrical input energy to the diode arrays of the Nd:YAG pump laser.

The large nonlinear coefficient of PPLN in combination with significant advances in manufacturing of PPLN now allow for the production of long crystals with excellent quality. This means that efficient operation of OPOs is no longer limited to high peak powers, thereby easing the requirements on the pump source for cw OPOs. The flexibility of grating-engineered phase matching has been particularly significant for cw OPOs and allowed a drastic reduction of the threshold of cw singly resonant OPOs. Threshold can be reduced to a few watts that make it possible that for example the devices can be directly pumped with diode lasers [10.112]. Continuous-wave OPOs have been established as practical and efficient sources of tunable radiation in the near- to mid-infrared spectral region. Devices for the ultraviolet and visible spectrum have not reached the same level of maturity.

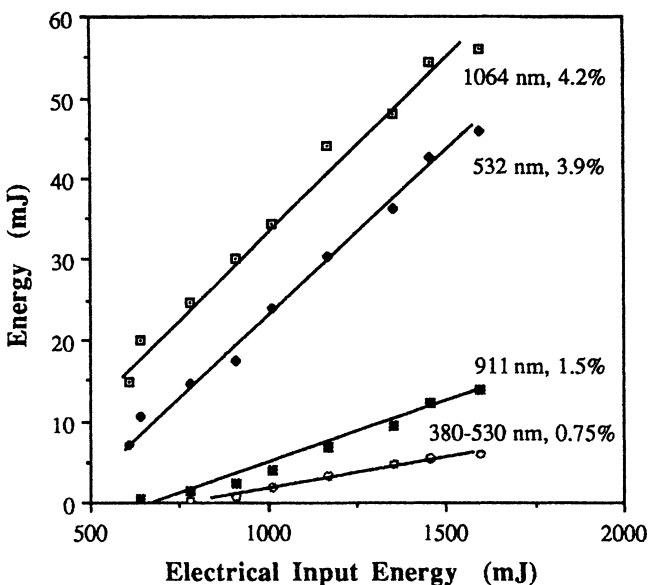


Fig. 10.40. Output at various wavelengths of the OPO depicted in Fig. 10.39 as a function of electrical input to the Nd:YAG pump laser

A common configuration for singly resonant cw OPOs is a four-mirror ring resonator with PPLN as the nonlinear crystal as depicted in Fig. 10.41 [10.112–115]. The bow-tie ring cavity is formed by two concave and two flat mirrors. Singly resonant operation is achieved with resonator mirrors that are highly reflecting for the signal beam and transmitting for the idler and pump beam. The concave mirrors which serve as input and output couplers generate a beam waist for the signal wave in the middle of the crystal. Many cw OPOs employ crystals in length up to 50 mm. The pump beam is usually mode-matched to the OPO cavity with a single lens which creates the appropriate beam waist inside the crystal.

It was found that a four-mirror resonator produces a higher output and has a narrower line width compared to a linear resonator [10.115]. Therefore ring resonators

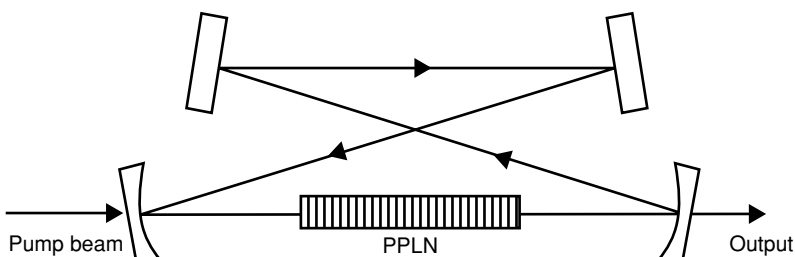


Fig. 10.41. Four-mirror ring cavity of a singly resonant cw OPO

are the most common resonator configuration for cw OPOs. The pump source is in most cases the fundamental or second harmonic of an Nd:YAG laser, but cw OPOs have also been designed with a diode laser as the pump source [10.112]. In this latter approach the singly resonant OPO was pumped by 2.25 W of 924-nm radiation from a InGaAs diode laser which generated up to 200 mW of 2.1- μm idler radiation.

The versatility of engineering and fabricating PPLN with nearly arbitrary grating periods is demonstrated in a system that integrates two separate frequency conversion steps in a single crystal [10.114]. The PPLN crystal has two grating periods in series. The first region is designed to produce a signal beam at 1540 nm and idler at 3450 nm from a 1064-nm Nd:YAG pump. The second region is designed to quasi-phase-match a sum frequency process whereby the signal and idler beams are combined to produce red light at 629 nm. The conversion of 1064 nm to 629 nm was 21% efficient and produced 2.5 W of red output.

A very efficient intracavity singly resonant cw-OPO-pumped Nd:YVO₄ laser is described in [10.116]. The high intracavity circulating power reduces the pump power requirement and an extremely low pump threshold for oscillations can be achieved. In the above system the pump source was a longitudinally pumped cw Nd:YVO₄ mini laser. At 1 W output from the laser diode, the single resonant OPO featuring a 50-mm-long PPLN crystal delivered 70 mW of output power at the idler wavelength of 3.66 μm .

Although most cw OPOs contain PPLN as the nonlinear material, other crystals such as periodically poled LiTaO₃ [10.117] and RbTiOAsO [10.118] have also been used.

OPOs have also been employed to provide tunable output from mode-locked lasers. The short pulse width of pico- or femtosecond pulses precludes the use of the standard OPO cavity in which the oscillating field builds up during the pump pulse. Such a cavity would have to be on the order of a few millimeters or less.

The basic approach that has been followed is synchronous pumping of OPO in which the resonator length of the OPO is matched to that of the pump laser cavity. This requires that one of the mirrors of the OPO is mounted on a piezoelectric transducer for precision adjustment of the OPO cavity length via a servo loop. Most synchronously pumped OPOs employ PPLN as the nonlinear material within a four-mirror ring resonator.

More than 12 W total output at the 1.85- μm signal and 2.5- μm idler has been obtained from a synchronously pumped OPO. The 47-mm-long and 1-mm-thick PPLN crystal was pumped by 80-ps-long pulses at 1064 nm with a repetition rate of 76 MHz [10.119]. The two concave mirrors of the four mirror resonator created a waist of the pump beam of 37 μm , and the signal and idler beams had a waist of 58 and 66 μm , respectively.

Synchronously pumped OPOs generating short pulses including femtosecond pulses have been reported in [10.99,119].

Figure 10.42 illustrates the technique of injection seeding an OPO in order to generate narrow-bandwidth output; [10.69]. A three-mirror L-shaped cavity configuration, containing a 50-mm-long LiNbO₃ crystal, was used to couple the pump and

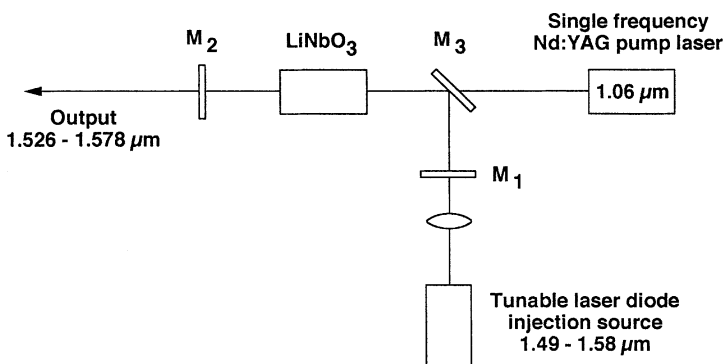


Fig. 10.42. Schematic diagram of an injection-seeded OPO

seed beam into the crystal. The OPO was pumped at $1.064\text{ }\mu\text{m}$ by an Nd:YAG laser with a pulse length of 8 ns and a pump energy of 75 mJ. The injection source was a grating tuned, external cavity InGaAsP diode laser tunable from 1.49 to $1.58\text{ }\mu\text{m}$ with a line width of 150 kHz.

The rear mirror (**M₁**) had a reflectivity of 90% at the signal wavelength and was mounted upon a piezoelectric stack that was used to adjust the length of the cavity. Mirrors **M₂** and **M₃** had signal reflectivities of 74 and 95%, respectively. All three mirrors had high transmission at $1.06\text{ }\mu\text{m}$. A 50-cm lens was used to focus the seed radiation into the cavity.

The nonlinear medium used for the OPO was a 5-cm-long lithium niobate crystal cut at 47° to the optic axis and antireflection coated at the signal wavelength. The crystal was kept at a constant temperature of 38°C and was angle-tuned by type I phase matching. In the unseeded operation, a pump energy of 75 mJ generated an output of 22 mJ at $1.535\text{ }\mu\text{m}$ with a bandwidth of 50 GHz. With injection seeding, the output was 7.6 mJ and the bandwidth was reduced to 180 MHz. Injection seeding was achieved over a signal wavelength ranging from 1.526 to $1.578\text{ }\mu\text{m}$, with a corresponding idler of 3.26 – $3.51\text{ }\mu\text{m}$.

10.4 Raman Laser

Raman scattering occurs when a molecule or atom absorbs a photon and then emits a photon with a different energy. The difference in energy changes the energy state of the molecule or atom. The particular wavelength shift depends on the material in which Raman scattering takes place. The process can either raise or lower the energy state of a molecule or atom, but the effect is stronger if the emitted photon has a lower energy than the incident photon. If a Raman material is pumped by a high-power laser, a fraction of the beam is shifted to a longer wavelength. If the power level of the pump source is increased, additional spectral lines will appear at longer as well as shorter wavelengths with respect to the pump wavelength.

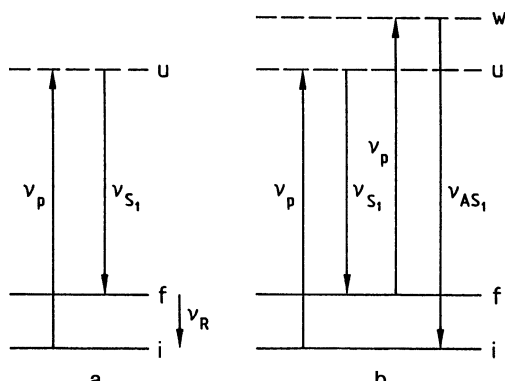


Fig. 10.43. Raman process. Generation of first Stokes light (a) and first anti-Stokes light (b)

Stimulated Raman scattering (SRS) occurs when a strong pump beam and a weak signal beam at a longer wavelength pass the Raman medium simultaneously. The molecule or atom, excited by the pump beam, releases energy to the signal wavelength thereby providing gain for the signal beam.

In its basic form, a Raman laser consists of a Raman medium such as a high-pressure gas cell or a crystal, a resonator that provides feedback for the Raman shifted wavelength, and a powerful pump beam.

10.4.1 Theory

The basic Raman effect is an inelastic light scattering process. The energy levels of interest for Raman scattering are shown in Fig. 10.43. An incident quantum $h\nu_p$ is scattered into a quantum $h\nu_s$, while the difference in energy $h(\nu_p - \nu_s) = h\nu_R$ is absorbed by the material. In Fig. 10.43 the u is upper state of the molecule, and i and f are the initial and final states. In principle, the excitation of the material may be a pure electronic excitation, or a vibrational or rotational excitation of a molecule. Solid-state-laser-pumped Raman lasers typically employ gases such as hydrogen or methane; therefore level i and f are the vibrational levels of the ground state of the molecule. The upper level u can be a real state or a “virtual” upper state. The frequency ν_s is called a Stokes frequency and is lower than the incident light frequency ν_p . The difference between ν_p and ν_s

$$\nu_p - \nu_s = \nu_R \quad (10.90)$$

is the Raman shift, which is characteristic of the material in which the Raman process is observed.

If the system is in an excited state to begin with, it may make a transition downward while the light is scattered. In that case the scattered light contains anti-Stokes frequencies which are higher than the incident frequency.

In the stimulated Raman effect, the pump laser at the frequency ν_p excites molecules to the level u , and if a population inversion exists between levels u and f , it can produce lasing action. In this case the radiation ν_s becomes amplified, while the

pump radiation ν_p loses energy. The process has typical laser characteristics, such as a pump energy threshold, exponential gain, and narrow line width. The emission in Fig. 10.43a is called the first Stokes line, usually written S_1 . If a high-power laser is focused into a Raman medium, additional lines will appear at the output. Actually, a single laser frequency interacting with molecules will produce a “comb” of frequencies, each separated from its neighbor by the frequency spacing ν_R . These additional lines will be to the left and right of the wavelength scale with regard to the laser pump wavelength.

The additional lines are produced by parametric four-wave mixing of the various waves propagating in the Raman medium. As an example Fig. 10.43b illustrates the generation of one such line, having a wavelength shorter than the pump wavelength. This so-called anti-Stokes line is the result of the interaction of ν_p and ν_{S1} both propagating in the same direction. The parametric four-wave mixing process does not require a population inversion between w and i, and therefore there is no well-defined threshold. The simplest way of looking at this interaction is that the two frequencies beat together to produce polarization (induced dipole moments in the molecules) at the difference frequency. This polarization then modulates the laser-molecule interaction and produces light beams at the side frequencies.

Stokes lines have lower frequency (longer wavelength) and anti-Stokes lines have higher frequency (shorter wavelength). In each case the line is labeled first, second, etc., by counting the number of frequency shifts from the pump laser.

The gain equations given below, which are taken from [10.120], provide the basic design parameters of the Raman lasers. A rigorous mathematical treatment of stimulated Raman scattering can be found in [10.121–123]. These references also provide comprehensive introductions to all areas of coherent Raman spectroscopy.

SRS can be described as a nonlinear interaction involving the third-order nonlinear susceptibility χ^3 . At a medium’s Raman resonance, the third-order susceptibility reduces to the peak Raman susceptibility χ''_R , where the double prime indicates the imaginary part of the total susceptibility.

The growth of the electric field E_2 at the Stokes wavelength and depletion of the pump field E_1 is governed by the equations

$$\frac{\partial E_1}{\partial z} = -\frac{\omega_p}{2cn_p} \chi''_R |E_2|^2 E_1, \quad (10.91)$$

$$\frac{\partial E_2}{\partial z} = \frac{\omega_s}{2cn_s} \chi''_R |E_1|^2 E_2, \quad (10.92)$$

where $\omega_p - \omega_s = \omega_R$ are the frequencies, n_s and n_p are the indices of refraction, and c is the velocity of light. For a constant pump field, the Stokes field grows exponentially with a power gain given by

$$P_s(l) = P_s(0) \exp(g_s l), \quad (10.93)$$

where g_s is the gain coefficient and l the interaction length in the Raman medium.

$$g_s = \frac{\omega_s \chi''_R |E_1|^2}{n_s c} = \frac{4\pi \chi''_R I_p}{\lambda_s n_s n_p \epsilon_0 c}. \quad (10.94)$$

Table 10.4. Stokes shift and Raman scattering cross section for several gases

Medium	$\nu_R [\text{cm}^{-1}]$	$d\sigma/d\Omega [\text{cm}^2/\text{Ster}]$
H ₂	4155	8.1×10^{-31}
CH ₄	2914	3.0×10^{-30}
N ₂	2330	3.7×10^{-31}
HF	3962	4.8×10^{-31}

If one expresses the third-order Raman susceptibility, χ''_R in terms of spontaneous Raman scattering cross section, $d\sigma/d\Omega$, one obtains

$$g_s = \frac{\lambda_p \lambda_s^2 N(d\sigma/d\Omega) I_p}{n_s^2 h c \pi \Delta \nu_R}, \quad (10.95)$$

where λ_s is the Stokes wavelength, I_p is the pump intensity, N is the number density of molecules, h is Planck's constant, and $\Delta \nu_R$ is the full-width, half-maximum Raman line width.

From these equations follows that the gain for a single-pass Raman medium is proportional to the incident intensity, the active media cross section (which includes pressure and line width dependencies), and the length of the Raman cell.

The threshold of a Raman laser is usually defined as the gain required to achieve an output power at the Stokes wavelength that is of the same order as the pump radiation. For example, to achieve a 1 MW Stokes shifted power output, one requires a gain-length product of $g_s l = 36$ in the Raman medium in order for the radiation to build up from the initial spontaneous noise level which is $P_s = h \nu_s \Delta \nu_s \approx 10^{-9}$ W in the visible. Quantitative information such as gain coefficient and Stokes wavelength for many gases, liquids, and solids are listed in [10.124]. Table 10.4 summarizes the data for the most important Raman media.

The maximum theoretical conversion efficiency of a Raman laser is

$$\eta_{\text{Ram}} = \frac{\nu_p - \nu_R}{\nu_p}. \quad (10.96)$$

If one introduces into (10.96) the numbers given for ν_R in Table 10.4, it is obvious that the conversion efficiency can be very high. For example, a frequency-doubled Nd:YAG laser Raman-shifted with CH₄ provides an output at 630 nm. With $\nu_R = 2914 \text{ cm}^{-1}$ and $\nu_p = 18,797 \text{ cm}^{-1}$ one obtains $\eta = 84\%$.

Stimulated Raman scattering in crystals does not have as long a history as the well-established technique of frequency conversion in pressurized gases. The design of a practical device is very challenging because high power density is required to obtain efficient conversion in a Raman active material, and at the same time damage to the crystal must be avoided. Also, in contrast to harmonic generation which is a lossless process, Raman conversion deposits heat into the crystal which leads to strong thermal lensing and birefringence.

Despite these difficulties, a number of diode-pumped solid-state Raman lasers have been successfully operated at the 1 W level and above. For example, an externally

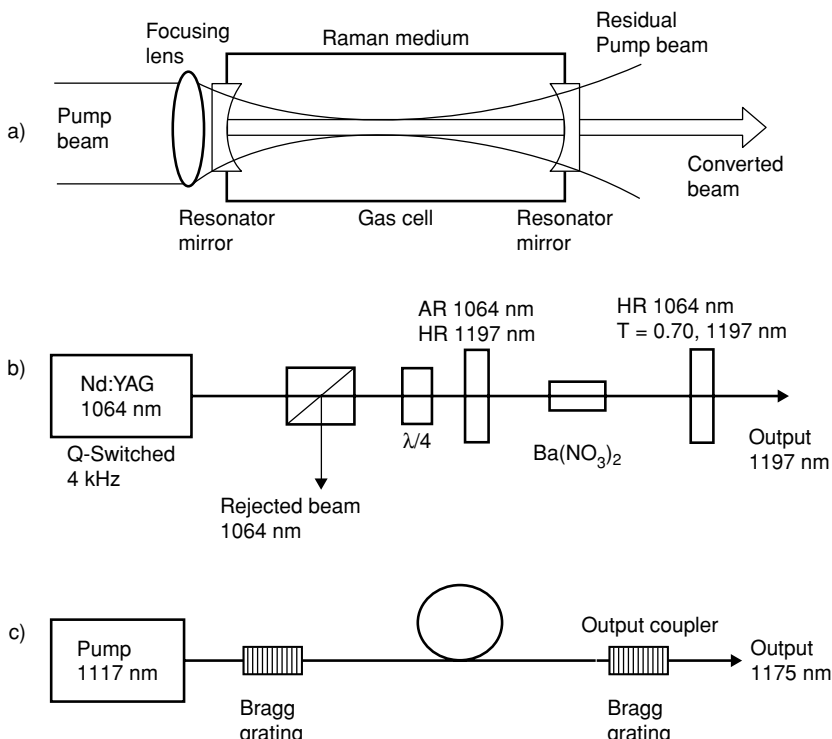


Fig. 10.44. Raman laser configurations. (a) Stimulated Raman scattering in a high-pressure gas cell; (b) solid-state Raman laser; (c) Raman fiber laser

pumped Raman laser containing a Ba(NO₃)₂ crystal produced up to 1.3 W at the first Stokes wavelength of 1197 nm [10.125]. The pump laser was a diode-pumped Nd:YAG slab laser and the optical design was similar to the schematic of Fig. 10.44b.

Similar to intracavity frequency doubling, a Raman laser can also be designed to share the resonator of the pump laser. Intracavity Raman lasers are described in [10.126, 127]. The conversion efficiency can be very high and a nearly quantum limited conversion of 85% has been reported for 35-ps pulses at 532 nm, which were wavelength-shifted in BaWO₄ to 559 nm [10.127].

Table 10.5 lists properties of crystal that have been used in the design of solid-state Raman laser [10.128]. The materials include crystalline Ba(NO₃)₂, LiIO₃, and various tungstates. The first column shows the Raman shift which is larger for Ba (NO₃)₂. The Raman gain is expressed by g_s/I_p [see Eq. (10.95)] and the last column lists the output wavelength if the crystal is pumped by an Nd:YAG laser at 1064 nm.

10.4.2 Device Implementation

The most important parameters for a Raman laser medium are the Raman gain which is a function of the cross section for Raman scattering, the Raman frequency shift,

Table 10.5. Properties of crystals used in Raman lasers

Crystal	Raman shift [cm ⁻¹]	Gain [cm/GW]	Stokes output ^a [nm]
Ba (NO ₃) ₂	1048	11	1197
LiIO ₃	770	4.8	1156
KGd (WO ₄) ₂	901, 768	3.3, 4.4	1158, 1177
Pb WO ₄	901	3.1	1170

^aPumped at 1064 nm.

and the damage threshold of the material. The latter is important because gain for Raman scattering must occur at power densities well below the onset of self-focusing and catastrophic damage.

Stimulated Raman scattering in high-pressure gas cells has been utilized for frequency conversion of high-power Q-switched solid-state lasers for many years. A typical optical design is depicted in Fig. 10.44a. A focusing lens concentrates the pump beam inside the pressurized cell containing the Raman medium. The resonator mirrors can either be located outside the cell or serve also as windows.

Liquids such as the tetrachlorides (GeCl₄, SiCl₄, SnCl₄) have also been used in Raman lasers. However, chemical stability, and heating by the intense laser beam due to submicron particles suspended in the liquid, has been a problem.

More recently, crystals have been recognized as an efficient Raman medium for low-average-power systems. Owing to the inelastic nature of the nonlinear process, a fraction of the pump power is deposited as heat in the Raman medium. This limits Raman lasers to the realm of low-repetition-rate or low-average-power systems. Figure 10.44b depicts a solid-state Raman laser containing a Ba(NO₃)₂ crystal. The resonator mirrors are coated to provide feedback only at the first Stokes wavelength. The figure shows an externally pumped Raman laser. The combination of a quarter waveplate and a polarization beam splitting cube protects the Nd:YAG laser from feedback of the Raman resonator.

Raman lasers require high peak power Q-switched lasers as pump sources. However, in fibers where the beam is confined to the 8-μm core of a single-mode fiber, the Raman process becomes very strong and efficient even at a few watts of continuous power. In a typical Raman fiber laser, the output from a 20- to 50-W fiber-coupled diode bar is used to pump the cladding of a double-clad yttrium fiber laser. The radiation from the Yb fiber laser is then used to pump a Raman laser.

Figure 10.44c depicts a Raman fiber laser that shifts the pump source at 1117 nm to a wavelength of 1175 nm. Fiber Bragg gratings at 1175 nm are incorporated at both ends of a long single-mode fiber. In glass the pump radiation is down-shifted by the vibrational modes of the molecular bonds in the glass. Both the Raman scattering cross sections and wavelength shifts are different for silica, germanium, phosphorus, and borate glasses.

The design and performance of a hydrogen gas Raman laser which converts the frequency-doubled output of an Nd:YAG laser from 532 to 683 nm with an efficiency of up to 40% will be illustrated below [10.129].

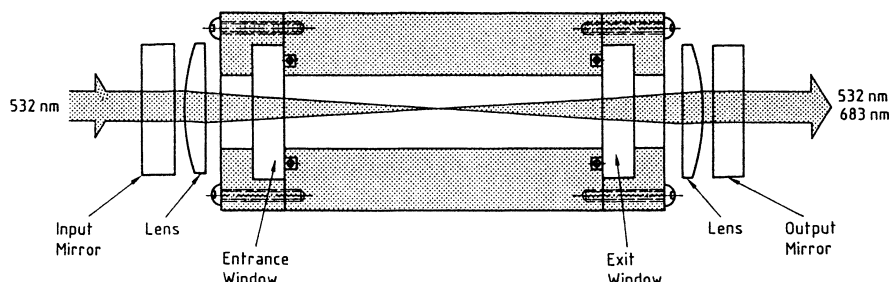


Fig. 10.45. Schematic diagram of a high-energy Raman cell

The 532-nm pump beam had an output energy up to 210 mJ, a pulse width of 24 ns, a beam diameter of 4.9 mm, and a beam divergence of 7 mrad. The repetition rate of the system was 2 Hz. The Raman laser consisted of the gas-pressure cell and the resonator optics, as shown in Fig. 10.45. The Raman cell is made from a block of aluminum bored with a 16-mm-diameter hole, fitted with O-ring grooves and windows held together by end caps. The 25-mm diameter by 12.5-mm thick fused silica windows are antireflection-coated at both the pump and the first Stokes wavelengths. The output of the Raman laser was measured as a function of input power with gas pressure, resonator configuration, and length as parameters. Figure 10.45 depicts the concentric resonator configuration comprising two flat mirrors and a pair of plano-convex lenses. The resonator length was 20 cm. The entrance mirror has high transmission at 532 nm and high reflection at 683 nm. The exit mirror has high transmission for the pump wavelength at 532 nm and 50% reflectance at the first Stokes wavelength. The reflectance for the second Stokes (954 nm) and first anti-Stokes (436 nm) wavelength was only a few percent at both mirrors.

Figure 10.46 exhibits the output vs. input for the resonator at the exact length for the concentric geometry (solid line) and for slight variations in length. As is apparent

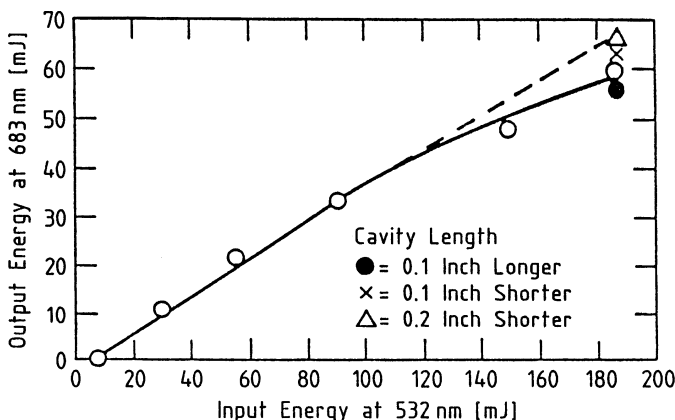


Fig. 10.46. Concentric resonator output energy for different pump input energies and cavity lengths. The solid line corresponds to the concentric position. (Hydrogen pressure: 1000 psi, output reflector 50% at 683 nm, 20 cm resonator)

from the data, the resonator length becomes more critical for the higher input energies, and a change of (1–2)% in resonator length has a noticeable effect. The output energy of 65 mJ at 683 nm for 185 mJ input at 532 nm was the highest energy achieved with the concentric resonator. Optical breakdown, probably caused by small particles and impurities in the gas, set this upper limit.

10.5 Optical Phase Conjugation

Optical phase conjugation, also referred to as wavefront reversal, has been demonstrated in solids, liquids, and gaseous media using a number of nonlinear optical interactions, such as three-wave and four-wave mixing, stimulated Brillouin scattering (SBS), stimulated Raman scattering (SRS), and photon echoes.

From the standpoint of solid-state laser engineering, phase conjugation via SBS is particularly important because it provides the simplest and most efficient interaction, and initial work in this area carried out by Zel'dovich et al. [10.130] revealed that optical aberrations produced by a laser amplifier stage could be corrected. The concept of reflecting an amplifier beam off an SBS cell and passing it back a second time through the amplifier was first used to compensate phase distortions in a ruby amplifier [10.131]. Following that initial work, SBS mirrors have been investigated in a number of solid-state lasers, using different nonlinear materials and optical arrangements [10.132–134]. Comprehensive descriptions of the principle of phase conjugation are contained in [10.135–138].

10.5.1 Basic Considerations

From a mathematical point of view, phase conjugation can be explained by considering an optical wave of frequency ω moving in the ($+z$) direction,

$$E_1(x, y, z, t) = A(x, y) \exp\{j[kz + \varphi(x, y)] - j\omega t\}, \quad (10.97)$$

where E_1 is the electric field of the wave with wavelength $\lambda = 2\pi/k$. The transverse beam profile is given by the function $A(x, y)$ and the phase factor $\varphi(x, y)$, indicating how the wave deviates from a uniform, ideal plane wave. In particular, the phase factor carries all the information about how the wave is aberrated.

If the beam given by (10.97) is incident upon an ordinary mirror, it is reflected upon itself and the sign of z changes to $-z$, and all other terms of the equation remain unchanged. However, if the beam is incident upon a phase-conjugate mirror it will be reflected as a conjugated wave E_2 given by

$$E_2(x, y, z, t) = A(x, y) \exp\{j[-kz - \varphi(x, y)] - j\omega t\}. \quad (10.98)$$

In addition to the sign change of z , the phase term has a changed sign too. The conjugate beam corresponds to a wave moving in the ($-z$)-direction, with the phase $\varphi(x, y)$ reversed relative to the incident wave. We can think of the process as a reflection combined with phase or wavefront reversal. The phase reversal expressed by (10.98), for example, means that a diverging beam emitted from a point source,

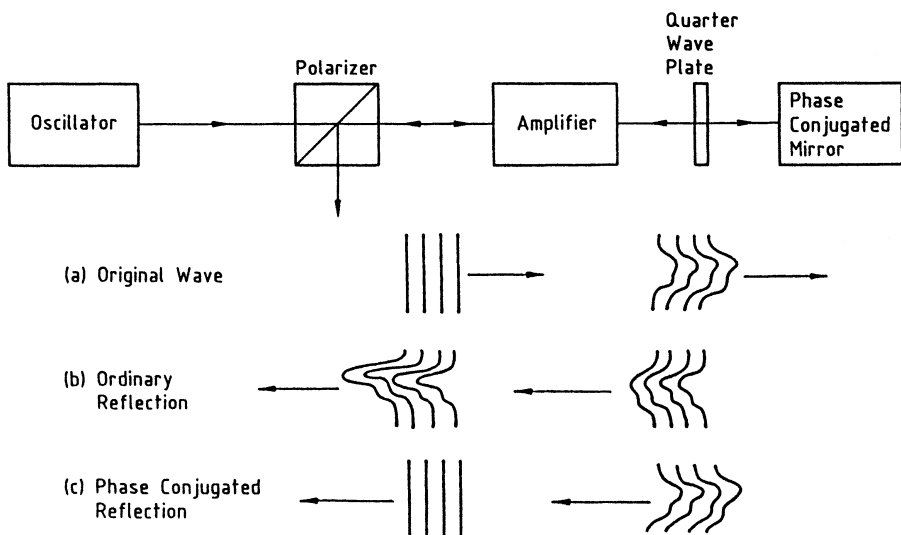


Fig. 10.47. Compensation for optical phase distortions caused by an amplifying medium using optical phase conjugation

after reflection at a phase-conjugate mirror, will be converging and be focused back to the point of origin.

A practical application of phase reversal in a laser system is depicted in Fig. 10.47. Shown is an oscillator which produces an output with a uniform flat wave front that is distorted in the amplifier medium. An ordinary mirror merely inverts the distortion as it reflects the beam, thereby keeping the distortion fixed with respect to the propagation direction. With a second pass through the amplifier, the distortion is essentially doubled. A phase-conjugate mirror, on the other hand, reverses the wavefronts relative to the wave propagation direction; hence, the same region of the amplifier that originally created the distortion compensates for it during the second pass through the amplifier.

However, it should be noted that although the wavefront is conjugated, the polarization state of the backward-going field is not conjugated. As far as the polarization vector is concerned, the SBS mirror behaves like an ordinary mirror. As we shall see, this has important implications with regard to the compensation of optical distortions caused by thermally induced birefringence in the amplifier rods.

As already mentioned, SBS of laser radiation in liquids or gases is the preferred approach for designing phase-conjugate mirrors. SBS involves the scattering of light by sound waves, i.e., acoustic phonons, or pressure/density waves. The incoming laser radiation generates an ultrasound wave by electrostriction corresponding to a spatial density modulation in the material. This modulation changes the refractive index and therefore a refractive index grating is created in the material.

The resultant Stokes scattered light is down-shifted in frequency by a relatively small amount ($\approx 10^9 - 10^{10}$ Hz). The gain of the Stokes-shifted wave is generally

the highest in a direction opposite to that of the incident beam. The efficiency of the SBS process (defined as the ratio of the Stokes-shifted, backward-going energy or power to the incident optical energy or power) can be as high as 90%. SBS has been studied extensively in liquids, solids, and gases. The steady-state gain factor of SBS is generally large, making SBS the dominant stimulated scattering process in many substances. Phase-conjugate mirrors can be employed to compensate thermal lensing in double-pass amplifiers if the beam intensity is high enough to provide sufficient reflectivity from the SBS process.

Reflectivity is an important parameter in designing an SBS mirror since it greatly influences the overall laser-system efficiency. The calculation of the reflectivity of SBS mirrors requires the solution of coupled differential equations for the incident and reflected light waves and the sound wave grating. The calculations of the scattering processes require a great numerical effort, assuming steady-state, or plane wave approximations solutions have been derived in [10.139–141].

The reflectivities of SBS mirrors depend on the excitation condition and the material properties of the nonlinear medium. Reflectivity vs. pump power or energy can be described by a threshold condition and a nonlinear power relationship. Threshold depends mainly on materials properties and cell geometry, whereas the increase of reflectivity is a function of the pump-beam power. Both threshold and the slope of reflectivity depend on the coherence properties of the beam. As will be explained later, there is a minimum requirement on the coherence or line width of the incident beam such that a coherent spatial and temporal interaction with the sound-wave grating is possible.

Design parameters which affect the performance of an SBS mirror will be examined in the following section.

10.5.2 Material Properties

Pressurized gases such as CH₄ and SF₆ or liquids such as CCl₄, acetone, and CS₂ are usually employed to provide efficient SBS for a 1.06-μm pump. SBS materials can be characterized by a gain coefficient and an acoustic decay time. The gain coefficient g_B determines threshold and slope of the reflectivity curve. Materials with a lower gain show a higher threshold and a slower increase of the reflectivity with increased pumping.

The acoustic-decay time τ_B establishes a criterion for the coherence or line width of the pump beam. For efficient interaction with the sound-wave grating, a coherent interaction on the order of the acoustic decay time is required. An inverse bandwidth of the pump pulse which is larger than the acoustic-phonon damping time describes the steady-state condition, i.e., $(\Delta\nu)^{-1} > \tau_B$. Maximum gain is achieved if this condition is satisfied. Most calculations, as well as the simple relationships for gain and threshold given below, are for this case.

Table 10.6 lists steady-state SBS gain coefficient g_B and acoustic decay time τ_B of representative gases and fluids.

Quite noticeable is the longer phonon lifetime in gases compared to liquids. Single longitudinal mode Q-switched lasers have a pulse length of 10–20 ns; therefore, the

Table 10.6. Steady-state SBS gain coefficients and acoustic decay time of representative gases and fluids, taken from [10.133, 134, 142]

Medium	g_B [cm/GW]	τ_B [ns]
CH ₄ (30 atm)	8	6
CH ₄ (100 atm)	65	17
SF ₆ (20 bar)	14	17
SF ₆ (22 atm)	35	24
CCl ₄	6	0.6
Acetone	20	2.1
CS ₂	130	5.2

coherence requirement for steady-state conditions, stated above, will barely be met in gases. SBS in gases will be highly transient, while in liquids, it will reach a steady state. This has the important implication that the effective gain for gases is actually considerably lower than the values in Table 10.6. The effective gain in a transient SBS process can be as much as 5–10 times less than the value given in the table. The lower SBS threshold and higher gain is the reason most current systems employ liquids as the nonlinear medium. Also, liquid cells are not as long as gas-filled cells. liquid cells are typically 10–15 cm long, whereas gas cells are between 30 and 100 cm in length.

Gases employed as nonlinear elements have the advantage that they eliminate problems which can arise in liquids owing to optical breakdown caused by bubbles or suspended particles.

The gain of an SBS process is a function of the frequency ω of the pump radiation, the phonon lifetime τ_B , the electrostrictive coefficient γ , the velocity of light and sound c and v , and the refractive index n_0 and density p_o of the material [10.141].

$$g_B = \frac{\omega^2 \gamma^2 \tau_B}{c^3 v n_0 \rho_0} \quad (10.99)$$

The threshold pump power for SBS is a parameter of practical importance. If one measures reflectivity versus pump power input, one observes that at a particular input power, reflectivity changes over many orders of magnitude for just a few percent increase in power. In this regime of rapid signal growth, a threshold is usually defined if the gain has reached $\exp(30)$.

The gain of the backward reflected Stokes wave over a length l of the nonlinear medium is $\exp(g_B I_p l)$ for a plane wave of pump intensity I_p . If the threshold P_{th} is defined as the condition when the gain reaches $\exp(30)$, then one obtains [10.133] for a high-pressure CH₄ gas as the SBS medium

$$P_{th} = \frac{30A}{g_B l} \quad (10.100)$$

where A is the area of the pump beam.

For a Gaussian pump beam, one obtains [10.143]

$$P_{\text{th}} = \frac{\lambda_p}{4g_B} \{1 + [1 + 30/\arctan(l/b)]^{1/2}\}^2, \quad (10.101)$$

where b is the confocal parameter defined in (5.7) and l is the length of the SBS cell. If the cell is long compared to the confocal parameter $l \gg b$, the lowest threshold is obtained, since $\arctan(l/b) = \pi/2$ and (10.101) reduces to

$$P_{\text{th}} = 7.5 \frac{\lambda_p}{g_B}. \quad (10.102)$$

10.5.3 Focusing Geometry

An SBS mirror in its most common form consists of a lens which focuses the incident beam into the bulk nonlinear material. The first buildup of the sound-wave amplitude is concentrated in the focal region of the incident beam. However, the sound wave can have a wide distribution over large parts of the cell.

As confirmed in experiments [10.141], in a first approximation, a change in focal length should not affect threshold or reflectivity, since a shorter focal length, which leads to a shorter interaction length l in (10.100) is compensated by stronger focusing leading to a smaller area A of the pump beam. Choosing short focal lengths will lead to a very compact sound-wave distribution with the advantage of a lower demand on the coherence of the laser radiation. The main disadvantage of a very short focal length is the high intensity and therefore the occurrence of optical breakdown.

Depending on the focal length of the lens, the sound wave may be sharply concentrated in the cell or distributed over the whole cell length.

There is also a difference whether the lens is the front window of the cell, and the nonlinear medium fills the space between the lens and the beam waist, or if the lens is positioned outside the cell and only the area around the beam waist is covered by the medium. The choice of a focusing lens, for an incident laser beam of given pulse energy and duration, has to be such that at the focal region the intensity is well above threshold but below optical breakdown.

10.5.4 Pump-Beam Properties

The pump power has to be well above the threshold of the nonlinear reflectivity curve. Otherwise, the fidelity of the reflected signal becomes small, because the parts of the beam away from the central peak, with energies below this threshold value are not reflected. The useful power range of the incident radiation is limited by the SBS threshold at the lower limit and by optical breakdown at the upper end.

A typical curve for SBS reflectivity vs. input energy is shown in Fig. 10.48. These experimental data were obtained by focusing a Q-switched Nd:YAG laser into a CCl_4 cell with a 80-mm-long focal length lens [10.142]. The general shape of the increase

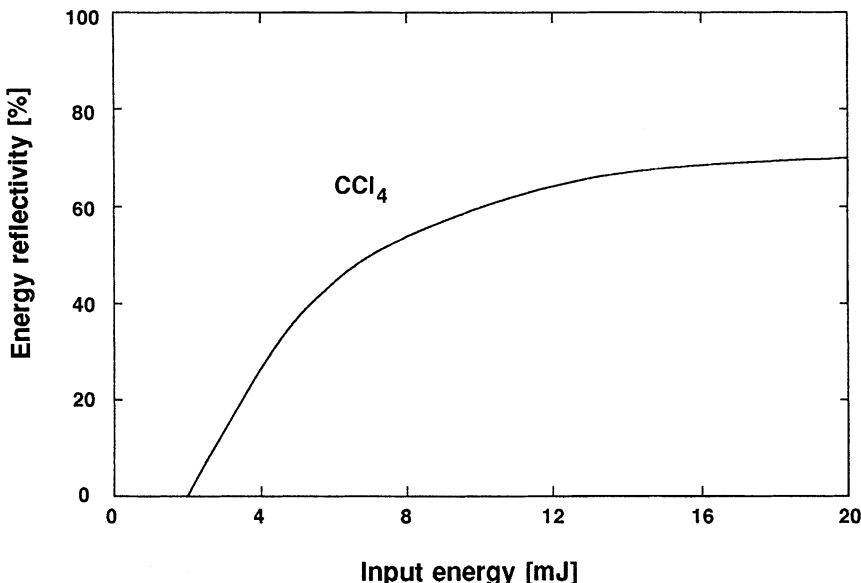


Fig. 10.48. SBS energy reflectivity of CCl_4 as a function of pump energy for a Q-switched Nd:YAG laser [10.142]. Curve represents a best fit of experimental data

in reflectivity with intensity can be approximated by a simple expression [10.139]

$$R = \frac{C(E_{\text{in}}/E_{\text{th}})}{1 + C(E_{\text{in}}/E_{\text{th}})} \quad \text{for } E_{\text{in}} \gg E_{\text{th}}, \quad (10.103)$$

where E_{in} , and E_{th} are the input energy of the incident beam and threshold value, respectively, and C is a constant which depends on the beam and nonlinear material properties.

In order to obtain a low SBS threshold and high reflectivity, an efficient coherent wave interaction is necessary between the pump beam and the sound-wave grating. There is a spatial and temporal requirement on the coherence of the incident beam. First, the coherence length of the beam should exceed the longitudinal sound-wave extension. If the pump beam has a Gaussian spatial profile, the sound wave has a longitudinal extent approximately given by the confocal parameter. Second, the coherence time (i-e., the inverse of the line width, $1/\Delta\nu$) of the pump beam should exceed the response time τ_B of the acoustic phonons. Typically, τ_B is on the order of nanoseconds for liquids, and tens of nanoseconds for pressurized gases. Therefore, high-efficiency SBS requires line width narrowing or preferably single longitudinal mode operation. If the laser operates in a single longitudinal mode, this means that the pulse length should be longer than τ_B .

If these conditions are not met, the steady-state SBS process changes to transient SBS with a correspondingly lower gain parameter. The effect of multimode lasers on the SBS threshold and experiments which address the issue of multimode operation will be discussed next.

Carr and Hanna [10.133] investigated SBS with a Q-switched single transverse and longitudinal mode Nd-YAG laser which had a pulse duration of 30 ns and a coherence length of 6 m. The 1-m-long cell filled with CH₄ at 30 atm results in a 6-ns acoustic decay time and a gain coefficient of 8 cm/GW. The beam was focused to a waist of $w_T = 150 \mu\text{m}$, from which follows, with $\lambda = 1.06 \mu\text{m}$, a confocal parameter of $b = 13 \text{ cm}$ [see (5.7)]. Introducing these parameters into (10.102) yields a threshold for SBS of $P_{\text{th}} = 100 \text{ kW}$. Even for a ratio of pulse width to phonon decay time of a factor of 5 ($t_p/\tau_p = 5$), a significant degradation from steady-state conditions can be expected. The theory predicts a threshold 2.5 times greater than for steady-state conditions or 250 kW in this particular case [10.144]. The actual observed threshold was 400 kW. Since the coherence length l_{coh} was 6 m and the confocal parameter b was 13 cm, the condition $l_{\text{coh}} \gg b$ in (10.102) is clearly satisfied.

The coherence length is reduced for multimode operation according to $l_{\text{coh}} = 2L/n$, where L is the length of the resonator and n the number of longitudinal modes. For the 1-m-long resonator, the condition $l_{\text{coh}} \gg b$ is satisfied even in the presence of several modes. The experimental results confirmed that the SBS threshold was little affected if the laser was operated in several modes. However, when the oscillator was operated on 15 modes ($l_{\text{coh}} = 15 \text{ cm}$ or a bandwidth of $\approx 2 \text{ GHz}$) threshold increased by 75%. Phase conjugation still occurred, but was less reliable and resulted in poor beam reconstruction.

The dependence of SBS reflectivity on coherence length and input energy is illustrated in Fig. 10.49. In this experiment, radiation from a Nd:YAG laser was

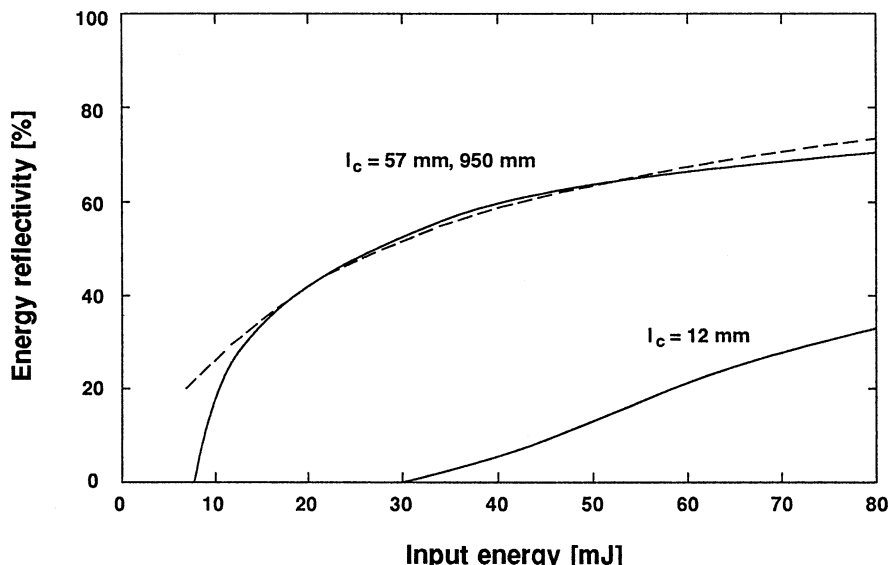


Fig. 10.49. SBS energy reflectivity in SF₆ for a Q-switched Nd:YAG laser with different coherence lengths l_c . Dashed line is an approximation according to (10.103) with $C = 0.25$

focused with a lens of 100-mm focal length into a cell containing SF₆ at a pressure of 20 bar [10.142].

The lens was positioned about 40 mm in front of the cell entrance window. In Fig. 10.49, measured energy reflectivities with different coherent laser pulses are shown. As can be seen from this figure, the energy reflectivity is different for the shortest coherence length of 12 mm compared to the two others. No difference was detectable between the pulses with 57 mm and 950 mm coherence length. In both cases, the coherence length was longer than the whole interaction length between the entrance window of the cell and the focus of the beams inside. The measured data agreed quite well with predicted values calculated from the theory described in [10.141].

10.5.5 System Design

In Fig. 7.21 we have already exhibited the most common configuration of compensating thermally induced lensing in amplifiers with an SBS mirror. The output from the oscillator passes through the amplifiers, is reflected by the SBS mirror, and propagates a second time through the amplifier chain. Output coupling is realized by a polarizer and a 90° polarization rotation carried out by a $\lambda/4$ waveplate which is passed twice. Conjugate reflectivities in this type of configuration are typically 50–80%, so that the efficiency of the amplifier stage is reduced by a fraction which depends on the ratio of energy extraction between the first and second pass in the amplifiers.

As already pointed out, phase conjugation will invert the wavefront and correct thermal lensing introduced by the amplifier chain; however, it will not correct for depolarization caused by birefringence. Depolarization causes distortion of the output beam profile, leads to polarization losses, and the wrongly polarized light is back-reflected toward the oscillator.

Several approaches have been explored to deal with this problem. One approach is to minimize the effect of birefringence as one would in any system independent of the use of an SBS mirror. This includes rotation of the birefringence axis in single- and double-stage amplifiers and the use of a naturally birefringent laser crystal. The second approach is unique to SBS and involves separating the depolarized beam into its two components of orthogonal polarization and individual conjugation of each polarization state. These approaches will be illustrated in more detail in the following section.

One approach of minimizing birefringence is utilized in the design exhibited in Fig. 7.21 in which a 90° rotator is placed between two identical amplifier stages. A ray passing through the amplifier has its electric field component along the fast birefringence axis rotated by 90° so that it lies along the slow axis in the second amplifier, and vice versa. Thus, regardless of the orientation of the fast and slow axes, the birefringence in one amplifier is canceled in the second. A commercially available Nd:YAG oscillator–amplifier system with an SBS mirror uses this architecture.

If the laser system employs only a single amplifier, a Faraday rotator with 45° rotation placed between the amplifier and mirror is equivalent to a 90° rotation between two identical amplifier stages. With the arrangement shown in Fig. 10.50 and using

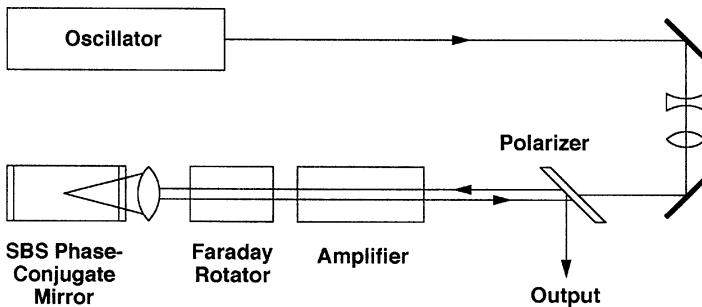


Fig. 10.50. Depolarization compensation in a single amplifier with a Faraday rotator in a double-pass configuration using an SBS mirror [10.133]

methane at 30 atm, nearly 300 mJ of diffraction-limited output was obtained in an Nd:YAG amplifier operating at 15 Hz [10.133].

Thermally induced birefringence effects can be greatly reduced if an anisotropic crystal such as Nd:YAlO or Nd:YLF is used as laser rod. These crystals have a poorer thermal conductivity compared to Nd:YAG, and therefore exhibit higher thermal lensing. But the latter can be compensated with a phase-conjugate mirror. Using this rationale, Eichler et al. [10.145] constructed an Nd:YAlO oscillator–amplifier system which produces 100-W average power in a 1.2 diffraction-limited beam. The amplifier had negligible depolarization losses but a strong thermal lens of less than 15 cm at the maximum lamp input of 8 kW. The experimental setup is depicted in Fig. 10.51. The oscillator, which was passively Q-switched with a LiF:F₂ color center crystal, contained two intracavity etalons with thicknesses of 2 and 20 mm, which resulted in a coherence length of 2.5 m. The output from the amplifier was focused with a 200-mm lens into the SBS cell, which contained CS₂ as the nonlinear material.

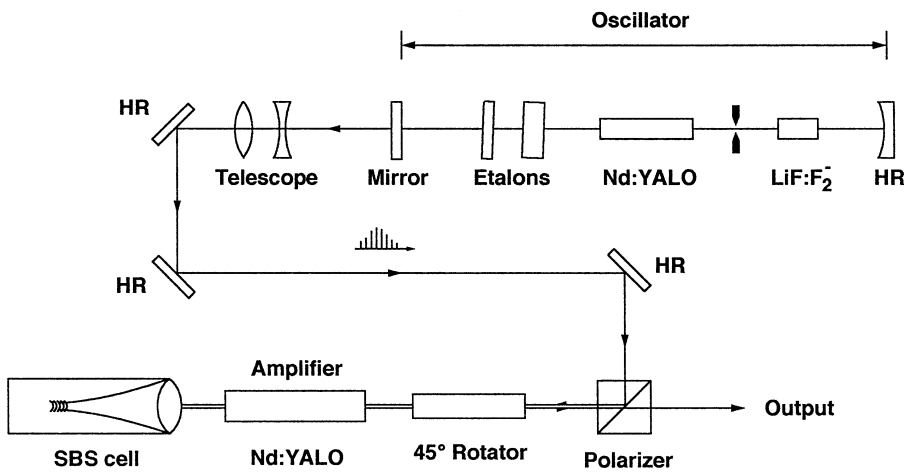


Fig. 10.51. Nd: YAlO oscillator and double pass single amplifier with SBS mirror [10.145]

An extension of this work covering phase conjugation in multi-amplifier architectures is described in [10.146].

In the approaches described so far, birefringence effects are minimized before the beam enters the SBS cell. There is a limit to the compensation capabilities of these schemes. Compensation will be acceptable if bifocusing effects are not too strong, otherwise the second-pass beam will not return exactly along the path of the first beam and the fidelity of beam restoration will suffer [10.147]. The best compensation can be achieved if the polarization is uniform and linear at the SBS cell.

An approach investigated by Basov et al. [10.148] is to split the beam into two orthogonal polarizations after passing through the amplifier. One of the beams is then rotated 90° so it has the same polarization as the other. The two beams will cooperatively reflect from the SBS phase-conjugate mirror. The back-reflected phase-conjugated beams then pass back through their respective optical paths and are recombined at the beam splitter before propagating through the amplifier for a second time. The beam emerging from the amplifier has the same beam quality and polarization as the original incident beam. A more recent implementation of this general approach was described in [10.149].

From a design point, the question that needs to be answered is whether a phase-conjugation system is necessary, or whether insertion of internal elements such as lenses, phase plates, or 90° rotators is sufficient to remove troublesome distortions associated with the amplifier stages. Other techniques which reduce beam aberrations are diode pumping and a zigzag slab design. The former reduces the heat load on the laser crystal and the latter compensates to a first-order beam distortion by virtue of its geometry. Of course, these techniques are not exclusive of each other and can be combined in one system. It should be mentioned that besides compensating for thermal lensing, a phase-conjugating mirror has some additional interesting features. Misalignment of a conventional rear mirror caused by mechanical, thermal, or vibration effects which will lead to beam wander and power loss is eliminated because the beam reflected from the phase-conjugated mirror is self-aligned. It greatly depends on the particular application and average-power requirements of the system, when it is justified to remove the troublesome aberrations associated with the amplifier stages by means of a phase-conjugate mirror. Also, a simple SBS mirror arrangement does not remove aberrations and losses due to birefringence, and the schemes for correction of stress birefringence by resolving the depolarized beam into components for separate conjugation are too complicated and require a large number of additional optical components.

Conceptually, the replacement of a conventional mirror at the end of an amplifier chain with an SBS cell and a lens appears straight-forward. However, a number of issues have to be resolved in a practical implementation of this technique. In order to achieve an acceptable overall system efficiency, the oscillator requires longitudinal mode selection, and the cell has to be operated at high beam intensities without causing optical breakdown. The latter is always a concern because impurities in the liquid could cause breakdown at the GW/cm^2 power levels, which are required to achieve a high SBS reflectivity.

Oscillators with SBS Q-Switching Mirrors. By far the most common application of SBS mirrors is in double-pass amplifier configurations. However, SBS mirrors have also been employed in oscillators. Since the amplified spontaneous emission is too small to start the SBS process, a conventional mirror is placed behind the SBS cell to start lasing action. As soon as the reflectivity of the SBS mirror is high enough, it will take over and form the main resonator. Since the losses decrease (i.e., reflectivity increases) as the flux in the resonator builds up, Q-switching occurs. Oscillators employing SBS Q-switching mirrors have been described in [10.150, 151].

11. Damage of Optical Elements

Optically induced damage to the laser medium and to components of the laser system generally determine the limit of useful performance of solid-state lasers. The performance of a laser system in terms of pump efficiency, gain, nonlinear conversion, brightness, and beam quality increases with power density of the beam. Power density is fairly independent of the size of the laser, output power scales mostly with beam diameter rather than beam intensity. As a consequence, it is desirable to operate all lasers at the highest beam intensity consistent with reliable operation, which, in turn, is determined by the optical-damage threshold of the various components. Therefore, an understanding of the mechanisms which cause radiation damage to optical components and a knowledge of the damage threshold of the materials employed in a laser are of great importance to the engineer who is designing a laser system.

Damage may occur either internally or at the surface of an optical component owing to a number of intrinsic and extrinsic factors. Intrinsic processes that limit the optical strength of materials include linear absorption, color-center formation, and a variety of nonlinear processes such as self-focusing, multiphoton absorption, and electron avalanche breakdown. Extrinsic factors include impurities, material defects (voids, dislocations, etc.), and in particular surface scratches and digs and surface contamination. In general, damage threshold is determined by the condition of the optical surfaces and the quality of optical coatings rather than by the bulk material. The problem of surface damage is compounded because most laser systems contain many surfaces.

There are different ways of defining damage threshold. One might define damage as the physical appearance of a defect in the material or by a degradation in the output performance of the laser system. From the standpoint of the user of the laser system, the performance deterioration is of more importance than the physical appearance of a defect in the material. Often the occurrence of a small blemish or defect does not alter system performance. In this case it is important to determine whether the defect remains constant or increases with time.

Quantitative measurements of the damage threshold of an optical component should be performed following a procedure specified by the International Standards Organization [11.1–3]. A test sample is irradiated with a well-characterized laser at different sites. The fluence levels are chosen so that at the higher fluence a high probability of damage exists, whereas at the lower levels the probability of damage is low. The percentage of failures is plotted vs. fluence. A least-squares linear fit to this data is calculated.

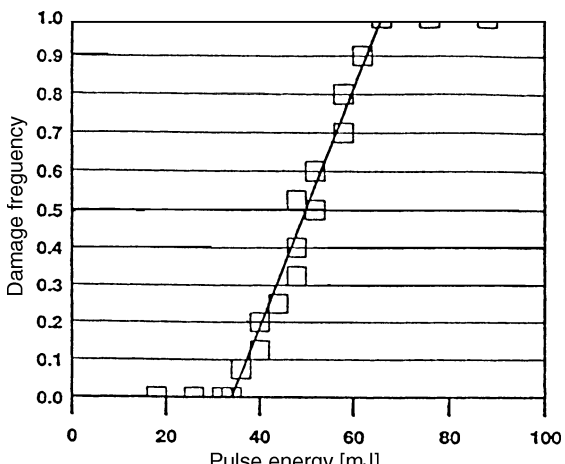


Fig. 11.1. Damage frequency plot for defining 0% damage probability according to ISO 11254

The linear data extrapolation to 0% damage frequency is defined as the damage threshold. The testing sites are inspected for damage with a Nomarski microscope at a magnification of 150. Figure 11.1 shows a damage frequency plot according to ISO 11254.

The results of experimental and theoretical investigations of laser-induced damage in dielectric and sol-gel coatings, optical glasses, metal films, laser crystals and glasses, crystals used in polarizers, Q-switches, harmonic generators, and parametric oscillators are presented annually at the Boulder Damage Symposium held since 1969. The earlier proceedings of these symposia have been published by the National Bureau of Standards [11.4] and since 1990 by the International Society for Optical Engineering (SPIE) [11.5]. Selected papers from the earlier symposia have also been published in a book [11.6].

11.1 Surface Damage

Undoubtedly the weakest parts in a well-designed laser are the surfaces of the optical components. It has been found that surfaces, even those that are scrupulously cleaned, have a lower damage threshold than the bulk.

One reason for the lower surface-damage threshold compared to bulk damage stems from the fact that even after the polishing process used in the finishing of optical elements, there are residual scratches, defects, and imperfections on the surface. At these points, the electric field of the light wave is greatly intensified so that the effective field value just inside the surface is much greater than the average field. When breakdown or failure of the surface occurs, it occurs near one of these imperfections [11.7]. Furthermore, as a consequence of the polishing process, minute inclusions of polishing material or other impurities are embedded in the surface. These impurities

may be strongly absorbing and, if so, can provide a nucleus around which damage may occur. Other factors tending to lower the damage threshold at the surface are contamination of the surface due to airborne particles, fingerprints, and residue from outgassing of nearby components.

From the foregoing it follows that surface damage is caused either by absorption of submicrometer inclusions or by the formation of a plasma at the surface because of electron avalanche breakdown in the dielectric materials. In the former case, microexplosions of isolated inclusions occur just under the surface [11.8]. In the latter case, the electric field produced by an intense laser beam is so high that the dielectric material will break down [11.9].

This avalanche ionization represents the ultimate failure mode of dielectric materials. In this process, a few free charge carriers from easily ionized impurities, or as a result of multiphoton ionization, absorb energy from the oscillating electric field of the light wave. Hence, they gain kinetic energy and multiply by impact ionization of the solid-state lattice. As a result of avalanching, the concentration of electrons increases significantly, which leads eventually to a complete absorption of radiation. The avalanche breakdown is usually associated with a luminous plasma formed in the material. The avalanche process is the high-frequency analog of dc breakdown. Avalanche ionization is the primary cause of surface damage, once absorbing impurities are removed. Because of field intensification effects, avalanche ionization is more likely to occur in the vicinity of pits and scratches at the surface.

The reduction of damage threshold at imperfect surfaces owing to multiple reflections has been analyzed in [11.7]. It was found that depending on the defect geometry, the presence of surface pits, grooves, cracks, nodules, or voids can increase the local field intensity by a factor up to n^4 , where n is the refractive index.

More recently it was reported that interference of internal reflections at a crack and the surface can locally cause much higher radiation intensification [11.10]. The numerical calculations revealed that light intensity enhancements are very sensitive to the polarization and angle of incidence of the beam, and the orientation and width of a crack with respect to the surface. For conical cracks the light intensity enhancement factor can locally reach two orders of magnitude.

In some cases a dielectric coating applied to a surface raises the damage threshold. Micropits and scratches are filled in by the coating material, which then reduces the reflectivity and standing wave ratio in association with smoothing of the surface. This effect has been observed in such cases as MgF_2 on glass, ThF_4 on LiNbO_3 , and sol-gel AR coatings on fused silica.

Super-polishing techniques, such as ion polishing and chemical etching, lead to higher damage thresholds than those for conventionally polished optical surfaces. Superpolish produces surfaces with a rms roughness of less than 1 Å, whereas a normal high-quality polish has a surface roughness of 10–20 Å.

Surface damage typically takes the form of a pit and is observed more frequently at the exit surface rather than the entrance surface of an optical component. Several models have been proposed to explain these observations.

In one model, pit formation and the difference of damage between front and back surface have been explained to be the results of reflections occurring at the various

boundaries [11.11, 12]. The formation of pits in glass is assumed to be the result of a standing wave which is formed inside the glass near the surface. The standing wave is caused by reflections from the plasma-glass boundary. After plasma initiation there is a layer of plasma several wavelengths thick contiguous to the surface. This plasma is densest at its source, that is, next to the surface. The electric field at the antinodes of this standing wave can become twice as large as the electric field of the incident beam. The first antinode is within one-quarter wavelength of the surface. It is this large electric field at the antinode that initiates pitting at, or just inside, the surface.

The fact that a sample of transparent dielectric material exposed to a collimated beam of light will usually damage at the exit surface at a lower power level than at the entrance surface can also be explained by the effect of Fresnel reflection. When a light pulse enters an isotropic optical material at near-normal incidence, there is a reflection at the air-to-sample boundary. Since the index of refraction n of the material is higher than that of air, the reflected light wave suffers a phase shift of 180° with respect to the incident light wave. This phase shift results in a partially destructive interference of the two light waves within a distance of $\lambda/4$ of the entrance surface. As a result the light intensity I_{en} at the entrance surface is related to the incident intensity I_0 by

$$I_{\text{en}} = \frac{4}{(n+1)^2} I_0. \quad (11.1)$$

At the exit surface, the reflected wave suffers no phase shift, so that the intensity at the exit surface I_{ex} is related to the intensity incident on the sample by

$$I_{\text{ex}} = \left(\frac{4n}{(n+1)^2} \right)^2 I_0. \quad (11.2)$$

Thus the ratio of the intensity inside the medium at the exit surface to the intensity inside the medium at the entrance surface is

$$\frac{I_{\text{ex}}}{I_{\text{en}}} = \left(\frac{2n}{n+1} \right)^2. \quad (11.3)$$

For $n = 1.55$, this ratio is 1.48.

A model which explains another difference between contaminated entrance and exit surfaces was put forward in [11.13]. However, the same conclusion is reached, namely, that particles on the front surface cause less damage than on the back surface. On the exit surface, a plasma is formed and confined between two solid materials, i.e., the substrate and the particle. The high density of the plasma and associated pressure cause the particle to be ejected rapidly on heating. The reaction force leads to a small pit on the surface, which then leads to damage. On the front surface, the plasma can expand and only a weak shockwave is launched into the substrate, and the surface is not pitted or damaged. Small particles may be completely vaporized in the process.

Consistent with the particle ejection model is the observation that internal reflective surfaces of Porro prisms and corner cubes have generally a higher damage threshold if the reflective surfaces are coated with SiO_2 coatings of about $2 \mu\text{m}$ thickness. The coating prevents the field of the evanescent wave from reaching the particles and therefore prevents the initiation of reaction pits.

11.2 Inclusion Damage

Optical components tend to exhibit minute inhomogeneities, which generally form in the process of fabricating the material. The inhomogeneities can consist of small bubbles, dielectric inclusions, or platinum particles in the case of laser glass. In crystalline materials, although some microinhomogeneities do occur during the growth process, there is less evidence that particulate damage is the limiting factor. In glass, however, during the course of melting, crucible material finds its way into the melt and upon cooling condenses out in the form of particulate inclusions. This has been a particularly difficult problem in the fabrication of laser glass, which is manufactured in platinum containers. The problem of platinum inclusions has been solved by glass manufacturers either by using crucibles of ceramic and clay materials or by carefully controlling the oxygen content in the melt. If the material contains minute inhomogeneities such as particulate inclusions, especially metallic inclusions, they can absorb the laser radiation, giving rise to local heating and melting of the surrounding laser host material. This in turn causes stress concentrations sufficient to rupture the material. Elaborate theoretical treatments of the problem of stress formation in the vicinity of an absorbing particle have been published [11.14].

To summarize the considerations that apply, let us consider an absorbing particle embedded in a laser material, illuminated by a brief and intense pulse of light. If the particle is a sphere of diameter d , it presents an absorbing area to the incident light of $\pi d^2/4$. The total energy absorbed in the particle is approximately

$$\Delta E = I t_p \left(\frac{\pi d^2}{4} \right) (1 - e^{-\alpha d}), \quad (11.4)$$

where I is the power density, t_p is the pulse duration, and α is the material absorption coefficient. The maximum temperature rise experienced by the particle will be given by

$$\Delta T = \frac{\Delta E}{C_p(\pi d^3/6)\gamma}, \quad (11.5)$$

neglecting heat conduction during the pulse. In the above equation C_p is the specific heat and γ is the density of the inclusion.

Equation (11.5) indicates that the temperature of metal particles subject to a 20-J/cm², 30-ns laser pulse can exceed 10,000 K for typical particle sizes. These high temperatures produce stress in the glass adjacent to the particles, which can exceed the theoretical strength of glass and result in failure.

11.3 Damage Threshold of Optical Materials

The data presented here on bulk, surface, and dielectric thin-film damage levels should only be used as a guide, since damage thresholds depend on a great number of laser and materials parameters, as well as sample cleanliness and prior history. Laser

parameters, such as wavelength, energy, pulse duration, transverse and longitudinal mode structure, beam size, location of beam waist, all play an important part in the definition of damage threshold. For example, multimode beams usually contain “hot spots” at which the peak power is many times the average value estimated from the pulse energy, pulse duration, and beam cross section.

Experience also shows that the damage threshold can vary greatly even within one particular sample because of compositional variations, localized imperfections, absorption centers, etc. It has also been shown that the prior history of a sample can have a large influence on the damage level.

11.3.1 Scaling Laws

Although the specific threshold at which laser damage is observed depends on a great many factors, empirical scaling laws offer a guide to the parametric variation of the thresholds for a given material.

In this subsection, the dependence of damage threshold on pulse width, wavelength, beam diameter, and laser conditioning is discussed.

Pulse Width. We can distinguish two different behavioral regimes. For pulses longer than about 100 ps, damage is caused by conventional heat deposition resulting in melting and boiling [11.15, 16]. Energy is absorbed by conduction band electrons from the external field and transferred to the lattice. In this regime, the source of the initial seed electrons can be local defects or impurities. For damage to occur, the temperature near the local absorption centers must be sufficiently high to cause fracture or melting.

Because the limiting process for temperature growth is thermal conduction and diffusion into the lattice, the fluence required to raise the heated region to some critical temperature is proportional to $t_p^{0.5}$ where t_p is the pulse duration [11.17]. This is in reasonably good agreement with numerous experiments which have observed a t_p^α scaling with α between 0.3 and 0.6 in a variety of dielectric materials from 20 ps to over 100 ns, including samples with defects.

Figure 11.2 illustrates the dependence of damage threshold on pulse width for a number of materials. The data presented are the results of numerous measurements performed at the Lawrence Livermore National Laboratory over a period of 10 years [11.18]. The materials include silicate glasses, such as borosilicate BK-7, low-expansion TiO_2-SiO_2 (ULE), fused silica, a commercial phosphate glass (LG 750), fluorophosphate glass, a sol-gel AR coating and a high reflectivity dielectric coating HfO_2 on a fused silica substrate.

The pulse-width dependence ranges from $t_p^{0.5}$ for fused silica at 355 nm and the sol-gel AR coating to $t_p^{0.4}$ for fused silica, BK-7, ULE, LG 750, and fluorophosphate at 1064 nm, and to $t_p^{0.3}$ for the HfO_2 coating.

As the pulse width decreases below 100 ps, a gradual transition takes place from the long pulse, thermally dominated regime to an ablative regime dominated by collisional and multiphoton ionization and plasma formation [11.19–21]. For pulses shorter than

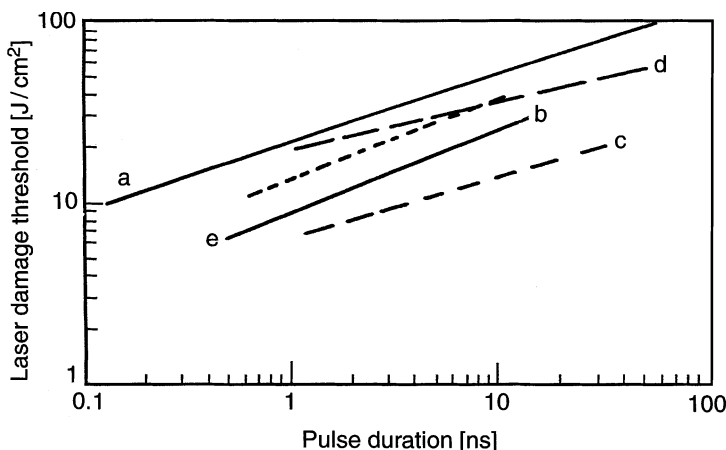


Fig. 11.2. Damage threshold vs. pulse duration for fused silica, BK-7, ULE, LG 750, and fluorophosphate glass at 1064 nm (a); fused silica at 355 nm (b); HfO₂/SiO₂ HR coating at 1064 nm, unconditioned (c) and laser conditioned (d); sol-gel AR coating on fused silica at 1064 nm and 355 nm (e) [11.18]

about 20 ps, electrons have insufficient time to couple to the lattice during the laser pulse. The damage threshold continues to decrease with decreasing pulse width, but at a rate slower than $t_p^{0.5}$. This departure is accompanied by a qualitative change in the damage morphology indicative of rapid plasma formation and surface ablation. The damage site is limited to only a small region where the laser intensity is sufficient to produce a plasma with essentially no collateral damage.

Optical breakdown occurs because of an electron avalanche in which conduction-band electrons, oscillating in response to the laser field, achieve energy equal to the bandgap, and subsequent impact ionization promotes another valence electron into the conduction band. Because the pulses are so short, collisional heating of the electrons occurs before there is significant transfer of energy from the electrons to the lattice. Impact ionization eventually results in an electron avalanche [11.9, 22].

Wavelength Dependence. Typically, the damage threshold decreases for shorter wavelengths and drops off rather sharply at the shortest wavelengths. This behavior is illustrated in Fig. 11.3 which summarizes the results of over 1000 damage measurements on KDP crystals [11.23]. The sharp drop in bulk damage threshold for very short wavelengths has also been measured in fused quartz and synthetic fused silica [11.24]. Fused quartz is produced by melting natural quartz powder, and synthetic fused silica is produced directly by flame hydrolysis of SiCl₄ in an H₂/O₂ flame. Measurements were performed with a Q-switched laser at 1064, 532, 355, and 266 nm with pulses of about 1 ns. For silica glass the laser-induced bulk damage threshold can be expressed as

$$J_{th} = 1.45\lambda^{0.43}, \quad (11.6)$$

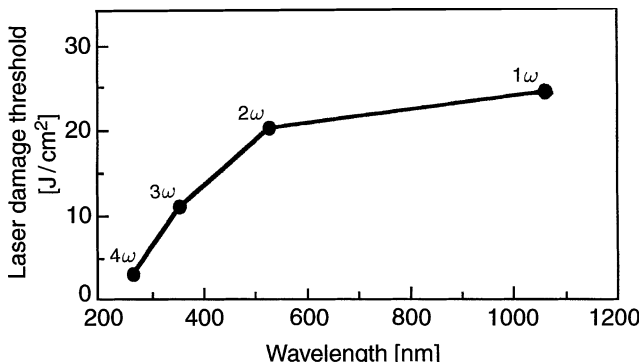


Fig. 11.3. Bulk laser damage threshold of KDP crystals measured with 3-ns pulses at the fundamental and harmonics of an Nd:YAG laser [11.23]

where J_{th} is in J/cm^2 and λ is the wavelength in nm. This relationship holds for wavelengths between 1064 and 355 nm. At 266 nm the threshold is about a factor 2 lower than that calculated from the above equation. It was concluded that the damage mechanism at wavelengths shorter than 355 nm is determined by two photon absorption. At 1064 nm no difference was found between the various types of SiO_2 ; at shorter wavelengths fused quartz samples had a slightly smaller damage threshold compared to synthetic fused silica.

Other experimental data for bulk and sol-gel AR-coated fused silica show a similar decrease in damage threshold in changing the wavelength from 1064 to 355 nm [11.18, 25].

Spot-Size Dependence. Surface damage is usually initiated by defects, such as pits, inclusions, or scratches. Probing the surface with a beam smaller than the separation of isolated defects will measure the damage threshold of the basic substrate or coating material. A larger spot size will increase the probability that surface defects will be within the beam area. Therefore, there is a dimensional dependence of the damage threshold. Depending on the density and distribution of these imperfections at a certain spot size, the dimensional dependence will disappear.

The dimensional dependence indicates that the failure mechanism is due to defect-driven localized failures rather than the basic coating or substrate material. In testing for damage, it is important that the beam spot size is large enough to provide meaningful results. Figure 11.4 illustrates a typical result of a dielectric coating tested at different spot diameters [11.26]. The dimensional dependence of the damage threshold disappears for spot sizes larger than 100 μm .

Laser Conditioning. It has been consistently observed in a number of optical materials, both bulk and thin film, that the damage threshold can be substantially and permanently improved by a process which consists of exposing a component to

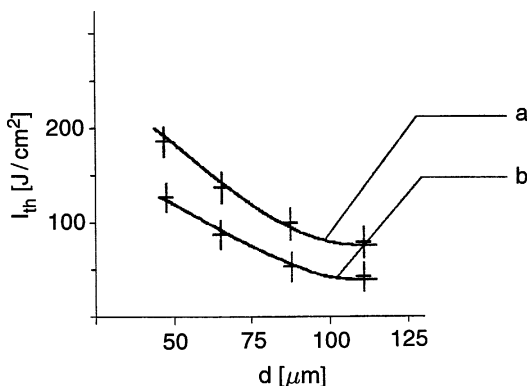


Fig. 11.4. Damage threshold dependence on beam diameter of a $\text{ZrO}_2/\text{SiO}_2$ (curve a) $\text{TiO}_2/\text{SiO}_2$ (curve b) multilayer coating [11.26]

incrementally higher and higher fluence levels beginning well below the single-shot damage threshold [11.27–30].

Multilayer HfO_2 coatings on fused silica substrates show the most consistent improvement with laser conditioning. In general, conditioning produces about a two to threefold improvement in the damage threshold. The curves (c and d) in Fig. 11.2 illustrate this improvement. The conditioning effect has been associated with the gentle removal of nodular-shaped defects, which are known to limit the damage threshold of these multilayer coatings. Other dielectric coatings which have been reported to respond to laser conditioning are MgF_2 , LaF_3 , and ZrO_2 [11.31, 32]. The bulk damage of KDP crystals can also be increased by a factor of 2 or more over the unconditioned threshold [11.23].

Actually, laser conditioning may represent the greatest single practical improvement in thin-film damage thresholds in the past 10 years. As a general rule of thumb at least five shots are needed to condition the optic to $\approx 85\%$ of the maximum conditioned threshold. Furthermore, the first shot in the conditioning sequence should be at a fluence of about one-half the unconditioned damage threshold.

11.3.2 Laser Host Materials

The damage threshold of the laser medium is usually determined by the coatings rather than the bulk material. Internal damage occurs relatively seldom, unless an internal focus is created because of self-focusing, or as a result of back reflections from an optical element.

Bulk damage using 47-ps pulses from a mode-locked Nd:YAG laser at 1.06 μm has been measured for a number of materials by focusing the beam inside the sample [11.33]. The samples tested included LiSAF, LiCAF, and LiSCAF, with different chromium dopings, along with Nd:YAG, fused silica, and BK-7. The threshold value of the Cr-doped laser crystals was about 20 J/cm² or 400 GW/cm², which are comparable with those of fused silica and BK-7 and about a factor of 2 larger than Nd:YAG.

Bulk damage threshold measurements with a Q-switched Nd:YAG laser which had a pulse width of 10 ns are reported in [11.34]. The lowest power density for which

damage was observed in the Nd:YAG sample was 3.6 GW/cm^2 , and 2.6 GW/cm^2 for Nd:YALO. As a comparison, the intrinsic damage thresholds for LiNbO₃ and calcite were at least a factor 6 lower compared to the laser crystals. Bulk damage thresholds for a number of Nd:Glasses have already been summarized in the previous section.

Although this chapter is concerned with laser-induced damage to optical materials, it might be of interest to some readers to briefly mention damage to laser crystals induced by gamma and proton radiation. Solid-state lasers in space are exposed to charged particles, such as electrons, protons, and high-energy cosmic rays. The effect of gamma rays and high-energy protons on Nd:YAG and Nd:YLF crystals has been described in [11.35]. It was found that both forms of radiation create color centers in the crystals which reduced optical output primarily by absorbing the laser radiation.

For Nd:YAG the induced absorption loss reached a limiting value of about 0.015 cm^{-1} at 100 krad exposure levels; the loss in Nd:YLF was higher and did not reach a limiting value. Codoping Nd with Cr³⁺ significantly reduced radiation susceptibility of Nd:YAG. The result of the experiments suggested that diode-pumped Nd:YAG lasers can be effectively radiation-hardened to withstand exposure to charged particles in space. Design features which improve radiation hardness include codoping of the Nd:YAG crystal with Cr³⁺, a short laser crystal, and pulsed Q-switched rather than cw operation, because the higher gain can more readily overcome the induced losses created by color centers.

11.3.3 Optical Glass

Data on bulk damage thresholds for a number of glasses have been provided in Sect. 11.3.1. In inclusion-free silica, damage threshold is limited by the surface. Extensive measurements at different wavelengths and pulse widths give a simple empirical relationship governing the safe operating limit for fused silica [11.25]

$$\begin{aligned} J_{\text{th}} &= (22 - 25)t_p^{0.4} && \text{at } 1064 \text{ nm,} \\ J_{\text{th}} &= (9 - 14)t_p^{0.5} && \text{at } 355 \text{ nm.} \end{aligned}$$

The lower values are for bare surface fused silica, and the higher values are measured after a sol-gel AR coating is applied to the surface. J_{th} is the damage threshold (J/cm^2) and t_p is the pulse length (ns). In agreement with the common trend in optical materials, the measurements also reveal a substantial decrease of the damage threshold for the shorter wavelength.

For pulses shorter than 20 ps, the damage fluence no longer follows the $t_p^{0.5}$ dependence. As explained earlier, for such short pulses there is insufficient time for lattice coupling. Figure 11.5 summarizes measurements of the damage fluence for fused silica at very short pulse widths [11.21]. Summaries of the damage threshold of a large number of different optical glasses including absorption filters can be found in [11.36].

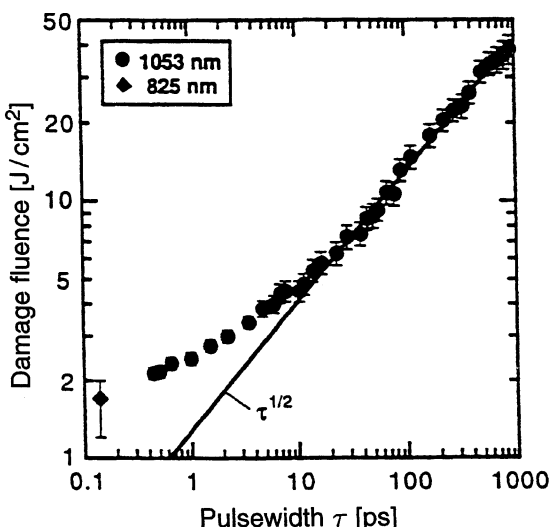


Fig. 11.5. Threshold damage fluence for fused silica as a function of pulse width [11.21]

11.3.4 Nonlinear Crystals

From all the optical components and materials employed in solid-state laser systems the largest spread in damage thresholds occurs with nonlinear crystals. Table 11.1 summarizes the nominal damage levels of important crystals employed in nonlinear process of solid-state lasers. It shows a spread of over two orders of magnitude from KDP/KD*P to the AsGaSe₂/AsGaS₂ crystals.

In addition to exhibiting damage mechanisms operative in other dielectric materials, such as thermal heating, and creation of an electron avalanche by impact ionization, nonlinear materials are subject to damage by virtue of their nonlinear properties. It is frequently observed that the damage levels observed in harmonic generation are far lower in the presence of the harmonic than those observed with just the fundamental present. This effect is often caused by multiphoton absorption, which plays a major role in laser-induced damage in nonlinear crystals. In this process, 2-photons or 3-photons can generate radiation at a wavelength which is below the absorption edge of the crystal. Absorption of UV radiation typically leads to color center formation.

Table 11.1. Typical damage thresholds for nonlinear crystals

Nonlinear crystal	KDP	KD*P	LBO	BBO	KTP KTA	LiNbO ₃ PPLN	AsGaS ₂ AsGaSe
Damage threshold [GW/cm ²]	8	4	2.5	1.5	0.5	0.2	0.03

Laser-induced damage in KDP and KD*P has been studied in great detail because these crystals are employed in inertial confinement fusion lasers for the generation of the second and third harmonics from Nd:Glass lasers. Laser damage threshold for KDP as a function of wavelength is depicted in Fig. 11.3. The damage threshold for KD*P is about a factor 2 lower compared to KDP. As already mentioned the threshold for bulk damage can be increased by subjecting the crystals to a series of gradually increasing fluence levels beginning below unconditioned threshold levels [11.37, 38].

The borate crystals LBO and BBO also have very high damage thresholds. LBO is emerging as an alternative to KTP for harmonic generation of Nd:lasers. This crystal does not suffer from nonlinear absorption or photo-refractive effects; however, the nonlinear coefficient and thermal acceptance parameter of LBO are about one third those of KTP. Lifetimes in excess of 1000 hours have been reported in LBO at a second-harmonic output close to 180 W [11.39]. BBO has a transmission band which extends to 200 nm; therefore, multiphoton absorption is not a problem. This material is of particular interest for harmonic generation in the blue region of the spectrum.

KTP crystals are primarily employed for frequency doubling of Nd:lasers, and in OPOs for the generation of the eye-safe wavelength of 1.5 μm . Although the bulk and surface damage thresholds for KTP are quite high at 1.06 μm , employed in a second harmonic generator or as an OPO, a number of failure mechanisms set in which are related to the conversion process.

At around 1.06 μm , laser-induced damage in KTP is associated with surface coatings and macroscopic flaws in crystals. The damage threshold of KTP at 1.06 μm , measured with a Q-switched Nd:YAG laser with a pulse width of 20 ns, is depicted in Fig. 11.6.

Nonlinear effects were minimized in these tests by appropriate orientation of the crystal. Surface failure for uncoated crystals is typically 15–20 J/cm² for pulse width

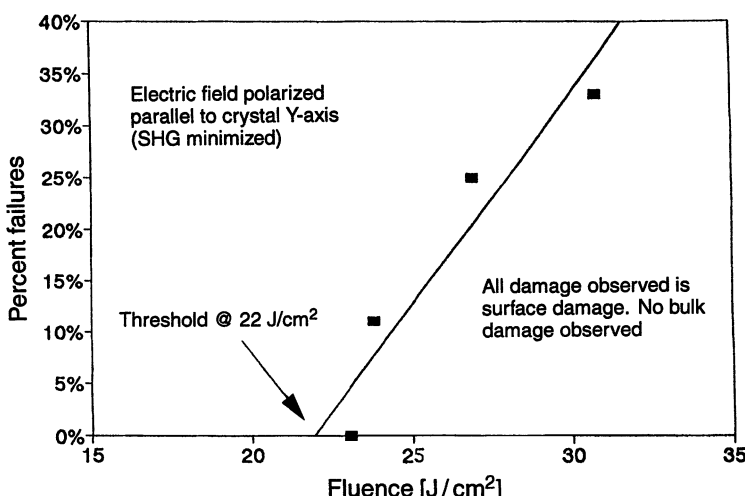


Fig. 11.6. Damage frequency plot of KTP at 1064 nm [11.40]

of 10–20 ns. Bulk failure thresholds have been measured as high as 30 GW/cm^2 [11.40, 41].

When KTP is used in a noncritical phase-matched OPO, it is subject to thermal heating owing to $3.3\text{-}\mu\text{m}$ idler absorption. In high-average-power systems this absorption results in a substantial lowering of the damage threshold. With a 20 Hz Nd:YAG laser, massive bulk and surface damage was observed at fluence levels as low as 5 J/cm^2 [11.40, 41].

KTA, a crystal very similar to KTP, has much lower absorption at the idler wavelength (Fig. 10.12). KTA avoids the problems associated with thermal heating due to absorption in the $2.8\text{--}3.5 \mu\text{m}$ region. Consequently KTA, rather than KTP, is usually employed in high-average-power OPOs designed for the generation of infrared radiation from an Nd:laser.

Damage of KTP in a harmonic generator results from a photochromic process which forms laser-induced color centers commonly referred to as gray tracks. Absorption of both the fundamental and harmonic radiation along the beam volume leads eventually to catastrophic failure of the crystal.

Different crystalline defects such as the presence of Ti^{3+} or Fe^{3+} chemical impurities, or a stoichiometric imbalance creating oxygen vacancies, can lead to different damage mechanisms [11.42]. The cause of damage is generally believed to be a nonlinear photoionization process such as multiphoton absorption, third harmonic, or sum frequency generation. These processes can produce photons with energies greater than the bandgap energy of KTP. These energetic photons will create free electrons and holes, some of which will become trapped at defect sites in the crystal. These defects may initially be nonabsorbing, but when ionized they become strongly absorbing. Active hole traps are Fe^{3+} impurities and active electron traps are Ti^{4+} ions which are adjacent to an oxygen vacancy [11.43]. Another damage mechanism leading to gray tracks at 532 nm is two-photon absorption by Ti^{3+} color centers [11.44].

Gray tracking in KTP has been extensively investigated [11.42–53]. Gray-tracking damage can be removed by heating the crystal during operation to about $70\text{--}100^\circ\text{C}$. At this elevated temperature darkening due to the photochromic process is annealed out fast enough to achieve long-term stable operation. Higher temperatures will accelerate the annealing process even more.

Gray tracking decreases as the temperature increases and vanishes for temperatures above 170°C [11.44]. In a laser system a higher temperature has to be weighted against potential contamination problems from outgassing of the hot components of the crystal oven (Sect. 11.4).

In a test conducted at 75°C , exposure to 12 J/cm^2 and 10,000 shots produced no bulk darkening; the same experiment performed at 30°C caused a transmission loss ranging from 4 to 8% [11.47].

Intracavity-doubled Nd:YAG lasers have produced over 100 W of second-harmonic power using KTP. In one of these high-power systems a degradation rate was measured of 0.04% per hour during a 300-h test run at 150 W of green output and a repetition rate of 13 kHz. Most of the degradation was attributed to gray tracking in the KTP crystal [11.39]. Because of this high degradation rate, the KTP crystal was

replaced by an LBO crystal. Degradation of LBO operated at 30°C was negligible at an average green output of 180 W.

In our laboratory, we have built a number of diode-pumped Nd:YAG lasers which produce between 250 and 500 mJ per pulse of green output at a pulse width of 10–20 ns and repetition rates up to 100 Hz. At a fluence level of about 1–2 J/cm² at 1.06 μm, degradation in KTP is minimal for a pulse count up to 10⁸–10⁹. The KTP crystals are operated typically at 90°C. One investigation revealed that the dependence of the induced absorption of 532-nm radiation is nonlinear and has a threshold of 80 MW/cm² [11.52].

Experiments have also shown that the peak power threshold for gray-tracking damage strongly depends on the repetition rate of the laser. An exponential decrease of damage threshold as a function of repetition rate was observed, ranging from 125 MW/cm² at 1 kHz to 18 MW/cm² at 6.3 kHz, to a few MW/cm² for frequencies above 10 kHz [11.50].

Lithium niobate has a relatively low damage threshold in comparison with other common nonlinear materials. For example, at 1.06 μm, a surface damage threshold of 180 MW/cm² has been measured for a 10-ns pulse with a Gaussian intensity profile [11.54]. At a wavelength of 1.54 μm, a damage level of 20 J/cm² with a 50-ns long pulse has been reported [11.26].

LiNbO₃ is plagued by photorefractive effects resulting from propagation of visible or UV radiation. Photorefractive effects cause refractive index inhomogeneities which seriously degrade beam quality and distort the index-match condition necessary for efficient second-harmonic generation [11.55, 56]. The occurrence of refractive index gradients is reversible if the temperature of the crystal is increased during operation to about 160°C. The index inhomogeneities are associated with imperfections in the crystal. Photons at the shorter wavelength have enough energy to break the binding energy which traps electrons at the vacant lattice site. The electrons are then free to move away, leaving behind a local electric field distribution in the crystal. Because of the large electro-optic effect of LiNbO₃, this local electric field causes refractive index gradients. Annealing the crystal at an elevated temperature increases the mobility of electrons in the crystal enough to permit neutralization of the charged vacancy, thereby removing the refractive index gradients. Also, doping with MgO has been used to reduce photorefractive damage; but doped crystals do not exhibit the same high quality that is available in undoped crystals.

There have been several reports that periodically poled lithium niobate is more resistant to photorefractive damage than are homogeneously poled crystals [11.57–59].

The large transparency range of 0.8–18 μm makes silver gallium selenide (AgGaSe₂) an excellent candidate for OPOs in the infrared region. Unfortunately, the crystal has a very low damage threshold which must be taken into account when engineering specific OPO devices. Measurements with a pump laser at 2.09 μm revealed an average surface damage threshold for coated and uncoated crystals of around 1 J/cm² at a pulse width of 50 ns [11.60].

Silver gallium sulfide (AgGaS₂) with a transmission range of 0.5–12 μm is another crystal for OPO devices in the mid- and far-infrared region. A surface damage

threshold of 25–50 MW/cm² for 10-ns pulses at 1.064 μm has been measured [11.61]. Since the bulk damage threshold of this crystal is an order of magnitude higher, further improvements of the crystal might lead to a higher surface damage threshold.

11.3.5 Dielectric Thin Films

Multilayer dielectric films are generally the weakest elements of any laser system. Because of the relative complexity and variety of deposition factors, thin films vary greatly in purity, morphology, uniformity, and composition, depending, to a great extent, on the specifics of the fabrication process. In addition, residual stress, substrate cleanliness, and other extrinsic factors tend to reduce the thin-film damage level well below that expected for the same material in bulk form.

The usefulness of a dielectric coating for high-power applications depends on the choice of coating material, thin-film design, and deposition technique. Today's knowledge of coating failures distinguishes between homogeneous background absorption in the film and absorption at localized defects. Many investigations have shown that microscopic absorbing defects in the film are the initial sites of failure [11.62–65].

During evaporation, ejected particles of coating material from the source, or particles flaking from the chamber walls, can become embedded in the film and can initiate the growth of so-called nodular defects. Inclusions form a discontinuity in the coating stack disrupt the electric field distribution, resulting in localized electric field enhancement in the vicinity of the nodule. This leads eventually to significant heating of the localized region. The effects of laser conditioning are now commonly seen to be a result of the heating and subsequent ejection of such inclusions.

Numerous measurements have conclusively shown that the defect density and film roughness, caused by overcoated particles, are key indicators in determining the threshold of a dielectric coating [11.63, 64, 66]. In AR coatings, the field intensity is near maximum at the substrate surface, where the coating is most vulnerable owing to surface imperfection, embedded polishing materials, and poor film structure.

Therefore, the ultimate limit for AR coatings is the damage threshold of the uncoated substrate material. With HR coatings the substrate surface is shielded from the high field strength, and the ultimate limit of a perfect coating is determined by bulk values of the coating materials.

Thin films and multilayer stacks for optical components of solid-state lasers are usually produced by electron-beam (e-beam) evaporation.

The e-beam deposition process consists of an electron beam generated by thermionic emission from a filament. The beam is focused and directed by permanent magnets to a grounded source material. Advanced deposition techniques include the ion-assisted deposition technique and ion-beam sputtering. The former technique uses a conventional e-beam source to generate the deposition and an ion gun pointed at the optical substrate to increase the energy of the deposited particles. Ion beam sputtering uses an ion source that strikes a target to sputter atoms with high arrival energies onto the substrate. The higher energy of the deposited particles compared to e-beam deposition generates denser films with lower porosity.

Very large pieces of optics, such as employed in inertial confinement fusion drivers, are AR-coated by a sol-gel process [11.67]. Sol-gel coatings are very cost-effective methods to produce coatings on large optical substrates since these coatings can be applied in a dip or spin process at room temperature. The procedure involves the preparation of a solution of metal alkoxides which is converted by hydrolysis or heat to an oxide in a gelation stage. For example, from a solution of $\text{Si}(\text{OCH}_3)_4$ a SiO_2 coating can be produced. Very high damage thresholds can be achieved with sol-gel coatings. Drawbacks include their fragile nature and difficulty in cleaning the optical components. For this reason, sol-gel coatings are not often used in standard solid-state lasers. The AR coating of choice is usually vacuum-deposited MgF_2 .

We will briefly review the laser-induced damage thresholds and major issues for thin-film coatings from the UV to the mid-infrared regime, which covers the range from frequency-quadrupled Nd:YAG lasers to OPOs operating in the 2–4 μm region.

The most detailed damage studies have been carried out for high-reflectivity $\text{HfO}_2/\text{SiO}_2$ coatings and for AR sol-gel coatings at the wavelengths of 1054 and 355 nm, because these coatings are used for the optical components of the large Nd:Glass lasers at the Lawrence Livermore National Laboratory.

UV Spectral Region. The damage threshold of dielectric thin films is lower in the UV region as compared to the longer wavelengths. One reason is the increased absorption, the other is the higher photon energy. Ionization and multiphoton absorption are more likely to occur at shorter wavelengths. The substrate materials transparent in the UV region are fused silica, MgF_2 , and CaF_2 . The choice of coating materials at the shortest wavelengths around 266 nm include MgF_2 , LaF_3 , SiO_2 and Al_2O_3 . At the wavelength around 355 nm, ZrO_2 and HfO_2 can be added to the above-listed materials.

Table 11.2 lists laser-induced damage thresholds for common substrates and thin films employed in the UV region [11.68]. At 355 nm, the damage threshold of a $\text{HfO}_2/\text{SiO}_2$ high-reflectivity coating was measured between 5 and 8 J/cm^2 for a 3-ns

Table 11.2. Damage threshold [J/cm^2] at 248 nm of various substrates and coatings [11.68]

Substrate	
MgF_2 crystal	20
Quartz crystal	10
Suprasil 300	8
CaF_2	3
AR coatings	
MgF_2	9
$\text{LaF}_3/\text{MgF}_2$	10
$\text{Al}_2\text{O}_3/\text{SiO}_2$	3
$\text{Al}_2\text{O}_3/\text{MgF}_2$	3
HR coatings	
$\text{Al}_2\text{O}_3/\text{SiO}_2$	25
$\text{LaF}_3/\text{MgF}_2$	20

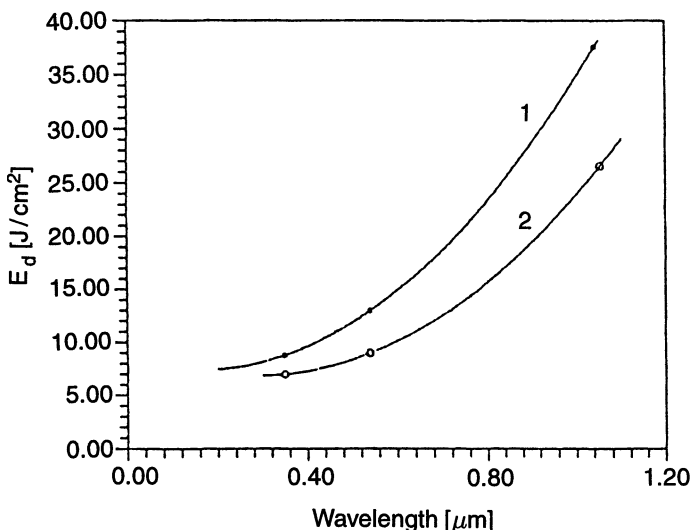


Fig. 11.7. Damage threshold of a multilayer $\text{ZrO}_2/\text{SiO}_2$ coating vs. wavelength for a defect density of $280/\text{mm}^2$ (curve 1) and $320/\text{mm}^2$ (curve 2) [11.69]

pulse. The damage threshold for $\text{ZrO}_2/\text{SiO}_2$ coatings was slightly lower, whereas $\text{Al}_2\text{O}_3/\text{SiO}_2$ coatings had damage thresholds around 10 J/cm^2 [11.66].

Visible and Near-Infrared Region. Multilayer thin films for this wavelength region usually consist of alternating layers of a metal oxide which provides the high-index material and SiO_2 . Common combinations are $\text{HfO}_2/\text{SiO}_2$, $\text{ZrO}_2/\text{SiO}_2$, $\text{TiO}_2/\text{SiO}_2$, and $\text{Ta}_2\text{O}_5/\text{SiO}_2$. In particular, $\text{HfO}_2/\text{SiO}_2$ has a very high laser-induced damage threshold; it can be further improved with laser conditioning.

Damage threshold for a multilayer $\text{HfO}_2/\text{SiO}_2$ coating at $1.06 \mu\text{m}$ as a function of pulse width is depicted in Fig. 11.2. The damage threshold for a multilayer $\text{ZrO}_2/\text{SiO}_2$ coating measured versus wavelength with a 10-ns-long pulse and a Gaussian beam profile is shown in Fig. 11.7. The curves also illustrate the dependence of the damage threshold on defect density. Similar to the observation made with bulk materials (Fig. 11.5), there is a transition region with regard to the pulse width, where the damage morphology changes from heating and melting at the longer pulses, to ablation of the individual dielectric layers at very short pulses. At the short pulse-width regime, pulse-width scaling is less than $t_p^{0.5}$. Figure 11.8 depicts the dependence of the damage threshold on pulse width of very short pulses for two multilayer dielectric polarizers [11.21]. Damage thresholds for polarizer coatings are typically lower than those of similar mirror coatings. For example, for 3-ns pulses, $\text{HfO}_2/\text{SiO}_2$ thin-film polarizers have a damage threshold after laser conditioning of around $15\text{--}20 \text{ J/cm}^2$, which is half the value compared to mirror coatings.

In [11.70] damage thresholds were reported for monolayer and multilayer coatings produced by different commercial suppliers. The results of the tests performed with 25-ps and 8-ns pulses at 1064 nm are summarized in Table 11.3. The data illustrate the large spread in the damage threshold for coatings from different vendors.

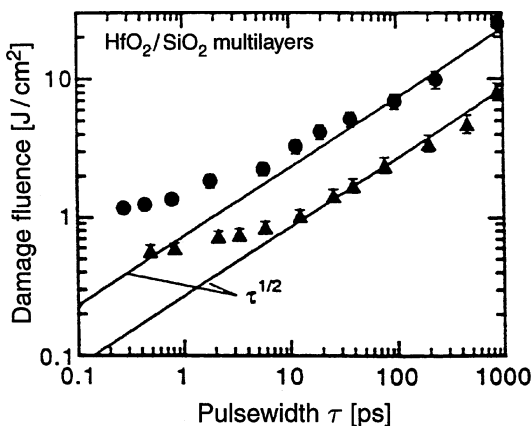


Fig. 11.8. Damage threshold at 1053 nm for $\text{HfO}_2/\text{SiO}_2$ multilayer 45° (\blacktriangle) and 57° (\bullet) polarizer [11.21]

The design and development of eye-safe rangefinders and LIDAR systems require high-damage-threshold coatings for the wavelength region around 1.5 μm . Measured values of the laser-induced damage threshold at this wavelength at a pulse width of 50 ns are listed in Table 11.4 for different coatings [11.26].

The damage threshold for $\text{ZrO}_2/\text{SiO}_2$ coatings were found to be higher as compared to $\text{TiO}_2/\text{SiO}_2$ (see also Fig. 11.4). The tests also revealed that the damage threshold for both types of coatings is about 20–30% higher at 1.5 μm as compared to 1.06 μm .

Mid-Infrared Spectral Range. Interest in high-power coatings for this wavelength regime is driven by the development of solid-state laser pumped OPOs with outputs between 2.5 and 4 μm . The availability of nonlinear crystals, such as KTA and PPLN, has opened the mid-infrared regime to solid-state lasers for a number of important applications such as atmospheric studies, spectroscopy, and IR countermeasures.

Table 11.3. Range of damage thresholds at 1064 nm (after preconditioning) for coatings produced by different commercial vendors [11.70]

	Damage threshold [J/cm^2]	
	25 ps	8 ns
Monolayers		
Ta ₂ O ₅	4.6–5.4	25
TiO ₂	3.1–3.4	9–18
SiO ₂	15–16	140
Multilayer coatings		
ZrO ₂ /SiO ₂	6.5–21.5	44–155
Al ₂ O ₃ /MgF ₂	13–15	120–130
Substrate bare surfaces		
Fused silica	17.8–21.5	–
BK-7	20–21.5	–
Nd:YLF	10–12.5	–

Table 11.4. Damage threshold of multilayer coatings at 1.54 μm [11.26]

Materials and type of coatings	Number of layers	Laser-damage threshold at 1.54 μm [J/cm^2]
ZrO ₂ –SiO ₂ high reflection	25	65 ÷ 80
ZrO ₂ –SiO ₂ Partially reflective	10	No less than 100
TiO ₂ –SiO ₂ high reflection	23	40 ÷ 60
ZrO ₂ –SiO ₂ antireflection	2	No less than 100

Coatings have been well developed in this region as a result of DF and HF chemical laser systems. Dielectric thin films for optical parametric oscillators have special requirements, such as multi-wavelength and dichroic coatings.

Values for the laser damage threshold were reported in [11.71] for a number of dielectric thin films composed of different materials and deposited by different methods. The stacks were designed around the requirements for OPOs with reflection bands between 2.5 and 4 μm . The highest damage thresholds were found for the ZnS/Al₂O₃ films deposited by e-beam evaporation on either silicon, CaF₂, or ZnS substrates. Damage levels at 3.8 μm for a 55-ns pulse were around 50 J/cm^2 , which is close to the damage level of the bare silicon substrate. Stacks of SiO₂/TiO₂ thin films also performed well with damage levels on the order of 45 J/cm^2 .

11.4 System Design Considerations

The designer of a laser system, although he cannot change the damage thresholds of the materials employed in a laser, can reduce the damage susceptibility and improve the reliability of his system by the right choice of materials and by proper design and operation of the laser. We will enumerate a few design, inspection, and operating procedures which need to be followed to reduce the likelihood of optical damage to the laser components.

11.4.1 Choice of Materials

In powerful lasers it is important that only high-damage-resistance AR and multilayer coatings are employed. These coatings usually include ZrO₂, SiO₂, TiO₂, Al₂O₃, HfO₂, and MgF₂ compositions which are evaporated with an e-beam gun. Beam splitters, lenses, and prisms located in the beam have to be fabricated from fused silica, sapphire, or highly damage-resistant glass, such as BK-7. The surfaces of these components should be pitch-polished to a 5/10 or 0/0 surface quality. Surface conditioning or “superpolishing,” such as chemical etching, ion-beam polishing,

laser conditioning, or bowl-feed polishing, are very effective in raising the damage threshold.

All components of the laser system should be inspected for surface defects, such as scratches, fingerprints, “orange peel,” and bulk defects, such as inclusions, bubbles, striation, schlieren, and internal stress.

Inclusions in a laser rod can be best checked by illuminating the rod from the side and observing the presence of scatter centers. The fringe pattern obtained from the Twyman-Green interferometer will reveal any density gradients and optical inhomogeneities in the laser rod. Inspection of the laser rod, Q-switch crystal, frequency doubling crystal, etc. between cross-polarizers will reveal internal stresses, striation, and schlieren. Optical surfaces are best inspected under a binocular microscope (magnification of $50\times$) with a strong collimated light beam reflected off the surface.

11.4.2 Design of System

One of the most, important considerations in the design of a laser system is the choice of beam size. This usually requires a trade-off between performance, which increases with higher fluence levels, and damage considerations which favor a larger beam size. Reliable operation requires that the beam diameter and, therefore, the aperture of all optical elements are large enough so that the power and energy densities are well below the damage threshold levels for the particular mode of operation.

The average power density of the beam is only an indicator, but not a reliable measure with regard to damage considerations. With Gaussian beams the peak intensity at the center rather than the average value has to be considered.

Hot spots in a multimode beam can far exceed average values; likewise, temporal fluctuations as a result of mode beating in multilongitudinal lasers can cause high-intensity temporal spikes.

As was discussed in Sect. 4.6 temporal spikes or disturbances in the spatial profile can lead to catastrophic self-focusing in high-power Q-switched lasers. A smooth temporal and spatial profile can be achieved with a laser operating in TEM_{00} mode and single line. To avoid self-focusing, high-power systems typically employ an injection-seeded oscillator lasing in a single transverse and longitudinal mode. Modulation of the beam profile by diffraction effects is reduced by employing spatial filters between amplifier stages.

The damage levels listed in this chapter have usually been measured in a carefully controlled laboratory environment, with smooth Gaussian beams, meticulously clean optics, and materials of excellent optical quality. The numbers clearly present upper limits. For a typical industrial or military laser employing industrial grade components and coatings the operating fluence and fluxes should be far below the numbers given for damage threshold.

A very important design consideration is the avoidance of damage caused by reflections from optical surfaces in the laser system. For example, very often a telescope is employed between amplifier stages to increase the beam diameter. The design and location of the negative lens employed in such a telescope is very critical, because if reflections from the concave surface are focused into the preceding laser rod, damage

will most certainly occur. Therefore, a plano-concave rather than a concave-concave lens should be used and the curved surface should be faced away from the preceding optical components. In this case the reflected light from this surface is diverging rather than converging.

Reflections from the rear surface of an amplifier rod are very dangerous because the reflected radiation is amplified in passing through the amplifier stage, and optical elements at the input side of the amplifier, which are normally operated at much lower energy densities, can be damaged. This is especially the case if a telescope is employed between the oscillator and amplifier stage. If the beam travels backwards through the amplifier chain, the beam diameter decreases for increasing intensities, and damage thresholds are easily exceeded. One way to minimize this kind of damage is to tilt the various amplifier stages and separate them as far as possible from each other. A beam traveling backwards through an amplifier will then miss the aperture of the preceding stage. In order to suppress prelasing, which can cause the same type of damage, the amplifier rod should have wedged ends. Damage to optical surfaces can be minimized by employing highly damage-resistant coatings or by arranging the surfaces at Brewster's angle.

11.4.3 System Operation

Two common sources of damage are "hot spots" in the laser beam structure and contamination of optical surfaces. The peak fluence in a hot spot can exceed the average value by more than an order of magnitude. Damage sites caused by hot spots are usually much smaller than the beam area. Hot spots usually occur in multimode beams or they can be caused by diffraction effects. A small resonator misalignment brought about by vibration, or a change in the thermal conditions can lead to a change in mode structure with regions of high fluence.

Contamination of optical surfaces includes absorption sites such as dust or lint or debris from side lobes of the laser beam striking mirror mounts or other components, and absorption from fingerprints, water vapor, airborne oil from pumps, and outgassing from adhesives. Water vapor from a highly humid environment causing condensation leaves a residue after drying because it carries air pollutants, traces of tobacco smoke, sulfur compounds, etc.

Enclosing the beam path and filling the enclosure with a positive pressure of dry air usually eliminates the problem. From an operational point of view, the most important factors to consider, if damage is to be avoided, are proper alignment of components and absolute cleanliness of all surfaces. Misalignment of the oscillator components can cause a change of the transverse-mode structure, hot spots and beam uniformities can occur. Misaligned components outside the resonator cavity can cause undesirable secondary reflection leading to damage.

Surfaces which are contaminated by dust, dirt, or fingerprints will rapidly degrade and cause nonuniform beam intensities which, in turn, can cause damage in more expensive optical components. Surfaces should be inspected frequently and cleaned with an airblast or with alcohol. A dental mirror and a flashlight are very convenient for the inspection of optical surfaces in a laser system. Very often components are

mounted close together and surfaces are hard to see. For the cleaning of surfaces which are relatively inaccessible, a stream of pressurized clean air or gas should be used. A useful device for cleaning optical surfaces is an ionizing airgun sold by 3M Company. The unit, which contains an α -particle source of polonium isotope 210 in the valve and nozzle sections, can be connected to a gas cylinder. The gas stream containing α -radiation can remove very efficiently statically charged particles from a surface.

The degradation and subsequent damage of optical surfaces by atmospheric dust particles and by cleaning residue has been studied by Barber [11.72]. It was found that dust particles consisting of minerals are melted onto the surface, leaving a circular indentation after the particle is dislodged by subsequent pulses.

In another type of degradation, craters are caused by liquids being absorbed a few micrometers into the glass surface during the cleaning operation, and then producing miniature explosions when a strong laser pulse strikes the absorbed liquid. Experiments showed that laser rod ends were badly pitted after liquid cleaning without drying, and no damage occurred on rods which were vacuum-dried.

From the foregoing it follows that the working area around a laser should be kept as clean as possible, free from dust and contaminants, such as cigarette smoke, so as to have clean room conditions as closely as possible.

After a laser is aligned and ready to be operated, the fluence level should be gradually increased starting at a level not higher than half the final output. This provides a chance for the removal of surface defects, and for particles to be evaporated or blown off by the shock wave created by the laser beam. Laser conditioning of coatings and bulk materials is an important procedure in achieving higher damage thresholds, as was discussed earlier in this chapter.

For lasers which are hermetically sealed, a few precautions are necessary to avoid contamination of optical surfaces by the environment created within the enclosure. It has been shown that trace levels of gas-phase contaminants of hermetically sealed Q-switched Nd:lasers can reduce the laser reliability and lifetime, especially for operation at elevated temperatures, i.e., above 50°C [11.73]. In these life tests, outgassing from silicone materials used in o-rings, potting materials, and thermally conductive pads were evaluated for their damage potential, along with trace levels of solvents used in cleaning mechanical and optical components.

All silicone materials, except a space-grade encapsulant (Dow Corning 93–500) were found to have a high probability of inducing contamination damage in sealed Nd:YAG lasers. With regard to the cleaning fluids, the aromatic hydrocarbons (benzene derivatives, i.e., toluene) more readily caused damage than nonaromatics, i.e., acetone. Additionally, the presence of oxygen was shown to dramatically inhibit contamination damage due to hydrocarbons. Therefore, purging a hermetically sealed laser with dry air rather than dry nitrogen can significantly reduce optical damage due to outgassing. Implementation of the test results increased the laser operation at 70°C from less than 20 h to over 500 h without significant optical damage.

Appendix A

Laser Safety

Hazards associated with solid-state lasers can be separated into two broad categories: those hazards related to the laser beam itself and those hazards related to the electronic equipment.

Radiation Hazards

Although high-power solid-state lasers have the capability of inflicting burns on the skin, the possibility of eye injury is immensely important. The property of lasers that is of primary concern with regard to eye hazards is their high radiance, i.e. the combination of high power density and directionality. The latter property causes the eye lens to focus the parallel beam emitted from a laser to a tiny spot on the retina. It also makes the laser hazardous over long distances.

Figure A.1 shows a cross section of the human eye. The figure shows a collimated beam of visible light impinging onto the cornea, being focused by the eye lens, passing through the aqueous humor, and impinging onto the retina. At the retina the light is absorbed. Under normal conditions the photon energy is converted by the retina into chemical energy, stimulating optical sensations.

Figure A.1 illustrates the principal reason for possible eye injury from a laser. The parallel rays of a laser can be focused through the eye lens to a point image of about $10\text{--}20 \mu\text{m}$ in diameter. If the pupil is dilated sufficiently to admit the entire beam of a laser, even lasers having power outputs of only a few milliwatts will produce power densities of kilowatts per square centimeter on the retina. Obviously, power densities of this magnitude may cause severe damage to the retina. For worst-case conditions—the eye focused at infinity and the pupil fully dilated (about 0.7 cm diameter)—the ratio of power density at the eye lens to that at the retina will be about 10^5 .

By comparison, conventional sources of illumination are extended, they are considerably less bright, and they emit light in all directions. These light sources produce a sizable image on the retina with a corresponding lower power density. For example, looking directly into the sun, the image of it on the retina is approximately $160 \mu\text{m}$ in diameter which yields a radiation intensity of around $30\text{W}/\text{cm}^2$.

The maximum permissible exposure of laser radiation to the eye depends on the wavelength and is dependent on the spectral transmission of the eye. Figure A.2. illustrates the spectral transmission characteristics of the human eye [A.1]. Retinal damage is possible from exposure to laser energy in the wavelength region between 400 and

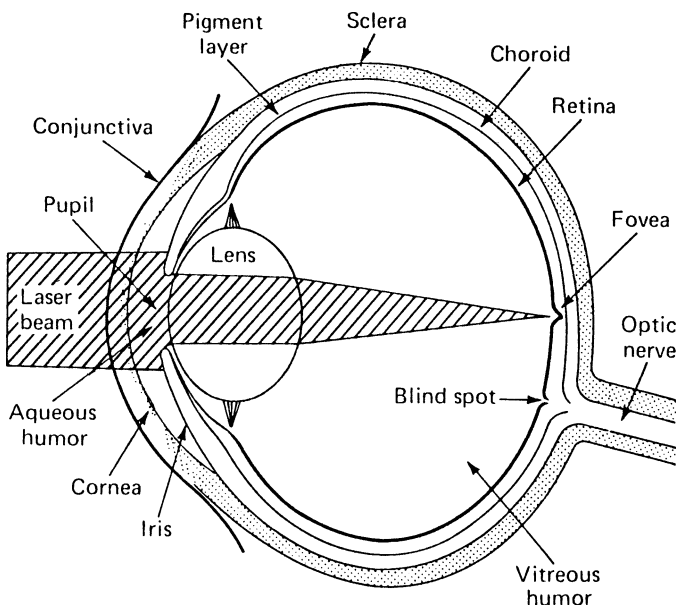


Fig. A.1. Cross section of the human eye

1400 nm (Fig. A.2c). In particular, radiation between 400 and 700 nm represents the greatest hazard, because the transmission of the anterior parts of the eye (cornea, aqueous humor, lens) is highest for this spectral region. At wavelengths longer than 700 nm, there is some absorption of the radiation before it reaches the retina. At IR

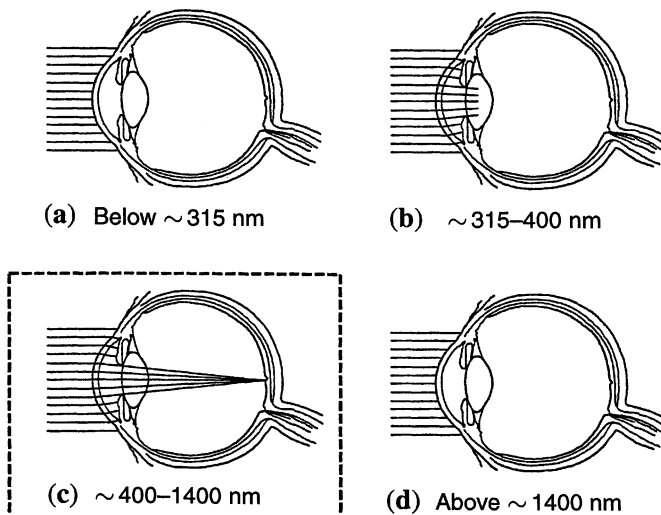


Fig. A.2. Spectral transmission characteristics of the human eye [A.1]

wavelengths greater than 1.4 μm , absorption of incident radiation occurs in the cornea and aqueous humor, and at wavelengths beyond 1.9 μm , absorption is restricted to the cornea alone (Fig. A.2d). Also ultraviolet radiation with a wavelength shorter than 315 nm is completely absorbed by the cornea (Fig. A.2a). Between 315 and 400 nm, radiation is absorbed at the lens of the eye (Fig. A.2b).

Electrical Hazards

Although the hazards of laser radiation are receiving deserved attention from government agencies, users, and manufacturers, the chief hazard of flashlamp pumped solid-state lasers is electrical rather than optical. Many solid-state lasers require high-voltage power supplies and energy-storage capacitors charged to lethal voltages. Furthermore, associated equipment such as Q-switches, optical gates, modulators, etc., are operated at high voltages. The power supply and associated electrical equipment of a laser can produce serious shock and burns and, in extreme cases, can lead to electrocution.

Safety Precautions Applicable to Solid-State Lasers

Enclosure of the beam and target in an opaque housing is the safest way of operating a laser. This level of safety precaution is mandatory for laser materials-processing systems operated in an industrial environment. In these systems interlocked doors, warning signs and lights, key-locked power switches, and emergency circuit breakers, and similar precautions are taken to protect operators and passers-by from electrical and radiation hazards of the laser equipment. Also, microscopes and viewing ports are filtered or blocked to prevent the issuance of laser radiation, and laser impact points are surrounded by shields. At points of access for routine maintenance and set-up, warning signs are displayed prominently, and interlocks prevent firing of the laser while doors or ports are open.

In the laboratory it is often not possible to completely enclose a high-power laser. In these situations the following safety precautions should be observed:

- Wear laser safety glasses at all times! Make sure that their attenuation factor is sufficient at the wavelengths present.
- Never look directly into the laser light source or at scattered laser light from any reflective surface. Never sight down the beam into the source.
- Set up the laser and all optical components used with it below eye level. Provide enclosures for the beam. Do not direct the beam outside the table on which the laser is positioned without using protective tubing.
- The output from Nd lasers and other IR lasers is invisible to the human eye. Use a IR viewing scope to check for specular reflected beams.
- Avoid operating the laser in a darkened environment. At low light levels the size of the iris is large and can hence accept a large amount of light. Work under as bright light conditions as possible (small iris).

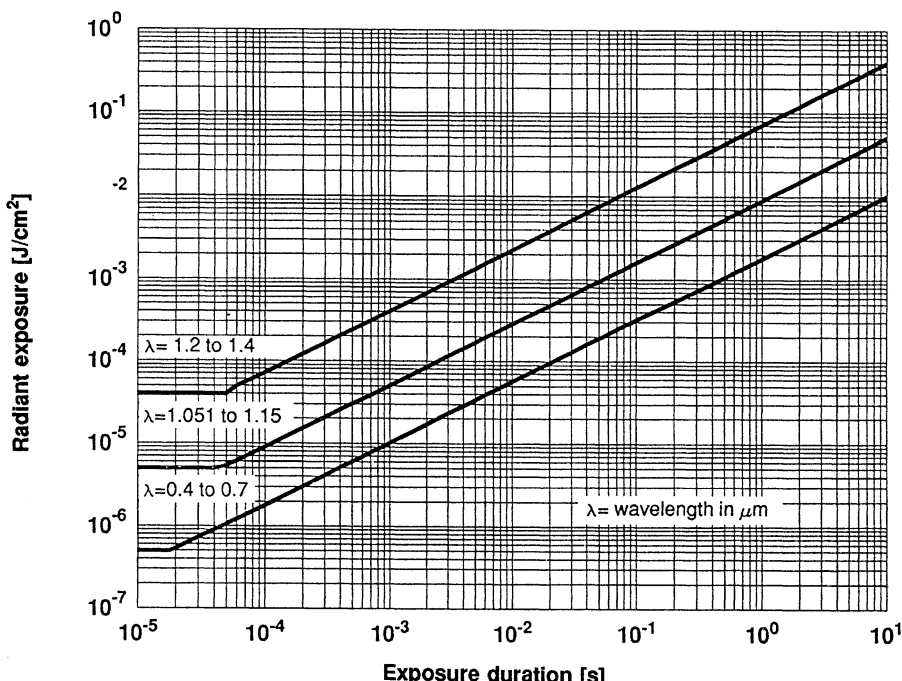


Fig. A.3. Exposure limits for direct viewing of a laser beam as a function of pulse width. Ranges are for visible and near-infrared spectral regions [A.2]

- Employ a countdown or other audible warning before the laser is fired.
- Post the appropriate hazard warning signs as specified in ANSI Z136.1 (1993) at the entrance to the laboratory.
- Control access to the laser area and have a flashing red light on the door when the laser is in operation. Operation of very large laser systems, such as used in inertial confinement fusion experiments, actually require the installation of safety interlocks at the entrance of the laser facility to prevent entry of unauthorized personnel into the facility while the laser power supply is charged and capable of firing the laser.
- Provide protection against accidentally contacting charged-up capacitors in energy-storage banks, high-voltage power supplies, etc. These components should be installed in cabinets having interlocked doors. Furthermore, capacitor banks should be equipped with gravity-operated dump solenoids.

The key to a successful safety program is the training and familiarization of the personnel involved with laser hazards and subsequent control measures. The appointment of a Laser Safety Officer is essential for companies or laboratories engaged in the manufacture or use of class III and class IV laser systems.

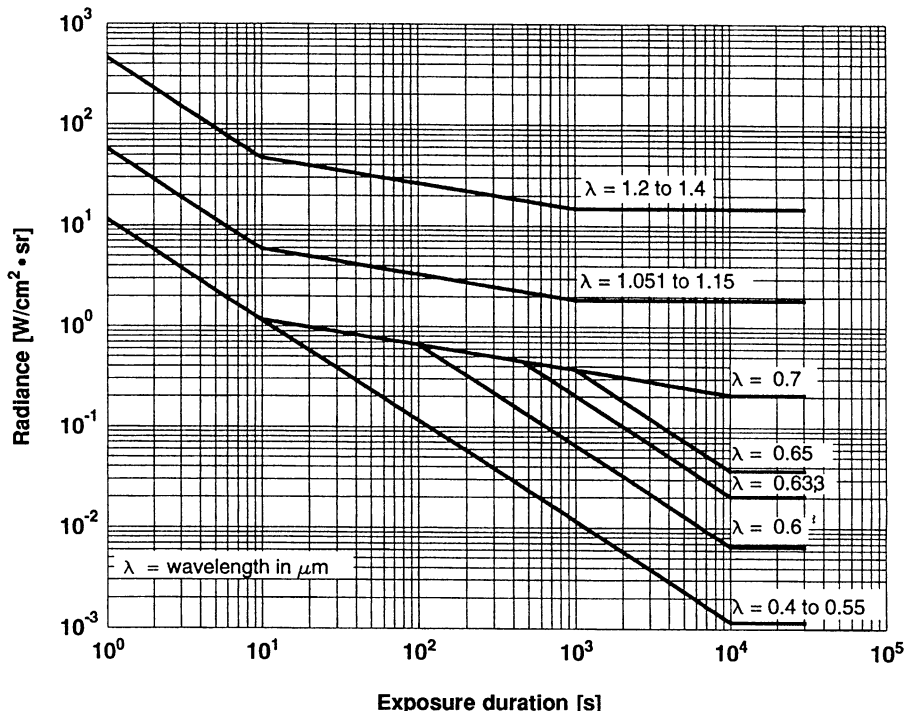


Fig. A.4. Exposure limits for direct viewing of a cw laser beam [A.2]

Laser Safety Standards

The potential of lasers for inflicting injury, particularly to the eyes, was recognised early, and as a consequence extensive studies have been undertaken into the biological mechanisms of laser damage, in an attempt to define safe working levels of optical radiation.

A document which is very useful as a guide for the safe use of lasers and systems is the standard published by the American National Standards Institute [A.2]. A comprehensive reference work covering every aspect of safety with lasers and other optical sources is the handbook written by D. Sliney et al. [A.3]. Additional information on laser safety can be found in [A.4].

In the United States, regulations for manufacturers are published by the Center for Devices and Radiological Health (formerly Bureau of Radiological Health), under the Food and Drug Administration [A.5]. User requirements in the United States are the responsibility of the individual states, but only a few states have such laws.

Under the federal safety standard, four classes of lasers have been created to allow manufacturers to categorize a product based on its potential hazard to a user. These classes are labeled I through IV, from the most safe to the most hazardous. Class I and II are used for lasers of cw outputs of less than 0.39 μW and 1 mW, respectively. Class III

and IV include lasers which represent a definite hazard to the eye from direct or scattered radiation. Solid-state lasers generally fall into class III or IV of that standard, which requires that warning signs, labels, and protective housings be installed to prevent human irradiation at levels in excess of a “safe” limit. Safety interlocks must be provided for each portion of the protective housing that can be removed by the user during normal operation or maintenance. In the event that the design of the safety interlock allows the user to defeat the system manually, the manufacturer must incorporate visible or audible warnings of this interlock override during laser operation. In addition, key-lock switches and warning lights are required along with other safety devices. Outside the United States, most countries have adopted the ANSI standard, or a similar standard generated by the International Electrotechnical Commission [A.6].

The author found the information presented in Figs. A.3 and A.4 quite useful in calculating the safe distance at which accidental direct viewing of the laser beam does not present a hazard. These situations occur quite frequently in field tests involving rangefinders, LIDAR's and similar equipment. Figure A.3 provides the occupational health and safety limits for pulsed laser radiation in the visible and near infrared spectrum. The curves show the safe fluence limits vs. pulselength for the visible and NIR. Compared to the visible regime, the threshold for eye damage is higher in the NIR because the focused spot on the retina is larger, furthermore higher transmission losses are encountered for the longer wavelength. The increase in fluence level with longer pulses reflects the fact that heat produced at the retina can be more effectively dissipated to the surrounding tissue as the exposure time increases. For exposure times shorter than about 50 μs , heat dissipation is insignificant and the damage threshold does not depend on pulselength. For exposure levels 10 times as high as indicated in Fig. A.3, there is a 50% probability of the occurrence of ophthalmologically visible retinal lesions [A.3].

Figure [A.4] gives the exposure limits for direct viewing of a cw laser beam for wavelengths ranging from 0.4 to 1.4 μm . The damage threshold for the longer wavelengths is higher for the same reasons as stated above. The reader is reminded that the data presented in these figures should only be considered as guidelines.

Appendix B

Conversion Factors and Constants

In this appendix we have listed some of the most frequently used conversion factors, constants, and definitions.

Physical Constants

h	$= 6.626 \times 10^{-34} \text{ J s}$	Planck constant
e	$= 1.602 \times 10^{-19} \text{ A s}$	Charge of an electron
k	$= 1.381 \times 10^{-23} \text{ J K}^{-1}$	Boltzmann constant
c	$= 2.998 \times 10^8 \text{ m s}^{-1}$	Speed of light in vacuum
ε_0	$= 8.854 \times 10^{-12} \text{ A s V}^{-1} \text{ m}^{-1}$	Permittivity of free space
μ_0	$= 1.257 \times 10^{-6} \text{ V s A}^{-1} \text{ m}^{-1}$	Permeability of free space
Z_0	$= \sqrt{\mu_0/\varepsilon_0} = 376.7 \Omega$	Impedance of free space
g	$= 9.81 \text{ m s}^{-2}$	Acceleration due to gravity

Force Conversions

$$\begin{aligned}1 \text{ dyne} &= 1 \text{ g cm s}^{-2} \\1 \text{ N} &= 1 \text{ kg m s}^{-2} = 10^5 \text{ dyne} \\1 \text{ kp} &= 9.81 \text{ kg m s}^{-2}\end{aligned}$$

Energy Conversions

$$\begin{aligned}1 \text{ J} &= 1 \text{ W s} \\1 \text{ cal} &= 4.19 \text{ J} \\1 \text{ eV} &= 1.60 \times 10^{-19} \text{ J} \\1 \text{ erg} &= 10^{-7} \text{ J}\end{aligned}$$

Pressure Conversions

$$\begin{aligned}1 \text{ Pa} &= 1 \text{ N m}^{-2} \\1 \text{ atm} &= 1.013 \text{ bar} = 1.033 \text{ kp cm}^{-2} \\1 \text{ bar} &= 10^6 \text{ dyne cm}^{-2} = 10^5 \text{ N m}^{-2} \\1 \text{ torr} &= 133.3 \text{ N m}^{-2} \\1 \text{ Pa} &= 9.87 \times 10^{-6} \text{ atm} = 145.1 \times 10^{-6} \text{ psi}\end{aligned}$$

Conversion of English Units into the MKS System

1 inch	= 2.540 cm
1 gal	= 3.785 l
1 lbs	= 0.453 kg
1 atm	= 14.7 psi
1 Btu	= 1055.8 W s
$T [{}^{\circ}\text{C}]$	= $\frac{5}{9}(T [{}^{\circ}\text{F}] - 32)$
$\Delta T [{}^{\circ}\text{C}]$	= $\frac{5}{9}\Delta T [{}^{\circ}\text{F}]$
$1 \text{ cal cm}^{-1} \text{ C}^{-1} \text{ s}^{-1}$	= 242 Btu/hr ft F
1 cal g^{-1}	= 1.8 Btu/lb

Conversion of Angles

$$1^{\circ} = 17.45 \text{ mrad}; 1' = 0.29 \text{ mrad}; 1'' = 4.85 \mu\text{rad}$$

$$1 \text{ rad} = 57^{\circ} 17' 45'', 1 \text{ mrad} = 3' 26''$$

Conversion of Wavenumber $n [\text{cm}^{-1}]$ to Energy

$$E = n \text{ hc}$$

$$\text{hc} = 1.986 \times 10^{-23} \text{ W s cm}$$

Conversion of Linewidth Given in Wavelength ($\Delta\lambda$) or Wavenumber (Δn) to Bandwidth ($\Delta\nu$)

$$\Delta\nu/\nu = \Delta\lambda/\lambda = \Delta n/n$$

$$\Delta\nu = c \Delta n$$

$$\Delta\lambda = \Delta n \lambda^2 = \Delta\nu \lambda^2/c$$

Amplifier Gain

$$g(\text{dB}) = 10 \log(E_2/E_1)$$

Optical Units

Wave number	$n [1/\text{cm}] = 10^4/(\lambda [\mu\text{m}])$
Frequency	$\nu [\text{Hz}] = 3 \times 10^{14}/(\lambda [\mu\text{m}])$
Photon energy	$E [\text{J}] = 1.987 \times 10^{-19}/(\lambda [\mu\text{m}])$
Photon energy	$E [\text{eV}] = 1.24/(\lambda [\mu\text{m}])$

Conversion of Transmission T to Optical Density D

$$T = 10^{-D}$$

Conversion of Units for the Nonlinear Index of Refraction n_2

$$n_2[\text{esu}] = 238.6 n_0 n_2 [\text{cm}^2/\text{W}]$$

$$n_2[\text{cm}^2/\text{W}] = 4.19 \times 10^{-3} (n_2/n_0) [\text{esu}]$$

Conversion of Beam Quality Factor M to Beam Diameter-Divergence Product $D\Theta$

$$M^2 = D\Theta/(4\lambda/\pi)$$

D = beam diameter (mm)

Θ = full beam angle (mr)

λ = wavelength (mm)

M = beam quality factor

Diffraction Limited Beam (TEM₀₀ Mode)

$$M^2 = 1$$

$$\Theta_0 D_0 = 4\lambda/\pi$$

$D_0 = 2w_0$, diameter of beam waist ($1/e^2$ points)

$\Theta_0 D_0 = 1.35$ mm mr at 1.064 μm

Appendix C

Definition of Symbols

A_{21}	Einstein coefficient (Chap. 1)
A^*	area
a	aperture radius
b	confocal parameter
B_{21}, B_{12}	Einstein coefficients (Chap. 1)
B	beam breakup integral (Chap. 4)
B_r	brightness (Chap. 4)
c, c_0	speed of light
c_p	specific heat (Chap. 7)
C	capacitance (Chap. 6)
C_T, C_r, C_ϕ, C_B	combination of material constants (Chap. 7)
d	thickness (Chaps. 5 and 9)
$d, d_{14}, d_{\text{eff}}$	coefficient of nonlinear polarization
D, D_0	beam diameter
e	electron charge
E	Young's modulus (Chap. 7)
E_1, E_2, E_3, E_0	energy levels (Chap. 1)
E_{st}	stored energy
ΔE	energy difference
E_{EL}	electrical input energy
E_{SC}	scale factor energy (Chap. 8)
$E_{\text{in}}, E_{\text{out}}, E_{\text{opt}}$	input, output, and optical energy (Chaps. 3 and 4)
E_{ex}	flashlamp explosion energy
E_i, E_0, E_s	input, output, and saturation fluence
E_1, E_2, E_3, E	electric field strength (Chap. 10)
E_j, E_z	electric field strength (Chap. 8)
$f, f', f'', f_x, f_y, f_{\text{ef}}$	focal length
F	finesse of interferometer (Chap. 5)
f	pulse repetition rate (Chap. 8)
$g_1, g_2, g(n_1), g(R_1), g(R_2)$	degeneracy of energy levels (Chaps. 1–3)
$g(v, v_0), g(v_0), g(v), g(v_s, v_0)$	atomic lineshape function (Chaps. 1 and 3)
g_0, g	gain coefficient

*Symbols whose definitions are not followed by chapter numbers are used throughout the book.

G, G_0	gain
g, g_1, g_2	parameters of resonator stability (Chaps. 5 and 9)
$h\nu$	photon energy
h	surface heat transfer coefficient (Chap. 7)
h	Planck constant (Chap. 6)
$I, I_L, I_R, I_{\text{circ}}, I_{\text{out}}, I_{\text{IN}}, I_P, I_0$	power density of laser beam
I_{av}, I_w	power density of pump radiation (Chap. 3)
I_{ASE}	fluorescence flux (Chap. 4)
$I_{\text{mn}}, I_{\text{pl}}$	intensity distribution of radial modes
I_{ac}	acoustic power density (Chap. 8)
I_S	saturation power density
i, i_P, i_S	current
$J_{\text{ST}}, J_{\text{th}}$	energy density (Chaps. 2 and 4)
K_0	flashlamp parameter (Chap. 6)
K	thermal conductivity
kT	thermal energy
k	diffusivity (Chap. 7)
K, K'	nonlinear coupling factor (Chap. 10)
K_1, K_2, K_3	combination of parameters (Chap. 10)
$k_p, k_s, k_i, k_w, k_{2W}, \Delta k$	wave number
$l, l(r), l_0$	length of active medium
Δl	pathlength difference (Chap. 7)
L, L_0, L_1, L_2	distances within resonator
l_C, l_a	coherence and aperture length
L	inductance (Chap. 6)
l, m, n, p	higher order modes (Chap. 5)
M	beam quality figure of merit (Chap. 5)
M	power ratio (Chap. 10)
m	magnification of unstable resonator (Chap. 5)
m	mass flow rate (Chap. 7)
M_{ac}	acoustic figure of merit (Chap. 8)
M_r, M_ϕ	thermal lensing sensitivity (Chap. 7)
$n_0, n_S, n_i, n_p, n_x, n_y$	refractive index
$\Delta n_0, \Delta n(r), \Delta n_\phi, \Delta n_r$	refractive index difference
$n_{1\omega}, n_{2\omega}, n_{3\omega}$	index at harmonic frequencies
n^0, n^e	ordinary and extraordinary refractive index
$n(r), n_r, n_\phi$	index in radial and tangential direction
dn/dT	temperature dependence of index
$dn/d\lambda$	wavelength dependence of index
$n(I)$	intensity dependence of index
n_2	nonlinear refractive index (Chaps. 4 and 9)
n_g, n_1	ground state and lower laser level population density
n_2, n	upper laser level population density
n_{tot}	total population density
$n_i, n_t, n_f, n_{\text{oo}}$	initial, threshold, final, and steady-state population density

Δn	perturbation of population density (Chap. 3)
$N_1, N_2, N_0, N_{\text{tot}}, N(v), \Delta N$	population of energy levels
N, N_{eq}	Fresnel number (Chap. 5)
N	number of axial modes (Chap. 9)
N	number of flashlamp firings (Chap. 6)
N_{ph}	number of photons (Chap. 5)
N	number density of molecules (Chap. 10)
$P_{\text{in}}, P_{\text{out}}, P_{\text{th}}, P, P_{\text{opt}}$	Input, output, threshold, intracavity, and optimum power
$P_{\text{av}}, P_{\text{p}}, P_{\text{cw}}$	average, peak, and cw power
$P_{\omega}, P_{2\omega}$	fundamental and harmonic power
P_{ac}	acoustic power (Chap. 8)
$P_{\text{a}}, P_{\text{h}}$	absorbed and dissipated power
$P_{\text{cr}}, P_{\text{f}}, P_{\lambda}$	critical, fluorescence, and spectral power
$P_{\text{avail}}, P_{\text{e}}$	available and incident power
p_{iklm}, p_{ij}	photoelastic tensor, coefficients
\mathbf{P}	induced polarization (Chap. 10)
p	gas pressure (Chap. 6)
$p, p_{\text{n}}, p_{\text{L}}$	resonator modes (Chaps. 1 and 5)
Q	resonator quality factor (Chap. 3)
Q	heat per volume (Chap. 7)
q	parameter (Chap. 7)
$R_1, R_2, R, R_{\text{opt}}, R_{\text{th}}, R'$	reflectivity
$r, r_0, r_{\text{L}}, r_{\text{R}}$	radius
$R(z), R_1, R_2, R, R_{\text{eff}}$	radius of curvature of resonator mirrors (Chap. 5)
R_d	electrical resistance (Chap. 6)
r_{ij}	electro-optic coefficients
R_S	thermal shock parameter (Chap. 7)
r_p	pump intensity distribution
$R(\lambda, T)$	flashlamp radiation
s	strain (Chap. 8)
s	Kerr lens sensitivity (Chap. 9)
S, S_1, S_2, S_0	combination of material constants (Chap. 7)
$T, T_{\text{opt}}, T_{\text{n}}, T_{\text{o}}, T_{\text{i}}, T_{\text{max}}$	transmission
t_p, t_{r}	pulse width, rise time
$T, T(r), T(r_0), T(\text{o}), T_F$	temperature
t	time
t_{r}	round trip time of photons
t_{LC}	time constant
u	nonlinear loss coefficient
V	volume (Chaps. 3 and 8)
$V, V_0, V_z, V_{1/2}$	voltage (Chaps. 6 and 8)
v, v_s, v_g	velocity
W	blackbody radiation (Chap. 1)
w	width
W_p	pump rate

W_{13}, W_{03}	pump parameter (Chap. 1)
W_{av}, W_s	energy density (Chap. 3)
$w_0, w, w_1, w_2, w_p, w_{\text{pl}}, w_m, w_n$	beam radius
x, y, z	distance
Z_0, Z	impedance
z	parameter
$\alpha_0, \alpha_0(v_s), \alpha_0(E)$	absorption coefficient
α	damping factor of current pulse (Chap. 6)
α	pulse shape factor (Chap. 9)
α	thermal expansion coefficient (Chap. 7)
α_p	angle (Chaps. 6 and 9)
β_0	propagation constant (Chap. 8)
β	combination of parameters (Chap. 4)
β_θ	angular sensitivity of doubling crystal (Chap. 10)
β	frequency chirp (Chap. 9)
β''	group dispersion in solids (Chap. 9)
χ	susceptibility (Chap. 10)
χ	heat deposition (Chap. 7)
$\delta, \delta_m, \delta_0, \delta_{\text{depol}}$	resonator losses
$\delta_{\text{AM}}, \delta_{\text{FM}}$	modulation depth
$\Delta_q, \Delta(2p+l), \Delta(m+n)$	frequency separation of axial modes (Chap. 5)
$\varepsilon(\lambda, T)$	emissivity (Chap. 6)
ε	resonator losses including output coupling (Chaps. 3 and 8)
$\varepsilon_0, \varepsilon$	permittivity (Chap. 10)
$\phi, \phi_0, \phi(r), \phi(x, t)$	photon density
ϕ	polar coordinate, azimuth angle
γ	factor determining three- or four-level laser
γ	nonlinear refractive coefficient (Chaps. 4 and 9)
γ	electrostrictive coefficient (Chap. 10)
η_Q, η_S, η_d	quantum, quantum defect, and differential quantum efficiency
$\eta_P, \eta_a, \eta_{\text{sys}}$	pump, absorption, and system efficiency
η_c, η_B, η_E	coupling, overlap, and extraction efficiency
$\eta_{\text{St}}, \eta_{\text{ASE}}, \eta_{\text{EQ}}$	Q-switch efficiencies
η_h	fractional heat load (Chap. 7)
$\eta_{\text{amp}}, \eta_{\text{par}}, \eta_{\text{Ram}}$	amplifier, parametric, and Raman efficiency
η, η'	combination of efficiency factors
$\varphi, \Delta\varphi, d\varphi, \varphi(t)$	phase angle
κ	combination of constants (Chap. 10)
κ	Boltzmann factor (Chap. 2)
$\lambda, \lambda_0, \lambda_1, \lambda_2, \lambda_p, \lambda_s, \lambda_i, \lambda_L$	wavelength
$\Delta\lambda$	wavelength difference
Λ	periodicity of grating (Chap. 10)
μ	factor determining Bragg deflection (Chap. 9)

μ_0	permeability of free space
ν	Poisson's ratio (Chap. 7)
$\nu_0, \nu_s, \nu_p, \nu_L, \nu_i, \nu_R, \nu_m, \nu_{rf}$	frequency
$\Delta\nu, \Delta\nu_L, \Delta\nu_c, d\nu$	bandwidth, linewidth
$\theta, \theta_c, \theta_D, \theta', \theta_m, \Delta\theta$	angle
ρ	walk-off angle (Chap. 10)
ρ	normalized beam radius (Chap. 5)
ρ_0	mass density (Chaps. 7, 8 and 10)
$\rho(\nu)$	radiation density per unit frequency (Chap. 1)
σ	stimulated emission cross section
σ_s	slope efficiency of laser output versus input
$\sigma_r, \sigma_\phi, \sigma_z, \sigma_{\max}$	thermal stress (Chap. 7)
$\sigma_{12}, \sigma_{gs}, \sigma_{es}$	absorption cross section
σ	Stefan–Boltzmann constant (Chap. 1)
τ_f, τ_{21}	spontaneous emission lifetime of upper laser level
τ_c	decay time of photon density in resonator
τ_B	phonon lifetime (Chap. 10)
τ_R	decay time of relaxation oscillations (Chap. 3)
τ_{ij}	spontaneous emission lifetime between states E_i and E_j
$\omega, \omega_0, \omega_p, \omega_1, \omega_2, \omega_3, \omega_4, \omega_s$	frequency
$\Delta\omega$	bandwidth
Ω	solid angle beam divergence (Chap. 4)
$\zeta, \zeta_{\max}, \zeta(t, \phi)$	cavity losses (Chap. 8)

References

Chapter 1

- 1.1 A. Yariv: *Quantum Electronics*, 4th edn. (Wiley, New York 1991)
1.2 A.E. Siegman: *Lasers* (University Science Books, Mill Valley, CA 1986)
1.3 H. Haken: *Laser Theory* (Springer, Berlin Heidelberg 1984)
1.4 I.I. Sobelman: *Atomic Spectra and Radiative Transitions*, 2nd edn. Springer Ser. Atoms and Plasmas, Vol. 12 (Springer, Berlin Heidelberg)
I.I. Sobelman, L.A. Vainshtein, E.A. Yukov: *Excitation of Atoms and Broadening of Spectral Lines*, 2nd edn. Springer Ser. Atoms and Plasmas, (Springer, Berlin Heidelberg, 1995)
1.5 H. Statz, G.A. de Mars: In *Quantum Electronics*, ed. by C.H. Townes (Columbia Univ. Press, New York, 1960) pp. 530–537

Chapter 2

- 2.1 S.E. Stokowski: In *Handbook of Laser Science and Technology*, ed. by M.J. Weber (CRC Press, Boca Raton, FL, 1982) pp. 215–264
2.2 P.F. Moulton: In *Handbook of Laser Science and Technology*, Vol. 1 ed. by M.J. Weber (CRC Press, Boca Raton, FL, 1986) pp. 21–295
2.3 L.G. DeShazer, S.C. Rund, B.A. Wechsler: In *Handbook of Laser Science and Technology*, Vol. 5, ed. by M.J. Weber (CRC Press, Boca Raton, FL, 1987) pp. 281–338
2.4 J.C. Walling: In *Tunable Lasers*, 2nd edn., ed. by L.F. Mollenauer, J.C. White, C.R. Pollock (Springer, Berlin, 1992) *Topics Appl. Phys.*, Vol. 59, Chap. 9
2.5 R.C. Powell: *Physics of Solid-State Laser Materials* (Springer, New York, 1998)
2.6 Special issue on solid-state lasers, IEEE J. Quantum Electron. **QE-24** (1988)
2.7 A.A. Kaminskii: *Crystalline Lasers* (CRC Press, Boca Raton, FL, 1996)
2.8 A.L. Schawlow, C.H. Townes: Phys. Rev. **112**, 1940 (1958)
2.9 T.H. Maiman: Nature **187**, 493 (1960)
2.10 J.E. Geusic, H.M. Marcos, L.G. Van Uitert: Appl. Phys. Lett. **4**, 182 (1964)
2.11 Kh.S. Bagdasarov, A.A. Kaminskii: JETP Lett. **9**, 303 (1969)
2.12 R.Wu, P.B. Phua, K.S. Lai: Appl. Opt. **39**, 431 (2000)
2.13 R.V. Alves, R.A. Buchanan, K.A. Wickersheim, E.A.C. Yates: J. Appl. Phys. **42**, 3043 (1971)
2.14 R.C. Ohlmann, K.B. Steinbruegge, R. Mazelsky: Appl. Opt. **7**, 905 (1968)
2.15 K.B. Steinbruegge, G.D. Baldwin: Appl. Phys. Lett. **25**, 220 (1974)
2.16 H.P. Weber, P.F. Liao, B.C. Tofield: IEEE J. Quantum Electron. **QE-10**, 563 (1974)
2.17 H.P. Weber, P.F. Liao, B.C. Tofield, P.M. Bridenbaugh: Appl. Phys. Lett. **26**, 692 (1975)
2.18 J.G. Gualtieri, T.R. Aucoin: Appl. Phys. Lett. **28**, 189 (1976)
2.19 H.G. Danielmeyer, G. Huber, W.W. Krühler, J.P. Jeser: Appl. Phys. **2**, 335 (1973)
2.20 V. Lupei, N. Pavel, Y. Sato, T. Taira: Opt. Lett. **28**, 2366 (2003)
2.21 J.R. O'Connor: Appl. Phys. Lett. **9**, 407 (1966)
2.22 T.Chin, R.C. Morris, O.Kafri, M. Long, D.F. Heller: In *High Power and Solid State Lasers*, SPIE Proc., Vol. 622, ed. By W.W. Simmons (SPIE, Bellingham, WA, 1986) p. 53

- 2.23 L.F. Johnson: J. Appl. Phys. **33**, 756 (1962); and **34**, 897 (1963)
- 2.24 P.P. Sorokin, M.J. Stevenson: Phys. Rev. Lett. **5**, 557 (1960); and in *Advances in Quantum Electronics*, ed. by J.R. Singer (Columbia Univ. Press, New York, 1961) p. 65
- 2.25 J. Lu, T. Murai, K. Takaichi, T. Uematsu, K. Misawa, M. Prabhu, J. Xu, K. Ueda, H. Yagi, T. Yanagitani, A.A. Kaminskii, A. Kudryashov: Appl. Phys. Lett. **78**, 3586 (2001)
- 2.26 I. Shoji, Y. Sato, S. Kurimura, V. Lupei, T. Taira, A. Ikesue, K. Yoshida: Opt. Lett. **27**, 234 (2002)
- 2.27 Y. Feng, J. Lu, K. Takaichi, K. Ueda, H. Yagi, T. Yanagitani, A.A. Kaminskii: Appl. Opt. **43**, 2944 (2004)
- 2.28 N.P. Barnes, D.J. Gettemy: IEEE J. Quantum Electron. **QE-17**, 1303 (1981)
- 2.29 G.J. Quarles, A. Rosenbaum, C.L. Marquardt, L. Esterowitz: In *Solid State Lasers*, SPIE Proc., Vol. 1223, ed. by G. Dubé (SPIE, Bellingham, WA, 1990) p. 221
- 2.30 T.Y. Fan, G. Huber, R.L. Byer, Mitzscherlich: IEEE J. Quantum Electron. **QE-24**, 924 (1988)
- 2.31 N.P. Barnes, D.J. Gettemy, L. Esterowitz, R.A. Allen: IEEE J. Quantum **QE-23**, 1434 (1987)
- 2.32 T. Kushida, H.M. Marcos, J.E. Geusic: Phys. Rev. **167**, 289 (1968)
- 2.33 W.F. Krupke, M.D. Shinn, J.E. Marion, J.A. Caird, S.E. Stokowski: J. Opt. Soc. Am. B **3**, 102 (1986)
- 2.34 J.K. Neeland, V. Evtuhov: Phys. Rev. **156**, 244 (1967)
- 2.35 M. Birnbaum, J.A. Gelbwachs: J. Appl. Phys. **43**, 2335 (1972)
- 2.36 M.J. Weber, T.E. Varitimos: J. Appl. Phys. **42**, 4996 (1971)
- 2.37 S. Singh, R.G. Smith, L.G. Van Uiter: Phys. Rev. B **10**, 2566 (1974)
- 2.38 H.G. Danielmeyer, M. Blätte, P. Balmer: Appl. Phys. **1**, 269 (1973)
- 2.39 R.G. Smith: IEEE J. Quantum Electron. **QE-4**, 505 (1968)
- 2.40 S. Singh, R.G. Smith, L.G. Van Uiter: Phys. Rev. B **10**, 2566–2572 (1974)
- 2.41 A.A. Kaminskii: Sov. Phys. JETP **37**, 201 (1968)
- 2.42 J. Marleng: IEEE J. Quantum Electron. **QE-14**, 56 (1978)
- 2.43 N. Barnes, B. Walsh, R. Davis: In *Advanced Solid-State Photonics, OSA Topical Mtg.*, San Antonio, TX, Feb 2003, Tech Digest, paper MB7-1
- 2.44 T.Y. Fan, R.L. Byer: IEEE J. Quantum Electron. **QE-23**, 605 (1987)
- 2.45 M. Birnbaum, C.F. Klein: J. Appl. Phys. **44**, 2928 (1973)
- 2.46 M.D. Thomas, G.A. Rines, E.P. Chicklis, W. Koechner: In *CLEO'86*, San Francisco, CA 1986, Paper WM4
- 2.47 Y. Inoue, S. Konno, T. Kojima, S. Fujikawa: IEEE J. Quantum Electron. **QE-35**, 1737 (1999)
- 2.48 Y. Inoue, S. Fujikawa: IEEE J. Quantum Electron. **36**, 751 (2000)
- 2.49 M.A. Kern, W.A. Clarkson, D.C. Hanna: In *Conf. on Lasers and Electro-Optics (CLEO)*, Washington, DC, 1997, Tech. Digest, paper CTuE4
- 2.50 M. Pierrou, F. Laurell, H. Karlsson, T. Kellner, C. Czeranowsky, G. Huber: Opt. Lett. **24**, 205 (1999)
- 2.51 V. Lupei, N. Pavel, T. Taira: Appl. Phys. Lett. **81**, 2677 (2002)
- 2.52 C. Czeranowsky, E. Heumann, G. Huber: Opt. Lett. **28**, 432 (2003)
- 2.53 S.M. Yarema, D. Milam: IEEE J. Quantum Electron. **QE-18**, 1941 (1982)
- 2.54 M.J. Weber: J. Non-Cryst. Solids **42**, 189 (1980)
- 2.55 S.E. Stokowski, R.A. Saroyan, M.J. Weber: Nd-doped laser glass spectroscopic and physical properties, Report M-095 (Rev.2) (Lawrence Livermore Nat'l Lab, 1981)
- 2.56 M.J. Weber, D. Milam, W.L. Smith: Opt. Eng. **17**, 463 (1978)
- 2.57 W.W. Simmons, J.T. Hunt, W.E. Warren: IEEE J. Quantum Electron. **QE-17**, 1727 (1981)
- 2.58 J.H. Campbell, T. Suratwala, C. Thorsness, P. Ehrmann, W. Steele, M. McLean: ICF Quarterly Report, Vol. 9, Jan–March 1999, p. 111, Lawrence Livermore Laboratory
- 2.59 C.F. Rapp: In *Handbook of Laser Science and Technology*, Vol. 5, Pt. 3, ed. by M.J. Weber (CRC Press, Boca Raton, FL, 1987) pp. 339–372
- 2.60 W.F. Krupke: IEEE J. Quantum Electron. **QE-10**, 450 (1974)
- 2.61 E.V. Zharikov, N.N. Il'ichev, V.V. Laptev, A.A. Mayutin, V.G. Ostroumov, P.P. Pashinin, I.A. Shcherbakov: Sov. J. Quantum Electron. **12**, 338–341 (1982)

- 2.62 D. Pruss, G. Huber, A. Beimowski: *Appl. Phys. B* **28**, 355–358 (1982)
2.63 D.S. Sumida, D.A. Rockwell: In *CLEO'86*, San Francisco, CA, 1986, Paper WQ3
2.64 P. Fuhrberg, W. Luhs, B. Struve, G. Litfin: In *Tunable Solid-State Lasers II*, ed. by A.B. Budgor, L. Esterowitz, L.G. DeShazer, (Springer, Berlin, 1987) Springer Ser. Opt. Sci., Vol. 52
2.65 Medium average power solid-state laser, Technical Information Seminar October, 1985, Lawrence Livermore National Laboratory
2.66 J.Y. Liu, C. Liu, M.G. Cohen: In *CLEO'86*, San Francisco, CA, 1986, Paper TuK33
2.67 E. Reed: *IEEE J. Quantum Electron.* **QE-21**, 1625 (1985)
2.68 S. Jackel, I. Moshe, R. Lallouz: In *OSA TOPS, Vol. 19, Adv. Solid State Lasers*, ed. by W.R. Bosenberg, M.M. Fejer (Optic Society of America, 1998)
2.69 L. Fornasiero, T. Kellner, S. Kueck, J.P. Meyn, P.E. Moebert, G. Huber: *Appl. Phys. B* **68**, 67 (1999)
2.70 Y. Louyer, P. Juncar, M. Himbert, M. Plimmer, F. Balembois, P. Georges: In *Adv. Solid-State Photonics*, San Antonio, TX, 2003, Tech Digest, Paper MB6-1
2.71 J.R. Lincoln, A.I. Ferguson: *Opt. Lett.* **19**, 1213, (1994)
2.72 G.R. Morrison, M. Ebrahimzadeh, C.F. Rae, M.H. Dunn: *Opt. Comm.* **118**, 55 (1995)
2.73 E.P. Chicklis: Private communication (1991)
2.74 M.G. Knights, G.A. Rines, J. McCarthy, T. Pollak, K.A. Smith, E.P. Chicklis: In *CLEO'84*, Anaheim, CA, 1984, Paper WM1
2.75 M.G. Knights, M.D. Thomas, E.P. Chicklis, G.A. Rines, W. Seka: *IEEE J. Quantum Electron.* **QE-24**, 712 (1988)
2.76 T.M. Pollak, W.F. Wing, R.J. Grasso, E.P. Chicklis, H.P. Jenssen: *IEEE J. Quantum Electron.* **QE-18**, 159–163 (1982)
2.77 R.A. Fields, M. Birnbaum, C.L. Fincher: *Appl. Phys. Lett.* **51**, 1885 (1987)
2.78 L. De Shazer: *Laser Focus World*, p. 88 (February 1994)
2.79 A. Brignon, G. Feugnet, J.P. Huignard, J.P. Pocholle: *IEEE J. Quantum Electron.* **QE-34**, 577 (1998)
2.80 A.I. Zagumennyi, V.A. Mikhailov, I.A. Shcherbakov: *Laser Phys.* **6**, 582 (1996)
2.81 Y.F. Chen: *IEEE J. Quantum Electron.* **35**, 234 (1999)
2.82 X. Peng, L. Xu, A. Asundi: *IEEE J. Quantum Electron.* **38**, 1291 (2002)
2.83 A. Di Lieto, P. Minguzzi, A. Pirastu, V. Magni: *IEEE J. Quantum Electron.* **39**, 903 (2003)
2.84 Y. Sato, T. Taira, N. Pavel, V. Lupei: *Appl. Phys. Lett.* **82**, 844 (2003)
2.85 V. Lupei, N. Pavel, T. Taira: *IEEE J. Quantum Electron.* **38**, 240 (2002)
2.86 Y.F. Chen, T.M. Huang, C.C. Liao, Y.P. Lan, S.C. Wang: *IEEE Photon. Technol. Lett.* **11**, 1241 (1999)
2.87 Y.F. Chen, Y.P. Lan, S.C. Wang: *Opt. Lett.* **25**, 1016 (2000)
2.88 Y.F. Chen, S.W. Tsai, Y.P. Lan, S.C. Wang, K.F. Huang: *Opt. Lett.* **26**, 199 (2001)
2.89 W.L. Nighan, N. Hodgson, E.Chen, D. Dudley: In *Conf. on Lasers and Electro-Optics (CLEO)*, Baltimore, MD, 1999, Paper CMA 1
2.90 L. Gonzalez, K. Kleine, L.R. Marshall: In *Conf. on Lasers and Electro-Optics (CLEO)*, Baltimore, MD, 1999, Paper CMA 2
2.91 E.V. Zharikov, V.I. Zhakov, L.A. Kulevskii, T.M. Murina, V.V. Osiko, A.M. Prokhorov, A.D. Savel'ev, V.V. Smirnov, B.P. Starikov, M.I. Timoshechkin: *Sov. J. Quantum Electron.* **4**, 1039 (1975)
2.92 V. Lupei, S. Georgescu: *Opt. Eng.* **35**, 1265 (1996)
2.93 B. Majaron, T. Rupnik, M. Lukac: *IEEE J. Quantum Electron.* **32**, 1636 (1996)
2.94 M. Bass, Wei-Qiang Shi, R. Kurtz, M. Kokta, H. Diegl: In *CLEO'86*, San Francisco, CA, 1986, Postdeadline paper ThT1-1
2.95 C. Ziolek, H. Ernst, G.F. Will, H. Lubatschowski, H. Welling, W. Ertmer: In *Adv. Solid-State Lasers*, Seattle, WA, 2001, Tech. Digest, p. 9
2.96 D.W. Chen, C.L. Fincher, T.S. Rose, F.L. Vernon, R.A. Fields: *Opt. Lett.* **24**, 385 (1999)
2.97 A. Hoegele, G. Hoerbe, H. Lubatschowski, H. Welling, W. Ertmer: *Opt. Comm.* **125**, 90 (1996)

- 2.98 K.L. Vodopyanov, R. Shori, O.M. Stafudd: *Appl. Phys. Lett.* **72**, 2211 (1998)
- 2.99 A. Dergachev, P. Moulton: In *Adv. Solid-State Photonics*, 2003, San Antonio, Texas, Tech. Digest, paper PD10-1
- 2.100 J.A. Hutchinson, M. Birnbaum, K. Spariosu, R. Stoltz, B. Zandi, D.S. Anker, T. Allik: In *Proc. IRIS Active Systems*, 1993, vol. II, p. 103
- 2.101 R. Wu, J.D. Myers, M.J. Myers: In *Proc. SPIE Conf. on Solid State Lasers VIII*, San Jose, CA, 1999, vol. 361, p. 221
- 2.102 W. Trussell, V. King, A. Hays, A. Hutchinson, S. Hamilin: In *Adv. Solid-State Photonics*, San Antonio, 2003, paper MA1-1, Tech. Digest
- 2.103 L.F. Johnson, R.E. Dietz, H.J. Guggenheim: *Phys. Rev. Lett.* **11**, 318–320 (1963)
- 2.104 L.F. Johnson, H.J. Guggenheim: *J. Appl. Phys.* **38**, 4837 (1967)
- 2.105 L.F. Johnson, H.J. Guggenheim: *IEEE J. Quantum Electron.* **QE-10** 442 (1974)
- 2.106 J.C. Walling, H.P. Jenssen, R.C. Morris, E.W. O'Dell, O.G. Peterson: *Opt. Lett.* **4**, 182–183 (1979)
- 2.107 J.C. Walling, O.G. Peterson, H.P. Jenssen, R.C. Morris, E.W. O'Dell: *IEEE J. Quantum Electron.* **QE-16**, 1302–1315 (1980)
- 2.108 P.F. Moulton, A. Mooradian: In *Laser Spectroscopy IV*, ed. by H. Walther, K.W. Rothe, (Springer, Berlin, 1979) Springer Ser. Opt. Sci., Vol. 21, pp. 584–589
- 2.109 P.F. Moulton: *Opt. News* **8**, 9 (1982)
- 2.110 B. Struve, G. Huber: *Appl. Phys. B* **30**, 117–120 (1983)
- 2.111 B. Struve, G. Huber: In *12th Int'l Quantum Electr. Conf.*, 1982, Paper ThR- 5
- 2.112 E.V. Zharikov, V.V. Laptev, E.I. Sidorova, Yu P. Timofeev, I.A. Shcherbakov: *Sov. J. Quantum Electron.* **12**, 1124 (1982)
- 2.113 H.P. Christensen, H.P. Jenssen: *IEEE J. Quantum Electron.* **QE-18**, 1197–1201 (1982)
- 2.114 U. Brauch, U. Dürr: *Opt. Commun.* **49**, 61 (1984)
- 2.115 H.R. Verdun, L.M. Thomas, D.M. Andrauskas, T. McCollum, A. Pinto: *Appl. Phys. Lett.* **53**, 2593 (1988)
- 2.116 V. Petricevic, S.K. Gayen, R.R. Alfano: *Appl. Phys. Lett.* **53**, 2590 (1988)
- 2.117 V. Petricevic, S.K. Gayen, R.R. Alfano: *Appl. Phys. Lett.* **52**, 1040 (1988)
- 2.118 J.G. Daly, C.A. Smith: *2 Micron Laser Applications*, SPIE Proc., Vol. 1627, ed. by J. Quarles (SPIE, Bellingham, WA, 1992) p.26, see also: Data sheet: Co-Lasers, Schwartz Electro-Optics, Inc.
- 2.119 B.T. McGuckin, R.T. Menzies: *IEEE J. Quantum Electron.* **QE-28**, 1025 (1992)
- 2.120 U. Brauch, A. Giesen, M. Karszewski, Chr. Stewen, A. Voss: *Opt. Lett.* **20**, 713 (1995)
- 2.121 J.C. Walling, O.G. Peterson, H.P. Jenssen, R.C. Morris, E.W. O'Dell: *IEEE J. Quantum Electron.* **QE-16**, 1302 (1980)
- 2.122 H. Samelson, J.C. Walling, D.F. Heller: *SPIE Proc.* **335**, 85 (1982)
- 2.123 R. Scheps, B.M. Gately, J.F. Myers, J.S. Krasinski, D.F. Heller: *Appl. Phys. Lett.* **56**, 2288 (1990)
- 2.124 S. Guch: In *CLEO'83*, Baltimore, MA, 1983, Paper ThR3
- 2.125 R.C. Sam, J.J. Yeh, K.R. Leslie, W.R. Rapoport: *IEEE J. Quantum Electron.* **QE-24**, 1151 (1988)
- 2.126 P.F. Moulton: *J. Opt. Soc. Am. B* **3**, 125 (1986); and *Laser Focus* **14**, 83 (1983)
- 2.127 E.G. Erickson: In *OSA Proc. on Tunable Solid State Lasers*, North Falmouth MA, 1989, Vol. 5, p. 26
- 2.128 A. Hoffstädt: *IEEE J. Quantum Electron.* **QE-33**, 1850 (1997)
- 2.129 R. Rao, G. Vaillancourt, H.S. Kwok, C.P. Khattak: In *OSA Proc. on Tunable Solid State Lasers*, North Falmouth, MA, 1989, Vol. 5, p. 39
- 2.130 T.R. Steele, D.C. Gerstenberger, A. Drobshoff, R.W. Wallace: *Opt. Lett.* **16**, 399 (1991)
- 2.131 G.T. Maker, A.I. Ferguson: *Opt. Lett.* **15**, 375 (1990)
- 2.132 J. Harrison, A. Finch, D.M. Rines, G.A. Rines, P.F. Moulton: *Opt. Lett.* **16**, 581 (1991)
- 2.133 S.A. Payne, L.L. Chase, L.K. Smith, W.L. Kway, H.W. Newkirk: *J. Appl. Phys.* **66**, 1051 (1989)
- 2.134 S.A. Payne, L.L. Chase, H.W. Newkirk, L.K. Smith, W.F. Krupke: *IEEE J. Quantum Electron.* **QE-24**, 2243 (1988)
- 2.135 P.A. Beaud, M. Richardson, E.J. Miesak: *IEEE J. Quantum Electron.* **QE-31**, 317 (1995)

- 2.136 M. Richardson, V. Castillo, P. Beaud, M. Bass, B. Chai, G. Quarles, W. Ignatuk: *Photonics Spectra*, p. 86 (October 1993)
- 2.137 R. Scheps, J.F. Myers, H. Serreze, A. Rosenberg, R.C. Morris, M. Long: *Opt. Lett.* **16**, 820 (1991)
- 2.138 Q. Zhang, B.H.T. Chai, G.J. Dixon: In *CLEO'91*, Baltimore, MD, 1991, Paper CThR6
- 2.139 S.A. Payne, W.F. Krupke, L.K. Smith, W.L. Kway, L.D. DeLoach, J.B. Tassano: *IEEE J. Quantum Electron.* **QE-28**, 1188 (1992)
- 2.140 R. Mellish, S.C.W. Hyde, N.P. Barry, R. Jones, P.M.W. French, J.R. Taylor, C.J. van der Poel, A. Valster: *Appl. Phys. B, Lasers Opt.* **65**, 221 (1997)
- 2.141 D. Kopf, K.J. Weingarten, G. Zhang, M. Moser, M.A. Emanuel, R.J. Beach, J.A. Skidmore, U. Keller: *Appl. Phys. B, Lasers Opt.* **65**, 235 (1997)
- 2.142 D. Kopf, A. Prasad, G. Zhang, M. Moser, U. Keller: *Opt. Lett.* **22**, 621 (1997)
- 2.143 P.J.M. Suni, S.W. Henderson: *Opt. Lett.* **16**, 817 (1991)
- 2.144 E.C. Honea, R.J. Beach, S.B. Sutton, J.A. Speth, S.C. Mitchell, J.A. Skidmore, M.A. Emanuel, S.A. Payne: *IEEE J. Quantum Electron.* **QE-33**, 1592 (1997); and in *TOPS, Advanced Solid State Lasers*, Vol. 10 (Opt. Soc. Am., Washington, DC, 1997) p. 307
- 2.145 G. Rustad, H. Hovland, K. Stenersen: In *OSA Advanced Solid State Lasers*, San Francisco, CA, 1996, Techn. digest, p. 48
- 2.146 R.C. Stoneman, L. Esterowitz: *Opt. Lett.* **15**, 486 (1990)
- 2.147 T. Yokozawa, H. Hara: *Appl. Opt.* **35**, 1424 (1996)
- 2.148 I.F. Elder, M.J.P. Payne: In *OSA Advanced Solid State Lasers*, San Francisco, CA, 1996 Techn. digest, p. 30; also *Appl. Opt.* **36**, 8606 (1997)
- 2.149 P.A. Budni, M.L. Lemons, J.R. Mosto, E.P. Chicklis: *IEEE J. Select. Topics Quantum Electron.* **6**, 629 (2000)
- 2.150 A. Dergachev, K. Wall, P.F. Moulton: In *OSA Trends in Optics and Photonics*, Vol. **68**, *Adv. Solid State Lasers*, ed. by M.E Fermann, L.R. Marshall (Optic Society of America, 2002) p. 343
- 2.151 J. Yu, U.N. Singh, N.P. Barnes, M. Petros: *Opt. Lett.* **23**, 780 (1998)
- 2.152 A. Finch, J.H. Flint: In *OSA Advanced Solid State Lasers*, San Francisco, CA, 1996, Techn. digest, p. 253
- 2.153 M.E. Storm: *IEEE J. Quantum Electron.* **QE-29**, 440 (1993)
- 2.154 T.S. Kubo, T.J. Kana: *IEEE J. Quantum Electron.* **QE-28**, 1033 (1992)
- 2.155 K.S. Lai, P.B. Phua, R.F. Wu, Y.L. Lim, E. Lau, S.W. Toh, B.T. Toh, A. Chng: *Opt. Lett.* **25**, 1591 (2000)
- 2.156 W.F. Krupke: *IEEE J. Select. Topics Quantum Electron.* **QE-6**, 1287 (2000)
- 2.157 D.S. Sumida, T.Y. Fan: In *Proc. Advanced Solid State Lasers*, Vol. 20 (Opt. Soc. Am., Washington, DC, 1994) p. 100; and *Opt. Lett.* **20**, 2384 (1995)
- 2.158 M. Karszewski, U. Brauch, K. Contag, A. Giesen, I. Johannsen, C. Stewen, A. Voss: In *OSA Advanced Solid State Lasers*, Coeur d'Alene, ID, 1998, Techn. Digest, p. 82
- 2.159 D.S. Sumida, H. Bruesselbach, R.W. Byren, M. Mangir, R. Reeder: *Proc. SPIE*, **3265**, 100 (1998)
- 2.160 C. Bibeau, R. Beach, C. Ebbers, M. Emanuel, J. Skidmore: In *TOPS Advanced Solid State Lasers*, Vol. 10 (Opt. Soc. Am., Washington, DC, 1997) p. 276
- 2.161 E.C. Honea, R.J. Beach, S.C. Mitchel, J. Skidmore, M.A. Emanuel, S.B. Sutton, S.A. Payne, P.V. Avizonis, R.S. Monroe, D.G. Harris: *Opt. Lett.* **25**, 805 (2000)
- 2.162 A. Giesen, M. Karszewski, C. Stewen, A. Voss: In *Proc. on Advanced Solid State Lasers*, Vol. 24 (Opt. Soc. Am., Washington, DC, 1995) p. 330
- 2.163 A. Giesen, M. Brauch, I. Johannsen, M. Karszewski, U. Schiegg, C. Stewen, A. Voss: In *TOPS Advanced Solid State Lasers*, Vol. 10 (Opt. Soc. Am., Washington, DC, 1997) p. 280
- 2.164 C. Stewen, K. Contag, M. Larionov, A. Giesen, H. Huegel: *IEEE J. Select. Topics Quantum Electron.* **6**, 650 (2000)

Chapter 3

- 3.1 W.W. Rigrod: *J. Appl. Phys.* **36**, 2487 (1965)
- 3.2 A.Y. Cabezas, R.P. Treat: *J. Appl. Phys.* **37**, 3556 (1966)

- 3.3 Yu. Kalinin, A.A. Mak: Opt. Tech. **37**, 129 (1970)
 3.4 D. Findlay, R.A. Clay: Phys. Lett. **20**, 277 (1966)
 3.5 T.Y. Fan, R.L. Byer: IEEE J. Quantum Electron. **QE-24**, 895 (1988)
 3.6 R. Dunsmuir: J. Electron. Control **10**, 453 (1961)
 3.7 H. Statz, G.A. Mars, D.T. Wilson, C.L. Tang: J. Appl. Phys. **36**, 1510 (1965)
 3.8 T.J. Kane: IEEE Photon. Technol. Lett. **2**, 244 (1990)
 3.9 K. Tsubono, S. Moriwaki: Jpn. J. Appl. Phys. **31**, 1241 (1992)
 3.10 C.C. Harb, M.B. Gray, H.A. Bachor, R. Schilling, P. Rottengatter, I. Freitag, H. Welling: IEEE J. Quantum Electron. **QE-30**, 2907 (1994)
 3.11 L.W. Casperson: J. Appl. Phys. **47**, 4555 (1976)
 3.12 A. Owyong G.R. Hadley, R. Eshierick, R.L. Schmitt, L.A. Rahn: Opt. Lett. **10**, 484 (1985)
 3.13 J.M. Eggleston, L. DeShazer, K. Kangas: IEEE J. Quantum Electron. **QE-24**, 1009 (1988)
 3.14 R. Burnham, Private Communication 1989, also A.D. Hays, R. Burnham, G.L. Harnagel: In *CLEO' 89* (Baltimore, MA) Postdeadline paper PO 9-1
 3.15 W. Koechner, H.R. Verdun: Diode laser pumped solid-state lasers, Final Rept. Contract N00014-85-C-0174, Naval Oceans Systems Command, San Diego, CA (1987)
 3.16 N. Barnes, M. Storm, P. Cross, M. Skolaut: IEEE J. Quantum Electron. **QE- 26**, 558 (1990)
 3.17 D.L. Sipes: Appl. Phys. Lett. **47**, 74–76 (1985)
 3.18 W.L. Nighan, N. Hodgson, E. Cheng, D. Dudley: In *CLEO' 99, Conf. on Lasers and Electro-Optics*, Baltimore, MD, May 1999, Tech. Digest, p. 1
 3.19 R.A. Fields, M. Birnbaum, C.L. Fincher: In *CLEO '87* (Baltimore, MD)
 3.20 N. Mermilliod, R. Romero, I. Chartier, C. Garapon, R. Moncorgé: IEEE J. Quantum Electron. **QE-28**, 1179 (1992)
 3.21 K.X. Liu, C.J. Flood, D.R. Walker, H.M. van Driel: Opt. Lett. **17**, 1361 (1992)
 3.22 J.R. Lincoln, A.I. Ferguson: Opt. Lett. **19**, 2119 (1994)
 3.23 R. Mellisk, P.M.W. French, J.R. Taylor, P.J. Delfyett, L.T. Florez: In *Proc. Adv. Solid State Lasers*, Vol. 20 (Opt. Soc. Am., Washington, DC, 1994) p. 239
 3.24 D. Kopf, K.J. Weingarten, L.R. Brovelli, M. Kamp, U. Keller: Opt. Lett. **19**, 2143 (1994)
 3.25 E.C. Honea, C.A. Ebbers, R.J. Beach, J.A. Speth, J.A. Skidmore, M.A. Emanuel, S.A. Payne: Opt. Lett. **23**, 1203 (1998)
 3.26 C. Bibeau, R. Beach, C. Ebbers, M. Emanuel, J. Skidmore: In *TOPS, Vol. 10: Advanced Solid State Lasers* (Opt. Soc. Am., Washington, DC, 1997) p. 276
 3.27 E.C. Honea, R.J. Beach, S.B. Sutton, J.A. Speth, S.C. Mitchell, J.A. Skidmore, M.A. Emanuel, S.A. Payne: IEEE J. Quantum Electron. **QE-33**, 1592 (1997)
 3.28 A.R. Clobes, M.J. Brienza: Appl. Phys. Lett. **21**, 265 (1972)
 3.29 A.M. Bonch-Bruevich, V. Yu. Petrun'kin, N.A. Esepkinsa, S.V. Krushalov, L.N. Pakhomov, V.A. Chernov, S.L. Galkin: Sov. Phys.-Tech. Phys. **12**, 1495 (1968)
 3.30 T.J. Kane, R.L. Byer: Opt. Lett. **10**, 65 (1985)
 3.31 W.R. Trutna, D.K. Donald, M. Nazarathy: Opt. Lett. **12**, 248 (1987)
 3.32 A.C. Nilsson, E.K. Gustafson, R.L. Byer: IEEE J. Quantum Electron. **QE-25**, 767 (1989)
 3.33 T.J. Kane, E.A.P. Cheng: Opt. Lett. **13**, 970 (1988)
 3.34 D.G. Scerbak: In *Solid-State Lasers*, SPIE Proc., Vol. 1223, ed. by G. Dubé (1990) p. 196
 3.35 J. Harrison, G.A. Rines, P.F. Moulton, J.R. Leger: Opt. Lett. **13**, 111 (1988)
 3.36 R. Scheps, J. Myers: In *Solid-State Lasers*, SPIE Proc., Vol. 1223, ed. by G. Dubé (1990) p. 186
 3.37 M.D. Selker, T.J. Johnston, G. Frangineas, J.L. Nightingale, D.K. Negus: In *Conf. on Lasers and Electro-Optics (CLEO)*, Anaheim, CA, June 1996, Tech. Digest, p. 602

Chapter 4

- 4.1 L.M. Frantz, J.S. Nodvik: J. Appl. Phys. **34**, 2346 (1963)
 4.2 P.G. Krukov, V.S. Letokhov: In *Laser Handbook I*, ed. by E.T. Arrechi, E.O. Schulz-DuBois (North-Holland, Amsterdam, 1972) pp. 561–595
 4.3 P.V. Avizonis, R.L. Grotbeck: J. Appl. Phys. **37**, 687 (1966)

- 4.4 T.G. Crow, T.J. Snyder: Techniques for achieving high-power Q-switched operation in YAG:Nd. Final Tech. Report AFAL-TR-70-69, Air Force, WPAFB (1970); and *Laser J.* **18**, (1970)
- 4.5 W. Koechner, R. Burnham, J. Kasinski, P. Bournes, D. DiBiase, K. Le, L. Marshall, A. Hays: In *Proc. Int'l. Conf. Optical Space Com.*, Munich, 10–14 June 1991, ed. by J. Franz (SPIE, Bellingham, WA, 1991), SPIE Proc., Vol. 1522, p. 169
- 4.6 C. Bibeau, D.R. Speck, R.B. Ehrlich, C.W. Laumann, D.T. Kyrazis, M.A. Henesian, J.K. Lawson, M.D. Perry, P.J. Wegner, T.L. Weiland: *Appl. Opt.* **31**, 5799 (1992)
- 4.7 B.M. Van Woertghem, J.R. Murray, J.H. Campbell, D.R. Speck, C.E. Barker, I.C. Smith, D.F. Browning, W.C. Behrendt: *Appl. Opt.* **36**, 4932 (1997)
- 4.8 Lawrence Livermore Lab. Laser Program Annual Reports UCRL-50021 and UCRL-LR-105821
- 4.9 W.E. Martin, D. Milam: *IEEE J. Quantum Electron.* **QE-18**, 1155 (1982)
- 4.10 C. Yamanaka, Y. Kato, Y. Izawa, K. Yoshida, T. Yamanaka, T. Sasaki, M. Nakatsuka, T. Mochizuki, J. Kuroda, S. Nakai: *IEEE J. Quantum Electron.* **QE-17**, 1639 (1981)
- 4.11 Chen, Y. Bai, J. Yu, U. Singh, M. Petros: In *Advanced Solid State Photonics*, San Antonio, TX, Feb. 2003, OAS Topical Mtg., Tech. Digest, p. 276
- 4.12 H. Kiriyama, K. Yamakawa, T. Nagai, N. Kageyama, H. Miyajima, H. Kan, H. Yoshida, M. Nakatsuka: *Opt. Lett.* **28**, 1671, 2003
- 4.13 S. Saraf, S. Sinha, A. Sridharan, R. Byer: In *Advanced Solid State Photonics*, San Antonio, TX, Feb. 2003, OAS Topical Mtg., Tech. Digest, p. 387
- 4.14 K.J. Snell, D. Lee, K.F. Wall, P.F. Moulton: In *OSA Trends in Optics and Photonics*, Vol. 34, *Advanced Solid State Lasers* (OSA, Washington, DC, 2000) p. 55
- 4.15 K.J. Snell, D. Lee: In *OSA Trends in Optics and Photonics*, Vol. 26, *Advanced Solid State Lasers* (OSA, Washington, DC, 1999) p. 295
- 4.16 B. Pati, Y. Isyanova, P. Moulton: In *Advanced Solid State Photonics*, San Antonio, TX, Feb. 2003, OAS Topical Mtg., Tech. Digest, p. 179
- 4.17 W.B. Jones, L.M. Goldman, J.P. Chernoch, W.S. Martin: *IEEE J. Quantum Electron.* **QE-8**, 534 (1972)
- 4.18 A. Yu. Dergachev, J.H. Flint, P.F. Moulton: In *CLEO Technical Digest* (OSA, Washington, DC, 2000) p. 564
- 4.19 T. Axenson, N. Barnes, D. Reichle: In *Advanced Solid State Photonics*, San Antonio, TX, Feb. 2003, OAS Topical Mtg., Postdeadline paper, Tech. Digest, p. 55
- 4.20 D. Mueller, S. Erhard, O. Ronsin, A. Giesen: In *Advanced Solid State Photonics*, San Antonio, TX, Feb. 2003, OAS Topical Mtg., Tech. Digest, p. 255
- 4.21 S. Forget, F. Balembois, P. Georges: In *OSA Proceedings*, Washington, DC, 2002, Vol. 68, p. 321
- 4.22 M. Gifford, K.J. Weingarten: *Opt. Lett.* **17**, 1788 (1992)
- 4.23 W.H. Lowdermilk, J.E. Murray: *J. Appl. Phys.* **51**, 2436 (1980)
- 4.24 J.E. Murray, W.H. Lowdermilk: *J. Appl. Phys.* **51**, 3548 (1980)
- 4.25 L. Turi, T. Juhasz: *Opt. Lett.* **20**, 154 (1995)
- 4.26 D.R. Walker, C.J. Flood, H.M. Van Driel, U.J. Greiner, H.H. Klingenberg: In *CLEO/Europe'94*, Amsterdam, 1994, Paper CThM1
- 4.27 M.D. Selker, R.S. Afzal, J.L. Dallas, A.W. Yu: *Opt. Lett.* **19**, 551 (1994)
- 4.28 M. Rhoades, K. Le, D. DiBiase, P. Bournes, W. Koechner, R. Burnham: In *Laser'95, Munich*, 1995, paper F
- 4.29 A.Y. Cabezas, R.P. Treat: *J. Appl. Phys.* **37**, 3556 (1966)
- 4.30 C. Kennedy: In *Advanced Solid State Photonics*, San Antonio, TX, Feb. 2003, OAS Topical Mtg., Tech. Digest, p. 217
- 4.31 D. Hoffmann, G. Bonati, P.F. Kayser, P. Loosen, R. Poprawe, R. Dinger, C.R. Haas, H. Martinen: In *Adv. Solid State Lasers*, TOPS Vol. 50 (Optical Soc. America 2001) p. 33
- 4.32 J. Bunkenberg, J. Boles, D.C. Brown, J. Eastman, J. Hoose, R. Hopkins, L. Iwan, S.D. Jacobs, J.H. Kelly, S. Kumpan, S. Letzring, D. Lonobile, L.D. Lund, G. Mourou, S. Refermat, S. Seka, J.M. Soures, K. Walsh: *IEEE J. Quantum Electron.* **QE-17**, 1620 (1981)

- 4.33 G.J. Linford, E.R. Peressini, W.R. Sooy, M.L. Spaeth: *Appl. Opt.* **13**, 379 (1974)
- 4.34 N.P. Barnes, V.J. Corcoran, I.A. Crabbe, L.L. Harper, R.W. Williams, J.W. Wragg: *IEEE J. QE-10*, 195 (1974)
- 4.35 E. Bridges, R.W. Boyd, G.P. Agrawal: *Opt. Lett.* **18**, 2026 (1993)
- 4.36 G. Fibich, A.L. Gaeta: *Opt. Lett.* **25**, 335 (2000)
- 4.37 S.A. Akhmanov, R.V. Khokhlov, A.P. Sukhorukov: In *Laser Handbook*, ed. by E.T. Arrechi, E.O. Schulz-DuBois (North-Holland, Amsterdam, 1972) p. 1151
- 4.38 R. DeSalvo, A.A. Said, D.J. Hagan, E.W. Van Stryland, M. Sheik-Bahae, *IEEE J. Quantum Electron.* **QE-32**, 1324 (1996)
- 4.39 Data sheets Schott and Hoya laser glasses
- 4.40 G. Arisholm: In *OSA TOPS, Vol. 10, Advanced Solid State Lasers* (Optical Soc. Am., 1997) p. 109
- 4.41 R.W. Boyd: *Nonlinear Optics* (Academic, San Diego, CA, 1992)
- 4.42 J. Herrmann: *Opt. Commun.* **98**, 111 (1993)
- 4.43 V.I. Bespalov, V.I. Talanov: *JETP Lett.* **3**, 307 (1966)
- 4.44 J.A. Glaze: High energy glass lasers: *Proc. Soc. Photo-Opt. Instr. Eng.* **69**, 45 (1975)
- 4.45 A.J. Campillo, S.L. Shapiro, B.R. Suydam: *Appl. Phys. Lett.* **24**, 178 (1974); and *Appl. Phys. Lett.* **23**, 628 (1973)
- 4.46 E.S. Bliss, D.R. Speck, J.F. Holzrichter, J.H. Erkkila, A.J. Glass: *Appl. Phys. Lett.* **25**, 448 (1974)
- 4.47 W.W. Simmons, J.T. Hunt, W.E. Warren: *IEEE J. Quantum Electron.* **QE-17**, 1727 (1981)
- 4.48 J.T. Hunt, D.R. Speck: *Opt. Eng.* **28**, 461 (1989)
- 4.49 J.T. Hunt, K.R. Manes, P.A. Renard: *Appl. Opt.* **32**, 5973 (1993)
- 4.50 D.R. Speck, E.S. Bliss, J.A. Glaze, J.W. Herris, F.W. Holloway, J.T. Hunt, B.C. Johnson, D.J. Kuizenga, R.G. Ozarski, H.G. Patton, P.R. Rupert, G.J. Suski, C.D. Swift, C.E. Thompson: *IEEE J. Quantum Electron.* **QE-17**, 1599 (1981)
- 4.51 U. Roth, F. Loewenthal, R. Tommasini, J.E. Balmer, H.P. Weber: *IEEE J. Quantum Electron.* **36**, 687 (2000)
- 4.52 O.A. Konoplev, D.D. Meyerhofer: *IEEE J. Select. Topics Quantum Electron.* **4**, 459 (1998)
- 4.53 K. Beckwitt, F.W. Wise, L. Qian, L.A. Walker, E. Canto-Said: *Opt. Lett.* **26**, 1696 (2001)

Chapter 5

- 5.1 A.G. Fox, T. Li: *Bell Syst. Tech. J.* **40**, 453 (1961)
- 5.2 G.D. Boyd, J.P. Gordon: *Bell Syst. Tech. J.* **40**, 489 (1961)
- 5.3 G.D. Boyd, H. Kogelnik: *Bell Syst. Tech. J.* **41**, 1347 (1962)
- 5.4 K. Kogelnik, T. Li: *Appl. Opt.* **5**, 1550 (1966); and *Proc. IEEE* **54**, 1312 (1966)
- 5.5 H. Kogelnik: In *Lasers I*, ed. by A.K. Levine (Dekker, New York, 1966) pp. 295–347
- 5.6 J.S. Kruger: *Electro-Opt. Syst. Design* 12 (September 1972)
- 5.7 R.J. Freiberg, A.S. Halsted: *Appl. Opt.* **8**, 335 (1969)
- 5.8 T. Li: *Bell Syst. Tech. J.* **44**, 917 (1965)
- 5.9 D.E. McCumber: *Bell Syst. Tech. J.* **44**, 333 (1965)
- 5.10 R.L. Phillips, L.C. Andrews: *Appl. Opt.* **22**, 643 (1983)
- 5.11 W.H. Carter: *Appl. Opt.* **19**, 1027 (1980)
- 5.12 A.E. Siegman, S.W. Townsend: *IEEE J. Quantum Electron.* **29**, 1212 (1993)
- 5.13 H. Kogelnik: *Bell Syst. Tech. J.* **44**, 455 (1965)
- 5.14 H. Steffen, J.P. Lörtscher, G. Herziger: *IEEE J. Quantum Electron.* **QE-8**, 239 (1972)
- 5.15 R.B. Chesler, D. Maydan: *J. Appl. Phys.* **43**, 2254 (1972)
- 5.16 N.K. Berger, N.A. Deryugin, Y.N. Lukyanov, Y.E. Studenikin: *Opt. Spectrosc. USSR* **43**, 176 (1977)
- 5.17 R. Hauck, H.P. Kortz, H. Weber: *Appl. Opt.* **19**, 598 (1980)
- 5.18 I.M. Belousova, O.B. Danilov: *Soc. Phys.* **12**, 1104 (1968)

- 5.19 E.A. Teppo: Nd:YAG laser laboratory experiments, Tech. Note 4051-2 (February 1972); and Tech. Note 4051-7, Naval Weapons Center, China Lake, CA (August 1973)
- 5.20 J.E. Geusic, H.J. Levingstein, S. Singh, R.C. Smith, L.G. Van Uitert: Appl. Phys. Lett. **12**, 306 (1968)
- 5.21 H.P. Kortz, R. Iffländer, H. Weber: Appl. Opt. **20**, 4124 (1981)
- 5.22 V. Magni: Appl. Opt. **25**, 107 (1986); and **25**, 2039 (1986)
- 5.23 V. Magni, G. Valentini, S. DeSilvestri: Opt. Quantum Electron. **23**, 1105 (1991)
- 5.24 S. DeSilvestri, P. Laporta, V. Magni: IEEE J. Quantum Electron. **QE-23**, 1999 (1987); and Opt. Lett. **11**, 513 (1986)
- 5.25 N. Pavel, T. Dascalu, V. Lupei: Opt. Eng. **35**, 1239 (May 1996)
- 5.26 D.C. Hanna, S.G. Sawyers, M.A. Yuratich: Opt. Quantum Electron. **13**, 493 (1981)
- 5.27 D.C. Hanna, S.G. Sawyers, M.A. Yuratich: Opt. Commun. **37**, 359 (1981)
- 5.28 P.H. Sarkies: Opt. Commun. **31**, 189 (1979)
- 5.29 H.W. Kogelnik, E.P. Ippen, A. Dienes, C.V. Shank: IEEE J. Quantum Electron. **QE-8**, 373 (1972)
- 5.30 D. Hanna: IEEE J. Quantum Electron. **QE-5**, 483 (1969)
- 5.31 A. Yariv, Optical Electronics, 4th edn. (Holt, Rinehart and Winston, Orlando, FL, 1971)
- 5.32 A.E. Siegman: Lasers, (University Science Book, Mill Valley, CA, 1986)
- 5.33 A.J. Kemp, G.J. Friel, T.K. Lake, R.S. Convoy, B.D. Sinclair: IEEE J. Quantum Electron. **36**, 228 (2000)
- 5.34 Applied Optics Research, Tuscon, AZ (GLAD); Script Enterprises, San Jose, CA (PARAXIA); Micro Systems Design, Munich, Germany (LASXAD); Breault Research Org. Tucson AZ (ASAP)
- 5.35 A. Rapaport, L. Weichman, B. Brickeen, S. Green, M. Bass: IEEE J. Quantum Electron. **37**, 1401 (2001)
- 5.36 F.A. Jenkins, H.E. White: *Fundamentals of Optics* (McGraw-Hill, New York, 1976)
- 5.37 M. Born, E. Wolf: *Principles of Optics* (Pergamon, New York, 1964)
- 5.38 C.L. Tang, H. Statz, G.A. DeMars, D.T. Wilson: Phys. Rev. **136**, A1 (1964)
- 5.39 A.R. Clobes, M.J. Brienza: Appl. Phys. Lett. **21**, 265 (1972)
- 5.40 T.J. Kane, R.J. Byer, Opt. Lett. **10**, 65 (1985)
- 5.41 D.A. Draegert: IEEE J. Quantum Electron. **QE-8**, 235 (1972)
- 5.42 H.G. Danielmeyer, W.G. Nilsen: Appl. Phys. Lett. **16**, 124 (1970)
- 5.43 H.G. Danielmeyer, E.H. Turner: Appl. Phys. Lett. **17**, 519 (1970)
- 5.44 A. Yariv: *Quantum Electronics*, 3rd edn. (Wiley, New York, 1988)
- 5.45 B. Zhou, T.J. Kane, G.I. Dixon, R.L. Byer: Opt. Lett. **10**, 62 (1985)
- 5.46 Y.K. Park, G. Giuliani, R.L. Byer: IEEE J. Quantum Electron. **QE-20**, 117 (1984)
- 5.47 N.P. Barnes, J.C. Barnes: IEEE J. Quantum Electron. **QE-29**, 2670 (1993)
- 5.48 L.A. Rahn: Appl. Opt. **24**, 940 (1985)
- 5.49 S.W. Henderson, E.H. Yuen, E.S. Fry: Opt. Lett. **11**, 715 (1986)
- 5.50 E.S. Fry, Q. Hu, X. Li: Appl. Opt. **30**, 1015 (1991)
- 5.51 V. Evtuhov, A.E. Siegman: Appl. Opt. **4**, 142 (1965)
- 5.52 K. Tsubono, S.Moriwaki: Jpn. J. Appl. Phys. **31**, 1241 (1992)
- 5.53 C.C. Harb, M.B. Gray, H.A. Bachor, R.Schilling, P. Rottengatter, I. Freitag, H. Welling: IEEE J. Quantum Electron. **QE-30**, 2907 (1994)
- 5.54 J. Harrison, A. Finch, J.H. Flint, P.F. Moulton: IEEE J. Quantum Electron. **QE-28**, 1123 (1992)
- 5.55 T.J. Kane, A.C. Nilsson, R.L. Byer: Opt. Lett. **12**, 175 (1987)
- 5.56 J.J. Zaykowski, J.A. Keszenheimer: IEEE J. Quantum Electron. **QE-28**, 1118 (1992)
- 5.57 J.A. Keszenheimer, J.J. Zaykowski: In CLEO '91, Baltimore, MD, 1991, paper CME8
- 5.58 A. Owyong, P. Esherick: Opt. Lett. **12**, 999 (1987)
- 5.59 T.J. Kane, E.A.P. Cheng: Opt. Lett. **13**, 970 (1988)
- 5.60 W.R. Trutna, D.K. Donald: Opt. Lett. **15**, 369 (1990)
- 5.61 P.A. Schultz, S.R. Henion: Opt. Lett. **16**, 578 (1991)
- 5.62 J.A. Keszenheimer, K.F. Wall, S.F. Root: In *OSA Proc. Adv. Solid-State Lasers*, Vol. 15, (1993) p. 283

- 5.63 P. Robrish: Opt. Lett. **19**, 813 (1994)
- 5.64 R.W.P. Drever, J.L. Hall, F.V. Kowalski, J. Hough, G.M. Ford, A.J. Munley, H. Ward: Appl. Phys. B, **31**, 97 (1983)
- 5.65 T. Day, E.K. Gustafson, R.L. Byer: IEEE J. Quantum Electron. **QE-28**, 1106 (1992)
- 5.66 N. Uehara, K. Ueda: Opt. Lett. **18**, 505 (1993)
- 5.67 K. Nakagawa, A.S. Shelkovnikov, T. Katsuda, M. Ohtsu: Appl. Opt. **33**, 6383 (1994)
- 5.68 A. Yu Nevsky, M. Eichenseer, J. von Zanthier, H. Walther: Opt. Commun. **210**, 91 (2002)
- 5.69 M. Musha, K. Nakagawa, K. Ueda: Opt. Lett. **22**, 1177 (1997)
- 5.70 B. Willke, S. Brozek, K. Danzmann, V. Quetschke, S. Gossler: Opt. Lett. **5**, (May 2000)
- 5.71 H.A. Macleod: *Thin-Film Optical Filters*, 2nd edn. (MacMillan, New York, 1986)
- 5.72 A.E. Siegman: Proc. IEEE **53**, 277 (1965)
- 5.73 A.E. Siegman: Appl. Opt. **13**, 353 (1974); and *Lasers* (University Science Books, Mill Valley, CA, 1986)
- 5.74 W.H. Steier: In *Laser Handbook*, Vol. 3, ed. by M. Stinch (North-Holland, Amsterdam, 1979)
- 5.75 R.L. Herbst, M. Komine, R.L. Byer: Opt. Commun. **21**, 5 (1977)
- 5.76 E. Armandillo, C. Norrie, A. Cosentino, P. Laporta, P. Wazan, P. Maine: Opt. Lett. **22**, 1168 (1997)
- 5.77 T.F. Ewanizky, J.M. Craig: Appl. Opt. **15**, 1465 (1976)
- 5.78 P.G. Gobbi, S. Morosi, G.C. Reali, A.S. Zarkasi: Appl. Opt. **24**, 26 (1985)
- 5.79 G. Giuliani, Y.K. Park, R.L. Byer: Opt. Lett. **5**, 491 (1980)
- 5.80 J.M. Eggleston, G. Giuliani, R.L. Byer: J. Opt. Soc. Am. **71**, 1264 (1982)
- 5.81 S. De Silvestri, P. Laporta, V. Magni, O. Svelto: Opt. Lett. **12**, 84 (1987)
- 5.82 N. McCarthy, P. Lavigne: Appl. Opt. **22**, 2704–2708 (1983)
- 5.83 N. McCarthy, P. Lavigne: Appl. Opt. **23**, 3845–3850 (1984)
- 5.84 P. Lavigne, N. McCarthy, J.G. Demers: Appl. Opt. **24**, 2581–2586 (1985)
- 5.85 N. McCarthy, P. Lavigne: Opt. Lett. **10**, 553–555 (1985)
- 5.86 A. Parent, P. Lavigne: Appl. Opt. **28**, 901–903 (1989)
- 5.87 G. Emiliani, A. Piegaro, S. De Silvestri, P. Laporta, V. Magni: Appl. Opt. **28**, 2832–2837 (1989)
- 5.88 S. De Silvestri, V. Magni, O. Svelto, G. Valentini: IEEE J. Quantum Electron. **QE-26**, 1500 (1990)
- 5.89 N. Hodgson, H. Weber: Opt. Quantum Electron. **22**, 39 (1990)
- 5.90 N. Hodgson, T. Haase: SPIE Proc. **1277**, 88 (1990)
- 5.91 V. Magni, S. DeSilvestri, O. Svelto, G.L. Valentini: Lasers Electro-Opt. **10**, 366 (1991)
- 5.92 V. Magni, S. DeSilvestri, L.-J. Qian, O. Svelto: Opt. Commun. **94**, 87 (1992)
- 5.93 N. Hodgson, G. Bostanjoglo, H. Weber: Opt. Commun. **99**, 75 (1993)
- 5.94 N. Hodgson, G. Bostanjoglo, H. Weber: Appl. Opt. **32**, 5902 (1993)
- 5.95 G. Bostanjoglo, G.A. Witt: Fibertek Report (February **14**, 1994)
- 5.96 W.F. Krupke, W.R. Sooy: IEEE J. Quantum Electron. **QE-5**, 575 (1969)
- 5.97 J.M. Yarborough, J. Hobart: In *Conf. on Laser Eng. Appl.*, Washington, DC, 1973, postdeadline paper
- 5.98 I.J. Hodgkinson, Vukusic: Opt. Commun. **24**, 133 (1978)
- 5.99 A.L. Bloom: J. Opt. Soc. Am. **64**, 447 (1974)

Chapter 6

- 6.1 J.H. Goncz: Instr. Soc. Am. Trans. **5**, 1 (1966)
- 6.2 J.H. Goncz, W.J. Mitchell: IEEE J. Quantum Electron. **QE-3**, 330 (1967)
- 6.3 J. Oliver, F.S. Barnes: IEEE J. Quantum Electron. **QE-5**, 225 (1969)
- 6.4 W.D. Fountain, L.M. Osterink, J.D. Foster: IEEE J. Quantum Electron. **QE-6**, 232, 684 (1970)
- 6.5 M.B. Davies, P. Scharman, J.K. Wright: IEEE J. Quantum Electron. **QE-4**, 424 (1968)
- 6.6 E.A. Teppo: Nd:YAG laser laboratory experiments, Tech. Note 4051-2 (Naval Weapons Center, China Lake, CA, 1972)

- 6.7 G.J. Linford: *Appl. Opt.* **33**, 8333 (1994)
- 6.8 J.L. Emmet, A.L. Schawlow: *J. Appl. Phys.* **35**, 2601 (1964)
- 6.9 J.R. Oliver, F.S. Barnes: *Proc. IEEE* **59**, 638 (1971)
- 6.10 J.H. Goncz, P.B. Newell: *J. Opt. Soc. Am.* **56**, 87 (1966)
- 6.11 J.H. Goncz: *J. Appl. Phys.* **36**, 742 (1965)
- 6.12 J.P. Markiewicz, J.L. Emmett: *IEEE J. Quantum Electron.* **QE-2**, 707 (1966)
- 6.13 J.F. Holzrichter, J.L. Emmett: *Appl. Opt.* **8**, 1459 (1969)
- 6.14 D.E. Perlman: *Rev. Sci. Instr.* **37**, 340 (1966)
- 6.15 K.R. Lang, F.S. Barnes: *J. Appl. Phys.* **35**, 107 (1964)
- 6.16 J.H. Rosolowski, R.J. Charles: *J. Appl. Phys.* **36**, 1792 (1965)
- 6.17 R.A. Dugdale, R.C. McVickers, S.D. Ford: *J. Nuclear Mater.* **12**, 1 (1964)
- 6.18 H.E. Edgerton, J.H. Goncz, J. Jameson: Xenon flashlamps, limits of operation. *Proc. 6th Int'l Congr. on High Speed Photography*, Haarlem, Netherlands (1963) p. 143
- 6.19 L. Waszak: *Microwaves* **130** (May 1969)
- 6.20 EG&G Linear Xeonon Flash Tubes, Data Sheet 1002-B
- 6.21 F. Schuda: In *Flashlamp-Pumped Laser Technology*, SPIE Proc. Vol. **609**, ed. by F. Schuda (SPIE, Bellingham, WA, 1986) p. 177
- 6.22 B. Newell, J.D. O'Brian: *IEEE J. Quantum Electron.* **QE-4**, 291 (1968)
- 6.23 J.F. Holzrichter, N. Dobeck, A. Pemberton: Flashlamp development, *Laser Progr. Ann. Rept.* UCRL-50021-74 (Lawrence Livermore Lab., 1974) pp. 107-115
- 6.24 L. Richter, F. Schuda, J. Degnan: In *Solid State Lasers*, SPIE Proc. Vol. 1223, ed. by G. Dubé (SPIE, Bellingham, WA, 1990) p. 142
- 6.25 W. Koechner, L. DeBenedictis, E. Matovich, G.E. Mevers: *IEEE J. Quantum Electron.* **QE-8**, 310 (1972)
- 6.26 J. Richards, D. Rees, K. Fueloop, B.A. See: *Appl. Opt.* **22**, 1325 (1983)
- 6.27 J.H. Kelly, D.C. Brown, K. Teegarden: *Appl. Opt.* **19**, 3817 (1980)
- 6.28 K. Yoshida, Y. Kato, H. Yoshida, C. Yamanaka: *Rev. Sci. Instr.* **55**, 1415 (1984)
- 6.29 G.N. Glascoe, J.V. Lebacqz: *Pulse Generators* (McGraw-Hill, New York, 1948)
- 6.30 J.R. Unternahrer: Private Communication (1994)
- 6.31 N.P. DePratt: *J. Phys. E.* **4**, 1 (1971)
- 6.32 V.J. Corcoran, R.W. McMillan, S.K. Barnoske: *IEEE J. Quantum Electron.* **QE-10**, 618 (1974)
- 6.33 F. Benjamin: *Electro-Optical System Designs*, **32** (March 1975)
- 6.34 W.L. Gagnon, G. Allen: Power conditioning, *Laser Progr. Ann. Rept.* UCRL-50021-74, (Lawrence Livermore Lab., 1974)
- 6.35 R.H. Dishington, W.R. Hook, R.P. Hilberg: *Appl. Opt.* **13**, 2300 (1974)
- 6.36 W.R. Hook, R.H. Dishington, R.P. Hilberg: *IEEE Trans. Electron Devices* **ED-19**, 308 (1972)
- 6.37 T.B. Read: *Appl. Phys. Lett.* **9**, 342 (1966)
- 6.38 W. Koechner: *Laser Focus* **5**, 29 (1969)
- 6.39 M. Grasis, L. Reed: Long-life krypton arc lamp for pumping Nd:YAG lasers, *Techn. Rept. AFAL-TR-73-156* (ILC Technologies, Sunnyvale, CA, 1973)
- 6.40 W.E. Thouret: *Illum. Eng.* **55**, 295 (1960)
- 6.41 S. Yoshikawa, K. Iwamoto, K. Washio: *Appl. Opt.* **10**, 1620 (1971)
- 6.42 L.M. Osterink, J.D. Foster: In *1969 IEEE Conf. on Laser Eng. Appl., Washington, DC*
- 6.43 W. Streifer, D.R. Scifres, G.L. Harnagel, D.F. Welch, J. Berger, M. Sakamoto: *IEEE J. Quantum Electron.* **QE-24**, 883 (1988)
- 6.44 T.Y. Fan, R.L. Byer: *IEEE J. Quantum Electron.* **24**, 895 (1988)
- 6.45 J.G. Endriz, M. Vakili, G.S. Browder, M. DeVito, J.M. Haden, G.L. Harnagel, W.E. Plano, M. Sakamoto, D.F. Welch, S. Willing, D.P. Worland, H.C. Yao: *IEEE J. Quantum Electron.* **QE-28**, 952 (1992)
- 6.46 A.A. Karpinski: *Laser Focus World* (October 1994) p. 155; and In *Nov. 1990 Annual Meeting OSA*, Boston Mass. Technical Digest, paper MK10
- 6.47 K.J. Linden, P.N. McDonnell: *NASA Conf. Publ.* **3249**, 233 (1993)

- 6.48 R. Beach, W.J. Bennett, B.L. Freitas, D. Mundinger, B.J. Comaskey, R.W. Solarz, M.A. Emanuel: IEEE J. Quantum Electron. **QE-28**, 966 (1992)
- 6.49 J.-H. Kim, R.J. Lang, A. Larson: Appl. Phys. Lett. **57**, 2048–2050 (1990)
- 6.50 N.W. Carlson, G. Evans, D. Bour, S. Liew: Appl. Phys. Lett. **56**, 16–18 (1990)
- 6.51 A. Scherer, J.L. Jewell, Y.H. Lee, J.P. Harbison, L.T. Florez: Appl. Phys. Lett. **55**, 2724 (1989)
- 6.52 M. Ettenberg: Laser Focus **22**, 86 (1985)
- 6.53 G. Harnagel, D. Welch, P. Cross, D. Scifers: 135 *Lasers Appl.* (June 1986)
- 6.54 K.A. Forrest, J.B. Abshire: IEEE J. Quantum Electron. **QE-23**, 1287 (1987)
- 6.55 E. Kapon: In *Handbook of Solid-State Lasers*, ed. by P.K. Cheo (Marcel Dekker, New York, 1989)
- 6.56 R. Burnham: Fibertek, Inc., private communication.
- 6.57 N.P. Barnes, M.E. Storm, P.L. Cross, M.W. Skolaut: IEEE J. Quantum Electron. **QE-26**, 558 (1990)
- 6.58 E.C. Honea, J.A. Skidmore, B.L. Freitas, E. Utterback, M.A. Emanuel: In *OSA Tops, Vol. 19, Adv. Solid State Lasers*, ed. by W.R. Rosenberg, M.M. Fejer (Opt. Soc. Am., 1998) p. 326
- 6.59 R.G. Waters, D.P. Bour, S.L. Yellen, N.F. Ruggieri: IEEE Photon. Techol. Lett. **2**, 531 (1990)
- 6.60 B. Li, G.L. Harnagel, R.R. Craig: Proc. SPIE **3285**, 93 (1998)
- 6.61 H. Asonen, J. Aarik, P. Bournes, F. Corvini, M. Fang, M. Finander, M. Hmelar, R. Nabiev, J. Nappi, K. Rakennus, A. Salokatve: Proc. SPIE **3628**, 11 (1999)
- 6.62 G.C. Osbourn, P.L. Gourley, I.J. Fritz, R.M. Biefeld, L.R. Dawson, T.E. Zipperian: In *Semiconductors and Semimetals, Vol. 24, Applications of Multiple Quantum Wells, Doping, and Superlattices*, ed. by R. Dingle (Academic, San Diego, CA, 1987) p. 459
- 6.63 R.G. Waters: In *LEOS'90*, Boston, 1990, paper SDL6.2
- 6.64 J.J. Coleman: In *LEOS'90*, Boston, 1990, paper SDL6.1
- 6.65 J.A. Skidmore, B.L. Freitas, J. Crawford, J. Satariano, E. Utterback, L. DiMercurio, K. Cutter, S. Sutton: Appl. Phys. Lett. **77**, 10 (2000)
- 6.66 J.L. Dallas, R.S. Afzal, M.A. Stephen: Appl. Opt. **35**, 1427 (1996)
- 6.67 D.A. Huchital: IEEE J. Quantum Electron. **QE-12** 1 (1976)
- 6.68 I.P. Lesnick, C.H. Church: IEEE J. Quantum Electron. **QE-2**, 16 (1966)
- 6.69 Yu.A. Kalinin: Sov. J. Opt. Techn. **37**, 1 (1970)
- 6.70 S.B. Schuldt, R.L. Aagard: Appl. Opt. **2**, 509 (1963)
- 6.71 C. Bowness: Appl. Opt. **4**, 103 (1965)
- 6.72 Yu.A. Kalinin, A.A. Mak: Opt. Tech. **37**, 129 (1970)
- 6.73 D.R. Skinner, J. Tregellas-Williams: Australian J. Phys. **19**, 1 (1966)
- 6.74 J. Whittle, D.R. Skinner: Appl. Opt. **5**, 1179 (1966)
- 6.75 D.R. Skinner: Appl. Opt. **8**, 1467 (1969)
- 6.76 W.R. Sooy, M.L. Stitch: J. Appl. Phys. **34**, 1719 (1963)
- 6.77 C.H. Cooke, J. McKenna, J.G. Skinner: Appl. Opt. **3**, 957 (1964)
- 6.78 D. Röss: *Lasers, Light Amplifiers and Oscillators* (Academic Press, New York, 1969) p. 426
- 6.79 H.U. Leuenberger, G. Herziger: Appl. Opt. **14**, 1190 (1975)
- 6.80 W. Koechner: Appl. Opt. **9**, 1429 (1970)
- 6.81 D.D. Bhawalkar, L. Pandit: IEEE J. Quantum Electron. **QE-9**, 43 (1973)
- 6.82 W.W. Morey: IEEE J. Quantum Electron. **QE-8**, 818 (1972)
- 6.83 A.N. Fletcher: Appl. Phys. B **37**, 31 (1985)
- 6.84 W.B. Jones: Laser Focus/Electro-Optic (September 1983) p. 107
- 6.85 W. Koechner, H. Verdun: Laser-diode array pumped solid state laser systems, Final Rept., (Naval Ocean Systems Command, Contract No. N00014-85-C-0174, 1986)
- 6.86 H. Bruesselbach, D.S. Sumida, R. Reeder, R.W. Byren: In *OSA TOPS, Vol. 10, Adv. Solid State Lasers*, ed. by C.R. Pollock, W.R. Bosenberg (Opt. Soc. Am., 1997) p. 285
- 6.87 R. Wu, P.B. Phua, K.S. Lai: Appl. Opt. **39**, 431 (2000)
- 6.88 J.J. Chang, E.P. Dragon, C.A. Ebbers, I.L. Bass, C.W. Cochran: In *OSA TOPS Vol. 19, Adv. Solid State Lasers*, ed. by W.R. Bosenberg, M.M. Fejer (Opt. Soc. Am., 1998) p. 300
- 6.89 N. Pavel, Y. Hirano, S. Yamamoto, Y. Koyata, T. Tajime: Appl. Opt. **39**, 986 (2000)

- 6.90 S. Lee, S.K. Kim, M. Yun, H.S. Kim, B.H. Cha, H.-J. Moon: *Appl. Opt.* **41**, 1089 (2002)
- 6.91 T.S. Rutherford, W.M. Tulloch, E.K. Gustafson, R.L. Byer: *IEEE J. Quantum Electron.* **QE-36**, 205 (2000)
- 6.92 A.D. Hays, G. Witt, N. Martin, D. DiBiase, R. Burnham: In *UV and Visible Lasers and Laser Crystal Growth*, Proc., SPIE, Vol. 2380 ed. by R. Scheps, M.R. Kokta (SPIE, Bellingham, WA, 1995) p. 88
- 6.93 R. Burnham, G. Moule, J. Unternahrer, M. McLaughlin, M. Kukla, M. Rhoades, D. DiBiase, W. Koehnner: In *Laser'95*, Munich 1995, Paper K9.
- 6.94 J.R. Lee, H.J. Baker, G.J. Friel, G.J. Hilton, D.R. Hall: *Opt. Lett.* **27**, 524 (2002)
- 6.95 J.E. Bernard, A.J. Alcock: *Opt. Lett.* **19**, 1861 (1994); and **18**, 968 (1993)
- 6.96 J. Richards, A. McInnes: *Opt. Lett.* **20**, 371 (1995)
- 6.97 C.E. Hamilton, R.J. Beach, S.B. Sutton, L.H. Furu, W.F. Krupke: *Opt. Lett.* **19**, 1627 (1994)
- 6.98 A.J. Alcock, J.E. Bernard: *IEEE J. Select. Topics Quantum Electron.* **3**, 3 (1997)
- 6.99 W. Zendzian, J.K. Jabczynski, Z. Mierczyk: In *ICM Int. Congress Center Muenchen*, June 1999, Postdeadline paper NPD2-1
- 6.100 A.J. Alcock, J.E. Bernard: U.S. patent number 5,315,612
- 6.101 D.G. Hall, R.J. Smith, R.R. Rice: *Appl. Opt.* **19**, 3041 (1980)
- 6.102 T.Y. Fan, R.L. Byer: *IEEE J. Quantum Electron.* **23**, 605 (1987)
- 6.103 T.Y. Fan, A. Sanchez: *IEEE J. Quantum Electron.* **26**, 311 (1990)
- 6.104 P. Laporta, M. Brussard: *IEEE J. Quantum Electron.* **27**, 2319 (1991)
- 6.105 Y.E. Chen, T.S. Liao, C.F. Kao, T.M. Huang, K.H. Lin, S.C. Wang: *IEEE J. Quantum Electron.* **32**, 2010 (1996)
- 6.106 Y.F. Chen, C.F. Kao, S.C. Wang: *Opt. Commun.* **133**, 517 (1997)
- 6.107 N. Pavel, T. Taira: *Opt. Eng.* **38**, 1806 (1999)
- 6.108 Y.F. Chen, C.F. Kao, T.M. Huang, C.L. Wang, S.C. Wang: *IEEE J. Select. Topics Quantum Electron.* **3**, 29 (1997)
- 6.109 Y.F. Chen, T.M. Huang, C.F. Kao, C.L. Wang, S.C. Wang: *IEEE J. Quantum Electron.* **33**, 1424 (1997)
- 6.110 A. Brignon, G. Feugnet, J.P. Huignard, J.P. Pocholle: *IEEE J. Quantum Electron.* **QE-34**, 577 (1998)
- 6.111 C. Rahlf, M.H. Dunn, B.D. Sinclair, W. Sibbett: In *CLEO'94*, Anaheim, CA. 1994, p. **308**, Paper CThG4
- 6.112 W.A. Clarkson, D.C. Hanna: *Opt. Lett.* **21**, 869 (1996)
- 6.113 H.R. Verdun, T. Chuang: *Opt. Lett.* **17**, 1000 (1992)
- 6.114 E.C. Holnea, C.A. Ebbers, R.J. Beach, J.A. Speth, J.A. Skidmore, M.A. Emanuel, S.A. Payne: *Opt. Lett.* **23**, 1203 (1998)
- 6.115 G.F. Albrecht, J.M. Eggleston, J.J. Ewing: *IEEE J. Quantum Electron.* **QE-22**, 2099 (1986)
- 6.116 J.M. Eggleston, G.F. Albrecht, R.A. Petr, J.F. Zumdiek: *IEEE J. Quantum Electron.* **QE-22**, 2092 (1986)
- 6.117 M.R. Siegrist: *Appl. Opt.* **15**, 2167 (1976)
- 6.118 J. Trenholme: Optimizing the design of a kilojoule laser amplifier chain, Laser Fusion Program, Semiannual Report (Lawrence Livermore Laboratory, 1973) p. 60.
- 6.119 Datasheet, *Jenoptik Laser*, Jena, Germany.
- 6.120 S. Erhard, A. Giesen, M. Karszewski, T. Rupp, C. Stewen, I. Johannsen, K. Contag: In *Proc. OSA Trends in Optics and Photonics, Adv. Solid State Lasers*, Washington, DC, 1999

Chapter 7

- 7.1 D.C. Brown: *IEEE J. Quantum Electron.* **34**, 560 (1998)
- 7.2 D.P. Devor, L.G. Shazer, R.C. Pastor: *IEEE J. Quantum Electron.* **25**, 1863 (1989)
- 7.3 B. Comaskey, B.D. Moran, G.F. Albrecht, R.J. Beach: *IEEE J. Quantum Electron.* **QE-31**, 1261 (1995)

- 7.4 T.Y. Fan: IEEE J. Quantum Electron. **QE-29**, 1457 (1993)
7.5 T.S. Chen, V.L. Anderson, O. Kahan: IEEE J. Quantum Electron. **QE-26**, 6 (1990)
7.6 M.S. Mangir, D.A. Rockwell: IEEE J. Quantum Electron. **QE-22**, 574 (1986)
7.7 D.S. Sumida, D.A. Rockwell, M.S. Mangir: IEEE J. Quantum Electron. **QE-24**, 985 (1988)
7.8 H.S. Carslaw, J.C. Jaeger: *Conduction of Heat in Solids* (Oxford University Press, London, 1948) p. 191
7.9 W. Koechner: Appl. Opt. **9**, 1429 (1970)
7.10 S.T. Hsu: *Engineering Heat Transfer* (Van Nostrand, Princeton, NJ, 1963) p. 274
7.11 G.D. Baldwin, E.P. Riedel: J. Appl. Phys. **38**, 2726 (1967)
7.12 M.K. Chun, J.T. Bischoff: IEEE J. Quantum Electron. **QE-7**, 200 (1971)
7.13 K.R. Richter, W. Koechner: Appl. Phys. **3**, 205 (1974)
7.14 W. Koechner: J. Appl. Phys. **44**, 3162 (1973)
7.15 B.A. Ermakov, A.V. Lukin: Sov. Phys. **15**, 1097 (1971)
7.16 S. Timoshenko, J.N. Goodier: *Theory of Elasticity*, 3rd ed. (McGraw-Hill, Singapore, 1982)
7.17 W. Koechner: Appl. Phys. **2**, 279 (1973)
7.18 M. Born, E. Wolf: *Principles of Optics* (Pergamon, London, 1965)
7.19 J.F. Nye: *Physical Properties of Crystals* (Clarendon, Oxford, UK, 1985), reprinted 1993
7.20 J.D. Foster, L.M. Osterink: J. Appl. Phys. **41**, 3656 (1970)
7.21 W. Koechner and D.K. Rice: IEEE J. Quantum Electron. **QE-6**, 557 (1970)
7.22 W. Koechner: Appl. Opt. **9**, 2548 (1970)
7.23 G.D. Baldwin: Q-switched evaluation of Nd:CaLaSOAP. Final Report AFAL-TR-72-334, Air Force Avionics Laboratory, Wright-Patterson AFB, Ohio (September 1972)
7.24 S.Z. Kurtev, O.E. Denchev, S.D. Savov: Appl. Opt. **32**, 278 (1993)
7.25 S. Jackel, I. Moshe, R. Lallouz: In *OSA Adv. Solid State Lasers*, Coeur d'Alene, ID, 1998, Tech. Digest, p. 127
7.26 J.J. Kasinski, R.L. Burnham: Appl. Opt. **35**, 5949 (1996)
7.27 Y. Hirano, Y. Koyata, S. Yamamoto, K. Kasahara, T. Tajime: Opt. Lett. **24**, 679 (1999)
7.28 J.M. Eggleston: IEEE J. Quantum Electron. **24**, 1821 (1988)
7.29 R. Byren: Hughes Aircraft Corp. Electro-Optical and Data Systems Group, private communication, 1991
7.30 S. Jackel, I. Moshe, R. Lallouz: In *OSA TOPS. Vol. 19: Advanced Solid-State Lasers*. ed. by W.R. Bosenberg, M.M. Fejer (Opt. Soc. Am., Washington, DC, 1998) p. 384
7.31 Q. Lü, N. Kugler, H. Weber, S. Dong, N. Müller, U. Wittrock: Opt. Quantum Electron. **28**, 57 (1996)
7.32 N. Kugler, S. Dong, Q. Lü, H. Weber: Appl. Opt. **36**, 9359 (1997)
7.33 J. Sherman: Appl. Opt. **37**, 7789 (1998)
7.34 J. Richards: Appl. Opt. **26**, 2514 (1987)
7.35 J.M. Eggleston, T.J. Kane, K. Kuhn, J. Unternahrer, R.L. Byer: IEEE J. Quantum Electron. **QE-20**, 289 (1984)
7.36 H.J. Baker, A. Chesworth, D.P. Millas, D.R. Hall: In *OSA TOPS. Vol. 19: Advanced Solid-State Lasers*. ed. by W.R. Bosenberg, M.M. Fejer (Opt. Soc. Am., Washington, DC, 1998) p. 407
7.37 J. Xu, J. Lee, H. Baker, D. Hall: In *Advanced Solid-State Photonics Topical Mtg.*, San Antonio, TX, February 2003, Postdeadline paper MB20-1
7.38 W.S. Martin, J.P. Chernoch: US Patent 3,633,126 (January 1972)
7.39 J.P. Chernoch, W.S. Martin, J.C. Almasi: Performance characteristics of a face-pumped, face-cooled laser, the mini-FPL. Tech. Rept. AFAL-TR-71-3, Air Force Avionics Lab., Wright Patterson AFB, OH, 1971
7.40 Lawrence Livermore National Lab., Medium Average Power Solid State Laser Technical Information Seminar, CA, October 1985
7.41 L.E. Zapata, K.R. Manes, D.J. Christie, J.M. Davin, J.A. Blink, J. Penland, R. Demaret, G. Dallum: Proc. Soc. Photo-Opt. Instrum. Eng. **1223**, 259 (1990)
7.42 N. Hodgson, S. Dong, Q. Lü: Opt. Lett. **18**, 1727 (1993); also in *CLEO'93* Baltimore, MD, paper CW16

- 7.43 R.J. Shine, A.J. Alfrey, R.L. Byer: Opt. Lett. **20**, 459 (1995)
- 7.44 W.B. Jones, L.M. Goldman, J.P. Chernoch, W.S. Martin: IEEE J. Quantum Electron. **QE-8**, 534 (1972); G.J. Hulme, W.B. Jones: Total internal reflection face pumped laser, Proc. Soc., Photo-Optical Inst. Eng. IEEE J. **QE-22**, 2092 (1986)
- 7.45 T. Kanabe, C. Yamanaka, N. Kitagawa, M. Takeda, M. Nakatsuka, S. Nakai: In *CLEO'92* (Anaheim, CA) paper CTUE5
- 7.46 A.D. Hays, G. Witt, N. Martin, D. DiBiase, R. Burnham: In *UV and Visible Lasers and Laser Crystal Growth*, SPIE Proc., Vol. 2380, ed. by R. Scheps, M.R. Kokta (1995) p. 88
- 7.47 R.S. Afzal, M.D. Selker: Opt. Lett. **20**, 465 (1995)
- 7.48 T.S. Rutherford, W.M. Tulloch, E.K. Gustafson, R.L. Byer: IEEE J. Quantum Electron. **36**, 205 (2000)
- 7.49 W.M. Tulloch, T.S. Rutherford, E.K. Gustafson, R.L. Byer: In *SPIE Vol. 3613: Solid-State Lasers VIII*, ed. by R. Scheps (SPIE, Wellington, WA, 1999)
- 7.50 M. Nigel, R. Burnham: Fibertek Inc., private communication, 2004
- 7.51 Lawrence Livermore Laboratory Laser Program Annual Reports UCRL-520021 (1974–1998)
- 7.52 W.W. Simmons, D.R. Speck, L.J. Hunt: Appl. Opt. **17**, 999 (1978)
- 7.53 W.E. Martin, J.B. Trenholme, G.T. Linford, S.M. Yarema, C.A. Hurley: IEEE J. Quantum Electrons. **QE-17**, 1744 (1981)
- 7.54 D.C. Brown: In *High-Peak-Power Nd:Glass Laser Systems*, Springer Ser. Opt. Sci., Vol. 25 (Springer, Berlin Heidelberg, 1981)
- 7.55 M.A. Summers, J.B. Trenholme, W.L. Gagnon, R.J. Gelinas, S.E. Stokowski, J.E. Marion, H.L. Julien, J.A. Blink, D.A. Bender, M.O. Riley, R.F. Steinkraus: *High Power and Solid State Lasers*, SPIE Proc., Vol. 622, ed. by W. Simmons (1986) P. 2
- 7.56 J.C. Almasi, W.S. Martin: US Patent 3,631,362 (December 1971)
- 7.57 D.C. Brown, J.H. Kelly, J.A. Abate: IEEE J. Quantum Electron. **QE-17**, 1755 (1981)
- 7.58 J.A. Abate, L. Lund, D. Brown, S. Jacobs, S. Refermat, J. Kelly, M. Gavin, J. Waldbillig, O. Lewis: Appl. Opt. **20**, 351 (1981); also Appl. Opt. **20**, 1588 (1981)
- 7.59 J.H. Kelly, D.L. Smith, J.C. Lee, S.D. Jacobs, D.J. Smith, J.C. Lambropoulos: In *CLEO'87* (Baltimore, MD), Tech. Digest, p. 114
- 7.60 A. Giesen, M. Karszewski, C. Stewen, A. Voss, L. Berger, U. Brauch: In *Proc. Adv. Solid-State Lasers*, Vol. 24 (Opt. Soc. Am., Washington, DC, 1995) p. 330
- 7.61 Y. Liao, R.J.D. Miller, M.R. Armstrong: Opt. Lett. **24**, 1343 (1999)
- 7.62 J. Frauchiger, P. Albers, H.P. Weber: IEEE J. Quantum Electron. **QE-28**, 1046 (1992)
- 7.63 M.E. Innocenzi, H.T. Yura, C.L. Fincher, R.A. Fields: Appl. Phys. Lett. **56**, 1831 (1990)
- 7.64 S.C. Tidwell, J.F. Seamans, M.S. Bowers, A.K. Cousins: IEEE J. Quantum Electron. **QE-28**, 997 (1992)
- 7.65 U.O. Farrukh, A.M. Buoncristiani, E.C. Byvik: IEEE J. Quantum Electron. **24**, 2253 (1988)
- 7.66 S.B. Sutton, G.F. Albrecht: Appl. Opt. **32**, 5256 (1983)
- 7.67 A.K. Cousins: IEEE J. Quantum Electron. **QE-28**, 1057 (1992)
- 7.68 C. Pfistner, R. Weber, H.P. Weber, S. Merazzi, R. Gruber: IEEE J. Quantum Electron. **QE-30**, 1605 (1994)
- 7.69 R. Weber, B. Neuenschwander, M. MacDonald, M.B. Roos, H.P. Weber: IEEE J. Quantum Electron. **QE-34**, 1046 (1998)
- 7.70 H.C. Lee, P.L. Brownlie, H.E. Meissner, E.C. Rea: SPIE Vol. 1624: Laser-Induced Damage in Optical Materials (SPIE, Bellingham, WA, 1991) p. 2
- 7.71 B. Neuenschwander, R. Weber, H.P. Weber: IEEE J. Quantum Electron. **QE-31** 1082 (1995)
- 7.72 X. Peng, A. Asundi, Y. Chen, Z. Xiong: Appl. Opt. **40**, 1396 (2001)
- 7.73 Y. Liao, R.J.D. Miller, M.R. Armstrong: Opt. Lett. **24**, 1343 (1999)
- 7.74 W.A. Clarkson, N.S. Felgate, D.C. Hanna: In *OSA TOPS. Vol.19: Advanced Solid-State Lasers*, ed. by W. Rosenberg, M.M. Feijer (Opt. Soc. Am., Washington, DC, 1998) p. 401
- 7.75 X. Peng, L. Xu, A. Asundi: IEEE J. Quantum Electron. **38**, 1291 (2002)
- 7.76 Y.F. Chen: IEEE J. Quantum Electron. **35**, 234 (1999)
- 7.77 J.L. Blows, T. Omatsu, J. Dawes, H. Pask, M. Tateda: IEEE Photon. Technol. Lett. **10**, 1727 (1998)

- 7.78 Y.F. Chen, H.J. Kuo: Opt. Lett. **23**, 846 (1998)
 7.79 A. Sennaroglu: Appl. Opt. **38**, 3253 (1999)
 7.80 Y.F. Chen, T.M. Huang, C.C. Liao, Y.P. Lan, S.C. Wang: IEEE Photonics Technol. Lett. **11**, 1241 (1999)
 7.81 Y.F. Chen, Y.P. Lan, S.C. Wang: Opt. Lett. **25**, 1016 (2000)
 7.82 M. Tsunekane, N. Taguchi, T. Kasamatsu, H. Inaba: IEEE J. Select. Topics Quantum Electron. **3**, 9 (1997)
 7.83 E.A. Teppo: Nd:YAG laser technology. NWC Tech. Memo 2534, Appendix C (1975); and Tech. Note 4051-2 (1972), Naval Weapons Center, China Lake, CA
 7.84 C.D. Marshall: Proc. Advanced Solid State Laser Conf. (Opt. Soc. Am., Washington, D.C., 1996)

Chapter 8

- 8.1 R.W. Hellwarth: In *Advances in Quantum Electronics* (Columbia Univ. Press, New York 1961) p. 334
 8.2 F.J. McClung, R.W. Hellwarth: Proc. IRE **51**, 46 (1963)
 8.3 W.G. Wagner, B.A. Lengyel: J. Appl. Phys. **34**, 2040 (1963)
 8.4 J.J. Degnan: IEEE J. Quantum Electron. **QE-25**, 214 (1989)
 8.5 J.E. Midwinter: Brit. J. Appl. Phys. **16**, 1125 (1965)
 8.6 G.D. Baldwin: IEEE J. Quantum Electron. **QE-7**, 220 (1971)
 8.7 R.B. Chesler, M.A. Karr, J.E. Geusic: Proc. IEEE **58**, 1899 (1970)
 8.8 R.J. Collins, P. Kisliuk: J. Appl. Phys. **33**, 2009 (1962)
 8.9 R.C. Benson, M.R. Mirarchi: IEEE Trans. Mil. Electron. **MIL-8**, 13 (1964)
 8.10 W. Buchman, W. Koehnert, D. Rice: IEEE J. Quantum Electron. **QE-6**, 747 (1970)
 8.11 I.W. Mackintosh: Appl. Opt. **8**, 1991 (1969)
 8.12 E.L. Steele, W.C. Davis, R.L. Treuthart: Appl. Opt. **5**, 5 (1966)
 8.13 Kh.S. Bagdasarov, V.I. Zhekov, T.M. Murina, A.A. Manenkov, M.I. Timoshechkin, A.M. Prokhorov: Sov. J. Quantum Electron. **8**, 83 (1978)
 8.14 Laser 1-2-3, Data Sheet, Schwartz Electro-Optics, Inc., Orlando, FL, 1997
 8.15 F. Konz, M. Frenz, V. Romano, M. Forrer, H.P. Weber: Opt. Commun. **103**, 298 (1993)
 8.16 H.J. Eichler, B. Liu, O. Sperlich: In *Solid State Lasers*, Vol. VII Proc. SPIE, Vol. 3265, ed. by R. Scheps, (SPIE Bellingham, WA, 1998) P. 75
 8.17 R.O'B. Carpenter: J. Opt. Soc. Am. **40**, 225 (1950)
 8.18 M. Born, E. Wolf: *Principles of Optics*, 2nd edn. (Macmillan, New York, 1964)
 8.19 I.P. Kaminow, E.H. Turner: Appl. Opt. **54**, 1374 (1966)
 8.20 F. Zernike Jr.: J. Opt. Soc. Am. **54**, 1215 (1964)
 8.21 J.H. Ott, T.R. Sliker: J. Opt. Soc. Am. **54**, 1442 (1964)
 8.22 M. Yamazaki, T. Ogawa: J. Opt. Soc. Am. **56**, 1407 (1966)
 8.23 E.V. Raevsky, V.L. Pavlovitch: Opt. Eng. **38**, 1781 (1999)
 8.24 S.Z. Kurtev, O.E. Denchev, S.D. Savov: Appl. Opt. **32**, 278 (1993)
 8.25 P.V. Lenzo, E.G. Spencer, K. Nassau: J. Opt. Soc. Am. **56**, 633 (1966)
 8.26 J.F. Ney: *Physical Properties of Crystals* (Oxford University Press, London, 1964)
 8.27 M.J.P. Payne, H.W. Evans: In *CLEO'84*, Anaheim, CA, 1984, Techn. Digest, Paper TUB16
 8.28 W.E. Schmid, IEEE J. Quantum Electron. **QE-16**, 790 (1980)
 8.29 Kh. S. Bagdasarov, V.P. Danilov, L.A. Kulevskii, V.A. Lobachev, T.M. Murina A.M. Prokhorov: Sov. J. Quantum Electron. **10**, 1127 (1980)
 8.30 E.A. Teppo: Nd:YAG Laser Lab. Experiments, January 1972 to June 1973, Technical Note 4051-7 (Naval Weapons Center, China Lake, CA, August 1973)
 8.31 R.P. Hilberg, W.R. Hook: Appl. Opt. **9**, 1939 (1970)
 8.32 T. Chuang, A.D. Hays, H.R. Verdun: OSA Proc.: Adv. Solid State Lasers **20**, 314 (1994); and Appl. Opt. **33**, 8355 (1994)
 8.33 M.B. Rankin, G.D. Ferguson: Proc. Soc. Photo-Opt. Instr. Eng. **160**, 67 (1978)
 8.34 J. Richards: Appl. Opt. **22**, 1306 (1983)

- 8.35 J. Richards: *Appl. Opt.* **26**, 2514 (1987)
- 8.36 E.A. Lundstrom: Waveplate for correcting thermally induced stress birefringence in solid state lasers, U.S. patent 4,408,334 (1983)
- 8.37 C.F. Quate, C.D. Wilkinson, D.K. Winslow: *Proc. IEEE* **53**, 1604 (1965)
- 8.38 N. Uchida, N. Niizeki: *Proc. IEEE* **61**, 1073 (1973)
- 8.39 R. Adler: *IEEE Spect.* **4**, 42 (1967)
- 8.40 R.W. Dixon: *IEEE J. Quantum Electron.* **QE-3**, 85 (1967)
- 8.41 R.W. Dixon: *J. Appl. Phys.* **38**, 5149 (1967)
- 8.42 P. Maak, L. Jakab, P. Richter, H.J. Eichler, B. Liu: *Appl. Opt.* **39**, 3054 (2000)
- 8.43 M. Hercher: *Appl. Opt.* **6**, 947 (1967)
- 8.44 Z. Burshtein, P. Blau, Y. Kalisky, Y. Shimony, M.R. Kokta: *IEEE J. Quantum Electron.* **QE-34**, 292 (1998)
- 8.45 Y.-S. Choi: *Appl. Opt.* **40**, 5417 (2001)
- 8.46 Y. Shimony, Z. Burshtein, Y. Kalisky: *IEEE J. Quantum Electron.* **QE- 31**, 1738 (1995)
- 8.47 J.J. Degnan: *IEEE J. Quantum Electron.* **QE-31**, 1890 (1995)
- 8.48 G. Xiao, M. Bass: *IEEE J. Quantum Electron.* **QE-33**, 41 (1997); and **QE-34**, 1142 (1998)
- 8.49 X. Zhang, S. Zhao, Q. Wang, Q. Zhang, L. Sun, S. Zhang: *IEEE J. Quantum Electron.* **QE-33**, 2286 (1997)
- 8.50 A. Agnesi, S. Dell' Acqua, E. Piccinini, G. Reali, G. Piccinno: *IEEE J. Quantum Electron.* **QE-34**, 1480 (1998)
- 8.51 T. Dascalu, N. Pavel, V. Lupei, G. Philippss, T. Beck, H. Weber: *Opt. Eng.* **35**, 1247 (May 1996)
- 8.52 A.D. Hays, R. Burnham: *Trends in Optics and Photonics*, Vol. 10, (Opt. Soc. Am., Washington, DC, 1997) P. 129
- 8.53 J.A. Morris, C.R. Pollock: *Opt. Lett.* **15**, 440 (1990)
- 8.54 J.J. Zaykowski, C. Dill: *Opt. Lett.* **19**, 1427 (1994)
- 8.55 J.J. Zaykowski, J. Ochoa, C. Dill: In *CLEO 1995*, P. 139, paper CTuM2
- 8.56 P. Wang, S.H. Zhou, K.K. Lee, Y.C. Chen: *Opt. Commun.* **114**, 439 (1995)
- 8.57 R. Wu, S. Hamlin, J.A. Hutchinson, L.T. Marshall: *Trends in Optics and Photonics*, Vol. 10, (Opt. Soc. Am., Washington, DC, 1997) P. 145
- 8.58 R.D. Stultz, M.B. Camargo, M. Lawler, D. Rockafellow, M. Birnbaum: In *OSA Advanced Solid State Lasers Conference*, Coeur d'Alene, ID, 1998, p. 330
- 8.59 Y.K. Kuo, Y.A. Chang: *Appl. Opt.* **42**, 1685 (2003)
- 8.60 B. Braun, F.X. Kaertner, G. Zhang, M. Moser, U. Keller: *Opt. Lett.* **22**, 381 (1997)
- 8.61 D. Maydan, R.B. Chesler: *J. Appl. Phys.* **42**, 1031 (1971)
- 8.62 R.B. Chesler, D. Maydan: *J. Appl. Phys.* **42**, 1028 (1971)
- 8.63 H.A. Kruegle, L. Klein: *Appl. Opt.* **15**, 466 (1976)
- 8.64 A. Hays: Fibertek, Inc., Private communication (1991)
- 8.65 J. Trenholme: Extraction of Energy from Laser Amplifiers. Laser Program Annual Report (1986) Chap. 7, Report UCRL 50021-86

Chapter 9

- 9.1 R. Bracewell: *The Fourier Transform and Its Applications* (McGraw-Hill, New York, 1965)
- 9.2 H.A. Haus, J.G. Fujimoto, E.P. Ippen: *IEEE J. Quantum Electron.* **QE-28**, 2086 (1992)
- 9.3 F. Krausz, M.E. Fermann, T. Brabec, P.F. Curley, M. Hofer, M.H. Ober, C. Spielmann, E. Wintner, A.J. Schmidt: *IEEE J. Quantum Electron.* **QE-28**, 2097 (1992)
- 9.4 W.T. Silfvast: *Laser Fundamentals* (Cambridge Univ. Press, Great Britain, 1996)
- 9.5 S.L. Shapiro (ed.): *Ultrashort Light Pulses*, Topics Appl. Phys., Vol. 18 (Springer, Berlin Heidelberg, 1977)
- 9.6 W. Kaiser (ed.) *Ultrashort Laser Pulses*, 2nd edn., Topics Appl. Phys., Vol. 60 (Springer, Berlin Heidelberg, 1993)

- 9.7 J.A. Fleck: Phys. Rev. B **1**, 84 (1970)
9.8 L.F. Mollenauer, R.H. Stolen: Opt. Lett. **9**, 13 (1984)
9.9 J. Goodberlet, J. Wang, J.G. Fujimoto, P.A. Schulz: Opt. Lett. **14**, 1125 (1989)
9.10 R.E. Bridges, R.W. Boyd, G.P. Agrawal: Optics Lett. **18**, 2026 (1993)
9.11 G. Cerullo, S.De Silvestri, V. Magni, O. Svelto: Opt. Lett. **19**, 1040 (1994), CLEO'94
(Anaheim, CA) paper CWA5 Tech. Digest p. 182
9.12 V. Magni, G. Cerullo, S. DeSilvestri: Opt. Commun. **101**, 365 (1993)
9.13 V. Magni, G. Cerullo, S. DeSilvestri: Opt. Commun. **96**, 348 (1993)
9.14 G. Cerullo, S. DeSilvestri, V. Magni, L. Pallaro: Opt. Lett. **19**, 807 (1994)
9.15 D.K. Negus, L. Spinelli, N. Goldblatt, G. Feuget: OSA Proc. Adv. Solid-State Lasers **10**, 120
(1991)
9.16 F. Krausz, C. Spielmann, T. Brabec, E. Wintner, A.J. Schmidt: Opt. Lett. **15**, 1082 (1990)
9.17 H.A. Haus, E.P. Ippen: Opt. Lett. **16**, 1331 (1991)
9.18 F. Salin, J. Squier, G. Mourou, M. Piché, N. McCarthy: OSA Proc. Ad. Solid-State Lasers **10**,
125 (1991)
9.19 D.E. Spence, P.N. Kean, W. Sibbett: Opt. Lett. **16**, 42–44 (1991)
9.20 D. Huang, M. Ulman, L.H. Acioli, H.A. Haus, J.G. Fujimoto: Opt. Lett. **17**, 511 (1992)
9.21 F. Salin, J. Squier, M. Piché: Opt. Lett. **16**, 1674 (1991)
9.22 M. Piché: Opt. Commun. **86**, 156 (1991)
9.23 T. Brabec, C. Spielmann, P.F. Curley, F. Krausz: Opt. Lett. **17**, 1292 (1992)
9.24 T. Brabec, P.F. Curley, C. Spielmann, E. Wintner, A.J. Schmidt: J. Opt. Soc. Am. B **10**, 1029
(1993)
9.25 U. Keller, D.A.B. Miller, G.D. Boyd, T.H. Chiu, J.F. Ferguson, M.T. Asom: Opt. Lett. **17**, 505
(1992); and In *OSA Proc. Adv. Solid State Lasers, Vol. 13*, L.L. Chase, A.A. Pinto (eds). (Opt.
Soc. Am., pp. 98–100, 1992)
9.26 U. Keller, K.J. Weingarten, F.X. Kärtner, D. Kopf, B. Braun, I.D. Jung, R. Fluk, C. Hönninger, N.
Matuschek, J. Aue de Au: IEEE Select. Topics Quantum Electron. **2**, 435 (1996)
9.27 I.D. Jung, F.X. Kärtner, N. Matuschek, D.H. Sutter, F. Morier-Genoud, G. Zhang, U. Keller: Opt.
Lett. **22**, 1009 (1997)
9.28 G.J. Spühler, R. Paschotta, U. Keller, M. Moser, M.J.P. Dymott, D. Kopf, J. Meyer, K.J. Wein-
garten, J.D. Kmetec, J. Alexander, G. Truong: Opt. Lett. **24**, 528 (1999)
9.29 J.M. Hopkins, G.J. Valentine, B. Agate, A.J. Kemp, U. Keller, W. Sibbett, IEEE J. Quantum
Electron. **38**, 360, (2002)
9.30 I.D. Jung, F.X. Kärtner, N. Matuschek, D.H. Sutter, F. Morier-Genoud, Z. Shi, V. Scheuer, M.
Tilsch, T. Tschudi, U. Keller: Appl. Phys. B **65**, 137 (1997)
9.31 J.L. Dallas: Appl. Opt. **33**, 6373 (1994)
9.32 D.J. Kuizenga, A.E. Siegman: IEEE J. Quantum Electron. **QE-6**, 694–709 (1970)
9.33 A.E. Siegman, D.J. Kuizenga: Appl. Phys. Lett. **14**, 181 (1969)
9.34 A.E. Siegman, D.J. Kuizenga: Opto-Electr. **6**, 43 (1974)
9.35 C.J. Flood, D.R. Walker, H.M. van Driel: Opt. Lett. **20**, 58 (1995)
9.36 D.J. Kuizenga, D.W. Phillion, T. Lund, A.E. Siegman: Opt. Commun. **9**, 221 (1973)
9.37 D.J. Kuizenga: IEEE J. Quantum Electron. **QE-17**, 1694 (1981)
9.38 A. Hays, L.R. Marshall, J.J. Kasinski, R. Burnham: IEEE J. Quantum Electron. **QE-28**, 1021
(1992)
9.39 R.P. Johnson, N.K. Moncur, L.D. Siebert: In *CLEO'87*, Baltimore, MD, 1987, paper FP2
9.40 T. Sizer, I.N. Duling: IEEE J. Quantum Electron. **QE-24**, 404 (1988)
9.41 G.T. Maker, A.I. Ferguson: Appl. Phys. Lett. **54**, 403 (1989); and Electron. Lett. **25**, 1025 (1989)
9.42 U. Keller, K.D. Li, B.T. Khuri-Yakub, D.M. Bloom, K.J. Weingarten, D.C. Gerstenberger: Opt.
Lett. **15**, 45 (1990)
9.43 L. Turi, C. Kuti, F. Krausz: IEEE J. Quantum Electron. **QE-26**, 1234 (1990)
9.44 F. Krausz, L. Turi, C. Kuti, A.J. Schmidt: Appl. Phys. Lett. **56**, 1415 (1990)
9.45 S.J. Walker, H. Avramopoulos, T. Sizer II: Opt. Lett. **15**, 1070 (1990)
9.46 J.H. Boyden: Microwaves **58** (March 1971)

- 9.47 G.T. Maker, A.I. Ferguson: Opt. Lett. **14**, 788 (1989)
- 9.48 T. Juhasz, S.T. Lai, M.A. Pessot: Opt. Lett. **15**, 1458 (1990)
- 9.49 G.P.A. Malcolm, J. Ebrahimzadeh, A.I. Ferguson: IEEE J. Quantum Electron. **QE-28**, 1172 (1992)
- 9.50 D.W. Hughes, M.W. Phillips, J.R.M. Barr, D.C. Hanna: IEEE J. Quantum Electron. **QE-28**, 1010 (1992)
- 9.51 F. Krausz, T. Brabec, E. Wintner, A.J. Schmidt: Appl. Phys. Lett. **55**, 2386 (1989)
- 9.52 R.L. Fork, O.E. Martinez, J.P. Gordon: Opt. Lett. **9**, 150 (1984)
- 9.53 J.P. Gordon, R.L. Fork: Opt. Lett. **9**, 153 (1984)
- 9.54 R. Szipočs, K. Ferencz, C. Spielmann, F. Krausz: Opt. Lett. **19**, 201 (1994)
- 9.55 F.X. Kaertner, N. Matuschek, T. Schibli, U. Keller, H.A. Haus, C. Heine, R. Morf, V. Scheuer, M. Tilsch, T. Tschudi: Opt. Lett. **22**, 831 (1997)
- 9.56 H.A. Haus, J.G. Fujimoto, E.P. Ippen: J. Opt. Soc. Am. B **8**, 2068 (1991)
- 9.57 C. Spielmann, F. Krausz, T. Brabec, E. Wintner, A.J. Schmidt: Opt. Lett. **16**, 1180 (1991)
- 9.58 U. Morgner, F.X. Kaertner, S.H. Cho, Y. Chen, H.A. Haus, J.G. Fujimoto, E.P. Ippen, V. Scheuer, G. Angelow, T. Tschudi: Opt. Lett. **24**, 411 (1999)
- 9.59 D.H. Sutter, G. Steinmeyer, L. Gallmann, N. Matuschek, F. Morier-Genoud, U. Keller, V. Scheuer, G. Angelow, T. Tschudi: Opt. Lett. **24**, 631 (1999)
- 9.60 Femtolasers Produktions GmbH, Vienna, Austria
- 9.61 P.R. Staver, W.T. Lotshaw: OSA Proc. Adv. Solid-State Lasers **20**, 252 (1994)
- 9.62 Y.M. Liu, P.R. Prucnal: IEEE J. Quantum Electron. **QE-29**, 2663 (1993)
- 9.63 M.T. Asaki, C.P. Huang, D. Garverey, J. Zhou, H.C. Kapteyn, M.M. Murnane: Opt. Lett. **18**, 977 (1993)
- 9.64 P.M. Mellish, P.M.W. French, J.R. Taylor, P.J. Delfyett, LT. Florez: Electron. Lett. **30**, 223 (1994)
- 9.65 D. Kopf, K.J. Weingarten, L.R. Brovelli, M. Kamp, and U. Keller, in *Conference on Lasers and Electro-Optics*, Vol. 15 of 1995 OSA Technical Digest Series (Optical Society of America, Washington, DC 1995). p. 252, paper CWM2
- 9.66 M. J. P. Dymott, A.I. Ferguson: Opt. Lett. **19**, 1988 (1994)
- 9.67 D. Kopf, K.J. Weingarten, G. Zhang, M. Moser, M.A. Emanuel, R.J. Beach, J.A. Skidmore, U. Keller: Appl. Phys. B-Lasers and Opt. **65**, 235–243 (1997)
- 9.68 D. Kopf, A. Prasad, G. Zhang, M. Moser, U. Keller: Opt. Lett. **22**, 621–623 (1997)
- 9.69 S. Uemura, K. Torizuka: IEEE J. Quantum Electron. **39**, 68 (2003)
- 9.70 J.M. Hopkins, G.J. Valentine, B. Agate, A.J. Kemp, U. Keller, W. Sibbett: IEEE J. Quantum Electron. **38**, 360 (2002)
- 9.71 A. Seas, V. Petričević, R.R. Alfano: Opt. Lett. **17**, 937 (1992)
- 9.72 A. Sennaroglu, C.R. Pollock, H. Nathel: Opt. Lett. **18**, 826 (1993)
- 9.73 Y. Pang, V. Yanovsky, F. Wise, B.I. Minkov: Opt. Lett. **18**, 1168 (1993)
- 9.74 V. Yanovsky, Y. Pang, F. Wise, B.I. Minkov: Opt. Lett. **18**, 1541 (1993)
- 9.75 A. Seas, V. Petričević, R.R. Alfano: Opt. Lett. **18**, 891 (1993)
- 9.76 E. Innerhofer, T. Suedmeyer, F. Brunner, R. Haering, A. Aschwanden, R. Paschotta, U. Keller, C. Hoenniger, M. Kumkar: In *Advanced Solid-State Photonics Topical Mtg.* San Antonio, TX, Feb. 2003, p. 376
- 9.77 D. Strickland, G. Mourou: Opt. Commun. **56**, 219 (1985)
- 9.78 G.A. Mourou, C.P.J. Barty, M.D. Perry: Phys. Today **51**, 22 (Jan. 1998)
- 9.79 K. Yamakawa, M. Aoyama, S. Matsuoka, H. Takuma, C.P.J. Barty, D. Fittinghoff: Opt. lett. **23**, 525 (1998)
- 9.80 C.P.J. Barty, T. Guo, C. Le Blanc, F. Raksi, C. Rose-Petruck, J. Squire, K.R. Wilson, V.V. Yakovlev, K. Yamakawa: Opt. Lett. **21**, 668 (1996)
- 9.81 P.A. Beaud, M. Richardson, E.J. Miesak: IEEE J. Quantum Electron. **QE-31**, 317 (1995)
- 9.82 P. Beaud, M. Richardson, E.J. Miesak, B. Chai: Opt. Lett. **18**, 1550 (1993)
- 9.83 A. Sullivan, H. Hamster, H.C. Kapteyn, S. Gordon, W. White, H. Nathel, R.J. Blair, R.W. Falcone: Opt. Lett. **16**, 1406 (1991)

Chapter 10

- 10.1 P.A. Franken, A.E. Hill, C.W. Peters, G. Weinreich: Phys. Rev. Lett. **7**, 118 (1961)
- 10.2 N. Bloembergen: *Nonlinear Optics* (Benjamin, New York), 4th printing.
- 10.3 F. Zernike, J.E. Midwinter: *Applied Nonlinear Optics* (Wiley, New York, 1973)
- 10.4 R.L. Sutherland: *Handbook of Nonlinear Optics* (Dekker, New York, 1973)
- 10.5 R.W. Boyd: *Nonlinear Optics* (Academic, San Diego, CA, 1992)
- 10.6 Y.R. Shen: *The Principles of Nonlinear Optics* (Wiley, New York, 1984)
- 10.7 D.A. Kleinman: In *Laser Handbook*, ed. by F.T. Arecchi, E.O. Schulz-DuBois, Vol. 2 (North-Holland, Amsterdam, 1972), pp. 1229–1258
- 10.8 J.A. Armstrong, N. Bloembergen, N. Ducuing, P.S. Pershan: Phys. Rev. **127**, 1918 (1962)
- 10.9 A. Yariv, P. Yeh: *Optical Waves in Crystals* (Wiley, New York, 1984)
- 10.10 D. Eimerl: IEEE J. Quantum Electron. **QE-23**, 575 (1987); and **QE-23**, 1361 (1981)
- 10.11 M.V. Hobden: J. Appl. Phys. **38**, 4365 (1967)
- 10.12 M. Born, E. Wolf: *Principles of Optics* (Macmillan, New York, 1964)
- 10.13 F.D. Bloss: *Crystallography and Crystal Chemistry* (Holt, Rinehart, Winston, New York, 1971)
- 10.14 N.F. Nye: *Physical Properties of Crystals* (Clarendon, Oxford, 1964)
- 10.15 Lasermetrics, Electro-Optics Div., Englewood Cliffs, NJ, Data Sheet 8701; In *Optical Harmonic Generating Crystals*, February 1987
- 10.16 R.C. Eckardt, H. Masuda, Y.X. Fan, R.L. Byer: IEEE J. Quantum Electron. **QE-26**, 922 (1990)
- 10.17 G.D. Boyd, A. Ashkin, J.M. Dziezic, D.A. Kleinman: Phys. Rev. **137**, A1305 (1965)
- 10.18 A.V. Smith, D.J. Armstrong, W.J. Alford: J. Opt. Soc., B **15**, 122 (1998)
- 10.19 R.S. Craxton, S.D. Jacobs, J.E. Rizzo, R. Boni: IEEE J. Quantum Electron. **QE-17**, 1762 (1981)
- 10.20 R.P. Jones: In *Solid-State Lasers and Nonlinear Crystals*, SPIE Proc., Vol. 2379, ed. G.J. Quarks, L. Esterowitz, L.K. Cheng (SPIE, Wellington, WA, 1995) p. 357
- 10.21 J.C. Jacco, G.M. Loiacono: Final Report under contract DAAK20-83-C-0139 Night Vision and Electronics Lab. Fort Belvoir, VA 22060, 1986
- 10.22 J.D. Bierlein: SPIE Proc. **1104**, 2 (1989)
- 10.23 L.K. Cheng, L.T. Chen, J.D. Bierlein, F.C. Zumsteg, A.A. Ballman: Appl. Phys. Lett. **62**, 346 (1993)
- 10.24 R. Wu: Appl. Opt. **32**, 971 (1993)
- 10.25 S. Zhao, C. Huang, H. Zhang: J. Cryst. Growth **99**, 805 (1990)
- 10.26 S. Lin, Z. Sun, B. Wu, C. Chen: J. Appl. Phys. **67**, 634 (1990)
- 10.27 K. Kato: IEEE J. Quantum Electron. **QE-22**, 1013 (1986)
- 10.28 W.J. Kozlovsky, C.D. Nabors, R.L. Byer: IEEE J. Quantum Electron. **QE-24**, 913 (1988)
- 10.29 R. Ono, T. Kamimura, S. Fukumoto, Y. Yap, M. Yoshimura, Y. Mori, T. Sasaki, K. Yoshida: J. Cryst. Growth **237**, 645 (2002)
- 10.30 H. Kitano, M. Matsui, K. Sato, N. Ushiyama, M. Yoshimura, Y. Mori, T. Sasaki: Opt. Lett. **28**, 263 (2003)
- 10.31 T. Sakuma, K. Deki, A. Finch, Y. Ohsako, T. Yokota: App. Opt. **39**, 5505 (2000)
- 10.32 T. Kojima, S. Konno, S. Fujikawa, K. Yasui, K. Yoshizawa: Opt. Lett. **25**, 58 (2000); also In *OSA TOPS, Vol. 68: Advanced Solid-State Lasers*, ed. by M.E. Fermann, L.R. Marshall (Opt. Soc. Am., Washington, DC, 2002) p. 464
- 10.33 U. Stamm, W. Zschocke, T. Schroeder, N. Deutsch, D. Basting: In *OSA TOPS, Vol. 10: Advanced Solid-State Lasers*, ed. by C.R. Pollock, W.R. Bosenberg (Opt. Soc. Am., Washington, DC, 1997)
- 10.34 D.C. Gerstenberger, T.M. Trautmann, M.S. Bowers: Opt. Lett. **28**, 1242 (2003)
- 10.35 P. Dekker, J. Dawes, P. Burns, J. Piper: In *OSA TOPS, Vol. 68: Advanced Solid-State Lasers*, ed. by M.E. Fermann, L.R. Marshall (Opt. Soc. Am., Washington, DC, 2002) p. 41
- 10.36 M. Yarborough, J. Falk, C.B. Hitz: Appl. Phys. Lett. **18**, 70 (1971)
- 10.37 B.J. Le Garrec, G.J. Raze, P.Y. Thro, M. Gilbert: Opt. Lett. **21**, 1990 (1996)
- 10.38 M.V. Ortiz, J.H. Fair, D.J. Kuizenga: In *OSA Proc. Adv. Solid State Lasers*, Vol. 13, (Opt. Soc. Am., Washington, DC, 1992) p. 361

- 10.39 R.G. Smith: IEEE J. Quantum Electron. **QE-6**, 215 (1970)
- 10.40 J.E. Geusic, H.J. Levinstein, S. Singh, R.G. Smith, L.G. van Uitert: Appl. Phys. Lett. **12**, 306 (1968)
- 10.41 T. Baer: J. Opt. Soc. Am., B **3**, 1175 (1986)
- 10.42 D.W. Anthon, D.L. Sipes, T.J. Pier, M.R. Ressl: IEEE J. Quantum Electron. **28**, 1148 (1992)
- 10.43 H. Nagai, M. Kume, I. Ohta, H. Shimizu, M. Kazumura: IEEE J. Quantum Electron. **28**, 1164 (1992)
- 10.44 Y.F. Chen, T.M. Huang, C.L. Wang, L.J. Lee: Appl. Opt. **37**, 5727 (1998)
- 10.45 M. Oka, S. Kubota: Opt. Lett. **13**, 805 (1988)
- 10.46 G.E. James, E.M. Harrell, C. Bracikowski, K. Wiesenfeld, R. Roy: Opt. Lett. **15**, 1141 (1990)
- 10.47 V. Magni, G. Cerullo, S. DeSilvestri, O. Svelto, L.J. Qian, M. Danailov: Opt. Lett. **18**, 2111 (1993)
- 10.48 J.J. Chang, E.P. Dragon, C.A. Ebbers, I.L. Bass, C.W. Cochran: In *OSA Adv. Solid-State Lasers*, February, 2–4, 1998, post deadline paper pd 15-1
- 10.49 E.C. Honea, C.A. Ebbers, R.J. Beach, J.A. Speth, J.A. Skidmore, M.A. Emanuel, S.A. Payne: Opt. Lett. **23**, 1203 (1998)
- 10.50 J.E. Murray, S.E. Harris: J. Appl. Phys. **41**, 609 (1970)
- 10.51 O. Bernecker: IEEE J. Quantum Electron. **QE-9**, 897 (1973)
- 10.52 J. Falk: IEEE J. Quantum Electron. **QE-11**, 21 (1975)
- 10.53 W. Seka, S.D. Jacobs, J.E. Rizzo, R. Boni, R.S. Craxton: Opt. Commun. **34**, 469–473 (1980)
- 10.54 R.S. Craxton: IEEE J. Quantum Electron. **QE-17**; 1771 (1981); Opt. Commun. **34**, 474 (1980)
- 10.55 A.D. Hays, L.R. Marshall, R. Burnham: In *Advanced Solid-State Lasers* (Hilton Head, SC) (OSA, Washington, DC, 1991), postdeadline paper PdP8
- 10.56 H. Hemmati, J.R. Lesh: Opt. Lett. **19**, 1322 (1994)
- 10.57 J. Kasinski, P. Bournes, D. DiBiase, R. Burnham: In *CLEO'93*, Baltimore, MD, paper CW11; *Tech. Digest Ser.* **11**, 274 (OSA, Washington, DC, 1993)
- 10.58 G.J. Linford, B.C. Johnson, J.S. Hildum, W.E. Martin, K. Snyder, R.D. Boyd, W.L. Smith, C.L. Vercimak, D. Eimerl, J.T. Hunt: Appl. Opt. **21**, 3633 (1982)
- 10.59 J.A. Giordmaine, R.C. Miller: Phys. Rev. Lett. **14**, 973 (1965)
- 10.60 R.G. Smith: In *Laser Handbook I*, ed. by F.T. Arecchi, E.O. Schultz-DuBois (North-Holland, Amsterdam, 1972) pp. 837–895; also *Lasers*, Vol. 4, ed. by A.K. Levine, A.J. De Maria (Dekker, New York, 1976) pp. 189–307
- 10.61 S.J. Brosnan, R.L. Byer: IEEE J. Quantum Electron. **QE-15**, 415–443 (1979)
- 10.62 R.L. Byer: In *Quantum Electronics: A Treatise*, Vol. I, Pt. B, ed. by H. Rabin, C.L. Tang (Academic, New York, 1973) pp. 587–702
- 10.63 G.D. Boyd, A. Ashkin: Phys. Rev. **146**, 198 (1966)
- 10.64 L.R. Marshall, A.D. Hays, J.J. Kasinski, R. Burnham: In *Adv. Solid-State Lasers*, Salt Lake City, UT (OSA Washington, DC, March 1990), postdeadline paper WC8PD-2
- 10.65 J.J. Kasinski, R. Burnham: In *CLEO'90* (Anaheim, CA), Dig. Tech. Papers, paper CMF5
- 10.66 L.R. Marshall, A.D. Hays, R. Burnham: In *CLEO'90* (Anaheim, CA), Dig. Tech. Paper, post-deadline paper CPDP35-1
- 10.67 Castech-Phoenix, Inc., Fuzhou, China, Data Sheet KTP
- 10.68 J.E. Bjorkholm: IEEE J. Quantum Electron. **QE-7**, 109 (1971)
- 10.69 M.J.T. Milton, T.D. Gardiner, G. Chourdakis, P.T. Woods: Opt. Lett. **19**, 281 (1994)
- 10.70 R.L. Burnham: Final Report Solid-State Mid Infrared Source, Contract: DAAB07-87-C-F074, Fibertek, Inc., 1998
- 10.71 J. Yao, W. Sheng, W. Shi: J. Opt. Soc. Am., B **9**, 891 (1992)
- 10.72 J.W. Yao, T.S. Fahlen: J. Appl. Phys. **55**, 65 (1984)
- 10.73 K. Kato: IEEE J. Quantum Electron. **QE-27**, 1137 (1991)
- 10.74 D. Eimerl: J. Appl. Phys. **62**, 1968 (1987)
- 10.75 C.L. Tang, W.R. Bosenberg, T. Ukachi, R. Lane, L. Cheng: Laser Focus World, (Oct. 1990) p. 107

- 10.76 K. Kato: IEEE J. Quantum Electron. **QE-27**, 1137 (1991)
- 10.77 J.T. Lin, J.L. Montgomery: Opt. Commun. **75**, 315–320 (1990)
- 10.78 R. Burnham, R.A. Stolzenberger, A. Pinto: IEEE Photon. Technol. Lett. **1**, 27–28 (1989)
- 10.79 R.P. Jones: In *Solid-State Lasers and Nonlinear Crystals*, SPIE Proc., Vol. 2379 ed. by G.J. Quarks, L. Esterowitz, L.K. Cheng, (1995) p. 357
- 10.80 W.R. Bosenberg, L.K. Cheng, J.D. Bierlein: In *Adv. Solid-State Lasers and Compact Blue-Green Lasers*, New Orleans, LA, Vol. 2 (OSA, Washington, DC, 1993) pp. 134–135
- 10.81 T. Chuang, J. Kasinski, H.R. Verdun: In *TOPS on Advanced Solid State Lasers*, Vol. 1, (OSA, Washington, DC, 1996) p. 150
- 10.82 S. Chandra, T.H. Allik, J.A. Hutchinson, R. Utano, G. Catella: In *TOPS Advanced Solid State Lasers*, Vol. 10, (OSA, Washington, DC, 1997) p. 270
- 10.83 S. Chandra, T.H. Allik, G. Catella, J.A. Hutchinson: In *Advanced Solid-State Lasers*, Coeur d'Alene, ID (OSA, Washington, DC, 1998) p. 102, paper AMD5-1
- 10.84 M.M. Fejer, G.A. Magel, D.H. Jundt, R.L. Byer: IEEE J. Quantum Electron. **QE-28**, 2631 (1992)
- 10.85 L.E. Myers, R.C. Eckardt, M.M. Fejer, R.L. Byer: J. Opt. Soc. Am., B **12**, 2102 (1995)
- 10.86 L.E. Myers, W.R. Bosenberg: IEEE J. Quantum Electron. **QE-33**, 1663 (1997)
- 10.87 D.H. Jundt: Opt. Lett. **22**, 1553 (1997)
- 10.88 L.E. Myers, W.R. Bosenberg, J.I. Alexander, M.A. Arbore, M.M. Fejer, R.L. Byer: In *Advanced Solid State Laser Conference*, San Francisco (OSA, Washington, DC, 1996), postdeadline paper PD5-1
- 10.89 W.R. Bosenberg, A. Drobshoff, L.E. Meyers: In *Advanced Solid State Laser Conference*, San Francisco (OSA, Washington, DC, 1996), Tech. Digest, p. 68, paper WD1-1
- 10.90 T. Chuang, R. Burnham: Opt. Lett. **23**, 43 (1998)
- 10.91 T. Chuang, R. Burnham: In *Advanced Solid-State Laser Conference*, Boston, MA (OSA, Washington, DC, 1999), Tech. Digest, p. 118, paper ME3-1
- 10.92 K.C. Burr, C.L. Tang: Opt. Lett. **22**, 1458 (1997)
- 10.93 T.P. Grayson, L.E. Myers, M.D. Nelson, V. Dominic: In *Advanced Solid State Laser Conference*, San Francisco, CA 1996 (OSA, Washington, DC), Tech. Digest, p. 71, paper WD2-1
- 10.94 G.D. Miller, R.G. Batchko, W.M. Tulloch, D.R. Weise, M.M. Fejer, R.L. Byer: Opt. Lett. **22**, 1834 (1997)
- 10.95 M. Taya, M.C. Bashaw, M.M. Fejer: Opt. Lett. **21**, 857 (1996)
- 10.96 Y. Furukawa, K. Kitamura, S. Takekawa, K. Niwa, H. Hatano: Opt. Lett. **23**, 1892 (1998)
- 10.97 J.P. Meyn, M.M. Fejer: Opt. Lett. **22**, 1214 (1997)
- 10.98 M.E. Klein, D.H. Lee, J.P. Meyn, B. Beier, K.J. Boller, R. Wallenstein: Opt. Lett. **23**, 831 (1998)
- 10.99 T. Kartaloglu, K.G. Köprülü, O. Aytür, M. Sundheimer, W.P. Risk: Opt. Lett. **23**, 61 (1998)
- 10.100 V. Pasiskevicius, S. Wang, H. Karlsson, J.A. Tellefsen, F. Laurell: In *Advanced Solid-State Lasers*, Coeur d'Alene, ID (OSA, Washington, DC, 1998) p. 183
- 10.101 T. Chang, R. Burnham: In *OSA TOPS Adv. Solid-State Lasers*, ed. by M.M. Fejer, H. Injeyan, U. Keller Vol. 26, (1999) p. 534
- 10.102 R. Dabu, A. Stratian, C. Fenic, C. Luculescu, L. Muscalu: Opt. Eng. **40**, 455 (2001)
- 10.103 P.B. Phua, K.S. Lai, R. Wu: Appl. Opt. **39**, 1435 (2000)
- 10.104 K.L. Vodopyanov, P.G. Schunemann: Opt. Lett. **28**, 441 (2003)
- 10.105 P.A. Budni, C.R. Ibach, S.D. Setzler, L.A. Pomeranz, M.L. Lemons, P.A. Ketteridge, E.J. Gustafson, Y.E. Young, P.G. Schunemann, T.M. Pollak, R.T. Castro, E.P. Chicklis: In *Adv. Solid-State Photonics*, February 2003, postdeadline paper PD12
- 10.106 M.J. Roskar, C.L. Tang: J. Opt. Soc. Am., B **2**, 691 (1985)
- 10.107 T.Y. Fan, R.C. Eckardt, R.L. Byer, J. Nolting, R. Wallenstein: Appl. Phys. Lett. **53**, 2014 (1988)
- 10.108 A. Fix, C. Huang, T. Shroder, R. Wallenstein: In *CLEO'90*, Anaheim, CA, Tech. Digest, p. 248, paper CWE8
- 10.109 J.G. Haub, M.J. Johnson, B.J. Orr, R. Wallenstein: In *CLEO'91*, Baltimore, MD, Tech. Digest, paper CFM1
- 10.110 W.L. Bosenberg, L.K. Cheng, C.L. Tang: Appl. Phys. Lett. **54**, 13 (1989)
- 10.111 L.R. Marshall, A. Kaz, O. Aytur: Opt. Lett. **18**, 817 (1993)

- 10.112 M.E. Klein, C.K. Laue, D.H. Lee, K.J. Boller, R. Wallenstein: Opt. Lett. **25**, 490 (2000)
- 10.113 U. Stroessner, J.P. Meyn, R. Wallenstein, P. Urenski, A. Arie, G. Rosenman, J. Mlynek, S. Schiller, A. Peters: J. Opt. Soc. Am. **19**, 1419 (2002)
- 10.114 W.R. Bosenberg, J.I. Alexander, L.E. Myers, R.W. Wallace: Opt. Lett. **23**, 207 (1998)
- 10.115 W.R. Bosenberg, A. Drobshoff, J.I. Alexander, L.E. Myers, R.L. Byer: Opt. Lett. **21**, 1336 (1996)
- 10.116 D.J.M. Stothard, M. Ebrahimzadeh, M.H. Dunn: Opt. Lett. **23**, 1895 (1998)
- 10.117 U. Stroessner, A. Peters, J. Mlynek, S. Schiller, J.P. Meyn, R. Wallenstein: Opt. Lett. **24**, 1602 (1999)
- 10.118 T.J. Edwards, G.A. Turnbull, M.H. Dunn, M. Ebrahimzadeh, H. Karlsson, G. Aridsson, F. Laurell: **23**, 837 (1998)
- 10.119 C.W. Hoyt, M. Sheik-Bahae, M. Ebrahimzadeh: Opt. Lett. **27**, 1543 (2002)
- 10.120 R.L. Byer: Frequency conversion via stimulated Raman scattering. Electro-Optical Systems Design, February 1980, pp. 24–29
- 10.121 Y.R. Shen: Stimulated Raman scattering, in *Topics Appl. Phys.*, Vol. 8: *Light Scattering in Solids I*, Vol 2nd edn., ed. by M. Cardona, (Springer, Berlin Heidelberg, 1983) Chap. 7
- 10.122 G.L. Eesley: *Coherent Raman Spectroscopy* (Pergamon, New York, 1981); A. Owyoung: In *Chemical Applications of Nonlinear Raman Spectroscopy*, ed. by B. Harvey (Academic, New York, 1981) pp. 281–320
- 10.123 W. Kaiser, M. Maier: In *Laser Handbook*, Vol. II, ed. by F.T. Arecchi, E.O. Schulz-DuBois (North-Holland, Amsterdam, 1972)
- 10.124 F.P. Milanovich: In *Handbook of Laser Science and Technology*, Vol. 3, ed. by M.J. Weber (CRC, Boca Raton, FL, 1986) p. 283
- 10.125 H.M. Pask, S. Myers, J.A. Piper, J. Richards, T. McKay: Opt. Lett. **28**, 435 (2003)
- 10.126 H.M. Pask, J.A. Piper: Opt. Lett. **24**, 1490 (1999)
- 10.127 P. Cerny, H. Jelinkova: Opt. Lett. **27**, 360 (2002)
- 10.128 H. Ogilvy, H. Pask, J. Piper, T. Omatsu: paper MB11-1. In Tech. Digest Adv. Solid-State Photonics, 2003 San Antonio, Texas (Opt. Soc. Am. Washington, D.C. 2003)
- 10.129 D.G. Bruns, D.A. Rockwell: High energy Raman resonator. Hughes Aircraft Comp. Culver City, CA, Final Report, Report FR-81-72-1035, 1981
- 10.130 B.Ya. Zel'dovich, Y.I. Popovichev, V.V. Ragul'skii, F.S. Faizullov: Sov. Phys. JETP **15**, 109 (1972)
- 10.131 O.Yu Nosach, V.I. Popovichev, V.V. Ragul'skii, F.S. Faizullov: JETP Lett. **16**, 435 (1972)
- 10.132 D.T. Hon: Opt. Eng. **21**, 252–256 (1982)
- 10.133 I.D. Carr, D.C. Hanna: Appl. Phys. B **36**, 83 (1985)
- 10.134 D.A. Rockwell: IEEE J. Quantum Electron. **QE-24**, 1124 (1988)
- 10.135 D.M. Pepper: Opt. Eng. **21**, 156–286 (1982), special issue on non-linear optical phase conjugation
- 10.136 R.A. Fisher (ed.): *Optical Phase Conjugation* (Academic, New York, 1983)
- 10.137 B.Ya. Zel'dovich, N.F. Pilipetsky, V.V. Shkunov: *Springer Ser. Opt. Sci.*, Vol. 42: *Principles of Phase Conjugation* (Springer, Berlin Heidelberg, 1985)
- 10.138 D.M. Pepper: In *Laser Handbook*, Vol. 4, ed. by M.L. Stich, M. Bass (North-Holland, Amsterdam, 1985) pp. 333–485
- 10.139 N.F. Andreev, M.A. Dvoretskii, A.A. Leshchev, V.G. Manishin, G.A. Pasmanik, T.P. Samarina: Sov. J. Quantum Electron. **15**, 928 (1985)
- 10.140 A. Kummrow, H. Meng: Opt. Commun. **83**, 342 (1991)
- 10.141 R. Menzel, H.J. Eichler: Phys. Rev. A **46**, 7139 (1992)
- 10.142 R. Menzel, D. Schulze: In *Proc. Int'l Summer School on Applications of Nonlinear Optics*, Prague, 1993
- 10.143 D. Cotter, D.C. Hanna, R. Wyatt: Appl. Phys. **8**, 333 (1975)
- 10.144 M. Maier, G. Renner: Phys. Lett. A **34**, 299–300 (1971)
- 10.145 H.J. Eichler, A. Haase, R. Menzel: IEEE J. Quantum Electron. **QE-31**, 1265 (1995)
- 10.146 H.J. Eichler, O. Mehl, J. Eichler: In *Conf. on Solid State Lasers VIII*, San Jose, CA, January 1999, SPIE. Proc., Vol. 3613 (1999) p. 166
- 10.147 V.N. Belousov, Yu.K. Nizienko: Opt. Spectrosc. (USSR) **58**, 563 (1985)

- 10.148 N.G. Basov, V.F. Efimkov, I.G. Zubarev, A.V. Kotov, S.I. Mikhailov, M.G. Smirnov: JETP Lett. **28**, 197 (1978)
- 10.149 H.J. Eichler, A. Haase, R. Menzel: In *Proc. Int'l Summer School and Top. Meeting on Applications on Nonlinear Optics*, Prague, 1993
- 10.150 J.J. Eichler, R. Menzel, D. Schumann: Appl. Opt. **31**, 5038 (1992)
- 10.151 M. Ostermeyer, A. Heuer, R. Menzel: IEEE J. Quantum Electron. **QE-34**, 372 (1998)

Chapter 11

- 11.1 Test method for the laser-radiation-induced damage threshold of optical surfaces. ISO 11254 (The International Organization for Standardization, 1992)
- 11.2 S.C. Seitel, A. Giesen, J. Becker: Proc. SPIE **1848**, 2 (1992)
- 11.3 J. Becker, A. Bernhardt: Proc. SPIE **2114**, 703 (1993)
- 11.4 *Laser-Induced Damage in Optical Materials* (1969–1989), National Bureau of Standards (National Institute of Standards and Technology after 1986), Special publication, ed. by H. E. Bennett, L.L. Chase, A.J. Glass, A.H. Guenther, D. Milam, B.E. Newman, M.J. Soileau
- 11.5 *Laser-Induced Damage in Optical Materials*: SPIE Proc. **1441** (1990), SPIE Proc. **1624** (1991), SPIE Proc. **1848** (1992), SPIE Proc. **2114** (1993), each ed. by H.E. Bennett, A.H. Guenther, L.O. Chase, B.E. Newnam, M.J. Soileau; SPIE Proc. **2428** (1994), SPIE Proc. **2714** (1995), SPIE Proc. **2966** (1996), ed. by H.E. Bennett, A.H. Guenther, M.R. Kozlowski, B.E. Newnam, M.J. Soileau; SPIE Proc. **3244** (1997), ed. by G.J. Exarhos, A.H. Guenther, M.R. Kozlowski, M.J. Soileau.
- 11.6 R.M. Wood (ed.): Selected papers on laser damage in optical materials. SPIE Milestone Series MS24, 1990
- 11.7 N. Bloembergen: Appl. Opt. **12**, 661 (1973)
- 11.8 N.L. Boling, G. Dubé: Appl. Phys. Lett. **23**, 658 (1973)
- 11.9 N. Bloembergen: IEEE J. Quantum Electron. **QE-10**, 375 (1974)
- 11.10 F.Y. Génin, A. Salleo, T.V. Pistor, L.L. Chase: J. Opt. Soc. Am. A **18**, 2607 (2001)
- 11.11 N.L. Boling, M.D. Crisp, G. Dubé: Appl. Opt. **12**, 650 (1973)
- 11.12 M.D. Crisp, N.L. Boling, G. Dubé: Appl. Phys. Lett. **21**, 364 (1972)
- 11.13 M.D. Feit, A.M. Rubenchik, D.R. Faux, R.A. Riddle, A. Shapiro, D.C. Eder, B.M. Penetrante, D. Milam, F.Y. Genin, M.R. Kozlowski: SPIE Proc. **2966**, 417 (1996)
- 11.14 R.W. Hopper, D.R. Uhlmann: J. Appl. Phys. **41**, 4023 (1970)
- 11.15 E.S. Bliss: Opto-electronics **3**, 99 (1971)
- 11.16 J.R. Bettis, R.A. House II, A.H. Guenther: Natl. Bur. Stand. (U.S.) Spec. Publ. **462**, 338 (1976)
- 11.17 R.M. Wood: *Laser Damage in Optical Materials* (Hilger, Boston, 1986)
- 11.18 J.H. Campbell, F. Rainer, M.R. Kozlowski, C.R. Wolfe, I.M. Thomas, F.P. Milanovich: Lawrence Livermore National Laboratory, ICF Quarterly Report (January–March 1991) p. 41
- 11.19 B.C. Stuart, M.D. Feit, S. Herman, A.M. Rubenchik, B.W. Shore, M.D. Perry: Phys. Rev. Lett. **74**, 2248 (1995)
- 11.20 B.C. Stuart, M.D. Feit, S. Herman, A.M. Rubenchik, B.W. Shore, M.D. Berry: Phys. Rev. B **53**, 1749 (1996)
- 11.21 B.C. Stuart, M.D. Perry, R.D. Boyd, J.A. Britten, B.W. Shore, M.D. Feit, A.M. Rubenchik: In *Generation, Amplification, and Measurement of Ultrashort Laser Pulses II*, SPIE Proc., Vol. 2377 ed. by F.W. Wise, C.P.J. Barty. (SPIE, Wellingham, WA, 1995) p. 247
- 11.22 S.C. Jones, P. Braunlich, R.T. Casper, X.A. Shen, P. Kelly: Opt. Eng. **28**, 1039 (1989)
- 11.23 F. Rainer, L.J. Atherton, J.T. DeYoreo: SPIE Proc. **1848**, 46 (1992)
- 11.24 N. Kuzuu, K. Yoshida, H. Yoshida, T. Kamimura, N. Kamisugi: Appl. Opt. **38**, 2510 (1999)
- 11.25 J.H. Campbell, F. Rainer: Report UCRL-JC-109255, Lawrence Livermore Laboratory, Livermore, CA; In *SPIE '92 Conf. Proc.*, San Diego, CA, 1992
- 11.26 G.Y. Kolodnyi, E.V. Levchuk, V.V. Novopashin, O.E. Sidoryuk: Laser Optoelektronika **28**, 61 (1996)
- 11.27 L. Sheehan, M. Kozlowski, F. Rainer, M. Staggs: SPIE Proc. **2114**, 559 (1994)

- 11.28 C.R. Wolfe, M.R. Kozlowski, J. Campbell, F. Rainer, A.J. Morgan, R.P. Gonzales: NIST (U.S.) Spec. Publ. **801**, 360 (1990)
- 11.29 M.R. Kozlowski, M. Staggs, F. Rainer, J. Stathis: SPIE Proc. **1441**, 269 (1991)
- 11.30 M.R. Kozlowski, I.M. Thomas, J.H. Campbell, R. Rainer: In *Thin Films for Optical Systems*, SPIE Proc., Vol. 1782 ed. by K.H. Guenther (SPIE, Wellingham, WA, 1992) p. 105
- 11.31 N. Kaiser, B. Anton, H. Jänen, K. Mann, E. Eva, C. Fischer, R. Henking, D. Ristau, P. Weissbrodt, D. Mademann, L. Raupach, E. Hacker: SPIE Proc. **2428**, 400 (1994)
- 11.32 A. Fornier, C. Cordillot, D. Bernardino, D. Ausserre, F. Paris: SPIE Proc. **2714**, 383 (1995)
- 11.33 M. Richardson, M.J. Soileau, P. Beaud, R. DeSalvo, S. Garnov, D.J. Hagan, S. Klimentov, K. Richardson, M. Sheik-Bahae, A.A. Said, E. Van Stryland, B.H.T. Chai: SPIE Proc. **1848**, 392 (1992)
- 11.34 R.M. Wood, R.T. Taylor, R.L. Rouse: Opt. Laser Technol. **6**, 105 (1975)
- 11.35 T.S. Rose, M.S. Hopkins, R.A. Fields: IEEE J. Quantum Electron. **QE-31**, 1593 (1995)
- 11.36 N. Neuroth, R. Hasse, A. Knecht: NBS Spec. Publ. **356**, 3–14 (1971); In *Damage in Laser Materials*, ed. by A.J. Glass, A.H. Guenther Natl. Bur. Standards (U.S.)
- 11.37 K.E. Montgomery, F.P. Milanovich: J. Appl. Phys. **68**, 15 (1990)
- 11.38 F. Rainer, L.J. Atherton, J.H. Campbell, F.P. DeMarco, M.R. Kozlowski, A.J. Morgan, M.C. Staggs: SPIE Proc. **1624**, 116 (1991)
- 11.39 J. Chang, E. Dragon, C. Ebbers, I. Bass, C. Cochran: In *OSA Trends in Optics and Photonics, Vol. 19: Advanced Solid-State Lasers*, ed. by W.R. Bosenberg, M.M. Fejer (Opt. Soc. Am., Washington, DC, 1998) p. 300
- 11.40 R.P. Jones, A.M. Floener, J.S. Runkel: Presented at *26th Annual Boulder Damage Symposium*, 1994
- 11.41 R.P. Jones: In *Solid-State Lasers and Nonlinear Crystals*, SPIE Proc., Vol. 2379 ed. by G.J. Quarles, L. Esterowitz, Z.K. Cheng (SPIE, Wellingham, WA, 1995) p. 357
- 11.42 M.P. Scripsick, G.E. Ruland: *OSA TOPS, Vol. 19: Advanced Solid-State Lasers*, ed. by W.R. Bosenberg, M.M. Fejer (Opt. Soc. Am., Washington, DC, 1998) p. 85
- 11.43 L.E. Halliburton, M.P. Scripsick: SPIE Proc. **2379**, 235 (1995)
- 11.44 B. Boulanger, J.P. Féve, Y. Guillien: Opt. Lett. **25**, 484 (2000)
- 11.45 F.C. Zumsteg, J.D. Bierlein, E.E. Gier: J. Appl. Phys. **47**, 4980 (1976)
- 11.46 J.K. Tyminski: J. Appl. Phys. **70**, 5570 (1991)
- 11.47 J.C. Jacco, D.R. Rockafellow, E.A. Teppo: Opt. Lett. **16**, 1307 (1991)
- 11.48 M.P. Scripsick, D.N. Loiacono, J. Rottenberg, S.H. Goellner, L.E. Halliburton, F.K. Hopkins: Appl. Phys. Lett. **66**, 3428 (1995)
- 11.49 G.M. Laiacono, D.N. Laiacono, T. McGee, M. Babb: J. Appl. Phys. **72**, 2705 (1992)
- 11.50 J.P. Féve, B. Boulanger, G. Marnier, H. Albrecht: Appl. Phys. Lett. **70**, 277 (1997)
- 11.51 M.P. Scripsick, G.J. Edwards, L.E. Halliburton, R.F. Belt, G.M. Loiacono: J. Appl. Phys. **76**, 733 (1994)
- 11.52 B. Boulanger, M.M. Fejer, R. Blachman, P.F. Bordui: Appl. Phys. Lett. **65**, 2401 (1994)
- 11.53 P.A. Morris, A. Ferretti, M.G. Roeloffs, J.D. Bierlein, T.M. Baer: SPIE Proc. **1848**, 24 (1992)
- 11.54 W.D. Fountain, L.M. Osterink, G.A. Massey: In NBS Spec. Publ. **356**, 91–103 (1971); In *Damage in Laser Materials*, ed. by A.J. Glass, A.H. Guenther Natl. Bur. Standards (U.S.)
- 11.55 A.M. Glass: Opt. Eng. **17**, 470 (1978)
- 11.56 D.A. Bryan, R.R. Rice, R. Gerson, H.E. Tomaschke, K.L. Sweeney, L.E. Halliburton: Opt. Eng. **24**, 138–143 (1985)
- 11.57 V. Pruner, P.G. Kazansky, J. Webjörn, P.St.J. Russell, D.C. Hanna: Appl. Phys. Lett. **67**, 1957 (1995)
- 11.58 G.A. Magel, M.M. Fejer, R.L. Byer: Appl. Phys. Lett. **56**, 108 (1990)
- 11.59 M. Taya, M.C. Bashaw, M.M. Fejer: Opt. Lett. **21**, 857 (1996)
- 11.60 M.A. Acharekar, L.H. Morton, E.W. Van Stryland: SPIE Proc. **2114**, 69 (1993)
- 11.61 S. Chandra, T.H. Allik, G. Catella, J.A. Hutchinson: In *Advanced Solid-State Laser Conf. 1998*, Coeur d'Alene, ID, p. 102
- 11.62 M.R. Kozlowski, R. Chow: SPIE Proc. **2114**, 640 (1993)

- 11.63 Q. Zhao, Z.X. Fan, H. Qiu, Y. Liu, Z.J. Wang: SPIE Proc. **2966**, 238 (1996)
11.64 B. Steiger, H. Brausse: SPIE Proc. **2428**, 559 (1994)
11.65 R.H. Sawicki, C.C. Shang, T.L. Swatloski: SPIE Proc. **2428**, 333 (1994)
11.66 A. Bodemann, N. Kaiser, M. Kozlowski, E. Pierce, C. Stoltz: SPIE Proc. **2714**, 395 (1995)
11.67 I.M. Thomas: SPIE Proc. **2114**, 232 (1993)
11.68 N. Kaiser: Laser Optoelektronik **28**, 52 (1996)
11.69 C. Li, Z. Li, Y. Sun: SPIE Proc. **2114**, 280 (1993)
11.70 S.V. Garnov, S.M. Klimentov, A.A. Said, M.J. Soileau: SPIE Proc. **1848**, 162 (1992)
11.71 K.L. Lewis, A.M. Pitt, M. Corbett, R. Blacker, J. Simpson: SPIE Proc. **2966**, 166 (1996)
11.72 T.L. Barber: Rev. Sci. Instrum. **40**, 1630 (1969)
11.73 F.E. Hovis, B. Shepherd, C. Radcliffe, H. Maliborski: SPIE Proc. **2428**, 72 (1994)

Appendix A

- A.1 Courtesy; Coherent, Inc. Laser Group, 5100 Patrick Henry Drive, Santa Clara, CA
A.2 American National Standards Institute, 11 West 42nd Street, New York, NY 10036
A.3 D. Sliney, M. Wolbarsht: *Safety with Lasers and Other Optical Sources* (Plenum, New York, 1980)
A.4 *LIA Laser Safety Guide*, Laser Institute of America, 12424 Research Parkway, Suite 125, Orlando, FL
A.5 Center for Devices and Radiological Health (HFZ-300), 8757 Georgia Avenue, Silver Spring, MD 20910. Performance Standards for Laser Products, Regulation 21CFR1040 (latest revision, April 1993)
A.6 International Electrotechnical Committee (IEC), Geneva, Switzerland. IEC Standard 825-1 (1993). Radiation Safety of Laser Products, Equipment Classifications, Requirements and User's Guide

Subject Index

- Absorption, definition 15, 22–25
curves 58, 64, 66, 72, 78, 85, 89, 92
efficiency, pump radiation 114, 115, 337,
338, 355, 377, 424
- Acoustooptic
modulator 562, 565, 569–572
Q-switch 514–522
- Actinides 50
- Active mirror amplifier 471
- Active mode locking; *see* Modelocking
- Additive pulse mode locking 546–548
- AgGaSe₂ nonlinear crystal 651, 650
- Airy disc 217
- Alexandrite laser 81, 84–88
- Alignment sensitivity, resonator 235–238, 295,
296
- Aluminate host 42
- AM modelocking 560–563, 569–572
- Amplified spontaneous emission 117, 118,
195–199
- Amplifier, pulse operation
theory 158–163
Nd:Glass 171–177
Nd:YAG 163–171
multipass 177–180
regenerative 180–187
distortions, losses 190–200
chirped pulse 584–586
- Amplifier, steady-state operation 188–190
- Amplitude fluctuation; *see* Output fluctuations
- Aperture length 611, 639
- Arc lamp; *see* Flashlamps or Krypton arc lamps
- Astigmatism, resonator 250–252, 552
- Atomic energy level; *see* Energy level
- Atomic line shapes 18–22
- Axial modes; *see* Longitudinal modes
- Ba₂NaNb₅O₁₅ crystal 595, 611, 621
- BBO crystal properties 612, 616, 637
- Beam divergence, definition 215–217, 225, 226
- Beam overlap efficiency 115, 116, 147, 151;
see also Mode matching efficiency
- Beam quality factor M 225–227
- BEL, laser host 44
- Beryllate, laser host 44
- Biaxial crystal 603, 612
- Birefringence
correction 242, 294, 453–457
electrically induced 499–508
thermally induced 445–451
- Birefringent filter 297, 298
- Blackbody radiation 12, 305
- Bleachable dye; *see* Saturable absorber
- Bohr's frequency relation 11
- Boltzmann distribution 13, 14, 26
- Bragg reflection 516–519
- Brewster angle 250, 251, 544, 553
- Brightness, definition 158
- Brillouin scattering; *see* Stimulated Brillouin
scattering
- Cavity dumping 529–533, 564–568
- CBO/CLBO crystal 617
- CDA crystal 596
- Ceramic, host material 45
- Cerium 49
- Charging unit, power supply 316–323
- Chirped mirrors 578, 579, 581
- Chromium lasers 81, 82; *see also* Ruby laser,
Alexandrite laser
- Circulating power 109–111, 258
- Cladding, active material 175, 197, 418
- Coatings; *see* Dielectric thin films
- Coherence length
frequency doubling 396
laser radiation 17, 262, 263
phase conjugation 674–676
- Compensation, thermal effects 451–457
- Collision line broadening 19
- Co:MgF₂ laser 82, 83
- Concave-convex resonator 219, 221, 241,
242–248
- Concentric resonator 219, 220
- Confocal parameter 215
- Confocal resonator 219, 220
- Continuous arc lamp; *see* Krypton arc lamps

- Conversion factors 200, 595, 708–710
 Cooling techniques
 laser medium 481–487
 arc lamps 301, 304, 313, 335, 336
 diode arrays 302, 346–350, 358–361,
 395–407
 conduction, 367, 402–404, 407, 485, 486
 gases, air 486, 487
 liquids 382–392, 481–485
 Coolant properties 482
 Coupling/transfer efficiency 117, 370, 373–376
 Cr:Forsterite laser 82, 575, 583
 Cr:GSGG laser 81, 82
 Cr:KZnF₃ laser 82
 Cr:LiCAF laser 92
 Cr:LiSAF laser 82, 91–94, 575, 582
 Critical phase matching 610, 611
 Cross section, stimulated emission 24, 25, 32,
 55, 61, 62, 68, 71, 74, 84, 90, 93, 96, 100
 CW arc lamps; *see* Krypton arc lamps
 Czochralski crystal growth 59

 Damage, optically induced 680–701
 Damage threshold 688–698
 Dielectric thin films 694–698
 laser crystals 688, 689
 nonlinear crystals 690–694
 Decay time, resonator 34, 35
 Degenerate energy level 14
 Dephasing factor, definition 597
 Depolarization losses 446–457, 505, 511–513
 Depopulation losses 117, 118, 194–199
 Dichroic mirror 619, 620, 630, 656–659
 Dielectric thin films 279–282, 578, 694–698
 Diffraction grating 584–586
 Diffraction losses, resonator 223–225
 Diode arrays; *see* laser diodes
 Dipolar line broadening 20
 Disk laser amplifier 172, 175–180, 418–422,
 469–473; *see also* Slab laser
 Dispersion compensation 576–579
 Dispersive mirrors; *see* Chirped mirrors
 Doppler broadening 21
 Dye saturable absorber 522, 523, 534, 535,
 542–546
 Dysprosium 50

 Edge pumped slab 467–469
 Efficiency factors 112–123, 143, 147, 151, 167,
 171, 394
 Einstein coefficients 14, 15, 17, 32
 Electronic feedback loop 270, 273, 277,
 572–574

 Electrooptic effect 499–508
 End-pumped lasers 148–152, 181, 266, 276,
 407–418, 473–481, 556, 560, 561, 582
 Energy extraction, amplifier 160–167, 176
 Energy level
 diagram 28, 29, 52, 56, 63, 74, 77, 86, 89, 95,
 98
 nomenclature 45–48
 Energy storage 118, 163, 170, 491
 Energy extraction efficiency 116, 117, 161–166,
 170, 171, 184, 492
 Energy storage efficiency 118, 158, 170, 173,
 491; *see also* Extraction efficiency
 Energy transfer input /output 112–118, 382,
 394, 420
 Erbium 48
 Er:Glass laser 75–79
 Er:YAG laser 73–75
 Er:YLF laser 75
 Etalon 255, 263–265
 Europium 49
 Excited state absorption 80, 81, 88, 524, 525
 Explosion energy, flashlamp 311, 312
 Extraction efficiency 117, 118, 122, 123,
 160–162, 170, 491, 492
 Eye damage 702–707

 Fabry-Perot interferometer 255–259, 558;
 see also Resonator, optical
 Face-pumped lasers 171–176, 418–422,
 469–473
 FAP laser host 43
 Faraday effect 153
 Faraday rotator 152, 155, 270, 677
 Feedback loop; *see* Electronic feedback loop
 Femtosecond lasers 555, 575–584
 Filament lamp; *see* Tungsten filament lamp
 Finesse, interferometer 257
 Flashlamps
 construction 301, 303, 304
 cooling 304, 313, 336, 384–392
 electrical characteristics 308, 309
 failure modes, lifetime 309–314
 operating conditions 314, 315
 optical characteristics 304–307
 Fluorescence 36, 107
 Fluorescent lifetime 36, 51, 55, 62, 64, 68, 71,
 78, 82, 84, 90, 93, 96, 100
 Fluorides, laser host 45
 FM modelocking 563, 564, 572–575
 Forbidden transition 31
 Fourier transform 539
 Four-level laser 29, 35, 36, 119–125

- Fractional thermal loading 423–425, 479
 Frequency control 274–276
 Frequency chirp 518, 540, 564
 Frequency doubling; *see* Second-harmonic generation
 Frequency stability 277, 278
 Fresnel number 223, 224, 282, 285
 Fringe visibility 262
 Fundamental mode, definition 215, 216;
see also Gaussian beam
- GaAlAs laser diodes; *see* Laser diodes
 g parameters, resonator 222, 232–236, 243
 Gadolinium 44, 49
 Gain coefficient, definition 119, 127, 162
 Gain, amplifier 159–161
 Gain saturation 108, 109, 122, 188
 Gain switching 133, 134
 Garnet, laser host 42
 Gaussian beam 215–217
 Gaussian temporal profile 537, 540
 Giant pulse; *see* Q-switch
 Glass, laser host 41
 Ground level 27–30
 GSGG, laser host 64–66
- Harmonic generation; *see* Second-harmonic generation
 Heat generation, laser material 423–426
 Heat removal; *see* Cooling techniques
 Heat transfer coefficient 427, 428
 Hemispherical resonator 219, 240
 Higher order modes 224–227
 Hole burning; *see* Spatial hole burning
 Holmium 49
 Homogeneous line broadening 19
 Hoop stress 438
 Host materials 40–45
- Idler wave 590, 634, 635
 Index matching; *see* Phase matching
 Indatrix, ellipsoid 440, 441, 502, 604–606
 Inhomogenous line broadening 20–22
 Injection seeding 268–271, 647, 662
 Interferometer; *see* Fabry-Perot interferometer
 Intracavity frequency doubling 618–624
 Inversion reduction factor 36
 Isolator; *see* Optical isolator
- KDP crystal, properties 502–506, 589, 602, 606, 612, 613, 628, 633
 Kerr effect 201–203, 501, 548–556, 591
- Kerr lens mode locking 543, 548–556
 sensitivity 549, 552, 553
 Krypton arc lamps
 electrical characteristics 336, 337
 mechanical design 301, 335
 spectral data 334, 336–339
 thermal considerations 335, 336
 KTP/KTA crystal properties 601–603, 612, 614, 615, 637, 641, 647–651, 690–693
- Large-radius mirror resonator 219
 Laser amplifier; *see* Amplifier
 Laser diode pumped systems
 end pumped 148–154, 266, 273–275, 407–418, 630
 side pumped 139–148, 165–171, 184–188, 287, 393–407, 567, 631, 656
 face pumped 179, 180, 367, 421, 472
 Laser diodes 340–366
 arrays 302, 345–351
 design 302, 342–351
 lifetime 361–363
 spatial profile 351–353
 spectral properties 353–358
 thermal issues 358–361, 347–350
 Laser rate equations 32–36
 Laser safety 702–707
 Laser oscillator
 threshold 103–108
 gain saturation 108, 109
 circulating power 109–111
 performance model 111–118
 output calculations 118–127
 diode pumped 139–152
 lamp pumped 134–139
 LBO crystal 612, 615, 616, 624, 637
 Lifetime broadening 19
 Light-pipe mode 199
 LiNbO_3 506–510, 603, 611, 612, 616, 651–655, 662
 Linewidth
 broadening effects 19–22
 control 263–268
 Schallow-Townes limit 267
 Longitudinal mode selection 263–268
 Longitudinal modes 210, 259–263
 Lorentzian lineshape 21, 22
- M-factor 225–227
 Metastable level 30, 31
 Microchip laser 276
 Mirror mounts 279
 Mode beating 271, 623, 624

- Modeling software 254, 255, 278, 398
 Mode locking, active 560–575
 system design 568–575
 theory 560–568
 transient 564–568
 Mode locking, passive 542–560
 theory 535–542
 coupled cavity modes 546–548
 Kerr lens 548–556, 580–583
 SESAM 556–560, 581, 582
 saturable dye 542–546
 Mode matching efficiency 409; *see also* Beam overlap efficiency
 Mode patterns 212, 214, 230
 radius 215, 226, 218–220, 224
 Mode selection
 longitudinal 263–273
 transverse 227–231
 Molybdates, laser host 44
 Monolithic laser 154, 265, 266, 270
 MOPA design 156–158, 166–170, 172, 670, 677
 Neodymium 48
 Nd:BEL crystal 44
 Nd:Cr:GSGG laser 64–66
 Nd:GdVO₄ crystal 44
 Nd:Glass laser
 systems 171–176, 418–420, 463–465,
 469–471
 material properties 61–64
 Nd:SOAP crystal 43
 Nd:YAB laser 619
 Nd:YAG laser
 flashlamp pumped 134–139, 164–166,
 384–387, 466
 diode side pumped 139–148, 165–171,
 184–187, 395–407, 567, 656
 end pumped 148–152, 266, 276, 407–418
 material properties 54–61
 damage 203–206, 688, 689
 thermal effects 428, 439, 445, 447–450,
 474–481
 Nd:YALO laser 42, 43, 677
 Nd:YLF laser 66–69, 181
 Nd:YVO₄ laser 69–73, 416, 417, 423–425, 468,
 528, 623,
 Neodymium 48
 Noncritical phase matching 610, 611
 Nonlinear coefficient 200, 548, 549, 575
 Nonlinear refractive index 200
 Nonlinear crystals, properties 611–617,
 649–655
 Nonlinear drive, definition 597
 Nonlinear optical effects 587–592
 Nonspherical aberration 191–193
 Nonuniform pumping 190, 378–381, 397, 431,
 450–452
 Optical coatings; *see* Dielectric thin films
 Optical isolator 152, 153, 181, 186, 270, 677
 Optical parametric oscillator 634–662
 configurations 634–637
 crystals 649–652
 examples 641–643, 645, 655–662
 performance modeling 637–646
 phase matching 634, 638, 641, 646, 653
 quasi phase matching 652–655
 wavelength/linewidth control 647–649
 Optical phase conjugation 669–679
 basic principles 669–671
 design issues 673–679
 materials 671–673
 Optical resonator; *see* Resonator
 Organic dye; *see* Saturable absorber
 Oscillator, threshold condition 103–108
 Output coupling 111, 117, 119, 121
 Output fluctuations 128–132, 271–273, 623,
 624
 Output vs input calculations 118–127
 Oxides, laser host 41–43
 Oxy sulfide, laser host 43
 Overlap integral 116
 Parasitic modes 199
 Passive mode locking 542–560
 Passive Q-switch 522–529
 Pentaphosphates 43, 44
 Periodically poled crystals 652–655
 PFN; *see* Pulse forming network
 Phase coherence, stimulated emission 17
 Phase matching 602–611, 634, 652–655
 Phase mismatch 593, 594, 638
 Phase conjugation; *see* Optical phase conjugation
 Phosphate, laser host 43
 Picosecond lasers 568–575
 Photoelastic effects 440–442
 Piezoelectric transducer 274, 276–278, 520, 572
 Piezooptic effect 509–511, 567, 570
 Planck's law 12
 Plane-parallel resonator 219, 221
 Plane wave impedance 595
 Plano-concave resonator 220
 Pockels cell Q-switch 499–516
 Population inversion 25–27, 159
 Porro prism resonator 252–254, 457, 512, 513
 Postlasing 508–511

- Potassium titanyl phosphate; *see* KTP
 Power supplies
 cw arc lamps 339, 340
 diode arrays 363–366
 flashlamps 315–334
 PPLN 637, 652–661
 Praeseodymium 49
 Prelasing 198, 199, 508, 509
 Pulse-bandwidth product 539–541, 562, 563
 Pulse forming network 323–331
 Pulse shape distortion 193, 194
 Pump band 28, 29
 Pump configurations 366–368
 Pump cavity, arc lamps
 radiation transfer 368–378
 mechanical design 381–392
 face pumped disks 418–420
 pump light distribution 378–381
 Pump arrangements, laser diodes
 side pumping, rods 393–401
 side pumping, slabs 401–407
 end pumping 407–418
 face pumped disks 421, 422
 Pump source efficiency 112, 113, 301, 337, 338, 355
 Pumping rate 33, 34, 119
 Quasi phasematching 652–655
 Quasi three or four level lasers 125, 126
 Q-switch, theory 117, 118, 488–498
 Q-switch devices
 acoustooptic 514–552
 electrooptical 499–516
 mechanical 498, 499
 passive 522–529
 Quality factor Q, definition 105
 Quantum efficiency 33, 36
 Quantum noise 272, 273
 Quantum well 343, 344, 557
 Quartz, optical transmission 306
 Radiation lifetime 15
 Radiation transfer efficiency 113
 Raman laser 662–669
 configurations 666
 examples 667–669
 theory 662–666
 Raman-Nath scattering 516
 Raman scattering; *see* Stimulated Raman scattering
 Rayleigh range 215, 217, 226
 Rare earth ions 46
 Rate equations 32–36, 159, 488, 489
 Rectangular slab laser 461–469
 Regenerative amplifiers 180–188
 Relaxation oscillations 128–132, 271–273, 567
 Resonant reflector 264
 Resonator, transverse modes
 configurations 217–222
 hardware 278–282
 losses 104, 105, 124, 125, 223–225, 228
 mode patterns 210–214
 misalignment sensitivity 235–238
 design software 254, 255
 stability diagram 222, 235, 243, 247
 internal lens 232–234, 248–250, 293
 Resonator, longitudinal modes
 mode structure 259–263
 linewidth reduction 263–271
 amplitude/frequency control 271–278
 wavelength selection 297–299
 Resonator, unstable; *see* Unstable resonator
 Ring laser 152–155
 Risley pair 253
 Ruby laser 51–54
 Safety; *see* Laser safety
 Samarium 50
 Sapphire, laser host 42
 Saturable absorber 522–529
 Saturation fluence/flux, definition 159, 172, 173, 188
 Second harmonic generation
 theory 590, 592–602
 phase matching 602–611
 intracavity 618–624
 crystal properties 611–618
 systems 629–633
 Self focusing 200–209
 Self mode locking; *see* Kerr lens mode locking
 Sellmeier equation 648
 SESAM 527, 528, 543, 556–560
 Semiconductor saturable absorber mirror;
 see SESAM
 Sensitizer, doping 49, 64, 75, 94, 95
 Servo loop; *see* Electronic feedback loop
 Side pumping 134–147, 366–406
 Signal distortions, amplifier 190–194
 Silicate, laser host 43
 Shot noise 272
 Slab laser 178, 179, 401–407, 458–469
 Slope efficiency, definition 120
 Small scale ripple growth 206, 207

- SOAP, laser host 43
 Soliton pulse shaping 579
 Spatial filter 171, 172, 208
 Spatial hole burning 265
 Spatial overlap 115, 116, 408–411
 Spectral characteristics, laser output 259–262
 Spherical resonator; *see* Concentric resonator
 Spike suppression 132, 133
 Spontaneous emission 15, 31
 Spot size, definition 215, 226
 Super Gaussian beam 192
 Stability diagram, resonator 222, 232, 235, 243, 247, 551
 Steady state amplification; *see* Amplifier, steady state
 Stefan-Boltzmann equation 13
 Stimulated Brillouin scattering 587, 590, 592, 669–679
 Stimulated emission, definition 16, 17, 24, 25; *see also* Cross section stimulated emission
 Stimulated Raman scattering 587, 590, 591, 662–669
 Stokes factor 115, 424
 Stokes lines 587, 664, 665
 Stress fracture limit 439, 459, 479–481
 Surface damage 681–684
 System efficiency 123, 151, 170, 171, 394
 Symbols, definition 711–715
- Telescopic resonator 248–250
 TEM_{mnq}, TEM_{plq} modes, definition 210–214
 Temporal distortions, amplifier 193, 194
 Thermal distortions, laser beam 193, 442–457 compensation 449–457
 Thermal line broadening 20
 Thermal effects, laser rod
 birefringence 445–449
 lensing 231–233, 442–445, 451–453
 photoelastic effect 440–442
 stress 437–440
 temperature distribution 426–437
 Thermal effects, slab laser 458–469
 Thermal effects, disk laser 469–473
 Thermal effects, end pumped laser 473–481
 Thermal lensing compensation 293, 294, 451, 452
 Thermal shock parameter 440, 480, 481
 Third harmonic generation 625–629
 Three level laser 27–29, 126, 127
- Threshold condition; *see* Oscillator threshold condition
 Threshold input 120
 Thulium 49, 50
 Ti:sapphire laser 83, 88–91, 575, 580–582
 Titanium 50
 Tm:YAG laser 94–97
 Tm:YLF laser 97
 Transform limited pulse 539–541
 Transition metals 50
 Transverse modes 210–254
 Travelling wave oscillator; *see* Ring laser
 Trigger circuit, flashlamp 331–334
 Tunable lasers 79–97
 Tungstate, laser host 44
 Tungsten filament lamp 300, 301
- Uniaxial crystal 603–608
 Unstable resonator 271, 282–296
 alignment sensitivity 295, 296
 negative branch 287–289
 positive branch 284–287
 Upper state efficiency 112, 115
- Vanadate, laser host 44
 Variable reflectivity mirror 270, 287, 289–292
 Vibronic lasers; *see* Tunable lasers
- Waist, Gaussian beam 215
 Wavefront distortion 190–193, 200–209, 442–449, 669–671
 Wavelength control; *see* frequency control
 Wavelength selection 297–299
 Whisper modes 199
 Wien's displacement law 13
 Whole beam self focusing 201–203
- Xenon arc lamp; *see* Flashlamps
- YAG laser host 42; *see also* Nd:YAG, Er:YAG, Yb:YAG lasers
 YAP, YALO, laser host 42
 Yb:YAG laser 97–101, 180, 421, 422, 424, 472, 583
 Yb:KGW laser 583
 YLF, laser host 45
 Ytterbium 49
- Zig-zag slab laser 402, 404, 461, 462
 ZnGeP₂ nonlinear crystal 651

Springer Series in OPTICAL SCIENCES

Volume 1

1 Solid-State Laser Engineering

By W. Koechner, 6th revised and updated ed. 2006, 447 figs., 45 tabs., XVI, 748 pages

Published titles since volume 80

85 Sensing with Terahertz Radiation

By D. Mittleman (Ed.), 2003, 207 figs., 14 tabs., XVI, 337 pages

86 Progress in Nano-Electro-Optics I

Basics and Theory of Near-Field Optics

By M. Ohtsu (Ed.), 2003, 118 figs., XIV, 161 pages

87 Optical Imaging and Microscopy

Techniques and Advanced Systems

By P. Török, F.-J. Kao (Eds.), 2003, 260 figs., XVII, 395 pages

88 Optical Interference Coatings

By N. Kaiser, H.K. Pulker (Eds.), 2003, 203 figs., 50 tabs., XVI, 504 pages

89 Progress in Nano-Electro-Optics II

Novel Devices and Atom Manipulation

By M. Ohtsu (Ed.), 2003, 115 figs., XIII, 188 pages

90/1 Raman Amplifiers for Telecommunications 1

Physical Principles

By M.N. Islam (Ed.), 2004, 488 figs., XXVIII, 328 pages

90/2 Raman Amplifiers for Telecommunications 2

Sub-Systems and Systems

By M.N. Islam (Ed.), 2004, 278 figs., XXVIII, 420 pages

91 Optical Super Resolution

By Z. Zalevsky, D. Mendlovic, 2004, 164 figs., XVIII, 232 pages

92 UV-Visible Reflection Spectroscopy of Liquids

By J.A. Räty, K.-E. Peiponen, T. Asakura, 2004, 131 figs., XII, 219 pages

93 Fundamentals of Semiconductor Lasers

By T. Numai, 2004, 166 figs., XII, 264 pages

94 Photonic Crystals

Physics, Fabrication and Applications

By K. Inoue, K. Ohtaka (Eds.), 2004, 209 figs., XV, 320 pages

95 Ultrafast Optics IV

Selected Contributions to the 4th International Conference on Ultrafast Optics, Vienna, Austria

By F. Krausz, G. Korn, P. Corkum, I.A. Walmsley (Eds.), 2004, 281 figs., XIV, 506 pages

96 Progress in Nano-Electro Optics III

Industrial Applications and Dynamics of the Nano-Optical System

By M. Ohtsu (Ed.), 2004, 186 figs., 8 tabs., XIV, 224 pages

97 Microoptics

From Technology to Applications

By J. Jahns, K.-H. Brenner, 2004, 303 figs., XI, 335 pages

- 98 **X-Ray Optics**
High-Energy-Resolution Applications
By Y. Shvyd'ko, 2004, 181 figs., XIV, 404 pages
- 99 **Mono-Cycle Photonics and Optical Scanning Tunneling Microscopy**
Route to Femtosecond Ångstrom Technology
By M. Yamashita, H. Shigekawa, R. Morita (Eds.) 2005, 241 figs., XX, 393 pages
- 100 **Quantum Interference and Coherence**
Theory and Experiments
By Z. Ficek and S. Swain, 2005, 178 figs., XV, 418 pages
- 101 **Polarization Optics in Telecommunications**
By J. Damask, 2005, 110 figs., XVI, 528 pages
- 102 **Lidar**
Range-Resolved Optical Remote Sensing of the Atmosphere
By C. Weitkamp (Ed.), 161 figs., XX, 416 pages
- 103 **Optical Fiber Fusion Splicing**
By A.D. Yablon, 2005, 137 figs., XIII, 306 pages
- 104 **Optoelectronics of Molecules and Polymers**
By A. Moliton, 2005, 229 figs., XXXI, 498 pages
- 105 **Solid-State Random Lasers**
By M. Noginov, 2005, 131 figs., XII, 238 pages
- 106 **Coherent Sources of XUV Radiation**
Soft X-Ray Lasers and High-Order Harmonic Generation
By P. Jaeglé, 2005, 150 figs., approx. 264 pages
- 107 **Optical Frequency-Modulated Continuous-Wave (FMCW) Interferometry**
By J. Zheng, 2005, 137 figs., XVIII, 254 pages
- 108 **Laser Resonators and Beam Propagation**
Fundamentals, Advanced Concepts and Applications
By N. Hodgson and H. Weber, 2005, 587 figs., XXV, 794 pages
- 109 **Progress in Nano-Electro Optics IV**
Characterization of Nano-Optical Materials and Optical Near-Field Interactions
By M. Ohtsu (Ed.), 2005, 123 figs., XIV, 206 pages
- 110 **Kramers-Kronig Relations in Optical Materials Research**
By V. Lucarini, J.J. Saarinen, K.-E. Peiponen, E.M. Vartiainen, 2005, 37 figs., X, 162 pages
- 111 **Semiconductor Lasers**
Stability, Instability and Chaos
By J. Ohtsubo, 2005, 169 figs., XII, 438 pages
- 112 **Photovoltaic Solar Energy Generation**
By A. Goetzberger and V.U. Hoffmann, 2005, 139 figs., XII, 234 pages
- 113 **Photorefractive Materials and Their Applications 1**
Basic Effects
By P. Günter and J.P. Huignard, 2005, 169 figs., approx. XII, 300 pages
- 114 **Photorefractive Materials and Their Applications 2**
Materials
By P. Günter and J.P. Huignard, 2005, 100 figs., approx. XII, 300 pages

- 115 **Photorefractive Materials and Their Applications 3**
Applications
By P. Günter and J.P. Huignard, 2005, 100 figs., approx. XII, 300 pages
- 116 **Spatial Filtering Velocimetry**
Fundamentals and Applications
By Y. Aizu and T. Asakura, 2006, 112 figs., approx. XII, 220 pages
- 117 **Progress in Nano-Electro-Optics V**
Nanophotonic Fabrications, Devices, Systems, and Their Theoretical Bases
By Motoichi Ohtsu, 2006, 122 figs., 3 tables, approx. 193 pages
- 118 **Mid-infrared Semiconductor Optoelectronics**
By A. Krier, 2006, 443 figs., approx. 776 pages
- 119 **Optical Interconnects**
The Silicon Approach
By L. Pavesi and G. Guillot, 2006, 265 figs., approx. 410 pages
- 120 **Relativistic Nonlinear Electrodynamics**
Interaction of Charged Particles with Strong and Super Strong Laser Fields
By H.K. Avetissian, 2006, 23 figs., XIV, 338 pages